Transactions of the ASME®

Technical Editor, LEWIS T. WHEELER (1997)

Department of Mechanical Engineering,
University of Houston,
Houston, TX 77204-4792

APPLIED MECHANICS DIVISION

Chairman, L. B. FREUND
Secretary, C. T. HERAKOVICH
Associate Technical Editors,
R. ABEYARATNE (1994)
T. R. AKYLAS (1994)
D. M. BARNETT (1996)
S. A. BERGER (1994)
I. M. DANIEL (1996)
G. J. DVORAK (1995)
E. J. HAUG, JR. (1996)
D. J. INMAN (1995)
S. LICHTER (1995)
W. K. LIU (1996)
X. MARKENSCOFF (1994)
D. M. PARKS (1995)
J. N. REDDY (1995)
J. W. RUDNICKI (1994)
W. N. SHARPE, JR. (1996)
C. F. SHIH (1995)
P. D. SPANOS (1994)
M. TAYA (1996)
F. Y. M. WAN (1994)

BOARD ON COMMUNICATIONS

Chairman and Vice-President
R. D. ROCKE

Members-at-Large
T. BARLOW, T. DEAR, L. M. KEER, J. KITTO,
W. MORGAN, E. M. PATTON, S. PATULSKI,
R. E. REDER, R. SHAH, A. VAN DER SLUYS,
F. M. WHITE, J. WHITEHEAD

OFFICERS OF THE ASME
President, J. H. FERNANDES
Exec. Director
D. L. BELDEN
Treasurer
R. A. BENNETT

PUBLISHING STAFF
Mng. Dir., Publ.,
CHARLES W. BEARDSLEY
Managing Editor,
CORNELIA MONAHAN
Production Editor,
JUDITH SIERANT
Production Assistant,
MARISOL ANDINO

Transactions of the ASME, Journal of Applied Mechanics (ISSN 0021-8936) is published quarterly (Mar., June, Sept., Dec.) for $165.00 per year by The American Society of Mechanical Engineers, 345 East 47th Street, New York, NY 10017. Second class postage paid at New York, NY and additional mailing office. POSTMASTER: Send address changes to Transactions of the ASME, Journal of Applied Mechanics, c/o THE AMERICAN SOCIETY OF MECHANICAL ENGINEERS, 22 Law Drive, Box 2300, Fairfield, NJ 07007-2300.

CHANGES OF ADDRESS must be received at Society headquarters seven weeks before they are to be effective. Please send old label and new address.

PRICES: To members, $40.00, annually: to nonmembers, $165.00.
Add $24.00 for postage to countries outside the United States and Canada.

STATEMENT from By-Laws. The Society shall not be responsible for statements or opinions advanced in papers or . . . printed in its publications (B7.1, Par. 3).

COPYRIGHT © 1993 by The American Society of Mechanical Engineers. Authorization to photocopy material for internal or personal use under circumstances not falling within the fair use provisions of the Copyright Act is granted by ASME to libraries and other users registered with the Copyright Clearance Center (CCC) Transactional Reporting Service provided that the base fee of $3.00 per article is paid directly to CCC, 27 Congress St., Salem, MA 01970. Request for special permission or bulk copying should be addressed to Reprints/Permission Department.

INDEXED by Applied Mechanics Reviews and Engineering Information, Inc. Canadian Goods & Services Tax Registration #126148048

Journal of Applied Mechanics

Published Quarterly by The American Society of Mechanical Engineers

VOLUME 60 • NUMBER 4 • DECEMBER 1993

TECHNICAL PAPERS

793 Crack Propagation in a Nonlinearly Viscoelastic Solid With Relevance to Adhesive Bond Failure
W. G. Knauss and G. U. Losi

802 Viscoelastic Microbuckling of Fiber Composites (93-WA/APM-16)
W. S. Slaughter and N. A. Fleck

807 Effect of Initial Void Shape on the Occurrence of Cavitation Instabilities in Elastic-Plastic Solids
V. Tvergaard and J. W. Hutchinson

813 Cyclic Viscoplastic Constitutive Equations, Part I: A Thermodynamically Consistent Formulation
J.-L. Chaboche

822 Cyclic Viscoplastic Constitutive Equations, Part II: Stored Energy—Comparison Between Models and Experiments
J.-L. Chaboche

829 Elastic-Plastic Finite Element Analysis of Repeated Indentation of a Half-Space by a Rigid Sphere
E. R. Kral, K. Komvopoulos, and D. B. Bogy

842 Rudnicki and Rice's Analysis of Strain Location Revisited (93-WA/APM-18)
G. Perrin and J. B. Leblond

847 Fundamental Solutions for a Poroelastic Half-Space With Compressible Constituents (93-WA/APM-13)
R. K. N. D. Rajapakse and T. Senjuntichai

857 Rayleigh-Type Wave Propagation on a Micropolar Cylindrical Surface
K. Mrithyumjaya Rao and M. Pratap Reddy

866 Dynamic Holographic-Electronic Speckle-Pattern Interferometry (93-WA/APM-17)
M. A. Ahmadshahi, S. Krishnaswamy, and S. Nemat-Nasser

875 An Experimental-Numerical Method for Nonlinear Structural Mechanics
F. J. M. Starmans, W. A. M. Brekelmans, and J. D. Janssen

883 Influence of Porosity on Plane Strain Tensile Crack-Tip Stress Fields in Elastic-Plastic Materials: Part II
Y. Miao and W. J. Drugan

890 Tunneling Cracks in Constrained Layers
S. Ho and Z. Suo

895 Local Delamination Growth in Layered Systems Under Compressive Load
E. Madenci and R. A. Westmann

903 The Initial Post-buckling and Growth Behavior of Internal Delaminations in Composite Plates (93-WA/APM-9)
G. A. Kardomateas

911 Reflection and Transmission by a Periodic Array of Coplanar Cracks: Normal and Oblique Incidence (93-WA/APM-10)
Y. Mikata

920 Interactions Among General Systems of Cracks and Anticracks: An Integral Equation Approach
K. X. Hu and A. Chandra

929 On the Mode Splitting of Degenerate Mechanical Systems Containing Cracks (93-WA/APM-5)
I. Y. Shen and C. D. Mote, Jr.

936 Near-Tip Fields in a Notched Body With Dislocations and Body Forces (93-WA/APM-15)
K.-C. Wu and F.-T. Chang

942 The Mechanism of Nip-Induced Tension in Wound Rolls
J. K. Good and Z. Wu

948 Active Stiffness Control of Cable Vibration
Y. Fujino, P. Warnitchai, and B. M. Pacheco

954 Conservation Laws in Systems With Variable Mass (93-WA/APM-14)
L. Cveticanin

959 Instability of Loaded Fractal Trees
J. B. Gómez, A. F. Pacheco, and A. J. Segui-Santonja

962 A Conservation Theorem for Constrained Multibody Systems (93-WA/APM-2)
J. T. Wang

970 Analytic Solutions for a Spinning Rigid Body Subject to Time-Varying Body-Fixed Torques, Part I: Constant Axial Torque
J. M. Longuski and P. Tsiotras

976 Analytic Solutions for a Spinning Rigid Body Subject to Time-Varying Body-Fixed Torques, Part II: Time-Varying Axial Torque
P. Tsiotras and J. M. Longuski

982 The Incremental Variational Principles for Frictional Contact Problems of Linear Elasticity
G. Zboinski

986 The Effect of Fiber Poisson Expansion in Micro-Indentation Tests
G. Meda, S. F. Hoysan, and P. S. Steif

(Contents continued on Inside Back Cover)

Downloaded 04 May 2010 to 171.66.16.49. Redistribution subject to ASME license or copyright; see http://www.asme.org/terms/Terms_Use.cfm

CONTENTS (CONTINUED)

992 **Stress and Notch-Stress Concentration Induced by Slight Depressions and Protrusions** (93-WA/APM-4)
C. H. Wu

998 **Free Vibration Analysis of Rectangular Plates With Nonuniform Lateral Elastic Edge Support** (93-WA/APM-6)
D. J. Gorman

1004 **Transfer Function Formulation of Constrained Distributed Parameter Systems, Part I: Theory** (93-WA/APM-11)
C. A. Tan and C. H. Chung

1012 **Transfer Function Formulation of Constrained Distributed Parameter Systems, Part II: Applications** (93-WA/APM-12)
C. H. Chung and C. A. Tan

1020 **Dualities in Free Vibration of Minimum Surface Membranes** (93-WA/APM-3)
B. Taborrok and L. Tong

1027 **Modeling of One-Dimensional Thermomechanical Erosion of High-Temperature Ablatives** (93-WA/APM-1)
B. C. Yang, F.-B. Cheung, and J. H. Koo

1033 **Localized Elasticae for the Strut on the Linear Foundation**
C. W. Hunt, M. K. Wadee, and N. Shiacolas

1039 **Asymmetric Indentation of a Finite Elastically Supported Beam** (93-WA/APM-7)
J. A. Peck and W. P. Schonberg

BRIEF NOTES

The Dynamic Energy Release Rate of Delaminations Based on Midlin-Type Nonlinear Theory 1046
A. E. Giannakopoulos and K.-F. Nilsson

Eshelby Tensor for an Elastic Inclusion With Slightly Weakened Interface 1048
J. Qu

End Shortening Relation and Stability of Columns on Nonlinear Foundation 1050
M. O. Oyesanya

1052 Multilayer Material With an Interface Crack
P. Gu

1054 Stresses in Narrow Regions
J. B. Keller

1056 On Neutral Holes in Tailored, Layered Sheets
B. Budiansky, J. W. Hutchinson, and A. G. Evans

1058 The Coefficient of Restitution for a Planar Two-Body Eccentric Impact
G. G. Adams and D. N. Tran

DISCUSSIONS

1061 **Complex Modes and Solvability of Nonclassical Linear Systems, by T. K. Caughey and F. Ma—Authors' Closure**

1061 **Singular Plastic Fields in Steady Penetration of a Rigid Cone, by D. Durban and N. A. Fleck—Discussion by H. S. Yu**

BOOK REVIEW

1063 ***Stress Intensity Factors Handbook, Vol. 3*, edited by Y. Murakami . . .** Reviewed by **L. M. Keer**

ANNOUNCEMENTS AND SPECIAL NOTES

1011 Europe-U.S. Workshop on Fracture of Quasibrittle Materials—Announcement

1003 Change of Address Form

1045 Symposium on Material Instabilities—Call for Papers

969 IUTAM Symposium—Announcement

1064 Books Received by the Office of the Technical Editor

1065 Worldwide Mechanics Meetings List

1067 1993 Author Index

1070 Information for Authors

Downloaded 04 May 2010 to 171.66.16.49. Redistribution subject to ASME license or copyright; see http://www.asme.org/terms/Terms_Use.cfm

Crack Propagation in a Nonlinearly Viscoelastic Solid With Relevance to Adhesive Bond Failure

W. G. Knauss
Mem. ASME.

G. U. Losi

Graduate Aeronautical Laboratories,
California Institute of Technology,
1201 E. California Boulevard
Pasadena, CA 91125

The problem of crack propagation through a material possessing nonlinearly viscoelastic material response is considered, including the influence of stress-induced free-volume changes on the rheology, as well as the formation of voids as material failure is approached. This particular material response is confined to a thin layer along the crack propagation axis, while the bulk of the material behaves in a linearly viscoelastic manner, thus simulating the situation arising in the growth of a crazeled crack, or the failure of a bonded joint with a thin adhesive layer strained uniformly across its thickness. The nonlinear material behavior thus governs simultaneously the stress and strain distribution at the crack tip as well as the crack speed solely in dependence on the applied load (stress intensity factor). Only quasi-static motion is considered, the velocities being understood to be "reduced" by temperature according to a time-temperature superposition principle. Comparisons with a model based on linearly viscoelastic considerations and rate-insensitive properties of the damaged material are presented.

1 Introduction

It is well known that polymers exhibit rate and time-dependent behavior which, as a function of temperature, can range over many decades of time. This fact is important because the projected use of polymers in engineering designs that are to last in service several decades of years requires an understanding and prediction of the long-term failure behavior. The controlling feature to understand is thus the rate of crack propagation as a function of the loads applied to the structure; for, if the crack propagation history can be determined then the time of failure can also be established.

Time-dependent crack propagation in polymers is influenced strongly by the physical properties of the solid, such as the relaxation or creep behavior, and by the history of the applied loading. Present day knowledge of this dependence derives principally from our understanding of polymer failure in terms of rate-dependent crack propagation when linear viscoelasticity is involved, but space limitations do not allow here a full review and discussion of these contributions; suffice it to say that Dugdale (1960), Barenblatt (1962), Williams (1963), Dietmann and Knauss (1970), Kostrov and Nikitin (1970), Mueller and Knauss (1971, 1975), Knauss (1974, 1976), and Schapery (1975) summarize the field. Common to the models discussed in these references is the neglect of any nonlinear kinematics and of the nonlinear material behavior of the failing material at the crack tip. Mostly based on a Dugdale/Barenblatt related crack-tip configuration, they allow for rate-dependent cohesive forces offered by the failing material with an attendant determination of the size of the cohesive zone, but none include the effect of the (nonlinear) "constitutive response" of the failing material. Although the details of the spatial distribution of the relevant cohesive forces appears to be of secondary importance, their magnitude as a function of the rate of crack propagation is significant (Knauss, 1974). In models referenced above, this cohesive force behavior needs to be prescribed as a separate function of material response with the help of which the rate of crack propagation can then be computed; in comparing experiments on an elastomeric material with theory it has been found that cohesive forces independent of crack speed provided the best agreement in that case (Knauss, 1974).

Instead of prescribing these cohesive forces as a separate material function[1] it would seem fundamentally preferable to compute their rate-dependent evolution from the constitutive behavior for the disintegrating material so that their development is coupled mutually to the (visco)elastic response of the surrounding bulk material. With this idea in mind we examine in this paper the effect of nonlinear material behavior on the growth of a crack when the nonlinear material response is confined to a narrow strip along the crack path. The determination of the crack speed under far-field loading is thus governed only through the complete description of the non-

Contributed by the Applied Mechanics Division of THE AMERICAN SOCIETY OF MECHANICAL ENGINEERS for publication in the ASME JOURNAL OF APPLIED MECHANICS.

Discussion on this paper should be addressed to the Technical Editor, Professor Lewis T. Wheeler, Department of Mechanical Engineering, University of Houston, Houston, TX 77204-4792, and will be accepted until four months after final publication of the paper itself in the ASME JOURNAL OF APPLIED MECHANICS.

Manuscript received by the ASME Applied Mechanics Division, Feb. 13, 1992; final revision, Oct. 26, 1992. Associate Technical Editor: W. N. Sharpe.

[1] This would be tantamount to consider this prescribed function as the basic, rate-dependent material behavior which controls crack propagation.

Copyright © 1993 by ASME
Downloaded 03 May 2010 to 171.66.16.245. Redistribution subject to ASME license or copyright; see http://www.asme.org/terms/Terms_Use.cfm

linear constitutive behavior (from zero strain to failure at a bounded strain) and no additional failure criterion, as used traditionally in fracture mechanics, is explicitly invoked. All computations are subject to small strain limitations.

The motivation for this work derived originally from the failure analysis of adhesive bonds, which involve primarily elastic adherends joined by a polymeric adhesive layer such that the nonlinear material behavior spans the layer thickness between the adherends (fully developed "plastic" zones). On the other hand, if the adherends are considered viscoelastic, this development addresses also the failure of adhesively bonded polymers; moreover, if in the limit of small strains, the properties of the viscoelastic adherends possess the (linearly) viscoelastic behavior of the cohesive zone material before it disintegrated, one would be dealing with crack propagation through a solid accompanied by a craze-like fracture. We consider here the latter problem. The present problem constitutes, therefore, also a generalization of the rate-independent formulations of the craze problem considered by Ungsuwarungsri and Knauss (1988). It turns out that the method produces results which contain the uniform failure of viscoelastic or elastic adhesive bonds. Some comments in this regard are offered in the later discussions.

In the sequel we delineate first the nature of the constitutive behavior employed and move then in Section 3 to the presentation of the analytical model. In Section 4 we analyze the numerical solution procedure and discuss the results in Section 5.

2 Nonlinear Material Description

From a materials point of view, the rupture of polymers is accompanied by two physical processes: As the strain increases, the response of the material deviates increasingly from linear behavior in its rate sensitivity, possibly developing strain softening; at sufficiently high strains, material damage accumulates in the form of small voids, which grow and coalesce to cause material disintegration. We shall incorporate both effects into the constitutive response of the material in the crack strip, albeit yet in an approximate manner. The nonlinearly viscoelastic behavior of the undamaged material follows the laws established by Emri and Knauss (1981, 1987), and Losi and Knauss (1992), while the process of void development and coalescence will be considered through inclusion of experimental results developed from the work of Knauss and Parvin (1990).

The Nonlinearly Viscoelastic Continuum. We start with the observation that dilatation of a polymer changes the time scale of the relaxation behavior by allowing changes in free volume to accommodate viscoelastic rearrangement of the polymer chains at different rates. Following Emri and Knauss (1981, 1987), the nonlinearly viscoelastic portion of the constitutive behavior relates the stress components τ_{ij} and small strains ϵ_{ij} in terms of deviator stresses S_{ij} and strains e_{ij}

$$S_{ij}=2\int_{-\infty}^{t}\mu(\zeta-\zeta')\frac{\partial e_{ij}(t')}{\partial t'}\,dt' \tag{1a}$$

$$\tau_{kk}=3\int_{-\infty}^{t}k(\zeta-\zeta')\frac{\partial \epsilon_{kk}(t')}{\partial t'}\,dt' \tag{1b}$$

$$\zeta=\zeta(t)=\int_{0}^{t}\frac{\mathrm{du}}{\Phi[\mathrm{T(u)},\epsilon_{kk}(u)]},\quad \zeta'=\zeta(t') \tag{1c}$$

where, $\mu(t)$ and $k(t)$ are, respectively, the shear and bulk relaxation moduli under small deformations for the isotropic material and Φ is a shift factor which controls the relaxation time spectrum according to the Doolittle Eq. (2*a*)

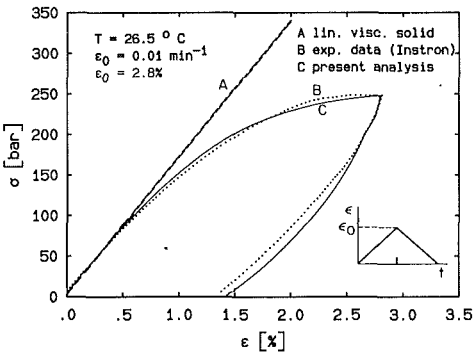


Fig. 1 Example of nonlinearly viscoelastic response modeled by Eqs. (1)-(4) (from Emri and Knauss (1987)).

$$\log_{10}\Phi=\frac{b}{2.303}\left[\frac{1}{f}-\frac{1}{f_0}\right] \tag{2a}$$

with

$$f=f_0+A\alpha(t)*dT+B\epsilon_{kk} \tag{2b}$$

denoting the fractional free volume (f_0 is a free volume reference value); the star notation implies convolution. A, B, and b are experimentally determined constants. For illustrative purposes, the thermal dilation

$$\alpha*dT=\int_{-\infty}^{t}\alpha(\zeta-\zeta')\frac{\partial T(x,t')}{dt'}\,dt' \tag{3}$$

has been included in terms of a convolution of the temperature with a time-dependent thermal volume expression characteristic $\alpha(t)$. The volume strain ϵ_{kk} is given by the inverse of (1*b*) as

$$\epsilon_{kk}=\frac{1}{3}M*d\tau_{kk}=\frac{1}{3}\int_{-\infty}^{t}M(\zeta-\zeta')\frac{\partial\tau_{kk}(x,t')}{\partial t'}\,dt' \tag{4}$$

with $M(t)$ representing the bulk creep compliance. As an example of the qualitative stress-strain behavior described by these equations we show in Fig. 1 the uniaxial response of polyvinylacetate (PVAc) resulting from the imposition of a constant rate of extension for the uniaxial modulus $E(t)$ and the bulk compliance $M(t)$ shown in Figs. 2 and 3.

Effect of void formation. In addition to this dilatation-induced strain softening (or dilatation-induced acceleration in creep or relaxation) there occurs damage-induced softening, occasioned by the appearance and growth of voids. Knauss and Parvin (1990) have studied the development of such damage at the tip of a crack and estimated the uniaxial stress-strain response of the damaged material when averaged over dimensions which are large compared to the void sizes. Figure 4 shows the stress-strain response reported in that reference, and reduced to a function Ψ representing the ratio of the stress σ to the strain, $\psi\equiv\sigma/\epsilon$, versus the uniaxial strain.

This function has been extrapolated to zero value at a maximum strain as shown by the solid line. However, the time or rate-dependent void response has not yet been studied, so that a more complete material response to failure as a function of deformation history is not yet available. Therefore, as a physically acceptable or even reasonable approximation we consider the nonlinearly viscoelastic model delineated in Eqs. (1) to (4), and account for the developing void damage through multiplication of the pertinent stress with the function Ψ of Fig. 4[2].

We deal thus with a nonlinearly viscoelastic constitutive

[2]It should be noted that this multiplication is incorporated at a state in the computations such that the related nonlinearity is reflected in the strain history of the failing material and in the latter's effect on the bulk polymer adjacent to the crack path.

Downloaded 03 May 2010 to 171.66.16.245. Redistribution subject to ASME license or copyright; see http://www.asme.org/terms/Terms_Use.cfm

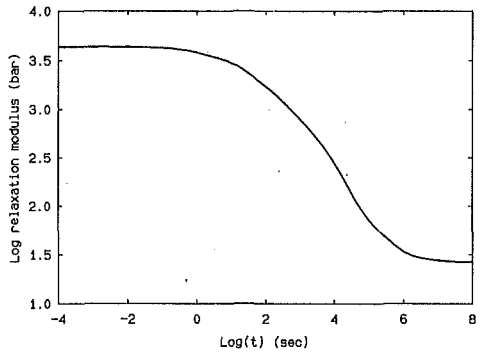


Fig. 2 Shear creep compliance of the model material

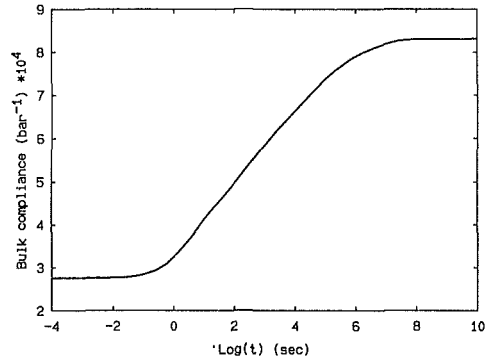


Fig. 3 Bulk creep compliance of the model material

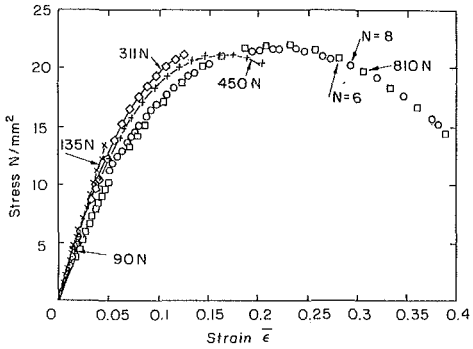


Fig. 4(*a*)

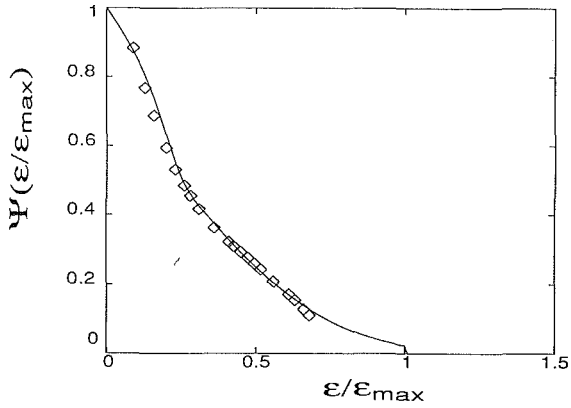


Fig. 4(*b*)

Fig. 4 Effect of void formation on global constitutive response (*a*) stress-strain behavior (from Knauss and Parvin (1990)); (*b*) the function Ψ

behavior which incorporates rate-dependent stress development in response to an arbitrary strain history, capped by a maximum strain (when the stress drops to zero as a result of strain softening). While this behavior is physically reasonable and acceptable, the actual material behavior may include also a rate-dependent maximum strain. The present model does not allow for this additional rate sensitive behavior, but retains the development of failure as a material description (attainment of zero stress at the crack tip) while also maintaining the development of rate-dependent stress levels in the failure zone[3]. It should be remembered here that experimental results agreed well with the linearly viscoelastic theory on the basis of an ultimate crack-tip strain as a failure criterions (Knauss, 1974). The nonlinear problem formulation delineated here is thus in keeping with this important linear limit behavior.

3 The Crack Propagation Model

We consider a small region containing the crack tip as shown in Fig. 5 and deforming under symmetric loading with respect to the crack axis. Two zones of material behavior are presumed to govern the time-dependent growth: A linearly viscoelastic bulk domain and a narrow line zone representing unstable and nonlinearly viscoelastic response of the material. While the model assumes ultimately a nonlinear zone of zero thickness ($h \to 0$) we show it in Fig. 5 to be finite in order to motivate a measure of strain across the strip.

In dealing with crack propagation in terms of a layer of nonlinearly responding material, one has essentially two options for a mathematical representation: One may cast the problem in terms of a mixed boundary value problem on a viscoelastic half-space with tractions to be determined in conformity with response of the nonlinear layer under some far-

[3]The development of a more realistic constitutive description allowing for rate-dependent formation and growth of voids poses a problem a great complexity and is clearly beyond the scope of the present investigation.

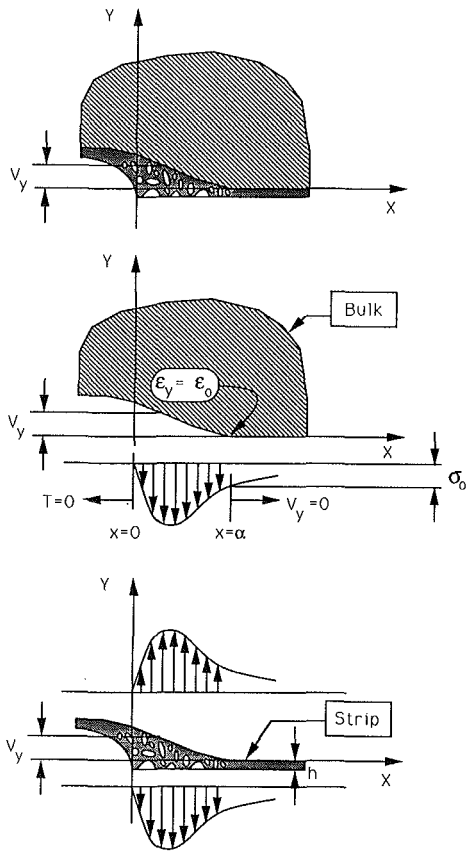


Fig. 5 Definition of crack-tip parameters

Downloaded 03 May 2010 to 171.66.16.245. Redistribution subject to ASME license or copyright; see http://www.asme.org/terms/Terms_Use.cfm

field loading with the assurance of bounded stresses in the crack-tip region (Anderson and Bergkvist, 1970). This description of crack behavior does not involve the stress intensity factor directly; the latter would have to be defined through the sum of tractions at the modeled "crack tip" once the solution to the boundary value problem has been established. The domain of integration could be defined along the crack axis on the range between the points where the normal traction drops to zero (the crack tip proper) and a location ahead of this point where the stress or the strain reach a predetermined value under a negative stress gradient. However, inasmuch as the material exhibits time-dependent behavior, the response of the strip material would affect its deformation and stress history and thus the definition of the size of the zone from which the stress intensity factor is determined; thus the stress intensity factor would become a function of the past history, if one were to insist on relating the model results to this fracture parameter.

Alternately, one may formulate the problem as one for a crack in terms of a stress intensity factor representing far-field loading. The crack-tip geometry and the history of material deformation or loading prior to entering the crack region must then be defined a priori as part of the geometry. Similarly, the initial conditions on the material entering the cohesive zone must be determined in conformity with the perceived previous load history. In terms of the crack model it appears easier in the context of the approximation to assign zero initial conditions to the material sufficiently far ahead of the cohesive zone (in the far past). It is primarily for this reason that we choose the latter model instead of the infinite half-space analog for this study.

The bulk domain. This domain obeys linearly viscoelastic behavior and occupies in the undeformed condition the space $y>0$; on $y=0$, $0<x<a$, it is bounded by a cohesive zone of thickness h which is small ($\rightarrow$zero) compared to any other dimension of the problem. To its left ($x<0$), zero tractions are specified, and zero y-displacement to its right ($x>\alpha$). At $x=a$ the strain, ϵ_{yy}, as determined from the solution for the bulk domain, attains a small preset value ϵ_0[4]. Over the length of the cohesive zone only normal tractions $T_y(x)$ act which are not known a priori, but which follow from the properties and deformation history of the adjacent strip in dependence on the crack speed.

We make use of the nonsingular solution for a trapezoidal traction distribution for $T(x)$ moving along a linearly viscoelastic domain (Knauss, 1974)[5], to construct the (as yet unknown) traction distribution T through superposition/addition; for such a piecewise linear distribution, the corresponding normal displacement $u_y(x-\dot{c}t, 0)$ is then also obtained through superposition of the results in Knauss (1974).

The displacement for a trapezoidal traction distribution (cf. Fig. 6) is given in terms of a complex potential ϕ as

$$v(x,0)=\frac{\kappa+1}{2}\,\mathrm{Im}\left[\int_0^x J(t-\xi)\left(\frac{\partial\phi(\zeta)}{\partial\xi}\right)d\xi\right] \tag{5}$$

where t is the time elapsed since the material particle at x has passed the point $x=\alpha$, $z=x-\dot{c}t+iy$ and Im denotes the imaginary part of the expression. Also in keeping with the assumption of a constant Poisson's ratio for the bulk material one has

$$\kappa=3-4\nu \text{ for plane strain}$$

$$=\frac{3-\nu}{1+\nu} \text{ for generalized plane stress.}$$

[4]This value sets the strain level on the crack axis at which nonlinear material description takes over.

[5]The referenced work deals with a constant Poisson's ratio, a simplification we retain in this work.

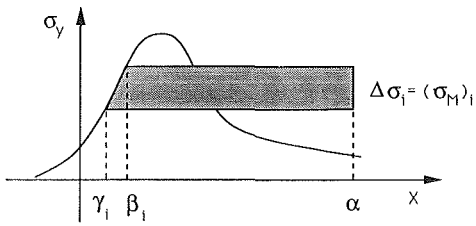


Fig. 6 Trapezoidal load distribution in the cohesive zone used for generating an arbitrary traction distribution

The stress function $\phi(z)$ has two additive components, $\phi_f(z)$ and $\phi_c(z)$ where

$$\phi_f(z)=\frac{K}{\sqrt{2\pi}}\sqrt{z-\alpha} \tag{6}$$

corresponds to far-field loading with a traction-free crack, and $\phi_c(z)$ corresponds to loading on the crack surfaces. For the case of trapezoidal loading illustrated in Fig. 6, along with the definitions of α, β, γ and the maximal stress σ_M, the imaginary part of the stress function ϕ_c is given in Knauss (1974) as

$$\mathrm{Im}(\phi_c(z))=\Bigg\{(-z^2+(\alpha+\beta)z=\alpha\beta)3\log\left(\frac{\sqrt{\alpha-z}+\sqrt{\alpha-\beta}}{\sqrt{\alpha-z}-\sqrt{\alpha-\beta}}\right)+(z^2-(\alpha+\gamma)z+\alpha\gamma)3\log\left(\frac{\sqrt{\alpha-z}+\sqrt{\alpha-\gamma}}{\sqrt{\alpha-z}-\sqrt{\alpha-\beta}}\right)-\sqrt{\alpha-z}[\sqrt{\alpha-\beta}(6z-4\beta-2\alpha)+\sqrt{\alpha-\gamma}(2\alpha-6z+4\gamma)]\Bigg\}\frac{\sigma_M}{\pi(\alpha-z)(6\beta-6\gamma)}$$

$$\text{for } z=x+iy, x<\alpha, y\rightarrow 0, \text{ and } \gamma<\alpha. \tag{7}$$

The finiteness condition

$$K=2\sqrt{2\pi}\lim_{z\rightarrow\alpha}\sqrt{z-\alpha}\,\phi_c'(z) \tag{8}$$

assures bounded stress in the crack-tip region. For the specification of the strain ϵ_0 which locates the beginning of the cohesive zone one needs to evaluate ϵ_{yy} on the boundary of the bulk phase as in

$$\epsilon_{yy}(0)=\epsilon_{yy}(\infty)+\frac{\kappa-1}{2}\,\mathrm{Re}\int_\infty^0 J(t-\tau)\,\frac{\partial\phi'(z(\tau))}{\partial\tau}\,d\tau \tag{9}$$

where

$$\mathrm{Re}(\phi'(z))=\Bigg\{3[z^2-(\alpha+\beta)z+\alpha\beta]\tan^{-1}\left(\frac{\sqrt{\alpha-\beta}}{\sqrt{z-\alpha}}\right)-\sqrt{(z-\alpha)(\alpha-\beta)}(3z-2\beta-\alpha)+[3z^2-3(\alpha+\gamma)z+3\alpha\gamma]\tan^{-1}\times\left(\frac{\sqrt{\alpha-\beta}}{\sqrt{z-\alpha}}\right)+\sqrt{(z-\alpha)(\alpha-\gamma)}(3z-2\gamma-\alpha)\Bigg\}\cdot\frac{\sigma_M}{3\pi(z-\alpha)(\beta-\gamma)}+\frac{K}{\sqrt{2\pi}\sqrt{z-\alpha}}\quad\text{for } z>0.$$

The displacement response under an arbitrary traction can then be constructed as the result of a summation of trapezoidal loadings as indicated in Fig. 6, where now the parameters β, γ, and σ_M need to be indexed for the summation. In effect, in Eqs. (5) to (9), the function ϕ is replaced by a summed indexed function. For example, Eq. (5) is replaced by

$$v(x,0,\dot{c})=\frac{\kappa+1}{2}\,\mathrm{Im}\left[\sum_i\int_0^x J(t-\zeta)\,\frac{\partial\phi_i(\zeta)}{\partial\zeta}\,d\zeta\right]. \tag{10}$$

It is clear that for any given degree of discretization of the cohesive zone, this approach is more accurate than the use of

Downloaded 03 May 2010 to 171.66.16.245. Redistribution subject to ASME license or copyright; see http://www.asme.org/terms/Terms_Use.cfm

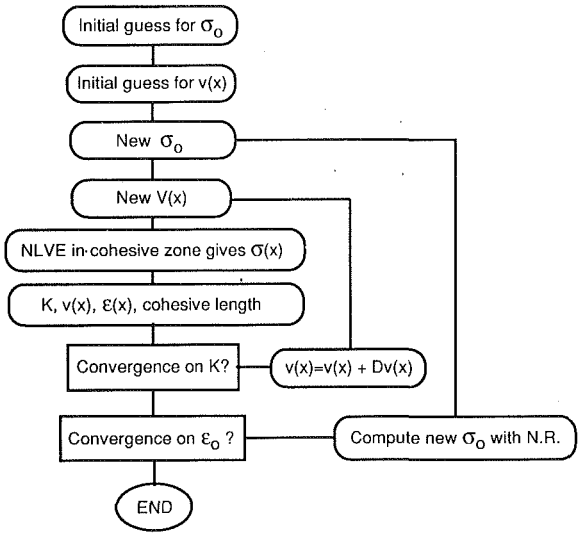


Fig. 7 Iteration scheme

a distribution of point forces to represent the cohesion of the failing material.

The Strip Domain. The tractions acting on the bulk domain within the cohesive zone result from the response of the strip. As strip material enters from the right into the cohesive zone at $x=\alpha$ it undergoes deformation normal to the direction of crack propagation; we allow only for purely uniaxial response characteristics of the strip material. The y-displacement $v(x-\dot{c}t,0)$ of the bulk domain boundary determines also the rate of straining as

$$\dot{\epsilon} = -\dot{c}\,\frac{\partial v}{\partial x}. \tag{11}$$

The strip material is taken to respond in a linearly viscoelastic manner until it enters the cohesive zone at $x=0$ at which moment it changes to the nonlinear behavior required by Eqs. (1*a–e*) and the voiding function Ψ. In keeping with the assumed uniaxial material response we employ the (uniaxial) constitutive response computed from the data in Figs. 2 and 3.[6] Accordingly, the average strain across the strip is given by

$$\bar{\epsilon}_y = \frac{v(x,o,\dot{c})}{h} \tag{12}$$

where the displacement $v(x,o,\dot{c})$ is found in (10).

The solution to the problem of the (steadily) propagating crack is now given by requiring that the tractions on the interface between the bulk domain and the strip as well as the displacements be matched. The solution is accomplished through Piccard iteration which is described, along with some additional observations on numerical procedures, in the following section.

4 Numerical Implementation

The convergence of the iterative scheme is not necessarily guaranteed a priori (Ungsuwarungsri and Knauss, 1987, 1988), because of the strongly nonlinear characteristics of the problem. One may be reasonably certain of approaching the correct solution if the computed parameters satisfy the test of physical/analytical reasonableness.

It was found convenient to start the iteration process by first choosing a speed of crack propagation $\dot{c}$, then estimating an initial value of the stress at the entrance to the cohesive zone (at $x=\alpha$) and prescribing an initial displacement function in the form appropriate to a single trapezoidal cohesive load for the bulk phase. This displacement function, applied to the deformation of the strip with nonlinear characteristics, would then generate a new traction distribution which can be represented by a sum of trapezoidal components, the discretization being accomplished along the x-axis, typically in 300 equal elements.[7] The new traction distribution generates a stress intensity factor according to (8) or its sum equivalent as well as a strain ϵ_0 in the bulk at $x=\alpha$.

Rather than describe the complete integration scheme in words, it is illustrated in Fig. 7. In practice, it turned out that a significant improvement in convergence was attained if in the iteration process the newly iterated traction distribution was not used to compute the next iteration of the boundary displacement, but instead, the old function plus a fraction of the difference between the old and the new one. This fraction was typically 20 percent, but when the traction distribution exhibited sharp peaks, this fraction needed to be reduced to as much as 5 percent.

5 Results and Discussion

Because the current model prescribes only the nonlinear constitutive behavior of the layer material and allows the model to freely determine fracture related parameters often prescribed a priori in linearized fracture models, it is of interest to examine several of these "parameters" and to draw comparisons between the linearized model(s) and the current results. Typical questions arise with regard to the rate-dependent distribution of the cohesive forces, limit behavior for "low" and "high" speeds, as well as the influence of the viscoelastic response of the bulk region. Also, observations are in order on the effect of concepts and parameters introduced for modeling purposes.

Time Scale and Stress Intensity Normalization. In order to discuss velocity effects we normalize the crack speed by a reference velocity defined as the ratio of the layer thickness "h" and an average relaxation time $\bar{\tau}$. The latter is defined in terms of the multiple relaxation time τ_i and the (discrete) spectral shear relaxation distribution μ_i as

$$\bar{\tau} \equiv \sum_{i=1}^{N} \mu_i \tau_i \Big/ \sum_{i-1}^{N} \mu_i. \tag{13}$$

All velocities are understood in units of this reference speed. It is also clear that the large values of "speeds" recorded here must be understood as "temperature-reduced" speeds rather than physical values which would clearly incur inertial considerations. The stress intensity factor is presented in units of the glassy modulus (4300 bar) and the square root of the layers thickness (0.7 mm).

Cohesive Force Distribution and Zone Size. In the following discussion it is convenient to consider variables as a function of the crack speed. In reality, the crack speed is, however, a consequence of the loading, i.e., the stress intensity. When we discuss parameters in terms of crack speed, it should therefore not be forgotten that this discussion should be interpreted in terms of dependence on the stress intensity factor.

Figures 8 and 9 present plots of the cohesive force distribution for two values of the strain ϵ_0 at the entrance to the cohesive zone. Inspection of these figures illustrates that the length of the cohesive zone changes nonmonotonically with crack speed, though this variation is more pronounced for the smaller value of the strain ϵ_0. This behavior is clearly at variance with the linearized theory based on energy principles and a rate-

[6] We note that the bulk behavior enters the problem explicitly only in the context of nonlinear material response in the cohesive zone, but not in the linearly viscoelastic portion of the problem because for that domain, the bulk and shear relaxation functions are assumed to possess the same time dependence. (See footnote 2.)

[7] Smaller numbers of elements could lead to unstable computations when high gradients of the cohesive tractions arose.

Downloaded 03 May 2010 to 171.66.16.245. Redistribution subject to ASME license or copyright; see http://www.asme.org/terms/Terms_Use.cfm

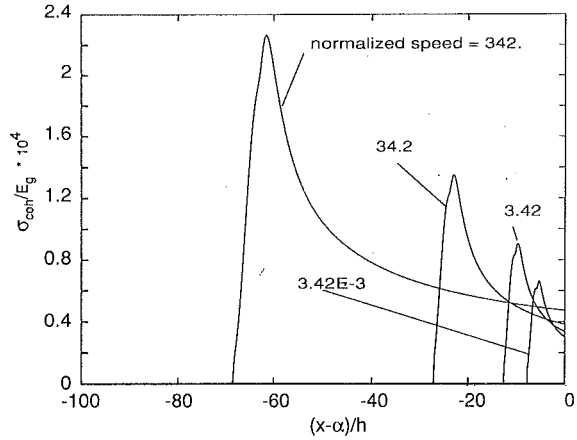


Fig. 8(*a*)

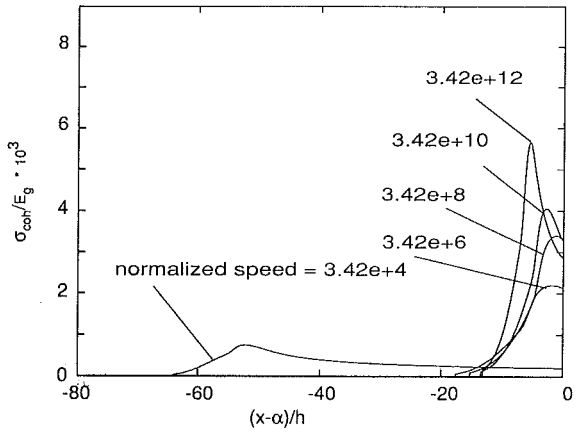


Fig. 8(*b*)

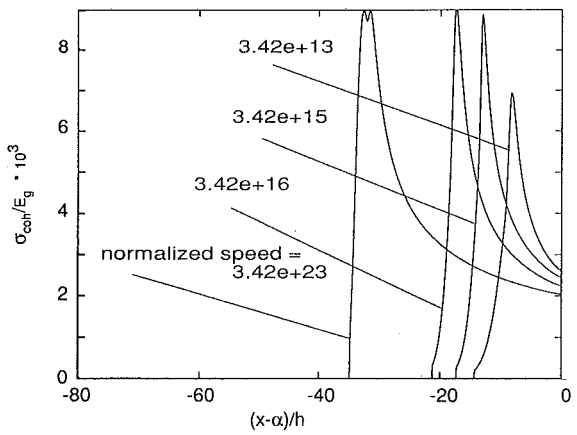


Fig. 8(*c*)

Fig. 8 Cohesive stress distribution for a range of crack speeds. Strain at entry to the nonlinear zone $\epsilon_0 = 0.3$ percent.

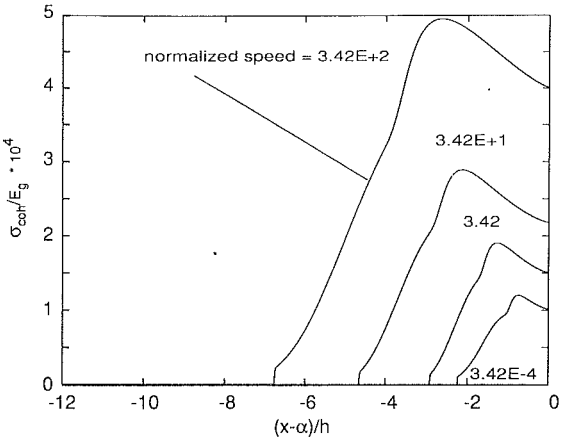


Fig. 9(*a*)

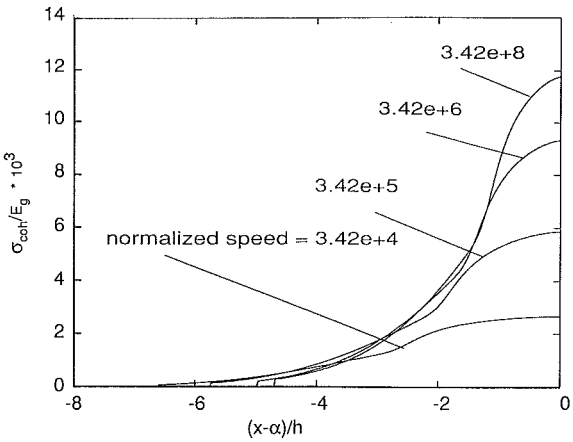


Fig. 9(*b*)

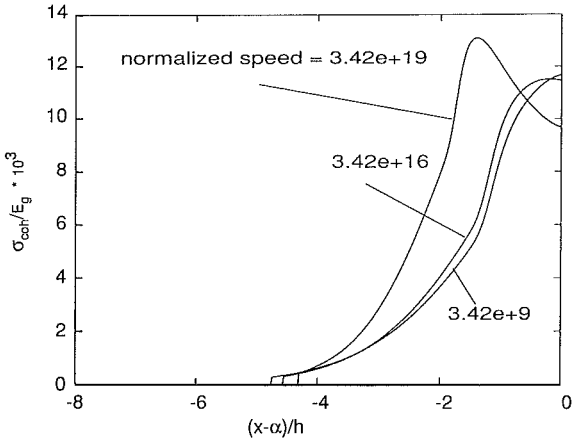


Fig. 9(*c*)

Fig. 9 Cohesive stress distribution for a range of crack speeds. Strain at entry to the nonlinear zone $\epsilon_0 = 1$ percent.

insensitive cohesive stress for which the nonlinear zone size increases monotonically with stress intensity (and thus with crack speed) (Mueller and Knauss, 1974).

It should be recognized that in this model the size of the cohesive zone is subject to the definition of where along the crack path the nonlinear material behavior becomes active. This determination is made through the choice of the strain ϵ_0: A small value for ϵ_0 places more of the crack axis into the cohesive zone than a larger value. This fact is quite clear from a comparison of Figs. 8 and 9.

The (initial) stress at the entry into the cohesive zone follows also a nonmonotonic dependence on the crack speed; however, with respect to the stress intensity factor the lack of monotonicity is not very pronounced as shown in Fig. 10. Here the initial stress is shown normalized by the product of the glassy modulus and the strain ϵ_0. This figure also indicates that for $\epsilon_0 = 0.3$ percent, the initial stress depends exponentially on the stress intensity factor for small values of the latter, while that seems not to be so clear for the larger value of ϵ_0. From Figs. 8 and 9 it is also clear that the maximum (peak) cohesive stress appears to increase monotonically with crack speed and thus with the stress intensity.

Downloaded 03 May 2010 to 171.66.16.245. Redistribution subject to ASME license or copyright; see http://www.asme.org/terms/Terms_Use.cfm

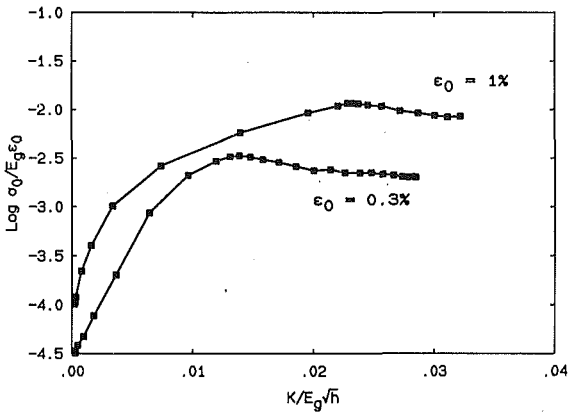


Fig. 10 The stress σ_y at entry to the cohesive zone as a function of the stress intensity factor

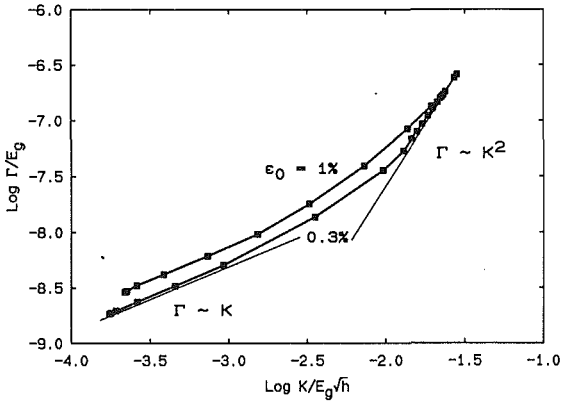


Fig. 12 Energy of fracture related to the stress intensity factor for the two choices of strain ϵ_0 at entry to the nonlinear zone

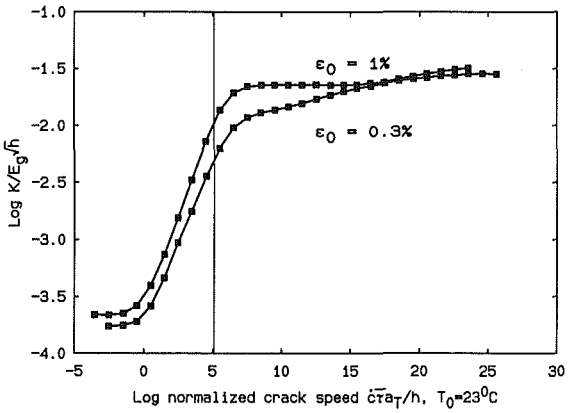


Fig. 11(*a*)

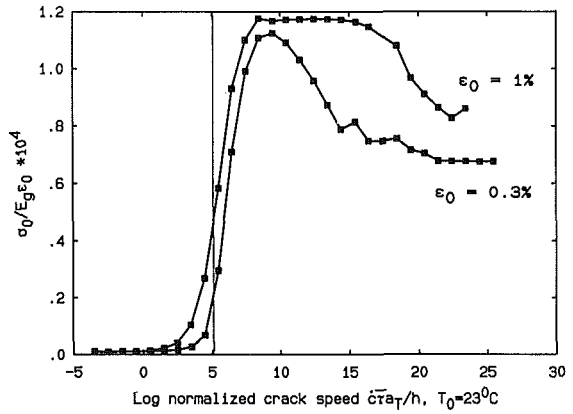


Fig. 11(*b*)

Fig. 11 Relation between the crack speed and (*a*) the stress intensity factor and (*b*) the σ_y stress at entry to the nonlinear zone

In plot (a) of Fig. 11 the relation between stress intensity factor and crack speed is summarized for the two initial strain conditions ϵ_0. This behavior is very similar for the two strains at the entry to the nonlinear zone, though details vary. Along with that data is also shown, in Fig. 11(*b*), the σ_y stress at the entry to nonlinear zone; the differences at the higher crack speeds are due to the differences in what is or is not included as part of the nonlinear zone through the prescription of the strain ϵ_0 (see earlier discussion). We note again that for the linearized models referenced initially (Williams, 1963; Mueller and Knauss, 1971; Knauss, 1974; and Schapery, 1975), the best data fit for *fracture of rubbery solids* is achieved with a *velocity independent value* for this stress. Beyond this observation we draw attention to the fact that the transition in the two plots from low-speed behavior (rubber-like behavior) to fast speed response (glass-like behavior) occurs at velocities which are different by about four orders of magnitude. Clearly, transition behavior of the cohesive stress from rubbery to glassy response and the time scales at which this occurs is an integral part of the nonlinear aspects of the fracture problem.

The Cohesive Fracture Energy. Energy expenditure in a fracture process is of intrinsic interest. In the linearized models the fracture energy has been taken to be a constant, which assumption has served well when rubber-like fracture behavior is involved. If one defines the fracture energy in the present situation through an integral over the cohesive zone α by

$$\Gamma = \int_{\alpha} \sigma d\epsilon(x)$$

as the work expended on the deformation of the material in the nonlinear zone, one can examine its behavior as a function of the applied stress intensity factor as shown in Fig. 12.

For the lower range of stress intensity factors the fracture energy (normalized by the glassy Young's modulus) increases somewhat in proportion to the applied load, while at the higher load levels it increases with its square. Thus the nonlinear model does not automatically generate the assumption in the linearized theory of a constant fracture energy in the rubbery region; for that (linearized) model, all the rate-dependent energy dissipation is derived from the deformations in the bulk domain. In the present nonlinear case, the model automatically adjusts the partition of dissipation between the bulk and the strip domain. As the stress intensity increases, the energy dissipation mechanisms shift increasingly to the nonlinear zone as represented by the approach to an asymptotic square power-law dependence.

It is of interest to consider this result in a simplified or qualitative context of the linearized fracture model by replacing the (constant) fracture energy by the present asymptotic representations. Using the approximate results for the linearized case (Knauss, 1974), one would then find that for the low-intensity case, when $\Gamma \sim bK$,

$$D\left(\frac{\alpha}{\dot{c}}\right)K^2 \sim bK,$$

which is a result reminiscent of the (linearized) displacement criterion (Knauss, 1974), while for the high-intensity case, when $\Gamma \sim bK^2$, there results

$$D\left(\frac{\alpha}{\dot{c}}\right)K^2 \sim bK^2,$$

Downloaded 03 May 2010 to 171.66.16.245. Redistribution subject to ASME license or copyright; see http://www.asme.org/terms/Terms_Use.cfm

indicating that this limit makes the crack speed independent of, or, at least, insensitive to the value of the stress intensity factor, which represents the region in Fig. 11(*a*) for $\dot{c}/(h/\bar{\tau}) > 10^8$.

In this context it is also of interest to briefly comment on the results with respect to the issue of quasi-constant failure propagation in a bonded joint, albeit in the sense of a "limit analysis." Note that for high rates of crack propagation, the bulk of the solid responds with its glassy (elastic) properties so that only the fracture zone contributes to the rate-dependent behavior; this is the high rate limit situation which corresponds to a bonded joint, though in the present case, with the stiff (glassy) properties of the polymer. This situation occurs for (normalized) stress intensity factors of about 0.01 and higher for which the crack propagation rate becomes increasingly insensitive to loading levels; it should be remembered that the "bond" failure involves a "plastic" zone that spans the bond line. In terms of Fig. 12, the energy expenditure for this situation follows the square dependence on the stress intensity, which observation is another way of saying that a bond formed of a stiff polymer is likely to show a strong variation of failure rate with relatively small changes in load levels as long as the current limit conditions apply.

Further Comparison With the Linearized Theory. In the reference by Knauss (1974), the linearized model was examined for the (constant) energy and the COD criterion. These criteria are reproduced in Fig. 13 where we have also chosen, for illustrative comparison, the present calculations with $\epsilon_0 = 1$ percent; the plots for the linearized theory have been evaluated for the relaxation properties of the present material, and the lower limit of the stress intensity factor has been adjusted so that all the curves possess the same asymptotic behavior for $\dot{c} \to 0$.

One notes first that the nonlinear results fall between the energy and displacement criteria: Thus crack propagation in the nonlinear case leads to slower crack growth rates than the linearized energy criterion predicts,[8] but to faster rates than the linearized displacement criterion would indicate. In fact, in an "overall sense" the present results appear to follow the displacement criterion more closely than the energy criterion.[9] There is clearly a transition from the near rubbery behavior to the glassy response in which the latter exhibits considerably more "toughness" than the linearized model would allow. This notion is attributed to the strong dependence of the fracture energy (dissipation) on load level as discussed in connection with Fig. 12.

6 Conclusion

We conclude this discussion of the characteristics of nonlinear fracture modeling with two caveats. While we have no direct evidence for the following conjecture, we point out that one (unintentional) aspect of the nonlinear material characterization may have an influence on this comparison between the nonlinear and the linearized model. The present model incorporates—for lack of better information at the moment—an ultimate constant strain for the nonlinear material response. This prescription may be viewed as being tantamount to a COD criterion. One must then wonder whether the current results are biased by this fact, although the present developments favor no preconceived notions as to which type of criterion should prevail; in fact, the present calculations were performed in order to circumvent the "question of the proper

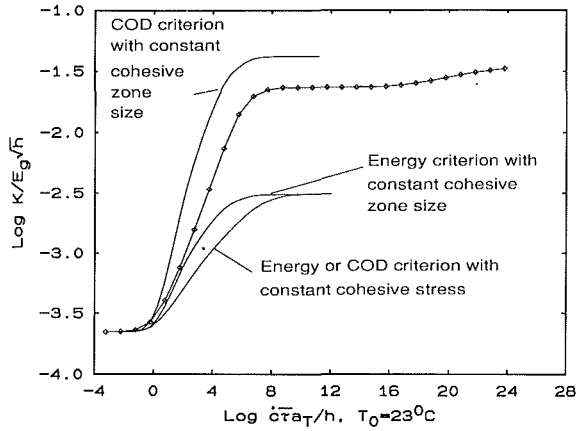


Fig. 13 Comparison of present computations ($\epsilon_0 = 1$ percent) and various linearly viscoelastic results from Knauss (1974)

criterion." Certainly, these computations are made under the most unrestricted material description presently available, except for the implicit assumption in the context of the maximum strain capability.

The other caveat relates to the implicit and widespread assumption that cracks propagate in a continuous manner, which was represented here by considering the continuous fracture process to occur with constant velocity. There is, however, increasing evidence that under both quasi-static and dynamic conditions cracks tend to propagate in a discontinuous, jump-like manner (Vasudevan and Knauss, 1988; Lee and Knauss, 1989; Washabaugh and Knauss, 1991; and Pulos, 1992). Such a behavior would, as a minimum, require different modeling, which would not be likely to generate globally different results, but which could change the results in details.

Acknowledgments

The authors would like to acknowledge the support of the Office of Naval Research, under grant # N00014-84-K-0424, under the supervision of Dr. Leighton H. Peebles. They would also like to acknowledge support of the National Science Foundation through the San Diego Supercomputer Center.

References

Anderson, H., and Bergkvist, H., 1970, "Analysis of a Nonlinear Crack Model," *J. Mech. Phys. Solids*, Vol. 18, pp. 1–28.

Barenblatt, G. I., 1962, "The Mathematical Theory of Equilibrium Cracks in Brittle Fracture," *Adv. Appl. Mech.*, Vol. 7, Academic Press, New York, p. 55.

Dietmann, H., and Knauss, W. G., 1970, "Crack Propagation under Variable Load Histories in Linearly Viscoelastic Solids," *Int. J. Eng. Sci.*, Vol. 8, pp. 643–656.

Dugdale, D. S., 1960, "Yielding of Steel Sheets Containing Slits," *J. Mech. Phy. Solids*, Vol. 8, p. 100.

Emri, I., and Knauss, W. G., 1981, "Nonlinear Viscoelasticity Based on Free Volume Consideration," *Computers and Structures*, Vol. 13, pp. 123–128.

Emri, I., and Knauss, W. G., 1987, "Volume Change and the Nonlinearly Thermo-Viscoelastic Constitution of Polymers," *Poly. Sci. Eng.*, A. Yee, ed., Vol. 27, pp. 86–100.

Knauss, W. G., 1974, "On the Steady Propagation of a Crack in a Viscoelastic Sheet: Experiments and Analysis," *Deformation & Fracture of High Polymers*, Kausch, Hassell and Jaffee, eds., Plenum Press.

Knauss, W. G., 1976, "Fracture of Solids Possessing Deformation Rate Sensitive Material Properties," *The Mechanics of Fracture*, F. Erdogan, ed., ASME, New York, AMD Vol. 19.

Knauss, W. G., and Parvin, M., 1990, "Damage Induced Constitutive Response of a Thermoplastic Related to Composites and Adhesive Bonding," *Int. J. Fract.*, Vol. 42, No. 1, pp. 57–72.

Kostrov, B. V., and Nikitin, L. V., 1970, "Some General Problems of Mechanics of Brittle Fracture," *Archiwum Mechaniki Stosowanej*, Vol. 22, No. 6, English version p. 749.

Lee, O. S., and Knauss, W. G., 1989, "Dynamic Crack Propagation Along a Weakly Bonded Polymeric Plane," *Exp. Mech.*, Vol. 29, pp. 342–346.

Losi, G. U., and Knauss, W. G., 1992, "Free Volume Theory and Nonlinear Thermo-Viscoelasticity," *Poly. Sci. Eng.*, Vol. 32, No. 8, pp. 542–557.

[8]In the nonlinear case the (required) fracture energy (dissipation) increases with crack speed, while the linear case assumes this quantity to be independent of speed.

[9]Note that the fracture model reported by Williams (1963) of a Voigt solid governed by a critical strain exhibits characteristics similar to the linear COD criterion in Fig. 15.

Downloaded 03 May 2010 to 171.66.16.245. Redistribution subject to ASME license or copyright; see http://www.asme.org/terms/Terms_Use.cfm

Muller, H. K., and Knauss, W. G., 1971, "Crack Propagation in a Linearly Viscoelastic Strip," ASME JOURNAL OF APPLIED MECHANICS, Vol. 38, pp. 483.

Muller, H. K., and Knauss, W. G., 1975, Discussion of "On the Governing Equation for Quasi-Static Crack Growth in a Linearly Viscoelastic Materials," by R. J. Nuismer, ASME JOURNAL OF APPLIED MECHANICS, Vol. 42, pp. 520–521.

Pulos, G., 1992, Current doctoral research, Graduate Aerospace Laboratories, California Institute of Technology, Pasadena, CA.

Schapery, R. A., 1975, "A Theory of Crack Initiation and Growth in Viscoelastic Media, I: Theoretical Development; II: Approximate Methods of Analysis; III: Analysis of Continuous Growth: *Int. J. Fract.*, Vol. 11, pp. 141; 339; 549.

Ungsuwarungsri, T., and Knauss, W. G., 1987, "The Role of Damage-Softened Material Behavior in the Fracture of Composite and Adhesives," *Int. J. Fract.*, Vol. 35, pp. 221–241.

Ungsuwarungsri, T., and Knauss, W. G., 1988, "A Nonlinear Analysis of an Equilibrium Crack, Part I: Problem Formulation and Solution; Part II: Simulations of Craze and Crack Growth," ASME JOURNAL OF APPLIED MECHANICS, Vol. 55, pp. 44–51; 52–58.

Vasudevan, N., and Knauss, W. G., 1988, "An Approximate Analysis of the Effect of Mocro Fractures on the Caustic of a Dynamically Moving Crack Tip," *Int. J. Fract.*, Vol. 36, pp. 121–135.

Washabaugh, P. D., and Knauss, W. G., 1993, "Non-Steady, Periodic Behavior in the Dynamic Fracture of PMMA," *Int. J. Fract.*, Vol. 59, pp. 189–197.

Williams, M. L., 1963, "The Fracture of Viscoelastic Material," *Fracture of Solids*, D. C. Drucker and J. J. Gilman, eds., pp. 157–188.

Downloaded 03 May 2010 to 171.66.16.245. Redistribution subject to ASME license or copyright; see http://www.asme.org/terms/Terms_Use.cfm

Viscoelastic Microbuckling of Fiber Composites

W. S. Slaughter

N. A. Fleck

Engineering Department,
Cambridge University,
Trumpington Street,
Cambridge, CB2 1PZ, England

A theoretical study is given of viscoelastic microbuckling of fiber composites. The analysis is formulated in terms of general linear viscoelastic behavior within the kink band. Material outside the kink band is assumed to behave elastically. Two specific forms of linear viscoelastic behavior are considered: a standard linear viscoelastic model and a logarithmically creeping model. Results are provided as deformation versus time histories and failure life versus applied stress. Failure is due to either the attainment of a critical failure strain in the kink band or to the intervention of a different failure mechanism such as plastic microbuckling.

Introduction

Microbuckling has been shown usually to be the dominant mechanism of compressive failure of aligned fiber composite materials (Argon, 1972; Budiansky and Fleck, 1993). The form of microbuckling under consideration here is an event in which the composite suffers localized buckling within a kink band. In laminates this is commonly observed in plies with fiber axes that are parallel to the loading direction. Matrix cracking of off-axis plies (plies with fiber axes not in the loading direction) and inter-ply delamination may occur concurrently, but microbuckling is thought to control failure when the proportion of off-axis plies is not large (Soutis, 1991). A physical understanding of the factors which control microbuckling is therefore important in order to design fiber composites of improved compressive strength.

Several studies of time-*independent* compressive failure have been undertaken. A preliminary theoretical analysis by Rosen (1965) treated microbuckling as an elastic buckling phenomenon. Results from this analysis, however, severely overestimate the critical stresses necessary for microbuckling. Subsequent theoretical analyses which have sought to modify the Rosen model to account for this discrepancy between predicted and measured strengths (e.g., Steif, 1988) have met with limited success. More recent studies by Argon (1972) and Budiansky and Fleck (1993) have included the effects of matrix yielding, initial fiber misalignment, and fiber extensibility. In these analyses, the assumption is made that a band of misaligned fibers exists and that the composite exhibits a predilection to microbuckle uniformly within this band. These latter studies form the foundation on which the current analysis is based.

Many fiber composites are known to exhibit time-*dependent* deformation behavior. Two of the more common examples, carbon fiber-reinforced PEEK and carbon fiber-reinforced epoxy resin, have been studied at ambient temperature (Horoschenkoff et al., 1988) and at elevated temperatures (Ha et al., 1991). In this paper, a linear viscoelastic composite behavior is assumed in order to examine time-dependent microbuckling of fiber composites in compression. The solution is formulated in terms of a general relaxation function and specific results are given for a standard linear viscoelastic solid and a logarithmically creeping solid. The logarithmic creep behavior is derived from the results of Horoschenkoff et al. (1988).

The results of this study may also be applicable to woods. Many woods fail by microbuckling in the S_2 layer of the cell wall (Grossman and Wold, 1971; Dinwoodie, 1981). The cell wall is composed of over 90 percent aligned tracheids by volume, which are natural fibers, bonded together by a weaker substance consisting principally of pectopolyuronides and lignin (Mark, 1967). These tracheids can be thought of as analogous to fibers in a fiber composite and the weaker bonding material as analogous to the matrix. Wood is also known to behave viscoelastically (Mark, 1967; Dinwoodie, 1981). Thus, to a first approximation, wood may be thought of as a viscoelastic fiber composite.

Viscoelastic Microbuckling

In microbuckling of uniform, aligned fiber composites, a kink band is formed in which the composite undergoes localized catastrophic failure. This kink band is on the order of ten fiber diameters in width and is generally *not* normal to the fiber axes. A schematic of the kink band is shown in Fig. 1. The kink band is at an angle β to the transverse direction and is of width w. It is assumed that the fibers are inextensible and that deformation within the band can be represented by the change in fiber direction ϕ. It is also assumed that an initial imperfection, or misalignment, can be represented by $\bar{\phi}$. Variations along the kink band are ignored. Let two cartesian coordinate systems, $(\underline{e}_1,\underline{e}_2)$ and $(\underline{\epsilon}_1,\underline{\epsilon}_2)$, aligned with the fiber direction outside and inside the kink, respectively, be defined

Contributed by the Applied Mechanics Division of THE AMERICAN SOCIETY OF MECHANICAL ENGINEERS for presentation at the ASME Winter Annual Meeting, New Orleans, LA, Nov. 28–Dec. 3, 1993.

Discussion on this paper should be addressed to the Technical Editor, Professor Lewis T. Wheeler, Department of Mechanical Engineering, University of Houston, Houston, TX 77204-4792, and will be accepted until four months after final publication of the paper itself in the ASME JOURNAL OF APPLIED MECHANICS.

Manuscript received by the ASME Applied Mechanics Division, Apr. 3, 1992; final revision, Dec. 3, 1992. Associate Technical Editor: G. J. Dvorak.

Paper No. 93-WA/APM-16.

Copyright © 1993 by ASME
Downloaded 03 May 2010 to 171.66.16.245. Redistribution subject to ASME license or copyright; see http://www.asme.org/terms/Terms_Use.cfm

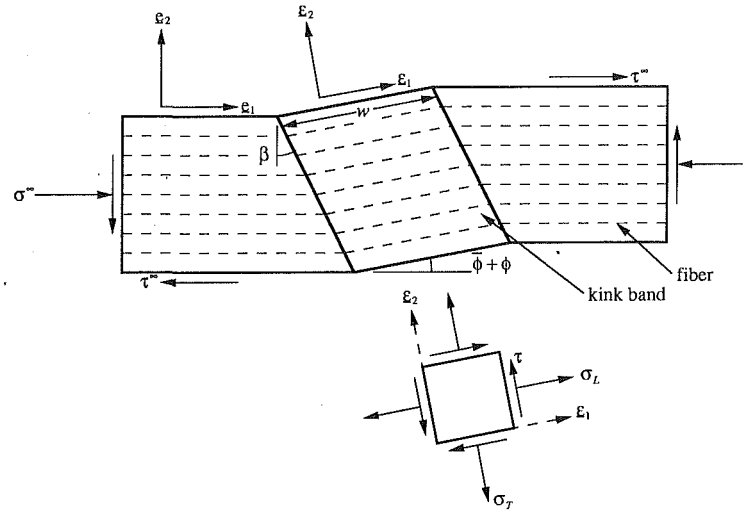


Fig. 1 Kink band geometry and notation

as shown in Fig. 1. For simplicity, remote loading $\underline{\sigma}^\infty = -\sigma^\infty \underline{\mathbf{e}}_1\underline{\mathbf{e}}_1 + \tau^\infty(\underline{\mathbf{e}}_1\underline{\mathbf{e}}_2 + \underline{\mathbf{e}}_2\underline{\mathbf{e}}_1)$ is restricted to be proportional and prescribed by the parameter $e \equiv \tau^\infty/\sigma^\infty$. We neglect remote loading perpendicular to the fibers.

A uniform state of stress and strain, related by a linear elastic response, is assumed to exist outside the kink band. Within the kink band the stress is given by $\underline{\sigma} = \sigma_L \underline{\epsilon}_1\underline{\epsilon}_1 + \sigma_T \underline{\epsilon}_2\underline{\epsilon}_2 + \tau(\underline{\epsilon}_1\underline{\epsilon}_2 + \underline{\epsilon}_2\underline{\epsilon}_1)$ and the strain is given by $\underline{\mathbf{e}} = e_T \underline{\epsilon}_2\underline{\epsilon}_2 + (1/2)\gamma(\underline{\epsilon}_1\underline{\epsilon}_2 + \underline{\epsilon}_2\underline{\epsilon}_1)$. Expressions for kinematic conditions and continuity of tractions across the kink band interface have been derived by Budiansky and Fleck (1993). In the $\underline{\epsilon}_2$-direction perpendicular to the kink band fibers, continuity of tractions requires

$$\sigma^\infty[\cos\beta\sin(\bar{\phi}+\phi) + e\cos(\beta+\bar{\phi}+\phi)] = \tau\cos(\beta-\bar{\phi}-\phi) + \sigma_T\sin(\beta-\bar{\phi}-\phi). \quad (1)$$

For small ϕ and $\bar{\phi}$ the approximate kinematic equations, relating strains within the kink band to ϕ, are (Budiansky and Fleck, 1993)

$$\gamma \approx \phi + \gamma^\infty = \phi + \frac{e\sigma^\infty}{G} \quad (2)$$

$$e_T \approx \phi\tan\beta \quad (3)$$

where γ^∞ is the shear strain outside the kink band and G is the composite shear modulus. The kink band angle β changes with remote shear strain γ^∞ according to

$$\tan\beta = \tan\beta_0 - \gamma^\infty$$

where β_0 is the initial value of β. For small γ^∞, $\beta \approx \beta_0$.

Within the kink band, the composite is assumed to have a linear viscoelastic response with independent transverse and shear constitutive relations; if $\lim_{t\to-\infty}\gamma(t) = \lim_{t\to-\infty} e_T(t) = 0$ then

$$\tau(t) = \int_{-\infty}^{t} K_s(t-s)\dot{\gamma}(s)ds = K_S(0)\gamma(t) + \int_{-\infty}^{t} \dot{K}_S(t-s)\gamma(s)ds \quad (4)$$

$$\sigma_T(t) = K_T(0)e_T(t) + \int_{-\infty}^{t} \dot{K}_T(t-s)e_T(s)ds \quad (5)$$

where t is time and $\dot{f}(t) \equiv \frac{d}{dt}f(t)$. $K_s(t)$ and $K_T(t)$ are the composite relaxation functions in shear and transverse straining, respectively. Substituting Eq. (2)–(5) into (1) gives

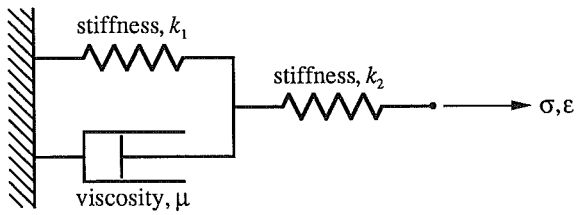


Fig. 2(*a*) Representative diagram for standard linear viscoelastic solid

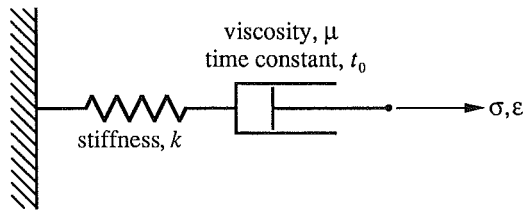


Fig. 2(*b*) Representative diagram for logarithmically creeping solid

$$\sigma^\infty[\cos\beta\sin(\bar{\phi}+\phi) + e\cos(\beta+\bar{\phi}+\phi)] - \left\{K_S(0)\left(\phi + \frac{e\sigma^\infty}{G}\right) + \int_{-\infty}^{t} \dot{K}_S(t-s)\left[\phi(s) + \frac{e\sigma^\infty(s)}{G}\right]ds\right\}\cos(\beta-\bar{\phi}-\phi) - \left\{\phi K_T(0) + \int_{-\infty}^{t} \dot{K}_T(t-s)\phi(s)ds\right\}\tan\beta\sin(\beta-\bar{\phi}-\phi) = 0. \quad (6)$$

Given composite relaxation functions and any loading history, $\sigma^\infty(t)$ with $\lim_{t\to-\infty}\sigma^\infty(t) = 0$, Eq. (6) can be solved numerically for the kink band deformation history, $\phi(t)$. Note that the kink band angle, β, is not determined by this analysis. In fact, β is a required independent variable. Typically, in carbon fiber composites $\beta \approx 20$ deg. Specific forms of the relaxation functions are now considered.

Standard Linear Viscoelastic Model. The standard linear viscoelastic material is sketched in Fig. 2(*a*). The material response satisfies the differential equation

Downloaded 03 May 2010 to 171.66.16.245. Redistribution subject to ASME license or copyright; see http://www.asme.org/terms/Terms_Use.cfm

$$\left(1+\frac{k_1}{k_2}\right)\sigma+\frac{\mu}{k_2}\,\dot{\sigma}=\mu\dot{\epsilon}+k_1\epsilon \tag{7}$$

where σ is stress, ϵ is strain, k_1 and k_2 are elastic moduli, and μ is viscosity. The relaxation function $K(t)$ is defined as the solution, $\sigma(t)$ for an 'input' $\epsilon=H(t)$ where $H(t)$ is the Heaviside step function. Thus, the relaxation function is

$$K(t)=\frac{k_1k_2}{k_1+k_2}\left\{1-\left(1-\frac{k_1+k_2}{k_1}\right)\exp\left[-\frac{t}{\mu}(k_1+k_2)\right]\right\}H(t). \tag{8}$$

Let (G_1,G_2,μ_S) and (E_1,E_2,μ_T) be the material properties (k_1,k_2,μ) for shear and transverse deformation, respectively.

Using Eq. (8), Eq. (6) can be rewritten for the standard linear viscoelastic model. The six dimensional material constants can be reduced to the following four nondimensional constants

$$\lambda\equiv\frac{E_2}{G_2},\ \eta\equiv\frac{\mu_SE_1}{\mu_TG_1},\ \overline{G}\equiv\frac{G_1+G_2}{G_1},\ \overline{E}\equiv\frac{E_1+E_2}{E_1}. \tag{9}$$

With the additional nondimensional substitutions

$$\overline{\sigma}^{\infty}\equiv\frac{\sigma^{\infty}}{G_2},\ \bar{t}\equiv\frac{G_1}{\mu_S}\,t,\ \bar{s}\equiv\frac{G_1}{\mu_S}\,s, \tag{10}$$

Eq. (6) becomes

$$\overline{\sigma}^{\infty}[\cos\beta\sin(\overline{\phi}+\phi)+e\cos(\beta+\overline{\phi}+\phi)]$$
$$-\left\{\phi+e\overline{\sigma}^{\infty}-\int_{-\infty}^{\bar{t}}\overline{K}_S(\bar{t}-\bar{s})[\phi(\bar{s})+e\overline{\sigma}^{\infty}(\bar{s})]d\bar{s}\right\}\cos(\beta-\overline{\phi}-\phi)$$
$$-\lambda\left\{\phi-\eta\int_{-\infty}^{\bar{t}}\overline{K}_T(\bar{t}-\bar{s})\phi(\bar{s})d\bar{s}\right\}\tan\beta\sin(\beta-\overline{\phi}-\phi)=0 \tag{11}$$

where

$$\overline{K}_S(\bar{t})=(\overline{G}-1)\exp(-\bar{t}\,\overline{G}) \tag{12}$$
$$\overline{K}_T(\bar{t})=(\overline{E}-1)\exp(-\eta\bar{t}\,\overline{E}). \tag{13}$$

Logarithmically Creeping Model. A logarithmically creeping model for composite behavior is proposed based on the results of Horoschenkoff et al. (1988). This material model is shown in Fig. 2(*b*). The response of the system must satisfy

$$\frac{1}{k}\,\dot{\sigma}+\frac{1}{\mu}\left(\frac{1}{t+t_0}\right)\sigma=\dot{\epsilon} \tag{14}$$

where σ is stress, ϵ is strain, k is an elastic modulus, μ is viscosity, and t_0 is a material time constant. The name for this constitutive law comes from the logarithmic nature of the *creep* function, i.e., the solution $\epsilon(t)$ when $\sigma(t)=H(t)$, given by

$$C(t)=\left[\frac{1}{k}+\frac{1}{\mu}\ln\left(\frac{t}{t_0}+1\right)\right]H(t).$$

The required *relaxation* function is

$$K(t)=k\left(\frac{t}{t_0}+1\right)^{-k/\mu}H(t). \tag{15}$$

Let (G,μ_S,t_{0S}) and (E_T,μ_T,t_{0T}) be the material properties (k,μ,t_0) for shear and transverse deformation, respectively.

For the logarithmically creeping model, the four nondimensional material constants are

$$\lambda\equiv\frac{E_T}{G},\ \eta\equiv\frac{t_{0S}}{t_{0T}},\ \overline{G}\equiv\frac{G}{\mu_S},\ \overline{E}\equiv\frac{E_T}{\mu_T}, \tag{16}$$

and the nondimensional substitutions are

$$\overline{\sigma}^{\infty}\equiv\frac{\sigma^{\infty}}{G},\ \bar{t}\equiv\frac{t}{t_{0S}},\ \bar{s}\equiv\frac{s}{t_{0S}}. \tag{17}$$

Rewriting Eq. (6) once again yields (11), but with new kernel functions

$$\overline{K}_S(\bar{t})=\overline{G}(\bar{t}+1)^{-\overline{G}-1} \tag{18}$$
$$\overline{K}_T(\bar{t})=\overline{E}(\eta\bar{t}+1)^{-\overline{E}-1}. \tag{19}$$

Material Properties. Both of the proposed viscoelastic models require four nondimensional material constants. The physical interpretation of these constants is similar for each model. The first constant, λ, is the ratio of the instantaneous transverse stiffness to the instantaneous shear stiffness. Experimental measurements suggest $\lambda=2$ (Hull, 1981). The second material constant, η, is the ratio of viscoelastic time scales in the shear and transverse directions. This ratio is taken to be unity ($\eta=1$) for simplicity. The third and fourth constants, $\overline{G}$ and $\overline{E}$, measure the viscoelastic response in comparison to the initial elastic response for the shear and transverse directions, respectively. Assuming that $\overline{G}=\overline{E}$, what are appropriate ranges of values for analysis? Based on the studies of Ha et al. (1991) and Horoschenkoff et al. (1988), carbon fiber-reinforced epoxy resins are modeled as standard linear viscoelastic materials with a range of $\overline{G}$ of 1.5–10.0 and carbon fiber-reinforced PEEK's are modeled as logarithmically creeping materials with a range of $\overline{G}$ of 0.1–0.4.

Failure Criterion. Failure is associated with debonding of the fiber-matrix interface, matrix microcracking, or with other mechanisms which result in a sharp decrease in the load bearing ability of the kink band. Several failure criteria are possible. It is proposed here that failure occurs when the following simple empirical criterion is satisfied:

$$\left(\frac{e_T}{e_{Tf}}\right)^2+\left(\frac{\gamma}{\gamma_f}\right)^2=1 \tag{20}$$

where e_{Tf} is the transverse failure strain and γ_f is the shear failure strain. It is further assumed that $e_{Tf}\ll\gamma_f$ so that, with Eq. (3),

$$\phi_f\approx\frac{e_{Tf}}{\tan\beta} \tag{21}$$

where ϕ_f is the critical kink band deformation angle at failure. For the purposes of this paper, $e_{Tf}=0.02$. All of these assumptions are in acceptable agreement with experimental evidence (see, for example, Hull, 1981).

A consequence of failure is the concept of failure time or viscoelastic life. Up to this point, only kink band deformation as a function of time, $\phi(t)$, has been discussed. As time, t, tends to infinity, $\phi(t)$ reaches a finite limit in the standard linear viscoelastic model or becomes unbounded in the logarithmically creeping model. Failure occurs at a finite time, t_f, when $\phi=\phi_f$, given by Eq. (21).

Results

Equation (11) is a nonlinear Volterra integral equation of the second kind with well-behaved difference kernels. This equation can be solved numerically by discretizing the integrals using Simpson's rule and stepping forward discretely in time, $t_n=n\Delta t$ where Δt is the step size. At each step, n, a root finding algorithm is used to calculate the deformation angle $\phi_n\equiv\phi(t_n)$ since the discrete solutions from previous steps, ϕ_i $(i=0,1,2,\ldots,n-1)$, are known. It is assumed that the solution is bounded by $0\le\phi<\pi/2$. Techniques for the numerical solution of integral equations can be found in Baker (1977).

Consideration is restricted to loading histories of the form

$$\sigma^{\infty}(t)=\sigma^{\infty}H(t) \tag{22}$$

with $e=0$ (i.e., $\tau^{\infty}=0$). Remote shear stress can be included but does not affect the qualitative features of the results. As previously discussed, $\lambda=2$, $\eta=1$, and $\overline{G}=\overline{E}$. The kink band

Downloaded 03 May 2010 to 171.66.16.245. Redistribution subject to ASME license or copyright; see http://www.asme.org/terms/Terms_Use.cfm

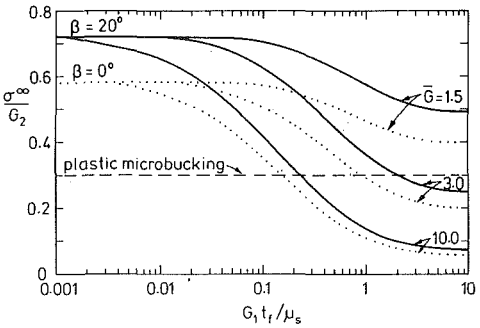


Fig. 3 Applied axial load versus time till failure for the standard linear viscoelastic model ($\lambda = 2$, $\eta = 1$, $\beta = 20$ deg and 0 deg, $\bar{\phi} = 2$ deg, $\phi_f = 3$ deg, $e = 0$, $\bar{E} = \bar{G}$)

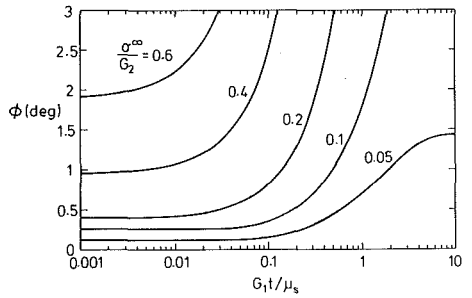


Fig. 4 Kink band deformation angle versus time for the standard linear viscoelastic model ($\lambda = 2$, $\eta = 1$, $\beta = 20$ deg, $\bar{\phi} = 2$ deg, $e = 0$, $\bar{E} = \bar{G} = 10$)

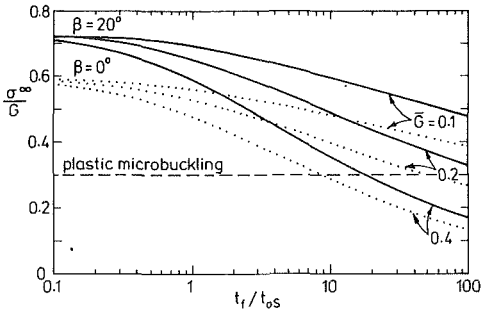


Fig. 5 Applied axial load versus time till failure for the logarithmically creeping model ($\lambda = 2$, $\eta = 1$, $\beta = 20$ deg and 0 deg, $\bar{\phi} = 2$ deg, $\phi_f = 3$ deg, $e = 0$, $\bar{E} = \bar{G}$)

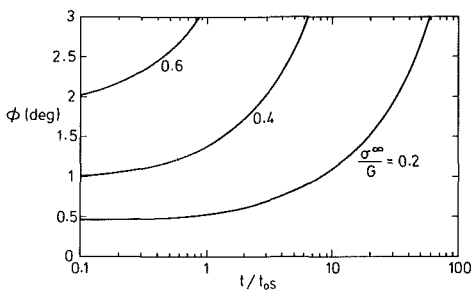


Fig. 6 Kink band deformation angle versus time for the logarithmically creeping model ($\lambda = 2$, $\eta = 1$, $\beta = 20$ deg, $\bar{\phi} = 2$ deg, $e = 0$, $\bar{E} = \bar{G} = 0.4$)

angle is taken to be $\beta = 20$ deg. The critical kink band deformation angle is $\phi_f = 3$ deg via Eq. (21). The case $\beta = 0$ deg is also considered, for comparison, but with $\phi_f = 3$ deg retained. An initial misalignment angle of $\bar{\phi} = 2$ deg is chosen in agreement with measurements on several composites (Budiansky and Fleck, 1993). Results for the standard linear viscoelastic model representing carbon fiber-reinforced epoxy resins are shown in Figs. 3 and 4 and those for the logarithmically creeping model representing carbon fiber-reinforced PEEK's are given in Figs. 5 and 6.

The applied axial stress σ^∞, as defined in Eq. (22), versus the failure time, t_f, is shown in Figs. 3 and 5 for representative $\bar{G}$ values. Experimental results (Ha et al., 1991; Horoschenkoff et al., 1988) indicate timescales t_{0S} and μ_S/G_1 both on the order of one hour. The necessary load for instantaneous failure ($t_f = 0$) is the same for both models and corresponds to the elastic microbuckling load with initial misalignment as calculated by Fleck and Budiansky (1991). The applied axial stress versus failure time for the standard linear viscoelastic model, when plotted on a logarithmic time scale (Fig. 3), has an "S" shaped profile. The applied axial stress versus failure time for the logarithmically creeping model, when plotted on a logarithmic time scale (Fig. 5), is nearly linear over a wide range of failure times. The evolution of kink band deformation, $\phi(t)$, is shown in Figs. 4 and 6 for different loads at a given $\bar{G}$. The ordinate of these plots is terminated at the critical fiber rotation angle $\phi_f = 3$ deg.

For the standard linear viscoelastic model there exists a critical stress, σ^∞_{cr}, below which $\phi(t) < \phi_f$ for all t and failure never occurs. At $\sigma^\infty = \sigma^\infty_{cr}$, $\phi(t \to \infty) = \phi_f$. For small $\bar{\phi}$ and ϕ_f, the critical stress in nondimensional form, $\bar{\sigma}^\infty_{cr} \equiv \sigma^\infty_{cr}/G_2$, follows from Eq. (11) as

$$\bar{\sigma}^\infty_{cr} \approx \left[\frac{1 + \lambda\left(\frac{\bar{G}}{\bar{E}}\right)\tan^2\beta}{(\bar{\phi} + \phi_f) + e\left(1 - \frac{1}{\bar{G}}\right)} \right] \frac{\phi_f}{\bar{G}}. \tag{23}$$

Note from Eq. (23) that $\bar{\sigma}^\infty_{cr}$ decreases linearly with decreasing ϕ_f and decreases with increasing $\bar{G}$. A graphical construction can be used to calculate $\bar{\sigma}^\infty_{cr}$ when $\beta = 0$ deg and $e = 0$ (see Fig. 7). The constitutive Eq. (1) reduces, for small ϕ and $\bar{\phi}$, to

$$\bar{\sigma}^\infty(\bar{\phi} + \phi) \approx \frac{\tau}{G_2}. \tag{24}$$

This equation is represented on the $(\phi, \tau/G_2)$ plane by a line of slope $\bar{\sigma}^\infty$ and intercept $(-\bar{\phi}, 0)$. At $t = 0$, the instantaneous elastic response gives

$$\frac{\tau}{G_2} = \phi \tag{25}$$

which defines a line of slope unity going through the origin on the $(\phi, \tau/G_2)$ plane. At $t \to \infty$, the response is

$$\frac{\tau}{G_2} = \frac{\phi}{\bar{G}} \tag{26}$$

which defines a line of slope $1/\bar{G}$ going through the origin on the $(\phi, \tau/G_2)$ plane. At $t = 0$, the $\tau - \phi$ state of the kink band material is given by the intersection of the lines defined by Eqs. (24) and (25). With increasing time, the $\tau - \phi$ state moves along the ray defined by Eq. (24). For $\bar{\sigma}^\infty$ sufficiently small (e.g., $\bar{\sigma}^\infty_1$ in Fig. 7), $\phi(t \to \infty) < \phi_f$ and failure does not occur; as $t \to \infty$ the $\tau - \phi$ state moves to the intersection of lines defined by Eqs. (24) and (26). At high values of $\bar{\sigma}^\infty$ (e.g., $\bar{\sigma}^\infty_2$ in Fig. 7), ϕ attains ϕ_f at a finite time and failure occurs. At $\bar{\sigma}^\infty = \bar{\sigma}^\infty_{cr}$, ϕ at the intersection of lines (24) and (26) equals ϕ_f.

Discussion

No mention has been made so far of plastic yielding within the kink band. An alternative failure mechanism to viscoelastic microbuckling is plastic instability by plastic microbuckling. A typical critical stress for plastic microbuckling in both PEEK and epoxy systems is $\bar{\sigma}^\infty = 0.3$ (Fleck and Budiansky, 1991). This stress level is shown in Figs. 3 and 5 as a dashed horizontal line. Above this line, failure is due to plastic microbuckling

Downloaded 03 May 2010 to 171.66.16.245. Redistribution subject to ASME license or copyright; see http://www.asme.org/terms/Terms_Use.cfm

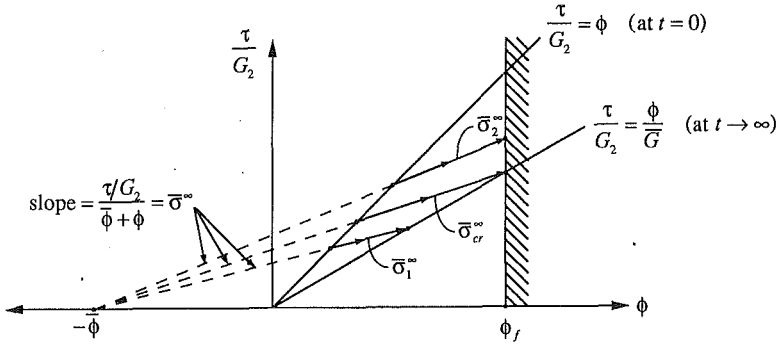


Fig. 7 Stress-strain diagram for the standard linear viscoelastic model when $\beta = 0$ deg and $e = 0$

and failure times from the viscoelastic analysis do not apply. Thus it is seen in Fig. 3 that a carbon fiber-epoxy composite, modeled as a standard linear viscoelastic material, will either fail by plastic microbuckling or not at all if $\bar{G} = 1.5$. For $\bar{G} = 3.0$ and $\bar{G} = 10.0$, viscoelastic microbuckling can occur at stress levels below the plastic microbuckling stress. In order to maximize viscoelastic strength for this material, ϕ_f should be maximized and $\bar{G}$ should be minimized. Figure 5 shows that a carbon fiber-PEEK composite, modeled as a logarithmically creeping solid, fails at low stress levels by viscoelastic microbuckling, for all $\bar{G}$. For example, for $\bar{\sigma}^\infty$, viscoelastic microbuckling requires a minimum of 100 hours ($t_{0S} \approx 1$ hour) at $\bar{G} = 0.2$.

The microbuckling analysis of Budiansky and Fleck (1993), on which this paper is based, follows the collapse response of an imperfect structure. It is not a bifurcation analysis. The effects of fiber bending stiffness are neglected, with the result that there is no length scale in the analysis. Previous studies have shown that this is a valid approximation (Budiansky, 1979). Fibers are implicitly assumed to be broken at the kink band interface, but without fiber bending stiffness this is not an issue. The issue of kink band initiation, in which the kink band might be imagined to begin at some region of local composite weakness or stress concentrator and then propagate out, has not been addressed. This is an important topic and kink bands are seen to form and grow in this way under certain conditions, e.g., at notch tips. However, the nature of the analysis presented here is that the kink band is treated as a one-dimensional structure. No variations in stress or deformation are allowed along the length of the kink band. The relative importance of kink band initiation is a topic for future investigation.

There is a dearth of experimental studies of viscoelastic failure in fiber composites under compression. In part this may be explained by the experimental difficulties that arise from a lack of knowledge of the time scales and loads involved. This situation is aggravated by the inevitable scatter in mechanical properties from one sample to the next. A load that may trigger plastic microbuckling in one sample may be insufficient to cause viscoelastic microbuckling in another. Hopefully, this study will help to alleviate these problems.

Acknowledgments

The authors are grateful for technical discussions with Prof. B. Budiansky. Support from ONR grant 0014-91-J-1916 is gratefully acknowledged.

References

Argon, A. S., 1972, "Fracture of Composites," *Treatise of Materials Science and Technology*, Vol. 1, Academic Press, New York.

Baker, C. H. T., 1977, *The Numerical Treatment of Integral Equations*, Oxford University Press, Oxford, U.K.

Budiansky, B., 1979, "Remarks on Kink Formation in Axially Compressed Fiber Bundles," Preliminary Reports, Memoranda and Technical Notes of the Materials Research Council Summer Conference, La Jolla, CA, July 1979, sponsored by DARPA.

Budiansky, B., and Fleck, N. A., 1993, "Compressive Failure of Fiber Composites," *J. Mech. Phys. Solids*, Vol. 41, No. 8, pp. 1265–1284.

Dinwoodie, J. M., 1981, *Timber: Its Nature and Behavior*, Van Nostrand Reinhold Company, Berkshire, U.K.

Fleck, N. A., and Budiansky, B., 1991, "Compressive Failure of Fiber Composites Due to Microbuckling," *Proc. IUTAM Symp. on Inelastic Deformation of Composite Materials*, J. Dvorak, ed., Troy, NY, May 29–June 1, 1990, Springer-Verlag, New York, pp. 235–273.

Grossman, P. U. A., and Wold, M. B., 1971, "Compressive Fracture of Wood Parallel to the Grain," *Wood Sci. Tech.*, Vol. 5, pp. 147–156.

Ha, S. K., Wang, Q., and Chang, F., 1991, "Modeling the Viscoplastic Behavior of Fiber-Reinforced Thermoplastic Matrix Composites at Elevated Temperatures," *J. Comp. Mat.*, Vol. 25, pp. 335–373.

Horoschenkoff, A., Brandt, J., Warnecke, J., and Brüller, O. S., 1988, "Creep Behavior of Carbon Fiber Reinforced Polyetheretherketone and Epoxy Resin," *New Generation Materials and Processes*, Milan.

Hull, D., 1981, *An Introduction to Composite Materials*, Cambridge University Press, Cambridge, U.K.

Mark, R. E., 1967, *Cell Wall Mechanics of Tracheids*, Yale University Press, New Haven, CT.

Rosen, B. W., 1965, "Mechanics of Composite Strengthening," *Fiber Composite Materials, Am. Soc. Metals Seminar*, Chapter 3.

Soutis, C., 1991, "Measurements of the Static Compressive Strength of Carbon Fiber-Epoxy Laminates," *Comp. Sci. Tech.*, Vol. 42, No. 4, pp. 373–392.

Steif, P. S., 1988, "A Simple Model for the Compressive Failure of Weakly Bonded, Fiber-Reinforced Composites," *J. Comp. Mat.*, Vol. 22, pp. 818–828.

Downloaded 03 May 2010 to 171.66.16.245. Redistribution subject to ASME license or copyright; see http://www.asme.org/terms/Terms_Use.cfm

Effect of Initial Void Shape on the Occurrence of Cavitation Instabilities in Elastic-Plastic Solids

V. Tvergaard
Department of Solid Mechanics,
The Technical University of Denmark,
DK-2800 Lyngby, Denmark

J. W. Hutchinson
Division of Applied Sciences,
Harvard University,
Cambridge, MA 02138
Fellow ASME

A void in an infinite elastic-plastic material grows without bound when a cavitation stress limit is reached. Such unstable void expansion, driven by the elastic energy stored in the surrounding material, has been studied for the relatively simple case of spherically symmetric conditions and also for a spherical void in an axisymmetric remote stress field. The analyses are here extended to consider the effect of a void with an initially prolate or oblate spheroidal shape. Numerical unit cell analyses are carried out for a power-hardening elastic-plastic material subject to various axisymmetric remote stress states. For the range of void shapes analyzed it is found that the critical cavitation stress state shows very little influence of the initial void shape.

1 Introduction

Cavitation instabilities in metals occur under rather rare conditions in which plastic flow is highly constrained leading to mean tensile stress levels which are more than four or five times the tensile flow stress of the solid. Although mean stress levels of that magnitude are seldom achieved, there are some important applications where such levels can occur and for which spontaneous cavitation is a potential failure mechanism. Situations where thin layers of a ductile metal are bonded to phases which are capable of only elastic deformation are likely candidates, as in ceramic particle reinforced metal matrix composites and in layered structures with ceramic layers alternating with metal layers. A striking example of cavitation instabilities was observed by Ashby, Blunt, and Bannister (1989) in tensile experiments on highly constrained ductile wires. In each specimen, a single void ballooned open in the region of highest triaxiality, most likely nucleated at some kind of second phase particle whose size would be measured in microns. These voids increased their volume by more than six orders of magnitude essentially spontaneously when critical conditions were reached. It is in this sense that a cavitation instability should be regarded as a material instability, quite distinct from conventional void growth which takes place incrementally and stably in proportion to imposed overall straining.

Early work on cavitation instabilities is summarized in Hill (1950). The earliest work was confined to either axisymmetric or spherical symmetric voids subject to stress loadings with the same symmetry. Recently these studies have been extended to the case of initially spherical voids under nonspherically symmetric stressing (Huang et al., 1991; Tvergaard et al., 1992; Hou and Abeyaratne, 1992). The critical remote stress states associated with the cavitation instability have been determined for an isolated initially spherical void in an infinite elastic-plastic medium. A somewhat different way of interpreting cavitation instabilities has been promulgated in studies of the phenomenon within the context of nonlinearly elastic solids. Ball (1982) views cavitation as a bifurcation from a homogeneously stressed state by allowing for bifurcation fields which are singular at the point of origin of the void (see Horgan (1992) for further discussion of the two interpretations and for further references to the elasticity literature). This alternative viewpoint lends itself naturally to the labelling of the phenomena as an inherent material instability.

With the exception of the three aforementioned papers, all the studies, whether for elastic or elastic-plastic solids, have been carried out under restrictions of either axial or spherical symmetry. The term material instability suggests that the critical cavitation stress states should not be a function of, for example, the initial shape of the void or, equivalently, of the details of any initial imperfection when viewed within the bifurcation context. This seems to be implicit in much of the literature, but it has not been established. The objective of this paper is to address this issue by determining to what extent, if any, the cavitation stress states are a function of the initial shape of the voids. Specifically, we will present results for an isolated void with an initially prolate or oblate spheroidal shape in an infinite elastic-plastic solid. The solid is subject to general

Contributed by the Applied Mechanics Division of THE AMERICAN SOCIETY OF MECHANICAL ENGINEERS for publication in the ASME JOURNAL OF APPLIED MECHANICS.

Discussion on this paper should be addressed to the Technical Editor, Professor Lewis T. Wheeler, Department of Mechanical Engineering, University of Houston, Houston, TX 77204-4792, and will be accepted until four months after final publication of the paper itself in the ASME JOURNAL OF APPLIED MECHANICS.

Manuscript received by the ASME Applied Mechanics Division, Jan. 20, 1992; final revision, Aug. 17, 1992. Associate Technical Editor: G. J. Dvorak.

Copyright © 1993 by ASME
Downloaded 03 May 2010 to 171.66.16.245. Redistribution subject to ASME license or copyright; see http://www.asme.org/terms/Terms_Use.cfm

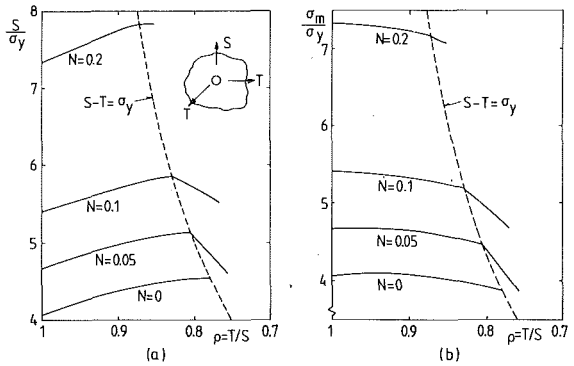


Fig. 1 Cavitation limits for a spherical void in an elastic-plastic power-hardening solid, with $\sigma_y/E = 0.003$ and $\nu = 0.3$; (*a*) axial tensile stress, (*b*) mean stress (from Tvergaard et al., 1992)

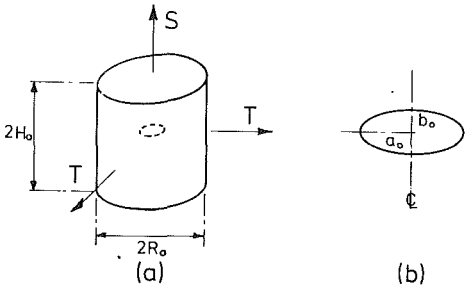


Fig. 2 (*a*) Cylindrical cell model used to analyze cavitation; (*b*) initial void shape

combinations of remote stress states sharing a common axis of symmetry with the void.

2 Cavitation in Axisymmetric Stress Field

For an isolated spherical void in an infinite, remotely stressed elastic-perfectly plastic solid the occurrence of cavitation instabilities has been analyzed by Huang et al. (1991), and the analysis was extended to power-hardening elastic-plastic solids by Tvergaard et al. (1992). The remote principal true stresses, leading to an axisymmetric stress state, were taken to be

$$\sigma_1^\infty = S, \quad \sigma_2^\infty = \sigma_3^\infty = T \tag{1}$$

and the analyses focussed on stress states where $S \geq T$. For the special case of a single spherical void in an elastic-plastic material subject to remote pure hydrostatic tension ($S = T$), where spherical symmetries apply, the analysis is relatively simple (Hill, 1950; Huang et al., 1991).

The dependence of the cavitation instability limit on the remote stress ratio T/S is shown in Fig. 1 (Tvergaard et al., 1992) for an elastic-plastic power-hardening material with initial yield stress $\sigma_y/E = 0.003$ and Poisson's ratio $\nu = 0.3$, including the result for an elastic-perfectly plastic solid ($N = 0$). These results for a spherical void include also the special case of spherical symmetry ($S = T$), and it is seen that the critical tensile stress S or mean stress σ_m for cavitation instability is strongly increased by strain hardening.

The solution procedure used by Huang et al. (1991) for general axisymmetric states of deformation is based on coupling an outer solution to a finite element representation of the solution in an inner region. The outer solution is either a purely elastic solution or a purely plastic solution, which consists of a uniform field corresponding to a uniform stress state equal to the remote stresses, with the lowest order perturbation superposed. The inner solution is a full finite strain solution, and the two solutions are coupled by requiring continuity of displacement increments and nominal traction increments across a spherical surface with radius $R = R^*$.

In the present analyses for voids with initial ellipsoidal shapes, it has been preferred to use a finite element approximation in the whole region analyzed. Thus a cylindrical cell model (Fig. 2) with a central void is analyzed. This type of cell model has been used previously (Tvergaard, 1982; Hutchinson and Tvergaard, 1989) to represent a periodic distribution of voids; but in the present computations, very low void volume fractions of about $2.5 \cdot 10^{-11}$ are considered so that the studies give a good approximation of the behavior of a single void in an infinite solid. The cell model analysis gives an accurate representation of the stress history in the material near the void, since the void surface is load free throughout the deformations. By contrast, in the analyses based on coupling an inner solution to an outer solution (Huang et al., 1991; Tvergaard et al., 1992), an initial uniform stress state is enforced by applying void surface loads, which are subsequently stepped down; but this gives a somewhat inaccurate stress history in the material near the void, which may result in an inaccuracy of the path-dependent elastic-plastic solution.

The cylindrical unit cell has the initial radius R_0 and height $2H_0$ (Fig. 2). Due to symmetry about the middle plane, only half of the cell needs to be analyzed. The void at the center of the cell is taken to be ellipsoidal, with initial half-axes a_0 and b_0 in the radial and axial directions, respectively. A cylindrical reference coordinate system is used, in which x^1 is the axial coordinate, x^2 is the radial coordinate, and x^3 is the circumferential angle. In terms of the displacement components u^i on the reference base vectors and the nominal surface tractions T^i, the boundary conditions for the unit cell are, on incremental form,

$$\dot{u}^1 = 0, \quad \dot{T}^2 = \dot{T}^3 = 0, \quad \text{at } x^1 = 0 \tag{2}$$

$$\dot{u}^1 = \dot{U}_I, \quad \dot{T}^2 = \dot{T}^3 = 0, \quad \text{at } x^1 = H_0 \tag{3}$$

$$\dot{u}^2 = \dot{U}_{II}, \quad \dot{T}^1 = \dot{T}^3 = 0, \quad \text{at } x^2 = R_0 \tag{4}$$

$$\dot{T}^i = 0, \quad \text{at } \left(\frac{x^1}{b_0}\right)^2 + \left(\frac{x^2}{a_0}\right)^2 = 1. \tag{5}$$

The two constants $\dot{U}_I$ and $\dot{U}_{II}$ are displacement increments and the ratio $\dot{U}_{II}/\dot{U}_I$ is calculated in each increment such that there is a fixed prescribed ratio, $\rho = T/S$, between the macroscopic true stresses (see Tvergaard, 1982).

Constitutive relations and equilibrium equations are given here in the context of a convected coordinate formulation of the field equations. The Lagrangian strain tensor is expressed in terms of the displacement components as

$$\eta_{ij} = \frac{1}{2}\left(u_{i,j} + u_{j,i} + u^k_{,i} u_{k,j}\right) \tag{6}$$

where $(\,)_{,j}$ denotes covariant differentiation in the reference frame, indices range from one to three, and the summation convention is adopted for repeated indices. The contravariant components of the Kirchhoff stress tensor τ^{ij} and the Cauchy stress tensor σ^{ij} are related by

$$\tau^{ij} = \sqrt{G/g}\ \sigma^{ij} \tag{7}$$

where g and G are the determinants for the metric tensors g_{ij} and G_{ij} in the reference configuration and the current configuration, respectively.

The elastic-plastic material behavior is represented by a finite strain generalization of J_2 flow theory (Hutchinson, 1973). The incremental stress-strain relationship is of the form $\dot{\tau}^{ij} = L^{ijkl}\,\dot{\eta}_{kl}$, with the tensor of instantaneous moduli given by

Downloaded 03 May 2010 to 171.66.16.245. Redistribution subject to ASME license or copyright; see http://www.asme.org/terms/Terms_Use.cfm

$$L^{ijkl}=\frac{E}{1+\nu}\left\{\frac{1}{2}\left(G^{ik}G^{jl}+G^{il}G^{jk}\right)+\frac{\nu}{1-2\nu}G^{ij}G^{kl}\right.$$
$$\left.-\beta\frac{3}{2}\frac{E/E_t-1}{E/E_t-(1-2\nu)/3}\frac{s^{ij}s^{kl}}{\sigma_y^2}\right\}$$
$$-\frac{1}{2}\left(G^{ik}\tau^{jl}+G^{il}\tau^{jk}+G^{jl}\tau^{ik}+G^{jk}\tau^{il}\right) \quad (8)$$

$$\beta=\begin{cases}1, & \text{for } \sigma_e=(\sigma_e)_{\max} \text{ and } \dot{\sigma}_e\geq 0\\ 0, & \text{for } \sigma_e<(\sigma_e)_{\max} \text{ or } \dot{\sigma}_e<0.\end{cases} \quad (9)$$

Here $\sigma_e = (3s_{ij}s^{ij}/2)^{1/2}$ is the effective Mises stress, $s^{ij} = \tau^{ij} - G^{ij}\tau^k_k/3$ is the stress deviator tensor, E is Young's modulus, and ν is Poisson's ratio. The tangent modulus E_t is the slope of the uniaxial true stress versus natural strain curve, which is here represented by a piecewise power law

$$\epsilon=\begin{cases}\dfrac{\sigma}{E}, & \text{for } \sigma\leq\sigma_y\\ \dfrac{\sigma_y}{E}\left(\dfrac{\sigma}{\sigma_y}\right)^{1/N}, & \text{for } \sigma>\sigma_y.\end{cases} \quad (10)$$

The finite strain generalization of J_2 flow theory employed here is formulated directly in terms of Kirchhoff stresses rather than Cauchy stresses (see Hutchinson, 1973), and thus the value of the effective Mises stress σ_e used in (8) and (9) is $\sqrt{G/g}$ times the corresponding effective stress value Σ_e defined in terms of Cauchy stresses. This difference is small, since G/g differs from unity only due to elastic compressibility.

3 Numerical Method

The equations of equilibrium are expressed in terms of the principle of virtual work, and a numerical solution is obtained by a linear incremental solution procedure. The equations governing the stress increments $\Delta\tau^{ij}$, the strain increments $\Delta\eta_{ij}$, etc., are obtained by expanding the principle of virtual work about the current state, using (6). To lowest order the incremental equation is

$$\int_V\left\{\Delta\tau^{ij}\delta\eta_{ij}+\tau^{ij}\Delta u^k_{,i}\delta u_{k,j}\right\}dV$$
$$=\int_A\Delta T^i\delta u_i dA-\left[\int_V\tau^{ij}\delta\eta_{ij}dV-\int_A T^i\delta u_i dA\right] \quad (11)$$

where V and A are the volume and surface, respectively, of the body in the reference configuration, and T^i are contravariant components of the nominal surface tractions. The bracketed terms are included to prevent drifting of the solution away from the true equilibrium path.

The meshes used in the incremental finite element solutions consists of quadrilaterals, each built up of four triangular, linear displacement elements. The integrals in (11) are evaluated at one central point within each element. An example of a mesh used for the analyses is shown in Fig. 3, illustrating both the outer mesh in the half unit cell analyzed and the central part of the mesh near a void with $a_0/b_0 = 4$.

A special Rayleigh-Ritz finite element method (Tvergaard, 1976) is used to be able to prescribe a node displacement at the void surface rather than the end displacement U_I without applying a load on the void surface. This improves the numerical stability near the occurrence of a cavitation instability where $\dot{U}_i \to 0$.

The average straining of the void is determined from the average displacement gradients F_{ij}, referring to a Cartesian frame, which are calculated as

$$F_{ij}=\delta_{ij}+\frac{1}{V}\int_A u_i n_j dA. \quad (12)$$

Here δ_{ij} is the Kronecker delta, V and A are the volume and surface, respectively, in the reference frame, and u_i and n_j are the Cartesian components of the displacements and the outward unit normal. The axial and transverse components of the gradient, F_{11} and $F_{22} = F_{33}$, respectively, are then used to define average half-axes a and b of the deformed void, such that

$$a=F_{22}a_0,\ b=F_{11}b_0. \quad (13)$$

Based on these average half-axes, the development of the ratio a/b will be used to illustrate the void shape changes during growth.

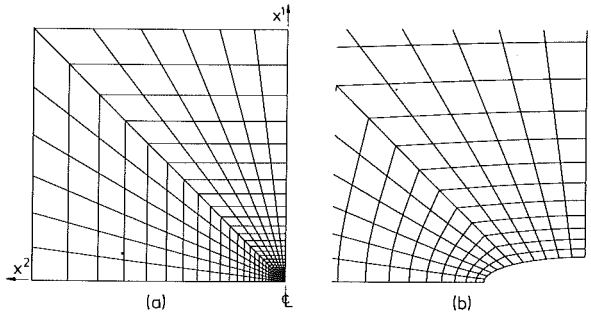


Fig. 3 Mesh used for numerical analyses; (*a*) outer mesh in half-unit cell, (*b*) inner mesh near a void with $a_0/b_0 = 4$

4 Results

The analyses to be presented here are carried out for a power-hardening material with $N = 0.1$ and $\sigma_y/E = 0.003$, and the value of Poisson's ratio is taken to be $\nu = 0.3$. Furthermore, the ratio of the average true stresses, $\rho = T/S$, is kept constant in each case studied, and thus the results to be presented are directly comparable with the curve for $N = 0.1$ shown in Fig. 1, obtained by Tvergaard et al. (1992) for initially spherical voids.

Figure 4 shows results obtained for remote hydrostatic tension, $T/S = 1$. Thus here the stress and strain fields far from the void satisfy conditions of spherical symmetry, as is directly shown by the numerical solutions, but near the voids spherical symmetry breaks down, and general axisymmetric fields develop due to the ellipsoidal initial void shapes.

As a measure of the void dilatation rate the development of $\dot{V}/(\dot{\epsilon}_1 V)$ is shown in Fig. 4(*a*), normalized by its value at $V/V_0 = 2$. Here, V_0 and V are the initial and current void volumes, respectively, and $\epsilon_1 = \ln(1 + U_1/H_0)$ denotes the average logarithmic strain in the x^1-direction. For $S \geq T$, where $\dot{\epsilon}_1 > 0$ if $\dot{S} > 0$, the occurrence of a cavitation state is determined by the condition that $\dot{V}/(\dot{\epsilon}_1 V)$ is unbounded as the stress state is approached from below. This is clearly illustrated by the plot of the normalized dilatation rate versus V/V_0 in Fig. 4(*a*), which shows that $\dot{V}/(\dot{\epsilon}_1 V)$ grows rapidly as the void volume increases. The occurrence of cavitation instabilities in this case of remote hydrostatic tension is also illustrated by the fact that the slope becomes zero for the curves of S/σ_y versus V/V_0 in Fig. 4(*c*). It is noted that the numerical stability of the computations decays as the void volume grows very large, leading to a strongly distorted mesh. Therefore, the predicted dilatation rates $\dot{V}/(\dot{\epsilon}_1 V)$ start to oscillate at the end of the computations shown in Fig. 4 after the stage illustrated by the curves in Fig. 4(*a*).

Downloaded 03 May 2010 to 171.66.16.245. Redistribution subject to ASME license or copyright; see http://www.asme.org/terms/Terms_Use.cfm

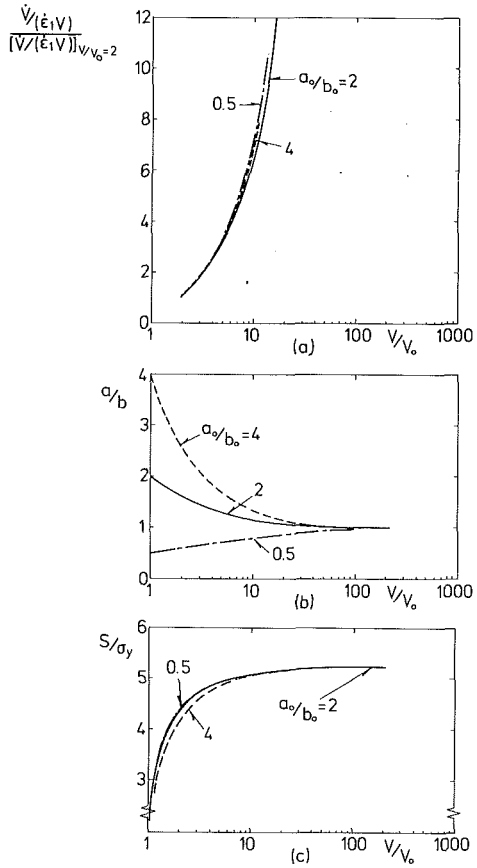


Fig. 4 Cavitation behavior versus void volume, for $T/S = 1$; (*a*) normalized dilatation rate, (*b*) void shape, (*c*) remote axial stress

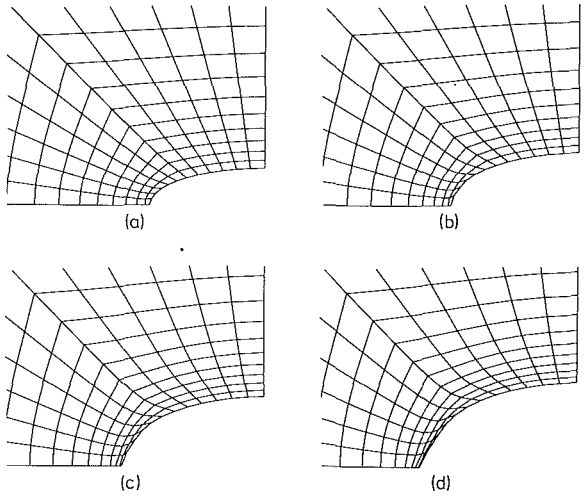


Fig. 5 Deformed inner meshes for $a_0/b_0 = 4$ and $T/S = 1$; (*a*) $V/V_0 = 1.70$, (*b*) $V/V_0 = 2.98$, (*c*) $V/V_0 = 4.67$, (*d*) $V/V_0 = 6.81$

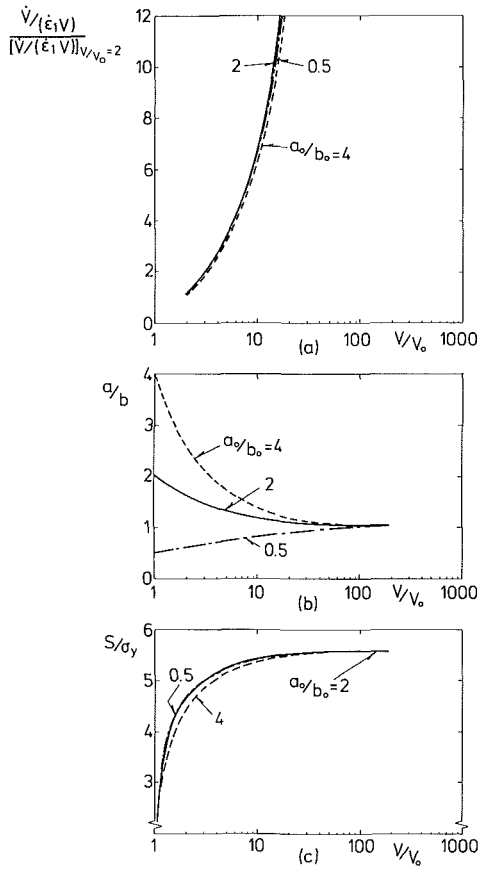


Fig. 6 Cavitation behavior versus void volume, for $T/S = 0.9$; (*a*) normalized dilatation rate, (*b*) void shape, (*c*) remote axial stress

The development of the void shape for increasing volume is illustrated by the curves of a/b versus V/V_0 in Fig. 4(b). Computations have been carried out for three different ellipsoidal shapes, $a_0/b_0 = 4$, $a_0/b_0 = 2$, and $a_0/b_0 = 0.5$, and it is seen that in all three cases the ratio a/b grows very close to unity, indicating that the growing voids become nearly spherical. Also, more extreme void shapes, $a_0/b_0 = 0.25$ and $a_0/b_0 = 6$, have been analyzed; but these computations break down numerically at an earlier stage than those shown in Fig. 4, due to strongly distorted meshes. Although these additional computations are not included in Fig. 4, it is noted that the trends are the same as those shown in the figure.

Both a circular cylindrical void and a spherical void were analyzed by Tvergaard et al. (1992), and it was found that the critical stress for cavitation instability is significantly lower in the case of a cylindrical void. Thus for the material considered here, with $N = 0.1$, $\sigma_y/E = 0.003$ and $\nu = 0.3$, the critical cavitation instability stress is 15 percent lower for a cylindrical void than that corresponding to a spherical void. In the case of ellipsoidal voids the behavior should approach that of cylindrical voids for very small values of a_0/b_0, but this tendency is not visible in Fig. 4(c). In fact, the cavitation instability stress found for $a_0/b_0 = 0.5$ is slightly smaller than that found for $a_0/b_0 = 4$, as expected, but the difference is only 0.4 percent. To obtain a cavitation instability stress closer to that for cylindrical voids, it is expected that the ratio a_0/b_0 would have to be so small that the void is still cylinder like when it has grown so large that the cavitation instability stress is approached.

Examples of mesh deformations near the void are shown in Fig. 5 for the case $a_0/b_0 = 4$, with $T/S = 1$, also illustrated in Fig. 4. These four deformed meshes correspond to rather early stages, at the values 1.70, 2.98, 4.67, and 6.81 of V/V_0; but it is seen from the corresponding curve in Fig. 4(b) that most of the void shape change takes place at this early stage. The elements around the void circumference are already strongly deformed in Fig. 5(d), since large strains develop in this region where the void surface was initially most strongly curved, and this is also the region where the most pronounced mesh distortions develop later on.

As the stress level approaches the cavitation instability limit, the strains grow very large at the void surface, and there is the

Downloaded 03 May 2010 to 171.66.16.245. Redistribution subject to ASME license or copyright; see http://www.asme.org/terms/Terms_Use.cfm

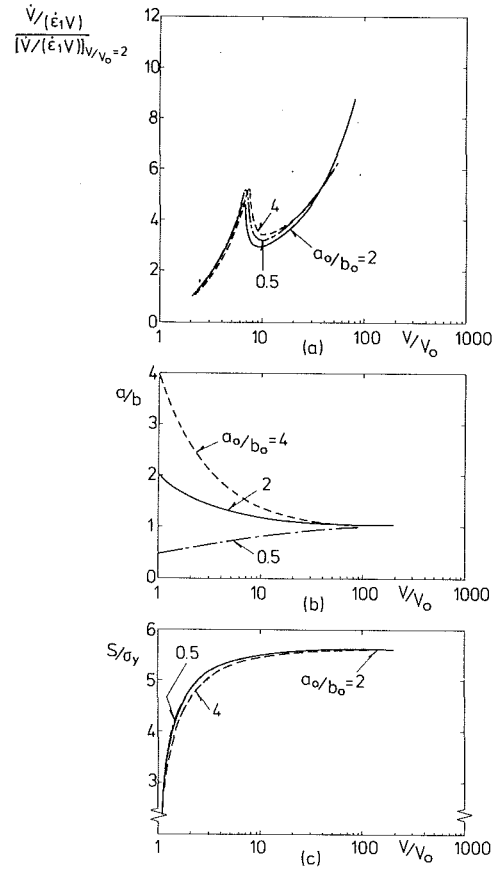


Fig. 7 Cavitation behavior versus void volume, for $T/S = 0.82$; (*a*) normalized dilatation rate, (*b*) void shape, (*c*) remote axial stress

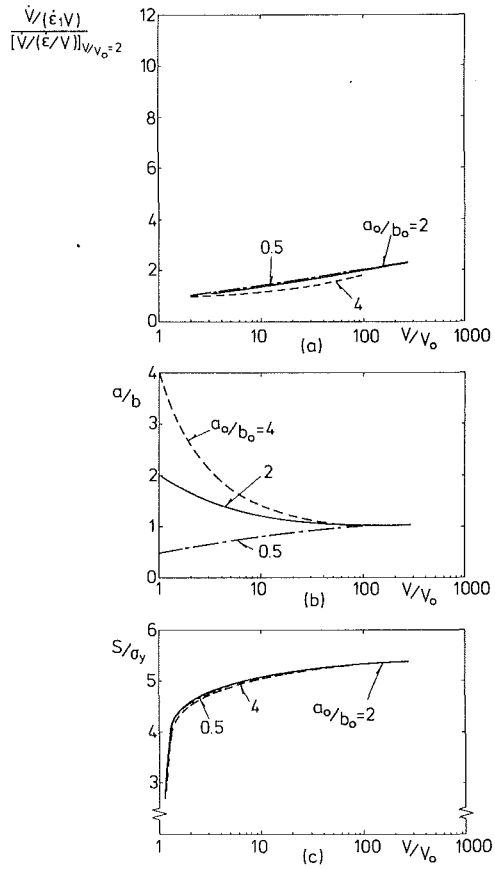


Fig. 8 Cavitation behavior versus void volume, for $T/S = 0.78$; (*a*) normalized dilatation rate, (*b*) void shape, (*c*) remote axial stress

possibility that bifurcation into a short wave surface instability takes place (see Hutchinson and Tvergaard, 1980). In the present computations the solid is characterized by the J_2 flow theory for which the surface wave bifurcation strain is essentially unattainable (apart from the special case of a very low-hardening material under plane-strain conditions). Thus in the present analyses, as well as the J_2 flow theory analyses of Huang et al. (1991) and Tvergaard et al. (1992), the occurrence of a surface instability prior to the cavitation instability is not likely. However, in analyses based on deformation theory (Hou and Abeyaratne, 1992; Tvergaard et al., 1992) the critical strains for surface instabilities and shear bands are not so large, and here the interaction with such modes of instability in the material near the void surface may have to be accounted in an accurate analysis of cavitation instabilities.

Computations have also been carried out for a remote axisymmetric stress state, $T/S = 0.9$, as illustrated in Fig. 6. As in Fig. 4, the normalized dilatation rate $\dot{V}/(\dot{\epsilon}_1 V)$ grows large at a rather early stage, indicating that a cavitation state will be reached, and this is also seen by the vanishing shape at the ends of the curves for S/σ_y versus V/V_0 in Fig. 6(*c*). Furthermore, it is noted from Fig. 6(*c*) that the limiting value of S/σ_y is larger for $T/S = 0.9$ than found in Fig. 4(*c*) for $T/S = 1$, in agreement with the results of Tvergaard et al. (1992) for initially spherical voids (see Fig. 1). Also the $T/S = 0.9$ the voids grow into a nearly spherical shape, as is seen from Fig. 6(*b*).

A common feature of the two cases $T/S = 1$ and $T/S = 0.9$ considered in Figs. 4 to 6 is that the fields far from the voids remain elastic (see also Fig. 1). For all cases in which the remote fields remain elastic Tvergaard et al. (1992) found that a cavitation state is reached, but in cases where remote plastic yielding occurs the conclusions were less clear. For an initially spherical void in a strain-hardening elastic-plastic solid, the results did indicate the occurrence of a cavitation instability under remote plastic yielding. However, for a circular cylindrical void the occurrence of an instability seemed more uncertain, even though a cavitation state was clearly predicted for the corresponding deformation theory solid, i.e., a nonlinear elastic solid (Tvergaard et al., 1992).

Figure 7 shows results for $T/S = 0.82$, which is just beyond the limit where remote yielding occurs for the material analyzed here. In this case the development of the normalized dilatation rate (Fig. 7(*a*)) differs significantly from that found in the previous two cases. Initially, the growth of $\dot{V}/(\dot{\epsilon}_1 V)$ is very similar to the results shown in Fig. 4(*a*) and 6(*a*); but then at $V/V_0 \simeq 7$, where plastic yielding initiates in regions far from the void, the normalized dilatation rates decay sharply. Subsequently, as plastic yielding continues in the outer regions of the circular cylindrical cell analyzed, $\dot{V}/(\dot{\epsilon}_1 V)$ starts to grow strongly again, and Fig. 7(*a*) as well as the vanishing slope at the ends of the curves in Fig. 7(*c*) indicate that a cavitation state will be reached for $T/S = 0.82$ during remote plastic yielding. Figure 7(*b*) shows that also in this stress state the initially ellipsoidal voids develop into near spherical shapes as they grow large.

For $T/S = 0.78$, plastic yielding in the remote fields occurs even earlier (Fig. 8). Thus remote yielding sets in at $V/V_0 < 2$ prior to the start of the curves in Fig. 8(*a*) so that these curves do not show a local maximum as that found in Fig. 7(*a*). Furthermore, the growth of the normalized dilatation rate $\dot{V}/(\dot{\epsilon}_1 V)$ as a function of V/V_0 is slow in Fig. 8(*a*), and the curves in Fig. 8(*c*) have clearly not yet reached a horizontal asymptote at the points where the computations are stopped due to numerical instabilities induced by a strongly distorted

Downloaded 03 May 2010 to 171.66.16.245. Redistribution subject to ASME license or copyright; see http://www.asme.org/terms/Terms_Use.cfm

mesh. Thus based on the computations illustrated in Fig. 8 it is not possible to conclude that a cavitation state will be reached in the J_2 flow theory solid for $T/S = 0.78$. A cavitation state may very well be reached at a later stage, but the curves in Fig. 8 indicate that the computations would have to be continued to values of V/V_0 much larger than 200 in order to approach a possible cavitation state.

5 Conclusions

The numerical results reported above demonstrate quite convincingly that, within the range of stress states for which cavitation occurs, the critical stresses themselves are virtually independent of the shape of the initial void. We suspect that the very small differences which have been computed (typically less than half a percent) are partly a consequence of numerical discretization. It has also been demonstrated that the cavitation stress states for infinitely long cylindrical voids, which are attained prior to those for finite aspect ratio voids, are not approaches for voids starting as prolate spheroids with aspect ratio less than about four ($a_0/b_0 > 0.25$). It remains an open question as to how large an aspect ratio would be required to reach a transition to the cylindrical cavitation states.

Acknowledgment

The work of JWH was supported in part by the National Science Foundation (Grant NSF-MSS-90-20141) and by the Division of Applied Sciences, Harvard University.

References

Ashby, M. F., Blunt, F. J., and Bannister, M., 1989, "Flow Characteristics of Highly Constrained Metal Wires," *Acta Metallurgica*, Vol. 37, pp. 1847–1857.

Ball, J. M., 1982, "Discontinuous Equilibrium Solutions and Cavitation in Nonlinear Elasticity," *Phil. Trans. R. Soc. Lond.*, Vol. A306, pp. 557–610.

Hill, R., 1950, *The Mathematical Theory of Plasticity*, Clarendon Press, Oxford, UK.

Horgan, C. O., 1992, "Void Nucleation and Growth for Compressible Nonlinearly Elastic Materials: an Example," *Int. J. Solids Structures*, Vol. 29, pp. 279–291.

Hou, H.-S., and Abeyaratne, R., 1992, "Cavitation in Elastic and Elastic-Plastic Solids," *J. Mech. Phys. Solids*, Vol. 40, pp. 571–592.

Huang, Y., Hutchinson, J. W., and Tvergaard, V., 1991, "Cavitation Instabilities in Elastic-Plastic Solids," *J. Mech. Phys. Solids*, Vol. 39, pp. 223–241.

Hutchinson, J. W., 1973, "Finite Strain Analysis of Elastic-Plastic Solids and Structures," *Numerical Solution of Nonlinear Structural Problems*, R. F. Hartung, ed., Vol. 17, ASME, New York.

Hutchinson, J. W., and Tvergaard, V., 1980, "Surface Instabilities on Statically Strained Plastic Solids," *Int. J. Mech. Sci.*, Vol. 22, pp. 339–354.

Hutchinson, J. W., and Tvergaard, V., 1989, "Softening Due to Void Nucleation in Metals," *Fracture Mechanics: Perspective and Directions*, ASTM STP 1020, R. P. Wei and R. P. Gongloff, eds., American Society for Testing and Materials, Philadelphia, pp. 61–83.

Tvergaard, V., 1976, "Effect of Thickness Inhomogeneities in Internally Pressurized Elastic-Plastic Spherical Shells," *J. Mech. Phys. Solids*, Vol. 24, pp. 291–304.

Tvergaard, V., 1982, "On Localization in Ductile Materials Containing Spherical Voids," *Int. J. Fracture*, Vol. 18, pp. 237–252.

Tvergaard, V., Huang, Y., and Hutchinson, J. W., 1992, "Cavitation Instabilities in a Power Hardening Elastic-Plastic Solid," *Eur. J. Mech. A/Solids*, Vol. 11, pp. 215–231.

Downloaded 03 May 2010 to 171.66.16.245. Redistribution subject to ASME license or copyright; see http://www.asme.org/terms/Terms_Use.cfm

Cyclic Viscoplastic Constitutive Equations, Part I: A Thermodynamically Consistent Formulation

J.-L. Chaboche
ONERA
29, av. de la Division Leclerc
92320 Chatillon, France

Cyclic viscoplastic constitutive equations are increasingly used for the inelastic analysis of structures under severe thermomechanical conditions. The purpose of the paper is to show how the classical models can be modified in order to follow the general principles of thermodynamics with internal variables. Using the restrictive framework of standard generalized materials, the state variables associated to various kinds of kinematic and isotropic hardening are selected. The evolution equations for these internal variables are then formulated in a slightly less restrictive form. For each hardening process, the separation of the total plastic work into energy dissipated as heat and energy stored in the material is discussed in detail.

1 Introduction

Plastic and viscoplastic constitutive equations have been greatly developed over the past 15 years, especially for applications under cyclic loadings and high temperatures. Though some of them do not consider directly the notion of back stresses (Bodner and Parton, 1975), the cyclic constitutive equations are generally based on linear and nonlinear kinematic hardening (Miller, 1976; Lee and Zaverl, 1978; Walker, 1981; Robinson, 1982; Lowe and Miller, 1983; Yao and Krempl, 1984; Watanabe and Atluri, 1986). Among these, the model developed at ONERA (Chaboche, 1977; Chaboche and Rousselier, 1983; Nouailhas, 1987, 1989) is based on the initial work of Armstrong and Frederick (1966) who have introduced what we called the nonlinear kinematic rule (NLK). It uses the superposition of several isotropic and kinematic hardening variables, each of the corresponding evolution equations being in a hardening/dynamic-recovery/thermal-recovery format.

On the other hand, thermodynamics with internal variables offers a good framework to introduce constitutive equations. It offers both a guideline and some constraints for the choice of thermodynamically consistent evolution equations. A special form uses the notion of standard generalized materials (Son and Halphen, 1975), where the complete thermoelastic-inelastic behavior is defined from the knowledge of two potentials: the thermodynamic potential to describe the present state and the dissipative potential for the irreversible evolutions (see, for example, Germain, 1973; Sidoroff, 1975; Germain et al., 1983). The constitutive equations that we have developed are thermodynamically consistent. It can be shown, either in the framework of standard generalized materials (Chaboche, 1985; Lemaître and Chaboche, 1990), or without explicitly using a dissipative potential (Chaboche, 1977; Chaboche, 1978). Such a procedure was discussed recently (Freed et al., 1991), and is used also in the present paper.

Introducing mechanical constitutive models into a thermodynamic framework allows the partition of the plastic work into the energy stored by the material and the one dissipated as heat. It is well known, from the works of Taylor and Quinney (1934) and many others, that the stored energy is only a small part of the total plastic work (between 5 and 50 percent) depending on the material and on the strain level.

The aim of the present paper is to introduce our constitutive equations into the thermodynamic framework, to discuss the various possibilities for the equations governing the different hardening variables, and to show the corresponding partitioning of the total plastic work between stored energy and energy dissipated as heat. The mechanical form of the considered constitutive equations is recalled in Section 2. The thermodynamic framework is then described in Section 3 and the consequences of the generalized normality hypothesis are discussed about the nature of the hardening state variables.

In Section 4, our viscoplastic constitutive equations are incorporated in the thermodynamic framework and the stored energies associated with the various hardening processes are considered in detail. Moreover, we discuss the form of the constitutive equations in the case of varying temperature.

We shall consider the thermomechanical behavior of viscoplastic materials; in particular, polycrystalline metals and their alloys. Each element of the material is assumed to be

Contributed by the Applied Mechanics Division of THE AMERICAN SOCIETY OF MECHANICAL ENGINEERS for publication in the ASME JOURNAL OF APPLIED MECHANICS.

Discussion on this paper should be addressed to the Technical Editor, Professor Lewis T. Wheeler, Department of Mechanical Engineering, University of Houston, Houston, TX 77204-4792, and will be accepted until four months after final publication of the paper itself in the ASME JOURNAL OF APPLIED MECHANICS.

Manuscript received by the ASME Applied Mechanics Division, Jan. 3, 1991; final revision, Aug. 17, 1992. Associate Technical Editor: C. F. Shih.

Copyright © 1993 by ASME
Downloaded 03 May 2010 to 171.66.16.245. Redistribution subject to ASME license or copyright; see http://www.asme.org/terms/Terms_Use.cfm

isotropic and to carry no stress in its initial virgin state. As the material deforms, however, anisotropies may become induced. Only kinematic anisotropy is considered in this paper. Small material displacements and rotations shall be considered to make up the deformation of the material. In a Cartesian reference configuration, the strain ϵ_{ij} is taken to be composed of elastic ϵ^e_{ij} (reversible—includes thermal strain) and inelastic or plastic ϵ^p_{ij} (irreversible) parts such that

$$\epsilon_{ij} = \epsilon^e_{ij} + \epsilon^p_{ij}, \tag{1}$$

and there is no inelastic strain in the stress-free virgin state.

In Part II of the paper, a systematic comparison of the constitutive laws with experiments is presented for both their mechanical and dissipative properties.

2 The Constitutive Equations

2.1 The Viscoplastic Potential and the Hardening Variables. They are developed in the framework of unified viscoplasticity, considering only one inelastic strain. We suppose the existence of a viscoplastic potential in the stress space. Its position, shape, and size depend on the various hardening variables. We limit ourselves to the case where the potential is a given function of the viscous stress (or overstress):

$$\Omega = DG\left(\frac{\sigma_v}{D}\right) = DG\left(\left\langle\frac{J(\sigma-\mathbf{X})-Y}{D}\right\rangle\right). \tag{2}$$

The shape of the equi-potentials is given by the distance J in the stress space. Though it is not necessary, we consider here the Von-Mises invariant

$$J(\sigma-X) = \left[\frac{3}{2}(\sigma'-\mathbf{X}'):(\sigma'-\mathbf{X}')\right]^{1/2}, \tag{3}$$

where σ' and $\mathbf{X}'$ are the deviators of the stress tensor σ and of the back stress tensor $\mathbf{X}$.[1]

Such a theory uses a combination of kinematic hardening, represented by X, and isotropic hardening, described by the evolution of the yield stress Y and of the drag stress D. The use of a yield stress introduces an elastic domain, corresponding to stress states where $J(\sigma - \mathbf{X}) - Y \leq 0$. The elastic domain can be reduced to a point by choosing $Y = 0$. In the old version of our model (Chaboche, 1977) isotropic hardening was present by the yield stress only, with a constant drag stress. On the other hand, many models use an evolutive drag stress with $Y = 0$ or a combination, like $Y = D$, in the viscoplastic theory of Perzyna. In our present developments we also use a combination, with only one independent variable R:

$$Y = k + R \qquad D = K + \omega R. \tag{4}$$

k and K are the initial values of, respectively, Y and D. However, in Sections 2 and 3 of the present paper we do not consider the restrictions (4) in order to discuss the constraints introduced by the thermodynamic framework. Let us note that, on the mechanical level, the use of one form or another is not without consequences. The isotropic hardening through the drag stress leads to an increase of the strain rate dependency, especially under cyclic conditions.

In the applications, the viscoplastic potential, that is the function G, could be particularized in various forms, power function, exponential or hyperbolic sine functions. The presently preferred choice is a sum of two power functions (as in Chaboche, 1989) which leads to a good compromise and does not increase the numerical integration difficulties associated with very stiff differential equations. Note that applications of Part II will be performed within the limiting rate-independent case. The viscoplastic strain rate is given by the normality assumption

$$\dot{\epsilon}_p = \frac{\partial\Omega}{\partial\sigma} = G'\left(\frac{\sigma_v}{D}\right)\frac{\partial\sigma_v}{\partial\sigma} = \frac{3}{2}G'\left(\frac{\sigma_v}{D}\right)\frac{\sigma'-\mathbf{X}'}{J(\sigma-\mathbf{X})} = \frac{3}{2}\dot{p}\,\frac{\sigma'-\mathbf{X}'}{J(\sigma-\mathbf{X})} \tag{5}$$

where

$$\dot{p} = \frac{\partial\Omega}{\partial\sigma_v} = G'\left(\frac{\sigma_v}{D}\right). \tag{6}$$

Let us note that p is the accumulated plastic strain, its derivative being the modulus of plastic strain rate. Here

$$\dot{p} = \left(\frac{2}{3}\,\dot{\epsilon}_p:\dot{\epsilon}_p\right)^{1/2}. \tag{7}$$

2.2 Evolution Equations for Hardening Variables. The rate equations for hardening variables obey a unique format. The back stress $\mathbf{X}$ is decomposed into independent variables $\mathbf{X}_i$, each of them being of the same rule. As shown in previous studies (McDowell and Moosbrugger, 1987; Watanabe and Atluri, 1986), two or three of such variables are sufficient to describe, very correctly, the real materials. The whole set of equations is given as follows:

$$\mathbf{X} = \sum_i \mathbf{X}_i \tag{8a}$$

$$\dot{\mathbf{X}}_i = \frac{2}{3}C_i\dot{\epsilon}_p - \Phi_{(R)}\left\langle 1 - \frac{X_{li}}{J(\mathbf{X}_i)}\right\rangle[\gamma_i\mathbf{X}_i\dot{p} + \gamma_{t_i}(J(\mathbf{X}_i))^{m_i-1}\mathbf{X}_i] \tag{8b}$$

$$\dot{R} = b(Q-R)\dot{p} - \gamma_r|R-Q_r|^{m_r}\mathrm{sign}(R-Q_r) \tag{8c}$$

$$\dot{D} = b'(Q'-D)\dot{p} - \gamma'_r|D-Q'_r|^{m'_r}\mathrm{sign}(D-Q'_r). \tag{8d}$$

In this section the yield stress Y and the drag stress D are considered as independent, as in Freed et al. (1991). In the above rate equations the hardening term is proportional to the strain rate or to its modulus $\dot{p}$. The dynamic recovery term is proportional to $\dot{p}$ and linear in the variable itself. The static recovery term (or thermal recovery) is a nonlinear function of the variable. The material coefficients C_i, bQ, $b'Q'$ indicate the rapidity of hardening (initial tangent modulus), the coefficients γ_i, b and b' play for the relative importance of dynamic recovery though γ_{t_i}, γ_r and γ'_r stands for the static thermal recovery. The temperature does not appear explicitly but all the material coefficients can be temperature dependent, especially the ones related to thermal recovery.

In the equation for back stresses $\mathbf{X}_i$, we have introduced a threshold X_{li} in the dynamic recovery term in order to improve the description of ratchetting effects (see Chaboche et al., 1991). Moreover, the function $\phi(R)$ is used to describe the change of the tangent modulus as a function of cyclic (isotropic) hardening. This function was introduced by Marquis (1979). Its form is taken as the one deduced from the endochronic theory (Valanis, 1980; Watanabe and Atluri, 1986; Chaboche, 1989).

$$\phi(R) = \frac{1}{1+R/\beta} \tag{9}$$

One of the back stresses, denoted X_p, may have an instantaneous linear hardening term, with $\gamma_p = X_{lp} = 0$ (Prager's rule). However, the corresponding thermal recovery is present ($\gamma_{tp} \neq 0$).

For the isotropic hardening, governed by R, we use for some materials the strain range memory concept (Chaboche et al., 1979), which introduces an additional variable keeping memory of the maximum plastic strain range. Such an additional possibility is not considered in the present paper.

In the practical applications of our model (see Nouailhas, 1989, 1990), we consider that yield stress and drag stress are

[1] $\langle\ \rangle$ is the MacCauley bracket, with $\langle x\rangle = x$ if $x > 0$, 0 if $x \leq 0$.

Downloaded 03 May 2010 to 171.66.16.245. Redistribution subject to ASME license or copyright; see http://www.asme.org/terms/Terms_Use.cfm

not independent with Eq. (4) which corresponds to the following values for the coefficients in Eq. (8*d*):

$$b' = b \qquad Q' = K + \omega Q$$

$$m_r' = m_r \quad Q_r' = K + \omega Q_r \quad \gamma_r' = \gamma_r \omega^{1-m_r}.$$

Let us note that the drag stress rate Eq. (8*d*) is not thermodynamically consistent, as it will be shown in Section 4. To consider independently the evolutions of the yield and of the drag stress it is necessary to drive the drag stress by the viscous part of the plastic power $\sigma_v \dot{p}$ instead of $\dot{p}$.

3 Thermodynamics With Internal Variables

3.1 Generalities.

3.1.1 The State Law. The present state of a material element is characterized by the observable variables, thermoelastic strain[2] ϵ_e, temperature T, thermal gradient ∇T, and the internal state variables denoted a_k. An inelastic material response brought about by a change in the internal variable a_k affects the future response of the material. If the a_k are taken to be scalar valued, the nonintersecting subsets of the a_k may be taken to be components of higher-order, irreducible, even-rank tensors associated with a reference configuration (Geary and Onat, 1974).

We choose the Helmoltz free energy as the thermodynamic potential

$$\Psi = u - ST \tag{10}$$

where u is the internal energy, S is the entropy, and Ψ is assumed to depend on all the independent state variables,

$$\Psi = \Psi(\epsilon_e, a_k, T, \nabla T). \tag{11}$$

Taking into account the conservation of energy, the second principle of thermodynamics reduces to the Clausius-Duhem inequality.

$$\sigma : \dot{\epsilon} - \dot{\Psi} - \dot{S}T - \frac{1}{T} q \cdot \nabla T \geq 0 \tag{12}$$

Therefore, using (11) and (1), Eq. (12) becomes

$$\left(\sigma - \frac{\partial \Psi}{\partial \epsilon_e}\right) : \dot{\epsilon}_e - \left(S + \frac{\partial \Psi}{\partial T}\right)\dot{T} - \frac{\partial \Psi}{\partial \nabla T} \cdot \frac{\partial \nabla T}{\partial t}$$

$$+ \sigma : \dot{\epsilon}_p - \frac{\partial \Psi}{\partial a_k}\dot{a}_k - \frac{1}{T} q \cdot \nabla T \geq 0. \tag{13}$$

If we assume the evolution equations for the plastic strain and the internal variables in the form

$$\dot{\epsilon}_p = \bar{\epsilon}_p(\epsilon_e, a_j, T, \nabla T)$$

$$\dot{a}_k = \bar{a}_k(\epsilon_e, a_j, T, \nabla T), \tag{14}$$

where $\bar{a}_k$ is zero for any instantaneous reversible change, we can follow the classical arguments of Coleman and Gurtin (1967). Inequality (13) must be valid for arbitrary *reversible* changes in the observable variables $\dot{\epsilon}_e$, T, $\partial \nabla T / \partial t$, so that the three first terms must vanish independently:

$$\sigma = \frac{\partial \Psi}{\partial \epsilon_e} \qquad S = -\frac{\partial \Psi}{\partial T} \qquad \frac{\partial \Psi}{\partial \nabla T} = 0. \tag{15}$$

The free energy does not depend on the thermal gradient. Equation (15*a*) is the expression for the thermoelastic law, which reduces to the Hookes law for isothermal conditions. By analogy, we express

$$A_k = \frac{\partial \Psi}{\partial a_k}, \tag{16}$$

the thermodynamic forces or affinities conjugate to the thermodynamic displacements a_k or fluxes $\dot{a}_k$. The remaining terms in (13) correspond to the dissipation inequality

$$\sigma : \dot{\epsilon}_p - A_k \dot{a}_k - \frac{1}{T} q \cdot \nabla T \geq 0. \tag{17}$$

Classically it is considered as separated into the intrinsic and thermal dissipation inequalities

$$\sigma : \dot{\epsilon}_p - A_k \dot{a}_k \geq 0 \qquad \frac{1}{T} q \cdot \nabla T \leq 0. \tag{18}$$

Usually the evolution of heat flux is represented by Fourier's equation

$$q = -\mathbf{k} \cdot \nabla T \tag{19}$$

where the symmetric tensor for thermal conductivity $\mathbf{k}$ must be positive definite in order to satisfy the thermal dissipation inequality.

Remark: The choice of evolution equations of the form (14*b*) is important. In some theories, reversible changes produce instantaneous changes of the internal variables (in the viscoplasticity theory based on overstress by Yao and Krempl (1984), for example). If we assume the evolution equation in the form

$$\dot{a}_k = \bar{a}_k(\epsilon_e, a_j, T, \nabla T) + \mathbf{H}_k(\epsilon_e, a_j, T, \nabla T) : \dot{\epsilon}_e, \tag{20}$$

we have to reconsider the Coleman's arguments and we now find

$$\sigma = \frac{\partial \Psi}{\partial \epsilon_e} + \mathbf{H}_k A_k, \tag{21}$$

which is a nonclassical form of the Hooke's law and changes the usual definition of the elastic strain. In the theory by Krempl ($k = 1$) for example, H may be considered as equal 1 and A is the equilibrium stress. Figure 1 shows schematically the isothermal tensile case, where $\sigma = E\epsilon_e + A$. In such situations, thermodynamic aspects must be reconsidered carefully. In our theory we do not accept such instantaneous reversible changes for the internal variables.

3.1.2 The Dissipative Potential. Standard Generalized Materials. In standard associated plasticity, the Hill's postulate of maximum dissipation, written in the stress space, leads to the quasi-convexity of the yield surface and defines the direction of the plastic strain rate as the outer normal to the yield surface at the present stress state. The same applies for vis-

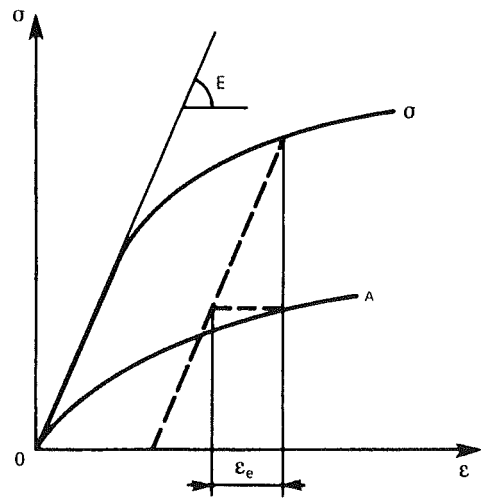


Fig. 1 The nonconventional definition of elastic strain corresponding to the introduction of a stress rate term in the evolutionary equations for the internal variables

[2]The observable variable is the total strain but for nonviscous elastic strains, provided by the use of Eq. (1), it is sufficient to consider the thermoelastic strain as the independent observable variable.

Downloaded 03 May 2010 to 171.66.16.245. Redistribution subject to ASME license or copyright; see http://www.asme.org/terms/Terms_Use.cfm

coplasticity, leading to the normality to the equi-potential surface.

Considering thermoviscoplasticity, it is possible to generalize such a postulate in order to check the second principle automatically. Materials (or constitutive theories) obeying such a principle are called "standard generalized materials." In the dissipation inequality (17), we observe the duality between rates of dissipative variables ($\dot{\epsilon}_p$, $-\dot{a}_k$, $-q/T$) and the corresponding thermodynamic forces (σ, A_k, ∇T). Following Germain (1973), we assume the existence of a potential of dissipations in the space of rate of dissipative variables

$$\phi = \phi(\dot{\epsilon}_p, \dot{\mathbf{a}}_k).$$

Here the space does not incorporate the heat flux, which was already taken into account leading to the Fourier's Eq. (19). ϕ is supposed to be positive, convex in its variables, and containing the origin—that is $\phi(0, 0) = 0$. The thermodynamic forces are obtained as

$$\sigma = \frac{\partial \phi}{\partial \dot{\epsilon}_P} \qquad A_k = \frac{\partial \phi}{\partial (-\dot{a}_k)}.$$

Applying to ϕ the Legendre-Fenchel transform, we obtain the complementary dissipative potential ϕ^* in the generalized space of thermodynamic forces (σ, A_k)

$$\phi^* = \min_{\dot{\epsilon}_p, -\dot{a}_k} [\sigma : \dot{\epsilon}_p - A_k \dot{a}_k - \phi(\dot{\epsilon}_p, -\dot{a}_k)] = \phi^*(\sigma, A_k).$$

Equations (23) are then replaced by

$$\dot{\epsilon}_p = \frac{\partial \phi^*}{\partial \sigma} \qquad \dot{a}_k = \frac{\partial \phi^*}{\partial A_k}. \tag{25}$$

Such a generalized normality, in the space (σ, A_k), confers interesting properties to the constitutive equations. In particular, the Second Principle is automatically verified due to the positiveness and convexity of ϕ^*. Provided $\phi^*(0, 0) = 0$, the intrinsic dissipation (18.a) writes as

$$\sigma : \dot{\epsilon}_p - A_k \dot{a}_k = \sigma : \frac{\partial \phi^*}{\partial \sigma} + A_k \frac{\partial \phi^*}{\partial A_k} \geq \phi^* \geq 0. \tag{26}$$

Remark: In fact, the convexity of ϕ^* is not necessary. A sufficient condition is the convexity of the domains $\phi \leq \phi^*(\sigma, A_k) \leq \phi_c^*$, for every positive value ϕ_c^*.

3.2 Some Consequences of the Generalized Normality Hypothesis. In the framework of classical viscoplasticity, the notion of standard generalized materials implies some interesting consequences about the nature of internal state variables. For the purpose of simplicity, we do not consider here the recovery effects (both dynamic and static) in the evolution equations of hardening variables. Then we assume the dissipative potential of the same form that the viscoplastic potential used for developing the mechanical part of the constitutive equations:

$$\phi^* = DG\left(\left\langle \frac{J(\sigma - \mathbf{X}) - R - k}{D} \right\rangle\right). \tag{27}$$

Here the thermodynamic forces A_k are, respectively, the back stress $\mathbf{X}$, the increase of the yield stress R, and the drag stress D. If we assume $k > 0$, $D > 0$ and $G(0) = 0$, and G convex, we can easily check that ϕ^* is positive, convex, and contains origin.

Let us note, respectively, α, r, δ, the internal state variables associated to the three hardening variables $\mathbf{X}$, R, D. The generalized normality hypothesis writes

$$\dot{\epsilon}_p = \frac{\partial \phi^*}{\partial \sigma}, \quad \dot{\alpha} = -\frac{\partial \phi^*}{\partial \mathbf{X}}, \quad \dot{r} = -\frac{\partial \phi^*}{\partial R}, \quad \dot{\delta} = -\frac{\partial \phi^*}{\partial D}. \tag{28}$$

From the classical choice (27) we obtain

$$\dot{\epsilon}_p = \frac{3}{2} G' \frac{\sigma' - \mathbf{X}'}{J(\sigma - \mathbf{X})} \qquad \dot{\alpha} = \dot{\epsilon}_p$$

$$\dot{r} = G' = \sqrt{\frac{2}{3} \dot{\epsilon}_p : \dot{\epsilon}_p} = \dot{p} \qquad \dot{\delta} = -G + G' \frac{\sigma_v}{D} \tag{29}$$

where we have denoted $\sigma_v = J(\sigma - \mathbf{X}) - R - k$ the viscous stress. Therefore the internal variable associated to the kinematic hardening is the plastic strain and the one corresponding to isotropic hardening described by the evolution of the yield stress is the accumulated plastic strain. For the isotropic hardening through the drag stress evolution a simple answer is only possible if we assume G as a power function $G(x) = x^{n+1}/(n + 1)$. In that case we obtain

$$\dot{\delta} = \frac{n}{n+1} \frac{\sigma_v \dot{p}}{D}, \tag{30}$$

where $\sigma_v \dot{p}$ represents the plastic power associated to viscosity.

When neglecting recovery effects, we have seen that the generalized normality hypothesis, applied to the classical form of the viscoplastic potential (which is needed to give a thermodynamic structure to the classical theories), proves that the internal state variables associated to the kinematic, isotropic (yield), and isotropic (drag) hardening are, respectively, the plastic strain, the accumulated plastic strain, and the accumulated plastic work corresponding to the viscous stress. For the last one, if we choose the free energy as quadratic in the internal variables (as it will be done below), we can easily prove that δ^2 is proportional to this accumulated viscoplastic work. Let us remark that several theories not considering the yield stress are based on the plastic work for describing isotropic hardening (for example, the constitutive equations developed by Bodner, 1975).

For a more complete description it is necessary to introduce dynamic and static recovery terms, which can be done by modifying the dissipative potential (27) (see Lemaître and Chaboche, 1990).

4 The Cyclic Viscoplastic Constitutive Equations in the Thermodynamic Framework

To some extent, it is possible to incorporate the constitutive equations of Section 2.2 into the thermodynamic approach presented. In Section 3, using two single potentials: the free energy, for example, and the potential of dissipations (see Chaboche, 1985; Lemaitre and Chaboche, 1990). However, the use of the potential of dissipations and of the generalized normality assumption is not a necessary condition to meet the thermodynamic principles. Often it introduces constraints that are too severe. As in a recent paper (Freed et al., 1991) we do not consider it systematically but impose the second principle by proper choices for the evolution equations of state variables.

The cases of kinematic hardening, isotropic hardening with the yield evolution, and isotropic hardening with a drag stress evolution are considered successively. In every case a viscoplastic potential Ω of the form (2) is assumed, so that the plastic strain rate is given by

$$\dot{\epsilon}_p = \frac{3}{2} \dot{p} \frac{\sigma' - \mathbf{X}'}{\mathbf{J}(\sigma - \mathbf{X})}$$

$$\dot{p} = G'\left(\frac{\sigma_v}{D}\right) = G'\left(\frac{J(\sigma - \mathbf{X}) - Y}{D}\right) = \left(\frac{2}{3} \dot{\epsilon}_p : \dot{\epsilon}_p\right)^{1/2}. \tag{31}$$

4.1 Evolution Equations for Kinematic Hardening. The choice given by the normality assumption (28*b*) is not acceptable: it leads to linear kinematic hardening. Introducing nonlinearity through a nonquadratic dependency of the free

Downloaded 03 May 2010 to 171.66.16.245. Redistribution subject to ASME license or copyright; see http://www.asme.org/terms/Terms_Use.cfm

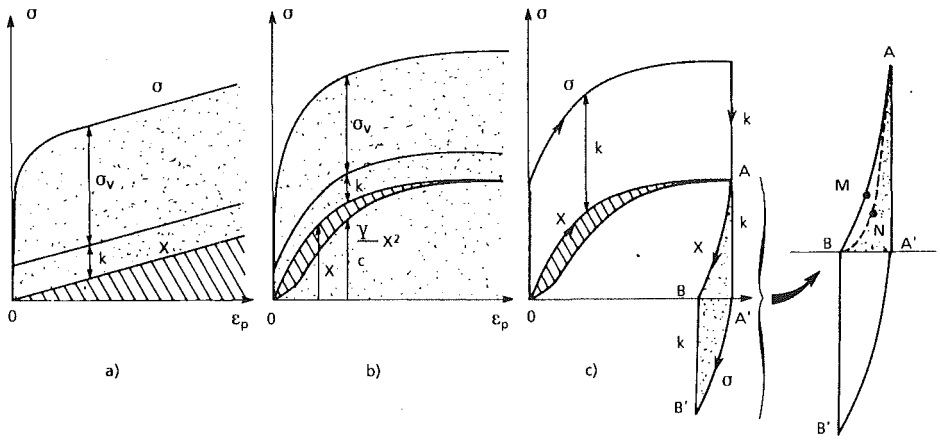


Fig. 2 Heat dissipated and stored energies for kinematic hardening; (*a*) linear kinematic hardening, (*b*) nonlinear kinematic hardening, (*c*) NLKH first compression in the rate independent case ($k = C/\gamma$)

energy upon α is not correct because it introduces a one-to-one nonlinear relationship between $\mathbf{X}$ and $\mathbf{e}_p$. The only solution is to incorporate the dynamic and static recovery terms in the rate equation of α. We continue to choose the driving (first) term as given by the normality assumption. For each individual α_i we write

$$\dot{\alpha}_i = \dot{\epsilon}_p - \frac{3}{2}\frac{\Phi(R)}{C_i}\left[\gamma_i \mathbf{X}_i \dot{p} + \gamma_{t_i}(J(\mathbf{X}_i)^{m_i - 1}\mathbf{X}_i\right]. \tag{32}$$

Moreover, the plastic part of the free energy is taken as

$$\Psi_p = \frac{1}{3}\sum_i C_i \boldsymbol{\alpha}_i : \boldsymbol{\alpha}_i \tag{33}$$

$$\mathbf{X}_i = \frac{\partial \Psi_p}{\partial \boldsymbol{\alpha}_i} = \frac{2}{3} C_i \boldsymbol{\alpha}_i \tag{34}$$

and Eq. (8*b*) is obtained for the back stress rate, at least for isothermal conditions (see Section 4.4 for the nonisothermal case). In Eq. (32) we have neglected the threshold X_{l_i} for simplicity, which does not alter the generality in that concerns dissipative aspects (when $J(\mathbf{X}_i) < X_{l_i}$ the rule (8*b*) works like the linear rule, already considered in Section 3.2).

In the case of pure kinematic hardening, the dissipation rate writes

$$\Phi = \boldsymbol{\sigma} : \dot{\boldsymbol{\epsilon}}_p - \mathbf{X}_i : \dot{\boldsymbol{\alpha}}_i = (\boldsymbol{\sigma} - \mathbf{X}) : \dot{\boldsymbol{\epsilon}}_p + \sum_i \frac{\Phi(R)}{C_i}\left[\gamma_i \dot{p} + \gamma_{t_i}(J(\mathbf{X}_i)^{m_i - 1}\right]\mathbf{J}(\mathbf{X}_i). \tag{35}$$

Taking into account the fact that $\sigma_v = \langle J(\sigma - \mathbf{X}) - k \rangle$ and $\dot{p} = 0$ if $\sigma_v = 0$, the first term equals $\sigma_v \dot{p} + k\dot{p}$ and is clearly positive as the second one, which checks easily the Second Principle (here the yield stress is constant, i.e., $R = 0$ and $Y = k$).

The dissipation rate indicates the part of the plastic power that is dissipated as heat. The difference is the stored energy rate that is also obtained by the time derivative of (33) and the use of (32). Neglecting the static recovery effects we have, for pure tension ($X_{11} = 2/3X$):

$$\dot{W}_s = \dot{\Psi}_p = \sum_i \left(X_i \dot{\epsilon}_p - \frac{\gamma_i}{C_i} X_i^2 |\dot{\epsilon}_p| \right). \tag{36}$$

Figure 2 shows schematically the parts of the plastic work which are dissipated as heat and stored in the material in simple individual cases. For a theory with one nonlinear kinematic variable (Fig. 2(*b*)), the stored energy is very small. First, its rate is increasing then decreasing, so that the ratio W_s/W_p of the stored energy to the total plastic work is increasing then decreasing. Here the total plastic work is given by integrating

$$\dot{W}_p = \sigma \dot{p} = \sigma_v \dot{p} + k\dot{p} + X\dot{p}. \tag{37}$$

We observe that the work done by the viscous stress and by the initial yield are dissipated as heat. In the case of the linear kinematic hardening ($\gamma = 0$) we have $W_s = 1/2C\epsilon_p^2$, and the ratio W_s/W_p is always increasing (Fig. 2(*a*)).

If now we consider a nonlinear kinematic rule with a tensile loading, followed by a compressive one, we observe the release of the previously stored energy when X is decreasing to zero (Fig. 2(*c*) drawn for time-independent plasticity with $X_o = C/\gamma = k$). In that case, the plastic work (area $A'B'B$) is smaller than energy dissipated as heat (area $A'B'B$ + area $AA'BM$ + area $AA'BN$). Under cyclic loadings, the energy stored by kinematic hardening is released every half cycle.

4.2 Evolution Equations for the Yield Stress. For the evolution equation of the yield stress we have two possible choices:

- *The first option* is to consider the state variable r as identical to the accumulated plastic strain for the instantaneous hardening as it is for a standard generalized material. In that case, the nonlinearity of the relationship between R and r is given by the choice of the free energy

$$\Psi_p = Qr + \frac{Q}{b}(e^{-br} - 1). \tag{38}$$

The thermodynamic force is given by

$$R = \frac{\partial \Psi}{\partial r} = Q(1 - e^{-br}) \tag{39}$$

and its rate equation (for isothermal conditions) is

$$\dot{R} = bQe^{-br}\dot{r} = b(Q - R)\dot{r}. \tag{40}$$

In order to describe static recovery we assume the evolution equation for r in the form

$$\dot{r} = \dot{p} - \frac{\gamma_r}{b}\frac{|R - Q_r|^{m_r}}{Q - R} Sg(R - Q_r). \tag{41}$$

Introduced in Eq. (40), this leads to the evolution equation of R, given by (8*c*).

Considering only the isotropic hardening ($\mathbf{X} = 0$), the dissipation rate writes

$$\Phi = \boldsymbol{\sigma} : \dot{\boldsymbol{\epsilon}}_p - R\dot{r} = J(\sigma)\dot{p} - R\dot{p} + \frac{\gamma_r}{b} R|R - Q_r|^{m_r - 1}\frac{R - Q_r}{Q - R} \tag{42}$$

with $\sigma_v = J(\sigma) - R - k$ in that case, and the two first terms write

Downloaded 03 May 2010 to 171.66.16.245. Redistribution subject to ASME license or copyright; see http://www.asme.org/terms/Terms_Use.cfm

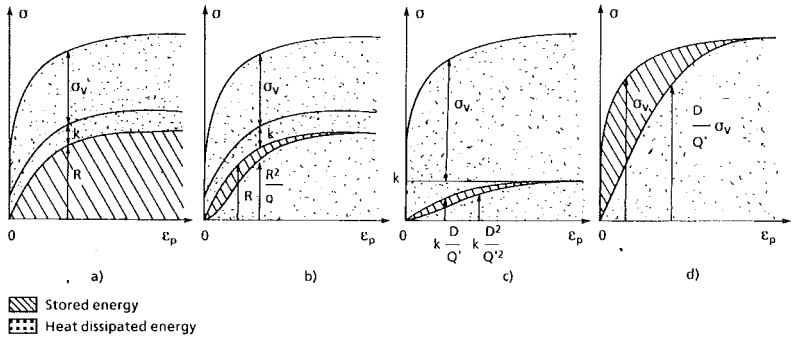


Fig. 3 Heat dissipated and stored energies for isotropic hardening; (*a*) with a yield stress, option 1; (*b*) with a yield stress, option 2, (*c*) with a drag stress, option 1, (*d*) with a drag stress, option 2

$$\sigma_v \dot{p} + k\dot{p}$$

and are positive, though the last one, corresponding to static recovery, is positive if

$$0 < Q_r < R < Q.$$

The second principle is verified if the above condition is observed. Let us note the importance of such a restriction. It eliminates the possibility for conditions such that

$$0 < R < Q_r < Q,$$

which could be used to describe some aging effects—that is hardening of the material due to time.

For this first option we observe that the stored energy associated to isotropic hardening corresponds to the whole work done by the variable R, that is the increase of the yield stress. Neglecting static recovery, we have

$$\dot{W}_s = \dot{\Psi}_p = R\dot{r} = R\dot{p}. \tag{43}$$

The work done by the viscous stress and by the initial yield is entirely dissipated as heat (Fig. 3(*a*)).

- *The second option* consists in choosing the free energy as quadratic in the internal variable r

$$\Psi_p = \frac{1}{2} bQr^2, \tag{44}$$

and the rate equation for r as

$$\dot{r} = \left(1 - \frac{R}{Q}\right)\dot{p} - \frac{\gamma_r}{bQ} |R - Q_r|^{m_r} Sg(R - Q_r). \tag{45}$$

The variable R is related to r by

$$R = \frac{\partial \Psi}{\partial r} = bQr \tag{46}$$

and its evolution equation is still identical to (8*c*).

Now the dissipation rate writes

$$\Phi = J(\sigma)\dot{p} - R\dot{p} + \frac{R^2}{Q}\dot{p} + \frac{\gamma_r}{bQ} |R - Q_r|^{m_r - 1} R(R - Q_r) \tag{47}$$

The sum of the three first terms reduces to

$$\sigma_v \dot{p} + k\dot{p} + \frac{R^2}{Q}\dot{p}$$

which is always positive, though the last one is positive if

$$0 < Q_r < R.$$

Here also it eliminates the possibility for aging effects where the static term of $\dot{R}$ is positive.

In that second option only a part of the work done by the variable R is stored in the material (neglecting static recovery)

$$\dot{W}_s = \dot{\Psi}_p = R\dot{r} = \left(R - \frac{R^2}{Q}\right)\dot{p}. \tag{48}$$

As for the nonlinear kinematic model, the ratio W_s/W_p is first increased then decreased as a function of the accumulated plastic strain (Fig. 3(*b*)). However, contrary to the kinematic model, the stored energy is not released under cyclic loadings ($\dot{p}$ is always positive). It can only be reached by the static recovery effect.

To conclude for the yield stress, the second principle is easy to verify with a restriction for Eq. (8*c*) which is that the static recovery term must be negative (a pure recovery effect)

$$\dot{R} = b(Q - R)\dot{p} - \gamma_r |R - Q_r|^{m_r}. \tag{49}$$

4.3 Evolution Equations for the Drag Stress. Here also we have two possibilities in order to respect thermodynamic restrictions. The first one can be used only if we accept a nonzero initial yield stress k. In the discussion below we neglect the static recovery terms.

- *The first option* considers the evolution equation for the state variable δ

$$\dot{\delta} = c\left(1 - \frac{D}{Q'}\right)\dot{p} \tag{50}$$

and the free energy is taken as quadratic in δ:

$$\Psi_p = \frac{1}{2}\frac{b'Q'}{c}\delta^2 \qquad D = \frac{1}{c} b'Q'\delta. \tag{51}$$

Combining (50) and (51*b*), we easily find the evolution equation (8*d*) for D (without the static recovery terms). The dissipation rate is (with $R = \mathbf{X} = 0$):

$$\Phi = \boldsymbol{\sigma} : \dot{\boldsymbol{\epsilon}}_p - D\dot{\delta} = J(\sigma)\dot{p} - cD\dot{p} + c\frac{D^2}{Q'}\dot{p} \tag{52}$$

which can be always positive only if the following condition applies.

Considering the viscous stress as $\sigma_v = J(\sigma) - k$ we obtain

$$\Phi = \sigma_v \dot{p} + \left[k - c\left(D - \frac{D^2}{Q'}\right)\right]\dot{p}$$

$$k - cD \geq 0. \tag{53}$$

The parameter c can be chosen freely. Taking $c \leq k/Q'$ is sufficient to meet the restriction. This option needs at least the use of a nonzero elastic domain ($k > 0$) but k can be chosen as small as we want. Let us note in that case the very small value of the stored energy associated to the drag stress evolution which is obtained from (with $c = k/Q'$):

$$\dot{W}_s = \dot{\Psi}_p = D\dot{\delta} = c\left(D - \frac{D^2}{Q'}\right)\dot{p} = k\frac{D}{Q'}\left(1 - \frac{D}{Q'}\right)\dot{p}. \tag{54}$$

The work done by the viscous stress is dissipated as heat and only a part of the work done by the initial yield k is stored into the material (Fig. 3(*c*) for tension).

Downloaded 03 May 2010 to 171.66.16.245. Redistribution subject to ASME license or copyright; see http://www.asme.org/terms/Terms_Use.cfm

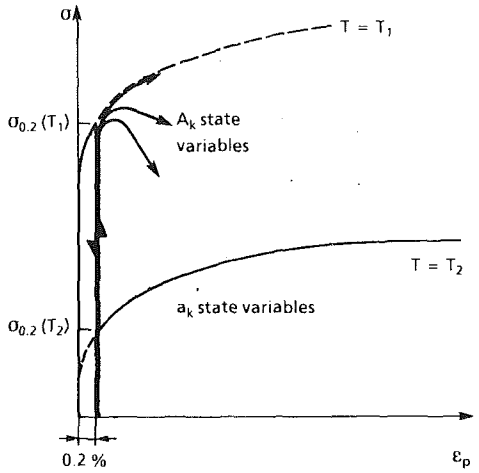


Fig. 4 Two hypothesis for the state variables after prior plastic flow under tension and a rapid temperature change from T_1 to T_2

• *The second option* consists in using in the evolution equation for δ a driving term proportional to the work done by the viscous stress, as obtained from the generalized normality assumption

$$\dot{\delta} = \left(1 - \frac{D}{Q'}\right) \frac{\sigma_v \dot{p}}{D}. \tag{55}$$

The free energy is taken as

$$\Psi_p = \frac{1}{2} b' Q' \delta^2 \qquad D = b' Q' \delta \tag{56}$$

and we obtain the dissipation rate (with $R = \mathbf{X} = 0$):

$$\Phi = J(\sigma)\dot{p} - \sigma_v \dot{p} + \frac{D}{Q'} \sigma_v \dot{p} = k\dot{p} + \frac{D}{Q'} \sigma_v \dot{p}, \tag{57}$$

which is clearly positive. Now the stored energy is defined by a small part of the work done by the viscous stress, the remaining being dissipated as heat.

$$\dot{W}_s = \dot{\Psi}_p = D\dot{\delta} = \left(1 - \frac{D}{Q'}\right) \sigma_v \dot{p} \tag{58}$$

Figure 3(*d*) illustrates this process for pure tension. Now the elastic domain may be reduced to a point ($k = 0$).

Concerning the static recovery terms, the same remarks apply than for the yield stress. Aging effect, that is static increase of the drag stress as a function of time (with $\dot{p} \simeq 0$), is not thermodynamically acceptable.

4.4 *Constitutive Equations Under Varying Temperature.* Until now the constitutive equations were considered under constant temperature. Their determination can be done at several temperature levels by isothermal tests. The coefficients of the model can depend explicitly on temperature. It is not the purpose here to define what kind of dependency. Some of the coefficients can be considered as constants and others must depend on temperature, especially the ones playing the role in the viscosity function G in (2) and in the thermal recovery terms of Eqs. (8*b–d*). Often these terms involve temperature explicitly through an Arhennius dependence.

Let us consider now the behavior of the models under varying temperature. In the present thermodynamic framework, the independent state variables are considered to be the "strain-like" variables appearing in the thermodynamic potential. They are independent of temperature in the following sense: if we consider a rapid temperature evolution that does not produce viscoplastic strains and where thermal recovery has not sufficient time to take place, the internal state variables (α_i, r, δ) do not change. However, the (dependent) associated thermodynamic forces ($\mathbf{X}_i$, R, D) can change instantaneously. In fact, the constitutive equations under varying temperature are easily deduced from the thermodynamic potential by the derivative of Eq. (16):

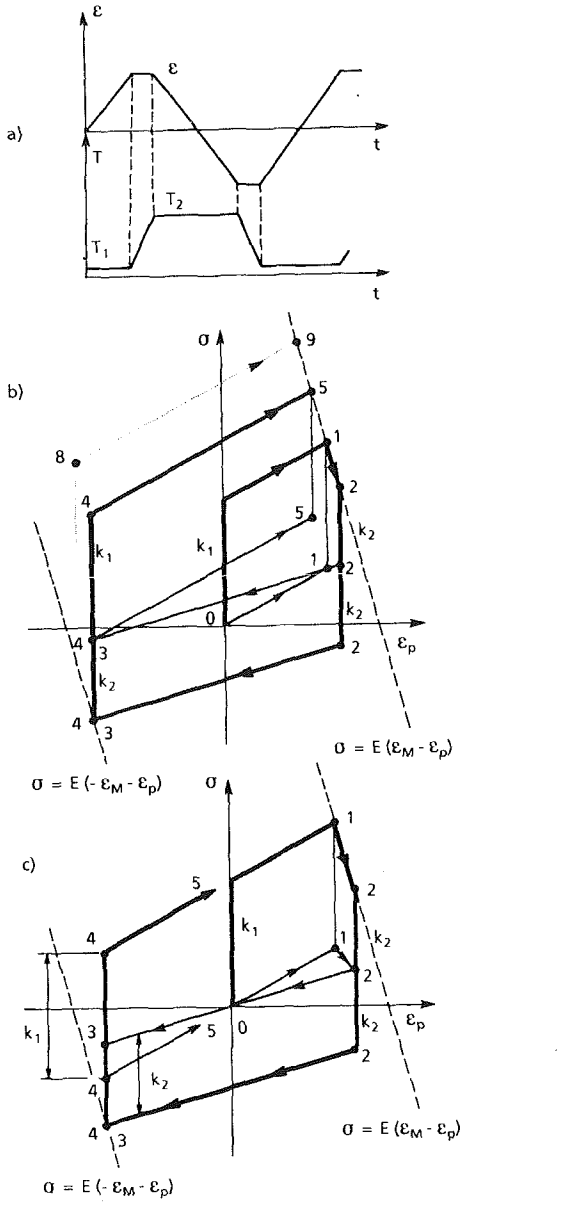


Fig. 5 A schematic example in the rate-independent case and for a linear kinematic hardening; (*a*) mechanical strain and temperature controls, (*b*) the cyclic response when considering the back stress as the state variable (without the $\dot{T}$ term in Eq. (60)), (*c*) the cyclic response when the state variables is α (with the $\dot{T}$ term in (60)).

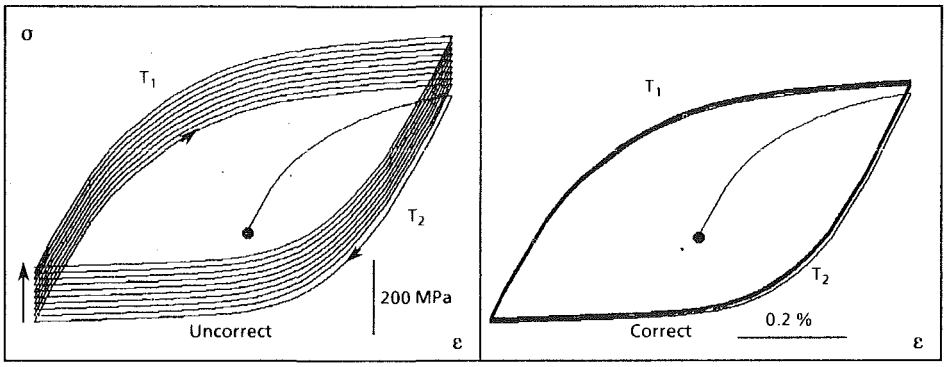
$$\dot{A}_k = \frac{\partial^2 \Psi}{\partial a_k \partial a_j} \dot{a}_j + \frac{\partial^2 \Psi}{\partial a_k \partial T} \dot{T}. \tag{59}$$

That introduces an additional temperature term in the rate equation for back stresses (with $X_{li} = 0$):

$$\dot{\mathbf{X}}_i = \frac{2}{3} C_i \dot{\epsilon}^p - \Phi(R)[\gamma_i \mathbf{X}_i \dot{p} + \gamma_{t_i} (J(\mathbf{X}_i))^{m_i - 1}] + \frac{1}{C_i} \frac{\partial C_i}{\partial T} \mathbf{X}_i \dot{T}. \tag{60}$$

Such an additional term was already considered in our first publication on constitutive models (Chaboche, 1977). It is also present in the Walker's model (1981) and, implicitly, in several other ones (as in the Miller's model (1983) where the back stress is implicitly proportional to the Young's modulus).

Downloaded 03 May 2010 to 171.66.16.245. Redistribution subject to ASME license or copyright; see http://www.asme.org/terms/Terms_Use.cfm



T_1 :	C_1 = 150 000 MPa	γ_1 = 1 000	$k(T_2) = 0.6\,k(T_1)$
	C_2 = 600 000 MPa	γ_2 = 10 000	$C_i(T_2) = 0.6\,C_i(T_1)$
	C_3 = 5 000 MPa	γ_3 = 0	$\gamma_i(T_2) = 1.8\,\gamma_i(T_1)$
	k = 50 MPa		

Fig. 6 *The same simulations as in Fig. 5 for the superposition of two NLK variables to the linear kinematic hardening; (a) no $\dot{T}$ term in Eq. (60), (b) with $\dot{T}$ term in Eq. (60).*

The presence of these additional terms has led to some discussions (see, for instance, Hartmann (1990) and Ohno et al. (1989)). It is the reason why we do insist on this point here. In fact, we may develop several arguments for the present way of writing the constitutive equations:

- On the physical level the true state is defined by the dislocation arrangements and the plastic strain incompatibilities (from grain to grain) are all quantities directly associated to the plastic strain. For the same dislocation state, if we rapidly change the temperature, we do change the Young's modulus, which immediately changes the stress fields associated to the various strain incompatibilities.
- On the phenomenological point of view we know that a great dependency of the 0.2 percent proof stress as a function of temperature is possible so that, for example,

$$\sigma_{0.2}(T_1) \gg \sigma_{\text{rupt}}(T_2) \quad \text{if} \quad T_1 \ll T_2.$$

If we imagine now a 0.2 percent monotonic tensile plastic strain at $T = T_1$, then a rapid unloading and a rapid temperature change to $T = T_2$ (without any new plastic flow) upon reloading, it is impossible to accept that the plastic flow will not begin before $\sigma_{0.2}(T_1)$. Clearly the correct behavior will be to begin plastic flow for a stress around $\sigma_{0.2}(T_2)$, as indicated schematically on Fig. 4 for a_k being the state variables.

- The last argument is given by a simple and schematic counter example where we assume only a linear kinematic hardening in the limit case of time-independent plasticity. Under uniaxial (tension compression we have $|\sigma - X| - k(T) \leq 0$) we consider a cyclic strain control (mechanical strain) between ϵ_M and $-\epsilon_M$. The strain increase is applied at the constant temperature T_1. Then strain is kept constant and the temperature changed to $T_2 > T_1$ (which produces plastic flow because $k_2 < k_1$). The strain is decreased to $-\epsilon_M$ at temperature T_2, then maintained during the temperature change. The responses corresponding to the two hypotheses are easily obtained and shown on Fig. 5(*b*) and 5(*c*). In the first case, $X = C_{(T)}\epsilon_p$ is the state variable, though in the second one the state variable is $\alpha = \epsilon_p$ and X changes during the temperature change. Clearly the first assumption leads to the ridiculous result involving a "stress ratchetting," illustrated in Fig. 5(*b*) by $\delta\sigma = \sigma_5 - \sigma_1 = \sigma_9 - \sigma_5 \ldots$, though the first cycle is correctly closed with the second assumption. Figure 6 shows a more realistic comparison where two NLK models are superposed to the linear one. The coefficients at T_1 are indicated on the figure and the ratio between values of k and C_i at T_2 and at T_1 is 0.6 (the ratio between values of γ_i is 1.8). Here also we observe the nonadmissible result given by the first hypothesis.

We may conclude this section by a short discussion about the temperature history effects. They are of two different natures:

- If coefficients in the dynamic recovery terms (γ_i for kinematic hardening, b for isotropic hardening) are depending on temperature, we may observe temperature history effects in the sense that the values of the internal variable (α and r) are different for two identical plastic strains with two different temperatures, provided

$$\dot{\alpha}_i = \dot{\epsilon}_p - \gamma_i \alpha_i \dot{p} \tag{61a}$$

$$\dot{r} = \dot{p} - br\dot{p}. \tag{61b}$$

However, this history effect is rapidly evanescent for the kinematic hardening and do not modify the asymptotic conditions for isotropic hardening. Wang and Ohno (1991) have used such a dependency, together with the "memory of maximum strain range" to describe some temperature history effects in stainless steels.

- If temperature history effects are significant and not evanescent they may be described by modifying the temperature rate terms in equations like (60), which is not consistent with the thermodynamic framework. Another way is to introduce such history effects with specific internal variables having the purpose to describe the corresponding changes in the microstructure.

5 Conclusion

In this paper we have shown how a set of cyclic viscoplastic constitutive equations may be incorporated into a general thermodynamic framework. Thermodynamics with internal variables uses the free energy to describe the present state of the material. From the second principle and classical arguments we deduce the constitutive equations for reversible processes.

The dissipative processes may be described by using a dissipative potential and a generalized normality hypothesis within the framework of the standard generalized materials. In that case we show that the independent state variables associated to the various hardening processes are, respectively, the plastic strain tensor for kinematic hardening, the accumulated plastic strain for the isotropic hardening based on a yield stress evolution, and the accumulated viscoplastic work for isotropic hardening with the drag stress.

The unified viscoplastic constitutive equations developed at

Downloaded 03 May 2010 to 171.66.16.245. Redistribution subject to ASME license or copyright; see http://www.asme.org/terms/Terms_Use.cfm

ONERA have been introduced in the thermodynamic framework without using the constraints of the standard generalized materials. Several options are possible for the various hardening equations. In each case we have checked the second principle and we have shown qualitatively what part of the plastic work is stored in the material. Let us point out here the following interesting result: the constitutive assumption for the free energy and the corresponding thermoelastoplastic coupling plays an important role in specifying the stored energy. In fact, for an isotropic hardening description, there are conceptually many different ways to construct the thermodynamic framework and define the free energy function and dissipation potential, all being consistent with the phenomenological evolution equations and satisfying the second law. The systematic comparison with experimental results is the subject of the Part II of the present paper.

References

Armstrong, P. J., and Frederick, C. O., 1966, "A Mathematical Representation of the Multiaxial Bauschinger Effect," CEGB Report RD/B/N 731.

Bodner, S. R., and Partom, Y., 1975, "Constitutive Equations for Elastic Viscoplastic Strain-Hardening Materials," ASME JOURNAL OF APPLIED MECHANICS, Vol. 42, pp. 385–389.

Chaboche, J. L., 1977, "Viscoplastic Constitutive Equations for the Description of Cyclic and Anisotropic Behaviour of Metals," *Bull. de l'Acad. Polonaise des Sciences*, Série Sc. et Techn., 17th Polish Conf. on Mechanics of Solids, Szczyrk, 1975, Vol. 25, pp. 33–41.

Chaboche, J. L., 1978, "Description Thermodynamique et Phénoménologique de la Viscoplasticité Cyclique Avec Endommagement," Thèse Paris VI.

Chaboche, J. L., 1985, "On the Constitutive Equations of Materials Under Monotonic or Cyclic Loadings," *La Recherche Aérospatiale, 1983-5*, pp. 31–43.

Chaboche, J. L., 1989, "Constitutive Equations for Cyclic Plasticity and Cyclic Viscoplasticity," *Int. J. of Plasticity*, Vol. 5, No. 3, pp. 247–302.

Chaboche, J. L., 1991, "On Some Modifications of Kinematic Hardening to Improve the Description of Ratchetting Effects," *Int. J. of Plasticity*, Vol. 7, No. 7, pp. 661–678.

Chaboche, J. L., Dang-Van K., and Cordier, G., 1979, "Modelization of the Strain Memory Effect on the Cyclic Hardening of 316 Stainless Steel," SMIRT-5, Division L, Berlin.

Chaboche, J. L., and Rousselier, G., 1983, "On the Plastic and Viscoplastic Constitutive Equations, Parts I and II," ASME *Journal of Pressure Vessel Technology*, Vol. 105, pp. 153–164.

Chaboche, J. L., Nouailhas, D., Pacou, D., and Paulmier, P., 1991, "Modeling of the Cyclic Response and Ratchetting Effects on INCONEL 718 Alloy," *European J. of Mechanics*, Vol. 10, No. 1, pp. 101–121.

Coleman, B. D., and Gurtin, M. E., 1967, "Thermodynamics With Internal State Variables," *J. Chem. Phys.*, Vol. 47, pp. 597–612.

Franchi, A., Genna, F., and Paterlini, F., 1990, "Research Note on Quasi-Connexity of the Yield Function and Its Relation to Drucker's Postulate," *Int. J. Plasticity*, Vol. 6, pp. 369–375.

Freed, A. D., et al., 1991, "Viscoplasticity: A Thermodynamic Formulation," NASA TM-102388.

Geary, J. A., and Onat, E. T., 1974, "Representation of Non-Linear Hereditary Mechanical Behavior," ORNL TM-4525.

Germain, P., 1973, *Cours de Mécanique des Milieux Continus*, Tome I, Masson, Paris.

Germain, P., Nguyen, Q. S., and Suquet, P., 1983, "Continuum Thermodynamics," ASME JOURNAL OF APPLIED MECHANICS, Vol. 50, pp. 1010.

Halpen, B., and Nguyen, Q. S., 1975, "Sur les Matériaux Standards Généralisés," *J. Mécanique*, Vol. 14, No. 1, pp. 39–63.

Hartmann, G., 1990, "Comparison of the Uniaxial Behavior of the Inelastic Constitutive Models of Miller and Walker by Numerical Experiments," *Int. J. Plasticity*, Vol. 6, pp. 189–206.

Lee, D., and Zaverl, Jr., F., 1978, "A Generalized Strain Rate Dependent Constitutive Equation for Anistropic Metals," *Acta Metallurgica*, Vol. 29, pp. 1771–1780.

Lemaitre, J., and Chaboche, J. L., 1990, *Le Mécanique des Matériaux Solides*, Dunod, Paris (English Ed. by Cambridge University Press, 1985).

Lowe, T. C., and Miller, A. K., 1983, "Improved Constitutive Equations for Modeling Strain Softening, Parts I and II," ASME *Journal of Engineering Materials and Technology*, Vol. 106, pp. 337–348.

McDowell, D. L., and Moosbrugger, J. C., 1987, "A Generalized Rate-Dependent Bounding Surface Model," ASME PVP-129, p. 1.

Marquis, D., 1979, "Etude Théorique et Vérification Expérimentale d'un Modèle de Plasticité Cyclique," Thèse, Paris VI.

Miller, A. K., 1976, "An Inelastic Constitutive Model for Monotonic Cyclic and Creep Deformation," ASME *Journal of Engineering Materials and Technology*, Vol. 98, No. 2, pp. 97–105; 106–113.

Nouailhas, D., 1987, "A Viscoplastic Modelling Applied to Stainless Steel Behaviour," Second Int. Conf. on Constitutive Laws for Engineering Materials: Theory and Application, Tucson, Desai et al. eds., pp. 717–724.

Nouailhas, D., 1989, "Unified Modelling of Cyclic Viscoplasticity: Application to Austenitic Stainless Steels," *Int. J. of Plasticity*, Vol. 5, pp. 501–520.

Nouailhas, D., 1990, "Prediction of Ratchetting and Creep Effects at Room Temperature on 304 Stainless Steel," *Res Mechanica*, Vol. 30, pp. 223–242.

Ohno, N., Takahuashi, Y., and Kuwabaka, K., 1989, "Constitutive Modeling of Anisothermal Cyclic Plasticity of 304 Stainless Steel," ASME *Journal of Engineering Materials and Technology*, Vol. 111, pp. 106–114.

Robinson, D. N., 1982, "Constitutive Relationships for Anisotropic High-Temperature Alloys," Int. Seminar on Inelastic Analysis and Life Prediction (SMIRT 7 Post Conference), Chicago, NASA TM 83437.

Sidoroff, F., 1975, "On the Formulation of Plasticity and Viscoplasticity with Internal Variables," *Arch. Mech.*, Warsaw, Vol. 27, No. 5–6, pp. 807–819.

Taylor, G. I., and Quinney, H., 1934, "The Latent Energy Remaining in a Metal After Cold Working," *Proc. Roy. Soc., London*, p. 307.

Valanis, K. C., 1980, "Fundamental Consequences of a New Intrinsic Time Measure Plasticity as a Limit of the Endochronic Theory," *Arch. Mech.*, Vol. 32, p. 171.

Walker, K. P., 1981, "Research and Development Program for Nonlinear Structural Modeling with Advanced Time-Temperature Dependent Constitutive Relationships," Report PWA-5700-50, NASA CR-165533.

Watanabe, O., and Atluri, S. N., 1986, "Internal Time, General Internal Variable and Multi-Yield-Surface Theories of Plasticity and Creep: a Unification of Concepts," *Int. J. of Plasticity*, Vol. 2, No. 1, pp. 37–57.

Yao, D., and Krempl, E., 1984, "Viscoplasticity Theory Based on Overstress. The Prediction of Monotonic and Cyclic Proportional and Non-Proportional Loading Paths of an Aluminum Alloy," *Int. J. of Plasticity*, Vol. 1, pp. 259–274.

Downloaded 03 May 2010 to 171.66.16.245. Redistribution subject to ASME license or copyright; see http://www.asme.org/terms/Terms_Use.cfm

Cyclic Viscoplastic Constitutive Equations, Part II: Stored Energy—Comparison Between Models and Experiments

J.-L. Chaboche
ONERA,
29, av. de la Division Leclerc,
92322 Chatillon, France

The cyclic constitutive equations developed at ONERA have been incorporated into a general thermodynamic framework (Part I). In the present part, systematic comparisons are given between the model predictions and experimental data for both the mechanical response and the energy stored in the material. The models are specified in their rate—independent-form and closed-form solutions are obtained for tension-compression monotonic and cyclic conditions. By superposing one or two nonlinear kinematic rules and one isotropic hardening equation, the available experimental data are fairly well reproduced. In particular it is possible to describe the low values of stored energy, the decrease of the ratio of stored energy to total plastic work as a function of strain, and the partial release of stored energy at every half cycle of a cyclic loading.

1 Introduction

In Part I of this paper, unified viscoplastic constitutive equations developed at ONERA to describe the cyclic behavior of metallic materials were presented. The thermodynamics with internal variables has been used in order to give to these constitutive equations such a structure that they follow thermodynamic constraints, especially the Second Principle. The stored energies associated to the various hardening processes have been established theoretically. Only a small part of the work done by the back stress is stored in the material, but is released at each half cycle. For the isotropic hardening described by the yield stress evolution we have two options, as well as for the isotropic hardening described by the evolution of the drag stress (which plays role on the viscous effect).

The purpose of this second part is to compare systematically the responses of the constitutive models with experimental results, especially that concerning the energy stored in the material. The literature in this domain shows that the stored energy is only a small part of the total plastic work: between 1 and 15 percent for the pure metals or single crystals and between 5 and 50 percent in more complex alloys (see the very complete review by Bever et al., 1972). More recently it was shown by Chrysochoos (1985, 1987) that the ratio of the stored energy to the total plastic work increases rapidly at small strains (say 0.5 to 2 percent) rather than decreasing continuously. The same trends were observed for a single crystal (Rönnpagel and Schwink, 1978) and in numerical simulations made with a self-consistent model (Corvasce et al., 1988).

In the present study, the experimental results are selected from the few papers mentioned above, where both the mechanical response and the stored energy data were indicated with sufficient details. The constitutive equations are applied under their time-independent form, which allow an easier treatment without modifying significantly the results. In that case, the drag stress does not play a role.

The experimental trends for stored energy are first briefly recalled in Section 2. Hence the constitutive equations are recalled in the framework of time-independent thermoplasticity, and their responses are determined analytically in the case of uniaxial tension-compression (Section 3). In Section 4 the possibilities of these models are compared with experimental data for monotonic as well as cyclic conditions.

2 Experimental Background

Since the works of Taylor and Quinney (1934) and many others, it is well known that only a small part of the plastic work done is stored in the material. The measurements are made through the energy that is evacuated as heat by the system, using various methods of calorimetry and various interpretations. The very complete review of these methods and of the corresponding results by Bever et al. (1972) shows both the experimental difficulties and significant differences between methods, between authors, and between materials. However, the general trends are as follows:

Contributed by the Applied Mechanics Division of THE AMERICAN SOCIETY OF MECHANICAL ENGINEERS for publication in the ASME JOURNAL OF APPLIED MECHANICS.

Discussion on this paper should be addressed to the Technical Editor, Professor Lewis T. Wheeler, Department of Mechanical Engineering, University of Houston, Houston, TX 77204-4792, and will be accepted until four months after final publication of the paper itself in the ASME JOURNAL OF APPLIED MECHANICS.

Manuscript received by the ASME Applied Mechanics Division, Jan. 3, 1991; final revision, Aug. 17, 1993. Associate Technical Editor: C. F. Shih.

Copyright © 1993 by ASME
Downloaded 03 May 2010 to 171.66.16.245. Redistribution subject to ASME license or copyright; see http://www.asme.org/terms/Terms_Use.cfm

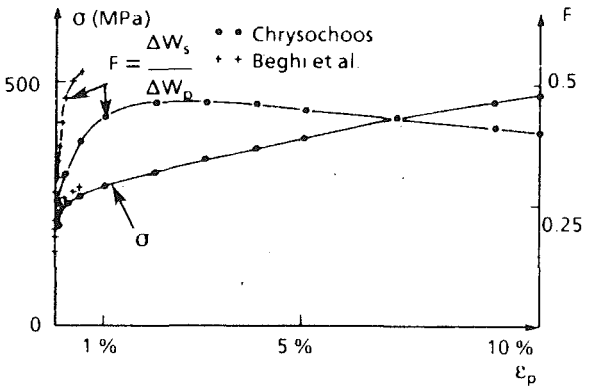


Fig. 1 The monotonous stress strain curve and the ratio $F = W_s/W_p$ for 316 stainless steel at room temperature. Data from Chrysochoos (1987) * * *, and from Beghi et al. (1986) + + +.

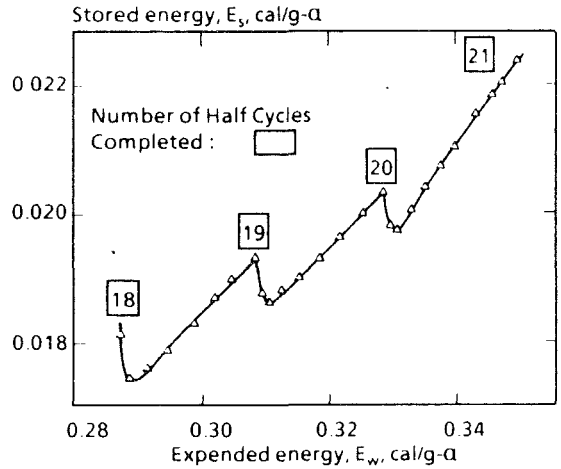


Fig. 2 Stored energy as a function of accumulated plastic work for OFHC copper. Reproduced from Halford (1966), energy units in Cal./gram-atom.

• The stored energy W_s is a very small fraction of the plastic work W_p at large strains (5 to 100 percent), especially in pure metals. Values between 1 and 15 percent are commonly reported.

• In fact, the rate of stored energy over the plastic power $\dot{W}_s/\dot{W}_p$ is great depending on the strain level, which explains the large discrepancies between global results. More often it is observed (still for significant strains) that the ratio W_s/W_p is decreasing with the plastic strain.

• The level of stored energy is larger for alloys and complex materials that have defects and complex dislocation arrangements. This is especially true for polycristalline metals used in industrial applications (see the recent study by Chrysochoos (1985, 1987) on three engineering materials). In such cases the ratio W_s/W_p may vary between 50 percent and 20 percent for moderate strains (1 percent to 10 percent).

• In some cases nonmonotonous evolution of the ratio $F = W_s/W_p$ has been reported, with an increasing evolution for small strain (lower than 0.5 to 2 percent), as shown in Fig. 1 for the 316 stainless steel (Chrysochoos, 1987; Beghi et al., 1986). The same trends were obtained in numerical simulations based on self-consistent models (see Corvasce et al., 1998, for example).

• Very few experiments have been made under cyclic strains. Figure 2 taken from Bever et al. (1972) shows results (W_s as a function of W_p) obtained by Halford (1966) on OFHC copper. At each reversal a part of the stored energy is released, the effect of which is clearly related to the kinematic nature of a part of the hardening.

Remark: The stored energy at the initial state is not necessarily zero. In the present paper W_s and W_p denote the changes of stored energy and plastic work since the initial state.

3 Study of the Model Properties in the Rate-Independent Limiting Case

One of the advantages of the unified viscoplasticity theory is to easily degenerate in a rate-independent plasticity theory when the function G in Eq. (2) of Part I is replaced by a discontinuous function (σ^* being given):

$$\sigma_v \le \sigma^* \rightarrow \Omega = 0$$

$$\sigma_v > \sigma^* \rightarrow \Omega = \infty.$$

It leads to replace the viscous stress by an increase of the elastic domain size ($k \rightarrow k + \sigma^*$). This elastic domain is of the Von-Mises type and is defined by

$$f = J(\sigma - \mathbf{X}) - R - k - \sigma^* \le 0. \tag{1}$$

Here we consider the limit viscous stress σ^* as incorporated in the initial size k of the elastic domain. In the absence of the drag effect we have to remember that the works done by k and σ_v are both dissipated as heat. Then the elastic domain is written:

$$f = J(\sigma - \mathbf{X}) - R - k \le 0. \tag{2}$$

We assume the associated plasticity and the normality rule so that the strain rate is given by

$$\dot{\epsilon}_p = \dot{\lambda} \frac{\partial f}{\partial \sigma} = \frac{3}{2} \dot{\lambda} \frac{\sigma' - \mathbf{X}'}{J(\sigma - \mathbf{X})} \tag{3}$$

where λ is the plastic multiplier determined by the consistency condition $f = \dot{f} = 0$. Here $\dot{\lambda}$ is identical to the modulus of the plastic strain rate

$$\dot{\lambda} = \dot{p} = \left(\frac{2}{3} \dot{\epsilon}_p : \dot{\epsilon}_p \right)^{1/2}. \tag{4}$$

In all comparisons made in this part of the paper, the models are taken under this rate-independent form.

The thermodynamic potential is still taken as the free energy, which plastic part contains the independent variables and is written here as follows:

$$\Psi_p = \frac{1}{3} \sum_i C_i \boldsymbol{\alpha}_i : \boldsymbol{\alpha}_i + Qp + \frac{Q - R_o}{b} (e^{-bp} - 1). \tag{5}$$

The tensors $\boldsymbol{\alpha}_i$ are the state variables associated to kinematic hardening. The back stress $\mathbf{X}$ is decomposed into the independent variables $\mathbf{X}_i$ that are the thermodynamic forces associated to $\boldsymbol{\alpha}_i$:

$$X = \sum_i \mathbf{X}_i \qquad \mathbf{X}_i = \frac{\partial \Psi_p}{\partial \boldsymbol{\alpha}_i} = \frac{2}{3} C_i \boldsymbol{\alpha}_i \tag{6}$$

For the isotropic hardening, we only consider the change of the yield stress (the drag stress does not play a role) through the first option proposed in Part I (Section 4.2). The state variable associated to isotropic hardening is the accumulated plastic strain (no thermal recovery) and we suppose that the associated force R may have a nonzero initial value R_o (due to some previous hardening). The first option corresponds to the choice of the two last terms in (5), with an exponential form leading to a simple rate equation for R (see Eq. (40) of Part I). As shown in the first part, this option leads to less heat dissipation than the second one. Then R expresses

$$R = \frac{\partial \Psi_p}{\partial p} = Q + (R_o - Q) e^{-bp}. \tag{7}$$

Downloaded 03 May 2010 to 171.66.16.245. Redistribution subject to ASME license or copyright; see http://www.asme.org/terms/Terms_Use.cfm

The evolution equations for the hardening variables associated to the kinematic hardening are taken the same as for the viscoplastic theory (Section 4.1 of Part I), but the thermal recovery terms are obviously deleted.

$$\dot{\boldsymbol{\alpha}}_i = \dot{\epsilon}_p - \frac{3}{2}\frac{\gamma_i}{C_i}\mathbf{X}_i\dot{p} \qquad \dot{\alpha}_p = \dot{\epsilon}_p \tag{8}$$

Here we neglect also the influence of isotropic hardening on the plastic tangent modulus through the function $\phi(R)$ in the recall term of (8) (compare with Eq. (32) in Part I). One of the kinematic variables may obey to the linear kinematic rule, with $\dot{\alpha}_p = \dot{\epsilon}_p$, $\mathbf{X}_p = 2/3C_p\boldsymbol{\alpha}_p$.

Let us consider one tension or compression loading with the initial conditions $p = p_o$, $X_i = X_{io}$, $R = R_o'$. In such a case, we have $\sigma = X + \nu R + \nu k$, where $\nu = \pm 1$ denotes the direction of plastic flow. $X = 2/3X_{11} = \Sigma X_i$ is the axial component of the back stress.

Integrating Eq. (8) and using $X_i = C_i\alpha_i$ and (7), we find the following relations for the hardening variables and for the current stress:

$$X_i = \nu\frac{C_i}{\gamma_i} + \left(X_{i_o} - \nu\frac{C_i}{\gamma_i}\right)e^{-\gamma_i(p-p_o)} \tag{9a}$$

$$X_p = C_p\epsilon_p = X_{p_o} + \nu C_p(p-p_o) \tag{9b}$$

$$R = Q + (R_o - Q)e^{-bp} = Q + (R_o' - Q)e^{-b(p-p_o)} \tag{9c}$$

$$\sigma = \sum_i X_i + X_p + \nu R + \nu k \tag{9d}$$

During the same loading, the plastic work done and the increment of stored energy are given by

$$\Delta W_p = \sum_i \frac{1}{\gamma_i}[C_i(p-p_o) + \nu(X_{i_o} - X_i)] + \frac{1}{2}\frac{1}{C_p}(X_p^2 - X_{p_o}^2) + Q(p-p_o) + \frac{R_o' - R}{b} + k(p-p_o) \tag{10}$$

$$\Delta W_s = \sum_i \frac{1}{2}\frac{1}{C_i}(X_i^2 - X_{o_i}^2) + \frac{1}{2}\frac{1}{C_p}(X_p^2 - X_{p_o}^2) + Q(p-p_o) + \frac{R_o' - R}{b}. \tag{11}$$

The case of the initial monotonic tension is obtained with $\nu = 1$, $R_o' = R_o$ and $X_{i_o} = X_{p_o} = p_o = 0$. We may notice several properties of the elementary models, especially in that concern the ratio of the stored energy W_s to the plastic work W_p. For the linear kinematic rule, with $C_i = Q = R_o = 0$ we have

$$W_p = kp + \frac{1}{2}C_p p^2 \qquad W_s = \frac{1}{2}C_p p^2$$

$$F = \frac{W_s}{W_p} = \frac{1}{1 + 2k/C_p p}.$$

The ratio W_s/W_p is increasing from 0 to 1, which is attained asymptotically. For the NLK model, with $C_p = Q = R_o = 0$ we find

$$W_p = \left(k + \frac{c}{\gamma}\right)p - \frac{c}{\gamma}(1 - e^{-\gamma p}) \qquad W_s = \frac{1}{2}\frac{c}{\gamma^2}(1 - e^{-\gamma p})^2$$

and the ratio W_s/W_p is firstly increasing rapidly to a maximum, then decreasing asymptotically to 0. For the isotropic model, with $C_i = C_p = 0$, we have

$$W_p = (k+Q)p - \frac{Q - R_o}{b}(1 - e^{-bp})$$

$$W_s = Qp - \frac{Q - R_o}{b}(1 - e^{-bp})$$

$$F = \frac{W_s}{W_p} = \frac{1}{1 + \dfrac{k}{Q - \dfrac{Q - R_o}{bp}(1 - e^{-bp})}}.$$

The ratio W_s/W_p is increasing from $R_o/(k+R_o)$ to $Q/(k+Q)$.

The corresponding evolutions are indicated in Fig. 3 as typical examples. In the experiments the decrease of the rate of stored energy and the decrease of the ratio W_s/W_p (see Bever et al., 1972) is usually observed. Clearly, the nonlinear kinematic model is the only one able to reproduce such trends qualitatively. Figure 4 shows the stress response and the ratio W_s/W_p for various combinations of the nonlinear kinematic models. In every case, we have the same asymptotic value $k + \Sigma_i C_i/\gamma_i$. The γ_i values are fixed and the values of C_i/γ_i are identical for the four nonlinear kinematic models. A linear kinematic model is superposed, with $C_p = 500$ MPa. We observe that the increase of nonlinearity improves both the shape of the stress strain curve and the trend for a decreasing ratio W_s/W_p.

4 Quantitative Comparisons With Experiments

4.1 Monotonic Loadings. We have selected experimental results showing both the stress strain curve and the ratio W_s/W_p. They are a single crystal of copper (99.997 percent) (Rönnpagel and Schwink, 1978) and there are engineering polycrystalline alloys, the steel XC 38, the austenitic stainless steel 316L, and the aluminum alloy 2024-T4 (Chrysochoos, 1985, 1987). All materials are tested at room temperature under uniaxial tension. Experimental results are shown by stars and dotted lines, together with the various model predictions, in Figs. 5 through 8.

The values of the parameters for every model are determined

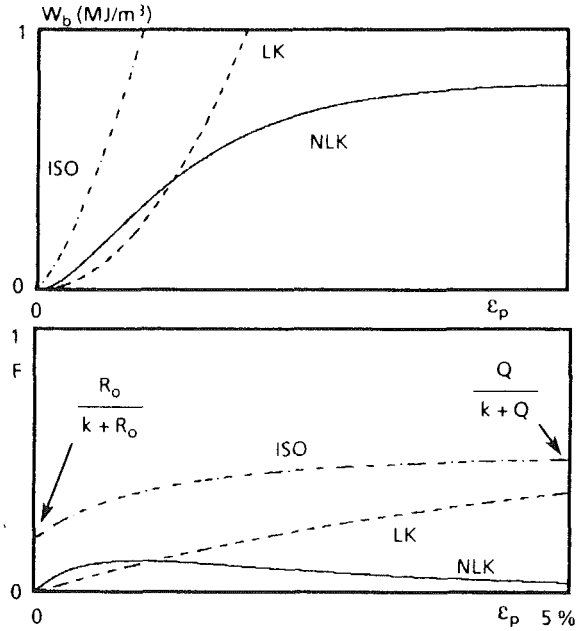


Fig. 3 Simulation of (*a*) the stored energy and (*b*) the ratio $F = W_s/W_p$. - - - - - linear kinematic hardening, $C_p = 5070$ MPa, $k = 200$ MPa ——— nonlinear kinematic hardening, $C = 16\,000$ MPa, $\gamma = 100$, $k = 200$ MPa, - · - · - · isotropic hardening, $Q = 160$ MPa, $b = 100$, $k = 160$ MPa, $R_o = 40$ MPa (the tensile curves are adjusted for ϵ_p = three percent, $\sigma = 352$ MPa).

Downloaded 03 May 2010 to 171.66.16.245. Redistribution subject to ASME license or copyright; see http://www.asme.org/terms/Terms_Use.cfm

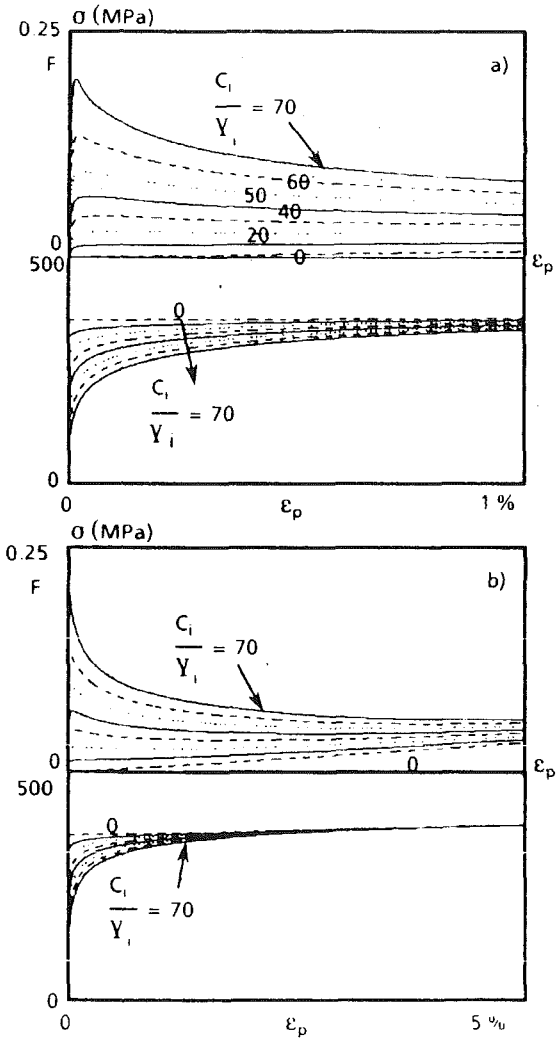


Fig. 4 Simulations of monotonic tensile curves and the ratio $F = W_s/W_p$ for NLK and LK models. C_p = 500 MMPa, γ_1 = 10 000, γ_2 = 2000, γ_3 = 500, γ_4 = 100. C_i/γ_i, i = 1, 2, 3, 4 have a common value, successively 0, 10, 20, 30, 40, 50, 60, 70 MPa. The sum $k + \Sigma C_i/\gamma_i$ = 360 MPa. (*a*) plastic strain scale: one percent; (*b*) plastic strain scale: five percent.

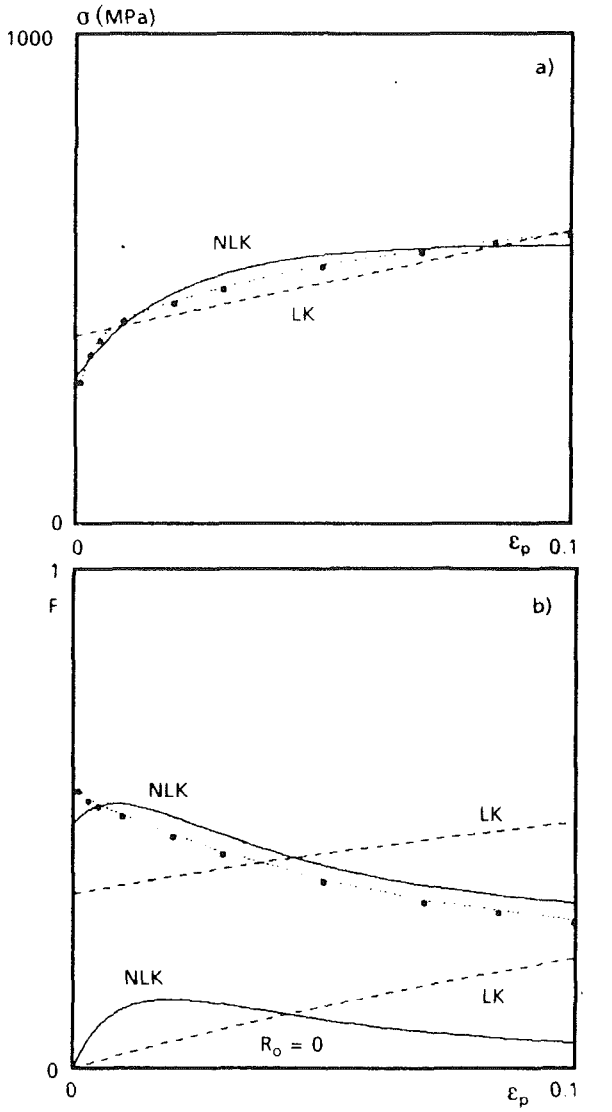


Fig. 5 Identifications of linear kinematic model and nonlinear kinematic model (one variable) with and without a saturated isotropic hardening, for XC 38 steel. (*a*) monotonic tensile curve; (*b*) corresponding ratio $F = W_s/W_p$. * - - - - * experimental data.

by the least square method from the tensile curve and the ratio $F = W_s/W_p$ (with the total scale fixed at 1000 MPa for σ and 1 for F). The weights chosen for σ and F are 3 and 1, respectively, in order to give less importance to the energy data.

Figure 5 illustrates, for the XC-38 steel, the possibilities of the simple models. The same kind of results have been obtained for the 316 SS and 2024 alloy:

- The linear kinematic hardening and the nonlinear kinematic hardening with $R_o = 0$ are able to describe approximately the tensile stress strain curve but for these polycrystalline materials, greatly underestimate the ratio F, that is the energy stored in the material.
- The superposition to them of a "saturated" isotropic hardening (given by $R_o = Q \neq 0$) does not change the stress strain curve but improves significantly the estimation of F. It corresponds to a partitioning of the initial yield stress into $k + R_o$, where the work done by k is dissipated as heat, the one corresponding to R_o being stored in the material (for the viscous model, k would be replaced by the viscous stress).
- The linear kinematic model gives an opposite trend compared to the experimental curve for the ratio F. Contrarily, the nonlinear kinematic model gives the good trends for the stress strain curve and the ratio $F = W_s/W_p$. This observation is also true for the two other polycrystals as shown by Fig. 6.

In order to improve the description of the stress strain curves, we have to superpose two nonlinear kinematic models and a saturated isotropic one for the XC 38 steel. For the 316 stainless steel and the 2023 alloy we have also superposed a nonsaturated isotropic hardening (where in fact $Q < 0$, which corresponds to softening). These better results are shown on Fig. 7. The stress strain curves and the evolution of F are well reproduced for the three materials, which can be considered as very satisfactory with such simple models. The values of the various parameters for the various models are indicated in Table 1.

In the case of single crystal, where the results depend on the tested direction, the anisotropic constitutive equations are not considered here, though the corresponding generalization of the present ones to single crystals do exist (Nouailhas and Freed, 1992). We have used three nonlinear kinematic models superposed to an isotropic one with option 1. In that case, the scale for the stress is 100 MPa. The values of the coefficients are indicated in Table 1. This simple modeling leads to fairly good simulations of both the stress strain curves and the evolutions of the ratio W_s/W_p of stored energy to plastic work (Fig. 8).

Downloaded 03 May 2010 to 171.66.16.245. Redistribution subject to ASME license or copyright; see http://www.asme.org/terms/Terms_Use.cfm

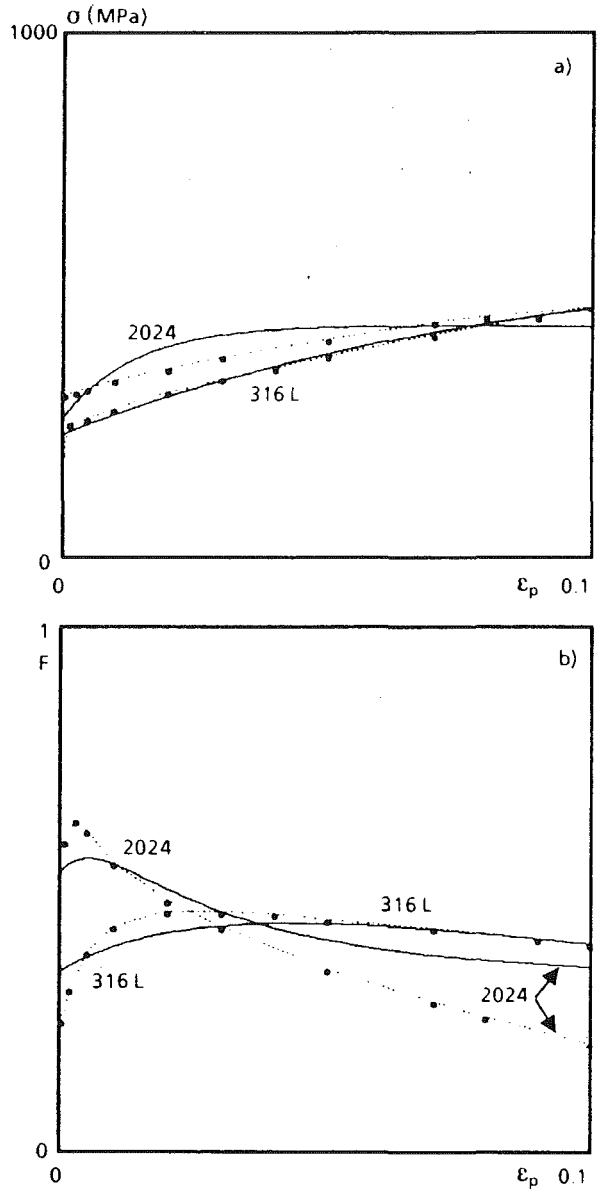


Fig. 6 Identification of nonlinear kinematic model (one variable) and a saturated isotropic hardening for 316 stainless steel and 2024 alu. alloy. (*a*) monotonic tensile curve; (*b*) corresponding ratio $F = W_s/W_p$. * - - - - * experimental data.

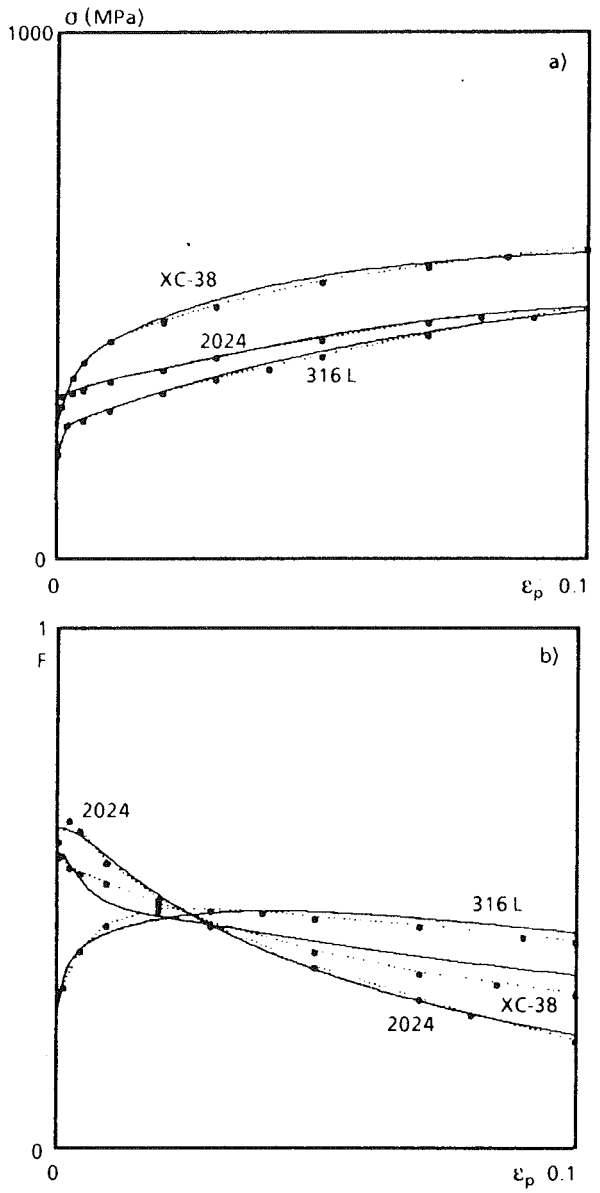


Fig. 7 The best identifications for the three materials. Two nonlinear kinematic models and one saturated isotropic hardening for XC 38. Two nonlinear kinematic models, one saturated and one nonsaturated isotropic variables for 316 stainless steel and 2024 alu. alloy. (*a*) monotonic tensile curve, (*b*) corresponding ratio $F = W_s/W_p$. * - - - - * experimental data.

4.2 Application to Cyclic Loads. In that case, we have the opportunity to observe the stored energy and its partial or complete release for each half cycle. If one uses, for example, a linear or a nonlinear kinematic hardening, the release will be complete as discussed in Section 4.1 of Part I. If we now suppose an isotropic model (option 1 or option 2), only the part corresponding to kinematic hardening is released so that we observe the evolution of the stored energy as a function of the total plastic work given by the solid line in Fig. 9. Parameters for the models are given in Table 1 and the stress-strain cyclic loops are shown Fig. 9(*a*). In that case we have selected option 2 presented in Section 4.2 of Part I for the isotropic hardening.

The solid line of Fig. 9(*b*) predicts very similar evolutions to the measurements made by Halford (1966) on an OFHC annealed copper (see also Bever et al. (1972)). Both the ratio of the accumulated values (stored energy to plastic work) and the increase/decrease at every half cycle compare satisfactorily (the experiment is given for the half cycles 19, 20, 21). Let us note here the complementarity of the mechanical measurements (stress strain curves) and energy measurements in order to make a correct partitioning between kinematic and isotropic hardening. Surprisingly, very few experimental results are reported in the literature for cyclic loadings.

In Fig. 9(*c*) for a larger number of cycles we may observe the difference between the two options for isotropic hardening (discussed in Section 4.2 of the Part I). For option 1, corresponding to Eq. (11) for ΔW_s, the average value of stored energy is increasing continuously, which seems to be the case for experimental results of Fig. 2. For option 2, the stored energy associated with isotropic hardening is $R^2/2bQ$ instead of $Q(p - p_o) + (R'_o - R)/b$, with R given by Eq. (9*c*). In that case the average stored energy increases and then stabilizes. Precise measurements under cyclic loadings for a larger number of cycles are needed in order to decide what assumption is the best one.

Downloaded 03 May 2010 to 171.66.16.245. Redistribution subject to ASME license or copyright; see http://www.asme.org/terms/Terms_Use.cfm

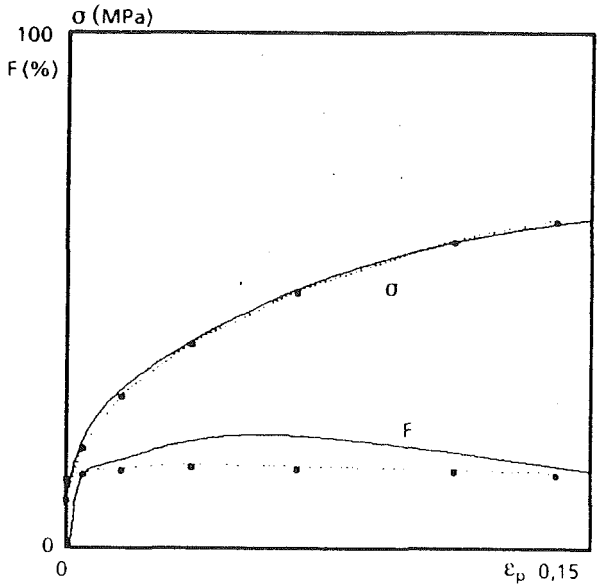


Fig. 8 Identification of the Copper single crystal (direction <100>) at room temperature (* - - - - * experimental data from Rönnpagel et al., 1978). Three nonlinear kinematic variables and one saturated isotropic variable.

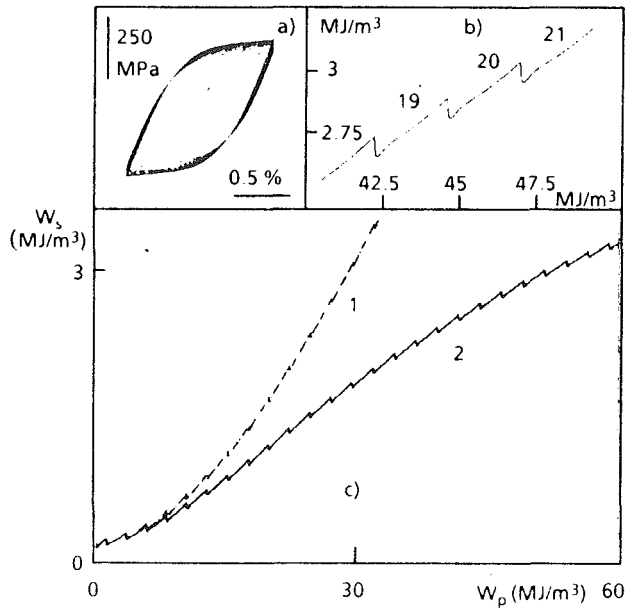


Fig. 9 Simulation with three nonlinear kinematic variables and one isotropic variable for a cyclic test under a ± 0.7 percent total strain control (E = 126 000 MPa). (*a*) the stress-strain response, (*b*) half cycles 19, 20, 21, (*c*) the 26 first half-cycles with option 1 and 2 for isotropic hardening.

Table 1. The coefficients for the various identifications and simulations

Material	Model	k	R_0	C_1 or C_p	γ_1	C_2	γ_2	C_3	γ_3	Q	b	Error
XC 38	LK without R_0	379	0	2 166	0							1 639 380
	LK with R_0	246	133	2 166	0							345 084
	NLK without R_0	295	0	13 600	50							1 389 320
	NLK with R_0	150	145	13 600	50							39 015
	2 × NLK with R_0	111	131	46 575	405	6 426	27					9 134
A 316	NLK with R_0	152	80	4 200	12							32 526
	2 × NLK + ISO + R_0	100.3	13.5	308 295	6 045	3 938	12.5			81	1 200	4 386
2024	NLK with R_0	121	137	14 060	76							127 749
	2 × NLK + ISO + R_0	117.5	184	10 764	138	7 152	24			- 173	68	1 762
Copper single crystal	3 × NLK with R_0	0.3	- 1.5	279 614	24 274	2 820	238.6	648	13.4			112.9
Cyclic simulations	LK + 3 × NLK + ISO C_p = 1 500 E = 180 000	200		10^6	10^4	200 000	1 000	15 000	100	130	8	

5 Conclusion

Unified viscoplastic constitutive equations are very useful for the complete inelastic analysis that is most often used now in the field of life prediction of structures, especially under cyclic thermomechanical loadings. The set of constitutive equations developed and used at ONERA offers good possibilities for describing many of the usually observed phenomena in the cyclic behavior of metallic materials.

Though already considered in the past (see, for example, Chaboche, 1983; Lemaître and Chaboche, 1990), the present paper was paying more attention to the thermodynamic aspects. In that case, two sets of hardening variables are used: the independent ones, or internal variables, that describe the present state of the material, and the associated thermodynamic forces (dependent variables) that play role in the viscoplastic potential.

Part I of this paper has given a simple but systematic method to incorporate the viscoplastic equation and the evolution equation for hardening variables into a thermodynamically acceptable form. For kinematic hardening, only one choice is possible though two options were proposed for each of the two forms of isotropic hardening, based either on the change of the yield stress or on the evolution of the drag stress. The partitioning of the total plastic work into energy stored in the

Downloaded 03 May 2010 to 171.66.16.245. Redistribution subject to ASME license or copyright; see http://www.asme.org/terms/Terms_Use.cfm

material and energy dissipated as heat has been qualitatively studied.

In this second part, the quantitative possibilities of the model were studied and compared to experimental data for both the mechanical behavior and the energy partitioning. The discussion was limited to the rate-independent form of the constitutive equations, which allows us to obtain closed-form solutions in the particular case of uniaxial tension compression. Several options have been studied for the part of the models which plays on the stored energy. These options do not affect the mechanical response. The model's simplest forms are selected and compared first, then for each material we study a more complicated form. The main results can be summarized as follows:

- The nonlinear kinematic hardening is the only model able to give sufficiently low values of stored energy and decreasing evolutions of the ratio W_s/W_p as a function of plastic strain that are observed experimentally under monotonic tension.
- In the case of copper single crystals (data from Rönnpagel and Schwink, 1978), the superposition of three nonlinear kinematic models is sufficient to correctly reproduce both the tensile curves and the evolution of stored energy.
- For polycrystals with complex microstructures (data from Chrysochoos, 1987), the combination of one or two nonlinear kinematic models and one isotropic hardening model is sufficient to represent the same kind of experimental results. The stored energy values being more important than for single crystals, the isotropic hardening, is taken with the first option—that is all the associated work done is stored in the material.
- Under cyclic tension compression loadings the energy stored associated to kinematic hardening is released at the beginning of every reverse loadings. The combination of nonlinear kinematic model and isotropic hardening agrees qualitatively with experimental data obtained by Halford (1966).

To our knowledge, this work is the first attempt to quantitatively check with experimental data the cyclic plastic and viscoplastic constitutive equations for their properties concerning the energy storage. The results are extremely satisfactory with the use of very simple models. Let us remark on the important role played by the isotropic hardening for the polycrystals. Two difficulties may appear: (i) the isotropic hardening induces cyclic hardening that has not been checked quantitatively due to the lack of cyclic data. (ii) the work done by the isotropic variable R is continuously stored in the material (with option 1), even when hardening is saturated (constant R value), which is difficult to interpret on a physical point of view. In order to answer these questions, systematic experimental studies under cyclic conditions could be extremely helpful including, at the same time, the measurements of the stress strain response and of the energy stored in the material.

References

Beghi, M. G., Bottani, C. E., and Caglioti, G., 1986, "Irreversible Thermo-Dynamics of Metals Under Stress," *Res. Mechanica*, Vol. 19, pp. 365–379.

Bever, M. B., Holt, D., and Titchener, A. L., 1972, "The Stored Energy of Cold Work," *Progress in Metal Science*, Vol. 17, B. Chalmers et al., eds., pp. 1–192.

Chaboche, J. L., 1983, "On the Constitutive Equations of Materials Under Monotonic or Cyclic Loadings," *La Recherche Aérospatiale, 1983–5*, pp. 31–43.

Chrysochoos, A., 1985, "Bilan énergétique en élastoplasticité, grandes déformations," *J. Mécanique Théorique et Appliquée*, Vol. 4, No. 5.

Chrysochoos, A., 1987, "Dissipation et Blocage d'énergie lors d'un écrouissage en traction simple," Thèse de Doctorat d'Etat, Université de Montpellier.

Corvasce, F., Lipinski, P., and Berveiller, M., 1988, "Stored Energy in Elasto-Plasticity of Metals," *Proceedings MECAMAT*, Int. Seminar on Inelastic Behaviour of Solids, Besançon, France, pp. 225–236.

Halford, G. R., 1966, "Stored Energy of Cold Work Changes Induced by Cyclic Deformation," Ph.D. Thesis, University of Illinois, Urbana, IL.

Lemaitre, J., and Chaboche, J. L., 1990, *La mécanique des matériaux solides*, Dunod, Paris, 1985 (English ed. by Cambridge University Press, Cambridge, MA).

Nouailhas, D., and Freed, A., 1992, "A Viscoplastic Theory for Anisotropic Materials," ASME *Engineering Materials and Technology*, Vol. 114, pp. 97–104.

Rönnpagel, D., and Schwink, C., 1978, "Measurement of the Stored Energy of Copper Single Crystals by Means of a New Deformation Calorimetry Method," *Acta Metallurgica*, Vol. 26, pp. 319–331.

Taylor, G. I., and Quinney, H., 1934, "The Latent Energy Remaining in a Metal After Cold Working," *Proc. Roy. Soc., London*, p. 307.

Downloaded 03 May 2010 to 171.66.16.245. Redistribution subject to ASME license or copyright; see http://www.asme.org/terms/Terms_Use.cfm

Elastic-Plastic Finite Element Analysis of Repeated Indentation of a Half-Space by a Rigid Sphere

E. R. Kral
Graduate Research Assistant,
Assoc. Mem. ASME.

K. Komvopoulos
Assoc. Professor,
Mem. ASME.

D. B. Bogy
Professor,
Fellow ASME.

Department of Mechanical Engineering,
University of California,
Berkeley, CA 94720

The elastic-plastic contact problem of a rigid sphere indenting a homogeneous half-space is analyzed with the finite element method. Emphasis is placed on the load range between elastic and fully plastic deformation, which has not yet been fully investigated. The rigid sphere is modeled by contact elements, thus eliminating the need to assume a particular pressure profile. Different elastic properties, with both elastic-perfectly plastic and isotropic strain hardening behaviors, are considered. Up to four complete frictionless load-unload cycles are applied to a peak load of 300 times the load necessary for the initiation of yielding. Results for the contact pressure, surface and subsurface stresses, initiation and growth of the plastic zone, and yielding of the half-space during unloading are presented. The effect of residual displacements on the contact pressure during subsequent load cycles is examined. The influence of strain hardening on the loading and residual stresses is analyzed and the consequences for crack initiation are discussed in light of these results. The accumulation of plastic strain in the yielding regions is tracked through the subsequent load cycles as the material approaches a steady-state elastic cycle, and the significance of the loading and residual stresses on the deformation characteristics is interpreted in the context of finite element results.

1 Introduction

As reliability, precision, and miniaturization of manufactured components become increasingly important, detailed analysis of the stresses and damage produced by contacting bodies becomes imperative. Knowledge of the stresses and deformations arising in contacting media, in conjunction with the resulting wear, is especially critical for precision mechanisms, such as computer hard disk drives and microelectromechanical devices, in which even small amounts of wear can be disastrous to the performance of the product. Thus understanding the stress, deformations, and stress cycles involved in the mechanics of contacting bodies is of paramount importance.

Outside the domain of metal forming, most analyses of contacting bodies involve the contact of a sphere or cylinder and a softer medium, which is also a frequently occurring phenomenon in engineering practice. The most direct macroscopic applications of such an investigation include hardness testing, the action of ball bearings in races, and the erosion of surfaces by low-velocity liquid or solid particle impact. On a smaller scale, the mechanics of precision machinery with smooth surfaces involves the contact of small surface asperities. In all these cases, the elastic behavior of the material can play an important role in the deformation behavior, even when the plastic zone is relatively large. Thus methods based on elastic-plastic constitutive models are necessary and more representative of the actual material behavior, rather than simple models based on rigid-perfectly plastic material, such as the slip-line theory of plasticity.

In the past few years, various aspects of elastic-plastic contact of rigid bodies on a half-space have been investigated. One of the earliest studies is that of Merwin and Johnson (1963), who analyzed the plane-strain rolling of a rigid cylinder on a half-space. Although important insight into the mechanics of rolling contact was obtained, several assumptions were made to allow a tractable problem. In particular, the contact pressure was assumed to remain Hertzian, the total strain cycle (elastic and plastic) was approximated by an equivalent Hertzian elastic strain cycle, and equilibrium was not necessarily satisfied during the strain cycle.

With the development of the finite element method, simplifying assumptions such as those used by Merwin and Johnson were overcome and results for various elastic-plastic contact problems were obtained. Akyuz and Merwin (1968) discussed a general methodology for the solution of elastic-plastic problems by the finite element method. Indentation was simulated by a predictor-corrector method applied to the surface nodal loads until the surface displacement matched the specified boundary of a rigid punch. Indentation by a rigid cylinder showed a significant flattening of the pressure profile and only subsurface growth of the plastic zone for the range of loads

Contributed by the Applied Mechanics Division of THE AMERICAN SOCIETY OF MECHANICAL ENGINEERS for publication in the ASME JOURNAL OF APPLIED MECHANICS.

Discussion on this paper should be addressed to the Technical Editor, Professor Lewis T. Wheeler, Department of Mechanical Engineering, University of Houston, Houston, TX 77204-4792, and will be accepted until four months after final publication of the paper itself in the ASME JOURNAL OF APPLIED MECHANICS.

Manuscript received by the ASME Applied Mechanics Division, July 17, 1992; final revision, Dec. 3, 1992. Associate Technical Editor: L. M. Keer.

Copyright © 1993 by ASME
Downloaded 03 May 2010 to 171.66.16.245. Redistribution subject to ASME license or copyright; see http://www.asme.org/terms/Terms_Use.cfm

studied. This observation was consistent with the analysis and experiments conducted by Johnson (1968), who also postulated the presence of a surface region just outside the maximum contact radius where yielding occurs upon removal of the load. Hardy et al. (1971) presented finite element results for the first load cycle of a rigid sphere indenting an elastic-perfectly plastic half-space for loads up to about 100 times the initial yield load. Indentation was simulated by specifying appropriate surface displacements. A significant departure of the contact pressure from the classical Hertzian profile was found, particularly at large loads when the pressure became almost uniform. Although the load range was sufficient to cause the plastic zone to reach the surface, a thin elastic surface region remained below the indenter even at stages of advanced plastic deformation. Dumas and Baronet (1971) performed a similar analysis for the plane-strain indentation of an elastic linear-hardening half-space by a rigid cylinder. It was again shown that flattening of the contact pressure profile occurs, and that the variation from the Hertzian pressure distribution became more pronounced for the least strain hardened material.

More recently, Follansbee and Sinclair (1984) and Sinclair et al. (1985) studied the indentation of an isotropically hardening half-space which was loaded well into the fully plastic regime, up to a load of five orders of magnitude above the initial yield load. Indentation by a rigid sphere was modeled by means of surface displacements applied to the half-space. Unloading was simulated by superposing the stresses resulting from a uniform tension applied over the contact area, which was justified on the basis of the approximate uniformity of the pressure profile in the fully plastic state. However, this approach neglected the possibility of yielding upon unloading. Hill et al. (1989) also studied indentation by a rigid sphere in the fully plastic regime using a nonlinear elastic power-law hardening model to approximate plastic behavior during loading. Bhargava et al. (1985a, 1985b) adopted the finite element technique to investigate the plane-strain problem of a cylinder rolling on a half-space, both for single and multiple passes. They assumed elastic-perfectly plastic behavior and represented the cylinder by a translating elliptical or modified elliptical pressure distribution. Based on the same assumptions and also including a linear kinematic hardening constitutive law, Kulkarni et al. (1990, 1991) analyzed the three-dimensional problem of a rigid sphere in frictionless contact with a half-space, using a translating Hertzian pressure profile to simulate loading by the sphere. Komvopoulos (1989) analyzed the plane-strain indentation of a layered half-space by a rigid cylinder using contact elements instead of an assumed pressure profile or direct application of surface displacements. It was again shown that the pressure distribution differed considerably from an elliptical profile, particularly for stiff and relatively thick layers and/or large plastic deformation, and that friction had only a secondary effect on the pressure profile.

This investigation extends the results of previous analyses by studying the mechanics of repeated elastic-plastic indentation of a half-space by a rigid sphere with loads up to 300 times the initial yield load. The sphere was modeled by contact elements, thus eliminating the need to assume a pressure profile *a priori*, and all contact was assumed to be frictionless. To study the effect of plasticity on the indentation process, both elastic-perfectly plastic and isotropic strain hardening behaviors were considered. Elastic indentation results will first be presented and compared with analytical solutions to assess the suitability of the finite element model. Results for repeated elastic-plastic indentation will then be given, and the effects of material properties on the contact pressure distribution, the evolution of the plastic zone, and the spatial variation of the stresses and strains will be investigated. The dependence of the maximum tensile principal stress on load cycles will be interpreted and the areas highly susceptible to crack initiation will be discussed. In addition, the effects of material properties on the residual displacements, the tendency for yielding due to unloading, and residual stresses produced from repeated indentation will be examined.

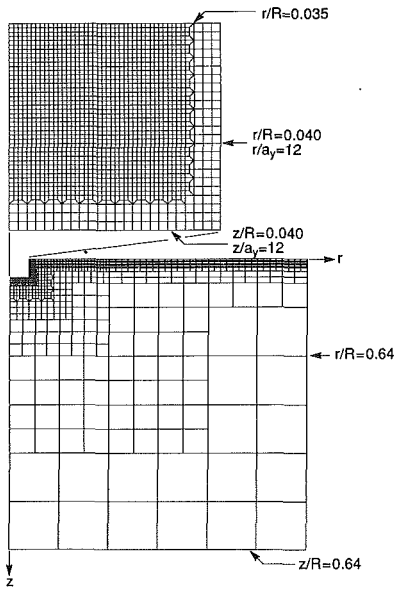


Fig. 1 Finite element discretization of the half-space

2 Modeling Procedures

2.1 Finite Element Mesh. The finite element mesh, shown in Fig. 1, consisted of 2721 four-node quadrilateral axisymmetric elements comprising 2848 nodes. A linear 2×2 integration scheme was used. The r- and z-dimensions of the mesh were equal to 960 nm. To analyze the indentation problem at a scale similar to that in microhardness testing and to avoid possible convergence problems arising from sharp edges, a rigid spherical indenter with a radius, R, equal to 1500 nm was modeled, giving a normalized mesh dimension of $r/R = z/R = 0.64$. In view of the significantly smaller magnitudes of indentation depths and contact radii, the model is representative of a blunt indenter on a half-space. Further enlargement of the mesh dimensions produced no significant effect on the results. The vertical boundaries of the mesh were constrained against displacement in the r-direction and the bottom boundary against displacement in the z-direction. The mesh is appropriate for modeling up to six 5-nm-thick layers, although only a homogeneous half-space was analyzed in this investigation. Results for repeated indentation of a layered half-space, based on the present mesh configuration, will be presented in forthcoming publications (Kral et al., 1994a,b). The central region of the mesh bounded by $r/R = 0.035$ and $z/R = 0.035$ was refined, as shown in the inset of Fig. 1, to account for the high stress gradients at the edge of the contact region. Mesh refinement was accomplished by using elements with a trapezoidal shape near the contact region and linear constraints farther away. The smallest elements were 1.25 nm square, which is about one-fourth the contact radius at initial yield. Despite some difficulties with proper contouring in the trapezoidal elements due to the nodal averaging of integration point data, the adopted refinement scheme proved satisfactory.

The sphere was modeled by a total of 44 three-node interface (contact) elements. Two nodes of each contact element corresponded to surface nodes of the half-space from the centerline to a distance $r/R = 0.04$, which was sufficient to model the anticipated contact radius. The third node was a common master node on the indenter, through which normal loads were applied incrementally to simulate the indentation process. The master node was constrained against rotation and radial dis-

Downloaded 03 May 2010 to 171.66.16.245. Redistribution subject to ASME license or copyright; see http://www.asme.org/terms/Terms_Use.cfm

placement. The contact elements calculate the penetration and interfacial sliding displacement of the rigid indenter on the deformable mesh. This information is used in surface constitutive models (contact and surface friction) to determine the surface traction. The traction is then decomposed into normal and tangential components based on the outward unit normal vector of the rigid body. In view of the marginal effect of friction in normal contact (Komvopoulos, 1988), only frictionless indentations were considered. For the zero-friction contact modeled, normal traction is applied only when the clearance between the nodes of the surface and the indenter is zero.

2.2 Plasticity Models. The simulations were performed with the multipurpose finite element code ABAQUS. This code uses an elastic-plastic constitutive model based on the assumption that the deformation gradient can be decomposed into elastic and plastic parts by a multiplicative decomposition. In order to guarantee the existence of such a decomposition, it is necessary to ensure that a stress-free configuration can be obtained without additional plastic deformation by the inverse of the elastic part of the deformation, which in turn requires that the stress at each point remains inside the yield surface (Casey and Naghdi, 1980). Since only isotropic hardening was assumed in this analysis, this condition is satisfied. According to the von Mises yield criterion adopted in this study, yielding occurred when

$$f = J_2 - k^2 = 0,$$

where k is a material constant and J_2 is the second invariant of the deviatoric stress tensor, given by

$$J_2 = \frac{1}{2} S_{ij}S_{ij}, \text{ where } S_{ij} = \sigma_{ij} - \frac{1}{3}\delta_{ij}\sigma_{kk}.$$

In terms of the uniaxial yield stress, the yield criterion reduces to

$$\sigma_M = \left[\frac{3}{2} S_{ij}S_{ij}\right]^{1/2} = \sigma^o,$$

where σ_M is the von Mises equivalent stress and σ^o is the yield stress. The material model used for plastic deformation was based on the flow rule

$$d\epsilon_{ij}^p = d\lambda S_{ij},$$

where $d\epsilon_{ij}^p$ are the components of plastic strain increment and $d\lambda$ is a function of the flow stress and the plastic strain rate. The usual assumption of negligible plastic volume change was maintained.

To examine the effect of the elastic and plastic deformation characteristics of the indented half-space on the resulting stress and strain fields, relatively compliant and stiff half-spaces with different strain hardening properties were considered. To account for boundary nonlinearities arising from the use of contact elements, an updated Lagrangian formulation was used. Isotropic strain hardening for plastically deforming material was assumed according to the relationship

$$\frac{\sigma^o}{\sigma_y} = \frac{K}{\sigma_y}\epsilon_{eq}^n,$$

where σ_y is the initial yield stress, K is the strength coefficient, n is the strain hardening exponent, and ϵ_{eq} is the equivalent plastic strain, defined as

$$\epsilon_{eq} = \int_S \left[\frac{2}{3} d\epsilon_{ij}^p d\epsilon_{ij}^p\right]^{1/2},$$

where S is the strain path. The hardening relation and flow rule apply only to yielding material for which $\sigma_M = \sigma^o$. When $\sigma_M < \sigma^o$, the usual elastic constitutive equations apply. The elastic and plastic material properties of the half-space are listed in Table 1. Poisson's ratio, ν, was assumed equal to 0.3 in all cases. The values of K were calculated from the strain hardening equation at the initial yield stress. Elastic moduli, stresses, and pressures were normalized by the initial yield stress σ_y. Loads and distances were normalized by the load, P_y, and the contact radius, a_y, respectively, corresponding to the initial yield of a half-space with properties $E/\sigma_y = 684.6$ and $n = 0.0$, known hereafter as the baseline case. Results are presented in terms of the elastic modulus ratio, β, which is obtained by normalizing the elastic modulus by that of the baseline case. The values of β used in the present study were 0.8 for a compliant half-space, 1.33 for a stiff half-space, and 1.0 for the baseline half-space. The elastic moduli were chosen to achieve contact radii at initial yield of 3.75, 5.0, and 6.25 nm for $\beta = 1.33$, 1.0, and 0.8, respectively. Small contact radii at initial yield were chosen to avoid using an excessively large number of contact elements at the highest loads.

Table 1 Elastic and plastic material properties

E/σ_y	ν	β	K/σ_y	n
547.7	0.3	0.8	1.00 6.63 23.40	0.0 0.3 0.5
684.6	0.3	1.0	1.00 7.09 26.17	0.0 0.3 0.5
912.8	0.3	1.33	1.00 7.73 30.21	0.0 0.3 0.5

2.3 Simulation of Repeated Indentation. For each set of material properties, interaction between the indenter and the half-space was studied by incrementally loading the rigid indenter in 20 steps to a maximum of 300 times the initial yield load, P_y, of the reference half-space ($\beta = 1.0$). The half-space was then unloaded incrementally following the same path. The convergence tolerance for establishing nodal force equilibrium was equal to $10^{-9}\ \sigma_y$. In most simulations, the load in each step was applied linearly in ten increments. At most 15 iterations were allowed in each increment in order to reach equilibrium within the specified tolerance. Repeated indentations were simulated by applying identical load-unload cycles until achieving either a purely elastic deformation (shakedown limit) or a maximum plastic strain increase several orders of magnitude smaller than that of the first load cycle (e.g., 10^{-6} or less).

Specialized programs were developed to analyze the results and generate plots of user-defined variables. For pre-processing, several FORTRAN subroutines were written to convert the finite element mesh data generated with the MENTAT preprocessor to input data files in the ABAQUS format. CAEDS was used to read ABAQUS results and generate contour plots of the data. The finite element calculations and post-processing were performed on an IBM RS6000 Model 540 workstation. Typical cpu times for single elastic and elastic-plastic indentations were about 10 minutes and 9.5 hours, respectively.

2.4 Verification of the Finite Element Model. To examine the suitability of the finite element mesh and modeling assumptions, elastic indentations were performed and the solutions for the surface and subsurface stresses were compared with results from the analysis of Hamilton and Goodman (1966). In the finite element simulation, the normalized modulus, E/σ_y, was equal to 103.25 and the contact radius, a, was about 27.5 nm, i.e., $a/R = 0.0183$. Stresses and coordinates were normalized by the yield stress, σ_y, and the contact radius, a, respectively.

Figure 2 shows surface and near-surface stresses obtained from the finite element simulation and the analysis of Hamilton and Goodman. Figures 2(*a*) and 2(*b*) show the radial variation of the stresses at the surface nodes. The agreement between finite element and analytical results is appreciably good. The

Downloaded 03 May 2010 to 171.66.16.245. Redistribution subject to ASME license or copyright; see http://www.asme.org/terms/Terms_Use.cfm

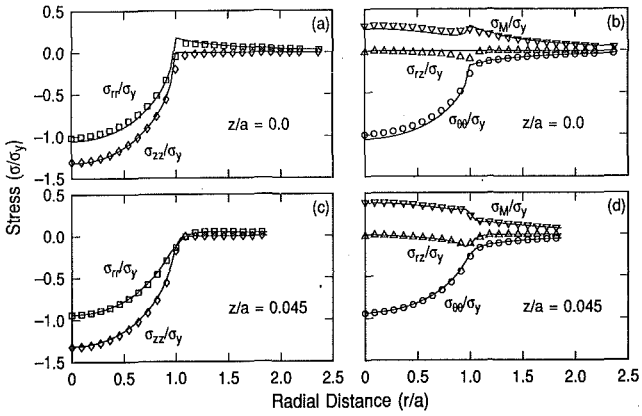


Fig. 2 Comparison of finite element (discrete points) and analytical (continuous lines) stress results for an elastic indentation: (*a*) and (*b*) stresses at the surface; (*c*) and (*d*) stresses near the surface

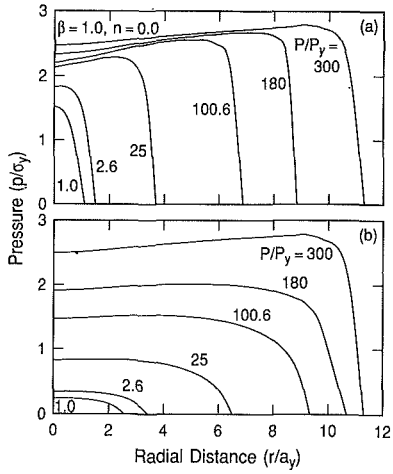


Fig. 3 Development of contact pressure distributions: (*a*) first and (*b*) second load half-cycles

small errors can be attributed to the discretization of the continuous surface and averaging of the stress data from the integration points to boundary nodes, which do not have elements on all sides. The problem caused by nodal averaging to boundary nodes is evident especially in the results for the shear stress, σ_{rz}, which shows small nonzero values near the contact edge, even though the shear traction output from the contact elements is zero. Figures 2(*c*) and 2(*d*) show the radial distribution of the stresses at a depth $z/a = 0.045$. The agreement between finite element and analytical results is excellent. The radial stress, σ_{rr}, becomes tensile at the contact edge, demonstrating the tendency for surface ring crack formation in normal contact loading. Comparison of finite element and analytical subsurface stress distributions on and near the axis of symmetry showed even closer agreement than the surface results shown in Fig. 2. In view of the favorable comparisons with analytical results, it may be concluded that the finite element mesh and modeling assumptions are appropriate for simulating the indentation of a half-space by a rigid sphere.

3 Results and Discussion

Elastic-plastic finite element solutions of the surface and subsurface stress and deformation fields resulting from indentation of half-spaces having nine different sets of elastic and plastic properties are presented and analyzed in this section. The emphasis has been on the interpretation of results which most reveal the significance of the indentation load, the number of load cycles, and the material properties on the resulting deformation behavior. The incremental increase of the load to its peak value, followed by the incremental unloading to a zero load will be referred to as a "load cycle." Either the loading or unloading portion of this entire cycle will be referred to as a "half-cycle."

3.1 Contact Pressure Distribution. Figure 3 shows the variation of the contact pressure as a function of load for the reference case of $\beta = 1.0$ and $n = 0.0$. During the first load half-cycle, Fig. 3(*a*) shows that the deviation of the pressure profile from the Hertzian profile ($P/P_y = 1.0$) increases with indentation load P/P_y, i.e., the initial pressure distribution changes significantly with the evolution of plastic deformation. In particular, increasing the load leads to a remarkable flattening of the pressure distribution, a shift of the maximum pressure toward the contact edge, and the simultaneous significant growth of the contact radius. These results are in agreement with previous indentation analyses, both plane-strain (Akyuz and Merwin, 1968; Dumas and Baronet, 1971; Komvopoulos, 1989) and axisymmetric (Hardy et al., 1971; Sinclair et al., 1985). Figure 3(*b*) shows the evolution of the contact pressure during the second load half-cycle, and is also largely valid for the first unload half-cycle. The figure illustrates that, in addition to the load, the contact pressure depends on the number of accumulated load cycles. The second load half-cycle, compared to the first, produces relatively uniform contact pressure distributions of much larger radius and lower maximum pressure. This is due to the increased interfacial conformity resulting from the residual deformation of the half-space. After the second load half-cycle, the contact pressure profiles are essentially the same as those shown in Fig. 3(*b*).

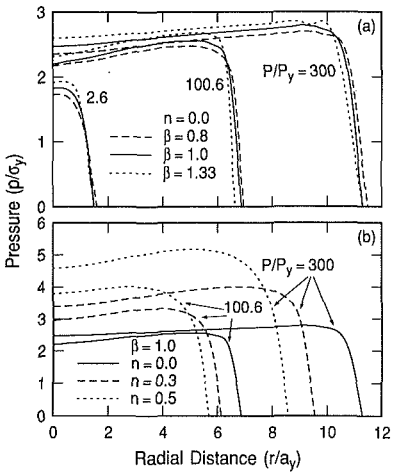


Fig. 4 Contact pressure distribution during the first load half-cycle as a function of elastic modulus (*a*) and strain hardening exponent (*b*) for various loads

Figure 4 shows the effect of the elastic and plastic properties on the contact pressure distribution during the first load half-cycle. Figure 4(*a*) shows that the stiffer material produces marginally higher pressures and slightly smaller contact radii. Figure 4(*b*) indicates that the effect of strain hardening on the pressure distribution is significantly more pronounced than the effect of the elastic modulus. The ability of the hardened material to support a higher stress promotes the development of significantly higher pressures and smaller contact radii. Consequently, the evolution of the contact pressure depends predominantly on the strain hardening characteristics and the accumulated plastic deformation at a given load rather than the modulus of elasticity.

Several previous elastic-plastic analyses of indentation and sliding have been based on an arbitrary selection of the maximum pressure (Merwin and Johnson, 1963) or an assumed contact pressure distribution, such as elliptical (Kulkarni et al., 1990, 1991) or modified elliptical (Bhargava et al., 1985a,

Downloaded 03 May 2010 to 171.66.16.245. Redistribution subject to ASME license or copyright; see http://www.asme.org/terms/Terms_Use.cfm

Table 2 Comparison of finite element and analytical results

P/P_y	Finite Element Method		Analytical Method	
	a/a_y	p_o/σ_y	a/a_y	p_o/σ_y
2.6	1.490	1.841	1.375	2.235
6.4	2.123	2.035	1.857	3.018
15.5	3.015	2.198	2.493	4.053

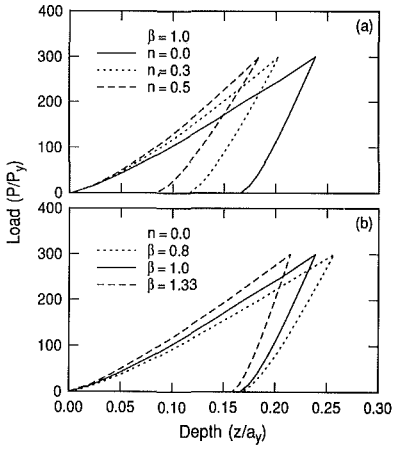


Fig. 5 Load versus indentation depth as a function of strain hardening exponent (*a*) and elastic modulus (*b*) for the first load cycle

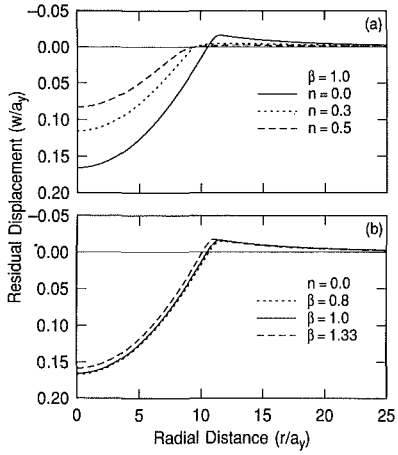


Fig. 6 Residual displacement as a function of strain hardening exponent (*a*) and elastic modulus (*b*) after the first load cycle

1985b). In view of the foregoing and the results of previous analyses (Hardy et al., 1971; Komvopoulos, 1989), it is apparent that when plasticity effects are dominant, such assumptions may influence the accuracy of the solution. The advantage of using contact elements to enforce a prescribed displacement at the contact surface and then calculating the equilibrium nodal forces according to a desirable surface constitutive model is that *a priori* assumptions for the contact pressure distribution are not necessary. Finite element and analytical results which further clarify this issue are listed in Table 2. The maximum contact pressure and contact radius from the present study are compared with data corresponding to "equivalent" Hertzian profiles for the same load (Timoshenko and Goodier, 1970). The table shows that even for a relatively light load, $P/P_y = 2.6$, there is a substantial difference between finite element and assumed Hertzian profiles for an equivalent load. In addition, the change in the contact pressure profile between the first and second load half-cycles shown in Figs. 3(*a*) and 3(*b*) is significant. Therefore, any analysis of repeated indentation or sliding must also account for the variation in the pressure profile resulting from the increased interfacial conformity after plastic deformation. However, it should also be pointed out that in rolling or sliding, changes in the contact geometry may not be as critical as in purely normal indentation, particularly for normal loads less than twice the yield load. Hence assuming an elliptical or modified elliptical contact pressure distribution may still yield reasonably accurate results under such conditions.

3.2 Load Versus Indentation Depth. The significance of material stiffness and strain hardening on the load versus indentation depth relationship is shown in Fig. 5. Figure 5(*a*) demonstrates that strain hardening has only a small effect on indentation depth for loads less than about $50P_y$, but results in significantly smaller indentation depths at heavier loads. The depth of the permanent (residual) indentation for the nonhardening material, $n = 0.0$, is about twice that for the maximum hardening material, $n = 0.5$. Figure 5(*b*) demonstrates that the effect of material stiffness also becomes increasingly significant at loads heavier than $50P_y$ for the nonhardening materials. Although the indentation depth increases with decreasing stiffness, the permanent indentation depth is essentially independent of the elastic modulus. Thus it may be concluded that the depth of the residual indentation, for loads at which the amount of plastic deformation is large, depends largely on the strain hardening behavior of the material.

The unloading curves shown in Fig. 5 exhibit an initially linear response. The linear response is due to the elastic recovery of the half-space and the small changes in the contact radius and pressure profile occurring at the initial stages of unloading. By extrapolating the linear portion of the unloading curves, the elastic moduli of the materials can be determined (Bhattacharya and Nix, 1988). However, as the unloading progresses, the curves show a nonlinearity which becomes more pronounced with increasing strain hardening. This is due to the evolution of the contact pressure from an essentially uniform distribution over a large contact area to an elliptical distribution over a much smaller area during the unload half-cycle, which is essentially similar to that shown in Fig. 3(*b*). Thus the pressure distribution resembles that of a sphere in a nearly spherical elastic seat produced by the residual deformation of the surface. The load versus indentation depth relationship then would be expected to approach that of the classical Hertzian solution, i.e., $z/a_y \propto P^{2/3}$ (Timoshenko and Goodier, 1970). Bhattacharya and Nix (1988) have shown that materials with a larger yield strength-to-elastic modulus ratio exhibit greater curvature in the nonlinear portion of the unloading curve, which is in agreement with the results presented in Fig. 5.

3.3 Residual Displacements. The effect of material properties on the residual vertical displacement of the surface, w, after the first complete load cycle is shown in Fig. 6. Figure 6(*a*) shows that hardening plays a significant role in the resulting permanent deformation. In all material cases, a residual pile-up occurs outside the maximum contact radius, with the nonhardening cases exhibiting a markedly greater amount and a relatively sharper transition from the contact region to the free boundary. The formation of these ridges is consistent with observations of residual pile-up at the contact edge of fully work-hardened materials, which exhibit approximately perfectly plastic behavior, and the absence of pile-up in annealed materials, which can harden during the indentation process (Tabor, 1970). In addition, the maximum residual displacement for the material with the largest strain hardening exponent is about one-half that of the nonhardening material (Fig. 6(*a*)). Figure 6(*b*) shows that the elastic properties have only a secondary effect on either the depth or the profile of the permanent indentation. The results shown in Fig. 6 confirm that the residual displacement is controlled primarily by the plastic properties of the material.

Downloaded 03 May 2010 to 171.66.16.245. Redistribution subject to ASME license or copyright; see http://www.asme.org/terms/Terms_Use.cfm

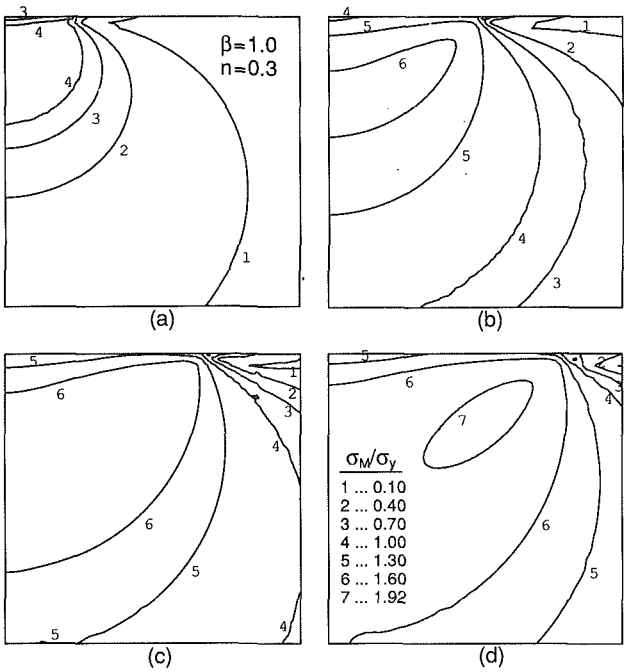


Fig. 7 Contours of von Mises equivalent stress during the first load half-cycle in the region $0 \le r/a_y \le 12$, $0 \le z/a_y \le 12$ for loads P/P_y equal to: (*a*) 15.5, (*b*) 100.6, (*c*) 200, and (*d*) 300

3.4 Surface and Subsurface Stresses. Figure 7 shows the evolution of the von Mises equivalent stress in the half-space during the first load half-cycle. Contour number 4 represents the boundary of the plastic zone. Figure 7(*a*) shows that the plastic zone has almost reached the surface at a load $P/P_y = 15.5$. A thin elastic core has developed over the plastic zone below the central region of the contact interface. The development of an elastic core has also been reported by Hardy et al. (1971) and Sinclair et al. (1985) prior to fully plastic deformation. Figures 7(*b*), 7(*c*), and 7(*d*) show that the elastic core diminishes and eventually disappears as the load increases, and the point of maximum Mises stress moves radially outward from the center and toward the surface. This excursion of the point of maximum Mises stress occurs as the plastically deforming material is squeezed between the rigid indenter (or the elastic core) and the elastic material surrounding the plastic zone. Additional information about the excursion of the maximum Mises stress away from the axis of symmetry, in terms of the position of the maximum equivalent plastic strain, is presented in the following section.

Figure 8 shows the effect of elastic and plastic material properties on both the maximum contact pressure and the maximum von Mises equivalent stress for the first load half-cycle. The stresses are plotted against a normalized strain parameter, $\Lambda = Ea/(1 - \nu^2)\sigma_R^o R$, where σ_R^o is a representative flow stress measured in simple compression at a representative strain $\epsilon_R \approx 0.2a/R$ for a spherical indenter (Johnson, 1985). For indentation by a sphere, values of Λ between approximately 2.4 and 30 are indicative of elastic-plastic deformation, while values of about 30 or greater are indicative of fully plastic deformation (Johnson, 1985). According to Fig. 8, the indentations considered in the present study are almost entirely in the elastic-plastic regime, with only the case $\beta = 1.33$, $n = 0.0$ having values of Λ exceeding 30. Figure 8(*a*) shows that the maximum contact pressure increases monotonically with the contact radius (and hence with the load). The rate of increase depends primarily on the hardening exponent and only secondarily on the elastic properties. In fact, as the indentation progresses toward the fully plastic regime, the maximum pressure approaches an asymptote whose slope is only a function

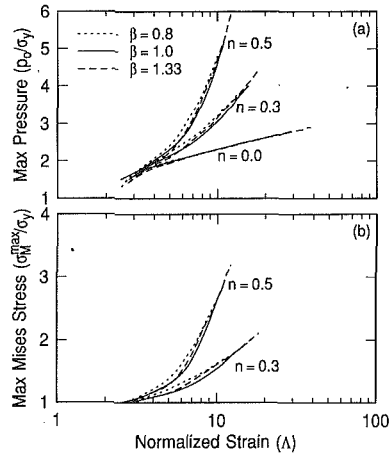


Fig. 8 Maximum contact pressure (*a*) and maximum von Mises equivalent stress (*b*) for the first load half-cycle versus normalized strain

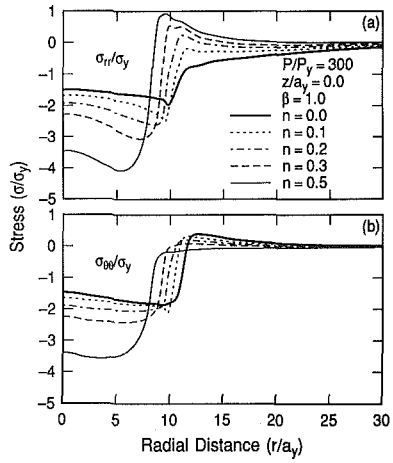


Fig. 9 Surface stresses for the first load half-cycle as a function of strain hardening exponent: (*a*) radial and (*b*) hoop stress

of the hardening exponent. Figure 8(*b*) shows a similar trend for the maximum von Mises equivalent stress. These results indicate that, for a given value of the hardening exponent, the stresses can be expressed as a function of Λ for sufficiently advanced plastic deformation, while for a given value of the normalized strain Λ, they depend only on the strain hardening exponent. These results are consistent with the analysis presented by Tabor (1970) and results for fully plastic indentation of nonlinear elastic materials exhibiting power-law hardening reported by Hill et al. (1989).

Stress distributions at the surface nodes for the peak load $P/P_y = 300$ are shown in Figs. 9 and 10. Figures 9(*a*) and 9(*b*) show the effect of strain hardening on the radial and hoop stresses, σ_{rr} and $\sigma_{\theta\theta}$, respectively. The radial stress for the nonhardening material is compressive everywhere, approaching zero as the radial distance increases. Hardening intensifies the compressive radial stress near the axis of symmetry and increases the peak radial stress near the contact edge. To better quantify the effect of hardening on the peak radial stress at the contact edge, four different nonzero strain hardening values were considered. Figure 9(*a*) shows that when $n = 0.1$ the peak radial stress is compressive, but for $n \ge 0.2$ it is tensile and increases with strain hardening. Radial stress contours, omitted for brevity, have demonstrated that for $n = 0.5$ the region of tensile radial stress at the contact edge extends to a depth $z/a_y \approx 1.0$. Figure 9(*b*) shows that hardening increases the compressive hoop stress below the indenter, but reduces the tensile hoop stress at the contact edge. For the maximum hardening material, the surface hoop stress is compressive

Downloaded 03 May 2010 to 171.66.16.245. Redistribution subject to ASME license or copyright; see http://www.asme.org/terms/Terms_Use.cfm

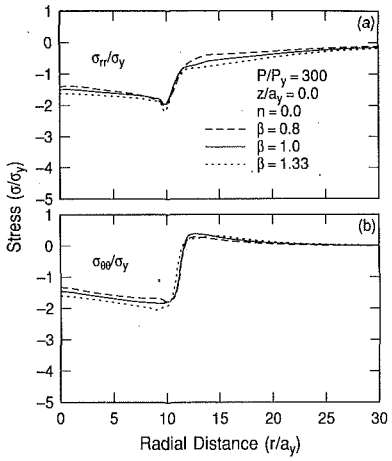


Fig. 10 Surface stresses for the first load half-cycle as a function of elastic modulus: (*a*) radial and (*b*) hoop stress

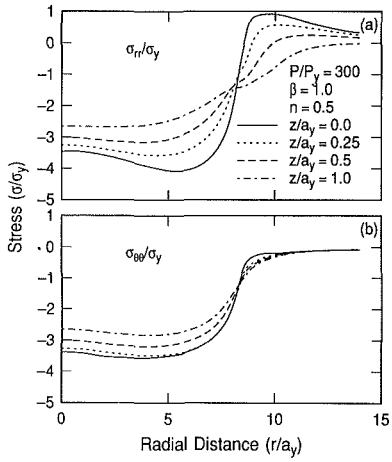


Fig. 11 Surface and near-surface stresses for the first load half-cycle obtained with the finer mesh: (*a*) radial and (*b*) hoop stress

everywhere. Stress contours have shown that the tensile hoop stress for the nonhardening material forms a band surrounding the plastic zone, closely matching the contour of tensile maximum principal stress. In fact, the hoop stress is the maximum principal stress in the tensile region, as will be shown later (Fig. 13(*d*)). For materials exhibiting greater hardening, this band of tensile hoop stress extends from the axis of symmetry toward the surface, but does not quite reach the surface. Thus the maximum principal stress at the surface remains the radial stress, as shown in Fig. 9. In summary, nonhardening and low-hardening materials exhibit a tensile surface hoop stress just outside the contact edge which decreases with increasing hardening. The radial stress in the same region increases with hardening, becoming tensile for a strain hardening exponent between 0.1 and 0.2.

The effect of elastic modulus on the surface stresses is shown in Fig. 10 for the nonhardening cases. The radial and hoop stresses show little sensitivity to variations in stiffness for the range of values studied. Since the same relative indifference to elastic modulus was found for all stresses, both loading and residual, additional results will be presented only for the effect of hardening, since the influence of elastic modulus is secondary.

To verify the stress results presented above and to assess the effect of nodal averaging on the stresses calculated at the surface nodes, additional simulations were performed with a mesh having the resolution of the interior region extended to a radius of $r/R = 0.048$, as compared to $r/R = 0.035$ in the previous model. This extension of the finer mesh region enhanced the determination of the peak radial and hoop stresses outside the contact radius at both surface and near-surface nodes. In addition, the interface to the coarser mesh consisted of triangular linear interpolation elements instead of the quadrilateral elements used previously. The modified mesh was used for several material cases to calculate the surface and near-surface stresses for the first load cycle and compare them with the stresses presented in Fig. 9.

Figure 11 shows the surface and near-surface stresses obtained with the finer mesh for $P/P_y = 300$, $\beta = 1.0$, and $n = 0.5$, which is the case with the largest tensile radial stress at the surface, as shown in Fig. 9(*a*). The surface stresses shown in Fig. 11 are very similar to those shown in Fig. 9 for the same material properties. Similar comparisons for the baseline case also showed excellent agreement between results obtained with the two meshes. Furthermore, Fig. 11(*a*) shows that the distributions of surface and subsurface radial stresses are similar. Figure 11(*b*) shows a similar behavior for the surface and subsurface hoop stresses. In view of these results, it may be concluded that the accuracy of nodal-averaged stresses at the surface nodes for the first load half-cycle is acceptable.

A comparison of the stress profiles shown in Figs. 9 and 11 with those of the elastic indentation shown in Fig. 2 reveals the effect of plastic deformation on the surface stresses. While the tensile peak of the surface radial stress in the elastic indentation occurs just outside the contact radius and the hoop stress asymptotically approaches zero, Fig. 9 shows an opposite trend for hardening exponents less than 0.2. Thus, as the amount of plastic deformation increases in the materials with little or no hardening, the peak tensile radial stress at the contact edge diminishes and the tensile hoop stress at the same location increases. This behavior of the surface stresses is in qualitative agreement with results of the spherical cavity expansion model for an elastic-perfectly plastic half-space under a blunt indenter (Johnson, 1985) and results of Hardy et al. (1971), although the stress profiles in the latter study do not extend sufficiently far in the radial direction to show the actual peak of the hoop stress. A comparison of the surface stress results presented here with those given by Sinclair et al. (1985) is also in order. In that work, the near-surface radial stress was solely compressive, while the hoop stress was slightly tensile outside the contact region. Moreover, the hardening exponent depended upon the load, rising from an initial value of about 0.15 to a final value of about 0.5. Since the reported results were for indentation loads of 45, 1300, and 52,000 times the initial yield load, it is considered that the stress distributions for $P/P_y = 45$ correspond to a hardening exponent equal to about 0.15. The maximum load $P/P_y = 300$ in this study is closer to the lowest load in Sinclair et al., and the results for $n = 0.0$ to 0.2 shown in Fig. 9 are qualitatively consistent with the results of that study.

Figure 12 shows the effect of strain hardening on the radial and normal stress distributions on the axis of symmetry at the maximum load $P/P_y = 300$. Increasing the strain hardening exponent intensifies the compressive normal stress in the region $z/a_y < 18$. Hardening also intensifies the compressive radial (and hoop) stress in the near-surface region, $z/a_y < 5$, but relaxes the stress at greater depths. For depths $z/a_y \geq 20$, the radial stress is slightly tensile and the stress field becomes insensitive to variations in the hardening exponent.

Contours of the maximum principal stress, σ_1, in the baseline material for different increments of the first load half-cycle are shown in Fig. 13. At $P/P_y = 39.8$, regions of tensile stress at the surface just outside the contact edge and in the subsurface extending from the axis of symmetry toward the surface are evident in Fig. 13(*a*). Contours of radial and hoop stresses have shown that the tensile principal stress at the surface is in

Downloaded 03 May 2010 to 171.66.16.245. Redistribution subject to ASME license or copyright; see http://www.asme.org/terms/Terms_Use.cfm

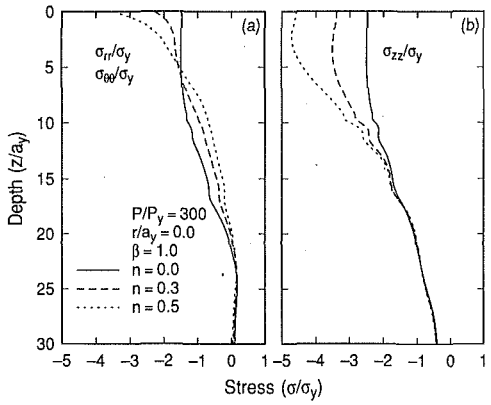


Fig. 12 Effect of strain hardening on the radial (*a*) and normal (*b*) stress on the axis of symmetry for the first load half-cycle

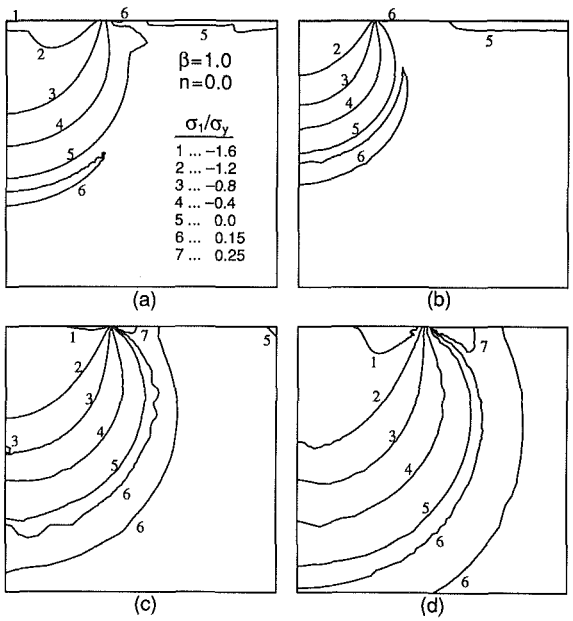


Fig. 13 Contours of maximum principal stress during the first load half-cycle for loads P/P_y equal to: (*a*) 39.8, (*b*) 100.6, (*c*) 200, and (*d*) 300. ((*a*) shows the region $0 \le r/a_y \le 12$, $0 \le z/a_y \le 12$, while (*b*), (*c*), and (*d*) show the region $0 \le r/a_y \le 24$, $0 \le z/a_y \le 24$)

the radial direction, while in the subsurface is in the hoop direction. As the load increases, the subsurface tensile region grows and eventually reaches the surface, as shown in Figs. 13(*b*) and 13(*c*), respectively. At that juncture, the maximum principal stress at the surface arises in the hoop direction, as demonstrated from a comparison with the results shown in Figs. 9(*a*) and 9(*b*). At the maximum load, Fig. 13(*d*) shows that the tensile stress band has expanded and thickened, and the surface tensile stress outside the contact edge has increased. The band of tensile hoop stress forms as the outlying elastic material resists the radial expansion of the plastically deformed material. This behavior will be most apparent for the nonhardening material, since an increasing load can be supported only through yielding of new material or an increase in hydrostatic pressure produced by the constraining tensile hoop stress band. Strain hardening delays the formation of the constraining tensile hoop stress band because the plastically deforming material directly supports more of the load by strain hardening.

The contours of maximum principal stress at the peak load for $\beta = 1.0$ and $n = 0.3$ and 0.5 are similar to those shown in Figs. 13(*c*) and 13(*b*), respectively, with the tensile hoop stress not quite reaching the surface. Thus for hardening materials, the maximum principal stress at the surface occurs in the radial direction, as shown for $n = 0.3$ and 0.5 in Fig. 9. The tensile stress on the axis of symmetry shown in Fig. 13(*d*) corresponds to the tensile radial (and hoop) stress on the centerline shown in Fig. 12(*a*). The tensile surface region shown in Fig. 13(*d*) exhibits the largest magnitude and gradient in maximum principal stress. The stress gradient occurs due to the tensile principal stress region becoming compressive as new interfacial contact points are established at heavier loads. As discussed previously, for indentations involving only small plastic deformation and materials exhibiting significant strain hardening, a tensile radial stress exists at the surface. Such a tensile stress may promote the formation of ring cracks at the contact edge, as is often encountered with indented brittle materials (Chaudhri and Phillips, 1990). For indentations producing large plastic deformation in materials possessing little or no hardening, the maximum principal stress at the surface will be in the hoop direction, thus enhancing the formation of radial cracks. The initiation of radial cracks due to a tensile surface hoop stress has been reported for silicon carbide demonstrating well-developed plasticity below a sharp indenter (Lankford and Davidson, 1979) and for the indentation of semi-brittle polymeric glasses, such as polymethylmethacrylate, by a sphere (Puttick et al., 1977). In addition, the subsurface region of tensile hoop stress is consistent with the formation of median cracks under sharp or blunt indenters carrying high loads (Lawn and Evans, 1977).

Finally, a comparison of the present results with those of a recent analysis by Hill et al. (1989) is in order. In the latter study, indentation of a nonlinear elastic half-space exhibiting a power-law hardening behavior was considered. Although there are results in agreement with those of the present study, particularly the dependence of stresses on only the strain hardening exponent for a given normalized strain (Fig. 8), there are also points of significant disagreement. In particular, Hill et al. show small deviations of the contact pressure from the Hertzian profile, and radial and hoop surface stresses at the contact edge that are both tensile for all hardening exponents investigated ($n = 0.1$, 0.25, 0.5, and 1.0). There are two possible reasons for the disagreements between the two studies. First, the approximation of the material as incompressible, nonlinear elastic with power-law hardening throughout the strain range indicates that the results will be most applicable to fully plastic deformation. As mentioned previously, the indentations considered in the present study are primarily in the elastic-plastic regime, i.e., $2.4 < \Lambda < 30$, where the effects of elastic compressibility may be significant. Second, the approximation of plastic deformation by nonlinear elastic deformation requires that the strain path is radial, i.e., the ratios between the strain components must remain constant throughout the loading process. Hill et al. themselves concede that the strain paths for a Brinell test can be only approximately radial at best, although they also show that strain paths at representative material points approach asymptotes at fixed ratios as the contact radius increases, indicating that the strain path is indeed radial for sufficiently advanced indentation. However, since indentations in the present investigation are primarily in the elastic-plastic rather than the fully plastic regime, the strain paths may not have reached the asymptotes predicted by Hill et al. Figure 14 demonstrates that this is indeed the case. The figure shows the strain paths at the material point $r/a_y = z/a_y = 3.0$ for the case $\beta = 1.33$ and $n = 0.0$, which is the only case in the present study approaching fully plastic behavior ($\Lambda > 30$). The strain components were normalized by the strain γ, evaluated at the same material point at the maximum load, given by

$$\gamma = \left[\frac{2}{3} e_{ij} e_{ij}\right]^{1/2}$$

where e_{ij} are the components of the deviatoric strain. Figure

Downloaded 03 May 2010 to 171.66.16.245. Redistribution subject to ASME license or copyright; see http://www.asme.org/terms/Terms_Use.cfm

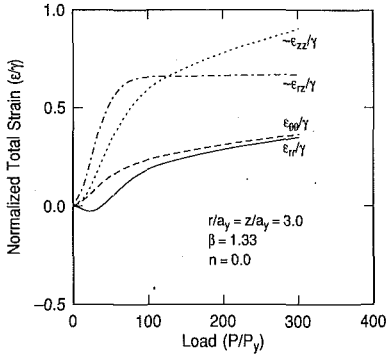


Fig. 14 Variation of normalized components of strain with load during the first load half-cycle

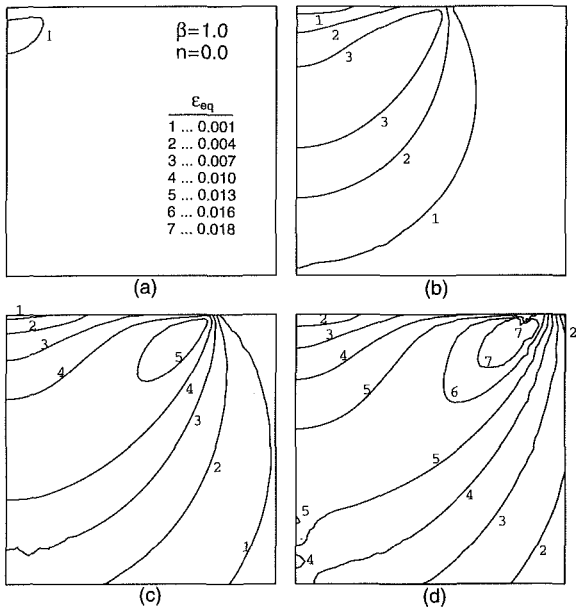


Fig. 15 Contours of equivalent plastic strain for the first load half-cycle in the region $0 \le r/a_y \le 12$, $0 \le z/a_y \le 12$ for loads P/P_y equal to: (*a*) 6.4, (*b*) 100.6, (*c*) 200, and (*d*) 300

14 shows that the normal strains approach fixed ratios for $P/P_y \ge 150$, but the shear strain approaches a constant value, which does not maintain a fixed ratio with other strain components. Hence the strain path during indentation in the load range investigated is not radial.

3.5 Evolution of Plasticity. Figure 15 shows the evolution of the equivalent plastic strain for the baseline material case in the first load half-cycle. Figure 15(*a*) shows that for small indentation loads, plastic deformation occurs only in the subsurface, with the maximum equivalent plastic strain located on the axis of symmetry. The plastic zone grows with indentation load, eventually reaching the surface, as shown in Fig. 15(*b*). Figures 15(*c*) and 15(*d*) demonstrate that as the size of the plastic zone increases, the location of the maximum equivalent plastic strain moves radially outward and toward the surface just inside the maximum contact radius. At the maximum load, large plastic strain gradients are produced near the contact edge and the elastic core at the center of the interface has disappeared (Fig. 15(*d*)).

Table 3 shows the effect of material properties on the excursion of the point of maximum equivalent plastic strain away from the axis of symmetry. The load P_i/P_y is that at which the point of maximum equivalent plastic strain permanently moves away from the axis of symmetry. Because nodal averaged values were used, a minor excursion to the next nodal line and a return to the centerline were occasionally encountered. These preliminary excursions were disregarded. The table also shows the depth on the axis of symmetry at which the excursion begins, z_i/a_y, and the final coordinates, r_f/a_y and z_f/a_y, of the point with the maximum equivalent plastic strain at the peak load $P/P_y = 300$. Hardening increases the load and depth at which the maximum plastic strain first moves away from the axis of symmetry. The maximum equivalent plastic strain at the peak load occurs closer to the axis of symmetry and farther below the surface as hardening increases. For the same hardening behavior, increasing the elastic modulus tends to decrease the load and depth at which the excursion occurs, as well as the depth of the point of maximum equivalent plastic strain at the peak load. As the indentation progresses, material near the surface becomes more constrained between the rigid indenter and the elastic material outside the contact radius, causing the accumulation of plastic strain away from the axis of symmetry. Since the indentation depth decreases with hardening, the constraint for a given load is reduced. Consequently, the maximum equivalent plastic strain occurs in the subsurface on the axis of symmetry until a greater indentation depth is reached.

Table 3 Effect of material properties on the excursion and final location of the point of maximum equivalent plastic strain

β	n = 0.0			n = 0.3			n = 0.5		
	P_i/P_y	z_i/a_y	r_f/a_y z_f/a_y	P_i/P_y	z_i/a_y	r_f/a_y z_f/a_y	P_i/P_y	z_i/a_y	r_f/a_y z_f/a_y
0.8	25.0	2.25	10.25 0.75	100.6	3.5	6.25 3.0	---	---	0.0 5.0
1.0	15.5	1.75	10.25 0.75	60.0	2.75	7.0 2.25	180.0	3.75	3.5 4.0
1.33	15.5	1.75	9.75 0.25	39.8*	2.25*	7.0 1.75	180.0	3.5	4.0 3.25

*For P/P_y between 6.4 and 39.8, the point of maximum equivalent plastic strain was on the next nodal line away from the axis of symmetry (r/a_y=0.25) from z/a_y=0.75 to 2.25. It is likely that this is due to the nodal averaging and that the given values are more representative of the actual case.

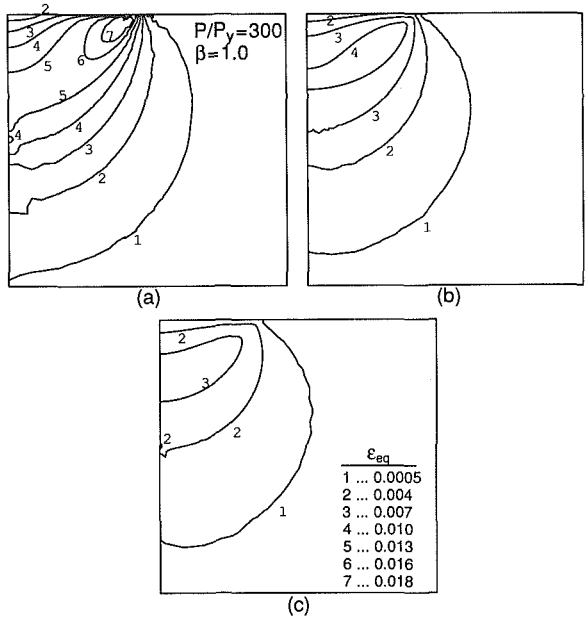


Fig. 16 Contours of equivalent plastic strain for the first load half-cycle in the region $0 \le r/a_y \le 24$, $0 \le z/a_y \le 24$ for strain hardening exponent n equal to: (*a*) 0.0, (*b*) 0.3, and (*c*) 0.5

The effect of hardening on the equivalent plastic strain is shown in Fig. 16. The movement of the maximum equivalent plastic strain away from the axis of symmetry and toward the surface is clearly evident for $n = 0.0$ (Fig. 16(*a*)) and $n = 0.3$ (Fig. 16(*b*)). However, Fig. 16(*c*) shows that for extreme hardening ($n = 0.5$) the maximum equivalent plastic strain still

Downloaded 03 May 2010 to 171.66.16.245. Redistribution subject to ASME license or copyright; see http://www.asme.org/terms/Terms_Use.cfm

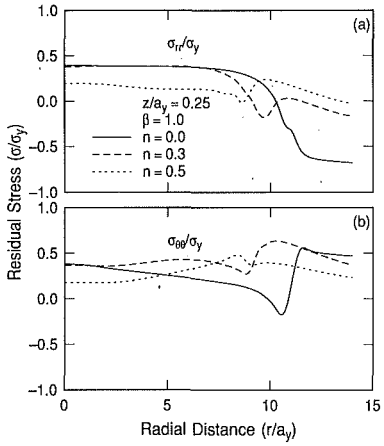


Fig. 17 Near-surface residual stresses after the first load cycle as a function of strain hardening exponent: (*a*) radial and (*b*) hoop residual stress

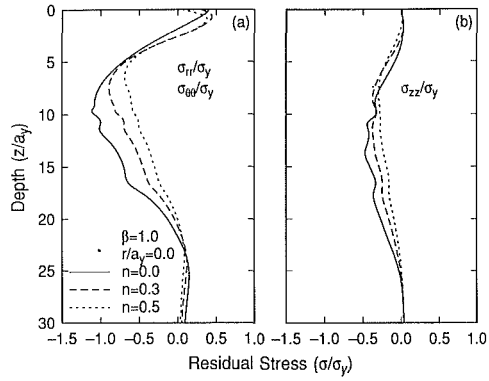


Fig. 18 Residual stresses on the axis of symmetry after the first load cycle as a function of strain hardening exponent: (*a*) radial (hoop) and (*b*) normal residual stress

occurs near the axis of symmetry. The size of the plastic zone and magnitude of the equivalent plastic strain decrease with hardening. This is attributable to the larger stress that can be supported by the hardened material for a given amount of plastic strain.

3.6 Residual Stresses. Residual stresses for the surface nodes of the mesh shown in Fig. 1 after the first load cycle were compared with similar results for surface and near-surface nodes of the finer mesh. The agreement was not satisfactory, indicating that the nodal averaging to the free surface was not reliable for the calculation of residual stresses. For this reason, residual stresses at the first subsurface nodal line of the finer mesh, i.e., at $z/a_y = 0.25$ extending radially to a distance $r/a_y = 14.25$, were chosen as being more representative of the actual residual stress state near the surface. Figure 17 shows the effect of strain hardening on the near-surface residual stresses. For nonhardening materials, the residual radial stress is tensile and fairly uniform from the axis of symmetry to $r \approx 10a_y$; it then becomes compressive at roughly the maximum contact radius of the first load half-cycle. Maximum hardening materials exhibit a smaller tensile radial stress, accompanied by a minimum at approximately the maximum contact radius. The minimum is followed by a tensile local maximum, after which the stress asymptotically approaches zero. Contours of radial stress, again omitted for brevity, have shown that the tensile region at the maximum contact radius extends to a depth of $z = 0.5a_y$ for $n = 0.3$ and $z = 0.75a_y$ for $n = 0.5$. Figure 17(*b*) shows that the hoop stress for the nonhardening material is tensile except near the maximum contact radius, while the hardening materials show an entirely tensile residual hoop stress profile. From Fig. 17(*a*), the surface residual radial stress on the axis of symmetry for $n = 0.0$ is equal to 0.39, which is close to the value of approximately 0.5 given by Johnson (1968) for contacting copper spheres with an estimated hardening exponent of about 0.016. The maximum hardening reduces the residual radial stress on the axis of symmetry to a value of 0.19. For nonhardening materials, the increase in the surface radial stress upon unloading indicates a tendency for ring crack formation. Alternatively, a comparison of the results shown in Figs. 9(*a*) and 17(*a*) indicates that hardening increases the likelihood of ring crack formation near the contact edge during the load half-cycle, because of the larger tensile radial stress. For hardening materials, the increase in the hoop stress from the values shown in Fig. 9(*b*) to the tensile values shown in Fig. 17(*b*) indicates a tendency to form radial cracks during the unload half-cycle, especially at the contact edge.

Figure 18 shows the distribution of the residual stresses on the axis of symmetry. Figure 18(*a*) reveals that the surface regions of tensile radial and hoop stress at the center of contact shown in Fig. 17 extend to a depth of 2 to $2.5a_y$, depending on the strain hardening. The thickness of the tensile region is about $2a_y$ for $n = 0.0$, with the maximum occurring at the surface, while for $n = 0.3$ and 0.5 the thickness is about $2.5a_y$ and the maximum occurs at $z \approx a_y$. Contours of residual hoop stress, again omitted for brevity, have shown a subsurface tensile band surrounding a compressive core, similar to the contours of maximum principal stress in the loaded condition shown in Fig. 13. The region of slightly tensile radial stress occurring at a depth of about $23a_y$, as shown in Fig. 18(*a*), corresponds to the intersection of this band of tensile hoop stress with the axis of symmetry. The tensile hoop stress in this region increases with decreasing hardening, thus promoting median crack formation. Figure 18(*b*) shows that the residual normal stress is slightly tensile near the surface, compressive below the surface to a depth of about $25a_y$, and slightly tensile at greater depths.

Comparison of the loading stresses shown in Figs. 9 and 12 with the residual stresses shown in Figs. 17 and 18 indicates that the surface may be more susceptible to cracking and accompanying wear after indentation loading. For all the material cases, the contact interface exhibits large compressive stresses under maximum load, but tensile residual stresses after unloading. Although surface tensile stresses can also be produced during loading, larger tensile residual stresses may develop upon unloading, as in the case of the radial stress just inside the contact edge for the nonhardening material shown in Fig. 17(*a*). Thus operations used to increase the resistance to cracking, such as peening, may produce surface tensile stresses under certain circumstances, making the surface more susceptible to cracking. Nevertheless, the surface tensile layer may be worn away quickly, leaving only the subsurface region with compressive stresses. Since the quasi-static process modeled here may differ considerably from the dynamic process of peening, more investigation is needed before such interpretations can be verified.

Upon unloading, yielding of both plastically deformed and previously elastic material occurred for some cases. The yielding region was always at the surface just outside the maximum contact radius, as predicted by Johnson (1985). Figure 19 shows the effect of hardening on the contours of residual von Mises equivalent stress. Figure 19(*a*) clearly shows the yielding region for the nonhardening material, given by contour number 7. There is no visible yielding region for $n = 0.3$, shown in Fig. 19(*b*), although a very small region exists (one integration point). Figure 19(*c*) shows that there is no yielding for $n = 0.5$. Table 4 gives the relative sizes of yielding regions in terms of the number of integration points which have accumulated plastic strain during the unload half-cycle and the number of yielding points which did not yield during the previous load half-cycle, i.e., newly yielding points. Additionally, Fig. 20

Downloaded 03 May 2010 to 171.66.16.245. Redistribution subject to ASME license or copyright; see http://www.asme.org/terms/Terms_Use.cfm

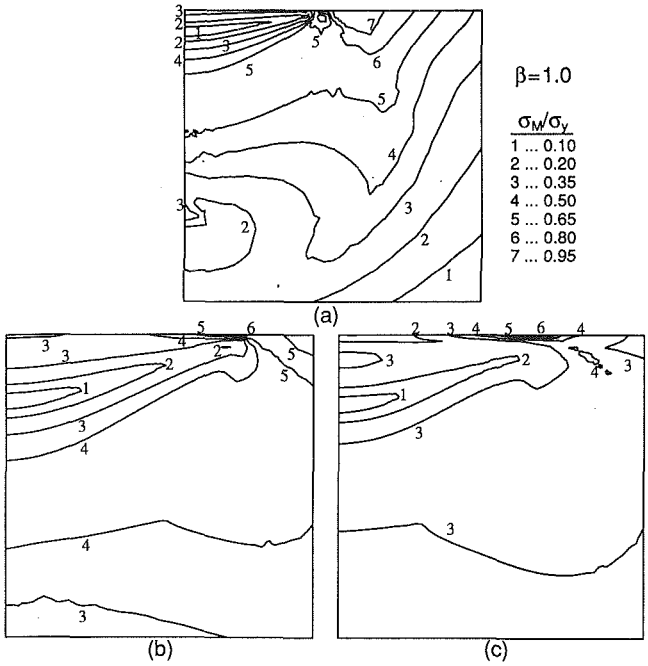


Fig. 19 *Contours of residual von Mises equivalent stress after the first load cycle for strain hardening exponent n equal to: (a) 0.0, (b) 0.3, and (c) 0.5. ((a) shows the region $0 \le r/a_y \le 24$, $0 \le z/a_y \le 24$, while (b) and (c) show the region $0 \le r/a_y \le 12$, $0 \le z/a_y \le 12$)*

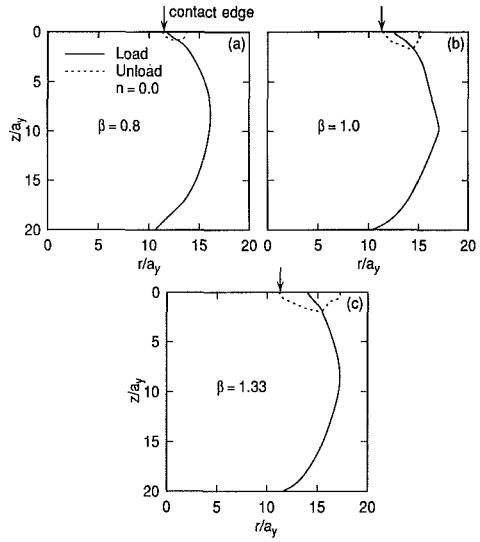


Fig. 20 **Yielding regions for the first load and unload half-cycles**

shows the boundaries of the yielded regions for the first load and unload half-cycles for the nonhardening cases. It is noted that the elastic-plastic boundary for the first load half-cycle exceeds the contact radius at the surface for the two cases closest to fully plastic deformation, namely $\beta = 1.0$ and 1.33, with $\Lambda = 28.8$ and 38.5, respectively. Furthermore, Table 4 and Figs. 19 and 20 show that the size of the unloaded yielding region generally increases with the modulus of elasticity and decreases with hardening. Since the hardening is isotropic, the uniform expansion of the yield surface during the load half-cycle makes yielding after unloading less likely for a hardening material. Although the two material cases with $\beta = 1.0$, $n = 0.3$ and $\beta = 0.8$, $n = 0.5$ exhibit yielding during the unload half-cycle, the sizes of these yielding regions are negligible (one and three integration points, respectively).

To ascertain whether yielding at the outer contact radius during unloading could have been an artifact of the increased

Table 4 **Yielding during the first unload half-cycle versus material properties**

n	β		
	0.8	1.0	1.33
0.0	y (18,11)	y (33,11)	y (47,9)
0.3	ny	y (1,0)	y (19,13)
0.5	y (3,0)	ny	ny

y = yielded upon unloading
ny = not yielded upon unloading
(a,b) = a: number of integration points with increased equivalent plastic strain during the unload half-cycle, and b: number of newly yielding integration points (included in a)

stiffness of the mesh where it becomes coarser, additional runs were performed using the finer mesh, since the yielding region would fall within the refined region. The finer mesh was used for one load cycle of the baseline material case. Results for the loading stresses, residual stresses, and yielding behavior were essentially the same as those for the coarser mesh.

Yielding during the unload half-cycle was further verified by elastically applying a uniform tension to the loaded half-space, as an approximation of the unloading of the pressure profile at maximum load shown in Fig. 3(*a*). This is the same procedure used by Sinclair et al. (1985) to model unloading. The uniform tensile stress was calculated to give a total load $P/P_y = 300$ and was applied over the same contact radius. Equations for the elastic stresses at the surface of a half-space subjected to a uniform tension over a circular region are given by (Johnson, 1985)

$$\sigma_{rr}(r,0) = \begin{cases} -\dfrac{p_o}{2}(1+2\nu), & 0 \le r \le a \\ \dfrac{p_o}{2}(1-2\nu)\left(\dfrac{a}{r}\right)^2, & a < r \end{cases}$$

$$\sigma_{\theta\theta}(r,0) = \begin{cases} -\dfrac{p_o}{2}(1+2\nu), & 0 \le r \le a \\ -\dfrac{p_o}{2}(1-2\nu)\left(\dfrac{a}{r}\right)^2, & a < r \end{cases}$$

$$\sigma_{zz}(r,0) = \begin{cases} -p_o, & 0 \le r \le a \\ 0, & a < r \end{cases}$$

where $-p_o$ represents the uniform tensile stress over the maximum contact region. The unloading stresses were added to the surface stresses of the finer mesh obtained for the baseline case at $P/P_y = 300$. The resulting residual stresses produced a Mises stress larger than unity (i.e., yielding) at $r/a_y = 11$ to 16, which very closely matched the surface yielding region given by the finite element simulation after the first unload half-cycle. Hence the presence of the unloaded yielding zone shown in Figs. 19(*a*) and 20(*b*) was verified. A comparison of the unloading stresses calculated from the above equations with the loading stresses for the nonhardening case shown in Fig. 9 indicates that yielding is due to the combined effect of the radial and hoop stresses just outside the maximum contact radius. In this region the unloading stresses increase the intensity of both the compressive radial stress and the tensile hoop stress, while the normal and shear stresses remain zero. Thus the addition of the unloading stresses increases the maximum shear stress. Since material in this region has already yielded or is close to yielding, the material will either reyield or will yield for the first time during unloading. As shown in Fig. 9, increasing hardening produces tensile radial and compressive hoop surface stresses just outside the contact radius.

Downloaded 03 May 2010 to 171.66.16.245. Redistribution subject to ASME license or copyright; see http://www.asme.org/terms/Terms_Use.cfm

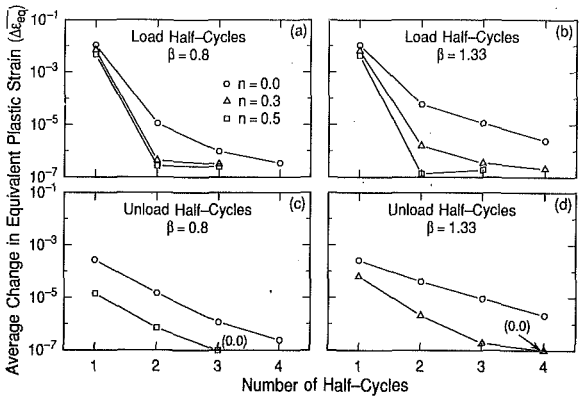


Fig. 21 Average change of total equivalent plastic strain in each half-cycle as a function of material properties: (*a*) and (*b*) load half-cycles; (*c*) and (*d*) unload half-cycles

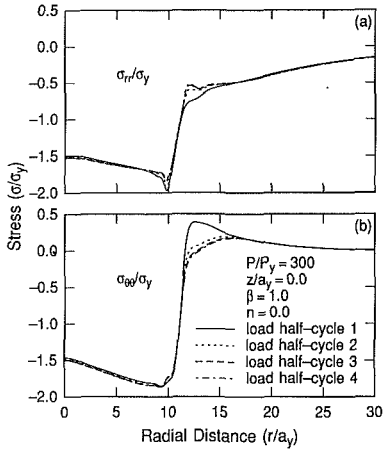


Fig. 22 Surface stresses as a function of load half-cycle: (*a*) radial and (*b*) hoop stress

Consequently, the addition of the compressive radial and tensile hoop unloading stresses is less likely to produce yielding in the hardening materials. The addition of the tensile unloading stresses inside the contact area raises the radial and hoop stresses to similar tensile values (Fig. 17) and produces a zero normal stress. Thus yielding will not occur inside the contact radius upon unloading.

Yielding during unloading is also related to the development of a residual pile-up at the contact edge. In Fig. 6, the residual surface displacements show a pronounced region of pile-up just at the maximum contact radius for the nonhardening case. The size of this ridge decreases considerably with hardening and increases slightly with elastic modulus. A similar trend is shown in Table 4 and Figs. 19 and 20 for the size of the unloaded yielding zone. The pile-up region is caused by the compressive residual radial stress at the surface outside the maximum contact radius. This stress is greatest for the nonhardening case and becomes less compressive with increasing hardening (Fig. 17(*a*)). Thus an increase in the compressive radial stress during unloading, coupled with an increase in the already tensile hoop stress, comprises the mechanism responsible for both yielding during unloading and the formation of a residual pile-up region.

3.7 Subsequent Load Cycles. The size and shape of the plastic zones established in the first load cycle did not change appreciably with subsequent load cycles. However, all material cases continued to yield and accumulate plastic strain during repeated indentation loading. Yielding during subsequent unloading occurred only for the materials undergoing yielding during the first unload half-cycle (see Table 4). Continued yielding was identified by those integration points which showed an increase in equivalent plastic strain during the half-cycle. The average increase in equivalent plastic strain, $\overline{\Delta\epsilon_{eq}}$, is given by the average computed over these points. Figure 21 shows $\overline{\Delta\epsilon_{eq}}$ as a function of load and unload half-cycles for different elastic and plastic properties. Load and unload half-cycles have been plotted separately because yielding occurs in different regions. Figures 21(*a*) and 21(*b*) show the variation of $\overline{\Delta\epsilon_{eq}}$ during the load half-cycles for $\beta = 0.8$ and 1.33, respectively, while Figs. 21(*c*) and 21(*d*) show corresponding curves for the unload half-cycles. For the materials that did not yield during the unload half-cycles, no curve is shown in Figs. 21(*c*) and 21(*d*). Points in the unloading graphs labelled 0.0 indicate no further increase in plastic strain during the particular half-cycle. Figures 21(*a*) and 21(*b*) show that the accumulation of plastic strain in each load half-cycle decreases rapidly by several orders of magnitude. Although in the material with $\beta = 1.33$, $n = 0.5$ the plastic strain increased in the third load half-cycle, the increase is negligible, i.e., of the order of 10^{-7}. A monotonic decrease in the accumulation of plastic strain occurs in all cases upon unloading. For the strain hardened materials, Figs. 21(*c*) and 21(*d*) show that the plastic strain does not increase after the third and fourth unload half-cycles, respectively, suggesting that the unloaded yielding region has reached shakedown. Similar trends were found for hardening materials with $\beta = 1.0$.

The effect of subsequent load half-cycles on the loading surface stresses is shown in Fig. 22 for the baseline case. Figure 22(*a*) shows negligible changes in the surface radial stress except at the contact edge, where repeated indentation produces a less compressive stress. The effect of repeated loading on the hoop stress, shown in Fig. 22(*b*), is also marginal except at the contact edge, where the stress becomes less tensile with each half-cycle. These two factors combine to decrease the tendency to yield during the following unload half-cycle. According to Fig. 22(*b*), the formation of radial cracks at the contact edge will be most likely in the first load half-cycle, when the tensile hoop stress is the greatest. The results shown in Fig. 22 are qualitatively similar to those of the other nonhardening materials. Plots of near-surface residual stresses for the baseline material, again omitted for brevity, have also shown a slight decrease in the tensile residual hoop stress at the contact edge, compared to the stresses shown in Fig. 17(*b*), and a marginal intensification of the compressive radial stress in the same region. In addition, the stresses on the axis of symmetry for both the load and unload half-cycles are almost identical to those shown in Figs. 12 and 18, respectively. Thus, the only significant changes in the stress field with subsequent cycles occur in the region near the contact edge.

The surface and subsurface stresses produced in subsequent load cycles for the hardening materials were virtually identical to those of the first load cycle, even for the case with $\beta = 1.33$ and $n = 0.3$, which exhibited a fairly large region of yielding during the first unload half-cycle (Table 4). Hence the presented stress fields for the first load cycle of all the hardening materials are also representative of the steady-state stresses at shakedown.

4 Conclusions

The elastic-plastic deformation characteristics resulting from repeated indentation of a half-space by a rigid spherical indenter were analyzed with the finite element method. Indentations with loads up to 300 times the load necessary for initial yield were performed on materials with different elastic and plastic properties. It was shown that resulting pressure profiles are significantly different from an "equivalent" Hertz profile. This is especially pronounced at large loads and in the second and subsequent load cycles, as the interfacial conformity is increased by the permanent deformation of the surface. This

Downloaded 03 May 2010 to 171.66.16.245. Redistribution subject to ASME license or copyright; see http://www.asme.org/terms/Terms_Use.cfm

conformity decreases the intensity of the peak contact pressure in subsequent cycles. The contact pressure is relatively insensitive to elastic properties in the range studied. Hardening produces significantly higher pressures and smaller contact radii.

Surface and subsurface stresses vary primarily with hardening. For nonhardening materials, a spherical band of tensile hoop stress develops from the axis of symmetry to the surface and prevents the expansion of the plastically deformed material. This produces a peak tensile hoop stress at the surface, thereby increasing the susceptibility to surface radial cracking. In hardening materials, which support more of the indenter load directly due to the increase of the material hardness, the tensile hoop stress band does not reach the surface. These materials exhibit a surface tensile radial stress at the contact edge, making them more susceptible to the formation of ring cracks.

Upon the first complete unloading, yielding occurs in a surface region just outside the maximum contact radius in the materials with larger elastic moduli and smaller strain hardening exponents. The yielding is caused by an increase in both the tensile hoop and compressive radial stresses upon the removal of the approximately uniform contact pressure. Since hardening increases the surface radial stress and decreases the surface hoop stress at the maximum load, yielding during unloading is inhibited. This yielding behavior is also related to the residual pile-up at the contact edge. This is consistent with experimental evidence from indentation hardness tests of both fully work-hardened materials and annealed materials. There is no other region of yielding in the half-space after the first unloading.

Subsequent load cycles produce continued yielding almost entirely within the plastically deformed region established in the first load cycle. Yielding during subsequent unload half-cycles occurs only in those materials that yield during the first unload half-cycle. The increase in average equivalent plastic strain decreases rapidly with each subsequent half-cycle, except for one hardening case, which shows a negligible increase between two load half-cycles. The surface stresses under maximum load for the nonhardening materials exhibit a decrease in both the compressive radial and tensile hoop stresses at the contact edge with loading cycles, which combine to decrease the tendency to yield during the subsequent unload half-cycles. The residual surface stresses change only slightly, while the stresses along the axis of symmetry are essentially independent of the number of subsequent cycles. For the hardening materials, the stresses on the surface and the axis of symmetry during the first load cycle are virtually identical to those produced in subsequent cycles.

Acknowledgments

This work was partially supported by the Surface Engineering and Tribology Program of the National Science Foundation under Grant No. MSS-8996309 and the Computer Mechanics Laboratory at the University of California at Berkeley.

References

Akyuz, F. A., and Merwin, J. E., 1968, "Solution of Nonlinear Problems of Elastoplasticity by Finite Element Method," *AIAA Journal*, Vol. 6, No. 10, pp. 1825–1831.

Bhargava, V., Hahn, G. T., and Rubin, C. A., 1985a, "An Elastic-Plastic Finite Element Model of Rolling Contact Part 1: Analysis of Single Contacts," ASME JOURNAL OF APPLIED MECHANICS, Vol. 52, pp. 67–74.

Bhargava, V., Hahn, G. T., and Rubin, C. A., 1985b, "An Elastic-Plastic Finite Element Model of Rolling Contact Part 2: Analysis of Repeated Contacts," ASME JOURNAL OF APPLIED MECHANICS, Vol. 52, pp. 75–82.

Bhattacharya, A. K., and Nix, W. D., 1988, "Finite Element Simulation of Indentation Experiments," *Int. J. Solids Structures*, Vol. 24, No. 9, pp. 881–891.

Casey, J., and Naghdi, P. M., 1980, "A Remark on the Use of the Decomposition $\mathbf{F} = \mathbf{F}_e\mathbf{F}_p$ in Plasticity," ASME JOURNAL OF APPLIED MECHANICS, Vol. 47, pp. 672–675.

Chaudhri, M. M., and Phillips, M. A., 1990, "Quasi-Static Indentation Cracking of Thermally Tempered Soda-Lime Glass With Spherical and Vickers Indenters," *Phil. Mag. A*, Vol. 62, No. 1, pp. 1–27.

Dumas, G., and Baronet, C. N., 1971, "Elastoplastic Indentation of a Half-Space by an Infinitely Long Rigid Circular Cylinder," *Int. J. Mech. Sci.*, Vol. 13, pp. 519–530.

Follansbee, P. S., and Sinclair, G. B., 1984, "Quasi-Static Normal Indentation of an Elasto-Plastic Half-Space by a Rigid Sphere—I. Analysis," *Int. J. Solids Structures*, Vol. 20, No. 1, pp. 81–91.

Hamilton, G. M., and Goodman, L. E., 1966, "The Stress Field Created by a Circular Sliding Contact," ASME JOURNAL OF APPLIED MECHANICS, Vol. 33, pp. 371–376.

Hardy, C., Baronet, C. N., and Tordion, G. V., 1971, "The Elasto-Plastic Indentation of a Half-Space by a Rigid Sphere," *Intl. J. Num. Meth. Engng.*, Vol. 3, pp. 451–462.

Hill, R., Storåkers, B., and Zdunek, A. B., 1989, "A Theoretical Study of the Brinell Hardness Test," *Proc. R. Soc. Lond.*, Vol. A423, pp. 301–330.

Johnson, K. L., 1968, "An Experimental Determination of the Contact Stresses Between Plastically Deformed Cylinders and Spheres," *Engineering Plasticity*, J. Heyman, and F. A. Leckie, eds., Cambridge University Press, Cambridge, U.K., pp. 341–361.

Johnson, K. L., 1985, *Contact Mechanics*, Cambridge University Press, Cambridge, U.K., pp. 171–184.

Komvopoulos, K., 1988, "Finite Element Analysis of a Layered Elastic Solid in Normal Contact With a Rigid Surface," *J. Tribol.*, Vol. 110, No. 3, pp. 477–485.

Komvopoulos, K., 1989, "Elastic-Plastic Finite Element Analysis of Indented Layered Media," *J. Tribol.*, Vol. 111, No. 3, pp. 430–439.

Kral, E. R., Komvopoulos, K., and Bogy, D. B., 1994a, "Finite Element Analysis of Repeated Indentation of an Elastic-Plastic Layered Medium by a Rigid Sphere, Part I: Surface Results," ASME JOURNAL OF APPLIED MECHANICS, Vol. 61, to be published.

Kral, E. R., Komvopoulos, K., and Bogy, D. B., 1994b, "Finite Element Analysis of Repeated Indentation of an Elastic-Plastic Layered Medium by a Rigid Sphere, Part II: Subsurface Results," ASME JOURNAL OF APPLIED MECHANICS, Vol. 61, to be published.

Kulkarni, S. M., Hahn, G. T., Rubin, C. A., and Bhargava, V., 1990, "Elastoplastic Finite Element Analysis of Three-Dimensional, Pure Rolling Contact at the Shakedown Limit," ASME JOURNAL OF APPLIED MECHANICS, Vol. 57, pp. 57–65.

Kulkarni, S. M., Hahn, G. T., Rubin, C. A., and Bhargava, V., 1991, "Elasto-Plastic Finite Element Analysis of Three-Dimensional Pure Rolling Contact Above the Shakedown Limit," ASME JOURNAL OF APPLIED MECHANICS, Vol. 58, pp. 347–353.

Lankford, J., and Davidson, D. L., 1979, "Indentation Plasticity and Microfracture in Silicon Carbide," *J. Mater. Sci.*, Vol. 14, pp. 1669–1675.

Lawn, B. R., and Evans, A. G., 1977, "A Model for Crack Initiation in Elastic/Plastic Indentation Fields," *J. Mater. Sci.*, Vol. 12, pp. 2195–2199.

Merwin, J. E., and Johnson, K. L., 1963, "An Analysis of Plastic Deformation in Rolling Contact," *Proc. Instn. Mech. Engrs.*, Vol. 177, No. 25, pp. 676–690.

Puttick, K. E., Smith, L. S. A., and Miller, L. E., 1977, "Stress Fields Round Indentations in Poly(methyl methacrylate)," *J. Phys. D: Appl. Phys.*, Vol. 10, pp. 617–632.

Sinclair, G. B., Follansbee, P. S., and Johnson, K. L., 1985, "Quasi-Static Normal Indentation of an Elasto-Plastic Half-Space by a Rigid Sphere—II. Results," *Int. J. Solids Structures*, Vol. 21, No. 8, pp. 865–888.

Tabor, D., 1970, "The Hardness of Solids," *Review Phys. Tech.*, Vol. 1, No. 3, pp. 145–179.

Timoshenko, S. P., and Goodier, J. N., 1970, *Theory of Elasticity*, 3rd ed., McGraw-Hill, New York, pp. 409–414.

Downloaded 03 May 2010 to 171.66.16.245. Redistribution subject to ASME license or copyright; see http://www.asme.org/terms/Terms_Use.cfm

Rudnicki and Rice's Analysis of Strain Localization Revisited

G. Perrin[1]
Laboratoire de Mécanique des Solides,
Ecole Polytechnique,
91128 Palaiseau, France

J. B. Leblond
Laboratoire de Modélisation en Mécanique,
Université Pierre et Marie Curie,
Tour 66, 4 place Jussieu,
75005 Paris, France

In a celebrated paper published in 1975, Rudnicki and Rice (RR) analyzed the conditions for strain localization in pressure-sensitive dilatant materials. This paper corrects certain results in their work that are relevant in exceptional cases. RR found that the normal to the plane of localization was generally *orthogonal to the direction of the intermediate principal stress; however, when a certain inequality was satisfied, it was orthogonal to the direction of the minimum principal stress. In contrast, it is shown here that the normal to the plane of localization is* always *orthogonal to the direction of the intermediate principal stress; but there is a special case where it is parallel to the direction of either the maximum or the minimum principal stress, and in this case the expression of the critical hardening modulus at localization differs from that given by RR.*

1 Introduction

In the mid 1970s Rudnicki and Rice (RR) published a paper on strain localization in pressure-sensitive dilatant materials that was soon to become famous (Rudnicki and Rice, 1975). Their fundamental result was a formula providing the critical value h_c of the hardening modulus below which bifurcation in the form of a shear band becomes possible for the first time. This formula corresponded to the case which they showed to be the most common one, where the normal to the plane of localization was perpendicular to the direction of the intermediate principal stress σ_{II}. The occurrence of this case was defined by an inequality involving the stress state and the model parameters. If this inequality was violated, the normal to the plane of localization was perpendicular to the direction of the minor principal stress σ_{III}, and the expression of h_c was different.

The aim of the present paper is to bring some corrections to the results of RR with regard to the particular case just mentioned. It will be seen that the normal to the plane of localization is in fact *always* perpendicular to the direction of σ_{II}. In general, it is collinear neither to the direction of the major principal stress σ_I nor to that of the minor one, σ_{III}; the expression of h_c is then exactly that given by RR. However, in the special case where the normal to the plane of localization is collinear to either of the directions of σ_I and σ_{III}, the expression of h_c differs from that given by RR. The inequalities defining the occurrence of this special case are also new; in particular they involve Poisson's ratio, which did not appear in RR's inequality.

These corrections are quite obviously of minor character. The authors nevertheless deem that they are worth mentioning, first because the occurrence of at least one of the particular cases might perhaps, as will be seen, be less exceptional in practice than was previously thought, and second because it is their opinion that papers of the importance and quality of that of RR deserve to be cleared of any ambiguity or error, no matter how small.

2 Statement of the Problem

We consider, just as RR did, a material obeying the following law in the plastic regime:

$$D'_{ij}=\frac{\dot{\sigma}'_{ij}}{2G}+\frac{1}{2h}\left(\frac{\sigma'_{kl}\dot{\sigma}_{kl}}{2\tau}+\beta'\,\frac{\dot{\sigma}_{kk}}{3}\right)\frac{\sigma'_{ij}}{\tau};$$

$$D_{kk}=\frac{\dot{\sigma}_{kk}}{3K}+\frac{\beta}{h}\left(\frac{\sigma'_{kl}\dot{\sigma}_{kl}}{2\tau}+\beta'\,\frac{\dot{\sigma}_{kk}}{3}\right). \quad (1)$$

The notations here are exactly identical to those of RR, except for their parameter μ which is denoted β' in order to avoid any possible confusion with Lamé's second coefficient. The dot denotes the ordinary time derivative, which means that a small strain formulation is used. It was shown by RR that introduction of an objective time derivative changes the expression of h_c/G, where h_c is the critical hardening modulus, only by a very small term (of order τ/G). Inversion of (1) yields

$$\dot{\sigma}_{ij}=\mathcal{L}_{ijkl}D_{kl},$$

where

$$\mathcal{L}_{ijkl}=G(\delta_{ik}\delta_{jl}+\delta_{il}\delta_{jk})+\left(K-\frac{2G}{3}\right)\delta_{ij}\delta_{kl}-\frac{\left(G\,\frac{\sigma'_{ij}}{\tau}+K\beta\delta_{ij}\right)\left(G\,\frac{\sigma'_{kl}}{\tau}+K\beta'\delta_{kl}\right)}{h+G+K\beta\beta'}.$$

[1]Currently with the Division of Applied Sciences, Harvard University, Cambridge, MA 02138.

Contributed by the Applied Mechanics Division of THE AMERICAN SOCIETY OF MECHANICAL ENGINEERS for presentation at the ASME Winter Annual Meeting, New Orleans, LA, Nov. 28–Dec. 3, 1993.

Discussion on this paper should be addressed to the Technical Editor, Professor Lewis T. Wheeler, Department of Mechanical Engineering, University of Houston, Houston, TX 77204-4792, and will be accepted until four months after final publication of the paper itself in the ASME JOURNAL OF APPLIED MECHANICS.

Manuscript received by the ASME Applied Mechanics Division, Dec. 11, 1991; final revision, Feb. 14, 1993. Associate Technical Editor: C. F. Shih.

Paper No. 93-WA/APM-18.

Copyright © 1993 by ASME
Downloaded 03 May 2010 to 171.66.16.245. Redistribution subject to ASME license or copyright; see http://www.asme.org/terms/Terms_Use.cfm

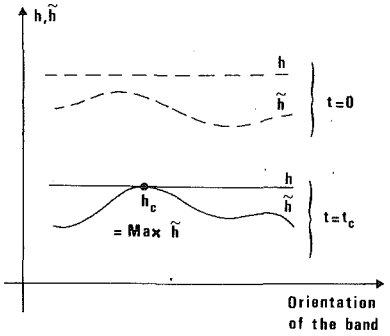


Fig. 1 Symbolic plot of $\tilde{h}$ versus the orientation of the band and of the actual hardening modulus, at the beginning of the loading ($t = 0$) and at the critical instant when bifurcation becomes possible for the first time ($t = t_c$)

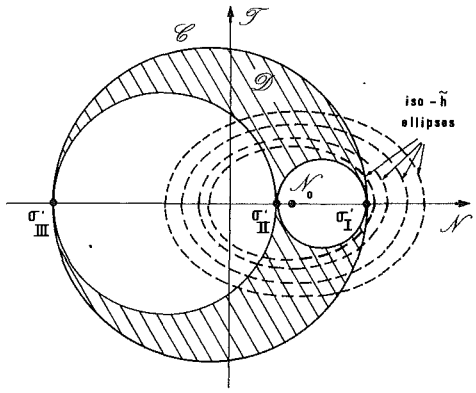


Fig. 2 The domain $\mathcal{D}$ and the iso $\tilde{h}$ ellipses

The condition for the possibility of the appearance of a planar localization band orthogonal to the x_2-direction reads

$$\underset{i,j}{\text{Det}}\ \mathcal{L}_{i2j2} = 0;$$

the corresponding value $\tilde{h}$ of the hardening modulus h is

$$\tilde{h} = \frac{(G\sigma'_{22} + K\beta\tau)(G\sigma'_{22} + K\beta'\tau)}{(K + 4G/3)\tau^2} + \frac{G(\sigma_{21}^2 + \sigma_{23}^2)}{\tau^2} - G - K\beta\beta'. \tag{2}$$

This value depends upon the orientation of the band. At the beginning of the loading, the actual value of the hardening modulus h is greater than $\tilde{h}$ for all envisageble orientations. As time passes, both h and $\tilde{h}$ evolve, until h reaches $\tilde{h}$ for the first time for some orientation, which necessarily corresponds to the absolute maximum h_c of $\tilde{h}$ over all possible ones (see Fig. 1). The problem is thus reduced to the determination of this maximum (which may be positive or negative, the latter possibility meaning that bifurcation is excluded for a hardening material).

3 Geometric Discussion

In contrast to RR's treatment, based on Lagrange multipliers, our approach will use the classical construction of Mohr's circles, which will allow for a simple geometric discussion.

We note that σ'_{22} and $\sigma_{21}^2 + \sigma_{23}^2$ are nothing but the normal component $\mathfrak{N}$ and the square of the tangential component $\mathfrak{T}$ of the force (corresponding to the stress *deviator* σ') exerted on a surface of unit area perpendicular to the x_2-direction. Therefore the expression (2) of $\tilde{h}$ is of the form

$$\tilde{h} = A(\mathfrak{N} - \mathfrak{N}_0)^2 + B\mathfrak{T}^2 + C, \tag{3}$$

with

$$A = \frac{G^2}{(K + 4G/3)\tau^2} = \frac{(1-2\nu)G}{2(1-\nu)\tau^2};$$

$$\mathfrak{N}_0 = -\frac{K(\beta+\beta')\tau}{2G} = -\frac{(1+\nu)(\beta+\beta')\tau}{3(1-2\nu)}; \quad B = \frac{G}{\tau^2};$$

$$C = -\frac{K^2(\beta-\beta')^2}{4(K+4G/3)} - G - K\beta\beta'$$

$$= -G\left[1 + \frac{2}{3}\frac{1+\nu}{1-2\nu}\beta\beta' + \frac{(1+\nu)^2(\beta-\beta')^2}{18(1-\nu)(1-2\nu)}\right]. \tag{4}$$

In Mohr's plane $\mathfrak{N}$, $\mathfrak{T}$, the iso $\tilde{h}$ curves are ellipses (denoted $\mathcal{E}_{\tilde{h}}$ in the sequel) with center at ($\mathfrak{N}_0$, 0) and major and minor axes along the $\mathfrak{N}$ and $\mathfrak{T}$-axes, respectively ($A < B$). All ellipses have identical eccentricities and differ only through their dimensions. Therefore, the maximum value h_c of $\tilde{h}$, when the

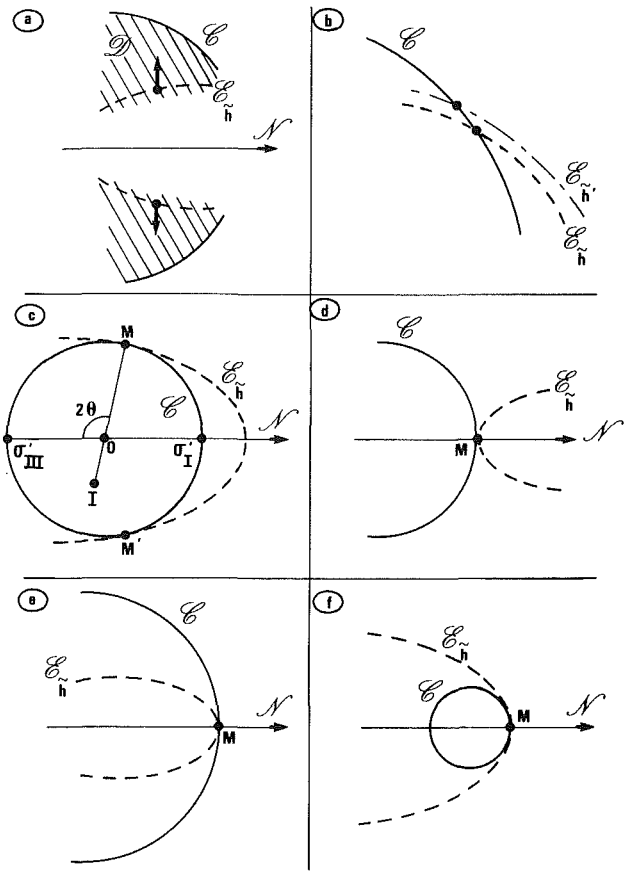


Fig. 3 Various configurations of the circle $\mathcal{C}$ and the ellipse $\mathcal{E}_{\tilde{h}}$. Only configurations 2(*c*) and 2(*f*) correspond to $\tilde{h} = h_c$.

normal to the band is varied, *corresponds to the largest ellipse* $\mathcal{E}_{h_c}$ *that still intersects the domain of variation* $\mathcal{D}$ *of the point* ($\mathfrak{N}$, $\mathfrak{T}$), i.e., the region comprised (in the broad sense) between the three Mohr circles (Fig. 2).

Let $\mathcal{C}$ denote the great Mohr circle of equation

$$(\mathfrak{N} - \sigma'_I)(\mathfrak{N} - \sigma'_{III}) + \mathfrak{T}^2 = 0 \tag{5}$$

where σ'_I, σ'_{II}, σ'_{III}, $\sigma'_I \geq \sigma'_{II} \geq \sigma'_{III}$, denote the ordered principal values of σ'. Any value $\tilde{h}$ corresponding to a point of $\mathcal{D}$ not lying on $\mathcal{C}$ can be increased (and therefore differs from h_c) by displacing this point slightly upwards or downwards, depending on whether it lies above or below the $\mathfrak{N}$-axis (Fig. 3(*a*)). Thus, any point of intersection of $\mathcal{E}_{h_c}$ and $\mathcal{D}$ must lie on $\mathcal{C}$. Since these points of intersection correspond to the possible orientations of the localization band (at first occurrence of

Downloaded 03 May 2010 to 171.66.16.245. Redistribution subject to ASME license or copyright; see http://www.asme.org/terms/Terms_Use.cfm

bifurcation), it follows that the normal to the band always lies in the plane determined by the directions of σ_I' and σ_{III}', i.e., that it is *always perpendicular to the direction of the intermediary principal stress*. This conclusion differs somewhat from that of RR in that these authors mentioned this result only as a general rule liable to be violated for some extreme values of the model parameters, the normal to the band being then perpendicular to the direction of σ_{III}' instead of σ_{II}'. The explanation of this contradiction is given in the Appendix.

It is also easy to see that at any point of intersection of $\mathcal{E}_{h_c}$ and $\mathcal{C}$ (or $\mathcal{D}$), these curves must be tangent to each other. Indeed, if the curves $\mathcal{E}_{\tilde{h}}$ and $\mathcal{C}$ cross themselves without being tangent, the ellipse $\mathcal{E}_{\tilde{h}'}$, for $\tilde{h}'$ slightly greater than $\tilde{h}$, still crosses $\mathcal{C}$, and therefore $\mathcal{D}$ (Fig. 3(*b*)).

We must now see whether the condition that $\mathcal{E}_{\tilde{h}}$ and $\mathcal{C}$ be tangent to each other at some point M is sufficient to warrant that $\tilde{h} = h_c$. This equality is equivalent to the property that $\mathcal{C}$ be everywhere interior in the broad sense to $\mathcal{E}_{\tilde{h}}$ (if this is true, larger ellipses do not intersect $\mathcal{C}$; if, conversely, there is a point on $\mathcal{C}$ which is strictly exterior to $\mathcal{E}_{\tilde{h}}$, the larger ellipse which contains it still intersects $\mathcal{C}$). Two cases must be distinguished.

- *$\mathcal{E}_{\tilde{h}}$ and $\mathcal{C}$ are tangent at some point not lying on the $\mathfrak{N}$-axis.* Let us write the equation of $\mathcal{E}_{\tilde{h}}$ under the parametric form

$$\mathfrak{N} - \mathfrak{N}_0 = a\cos\varphi,$$

$$\mathfrak{I} = b\sin\varphi \quad \left(a = \sqrt{(\tilde{h}-C)/A} > b = \sqrt{(\tilde{h}-C)/B}\right).$$

It is easy to calculate the radius of curvature and the $\mathfrak{I}$-coordinate of the center of curvature, namely

$$\frac{(a^2\sin^2\varphi + b^2\cos^2\varphi)^{3/2}}{ab} \text{ and } -\frac{a^2-b^2}{b}\sin^3\varphi.$$

It follows that for a point of the ellipse lying above the $\mathfrak{N}$-axis, the corresponding center of curvature lies below it. Now let 0 denote the center of $\mathcal{C}$ and I the center of curvature of $\mathcal{E}_{\tilde{h}}$ corresponding to the point M (Fig. 3(*c*)). These points are aligned with M since they lie on the common normal to $\mathcal{E}_{\tilde{h}}$ and $\mathcal{C}$. 0 lies on the $\mathfrak{N}$-axis. Because of symmetry with respect to this axis, M can be assumed to lie above it, and I then lies below it by what precedes. It follows that the radius of curvature of $\mathcal{E}_{\tilde{h}}$ is greater than that of $\mathcal{C}$ and therefore that the circle is locally (except at M) strictly interior to the ellipse. The same is true near the symmetric point M' of M with respect to the $\mathfrak{N}$-axis. If the circle were somewhere strictly exterior to the ellipse, there would necessarily exist a point of intersection distinct from the two double points M and M', which is impossible. It follows that $\mathcal{C}$ is everywhere interior in the broad sense to $\mathcal{E}_{\tilde{h}}$, and thus that $\tilde{h} = h_c$.

- *$\mathcal{E}_{\tilde{h}}$ and $\mathcal{C}$ are tangent on the $\mathfrak{N}$-axis.* If the concavities of the curves are oriented in opposite directions, $\mathcal{C}$ is not interior to $\mathcal{E}_{\tilde{h}}$ and therefore $\tilde{h} \neq h_c$ (Fig. 3(*d*)). The same conclusions hold if they are oriented in the same direction but the radius of curvature of $\mathcal{E}_{\tilde{h}}$ is smaller than that of $\mathcal{C}$ (Fig. 3(*e*)). There remains the case where they are oriented in the same direction and the radius of curvature of $\mathcal{E}_{\tilde{h}}$ is greater than or equal to that of $\mathcal{C}$ (Fig. 3(*f*)). If $\mathcal{C}$ were somewhere strictly exterior to $\mathcal{E}_{\tilde{h}}$, the major axis of the latter would have to be smaller than the radius of the former. But the major axis of $\mathcal{E}_{\tilde{h}}$ is greater than its radius of curvature at M (this immediately results from the formula given above, with $\varphi = 0$ or π), which is itself supposed to be greater than or equal to the radius of $\mathcal{C}$. Hence, this possibility must be excluded, and $\mathcal{C}$ is everywhere interior in the broad sense to $\mathcal{E}_{\tilde{h}}$; thus $\tilde{h} = h_c$.

In conclusion, the ellipse $\mathcal{E}_{h_c}$ corresponding to the absolute maximum of $\tilde{h}$ can be characterized as follows: *it is tangent to the great Mohr circle $\mathcal{C}$ at a point which lies*

- *either outside the $\mathfrak{N}$-axis* (general case);
- *or on the $\mathfrak{N}$-axis, the concavities of $\mathcal{E}_{h_c}$ and $\mathcal{C}$ being then oriented in the same direction and the radius of curvature of $\mathcal{E}_{h_c}$ being greater than or equal to that of $\mathcal{C}$* (particular case).

The "particular case" just evidenced corresponds to two special positions of the point of tangency of $\mathcal{E}_{h_c}$ and $\mathcal{C}$, namely $(\sigma_I', 0)$ and $(\sigma_{III}', 0)$. The corresponding orientations of the normal to the band are the directions of the major and minor principal stresses. In contrast, RR's "particular case" corresponded to orientations of this normal lying in the plane determined by the directions of the major and intermediate principal stresses.[2] The origin of this discrepancy is explained in the Appendix.

4 Analytical Treatment

4.1 General Case. Let us determine the expression of h_c. This requires to look for the points of tangency of $\mathcal{E}_{h_c}$ and $\mathcal{C}$. Combination of the Eqs. (3) and (5) of these curves and elimination of $\mathfrak{I}^2$ yields

$$(B-A)\mathfrak{N}^2 + (B\sigma_{II}' + 2A\mathfrak{N}_0)\mathfrak{N} + B(\sigma_{II}'^2 - \tau^2) - A\mathfrak{N}_0^2 + h_c - C = 0,$$

where the relations

$$\sigma_I' + \sigma_{II}' + \sigma_{III}' = 0$$

and

$$\sigma_I'^2 + \sigma_{II}'^2 + \sigma_{III}'^2 = 2\tau^2$$

have been used to express $\sigma_I' + \sigma_{III}'$ and $\sigma_I'\sigma_{III}'$ in terms of σ_{II}' and τ. For $\mathcal{E}_{h_c}$ and $\mathcal{C}$ to have a point of tangency outside the $\mathfrak{N}$-axis, this equation must have a double solution in $\mathfrak{N}$, i.e., its discriminant must be zero. This leads to the following expression of h_c:

$$h_c = C + B(\tau^2 - \sigma_{II}'^2) + A\mathfrak{N}_0^2 + \frac{(B\sigma_{II}' + 2A\mathfrak{N}_0)^2}{4(B-A)},$$

which can be put after some algebra, using the expressions (4) of A, $\mathfrak{N}_0$, B, C, under the form

$$\frac{h_c}{G} = \frac{1+\nu}{9(1-\nu)}(\beta-\beta')^2 - \frac{1+\nu}{2}\left(N + \frac{\beta+\beta'}{3}\right)^2, \tag{6}$$

where

$$N = \sigma_{II}'/\tau.$$

This is exactly RR's general formula (20).

The conditions of validity of this formula are easily found by noting that for the point of tangency of $\mathcal{E}_{h_c}$ and $\mathcal{C}$ to lie outside the $\mathfrak{N}$-axis, the double solution of the above equation must be strictly comprised between σ_{III}' and σ_I'. Hence, these conditions of validity read

$$\sigma_{III}' < -\frac{B\sigma_{II}' + 2A\mathfrak{N}_0}{2(B-A)} < \sigma_I',$$

or, equivalently,

$$N_{\min} + (1-\nu)N < \frac{(1+\nu)(\beta+\beta')}{3} < N_{\max} + (1-\nu)N, \tag{7}$$

where

$$N_{\min} = \sigma_{III}'/\tau$$

and

$$N_{\max} = \sigma_I'/\tau.$$

The explanation of the discrepancy with respect to the condition found by RR (their inequality (18)), namely

$$2\sigma_I' - \sigma_{II}' - \sigma_{III}' > 2\tau(\beta+\beta') \quad \Leftrightarrow \quad N_{\max} > \frac{2}{3}(\beta+\beta'),$$

is again explained in the Appendix.

[2] It is interesting to note, however, that the numerical results for the constitutive relation modified for the vertex effect reported in RR's Appendix II are consistent with the present findings; indeed the normal to the plane of localization appears to be always in the plane defined by σ_I and σ_{III}, and exceptionally parallel to the direction of σ_I.

Downloaded 03 May 2010 to 171.66.16.245. Redistribution subject to ASME license or copyright; see http://www.asme.org/terms/Terms_Use.cfm

Let us now look for the orientation of the band. Let θ denote, as in RR's work, the angle between the direction of σ'_{III} and the normal to the band. By a well-known property of Mohr's circles, 2θ is the angle shown in Fig. 3(*c*). Since the radius and $\mathfrak{N}$-coordinate of the center of $\mathcal{C}$ are $(\sigma'_I - \sigma'_{III})/2$ and $-\sigma'_{II}/2$, it follows that

$$\cos 2\theta = -\frac{\mathfrak{N} + \sigma'_{II}/2}{(\sigma'_I - \sigma'_{III})/2},$$

which is readily put, using the identity

$$\cos 2\theta = \frac{1 - \tan^2\theta}{1 + \tan^2\theta}$$

and the expressions of $\mathfrak{N}$, $\mathfrak{N}_0$, A, B, under the form

$$\tan^2\theta = \frac{\xi - N_{\min}}{N_{\max} - \xi},\ \xi = \frac{(1+\nu)(\beta+\beta')}{3} - (1-\nu)N. \tag{8}$$

(Note that the conditions (7) precisely ensure the positiveness of the numerator and the denominator of the expression of $\tan^2\theta$.) This result is identical to that of RR (Eq. (19) of their paper).

4.2 Particular Case. Let us first assume the point of tangency of $\mathcal{E}_{h_c}$ and $\mathcal{C}$ to be $(\sigma'_I, 0)$. Then (3) immediately yields

$$h_c = C + A(\sigma'_I - \mathfrak{N}_0)^2,$$

or, equivalently (after rearrangement),

$$\frac{h_c}{G} = \frac{1+\nu}{9(1-\nu)}(\beta - \beta')^2 - \frac{1+\nu}{1-\nu}\left(\frac{N_{\max}}{2} - \frac{\beta+\beta'}{3}\right)^2 - \frac{1}{4}(N - N_{\min})^2. \tag{9}$$

For this formula to be applicable, it is first necessary that the concavities of $\mathcal{E}_{h_c}$ and $\mathcal{C}$ be oriented in the same direction, or equivalently, that the center of the ellipse be located on the left of the point of tangency; this condition reads $\mathfrak{N}_0 \le \sigma'_I$. It is also necessary that the radius of curvature of $\mathcal{E}_{h_c}$ at the point of tangency be greater than or equal to $(\sigma'_I - \sigma'_{III})/2$. Using the expression of the radius of curvature given previously, this condition can be explicited as follows:

$$\frac{\sqrt{A(h_c - C)}}{B} = \frac{A}{B}(\sigma'_I - \mathfrak{N}_0) \ge \frac{1}{2}(\sigma'_I - \sigma'_{III})$$

(where account has been taken of the inequality $\sigma'_I \ge \mathfrak{N}_0$), which is equivalent to

$$N_{\max} + (1-\nu)N \le \frac{(1+\nu)(\beta+\beta')}{3}. \tag{10}$$

Conversely, this sole inequality is sufficient for (9) to be valid; indeed, since $\sigma'_I - \sigma'_{III} \ge 0$, it automatically implies the other condition $\sigma'_I - \mathfrak{N}_0 \ge 0$.

The expression (9) of h_c disagrees with that of RR (which these authors state to be just (6) with N replaced by $N_{\min}$), and the corresponding conditions of validity are also different. This is not surprising since, as remarked previously, RR's particular case and ours correspond to different situations (normal to the band perpendicular to the direction of σ'_{III} in the first case, parallel to that of σ'_I in the second one); more details are given in the Appendix.

The formulae relative to the case where the point of tangency of $\mathcal{E}_{h_c}$ and $\mathcal{C}$ is $(\sigma'_{III}, 0)$ can be derived in a completely analogous way:

$$\frac{h_c}{G} = \frac{1+\nu}{9(1-\nu)}(\beta - \beta')^2 - \frac{1+\nu}{1-\nu}\left(\frac{N_{\min}}{2} - \frac{\beta+\beta'}{3}\right)^2 - \frac{1}{4}(N_{\max} - N)^2 \tag{11}$$

provided that

$$N_{\min} + (1-\nu)N \ge \frac{(1+\nu)(\beta+\beta')}{3}. \tag{12}$$

4.3 Concluding Remarks. It should first be noted that in spite of their seemingly discontinuous character, the above expressions of h_c *are* continuous: it can be verified that if, for instance,

$$N_{\max} + (1-\nu)N = \frac{(1+\nu)(\beta+\beta')}{3},$$

both (6) and (9) yield the same result (use must be made of the relation $N_{\max} + N + N_{\min} = 0$ in the check). This means that the "$<$" signs in the validity conditions (7) could be replaced by "$\le$".

A major consequence of RR's work was that *if normality of the flow rule is obeyed and the hardening modulus is positive, strain localization is impossible*; this stemmed from the implications

$$(\text{normality}) \Rightarrow \beta = \beta' \Rightarrow h_c \le 0,$$

(h_c being supposed to be given by RR's Eq. (20), equivalent to (6)). It is important to note that *the present analysis does not modify this conclusion*; indeed, the h_c values given by the formulae (9) and (11), relevant in the particular case, are nonpositive for $\beta = \beta'$, just like that given by (6). Similarly, RR's conclusion that h_c *can be positive for a non-normal flow rule* is left unmodified.

Concerning the case defined by (12), it may be remarked that the left-hand side of this inequality is nonpositive (it is equal to $-(1-\nu)N_{\max} + \nu N_{\min}$, with $N_{\max} \ge 0$ and $N_{\min} \le 0$); hence this condition requires that $\beta + \beta'$ be nonpositive. It follows that this case is certainly exceptional in practice (see the short discussion at the end of Appendix I of RR's paper).

On the other hand, the case defined by (10) might be a possible occurrence in practice. Let us consider, for instance, a porous ductile metal described by the well-known Gurson criterion (Gurson, 1977). Using the identification of the parameters h, β, β' provided for instance by Yamamoto (1978), it is easy to check that the right-hand side of (10) is an increasing function of the mean stress and the porosity. On the other hand, the left-hand side depends only on the stress deviator. Hence inequality (10) should be satisfied for high triaxialities and/or high porosities.

Note: Since the first draft of this paper was written, the authors have become aware of the fact that the geometric method of Section 3 has been proposed by other authors in some recent papers (Benallal and Lemaitre, 1991; Benallal, 1992; Benallal and Comi, 1993), where it was used to study bifurcations for various constitutive laws incorporating notably the softening effect due to thermomechanical coupling. Benallal et al. did not, however, employ it to revisit RR's analysis.

References

Benallal, A., and Lemaître, J., 1991, "Localization Phenomena in Thermo-Elastoplasticity," *Creep in Structures* (Proceedings of an IUTAM Symposium held in Cracow, Poland, 1990), M. Zyczkowski, ed., Springer-Verlag, New York, pp. 223–235.

Benallal, A., 1992, "On Localization Phenomena in Thermo-Elastoplasticity," *Archives of Mechanics*, Vol. 44, pp. 15–29.

Benallal, A., and Comi, C., 1993, "A Geometrical Method to Solve Localization Problems," *Journal of the Mechanics and Physics of Solids*, submitted for publication.

Gurson, A. L., 1977, "Continuum Theory of Ductile Rupture by Void Nucleation and Growth: Part I—Yield Criteria and Flow Rules for Porous Ductile Media," ASME *Journal of Engineering Materials and Technology*, Vol. 99, pp. 2–15.

Rudnicki, J. W., and Rice, J. R., 1975, "Conditions for the Localization of Deformation in Pressure-Sensitive Dilatant Materials," *Journal of the Mechanics and Physics of Solids*, Vol. 23, pp. 371–394.

Yamamoto, H., 1978, "Conditions for Shear Localization in the Ductile Fracture of Void-Containing Materials," *International Journal of Fracture*, Vol. 14, pp. 347–365.

Downloaded 03 May 2010 to 171.66.16.245. Redistribution subject to ASME license or copyright; see http://www.asme.org/terms/Terms_Use.cfm

APPENDIX

Detailed Analysis of the Divergences With Respect to the Work of Rudnicki and Rice

The explanations of the discrepancies are to be found in RR's Appendix I; we refer to the notations and reasoning of this part of their paper. All differences are in fact the result of three factors.

(1) RR disregarded the case where two of the n_K's are zero, which does correspond to the particular case evidenced here (for $n_I = n_{II} = 0$ or $n_{II} = n_{III} = 0$). The reason for this was that the corresponding h_c values were smaller than that deduced from (6) for the values of β and β' they investigated. It has been shown in the present work, however, that this case is indeed possible, provided that conditions (10) or (12) are fulfilled.

(2) On the other hand, they found a particular case corresponding to $n_{III} = 0$, n_I and $n_{II} \neq 0$, which does not exist in our view. This was because they neglected to check the positiveness of the values of n_I^2 and n_{II}^2 resulting from their treatment in that case; indeed, let us show that such a check allows to establish the impossibility of the latter. The values of n_I^2 and n_{II}^2 are

$$n_I^2 = \frac{\frac{(1+\nu)(\beta+\beta')}{3} - N - (1-\nu)N_{\min}}{N_{\max} - N};$$

$$n_{II}^2 = \frac{N_{\max} + (1-\nu)N_{\min} - \frac{(1+\nu)(\beta+\beta')}{3}}{N_{\max} - N}.$$

Hence $n_{II}^2 > 0$ requires that

$$N_{\max} + (1-\nu)N_{\min} > \frac{(1+\nu)(\beta+\beta')}{3}.$$

Now, for the h_c value calculated with $n_{III} \simeq 0$, n_I and $n_{II} \neq 0$ to be greater than that corresponding to $n_{II} = 0$, n_I and $n_{III} \neq 0$, the inequality

$$N_{\max} < \frac{2}{3}(\beta+\beta')$$

(opposite of RR's condition (18)) must be satisfied; but this inequality is incompatible with that above, since

$$N = -N_{\min} - N_{\max} \geq N_{\min} \Rightarrow N_{\min} \leq -N_{\max}/2$$

$$\Rightarrow N_{\max} + (1-\nu)N_{\min} \leq \frac{1+\nu}{2} N_{\max}.$$

Hence the case $n_{III} = 0$, n_I and $n_{II} \neq 0$ is impossible.

(3) RR identified the conditions of validity of their general formula (20) as those excluding the (in fact, impossible) particular case $n_{III} = 0$, n_I and $n_{II} \neq 0$. The correct conditions could again have been derived by checking the positiveness of the values of n_I^2 and n_{III}^2 found for $n_{II} = 0$, n_I and $n_{III} \neq 0$. Indeed, these values are

$$n_I^2 = \frac{\frac{(1+\nu)(\beta+\beta')}{3} - N_{\min} - (1-\nu)N}{N_{\max} - N_{\min}};$$

$$n_{III}^2 = \frac{N_{\max} + (1-\nu)N - \frac{(1+\nu)(\beta+\beta')}{3}}{N_{\max} - N_{\min}},$$

which are positive under conditions (7).

Downloaded 03 May 2010 to 171.66.16.245. Redistribution subject to ASME license or copyright; see http://www.asme.org/terms/Terms_Use.cfm

Fundamental Solutions for a Poroelastic Half-Space With Compressible Constituents

R. K. N. D. Rajapakse

T. Senjuntichai

Department of Civil Engineering,
University of Manitoba,
Winnipeg, Manitoba R3T 2N2, Canada

This paper presents a comprehensive analytical treatment of the three-dimensional response of a poroelastic half-space with compressible constituents. General solutions for equations of equilibrium expressed in terms of displacements and variation of fluid volume are derived by applying Fourier expansion, Hankel transforms, and Laplace transforms with respect to the circumferential, radial, and time coordinates, respectively. The general solutions are used to derive a set of fundamental solutions corresponding to circular ring loads and to a fluid source applied at a finite depth below the free surface of a poroelastic half-space. The circumferential variation of the ring loads and the fluid source is described by appropriate trigonometric terms. Fundamental solutions presented in this paper can be used to model arbitrarily distributed loadings and a fluid source as well as a number of other problems encountered in geomechanics and energy resource explorations. In addition, these fundamental solutions can be used as the kernel functions in the development of boundary integral equation methods for a poroelastic half-space. Solutions for buried circular patch loads/fluid sink and concentrated loads/fluid sink are also deduced. Numerical evaluation of the fundamental solutions is also discussed. Comparisons are presented for time domain solutions obtained by using the Stehfest's and Schapery's schemes for Laplace inversion. A selected set of numerical solutions are presented to portray the features of consolidation process in six different poroelastic materials under buried patch loads and a sink.

Introduction

It is well known that several problems encountered in geomechanics (Terzaghi, 1923; McNamee and Gibson, 1960a,b; Ruina, 1978; Rudnicki, 1986a, 1987) are concerned with the consolidation process in geomaterials which are semi-infinite and composed of a solid matrix with fluid-saturated pore spaces. Therefore, the study of the mechanical response of such a medium, commonly known as a porous elastic solid, has been a subject of interest and an object of numerous investigations. The first theory of consolidation was originally developed by Terzaghi (1923) concerned with the one-dimensional vertical compression of loaded clay layers. Later, Biot (1941) presented the general theory of three-dimensional consolidation by adopting Terzaghi's concepts. In addition to the material constants in classical elasticity, Biot included some poroelastic constants in his theory. A number of problems related to the special case involving incompressible constituents have been considered in the past (McNamee and Gibson, 1960a,b; Schiffman and Fungaroli, 1965; Apirathvorakij and Karasudhi, 1980; Niumpradit and Karasudhi, 1981; Puswewala and Rajapakse, 1988; Kanok-Nukulchai and Chau, 1990; and others). Verruijt (1971) modified the displacement functions given by McNamee and Gibson to account for the compressibility of constituents. The incompressible case can be used to model the consolidation of the water-saturated clays but for the case of porous rocks, the compressibility of the pore fluid should be considered. The governing equations for fluid-saturated poroelastic media with compressible constituents were later reformulated by Rice and Cleary (1976) in terms of material constants which are more easily identifiable. Thereafter, their formulation has been widely used to study the quasi-static response of porous elastic solids containing compressible constituents. Cleary (1977) presented a set of fundamental solutions for an infinite poroelastic solid. Rudnicki (1986b) rederived Cleary's results for a suddenly applied point force, a fluid mass source and a fluid mass dipole. Problems related to a slip on a fault in a poroelastic medium were also considered by Rudnicki (1986a, 1987). Plane-strain problems related to a borehole has been considered by Detournay and Cheng (1988).

This paper is a further development of the formulation presented by Rice and Cleary (1976) for poroelastic solids with compressible constituents and it has three objectives. The first

Contributed by the Applied Mechanics Division of THE AMERICAN SOCIETY OF MECHANICAL ENGINEERS for presentation at the ASME Winter Annual Meeting, New Orleans, LA, Nov. 28–Dec. 3, 1993.

Discussion on this paper should be addressed to the Technical Editor, Professor Lewis T. Wheeler, Department of Mechanical Engineering, University of Houston, Houston, TX 77204-4792, and will be accepted until four months after final publication of the paper itself in the ASME JOURNAL OF APPLIED MECHANICS.

Manuscript received by the ASME Applied Mechanics Division, Apr. 21, 1992; final revision, Dec. 18, 1992. Associate Technical Editor: R. M. Bowen.

Paper No. 93-WA/APM-13.

Copyright © 1993 by ASME

Downloaded 03 May 2010 to 171.66.16.245. Redistribution subject to ASME license or copyright; see http://www.asme.org/terms/Terms_Use.cfm

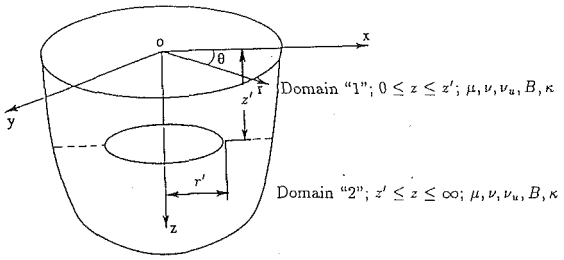


Fig. 1 Coordinate system and internal ring loading

objective is to present three-dimensional general solutions for the analysis of asymmetric problems related to a poroelastic solid with compressible constituents. Fourier expansion, Hankel transforms, and Laplace transforms with respect to the circumferential, radial, and time coordinates are used to obtain explicit general solutions. In essence, this work is similar to Muki's classical three-dimensional solutions for ideal elasticity (Muki, 1960) and the three-dimensional poroelastic solutions presented by Schiffman and Fungaroli (1965) for the case of incompressible constituents. Our second objective is to derive a set of fundamental solutions corresponding to asymmetric ring loads (radial, circumferential, and vertical) and to a fluid source applied at a finite depth below the free surface of a poroelastic half-space. Complete explicit solutions are presented in the Laplace transform space for the above loadings and it is shown that poroelastic counterparts of classical Mindlin's solution (Mindlin, 1936) and solutions for uniform patch loads/fluid source can be deduced from the ring load/source solutions. These fundamental solutions can be also used in the development of boundary integral equation methods (Nishimura and Kobayashi, 1989; Dargush and Banerjee, 1991; Dominguez, 1991; and Cheng et al., 1992) for the analysis of complicated problems related to poroelastic half-space regions, analysis of problems encountered in energy resource explorations, and in the development of solutions for anchors, buried footing, piles, etc. The final objective is to study the response of different poroelastic materials under a selected set of buried loads and a fluid sink by numerically evaluating the Laplace domain solutions. The influence of poroelastic material parameters on the response and the features of the consolidation process are discussed.

Governing Equations and General Solutions

Consider a poroelastic half-space with a cylindrical polar coordinate system (r, θ, z) defined as shown in Fig. 1. The quasi-static governing equations (Rice and Cleary, 1976) of a poroelastic medium with compressible constituents, expressed in terms of stresses and pore pressure as the basic variables, can be transformed into Navier equations with coupling terms and a diffusion equation by treating the displacements and the variation of fluid volume as the basic unknowns. The governing equations can be expressed as

$$\nabla^2 u_r + \frac{1}{1-2\nu_u}\frac{\partial \epsilon}{\partial r} - \frac{1}{r}\left[\frac{2}{r}\frac{\partial u_\theta}{\partial \theta} + \frac{u_r}{r}\right] - \frac{2B(1+\nu_u)}{3(1-2\nu_u)}\frac{\partial \zeta}{\partial r} = 0 \quad (1)$$

$$\nabla^2 u_\theta + \frac{1}{1-2\nu_u}\frac{\partial \epsilon}{r\partial \theta} - \frac{1}{r}\left[\frac{u_\theta}{r} - \frac{2}{r}\frac{\partial u_r}{\partial \theta}\right] - \frac{2B(1+\nu_u)}{3(1-2\nu_u)}\frac{1}{r}\frac{\partial \zeta}{\partial \theta} = 0 \quad (2)$$

$$\nabla^2 u_z + \frac{1}{1-2\nu_u}\frac{\partial \epsilon}{\partial z} - \frac{2B(1+\nu_u)}{3(1-2\nu_u)}\frac{\partial \zeta}{\partial z} = 0 \quad (3)$$

$$\nabla^2 \zeta = \frac{\partial \zeta}{c\partial t} \quad (4)$$

where

$$\nabla^2 = \frac{\partial^2}{\partial r^2} + \frac{1}{r}\frac{\partial}{\partial r} + \frac{1}{r^2}\frac{\partial^2}{\partial \theta^2} + \frac{\partial^2}{\partial z^2} \quad (5)$$

$$\epsilon = \frac{\partial u_r}{\partial r} + \frac{u_r}{r} + \frac{1}{r}\frac{\partial u_\theta}{\partial \theta} + \frac{\partial u_z}{\partial z} \quad (6)$$

$$c = \frac{2\mu\kappa B^2(1-\nu)(1+\nu_u)^2}{9(1-\nu_u)(\nu_u-\nu)}. \quad (7)$$

In the above equations, $u_r(r, \theta, z, t)$, $u_\theta(r, \theta, z, t)$, and $u_z(r, \theta, z, t)$ are displacements in the r, θ, and z directions, respectively; ζ denotes the variation of fluid volume per unit reference volume; μ, ν, ν_u, and κ are the shear modulus, drained and undrained Poisson's ratios, and the coefficient of permeability of the medium, respectively. In addition, B is the Skempton's pore pressure coefficient (Skempton, 1954). Also, note that Eq. (4) is based on the assumption that the solid dilatation and gradients in fluid mass content do not contribute significantly to mass flux.

The constitutive relations can be expressed by using standard indicial notation as

$$\sigma_{ij} = 2\mu\left[\epsilon_{ij} + \frac{\nu}{1-2\nu}\delta_{ij}\epsilon\right] - \frac{3(\nu_u-\nu)}{B(1-2\nu)(1+\nu_u)}\delta_{ij}p. \quad (8)$$

In Eq. (8), σ_{ij} and ϵ_{ij} denote the stresses and strains of the bulk material, respectively, ϵ is the dilatation which is defined in Eq. (6), δ_{ij} is the Kronecker delta, and p is the excess pore fluid pressure (suction is considered negative), which can be expressed in terms of dilatation and variation of fluid volume as

$$\frac{p}{2\mu} = -\frac{B(1+\nu_u)}{3(1-2\nu_u)}\epsilon + \frac{B^2(1-2\nu)(1+\nu_u)^2}{9(1-2\nu_u)(\nu_u-\nu)}\zeta. \quad (9)$$

At this stage, it is convenient to nondimensionalize all quantities including the coordinate frame with respect to length and time by selecting the radius of a loading area "a" as a unit length and "a^2/c" as a unit of time, respectively. All variables will be replaced by appropriate nondimensional variables, but the previous notations will be used for convenience.

Application of the Fourier expansion with respect to the circumferential coordinate θ for the displacements and the variation of fluid volume results in

$$u_r(r,\theta,z,t) = \sum_{m=0}^{\infty} u_{rm}(r,z,t)\cos m\theta + \sum_{m=0}^{\infty} \tilde{u}_{rm}(r,z,t)\sin m\theta \quad (10)$$

$$u_\theta(r,\theta,z,t) = \sum_{m=0}^{\infty} u_{\theta m}(r,z,t)\sin m\theta - \sum_{m=0}^{\infty} \tilde{u}_{\theta m}(r,z,t)\cos m\theta \quad (11)$$

$$u_z(r,\theta,z,t) = \sum_{m=0}^{\infty} u_{zm}(r,z,t)\cos m\theta + \sum_{m=0}^{\infty} \tilde{u}_{zm}(r,z,t)\sin m\theta \quad (12)$$

$$\zeta(r,\theta,z,t) = \sum_{m=0}^{\infty} \zeta_m(r,z,t)\cos m\theta + \sum_{m=0}^{\infty} \tilde{\zeta}_m(r,z,t)\sin m\theta. \quad (13)$$

In Eqs. (10)–(13), u_{rm}, $u_{\theta m}$, u_{zm}, and ζ_m are symmetric components and $\tilde{u}_{rm}$, $\tilde{u}_{\theta m}$, $\tilde{u}_{zm}$, and $\tilde{\zeta}_m$ are antisymmetric components corresponding to the mth harmonic. In the subsequent analysis, only symmetric components are considered without loss of generality. It is noted that the solution corresponding to antisymmetric components can be obtained by making the replacements $\cos m\theta \rightarrow -\sin m\theta$ and $\sin m\theta \rightarrow \cos m\theta$ (Muki, 1960).

Downloaded 03 May 2010 to 171.66.16.245. Redistribution subject to ASME license or copyright; see http://www.asme.org/terms/Terms_Use.cfm

The Laplace transform of function $\phi(r, z, t)$ with respect to time variable t is defined by (Sneddon, 1951)

$$\bar{\phi}(r,z,s) = \int_0^\infty \phi(r,z,t) e^{-st} dt \tag{14}$$

and

$$s\bar{\phi}(r,z,s) = \int_0^\infty \frac{\partial \phi(r,z,t)}{\partial t} e^{-st} dt. \tag{15}$$

In Eqs. (14) and (15), s is the Laplace transform parameter and $\phi(r, z, 0) = 0$. The inverse Laplace transform is given by

$$\phi(r,z,t) = \frac{1}{2\pi i} \int_{\alpha - i\infty}^{\alpha + i\infty} \bar{\phi}(r,z,s) e^{st} ds \tag{16}$$

where the line $\mathrm{Re}(s) = \alpha$ is to the right of all singularities of $\bar{\phi}$ and $i = \sqrt{-1}$.

The mth order Hankel integral transform of $\bar{\phi}(r, z, s)$ with respect to the radial coordinate is defined by (Sneddon, 1951)

$$\phi_m^*(\xi,z,s) = \int_0^\infty \bar{\phi}(r,z,s) J_m(\xi r) r dr \tag{17}$$

and the inverse relationship is given by

$$\bar{\phi}(r,z,s) = \int_0^\infty \phi_m^*(\xi,z,s) J_m(\xi r) \xi d\xi, \tag{18}$$

where $J_m(\xi r)$ denotes the Bessel function of the first kind of order m (Watson, 1962) and ξ is the Hankel transform parameter.

In all subsequent manipulations, the superposed bar denotes the Laplace transform of a function with respect to the time coordinate and the superscript $(^*)$ denotes the Hankel transform with respect to the radial coordinate of the Laplace transform of that function.

In view of Eqs. (10)–(18), Eq. (4) can be solved directly and the resulting solution can be expressed as

$$\zeta_m^* = A_m(\xi,s) e^{\gamma z} + B_m(\xi,s) e^{-\gamma z} \tag{19}$$

where

$$\gamma = (\xi^2 + s)^{1/2}, \tag{20}$$

and $A_m(\xi, s)$ and $B_m(\xi, s)$ are arbitrary functions.

Differentiation of Eqs. (1) to (3) and subsequent manipulations yield

$$\nabla^2 \epsilon = \eta \nabla^2 \zeta \tag{21}$$

where

$$\eta = \frac{B(1+\nu_u)}{3(1-\nu_u)} \tag{22}$$

and ∇^2 is defined as in Eq. (5).

Application of the Fourier expansion together with the Laplace and mth order Hankel integral transform in Eq. (21) and the substitution of Eq. (19) results in

$$\left[\frac{d^2}{dz^2} - \xi^2\right] \epsilon_m^* = \eta s (A_m(\xi,s) e^{\gamma z} + B_m(\xi,s) e^{-\gamma z}) \tag{23}$$

where

$$\epsilon_m^* = \frac{\partial u_{rm}^*}{\partial r} + \frac{u_{rm}^*}{r} + \frac{m}{r} u_{\theta m}^* + \frac{\partial u_{zm}^*}{\partial z}. \tag{24}$$

The following solution for Eq. (23) can be obtained by using the method of variation of parameters (Kreider et al., 1966)

$$\epsilon_m^* = \eta (A_m(\xi,s) e^{\gamma z} + B_m(\xi,s) e^{-\gamma z}) + C_m(\xi,s) e^{\xi z} + D_m(\xi,s) e^{-\xi z}, \tag{25}$$

where $C_m(\xi, s)$ and $D_m(\xi, s)$ are arbitrary functions.

After lengthy manipulations involving Eqs. (1)–(3), (6), (10)–(13), (19), and (25), the general solutions for the mth Fourier harmonic of displacement components in the Laplace transform space can be expressed as

$$\bar{u}_{rm} = \int_0^\infty \Bigg[\left\{ \frac{\xi\eta}{s} (A_m e^{\gamma z} + B_m e^{-\gamma z}) - a_1 z (C_m e^{\xi z} - D_m e^{-\xi z}) \right\} \times \{ J_{m-1}(\xi r) - J_{m+1}(\xi r) \} + \{ (E_m e^{\xi z} + F_m e^{-\xi z}) \times J_{m+1}(\xi r) + (G_m e^{\xi z} + H_m e^{-\xi z}) J_{m-1}(\xi r) \} \Bigg] \frac{\xi}{2} d\xi \tag{26}$$

$$\bar{u}_{\theta m} = \int_0^\infty \Bigg[\left\{ -\frac{\xi\eta}{s} (A_m e^{\gamma z} + B_m e^{-\gamma z}) + a_1 z (C_m e^{\xi z} - D_m e^{-\xi z}) \right\} \times \{ J_{m-1}(\xi r) + J_{m+1}(\xi r) \} + \{ (E_m e^{\xi z} + F_m e^{-\xi z}) \times J_{m+1}(\xi r) - (G_m e^{\xi z} + H_m e^{-\xi z}) J_{m-1}(\xi r) \} \Bigg] \frac{\xi}{2} d\xi \tag{27}$$

$$\bar{u}_{zm} = \int_0^\infty \Bigg[\frac{\gamma\eta}{s} (A_m e^{\gamma z} - B_m e^{-\gamma z}) - \left(a_1 z - \frac{a_2}{\xi}\right) C_m e^{\xi z} - \left(a_1 z + \frac{a_2}{\xi}\right) D_m e^{-\xi z} - \left(\frac{E_m - G_m}{2}\right) e^{\xi z} + \left(\frac{F_m - H_m}{2}\right) e^{-\xi z} \Bigg] \times \xi J_m(\xi r) d\xi \tag{28}$$

where

$$a_1 = \frac{1}{2(1-2\nu_u)} \quad \text{and} \quad a_2 = \frac{(3-4\nu_u)}{2(1-2\nu_u)} \tag{29}$$

and $E_m(\xi, s)$, $F_m(\xi, s)$, $G_m(\xi, s)$, and $H_m(\xi, s)$ are arbitrary functions.

Application of the Fourier expansion with respect to θ for the stress components and the pore pressure results in

$$\frac{\sigma_{ij}(r,\theta,z,t)}{2\mu} = \sum_{m=0}^{\infty} \sigma_{ijm}(r,z,t) f(\theta) \tag{30}$$

$$\frac{p(r,\theta,z,t)}{2\mu} = \sum_{m=0}^{\infty} p_m(r,z,t) \cos m\theta \tag{31}$$

In Eqs. (30) and (31), σ_{ijm} and p_m are symmetric components corresponding to the mth harmonic and

$$f(\theta) = \begin{cases} \cos m\theta, & (i,j \neq 0 \text{ or } i=j=\theta), \\ \sin m\theta, & (i \text{ or } j = \theta). \end{cases} \tag{32}$$

Thereafter, the general solutions for the mth Fourier harmonic of the stress components and the pore pressure, nondimensionalized with respect to the shear modulus of the medium, can be expressed as

$$\bar{\sigma}_{rrm} = \int_0^\infty \Bigg[(A_m e^{\gamma z} + B_m e^{-\gamma z}) \times \left\{ \frac{\xi\eta}{s} \left(\frac{(m-1)J_{m-1}(\xi r) + (m+1)J_{m+1}(\xi r)}{r} \right) - \frac{2\gamma^2\eta}{s} J_m(\xi r) \right\} + C_m e^{\xi z} \left\{ (2a_1\xi z + 2a_3) J_m(\xi r) - a_1 z \left(\frac{(m-1)J_{m-1}(\xi r) + (m+1)J_{m+1}(\xi r)}{r} \right) \right\} - D_m e^{-\xi z} \left\{ (2a_1\xi z - 2a_3) J_m(\xi r) - a_1 z \left(\frac{(m-1)J_{m-1}(\xi r) + (m+1)J_{m+1}(\xi r)}{r} \right) \right\}$$

Downloaded 03 May 2010 to 171.66.16.245. Redistribution subject to ASME license or copyright; see http://www.asme.org/terms/Terms_Use.cfm

$$+(E_m e^{\xi z}+F_m e^{-\xi z})\left\{\xi J_m(\xi r)-\frac{(m+1)J_{m+1}(\xi r)}{r}\right\}$$
$$-(G_m e^{\xi z}+H_m e^{-\xi z})\left\{\xi J_m(\xi r)-\frac{(m-1)J_{m-1}(\xi r)}{r}\right\}\Bigg]\frac{\xi}{2}\,d\xi \tag{33}$$

$$\bar{\sigma}_{\theta\theta m}=\int_0^\infty\Bigg[-(A_m e^{\gamma z}+B_m e^{-\gamma z})\times\left\{\frac{\xi\eta}{s}\left(\frac{(m-1)J_{m-1}(\xi r)+(m+1)J_{m+1}(\xi r)}{r}\right)+2\eta J_m(\xi r)\right\}$$
$$+C_m e^{\xi z}\left\{2a_3 J_m(\xi r)+a_1 z\left(\frac{(m-1)J_{m-1}(\xi r)+(m+1)J_{m+1}(\xi r)}{r}\right)\right\}$$
$$+D_m e^{-\xi z}\left\{2a_3 J_m(\xi r)-a_1 z\left(\frac{(m-1)J_{m-1}(\xi r)+(m+1)J_{m+1}(\xi r)}{r}\right)\right\}$$
$$+(E_m e^{\xi z}+F_m e^{-\xi z})\left\{\frac{(m+1)J_{m+1}(\xi r)}{r}\right\}$$
$$-(G_m e^{\xi z}+H_m e^{-\xi z})\left\{\frac{(m-1)J_{m-1}(\xi r)}{r}\right\}\Bigg]\frac{\xi}{2}\,d\xi \tag{34}$$

$$\bar{\sigma}_{zzm}=\int_0^\infty\left[\frac{\xi^2\eta}{s}(A_m e^{\gamma z}+B_m e^{-\gamma z})-(a_1\xi z-a_4)C_m e^{\xi z}+(a_1\xi z+a_4)D_m e^{-\xi z}-\xi\left(\frac{E_m-G_m}{2}\right)e^{\xi z}-\xi\left(\frac{F_m-H_m}{2}\right)e^{-\xi z}\right]\xi J_m(\xi r)\,d\xi \tag{35}$$

$$\bar{\sigma}_{r\theta m}=\int_0^\infty\Bigg[\left\{\frac{\xi\eta}{s}(A_m e^{\gamma z}+B_m e^{-\gamma z})-a_1 z(C_m e^{\xi z}-D_m e^{-\xi z})\right\}\times\left\{\frac{2(m+1)J_{m+1}(\xi r)-2(m-1)J_{m-1}(\xi r)}{r}\right\}$$
$$+(E_m e^{\xi z}+F_m e^{-\xi z})\left\{\xi J_m(\xi r)-\frac{2(m+1)J_{m+1}(\xi r)}{r}\right\}$$
$$+(G_m e^{\xi z}+H_m e^{-\xi z})\left\{\xi J_m(\xi r)-\frac{2(m-1)J_{m-1}(\xi r)}{r}\right\}\Bigg]\frac{\xi}{4}\,d\xi \tag{36}$$

$$\bar{\sigma}_{\theta zm}=\int_0^\infty\Bigg[\left\{-\frac{\xi\gamma\eta}{s}(A_m e^{\gamma z}-B_m e^{-\gamma z})+\left(\frac{2a_1\xi z-1}{2}\right)C_m e^{\xi z}\times\left(\frac{2a_1\xi z+1}{2}\right)D_m e^{-\xi z}\right\}\{J_{m-1}(\xi r)+J_{m+1}(\xi r)\}$$
$$+\frac{\xi}{4}(E_m e^{\xi z}-F_m e^{-\xi z})\{J_{m-1}(\xi r)+3J_{m+1}(\xi r)\}$$
$$-\frac{\xi}{4}(G_m e^{\xi z}-H_m e^{-\xi z})\{3J_{m-1}(\xi r)+J_{m+1}(\xi r)\}\Bigg]\frac{\xi}{2}\,d\xi \tag{37}$$

$$\bar{\sigma}_{zrm}=\int_0^\infty\Bigg[\left\{\frac{\xi\gamma\eta}{s}(A_m e^{\gamma z}-B_m e^{-\gamma z})-\left(\frac{2a_1\xi z-1}{2}\right)C_m e^{\xi z}-\left(\frac{2a_1\xi z+1}{2}\right)D_m e^{-\xi z}\right\}\{J_{m-1}(\xi r)-J_{m+1}(\xi r)\}$$
$$-\frac{\xi}{4}(E_m e^{\xi z}-F_m e^{-\xi z})\{J_{m-1}(\xi r)-3J_{m+1}(\xi r)\}$$
$$+\frac{\xi}{4}(G_m e^{\xi z}-H_m e^{-\xi z})\{3J_{m-1}(\xi r)-J_{m+1}(\xi r)\}\Bigg]\frac{\xi}{2}\,d\xi \tag{38}$$

$$\bar{p}_m=\int_0^\infty[a_5\eta(A_m e^{\gamma z}+B_m e^{-\gamma z})-a_4\eta(C_m e^{\xi z}+D_m e^{-\xi z})]\xi J_m(\xi r)\,d\xi \tag{39}$$

where

$$a_3=\frac{\nu_u}{1-2\nu_u},\quad a_4=\frac{(1-\nu_u)}{(1-2\nu_u)}\quad\text{and}\quad a_5=\frac{B(1-\nu)(1+\nu_u)}{3(\nu_u-\nu)}. \tag{40}$$

The fluid discharge in the i-direction, denoted by q_i, is given by

$$q_i=-\kappa\frac{\partial p}{\partial i},\quad (i=r,z)\quad\text{and}\quad q_\theta=-\kappa\frac{\partial p}{r\partial\theta}. \tag{41}$$

Solution of Boundary Value Problems

Boundary value problems involving an internally loaded poroelastic half-space are considered in this section. The solutions corresponding to the four basic loading configurations, i.e., a vertical ring load, a radial ring load, a circumferential ring load, and a ring fluid source, all of intensity equal to Heaviside unit step function $H(t)$ per unit arc length applied over a circular ring of radius "r'" at a depth $z = z'$, are presented. The circumferential distribution of the vertical and radial ring loads and the ring fluid source is of the form cos $m\theta$ and that of the circumferential ring load is sin $m\theta$. A solution to the internally loaded half-space can be derived by considering it as a two-domain boundary value problem (Karasudhi, 1990). A superscript i (i = 1, 2) is used to denote the domain number where domain "1" is bounded by $0 \le z \le z'$ and domain "2" by $z' \le z < \infty$. General solutions for each domain are given by Eqs. (26)–(28), (33)–(39), and (41) with arbitrary coefficients $A_m^i(\xi, s)$, $B_m^i(\xi, s)$, ..., $H_m^i(\xi, s)$ where a superscript i = 1, 2 is used to identify the domain number. Note that for domain "2," arbitrary functions $A_m^2(\xi, s)$, $C_m^2(\xi, s)$, $E_m^2(\xi, s)$, and $G_m^2(\xi, s) \equiv 0$ to ensure the regularity of the solutions at infinity.

In view of the prescribed circumferential distribution of the loading case only the mth Fourier harmonic in Eqs. (10)–(13), (30), and (31) need to be considered. Therefore, the boundary and continuity conditions can be expressed as

$$\bar{\sigma}^1_{z\alpha m}(r,0,s)=0,\quad \alpha=r,\theta,z \tag{42}$$
$$\bar{p}^1_m(r,0,s)=0, \tag{43}$$
$$\bar{u}^1_{\alpha m}(r,z',s)-\bar{u}^2_{\alpha m}(r,z',s)=0,\quad \alpha=r,\theta,z \tag{44}$$
$$\bar{p}^1_m(r,z',s)-\bar{p}^2_m(r,z',s)=0, \tag{45}$$
$$\bar{\sigma}^1_{z\alpha m}(r,z',s)-\bar{\sigma}^2_{z\alpha m}(r,z',s)=\frac{F_\alpha}{2\mu s},\quad \alpha=r,\theta,z \tag{46}$$
$$\left\{\kappa\frac{\partial\bar{p}^1_m}{\partial z}(r,z',s)\right\}-\left\{\kappa\frac{\partial\bar{p}^2_m}{\partial z}(r,z',s)\right\}=\frac{Q}{2\mu s}. \tag{47}$$

For a vertical ring load:

$$F_z=\delta(r-r')\quad\text{and}\quad F_r=F_\theta=Q=0, \tag{48}$$

where $\delta(\,)$ denotes Dirac's delta function.

For a radial ring load:

$$F_r=\delta(r-r')\quad\text{and}\quad F_\theta=F_z=Q=0. \tag{49}$$

Downloaded 03 May 2010 to 171.66.16.245. Redistribution subject to ASME license or copyright; see http://www.asme.org/terms/Terms_Use.cfm

For a circumferential ring load:

$$F_\theta = \delta(r-r') \quad \text{and} \quad F_r = F_z = Q = 0. \tag{50}$$

For a ring fluid source:

$$Q = \delta(r-r') \quad \text{and} \quad F_r = F_\theta = F_z = 0. \tag{51}$$

Substitution of general solutions for displacements, stresses, and pore pressure in Eqs. (42)–(47) together with Eqs. (48)–(51) and the following Hankel transform representation for $\delta(r - r')$ yields a set of linear simultaneous equations to determine arbitrary functions corresponding to the two domains.

$$\delta(r-r') = \int_0^\infty \xi r' J_m(\xi r') J_m(\xi r) d\xi \tag{52}$$

The following solutions are obtained for the nonzero arbitrary functions appearing in the general solutions given by Eqs. (26)–(28), (33)–(39), and (41).

Arbitrary Functions for Vertical Ring Loading.

$$A_m^1(\xi,s) = \frac{e^{-\gamma z'}}{4a_5\mu s} r' J_m(\xi r') \tag{53}$$

$$B_m^1(\xi,s) = \left(\frac{b_3 e^{-\xi z'} - b_2 e^{-\gamma z'}}{4a_5 b_1 \mu s}\right) r' J_m(\xi r') \tag{54}$$

$$B_m^2(\xi,s) = B_m^1(\xi,s) - A_m^1(\xi,s) e^{2\gamma z'} \tag{55}$$

$$C_m^1(\xi,s) = \frac{e^{-\xi z'}}{4a_4\mu s} r' J_m(\xi r') \tag{56}$$

$$D_m^1(\xi,s) = \left(\frac{b_4 e^{-\xi z'} - 2b_5\gamma e^{-\gamma z'}}{4a_4 b_1 \mu s}\right) r' J_m(\xi r') \tag{57}$$

$$D_m^2(\xi,s) = D_m^1(\xi,s) - C_m^1(\xi,s) e^{2\xi z'} \tag{58}$$

$$E_m^1(\xi,s) = \frac{b_6 e^{-\xi z'}}{4a_5\mu s^2} r' J_m(\xi r') \tag{59}$$

$$F_m^1(\xi,s) = \left(\frac{b_{10} e^{-\xi z'} - 2b_9\xi\gamma\eta e^{-\gamma z'}}{4a_5 b_1 \xi\mu s^2}\right) r' J_m(\xi r') \tag{60}$$

$$F_m^2(\xi,s) = F_m^1(\xi,s) - \frac{b_7 e^{\xi z'}}{4a_5\mu s^2} r' J_m(\xi r') \tag{61}$$

$$G_m^1(\xi,s) = -E_m^1(\xi,s) \tag{62}$$

$$H_m^i(\xi,s) = -F_m^i(\xi,s), \quad (i=1,2) \tag{63}$$

where

$$b_1 = a_5 s + 2(1-\nu_u)\xi\eta(\xi-\gamma) \tag{64}$$

$$b_2 = a_5 s + 2(1-\nu_u)\xi\eta(\xi+\gamma) \tag{65}$$

$$b_3 = 4(1-\nu_u)\xi^2\eta - 2(1-2\nu_u)a_5 s - 2a_5\xi s z' \tag{66}$$

$$b_4 = 2(1-\nu_u)\xi\eta(\xi+\gamma) - (3-4\nu_u)a_5 s - 2a_5\xi s z' \tag{67}$$

$$b_5 = 2(1-\nu_u)\xi\eta \tag{68}$$

$$b_6 = \xi\eta - \frac{a_5 s z'}{2(1-\nu_u)} \tag{69}$$

$$b_7 = \xi\eta + \frac{a_5 s z'}{2(1-\nu_u)} \tag{70}$$

$$b_8 = 2(1-\nu_u)\xi\eta(\xi+\gamma) + (3-4\nu_u)a_5 s \tag{71}$$

$$b_9 = 2(1-\nu_u)(\xi^2\eta + a_5 s) \tag{72}$$

$$b_{10} = b_6 b_8 \xi - b_{11} \quad \text{and} \quad b_{11} = \frac{a_5 b_9 s}{a_4}. \tag{73}$$

Arbitrary Functions for Radial and Circumferential Ring Loadings.

$$A_m^1(\xi,s) = \frac{\xi e^{-\gamma z'}}{8a_5\gamma\mu s} r' \{nJ_{m-1}(\xi r') + J_{m+1}(\xi r')\} \tag{74}$$

$$B_m^1(\xi,s) = \left(\frac{c_1\gamma e^{-\xi z'} - b_2\xi e^{-\gamma z'}}{8a_5 b_1\gamma\mu s}\right) r' \{nJ_{m-1}(\xi r') + J_{m+1}(\xi r')\} \tag{75}$$

$$B_m^2(\xi,s) = B_m^1(\xi,s) + A_m^1(\xi,s) e^{2\gamma z'} \tag{76}$$

$$C_m^1(\xi,s) = \frac{e^{-\xi z'}}{8a_4\mu s} r' \{nJ_{m-1}(\xi r') + J_{m+1}(\xi r')\} \tag{77}$$

$$D_m^1(\xi,s) = \left(\frac{c_2 e^{-\xi z'} - 2b_5\xi e^{-\gamma z'}}{8a_4 b_1\mu s}\right) r' \{nJ_{m-1}(\xi r') + J_{m+1}(\xi r')\} \tag{78}$$

$$D_m^2(\xi,s) = D_m^1(\xi,s) + C_m^1(\xi,s) e^{2\xi z'} \tag{79}$$

$$E_m^1(\xi,s) = \frac{e^{-\xi z'}}{8a_5\xi\mu s^2} r' \left\{c_3 nJ_{m-1}(\xi r') - c_4 J_{m+1}(\xi r')\right\} \tag{80}$$

$$F_m^1(\xi,s) = \left\{\frac{(b_9c_3 - c_4c_5 - b_{11})nJ_{m-1}(\xi r') - (b_9c_4 - c_3c_5 + b_{11})J_{m+1}(\xi r')}{8a_5 b_1\xi\mu s^2}\right\} r' e^{-\xi z'} - \frac{b_9\xi^2\eta e^{-\gamma z'}}{4a_5 b_1\xi\mu s^2} r' \{nJ_{m-1}(\xi r') + J_{m+1}(\xi r')\} \tag{81}$$

$$F_m^2(\xi,s) = F_m^1(\xi,s) + \frac{e^{\xi z'}}{8a_5\xi\mu s^2} r' [c_6 nJ_{m-1}(\xi r') - c_7 J_{m+1}(\xi r')\} \tag{82}$$

$$G_m^1(\xi,s) = \frac{e^{-\xi z'}}{8a_5\xi\mu s^2} r' \{c_4 nJ_{m-1}(\xi r') - c_3 J_{m+1}(\xi r')\} \tag{83}$$

$$H_m^1(\xi,s) = \left\{\frac{(b_9c_4 - c_3c_5 + b_{11})nJ_{m-1}(\xi r') - (b_9c_3 - c_4c_5 - b_{11})J_{m+1}(\xi r')}{8a_5 b_1\xi\mu s^2}\right\} r' e^{-\xi z'} + \frac{b_9\xi^2\eta e^{-\gamma z'}}{4a_5 b_1\xi\mu s^2} r' \{nJ_{m-1}(\xi r') + J_{m+1}(\xi r')\} \tag{84}$$

$$H_m^2(\xi,s) = H_m^1(\xi,s) + \frac{e^{\xi z'}}{8a_5\xi\mu s^2} r' \{c_7 nJ_{m-1}(\xi r') - c_6 J_{m+1}(\xi r')\} \tag{85}$$

where

$$c_1 = 4(1-\nu_u)\xi^2\eta + 4(1-\nu_u)a_5 s - 2a_5\xi s z' \tag{86}$$

$$c_2 = 2(1-\nu_u)\xi\eta(\xi+\gamma) + (3-4\nu_u)a_5 s - 2a_5\xi s z' \tag{87}$$

$$c_3 = b_6\xi - \frac{a_5 s}{2(1-\nu_u)} \tag{88}$$

$$c_4 = -b_6\xi - \frac{(7-8\nu_u)a_5 s}{2(1-\nu_u)} \tag{89}$$

$$c_5 = (1-2\nu_u)a_5 s + 2(1-\nu_u)\xi\gamma\eta \tag{90}$$

$$c_6 = b_7\xi - \frac{a_5 s}{2(1-\nu_u)} \tag{91}$$

Downloaded 03 May 2010 to 171.66.16.245. Redistribution subject to ASME license or copyright; see http://www.asme.org/terms/Terms_Use.cfm

$$c_7 = -b_7\xi - \frac{(7-8\nu_u)a_5 s}{2(1-\nu_u)} \tag{92}$$

and

$$n = \begin{cases} -1, & \text{for radial loading,} \\ 1, & \text{for circumferential loading.} \end{cases} \tag{93}$$

Arbitrary Functions for Ring Fluid Source.

$$A_m^1(\xi,s) = \frac{e^{-\gamma z'}}{4a_5\gamma\eta\mu s\kappa} r' J_m(\xi r') \tag{94}$$

$$B_m^1(\xi,s) = \left(\frac{2b_5\gamma e^{-\xi z'} - b_2 e^{-\gamma z'}}{4a_5 b_1 \gamma\eta\mu s\kappa}\right) r' J_m(\xi r') \tag{95}$$

$$B_m^2(\xi,s) = B_m^1(\xi,s) + A_m^1(\xi,s)e^{2\gamma z'} \tag{96}$$

$$C_m^1(\xi,s) = 0 \tag{97}$$

$$D_m^1(\xi,s) = b_5\left(\frac{e^{-\xi z'} - e^{-\gamma z'}}{2a_4 b_1 \eta\mu s\kappa}\right) r' J_m(\xi r') \tag{98}$$

$$D_m^2(\xi,s) = D_m^1(\xi,s) \tag{99}$$

$$E_m^1(\xi,s) = \frac{e^{-\xi z'}}{4a_5\mu s^2\kappa} r' J_m(\xi r') \tag{100}$$

$$F_m^1(\xi,s) = \left(\frac{b_8 e^{-\xi z'} - 2b_9 e^{-\gamma z'}}{4a_5 b_1 \mu s^2\kappa}\right) r' J_m(\xi r') \tag{101}$$

$$F_m^2(\xi,s) = F_m^1(\xi,s) + E_m^1(\xi,s)e^{2\xi z'} \tag{102}$$

$$G_m^1(\xi,s) = -E_m^1(\xi,s) \tag{103}$$

$$H_m^i(\xi,s) = -F_m^i(\xi,s), \quad (i=1,2) \tag{104}$$

Special Loading Cases.

(1) Vertical Patch Load (Fig. 2(a)) and a Point Load. Note that the deformation fields corresponding to the above loadings are axially symmetric about the z-axis and only the terms corresponding to $m = 0$ in Eqs. (10)–(13), (30), and (31) need to be considered. The arbitrary functions corresponding to a uniform patch loading of radius "a" and intensity $f_0H(t)$ as shown in Fig. 2(a) is given by Eqs. (53)–(63) with the term $r'J_0(\xi r')$ replaced by $f_0J_1(\xi)/\xi$. In addition, $\bar{u}_\theta = \bar{\sigma}_{r\theta} = \bar{\sigma}_{\theta z} = 0$ is obtained from Eqs. (27), (36), and (37), respectively, for axisymmetric vertical loading.

The arbitrary functions corresponding to a vertical concentrated load of magnitude $P_0H(t)$ applied at $z = z'$ (poroelastic counterpart of the classical Mindlin's solution for a vertical load (Mindlin, 1936)) is given by Eqs. (53)–(63) with $m = 0$ and the term $r'J_0(\xi r')$ replaced by $P_0/2\pi$.

(2) Horizontal Patch Load (Fig. 2(b)) and a Point Load. Note that the deformation fields corresponding to above loading cases are symmetric about $\theta = 0$ and only the symmetric terms corresponding to $m = 1$ in Eqs. (10)–(13), (30), and (31) need to be considered. The arbitrary functions corresponding to horizontal patch load can be obtained from Eqs. (74)–(85) by replacing the terms $nr'J_0(\xi r')$ and $r'J_2(\xi r')$ by $-2f_0J_1(\xi)/\xi$ and 0, respectively.

In the case of a concentrated load of magnitude $P_0H(t)$ applied at $z = z'$ (poroelastic counterpart of classical Mindlin's solution for a horizontal load (Mindlin, 1936)), the arbitrary coefficients are once again obtained by replacing the terms $nr'J_0(\xi r')$ and $r'J_2(\xi r')$ in Eqs. (74)–(85) by $-P_0/\pi$ and 0, respectively.

(3) Patch Fluid Sink (Fig. 2(c)) and a Point Sink. Note that the deformation fields corresponding to the above fluid sinks are axially symmetric about the z-axis and only the terms corresponding to $m = 0$ in Eqs. (10)–(13), (30), and (31) need to be considered. The arbitrary function corresponding to a circular fluid sink of radius "a" and uniform intensity $q_0H(t)$ is given by Eqs. (94)–(104) with the term $r'J_0(\xi r')$ replaced by $-q_0J_1(\xi)/\xi$. In the case of a point sink of intensity $Q_0H(t)$ applied at $z = z'$, the arbitrary functions are given by Eqs. (94)–(104) with $r'J_0(\xi r')$ replaced by $-Q_0/2\pi$. Note that $\bar{u}_\theta = \bar{\sigma}_{r\theta} = \bar{\sigma}_{\theta z} = 0$ for both patch fluid sink and a point sink.

(4) Loadings and Fluid Sources With Nonuniform Distribution. Arbitrary functions corresponding to loadings and fluid sources with nonuniform intensities applied over an axisymmetric domain (circular or annular) can be obtained by first developing a Fourier expansion of the intensity of applied loads/fluid sources with respect to θ and thereafter integrating with respect to r'. The integration with respect to r' can be obtained numerically or by analytical methods depending on the type of radial distribution of the load/fluid source. In addition, the solutions corresponding to loadings and fluid sources of different configurations (e.g., ring, patch, and annular loads) applied in a poroelastic full space can be obtained from the half-space solutions by setting z' approaching infinity and replacing $|z' - z|$ by z where the origin of the coordinate frame (r, θ, z) is now set at the level of the applied load/source with the z-axis coinciding with the axis of symmetry of the applied load/source.

Numerical Results and Discussion

The complete solutions for displacements, stresses, pore pressure, and fluid discharge corresponding to each boundary value problem are given by Eqs. (26)–(28), (33)–(39), and (41) together with the solutions for arbitrary functions, $A_m^i(\xi, s)$ to $H_m^i(\xi, s)$, given by Eqs. (53)–(63), (74)–(85), and (94)–(104). In this section, the response of poroelastic half-space regions of different material properties to a selected set of internal loading configurations is studied. It is noted that the solutions for displacements and stresses at an arbitrary point appear in terms of Lipschitz-Hankel-type semi-infinite integrals with respect to Hankel transform parameter ξ and a Bromwich integral with respect to the Laplace transform parameter s. It should be noted that the Laplace inversion can be carried out analytically when $(z = 0)$ and $(z' = 0)$ (McNamee and Gibson, 1960a,b). However, the resulting solutions would still involve Lipschitz-Hankel-type integrals with respect to ξ which can be evaluated only by numerical quadrature. Given the complexity of the integrands corresponding to the response at an arbitrary point due to a buried load/fluid source, it is proposed to develop an accurate numerical quadrature scheme to evaluate these integrals. The review of literature indicates that the Laplace inversion can be carried out very accurately (Piessen, 1975) by using the numerical inversion method proposed by Stehfest (1970). The formula due to Stehfest is given by

$$f(t) \simeq \frac{\ln 2}{t} \sum_{n=1}^{N} c_n \bar{f}\left(n\frac{\ln 2}{t}\right) \tag{105}$$

where $\bar{f}$ denotes the Laplace transform of $f(t)$ and

$$c_n = (-1)^{n+N/2} \sum_{k=[(n+1)/2]}^{\min(n,N/2)} \times \frac{k^{N/2}(2k)!}{(N/2-k)!k!(k-1)!(n-k)!(2k-n)!} \tag{106}$$

and N is even.

The application of Eq. (105) to evaluate the fundamental solutions involves the computation of a series of Lipschitz-Hankel integrals involving products of Bessel functions at N discrete values of s for each value of t. It is found that the semi-infinite integral with respect to ξ can be evaluated ac-

Downloaded 03 May 2010 to 171.66.16.245. Redistribution subject to ASME license or copyright; see http://www.asme.org/terms/Terms_Use.cfm

Table 1 Comparison of solutions for vertical displacement and pore pressure due to vertical patch load (Fig. 2(*a*)) for poroelastic material with incompressible constituents ($\nu = 0.25$)

t^*	$2\mu u_z(0,1,t^*)/f_0a$		$p(0,1,t^*)/f_0$	
(ct/a^2)	Stehfest	Schapery	Stehfest	Schapery
10^{-6}	0.813	0.814	1.424	1.424
10^{-5}	0.814	0.815	1.426	1.427
10^{-4}	0.817	0.819	1.431	1.433
0.001	0.827	0.830	1.448	1.453
0.01	0.853	0.859	1.492	1.497
0.1	0.902	0.905	1.470	1.471
1.0	0.961	0.966	0.045	0.048

Table 2 Comparison of solutions for pore pressure due to vertical patch load applied at the free surface for poroelastic material with incompressible constituents ($\nu = 0.0$)

t^*	$p(0.5,0.1,t^*)/f_0$		
(ct/a^2)	Schiffman and Fungaroli	Stehfest	Schapery
0.001	0.90	0.894	0.833
0.01	0.48	0.484	0.477
0.1	0.13	0.129	0.166
1.0	0.02	0.015	0.031

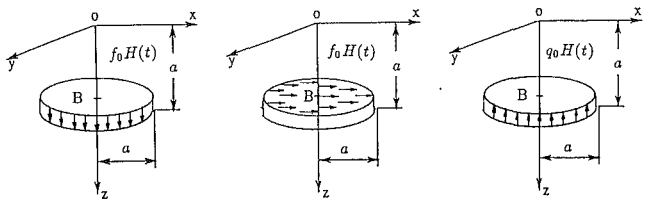
curately by applying an adaptive version of extended trapezoidal formula with $\Delta\xi = 0.1$. It is also found that accurate time-domain solutions are obtained from Eq. (105) with $N \geq 8$. It is important to note that the Stehfest method is computationally quite demanding although it is accurate. For example, in the boundary element method the fundamental solutions need to be computed repetitively at a considerable number of boundary nodes to compute the time-domain solutions. A more simple and computationally efficient scheme is given by Schapery (1962) which can be expressed as

$$f(t) \simeq [s\bar{f}(s)]_{s=0.5/t} \tag{107}$$

where $\bar{f}$ denotes the Laplace transform of $f(t)$ and s is the Laplace transform parameter.

Table 1 presents a comparison of vertical displacements and pore pressure obtained from Stehfest and Schapery schemes at the point (0,1) due to a uniform vertical patch load (Fig. 2(*a*)) applied at $z' = 1.0$. It is evident that the two solutions agree very closely. Table 2 presents the solutions for pore pressure at an internal point due to a vertical patch load applied at the surface. Comparison of solutions presented by Schiffman and Fungaroli (1965) with those obtained from Stehfest and Schapery schemes indicate that the pore pressure solutions corresponding to Schapery scheme is less accurate but still acceptable in a practical situation. The suitability of Schapery's scheme for a more complicated situation such as the boundary element method can be assessed only after a detailed numerical study involving a boundary element analysis. Nevertheless, Schapery's scheme is computationally very efficient and it also yields approximate explicit time-domain (see Eq. (107)) fundamental solutions which can be useful in the development of direct time-domain solution algorithms for more complicated boundary value problems.

In the numerical study, time histories of displacements and pore pressure due to buried patch loads and a buried patch fluid sink are investigated. Stehfest inversion scheme is used to obtain time domain solutions with high accuracy. The loadings and discharge are assumed to be uniformly distributed over a circular area of radius "a" with intensity f_0 and q_0, respectively, and acting at a depth "a" as shown in Fig. 2. A nondimensional time, t^*, where $t^* = ct/a^2$ is used in the numerical study. Six different poroelastic materials (Rice and Cleary, 1976), namely, a poroelastic material with incompressible constituents ($\nu = 0.25$, $\nu_u = 0.5$, $B = 1.0$), Ruhr Sandstone ($\nu = 0.12$, $\nu_u = 0.31$, $B = 0.88$), Tennessee Marble



(a) Vertical patch load (b) Horizontal patch load (c) Patch fluid sink

Fig. 2 Loading configurations considered in numerical study

($\nu = 0.25$, $\nu_u = 0.27$, $B = 0.51$), Berea Sandstone ($\nu = 0.2$, $\nu_u = 0.33$, $B = 0.62$), Westerly Granite ($\nu = 0.25$, $\nu_u = 0.34$, $B = 0.85$), and Weber Sandstone ($\nu = 0.15$, $\nu_u = 0.29$, $B = 0.73$), are considered in the numerical study to investigate the influence of poroelastic material parameters on the response and the features of the consolidation process. It is useful to note that $0 \leq B \leq 1$ and $\nu \leq \nu_u \leq 0.5$ for all poroelastic materials. The limiting cases of a poroelastic solid with incompressible constituents and an ideal elastic material are obtained when $\nu_u = 0.5$ and $B = 1$ and $\nu_u = \nu$, respectively.

The displacement histories at points O ($r = 0$, $z = 0$) and B ($r = 0$, $z = a$) are shown in Figs. 3(*a*), 3(*b*), and 3(*c*) for the uniform patch loadings shown in Figs. 2(*a*), 2(*b*), and 2(*c*), respectively. The trend of the displacement histories are quite similar for both vertical and horizontal loadings and the material with incompressible constituents has the lowest initial solution followed by Westerly Granite, Berea Sandstone, Ruhr Sandstone, Weber Sandstone, and Tennessee Marble. Comparison of this behavior with the material properties indicate that the initial response is mainly governed by the value of the undrained Poisson's ratio. The above dependence of the initial solution for displacements only on the undrained Poisson's ratio can be verified analytically by obtaining the initial ($t = 0^+$) solution through limit procedures. The following initial solutions are obtained for vertical displacement and pore pressure for a vertical patch load (Fig. 2(*a*))

$$u_z(r,z) = \frac{f_0}{8(1-\nu_u)\mu}\int_0^\infty [\{(3-4\nu_u)\xi(1+z) + 2\xi^2 z + (3-4\nu_u)^2 - 4(1-\nu_u)(1-2\nu_u)\} \times e^{-\xi(1+z)} + \{(3-4\nu_u) + \xi|1-z|\}e^{-\xi|1-z|}] \frac{J_1(\xi)J_0(\xi r)}{\xi} d\xi \tag{108}$$

$$p(r,z) = \frac{B(1+\nu_u)f_0}{6(1-\nu_u)}\int_0^\infty [\{(3-4\nu_u) + 2\xi\}e^{-\xi(1+z)} - h^* e^{-\xi|1-z|}]J_1(\xi)J_0(\xi r)d\xi \tag{109}$$

where

$$h^* = \begin{cases} 1, & 0 \leq z \leq 1, \\ -1, & 1 < z < \infty. \end{cases} \tag{110}$$

The initial solutions for horizontal displacement and pore pressure for a horizontal patch load (Fig. 2(*b*)) are given by

$$u_x(r,z) = \frac{f_0}{16(1-\nu_u)\mu}\int_0^\infty \Big[\{(-(3-4\nu_u)\xi(1+z) + 2\xi^2 z + 8(1-\nu_u)^2 + 1) \times e^{-\xi(1+z)} + ((7-8\nu_u) - \xi|1-z|)e^{-\xi|1-z|}\}J_0(\xi r) + \{((3-4\nu_u)\xi(1+z) - 2\xi^2 z + 8\nu_u(1-\nu_u) - 1) \times e^{-\xi(1+z)} + (1+\xi|1-z|) \times e^{-\xi|1-z|}\}J_2(\xi r)\Big] \frac{J_1(\xi)}{\xi} d\xi \tag{111}$$

Downloaded 03 May 2010 to 171.66.16.245. Redistribution subject to ASME license or copyright; see http://www.asme.org/terms/Terms_Use.cfm

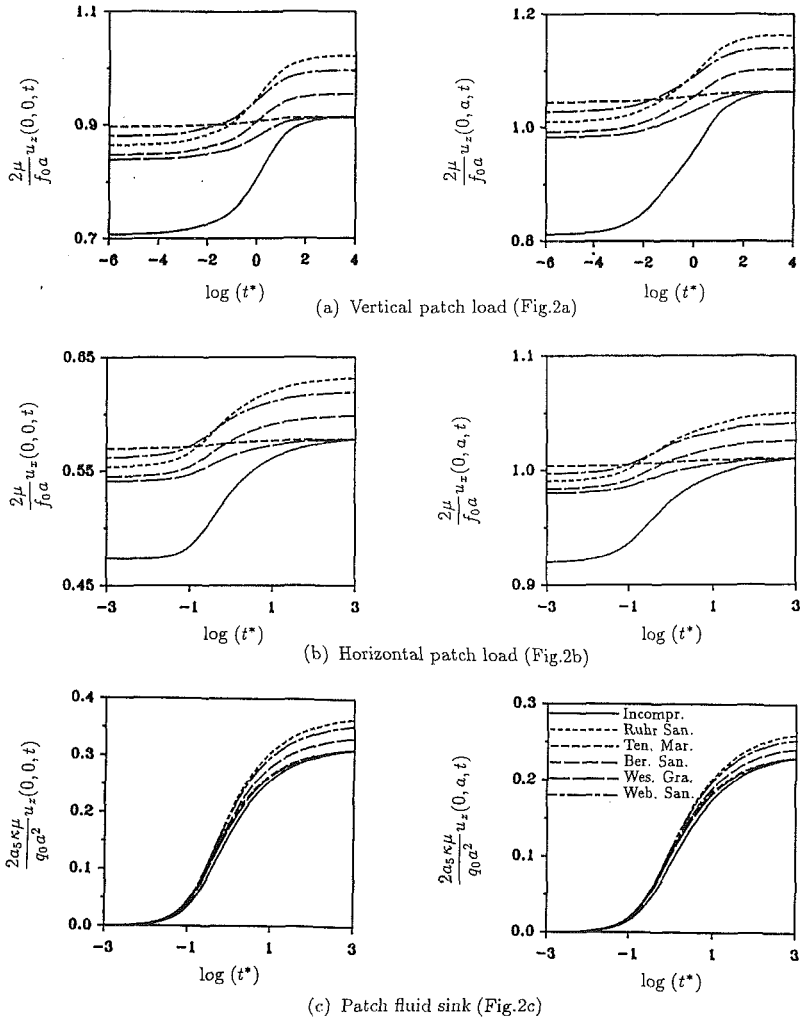


Fig. 3 Displacement histories at points O ($r = 0$, $z = 0$) and B ($r = 0$, $z = a$) for different materials under patch loadings shown in Fig. 2

$$p(r,z) = \frac{B(1+\nu_u)f_0}{6(1-\nu_u)} \int_0^\infty [\{2\xi - (3-4\nu_u)\} \times e^{-\xi(1+z)} + e^{-\xi|1-z|}] J_1(\xi) J_1(\xi r) d\xi. \quad (112)$$

It is interesting to note that the foregoing solutions for displacements are essentially elastic solutions with the Poisson's ratio equal to the undrained Poisson's ratio. In addition, the final solutions ($t \to \infty$) for displacements corresponding to loadings shown in Figs. 2(a) and 2(b) are given by Eqs. (108) and (111), respectively, where ν_u replaced by ν. The final solutions for pore pressure is zero for both loading cases. The numerical solutions shown in Figs. 3 indicate that the material with the lowest undrained Poisson's ratio has the largest initial displacements. Therefore, the material with incompressible constituents has the lowest initial displacements. On the other hand, the material with the lowest drained Poisson's ratio has the maximum final displacements. In view of Eqs. (108) and (111), it is evident that the material with incompressible constituents, Tennessee Marble, and Westerly Granite have identical final solutions for displacements since the drained Poisson's ratios of these materials are identical. This fact is also confirmed by the numerical solutions shown in Figs. 3(a) and 3(b). The order of magnitude of nondimensional final displacements is identical to that of the drained Poisson's ratio.

Naturally, the displacement at point O is always less than that at point B for loadings shown in Figs. 2(a) and 2(b). The displacement increases slowly when $0 < t^* < 0.1$ and more rapidly during the period $0.1 < t^* < 100$ reaching its final value when $t^* > 1000$ for vertical and horizontal loadings. The displacements shown in Fig. 3(c) under a patch fluid sink (Fig. 2(c)) have features different to those corresponding to vertical and horizontal loadings. Naturally, the initial displacement is zero for all materials in this case and increases rapidly with time within the period $0.1 < t^* < 100$. Final solution is reached when $t^* > 1000$ for all six materials. The displacement at point O is found to be higher than that at point B at all time instants. Similar behavior was also noted in the numerical solutions reported by Kanok-Nukulchai and Chau (1990) and may be due to the presence of the free-surface condition. The order of the final solutions for a fluid sink is identical to that of ν. Once again, the nondimensional final solutions for Tennessee Marble, Westerly Granite, and the material with incompressible constituents are identical due to identical drained Poisson's ratios.

Figure 4 presents the profiles of displacements and pore pressure for Ruhr Sandstone along the r and z-axes under a vertical patch load (Fig. 2(a)) and a fluid sink (Fig. 2(c)). It is noted that displacements at all points increase with time and the shape of the displacement profiles remain relatively unchanged with time in the case of vertical loading. Under vertical loading the highest displacement is observed at the level of loading and it decreases rapidly with the depth below the level of loading. Vertical displacement at the surface level also de-

Downloaded 03 May 2010 to 171.66.16.245. Redistribution subject to ASME license or copyright; see http://www.asme.org/terms/Terms_Use.cfm

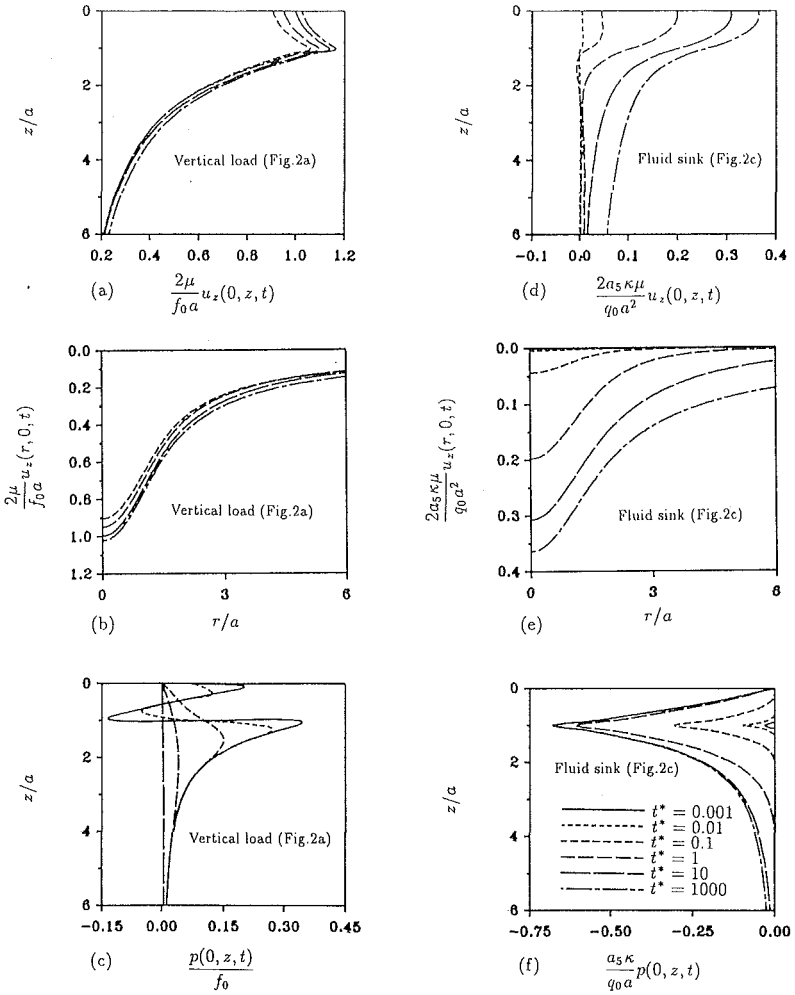


Fig. 4 Variation of displacements and pore pressure along the *z*-axis and the surface for Ruhr Sandstone under loadings shown in Figs. 2(*a*) and 2(*c*)

creases rapidly with the radial distance and the displacement at $r = 4a$ is about one-fifth of the displacement at $r = 0$. The difference between initial and final surface displacement profile is about 15 percent. Pore pressure profiles corresponding to the vertical loadings are shown in Fig. 4(*c*) and these show complicated variation with time. An examination of the explicit solution indicates that at $t^* = 0$ pore pressure is discontinuous within the domain of the loading. It becomes continuous for $t^* > 0$ and undergoes rapid changes with time in the vicinity of loading during the period $0 < t^* < 0.1$. Note that for $t^* < 0.01$, suction is developed in the region $0.5 < z/a < 1.0$. Pore pressure profile becomes much smoother when $t^* > 0.1$ and thereafter pore pressure decreases gradually with both the depth and time. Pore pressure within the domain is nearly dissipated when $t^* > 10$. The variation of vertical displacement along the z-axis and the free surface ($z = 0$) due to a fluid sink are shown in Figs. 4(*d*) and 4(*e*), respectively. These solutions show more dependence on time when compared to those presented in Figs. 4(*a*) and 4(*b*). Maximum displacement is observed near the surface but not at the level of loading and the displacement decreases rapidly near the sink level ($1.0 < z/a < 2.0$). More gradual variation of vertical displacement is noted for $z/a > 2.0$. Maximum surface displacement is noted at the origin ($r = 0$, $z = 0$) at all times and the surface displacement decreases rapidly with the radial distance. Comparison of numerical solutions for displacements at $t^* = 1000$ and $t^* = 10^6$ indicates that a final equilibrium state is reached when $t^* > 1000$. Similar behavior was also noted by Kanok-Nukulchai and Chau (1990) for an interior sink in a poroelastic half-space with incompressible constituents. Suction profiles shown in Fig. 4(*f*) indicate that it increases rapidly with time and reaching a final value when $t^* > 1000$. The initial solution yields zero suction in this case. The maximum value of suction is noted at $z = a$ and a sharp decrease is noted with the depth both above and below the sink level. Naturally, the suction profiles show a singularity at $z = a$ due to the applied sink.

Conclusions

A set of general solutions are presented in the Laplace transform space for equations governing asymmetric deformations of a poroelastic medium with compressible constituents. These general solutions are used to derive fundamental solutions corresponding to buried circular ring loads acting in the radial, circumferential, and vertical directions and to a fluid source. Solutions corresponding to uniform circular, point, and annular loadings/fluid sources can be derived from ring load/source solutions. In addition, the fundamental solutions for a poroelastic full space can be obtained by taking certain limits on the corresponding half-space solutions. It is noted that the fundamental solutions appear in terms of Lipschitz-Hankel integrals involving products of Bessel functions. The complexity of the fundamental solutions hinder any attempts to obtain time domain solutions by analytical Laplace inversion

Downloaded 03 May 2010 to 171.66.16.245. Redistribution subject to ASME license or copyright; see http://www.asme.org/terms/Terms_Use.cfm

methods. It is found that accurate time-domain solutions can be obtained by applying the numerical scheme proposed by Stehfest (1970) for Laplace inversion and applying direct numerical quadrature to evaluate the Lipschitz-Hankel integrals. The numerical study also confirms that the more simple and computationally efficient Schapery's scheme (Schapery, 1962) yields time-domain solutions with reasonable accuracy. The application of Schapery's scheme to the Laplace domain solutions presented in this paper results in approximate time domain fundamental solutions explicitly. The response of six different poroelastic half-spaces under buried patch loads and a fluid sink is investigated in the numerical study. It is noted from the limit solutions that the nondimensional initial displacements are governed by the undrained Poisson's ratio whereas the final response depends only on the drained Poisson's ratio. In all loading cases it is found that the rate of displacement is higher when $0.1 < t^* < 100$. Final solutions are reached when $t^* > 1000$ for all types of loadings. The difference between the initial and final displacements due to vertical and horizontal loadings is less than 20 percent of the final displacement for all six materials. The initial solutions for pore pressure and displacements are zero due to a fluid sink. Displacements and suction show more dependence and variation with time under a circular sink when compared to the solutions corresponding to vertical and horizontal loadings. It is also noted that under a sink the highest vertical displacement is not observed at the level of the sink. The fundamental solutions presented in this paper are very useful in the analysis of a wide variety of problems related to geomechanics, energy resource explorations, groundwater studies, biomechanics, and in the development of boundary integral equation methods for poroelastic materials. A numerical approach based on the general solutions presented in this paper can be developed for the analysis of a multilayered poroelastic half-space under three-dimensional loadings and fluid sources.

Acknowledgments

The work presented in this paper was supported by Natural Sciences and Engineering Research Council of Canada Grant A-6507.

References

Apirathvorakij, V., and Karasudhi, P., 1980, "Quasi-static Bending of a Cylindrical Elastic Bar Partially Embedded in a Saturated Elastic Half-Space," *Int. J. Solid Structures*, Vol. 16, pp. 625–644.

Biot, M. A., 1941, "General Theory of Three-Dimensional Consolidation," *J. Appl. Phys.*, Vol. 12, pp. 155–164.

Cheng, A. H-D., Abousleiman, Y., and Badmus, T., 1992, "A Laplace Transform BEM for Axisymmetric Diffusion Utilizing Pre-Tabulated Green's Function," *Engineering Analysis with Boundary Elements*, Vol. 9, pp. 39–46.

Cleary, M. P., 1977, "Fundamental Solutions for a Fluid-Saturated Porous Solid," *Int. J. Solid Structures*, Vol. 13, pp. 785–806.

Dargush, G. F., and Banerjee, P. K., 1991, "A New Boundary Element Method for Three Dimensional Coupled Problems of Consolidation and Thermoelasticity," ASME JOURNAL OF APPLIED MECHANICS, Vol. 58, pp. 28–36.

Detournay, E., and Cheng, A. H-D., 1988, "Poroelastic Response of a Borehole in a Non-hydrostatic Stress Field," *Int. J. Rock Mech. Min. Sci. and Geomech. Abstr.*, Vol. 25, pp. 171–182.

Dominguez, J., 1991, "An Integral Formulation for Dynamic Poroelasticity," ASME JOURNAL OF APPLIED MECHANICS, Vol. 58, pp. 588–591.

Kanok-Nukulchai, W., and Chau, K. T., 1990, "Point Sink Fundamental Solutions for Subsidence Prediction," *J. Engng. Mech.*, Vol. 116, pp. 1176–1182.

Karasudhi, P., 1990, *Foundation of Solid Mechanics*, Kluwer Academic Publishers, The Netherlands.

Kreider, D. L., Kuller, R. G., Ostberg, D. R., and Perkins, F. W., 1966, *An Introduction to Linear Analysis*, Addison-Wesley, Cambridge, MA.

McNamee, J., and Gibson, R. E., 1960a, "Displacement Functions and Linear Transforms Applied to Diffusion Through Porous Elastic Media," *Q. J. Mech. App. Math.*, Vol. 13, pp. 98–111.

McNamee, J., and Gibson, R. E., 1960b, "Plane Strain and Axially Symmetric Problems of the Consolidation of a Semi-Infinite Clay Stratrum," *Q. J. Mech. App. Math.*, Vol. 13, pp. 210–227.

Mindlin, R. D., 1936, "Force at a Point in the Interior of a Semi-Infinite Solid," *Physics*, Vol. 7, pp. 195–202.

Muki, R., 1960, "Asymmetric Problems of the Theory for a Semi-Infinite Solid and a Thick Plate," *Progress in Solid Mechanics*, I. N. Sneddon and R. Hill, eds., North Holland, Amsterdam, Vol. 1, pp. 399–439.

Nishimura, N., and Kobayashi, S., 1989, "A Boundary Integral Equation Method for Consolidation Problems," *Int. J. Solid Structures*, Vol. 25, pp. 1–21.

Niumpradit, B., and Karasudhi, P., 1981, "Load Transfer from an Elastic Pile to a Saturated Elastic Soil," *Int. J. Numer. Anal. Methods Geomech.*, Vol. 5, pp. 115–138.

Piessens, R., 1975, "Bibliography on Numerical Inversion of the Laplace Transform and Applications," *J. Comp. Appl. Math.*, Vol. 1, pp. 115–126.

Puswewala, U. G. A., and Rajapakse, R. K. N. D., 1988, "Axisymmetric Fundamental Solutions for a Completely Saturated Porous Elastic Solid," *Int. J. Engng. Sci.*, Vol. 26, pp. 419–436.

Rice, J. R., and Cleary, M. P., 1976, "Some Basic Stress-Diffusion Solutions for Fluid Saturated Elastic Porous Media with Compressible Constituents," *Rev. Geophys. Space Phys.*, Vol. 14, pp. 227–241.

Rudnicki, J. W., 1986a, "Slip on an Impermeable Fault in a Fluid-Saturated Rock Mass," *Earthquake Source Mechanics*, J. Das, J. Boatwright, and C. H. Scholz, eds., American Geophysical Union, Geophysical Monograph 37, pp. 81–89.

Rudnicki, J. W., 1986b, "Fluid Mass Sources and Point Forces in Linear Elastic Diffusive Solid," *Mechanics of Materials*, Vol. 5, pp. 383–393.

Rudnicki, J. W., 1987, "Plane Strain Dislocations in Linear Elastic Diffusive Solids," ASME JOURNAL OF APPLIED MECHANICS, Vol. 54, pp. 545–552.

Ruina, A., 1978, "Influence of Coupled Deformation-Diffusion Effects on the Retardation of Hydraulic Fracture," *Proc. 19th U.S. Rock Mechanics Symp.*, pp. 274–282.

Schapery, R. A., 1962, "Approximate Methods of Transform Inversion for Viscoelastic Stress Analysis," *Proc. 4th U.S. Nat. Congress on Appl. Mech.*, Vol. 2, pp. 1075–1085.

Schiffman, R. L., and Fungaroli, A. A., 1965, "Consolidation due to Tangential Loads," *Proc. 6th Int. Conf. Soil Mech. and Found. Engng.*, pp. 188–192.

Skempton, A. W., 1954, "The Pore Pressure Coefficients A and B," *Geotechnique*, Vol. 4, pp. 143–147.

Sneddon, I. N., 1951, *Fourier Transforms*, McGraw-Hill, New York.

Stehfest, H., 1970, "Numerical Inversion of Laplace Transforms," *Communs. Ass. Comput. Mach.*, Vol. 13, pp. 47–49.

Terzaghi, K., 1923, "Die Berechnung der Durchassigkeitsziffer des Tones aus dem Verlauf der hydrodynamischen Spannungsercheinungen," *Sitzungsber. Akad. Wiss. Wien. Math.-Naturwiss. Kl., Abt. 2A*, Vol. 132, pp. 105–124.

Verruijt, A., 1971, "Displacement Functions in the Theory of Consolidation or in Thermoelasticity," *J. Appl. Math. Phys.*, Vol. 22, pp. 891–898.

Watson, G. N., 1944, *A Treatise on the Theory of Bessel Functions*, University Press, Cambridge, U.K.

Downloaded 03 May 2010 to 171.66.16.245. Redistribution subject to ASME license or copyright; see http://www.asme.org/terms/Terms_Use.cfm

Rayleigh-Type Wave Propagation on a Micropolar Cylindrical Surface

K. Mrithyumjaya Rao

M. Pratap Reddy

Department of Mathematics,
Kakatiya University,
Warangal-50 6009, India

A detailed study of a Rayleigh wave propagating on the surface of a micropolar elastic circular cylinder in an azimuthal direction is considered. At the cutoff frequency if the particle displacement is purely azimuthal and equivoluminal, then only this type of wave exists. A number of deviations from the results of the classical theory are observed. For example, the phase velocity corresponding to the same branch is given to be single valued, whereas it seems to be multivalued at some intervals. Due to the micropolar effect there exists an extra wave whose frequency spectrum is also obtained. The dependence of the microrotation and couple stress amplitudes on depth are evaluated. The frequency of the Rayleigh wave increases due to the micropolar effect.

Introduction

In metals such as steel and aluminum, experiments confirm the theoretical results from the classical theory of elasticity. The points of a classical elastic material have translational degrees-of-freedom only, and the transmission of the load across a differential element of a surface is described by a force vector only. But polymeric foam, human bone, and bodies of polycrystalline materials do not confirm this. The latter materials are fibrous and composite in nature and display size effects in torsion, bending, and fatigue. These materials have additional microdeformational degrees-of-freedom, i.e., they possess a microstructure whose size cannot be neglected in comparison with length scales of interest. Various degrees-of-freedom of a microstructure were considered by different authors, viz., Cosserat (1909), Eringen and Suhubi (1964a), Mindlin (1964), Aero and Kuvshinski (1964), Polmov (1964) and Green and Rivlin (1964). Each one has given an independent set of governing equations. The force at a point of a surface element of bodies of these materials is completely characterized by a stress vector and a couple stress vector at that point. In the classical theory of elasticity, the effect of couple stress is neglected. If we also take into consideration the couple stress, the medium is known as the Cosserat elastic medium. Eringen (1966) has modified his earlier theory and renamed it as the "Linear Theory of Micropolar Elasticity." In the following we consider the theory of Eringen. This theory is one of the simplest extensions of classical theory and some important problems of elasticity have been solved using it. This theory has microrotation about the center of mass as an additional degree-of-freedom and the physical phenomenon under consideration must have a characteristic length (such as wave length) comparable with the size of grains in the body. Recently efforts have been made experimentally to identify materials whose behavior tallies with that of Cosserat materials, a detailed list of which can be found in Lakes (1986). Lakes has shown that the theoretical results based on the couple stress theory instead of the classical theory, tally with the experimental results in the case of (i) quasi-static bending of human bone (Lakes, 1982) and (ii) torsion and bending of two foam materials (Lakes, 1986).

The problem of the surface wave propagation on a cylindrical surface is having practical applications such as detection of surface flaws, internal flaws, incipient fatigue cracks, and determination of their depth and nature. In classical theory, Sezawa (1927) has studied the Rayleigh wave propagation on cylindrical surfaces. Ewing et al. (1957) have corrected the frequency equation given by Sezawa and tallied with some experimental results of Oliver (1955). Later, Viktorov (1967) studied the effect of the curvature on a Rayleigh wave and showed graphically and theoretically the phase velocity of this wave propagating on a cylindrical surface in the azimuthal direction. This leads to a Rayleigh wave velocity as the radius of the cylinder tends to infinity. The same problem is also known as plain-strain vibrations in a cylinder. Gazis (1957) studied this problem in hollow cylinders.

After the advent of high-speed computers a complete study of the wave propagation, whose frequency equation involved transcendental functions, became possible (Pao, 1962; Zamanak, 1971).

In this paper a detailed study of a Rayleigh-type surface wave, propagating on the surface in the azimuthal direction of an elastic circular cylinder of a micropolar elastic material,

Contributed by the Applied Mechanics Division of THE AMERICAN SOCIETY OF MECHANICAL ENGINEERS for publication in the ASME JOURNAL OF APPLIED MECHANICS.

Discussion on this paper should be addressed to the Technical Editor, Professor Lewis T. Wheeler, Department of Mechanical Engineering, University of Houston, Houston, TX 77204-4792, and will be accepted until four months after final publication of the paper itself in the ASME JOURNAL OF APPLIED MECHANICS.

Manuscript received by the ASME Applied Mechanics Division, May 17, 1989; final revision, Mar. 13, 1992. Associate Technical Editor: L. M. Keer.

Copyright © 1993 by ASME

Downloaded 03 May 2010 to 171.66.16.245. Redistribution subject to ASME license or copyright; see http://www.asme.org/terms/Terms_Use.cfm

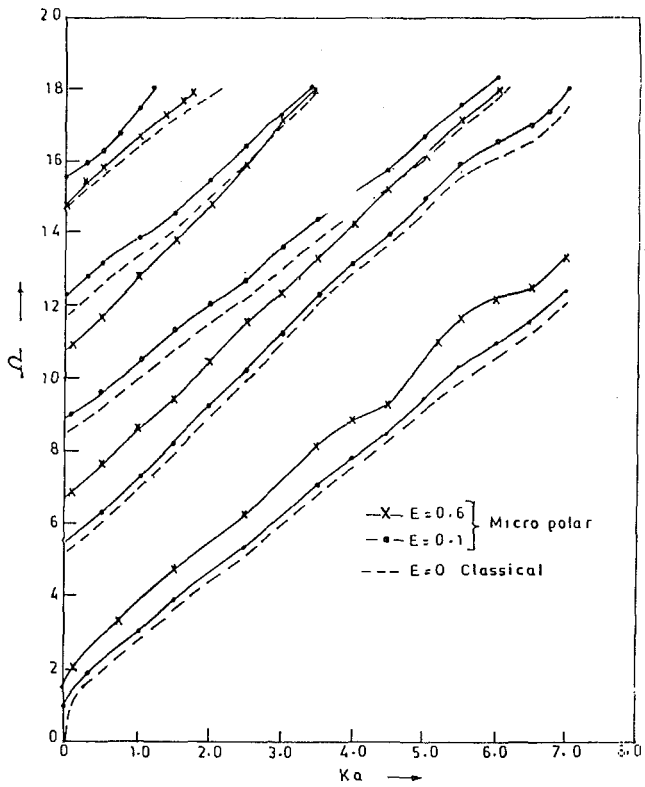


Fig. 1 Frequency versus wave number in (0, 7)

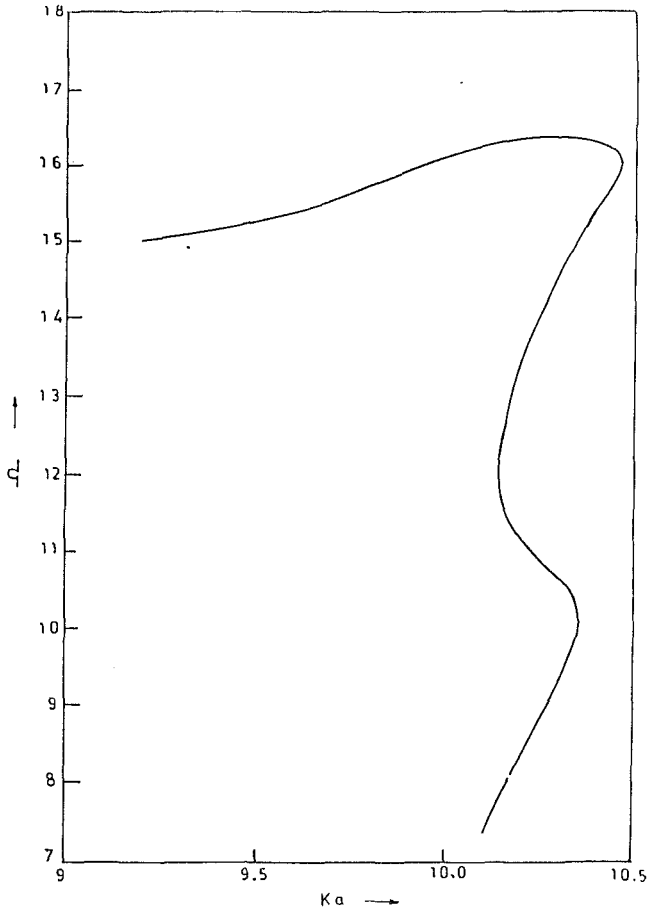


Fig. 2 Frequency versus wave number in (9, 10.5)

is considered. Supposing the surface of the cylinder to be stress-free the frequency equation is obtained. This equation can be factorized. The first factor is the counterpart of classical theory and the second depends only on micropolar effects from the first factor, using the procedure of Zamanak (1971). It is observed that this type of wave exists only if the particle displacement is purely azimuthal and equivoluminal at the cutoff frequency. The frequency spectrum in the case of classical theory was not given by Sezawa (1927), Ewing et al. (1957), or Viktorov (1967). Here it is given for both classical and micropolar cases in Fig. 1. The frequency is monotonic in (0, 10) of ka, where k is the wave number and a the radius of the cylinder, and oscillatory for $Ka > 10$, which is shown in Fig. 2. It implies that when $ka > 10$, the frequency is many valued instead of single valued for a given wave number.

The phase velocities are evaluated numerically by giving very small increments to the wave length $(2\pi/ka)$. In the case of classical theory the following deviations from the results given by Sezawa (1927), Ewing et al. (1957), and Viktorov (1967) are observed:

(i) The variation of phase velocity is not monotonic in the interval (0, 1.5) of $2\pi/ka$ as given by Ewing et al. (1957), but it is oscillatory as shown in Figs. 3 and 5.

(ii) From Figs. 7 and 10 we have that the phase velocity is greater than that given by Ewing et al. (1957) in the interval (0.13, 0.6).

(iii) The phase velocity of this Rayleigh-type surface wave tends to Rayleigh wave velocity as ka tends to very large values, but not near 50 as given by Viktorov (1967). This is due to evaluating phase velocities with greater step lengths of $(2\pi/ka)$.

The following effects are observed due to the presence of microrotation:

(i) There exists a new wave whose frequency depends purely on micropolar elastic constants, which is named as the new micropolar surface wave. The frequency spectrum of that new wave is the same as that of the frequency of the main wave.

(ii) The difference between the frequency of a micropolar case of a given wave number is greater with an increase in the wave number and for successive branches taken in ascending order.

(iii) For a very small wave number, the micropolar effect on a frequency is considerable in the first branch compared to other branches.

It is shown that the microrotation completely decays at a depth approximately equivalent to 4.5 times and 1.8 times the wavelength, respectively, in the case of $ka = 5$ and 25. So it is concluded that the rate of decay is faster with greater ka. The same behavior is also observed with the couple stress.

Rayleigh-Type Surface Wave Propagation on a Micropolar Cylindrical Surface

In this paper, the problem of propagation of a Rayleigh-type wave on a cylindrical surface in the azimuthal direction is considered. Therefore the displacement vector $\mathbf{U}$ $(u_r, u_\theta, 0)$ and microrotation ϕ $(0, 0, \phi)$ are taken as functions of r, θ and t only.

The displacements are expressed in terms of potential functions S and U as

$$u_r = \frac{\partial S}{\partial r} + \frac{1}{r}\frac{\partial U}{\partial \theta}$$

$$u_\theta = \frac{1}{r}\frac{\partial S}{\partial \theta} - \frac{\partial U}{\partial r}. \tag{1}$$

Let the micropolar medium be governed by the equations

Downloaded 03 May 2010 to 171.66.16.245. Redistribution subject to ASME license or copyright; see http://www.asme.org/terms/Terms_Use.cfm

given by Eringen (1968). Let S, U, ϕ, suitable to this problem, be

$$S = AJ_n(mr)e^{i(n\theta+\omega t)},$$
$$U = BJ_n(mr)e^{i(n\theta+\omega t)},$$
$$\phi = CJ_n(mr)e^{i(n\theta+\omega t)}, \quad (2)$$

where $n = ka$, k is the wave number "a" (the radius of the cylinder), and ω is the angular frequency. The potentials S, U, and ϕ that satisfy the equations of motion are given by

$$U = [A_1 J_n(m_1 r) + A_2 J_n(m_2 r)]e^{i(n\theta+\omega t)},$$
$$\phi = TA_2 J_n(m_2 r)e^{i(n\theta+\omega t)},$$
$$S = A_3 J_n(m_3 r)e^{i(n\theta+\omega t)}, \quad (3)$$

where

$$m_1^2 = \frac{\omega^2}{C_2^2 + C_3^2},\ m_2^2 = \frac{\omega^2}{C_4^2} - \frac{2\omega_0^2}{C_4^2},$$
$$m_3^2 = \frac{\omega^2}{C_1^2 + C_3^2},\ C_1^2 = \frac{\lambda + 2\mu}{\rho},\ C_2^2 = \frac{\mu}{\rho},\ C_3^2 = \frac{\kappa}{\rho},$$
$$C_4^2 = \frac{\gamma}{\rho j},\ \omega_0^2 = \frac{\kappa}{\rho j},\ \epsilon = \frac{C_3^2}{C_2^2}$$
$$T = (1+\epsilon)(m_2^2 - \omega^2/(C_2^2 + C_3^2)) \quad (4)$$

and λ, μ are Lame's constants and κ, γ are micropolar elastic constants. Let microeffects be not very strong so the terms of ϵ^2, ϵ^3 . . . are neglected.

Now the displacements are given by

$$u_r = \left\{A_3 \frac{d}{dr} J_n(m_3 r) + \frac{in}{r}[A_1 J_1(m_1 r) + A_2 J_n(m_2 r)]\right\} e^{i(n\theta+\omega t)},$$
$$u_\theta = \left\{\frac{in}{r} A_3 J_n(m_3 r) - A_1 \frac{d}{dr} J_n(m_1 r) - A_2 \frac{d}{dr} J_n(m_2 r)\right\} e^{i(n\theta+\omega t)},$$
$$\phi = TA_2 J_n(m_2 r)e^{i(n\theta+\omega t)}. \quad (5)$$

Assuming the boundary to be stress free, i.e.,

$$\sigma_{rr} = \sigma_{r\theta} = m_{rz} = 0 \text{ on } r = a \quad (6)$$

we get

$$(\lambda + 2\mu + \kappa)\frac{\partial u_r}{\partial r} + \lambda\left(\frac{1}{r} - \frac{\partial U_\theta}{\partial \theta}\frac{u_r}{r}\right) = 0,$$
$$\frac{(2\mu+\kappa)}{2}\left(\frac{1}{r}\frac{\partial u_r}{\partial \theta} + \frac{\partial u_\theta}{\partial \theta} - \frac{u_\theta}{r}\right) + \frac{\kappa}{2}\left(\frac{\partial u_\theta}{\partial r} + \frac{u_\theta}{r} - \frac{1}{r}\frac{\partial u_r}{\partial \theta}\right) - \kappa\phi = 0$$
$$\phi,\ r = 0. \quad (7)$$

Substituting (5) in (7), three homogeneous equations in A_1, A_2, A_3 are obtained. For a nontrivial solution we have

$$|B| = 0 \quad (8)$$

where

$$b_{11} = (2+\epsilon)\left[\frac{in}{r}\frac{d}{dr} J_n(m_1 r) - \frac{in}{r^2} J_n(m_1 r)\right]$$
$$b_{12} = (2+\epsilon)\left[\frac{in}{r}\frac{d}{dr} J_n(m_2 r) - \frac{in}{r^2} J_n(m_2 r)\right]$$
$$b_{13} = \left(2 - \frac{C_1^2}{C_2^2}\right) m_3^2 J_n(m_3 r) + (2+\epsilon)\frac{d^2}{dr^2} J_n(m_3 r)$$
$$b_{21} = \frac{1}{r}\frac{l}{dr} J_n(m_1 r) - \frac{n^2}{r^2} J_n(m_1 r) - (1+\epsilon)\frac{d^2}{dr^2} J_n(m_1 r)$$
$$b_{22} = \frac{1}{r}\frac{d}{dr} J_n(m_2 r) - \frac{n^2}{r^2} J_n(m_2 r) - (1+\epsilon)\frac{d^2}{dr^2} J_n(m_2 r) - TJ_n(m_2 r)$$
$$b_{23} = (2+\epsilon)\left[\frac{in}{r}\frac{d}{dr} J_n(m_3 r) - \frac{in}{r^2} J_n(m_3 r)\right]$$
$$b_{31} = 0$$
$$b_{32} = T\frac{d}{dr} J_n(m_2 r)$$
$$b_{33} = 0 \text{ at } r = a.$$

The frequency Eq. (8) splits into two factors out of which one is the counterpart of the classical theory. Therefore, when the micropolar effects are neglected, we obtain the equation of classical theory. The other factor gives a new equation

$$\frac{d}{dr} J_n(m_2 r) = 0 \text{ at } r = a, \quad (9)$$

which has no counterpart in classical theory and involves purely micropolar elastic constants.

Now we analyze the equation given by the first factor. Let us use the following notation:

$$\Omega = \omega a/C_2,\ \alpha = m_3 a,\ \beta = m_1 a,$$
$$p^2 = C_1^2/C_2^2 = 2(1-\nu)/(1-2\nu)$$

where ν is the Poisson's ratio.

Frequency Spectrum

This problem is also known as a problem of plain-strain vibrations in a circular cylinder. Gazis (1957) has studied this problem in classical theory. In this case, n is a positive integer.

In the case of a semi-infinite medium with circular cylindrical surface as its bounding surface, n is a continuous variable. The case of n being a continuous variable arose in the studies of Gilbert and Knopoff (1959), Norwood and Miklowitz (1967), Peck and Miklowitz (1969), and Viktorov (1967). The first three authors adopted the method known as wave form of a function and wave sum. This method was explained in detail by Friedlander (1958) and Miklowitz (1980). By adopting the wave form procedure, it is also observed that the frequency equation is the same as the equation given in (8). Also in this paper, n is treated as a continuous variable.

For constructing the frequency spectrum, we require the cutoff frequencies. These are obtained by using the condition that the dimensionless frequency Ω will be finite as $n = ka \to 0$. Taking these cutoff frequencies as the beginning points we construct the branches. Then det (8) reduces to

$$\beta(1+\epsilon)J_0(\beta) - (2+\epsilon)J_1(\beta) = 0, \quad (10)$$
$$(2+\epsilon)J_1(\alpha) - (p^2+\epsilon)\alpha J_0(\alpha) = 0. \quad (11)$$

From (8) and (10) we find that A_2 and A_3 are zero, and hence from (5) the displacement is purely azimuthal and equi-voluminal. The roots of this equation are independent of Poisson's ratio. These are given in Table 1.

From (11) and (8) we find that A_1, A_2 are zero and from (5) we can conclude that the displacement is purely radial and dilatational. The roots of this equation depend on the Poisson's ratio and the first three roots are given in Table 2.

By taking the cutoff frequencies as the starting points of the branches, the first five branches are constructed and are shown in Fig. 1. From that it can be observed that the branches are originating only from those cutoff frequencies given by (10), which do not depend on the Poisson's ratio. This implies that the branches are not originating from the cutoff frequencies depending on Poisson's ratio ν. Therefore, it is concluded that,

Downloaded 03 May 2010 to 171.66.16.245. Redistribution subject to ASME license or copyright; see http://www.asme.org/terms/Terms_Use.cfm

for the existence of a Rayleigh-type surface wave on a cylindrical surface, the particle displacement is purely azimuthal and equi-voluminal at cutoff frequencies.

In the frequency spectrum, the branches are shown to $ka = 7$. On calculating the frequencies for further values of ka, it is seen that frequencies increase monotonically up to $ka < 10$ in the first branch. But when $ka > 10$, the frequency is oscillating as shown in Fig. 2. That means the frequency is many valued. We will discuss such behavior later.

Micropolar Effect

Here the effect of micropolarity is studied when $\epsilon = 0.1$ and $\epsilon = 0.6$. In the former, the micropolarity of the medium is weak and in the later case the effect of micropolarity is relatively strong. In fact, Cowin (1970) has shown that ϵ can take values greater than 1 also. But in the present case, since ϵ^2 is neglected in the beginning, bigger values are not considered. The following points are observed due to the micropolar effect on the frequency spectrum:

(i) The difference between the frequency of a micropolar case and a classical case for a given wave number is greater with an increase in wave number, and for successive branches taken in ascending order.

(ii) From Table 3 it is seen that
(a) for very small wave numbers, the micropolar effect on frequency is considerable in the first branch; and
(b) the increase in frequency is 0.58 in the classical case, 0.17 when $\epsilon = 0.1$, and 0.05 for $\epsilon = 0.6$ as ka varies from 0 to 0.007.

Table 1 Cutoff frequencies

Sl. No.	Classical	Micropolar	
	$\epsilon=0$	$\epsilon=0.1$	$\epsilon=0.6$
1	0	0.6262606	1.501519
2	5.13646	5.404860	6.588914
3	8.4416960	8.839390	10.70353
4	11.62017	12.19519	14.73891
5	14.79585	15.52455	18.74764

Table 2 Cutoff frequencies

Sl. No.	Classical	Micropolar	
	$\epsilon=0$	$\epsilon=0.1$	$\epsilon=0.6$
1	0.8799041	0.9009237	1.067445
2	5.577357	5.605503	5.857740
3	12.80736	12.86701	13.44604

Table 3 Frequency versus wave number

Wave number ka	Frequency		
	Classical	Micropolar	
	$\epsilon=0$	$\epsilon=0.1$	$\epsilon=0.6$
0	0	0.6262606	1.501519
0.00001	0.1036450	0.6237671	1.501475
0.0001	0.2001497	0.627720	1.502090
0.001	0.354821	0.6611185	1.508297
0.002	0.4206353	0.6912563	1.515296
0.003	0.4674147	0.7150041	1.522404
0.004	0.5056288	0.7374506	1.529628
0.005	0.5338352	0.7575962	1.536969
0.006	0.5601032	0.7740775	1.544432
0.007	0.5821004	0.7920533	1.551602

Phase Velocity in the Case of a Short Wavelength

Following Ewing et al. (1957), for large values of ka it will be convenient to take phase velocity C/C_2 and $2\pi/ka$ instead of the frequency Ω and the wave number ka, respectively. Now, the phase velocity equation can be written as

$$\{[Y^2/(1+\epsilon)-2+x^2/\pi-\epsilon(1-x/2-Y^2/(1+\epsilon)]J_R(P) - [(2+\epsilon)(YX/2\pi\sqrt{1+\epsilon}]J_{R+1}(P)\} \times\{[-(P^2/(P^2+\epsilon))+Y^2+2 -X/\pi+\epsilon(1-X/2\pi-Y^2/(P^2+\epsilon)]J_R(Q)+[(2+\epsilon)/\sqrt{P^2+\epsilon} \times(XY/2\pi)J_{R+1}(Q)\}+4(1+\epsilon)\{(1-x/2\pi)J_R(Q) -(Y/\sqrt{p^2+\epsilon})J_R(Q)\}\{(1-x/2\pi)J_R(P) -(Y/\sqrt{1+\epsilon})J_{R+1}(P)=0 \quad (12)$$

where

$$X=2\pi/ka,\ Y=C/C_2,\ R=2\pi/x,$$
$$p=\frac{Y}{X}\cdot\frac{2\pi}{\sqrt{1+\epsilon}},\ Q=\frac{Y}{X}\cdot\frac{2\pi}{\sqrt{p^2+\epsilon}}. \quad (13)$$

From this equation for $\epsilon = 0$, we obtain the equation of the

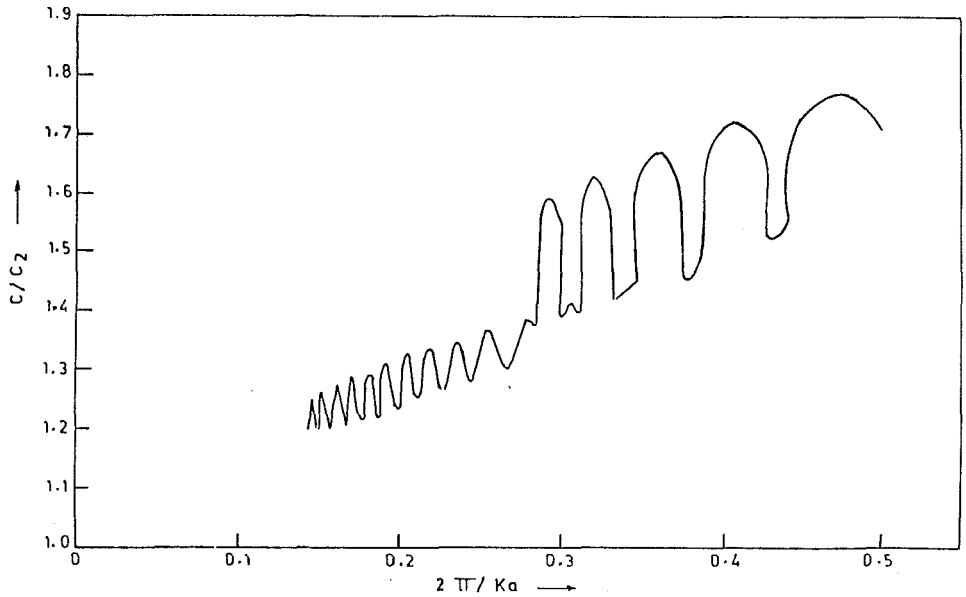


Fig. 3 Phase velocity versus reciprocal wave number in (0, 0.6)

Downloaded 03 May 2010 to 171.66.16.245. Redistribution subject to ASME license or copyright; see http://www.asme.org/terms/Terms_Use.cfm

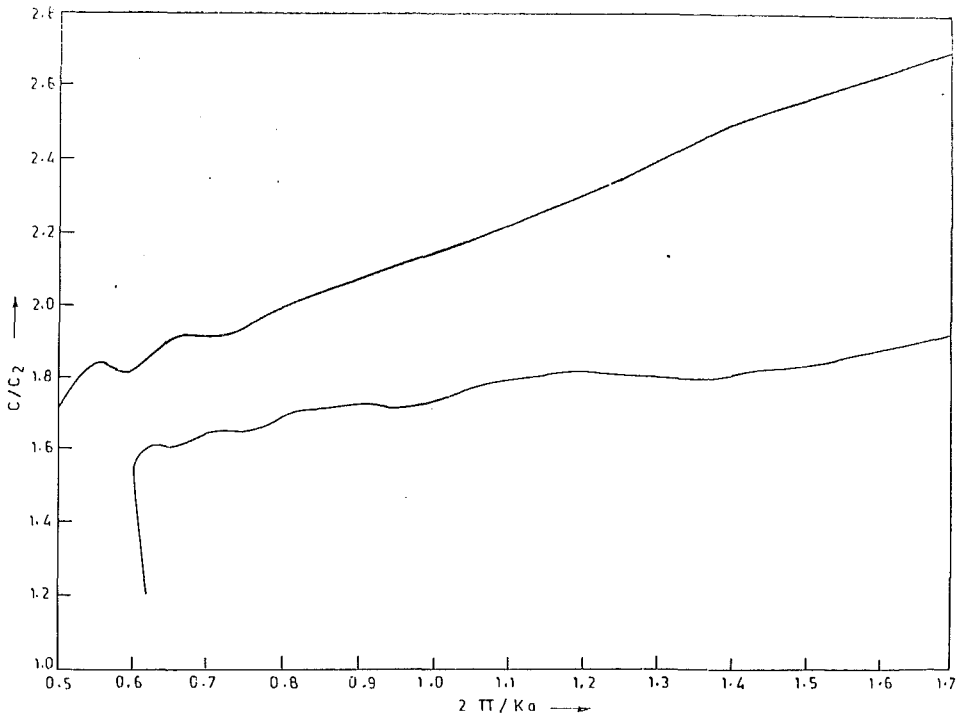


Fig. 4 Phase velocity versus reciprocal wave number in (0.5, 1.7)

Table 4 Phase velocity versus reciprocal wave number

C/C_2 for $\frac{2\pi}{ka}=0.0000002$	C/C_2 for $\frac{2\pi}{ka}=0.0000003$	C/C_2 for $\frac{2\pi}{ka}=0.0000004$
0.09984107	0.09251869	0.06160823
0.2799114	0.1636568	0.1295193
0.3210959	0.3708008	0.1702065
0.5456388	0.4252898	0.2214639
0.6478803	0.4586116	0.2904462
0.6557882	0.7238415	0.3814466
0.7262158	0.7704883	0.4098405
0.7720585	0.8135084	0.4875593
0.8945689	0.8622605	0.5409092
1.034664	0.9329552	0.6147524
1.056141	0.9833428	0.6531078
1.135143	1.041278	0.7936540
1.176022	1.051153	0.8371840
	1.147310	0.9101262
	1.165602	1.177974

classical theory (Ewing et al., 1957). The phase velocity is evaluated in single precision on an I.B.M. compatible P.C. The phase velocity C/C_2 versus $2\pi/ka$ is shown in Figs. 3–6. The curve is split into four segments based on pecularities in each of the intervals (0, 0.5), (0.5, 1.7), (0.6, 1.8), (1.8, 3.0), respectively.

Initially for small values of $2\pi/ka$, Eq. (12) is solved for C/C_2 and it is found to be very confusing and no clear curve is emerging. Typical data in the range (0, 1.2) of C/C_2 are given in Table 4. Then the Eq. (12) is solved for $2\pi/ka = 1.5$ and the roots in the range (0, 1.2) of C/C_2, are found to be 0.339872, 0.8404288, and 1.09374. Taking this as the basis, the phase velocity curve is constructed towards the left and right of 1.5 of $2\pi/ka$. From Fig. 6 we observe that the three values of C/C_2 belong to the same branch. Thus we can conclude that the curve shown in Figs. 3 to 6 is that of first branch (mode) only.

The curve exhibits an interesting feature at 1.4768249 and 1.2566329. The corresponding data are given in Table 5. From the table it is observed that as $2\pi/$ka approaches 1.4768240, the values of C/C_2 approaches 1.000001. Then for 1.4768249, there is no root in the range (0.95, 1.15). This implies that this branch does not extend further. Since the phase velocity curve of a wave is a continuous one under nondissipative conditions, it is supposed that the curve turns back such that the value of C/C_2 is 0.9999974 at 1.4768250 of $2\pi/ka$. This type of conclusion is made at many other parts of the curve, for example at 1.2566330 also, the data of which is shown in Table 5.

From Fig. 6 it is observed that the phase velocity is oscillatory following a pattern in (0.6, 1.5) of $2\pi/ka$. The width of the period of this pattern is decreasing as $2\pi/ka$ decreases. The phase velocity has locally many maxima and minima. The maxima can be grouped into two sets. They come alternately from those sets. The second set is approaching the first as $2\pi/ka$ decreases.

From Fig. 3 it is seen that this pattern is not followed in the range (0, 0.6) and two new different patterns are observed approximately in (0.28, 0.6) and (0.13, 0.28). At 0.60148, the curve turns back and the phase velocity goes on increasing to 1.92 at 1.7 of $2\pi/ka$ as shown in Fig. 4 to the extent it is investigated. At 0.6, the first root of Eq. (12) is found to be 1.910318. It is also observed that there is no root of this equation between 0.6 and 0.60148 in (0, 1.8) of C/C_2. Therefore the curve is investigated toward left and right from 1.810318. Toward the right, the phase velocity curve goes on increasing from 1.810318 to 2.7 at 1.7 of $2\pi/ka$. By the continuity property, the above two parts of this curve should meet.

The phase velocity in the range (0, 0.13) of $2\pi/ka$ can not be graphically represented as phase velocity changes violently.

From Figs. 3–6 we can observe that the phase velocity has a smooth behavior for $2\pi/ka > 1.5$ or $ka < 4.2$ and oscillating behavior, or many valued, for $2\pi/ka < 1.5$ or $ka > 4.2$. The same behavior is observed for the frequency in the first branch of the frequency spectrum.

The curve of phase velocity versus $2\pi/ka$ is given by Ewing et al. (1957), which is reproduced in Fig. 7. We can observe the difference between Figs. 3 to 6 and Fig. 7. The common points between the two curves are shown as points enclosed by squares. If we draw a curve joining these points in squares,

Downloaded 03 May 2010 to 171.66.16.245. Redistribution subject to ASME license or copyright; see http://www.asme.org/terms/Terms_Use.cfm

Table 5 Phase velocity versus reciprocal wave number

$2\pi/ka$	C/C_2	$2\pi/ka$	C/C_2
1.48	1.026584, 0.9514977	1.2567	0.091164 , 0,2526515
1.478	1.00947 , 0.9806886	1.25668	0.07765884, 0.2280187
1.477	1.001382, 0.9970155	1.25666	0.08154214, 0.1998727
1.4769	1.000591, 0.998717	1.35664	0.04110553, 0.1625753
1.47688	1.000431, 0.9990618	1.256638	0.0607064 , 0,1606718
1.47686	1.000273, 0.9994052	1.256636	0.06007281, 0.1251151
1.47684	1.000112, 0.9997553	1.256634	0.1667677 , 0.1102452
1.47683	1.000033, 0.9999275	1.256633	0.1499271 , 0.0618788
1.476828	1.000020, 0.9999560	1.2566329	No root between
1.476825	1.000001, 0.9999974		(0.001, 0.201)
1.4768249	No root between (0.95, 1.15)		

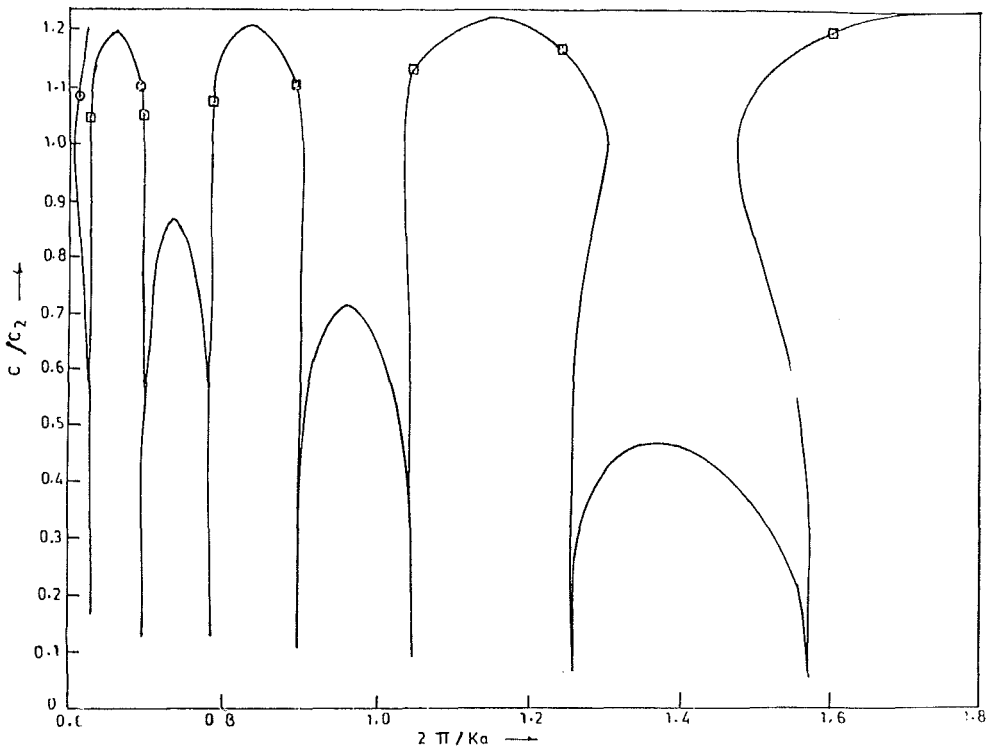


Fig. 5 Phase velocity versus reciprocal wave number (0.6, 1.8)

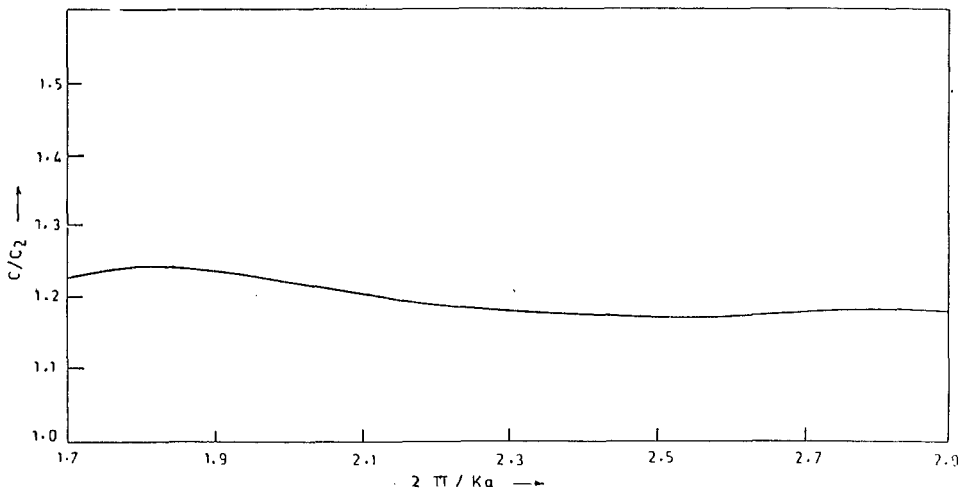


Fig. 6 Phase velocity versus reciprocal wave number in (1.7, 2.9)

Downloaded 03 May 2010 to 171.66.16.245. Redistribution subject to ASME license or copyright; see http://www.asme.org/terms/Terms_Use.cfm

we obtain the curve given by Ewing et al. (1957). The curve given here differs from that of Ewing et al. (1957) in the range (0.13, 0.6). The experimental values that are obtained by Oliver (1955) for Poisson's ratio 0.28 are available in the range (0, 1) of $2\pi/ka$ from Ewing et al. (1957). These points are shown as points enclosed by circles in the graph.

Curvature Effect

Viktorov (1967) has studied the influence of curvature on phase velocity C_R of a plane harmonic Rayleigh wave by calculating the ratio C/C_R, where C is the phase velocity of the surface wave of the present problem. In the graph presented there (reproduced in Fig. 8), he has shown that C/C_R tends to 1 as ka approaches 50. Viktorov has also observed that the same result can be derived by reducing the frequency equation of the present problem to the frequency equation of the Rayleigh wave.

The frequency equation obtained by Viktorov can be obtained as a particular case of (12) by taking $\epsilon = 0$ and using recurrence relations of Bessel functions.

When the Eq. (12) is numerically solved for C/C_R for varying ka, the following points are observed:

(i) The curve is not smooth as shown in Fig. 8 in the intervals (3, 4) and (25, 26) of ka, but C/C_R first increases and then decreases. Those are given in Table 6. A similar variation is also observed for some more intervals of ka.

(ii) When ka takes the integer values 29, 31, 35, 37, 39, 40, 42, 44, 45, 50, 52, 54, we do not find a root between 1 and 1.2 as shown in Fig. 8. But we find values for C/C_R in this interval for all integer values of ka from 6 to 55, and also we do not find roots in this interval for many noninteger values of ka as shown in Fig. 8.

From these observations it is concluded that the ratio C/C_R will be oscillating as ka varies. The same type of behavior is observed for C/C_2 when $2\pi/ka$ is small, i.e., ka is large (see Figs. 3 and 5). So it can be concluded that the phase velocity of the surface wave does not tend to the Rayleigh wave velocity so smoothly as ka tends to near 50. But by taking the Debey's (Abramowitz and Stegun, 1972) asymptotic expansions for Bessel functions and ka to infinity, Eq. (12) reduces to

$$\left(-\frac{C^2}{C_2^2}-2-\epsilon\right)^2 = 4(1+\epsilon)\left[\left(1-\frac{C^2}{C_2^2}\right)\frac{1.}{(p^2+\epsilon)}\right]^{1/2}\left[1-\frac{C^2}{C_2^2}\right]^{1/2}.$$

This equation tallies with that of Eringen and Suhubi (1964b) in the case of Rayleigh wave propagation in a micropolar half-space. When $\epsilon = 0$, this equation leads to Rayleigh's equation of classical theory. Hence as ka tends to infinity, the phase velocity of this surface wave tends to Rayleigh wave velocity.

Therefore this is possible only when ka is very large but not as ka tends to a value around 50.

New Micropolar Surface Wave

Since Eq. (9) involves purely micropolar elastic constants κ, γ it is concluded that a new surface wave exists which is named as the micropolar surface wave. Let us introduce the notation

$$\Omega' = \frac{C}{C_4}\cdot ka,\ D = \frac{\omega_o}{C_4}\,a = \frac{\kappa}{\gamma}\,a \tag{14}$$

where Ω' is a dimensionless frequency. Now (9) takes the form

$$(ka)J_{ka}(\sqrt{\Omega'^2-2D^2}) - \sqrt{\Omega'^2-2D^2}\,J_{ka+1}(\sqrt{\Omega'^2-2D^2}) = 0. \tag{15}$$

By using the above equation, the frequency spectrum of the new micropolar surface wave is given in Fig. 9 for two values of D, i.e., $D = 0.5$ and $D = 1.3$. The former case corresponds to a medium in which the micropolar elastic constant κ, which is related to stress is numerically greater than γ, which is related to the couple stress. In the later case, it is vice versa. From the frequency spectrum Fig. 9, it can be seen that the difference between the frequencies of the above two cases is decreasing for successive branches taken in ascending order. In the first branch, the difference between the frequencies is more for small wave numbers.

By comparing the frequency spectra given in Fig. 1 and Fig. 9, it can be concluded that the behavior of the frequencies of the two waves is same. It is an interesting result when compared

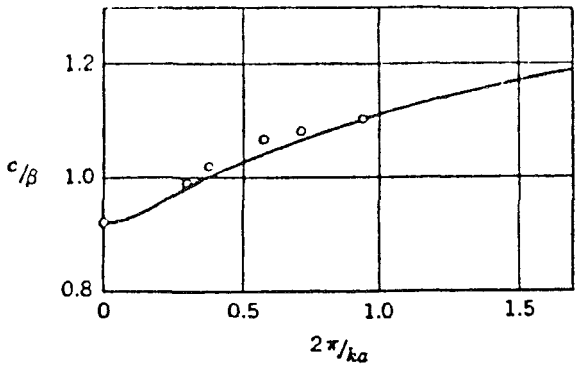


Fig. 7 Phase velocity versus reciprocal wave number

Table 6 Phase velocity versus wave number

k/a	C/C_R	ka	C/C_R
3.0	1.305096	25.0	1.052341
3.01	1.306168	25.001	1.13517
3.05	1.310571	25.01	1.152088
3.1	1.316241	25.1	1.179842
3.2	1.327476	25.2	1.205870
3.3	1.337273	25.3	1.222400
3.4	1.344005	25.4	1.233276
3.5	1.346217	25.5	1.236943
3.6	1.342954	25.6	1.232844
3.7	1.334026	25.7	1.221554
3.8	1.320104	25.8	1.204641
3.9	1.302560	25.95	1.163091
3.95	1.288716	25.98	1.154040
4.0	1.273118	25.999	1.134375
		25.9999	1.066910
		26.0	1.055363

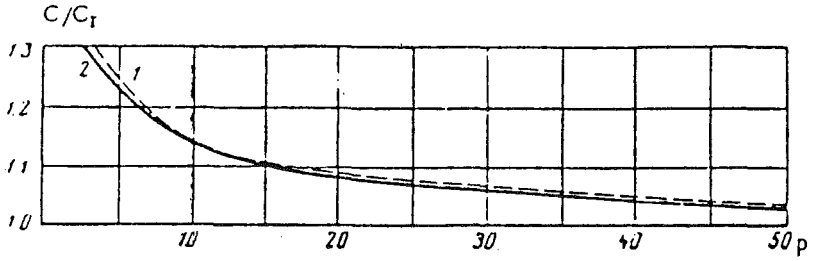


Fig. 8 Phase velocity versus wave number

Downloaded 03 May 2010 to 171.66.16.245. Redistribution subject to ASME license or copyright; see http://www.asme.org/terms/Terms_Use.cfm

to the results of Mrithyumjaya Rao and Kesava Rao (1983) and Mrithyumjaya Rao (1988). It is observed that the behavior of the phase velocity of the new micropolar longitudinal wave propgation in a cylinder is that of a torsional wave (Mrithyumjaya Rao and Kesava Rao, 1983). It is also observed that the behavior of the phase velocity of the new micropolar longitudinal wave propagating in a wave guide is that of a SH-type wave (Mrithyumjaya Rao, 1988).

Just as in the case of the main surface wave, it can be shown that the frequency equation of the new micropolar wave tends to the frequency equation of a new Rayleigh wave that exists in a micropolar half-space as $ka \to \infty$. For that we take the Debey's asymptotic expansion of the Bessel function and $ka \to \infty$, then Eq. (15) reduces to

$$1-(C/C_4)^2+2(\omega_0/\kappa C_4)^2=0. \tag{16}$$

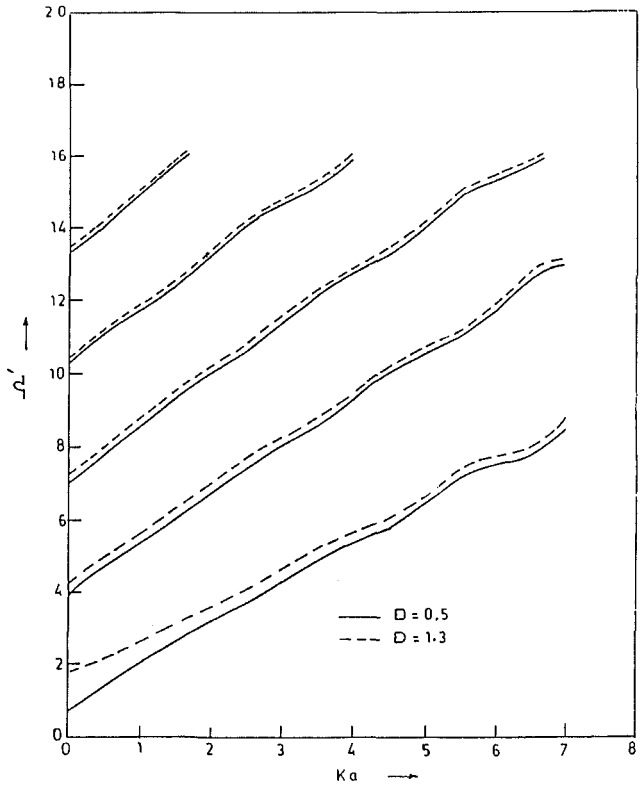


Fig. 9 Micropolar frequency versus wave number in (0, 7)

This equation tallies with the equation that is obtained by Eringen and Suhubi (1964b) for a new Rayleigh wave in a micropolar half-space.

The dependence of the microrotation amplitudes on depth are calculated by using (5) and are shown in Fig. 10 for two values of ka, i.e., $ka = 5$ and 25 taking $D = 0.5$. The curve is given in terms of a dimensionless microrotation amplitudes ϕ/ϕ_0 and fractions of wave length $k(a-r)$. Here ϕ_0 is the amplitudes of the microrotation on the surface of the cylinder, i.e., $r = a$. From Fig. 10 it can be observed that the microrotation in the new surface wave completely decays at a depth approximately equal to 4.5 times and 1.8 times of wave length, respectively, in the cases of $ka = 5$ and 25. That means the rate of decay is faster with increasing ka. The same analysis will also hold good in the case of $D = 1.3$.

The dependence of couple stress amplitudes on depth are calculated and shown in Table 7 for $ka = 5$ and 25. From the table it is observed that the rate of decay of couple stress is faster with increasing ka just as in microrotation.

Conclusions

It is shown that the Rayleigh type of surface wave can propagate on a micropolar cylindrical surface if the particle displacement is purely azimuthal and equivoluminal at the cutoff frequency. It is observed that, corresponding to the same

Table 7 Depth of couple stress

$ka=5$		$ka=25$	
$K\ (a-r)$	m_{rz}/m_{rzla}	$k\ (a-r)$	m_{rz}/m_{rzla}
0	1.0	0	1.0
0.0005	11.3555	0.001	23.8320
0.005	104.126	0.01	228.996
0.05	1023.64	0.1	2275.72
0.6	10192.6	0.5	10893.38
1.0	13776.6	1.0	19494.4
1.4	14610.0	1.5	24606.6
2.C	11909.1	2.C	25734.9
3.C	4138.64	3.C	18190.6
3.5	1567.93	3.6	10220.4
4.C	350.559	4.2	2166.29
4.6	9.41518	4.36	217.325
4.7	2.64927	4.37	99.6536
4.74	1.18752	4.376	27.179
4.78	0.28735	4.378	5.73999
4.79	0.140709	4.3782	3.42204
4.792	0.0191573	4.3784	1.14184
4.794	0.0226667		
4.8	0.00661159		

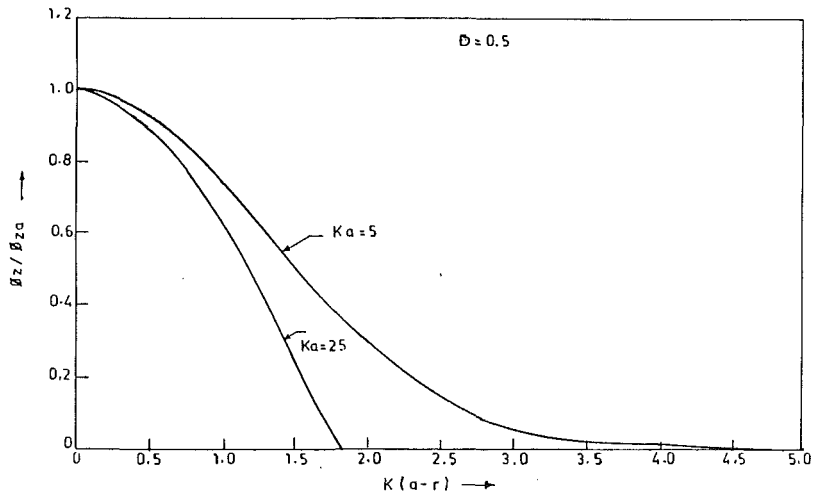


Fig. 10 Depth of microrotation

Downloaded 03 May 2010 to 171.66.16.245. Redistribution subject to ASME license or copyright; see http://www.asme.org/terms/Terms_Use.cfm

branch, the frequency is multivalued in some intervals of the wave number instead of single valued as reported previously. Due to the micropolar effect, the velocity of Rayleigh wave increases.

Acknowledgments

The authors acknowledge with thanks the suggestions given by Dr. G. S. Murthy, Head—Seismology Division, Babha Atomic Research Centre, Bombay, India and also the reviewers for their critical review and suggestions in improving the quality of this paper.

References

Abramowitz, M., and Stegun, 1972, *Handbook of Mathematical Functions*, Dover, New York.

Aero, E. L., and Kuvshinski, E. V., 1963, "Continuum Theory of Asymmetric Elasticity," *Soviet Phys. Solid State*, Vol. 5, p. 1892.

Cosserat, E. F., 1909, *Theorie des Corps Deformables*, A. Hermann et Fils, Paris.

Cowin, S. C., 1970, "An Incorrect Inequality in Micropolar Elasticity Theory," *Journal of Applied of Mathematical Physics* (*Z.A.M.P.*), Vol. 21, pp. 494–497.

Eringen, A. C., and Suhubi, E. S., 1984a, "Nonlinear Theory of Simple Microelastic Solids—I," *Int. J. Engng. Sci.*, Vol. 2, pp. 189–203.

Eringen, A. C., and Suhubi, E. S., 1964b, "Nonlinear Theory of Simple Microelastic Solids—II," *Int. J. Engng. Sci.*, Vol. 2, pp. 389–404.

Eringen, A. C., 1966, "Linear Theory of Micropolar Elasticity," *J. Math. Mech.*, Vol. 15, pp. 909–924.

Eringen, A. C., 1968, "Theory of Micropolar Elasticity," *Fracture*, Vol. II, H. Liebouritz, ed., Academic Press, New York.

Ewing, Jardetzky, and Press, 1957, *Elastic Waves in Layered Media*, McGraw-Hill, London.

Friedlander, F. G., 1958, *Sound Pulses*, Cambridge University Press, London, Chapter 6.

Gazis, D. C., 1958, "Exact Analysis of the Plane-Strain Vibrations of Thick Walled Hollow Cylinders," *J. Acoust. Soc. Am.*, Vol. 30, pp. 786–794.

Gilbert, F., and Knopoff, L., 1959, "Scattering of Impulsive Elastic Waves by a Circular Cylinder," *J. Acoust. Soc. Am.*, Vol. 31, pp. 1169–1175.

Green, A. E., and Rivlin, R. S., 1964, "Multipolar Continuum Mechanics," *Arch. Rat. Mech. Anal.*, Vol. 17, pp. 113–147.

Lakes, R. S., and Yang, J. F. C., 1982, "Experimental Study of Micropolar and Couple Stress Elasticity in Compact Bone in Bending," *J. Biomechanics*, Vol. 15, pp. 91–98.

Lakes, R. S., 1986, "Experimental Microelasticity of Two Porous Solids," *Int. J. Solids Structures*, Vol. 22, pp. 55–63.

Miklowitz, J., 1980, *The Theory of Waves and Waveguides*, North-Holland, Amsterdam, The Netherlands.

Mindlin, R. D., 1964, "Microstructure in Linear Elasticity," *Arch. Rat. Mech. Anal.*, Vol. 16, pp. 51–72.

Mrithyumjaya Rao, K., and Kesava Rao, B., 1983, "Longitudinal Wave Propagation in a Micropolar Wave Guide of Circular Cross-Section," *Int. J. Engng. Sci.*, Vol. 21, pp. 1137–1144.

Mrithyumjaya Rao, K., 1988, "Longitudinal Wave Propagation in a Micropolar Wave Guide," *Int. J. Engng. Sci.*, Vol. 26, pp. 135–141.

Norwood, F. R., and Miklowitz, J., 1967, "Diffraction of Transient Elastic Waves by a Spherical Cavity," ASME JOURNAL OF APPLIED MECHANICS, Vol. 34, pp. 735–744.

Oliver, J., 1955, "Rayleigh Waves on a Cylindrical Curved Surface," *Earthquake Notes*, Vol. 26, pp. 24–25.

Pao, Y. H., 1962, "The Dispersion of Flexural Waves in an Elastic, Circular Cylinder," ASME JOURNAL OF APPLIED MECHANICS, Vol. 29, pp. 61–64.

Peck, J. C., and Miklowitz, J., 1969, "Shadow-Zone Response in the Diffraction of a Plane Compressional Pulse by a Circular Cavity," *Int. J. Solids Structures*, Vol. 5, pp. 437–454.

Polmov, N. A., 1964, "Fundamental Equations of Theory of Asymmetric Elasticity," *Prikl. Mat. Mekh.*, Vol. 28, pp. 401–420.

Sezawa, K., 1927, "Dispersion of Elastic Waves Propagated on the Surface of Stratified Bodies and on Curved Surfaces," *Bull. Earthquake Research Inst.*, Vol. 3, pp. 1–18.

Viktorov, I. A., 1967, *Rayleigh and Lamb Waves*, Plenum Press, New York.

Zamanak, J., 1971, "An Experimental and Theoretical Investigation of Elastic Wave Propagation in a Cylinder," *J. Acoust. Soc. Am.*, Vol. 51, pp. 265–283.

Downloaded 03 May 2010 to 171.66.16.245. Redistribution subject to ASME license or copyright; see http://www.asme.org/terms/Terms_Use.cfm

Dynamic Holographic-Electronic Speckle-Pattern Interferometry

M. A. Ahmadshahi[1]

Sridhar Krishnaswamy[2]
Assoc. Mem. ASME.

S. Nemat-Nasser
Fellow ASME.

Center of Excellence for Advanced Materials,
Department of Applied Mechanics
and Engineering Sciences,
University of California, San Diego,
La Jolla, CA 92093-0411

The development of a nondestructive, full-field, quantitative optical technique, and its feasibility to study dynamic deformations of opaque and diffusively reflecting solids under transient loads, are discussed. The technique involves recording a sequence of dynamically changing two-beam speckle interference patterns (also called holographic speckle patterns) of a rapidly deforming body which is doubly illuminated by a laser light source. The time sequence of speckle patterns is recorded by means of a high-speed camera on an ultra-sensitive 35-mm film. The developed negatives are then digitized by a CCD camera into an image processing system. An initial speckle pattern corresponding to the undeformed state of the object is taken as the reference, and subsequent speckle patterns are digitally subtracted (reconstructed) from it to produce time-varying fringe patterns corresponding to the relative deformation of the test object. In order to gain confidence that the technique can be used to record truly transient deformation, it is tested here on a vibrating plate at resonance, thereby obtaining the evolution of the fringe pattern during 1/2 cycle of deformation corresponding to 160 μs.

1 Introduction

Optical techniques such as holographic and speckle interferometry provide means by which one can obtain full-field, quantitative measurements of deformations of objects under different loading conditions. The nondestructive nature of such techniques makes them suitable for use in hostile environments where other types of probes may be damaged, or may interfere with the implementation of the experiment, rendering them ineffective.

Speckle patterns are random intensity distributions, produced by a coherent light source, such as a laser, as it illuminates a diffusely reflecting body (Dainty, 1975). There are two types of fundamentally different speckle patterns; holographic speckle patterns which contain both phase and amplitude information simultaneously; and photographic speckle patterns which contain information pertaining only to the amplitude of the lightwave. In the latter case, the speckle patterns are obtained when a diffuse surface of an object is illuminated by a single coherent beam and the resulting scattered wavefront is recorded on a photographic emulsion medium. A double exposure of such speckle photographs, one exposure taken before and another taken after deformation of the object, is then illuminated by laser beams at discrete points to generate the corresponding Young's fringes, used to quantify the displacement components. Considerable effort has been devoted to this type of speckle-pattern photography, and detailed studies can be found in Francon (1979). Holographic speckle patterns, on the other hand, are obtained when the scattered wavefront emanating from the diffuse surface of the object is recorded simultaneously with a reference wavefront on the photographic emulsion medium. The speckle pattern recorded in the original experiment of Gabor's in-line holography (Gabor, 1948), leading to the hologram of the object, is an example of a holographic speckle pattern. Holographic interferometry is, in essence, the interference of two recorded holographic speckle patterns. Two such speckle patterns, corresponding to the undeformed and deformed state of the object, are recorded on the same photographic emulsion medium, hence involving double-exposure holography. The addition of these intensity variations produces fringe patterns that are directly related to the displacement of the object (Solid, 1969). Cartesian components of the displacement vector can be separated and individually recorded by holographic interferometric techniques (Sciammarella and Gilbert, 1976). These methods have been complemented by powerful image processing techniques and, during the past decade, considerable research has been devoted toward facilitating computer-based holographic interferometric techniques for quantitative measurements of displacement and strain fields of deforming bodies, making them an effective tool for experimental stress analysis (Sciammarella and Ahmadshahi, 1984, 1986, 1988). Further advances in this field have led to what is known as electronic speckle-pattern interferometry, sometimes referred to as electronic holography (Stetson and Brohinsky, 1985).

Speckle-pattern interferometry, be it holographic or pho-

[1]Presently, Senior Engineer, C. E. Niehoff & Co., 2021 Lee Street, Evanston, IL 60202.

[2]Presently, Assistant Professor, Department of Mechanical Engineering, Northwestern University, Evanston, IL 60208-3020.

Contributed by the Applied Mechanics Division of THE AMERICAN SOCIETY OF MECHANICAL ENGINEERS for presentation at the ASME Winter Annual Meeting, New Orleans, LA, Nov. 28–Dec. 3, 1993.

Discussion on this paper should be addressed to the Technical Editor, Professor Lewis T. Wheeler, Department of Mechanical Engineering, University of Houston, Houston, TX 77204-4792, and will be accepted until four months after final publication of the paper itself in the ASME JOURNAL OF APPLIED MECHANICS.

Manuscript received by the ASME Applied Mechanics Division, June 26, 1991; final revision, Oct. 7, 1992. Associate Technical Editor: M. E. Fourney. Paper No. 93-WA/APM-17.

Copyright © 1993 by ASME
Downloaded 03 May 2010 to 171.66.16.245. Redistribution subject to ASME license or copyright; see http://www.asme.org/terms/Terms_Use.cfm

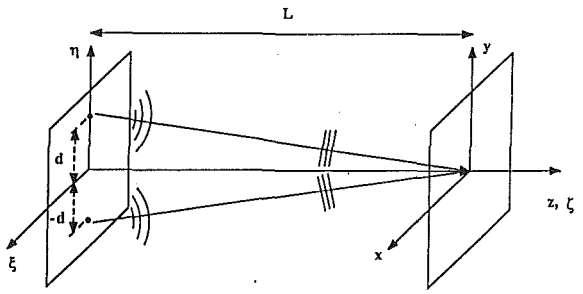


Fig. 1 Two point sources located on the ξ, η-plane; the x, y-plane lies on the photographic emulsion plate

tographic, has until now been limited to the study of static deformations, or at most, periodic deformations which occur when an object is under steady-state vibration. In the latter case, temporal modulation of the amplitude and/or phase of the illuminating lightwave (Aleksoff, 1971; and Ahmadshahi, 1988) has made full-field quantitative measurements of displacement and strain of vibrating bodies possible. However, in view of many technical problems, it has been stated as recently as 1989 that "dynamic speckle-pattern interferometry is not possible" (see Jones and Wykes, 1989). Although there are in principle no inherent limitations preventing the use of such techniques to record transient deformation, a number of technical difficulties must be overcome before dynamic speckle interferometry becomes a viable technique. Among these, intensity, resolution, and perhaps most importantly, image registration, have accounted for the preclusion of speckle techniques in the study of transient deformations until now.

In this paper, we discuss the development of dynamic holographic-electronic speckle-pattern interferometry and its application to analyze the deformations of diffusely reflecting bodies under transient loads. The objective of this research is to show that holographic speckle interferometry is applicable to dynamic problems, and more importantly, to demonstrate how this technique can be realized. Other optical methods, such as photoelasticity (Dally, Riley, and Durelli, 1959; Dally, Durelli and Riley, 1960; Durelli and Riley, 1961) and moiré (Riley and Durelli, 1962; Huntley and Field, 1989), have been employed with considerable success for dynamic stress and displacement analysis. However, they have many limitations. Michelson interferometry and some shearing interferometers (Krishnaswamy, Tippur, and Rosakis, 1992) require that the material be either transparent or, when it is opaque, be highly polishable. Photoelastic studies can only be performed on transparent, birefringent materials. It is further limited because auxiliary information is needed for the separation of the principal stresses. Moiré methods utilize gratings that need to be ruled, etched, or embedded onto the specimen and thus do not qualify as nondestructive testing techniques. Even in those circumstances where gratings with minimal surface intrusion are used, elevated temperature may compromise the integrity of the grating.

The technique described in this paper is complementary to the existing optical techniques in that it makes possible full-field, nondestructive, time-sequence measurements of components of the surface displacements of deforming bodies which are opaque and whose surfaces may not be polishable or which may degrade with temperature. The proposed method of dynamic holographic-electronic speckle-pattern interferometry can therefore be a valuable tool in the analysis of structural and/or material behavior over a relatively wide range of deformation rates and temperatures.

In the following sections, the principles of holographic speckle interferometry and the requirements of speckle correlation are first briefly outlined to lay the basis for the subsequent description of the proposed technique.

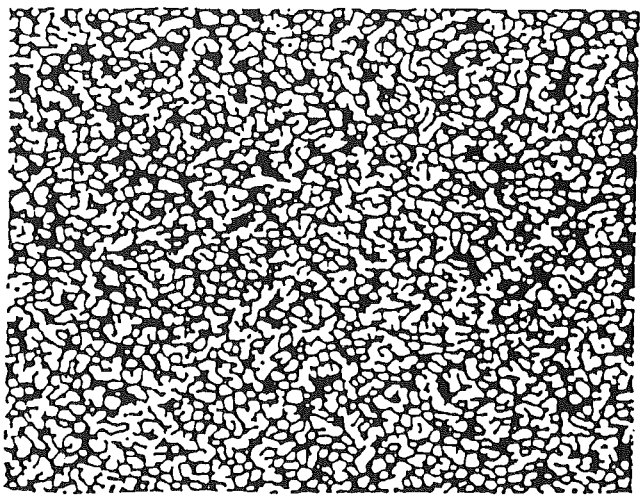


Fig. 2 Photograph of a typical speckle pattern

2 Holographic Speckle-Pattern Interferometry

Consider two point sources located on the ξ, η-plane which are mutually coherent, linearly polarized, and are emitting light waves of wavelength λ; (Fig. 1). If the x, y-plane (photographic emulsion plane) is relatively far from the ξ, η-plane, the optical field on this plane is the sum of two plane waves, and the intensity recorded by the photographic emulsion is in the form of sinusoidal fringes, the orientation and spatial frequency of which depend on the location of the points on the ξ, η-plane, the distance L, and the wavelength λ (Smith, 1969). The presence of a third point will result in recording the sum of three different sinusoidal fringes with different orientations and spatial frequencies. This is due to interference between point 1 and point 2, point 1 and point 3, and point 2 and point 3. Introducing a fourth point source on the ξ, η-plane will lead to an intensity distribution which is the sum of the intensities of six different sinusoidal fringe patterns with distinct spatial frequencies and orientations. If, now, the ξ, η-plane is taken as a rough (diffuse) surface which is being illuminated by a coherent light source, according to Huygen's principle, each point on the surface acts as a point source similar to those shown in Fig. 1. The collection of the optical field of all such points on the photographic emulsion medium gives rise to a random intensity distribution known as the speckle pattern; (see Fig. 2 and Dainty (1975)). For those who are involved with the study of deformations of solids, a speckle pattern can be thought of as a collection of fictitious marks on the surface of the specimen, and holographic interferometry is a process of monitoring their displacements.

In typical off-axis holographic interferometry (Leith and Upatnieks, 1962; and Sciammarella, 1982) two speckle patterns are recorded on the same photographic emulsion medium. Furthermore, these speckle patterns are holographic; that is, the optical setup includes a reference beam and/or a double illumination of the surface of the object. We will consider the latter case in which two mutually coherent collimated beams illuminate the surface of the object. The corresponding scattered wavefronts, W_1 and W_2, are simultaneously recorded on the film (Fig. 3). The electric fields of W_1 and W_2 at the film plane can be expressed as

$$E_1(x,y) = A(x,y)\exp[i\psi_1(x,y)], \tag{1}$$

$$E_2(x,y) = B(x,y)\exp[i\psi_2(x,y)]. \tag{2}$$

The recorded intensity then becomes

Downloaded 03 May 2010 to 171.66.16.245. Redistribution subject to ASME license or copyright; see http://www.asme.org/terms/Terms_Use.cfm

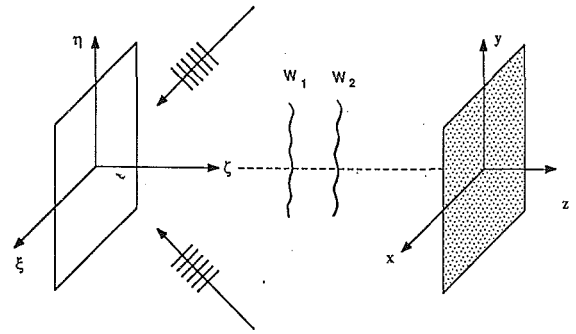


Fig. 3 Double illumination of a diffused surface

$$I_1(x,y)=\int_{-T/2}^{T/2}[E_1(x,y)+E_2(x,y)][\overline{E}_1(x,y)+\overline{E}_2(x,y)]dt,$$

$$=T\{A^2(x,y)+B^2(x,y)+2A(x,y)B(x,y)\cos[\psi(x,y)]\}, \quad (3)$$

where

$$\psi(x,y)=\psi_1(x,y)-\psi_2(x,y), \quad (4)$$

an overbar indicates the complex conjugate; T is the time interval during which the film is exposed; $A(x, y)$ and $B(x, y)$ are amplitudes, and $\psi_1(x, y)$ and $\psi_2(x, y)$ are the phases (related to the random height variations of the points on the surface) of the two scattered wavefronts; and $i=\sqrt{-1}$. A second speckle pattern is recorded after the body has been deformed, and its intensity distribution is recorded as

$$I_2(x,y)=T\{A^2(x,y)+B^2(x,y)+2A(x,y)B(x,y)\times\cos[\psi(x,y)+(\mathbf{K}_1-\mathbf{K}_2)\cdot\mathbf{d}(\mathbf{x},\mathbf{y})]\}. \quad (5)$$

The sum of the two speckle patterns produces holographic interferometric fringes,

$$I(x,y)=I_1(x,y)+I_2(x,y),$$

or

$$I(x,y)=T\{2[A^2(x,y)+B^2(x,y)]+4A(x,y)B(x,y)\times\cos[\psi(x,y)+(1/2)(\mathbf{K}_1-\mathbf{K}_2)\cdot\mathbf{d}(\mathbf{x},\mathbf{y})]\times\cos[(1/2)(\mathbf{K}_1-\mathbf{K}_2)\cdot\mathbf{d}(\mathbf{x},\mathbf{y})]\}, \quad (6)$$

with $\mathbf{K}_1$ and $\mathbf{K}_2$ representing the two illumination vectors (Solid, 1969) and $\mathbf{d}(\mathbf{x}, \mathbf{y})$ is the displacement vector. The corresponding scalar quantities K and $d(x, y)$ represent the magnitude of the difference between the illumination vectors, and the projection of the displacement vector in the corresponding direction, respectively. In Eq. (6), the first term in the right-hand side is the background intensity and the second term is composed of two sinusoidal parts: one part contains information regarding both surface roughness and deformation while the other part is related only to deformation of the object. It is this term that dramatically displays the fringe pattern seen in double exposure holography. Separate in-plane components of the displacement vector can be obtained by symmetric illumination of the object (Sciammarella and Gilbert, 1976), if the sensitivity vectors lie on the x, z and y, z-planes (Fig. 3); and the corresponding fringe patterns are then proportional to the x and y-components of the displacement vector, respectively.

3 Speckle Correlation

Experimentalists who employ the holographic interferometry technique to study object deformations are well aware of the stability requirements of the optical setup, and the recording medium in particular. Any small disturbance to the photographic emulsion medium will result in degradation of the contrast of the fringe pattern, to the extent that rigid-body motions of the hologram plane of the order of microns, could diminish them altogether. This behavior can be explained if we consider Eqs. (3) and (6), which are the speckle patterns before and after deformation. Suppose that before recording the second exposure, there is a rigid-body translation of the photographic recording medium by an amount x_0 and y_0, in the x and y-directions, respectively. Then Eq. (5) would take on the following form:

$$I_2(x,y)=T\{A^2(x,y)+B^2(x,y)+2A(x,y)B(x,y)\times\cos[\psi(x-x_0,y-y_0)+Kd(x,y)]\}. \quad (7)$$

In Eq. (7), we have assumed that $A(x, y)$, $B(x, y)$, and $d(x, y)$ are all relatively slowly varying functions. Consequently, small shifts of the amount x_0 or y_0 will not change their form. The only term, however, that should be considered is the function $\psi(x, y)$, which is randomly varying and proportional to the roughness. Thus it changes completely, if small shifts are introduced. Finally, if the two speckle patterns of Eqs. (3) and (7) are added, the resulting intensity distribution will be

$$I(x,y)=T\{2[A^2(x,y)+B^2(x,y)]+4A(x,y)B(x,y)\times\cos[(1/2)[\psi(x,y)+\psi(x-x_0,y-y_0)+Kd(x,y)]\times\cos[(1/2)[\psi(x,y)-\psi(x-x_0,y-y_0)+Kd(x,y)]\}. \quad (8)$$

In Eq. (8), the difference between $\psi(x, y)$ and its shifted version (the last line of the equation) is another random function which will overwhelm the term $Kd(x, y)$, and thus no discernible fringes can be seen if such rigid-body translations occur. One can see, therefore, that holographic interferometric fringes are formed only when the speckle patterns corresponding to the undeformed and deformed states of the object are well aligned, and fringe contrast strongly depends on how precisely the two speckle patterns are correlated.

4 Recording Dynamic Speckle Patterns

The principle of the DHESPI (Dynamic Holographic-Electronic Speckle-Pattern Interferometry) technique is based on recording a sequence of holographic speckle patterns on a photographic emulsion medium using a high-speed camera, and subsequently digitizing the negatives by means of a CCD camera and an image processing system. The digitized speckle patterns are then registered utilizing image correlation techniques. A reference speckle pattern corresponding to the undeformed (or a suitable preceding deformed) state of the object is subtracted from the remaining speckle patterns which are obtained during subsequent deformation.

Figure 4 illustrates the dynamic recording of time-varying speckle patterns using a high-speed camera (Cordin model 330A) and an image processing system. The scattered waves due to double illumination of the object are recorded by the high-speed camera as a sequence of snapshots on T-Max P3200 Kodak film. The electric field due to the scattered waves at the film plane is

$$E(x,y,t)=E_1(x,y,t)+E_2(x,y,t)=A(x,y,t)\exp[i\psi_{T1}(x,y,t)]+B(x,y,t)\exp[i\psi_{T2}(x,y,t)], \quad (9)$$

$$\psi_{T1}(x,y,t)=\psi_1(x,y)+(K_1-K_0)d(x,y,t), \quad (10)$$

$$\psi_{T2}(x,y,t)=\psi_2(x,y)+(K_2-K_0)d(x,y,t), \quad (11)$$

where $(K_1 - K_0)$ and $(K_2 - K_0)$ are sensitivity constants and $d(x, y)$ is a component of the displacement vector in the direction of the sensitivity vectors. We will postpone to the next section the description of the procedure to separate and individually obtain the three components of the displacement vector.

The sequence of exposures obtained by the high-speed camera can be analyzed best through the use of a shuttering se-

Downloaded 03 May 2010 to 171.66.16.245. Redistribution subject to ASME license or copyright; see http://www.asme.org/terms/Terms_Use.cfm

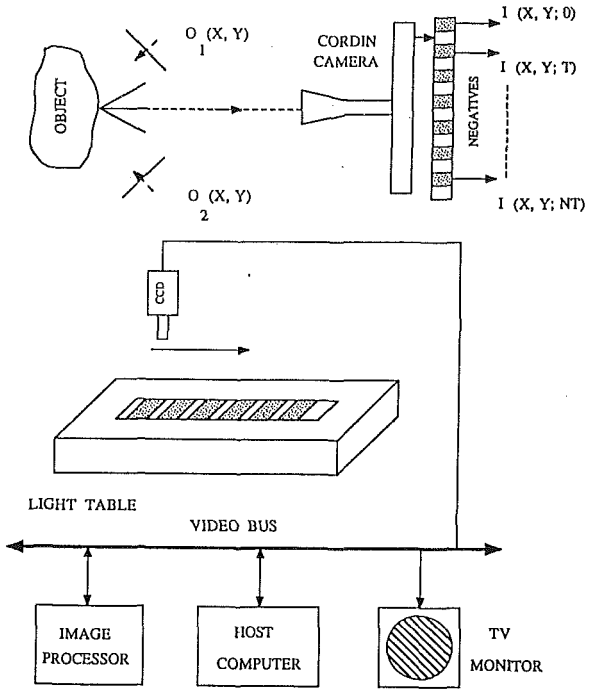


Fig. 4 Schematic representation of dynamic recording of time-varying speckle patterns, and the image processing system

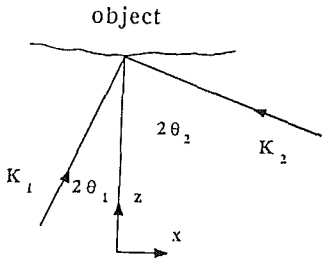


Fig. 5 Schematic representation of double illumination beams and the corresponding illumination vectors

quence $S_n(t; T)$, where T is the period of the shutter sequence and the index n signifies the elements of the sequence. The intensity distribution of each negative is then

$$I_1(x,y;nT) = \int_{-\infty}^{\infty} E(x,y,t) \times \bar{E}(x,y,t) \times S_n(t;T)dt, \quad n=0, 1, 2, 3, \ldots, N, \quad (12)$$

where the elements of the sequence $\{S_n\}$ are functions such that

$$S_n(t;T) = \begin{cases} n\text{th arbitrary function} & 0 \le t \le T \\ 0 & \text{otherwise.} \end{cases} \quad (13)$$

The most useful function, achieved through the on-off switching of the light source, is the Dirac-Delta distribution, i.e.,

$$S_n(t;T) = \delta(t-nT) \quad n=0, 1, 2, 3, \ldots, N, \quad (14)$$

so that each of the $N + 1$ arbitrary functions is an impulse and that they differ only by a shift in time. Therefore, the sequence of intensity distributions is

$$I(x,y;nT) = E(x,y,nT) \times \bar{E}(x,y,nT) = [A^2(x,y,nT) + B^2(x,y,nT) + 2A(x,y,nT) \times B(x,y,nT)\cos[\psi(x,y) + (K_1 - K_2)d(x,y,nT)] \quad n=0, 1, 2, 3, \ldots, N \quad (15)$$

with $\psi(x, y)$ defined by Eq. (4). These intensity distributions are digitized and stored by the image processing system to be correlated and reconstructed to produce time-varying fringe patterns.

5 Quantitative Measurement

The information carried by the speckle pattern of Eq. (15) relates to the surface roughness and a component of the displacement vector. The corresponding in-plane components can be obtained in the following manner. Consider the case where the propagation vectors of the two collimated illumination beams lie on the x, z-plane (Fig. 5) and are written as

$$\mathbf{K}_1 = \frac{2\pi}{\lambda}(\sin 2\theta_1 \mathbf{e}_x + \cos 2\theta_1 \mathbf{e}_z), \quad (16)$$

$$\mathbf{K}_2 = \frac{2\pi}{\lambda}(-\sin 2\theta_2 \mathbf{e}_x + \cos 2\theta_2 \mathbf{e}_z), \quad (17)$$

where $2\theta_1$ and $2\theta_2$ are the angles between the illumination vectors and the z-axis, taking on only positive values. The object displacement vector at any point in space and time is written as

$$\mathbf{d}(x,y,t) = u(x,y,t)\mathbf{e}_x + v(x,y,t)\mathbf{e}_y + w(x,y,t)\mathbf{e}_z, \quad (18)$$

where $u(x, y, t)$ and $v(x, y, t)$ are the in-plane and $w(x, y, t)$ the out-of-plane displacement components. Furthermore, the displacement vector at $t = 0$, corresponding to the undeformed state of the object, is taken as zero,

$$\mathbf{d}(x,y,0) = \mathbf{0}. \quad (19)$$

The digitized speckle patterns obtained from the intensity distributions recorded on the film are then correlated and, as in the case of ESPI (Electronic Speckle-Pattern Interferometry), subtracted in order to generate holographic interferometric fringes. The recorded speckle pattern corresponding to time $t = 0$ is selected as the reference image and subsequent images are subtracted from it, which results in a sequence of intensity distributions as

$$q(x,y;nT) = I(x,y;nT) - I(x,y;0), \quad n=1, 2, 3, \ldots, N. \quad (20)$$

For example, if we consider the case where the illumination vectors lie on the x, z-plane, the speckle-pattern intensity distribution can be represented as

$$I(x,y;nT) = [A^2(x,y) + B^2(x,y)] + 2A(x,y) \times B(x,y)\{\cos[\psi(x,y) + k_x u(x,y,nT) + k_z w(x,y,nT)]\}, \quad n=0, 1, 2, 3, \ldots, N, \quad (21)$$

where

$$k_x = \frac{\pi}{\lambda}(\sin 2\theta_1 + \sin 2\theta_2), \quad (22)$$

$$k_z = \frac{\pi}{\lambda}(\cos 2\theta_1 - \cos 2\theta_2). \quad (23)$$

In this way Eq. (20) can be expanded to give

$$q(x,y;nT) = 4A(x,y)B(x,y) \times \sin[\psi(x,y) + k_x u(x,y,nT) + k_z w(x,y,nT)] \times \sin[k_x u(x,y,nT) + k_z w(x,y,nT)], \quad n=1, 2, 3, \ldots, N. \quad (24)$$

Symmetric illumination of the specimen ($2\theta_1 = 2\theta_2$) results in

$$q(x,y;nT) = 4A(x,y)B(x,y) \times \sin[k_x u(x,y,nT)] \times \sin[\psi(x,y) + k_x u(x,y,nT)], \quad n=1, 2, 3, \ldots, N. \quad (25)$$

Similar results can be obtained for the other in-plane component of the displacement vector, if we symmetrically illuminate the specimen such that the propagation vectors lie on the y, z-plane,

Downloaded 03 May 2010 to 171.66.16.245. Redistribution subject to ASME license or copyright; see http://www.asme.org/terms/Terms_Use.cfm

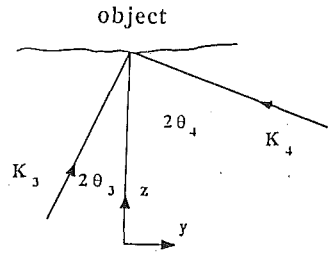


Fig. 6 Schematic representation of double illumination beams and the corresponding illumination vectors

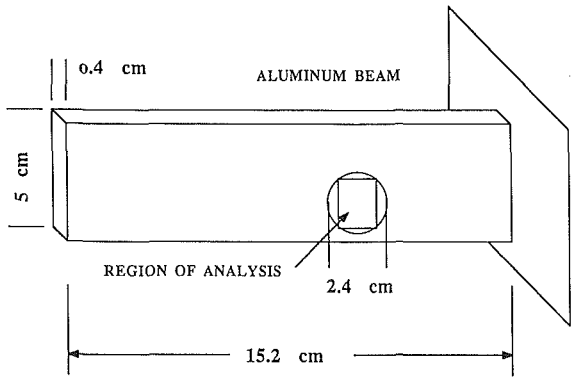


Fig. 7 Cantilever beam and the region of analysis

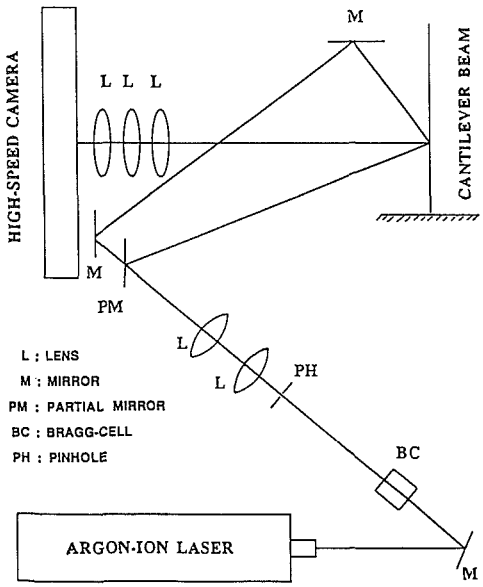


Fig. 8 Optical setup

$$q(x,y;nT) = 4A(x,y)B(x,y) \times \sin[k_y v(x,y,nT)] \times \sin[\psi(x,y) + k_y v(x,y,nT)], \quad n = 1, 2, 3, \ldots, N, \quad (26)$$

with

$$k_y = \frac{\pi}{\lambda}(\sin 2\theta_3 + \sin 2\theta_3) = \frac{2\pi}{\lambda} \sin 2\theta_3. \quad (27)$$

It should be mentioned that, although some of the above equations are limited to small deformations, large deformations can also be accommodated by an incremental method. That is, consecutive pairs of speckle patterns may be subtracted, instead of using the initial speckle pattern as the reference, to generate the interferometric fringes, and the total displacement would be obtained by the addition of all the corresponding increments.

6 Experiment

To demonstrate the feasibility of the technique, the proposed method was used to get a time sequence of a periodically deforming object in order to enable direct comparison with conventional stroboscopic speckle methods. This is essential to gain confidence in the technique prior to using it to recover truly transient deformation. Thus the time evolution of the displacement of a vibrating cantilever beam at resonance is studied. The aluminum cantilever beam is 15.2 cm long, 5 cm wide, and 0.4 cm thick (Fig. 7). An argon-ion cw laser is used as the light source which delivers 1.2 w/cm^2 power. Laser intensity limitations restrict the field of analysis to a rectangular region inscribed in a circular region 2.4 cm in diameter, as shown in Fig. 7. The cantilever beam is excited by an electromagnetic shaker. At a frequency of 3125 Hz, a plate-mode resonance is detected. The optical setup is shown in Fig. 8. The laser beam is passed through a Bragg-Cell, which provides a flash of light equal to 3.2 ms. This period is long enough to expose 80 frames of the high-speed camera which was set to operate at 25,000 frames per second. This corresponds to exposure and interframe times of 20 μs each. The beam is then passed through a pinhole and two well-corrected lenses of 175 mm focal length, to produce a collimated beam 2.4 cm in diameter. This beam is passed through a 50/50 partial mirror, providing two equal intensity collimated beams, one of which illuminates the cantilever beam at an angle of 20 deg with the normal, and the other at an angle of 55 deg with the normal; Fig. 8. The region is imaged onto the film track of the high-speed camera by its internal lens system and three well-corrected lenses of 381 mm, 381 mm, and 175 mm focal lengths, as shown in Fig. 8. The recording medium, T-MAX P3200 Kodak film, is reported by the manufacturer to have a resolution of approximately 40 l/mm. The high-speed Cordin camera used in this experiment is capable of at least the same resolving power since its resolution is reported to be 40 l/mm at a speed of 2,000,000 frame per second. Therefore, it is expected that at lower speeds, specifically 25,000 frames per second used in this experiment, the resolution of the camera is considerably higher than the film, and consequently, it is the film that determines the spatial resolution of the system. One of the internal relay lenses of the camera has a focal distance of approximately 300 mm, and an effective aperture was taken to be the width of the beam-splitting cube of the camera which was 8.5 mm. This gives a speckle size of roughly 20 μ. As mentioned previously, the illuminations were not symmetric, so that the fringe patterns are due to a combination of in-plane and out-of-plane displacement components. Utilizing Eqs. (22) and (23) we get for the sensitivity constants K_x and K_z the values of 9.67 rad/μ and 6.77 rad/μ, respectively. The modulus of the resulting sensitivity vector is then, K = 11.8 rad/μ and the corresponding direction of approximately Θ_k = 35 deg. Therefore, the fringes can be thought of as representing the component of the displacement vector, making an angle of 35 deg to the normal of the cantilever beam, and each fringe corresponds to 0.53 μ of this displacement.

7 Results

Figure 9 shows the time-frozen fringes of the vibrating beam corresponding to the maximum displacement, using ESPI and strobing technique. This was intended to verify the dynamic analysis of the subregion shown in the same figure. Figure 10 shows the sinusoidal amplitude of the time-varying displacement which can be written as

$$w(x,y,t) = \cos(2\pi\Omega t) f(x,y), \quad (28)$$

where Ω = 3215 Hz, and $f(x, y)$ is the mode shape whose interferometric fringe pattern is shown in Fig. 9.

The experiment is conducted in such a way that while the

Downloaded 03 May 2010 to 171.66.16.245. Redistribution subject to ASME license or copyright; see http://www.asme.org/terms/Terms_Use.cfm

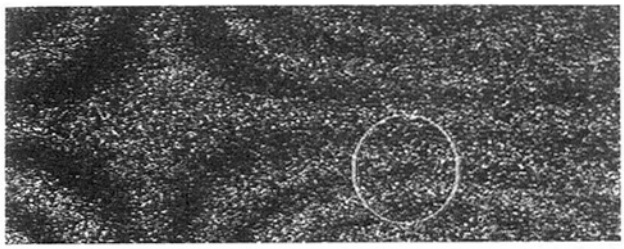


Fig. 9 Time-frozen fringes corresponding to the maximum displacement using electronic speckle-pattern interferometry and strobing technique; the evolution of fringe pattern in the rectangular subregion is studied by dynamic holographic-electronic speckle-pattern interferometry

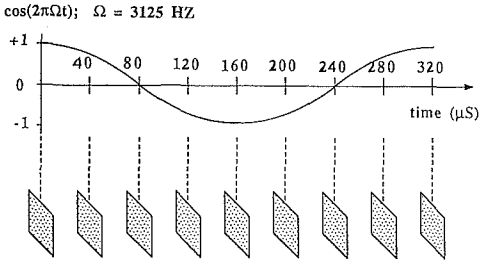


Fig. 10 Time-varying amplitude of the mode function; dotted parallelograms are schematic representations of the holographic speckle patterns obtained at discrete times using a high-speed camera

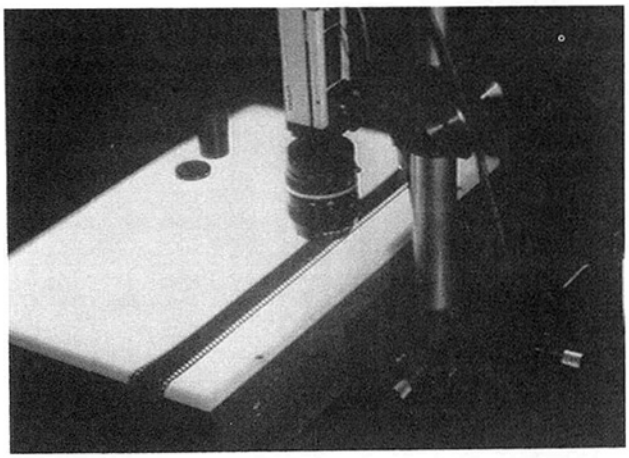


Fig. 11 Image digitization system

cantilever beam is vibrating and the rotating mirror of the high-speed camera is rotating, a pulse of light of period 3.2 μs is applied by the Bragg-Cell, corresponding to 80 frames, eight of which are sufficient to complete one cycle of vibration. Taking the first exposure frame at the maximum or the minimum of the amplitude of vibration (of which we have chosen the former), the deformation during the subsequent one-half cycle of vibration is analyzed. It should be noted that the two illumination beams, as described in Section 6, are not symmetric, and thus, both components $u(x, y, t)$ and $w(x, y, t)$ contribute to the total phase, Eq. (24). This is because symmetric illumination annihilates the term $w(x, y, t)$, and the displacement component $u(x, y, t)$ alone could not produce a sufficient number of fringes in the subregion shown in Fig. 9. This is expected since the thickness of the cantilever beam is small compared to its other dimensions, and, therefore, membrane deflections are much higher in magnitude than in-plane stretches. Hence the fringes obtained and shown in what follows are predominantly due to the out-of-plane displacement component.

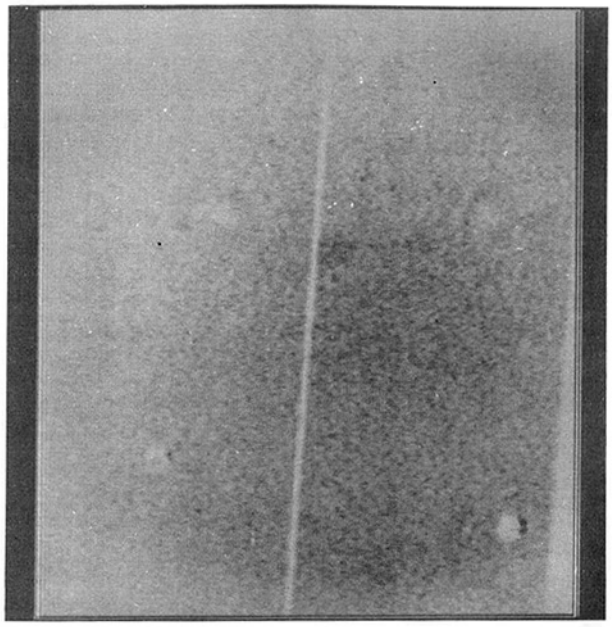


Fig. 12 Holographic speckle pattern obtained at $t = 0$ μs

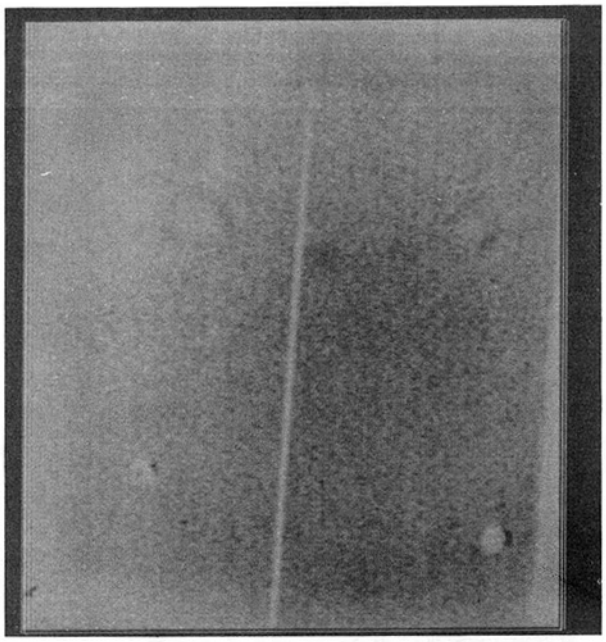


Fig. 13 Holographic speckle pattern obtained at $t = 40$ μs

Figure 11 shows the setup used to digitize the negatives. A CCD camera and an image processing system are used to digitize the developed negatives, mounted on a light table. Careful registration of the negatives is accomplished by (1) marking the specimen with three noncollinear dots at arbitrary locations, for course alignment; (2) mounting the CCD camera on a translation stage (Newport model 400) for fine alignment; and, finally, (3) by cross-correlation of the digital images.

Figures 12 and 13 show two digitized speckle patterns corresponding to $t = 0$ μs and $t = 40$ μs, respectively. After registration, the two images are subtracted and the results, obtained through the use of image processing techniques, is shown in Fig. 14. The intermediate processing stages leading to the final result involve: a 2-D low-pass filter, a narrow-band band-pass filtering in the vertical direction, followed by a narrow-band band-pass Hilbert transform combination filtering in the vertical direction to normalize the amplitude variation of the fringe pattern (Ahmadshahi, 1998). Figure 15 shows the

Downloaded 03 May 2010 to 171.66.16.245. Redistribution subject to ASME license or copyright; see http://www.asme.org/terms/Terms_Use.cfm

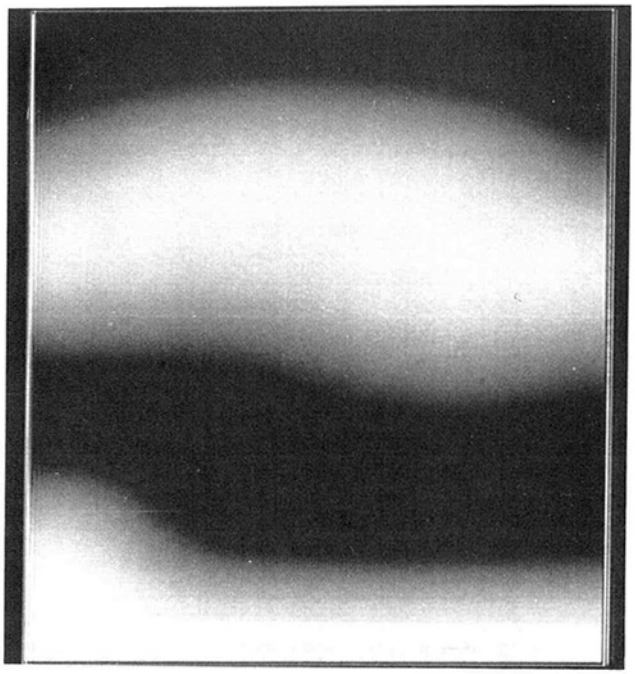


Fig. 14 Enhanced fringe pattern obtained by subtracting the image shown in Fig. 13 from that shown in Fig. 12; the fringe pattern corresponds to the difference between the maximum displacement and the displacement 40 μs later in time

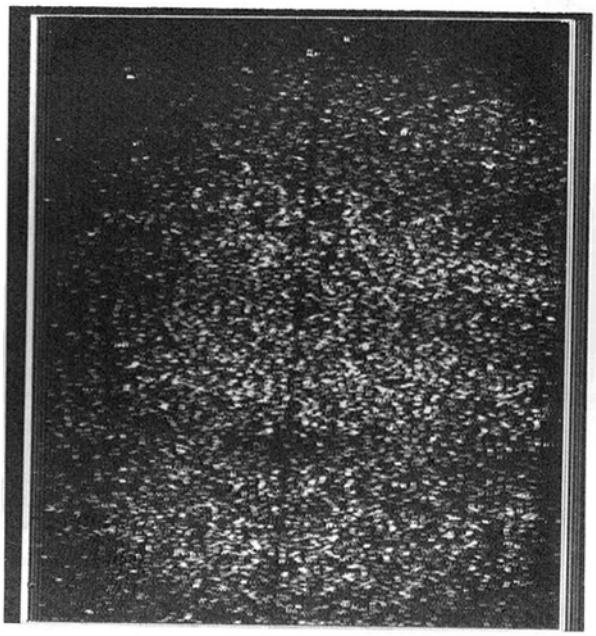


Fig. 15 The result of subtraction of two holographic speckle patterns obtained at $t = 0$ μs and $t = 120$ μs

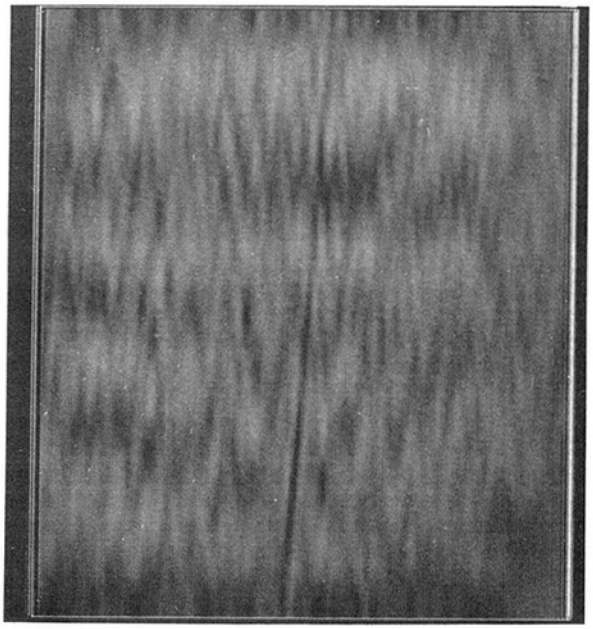


Fig. 16 The result of 2-D band-pass filter applied to Fig. 15

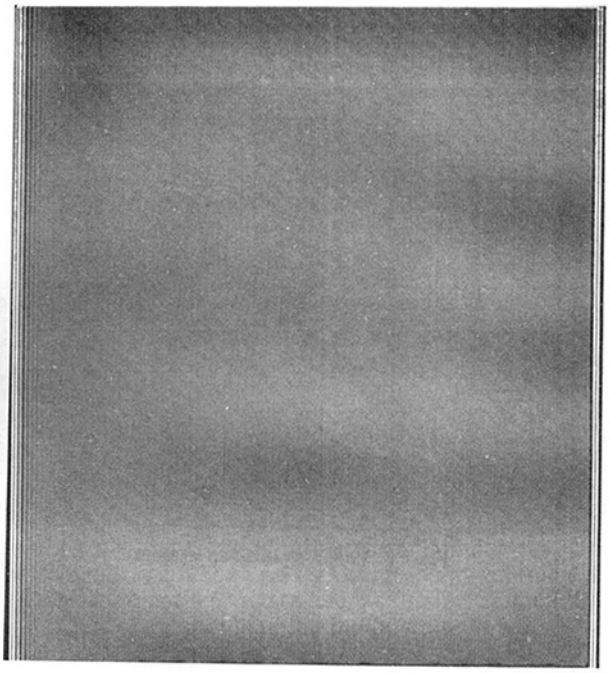


Fig. 17 The result of 1-D low-pass filter applied in the horizontal direction to Fig. 16

result of subtraction of the digitized speckle pattern corresponding to $t = 120$ μs from that obtained at $t = 0$ μs. Figure 16 shows the result of 2-D low-pass and a 1-D narrow-band band-pass filtering of the image shown in Fig. 15. Figure 17 shows the result of 1-D narrow-band low-pass filtering applied in the horizontal direction to Fig. 16. Finally, this image is normalized by generating an in-quadrature image using a combination of a narrow-band band-pass filter and a narrow-band band-pass Hilbert transform; Fig. 18. All 1-D filters are of finite-impulse-response linear-phase type, and their band-pass widths are ± 1 harmonic around the central frequency based on a 512 pixel resolution. Typical filter length is 101 samples. Figure 19 is the composite image of the evolution of the fringe pattern during 160 μs. The figure represents the subtracted speckle patterns obtained at $t = 40$ μs, $t = 80$ μs, $t = 120$ μs and $t = 160$ μs, from the reference speckle pattern obtained at $t = 0$ μs.

It is not possible to directly ascertain the accuracy of our results, since we have no theoretical solution to this particular problem. Furthermore, because of the asymmetric illumination of the specimen, the obtained fringe patterns are a combination of the in-plane and the out-of-plane components of the displacement vector. Consequently, we have adopted a consistency test and the accuracy of the results will be based upon how consistent the fringe patterns are with respect to each other. Specifically, we have chosen the fringe pattern corresponding to deformation at $t = 120$ μs as the base image to obtain the mode shape as given in Eq. (28). This is because

Downloaded 03 May 2010 to 171.66.16.245. Redistribution subject to ASME license or copyright; see http://www.asme.org/terms/Terms_Use.cfm

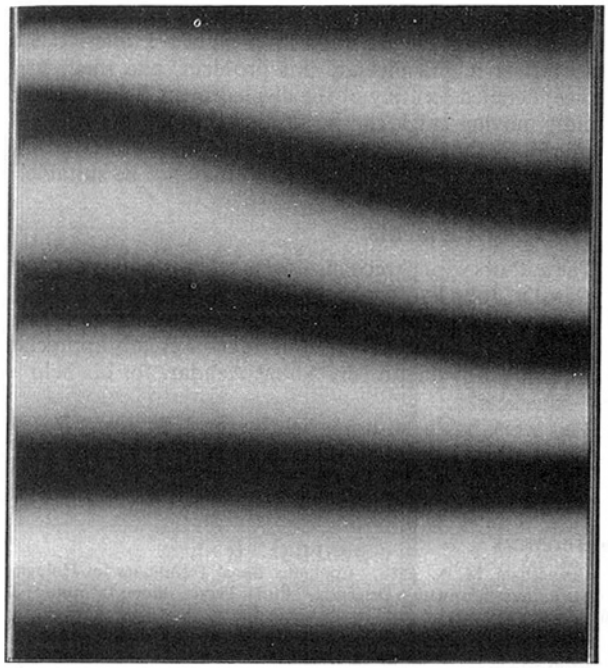


Fig. 18 Normalized fringes

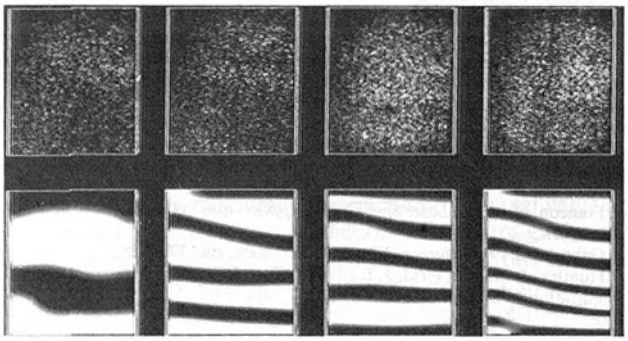


Fig. 19 Evolution of displacement in a rectangular subregion of a cantilever beam during 1/2 cycle of vibration obtained at $t = 40\ \mu s$, $t = 80\ \mu s$, $t = 120\ \mu s$, and $t = 160\ \mu s$, from the reference obtained at $t = 0\ \mu s$

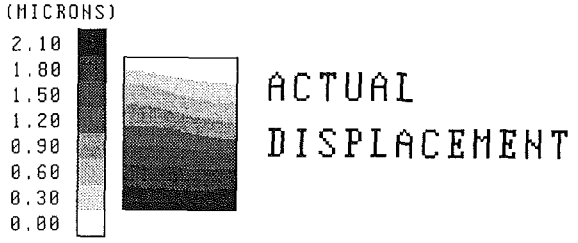


Fig. 20 Actual displacement levels obtained from the fringe patterns at $t = 120\ \mu s$

the signal-to-noise ratio of this image was found to be the highest compared to the other three fringe patterns. Figure 20 shows the levels of displacements obtained from the fringe patterns shown in Fig. 18. Figures 21–23 show the comparison between the "actual" displacements and the "compared" displacements occurring at $t = 40\ \mu s$, $t = 80\ \mu s$, $t = 160\ \mu s$, and the corresponding absolute errors. By "actual" displacement we mean those calculated from the fringe patterns corresponding to $t = 40\ \mu s$, $t = 80\ \mu s$, $t = 160\ \mu s$. The "compared" displacements are simply those obtained by multiplying the displacement levels of the base image at $t = 120\ \mu s$, Fig. 20, by the appropriate time-dependent factors (obtained from Eq. (28)) which are 0.41, 0.59, and 1.18, respectively.

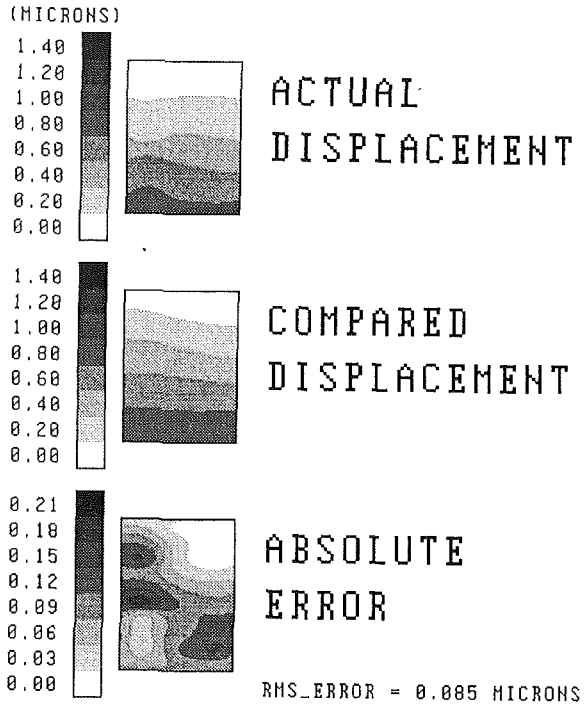


Fig. 21 Actual displacements obtained from the fringe pattern at $t = 40\ \mu s$ compared for consistency with the displacements expected from appropriate time-dependent scaling of the base image at $t = 120\ \mu s$

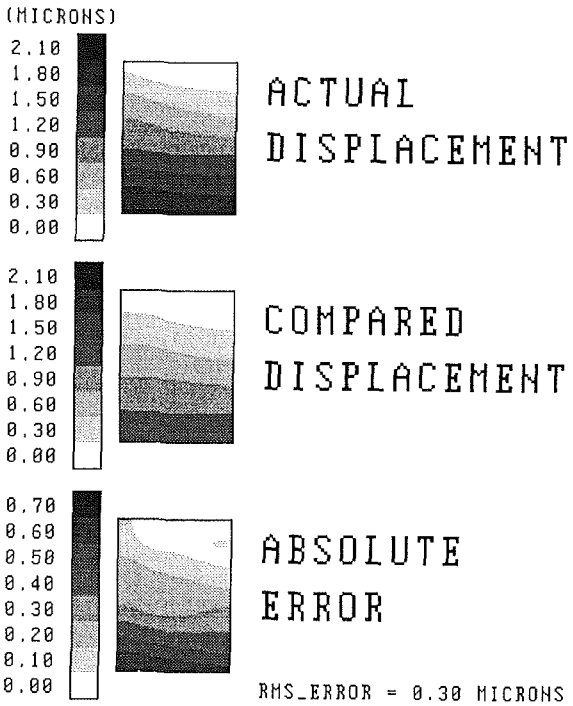


Fig. 22 Actual displacements obtained from the fringe pattern at $t = 80\ \mu s$ compared for consistency with the displacements expected from appropriate time-dependent scaling of the base image at $t = 120\ \mu s$

It is observed that the main contribution to the absolute error arises from the edges and the corners of the images. This is most likely due to the well-known edge distortions associated with discretized and finite length convolution operations used in the image processing. Furthermore, relatively long exposure times (20 μs for each frame) are likely to introduce additional errors, since the fringe patterns involve some time-averaging, and therefore are not the sinusoidal ones which govern the

Downloaded 03 May 2010 to 171.66.16.245. Redistribution subject to ASME license or copyright; see http://www.asme.org/terms/Terms_Use.cfm

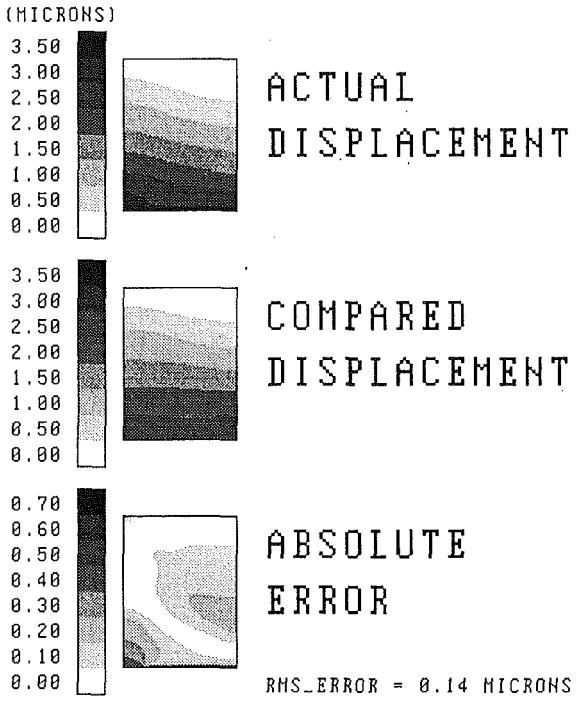


Fig. 23 Actual displacements obtained from the fringe pattern at t = 160 μs compared for consistency with the displacements expected from appropriate time-dependent scaling of the base image at t = 120 μs

static or stroboscopic interferometric fringes. This error can be minimized by reducing the exposure time of each frame via synchronized ultra-short-duration laser pulses of sufficiently high power.

8 Conclusions

A nondestructive optical technique to quantitatively study the full-field transient deformation of diffusely reflecting bodies is reported in this paper. The technique is a two-step process whereby a sequence of holographic speckle patterns generated by doubly illuminating the surface of the specimen is first recorded by means of a high-speed camera during deformation of the object, and the developed negatives containing the record of the dynamic speckle patterns are subsequently sequentially digitized by a CCD camera and an image processing system. A reference speckle pattern corresponding to the undeformed state of the object, is used to subtract the remaining speckle patterns from it, and the result has been shown to produce fringe patterns of the components of the time-varying displacement vector.

For illustration purposes, the technique is applied to the case of a vibrating cantilever beam, and the evolution, a combined in-plane and out-of-plane components of the displacement vector during one-half cycle of the vibration, is determined. It is shown, however, that due to nonperfect alignment of the digitized speckle patterns, the interferometric fringes produced by subtracting pairs of speckle patterns are of rather low contrast. Therefore, it is essential to employ image processing techniques to enhance the fringe contrast prior to making quantitative measurements.

The high-speed camera used in our experiment has the capability of operating at 2,000,000 frames per second. For 80 frames at this speed, the time resolution is 0.5 μs, and so events that last tens of microseconds can be analyzed using DHESPI. Lack of laser intensity, however, currently limits our analysis to relatively small regions and long exposure times. Use of a pulsed laser might alleviate this problem, and then, for instance, detailed scrutiny of the displacement fields ahead of a rapidly moving crack can be studied through the use of Dynamic Holographic-Electronic Speckle-Pattern Interferometry in situations where other techniques may not be suitable.

9 Acknowledgments

The authors wish to recognize their colleague and dear friend, the late Dr. John E. Starrett, for his contributions to theoretical and practical aspects of this research. The technical assistance of Mr. David Lischer and Mr. Jon Isaacs is greatly appreciated. Thanks are also due to Mr. Abbas Azhdari for his help with the experiments.

This work has been supported by the U.S. Army Research Office under Contract No. DAAL-03-86-K-0169 with the University of California, San Diego.

References

Ahmadshahi, M. A., 1988, "Computer Based Techniques for Holographic Fringe Pattern Information Detection," Ph.D. Thesis, Illinois Institute of Technology.

Aleksoff, C. C., 1971, "Temporally Modulated Holography," *Appl. Opt.*, Vol. 10, No. 6, pp. 1329–1341.

Dainty, J. C., ed., 1975, *Laser Speckle and Related Phenomena*, Springer-Verlag, Berlin.

Dally, J. W., Durelli, A. J., and Riley, W. F., 1960, "Photoelastic Study of Stress Wave Propagation in Large Plates," *Proc. of SESA*, Vol. 17, pp. 33–50.

Dally, J. W., Riley, W. F., and Durelli, A. J., 1959, "A Photoelastic Approach to Transient Stress Problems Employing Low-Modulus Materials," ASME JOURNAL OF APPLIED MECHANICS, Vol. 26, Vol. 81, pp. 613–620.

Durelli, A. J., and Riley, W. F., 1961, "Stress Distribution on the Boundary of a Circular Hole in a Large Plate During Passage of a Stress Pulse of Long Duration," ASME JOURNAL OF APPLIED MECHANICS, Vol. 28, Vol. 83, pp. 245–251.

Francon, M., 1975, *Laser Speckle and Applications in Optics*, Academic Press, New York.

Gabor, D., 1948, *Nature*, Vol. 161, No. 4098, pp. 777–778.

Huntley, J. M., and Field, J. E., 1989, "High Resolution Moire Photography: Application to Dynamic Stress Analysis," *Opt. Eng.*, Vol. 28, No. 8, pp. 926–933.

Jones, R., and Wykes, C., 1989, *Holographic and Speckle Interferometry*, Cambridge University Press, Cambridge, U.K.

Krishnaswamy, S., Tippur, H. V., and Rosakis, A. J., 1992, "Measurement of Transient Crack Fields Using the Method of Coherent Gradient Sensing," *J. Mech. Phys. Solids*, Vol. 40, No. 2, pp. 339–372.

Leith, E. N., and Upatnieks, J., 1962, "Reconstructed Wavefronts and Communication Theory," *J. Opt. Soc. Amer.*, Vol. 52, pp. 1123–1130.

Riley, W. F., and Durelli, A. J., 1962, "Application of Moire Method to the Determination of Transient Stress and Strain Distribution," ASME JOURNAL OF APPLIED MECHANICS, Vol. 29, pp. 23–29.

Sciammarella, C. A., 1982, "Holographic Moire, an Optical Tool for the Determination of Displacements, Strains, Contours and Slopes of Surfaces," *Opt. Eng.*, Vol. 21, No. 3, pp. 447–457.

Sciammarella, C. A., and Ahmadshahi, M. A., 1984, "A Computer Based Method for Fringe Pattern Analysis," *Proc. of the 1984 SEM Fall Meeting*, pp. 61–69.

Sciammarella, C. A., and Ahmadshahi, M. A., 1986, "An Optoelectronic System for Fringe Pattern Analysis," *Exper. Tech.*, Vol. 10, No. 7, pp. 8–13.

Sciammarella, C. A., and Ahmadshahi, M. A., 1988, "A Computer Based Holographic Interferometry to Analyze 3-D Surfaces," *Proc. of IMEKO XI World Congress of the International Measurement Confederation*, pp. 167–175.

Sciammarella, C. A., and Gilbert, J. A., 1976, "A Holographic-Moire Technique to Obtain Separate Patterns for Components of Displacement," *Exper. Mech.*, Vol. 16, No. 6, pp. 215–220.

Smith, H. M., 1969, *Principles of Holography*, John Wiley and Sons, New York.

Solid, J. E., 1969, "Holographic Interferometry Applied to Measurements of Small Static Displacements of Diffusely Reflecting Surfaces," *Appl. Opt.*, Vol. 8, pp. 1587–1595.

Stetson, K. A., and Brohinsky, W. R., 1985, "Electronic Holography and Its Application to Hologram Interferometry," *Appl. Opt.*, Vol. 24, No. 21, pp. 3631–3637.

Downloaded 03 May 2010 to 171.66.16.245. Redistribution subject to ASME license or copyright; see http://www.asme.org/terms/Terms_Use.cfm

F. J. M. Starmans[1]
Research Fellow.

W. A. M. Brekelmans
Associate Professor.

J. D. Janssen
Professor.

Faculty of Mechanical Engineering,
Eindhoven University of Technology,
5600 MB Eindhoven, The Netherlands

An Experimental-Numerical Method for Nonlinear Structural Mechanics

A maximum likelihood estimator and the finite element method are used to construct a tool for estimating the state of continuous structures from measured structural data. These structural data can, for example, consist of displacements of material points and stresses or strains at material points. The statistical uncertainty of the measured data is supposed to be known. An approximation for the uncertainty of the estimated state can be given. The analyzing tool, elaborated for the geometrically nonlinear rigid plastic case, is useful for evaluation of feasibility and accuracy of experimental set-ups. An example of application of the tool is presented.

1 Introduction

In experimental mechanics the determination of the accuracy of the results gathered from measurements should be an integral part of the research. In cases in which the quantity of interest is directly measured, a prediction of the real value and an inaccuracy limit for this prediction follows straightforward from the measuring technique. An example of this is the experimental determination of the limit load of a structure by use of force transducers. In other cases the interesting figures are often derived from plain numerical manipulation of measured data values. Standard error propagation or probability analysis can be used to establish accuracy limits for the resulting data in an analytical way. A quite trivial example is the determination of the elastic moduli of some material from traditional material testing experiments like the tension test and the torsion test.

If the configuration under consideration is complex with a large amount of measured data, it may become necessary to combine numerical structural analysis with stochastic theories to be able to predict the values of desired data from measured data, as well as to assess the accuracy of the predicted values. Quite a lot research has already been performed in this field. A distinction can be made regarding developments making use of probability analysis and those making use of estimation theory.

The first category focusses on the prediction of statistical properties, resulting from variations in applied loads, material properties, and so on (e.g., Handa and Andersson, 1981; Drewniak and Pawicki, 1985; Liu et al., 1987). These methods are especially useful for reliability studies and risk analyses. The second category involves the prediction of the behavior of a structure or of uncertain parameters given a set of observations (e.g., Contreras, 1980; Mura et al., 1986; Oda and Shinada, 1987). These methods are often called (hybrid) experimental-numerical methods.

In this paper a development with respect to the second category is presented. It is a combination of the finite element method for structural analysis of isothermal quasistatic problems and the maximum likelihood method, known from estimation theory. It is suited for geometrically nonlinear problems, i.e., large displacements and rotations, with history-dependent material behavior, more specifically rigid plastic. The application is demonstrated in the field of contact and friction research. With the nonlinear method, the upsetting test is analyzed. The calculation gives directives for the quantities to be measured and their measuring accuracy needed for a reliable prediction of the contact stresses during upsetting.

In the following, a general description of the kind of problems is considered. Then the finite element method, for taking into account the physical behavior and the maximum likelihood method for dealing with the observation data, is discussed. After some remarks about their combined numerical implementation, the method is applied in the example of upsetting. Finally, some conclusions are given.

2 General Description of the Nonlinear Problem

An irreversible behaving body B enclosed by boundary ∂B is considered with a known initial state at some reference time t_o. Both the body and its boundary consist of an invariant set of material points. Due to mechanical loads the displacements of the material points are large, which causes geometrical nonlinearity. Thermal effects, inertial effects, and distributed loads are supposed to be negligibly small.

The deformation of the body is considered during a time interval $t_o \leq \tau \leq t$. At any time and at any internal point of

[1]Currently at Philips Research, Eindhoven, The Netherlands. Please address all correspondence to F. Starmans, Hagenkampweg Noord 2, 5616 TA Eindhoven, The Netherlands.

Contributed by the Applied Mechanics Division of THE AMERICAN SOCIETY OF MECHANICAL ENGINEERS for publication in the ASME JOURNAL OF APPLIED MECHANICS.

Discussion on this paper should be addressed to the Technical Editor, Professor Lewis T. Wheeler, Department of Mechanical Engineering, University of Houston, Houston, TX 77204-4792, and will be accepted until four months after final publication of the paper itself in the ASME JOURNAL OF APPLIED MECHANICS.

Manuscript received by the ASME Applied Mechanics Division, Mar. 1, 1991; final revision, May 2, 1992. Associate Technical Editor: A. K. Noor.

Copyright © 1993 by ASME
Downloaded 03 May 2010 to 171.66.16.245. Redistribution subject to ASME license or copyright; see http://www.asme.org/terms/Terms_Use.cfm

the body, local equilibrium requires the Cauchy stress tensor $\mathbb{T}$ to satisfy (see, e.g., Hunter, 1976)

$$\nabla \cdot \mathbb{T} = \mathbf{0} \tag{1}$$

with ∇ the gradient operator, $\mathbf{0}$ the zero vector, and $\cdot$ the inner product. The actual value of $\mathbb{T}$ at time t depends on the history ($t_o \leq \tau \leq t$) of the deformation gradient $\mathbb{F}$, expressible by means of a constitutive functional $\mathcal{G}$

$$\mathbb{T} = \underset{\tau = t_0}{\overset{t}{\mathcal{G}}} [\mathbb{F}(\tau)]. \tag{2}$$

Mechanical properties figuring in $\mathcal{G}$ should be known for the material under consideration. With three independent boundary conditions at each point of ∂B, explicitly described during $t_o \leq \tau \leq t$, Eqs. (1) and (2) define a so-called direct problem (Kubo, 1988). The solution can be approximated by a straightforward analysis using a numerical scheme such as the finite element method.

In physical reality, however, sometimes boundary loads or displacements are not explicitly known or can only be measured with limited accuracy. To calculate for such cases the solution with a certain reliability, sufficient information about other quantities at the boundary or at interior points has to be determined and incorporated in the calculation, then called an inverse analysis. For this continuum problem a discretized approach, in space and in time, is adopted. Extension of the set of discretization points in space and time increases the accuracy of the approximation.

From the literature such types of analyses are known, especially in the field of contact problems between linear elastic bodies, e.g., Chambless et al. (1986), Oda and Shinada (1987), Turner et al. (1988). The (least squares or penalty) methods used are able to calculate the unknown interaction in the contact regions, but give neither indication on the weighting of the experimental data nor about the reliability of the results. Combined applications of numerical approximation techniques and estimation theories to contact problems with nonlinear materials involved are not known to the authors.

With the foregoing in mind, an incremental finite element formulation is chosen. The material behavior is assumed to be rigid plastic. As the estimation strategy for the incremental displacement field of the body with partly uncertain boundary conditions, the maximum likelihood method is used, which takes the stochastic behavior of the different boundary conditions into account. Information about the uncertainty of the displacement field and derivative quantities can be obtained.

3 Strategy for the Nonlinear Behavior

A well-known strategy used to solve approximately differential equations is the method of weighted residuals. The equilibrium Eq. (1) reads in the weak formulation

$$\int_B (\nabla \boldsymbol{w})^c : \mathbb{T}\, dV = \int_{\partial B} \boldsymbol{w} \cdot \boldsymbol{b}\, dA \tag{3}$$

with : the double inner product, $\boldsymbol{w}$ the weighting vector field, and $\boldsymbol{b}$ the external boundary load vector on the boundary ∂B. This load is related to the material stress state by $\boldsymbol{b} = \mathbb{T} \cdot \boldsymbol{n}$ with $\boldsymbol{n}$ the unit outward normal vector on ∂B. Substitution of the constitutive Eq. (2) yields an integral equation for the displacement field of the material points of the body. Elaboration of that equation depends on the nature of the constitutive equation. Here rigid plastic material behavior, obeying the Levy-Von Mises flow rule presupposing isotropic hardening, is chosen:

$$\mathbb{T} = -p\mathbb{I} + \frac{2}{3}(\dot{\bar{\epsilon}})^{-1} Y \mathbb{D},\quad p = -\frac{1}{3}\operatorname{tr}(\mathbb{T}),\quad \dot{\bar{\epsilon}} = \left(\frac{2}{3}\mathbb{D}:\mathbb{D}\right)^{1/2} \tag{4}$$

with $\mathbb{D}$ the deformation rate tensor, p the pressure, $\bar{\epsilon}$ the equivalent plastic strain, and Y the yield stress. Equation (4) supposes $\mathbb{D}$ unequal the second order null tensor. The Cauchy stress tensor $\mathbb{T}$ satisfies Von Mises' flow criterion

$$\frac{3}{2}\mathbb{T}^d : \mathbb{T}^d = Y^2,\quad \mathbb{T}^d = \mathbb{T} + p\mathbb{I} = \mathbb{T} - \frac{1}{3}\operatorname{tr}(\mathbb{T})\mathbb{I}, \tag{5}$$

where $\mathbb{T}^d$ is the deviatoric stress tensor. For many metals under cold-forming conditions in noncyclic processes, the yield stress depends only on the history parameter $\bar{\epsilon}$. Elastic effects are not modeled by (4), as they may be neglected in case of large plastic strains. In the constitutive model the pressure p occurs as an extra unknown. This pressure should result from the requirement of incompressibility, $\operatorname{tr}(\mathbb{D}) = 0$. This requirement is taken into account, weighted over B with a scalar weighting field q

$$\int_B q \operatorname{tr}(\mathbb{D})\, dV = 0. \tag{6}$$

The time domain $t_o \leq \tau \leq t$ is discretized in finite steps Δt, called increments. For small incremental displacements $\boldsymbol{u}$, the tensor $\mathbb{D}$ can be approximated by

$$\mathbb{D} = \frac{\mathbb{A}}{\Delta t},\quad \mathbb{A} = \frac{1}{2}(\nabla \boldsymbol{u} + (\nabla \boldsymbol{u})^c) \tag{7}$$

where the gradient operator ∇ is defined with respect to the configuration at the end of the increment. From (4) and (7) it follows for the end of the increment that

$$\mathbb{T} = -p\mathbb{I} + \frac{2}{3}(\Delta\bar{\epsilon})^{-1} Y_e \mathbb{A},\quad \Delta\bar{\epsilon} = \left(\frac{2}{3}\mathbb{A}:\mathbb{A}\right)^{1/2} \tag{8}$$

where Y_e is the equivalent stress at the end of the increment, expressible in $\Delta\bar{\epsilon}$. The Eqs. (3), with (8) substituted in it, and (6), with (7) substituted in it, should hold at the end of each increment for arbitrary admissible weighting fields, $\boldsymbol{w}$ and q, respectively.

The domain B is divided into material elements (Lagrangian formulation). In the elements the displacements, the pressure, and the weighting fields are interpolated between the nodal points using a Galerkin approach, i.e., equal interpolation functions for $\boldsymbol{u}$ and $\boldsymbol{w}$, as well as for p and q. Requiring that the elaborated Eqs. (3) and (6) are satisfied for all admissible weighting fields results in a set of vector equations (related to equilibrium) and scalar equations (related to volume invariance) for each increment. With respect to some vector base, these equations can formally be written as

$$\begin{bmatrix} \mathbf{f(u,p)} \\ \mathbf{c(u)} \end{bmatrix} = \begin{bmatrix} \mathbf{0} \\ \mathbf{0} \end{bmatrix} \tag{9}$$

where $\mathbf{u}$ and $\mathbf{p}$ are composed of the nodal values of the displacements and the pressures. As the set (9) is nonlinear in the nodal displacements and pressures, necessitating an iterative solution procedure, the iterative changes of $\mathbf{f}$ and $\mathbf{c}$ are of interest. From (9), analytical expressions for these iterative changes, $\delta\mathbf{f}$ and $\delta\mathbf{c}$, in the iterative changes, $\delta\mathbf{u}$ and $\delta\mathbf{p}$, can be obtained.

When displacement and pressure fields are known, the stresses at an arbitrary point of B can be calculated using (8) and the interpolations per element. To obtain stresses continuous over the element boundaries, a straightforward unweighted averaging of stresses in the nodal points at the element boundaries is used.

4 Strategy for the State Estimation

In the previous section the behavior of a body of rigid plastic material is approximated by a discretized incremental technique. Assuming the initial conditions and material behavior

Downloaded 03 May 2010 to 171.66.16.245. Redistribution subject to ASME license or copyright; see http://www.asme.org/terms/Terms_Use.cfm

to be known, the mechanical condition of the body after the first increment is described by $3n + m$ nodal unknowns composed of $3n$ displacements (n displacement nodes) and m pressures (m pressure nodes), previously denoted by $\mathbf{u}$ and $\mathbf{p}$, respectively. The $3n$ displacements can arbitrarily be replaced by $3n$ nodal locations in the sequel.

For some kth increment the condition of the body at the end of the increment depends on $3n$ location degrees-of-freedom and m pressure degrees-of-freedom more than its condition at the beginning of the increment. These degrees-of-freedom are gathered in the column $\mathbf{s}(k)$, further called the incremental state extension of the kth increment. After k increments, the total of $(3n + m)k$ unknowns is gathered in the accumulated state $\mathbf{s}_K$,

$$\mathbf{s}_K^T = [\mathbf{s}(1)^T \mathbf{s}(2)^T \ldots \mathbf{s}(k)^T] \tag{10}$$

which is the combination of the incremental state extensions $\mathbf{s}(1)$ to $\mathbf{s}(k)$.

To quantify the accumulated state $\mathbf{s}_N$, belonging to a deformation process over a time period divided into N increments, at least $(3n + m)N$ values of relevant quantities with respect to the condition of the body during the time period have to be known. A part $\mathbf{h}_e$ of these quantities will be exactly known, the rest ($\mathbf{h}_m$) of them will be measurable with only a limited accuracy. As relevant quantities, not only do the nodal degrees-of-freedom have to be considered, but also quantities like stresses, strains, and forces. The relevant quantities $\mathbf{h}_e(k)$ and $\mathbf{h}_m(k)$ of the kth increment can be uniquely expressed in the accumulated state $\mathbf{s}_K$, so $\mathbf{h}_e(k) = \mathbf{h}_e(\mathbf{s}_K)$ and $\mathbf{h}_m(k) = \mathbf{h}_m(\mathbf{s}_K)$. The quantities $\mathbf{h}_e(k)$ are called exact state-dependent quantities and $\mathbf{h}_m(k)$ are the measurable state-dependent quantities. The actual data values for $\mathbf{h}_e(k)$ compose the column $\mathbf{z}_e(k)$ and are called exact observation data, and the actual data values for $\mathbf{h}_m(k)$ compose the column $\mathbf{z}_m(k)$ called measured observation data. Per increment, the incremental exact observation data $\mathbf{z}_e(k)$ are equal to $\mathbf{h}_e(k)$, whereas the incremental measured observation data $\mathbf{z}_m(k)$ will deviate from $\mathbf{h}_m(k)$ with an unknown stochastic column $\mathbf{v}(k)$ containing incremental observation errors

$$\mathbf{z}_e(k) = \mathbf{h}_e(\mathbf{s}_K), \quad \mathbf{z}_m(k) = \mathbf{h}_m(\mathbf{s}_K) + \mathbf{v}(k). \tag{11}$$

Note that modeling errors, e.g., due to the discretization, are assumed to be negligibly small. With the same notation convention (10), accumulated columns $\mathbf{h}_{e,K}$, $\mathbf{h}_{m,K}$, $\mathbf{z}_{e,K}$ and $\mathbf{z}_{m,K}$ are defined using the incremental columns $\mathbf{h}_e(k)$, $\mathbf{h}_m(k)$, $\mathbf{z}_e(k)$, and $\mathbf{z}_m(k)$. So it can be stated for the accumulated exact and measurable state-dependent quantities that

$$\mathbf{h}_{e,K} = \mathbf{h}_{e,K}(\mathbf{s}_K), \quad \mathbf{h}_{m,K} = \mathbf{h}_{m,K}(\mathbf{s}_K). \tag{12}$$

The incremental observation errors of k increments compose the accumulated observation error column $\mathbf{v}_K = \mathbf{z}_{m,K} - \mathbf{h}_{m,K}(\mathbf{s}_K)$.

The problem to be solved for the deforming body (over a time period divided into a total of N increments) can now be stated as searching for that approximation $\hat{\mathbf{s}}_N$ for $\mathbf{s}_N$ which obeys

$$\mathbf{z}_{e,N} = \mathbf{h}_{e,N}(\hat{\mathbf{s}}_N) \tag{13}$$

and satisfies some criterion expressed in $\mathbf{z}_{m,N}$, $\mathbf{h}_{m,N}$, $\mathbf{v}_N$, and $\hat{\mathbf{s}}_N$. This formulation constitutes a static nonlinear estimation problem with constraints. A reliable estimate $\hat{\mathbf{s}}_N$ can be obtained with a maximum likelihood estimator (see, e.g., Schweppe (1973) and Norton (1986)). Generally for measuring errors, a Gaussian probability applies. Therefore, $\mathbf{v}_N$ is supposed to have such a probability density $p(\mathbf{v}_N)$ with zero mean and covariance matrix $\underline{\mathbf{R}}_N$. The likelihood function $p(\mathbf{z}_N : \mathbf{s}_N)$, defined as the density function of the observation data $\mathbf{z}_N$ given state $\mathbf{s}_N$, then results in

$$((2\pi)^L \det(\underline{\mathbf{R}}_N))^{-1/2} \times \exp\left(-\frac{1}{2}[\mathbf{z}_{m,N} - \mathbf{h}_{m,N}(\mathbf{s}_N)]^T \underline{\mathbf{R}}_N^{-1} [\mathbf{z}_{m,N} - \mathbf{h}_{m,N}(\mathbf{s}_N)]\right) \tag{14}$$

with L the length of $\mathbf{v}_N$, i.e., the total number of measured observations. Maximizing this function for the actual observation data $\mathbf{z}_{m,N}$ under the constraints (13) yields the desired estimate $\hat{\mathbf{s}}_N$. Unicity of this estimate depends, among others, on the available exact and measurable state-dependent quantities and is not generally guaranteed. Physical insight and further research are needed to investigate this.

A disadvantage of the above method is of computational origin. To obtain a reasonable approximation of the nonlinear behavior of body B, the incremental state extension columns with each $3n + m$ nodal degrees-of-freedom and the total number of increments N have to be relatively large. To deal with the accumulated state column $\mathbf{s}_N$ of length $(3n + m)N$ in a maximization process of the function (14) would need large computation time and memory. For this reason, among others, in estimation theory for dynamic systems, filtering techniques are developed to determine estimates for successive time steps instead of simultaneously for the total set of time steps. The estimation of the incremental state extension $\mathbf{s}(k)$ for the kth time step is then based on momentary observation data and some estimate $\hat{\mathbf{s}}_{K-1}$ for the accumulated state $\mathbf{s}_{K-1}$. For the estimation of $\mathbf{s}(k)$ in the considered case a simple "filter" is proposed in the sequel based on the previous incremental state extension estimate $\hat{\mathbf{s}}(k-1)$ and the incremental observation data $\mathbf{z}(k)$.

In the foregoing, $\mathbf{h}_e(k)$ and $\mathbf{h}_m(k)$ are introduced as functions of $\mathbf{s}_K$, and thus of the combination of $\mathbf{s}_{K-1}$ and $\mathbf{s}(k)$. For the particular history-dependent material behavior these variables may be replaced by $\mathbf{s}(k)$, $\Delta\mathbf{s}(k)$ and $\mathbf{H}(k)$, with $\Delta\mathbf{s}(k)$, the change of the incremental state extension defined by

$$\Delta\mathbf{s}(k) = \mathbf{s}(k) - \mathbf{s}(k-1) \tag{15}$$

and $\mathbf{H}(k)$, a column with the history parameters resulting after the kth increment, i.e., the equivalent plastic strains at a discrete number of material points. The choice of the material behavior enables that they can be expressed additively as

$$\mathbf{H}(k) = \mathbf{H}(k-1) + \Delta\mathbf{H}(\mathbf{s}(k), \Delta\mathbf{s}(k)) \tag{16}$$

with $\Delta\mathbf{H}$ a nonlinear function of $\mathbf{s}(k)$ and $\Delta\mathbf{s}(k)$. It is noticed that the change of the incremental state extensions contains the nodal incremental displacements and the changes of the pressure degrees-of-freedom of the kth increment. If an estimate $\hat{\mathbf{s}}(k-1)$ for the incremental state extension $\mathbf{s}(k-1)$ is available, $\mathbf{s}(k-1)$ can be written as

$$\mathbf{s}(k-1) = \hat{\mathbf{s}}(k-1) + \delta\mathbf{s}(k-1) \tag{17}$$

with errors $\delta\mathbf{s}(k-1)$. Also, errors $\delta\mathbf{H}(k-1)$ will apply for the estimate $\hat{\mathbf{H}}(k-1)$. Assuming these errors are relatively small, the quantities $\mathbf{h}_e(k)$ are written as

$$\mathbf{h}_e(k) = \mathbf{h}_e(\mathbf{s}(k), \mathbf{s}(k) - \hat{\mathbf{s}}(k-1), \hat{\mathbf{H}}(k-1) + \Delta\mathbf{H}(\mathbf{s}(k), \mathbf{s}(k) - \hat{\mathbf{s}}(k-1))) - \left(\frac{\partial}{\partial\Delta\mathbf{s}}(\mathbf{h}_e^T)\right)^T \delta\mathbf{s}(k-1) + \left(\frac{\partial}{\partial\mathbf{H}}(\mathbf{h}_e^T)\right)^T \left(\delta\mathbf{H}(k-1) - \left(\frac{\partial}{\partial\Delta\mathbf{s}}(\Delta\mathbf{H}^T)\right)^T \delta\mathbf{s}(k-1)\right) \tag{18}$$

where quadratic and higher-order terms in the errors are neglected. A similar relationship for $\mathbf{h}_m(k)$ can be formulated. The only unknown in the zeroth-order terms of $\mathbf{h}_e(k)$ and $\mathbf{h}_m(k)$ is the incremental state extension $\mathbf{s}(k)$. If the first-order terms in the errors are negligible, a maximum likelihood estimate $\hat{\mathbf{s}}(k)$ for $\mathbf{s}(k)$ can be obtained in a straightforward way. If the first-order terms are not negligible, the estimate $\hat{\mathbf{s}}(k)$ solely based on the zeroth-order term will contain an extra bias

Downloaded 03 May 2010 to 171.66.16.245. Redistribution subject to ASME license or copyright; see http://www.asme.org/terms/Terms_Use.cfm

error, besides the bias error caused by the estimation method. As usual, the bias error $\mathbf{b}(k)$ of the estimate $\hat{\mathbf{s}}(k)$ is defined by $\mathbf{b}(k) = E(\hat{\mathbf{s}}(k)) - \mathbf{s}_t(k)$ with $E(\hat{\mathbf{s}}(k))$, the expected value of $\hat{\mathbf{s}}(k)$, and $\mathbf{s}_t(k)$, the true but unknown incremental state extension.

For the analysis of the upsetting experiment, the maximum likelihood estimator using only the zeroth-order terms is chosen, as the bias errors are expected to remain small. A part of the exact and measurable state-dependent quantities consists of positions of boundary nodes, which are linear in $\mathbf{s}(k)$. This contributes to a bounding of the bias terms for two reasons. First, the maximum likelihood method delivers bias-free estimates for models with only linear state-dependent quantities. Secondly, such state-dependent quantities force the estimator to choose $\hat{\mathbf{s}}(k)$ close to the true incremental state extension $\mathbf{s}_t(k)$, despite possible bias errors in $\hat{\mathbf{H}}(k-1)$ caused by the maximum likelihood method. Assuming the estimate $\hat{\mathbf{s}}(k)$ is unbiased and not too far from the true state, an approximation for its error covariance matrix $\underline{\Sigma}$ can be given,

$$\underline{\Sigma} \approx \underline{Z}_e^T (\underline{Z}_e \underline{J}_m^T \underline{R}^{-1} \underline{J}_m \underline{Z}_e^T)^{-1} \underline{Z}_e, \quad \underline{Z}_e \underline{J}_e^T = \underline{0}, \tag{19}$$

with $\underline{R} = \underline{R}(k)$ the covariance matrix of $\mathbf{v}(k)$, and the Jacobian matrices $\underline{J}_m^T = (\partial/\partial \mathbf{s})(\mathbf{h}_m^T)$ and $\underline{J}_e^T = (\partial/\partial \mathbf{s})(\mathbf{h}_e^T)$. Note that the rows of $\underline{Z}_e$ span the orthogonal complement of the space spanned by the rows of $\underline{J}_e$. Equations (19) offer a lower bound for the reliability of the resulting incremental state extension estimate.

5 Numerical Implementation

Because of the promising numerical results for incompressible flow, an axisymmetric triangular isoparametric $P_2^+ - P_1$ Crouzeix-Raviart element is applied for the numerical simulations. This element, with an extended quadratic interpolation for the shape and position field and a linear pressure field discontinuous over the element boundaries, provides accurate results for quite coarse meshes. It further shows the capability of numerical smoothing in the neighborhood of singular points. Such singularities can occur under sticking conditions at the outer edges of contact boundaries.

Various solution methods exist to tackle optimization problems (see, e.g., Gill et al., 1981). For the optimization considered here, the solution method has to minimize the following function

$$(\mathbf{z}_m - \mathbf{h}_m(\mathbf{s}))^T \underline{R}^{-1} (\mathbf{z}_m - \mathbf{h}_m(\mathbf{s})) \tag{20}$$

with respect to the unknowns $\mathbf{s}$, with the nonlinear equality constraints

$$\mathbf{z}_e = \mathbf{h}_e(\mathbf{s}). \tag{21}$$

Again, unicity of the solution is not generally guaranteed. The penalty function approach is a very elegant and comprehensible method to deal with the constraints (21). This method transforms the constrained minimization of (20) into the unconstrained minimization of

$$F(\mathbf{s}) = (\mathbf{z}_m - \mathbf{h}_m(\mathbf{s}))^T \underline{R}^{-1} (\mathbf{z}_m - \mathbf{h}_m(\mathbf{s})) + (\mathbf{z}_e - \mathbf{h}_e(\mathbf{s}))^T \underline{Q}^{-1} (\mathbf{z}_e - \mathbf{h}_e(\mathbf{s})). \tag{22}$$

The penalty matrix $\underline{Q}^{-1}$, not necessarily diagonal, may be interpreted as a fictitious inverse covariance matrix of the exact observation data $\mathbf{z}_e$. This interpretation is helpful in choosing reasonable values for $\underline{Q}^{-1}$ in relation to $\underline{R}^{-1}$, i.e., smaller covariances for $\mathbf{z}_e$ than the covariances of comparable quantities of $\mathbf{z}_m$, but not too small in order to avoid computational difficulties. Because of its robustness, the Newton method is used to perform the unconstrained minimization in an iterative manner. With the use of iterative equations as indicated in Section 3, the underlying equations are analytically known. Therefore, advantage can be taken of their structure, resulting in savings in computation time and memory. For the one-dimensional optimization along the search direction, a golden section search is employed, needing only the evaluation of function values.

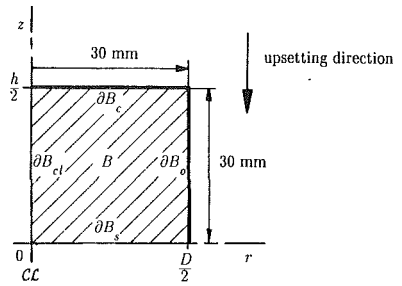


Fig. 1 The upsetting configuration in the reference state

In the upsetting experiment, given as an example in the next section, the boundary conditions are kinematical (prescribed positions of boundary nodes) and dynamical (prescribed stresses or forces). These quantities are partly considered as exact boundary conditions, depending on the problem studied. In the interior of the body there are constraints of zero nodal forces and equations following from volume invariance. The exact boundary conditions (except exact nodal point positions as these can be prescribed easily) and all constraints are taken in account as exact observation data.

6 Simulations of an Upsetting Experiment

It is the aim of the calculations to gain insight in the accuracy of the contact quantities which can be expected for different sets of boundary conditions, each representing a possible experimental set-up. With these results the upsetting experiment can be evaluated with respect to its usefulness for the measuring of contact behavior in forming processes.

The calculations are executed on an axisymmetric workpiece within the undeformed state, a diameter of 60 mm and a diameter-to-height ratio equal to 1. Because of axisymmetry and the assumption of symmetry with respect to the midplane of the workpiece, only one quarter of the cross-section has to be divided into elements. In Fig. 1 the different boundary parts are indicated. The workpiece is assumed to be made of pure aluminum. The yield stress Y as function of the equivalent plastic strain is taken as

$$Y = 32 + 120\bar{\epsilon} - 60\bar{\epsilon}^2 + 99\bar{\epsilon}^3 \ (\mathrm{N/mm^2}) \tag{23}$$

which results from a fit through data of a Rastegaev test on pure aluminum of Reiss and Pöhlandt (1985). In 10 increments of 3 mm upsetting each, the workpiece is pressed to a total height of 30 mm (50 percent height reduction). As a constitutive equation for the friction along the contact boundary ∂B_c, the Von Mises model is used:

$$|\tau| = \frac{1}{3}\sqrt{3} m Y, \tag{24}$$

with m being the constant friction factor ($0 \le m \le 1$). The direction of the friction stress is equal to that of the relative displacement of the contact partner.

The nontrivial contact quantities of interest at the boundary part ∂B_c are the radial displacements $\Delta r = r - r_0$ with respect to the reference configuration at time point t_0, the normal stress σ_n, and the (frictional) shear stress τ. For the configuration considered, σ_n acts in the negative axial direction and τ acts in the negative radial direction. For the boundary parts ∂B_c and ∂B_o the boundary conditions, used for the calculations, are varied as indicated in Table 1. For all cases the boundary conditions along ∂B_{cl} and ∂B_s are reflecting the symmetry conditions (∂B_{cl}: radial displacement suppressed; ∂B_s: axial displacement suppressed). Results from Case 1 will serve as input

Downloaded 03 May 2010 to 171.66.16.245. Redistribution subject to ASME license or copyright; see http://www.asme.org/terms/Terms_Use.cfm

Table 1 The boundary conditions of the five cases considered (crosses (x) indicate presence of a boundary condition)

BOUNDARY CONDITIONS		CASES				
PART	CONDITION	1	2	3	4	5
∂B_c	MEASURED AXIAL DISPLACEMENT	×	×	×	×	×
	VON MISES FRICTION MODEL	×				
	MEASURED NORMAL CONTACT STRESS				×	×
	MEASURED UPSETTING FORCE			×		
∂B_o	STRESS FREE	×	×	×	×	×
	MEASURED DISPLACEMENTS		×	×		×

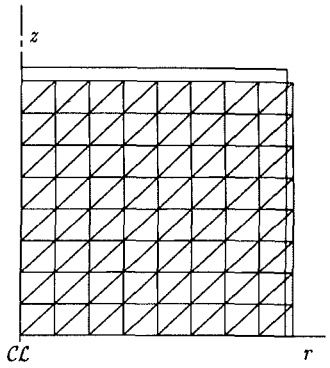


Fig. 2(*a*)

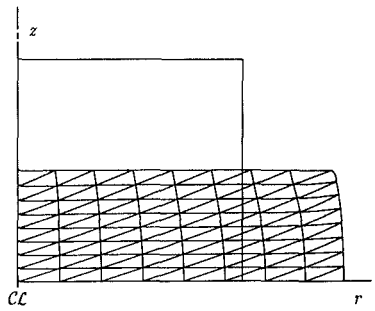


Fig. 2(*b*)

Fig. 2 Deformed meshes after 3 mm (*a*) and 30 mm (*b*) upsetting

for the other calculations, which in fact should result in the same solution. The covariance estimates according to Eq. (19) are used to study for each case the reliability of this solution at the contact boundary. Case 3 is meant to study the influence of the measured upsetting force as extra boundary condition with respect to Case 2. Case 5 aims to investigate whether measured displacements of the outer unloaded surface contribute to an improvement of the contact quantities accuracy as resulting from Case 4. For all cases the standard deviation of the axial displacement at the contact boundary is supposed to be 0.01 mm, which is quite accurate. All measured quantities are supposed to be mutual independent. The experiences obtained from the different problem formulations are discussed sequentially.

Case 1. The boundary conditions as specified in Table 1, together with the symmetry boundary conditions, constitute a direct problem. For the constant friction factor m a value of 0.1 is applied. The standard deviation of the friction stress calculated with this model is assumed to be 0.1 N/mm^2. In Fig. 2 the deformed meshes after 3 mm and 30 mm upsetting are shown. In the sequel the results will be presented always for these two upsetting stages.

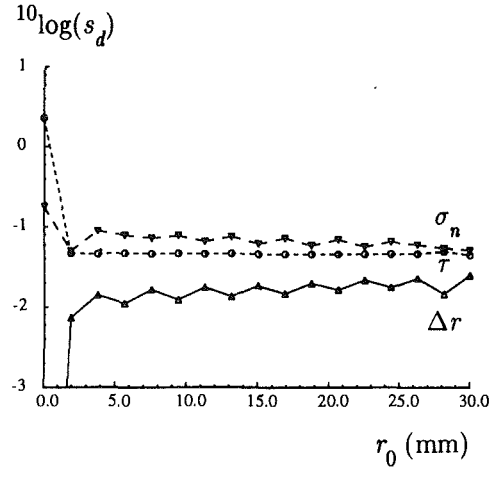


Fig. 3(*a*)

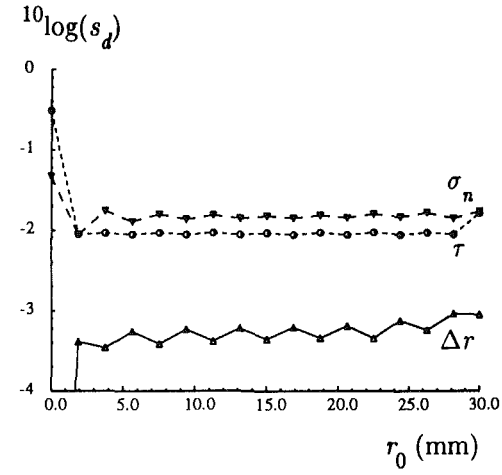


Fig. 3(*b*)

Fig. 3 The dimensionless standard deviations for Case 1

As a measure for the reliability of the contact quantities a dimensionless standard deviation s_d is introduced, which is comparable to the coefficient of variation from statistics. For each contact quantity s_d is defined as a function of the position at the contact surface by

$$s_d = \frac{\hat{s}}{\hat{\mu}_m} \tag{25}$$

with $\hat{\mu}_m$ the maximum of the absolute estimation of the quantity along the contact surface, and $\hat{s}$ the locally estimated standard deviation. It can be interpreted as a relative error. The advantage of this definition is that the accuracy of the contact quantities, with mutually very different ranges, can be compared. The calculated values of s_d for the radial displacement, normal stress, and friction stress after 3 mm and 30 mm upsetting are given in Fig. 3 as a function of the reference radial position r_0.

Case 2. In the second case, the knowledge on the contact model is not taken into account. For compensation, the measured axial and radial displacement of the free surface, with a standard deviation of 0.01 mm, are used as boundary conditions. It should be noted that for each increment the measured displacements are referenced to the original state, so it is assumed that no accumulation of measuring errors occurs. This second problem appears to be very ill-conditioned. Because of this, lack of convergence occurred in the calculation when this was started for each increment from a first guess for the solution which was too far from the actual solution. Therefore,

Downloaded 03 May 2010 to 171.66.16.245. Redistribution subject to ASME license or copyright; see http://www.asme.org/terms/Terms_Use.cfm

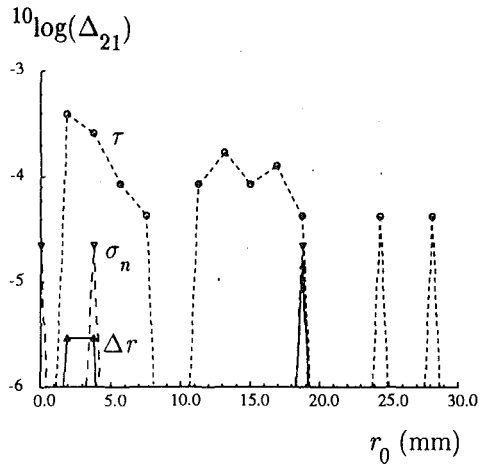


Fig. 4(a)

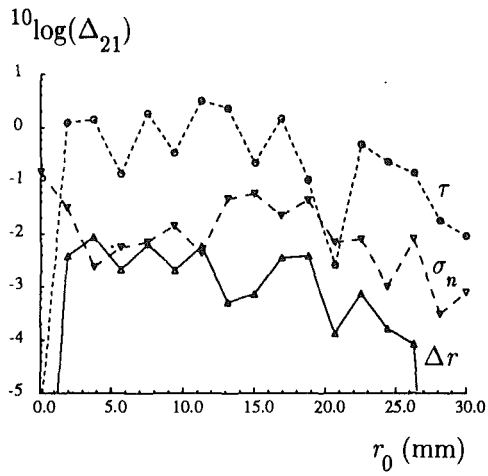


Fig. 4(b)

Fig. 4 Dimensionless absolute differences of Case 2 with respect to Case 1

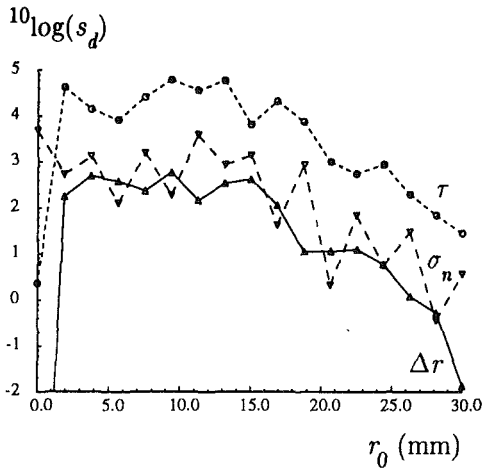


Fig. 5(a)

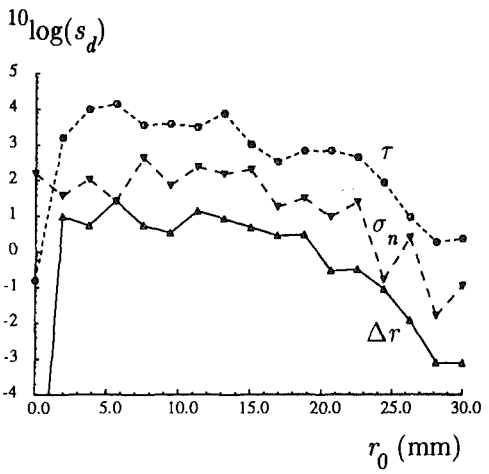


Fig. 5(b)

Fig. 5 The dimensionless standard deviations for Case 2

the incremental first guesses are taken to be equal to the incremental solutions of the direct problem of Case 1. The solution then calculated shows differences (increasing per increment) from the solution of the direct problem.

To illustrate this phenomenon, Fig. 4 shows the dimensionless absolute differences Δ_{21} between the solution of the current case and the solution of Case 1. The method to make the differences dimensionless is equal to the one used in Eq. (25). The differences are caused by the truncation of the displacements of the outer surface calculated for Case 1 before they are used as boundary conditions in the current case. In fact, these truncation errors act as very small measuring errors. The ill-conditioning is also illustrated by the resulting dimensionless standard deviations of the contact quantities, given in Fig. 5. The accuracy of the measured displacements at ∂B_o should be increased beyond physical possibilities to obtain acceptably accurate contact quantities.

Case 3. With respect to Case 2, as extra input the measured upsetting force is used. It is supposed that this force (in the order of 0.1 MN) is very accurately known with a standard deviation of 100 N. To achieve convergence of the solution process the same procedure as in the previous case was necessary. The dimensionless standard deviations become smaller, see Fig. 6; however, not small enough to reach usefulness.

Case 4. Instead of the knowledge of the contact model of Case 1 the measured normal stresses are applied as boundary conditions at the contact surface. The standard deviation of this stress is very conservatively supposed to be 10 N/mm^2. For this case as well as the next, the previously described special treatment of the incremental first guesses was no longer needed to obtain convergence. The resulting dimensionless standard deviations are given in Fig. 7. The large value of s_d for the friction stress τ is caused by the small absolute values of τ.

Case 5. In this case it is considered whether the estimates of Case 4 can be improved by measured contour data. As in the Cases 2 and 3, a standard deviation of 0.01 mm is supposed for the displacements of the contour points. In Fig. 8 improvements can be observed, especially for the high upsetting range and near the outer radius. In contrast to the reliability of the radial displacement and normal stress, the reliability of the friction stress is unsatisfactory. This has to be improved before calculated results for the friction stress can be used for quantifying contact models.

Three ways are mentioned to reach extra improvement. At first the standard deviation of the normal stress is taken to be quite large in the actual calculation. Measurement of the normal stress with a higher accuracy will reduce the standard deviation of the friction stress. Secondly, use can be made of

Downloaded 03 May 2010 to 171.66.16.245. Redistribution subject to ASME license or copyright; see http://www.asme.org/terms/Terms_Use.cfm

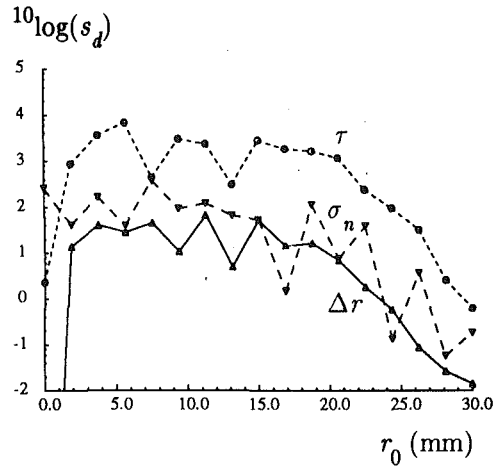


Fig. 6(*a*)

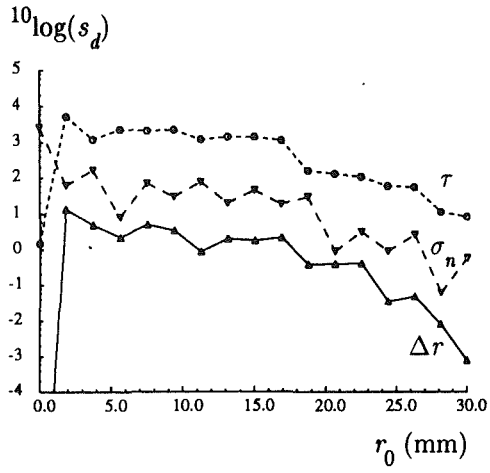


Fig. 6(*b*)

Fig. 6 The dimensionless standard deviations for Case 3

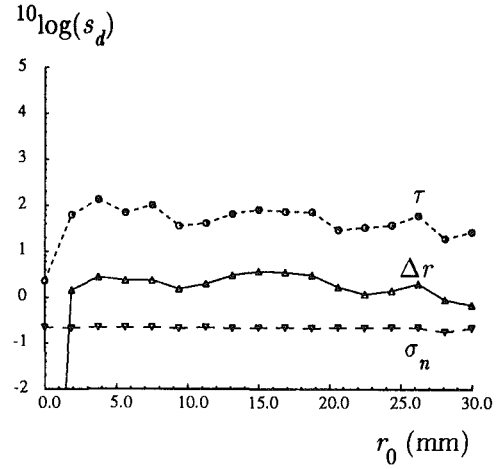


Fig. 7(*a*)

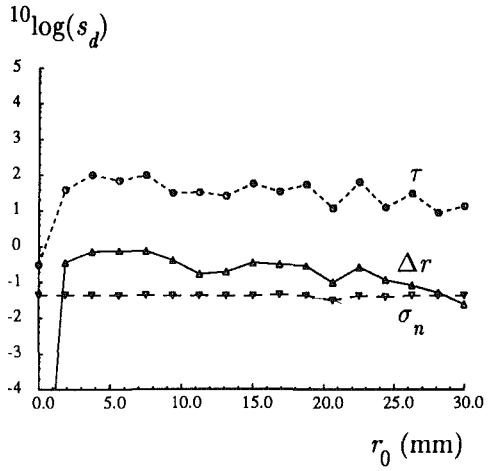


Fig. 7(*b*)

Fig. 7 The dimensionless standard deviations for Case 4

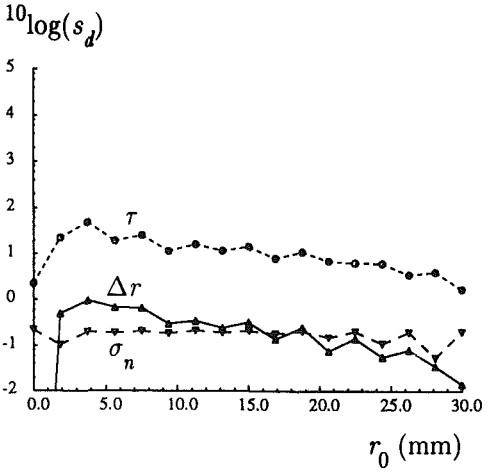


Fig. 8(*a*)

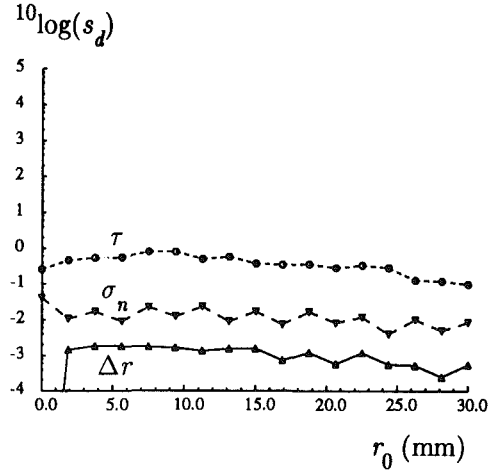


Fig. 8(*b*)

Fig. 8 The dimensionless standard deviations for Case 5

the smoothness of the contact stress pattern. Decrease in the number of contact stress unknowns will result in a higher accuracy for the contact quantities. This strategy was applied for calculations on a (linear elastic) stress measuring tool by Starmans et al. (1992). It turned out that the friction stress can be measured together with the normal stress, thus offering a third way for raising the reliability of the friction stress. The fitting quality of the (with a reduced number of contact stress unknowns) estimated contact stress pattern can be judged by using the reached minimum value of $F(s)$ according to Eq.

Downloaded 03 May 2010 to 171.66.16.245. Redistribution subject to ASME license or copyright; see http://www.asme.org/terms/Terms_Use.cfm

(22). A quantitative measure for the fitting quality can be obtained by the χ^2-test.

It is concluded that the use of measured displacements of the contour, the upsetting displacement, and the upsetting force only cannot lead to a successful estimate of the contact quantities. This is in accordance with experimental results as reported in the literature (Herbertz and Wiegels, 1981). Measurement of the stresses at the contact area is necessary. This can be done with a stress measuring tool as described by Starmans et al. (1992), or with some other method (see e.g., Tuncer and Dean (1987) for a review). Improvement of the results calculated from contact stress data may be obtained if additional quite accurate contour displacements are available.

7 Conclusions

In the foregoing a combined elaboration of the finite element method for quasi-static structural problems and the maximum likelihood method is described. It is applied to evaluate possible experimental set-ups in the field of contact and friction research in order to show its usefulness in experimental mechanics.

For the nonlinear problems an asymptotic unbiased estimation tool was formulated. This was, however, discarded on the basis of the current numerical limitations. A filter approach was presented instead, and elaborated for rigid plastic material behavior. Although this method needs still further evaluation it showed to be possible, in the example of the upsetting experiment, to take different kinds of measured data into account. Further, the covariance estimate proved useful to evaluate various experimental set-ups and to improve these set-ups. A further investigation of the behavior of this nonlinear tool is recommended. Via Monte Carlo simulations, the performance should be examined in further research. Also attention should be paid to the conditions for existence and unicity.

References

Chambless, D. A., Swinson, W. F., Suhling, J. C., and Turner, J. L., 1986, "New Hybrid Photoelastic Finite Element Technique for Stress Analysis," *Proceedings of the 1986 SEM Spring Conference on Experimental Mechanics*, Society for Experimental Mechanics, Bethel, PA, pp. 991–998.

Contreras, H., 1980, "The Stochastic Finite-Element-Method," *Computers & Structures*, Vol. 12, pp. 341–348.

Drewniak, J., and Pawicki, Z., 1985, "Boundary Element Method for Fluctuations of Boundary Conditions," *Mechanics Research Communications*, Vol. 12, pp. 113–118.

Gill, P. E., Murray, W., and Wright, M. H., 1981, *Practical Optimization*, Academic Press, London.

Handa, K., and Andersson, K., 1981, "Application of Finite Element Methods in the Statistical Analysis of Structures," *Proceedings of the 3rd International Conference on Structural Safety and Reliability*, T. Moan and M. Shinozuka, eds., Elsevier, Amsterdam, pp. 409–417.

Herbertz, R., and Wiegels, H., 1981, "A Method for Frictionless Upsetting of Cylindrical Workpieces for Registering Flow Curves," (in German), *Stahl und Eisen*, Vol. 101, pp. 89–92.

Hunter, S. C., 1976, *Mechanics of Continuous Media*, John Wiley and Sons, New York.

Kubo, S., 1988, "Inverse Problems Related to the Mechanics and Fracture of Solids and Structures," *JSME International Journal, Series I*, Vol. 31, pp. 157–166.

Liu, W. K., Mani, A., and Belytschko, T., 1987, "Finite Element Methods in Probabilistic Mechanics," *Probabilistic Engineering Mechanics*, Vol. 2, pp. 201–213.

Mura, T., Cox, B., and Gao, Z., 1986, "Computer-Aided Nondestructive Measurements of Plastic Strains from Surface Displacements," *Proceedings of the International Conference on Computational Mechanics 1986*, G. Yagawa and S. N. Atluri, eds., Springer-Verlag, Tokyo, pp. II.43–II.48.

Norton, J. P., 1986, *An Introduction to Identification*, Academic Press, London.

Oda, J., and Shinada, T., 1987, "An Inverse Analysis Technique to Obtain Contact Stress Distributions," (in Japanese), *Transactions of the Japanese Society of Mechanical Engineers*, Vol. 53, pp. 1614–1621.

Reiss, W., and Pöhlandt, K., 1985, "Behaviour and Manipulation of Wrought Materials under Homogeneous Deformation," (in German), *Materialprüfung*, Vol. 27, pp. 100–104.

Schweppe, F. C., 1973, *Uncertain Dynamic Systems*, Prentice-Hall, Englewood Cliffs, NJ.

Starmans, F. J. M., Brekelmans, W. A. M., and Janssen, J. D., 1992, "A Hybrid-Experimental-Numerical Method for Linear Structural Mechanics," *Computers & Structures*, Vol. 43, pp. 61–68.

Tuncer, C., and Dean, T. A., 1987, "A New Pin Design for Pressure Measurement in Metal Forming Processes," *International Journal of Machine Tools and Manufacture*, Vol. 27, pp. 325–331.

Turner, J. L., McNeill, S. R., Chao, Y. J., Sutton, M. A., and Peters, W. H., 1988, "Hybrid Methods in Experimental Mechanics," *Proceedings of the International Conference on Computational Engineering Science 1988*, S. N. Atluri and G. Yagawa, eds., Springer-Verlag, New York, pp. 48.ix.1–48.ix.4.

Downloaded 03 May 2010 to 171.66.16.245. Redistribution subject to ASME license or copyright; see http://www.asme.org/terms/Terms_Use.cfm

Influence of Porosity on Plane Strain Tensile Crack-Tip Stress Fields in Elastic-Plastic Materials: Part II

Y. Miao
Graduate Research Assistant.

W. J. Drugan
Professor,
Mem. ASME.

Department of Engineering Mechanics and Astronautics,
1415 Johnson Drive,
University of Wisconsin-Madison,
Madison, WI 53706

This paper continues the investigation of Drugan and Miao (1992). There we studied analytically the influence of a uniform porosity distribution on the stress field near a plane strain tensile crack tip in ductile (elastic-ideally plastic) material, assuming that material very near the tip is at yield at all angles about the tip. Our solutions exhibited completely continuous stress fields for porosity $f \leq 0.02979$, *but for higher porosities they involved radial surfaces of radial normal stress jumps. Here we investigate whether, for this higher range of porosity, relaxing our assumption of yield at all angles about the tip will facilitate solutions exhibiting fully continuous stress fields. The answer to this is shown to be yes, with a single near-tip sector assembly providing such solutions for this entire higher porosity range. On either side of the crack symmetry plane, this solution configuration consists of a leading plastic sector possessing radial stress characteristics ("generalized centered fan"), followed by a plastic sector of constant Cartesian components of stress, followed finally by a sector of purely elastic material adjacent to the crack flank. The angular extents of these sectors vary substantially with porosity level. In regions of purely elastic response, we have accounted for the influence of porosity on the overall, or effective, elastic moduli. Among the interesting features of these new solutions are a significantly enlarged generalized centered fan sector as compared to that of the fully plastic Part I solutions for the same* f *values, and for* f *values just slightly above the 0.02979 level, a narrow elastic sector exists in which stresses vary so rapidly with angle that they appear to be nearly discontinuous. This rapid variation spreads out as the elastic sector enlarges with increasing* f, *and, in contrast to the fully plastic solutions, the radial normal component of stress becomes negative near the crack flank.*

1 Introduction

This paper continues the investigation begun in Drugan and Miao (1992), hereafter referred to as Part I. That study provided an analytical first examination of the influence of the entire range of material porosity level on the stress field near a stationary plane strain tensile crack tip in ductile (elastic-ideally plastic) material with a uniform porosity distribution, which arises approximately in, e.g., incompletely sintered or previously deformed metals and alloys. Such porosity also occurs in hot-isostatic-pressed material that is subjected to a subsequent heat treatment, since gas trapped at high pressures then opens voids. We assumed that the material is at yield at all angles around the crack tip, obeying the Gurson-Tvergaard yield criterion, and that in plastically deforming near-tip regions plastic strain dominates elastic. Under these assumptions only two types of near-tip plastic solution sector are possible: generalized centered fan, and constant stress (Cartesian components); the appropriate assembly of these provides the complete near-tip stress field. We showed that there are three permissible types of near-tip solution configuration; the applicable one depends on the porosity level, f. One is a generalized Prandtl field which exists for small f, between 0 and $.04468/q_1 \equiv f_1$, and reduces, as $f \to 0$, to the classical Prandtl field of a tensile crack in fully dense Huber-Mises material (Rice, 1967, 1982). Here q_1 is one of the parameters Tvergaard (1981) introduced to improve the Gurson yield condition; it is typically suggested, on the basis of numerical finite element simulations of elastic-plastic response of voided media, that

Contributed by the Applied Mechanics Division of THE AMERICAN SOCIETY OF MECHANICAL ENGINEERS for publication in the ASME JOURNAL OF APPLIED MECHANICS.

Discussion on this paper should be addressed to the Technical Editor, Professor Lewis T. Wheeler, Department of Mechanical Engineering, University of Houston, Houston, TX 77204-4792, and will be accepted until four months after final publication of the paper itself in the ASME JOURNAL OF APPLIED MECHANICS.

Manuscript received by the ASME Applied Mechanics Division, Aug. 20, 1991; final revision, Aug. 14, 1992. Associate Technical Editor: R. M. Bowen.

Copyright © 1993 by ASME
Downloaded 03 May 2010 to 171.66.16.245. Redistribution subject to ASME license or copyright; see http://www.asme.org/terms/Terms_Use.cfm

$q_1 \approx 1.5$ (see Part I). Another near-tip solution type is a plane-stress-like configuration, resembling Hutchinson's (1968) plane stress tensile crack solution for fully dense Huber-Mises material, which exists for $f_1 \le f \le 0.18043/q_1 \equiv f_2$. This consists of a generalized centered fan sector beginning at the crack symmetry line, followed by two constant stress plastic sectors with stress jumps in radial and out-of-plane normal components across their mutual border. For the remaining higher porosities $f_2 \le f \le 1/q_1$, the stress field is an assembly of two constant stress plastic sectors with stress jumps across their unchanged mutual border; this configuration exists for the entire porosity range from 0 to $1/q_1$.

Among these three distinct types of near-tip solution configuration, the generalized Prandtl field is the only one with fully continuous stress fields. Although stress discontinuities in radial and out-of-plane normal components cannot be ruled out on the basis of the elastic-plastic governing equations, and hence the other near-tip configurations *are* valid solutions to these equations and the boundary conditions, one wonders whether a continuous stress field can also be found for f larger than f_1, which is far below, e.g., the critical value $f \approx 0.15$ suggested by Tvergaard and Needleman (1984), on the basis of comparisons with experiments, to correspond to the onset of substantial void coalescence. Thus the objective of this work is to seek for $f > f_1$ possible completely continuous stress fields by relaxing the assumption that the material experiences plastic response at all angles about the tip, while maintaining the other assumptions reviewed above. Hence possible near-tip solution sector types for $f > f_1$ include the plastic generalized centered fan and constant stress types already analyzed, and now in addition a sector of purely elastic response.

Solutions involving such elastic sectors for stationary crack-tip fields in elastic-plastic materials have been exhibited in other contexts. For example, Gao's (1980) asymptotic mixed-mode plane strain near-tip solutions exhibited these, and Sakata et al.'s (1986) numerical finite element analysis of the same problem class also displayed a near-tip sector of elastic response. In a situation more similar to the present problem, Dong and Pan (1991) analyzed near-tip plane strain tensile crack fields in an elastic-plastic pressure-sensitive model based on a simple yield criterion that is a linear combination of the effective and hydrostatic stresses. For nonhardening materials, their solutions exhibit sectors of elastic response adjacent to the crack flanks, as do our solutions.

We here continue to consider a plane strain Mode I stationary crack in porous elastic-ideally plastic material with spherical microvoids uniformly distributed in the three dimensions so that the material is macroscopically homogeneous, isotropic, and hence so are its overall, or effective, elastic moduli. We assume that the material obeys Tvergaard's (1981, 1982) modification of Gurson's (1977) yield criterion and associated plastic flow rule, and we employ a small-displacement-gradient formulation. Thus for the same reasons stated in Section 7 of Part I, on the basis of full-field numerical finite element solutions referenced there, the present results are expected to be physically meaningful in an annular region surrounding a crack tip, whose inner radius is on the order of two to three times the crack-tip opening displacement and whose outer radius is sufficiently small compared with, e.g., the maximum plastic zone radius. For purely elastic deformations, generalized Hooke's Law is written in terms of the effective (macroscopic) moduli E (Young's modulus) and ν (Poisson's ratio) and hence applies to macroscopic stresses and strains.

Similarly to Part I, let Cartesian axes x_1, x_2 and x_3 be chosen so that x_3 and x_1 are parallel, respectively, to the crack front and the crack surfaces, the latter being assumed traction-free. Throughout the paper, components of tensors with respect to this Cartesian system will be denoted by Latin indices i, j, k, l with range 1, 2, 3; the summation convention for repeated subscripts applies to these indices. Let r, θ be polar coordinates

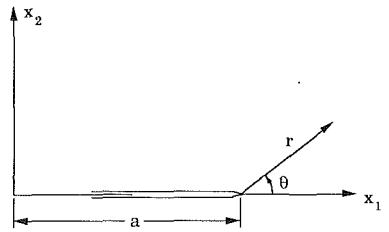


Fig. 1 Cartesian coordinates x_1, x_2, x_3 are fixed in the body; polar coordinates r, θ are centered at the crack tip; a measures crack length

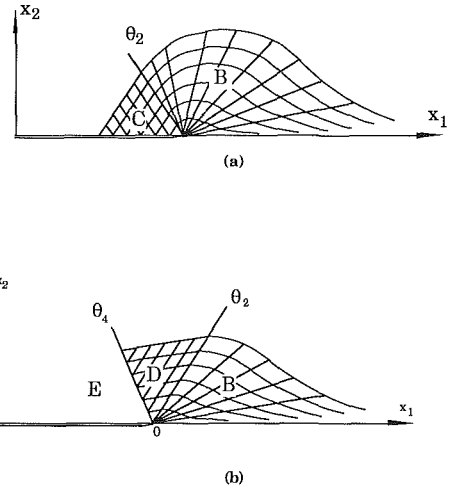


Fig. 2 (*a*) The limiting ($f = f_1$) generalized Prandtl stress field in terms of stress characteristics ($\theta_2 \approx 2.3378$); (*b*) the continuous asymptotic stress field configuration in terms of stress characteristics for $f_1 < f < 1/q_1$

in the x_1-x_2 plane and centered at the crack tip with $\theta = 0$ coinciding with the positive x_1-axis, as shown in Fig. 1.

As explained in Part I, the three types of fully plastic near-tip sector configuration derived there evolve consistently from one to the next as the porosity level increases. It is thus desired that the new continuous solutions for $f > f_1$ we seek here would reduce, as f approaches f_1 from above, to the limiting generalized Prandtl field that applies at $f = f_1$, as illustrated in Fig. 2(*a*). On the other hand, the structure of the plane-stress-like distribution, which is obtained by adding a plastic constant stress sector to the configuration of Fig. 2(*a*) for $f > f_1$, implies that a possible configuration for a *continuous* stress field for $f > f_1$ could be one or both of the following assemblies of those three different sectors: a generalized centered fan plastic sector B, beginning at the symmetry line ($\theta = 0$), followed either by a constant stress plastic sector D and then an elastic sector E adjacent to the crack surface, as shown in Fig. 2(*b*); or, by an elastic sector first and then a constant stress plastic sector which ends at the crack surface. However, numerical computations show that a solution with this latter configuration cannot exist because full stress continuity, stress symmetry and the traction-free crack surface boundary conditions demand a number of restrictions greater than that of the total undetermined constants; hence all the restrictions cannot be satisfied simultaneously. Thus, we shall investigate the first configuration in this paper. We define θ_2 and θ_4 to be the mutual borders between Sectors B and D, and D and E, respectively, as shown in Fig. 2(*b*).

2 Asymptotic Governing Equations and Stress Distributions

As noted in the Introduction, we have made here the same assumptions in plastically deforming near-tip sectors as we did

Downloaded 03 May 2010 to 171.66.16.245. Redistribution subject to ASME license or copyright; see http://www.asme.org/terms/Terms_Use.cfm

in Part I. Thus, the asymptotic governing equations in such sectors are exactly the same as those previously derived, and so are their stress field solutions; these are reviewed as in the following. Stresses in a purely elastic sector (with no prior plastic straining) are derived here; they must satisfy the equilibrium equations, plane strain and compatibility conditions, and meanwhile must not violate the yield condition.

2.1 Near-Tip Plastic Sectors. We showed in Part I that the asymptotic ($r\to 0$) governing equations in plastically deforming near-tip sectors with singular straining are

$$[\sigma'_{rr}+\sigma'_{\theta\theta}]\left\{3s_{rr}+q_1q_2f\sinh\left[\frac{q_2\sigma_{kk}}{2}\right]\right\}=0 \tag{1a}$$

$$3s_{33}+q_1q_2f\sinh\left[\frac{q_2\sigma_{kk}}{2}\right]=0 \tag{1b}$$

$$\sigma_{rr}-\sigma_{\theta\theta}+\sigma'_{r\theta}=0,\quad \sigma'_{\theta\theta}+2\sigma_{r\theta}=0 \tag{1c}$$

$$\sigma'_{11}\sin\theta=\sigma'_{12}\cos\theta,\quad \sigma'_{22}\cos\theta=\sigma'_{12}\sin\theta, \tag{1d}$$

where (1*b*) is the plane strain condition; (1*c*) and (1*d*) are the equilibrium equations in polar and Cartesian coordinates, respectively; and (1*a*) is a differential form of the Gurson-Tvergaard yield condition, having employed (1*b*). Stress components σ_{ij} are normalized by the matrix material's uniaxial yield stress. The notation σ'_{ij} is defined as

$$\sigma'_{ij}\equiv\lim_{r\to 0}\frac{\partial\sigma_{ij}(r,\theta)}{\partial\theta}, \tag{1e}$$

and $\mathbf{s}=\boldsymbol{\sigma}-\mathbf{I}\,\mathrm{trace}(\boldsymbol{\sigma})/3$ is the deviatoric stress tensor with $\mathbf{I}$ being the identity tensor.

As detailed in Part I, the only possible solutions to this equation set are plastic sectors in the form of either:

(*i*) *generalized centered fan type*, when the braced term in (1*a*) vanishes, and (1*b*) and (1*c*) are satisfied. When this sector type begins at the symmetry line $\theta=0$, the stresses are obtained by numerical integration of the rearranged asymptotic governing equations:

$$\sigma_{33}=\sigma_{rr} \tag{2a}$$

$$\sigma'_{r\theta}=\sigma_{\theta\theta}-\sigma_{rr} \tag{2b}$$

$$\sigma'_{\theta\theta}=-2\sigma_{r\theta} \tag{2c}$$

$$\sigma'_{rr}=\sigma_{r\theta}\frac{q_1q_2^2f\cosh\left[q_2\left(\sigma_{rr}+\frac{1}{2}\sigma_{\theta\theta}\right)\right]-2}{q_1q_2^2f\cosh\left[q_2\left(\sigma_{rr}+\frac{1}{2}\sigma_{\theta\theta}\right)\right]+1}, \tag{2d}$$

with the following boundary values at $\theta=0$ (explained in Part I):

$$\sigma_{r\theta}(0)=0 \tag{3a}$$

$$\sigma_{\theta\theta}(0)=\frac{2}{3}\left[Q+\frac{1}{q_2}\ln\left\{[(1+q_2^2)(1+q_1^2q_2^2f^2)]^{1/2}-1+q_2Q\right\}-\frac{1}{q_2}\ln(q_1q_2^2f)\right] \tag{3b}$$

$$\sigma_{33}(0)=\sigma_{rr}(0)=\sigma_{\theta\theta}(0)-Q \tag{3c}$$

where

$$Q=\frac{1}{q_2}\left\{2+q_2^2(1+q_1^2f^2)-2[(1+q_2^2)(1+q_1^2q_2^2f^2)]^{1/2}\right\}^{1/2}; \tag{3d}$$

or:

(*ii*) *constant stress plastic type*, when the first bracket in (1*a*) vanishes, and (1*b*) and (1*d*) are satisfied (characterized by $\sigma_{11}=$ constant, $\sigma_{22}=$ constant, $\sigma_{12}=\sigma_{21}=$ constant, and σ_{33} is also proved to be constant; see Part I). The polar components of stress thus have general (asymptotic) closed-form representations in terms of the variable θ and integration constants c_n (which must satisfy the plane strain condition (1*b*) and the yield condition):

$$\sigma_{rr}=c_1+c_2\cos 2\theta+c_4\sin 2\theta \tag{4a}$$

$$\sigma_{\theta\theta}=c_1-c_2\cos 2\theta-c_4\sin 2\theta \tag{4b}$$

$$\sigma_{r\theta}=-c_2\sin 2\theta+c_4\cos 2\theta \tag{4c}$$

$$\sigma_{33}=c_3. \tag{4d}$$

2.2 Near-Tip Elastic Sectors. As mentioned in the Introduction, generalized Hooke's Law in terms of effective elastic moduli applies here to macroscopic stresses and strains. This and the plane strain condition together imply

$$\sigma_{33}=\nu(\sigma_{rr}+\sigma_{\theta\theta}) \tag{5}$$

with which the compatibility equation in terms of stresses without body forces becomes, for arbitrary elastic moduli

$$\left(\frac{\partial^2}{\partial r^2}+\frac{1}{r}\frac{\partial}{\partial r}+\frac{1}{r^2}\frac{\partial^2}{\partial\theta^2}\right)(\sigma_{rr}+\sigma_{\theta\theta})=0. \tag{6}$$

It was proved in Part I that all components of stress at an arbitrary material point must be bounded; thus, a result proved by Drugan (1985) applies:

$$r\frac{\partial\sigma_{ij}}{\partial r}=o\left(\frac{1}{\ln(R/r)}\right)\quad\text{as}\quad r\to 0, \tag{7}$$

where R is a constant with length dimensions. Taking an r-partial derivative of this, multiplying the resulting equation by r, and then applying (7) gives

$$r^2\frac{\partial^2\sigma_{ij}}{\partial r^2}=o\left(\frac{1}{\ln(R/r)}\right)\quad\text{as}\quad r\to 0. \tag{8}$$

Therefore, after multiplying (6) by r^2, applying these asymptotic relations (7) and (8) to the resulting equation, and using notation like that of (1*e*) (i.e., $\sigma''_{ij}\equiv\lim_{r\to 0}[\partial^2\sigma_{ij}(r,\theta)/\partial\theta^2]$), the compatibility condition (6) takes the asymptotic ($r\to 0$) form

$$\sigma''_{rr}(\theta)+\sigma''_{\theta\theta}(\theta)=0. \tag{9}$$

Hence the asymptotic governing equations in an elastic sector are the equilibrium Eqs. (1*c*), the plane-strain condition (5) and compatibility (9), which have the following general solution for stresses in terms of the variable θ and integration constants A, B, C, and D:

$$\sigma_{rr}(\theta)=D+2C\theta+A\cos 2\theta+B\sin 2\theta \tag{10a}$$

$$\sigma_{\theta\theta}(\theta)=D+2C\theta-A\cos 2\theta-B\sin 2\theta \tag{10b}$$

$$\sigma_{r\theta}(\theta)=-C-A\sin 2\theta+B\cos 2\theta \tag{10c}$$

$$\sigma_{33}(\theta)=2\nu(D+2C\theta). \tag{10d}$$

These elastic sector stress expressions are the same as those obtained by Gao (1980) who simply *assumed* an asymptotic form for the Airy stress function.

3 Asymptotic Sector Assembly Procedure

We now attempt to establish a completely continuous asymptotic stress field for $f>f_1$ by near-tip assembly, in the manner illustrated in Fig. 2(*b*), of these three different stress sectors: a generalized centered fan, a constant stress plastic sector, and an elastic stress distribution. Hence all parameters to be determined are: A, B, C, D in (10); c_1, c_2, c_3, c_4 in (4); and θ_2 and θ_4 of Fig. 2(*b*). As shown in Part I, the governing equations require *all* components of stress to be continuous across the mutual border between a constant stress plastic sector and a generalized centered fan plastic sector (i.e., $\theta=\theta_2$), which, together with the assumption of stress continuity across the mu-

Downloaded 03 May 2010 to 171.66.16.245. Redistribution subject to ASME license or copyright; see http://www.asme.org/terms/Terms_Use.cfm

tual border between Sectors D and E (i.e., $\theta=\theta_4$) and the traction-free crack-face conditions, will be applied to determine all these unknown parameters. The parameters must be chosen such that $\theta_4 \geq \theta_2$ and the yield condition is not violated in Sector E, for a physically appropriate solution to exist.

Evidently, full stress continuity results in

$$[\![\sigma_{\theta\theta}+\sigma_{rr}]\!]=0 \quad \text{across} \quad \theta=\theta_2,\ \theta_4, \tag{11}$$

where

$$[\![\sigma(\theta)]\!] \equiv \sigma(\theta^+)-\sigma(\theta^-); \tag{12}$$

(11) leads, via (10a,b) and (4a,b), to

$$2c_1=2(D+2C\theta_4) \tag{13a}$$

$$2c_1=\sigma_{\theta\theta}(\theta_2^-)+\sigma_{rr}(\theta_2^-). \tag{13b}$$

Furthermore, continuity of σ_{33} across $\theta=\theta_2$, θ_4 together with (10d), (4d), and (2a) gives

$$c_3=2\nu(D+2C\theta_4)=\sigma_{rr}(\theta_2^-), \tag{14}$$

which, via (13), implies

$$\sigma_{\theta\theta}(\theta_2^-)=\frac{1-\nu}{\nu}\sigma_{rr}(\theta_2^-). \tag{15}$$

Application of this condition to the numerical integration of (2) in the generalized centered fan sector determines the value of θ_2, showing where that sector ends. The other unknown parameters in Sector D of Fig. 2(b) are then immediately determined by enforcing full stress continuity across θ_2, which implies that both the plane strain and yield conditions are automatically satisfied and results in

$$c_1=\frac{1}{2}[\sigma_{\theta\theta}(\theta_2^-)+\sigma_{rr}(\theta_2^-)] \tag{16a}$$

$$c_2=-\sigma_{r\theta}(\theta_2^-)\sin 2\theta_2+\frac{1}{2}[\sigma_{rr}(\theta_2^-)-\sigma_{\theta\theta}(\theta_2^-)]\cos 2\theta_2 \tag{16b}$$

$$c_3=\sigma_{rr}(\theta_2^-) \tag{16c}$$

$$c_4=\sigma_{r\theta}(\theta_2^-)\cos 2\theta_2+\frac{1}{2}[\sigma_{rr}(\theta_2^-)-\sigma_{\theta\theta}(\theta_2^-)]\sin 2\theta_2. \tag{16d}$$

To determine the remaining unknown parameters, we first apply the traction-free boundary conditions at $\theta=\pi$ using (10b,c):

$$B=C; \quad A=D+2\pi C. \tag{17a,b}$$

Also, continuity of $(\sigma_{rr}(\theta)-\sigma_{\theta\theta}(\theta))$ and $\sigma_{12}(\theta)$ across θ_4 altogether with (17), (10a,b,c) and (4a,b,c) results in

$$[c_2-(D+2\pi C)]\cos 2\theta_4+(c_4-C)\sin 2\theta_4=0 \tag{18a}$$

$$C(1-\cos 2\theta_4)=c_4. \tag{18b}$$

Obviously, for $\theta_4 \neq 0$ or π, the above can be solved for D and C in terms of c_2, c_4 and θ_4; these expressions are used in (13a) to obtain an algebraic equation for θ_4 alone. The resulting equations are

$$c_1-c_2+c_4\frac{\sin 2\theta_4+2(\pi-\theta_4)}{1-\cos 2\theta_4}=0 \tag{19}$$

$$D=c_2-\frac{\sin 2\theta_4+2\pi}{1-\cos 2\theta_4}c_4 \tag{20a}$$

$$C=\frac{1}{1-\cos 2\theta_4}c_4. \tag{20b}$$

By solving (19) numerically (having substituted (16)), satisfying $0\leq\theta_2\leq\theta_4\leq\pi$, the parameters A, B, C, D will be determined by using (20) and then (17). These results are acceptable if and only if the stresses in (10) with the coefficients given by (20) and (17) do not violate yield for all $\theta_4\leq\theta\leq\pi$.

As far as the special case $\theta_4=\pi$ is concerned, one observes that in the limit $\theta_4\to\pi$, l'Hopital's rule shows that in (19) the term $[\sin 2\theta_4+2(\pi\theta_4)]/[1-\cos 2\theta_4]$ has a limit of zero, which together with the boundedness of all the c_n's given by (16) implies

$$\lim_{\theta_4\to\pi} c_1=\lim_{\theta_4\to\pi} c_2. \tag{21}$$

On the other hand, (18a) and (13a) show, via (21) and the boundedness of c_4, that $C\sin 2\theta_4\to 0$, or $C=o(1/\sin\theta_4)$ as $\theta_4\to\pi$. Application of this asymptotic equation to (18b) further implies that $c_4=o(\sin\theta_4)$; that is

$$\lim_{\theta_4\to\pi} c_4=0. \tag{22}$$

Evidently, (21) and (22) show that $\theta_4=\pi$ would result in a physically appropriate solution if and only if $c_1=c_2$ and $c_4=0$, which are indeed the two traction-free conditions on the crack surface when the elastic sector vanishes, and thus the constant stress Sector D ends at the crack surface. In this situation, the features of stresses in Sector D here and those in Sector C in the limiting generalized Prandtl field of Fig. 2(a) are the same. Numerical calculations show that this situation can occur, with the complete solution reducing precisely to the limiting Prandtl field, if and only if the porosity f decreases to f_1. This indicates a smooth evolution from the continuous generalized Prandtl field to the current continuous solution.

Now consider the other special case, namely $\theta_4=0$. As a limiting case of the solution having the configuration of Fig. 2(b), this could be true only if $\theta_2=0$ holds as well, which requires $\nu=\sigma_{rr}(0)/[\sigma_{\theta\theta}(0)+\sigma_{rr}(0)]$ as detailed later. Consequently, (16d) gives $c_4=0$ and thus (18b) demands C be finite, while (18a) and (13a) together imply $D=c_1$ and $C=(c_1-c_2)/2\pi$. With these and (17) and the particular value of ν as well, full stress continuity across the internal borders is satisfied and so are the traction-free crack surface and stress symmetry conditions. However, the numerical computations to be described show that this purely elastic stress field as a limiting case of the solution we seek here cannot occur.

4 Existence of the Solution and Solvability Conditions

In order to obtain a complete stress field with the assumed configuration shown in Fig. 2(b) it is necessary for the key Eqs. (15) and (19), which determine the sector boundary locations θ_2 and θ_4, respectively, to have solutions satisfying the basic requirement

$$0\leq\theta_2\leq\theta_4\leq\pi. \tag{23}$$

We first prove that for each fixed value of f in the range

$$f_1\leq f<1/q_1, \tag{24}$$

(15) has a unique solution for θ_2 for a certain *range* of Poisson's ratios. Recalling the plane strain condition in the generalized centered fan sector (see Part I), we have

$$\sigma_{\theta\theta}-\sigma_{rr}=q_1q_2f\sinh\left[q_2\left(\sigma_{rr}+\frac{1}{2}\sigma_{\theta\theta}\right)\right]. \tag{25}$$

With reference to the numerical calculations of Part I, we found that for every fixed f satisfying (24), there is a unique $0<\bar{\theta}(f)<\pi$ in a generalized centered fan sector bordering $\theta=0$ such that $\sigma_{kk}(\bar{\theta})=0$ and $\sigma_{\theta\theta}(\bar{\theta})=0=\sigma_{rr}(\bar{\theta})$; and for all $0\leq\theta<\bar{\theta}(f)$, $\sigma_{kk}(\theta)>0$, $\sigma_{rr}(\theta)>0$ and $\sigma_{\theta\theta}(\theta)>0$, which together with (25) indicates $\sigma_{\theta\theta}(\theta)>\sigma_{rr}(\theta)$. Also, the continuous function $\sigma_{\theta\theta}(\theta)/\sigma_{rr}(\theta)$ decreases monotonically as θ increases. Thus by using these results and rewriting (15) as

$$\frac{1}{\nu}=1+\frac{\sigma_{\theta\theta}(\theta_2^-)}{\sigma_{rr}(\theta_2^-)}, \tag{26}$$

one can easily find that $1+[\sigma_{\theta\theta}(\theta_2^-)/\sigma_{rr}(\theta_2^-)]>2$, and hence for each f in the range (24) and each $\sigma_{rr}(0)/[\sigma_{\theta\theta}(0)+\sigma_{rr}(0)]\leq\nu<(1/2)$, there is a unique $\theta_2\in(0,\ \bar{\theta}(f))$ such that (26), or (15), holds; and the larger the ν, the larger the value of θ_2. It is noticed that for $\theta_2=0$ with $\nu=\sigma_{rr}(0)/[\sigma_{\theta\theta}(0)+\sigma_{rr}(0)]$, the generalized

Downloaded 03 May 2010 to 171.66.16.245. Redistribution subject to ASME license or copyright; see http://www.asme.org/terms/Terms_Use.cfm

centered fan sector vanishes. It is also noticed that ν must be less than 1/2, which means that the porous material considered here must also be elastically compressible. In fact, as mentioned in the Introduction, for porous materials the ν used here is indeed the macroscopic (effective) Poisson's ratio and hence it is smaller than that of the matrix material, even if the matrix material is elastically incompressible, because material with nonzero porosity is no longer macroscopically elastically incompressible.

To investigate conditions under which (19) will have solutions $\theta_4 \in (0, \pi)$, we first rewrite it, for $c_4 \neq 0$, as

$$\frac{c_1 - c_2}{c_4} + \frac{\sin 2\theta_4 + 2(\pi - \theta_4)}{(1 - \cos 2\theta_4)} = 0, \tag{27}$$

and we define

$$\alpha = \frac{c_1 - c_2}{c_4}, \tag{28a}$$

$$G(x, \alpha) = \alpha + \frac{\sin 2x + 2(\pi - x)}{(1 - \cos 2x)}. \tag{28b}$$

Thus the root of Eq. (27) is the same as the zero point of the function $G(x, \alpha)$; the latter can be more easily studied by analyzing the features of $G(x, \alpha)$. Evidently, via (28b), we have for each fixed α

$$G(0, \alpha) = +\infty, \quad G(\pi, \alpha) = \alpha. \tag{29}$$

Also the function $G(x, \alpha)$ decreases monotonically on the interval $[0, \pi]$ for each fixed α since for every $x \in (0, \pi)$ its first-order derivative with respect to x is always negative:

$$\frac{\partial G}{\partial x}(x, \alpha) = -\frac{2}{\sin^3 x}[\sin x + \cos x(\pi - x)] < 0. \tag{30}$$

Hence, (27) will have a unique solution on the interval $(0, \pi)$ if and only if $\alpha < 0$, which via (28a) requires $(c_1 - c_2)/c_4 < 0$ (according to (4), this means that σ_{22} and σ_{12} in the constant stress plastic Sector D must have opposite signs), and it will have a root $x = \pi$ and $\alpha = 0$. This latter case, as mentioned earlier, cannot result in an acceptable stress field unless both the conditions $c_1 = c_2$ for $c_4 = 0$, representing the traction-free boundary conditions, can be satisfied.

As regards the special situation $c_4 = 0$, (18b) demands either $C = 0$, or $\theta_4 = 0$ or π. With $C = 0$ and $c_4 = 0$, (17a) gives $B = 0$; (18a) and (17b) require $A = D = c_2$, while 13(a) and (17b) demand $A = D = c_1$. Thus if $c_1 \neq c_2$, no such solution can exist; otherwise (10) gives, after substituting all these results for those parameters, exactly the same stress distribution in the elastic Sector E as that in the constant stress Sector D given by (4) with $c_4 = 0$ and $c_1 = c_2$. In this case, θ_4 is arbitrary, and indeed Sectors E and D join to become one constant stress plastic sector; the features of the entire stress field are hence similar to those of the limiting Prandtl field of Fig. 2(a) (see Part I). Similarly, as in Section 3, $\theta_4 = \pi$ with $c_4 = 0$ may lead to a solution if and only if $c_1 = c_2$. As mentioned previously, this will take place only when f approaches f_1. However, with $\theta_4 = 0$, one has to require $\theta_2 = 0$, otherwise no solution will exist.

Thus we have shown that there is a unique θ_2 for each f in the range (24) and some $\sigma_{rr}(0)/[\sigma_{\theta\theta}(0) + \sigma_{rr}(0)] < \nu < 1/2$; and with $(c_1 - c_2)/c_4 < 0$ there is a unique $\theta_4 \in (0, \pi)$. As long as (23) is satisfied and yield is not violated in the elastic Sector E, an acceptable solution for such an f and ν is thus found.

5 Results

Since the stresses in the generalized centered fan sector must be determined by numerical integration, all the unknown parameters satisfying (15), (16), (17), (19), (20), and (23) are thus numerically determined. The results show that a stress field with the configuration illustrated in Fig. 2(b) does exist for all f in the range (24) and for certain ranges of Poisson's ratio which depend on the value of f. The results also indicate that the locations of both internal boundaries θ_2 and θ_4 and the angular extent of each of the sectors are strongly influenced by not only the void volume fraction f but also Poisson's ratio ν: both θ_2 and θ_4 decrease as f increases (see Table 1); but for each fixed f, they increase as Poisson's ratio does on its corresponding range, as do the angular spans of the constant stress plastic Sector D and the generalized centered fan Sector B. The angular extent of the elastic Sector E decreases as ν increases. These trends will be seen in Figs. 3 and 4.

As regards the solution existence range, the results clearly indicate that for each f in the range (24), there is a smallest value of ν, which is larger than $\sigma_{rr}(0)/[\sigma_{\theta\theta}(0) + \sigma_{rr}(0)]$ and is here called $\nu_{\min}$, at which $\theta_4 = \theta_2$, meaning the constant stress plastic Sector D vanishes, and below which $\theta_4 < \theta_2$ so that the solution does not hold. In this situation, both θ_4 and θ_2 attain their smallest values over the interval $(\nu_{\min}, \nu_{\max})$, as defined later. Similarly, there is a $\nu_{\max}$ such that if $\nu > \nu_{\max}$, the yield condition is violated in the elastic sector. Values of both $\nu_{\min}$ and $\nu_{\max}$ are dependent on the void volume fraction f, which indicates in one way the inner link between the macroscopic elastic moduli and the porosity level. Therefore, the solution exists only on the interval $(\nu_{\min}, \nu_{\max})$, and the extent of this interval varies with f: it is nearly 0 in the limits $f \to f_1$ and $f \to 1/q_1$. It is also observed that both the values of $\nu_{\min}$ and $\nu_{\max}$ decrease as f increases. This $\nu_{\max}$ is smaller than 1/2, the value of Poisson's ratio for elastically incompressible materials; this shows that in the present $f > 0$ analysis the material must be macroscopically elastically compressible for a solution to exist.

Since the solution can exist only for $\nu \leq \nu_{\max}(f)$, one wonders what this $\nu_{\max}(f)$ means. Does it correspond to the actual

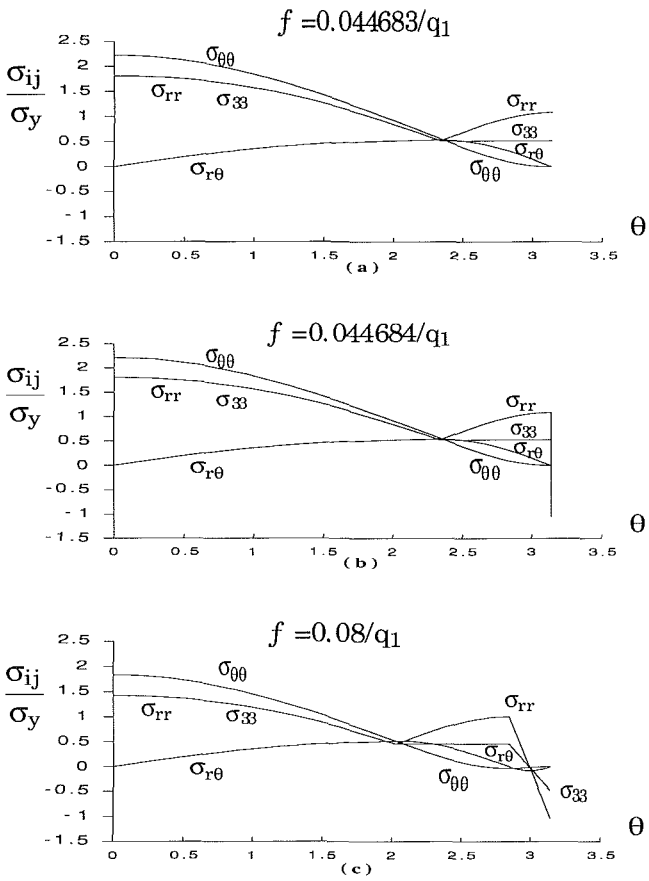


Fig. 3 Polar components of stress as functions of angle θ with the solution configuration of Fig. 2(b): (a) for $f = f_1$ (or, $f \to f_1^+$), with $\nu \approx .481611$, $\theta_2 \approx 2.3378$, $\theta_4 \approx \pi$; (b) for $f \approx .044684/q_1$, with $\nu \approx .481610$, $\theta_2 \approx 2.33779$, $\theta_4 \approx 3.14157$; (c) for $f \approx .08/q_1$, with $\nu \approx .468081$, $\theta_2 \approx 2.02623$, $\theta_4 \approx 2.84110$

Downloaded 03 May 2010 to 171.66.16.245. Redistribution subject to ASME license or copyright; see http://www.asme.org/terms/Terms_Use.cfm

effective Poisson's ratio for this porous material? The approximate effective elastic moduli in porous material have been investigated by several researchers including, for example, Zhao et al. (1989). By employing their work, we determine the effective Poisson's ratio, ν_e (see the Appendix and Table 1), for the porous material considered in this study. Specifically, when the matrix material is assumed to be elastically incompressible, as in our solutions, ν_e values for small f are very close to our ν_{max}. For instance, for $f=f_1$, the relative difference $(\nu_e-\nu_{max})/\nu_{max}\approx .006$; and for $f\approx .25/q_1$, $(\nu_e-\nu_{max})/\nu_{max}\approx .061$. These comparisons show that $\nu_{max}(f)$ appears to be the actual effective Poisson's ratio for a given f. Both ν_e and ν_{max} for selected f values are shown in Table 1.

An interesting related phenomenon is that as $f\to f_1$, θ_2 and θ_4 corresponding to $\nu_{max}(f)=.481611$ approach 2.3378 and π, respectively, and the elastic sector vanishes in this limit. Also conditions (21) and (22) are satisfied. This shows that the solution family corresponding to the set of $\nu_{max}(f)$ reduces to the limiting generalized Prandtl field of Fig. 2(*a*), derived in Part I, as $f\to f_1$. Thus this solution family will be taken as the new continuous solutions for those porosities in the range (24), since it evolves consistently from the generalized Prandtl field. Stress distributions for selected values of f corresponding to this solution family having $\nu=\nu_{max}$ are displayed in Figs. 3 and 4.

One observes, see e.g., Fig. 3(*b*), that for f very close to f_1^+, the angular extent of the elastic sector is almost zero: for $f\approx f_1+1.0\times10^{-6}/q_1$, $\theta_4\approx\pi-2.0\times10^{-5}$ rad., and stress components σ_{rr} and σ_{33} seem to "jump" from positive to negative values within a small transition zone of angular width less than 2.0×10^{-5} radian. As f increases, θ_4 corresponding to $\nu_{max}(f)$ decreases (see Table 1) so that the angular span of the elastic sector increases, and the apparent "stress jump" is smoothed out.

The solution configuration shown in Fig. 2(*b*) is maintained for all f in the range (24). In addition, as predicted by the yield criterion, the magnitudes of the stress components and the hydrostatic stress decrease as the porosity level increases. That this decrease in hydrostatic stress level with increasing porosity is substantial is illustrated in Fig. 5, which shows hydrostatic stress directly ahead of the tip as a function of f. The superscripts I and II correspond to the predictions from the fully plastic solutions of Part I and those of the present solutions, respectively. The close agreement between these two predictions is remarkable, especially over the practically important range of, say, $0\le f\le 0.15$.

Comparing Fig. 5 in Part I with Fig. 3 here, one observes that the border between the generalized centered fan sector and the constant stress plastic sector shifts backward substantially, and what were stress jumps in the fully plastic solutions are now rapid but continuous variations in the elastic stress sector. Thus the extent of the generalized centered fan sector

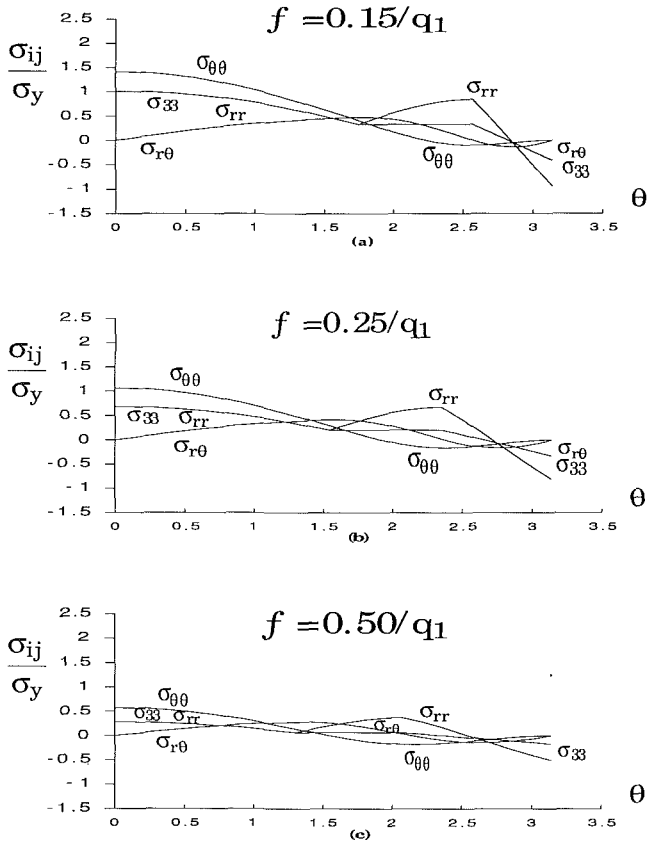


Fig. 4 Polar components of stress as functions of angle θ with the solution configuration of Fig. 2(*b*) (continued): (*a*) for $f\approx .15/q_1$, with $\nu\approx .443256$, $\theta_2\approx 1.73909$, $\theta_4\approx 2.56225$; (*b*) for $f\approx .25/q_1$, with $\nu\approx .409936$, $\theta_2\approx 1.53475$, $\theta_4\approx 2.35114$; (*c*) for $f\approx .50/q_1$ with $\nu\approx .332823$, $\theta_2\approx 1.29846$, $\theta_4\approx 2.05549$

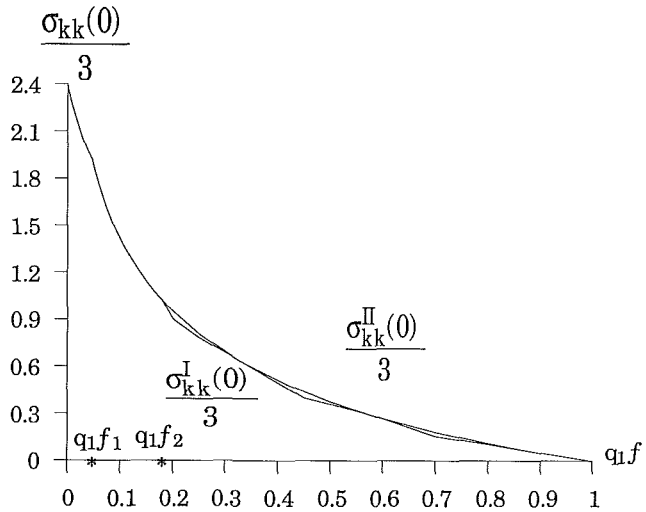


Fig. 5 Hydrostatic stress level (normalized by the matrix material's uniaxial yield stress) directly ahead of the crack tip versus void volume fraction, as predicted by the fully plastic solutions of Part I (superscript I) and the present elastic-plastic solutions (superscript II).

Table 1 Parameter values for fully continuous stress field solutions having the configuration of Fig. 2(*b*) ($f\ge f_1$)

q_1f	θ_2(rad)	θ_4(rad)	c_1	c_2	c_3	c_4	A	B=C	D	ν_{max}	ν_e
.044683	2.33780	3.14159	.5422	.5422	.52222	.00000				.48161	.48449
.044684	2.33779	3.14156	.54216	.54216	.52222	-.00001	-.63863	-13442	84458	.48161	.48449
.080000	2.02623	2.84110	.48623	.42701	.45519	-.29207	-.51550	-1.6668	9.9574	.46808	.47379
.150000	1.73909	2.56225	.37092	.19598	.32883	-.43262	-.46529	-.72169	4.0692	.44326	.45574
.250000	1.53475	2.35114	.25710	.01618	.21079	-.41887	-.39847	-.41468	2.2070	.40994	.43541
.500000	1.29846	2.05549	.10788	-.11400	.07181	-.25779	-.24974	-.16463	.78469	.33282	.40146

Downloaded 03 May 2010 to 171.66.16.245. Redistribution subject to ASME license or copyright; see http://www.asme.org/terms/Terms_Use.cfm

is enlarged, the magnitude of the stress in the constant stress plastic sector is reduced and hence the stresses become negative near the crack surfaces.

Acknowledgments

Support of this work by the Mechanics Division of the Office of Naval Research under Grants N00014-89-J-1206 and N00014-92-J-1314 and by the National Science Foundation under Grant MSS-8552486 is gratefully acknowledged.

References

Dong, P., and Pan, J., 1991, "Elastic-Plastic Analysis of Cracks in Pressure-Sensitive Materials," *International Journal of Solids and Structures*, Vol. 28, pp. 1113–1127.

Drugan, W. J., 1985, "On the Asymptotic Continuum Analysis of Quasi-Static Elastic-Plastic Crack Growth and Related Problems," ASME JOURNAL OF APPLIED MECHANICS, Vol. 52, pp. 601–605.

Drugan, W. J., and Miao, Y., 1992, "Influence of Porosity on Plane Strain Tensile Crack Tip Stress Fields in Elastic-Plastic Materials: Part I," ASME JOURNAL OF APPLIED MECHANICS, Vol. 59, pp. 559–567.

Gao, Y. C., 1980, "Elastic-Plastic Field of a Crack Before Growing in Perfectly Plastic Medium," *Acta Solid Mechanica Sinica*, Vol. 1, pp. 69–75.

Gurson, A. L., 1977, "Continuum Theory of Ductile Rupture by Void Nucleation and Growth: Part I—Yield Criteria and Flow Rules for Porous Ductile Media," ASME *Journal of Engineering Materials and Technology*, Vol. 99, pp. 2–15.

Hutchinson, J. W., 1968, "Plastic Stress and Strain Fields at a Crack Tip," *Journal of the Mechanics and Physics of Solids*, Vol. 16, pp. 337–347.

Rice, J. R., 1967, "Mechanics of Crack Tip Deformation and Extension by Fatigue," *Fatigue Crack Propagation*, ASTM-STP 415, American Society for Testing and Materials, Philadelphia, pp. 247–311.

Rice, J. R., 1982, "Elastic-Plastic Crack Growth," *Mechanics of Solids: The R. Hill 60th Anniversary Volume*, H. G. Hopkins and M. J. Sewell, eds., Pergamon Press, Oxford, pp. 539–562.

Sakata, M., Abe, H., and Tanaka, S., 1986, "Numerical Analysis of Blunting of a Crack Tip in a Ductile Material Under Small-Scale Yielding and Mixed Mode Loading," *Computational Mechanics*, Vol. 1, pp. 11–19.

Tvergaard, V., 1981, "Influence of Voids on Shear Band Instabilities Under Plane Strain Conditions," *International Journal of Fracture*, Vol. 17, pp. 389–407.

Tvergaard, V., 1982, "On Localization in Ductile Materials Containing Spherical Voids," *International Journal of Fracture*, Vol. 18, pp. 237–252.

Tvergaard, V., and Needleman, A., 1984, "Analysis of the Cup-Cone Fracture in a Round Tensile Bar," *Acta Metallurgica*, Vol. 32, pp. 157–169.

Zhao, Y. H., Tandon, G. P., and Weng, G. J., 1989, "Elastic Moduli for a Class of Porous Materials," *Acta Mechanica*, Vol. 76, pp. 105–130.

APPENDIX

The Effective Poisson's Ratio

For a material which is an aggregate of an isotropic elastic matrix and three-dimensional randomly distributed voids, the effective bulk and shear moduli are given approximately, as suggested in Zhao et al. (1989), by

$$\frac{\kappa}{\kappa_0}=\frac{1}{1+fp}, \qquad \frac{\mu}{\mu_0}=\frac{1}{1+fq}, \tag{A1}$$

where p and q are functions of Poisson's ratio, and quantities with or without the subscript "0" denote, respectively, those of matrix material and the corresponding effective one. With reference to Zhao et al. these functions simplify, for spherical voids, to

$$p=\frac{3}{2}\frac{1-\nu_0}{1-2\nu_0}, \qquad q=14f\frac{1-\nu_0}{7-5\nu_0}. \tag{A2}$$

By using the definition of the bulk modulus and the relation among the elastic moduli, and via (A2), (A1) become

$$\frac{1-2\nu_0}{1-2\nu}\frac{E}{E_0}=\frac{\kappa}{\kappa_0}=\frac{2(1-2\nu_0)}{2(1-2\nu_0)+3f(1-\nu_0)}, \tag{A3a}$$

$$\frac{1+\nu_0}{1+\nu}\frac{E}{E_0}=\frac{\mu}{\mu_0}=\frac{7-5\nu_0}{7-5\nu_0+14f(1-\nu_0)}. \tag{A3b}$$

Elimination of E/E_0 from the above equations and rearrangement of the resulting equation gives the effective Poisson's ratio as a function of that of the matrix material and the void volume fraction:

$$\nu_e=\frac{6(7-5\nu_0)\nu_0+f(1-\nu_0)(7+43\nu_0)}{6(7-5\nu_0)+f(1-\nu_0)(77+41\nu_0)}. \tag{A4}$$

For an elastically incompressible matrix material ($\nu_0=1/2$), the effective Poisson's ratio, via (A4), becomes

$$\nu_e=\frac{18+19f}{36+65f}. \tag{A5}$$

Downloaded 03 May 2010 to 171.66.16.245. Redistribution subject to ASME license or copyright; see http://www.asme.org/terms/Terms_Use.cfm

Tunneling Cracks in Constrained Layers

S. Ho[1]

Z. Suo
Mem. ASME.

Mechanical Engineering Department,
University of California,
Santa Barbara, CA 93106-5070

A thin, brittle layer bonded between tougher substrates is susceptible to cracking under residual and applied stresses. Such a crack initiates from an equi-axed flaw, confined by the substrates, tunneling in the brittle layer. Although tunneling is a three-dimensional process, the energy release rate at the front of a steady-state tunnel can be computed using plane strain fields. Several technically important problems are analyzed, including tunnels in adhesive joints, shear fracture, and kinked tunnels in a reaction product layer. The concept is finally applied to microcracking in brittle matrix composites caused by thermal expansion mismatch.

Introduction

Layered materials subjected to residual and applied stresses are susceptible to cracking. Depending on the application, such cracks can either fail device or degrade material. For example, cracks in multilayer capacitors form easy conducting paths, leading to electrical leak. For metal matrix composites, microcracks in fiber coating can be the nucleation sites for fatigue cracks in the matrix. A commonly observed cracking process, tunneling, is examined in this paper.

Figure 1 illustrates a thin, brittle layer of thickness h, bonding two tougher substrates, subjected to both applied and residual stresses. If the net stress in the layer is tensile and sufficiently high, it drives pre-existing flaws to tunnel through the layer. The energy release rate at the *front*, G_F, varies from point to point, and depends on the tunnel length a. A long tunnel ($a/h \to \infty$) reaches a *steady-state*: the front self-adjusts to a shape such that G_F is the same at every point along the front, which no longer depends on the tunnel length, nor on the initial flaw geometry. This steady-state energy release rate is denoted as G_{ss} in Fig. 1.

Two facts, to be elaborated upon later suggest that G_{ss} is suitable for design of constrained thin layers. First, G_{ss} is relatively easy to compute (only plane-strain analyses are required). Second, the steady-state is readily reached if pre-existing flaw size is close to layer thickness. These concepts have evolved from studies of layered materials of many varieties: composite laminates (Parvizi et al., 1978; Wang, 1984; Dvorak and Laws, 1986; Fang et al., 1989), thin films (Gille, 1985; Hu et al., 1988; Bueth, 1992; Ye et al., 1992), and brittle adhesive layers (Suo, 1990).

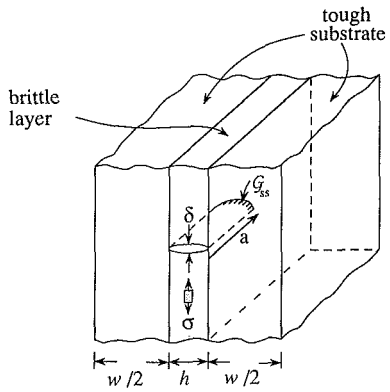


Fig. 1 A crack tunnels in a bonded layer

In this paper a new formula for G_{ss}, convenient for finite element analyses, is presented. We then discuss tunnel nucleation and the relevance of G_{ss} in design. The versatility of the concepts is demonstrated by several technically significant problems, including cracking in adhesive joints, shear fracture, and kinked cracks. The concepts are finally applied to microcracking in brittle matrix composites caused by thermal expansion mismatch.

Driving Force for Steady-State Tunneling

As sketched in Fig. 1, tunneling is a three-dimensional process. However, when the steady-state is reached, i.e., as $a/h \to \infty$, G_{ss} can be calculated using plane-strain elasticity solutions. Two alternative formulas are derived below. The tunnel is assumed to be perfectly constrained at the edges so that neither interface nor substrates crack. The significance of interface debonding and substrate cracking is reported elsewhere (Ye et al., 1992).

For such a semi-infinite tunnel the process that the front advances a unit distance is equivalent to (i) remove a unit thickness of material far ahead of the tunnel and, (ii) append a unit thickness of material in the wake. Let U be the difference in the strain energy stored in the two slices. By definition, it follows that

---

[1] Present address: Department of Theoretical and Applied Mechanics, University of Illinois, Urbana, IL 61801.

Contributed by the Applied Mechanics Division of THE AMERICAN SOCIETY OF MECHANICAL ENGINEERS for publication in the ASME JOURNAL OF APPLIED MECHANICS.

Discussion on this paper should be addressed to the Technical Editor, Professor Lewis T. Wheeler, Department of Mechanical Engineering, University of Houston, Houston, TX 77204-4792, and will be accepted until four months after final publication of the paper itself in the ASME JOURNAL OF APPLIED MECHANICS.

Manuscript received by the ASME Applied Mechanics Division, May 30, 1991; final revision, Aug. 17, 1992. Associate Technical Editor: F. Y. M. Wan.

Copyright © 1993 by ASME
Downloaded 03 May 2010 to 171.66.16.245. Redistribution subject to ASME license or copyright; see http://www.asme.org/terms/Terms_Use.cfm

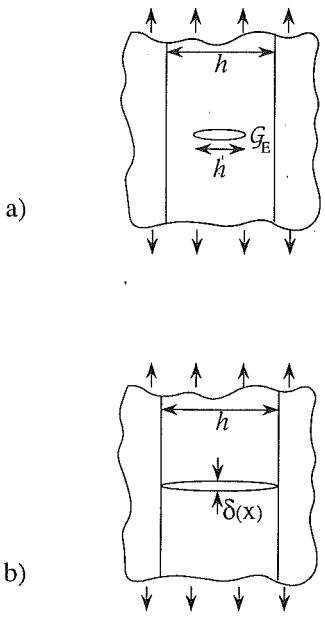


Fig. 2 (*a*) A plane-strain crack of size $h' < h$ used for formula (2); (*b*) a plane-strain crack of size h used for formula (3)

$$G_{ss} = U/h. \tag{1}$$

Observe that U equals the strain energy increase, at constant applied stress, due to introduction of a plane-strain crack in the unit slice. Let G_E be the energy release rate at the *edge* of a plane-strain crack of width $h' < h$ (Fig. 2(*a*)). It has been shown that (Gille, 1985; Dvorak and Laws, 1986)

$$G_{ss} = \frac{1}{h}\int_0^h G_E(h')dh'. \tag{2}$$

This formula requires G_E for plane-strain cracks of *various* width, $0 < h' < h$. As pointed out by these authors, such information is available in the literature only for a few inhomogeneous systems within limited parameter ranges, and finite element computation of G_E for various crack lengths is tedious.

Alternatively, U equals the work done by the stress through the crack opening (Fig. 2(*b*)), so that

$$G_{ss} = \frac{1}{2h}\int_0^h \sigma(x)\delta(x)dx. \tag{3}$$

Here $\sigma(x)$ is the stress distribution on the prospective crack plane prior to cracking; and $\delta(x)$ is the opening profile in the wake. Although (2) and (3) are equivalent, the latter is considerably more efficient in computation, since only two instead of many configurations need be analyzed: the stress in the uncracked body and the displacement for a plane-strain crack of *final width* h (Fig. 2(*b*)). Each of the two independent problems is under plane-strain conditions readily analyzed by commercial finite element codes.

Both (2) and (3) are valid for linear elastic systems uniform in geometry, material, and loading along the tunneling direction. In the following, (2) is used if G_E for the corresponding plane-strain cracks, with width varying from zero to the final tunnel size, is available in the literature; but (3) is used whenever finite element analysis is required.

Tunnel Nucleation

Tunnel nucleation is a complicated process. The nature of pre-existing flaws plays a predominant role—a gas bubble would behave differently from a microcrack. Several idealizations are invoked as follows. The pre-existing flaw is taken

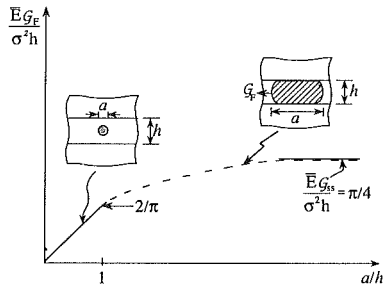


Fig. 3 The frontal energy release rate increases with the tunnel length, approaching quickly to an asymptote

to be a penny-shaped crack of initial diameter, a_0, less than layer thickness (Fig. 3). Some time-dependent subcritical cracking mechanism is assumed, so that the flaw grows slowly into a long tunnel under a constant applied stress, σ. The thin layer and the substrates are assumed to have identical elastic constants, and substrates are semi-infinite. The main objective of the following discussion is to provide a rough estimate of the tunnel length needed to attain the steady-state. None of the foregoing simplifications will change the conclusions qualitatively.

Let a be the current size of the crack (Fig. 3). When $a/h < 1$, the growing crack remains penny-shaped, since the energy release rate is the same at every point along the front. This energy release rate is given by (Tada et al., 1985)

$$G_F = \frac{2}{\pi}\sigma^2 a/\bar{E} \tag{4}$$

with $\bar{E} = E/(1-\nu^2)$, E and ν being Young's modulus and Poisson's ratio. Equation (4) is the straight line in Fig. 3, up to $a/h = 1$. After touching the interfaces, the crack is confined by the tough substrates and becomes noncircular, so that (4) is not valid when $a/h > 1$.

The crack will finally become a long tunnel and reach the steady-state. To compute G_{ss}, the classical solution is needed for G_E of a plane-strain crack of width h' (Fig. 2(*a*)):

$$G_E = \frac{\pi}{2}\sigma^2 h'/\bar{E}. \tag{5}$$

Integral (2) gives

$$G_{ss} = \frac{\pi}{4}\sigma^2 h/\bar{E}. \tag{6}$$

This result is indicated in Fig. 3 as the asymptotic value for $a/h \to \infty$.

Observe that the solutions for two limiting cases, $a/h = 1$ and $a/h \to \infty$, differ only by 23 percent. Consequently, for practical purposes, the tunnel attains the steady-state as soon as $a/h \sim 1$. The fact that the solution around $a/h \approx 1$ depends on the initial flaw geometry and the growth law of subcritical cracking discourages further elaboration in this region. The dashed line in Fig. 3 is the anticipated trend.

Now consider a brittle layer without subcritical cracking mechanism, but with a well-defined fracture energy Γ—that is, the crack will not grow if $G_F < \Gamma$. Following Dvorak and Laws (1986), we distinguish *thin* and *thick* layers by the ratio of the pre-existing flaw size to the layer thickness, a_0/h.

For a *thick* layer, where $a_0/h \ll$, the critical stress for the flaw to grow is governed by the flaw size

$$\sigma_c = (\pi\Gamma\bar{E}/2a_0)^{1/2}. \tag{7}$$

As suggested by Fig. 3, under a constant applied stress $\sigma = \sigma_c$, the flaw grows dynamically into a long tunnel. For example, the flaw size for a dense ceramic scales with grain diameter, typically $a_0 = 1 \sim 10$ μm. If the layer thickness is much larger than the grain diameter, the stress needed to nucleate a tunnel

Downloaded 03 May 2010 to 171.66.16.245. Redistribution subject to ASME license or copyright; see http://www.asme.org/terms/Terms_Use.cfm

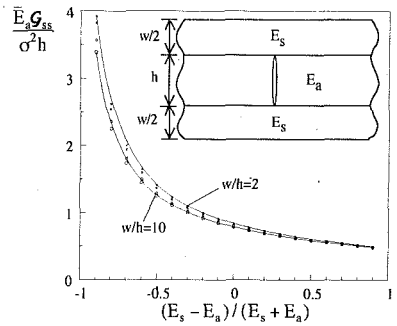


Fig. 4 Driving force for tunneling in an adhesive layer

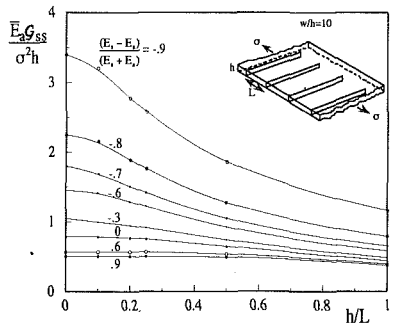


Fig. 5 Driving force for periodic tunnels

is given by (7). Consequently, the critical stress for a thick layer is identical to the strength of the material in bulk.

For a *thin* bonded layer, where the pre-existing flaws are on the other of layer thickness, i.e., $a_0/h \sim 1$, the steady-state energy release rate G_{ss} becomes relevant. From (6), one finds that the critical stress to maintain tunnel growth is

$$\sigma_c = (4\Gamma\bar{E}/\pi h)^{1/2}. \tag{8}$$

This critical stress is well defined: no knowledge of flaw geometry or microstructure is needed. It is conservative: any flaw, regardless of its initial size or shape, cannot grow into a long tunnel if the applied stress is below σ_c. Consequently, the critical stress derived from G_{ss} can serve as a well-defined, conservative design criterion for avoidance of tunnel cracks in brittle thin layers. It is clear from Fig. 3 that the criterion becomes overly conservative for very thick layers ($a_0/h \ll 1$).

Observe that the critical stress (8) is governed by layer thickness; the thinner the layer, the higher the strength, everything else being equal. This has motivated the conception of microlaminates, consisting of alternate metal and ceramic, each layer submicron thick, fabricated by a variety of thin film deposition techniques (Evans, private communication). Because cracks in a ceramic layer are confined by the adjacent metal layers, and dislocations in a metal layer is confined by the adjacent ceramic layers (Freund, 1990), the microlaminates can have very high elastic limit, unprecedented by bulk solids.

The rest of the paper will focus on applying tunneling concepts to a variety of technical problems, with nucleation stage ignored. Each individual application of the following results must be validated on the basis that the pre-existing flaw size is close to the layer thickness.

Adhesive Layer

Inserted in Fig. 4 is a cross-section of a tunnel wake. In finite element calculations, Poisson's ratios are taken to be $\nu_a = \nu_s = 1/3$, so that elastic mismatch is specified by $(E_s - E_a)/(E_s + E_a)$. The plane-strain conditions prevail in the tunnel wake. We analyze the plane-strain field using finite elements; the computed opening profile is integrated according to (3). The normalized G_{ss} is plotted in Fig. 4, varying the elastic mismatch and thickness ratio. Substrate thickness has little effect; the curve for semi-infinite substrates is nearly identical to the curve for $w/h = 10$ with the resolution of Fig. 4. Figure 4 is therefore sufficiently complete for practical purposes. The following illustrates an application.

In an experiment by Zdaniewski et al. (1987), different glasses were used to bond alumina substrates. Gas bubbles of size of layer thickness formed in the glass during bonding, acting as tunnel nuclei. The residual stresses for the four glasses used in the experiment were $\sigma_R = 63, 50, 131, 132$ MPa, respectively. Tunnels were observed to radiate from the bubbles in the last two glasses, but not the first two. Take $E_{\text{glass}} = 70$ GPa and $E_{\text{alumina}} = 350$ GPa. From Fig. 4, this elastic mismatch corresponds to $G_{ss}\bar{E}_a/\sigma^2 h = 0.6$. Given that $h = 50$ μm and $\Gamma_{\text{glass}} = 5$ Jm^{-2}, the predicted critical stress is $\sigma_c = 120$ MPa. The predicted critical stress indeed discriminates glass layers with and without tunnels.

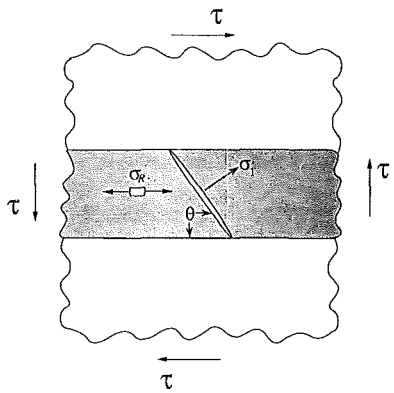


Fig. 6 Microcrack under combined residual stress and applied shear

Periodic Tunnels

Periodic tunnels can form under uniaxial tension (e.g., Parvizi et al., 1978; Laws and Dvorak, 1988). Figure 5 illustrates tunnels with spacing L. The opening profile, $\delta(x)$, is for one of the cracks which is computed using finite elements. The computed energy release rate G_{ss} is plotted in Fig. 5 for $w/h = 10$. Observe that, except for very compliant substrates, G_{ss} does not vary substantially with spacing L/h. Consequently, once the stress is sufficient to drive one tunnel, many tunnels will follow with a slightly higher stress, so long as the nucleation sites are readily available.

In Fig. 5, all the cracks are assumed to tunnel simultaneously. With a proper rearrangement of the results in Fig. 5, the driving force for new tunnels forming between existing tunnels can also be obtained (Hutchinson and Suo, 1992).

Shear Fracture

Upon closer examination of shear fracture in a laminate, one sees microcracks normal to the principal tensile stress nucleate and connect, causing macroscopic fracture (Chai, 1988). As an example consider a brittle thin layer bonded between tough substrates, subjected to shear stress τ and residual stress σ_R (Fig. 6). The larger principal stress, σ_1, and the angle between the interface and the plane of the principal stress, θ, are given by

$$\tan\theta = \sigma_1/\tau = \sigma_R/2\tau + \sqrt{(\sigma_R/2\tau)^2 + 1}. \tag{9}$$

Regardless of the sign of σ_R, σ_1 is always tensile; $\theta < 45$ deg if $\sigma_R < 0$, and $\theta > 45$ deg if $\sigma_R > 0$.

A tunnel is assumed to form perpendicular to σ_1. For simplicity, the elastic moduli of the substrates and the bonded

Downloaded 03 May 2010 to 171.66.16.245. Redistribution subject to ASME license or copyright; see http://www.asme.org/terms/Terms_Use.cfm

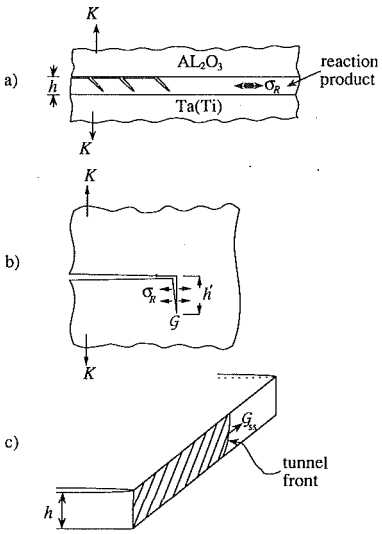


Fig. 7 Kinked tunnels

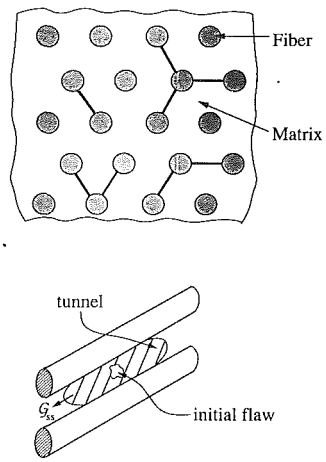


Fig. 8 Matrix cracking due to thermal mismatch

layer are taken to be identical and substrates are semi-infinite. The cross-section of the tunnel wake is a Griffith crack, so that (6) is applicable. Identifying the net stress σ_1 and tunnel width $h/\sin\theta$, one obtains

$$G_{ss}\bar{E}/h\tau^2 = \frac{\pi}{4}\sin\theta/\cos^2\theta. \tag{10}$$

For layers with different elastic constants, the tunnel angle should still be determined by (9), but finite element analysis is needed to calculate G_{ss}. Judged from Fig. 4, however, the results should be insensitive to elastic mismatch if substrates are stiffer than the layer.

Kinked Tunnels

When a Al_2O_3 plate is diffusion bonded to a Ta(Ti) alloy, a reaction product layer (RPL) of thickness 2 μm forms (He et al., 1991). The system debonds along the Al_2O_3-RPL interface upon loading, leaving behind a trail of microcracks in the RPL (Fig. 7(*a*)).

The tunnel is driven by the stress intensity at the parent crack front, K, and by the residual stress in the layer, σ_R. For simplicity the remote load is assumed to be mode I, and the microcracks are taken to be perpendicular to the interface. The system is taken to be elastically homogeneous and the two substrates are semi-infinite. None of these assumptions will affect the conclusions qualitatively.

For a kink of depth h' under the plane-strain conditions (Fig. 7(*b*)), the stress intensity factor is (He et al., 1991)

$$K_I = 0.374K + 1.766\sigma_R\sqrt{h'},\quad K_{II} = -0.347K + 0.201\sigma_R\sqrt{h'}. \tag{11}$$

The energy release rate at the kink tip can be computed from Irwin's relation

$$G_E = (K_I^2 + K_{II}^2)/\bar{E}. \tag{12}$$

The energy release rate at the tunnel front G_{ss} (Fig. 7(*c*)) can be integrated according to (2), giving

$$\bar{E}G_{ss}/K^2 = 0.260 + 0.788\eta + 1.58\eta^2,\quad \eta = \sigma_R\sqrt{h}/K. \tag{13}$$

The parameter η reflects the effect of the residual stress. When a tunnel forms, the residual tension is locally relieved. As the interface crack grows further, the residual tension recovers, driving a new tunnel.

Kinked tunnels were also observed by Chai (1987) in an epoxy bonded between aluminum substrates. He observed that the main crack ran alternating on the two interfaces, leaving behind a wavy fracture surface. This did not happen in the system of He et al. (1991), presumably because the Ta(Ti)-RPL interface is much tougher.

Thermal Cracking in Brittle Matrix Composites

All previous examples are related to layered materials. But tunneling is more prevalent. To illustrate, consider matrix cracking caused by thermal mismatch. An intermetallic reinforced by ceramic fibers, such as $MoSi_2$-SiC, usually has higher thermal expansion coefficient in the matrix than in the fibers. Upon cooling from the processing temperature, the matrix is subjected to tensile hoop stress and susceptible to cracking (Lu et al., 1991). One experimental finding is that cracking is more likely to occur in the matrix reinforced by fibers of larger radius, so that a critical fiber radius exists, below which matrix cracking is suppressed.

Focus on the radial crack in Fig.8. The thermal mismatch strain is

$$\epsilon_0 = \int_{T_r}^{T_p}(\alpha_m - \alpha_f)dT, \tag{14}$$

where α_m and α_f are thermal expansion coefficients of the matrix and fiber, and T_p and T_r are the processing temperature and room temperature. The residual stress estimated from the mismatch strain for $MoSi_2$-SiC is high (~ 2 GPa), well in excess of the bulk strength of $MoSi_2$. Also note that the residual stress is *independent* of fiber radius for a fixed fiber volume. These two facts eliminate the possibility of explaining the experimental finding on the basis of bulk strength.

We assume porosity exists, of size limited only by the fiber spacing, which tunnels through the matrix under sufficiently high thermal stress (Fig. 8). On dimensional grounds, the steady-state energy release rate takes the form

$$G_{ss} = \Omega\epsilon_0^2 E_m R, \tag{15}$$

where R is fiber radius and E_m is the Young's modulus of the matrix. The dimensionless prefactor, Ω, depends on fiber volume fraction, fiber arrangement, elastic mismatch, and interface properties, which has been computed using finite elements on the basis of the tunneling crack concepts developed in the previous sections (Ho and Suo, 1992).

The tunnel will not form if $G_{ss} < \Gamma_m$, Γ_m being the fracture energy of the matrix. Thus (15) gives

$$\Gamma_m/\epsilon_0^2 E_m R > \Omega. \tag{16}$$

The dimensionless group on the left-hand side consists of measurable parameters and predicts, among other things, that the larger the fiber radius, the more likely will the matrix crack, which is in agreement with the experimental findings.

Downloaded 03 May 2010 to 171.66.16.245. Redistribution subject to ASME license or copyright; see http://www.asme.org/terms/Terms_Use.cfm

Concluding Remarks

Cracks tunnel in confined geometries. The steady-state tunneling defines a conservative design limit. The energy release rate at the tunnel front is computed for a number of cases. To demonstrate the versatility of the concepts without going into technical details we have treated each problem in its simplest form. Many more computations are needed to take key variables into account, so that rigorous design criteria will emerge. Nevertheless, results presented here can be used as a base line for such purposes. Although this paper has focused on cracking in brittle layers, tunnels can form in ductile metal or polymer layers under cyclic loading. The fatigue life is dictated by the steady-state energy release rate, provided large flaws are available and tunnels do not take many cycles to nucleate.

Acknowledgment

Support is provided by ONR/URI contract N-0014-92-J-1808, and by NSF Young Investigator Award MSS-9258115. Finite element analyses are carried out using ABAQUS.

References

Beuth, J. L., 1992, "Cracking of Thin Bonded Films in Residual Tension," *Int. J. Solids and Structures*, Vol. 29, pp. 1657–1675.

Chai, H., 1987, "A Note on Crack Trajectory in an Elastic Strip Bounded by Rigid Substrates," *Int. J. Fracture*, Vol. 32, pp. 211–213.

Chai, H., 1988, "Shear Fracture," *Int. J. Fracture*, Vol. 37, pp. 137–159.

Dvorak, G. J., and Laws, N., 1986, "Analysis of First Ply Failure in Composite Laminates," *Engng. Fracture Mech.*, Vol. 25, pp. 763–770.

Dvorak, G. J., and Laws, N., 1988, "Progressive Transverse Cracking in Composite Laminates," *J. Composite Materials*, Vol. 22, pp. 900–916.

Fang, G. P., Schapery, R. A., and Weitsman, Y., 1989, "Thermally-Induced Fracture in Composites," *Engng. Fracture Mech.*, Vol. 33, pp. 619–623.

Freund, L. B., 1990, "The Driving Force for Gliding of a Threading Dislocation in a Strained Epitaxial Layer on a Substrate," *J. Mech. Phys. Solids*, Vol. 38, pp. 657–679.

Gille, G., 1985, "Strength of Thin Films and Coatings," *Current Topics in Materials Science*, Vol. 12, E. Kaldis, ed., North Holland, Amsterdam.

He, M.-Y., Bartlett, A., Evans, A. G., and Hutchinson, J. W., 1991, "Kinking of a Crack Out of an Interface: Role of In-Plane Stress," *J. Am. Ceram. Soc.*, Vol. 74, pp. 767–771:

Ho, S., and Suo, Z., 1992, "Microcracks Tunneling in Brittle Matrix Composites Driven by Thermal Expansion Mismatch," *Acta. Mer. Mater.*, Vol. 40, pp. 1685–1690.

Hu, M. S., Thouless, M. D., and Evans A. G., 1988, "The Decohesion of Thin Films from Brittle Substrates," *Acta Met.*, Vol. 36, pp. 1301–1307.

Hutchinson, J. W., and Suo, Z., 1992, "Mixed-Mode Cracking in Layered Materials," *Advances in Applied Mechanics*, Vol. 29, pp. 63–191.

Lu, T. C., Yang, J., Suo, Z., Evans, A. G., Hecht, R., and Mehrabian, R., 1991, "Matrix Cracking in Intermetallic Composites Caused by Thermal Expansion Mismatch," *Acta. Metall. Mater.*, Vol. 39, pp. 1883–1890.

Parvizi, A., Garrett, K. W., and Bailet, J. E., 1978, "Constrained Cracking in Glass Fiber-Reinforced Epoxy Cross-Ply Laminates," *J. Matter Sci.*, Vol. 13, pp. 195–201.

Suo, Z., 1990, "Failure of Brittle Adhesive Joints," ASME *Applied Mechanics Reviews*, Vol. 43, pp. S276–S279.

Tada, H., Paris, P. C., and Irwin, G. R., 1985, *The Stress Analysis of Cracks Handbook*, Del Research, St. Louis, MO.

Wang, A. S. D., 1984, "Fracture Mechanics of Sublaminate Cracks in Composite Materials," *Composite Tech. Rev.*, Vol. 6, pp. 45–62.

Ye, T., Suo, Z., and Evans, A. G., 1992, "Thin Film Cracking and the Roles of Interface and Substrate," *Int. J. Solids Structures*, Vol. 29, pp. 2639–2648.

Zdaniewski, W. A., Conway, J. C., and Kirchner, H. P., 1987, "Effects of Joint Thickness and Residual Stresses on the Properties of Ceramic Adhesive Joints," *J. Am. Ceram. Soc.*, Vol. 70, pp. 104–109.

Downloaded 03 May 2010 to 171.66.16.245. Redistribution subject to ASME license or copyright; see http://www.asme.org/terms/Terms_Use.cfm

E. Madenci
Department of Aerospace and Mechanical Engineering, The University of Arizona, Tucson, AZ 85721
Mem. ASME

R. A. Westmann
Mechanical, Aerospace, and Nuclear Engineering Department, University of California, Los Angeles, CA 90024-1597
Mem. ASME

Local Delamination Growth in Layered Systems Under Compressive Load

This paper addresses the problem of delamination growth prior to its buckling using mathematical techniques appropriate for mixed boundary value problems. The formulation presented herein does not require buckling as a necessary condition for delamination growth. By employing the stability equations of elasticity theory, solutions to the problem of an infinite layer with a slightly imperfect circular delamination subjected to axisymmetric and uniaxial in-plane compressive loading are presented. This approach permits the determination of the stress intensity factors under specified initial imperfections for applied compressive stress.

1 Introduction

Local delamination buckling and growth is a frequently observed failure mode in laminated structures subjected to compressive loads. Delaminations in the form of inclusions, wrinkles, or gas bubbles may result from the manufacturing process for layered systems. Delaminations may also result from low-velocity impact damage during service. As shown experimentally by Chai et al. (1983), McCarty and Ratwani (1983), and Starnes and Williams (1984), the presence of a debond may reduce the compressive strength of the layered structure to a level where premature failure occurs as a result of delamination growth and/or catastrophic failure.

The specific nature of this failure mode is unlike that usually encountered in fracture mechanics. The uniqueness of this failure mechanism prompted many researchers to investigate this problem. However, these investigations employ structural mechanics theories which entail significant limitations. First, in order to model the delaminated layer as a beam or as a plate, the ratio of delamination length to its depth must be large. Second, the edges of the delamination are assumed to be either clamped or simply supported, and the delamination cannot grow unless the delaminated layer buckles. While suitable for initial strength evaluations of the delaminated composite, such approximations do not permit detailed fracture mechanics examination. Madenci (1987) provides an extensive review of these investigations.

Madenci and Westmann (1991) studied the problem of local delamination buckling by employing stability equations of elasticity theory which overcome these limitations. This paper addresses the growth of an initially imperfect delamination subjected to compressive loads. The formulation presented by Madenci and Westmann has been extended to account for the effect of slightly perturbed boundaries due to the presence of an initially imperfect delamination. Under this formulation, buckling is not a necessary condition for delamination growth, because the imperfection permits the determination of the stress field. This approach allows the study of the growth process which might eventually lead to buckling. This interaction has been illustrated by Madenci (1991) for delamination growth and buckling in an orthotropic strip. The initial direction of delamination growth can be predicted as well.

Section 2 presents the mathematical model for the two-dimensional loading conditions of axisymmetric and uniaxial in-plane compressive loading when the delamination and bounding surfaces are slightly perturbed. In Section 3 the solution for the case of axisymmetric loading is obtained by first reducing the problem to a pair of dual integral equations and then to the solution of a single nonhomogeneous Fredholm integral equation of the second kind. Section 4 addresses the uniaxial loading case with a mathematical approximation which permits the problem to be stated in terms of two pairs of simultaneous dual integral equations. Again, these equations are converted to a pair of coupled, nonhomogeneous Fredholm integral equations of the second kind.

In both Sections 3 and 4 the effect of initial imperfections, formulated in Section 2, provides the stress intensity factors for applied compressive stress under specified initial imperfections. The stress intensity factors are complex functions of the applied stress, unlike those usually encountered in linear elastic fracture mechanics. Section 5 presents the numerical results for the stress intensity factors under axisymmetric and uniaxial loading.

2 Problem Statement

This study addresses the growth of an imperfect delamination embedded in a flat elastic layer subjected to in-plane

Contributed by the Applied Mechanics Division of THE AMERICAN SOCIETY OF MECHANICAL ENGINEERS for publication in the ASME JOURNAL OF APPLIED MECHANICS.

Discussion on this paper should be addressed to the Technical Editor, Professor Lewis T. Wheeler, Department of Mechanical Engineering, University of Houston, Houston, TX 77204-4792, and will be accepted until four months after final publication of the paper itself in the ASME JOURNAL OF APPLIED MECHANICS.

Manuscript received by the ASME Applied Mechanics Division, Sept. 25, 1991; final revision July 1, 1992. Associate Technical Editor: G. J. Dvorak.

Copyright © 1993 by ASME
Downloaded 03 May 2010 to 171.66.16.245. Redistribution subject to ASME license or copyright; see http://www.asme.org/terms/Terms_Use.cfm

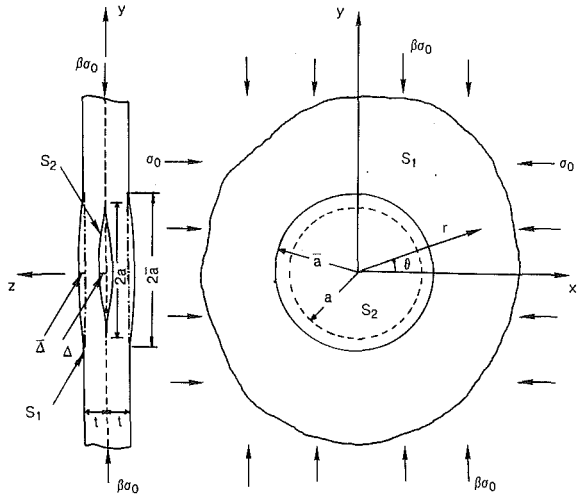


Fig. 1 Layered structure with imperfect circular delamination

compressive loads. A cylindrical coordinate system (r, θ, z) is employed in which the symmetry plane $z=0$ coincides with the midsurface of the layer (Fig. 1). The total layer thickness is taken to be $2t$, and the bounding surface of the layer becomes

$$S_1 = \{r, \theta, z \mp \bar{\Delta}(r): r \in [0, \infty), \theta \in [0, 2\pi], z = \mp t\}.$$

The imperfect circular delamination, radius $a=1$, is located in the midplane of the layer and centered at $r=0$; the delamination surface S_2 is therefore described by[1]

$$S_2 = \{r, \theta, z \mp \Delta(r): r \in [0, \infty), \theta \in [0, 2\pi], z = \mp 0\}.$$

The layer is composed of a homogeneous, elastic, isotropic material with shear modulus μ and Poisson's ratio ν.

Since delamination imperfections, in the form of voids or inclusions, result either from a lateral impact or from poor bonding during manufacturing, it is assumed that the region where the imperfection is embedded is slightly perturbed from the perfect configuration. This perturbation is the result of a permanent shape change of the delamination surfaces and also causes a perturbation on the bounding surfaces that is of a smaller magnitude but extends over a larger area.

The initially imperfect bounding surfaces and delamination surfaces, which deviate only slightly from the perfect configurations ($z = \mp t$ and $z=0$), can be described by the following functions, $\bar{\Delta}(r)$ and $\Delta(r)$, respectively.[2]

$$\bar{\Delta}(r) = \frac{\bar{\delta}}{2}\left[1 + \cos\frac{\pi r}{\bar{a}}\right] H(\bar{a} - r)$$

$$\Delta(r) = \frac{\delta}{2}\left[1 + \cos\frac{\pi r}{a}\right] H(a - r). \tag{1}$$

These functions possess small gradients and thus preserve the initial stress state as spatially constant.

Based on the foregoing discussion, the relationship between the primary parameters $\bar{\delta}$ and δ, the amplitudes of the imperfections, can be established from the constant volume requirement of the material and from the assumption that $\bar{a} = a + t$. This results in the relationship

$$\bar{\delta} = \frac{\delta}{a+t} \tag{2}$$

for the functions specified in (1).

The layer is subjected to an in-plane compressive loading σ_0 resulting from the initial equilibrium stress state, with surfaces S_1 and S_2 remaining traction-free.

In the derivation of equations of elastic stability concerning bifurcation, it is assumed that the unit normal to the bounding surfaces is perpendicular to the direction of the applied load and/or that uniform loading is achieved at every cross-section. If this assumption does not hold, the nature of the stability problem is altered. In order to account for the initial imperfection, the traction equations given by Madenci and Westmann (1991) are modified while the equilibrium equations remain unaffected. The mathematical boundary value problem then reduces to the determination of the nontrivial stress field induced by the specified initial imperfection and the applied traction conditions on S_1 and S_2. The solution to this problem provides the stress intensity factors for detailed fracture mechanics examination.

3 Solution for Axisymmetric Compression

The displacement equilibrium equations for the case of axisymmetric compression, $\beta = 1$ in Fig. 1, may be expressed as

$$\frac{2(1-\nu)}{(1-2\nu)}\left[\frac{1}{r}(ru_r)_{,r} + u_{z,z}\right]_{,r} - (u_{z,r} - u_{r,z})_{,z} - \frac{\sigma_0}{\mu}\left[\frac{1}{r}(ru_r)_{,r}\right]_{,r} = 0$$

$$\frac{2(1-\nu)}{(1-2\nu)}\left[\frac{1}{r}(ru_r)_{,r} + u_{z,z}\right]_{,z} + \frac{1}{r}[r(u_{z,r} - u_{r,z})]_{,r} - \frac{\sigma_0}{\mu}\frac{1}{r}(ru_{z,r})_{,r} = 0 \tag{3}$$

where u_r, u_θ, and u_z are the components of the displacement field referenced to the cylindrical coordinates (r, θ, z). Due to the axial symmetry of the geometric and loading configurations, the displacement component u_θ and derivatives with respect to θ vanish in Eq. (3).

Boundary conditions associated with the traction-free surface S_1 then become

$$\left.\begin{aligned} &\frac{2\mu}{(1-2\nu)}\left[(1-\nu)u_{z,z} + \nu\frac{1}{r}(ru_r)_{,r}\right] = 0 && (4a)\\ &\mu[u_{r,z} + u_{z,r}] + \sigma_0\bar{\Delta}_{,r} = 0 && (4b)\end{aligned}\right\} z = \mp t,\ r \in [0, \infty).$$

The presence of symmetry with respect to the midplane ($z=0$) and the requirement that the delamination surface S_2 be traction-free result in the following boundary conditions:

$$\mu(u_{r,z} + u_{z,r}) + \sigma_0\Delta_{,r} = 0 \qquad z = 0^+,\ r \in [0, \infty) \tag{5a}$$

$$\frac{2\mu}{(1-2\nu)}\left[(1-\nu)u_{z,z} + \nu\frac{1}{r}(ru_r)_{,r}\right] = 0 \qquad z = 0^+,\ r \in [0, 1) \tag{5b}$$

$$u_z = 0 \qquad z = 0^+,\ r \in (1, \infty). \tag{5c}$$

Further, the far-field regularity conditions require that

$$u_r,\ u_z \to 0 \quad \text{for} \quad z \in [0, t],\ r \to \infty.$$

Adopting the identical solution procedure presented in Section 3 of Madenci and Westmann (1991) and imposing the conditions (5), (6) result in the following pair of nonhomogeneous dual integral equations:

$$\int_0^\infty C(\xi)\xi J_0(r\xi)d\xi = f_0(r) + \int_0^\infty G(\xi; \sigma_0, t)C(\xi)\xi J_0(r\xi)d\xi \quad r \in [0, 1) \tag{6a}$$

$$\int_0^\infty C(\xi)J_0(r\xi)d\xi = g_0(r) \quad r \in (1, \infty). \tag{6b}$$

The expression for the functions and the constants in these equations are the same as in Madenci and Westmann except

[1] The delamination radius is taken to be unity so that the problem statement is in dimensionless form.

[2] Here and in the following, $H(r)$ denotes the Heaviside step function.

Downloaded 03 May 2010 to 171.66.16.245. Redistribution subject to ASME license or copyright; see http://www.asme.org/terms/Terms_Use.cfm

for $f_0(r)$ and $g_0(r)$. These forcing functions which appear in the formulation as a result of the initial imperfections depend on the amplitude of the imperfection and are in the form

$$f_0(r)=\sqrt{\frac{\pi}{2}}\frac{\sigma_0}{\mu}\frac{\delta}{(1-\tau)(1+\tau_2^2)}\int_0^\infty [D_1(\xi)\bar{S}_2(\xi) + D_2(\xi)\bar{S}_1(\xi)]\xi J_0(r\xi)d\xi \quad (7a)$$

$$g_0(r)=\sqrt{\frac{\pi}{2}}\frac{\sigma_0}{\mu}\frac{\delta}{(1+\tau_2^2)}\int_0^\infty [D_3(\xi)\bar{S}_2(\xi) + D_4(\xi)\bar{S}_1(\xi)]J_0(r\xi)d\xi \quad (7b)$$

where

$$D_1(\xi)=-\frac{(1-\tau)-(1+\tau)e^{-2\tau_1\xi t}+2\tau e^{-(\tau_1+\tau_2)\xi t}}{D(\xi)}$$

$$D_2(\xi)=-\frac{2\tau e^{-\tau_1\xi t}-(1+\tau)e^{-\tau_2\xi t}+(1-\tau)e^{-(\tau_1+\tau_2)\xi t}}{D(\xi)}$$

$$D_3(\xi)=\frac{(1-\tau)(1+\tau_2^2)+(1+\tau)(1+\tau_2^2)e^{-2\tau_1\xi t}-4e^{-(\tau_1+\tau_2)\xi t}}{(1-\tau_2^2)D(\xi)}$$

$$D_4(\xi)=\frac{e^{-\tau_2\xi t}+e^{-(2\tau_1+\tau_2)\xi t}}{D(\xi)}$$

in which

$$D(\xi)=-2[(1-\tau)+(1+\tau)e^{-2\tau_1\xi t}-2e^{-(\tau_1+\tau_2)\xi t}].$$

The functions $\bar{S}_1(\xi)$ and $\bar{S}_2(\xi)$, arising from the presence of initial imperfections, are expressed as

$$\bar{S}_1(\xi)=-\sqrt{\frac{\pi}{2}}\frac{a}{(a+t)^2}B(a+t,\ \xi)\quad \bar{S}_2(\xi)=-\sqrt{\frac{\pi}{2}}\frac{1}{a}B(a,\ \xi) \quad (8)$$

where $B(c, \xi)$ is presented in the Appendix. The dual integral Eqs. (6) are converted to a nonhomogeneous Fredholm integral equation of the second kind (Sneddon and Lowengrub, 1969) by means of the following integral representation for $C(\xi)$ (Copson, 1961):

$$C(\xi)=\delta\xi^{1/2}\left[\int_0^1 \alpha^{1/2}\Psi_1(\alpha)J_{1/2}(\xi\alpha)d\alpha + \int_1^\infty \alpha^{1/2}\Psi_2(\alpha)J_{1/2}(\xi\alpha)d\alpha\right] \quad (9)$$

In this representation, $\Psi_1(\alpha)$ and $\Psi_2(\alpha)$ are assumed to be continuous over [0, 1) and (1, ∞), respectively, and are required to satisfy the conditions

$$\lim_{\alpha\to 0^+}\alpha^{1/2}\Psi_1(\alpha)=0 \quad \text{and} \quad \lim_{\alpha\to\infty}\alpha^{1/2}\Psi_2(\alpha)=0.$$

Substituting (9) into (6b) and utilizing the Weber-Schaftheitlin integral (Watson, 1944) lead to an Abel integral equation for $\Psi_2(\alpha)$

$$\sqrt{\frac{2}{\pi}}\delta\int_r^\infty \Psi_2(\alpha)\frac{d\alpha}{\sqrt{\alpha^2-r^2}}=g_0(r) \quad r\in(1,\ \infty). \quad (10)$$

Applying Abel's solution method (Whittaker and Watson, 1920) to invert the left-hand side of Eq. (10) and then substituting from (7b) give the final equation for $\Psi_2(\alpha)$,

$$\Psi_2(\alpha)=\frac{\sigma_0}{\mu}\frac{1}{(1+\tau_2^2)}\int_0^\infty [D_3(\xi)\bar{S}_2(\xi) + D_4(\xi)\bar{S}_1(\xi)]\sin(\alpha\xi)d\xi \quad \alpha\in(1,\ \infty). \quad (11)$$

Modifying $C(\xi)$ by integration by parts and substituting the resulting expression into (6a) yield the second Abel integral equation

$$\sqrt{\frac{2}{\pi}}\delta\int_0^r \frac{d[\Psi_1(\alpha)]}{d\alpha}\frac{d\alpha}{\sqrt{r^2-\alpha^2}} = \int_0^\infty G(\xi;\ \sigma_0,\ t)C(\xi)\xi J_0(r\xi)d\xi + f_0(r) \quad r\in[0,\ 1). \quad (12)$$

Applying Abel's solution method and substituting the expression for $C(\xi)$ into the right-hand side of (12) result in the final equation for $\Psi_1(\alpha)$,

$$\Psi_1(\alpha)=\int_0^1 K(\alpha,\ \eta;\ \sigma_0,\ t)\Psi_1(\eta)d\eta+\int_1^\infty K(\alpha,\ \eta;\ \sigma_0,\ t)\Psi_2(\eta)d\eta + \frac{\sigma_0}{\mu}\frac{1}{(1-\tau)(1+\tau_2^2)}\int_0^\infty [D_1(\xi)\bar{S}_2(\xi)+D_2(\xi)\bar{S}_1(\xi)]\sin(\alpha\xi)d\xi \quad \alpha\in[0,\ 1), \quad (13)$$

where the kernel $K(\alpha, \eta; \sigma_0, t)$ is the same as that defined by Madenci and Westmann.

The evaluation of Eq. (11) and the solution of Eq. (13) permit the determination of the stress intensity factor which can be identified as a growth parameter. The stress intensity factor, which is a measure of the severity of the singular stress field at the delamination edge, depends on the delamination geometry, boundary conditions, and the applied load. The well-known asymptotic expression for the normal stress in the vicinity of the delamination edge is of the form

$$\sigma_{zz}(r,\ 0)=\frac{K_I}{\sqrt{2\pi\rho}} \quad \text{as} \quad \rho\to 0^+ \quad (14)$$

where K_I is the stress intensity factor and ρ is the distance away from the delamination edge.

For the present problem, the stress intensity factor K_I for the delamination edge is obtained from the following expression:

$$\sigma_{zz}(r,\ 0)=\frac{4\mu\tau_2(1-\tau)}{\tau}\left[\int_0^\infty C(\xi)\xi J_0(r\xi)d\xi - \int_0^\infty G(\xi)C(\xi)\xi J_0(r\xi)d\xi - f_0(r)\right] \quad r\in(1,\ \infty). \quad (15)$$

Modifying $C(\xi)$ by integration by parts and substituting into (15) in conjunction with the use of the Weber-Schaftheitlin integral yield the following:

$$\frac{\sigma_{zz}}{\mu}(r,\ 0)=\sqrt{\frac{2}{\pi}}\frac{4\tau_2(1-\tau)}{\tau}\delta[\Psi_1(1)-\Psi_2(1)]\frac{H(r-1)}{\sqrt{r^2-1}} + \sqrt{\frac{2}{\pi}}\frac{4\tau_2(1-\tau)}{\tau}\delta\left[\int_0^1\frac{d\Psi_1(\alpha)}{d\alpha}\frac{H(r-\alpha)}{\sqrt{r^2-\alpha^2}}d\alpha + \int_1^\infty\frac{d\Psi_2(\alpha)}{d\alpha}\frac{H(r-\alpha)}{\sqrt{r^2-\alpha^2}}d\alpha\right] - \frac{4\tau_2(1-\tau)}{\tau}\delta\left[\int_0^1\alpha^{1/2}\Psi_1(\alpha)\int_0^\infty G(\xi)\xi^{3/2}J_{1/2}(\alpha\xi)J_0(r\xi)d\xi\,d\alpha + \int_1^\infty\alpha^{1/2}\Psi_2(\alpha)\int_0^\infty G(\xi)\xi^{3/2}J_{1/2}(\alpha\xi)J_0(r\xi)d\xi\,d\alpha + f_0(r)\right]. \quad (16)$$

Except for the first term in Eq. (16), all the remaining terms are bounded when r approaches 1. Integrating the first two

Downloaded 03 May 2010 to 171.66.16.245. Redistribution subject to ASME license or copyright; see http://www.asme.org/terms/Terms_Use.cfm

integrals by parts demonstrates their boundedness. By using the Weierstrass-M and Drichlet tests for uniform convergence, the remaining integrals can be shown to be continuous functions in the interval $(1, \infty)$.

Defining

$$\rho = r - 1$$

and retaining the first term in Eq. (16) result in the near-field solution for the normal stress as follows:

$$\frac{\sigma_{zz}}{\mu}(r, 0) = \frac{4\sqrt{2}\tau_2(\tau-1)}{\tau}\delta[\Psi_1(1) - \Psi_2(1)]\frac{1}{\sqrt{2\pi\rho}} \quad \text{as} \quad \rho \to 0^+. \tag{17}$$

From Eqs. (14) and (17), the stress intensity factor can be expressed as

$$K_I = \frac{4\sqrt{2}\mu\tau_2(\tau-1)}{\tau}[\Psi_1(1) - \Psi_2(1)]\delta. \tag{18}$$

4 Solution for Uniaxial Compression

In the case of uniaxial compression ($\beta = 0$ in Fig. 1), the displacement equilibrium equations in cylindrical coordinates reduce to

$$\nabla^2 u_r + \frac{1}{(1-2\nu)}\Delta_{,r} - \frac{1}{r^2}(2u_{\theta,\theta} + u_r) - \frac{\sigma_0}{2\mu}\left\{\left[\frac{1}{r}(ru_r)_{,r}\right]_{,r} + \frac{1}{r^2}(u_{r,\theta} - 2u_\theta)_{,\theta}\right\} - \frac{\sigma_0}{2\mu}\left\{\left[r\left(\frac{1}{r}u_r\right)_{,r}\right]_{,r} - \frac{1}{r^2}(u_{r,\theta} - 2u_\theta)_{,\theta}\right\}\cos 2\theta + \frac{\sigma_0}{2\mu}\left\{2\left[\frac{1}{r}(u_{r,\theta} - u_\theta)\right]_{,r}\right\}\sin 2\theta = 0 \tag{19a}$$

$$\nabla^2 u_\theta + \frac{1}{(1-2\nu)}\frac{1}{r}\Delta_{,\theta} + \frac{1}{r^2}(2u_{r,\theta} + u_\theta) - \frac{\sigma_0}{2\mu}\left\{\left[\frac{1}{r}(ru_\theta)_{,r}\right]_{,r} + \frac{1}{r^2}(u_{\theta,\theta} + 2u_r)_{,\theta}\right\} - \frac{\sigma_0}{2\mu}\left\{\left[r\left(\frac{1}{r}u_\theta\right)_{,r}\right]_{,r} - \frac{1}{r^2}(u_{\theta,\theta} + 2u_r)_{,\theta}\right\}\cos 2\theta + \frac{\sigma_0}{2\mu}\left\{2\left[\frac{1}{r}(u_{\theta,\theta} + u_r)\right]_{,r}\right\}\sin 2\theta = 0 \tag{19b}$$

$$\nabla^2 u_z + \frac{1}{(1-2\nu)}\Delta_{,z} - \frac{\sigma_0}{2\mu}\left[\frac{1}{r}(ru_{z,r})_{,r} + \frac{1}{r^2}u_{z,\theta\theta}\right] - \frac{\sigma_0}{2\mu}\left[r\left(\frac{1}{r}u_{z,r}\right)_{,r} - \frac{1}{r^2}u_{z,\theta\theta}\right]\cos 2\theta + \frac{\sigma_0}{2\mu}\left[2\left(\frac{1}{r}u_{z,\theta}\right)_{,r}\right]\sin 2\theta = 0 \tag{19c}$$

in which

$$\Delta = u_{r,r} + \frac{1}{r}u_r + \frac{1}{r^2}u_{\theta,\theta} + u_{z,r}$$

$$\nabla^2 = \frac{\partial^2}{\partial r^2} + \frac{1}{r}\frac{\partial}{\partial r} + \frac{1}{r^2}\frac{\partial^2}{\partial\theta^2} + \frac{\partial^2}{\partial z^2}.$$

The traction-free boundary conditions on S_1 are stated as follows:

$$\left.\begin{aligned} &\frac{2\mu}{(1-2\nu)}\left\{(1-\nu)u_{z,z} + \nu\left[u_{r,r} + \frac{1}{r}(u_{\theta,\theta} + u_r)\right]\right\} = 0 && (20a)\\ &\mu[u_{r,z} + u_{z,r}] + \frac{\sigma_0}{2}\overline{\Delta}_{,r}[1 + \cos 2\theta] = 0 && (20b)\\ &\mu\left[\frac{1}{r}u_{z,\theta} + u_{\theta,z}\right] - \frac{\sigma_0}{2}\overline{\Delta}_{,r}\sin 2\theta = 0 && (20c)\end{aligned}\right\} z = \mp t \quad r \in [0, \infty).$$

Symmetry of the solution with respect to the midplane ($z = 0$) and the requirement that the delamination surface S_2 be traction-free result in the following boundary conditions:

$$\left.\begin{aligned} &\mu[u_{r,z} + u_{z,r}] + \frac{\sigma_0}{2}\Delta_{,r}[1 + \cos 2\theta] = 0 && r \in [0, \infty) \quad (20d)\\ &\mu\left[\frac{1}{r}u_{z,\theta} + u_{\theta,z}\right] - \frac{\sigma_0}{2}\Delta_{,r}\sin 2\theta = 0 && r \in [0, \infty) \quad (20e)\\ &\frac{2\mu}{(1-2\nu)}\left\{(1-\nu)u_{z,z} + \nu\left[u_{r,r} + \frac{1}{r}(u_{\theta,\theta} + u_r)\right]\right\} = 0 && r \in [0, 1) \quad (20f)\\ &u_z = 0 && r \in (1, \infty). \quad (20g)\end{aligned}\right\} z = 0^+$$

Finally, the far-field regularity conditions require that

$$u_r, u_\theta, u_z \to 0 \quad \text{for} \quad |z| \in [0, t], \quad r \to \infty.$$

The solution procedure, as with the axisymmetric loading case, involves the steps outlined in Section 4 of Madenci and Westmann (1991). The application of the boundary conditions (20) leads to a system of coupled nonhomogeneous dual integral equations

$$\int_0^\infty [\kappa_1 S(\xi) + \kappa_2 D(\xi)]\xi J_0(r\xi)d\xi = \int_0^\infty [h(\xi; \sigma_0, t)S(\xi) + g(\xi; \sigma_0, t)D(\xi)]\xi J_0(r\xi)d\xi + F_0(r) \quad r \in [0, 1) \tag{21a}$$

$$\int_0^\infty [\kappa_2 S(\xi) + \kappa_1 D(\xi)]\xi J_2(r\xi)d\xi = \int_0^\infty [g(\xi; \sigma_0, t)S(\xi) + h(\xi; \sigma_0, t)D(\xi)]\xi J_2(r\xi)d\xi + F_2(r) \quad r \in [0, 1) \tag{21b}$$

$$\int_0^\infty D(\xi)J_0(r\xi)d\xi = G_0(r) \quad r \in (1, \infty) \tag{21c}$$

Downloaded 03 May 2010 to 171.66.16.245. Redistribution subject to ASME license or copyright; see http://www.asme.org/terms/Terms_Use.cfm

$$\int_0^\infty S(\xi)J_2(r\xi)d\xi = G_2(r) \qquad r\in(1,\ \infty) \qquad (21d)$$

where $S(\xi)$ and $D(\xi)$ are the unknown functions. The expressions for the functions and the constants in these equations are the same as those given by Madenci and Westmann (1991), except for $F_0(r)$, $F_2(r)$, $G_0(r)$, and $G_2(r)$. These forcing functions which arise due to the initially imperfect boundaries are given in the Appendix.

These coupled dual integral Eqs. (21) are converted to a pair of coupled nonhomogeneous Fredholm integral equations of the second kind. This is achieved by means of the following integral respresentations for $S(\xi)$ and $D(\xi)$ (Westmann, 1965):

$$S(\xi) = \delta\xi^{1/2}\left[\int_0^1 \alpha^{1/2}\Phi_2(\alpha)J_{5/2}(\xi\alpha)d\alpha + \int_1^\infty \alpha^{1/2}\Phi_3(\alpha)J_{5/2}(\xi\alpha)d\alpha\right] \qquad (22a)$$

$$D(\xi) = \delta\xi^{1/2}\left[\int_0^1 \alpha^{1/2}\Phi_1(\alpha)J_{1/2}(\xi\alpha)d\alpha - \frac{\kappa_1}{\kappa_2}\int_0^1 \alpha^{1/2}\Phi_2(\alpha)J_{5/2}(\xi\alpha)d\alpha - \frac{\kappa_1}{\kappa_2}\int_1^\infty \alpha^{1/2}\Phi_3(\alpha)J_{5/2}(\xi\alpha)d\alpha + \int_1^\infty \alpha^{1/2}\Phi_4(\alpha)J_{1/2}(\xi\alpha)d\alpha\right] \qquad (22b)$$

in which $\Phi_1(\alpha)$ to $\Phi_4(\alpha)$ are the unknown functions to be determined. The functions $\Phi_1(\alpha)$ to $\Phi_4(\alpha)$ are required to be continuous over the intervals [0, 1) and (1, ∞), respectively, and must satisfy the conditions

$$\lim_{\alpha\to 0^+}[\alpha^{1/2}\Phi_1(\alpha)] = 0, \quad \lim_{\alpha\to 0^+}[\alpha^{1/2}\Phi_2(\alpha)] = 0$$

$$\lim_{\alpha\to\infty}[\alpha^{1/2}\Phi_3(\alpha)] = 0, \quad \lim_{\alpha\to\infty}[\alpha^{1/2}\Phi_4(\alpha)] = 0.$$

From the Weber-Schaftheitlin integral, substitution of $D(\xi)$ and $S(\xi)$ into (21c) and (21d), respectively, result in the following Abel integral equations:

$$\delta\int_r^\infty \Phi_4(\alpha)\frac{d\alpha}{\sqrt{\alpha^2-r^2}} = \sqrt{\frac{\pi}{2}}\,G_0(r) + \delta\frac{\kappa_1}{\kappa_2}\int_r^\infty \frac{d}{d\alpha}[\alpha^2\Phi_3(\alpha)]\alpha^{-3}\sqrt{\alpha^2-r^2}\,d\alpha \quad r\in(1,\ \infty) \qquad (23)$$

$$\delta\int_r^\infty \Phi_3(\alpha)\alpha^{-2}\frac{d\alpha}{\sqrt{\alpha^2-r^2}} = \sqrt{\frac{\pi}{2}}\,G_2(r)r^{-2} \quad r\in(1,\ \infty). \qquad (24)$$

Inverting Eqs. (23) and (24) and substituting for $G_0(r)$ and $G_2(r)$, after exchanging orders of integration, yield

$$\Phi_3(\alpha) = -2\sqrt{\frac{\pi}{2}}\frac{\sigma_0}{\mu}\alpha^{1/2}\int_0^\infty [g_2(\xi) - g_1(\xi)]\xi^{1/2}J_{5/2}(\alpha\xi)d\xi \quad \alpha\in(1,\ \infty) \qquad (25)$$

$$\Phi_4(\alpha) = \sqrt{\frac{\pi}{2}}\frac{\sigma_0}{\mu}\alpha^{1/2}\int_0^\infty \left\{[g_2(\xi)+g_1(\xi)] - \frac{16}{3}\frac{\kappa_1}{\kappa_2}[g_2(\xi)-g_1(\xi)]\right\}\xi^{1/2}J_{1/2}(\alpha\xi)d\xi \quad \alpha\in(1,\ \infty). \qquad (26)$$

Modifying the expressions for $(\kappa_1 S+\kappa_2 D)$ and $(\kappa_2 S+\kappa_1 D)$ by integrating by parts and then substituting these into (21a) and (21b), respectively, results in the following Abel's integral equations:

$$\sqrt{\frac{2}{\pi}}\kappa_2\delta\int_0^r \frac{d[\Phi_1(\alpha)]}{d\alpha}\frac{d\alpha}{\sqrt{r^2-\alpha^2}} = \int_0^\infty [h(\xi)S(\xi) + g(\xi)D(\xi)]\xi J_0(\xi)d\xi + F_0(r) \quad r\in[0,\ 1) \qquad (27)$$

$$\sqrt{\frac{2}{\pi}}\delta\frac{1}{r^2}\int_0^r \left\{\frac{(\kappa_2^2-\kappa_1^2)}{\kappa_2}\frac{d}{d\alpha}[\alpha^2\Phi_2(\alpha)] - \kappa_1\alpha^3\frac{\mathrm{d}}{\mathrm{d}\alpha}[\alpha^{-1}\Phi_1(\alpha)]\right\}\frac{d\alpha}{\sqrt{r^2-\alpha^2}} = \int_0^\infty [g(\xi)S(\xi)+h(\xi)D(\xi)]\xi J_2(r\xi)d\xi + F_2(r) \quad r\in[0,\ 1). \qquad (28)$$

Applying Abel's solution method to Eqs. (27) and (28) and substituting the expressions for $S(\xi)$ and $D(\xi)$, Eq. (22), into the right-hand side of (27) and (28) result in the final integral equations for $\Phi_1(\alpha)$ and $\Phi_2(\alpha)$

$$\begin{bmatrix} \kappa_2 & 0 \\ -\kappa_1 & (\kappa_2^2-\kappa_1^2)/\kappa_2 \end{bmatrix}\begin{Bmatrix}\Phi_1(\alpha)\\ \Phi_2(\alpha)\end{Bmatrix} = \int_0^1 \begin{bmatrix} K_{11}(\alpha,\eta;\alpha_0,t) & K_{12}(\alpha,\eta;\sigma_0,t) \\ K_{21}(\alpha,\eta;\alpha_0,t) & K_{22}(\alpha,\eta;\sigma_0,t)\end{bmatrix}\begin{Bmatrix}\Phi_1(\eta)\\ \Phi_2(\eta)\end{Bmatrix}d\eta + \int_1^\infty \begin{bmatrix} K_{13}(\alpha,\eta;\sigma_0,t) & K_{14}(\alpha,\eta;\sigma_0,t) \\ K_{23}(\alpha,\eta;\sigma_0,t) & K_{24}(\alpha,\eta;\sigma_0,t)\end{bmatrix}\begin{Bmatrix}\Phi_3(\eta)\\ \Phi_4(\eta)\end{Bmatrix}d\eta + \begin{Bmatrix}N_1(\alpha)\\ N_2(\alpha)\end{Bmatrix} \quad \alpha\in[0,\ 1). \qquad (29)$$

In this coupled system of nonhomogeneous Fredholm integral equations of the second kind (29), the kernels associated with $\Phi_1(\alpha)$ and $\Phi_2(\alpha)$ are the same as those given by Madenci and Westmann (1991). The kernels associated with $\Phi_3(\alpha)$ and $\Phi_4(\alpha)$ are expressed in terms of the following integrals:

$$K_{13}(\alpha,\eta) = \sqrt{\alpha\eta}\int_0^\infty \left[h(\xi;\sigma_0,t) - \frac{\kappa_1}{\kappa_2}g(\xi;\sigma_0,t)\right]\xi J_{1/2}(\alpha\xi)J_{5/2}(\eta\xi)d\xi$$

$$K_{14}(\alpha,\eta) = \sqrt{\alpha\eta}\int_0^\infty g(\xi;\sigma_0,t)\xi J_{1/2}(\alpha\xi)J_{1/2}(\eta\xi)d\xi$$

$$K_{23}(\alpha,\eta) = \sqrt{\alpha\eta}\int_0^\infty \left[g(\xi;\sigma_0,t) - \frac{\kappa_1}{\kappa_2}h(\xi;\sigma_0,t)\right]\xi J_{5/2}(\alpha\xi)J_{5/2}(\eta\xi)d\xi$$

$$K_{24}(\alpha,\eta) = \sqrt{\alpha\eta}\int_0^\infty h(\xi;\sigma_0,t)\xi J_{5/2}(\alpha\xi)J_{1/2}(\eta\xi)d\xi.$$

The functions $N_1(\alpha)$ and $N_2(\alpha)$ can be written as

$$N_1(\alpha) = 2\sqrt{\frac{\pi}{2}}\frac{\sigma_0}{\mu}\alpha^{1/2}\int_0^\infty [f_2(\xi)+f_1(\xi)]\xi^{1/2}J_{1/2}(\alpha\xi)d\xi$$

$$N_2(\alpha) = 2\sqrt{\frac{\pi}{2}}\frac{\sigma_0}{\mu}\alpha^{1/2}\int_0^\infty [f_2(\xi)-f_1(\xi)]\xi^{1/2}J_{5/2}(\alpha\xi)d\xi.$$

The evaluation of equations for $\Phi_2(\alpha)$ and $\Phi_4(\alpha)$ and then their substitution into Eq. (29) allow for the solution of $\Phi_1(\alpha)$ and $\Phi_2(\alpha)$.

For the present problem, the stress intensity factor K_I near

Downloaded 03 May 2010 to 171.66.16.245. Redistribution subject to ASME license or copyright; see http://www.asme.org/terms/Terms_Use.cfm

the delamination edge is obtained from the following expression:

$$\sigma_{zz}(r,\theta,0) = -\frac{\mu}{2}\left\{\int_0^\infty [\kappa_1 S(\xi)+\kappa_2 D(\xi)]\xi J_0(r\xi)d\xi - \int_0^\infty [h(\xi)S(\xi)+g(\xi)D(\xi)]\xi J_0(r\xi)d\xi - F_0(r)\right\} + \frac{\mu}{\sqrt{2}}\left\{\int_0^\infty [\kappa_2 S(\xi)+\kappa_1 D(\xi)]\xi J_2(r\xi)d\xi - \int_0^\infty [g(\xi)S(\xi)+h(\xi)D(\xi)]\xi J_2(r\xi)d\xi - F_2(r)\right\}\cos(2\theta) \quad r\in(1,\infty). \quad (30)$$

Substituting the modified forms of $[\kappa_1 S(\xi)+\kappa_2 D(\xi)]$ and $[\kappa_2 S(\xi)+\kappa_1 D(\xi)]$ in conjunction with the use of Weber-Schaftheitlin integral yields the following:

$$\frac{2}{\mu}\sigma_{zz}(r,\theta,0) = \kappa_2\delta[\Phi_1(1)-\Phi_4(1)]\sqrt{\frac{2}{\pi}}\frac{H(r-1)}{\sqrt{r^2-1}} + \delta\sqrt{2}\left\{\kappa_1[\Phi_1(1)-\Phi_4(1)] - \frac{\kappa_2^2-\kappa_1^2}{\kappa_2}[\Phi_2(1)-\Phi_3(1)]\right\}\sqrt{\frac{2}{\pi}}\frac{1}{r^2}\frac{H(r-1)}{\sqrt{r^2-1}}\cos(2\theta) - \kappa_2\delta\sqrt{\frac{2}{\pi}}\left[\int_0^1 \frac{d[\Phi_1(\alpha)]}{d\alpha}\frac{H(r-\alpha)}{\sqrt{r^2-\alpha^2}}d\alpha + \int_1^\infty \frac{d[\Phi_4(\alpha)]}{d\alpha}\frac{H(r-\alpha)}{\sqrt{r^2-\alpha^2}}d\alpha\right] + \delta\sqrt{\frac{2}{\pi}}\left[\int_0^1\left\{\frac{(\kappa_2^2-\kappa_1^2)}{\kappa_2}\frac{d}{d\alpha}[\alpha^2\Phi_2(\alpha)] - \kappa_1\alpha^3\frac{d}{d\alpha}[\alpha^{-1}\Phi_1(\alpha)]\right\}\frac{1}{r^2}\times\frac{H(r-\alpha)}{\sqrt{r^2-\alpha^2}}d\alpha + \int_1^\infty\left\{\frac{(\kappa_2^2-\kappa_1^2)}{\kappa_2}\frac{d}{d\alpha}[\alpha^2\Phi_3(\alpha)] - \kappa_1\alpha^3\frac{d}{d\alpha}[\alpha^{-1}\Phi_4(\alpha)]\right\}\frac{1}{r^2}\frac{H(r-\alpha)}{\sqrt{r^2-\alpha^2}}d\alpha\right]\cos(2\theta) + \int_0^\infty [h(\xi)S(\xi)+g(\xi)D(\xi)]\xi J_0(r\xi)d\xi + F_0(r) - \left[\int_0^\infty [g(\xi)S(\xi)+h(\xi)D(\xi)]\xi J_2(r\xi)d\xi + F_2(r)\right]\cos(2\theta). \quad (31)$$

All the terms in Eq. (31) except the first two are bounded when r approaches 1. Integration by parts demonstrates the boundedness of the integrals involving the $1/\sqrt{r^2-\alpha^2}$ term. By using the Weierstrass-M and Drichlet tests for uniform convergence, the remaining integrals can be shown to be continuous functions in the interval $(1,\infty)$. From Eqs. (14) and (31), the stress intensity factor can be obtained as

$$K_I = \mu\delta\left[\frac{\kappa_2}{\sqrt{2}}[\Phi_1(1)-\Phi_4(1)] + \left\{\kappa_1[\Phi_1(1)-\Phi_4(1)] - \frac{(\kappa_2^2-\kappa_1^2)}{\kappa_2}[\Phi_2(1)-\Phi_3(1)]\right\}\cos(2\theta)\right].$$

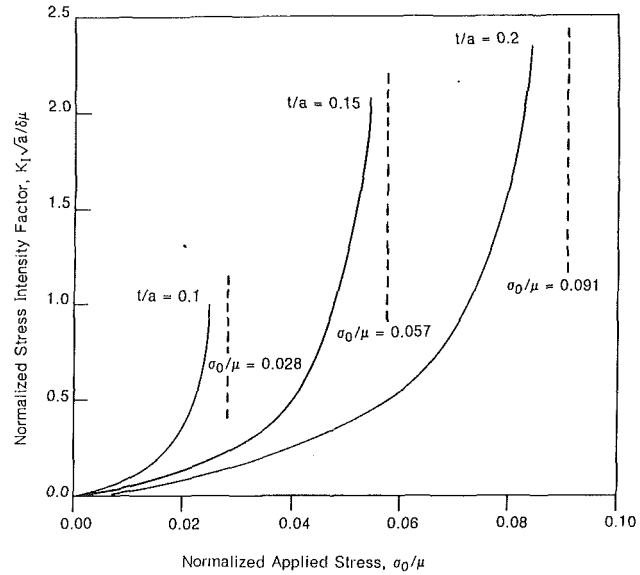


Fig. 2 Normalized stress intensity factor as a function of normalized applied stress—axisymmetric load

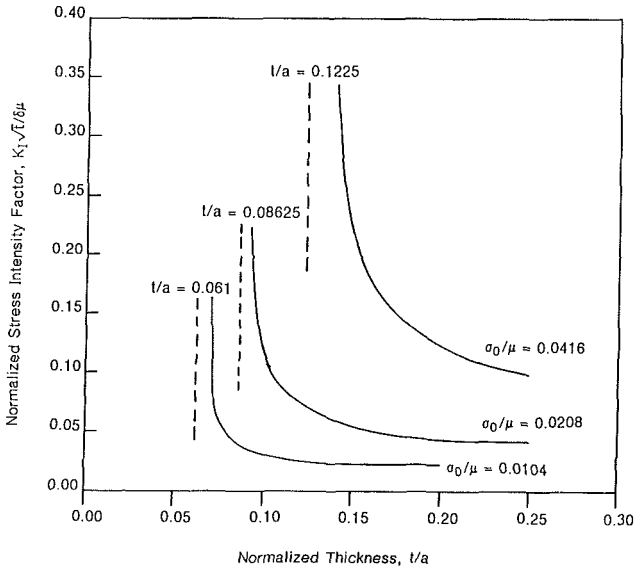


Fig. 3 Normalized stress intensity factor as a function of normalized thickness—axisymmetric load

5 Numerical Results

The complexity of the kernels in the integral Eqs. (13), (29) requires a numerical solution, the treatment of which is well documented (Baker, 1977). The solutions to Eqs. (13), (29) exist only if the applied stress is less than the value of the buckling stress, σ_0. The general form of these integral equations is the same as that presented by Madenci and Westmann (1991), but with forcing functions which are proportional to the magnitude of the initial imperfections. Therefore, the numerical discretization procedure adopted in this paper is the same. In all calculations, the value of Poisson's ratio is taken to be 0.3, and the number of integration intervals is taken to be $N=40$ as a result of a convergence study.

In the axisymmetric compression case, the normalized stress intensity factor, $K_I\sqrt{a}/\mu\delta$, is calculated for a range of normalized applied stresses, σ_0/μ. The results are depicted in Fig. 2 for a specified dimensionless thickness, t/a. In order to identify the nature of the delamination growth process, the normalized stress intensity factor, $K_I\sqrt{t}/\mu\delta$, is calculated as a function of dimensionless thickness, t/a, for specified applied stress, σ_0/μ. This relationship is illustrated in Fig. 3 for a range of σ_0/μ values.

Downloaded 03 May 2010 to 171.66.16.245. Redistribution subject to ASME license or copyright; see http://www.asme.org/terms/Terms_Use.cfm

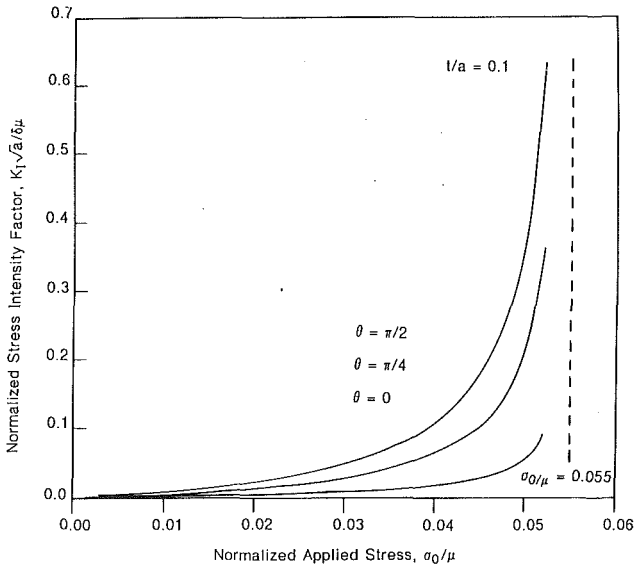


Fig. 4 Normalized stress intensity factor as a function of normalized applied stress for $t = 0.1$—uniaxial load

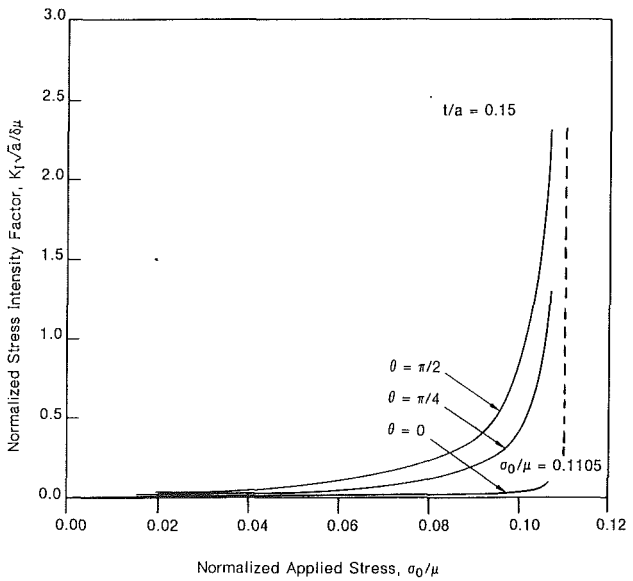


Fig. 6 Normalized stress intensity factor as a function of normalized applied stress for $t = 0.2$—uniaxial load

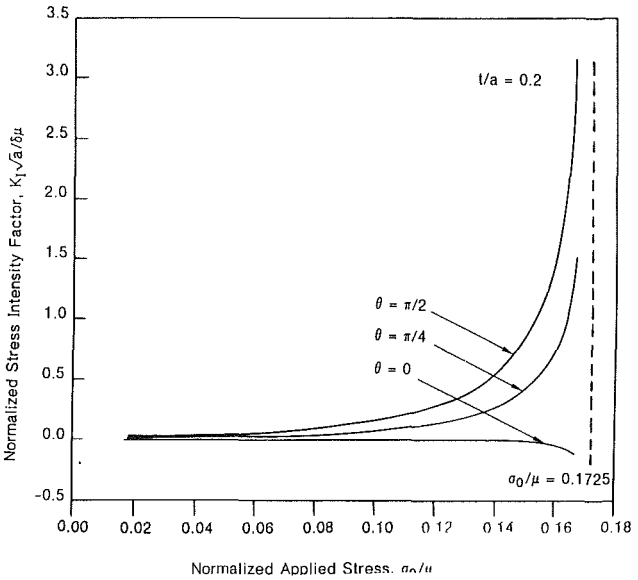


Fig. 5 Normalized stress intensity factor as a function of normalized applied stress for $t = 0.15$—uniaxial load

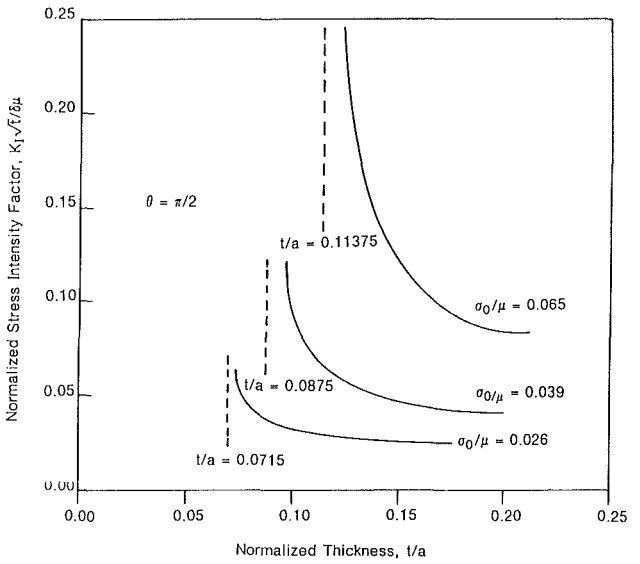


Fig. 7 Normalized stress intensity factor as a function of normalized thickness for $\theta = 90$—uniaxial load

The coupled system of integral equations for uniaxial compression is solved by extending the method used by Madenci and Westmann (1991). The variation of the dimensionless stress intensity factor, $K_I\sqrt{a}/\mu\delta$, against the dimensionless applied stress, σ_0/μ, for 0, 45, and 90 deg is presented in Figs. 4, 5, and 6, each of which corresponds to specified dimensionless thickness, t/a. Along the direction of applied load ($\theta = 0$ deg), the dimensionless stress intensity factor, $K_I\sqrt{t}/\mu\delta$, as a function of the dimensionless thickness, t/a, is depicted in Fig. 7 for a range of specified stresses.

6 Final Comments

The present analysis focuses on the assessment of the delamination growth parameter, K_I, due to the magnitude of imperfections, δ. The axisymmetric and uniaxial loading conditions are considered while addressing this problem.

As mentioned previously, the solution of the governing equations leading to the integral equations (13), (29) is carried out by the procedure employed by Madenci and Westmann (1991). The governing equations for the axisymmetric loading case involves an approximation in order to make the formulation tractable. The effect of this approximation was discussed in detail and shown to be insignificant by Madenci and Westmann.

The stress intensity factors are determined to be a complex function of the applied stress, unlike those encountered in linear elastic fracture mechanics where the stress intensity factor is proportional to the applied load. The present analysis indicates unstable delamination growth, even before the buckling stress is reached if the stress intensity factor is greater than or equal to the fracture toughness of the interface. This prediction has been experimentally observed by Pavier and Chester (1990) for delaminations embedded in carbon fiber-reinforced epoxy. The study of delamination growth prior to buckling is made possible by determining the stress intensity factor. The prediction of the initial direction of delamination growth is also an important outcome of this approach, as previous analyses by other authors could not account for delamination growth before buckling. The present analysis disregards the

Downloaded 03 May 2010 to 171.66.16.245. Redistribution subject to ASME license or copyright; see http://www.asme.org/terms/Terms_Use.cfm

effect of nonlinearities which result in unbounded stress intensity factors as the applied stress approaches the buckling stress because of the assumptions involved in the derivation of governing equations.

For two layers bonded together, the fracture toughness of the interface may be much smaller than that of the parent metal. As shown in Figs. 3 and 7, the stress intensity factor increases for fixed delamination length under increasing applied stress. Once the fracture toughness of the interface is reached, then delamination growth occurs. As delamination grows, the stress intensity factor increases. This relationship is depicted for certain values of σ_0/μ in Figs. 3 and 7. Once the delamination growth begins, it accelerates, and the ratio of delamination length to thickness, t/a, decreases to the point where buckling occurs under the specified applied stress. As shown in Figs. 4 through 6, the initial direction of delamination growth under uniaxial compression is in the direction perpendicular to that of the load. This prediction is in agreement with the test results reported by Chai and Babcock (1985) for a specific laminate lay-up. This prediction is also in agreement with the numerical study conducted by Whitcomb (1989).

The modeling of the layered systems of materials presented in this study is far from the real-life laminated composite materials. However, the purpose of this analysis was to better understand the interaction between delamination growth and buckling and to establish bench-mark solutions for related problems.

References

Baker, C. T. H., 1977, *The Numerical Treatment of Integral Equations*, Claredon Press, Oxford, U.K.

Chai, H., and Babcock, C. D., 1985, "Two-Dimensional Modelling of Compressive Failure in Delaminated Laminates," *J. Composite Materials*, Vol. 19, pp. 67–98.

Chai, H., Knauss, W. G., and Babcock, C. D., 1983, "Observation of Damage Growth in Compressively Loaded Laminates," *Experimental Mechanics*, Vol. 23, pp. 329–337.

Copson, E. T., 1961, "On Certain Dual Integral Equations," *Proc. Glasgow Math. Assoc.*, Vol. 5, pp. 21–24.

McCarty, J. E., and Ratwani, M. M., 1983, "Damage Tolerance of Composites," F33615-82-C3212, Interim Report No. 2, Boeing Military Airplane Company, Seattle, WA.

Madenci, E., 1987, "Local Delamination Buckling in Layered Structures," Ph.D. Thesis, University of California, Los Angeles, CA.

Madenci, E., 1991, "Delamination Growth and Buckling in an Orthotropic Strip," *Int. J. Solids and Structures*, Vol. 27, pp. 1773–1788.

Madenci, E., and Westmann, R. A., 1991, "Local Delamination Buckling in Layered Systems," ASME JOURNAL OF APPLIED MECHANICS, Vol. 58, pp. 157–166.

Pavier, M. J., and Chester, T. W., 1990, "Compression Failure of Carbon Fiber-Reinforced Coupons Containing Central Delaminations," *Composites*, Vol. 21, pp. 23-31.

Starnes, J. H., and Williams, J. G., 1984, "Failure Characteristics of Graphite/Epoxy Structural Components Loaded in Compression," NASA TM 84552.

Sneddon, I. N., and Lowengrub, M., 1969, *Crack Problem in the Classical Theory of Elasticity*, John Wiley and Sons, New York.

Watson, G. N., 1962, *Theory of Bessel Functions*, University Press, Cambridge, U.K.

Westmann, R. A., 1965, "Simultaneous Pairs of Dual Integral Equations," *Society of Industrial Applied Mathematics Review*, Vol. 7, pp. 341–348.

Whitcomb, J. D., 1989, "Three-Dimensional Analysis of a Postbuckled Embedded Delamination," *J. Composite Materials*, Vol. 23, pp. 862–887.

Whittaker, E. T., and Watson, G. N., 1920, *A Course of Modern Analysis*, University Press, Cambridge, U.K.

APPENDIX

In Eq. (8), the function $B(c, \xi)$ is expressed as

$$B(c, \xi) = \int_0^c r \sin\frac{\pi r}{c} J_1(r\xi)\, dr.$$

The forcing functions that appear in the pair of coupled dual integral Eqs. (21) are the following:

$$F_0(r) = 2\sqrt{\frac{\pi}{2}}\frac{\sigma_0}{\mu}\delta\int_0^\infty [f_2(\xi) + f_1(\xi)]\xi J_0(r\xi)\, d\xi$$

$$F_2(r) = 2\sqrt{\frac{\pi}{2}}\frac{\sigma_0}{\mu}\delta\int_0^\infty [f_2(\xi) - f_1(\xi)]\xi J_2(r\xi)\, d\xi$$

$$G_0(r) = \sqrt{\frac{\pi}{2}}\frac{\sigma_0}{\mu}\delta\int_0^\infty [g_2(\xi) + g_1(\xi)]J_0(r\xi)\, d\xi$$

$$G_2(r) = \sqrt{\frac{\pi}{2}}\frac{\sigma_0}{\mu}\delta\int_0^\infty [g_2(\xi) - g_1(\xi)]J_2(r\xi)\, d\xi$$

where

$$f_1(\xi) = (k_1' + k_2')a_{31} + k_3' a_{33}; \quad f_2(\xi) = (k_5' + k_6')a_{35} + k_7' a_{37}$$

$$g_1(\xi) = (k_1' - k_2')\rho(\gamma_1) + k_3'\rho(\gamma_2);$$

$$g_2(\xi) = (k_5' - k_6')\rho(\gamma_3) + k_7'\rho(\gamma_4)$$

in which

$$k_1' = e_1 - (b_1' e^{-\gamma_1\xi t} + b_2' e^{\gamma_2\xi t})\bar{S}_1(\xi) + (b_1' + b_2')e^{-(\gamma_1-\gamma_2)\xi t}\bar{S}_2(\xi)]/\Delta_1(\xi)$$

$$k_2' = e_1[(b_1' e^{\gamma_1\xi t} - b_2' e^{\gamma_2\xi t})\bar{S}_1(\xi) + (b_2' - b_1')e^{(\gamma_1+\gamma_2)\xi t}\bar{S}_2(\xi)]/\Delta_1(\xi)$$

$$k_3' = e_2 b_3'[(e^{\gamma_1\xi t} + e^{-\gamma_1\xi t})\bar{S}_1(\xi) - 2\bar{S}_2(\xi)]/\Delta_1(\xi)$$

$$k_5' = e_2[-(c_1' e^{-\gamma_3\xi t} + c_2' e^{\gamma_4\xi t})\bar{S}_1(\xi) + (c_1' + c_2')e^{-(\gamma_3-\gamma_4)\xi t}\bar{S}_2(\xi)]/\Delta_2(\xi)$$

$$k_6' = e_2[(c_1' e^{\gamma_3\xi t} - c_2' e^{\gamma_4\xi t})\bar{S}_1(\xi) + (c_2' - c_1')e^{(\gamma_3+\gamma_4)\xi t}\bar{S}_2(\xi)]/\Delta_2(\xi)$$

$$k_7' = e_2 c_3'[(e^{\gamma_3\xi t} + e^{-\gamma_3\xi t})\bar{S}_1(\xi) - 2\bar{S}_2(\xi)]/\Delta_2(\xi).$$

The constants which appear in the expressions for $k_1' - k_7'$ are defined as follows:

$$e_1 = (1 - 1/\sqrt{2})/4, \quad e_2 = (1 + 1/\sqrt{2})/4$$

$$b_1' = a_{31}a_{13}, \quad b_2' = a_{11}a_{33}, \quad b_3' = a_{11}a_{31}$$

$$c_1' = a_{35}a_{17}, \quad c_2' = a_{15}a_{37}, \quad c_3' = a_{15}a_{35}.$$

The functions $\bar{S}_1(\xi)$ and $\bar{S}_2(\xi)$ are already given in Section 3. The rest of the constants and functions are defined in the Appendix of Madenci and Westmann (1990).

Downloaded 03 May 2010 to 171.66.16.245. Redistribution subject to ASME license or copyright; see http://www.asme.org/terms/Terms_Use.cfm

The Initial Post-buckling and Growth Behavior of Internal Delaminations in Composite Plates

G. A. Kardomateas
Assoc. Professor,
School of Aerospace Engineering,
Georgia Institute of Technology,
Atlanta, GA 30332-0150
Mem. ASME

The initial post-buckling and growth behavior of delaminations in plates is studied by a perturbation procedure. In this work, no restrictive assumptions regarding the delamination thickness and plate length are made, i.e., the usual thin film assumptions are relaxed. The perturbation procedure is based on an asymptotic expansion of the load and deformation quantities in terms of the distortion parameter of the delaminated layer, the latter being considered a compressive elastica. Closed-form solutions for the load and midpoint delamination deflection versus applied compressive displacement during the initial post-buckling phase are derived. Moreover, closed-form expressions for the energy release rate and the mixity ratio (i.e., Mode II versus Mode I) at the delamination tip are produced. A higher Mode I component is found to be present during the initial post-buckling phase for delaminations of increasing ratio of delamination thickness over plate thickness, h/T *(i.e., delaminations further away from the surface). Moreover, the energy release rate corresponding to the same applied strain is larger for a higher* h/T *ratio. The reduced growth resistance of these configurations is verified by experimental results on unidirectional composite specimens with internal delaminations.*

Introduction

Delaminations or interlayer cracks are developed as a result of imperfections in production technology or due to service loads which may include impact by foreign objects. As a consequence, structural elements with delaminations under compression suffer a degradation of their stiffness and buckling strength and potential loss of integrity from possible growth of the interlayer crack. Besides strength, delaminations can influence other performance characteristics, such as the energy absorption capacity of composite beam systems (Kardomateas and Schmueser, 1988).

Delamination buckling in plates under compression has received considerable attention and numerous contributions have addressed related issues in both one-dimensional and two-dimensional treatments (e.g., Chai et al., 1981; Simitses et al., 1985; Wang et al., 1985; Evans and Hutchinson, 1984; Chai and Babcock, 1985). However, although the critical point can be fairly well determined and has been extensively studied, limited work has focused on the post-buckling behavior, which ultimately governs the growth characteristics of the delamination.

The one configuration most thoroughly studied is the one-dimensional delamination, consisting of a delamination in an infinitely thick plate. In this model (Chai, Babcock, and Knauss, 1981), which has also been called "thin film" model, the unbuckled (base) plate is assumed to be subject to a uniform compressive strain. Closed-form expressions for the energy release rate from the thin film model were derived by Chai et al. (1981) by using the strain energy expressions before and after delamination buckling.

The other configuration most extensively studied is the axisymmetric counterpart to the one-dimensional delamination, i.e., a circular delamination in a perfectly rigid supporting plate. The latter relates also to the so-called blister test used to determine adhesive and cohesive material properties. For this configuration, Evans and Hutchinson (1984) derived a formula for the energy release rate by using an asymptotically valid solution to the system of governing equations for small buckling deflections. Results for the energy release rate of a circular delamination were also given by Chai (1990) and calculated through a path-independent integral approach by Yin (1985). In the same context, Storåkers and Andersson (1988) derived general potential energy theorems and associated bounds for composite plates within the kinematical assumptions usually attributed to von Karman, and studied in detail the efficiency of different analytical and numerical means for this circular delamination case.

For delaminations in plates that cannot fulfill the "thin

Contributed by the Applied Mechanics Division of THE AMERICAN SOCIETY OF MECHANICAL ENGINEERS for presentation at the ASME Winter Annual Meeting, New Orleans, LA, Nov. 28–Dec. 3, 1993.
Discussion on this paper should be addressed to the Technical Editor, Professor Lewis T. Wheeler, Department of Mechanical Engineering, University of Houston, Houston, TX 77204-4792, and will accepted until four months after final publication of the paper itself in the ASME JOURNAL OF APPLIED MECHANICS.
Manuscript received by the ASME Applied Mechanics Division, Aug. 10, 1992; final revision, Jan. 15, 1993. Associate Technical Editor: J. N. Reddy.
Paper No. 93-WA/APM-9.

Copyright © 1993 by ASME
Downloaded 03 May 2010 to 171.66.16.245. Redistribution subject to ASME license or copyright; see http://www.asme.org/terms/Terms_Use.cfm

film'' model assumptions, both the critical load and the post-critical behavior are expected to deviate from the predictions of Chai et al. (1981). To this extent, Simitses et al. (1985) studied the critical load for a delamination of arbitrary thickness and size in a finite plate. Their results showed indeed a range of critical load versus thin film load ratios, depending on delamination and base plate dimensions, as well as base plate end fixity (simply supported versus clamped). Concerning the post-critical behavior of delaminations of arbitrary size, Kardomateas (1989a) provided a formulation for studying the post-buckling behavior by using elastica theory for representing the deflections of the buckled layer; this work resulted in a system of nonlinear equations rather than closed-form expressions.

In this paper, the initial post-buckling behavior of delaminated composites (with no restrictive assumptions on the delamination dimensions) is studied by using a perturbation procedure based on an asymptotic expansion of the load and deformation quantities in terms of the distortion parameter of the delaminated layer, the latter being considered a compressive elastica. The analysis will lead to closed-form solutions for the load versus applied compressive displacement and the near-tip resultant moments and forces. Subsequently, the bi-material interface crack solutions for the energy release rate and the mode mixity in terms of the resultant moments and forces, as derived by Suo and Hutchinson (1990) will be employed to study the growth characteristics of the delamination. Numerical results for a range of relative delamination thicknesses and lengths are presented and discussed. Moreover, the predicted growth characteristics are compared with experimental observations from compression tests of unidirectional composite specimens with internal debonds.

Initial Post-buckling Solution

In a delaminated system, which can be thought of as an aggregate of constitutive parts such as the delaminated layer, substrate layer, and the base plate, the conditions of geometrical continuity at the common sections (i.e., where the delamination starts or ends) play a particularly important part in the realization of equilibrium states which follow nonlinear paths. The exact laws that govern the behavior of single compressive elements elastically restrained at the ends by means of concentrated forces and moments constitutes the elastica theory (e.g., Britvek, 1973). Generalized coordinates of deformation are the distortion parameter, α, which represents the tangent rotation at an inflection point from the straight position, and the amplitude variable $\Phi(x)$. The initial post-buckling deformations are relatively small, so the exact expressions may be expanded in Taylor series in terms of the distortion parameter. Exact dependence of the end moments, end rotations, and the flexural contraction is through elliptic functions; however, the asymptotic expressions that will be given in this work are in terms of trigonometric functions.

Consider a plate of half-length L (and unit width) with a through-the-width delamination of half-length ℓ, symmetrically located (Fig. 1). The delamination is at an arbitrary position through the thickness T. Over the delaminated region, the laminate consists of the part above the delamination, of thickness h referred to as the ''delaminated'' part, and the part below the delamination, of thickness $H=T-h$, referred to as the ''substrate'' part. The remaining, intact laminate, of thickness T and length $b=L-\ell$, is referred to as the ''base'' plate. Without loss of generality, it may be assumed that $h<T/2$. Accordingly, the subscript $i=d, s, b$ refers to the delaminated part, the substrate or the base plate, respectively. In the following, we shall also denote by D_i the bending stiffness, $D_i=Et_i^3/[12(1-\nu^2)]$, t_i being the thickness of the corresponding part, E the modulus of elasticity, and ν the Poisson's ratio. For simplicity reasons, the properties of the material are assumed homogeneous, linearly elastic, and isotropic (orthotropic properties can be accounted by using $\nu_{12}\nu_{21}$ instead of ν^2 and E the modulus of elasticity along the $x\equiv 1$ axis). Notice also that in Fig. 1 the end moments and tangent rotations are assumed positive clockwise.

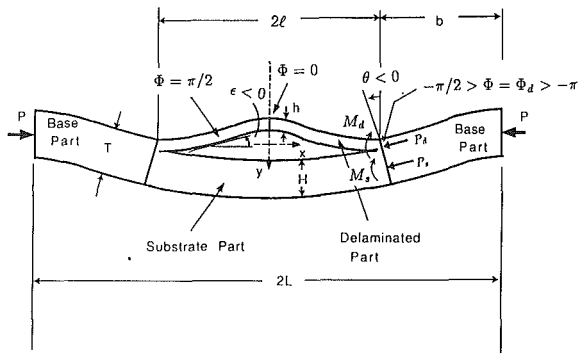


Fig. 1 Definition of the geometry

The buckled configuration of the delaminated layer is part of an inflectional elastica with end amplitude Φ_d and distortion parameter ϵ. At the critical state, the end amplitude is Φ_d^0. Suppose that in the slightly buckled configuration, Φ_d can be expanded in the form

$$\Phi_d=\Phi_d^0+\phi_d^{(1)}\epsilon+\phi_d^{(2)}\epsilon^2+O(\epsilon^3). \tag{1}$$

Then the end rotation at the common section, θ, is given by expanding the relevant expression (Britvek, 1973) in the Taylor series in terms of ϵ (notice that at the critical state $\theta^0=0$):

$$\theta=(\sin\Phi_d)\epsilon-\frac{1}{24}(\sin\Phi_d\cos^2\Phi_d)\epsilon^3+\ldots=(\sin\Phi_d^0)\epsilon+(\cos\Phi_d^0)\phi_d^{(1)}\epsilon^2+\left[(\cos\Phi_d^0)\phi_d^{(2)}-(\sin\Phi_d^0)\frac{\phi_d^{(1)2}}{2}-\frac{1}{24}\sin\Phi_d^0\cos^2\Phi_d^0\right]\epsilon^3+\ldots=\theta^{(1)}\epsilon+\theta^{(2)}\epsilon^2+\theta^{(3)}\epsilon^3+O(\epsilon^4). \tag{2}$$

Notice that by the continuity condition, θ is the same for both the delaminated and substrate parts as well as the base plate.

The asymptotic expansion for the end moment, M_d, is similarly found by substituting (1) into the relevant expression (Britvek, 1973) and subsequently expanding in Taylor series (again $M_d^0=0$):

$$\frac{\ell M_d}{D_d}=(\Phi_d\cos\Phi_d)\epsilon+\frac{\Phi_d}{16}\left(\frac{1}{3}-\frac{\sin 2\Phi_d}{2\Phi_d}\right)(\cos\Phi_d)\epsilon^3+\ldots=\frac{\ell}{D_d}\left(M_d^{(1)}\epsilon+M_d^{(2)}\epsilon^2+M_d^{(3)}\epsilon^3\right)+O(\epsilon^4), \tag{3a}$$

where

$$\frac{\ell M_d^{(1)}}{D_d}=\Phi_d^0\cos\Phi_d^0;\quad\frac{\ell M_d^{(2)}}{D_d}=(\cos\Phi_d^0-\Phi_d^0\sin\Phi_d^0)\,\phi_d^{(1)}, \tag{3b}$$

$$\frac{\ell M_d^{(3)}}{D_d}=(\cos\Phi_d^0-\Phi_d^0\sin\Phi_d^0)\phi_d^{(2)}-\left(\sin\Phi_d^0+\frac{\Phi_d^0}{2}\cos\Phi_d^0\right)\phi_d^{(1)2}+\frac{\Phi_d^0}{16}\left(\frac{1}{3}-\frac{\sin 2\Phi_d^0}{2\Phi_d^0}\right)(\cos\Phi_d^0). \tag{3c}$$

Likewise, the axial force is given by

$$\frac{\ell^2 P_d}{D_d}=\Phi^2+\frac{\Phi^2}{8}\left(1-\frac{\sin 2\Phi}{2\Phi}\right)\epsilon^2+\ldots=\Phi_d^{02}+2\Phi_d^0\phi_d^{(1)}\epsilon$$

Downloaded 03 May 2010 to 171.66.16.245. Redistribution subject to ASME license or copyright; see http://www.asme.org/terms/Terms_Use.cfm

$$+\left[\phi_d^{(1)2}+2\Phi_d^0\phi_d^{(2)}+\frac{\Phi_d^{02}}{8}\left(1-\frac{\sin 2\Phi_d^0}{2\Phi_d^0}\right)\right]\epsilon^2+\ldots$$

$$=\frac{\ell^2}{D_d}\,(P_d^0+P_d^{(1)}\epsilon+P_d^{(2)}\epsilon^2)+O(\epsilon^3). \quad (4)$$

Finally, the flexural contraction, f_d, is

$$f_d=\frac{\ell}{2}\left(1-\frac{\sin 2\Phi_d}{2\Phi_d}\right)\epsilon^2+O(\epsilon^4)=\frac{\ell}{2}\left(1-\frac{\sin 2\Phi_d^0}{2\Phi_d^0}\right)\epsilon^2$$

$$+\frac{\ell}{4}\left(\frac{\sin 2\Phi_d^0}{\Phi_d^0}-\frac{2\cos 2\Phi_d^{02}}{\Phi_d^0}\right)\phi_d^{(1)}\epsilon^3+\ldots=f_d^{(2)}\epsilon^2+f_d^{(3)}\epsilon^3+O(\epsilon^4). \quad (5)$$

Although the substrate part and the base plate undergo moderate bending with no inflection point, we may also use the elastic theory to describe their (nonlinear) deformation; in this case the inflection points are outside the actual elastic curve. For the substrate part, we have to expand not only the amplitude Φ_s, but also the distortion parameter α_s in a perturbation series with respect to the distortion parameter of the delamination layer ϵ:

$$\Phi_s=\Phi_s^0+\phi_s^{(1)}\epsilon+\phi_s^{(2)}\epsilon^2+O(\epsilon^3), \quad (6a)$$

$$\alpha_s=\alpha_s^{(1)}\epsilon+\alpha_s^{(2)}\epsilon^2+\alpha_s^{(3)}\epsilon^3+O(\epsilon^4). \quad (6b)$$

Then the end rotation at the common section θ is given by expanding again in Taylor series in terms of ϵ:

$$\theta=(\sin\Phi_s)\alpha_s-\frac{1}{24}(\sin\Phi_s\cos^2\Phi_s)\alpha_s^3+\ldots$$

$$=\theta_s^{(1)}\epsilon+\theta_s^{(2)}\epsilon^2+\theta_s^{(3)}\epsilon^3+O(\epsilon^4), \quad (7a)$$

where

$$\theta_s^{(1)}=(\sin\Phi_s^0)\alpha_s^{(1)};\ \theta_s^{(2)}=(\cos\Phi_s^0)\phi_s^{(1)}\alpha_s^{(1)}+(\sin\Phi_s^0)\alpha_s^{(2)}, \quad (7b)$$

$$\theta_s^{(3)}=\left[(\cos\Phi_s^0)\phi_s^{(2)}-(\sin\Phi_s^0)\frac{\phi_s^{(1)2}}{2}\right]\alpha_s^{(1)}+(\cos\Phi_s^0)\phi_s^{(1)}\alpha_s^{(2)}$$

$$+(\sin\Phi_s^0)\alpha_s^{(3)}-\frac{1}{24}\sin\Phi_s^0\cos^2\Phi_s^0\alpha_s^{(1)3}. \quad (7c)$$

In a similar fashion, by using the expressions (6), the asymptotic expansion for the end moment, M_s is (again $M_s^0=0$):

$$\frac{\ell M_s}{D_s}=(\Phi_s\cos\Phi_s)\alpha_s+\frac{\Phi_s}{16}\left(\frac{1}{3}-\frac{\sin 2\Phi_s}{2\Phi_s}\right)(\cos\Phi_s)\alpha_s^3+\ldots$$

$$=\frac{\ell}{D_s}\left(M_s^{(1)}\epsilon+M_s^{(2)}\epsilon^2+M_s^{(3)}\epsilon^3\right)+O(\epsilon^4), \quad (8a)$$

where

$$\frac{\ell M_s^{(1)}}{D_s}=(\Phi_s^0\cos\Phi_s^0)\alpha_s^{(1)}, \quad (8b)$$

$$\frac{\ell M_s^{(2)}}{D_s}=(\cos\Phi_s^0-\Phi_s^0\sin\Phi_s^0)\,\phi_s^{(1)}\alpha_s^{(1)}+(\Phi_s^0\cos\Phi_s^0)\alpha_s^{(2)}, \quad (8c)$$

$$\frac{\ell M_s^{(3)}}{D_s}=(\Phi_s^0\cos\Phi_s^0)\alpha_s^{(3)}+(\cos\Phi_s^0-\Phi_s^0\sin\Phi_s^0)\,(\phi_s^{(2)}\alpha_s^{(1)}+\phi_s^{(1)}\alpha_s^{(2)})$$

$$-\left(\sin\Phi_s^0+\frac{\Phi_s^0}{2}\cos\Phi_s^0\right)\phi_s^{(1)2}\alpha_s^{(1)}$$

$$+\frac{\Phi_s^0}{16}\left(\frac{1}{3}-\frac{\sin 2\Phi_s^0}{2\Phi_s^0}\right)(\cos\Phi_s^0)\,\alpha_s^{(1)3}. \quad (8d)$$

Likewise, the axial force is given by

$$\frac{\ell^2 P_s}{D_s}=\Phi_s^2+\frac{\Phi_s^2}{8}\left(1-\frac{\sin 2\Phi_s}{2\Phi_s}\right)\epsilon^2+\ldots$$

$$=\frac{\ell^2}{D_s}\,(P_s^0+P_s^{(1)}\epsilon+P_s^{(2)}\epsilon^2)+O(\epsilon^3), \quad (9a)$$

where

$$\frac{\ell^2 P_s^0}{D_s}=\Phi_s^{02};\qquad \frac{\ell^2 P_s^{(1)}}{D_s}=2\Phi_s^0\phi_s^{(1)}, \quad (9b)$$

$$\frac{\ell^2 P_s^{(2)}}{D_s}=\phi_s^{(1)2}+2\Phi_s^0\phi_s^{(2)}+\frac{\Phi_s^{02}}{8}\left(1-\frac{\sin 2\Phi_s^0}{2\Phi_s^0}\right)\alpha_s^{(1)2}. \quad (9c)$$

Finally, the asymptotic expansion for the flexural contraction, f_s, is found to be

$$f_s=\frac{\ell}{2}\left(1-\frac{\sin 2\Phi_s}{2\Phi_s}\right)\alpha_s^2+O(\alpha_s^4)$$

$$=f_s^{(2)}\epsilon^2+f_s^{(3)}\epsilon^3+O(\epsilon^4), \quad (10a)$$

where

$$f_s^{(2)}=\frac{\ell}{2}\left(1-\frac{\sin 2\Phi_s^0}{2\Phi_s^0}\right)\alpha_s^{(1)2}, \quad (10b)$$

$$f_s^{(3)}=\frac{\ell}{4}\left(\frac{\sin 2\Phi_s^0}{\Phi_s^{02}}-\frac{2\cos 2\Phi_s^0}{\Phi_s^0}\right)\phi_s^{(1)}\alpha_s^{(1)2}$$

$$+\ell\left(1-\frac{\sin 2\Phi_s^0}{2\Phi_s^0}\right)\alpha^{(1)}\alpha_s^{(2)}. \quad (10c)$$

The base plate is assumed to be simply supported, so at the simply supported end, the amplitude $\Phi=-\pi/2$ and at the common section $\Phi=\Phi_b$. The amplitude at the common section and the distortion parameter of the base plate are now expanded in terms of the distortion parameter of the delaminated part ϵ:

$$\Phi_b=\Phi_b^0+\phi_b^{(1)}\epsilon+\phi_b^{(2)}\epsilon^2+O(\epsilon^3), \quad (11a)$$

$$\alpha_b=\alpha_b^{(1)}\epsilon+\alpha_b^{(2)}\epsilon^2+\alpha_b^{(3)}\epsilon^3+O(\epsilon^4). \quad (11b)$$

Moreover, the end rotation at the common section θ is given by expanding again the relevant expression from Britvek (1973) in Taylor series in terms of ϵ:

$$\theta=\left[\sin\Phi_b+\frac{\cos\Phi_b}{\Phi_b+(\pi/2)}\right]\alpha_b+R(\Phi_b)\alpha_b^3+\ldots$$

$$=\theta_b^{(1)}\epsilon+\theta_b^{(2)}\epsilon^2+\theta_b^{(3)}\epsilon^3+O(\epsilon^4), \quad (12a)$$

where $R(\Phi_b)$ is defined by

$$R(\Phi_b)=\frac{7}{48}\frac{\cos\Phi_b}{\Phi_b+(\pi/2)}-\frac{3}{32}\frac{\cos\Phi_b\sin 2\Phi_b}{[\Phi_b+(\pi/2)]^2}-\frac{1}{3}\frac{\cos^3\Phi_b}{[\Phi_b+(\pi/2)]^3}$$

$$-\frac{1}{24}\sin\Phi_b\cos^2\Phi_b. \quad (12b)$$

In terms of

$$\beta=\sin\Phi_b^0+\frac{\cos\Phi_b^0}{\Phi_b^0+(\pi/2)};\quad q=\cos\Phi_b^0-\left(\Phi_b^0+\frac{\pi}{2}\right)\sin\Phi_b^0, \quad (12c)$$

$$\xi=\cos\Phi_b^0-\frac{\sin\Phi_b^0}{\Phi_b^0+(\pi/2)}-\frac{\cos\Phi_b^0}{[\Phi_b^0+(\pi/2)]^2}, \quad (12d)$$

$$\chi=\frac{\cos\Phi_b^0}{[\Phi_b^0+(\pi/2)]^3)}+\frac{\sin\Phi_b^0}{[\Phi_b^0+(\pi/2)]^2}-\frac{\cos\Phi_b^0}{2[\Phi_b^0+(\pi/2)]}-\frac{\sin\Phi_b^0}{2}, \quad (12e)$$

we obtain

$$\theta_b^{(1)}=\beta\alpha_b^{(1)};\quad \theta_b^{(2)}=\xi\phi_b^{(1)}\alpha_b^{(1)}+\beta\alpha_b^{(2)}, \quad (12f)$$

$$\theta_b^{(3)}=\beta\alpha_b^{(3)}+\xi[\phi_b^{(1)}\alpha_b^{(2)}+\phi_b^{(2)}\alpha_b^{(1)}]$$

$$+\chi\phi_b^{(1)2}\alpha_b^{(1)}+R(\Phi_b^0)\,\alpha_b^{(1)3}. \quad (12g)$$

Concerning the end moment, M_b, use of (11) gives the following asymptotic expansion (again $M_b^0=0$):

$$\frac{bM_b}{D_b}=\left(\Phi_b+\frac{\pi}{2}\right)(\cos\Phi_b)\alpha_b+\frac{1}{16}\left(\Phi_b+\frac{\pi}{2}\right)$$

Downloaded 03 May 2010 to 171.66.16.245. Redistribution subject to ASME license or copyright; see http://www.asme.org/terms/Terms_Use.cfm

$$\times\left(\frac{1}{3}-\frac{\sin 2\Phi_b}{2[\Phi_b^0+(\pi/2)]}\right)(\cos\Phi_b)\alpha_b^3+\ldots$$

$$=\frac{b}{D_b}\,(M_b^{(1)}\epsilon+M_b^{(2)}\epsilon^2+M_b^{(3)}\epsilon^3)+O(\epsilon^4), \quad (13a)$$

where

$$\frac{bM_b^{(1)}}{D_b}=\left(\Phi_b^0+\frac{\pi}{2}\right)(\cos\Phi_b^0)\alpha_b^{(1)}, \quad (13b)$$

$$\frac{bM_b^{(2)}}{D_b}=q\phi_b^{(1)}\alpha_b^{(1)}+\left(\Phi_b^0+\frac{\pi}{2}\right)(\cos\Phi_b^0)\alpha_b^{(2)}, \quad (13c)$$

$$\frac{bM_b^{(3)}}{D_b}=\left(\Phi_b^0+\frac{\pi}{2}\right)(\cos\Phi_b^0)\alpha_b^{(3)}$$

$$-\left[\sin\Phi_b^0+\left(\Phi_b^0+\frac{\pi}{2}\right)\frac{\cos\Phi_b^0}{2}\right]\phi_b^{(1)2}\alpha_b^{(1)}+q(\alpha_b^{(1)}\alpha_b^{(2)}+\phi_b^{(2)}\alpha_b^{(1)})$$

$$+\frac{1}{16}\left(\Phi_b^0+\frac{\pi}{2}\right)\left(\frac{1}{3}-\frac{\sin 2\Phi_b^0}{2[\Phi_b^0+(\pi/2)]}\right)(\cos\Phi_b^0)\alpha_b^{(1)3}. \quad (13d)$$

Likewise, the axial force at the base plate (which is also the applied force) is given by

$$\frac{b^2P}{D_p}=\left(\Phi_b+\frac{\pi}{2}\right)^2+\left(\Phi_b+\frac{\pi}{2}\right)^2\left[\frac{1}{8}-\frac{1}{16}\frac{\sin 2\Phi_b}{[\Phi_b+(\pi/2)]}\right.$$

$$\left.-\frac{1}{2}\frac{\cos^2\Phi_b}{[\Phi_b+(\pi/2)]^2}\right]\alpha_b^2=\frac{b^2}{D_b}\,(P^0+P^{(1)}\epsilon+P^{(2)}\epsilon^2)+O(\epsilon^3), \quad (14a)$$

where

$$\frac{b^2P^0}{D_b}=\left(\Phi_b^0+\frac{\pi}{2}\right)^2;\quad \frac{b^2P^{(1)}}{D_b}=2\left(\Phi_b^0+\frac{\pi}{2}\right)\phi_b^{(1)}, \quad (14b)$$

$$\frac{b^2P^{(2)}}{D_b}=\phi_b^{(1)2}+2\left(\Phi_b^0+\frac{\pi}{2}\right)\phi_b^{(2)}$$

$$+\frac{1}{8}\left(\Phi_b^0+\frac{\pi}{2}\right)^2\left[1-\frac{\sin 2\Phi_b^0}{2[\Phi_b^0+(\pi/2)]}-\frac{4\cos^2\Phi_b^0}{[\Phi_b^0+(\pi/2)]^2}\right]\alpha_b^{(1)2}. \quad (14c)$$

Finally, the flexural contraction, f_b, between the simply supported end and the common section is

$$f=\frac{b}{4}\left[1-\frac{\sin 2\Phi_b}{2[\Phi_b+(\pi/2)]}-\frac{2\cos^2\Phi_b}{[\Phi_b+(\pi/2)]^2}\right]\alpha_b^2+\ldots$$

$$=f_b^{(2)}\epsilon^2+O(\epsilon^3), \quad (15a)$$

where

$$f_b^{(2)}=\frac{b}{4}\left[1-\frac{\sin 2\Phi_b^0}{2[\Phi_b^0+(\pi/2)]}-\frac{2\cos^2\Phi_b^0}{[\Phi_b^0+(\pi/2)]^2}\right]\alpha_b^{(1)2}. \quad (15b)$$

Having obtained the asymptotic expressions for the force and deformation quantities, we shall discuss the formulation of the equilibrium and compatibility requirements that will ultimately define the nonlinear post-critical path. Force and moment equilibrium at the common section require

$$P_d+P_s-P=0, \quad (16a)$$

$$M_d+M_s+M_b-P_d\frac{H}{2}+P_s\frac{h}{2}=0. \quad (16b)$$

The deflections of the delaminated and substrate parts should be geometrically compatible. Thus, a second condition necessary for a solution involves the compatible shortening of the delaminated and substrate parts, which consists, in turn, of the compressive and flexural shortening:

$$\left(f_d+2\frac{P_d\ell}{Eh}\right)-\left(f_s+2\frac{P_s\ell}{EH}\right)+\theta T=0. \quad (17)$$

As the compressive load P is applied, the plate remains flat and a primary state solution (pure compression) is characterized by $P^0=P_d^0T/h$ and $P_s^0=P_d^0H/h$, which gives

$$\Phi_s^0=\Phi_d^0\sqrt{\frac{D_dH}{D_sh}};\quad \Phi_b^0=-\Phi_d^0\frac{b}{\ell}\sqrt{\frac{D_dT}{D_bh}}-\pi/2. \quad (18a)$$

Although determination of the critical point is not a primary objective of this paper and the buckling analysis has been thoroughly carried out in other works (e.g., Simitses et al., 1985), we shall briefly describe the equations for the critical point (in terms of Φ_d^0) for the sake of completeness, and because the formulation for the initial post-buckling naturally follows that for the critical point.

By equating the first-order rotation at the common section we obtain $\alpha_s^{(1)}$ and $\alpha_b^{(1)}$:

$$\alpha_s^{(1)}=\frac{\sin\Phi_d^0}{\sin\Phi_s^0};\quad \alpha_b^{(1)}=\frac{\sin\Phi_d^0}{\beta}. \quad (18b)$$

Writing the moment equilibrium (16b) and the geometric compatibility (17) for the first-order terms and eliminating the quantity $[P_d^{(1)}H-P_s^{(1)}h]$ leads to the characteristic equation, for the determination of Φ_d^0:

$$\frac{D_d}{\ell}\Phi_d^0\cos\Phi_d^0+\sin\Phi_d^0\left[\frac{D_s}{\ell}\Phi_s^0\cot\Phi_s^0\right.$$

$$\left.+\frac{D_b}{b}\left(\Phi_b^0+\frac{\pi}{2}\right)\frac{\cos\Phi_b^0}{\beta}+\frac{EThH}{4\ell}\right]=0. \quad (18c)$$

Next, the initial post-buckling behavior is considered.

First-Order Forces. Force equilibrium, Eq. (16a) for the first-order terms, and use of (4), (9b), and (14b) for the first-order forces gives

$$\phi_b^{(1)}=\frac{\Phi_d^0}{\Phi_b^0+(\pi/2)}\frac{D_db^2}{D_b\ell^2}\phi_d^{(1)}+\frac{\Phi_s^0}{\Phi_b^0+(\pi/2)}\frac{D_sb^2}{D_b\ell^2}\phi_s^{(1)}$$

$$=\rho_d\phi_d^{(1)}+\rho_s\phi_s^{(1)}. \quad (19a)$$

By equating the second-order terms in the expressions for the slope at the common section, $\theta^{(2)}$, Eqs. (2), (7b), and (12f) we can find $\alpha_s^{(2)}$ and $\alpha_b^{(2)}$ as follows:

$$\alpha_s^{(2)}=\frac{\cos\Phi_d^0}{\sin\Phi_s^0}\phi_d^{(1)}-\frac{(\cos\Phi_s^0)\alpha_s^{(1)}}{\sin\Phi_s^0}\phi_s^{(1)}=\gamma_d\phi_d^{(1)}+\phi_s\phi_s^{(1)}, \quad (19b)$$

$$\alpha_b^{(2)}=\frac{\cos\Phi_d^0}{\beta}\phi_d^{(1)}-\frac{\xi\alpha_b^{(1)}}{\beta}\phi_b^{(1)}. \quad (19c)$$

Using (19a) we can write $\alpha_b^{(2)}$ in the form

$$\alpha_b^{(2)}=\eta_d\phi_d^{(1)}+\eta_s\phi_s^{(1)}, \quad (19d)$$

where

$$\eta_d=\frac{\cos\Phi_d^0}{\beta}-\frac{\xi\alpha_b^{(1)}}{\beta}\rho_d;\quad \eta_s=-\frac{\xi\alpha_b^{(1)}}{\beta}\rho_s. \quad (19e)$$

Determination of the first-order forces requires deriving $\phi_d^{(1)}$ and $\phi_s^{(1)}$ and this will be discussed next. The moment equilibrium Eq. (16b) for the second-order terms is

$$M_d^{(2)}+M_s^{(2)}+M_b^{(2)}=\frac{1}{2}\,[P_d^{(2)}H-P_s^{(2)}h]. \quad (20)$$

The geometric compatibility Eq. (17) for the second-order terms gives

$$f_d^{(2)}-f_s^{(2)}+\theta^{(2)}T=[P_s^{(2)}h-P_d^{(2)}H]\frac{2\ell}{EhH}. \quad (21)$$

Eliminating the quantity $[P_s^{(2)}h-P_d^{(2)}H]$ from Eqs. (20) and (21) gives the following first linear equation for $\phi_d^{(1)}$ and $\phi_s^{(1)}$:

$$a_{11}\phi_d^{(1)}+a_{12}\phi_s^{(1)}=\left[\frac{\ell}{2}\left(1-\frac{\sin 2\Phi_s^0}{2\Phi_s^0}\right)\alpha_s^{(1)2}\right.$$

$$\left.-\frac{\ell}{2}\left(1-\frac{\sin 2\Phi_d^0}{2\Phi_d^0}\right)\right]\frac{EhH}{4\ell}, \quad (22a)$$

where

Downloaded 03 May 2010 to 171.66.16.245. Redistribution subject to ASME license or copyright; see http://www.asme.org/terms/Terms_Use.cfm

$$a_{11}=\frac{D_d}{\ell}(\cos\Phi_d^0-\Phi_d^0\sin\Phi_d^0)+\frac{D_s}{\ell}\Phi_s^0(\cos\Phi_s^0)\gamma_d+(\cos\Phi_d^0)$$
$$\times\frac{EhHT}{4\ell}+\frac{D_b}{b}\left[q\alpha_b^{(1)}\rho_d+\left(\Phi_b^0+\frac{\pi}{2}\right)(\cos\Phi_b^0)\eta_d\right], \quad (22b)$$

$$a_{12}=\frac{D_s}{\ell}(\cos\Phi_s^0-\Phi_s^0\sin\Phi_s^0)\alpha_s^{(1)}+\Phi_s^0(\cos\Phi_s^0)\gamma_s$$
$$+\frac{D_b}{b}\left[q\alpha_b^{(1)}\rho_s+\left(\Phi_b^0+\frac{\pi}{2}\right)(\cos\Phi_b^0)\eta_s\right]. \quad (22c)$$

The second equation needed to find $\phi_d^{(1)}$ and $\phi_s^{(1)}$ is the first-order geometric compatibility Eq. (17) at the common section, which becomes after the expressions (4) and (9*b*) for the first-order delamination and substrate forces, and (2) for the first-order rotation, are substituted:

$$\frac{D_s}{\ell^2}\Phi_s^0h\phi_s^{(1)}-\frac{D_d}{\ell^2}\Phi_d^0H\phi_d^{(1)}=\frac{EhHT}{4\ell}\sin\Phi_d^0. \quad (23)$$

The foregoing system of two linear Eqs., (22*a*) and (23), allows finding $\phi_d^{(1)}$ and $\phi_s^{(1)}$, and hence the first-order forces $P_d^{(1)}$, $P_s^{(1)}$ and the first-order applied force $P^{(1)}=P_d^{(1)}+P_s^{(1)}$.

Second-Order Forces. Second-order force equilibrium (16*a*), together with (4), (9*c*), and (14*c*), gives

$$\phi_b^{(2)}=\rho_d\phi_d^{(2)}+\rho_s\phi_s^{(2)}+\rho_c, \quad (24a)$$

where

$$\rho_c=\rho_d\left[\frac{\phi_d^{(1)2}}{2\Phi_d^0}+\frac{\Phi_d^0}{16}\left(1-\frac{\sin 2\Phi_d^0}{2\Phi_d^0}\right)\right]$$
$$+\rho_s\left[\frac{\phi_s^{(1)2}}{2\Phi_s^0}+\frac{\Phi_s^0}{16}\left(1-\frac{\sin 2\Phi_s^0}{2\Phi_s^0}\right)\alpha_s^{(1)2}\right]-\frac{\phi_b^{(1)2}}{2[\Phi_b^0+(\pi/2)]}$$
$$-\frac{1}{16}\left(\Phi_b^0+\frac{\pi}{2}\right)\left[1-\frac{\sin 2\Phi_b^0}{2[\Phi_b^0+(\pi/2)]}-\frac{4\cos^2\Phi_b^0}{[\Phi_b^0+(\pi/2)]^2}\right]\alpha_b^{(1)2}. \quad (24b)$$

By equating the third-order terms in the expressions for the slope at the common section for the delaminated and the substrate parts, $\theta^{(3)}$, Eqs. (2) and (7*c*), we can find $\alpha_s^{(3)}$,

$$\alpha_s^{(3)}=\gamma_d\phi_d^{(2)}+\gamma_s\phi_s^{(2)}+\gamma_c, \quad (25a)$$

where γ_c is given in terms of the following quantities:

$$\psi_d=-\left(\frac{\phi_d^{(1)2}}{2}+\frac{1}{24}\cos^2\Phi_d^0\right)\sin\Phi_d^0, \quad (25b)$$

$$\psi_s=-\left(\frac{\phi_s^{(1)2}}{2}+\frac{1}{24}\alpha_s^{(1)2}\cos^2\Phi_s^0\right)\alpha_s^{(1)}\sin\Phi_s^0$$
$$+\phi_s^{(1)}\alpha_s^{(2)}\cos\Phi_s^0 \quad (25c)$$

as follows:

$$\gamma_c=\frac{\psi_d-\psi_s}{\sin\Phi_s^0}. \quad (25d)$$

In a similar fashion, by equating the third-order terms in the expressions for the slope at the common section for the delaminated and the base parts, and using (24*a*) we can write $\alpha_b^{(3)}$ in the form

$$\alpha_b^{(3)}=\eta_d\phi_d^{(2)}+\eta_s\phi_s^{(2)}+\eta_c, \quad (26a)$$

where

$$\beta\eta_c=\psi_d-(\xi\rho_c+\chi)\alpha_b^{(1)}-\xi\phi_b^{(1)}\alpha_b^{(2)}-R(\Phi_b^0)\alpha_b^{(1)3}. \quad (26b)$$

Determination of the second-order forces requires deriving $\phi_d^{(2)}$ and $\phi_s^{(2)}$ and this will be discussed next. The moment equilibrium Eq. (16*b*) for the third-order terms is

$$M_d^{(3)}+M_s^{(3)}+M_b^{(3)}=\frac{1}{2}[P_d^{(3)}H-P_s^{(3)}h]. \quad (27a)$$

The geometric compatibility Eq. (17) for the third-order terms gives

$$f_d^{(3)}-f_s^{(3)}+\theta^{(3)}T=[P_s^{(3)}h-P_d^{(3)}H]\frac{2\ell}{EhH}. \quad (27b)$$

Eliminating now the quantity $[P_s^{(3)}h-P_d^{(3)}H]$ from Eqs. (27*a*) and (27*b*) gives the following first linear equation for $\phi_d^{(2)}$ and $\phi_s^{(2)}$:

$$a_{11}\phi_d^{(2)}+a_{12}\phi_s^{(2)}=c_1, \quad (28)$$

where the coefficients a_{11} and a_{12} are the same as in the first-order problem, Eqs. (22*b*, *c*), and c_1 is given in Appendix A.

The second equation needed to find $\phi_d^{(2)}$ and $\phi_s^{(2)}$ is the second-order geometric compatibility Eq. (17) at the common section, which becomes after the expressions (4) and (9*c*) for the second-order forces, and (2) for the second-order rotation, are substituted:

$$\frac{D_s}{\ell^2}\Phi_s^0h\phi_s^{(2)}-\frac{D_d}{\ell^2}\Phi_d^0H\phi_d^{(2)}=\left[1-\frac{\sin 2\Phi_d^0}{2\Phi_d^0}-\left(1-\frac{\sin 2\Phi_s^0}{2\Phi_s^0}\right)\alpha_s^{(1)2}\right.$$
$$\left.+\frac{2T}{\ell}\phi_d^{(1)}\cos\Phi_d^0\right]\frac{EhH}{8}+\left[\phi_d^{(1)2}+\frac{\Phi_d^{02}}{8}\left(1-\frac{\sin 2\Phi_d^0}{2\Phi_d^0}\right)\right]\frac{D_dH}{2\ell^2}$$
$$-\left[\phi_s^{(1)2}+\frac{\Phi_s^{02}}{8}\left(1-\frac{\sin 2\Phi_s^0}{2\Phi_s^0}\right)\alpha_s^{(1)2}\right]\frac{D_sh}{2\ell^2}. \quad (29)$$

The foregoing system of two linear Eqs. (28) and (29) allows finding $\phi_d^{(2)}$ and $\phi_s^{(2)}$, and hence the second-order forces $P_d^{(2)}$, $P_s^{(2)}$ and the second-order applied force $P^{(2)}=P_d^{(2)}+P_s^{(2)}$.

Displacements. Next we shall discuss the expressions during the initial post-buckling stage for two additional quantities, which are typically needed for correlation with experimental data: the midpoint deflection of the delaminated layer and the substrate part, and the applied compressive displacement (or applied strain).

First, it should be noted that at each point x there corresponds a value of the variable amplitude $\Phi(x)$; the value at the common section $x=\ell$ is Φ_i, $i=d, s$. Furthermore, at the midpoint $x=0$, where the slope is zero, $\Phi=0$ and at the inflection point, where the slope is α_i, $\Phi=\pi/2$. The deflection increment on the elastica is given by (Britvek, 1973)

$$dw_i=2\sin\left(\frac{\alpha_i}{2}\right)\sqrt{\frac{D_d}{P_d}}\sin\Phi d\Phi. \quad (30a)$$

Integrating between the midpoint ($x=0$) and the common interface ($x=\ell$) gives the midpoint deflection

$$w_{im}=2\sin\left(\frac{\alpha_i}{2}\right)\sqrt{\frac{D_d}{P_d}}(\cos\Phi_i-1). \quad (30b)$$

Substituting the asymptotic expansions for the force P_i and for the amplitude Φ_i, gives the midpoint displacement of the delaminated layer or the substrate part ($i=d, s$) as follows:

$$w_{im}=w_{im}^{(1)}\epsilon+w_{im}^{(2)}\epsilon^2+\ldots, \quad (31a)$$

where for the delaminated layer

$$w_{dm}^{(1)}=\frac{\ell}{\Phi_d^0}(\cos\Phi_d^0-1), \quad (31b)$$

$$w_{dm}^{(2)}=\frac{\ell}{\Phi_d^0}\left[\frac{(1-\cos\Phi_d^0)}{\Phi_d^0}-\sin\Phi_d^0\right]\phi_d^{(1)}, \quad (31c)$$

and for the substrate part after substitution of (6*b*),

$$w_{sm}^{(1)}\frac{\Phi_i^0}{\ell}=(\cos\Phi_s^0-1)\alpha_s^{(1)}, \quad (31d)$$

$$w_{sm}^{(2)}\frac{\Phi_i^0}{\ell}=\left[\frac{(1-\cos\Phi_s^0)}{\Phi_s^0}-\sin\Phi_s^0\right]\phi_s^{(1)}\alpha_s^{(1)}$$
$$+(\cos\Phi_s^0-1)\alpha_s^{(2)}. \quad (31e)$$

Finally, the previous analysis allows finding a direct expression for the applied strain, ϵ_0, as follows:

Downloaded 03 May 2010 to 171.66.16.245. Redistribution subject to ASME license or copyright; see http://www.asme.org/terms/Terms_Use.cfm

$$\epsilon_0 L = \frac{P^0 L}{ET} + \left[\frac{P^{(1)} b}{ET} + \frac{P_d^{(1)}\ell}{Eh} + \frac{H}{2}\theta^{(1)}\right]\epsilon + \left[\frac{f_d^{(2)}}{2} + \frac{P_d^{(2)}\ell}{Eh} + f_b^{(2)} + \frac{P^{(2)} b}{ET} + \frac{H}{2}\theta^{(2)}\right]\epsilon^2 + \ldots . \quad (32)$$

Delamination Growth Characteristics

Before applying the initial post-buckling solution that has just been presented, the basic interface crack solutions that are needed in the analysis will be reviewed. For a general bimaterial interface crack, these solutions depend on the Dundurs (1969) parameters, $\tilde{\alpha}$, $\tilde{\beta}$ and the bimaterial constant $\tilde{\epsilon}$. For the homogeneous system under consideration, $\tilde{\alpha} = \tilde{\beta} = \tilde{\epsilon} = 0$. Therefore, the formulas of Suo and Hutchinson (1990) will be presented with the homogeneous material assumption into consideration.

For the plane-strain interface crack shown in Fig. 1, the energy release rate G is

$$G = \frac{1-\nu}{4\mu}\left[\frac{P^{*2}}{Ah} + \frac{M^{*2}}{Ih^3} + 2\frac{P^* M^*}{\sqrt{AI}h^2}\sin\gamma\right] \quad (33)$$

where μ is the shear modulus. In terms of

$$\eta = h/H;\ C_1 = \frac{h}{T};\ C_2 = \frac{6h^2 H}{T^3};\ C_3 = \frac{h^3}{T^3} \quad (34)$$

P^* and M^* are linear combinations of the loads from the previous post-buckling solution:

$$P^* = P_d - C_1 P - C_2\frac{M_b}{h}, \quad (35a)$$

$$M^* = M_d - C_3 M_b. \quad (35b)$$

Moreover, A and I are positive dimensionless numbers and the angle γ is restricted such that $\gamma \le \pi/2$. These quantities are given by

$$A = \frac{1}{1+4\eta+6\eta^2+3\eta^3};\ I = \frac{1}{12(1+\eta^3)};\ \sin\gamma = 6\eta^2(1+\eta)\sqrt{AI}. \quad (36)$$

The preceding formula does not separate the opening and shearing components. Instead, the following two expressions give the Mode I and Mode II stress intensity factors

$$K_I = \frac{1}{\sqrt{2}}\left[\frac{P^*}{\sqrt{Ah}}\cos\omega + \frac{M^*}{\sqrt{Ih^3}}\sin(\omega+\gamma)\right] \quad (37a)$$

$$K_{II} = \frac{1}{\sqrt{2}}\left[\frac{P^*}{\sqrt{Ah}}\sin\omega - \frac{M^*}{\sqrt{Ih^3}}\cos(\omega+\gamma)\right]. \quad (37b)$$

Accurate determination of ω, which depends only on η (for a fixed set of Dundurs constants $\tilde{\alpha}$, $\tilde{\beta}$), requires the numerical solution of an integral equation and has been reported in Suo and Hutchinson (1990). The extracted ω, however, varies slowly with η in the entire range $0 \le \eta \le 1$, in accordance with the approximate formula (Hutchinson and Suo, 1991)

$$\omega = 52.1^0 - 3^0\eta. \quad (38)$$

The mode mixity is defined by

$$\psi = \tan^{-1}(K_{II}/K_I) = \tan^{-1}\left[\frac{\lambda\sin\omega - \cos(\omega+\gamma)}{\lambda\cos\omega + \sin(\omega+\gamma)}\right], \quad (39a)$$

where λ measures the loading combination as

$$\lambda = \sqrt{\frac{I}{A}}\frac{P^* h}{M^*}. \quad (39b)$$

Substituting the asymptotic expressions for the forces and moments from the post-buckling solution already presented, gives

$$P^* = \epsilon P^{*(1)} + \epsilon^2 P^{*(2)} + \ldots \quad M^* = \epsilon M^{*(1)} + \epsilon^2 M^{*(2)} + \ldots \quad (40a)$$

where the first and second-order terms (i.e., $k = 1,2$) are (notice that the zero-order quantities in the expression for P^* cancel out)

$$P^{*(k)} = \frac{H}{T}P_d^{(k)} - \frac{h}{T}P_s^{(k)} - \frac{6hH}{T^3}M_b^{(k)}, \quad (40b)$$

$$M^{*(k)} = M_d^{(k)} - \frac{h^3}{T^3}M_b^{(k)}. \quad (40c)$$

In the previous relations, the first and second-order forces and moments, $P_d^{(k)}$, $P_s^{(k)}$, $M_d^{(k)}$, $M_b^{(k)}$, $k = 1, 2$ have already been found from the initial post-buckling solution described in the previous section.

Now the energy release rate and the Mode I and II stress intensity factors can be written in the form:

$$G = \epsilon^2 G^{(2)} + \epsilon^3 G^{(3)} + \ldots, \quad (41a)$$

$$K_{I,II} = \epsilon K_{I,II}^{(1)} + \epsilon^2 K_{I,II}^{(2)} + \ldots, \quad (41b)$$

where $K_{I,II}^{(1)}$, $K_{I,II}^{(2)}$ are found by substituting in (37) the first or second-order forces and moments, respectively, $G^{(2)}$ is found from (33) by substituting directly the first-order forces and moments and

$$G^{(3)} = \frac{1-\nu}{2\mu}\left[\frac{P^{*(1)}P^{*(2)}}{Ah} + \frac{M^{*(1)}M^{*(2)}}{Ih^3} + \frac{\sin\gamma}{\sqrt{AI}h^2}\left(P^{*(1)}M^{*(2)} + P^{*(2)}M^{*(1)}\right)\right]. \quad (41c)$$

Discussion of Results

The thin film model of Chai et al. (1981), which is a closed-form solution for the initial post-buckling and growth behavior, represents the limiting solution for a very large value of the ratio h/T, i.e., for a delamination in an infinitely thick base plate. This solution predicts an energy release rate

$$G(\epsilon_0, \ell) = \frac{1}{2}Eh(1-\nu^2)(\epsilon_0 - \epsilon_{cr})(\epsilon_0 + 3\epsilon_{cr}), \quad (42a)$$

where

$$\epsilon_{cr} = \frac{\pi^2 h^2}{12(1-\nu^2)\ell^2}, \quad (42b)$$

is the Euler's critical strain for the delaminated layer (treated as a column with built-in ends) and ϵ_0 is the applied strain. The applied load is $P = E\epsilon_0$ and the midpoint deflection is

$$w_{dm} = -\frac{4\ell}{\pi}\sqrt{(\epsilon_0 - \epsilon_{cr})(1-\nu^2)}. \quad (42c)$$

For this model, the mode mixity is given by the following relation (Hutchinson and Suo, 1991):

$$\tan\psi = \frac{4\cos\omega + \sqrt{3}\xi\sin\omega}{-4\sin\omega + \sqrt{3}\xi\cos\omega}. \quad (43a)$$

Since the thin film model postulates that $\eta = h/H \to 0$, $\omega = 52.1^0$. Futhermore, ξ is defined by

$$\xi = \left[\frac{4}{3}\left(\frac{\epsilon_0}{\epsilon_{cr}} - 1\right)\right]^{1/2}. \quad (43b)$$

These results from the limiting thin film model are a very useful approximation and a comparison with the present general post-buckling solution is noteworthy. In applying the formulas presented in this paper, it should be remarked that in general, the critical end-amplitude for the delamination (that normally buckles with an inflection point) is $-\pi/2 > \Phi_d^0 > -\pi$ (the thin film model assumes $\Phi_d = -\pi$), whereas for the substrate part that normally shows no inflection point, $0 > \Phi_s^0 > -\pi/2$, and

Downloaded 03 May 2010 to 171.66.16.245. Redistribution subject to ASME license or copyright; see http://www.asme.org/terms/Terms_Use.cfm

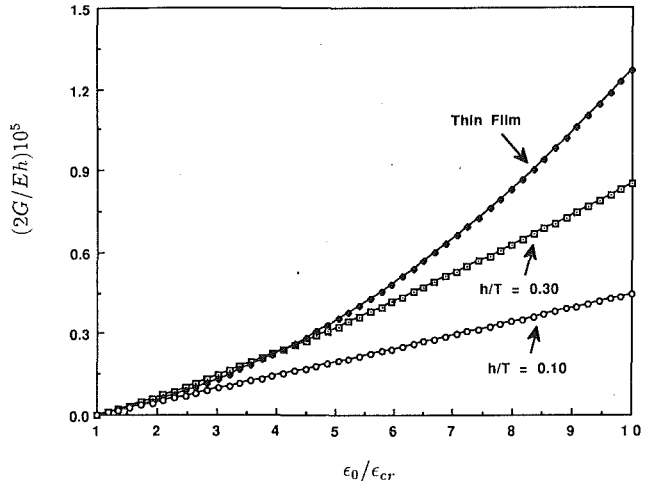


Fig. 2 Energy release rate, $(2G/Eh)10^5$, as a function of the applied strain

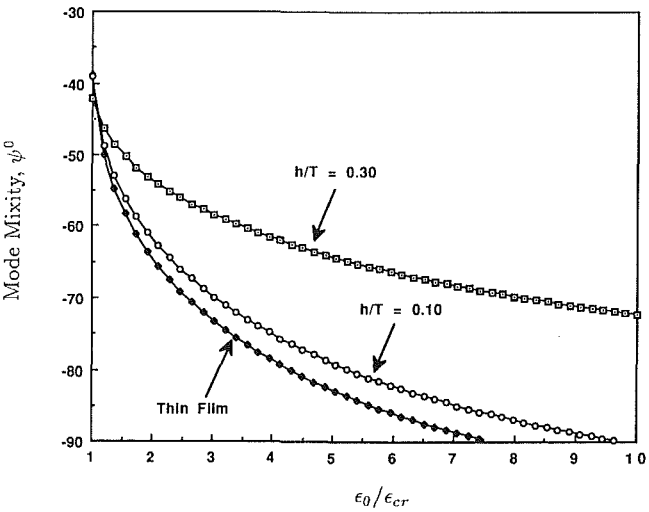


Fig. 3 Mode mixity, ψ^0, versus applied strain

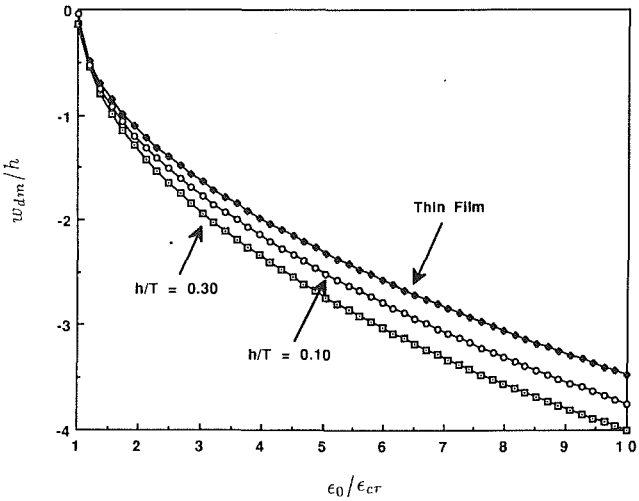


Fig. 4 Midpoint deflection of the delamination, w_{dm}/h, as a function of the applied strain

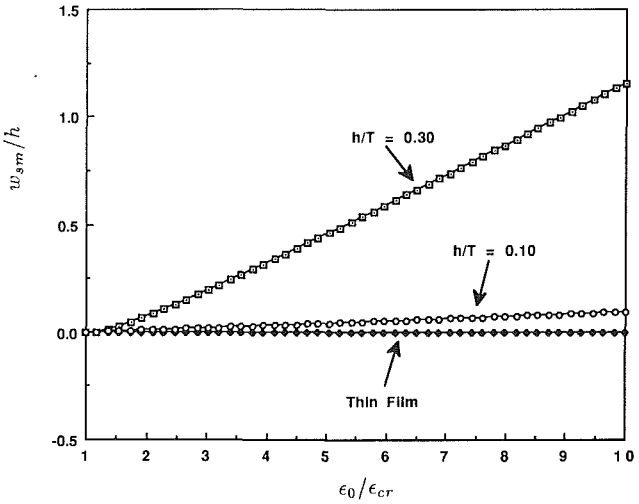


Fig. 5 Midpoint deflection of the substrate part, w_{sm}/h, versus applied strain

likewise for the base part, $\pi/2 > \Phi_b^0 > -\pi/2$. Moreover, the distortion parameter for the delamination is $\epsilon < 0$ (Fig. 1).

For an illustration of the results from the previous analysis consider a delaminated plate with $E = 10$ GPa and $\nu = 0.3$ and delamination and plate length $\ell = 20$ mm and $L = 60$ mm, respectively, and delamination thickness $h = 0.4$ mm. These dimensions correspond to our specimen dimensions (a width of 10 mm has been considered and is appropriately accounted in the results). To keep the critical strain ϵ_{cr} constant we keep the delamination length and thickness constant and vary only the plate thickness to get a varying ratio h/T; this would ensure the same thin film model solution.

Figure 2 shows the energy release rate $(2G/Eh)10^5$, as a function of the applied strain for $h/T = 0.10$ and $h/T = 0.30$. It is seen that for the same applied strain, the energy release rate for the case of the delamination located further away from the surface ($h/T = 0.3$) is always higher than the one for the delamination close to the surface ($h/T = 0.1$). In the beginning, i.e., for relatively small applied strain, the curves tend toward the thin film solution for a decreasing ratio h/T (as expected); however, as the applied strain is increased, the thin film model solution rises even above the $h/T = 0.3$ solution and predicts a much higher energy release rate. Experimental results that have been previously reported by Kardomateas (1989b, 1990) confirm clearly the reduced growth resistance of the "large ratio" case, $h/T = 0.3$, versus the "small ratio" one, $h/T = 0.1$). In fact, the small ratio delamination in these studies did not grow at all despite a very large increase in the applied strain. Notice that this important difference in growth behavior cannot obviously be predicted by the thin film model, which, because of its strongly nonlinearly increasing $G - \epsilon_0$ curve, would predict growth even for the small ratio delamination if the applied strain would be sufficiently increased.

Another very interesting result is the variation of the mode mixity (Mode II versus Mode I) at the delamination tip. Figure 3 shows the mode mixity ψ versus applied strain. It is seen that for the same applied strain the delamination located further away from the surface ($h/T = 0.3$) shows a higher mode I proportion than the one for the delamination close to the surface ($h/T = 0.1$). As a consequence, the value of the applied strain at which the delamination tip loading becomes pure Mode II ($\psi = -90$ deg) is increased. This point for the thin film model is at $\epsilon_0/\epsilon_{cr} = 7.55$. The curve show a trend toward the thin film solution for a decreasing ratio h/T.

Figure 4 shows the midpoint deflection of the delamination, w_{dm}/h, and Fig. 5 shows the midpoint deflection of the substrate part, w_{sm}/h, both as a function of the applied strain. It is seen that both curves show a trend toward the thin film solution for a decreasing ratio h/T and that the midpoint deflections are higher for a larger value of h/T (delaminations located further away from the surface).

Figure 6 shows the applied load P versus applied strain curves. It is seen that for the same value of applied strain, the delamination located further away from the surface ($h/t = 0.3$) exhibits a lower applied load and hence a larger loss of stiffness than the delamination close to the surface ($h/t = 0.1$). Again,

Downloaded 03 May 2010 to 171.66.16.245. Redistribution subject to ASME license or copyright; see http://www.asme.org/terms/Terms_Use.cfm

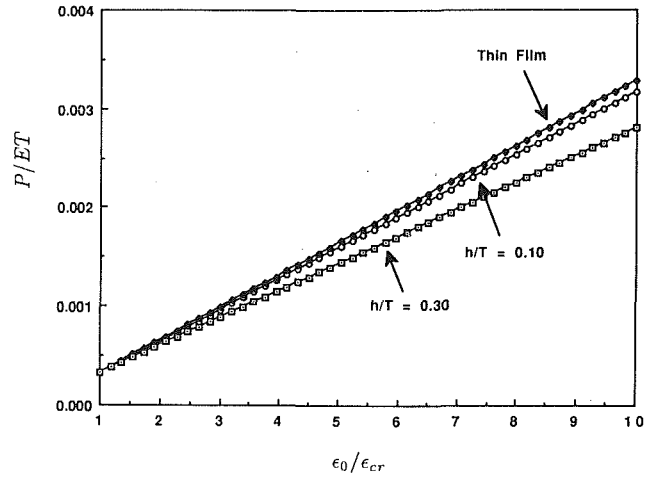


Fig. 6 Applied load *P* versus applied strain curves

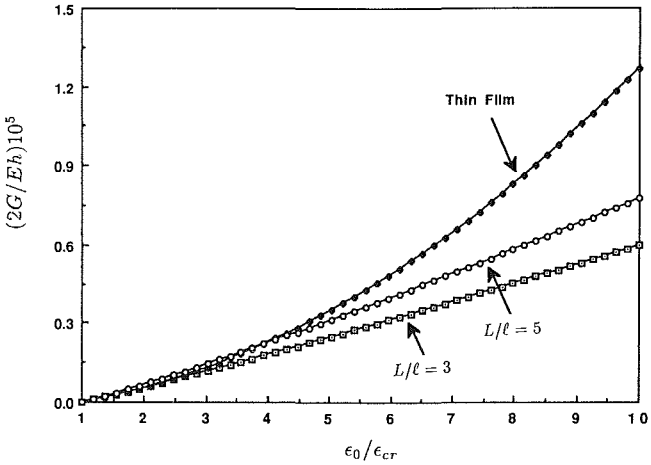


Fig. 7 Energy release rate as a function of the applied strain illustrating the effect of relative plate length

the curves tend to the thin film limit for a decreasing h/T value.

Next, the influence of the base plate length is studied by keeping the delamination length and thickness constant, and varying only the plate length to get a ratio L/ℓ of 3 and 5. In this example the plate thickness was chosen so that $h/T = 0.20$. This effect is mostly evident on the energy release rate, which is shown in Fig. 7 as a function of the applied strain. It is seen that the effect of plate length is evident at higher values of applied strain with the longer plate exhibiting higher energy release rates (and closer to the thin film solution).

Acknowledgment

The financial support of the Office of Naval Research, Mechanics Division, Grant N00014-91-J-1892, and the interest and encouragement of the Project Monitor, Dr. Y. Rajapakse, are both gratefully acknowledged.

References

Britvek, S. J., 1973, *The Stability of Elastic Systems*, Pergamon, New York.

Chai, H., Babcock, C. D., and Knauss, W. G., 1981, "One Dimensional Modelling of Failure in Laminated Plates by Delamination Buckling," *Int. J. Solids Structures*, Vol. 17, pp. 1069–1083.

Chai, H., and Babcock, C. D., 1985, "Two-Dimensional Modelling of Compressive Failure in Delaminated Laminates," *J. Comp. Mat.*, Vol. 19, pp. 67–97.

Chai, H., 1990, "Three-Dimensional Fracture Analysis of Thin Film Debonding," *Int. J. Fracture*, Vol. 46, pp. 237–256.

Dundurs, J., 1969, *Mathematical Theory of Dislocations*, ASME, New York, pp. 70–115.

Evans, A. G., and Hutchinson, J. W., 1984, "On the Mechanics of Delamination and Spalling in Compressed Films," *Int. J. Solids Structures*, Vol. 20, No. 5, pp. 455–466.

Hutchinson, J. W., and Suo, Z., 1992, "Mixed Mode Cracking in Layered Materials," *Advances in Applied Mechanics*, Vol. 29, Academic Press, New York, pp. 63–191.

Kardomateas, G. A., and Schmueser, D. W., 1988, "Buckling and Postbuckling of Delaminated Composites Under Compressive Loads Including Transverse Shear Effects," *AIAA Journal*, Vol. 26, pp. 337–343.

Kardomateas, G. A., 1989a, "Large Deformation Effects in the Postbuckling Behavior of Composites With Thin Delaminations," *AIAA Journal*, Vol. 27, pp. 624–631.

Kardomateas, G. A., 1989b, "Geometric Nonlinearities in the Postbuckling Behavior of Delaminated Composites," *Interlaminar Fracture in Composites* ("Key Engineering Materials," series), Trans. Tech. Publications, Switzerland, pp. 269–284.

Kardomateas, G. A., 1990, "Postbuckling Characteristics in Delaminated Kevlar/Epoxy Laminates: An Experimental Study," *Journal of Composites Technology and Research (ASTM)*, Vol. 12, No. 2, pp. 85–90.

Simitses, G. J., Sallam, S., and Yin, W. L., 1985, "Effect of Delamination on Axially Loaded Homogeneous Laminated Plates," *AIAA Journal*, Vol. 23, No. 9, pp. 1437–1444.

Storåkers, B., and Andersson, B., 1988, "Nonlinear Plate Theory Applied to Delamination in Composites," *J. Mech. Phys. Solids*, Vol. 36, No. 6, pp. 689–718.

Suo, Z., and Hutchinson, J. W., 1990, "Interface Crack Between Two Elastic Layers," *International Journal of Fracture*, Vol. 43, pp. 1–18.

Wang, S. S., Zahlan, N. M., and Suemasu, H., 1985, "Compressive Stability of Delaminated Random Short-Fiber Composites, Part I—Modeling and Methods of Analysis," *J. Comp. Mat.*, Vol. 19, pp. 296–316.

Yin, W. L., 1985, "Axisymmetric Buckling and Growth of a Circular Delamination in a Compressed Laminate," *Int. J. Solids Structures*, Vol. 21, pp. 503–514.

APPENDIX A

The constant c_1 in Eq. (28) is given as follows:

$$c_1 = \frac{D_d}{\ell} c_{1d} + \frac{D_s}{\ell} c_{1s} + \frac{D_b}{b} c_{1b} + c_{1c}, \tag{A1}$$

where

$$c_{1d} = \left(\frac{\Phi_d^0}{2}\cos\Phi_d^0 + \sin\Phi_d^0\right)\phi_d^{(1)2} - \frac{\Phi_d^0}{16}\cos\Phi_d^0\left(\frac{1}{3} - \frac{\sin 2\Phi_d^0}{2\Phi_d^0}\right), \tag{A2a}$$

$$c_{1s} = \alpha_s^{(1)}\left[\left(\frac{\Phi_s^0}{2}\cos\Phi_s^0 + \sin\Phi_s^0\right)\phi_s^{(1)2} - \frac{\Phi_s^0}{16}\cos\Phi_s^0\left(\frac{1}{3} - \frac{\sin 2\Phi_s^0}{2\Phi_s^0}\right)\alpha_s^{(1)2}\right] - (\cos\Phi_s^0 - \Phi_s^0\sin\Phi_s^0)\phi_s^{(1)}\alpha_s^{(2)} + \gamma_c\Phi_s^0\cos\Phi_s^0, \tag{A2b}$$

$$c_{1b} = -q(\alpha_b^{(1)}\rho_c + \phi_b^{(1)}\alpha_b^{(2)}) - \left(\Phi_b^0 + \frac{\pi}{2}\right)\cos\Phi_b^0 \times\left[\eta_c + \left(\frac{1}{3} - \frac{\sin 2\Phi_b^0}{2[\Phi_b^0 + (\pi/2)]}\right)\frac{\alpha_b^{(1)3}}{16}\right] + \left[\sin\Phi_b^0 + \left(\Phi_b^0 + \frac{\pi}{2}\right)\frac{\cos\Phi_b^0}{2}\right]\phi_b^{(1)2}\alpha_b^{(1)}, \tag{A2c}$$

and

$$c_{1c} = \left[\left(\frac{\sin 2\Phi_s^0}{\Phi_s^0} - 2\cos 2\Phi_s^0\right)\frac{\phi_s^{(1)}\alpha_s^{(1)2}}{4\Phi_s^0} + \left(1 - \frac{\sin 2\Phi_s^0}{2\Phi_s^0}\right)\alpha_s^{(1)}\alpha_s^{(2)} - \left(\frac{\sin 2\Phi_d^0}{\Phi_d^0} - 2\cos 2\Phi_d^0\right)\frac{\phi_d^{(1)}}{4\Phi_d^0} - \frac{\psi_c T}{\ell}\right]\frac{EhH}{4} \tag{A2d}$$

Downloaded 03 May 2010 to 171.66.16.245. Redistribution subject to ASME license or copyright; see http://www.asme.org/terms/Terms_Use.cfm

Reflection and Transmission by a Periodic Array of Coplanar Cracks: Normal and Oblique Incidence

Yozo Mikata
Department of Mechanical Engineering and Mechanics,
Old Dominion University,
Norfolk, VA 23529-0247
Assoc. Mem. ASME

Scattering of in-plane elastic waves by a periodic array of coplanar cracks is investigated. This problem was first treated by Angel and Achenbach. The method of their solution was based on the Fourier series expansion of the Green-Lamé potentials. In this paper, we have extended van der Hijden and Neerhoff's treatment of scattering of in-plane elastic waves by a single crack to the periodic case. Major advantages of our treatment over Angel and Achenbach are: (1) the formulation is relatively simple, straightforward, and unified for both normal and oblique incidence, and (2) more importantly, there is no need for numerical integrations, because all the integrations involved in the formulation can be analytically evaluated thanks to the periodicity of the problem and the coplanarity of the cracks. Numerical results are presented and compared with those of Angel and Achenbach. Some new numerical results are also presented.

1 Introduction

Scattering of elastic waves by cracks has attracted considerable attention (see Achenbach and Li, 1986; Angel and Achenbach, 1985a,b; Kraut, 1976; Mal, 1970, 1972; Mikata and Achenbach, 1988a,b; van den Berg, 1982; van der Hijden and Neerhoff, 1984; Visscher, 1981) over the years for its fundamental importance towards the nondestructive evaluation of materials and the detection of the fault zones in seismology. The concise review article has been written by Kraut (1976). In the present paper, the problem of scattering of in-plane longitudinal as well as transverse waves by a periodic array of coplanar cracks is investigated.

Mal (1970, 1972) studied the problem of the diffraction of normally incident antiplane shear waves and normally incident in-plane longitudinal waves by a Griffith crack in an infinite isotropic elastic medium. An exact solution was obtained numerically by solving a Fredholm integral equation after using the integral transform technique (Mal 1970). The transition matrix (Waterman, 1969) for elastic wave scattering by a Griffith crack was obtained by van den Berg (1982). Scattering of in-plane longitudinal and transverse waves by a Griffith crack was treated by van der Hijden and Neerhoff (1984) for an arbitrary angle of incidence. Starting from the Betti-Rayleigh reciprocity relation, they derived a pair of singular integral equations for the unknown crack-opening displacements. These integral equations were solved by Chebyshev polynomial expansions of the unknown crack-opening displacements. Rayleigh limit of elastic wave scattering by an arbitrary shaped flat crack was investigated by Visscher (1981), and certain symmetry properties pertaining to the problem were discussed.

Reflection and transmission of elastic waves by a periodic structure has been intensively studied in recent years for the quantitative nondestructive evaluation of micro-defects in solids (Achenbach and Kitahara, 1986; Achenbach and Li, 1986; Angel and Achenbach, 1985a,b; Mikata and Achenbach, 1988a,b). Reflection and transmission coefficients have been obtained by Achenbach and Kitahara (1986) for an obliquely incident three-dimensional plane wave going through a doubly periodic array of spherical cavities by using the boundary integral equation method. Scattering of scalar waves by a periodic array of screen was treated by Achenbach and Li (1986). An integral equation was derived for the unknown jump of the scalar potential across the screen, and this equation was solved by the Chebyshev polynomial expansion of the unknown jump. Reflection and transmission of elastic waves by a periodic array of coplanar cracks was first treated by Angel and Achenbach for both normal incidence (1985a) and oblique incidence (1985b). The method of their solution was based on the Fourier series expansions of the Green-Lamé potentials. Reflection and transmission of a plane longitudinal wave by a periodic array of inclined cracks was solved by Mikata and Achenbach (1988a) for both normal incidence and oblique

Contributed by the Applied Mechanics Division of THE AMERICAN SOCIETY OF MECHANICAL ENGINEERS for presentation at the ASME Winter Annual Meeting, New Orleans, LA, Nov. 28–Dec. 3, 1993.

Discussion on this paper should be addressed to the Technical Editor, Professor Lewis T. Wheeler, Department of Mechanical Engineering, University of Houston, Houston, TX 77204-4792, and will be accepted until four months after final publication of the paper itself in the ASME JOURNAL OF APPLIED MECHANICS.

Manuscript received by the ASME Applied Mechanics Division, Sept. 25, 1991; final revision, Oct. 23, 1992. Associate Technical Editor: S. K. Datta.

Paper No. 93-WA/APM-10.

Copyright © 1993 by ASME
Downloaded 03 May 2010 to 171.66.16.245. Redistribution subject to ASME license or copyright; see http://www.asme.org/terms/Terms_Use.cfm

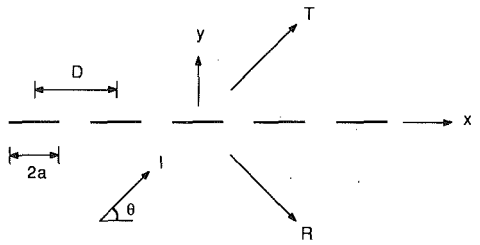


Fig. 1 In-plane wave incident on a periodic array of coplanar cracks

incidence by using the boundary integral equation method. The scattering by a periodic array of coplanar cracks was treated as a special case (Mikata and Achenbach 1988a). Reflection and transmission of an anti-plane shear wave by an infinite array of equally spaced but randomly oriented cracks in an isotropic elastic medium was also treated by Mikata and Achenbach (1988b). They derived a singular integral equation for the conditionally averaged crack-opening displacement using Lax's quasi-crystalline approximation. They also developed an approximate method to solve the integral equation based on a point scatterer.

The present paper also deals with reflection and transmission of elastic waves by a periodic array of coplanar cracks, but with a different approach. We have extended van der Hijden and Neerhoff's treatment (1984) of scattering of in-plane elastic waves by a single crack to the periodic case. The advantages of our treatment over Angel and Achenbach (1985a,b) will become clear in the section of mathematical formulation. These are: (1) the formulation is relatively simple, straightforward, and unified for both normal and oblique incidence, and (2) more importantly, there is no need for numerical integrations, because all the integrations involved in the formulation can be analytically evaluated thanks to the periodicity of the problem and the coplanarity of the cracks. The second point is remarkable considering that even the solution for a single crack (van der Hijden and Neerhoff 1984) needed numerical integrations.

2 Statement of the Problem

A time-harmonic in-plane wave of the form $\mathbf{u}^{in}(x, y)$ exp $(-i\omega t)$ is incident on a periodic array of coplanar cracks in an isotropic elastic medium as shown in Fig. 1. The incident wave is represented as I in Fig. 1. Every crack has length $2a$, and the center points of the adjacent coplanar cracks are separated from each other by distance D. The propagation vector of the incident wave makes an angle θ with the x-axis. Transmitted as well as reflected waves are also shown in Fig. 1.

Our problem is to obtain a time-harmonic displacement wave of the form $\mathbf{u}(x, y)$ exp $(-i\omega t)$ in the medium under the foregoing condition. Here $\mathbf{u}(x, y)$ and ω are the amplitude and the angular frequency of the wave, respectively. Since the time-harmonic wave can be discussed without any reference to its time-harmonic factor, in the following analysis, there will be no mention of the time-harmonic factor exp $(-i\omega t)$. The governing equation for $\mathbf{u}(x, y)$ is given by the Navier's equation:

$$\mu u_{i,jj} + (\lambda+\mu) u_{j,ji} + \rho\omega^2 u_i = 0 \tag{1}$$

where μ and λ are Lamé constants, ρ is the mass density of the medium, and i and j run through 1 to 2, which correspond to x and y-axes. Differentiation is signified by a comma, and Einstein's summation convention has been used. The displacement field is now expressed as a sum of two parts, the incident field $\mathbf{u}^{in}$ and the scattered field $\mathbf{u}^{sc}$:

$$u_i(x,y) = u_i^{in}(x,y) + u_i^{sc}(x,y) \tag{2}$$

The incident field is taken as either a plane longitudinal wave or a plane transverse wave,

$$\mathbf{u}^{in}(\mathbf{x}) = \mathbf{u}^L(\mathbf{x}) \text{ or } \mathbf{u}^T(\mathbf{x}), \tag{3}$$

where

$$\mathbf{u}^L(\mathbf{x}) = \begin{pmatrix} \cos\theta \\ \sin\theta \end{pmatrix} \exp(ik_L \mathbf{p}\cdot\mathbf{x}),$$

$$\mathbf{u}^T(\mathbf{x}) = \begin{pmatrix} -\sin\theta \\ \cos\theta \end{pmatrix} \exp(ik_T \mathbf{p}\cdot\mathbf{x}). \tag{4}$$

Here $\mathbf{p}$ is the propagation vector which is given by

$$\mathbf{p} = (\cos\theta, \sin\theta), \tag{5}$$

and the wave numbers k_L and k_T are defined as

$$k_L = \frac{\omega}{c_L},\ c_L = \sqrt{\frac{\lambda+2\mu}{\rho}},$$

$$k_T = \frac{\omega}{c_T},\ c_T = \sqrt{\frac{\mu}{\rho}}, \tag{6}$$

where c_L and c_T are the longitudinal and transverse wave velocities, respectively. Since the incident field $\mathbf{u}^{in}$ satisfies the Eq. (1), the scattered field $\mathbf{u}^{sc}$ must also satisfy the same equation. The traction-free condition on the faces of the crack gives the following boundary conditions:

$$\sigma_{kl}^{sc}(\mathbf{x}) n_l^- = -\sigma_{kl}^{in}(\mathbf{x}) n_l^-,\ \mathbf{x}\in\Gamma_m^-,\ m = 0, \pm 1, \pm 2, \ldots, \tag{7}$$

where Γ_m^- is the lower face of the mth crack, and σ_{kl}^{sc}, σ_{kl}^{in}, and n_l^- are given by

$$\sigma_{kl}^{sc}(\mathbf{x}) = C_{klmn} u_{m,n}^{sc}(\mathbf{x}), \tag{8}$$

$$\sigma_{kl}^{in}(\mathbf{x}) = C_{klmn} u_{m,n}^{in}(\mathbf{x}), \tag{9}$$

$$n_l^- = (0,1). \tag{10}$$

Here C_{klmn} is the component of the elasticity tensor of the medium, and is given by

$$C_{klmn} = \mu(\delta_{km}\delta_{ln} + \delta_{kn}\delta_{lm}) + \lambda\delta_{kl}\delta_{mn}. \tag{11}$$

In addition to the boundary condition (7), the scattered field must also satisfy the Sommerfeld radiation condition.

3 Mathematical Formulation

The procedure to obtain the governing singular integral equations for the unknown crack-opening displacements is exactly the same as the one used in Mikata and Achenbach (1988a). For the sake of clarity, however, the essential steps are given here.

Using the Betti-Rayleigh reciprocity relation of elastodynamics (Achenbach, Gautesen, and McMaken, 1982) along with the Sommerfeld radiation condition, we arrive at the following integral representation for the scattered field:

$$u_k^{sc}(\mathbf{x}) = \sum_{m=-\infty}^{\infty} \int_{\Gamma_m^-} \psi_i^m(\mathbf{x}') \sigma_{ij;k}^G(\mathbf{x},\mathbf{x}') n_j^- \, ds_m', \tag{12}$$

where $\psi_i^m (i = 1, 2)$ are the unknown crack-opening displacements for the mth crack

$$\psi_i^m(\mathbf{x}') = \mathbf{u}_i^{sc}(\mathbf{x}')|_{\mathbf{x}'\in\Gamma_m^+} - u_i^{sc}(\mathbf{x}')|_{\mathbf{x}'\in\Gamma_m^-}, \tag{13}$$

while the Green's stress tensor $\sigma_{ij;k}^G$ is given by

$$\sigma_{ij;k}^G(\mathbf{x},\mathbf{x}') = C_{ijln} \frac{\partial}{\partial x_n'} u_{l;k}^G(\mathbf{x},\mathbf{x}'). \tag{14}$$

Here $u_{l;k}^G(\mathbf{x}, \mathbf{x}')$, which is the displacement in the l-direction due to a unit force in the k-direction applied at $\mathbf{x}$, is given by

$$u_{l;k}^G(\mathbf{x},\mathbf{x}') = \frac{i}{4\mu k_T^2} [\partial_k' \partial_l' \{H_0^{(1)}(k_T R) - H_0^{(1)}(k_L R)\} + \delta_{kl} k_T^2 H_0^{(1)}(k_T R)], \tag{15}$$

Downloaded 03 May 2010 to 171.66.16.245. Redistribution subject to ASME license or copyright; see http://www.asme.org/terms/Terms_Use.cfm

where $H_0^{(1)}$ is the zeroth-order Hankel function of the first kind, and

$$R = |\mathbf{x} - \mathbf{x}'|. \tag{16}$$

The relation between the crack coordinate s_m' and the global coordinates (x', y') is given by

$$\begin{pmatrix} x' \\ y' \end{pmatrix} = s_m' \begin{pmatrix} 1 \\ 0 \end{pmatrix} + \begin{pmatrix} mD \\ 0 \end{pmatrix}, \quad -a \le s_m' \le a. \tag{17}$$

Substitution of Eq. (17) into (12) yields

$$u_k^{sc}(\mathbf{x}) = \sum_{m=-\infty}^{\infty} \int_{-a}^{a} \psi_i^m(s_m') \sigma_{ij;k}^G(\mathbf{x}, s_m'; m) n_j^- \, ds_m'. \tag{18}$$

Since s_m' is a dummy variable of the integration, (18) can be rewritten as

$$u_k^{sc}(\mathbf{x}) = \sum_{m=-\infty}^{\infty} \int_{-a}^{a} \psi_i^m(s') \sigma_{ij;k}^G(\mathbf{x}, s'; m) n_j^- \, ds'. \tag{19}$$

It follows from the periodicity of the problem that

$$\psi_i^m(s') = \exp(imDk_{L,T} \cos\theta) \psi_i(s'), \tag{20}$$

where ψ_i $(i = 1, 2,)$ are the unknown crack-opening displacements for the zeroth crack, and

$$k_{L,T} = \begin{cases} k_L & \text{for an incident longitudinal wave} \\ k_T & \text{for an incident transverse wave.} \end{cases} \tag{21}$$

Substituting (20) into (19) we obtain

$$u_k^{sc}(\mathbf{x}) = \int_{-a}^{a} \psi_i(s') \, ds' \times \sum_{m=-\infty}^{\infty} \exp(imDk_{L,T} \cos\theta) \sigma_{ij;k}^G(\mathbf{x}, s'; m) n_j^-. \tag{22}$$

The periodicity of the problem also implies that we only have to consider one of the infinite number of boundary conditions (7), since the conditions are equivalent. The stresses corresponding to (22) follow from (8), and (7) subsequently yields

$$f_k(x) = \int_{-a}^{a} \psi_i(s') G_{ik}(x, s') ds', \quad -a \le x \le a, \; k = 1,2, \tag{23}$$

where

$$f_k(x) = -\sigma_{kl}^{in}(\mathbf{x}) n_l^- |_{\mathbf{x} \in \Gamma_0^-}, \tag{24}$$

$$G_{ij}(x, s') = \sum_{m=-\infty}^{\infty} \exp(imDk_{L,T} \cos\theta) F_{ik}(x, s'; m), \tag{25}$$

$$F_{ik}(x, s'; m) = [\mu(\sigma_{ij;k,l}^G + \sigma_{ij;l,k}^G) + \lambda \sigma_{ij;p,p}^G \delta_{kl}] n_j^- n_l^- |_{\mathbf{x} \in \Gamma_0^-}. \tag{26}$$

Equation (23) is a pair of singular integral equations for the unknown crack-opening displacements $\psi_i (i = 1, 2)$ of the zeroth crack.

In order to solve the integral Eq. (23) for ψ_i, let us expand ψ_i as

$$\psi_i(s') = \sum_{n=1}^{\infty} C_{in} \phi_n(s'), \; i = 1,2, \tag{27}$$

where C_{in} are the unknown coefficients, and ϕ_n are the Chebyshev polynomials (Mikata and Achenbach, 1988b; van der Hijden and Neerhoff, 1984) defined by

$$\phi_n(s') = \begin{cases} \cos\left(n \sin^{-1} \dfrac{s'}{a}\right), & n = \text{odd} \\ i \sin\left(n \sin^{-1} \dfrac{s'}{a}\right), & n = \text{even} \end{cases}. \tag{28}$$

The key to the success of our method is the following representation of Hankel function:

$$H_0^{(1)}(kR) = \frac{1}{\pi} \int_{-\infty}^{\infty} \frac{1}{\sqrt{k^2 - \zeta^2}} \exp[i\zeta(x - x') + i\sqrt{k^2 - \zeta^2} |y - y'|] d\zeta, \tag{29}$$

where the sign of $(k^2 - \zeta^2)^{1/2}$ is taken as

$$(k^2 - \zeta^2)^{1/2} = i(\zeta^2 - k^2)^{1/2} \text{ for } |\zeta| > k. \tag{30}$$

Substituting (29) into (15), and subsequently using the Eqs. (14), (17), and (26), we obtain

$$F_{11}(x, s'; m) = \frac{i\mu}{4\pi k_T^2} \int_{-\infty}^{\infty} \frac{1}{\gamma_T} [4\zeta^2 \gamma_L \gamma_T + (k_T^2 - 2\zeta^2)^2] \times \exp\{i\zeta(x - s' - mD)\} d\zeta,$$

$$F_{22}(x, s'; m) = \frac{i\mu}{4\pi k_T^2} \int_{-\infty}^{\infty} \frac{1}{\gamma_L} [4\zeta^2 \gamma_L \gamma_T + (k_T^2 - 2\zeta^2)^2] \times \exp\{i\zeta(x - s' - mD)\} d\zeta,$$

$$F_{12} = F_{21} = 0, \tag{31}$$

where

$$\gamma_L = \sqrt{k_L^2 - \zeta^2}, \; \gamma_T = \sqrt{k_T^2 - \zeta^2}. \tag{32}$$

Next, an infinite system of linear algebraic equations for $C_{in} (i = 1, 2)$ is obtained by multiplying both sides of Eq. (23) by the complex conjugate of $\phi_j(x)$ (i.e., $\phi_j^*(x)$), and integrating them over $x \in [-a, a]$. By using Eqs. (24), (25), (27), and (31), the resulting system is obtained for an incident P-wave as

$$d_{1j}^L = \sum_{n=1}^{\infty} K_{11jn}^L C_{1n}, \; d_{2j}^L = \sum_{n=1}^{\infty} K_{22jn}^L C_{2n}, \; j \in \mathbf{Z}^+, \tag{33}$$

and for an incident SV-wave as

$$d_{1j}^T = \sum_{n=1}^{\infty} K_{11jn}^T C_{1n}, \; d_{2j}^T = \sum_{n=1}^{\infty} K_{22jn}^T C_{2n}, \; j \in \mathbf{Z}^+, \tag{34}$$

where $\mathbf{Z}^+ = \{1, 2, 3 \ldots\}$, and

$$d_{1j}^L = -2j \sin\theta J_j(ak_L \cos\theta),$$

$$d_{2j}^L = -\frac{j}{\cos\theta} \left[\left(\frac{k_T}{k_L}\right)^2 - 2\cos^2\theta \right] J_j(ak_L \cos\theta), \tag{35}$$

$$d_{1j}^T = -j \frac{\cos 2\theta}{\cos\theta} J_j(ak_T \cos\theta),$$

$$d_{2j}^T = -2j \sin\theta J_j(ak_T \cos\theta), \tag{36}$$

$$K_{11jn}^{L,T} = \frac{\pi}{2aDk_T^2} jn \sum_{m=-\infty}^{\infty} \frac{1}{(a\zeta_m^{L,T})^2} J_j(a\zeta_m^{L,T}) J_n(a\zeta_m^{L,T}) M_1(a\zeta_m^{L,T}),$$

$$K_{22jn}^{L,T} = \frac{\pi}{2aDk_T^2} jn \sum_{m=-\infty}^{\infty} \times \frac{1}{(a\zeta_m^{L,T})^2} J_j(a\zeta_m^{L,T}) J_n(a\zeta_m^{L,T}) M_2(a\zeta_m^{L,T}), \tag{37}$$

$$M_1(t) = \frac{[(ak_T)^2 - 2t^2]^2}{\sqrt{(ak_T)^2 - t^2}} + 4t^2 \sqrt{(ak_L)^2 - t^2},$$

$$M_2(t) = \frac{[(ak_T)^2 - 2t^2]^2}{\sqrt{(ak_L)^2 - t^2}} + 4t^2 \sqrt{(ak_T)^2 - t^2}, \tag{38}$$

$$\zeta_m^{L,T} = k_{L,T} \cos\theta + \frac{2\pi}{D} m. \tag{39}$$

In deriving Eqs. (33)–(39), we have used the following formulas:

Downloaded 03 May 2010 to 171.66.16.245. Redistribution subject to ASME license or copyright; see http://www.asme.org/terms/Terms_Use.cfm

$$\int_{-a}^{a} \phi_n(s')e^{-i\zeta s'}ds' = \frac{\pi n}{\zeta} J_n(a\zeta),$$

$$\int_{-a}^{a} \phi_j^*(x)e^{i\zeta x}dx = \frac{\pi j}{\zeta} J_j(a\zeta), \tag{40}$$

$$\sum_{m=-\infty}^{\infty} \delta(z-m) = \sum_{m=-\infty}^{\infty} e^{2\pi imz}, \tag{41}$$

where J_n is the Bessel function of order n and $\delta(z)$ is the Dirac delta function. It should be also noted here that the Poisson's summation formula (41), which plays an important role in such diverse fields as number theory (Terras, 1985) and the theory of elliptic functions (Bellman, 1961), has to be understood in the sense of distribution (Stakgold, 1979).

4 Reflection and Transmission Coefficients and Power Balance

Once the solutions to the Eqs. (33) and (34) are obtained, the scattered fields are obtained through (19) for an incident P-wave as

$$\mathbf{u}^{sc}(\mathbf{x}) = \sum_{m=-\infty}^{\infty} \left[\begin{pmatrix} W_x^{L+}(\zeta_m^L) \\ W_y^{L+}(\zeta_m^L) \end{pmatrix} e^{s^+(\mathbf{x},\zeta_m^L,k_L)} + \begin{pmatrix} W_x^{T+}(\zeta_m^L) \\ W_y^{T+}(\zeta_m^L) \end{pmatrix} e^{s^+(\mathbf{x},\zeta_m^L,k_T)} \right], \quad y>0$$

$$\mathbf{u}^{sc}(\mathbf{x}) = \sum_{m=-\infty}^{\infty} \left[\begin{pmatrix} W_x^{L-}(\zeta_m^L) \\ W_y^{L-}(\zeta_m^L) \end{pmatrix} e^{s^-(\mathbf{x},\zeta_m^L,k_L)} + \begin{pmatrix} W_x^{T-}(\zeta_m^L) \\ W_y^{T-}(\zeta_m^L) \end{pmatrix} e^{s^-(\mathbf{x},\zeta_m^L,k_T)} \right], \quad y<0 \tag{42}$$

and for an incident SV-wave as

$$\mathbf{u}^{sc}(\mathbf{x}) = \sum_{m=-\infty}^{\infty} \left[\begin{pmatrix} W_x^{T+}(\zeta_m^T) \\ W_y^{T+}(\zeta_m^T) \end{pmatrix} e^{s^+(\mathbf{x},\zeta_m^T,k_T)} + \begin{pmatrix} W_x^{L+}(\zeta_m^T) \\ W_y^{L+}(\zeta_m^T) \end{pmatrix} e^{s^+(\mathbf{x},\zeta_m^T,k_L)} \right], \quad y>0$$

$$\mathbf{u}^{sc}(\mathbf{x}) = \sum_{m=-\infty}^{\infty} \left[\begin{pmatrix} W_x^{T-}(\zeta_m^T) \\ W_y^{T-}(\zeta_m^T) \end{pmatrix} e^{s^-(\mathbf{x},\zeta_m^T,k_T)} + \begin{pmatrix} W_x^{L-}(\zeta_m^T) \\ W_y^{L-}(\zeta_m^T) \end{pmatrix} e^{s^-(\mathbf{x},\zeta_m^T,k_L)} \right], \quad y<0 \tag{43}$$

where

$$W_x^{L\pm}(\zeta) = \frac{\pi}{2Dk_T^2} \sum_{n=1}^{\infty} nC_{\alpha n} I_{\alpha\pm}^{11}(\zeta) J_n(a\zeta),$$

$$W_y^{L\pm}(\zeta) = \frac{\pi}{2Dk_T^2} \sum_{n=1}^{\infty} nC_{\alpha n} I_{\alpha\pm}^{12}(\zeta) J_n(a\zeta),$$

$$W_x^{T\pm}(\zeta) = \frac{\pi}{2Dk_T^2} \sum_{n=1}^{\infty} nC_{\alpha n} I_{\alpha\pm}^{21}(\zeta) J_n(a\zeta),$$

$$W_y^{T\pm}(\zeta) = \frac{\pi}{2Dk_T^2} \sum_{n=1}^{\infty} nC_{\alpha n} I_{\alpha\pm}^{22}(\zeta) J_n(a\zeta), \tag{44}$$

$$S^{\pm}(\mathbf{x},\zeta,k) = i\zeta x \pm iy\sqrt{k^2-\zeta^2}, \tag{45}$$

and

$$I_{1\pm}^{11}(\zeta) = \pm 2\zeta, \; I_{2\pm}^{11}(\zeta) = \frac{k_T^2 - 2\zeta^2}{\gamma_L},$$

$$I_{1\pm}^{12}(\zeta) = 2\gamma_L, \; I_{2\pm}^{12}(\zeta) = \pm\frac{k_T^2 - 2\zeta^2}{\zeta},$$

$$I_{1\pm}^{21}(\zeta) = \pm\frac{k_T^2 - 2\zeta^2}{\zeta}, \; I_{2\pm}^{21}(\zeta) = -2\gamma_T,$$

$$I_{1\pm}^{22}(\zeta) = -\frac{k_T^2 - 2\zeta^2}{\gamma_T}, \; I_{2\pm}^{22}(\zeta) = \pm 2\zeta. \tag{46}$$

In the Eq. (44), a summation is taken on α (= 1 ,2). The scattered fields of zeroth order are defined for an incident P-wave as

$$\mathbf{u}_0^{sc}(\mathbf{x}) = \begin{pmatrix} W_x^{L\pm}(\zeta_0^L) \\ W_y^{L\pm}(\zeta_0^L) \end{pmatrix} e^{s^{\pm}(\mathbf{x},\zeta_0^L,k_L)} + \begin{pmatrix} W_x^{T\pm}(\zeta_0^L) \\ W_y^{T\pm}(\zeta_0^L) \end{pmatrix} e^{s^{\pm}(\mathbf{x},\zeta_0^L,k_T)}, \; y \gtrless 0 \tag{47}$$

and for an incident SV-wave as

$$\mathbf{u}_0^{sc}(\mathbf{x}) = \begin{pmatrix} W_x^{T\pm}(\zeta_0^T) \\ W_y^{T\pm}(\zeta_0^T) \end{pmatrix} e^{s^{\pm}(\mathbf{x},\zeta_0^T,k_T)} + \begin{pmatrix} W_x^{L\pm}(\zeta_0^T) \\ W_y^{L\pm}(\zeta_0^T) \end{pmatrix} e^{s^{\pm}(\mathbf{x},\zeta_0^T,k_L)}, \; y \gtrless 0. \tag{48}$$

Substituting (39), (44), and (45) into (47) and (48), we obtain the scattered fields of zeroth order for an incident P-wave as

$$\mathbf{u}_0^{sc}(\mathbf{x}) = \mathbf{d}_L^{L+}(T_L^L - 1)\exp(ik_L\mathbf{x}\cdot\mathbf{p}_L^{L+}) + \mathbf{d}_L^{T+}T_L^T \exp(ik_T\mathbf{x}\cdot\mathbf{p}_L^{T+}), \; y>0$$

$$\mathbf{u}_0^{sc}(\mathbf{x}) = \mathbf{d}_L^{L-}R_L^L \exp(ik_L\mathbf{x}\cdot\mathbf{p}_L^{L-}) + \mathbf{d}_L^{T-}R_L^T \exp(ik_T\mathbf{x}\cdot\mathbf{p}_L^{T-}), \; y<0 \tag{49}$$

and for an incident SV-wave as

$$\mathbf{u}_0^{sc}(\mathbf{x}) = \mathbf{d}_T^{T+}(T_T^T - 1)\exp(ik_T\mathbf{x}\cdot\mathbf{p}_T^{T+}) + \mathbf{d}_T^{L+}T_T^L \exp(ik_L\mathbf{x}\cdot\mathbf{p}_T^{L+}), \; y>0$$

$$\mathbf{u}_0^{sc}(\mathbf{x}) = \mathbf{d}_T^{T-}R_T^T \exp(ik_T\mathbf{x}\cdot\mathbf{p}_T^{T-}) + \mathbf{d}_T^{L-}R_T^L \exp(ik_L\mathbf{x}\cdot\mathbf{p}_T^{L-}), \; y<0 \tag{50}$$

where

$$\begin{aligned}
&\mathbf{d}_L^{L+} = (\cos\theta, \sin\theta), && \mathbf{p}_L^{L+} = (\cos\theta, \sin\theta),\\
&\mathbf{d}_L^{T+} = (-\sin\theta_T, \cos\theta_T), && \mathbf{p}_L^{T+} = (\cos\theta_T, \sin\theta_T),\\
&\mathbf{d}_L^{L-} = (\cos\theta, -\sin\theta), && \mathbf{p}_L^{L-} = (\cos\theta, -\sin\theta),\\
&\mathbf{d}_L^{T-} = (\sin\theta_T, \cos\theta_T), && \mathbf{p}_L^{T-} = (\cos\theta_T, -\sin\theta_T),\\
&\mathbf{d}_T^{T+} = (-\sin\theta, \cos\theta), && \mathbf{p}_T^{T+} = (\cos\theta, \sin\theta),\\
&\mathbf{d}_T^{L+} = (\cos\theta_L, \sin\theta_L), && \mathbf{p}_T^{L+} = (\cos\theta_L, \sin\theta_L),\\
&\mathbf{d}_T^{T-} = (\sin\theta, \cos\theta), && \mathbf{p}_T^{T-} = (\cos\theta, -\sin\theta),\\
&\mathbf{d}_T^{L-} = (\cos\theta_L, -\sin\theta_L), && \mathbf{p}_T^{L-} = (\cos\theta_L, -\sin\theta_L),
\end{aligned} \tag{51, 52}$$

$$\cos\theta_T = \frac{k_L}{k_T}\cos\theta, \quad \sin\theta_T = \sqrt{1-\cos^2\theta_T},$$

$$\cos\theta_L = \frac{k_T}{k_L}\cos\theta, \quad \sin\theta_L = \sqrt{1-\cos^2\theta_L}. \tag{53}$$

Here T_L^L and T_L^T are the transmission coefficients of an incident P-wave for transmitted longitudinal and transverse waves, and R_L^L and R_L^T are the reflection coefficients of an incident P-wave for reflected longitudinal and transverse waves, and they are expressed as

$$T_L^L = 1 + \frac{\pi}{2Dk_L}\frac{1}{\sin\theta\cos\theta} \times \sum_{n=1}^{\infty} nJ_n(ak_L\cos\theta)\left[C_{1n}\left(\frac{k_L}{k_T}\right)^2 \sin 2\theta - C_{2n}\cos 2\theta_T \right],$$

Downloaded 03 May 2010 to 171.66.16.245. Redistribution subject to ASME license or copyright; see http://www.asme.org/terms/Terms_Use.cfm

$$T_L^T=\frac{\pi}{2Dk_T}\frac{1}{\sin\theta_T\cos\theta_T}\sum_{n=1}^{\infty}nJ_n(ak_T\cos\theta_T)[C_{1n}\cos 2\theta_T + C_{2n}\sin 2\theta_T]$$

$$R_L^L=-\frac{\pi}{2Dk_L}\frac{1}{\sin\theta\cos\theta}\sum_{n=1}^{\infty}nJ_n(ak_L\cos\theta)\times\left[C_{1n}\left(\frac{k_L}{k_T}\right)^2\sin 2\theta+C_{2n}\cos 2\theta_T\right],$$

$$R_L^T=\frac{\pi}{2Dk_T}\frac{1}{\sin\theta_T\cos\theta_T}\sum_{n=1}^{\infty}nJ_n(ak_T\cos\theta_T)[C_{1n}\cos 2\theta_T - C_{2n}\sin 2\theta_T]. \quad (54)$$

Similarly, T_T^T and T_T^L are the transmission coefficients of an incident SV-wave for transmitted transverse and longitudinal waves, and R_T^T and R_T^L are the reflection coefficients of an incident SV-wave for reflected transverse and longitudinal waves, and they are expressed as

$$T_T^T=1+\frac{\pi}{2Dk_T}\frac{1}{\sin\theta\cos\theta}\times\sum_{n=1}^{\infty}nJ_n(ak_T\cos\theta)[C_{1n}\cos 2\theta+C_{2n}\sin 2\theta]$$

$$T_T^L=\frac{\pi}{2Dk_L}\frac{1}{\sin\theta_L\cos\theta_L}\times\sum_{n=1}^{\infty}nJ_n(ak_L\cos\theta_L)\left[C_{1n}\left(\frac{k_L}{k_T}\right)^2\sin 2\theta_L-C_{2n}\cos 2\theta\right]$$

$$R_T^T=\frac{\pi}{2Dk_T}\frac{1}{\sin\theta\cos\theta}\sum_{n=1}^{\infty}nJ_n(ak_T\cos\theta)\times[C_{1n}\cos 2\theta-C_{2n}\sin 2\theta]$$

$$R_T^L=-\frac{\pi}{2Dk_L}\frac{1}{\sin\theta_L\cos\theta_L}\sum_{n=1}^{\infty}nJ_n(ak_L\cos\theta_L)\times\left[C_{1n}\left(\frac{k_L}{k_T}\right)^2\sin 2\theta_L+C_{2n}\cos 2\theta\right]. \quad (55)$$

It is seen from Eqs. (6), (50), (52), and (53*b*) that there is a critical incident angle for an incident SV-wave with which the reflected and transmitted P-waves propagate along the x-axis. There is only one such angle in the range of $[0, \pi/2]$. From (53*b*), the critical angle θ_{cr} is given by

$$\theta_{cr}=\cos^{-1}\frac{k_L}{k_T}. \quad (56)$$

It follows from the Eqs. (50), (52), and (53*b*) that when $0 \le \theta \le \theta_{cr}$, the reflected and transmitted P-waves become evanescent. Therefore, it may be defined that

$$T_T^L=R_T^L=0, \text{ if } 0\le\theta\le\theta_{cr}. \quad (57)$$

This does not mean that the numerical values for T_T^L and R_T^L computed by (55) become actually zero. They do have some values. However, they no longer possess any useful meaning as transmission or reflection coefficients. It should be also mentioned that the power balance equation given below for an incident SV-wave has been derived with (57) as an implicit condition.

The power balance equation for an incident P-wave in terms of reflection and transmission coefficients has been obtained by Mikata and Achenbach (1988a) as

$$|R_L^L|^2+|T_L^L|^2+\frac{k_L\sin\theta_T}{k_T\sin\theta}(|R_L^T|^2+|T_L^T|^2)=1. \quad (58)$$

Performing the same procedure for an incident SV-wave, the power balance equation is obtained as

$$|R_T^T|^2+|T_T^T|^2+\frac{k_T\sin\theta_L}{k_L\sin\theta}(|R_T^L|^2+|T_T^L|^2)=1. \quad (59)$$

In deriving the power balance Eqs. (58) and (59), it was assumed that the only propagating wave is the zeroth-order wave. Therefore, these equations are valid only when the frequency is smaller than a certain value.

5 Critical Wave Number

The scattered fields for an incident P-wave and an incident SV-wave are given by (42) and (43). It is seen from these equations that the scattered fields are composed of an infinite number of different wave modes, each corresponding to a different m. It is now clear from (42), (43), and (45) that a particular mode is propagating when $\sqrt{k^2-\zeta^2}$ is real, and evanescent otherwise. Since $k_T > k_L$, the zeroth-order wave ($m = 0$) is always propagating for an incident P-wave, and is also propagating for an incident SV-wave when $\theta_{cr} < \theta < \pi/2$ for all the frequency range. A higher-order wave ($m \neq 0$) can be propagating if the frequency is higher than a certain value. For an incident P-wave, we have

$$\begin{aligned}&(ak_L)^2-(a\zeta_m^L)^2\ge 0\rightarrow\text{a propagating P-wave of order } m\\&(ak_T)^2-(a\zeta_m^L)^2\ge 0\rightarrow\text{a propagating SV-wave of order } m.\end{aligned} \quad (60)$$

For an incident SV-wave, we have

$$\begin{aligned}&(ak_L)^2-(a\zeta_m^T)^2\ge 0\rightarrow\text{a propagating P-wave of order } m\\&(ak_T)^2-(a\zeta_m^T)^2\ge 0\rightarrow\text{a propagating SV-wave of order } m.\end{aligned} \quad (61)$$

Substituting (39) into (60) and solving the resulting inequality for a nondimensional wave number, we obtain the following results for an incident P-wave:

$$ak_L\ge\frac{2\pi m}{1-\cos\theta}\frac{a}{D}\ (m>0) \text{ or } ak_L\ge-\frac{2\pi m}{1+\cos\theta}\frac{a}{D}\ (m<0)$$
$$\rightarrow\text{a propagating P-wave of order } m \quad (62a)$$

$$ak_L\ge\frac{2\pi m}{\epsilon-\cos\theta}\frac{a}{D}\ (m>0) \text{ or } ak_L\ge-\frac{2\pi m}{\epsilon+\cos\theta}\frac{a}{D}\ (m<0)$$
$$\rightarrow\text{a propagating SV-wave of order } m \quad (62b)$$

where

$$\epsilon=\frac{k_T}{k_L}=\sqrt{\frac{2\mu+\lambda}{\mu}}=\sqrt{\frac{2(1-\nu)}{1-2\nu}}>1. \quad (63)$$

Here, ν is the Poisson ratio. Similarly, for an incident SV-wave, we obtain the following results: when $0<\theta<\theta_{cr}$,

$$-\frac{2\pi m}{1+\epsilon\cos\theta}\frac{a}{D}\le ak_L\le\frac{2\pi m}{1-\epsilon\cos\theta}\frac{a}{D}\ (m<0)$$
$$\rightarrow\text{a propagating P-wave of order } m. \quad (64a)$$

when $\theta_{cr} < \theta < \pi/2$,

$$ak_L\ge\frac{2\pi m}{1-\epsilon\cos\theta}\frac{a}{D}\ (m>0) \text{ or } ak_L\ge-\frac{2\pi m}{1+\epsilon\cos\theta}\frac{a}{D}\ (m<0)$$
$$\rightarrow\text{a propagating P-wave of order } m. \quad (64b)$$

Regardless of the value of θ,

$$ak_T\ge\frac{2\pi m}{1-\cos\theta}\frac{a}{D}\ (m>0) \text{ or } ak_T\ge-\frac{2\pi m}{1+\cos\theta}\frac{a}{D}\ (m<0)$$
$$\rightarrow\text{a propagating SV-wave of order } m. \quad (64c)$$

It can be seen from (62) and (64) that, for the same order m,

Downloaded 03 May 2010 to 171.66.16.245. Redistribution subject to ASME license or copyright; see http://www.asme.org/terms/Terms_Use.cfm

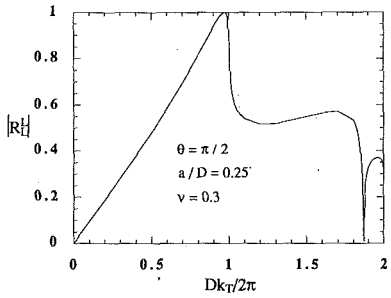


Fig. 2(*a*)

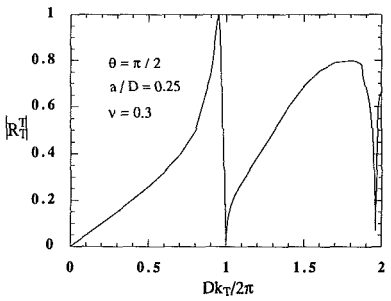


Fig. 2(*b*)

Fig. 2 Absolute values of reflection coefficients of normally incident (*a*) P- and (*b*) SV- waves for various values of $Dk_T/2\pi$

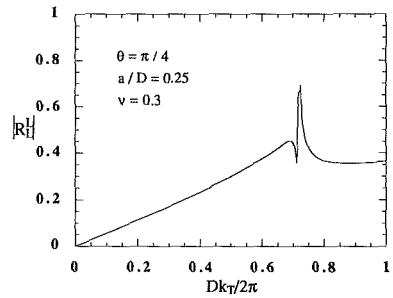


Fig. 3(*a*)

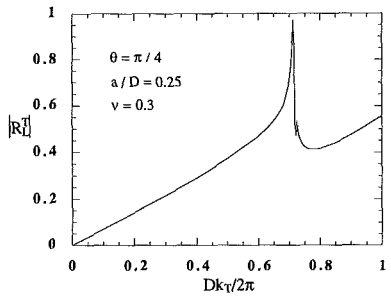


Fig. 3(*b*)

Fig. 3 Absolute values of reflection coefficients ((*a*) $|R_L^L|$ and (*b*) $|R_L^T|$) of an obliquely incident ($\theta = \pi/4$) P-wave for various values of $Dk_T/2\pi$

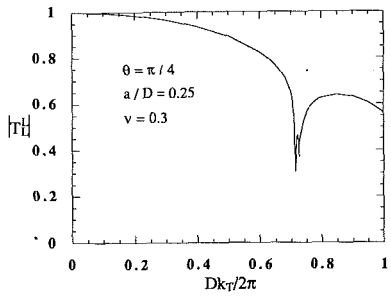


Fig. 4(*a*)

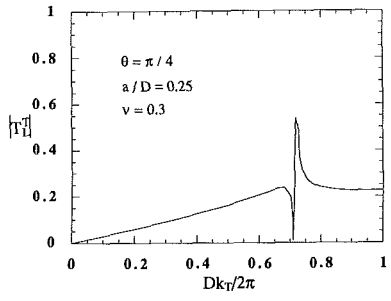


Fig. 4(*b*)

Fig. 4 Absolute values of transmission coefficients ((*a*) $|T_L^L|$ and (*b*) $|T_L^T|$) of an obliquely incident ($\theta = \pi/4$) P-wave for various values of $Dk_T/2\pi$

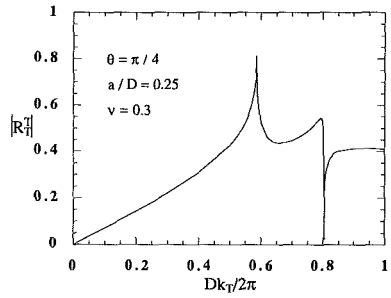


Fig. 5(*a*)

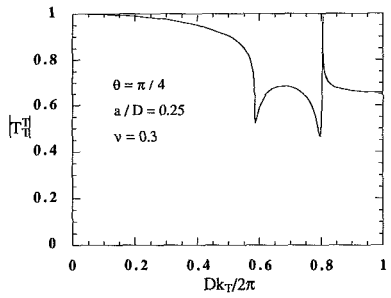


Fig. 5(*b*)

Fig. 5 Absolute values of reflection and transmission coefficients ((*a*) $|R_T^T|$ and (*b*) $|T_T^T|$) of an obliquely incident ($\theta = \pi/4$) SV-wave for various values of $Dk_T/2\pi$

an SV-wave starts propagating at a lower frequency than a P-wave. Also, by comparing a wave of order m (>0) and a wave of order, $-m$, we always have the following inequality:

$$\text{the propagating frequency of a wave of order } -m \leq \text{the propagating frequency of a wave of order } m. \quad (65)$$

Thus, the lowest frequency for a wave of a higher order ($m \neq 0$) to propagate is the propagating frequency of an SV-wave of order -1 for both types (P and SV) of incident waves. Let us call this frequency a critical frequency and the corresponding wave number a critical wave number. Then nondimensional critical wave numbers are obtained as

$$(ak_T)_{cr} = \frac{2\pi}{1 + \frac{1}{\epsilon}\cos\theta}\frac{a}{D} \quad \text{for an incident P-wave}$$

$$(ak_T)_{cr} = \frac{2\pi}{1 + \cos\theta}\frac{a}{D} \quad \text{for an incident SV-wave.} \quad (66)$$

Downloaded 03 May 2010 to 171.66.16.245. Redistribution subject to ASME license or copyright; see http://www.asme.org/terms/Terms_Use.cfm

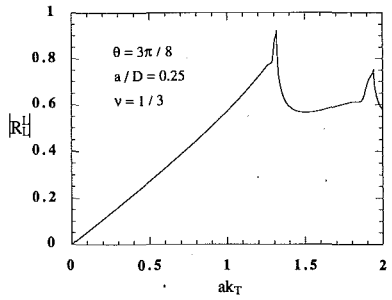


Fig. 6(*a*)

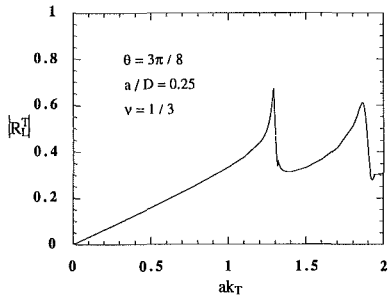


Fig. 6(*b*)

Fig. 6 Absolute values of reflection coefficients ((*a*) $|R_L^L|$ and (*b*) $|R_L^T|$) of an obliquely incident ($\theta = 3\pi/8$) P-wave for various values of ak_T

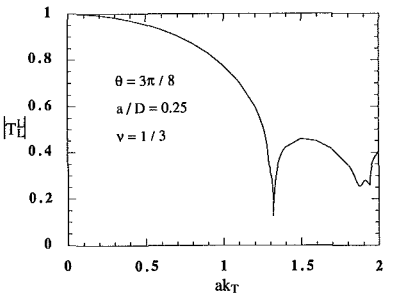


Fig. 7(*a*)

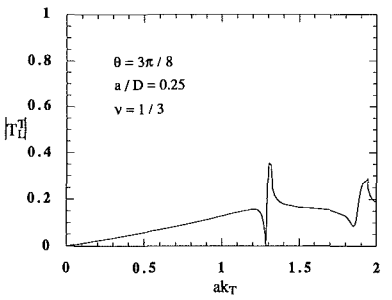


Fig. 7(*b*)

Fig. 7 Absolute values of transmission coefficients ((*a*) $|T_L^L|$ and (*b*) $|T_L^T|$) of an obliquely incident ($\theta = 3\pi/8$) P-wave for various values of ak_T

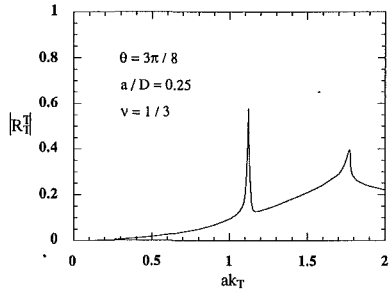


Fig. 8(*a*)

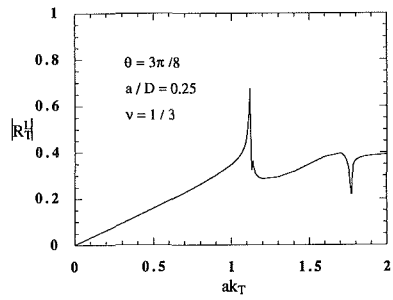


Fig. 8(*b*)

Fig. 8 Absolute values of reflection coefficients ((*a*) $|R_T^T|$ and (*b*) $|R_T^L|$) of an obliquely incident ($\theta = 3\pi/8$) SV-wave for various values of ak_T

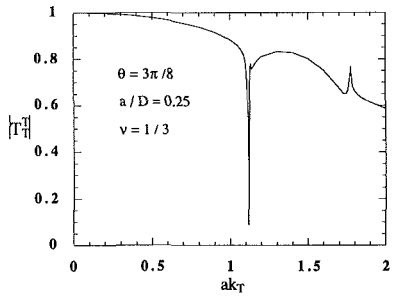


Fig. 9(*a*)

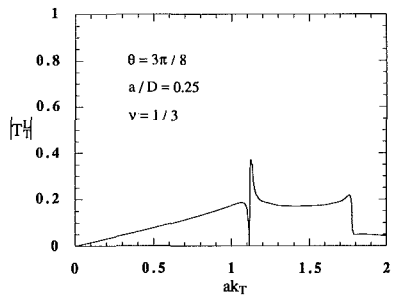


Fig. 9(*b*)

Fig. 9 Absolute values of transmission coefficients ((*a*) $|T_T^T|$ and (*b*) $|T_T^L|$) of an obliquely incident ($\theta = 3\pi/8$) SV-wave for various values of ak_T

It should be mentioned here that the power balance Eqs. (58) and (59) are valid when the frequency is less than the respective critical frequency.

6 Results and Discussion

By using Eqs. (54) and (55), the reflection and transmission coefficients for incident longitudinal and transverse waves have been calculated for both normal and oblique incidence. The absolute values of these coefficients are shown in Figs. 2–9. The horizontal axis corresponds to nondimensional wave numbers, $Dk_T/2\pi$ for Figs. 2–5, and ak_T for Figs. 6–9, respectively. The ratio of half-crack length to crack spacing, a/D, and the Poisson ratio ν have been set to be 0.25 and 0.3 in Figs. 2–5, and 0.25 and 1/3 in Figs. 6–9, respectively. In solving the Eqs. (33) and (34) for the expansion coefficients C_{1n} and C_{2n}, we need to truncate the infinite system of equations. In all of the following results, we have truncated the infinite system after the first ten equations. In evaluating the coefficients $K_{11jn}^{L,T}$ and $K_{22jn}^{L,T}$, we also need to truncate a pair of infinite series (37). In all of the following results, we have truncated the infinite series (37) by retaining 61 terms corresponding to $m = \{-30, \ldots$

Downloaded 03 May 2010 to 171.66.16.245. Redistribution subject to ASME license or copyright; see http://www.asme.org/terms/Terms_Use.cfm

. . , 30}. The power balance Eqs. (58) and (59) have been used to check the accuracy of the calculations. It has been found in all of the following results that (58) and (59) are easily satisfied up to at least four or five significant digits.

The results shown in Figs. 2–5 correspond to those of Angel and Achenbach (1985a,b). The present results for the normal incidence (Fig. 2) seem to agree with those of Angel and Achenbach, although the direct comparison is rather difficult. Overall results (Figs. 3–5) for the oblique incidence ($\theta = \pi/4$) also seem to be the same as those of Angel and Achenbach. There are, however, some finer differences between the two, if we look into the details of the results. For this purpose, let us tabulate the peak and plunge values for reflection and transmission coefficients from Figs. 3–5. These are

$$
\begin{aligned}
&|R_L^L| \simeq 0.357 && \text{at} && \bar{k} = 0.7115\\
&|R_L^L| \simeq 0.692 && \text{at} && \bar{k} = 0.7257\\
&|R_L^T| \simeq 0.973 \text{ or } 0.814 && \text{at} && \bar{k} = 0.7125\\
&|R_L^T| \simeq 0.536 \text{ or } 0.449 && \text{at} && \bar{k} = 0.7257\\
&|T_L^L| \simeq 0.307 && \text{at} && \bar{k} = 0.715\\
&|T_L^L| \simeq 0.370 && \text{at} && \bar{k} = 0.7257\\
&|T_L^T| \simeq 0.0107 \text{ or } 0.0090 && \text{at} && \bar{k} = 0.71\\
&|T_L^T| \simeq 0.538 \text{ or } 0.450 && \text{at} && \bar{k} = 0.718\\
&|T_L^T| \simeq 0.512 \text{ or } 0.428 && \text{at} && \bar{k} = 0.7257\\
&|R_T^T| \simeq 0.813 && \text{at} && \bar{k} = 0.5858\\
&|R_T^T| \simeq 0.0220 && \text{at} && \bar{k} = 0.8051\\
&|T_T^T| \simeq 0.522 && \text{at} && \bar{k} = 0.5871\\
&|T_T^T| \simeq 0.991 && \text{at} && \bar{k} = 0.8053
\end{aligned}
\tag{67}
$$

where

$$\bar{k} = \frac{Dk_T}{2\pi}. \tag{68}$$

First, it should be mentioned that there are two numbers attached to absolute values of certain reflection and transmission coefficients in (67). This is because there are differences between the present paper and Angel and Achenbach in the definitions for certain reflection and transmission coefficients. The first number corresponds to the present definitions (49) and (50), while the second number corresponds to their definitions (see (6.12) and (6.13) in Angel and Achenbach (1985b)). Comparing the above results with those of Angel and Achenbach, we find some differences in the peak and plunge values as well as in their corresponding nondimensional wave numbers. It should also be mentioned that some of the peaks and the plunges in (67) are very tiny ones. Another observation to be made about the above results is that some of those peaks and plunges occur very near the critical wave number or the propagating wave numbers of a respective incident wave. This fact was also pointed out by Angel and Achenbach but in a somewhat less general perspective. Using (64) and (66) for the present case, we obtain

$$\bar{k}_{cr}^L = \frac{1}{1+\frac{1}{\sqrt{7}}} \simeq 0.7257 \text{ for an incident P-wave}$$

$$\bar{k}_{cr}^T = \frac{1}{1+\frac{1}{\sqrt{2}}} \simeq 0.5858 \text{ for an incident SV-wave}$$

$\bar{k}_{-1} \equiv$ a nondimensional propagating wave number of a P-wave of order -1 for an incident SV-wave

$$= \frac{1}{\sqrt{\frac{2}{7}}+\frac{1}{\sqrt{2}}} \simeq 0.8054. \tag{69}$$

Comparing the nondimensional wave numbers corresponding to the peaks and plunges in (67) with the nondimensional critical and propagating wave numbers in (69), we find a closer correlation between these two wave numbers than is found in Angel and Achenbach.

New results for an oblique incidence ($\theta = 3\pi/8$) are shown in Figs. 6–9. Again, many peaks and plunges are seen in these graphs. Let us tabulate the peak and plunge values for reflection and transmission coefficients from Figs. 6–9. These are

$$
\begin{aligned}
&|R_L^L| \simeq 0.922 && \text{at} && ak_T = 1.3185\\
&|R_L^L| \simeq 0.755 && \text{at} && ak_T = 1.9424\\
&|R_L^T| \simeq 0.670 && \text{at} && ak_T = 1.289\\
&|R_L^T| \simeq 0.363 && \text{at} && ak_T = 1.3185\\
&|R_L^T| \simeq 0.612 && \text{at} && ak_T = 1.863\\
&|R_L^T| \simeq 0.304 && \text{at} && ak_T = 1.9425\\
&|T_L^L| \simeq 0.125 && \text{at} && ak_T = 1.3185\\
&|T_L^L| \simeq 0.258 && \text{at} && ak_T = 1.941\\
&|T_L^T| \simeq 0.0026 && \text{at} && ak_T = 1.2835\\
&|T_L^T| \simeq 0.354 && \text{at} && ak_T = 1.3065\\
&|T_L^T| \simeq 0.346 && \text{at} && ak_T = 1.3185\\
&|T_L^T| \simeq 0.290 && \text{at} && ak_T = 1.9424\\
&|R_T^T| \simeq 0.578 && \text{at} && ak_T = 1.1195\\
&|R_T^T| \simeq 0.396 && \text{at} && ak_T = 1.771\\
&|R_T^L| \simeq 0.675 && \text{at} && ak_T = 1.117\\
&|R_T^L| \simeq 0.365 && \text{at} && ak_T = 1.136\\
&|R_T^L| \simeq 0.220 && \text{at} && ak_T = 1.773\\
&|T_T^T| \simeq 0.087 && \text{at} && ak_T = 1.1185\\
&|T_T^T| \simeq 0.780 && \text{at} && ak_T = 1.133\\
&|T_T^T| \simeq 0.767 && \text{at} && ak_T = 1.7785\\
&|T_T^L| \simeq 0.0034 && \text{at} && ak_T = 1.114\\
&|T_T^L| \simeq 0.371 && \text{at} && ak_T = 1.1245\\
&|T_T^L| \simeq 0.350 && \text{at} && ak_T = 1.136\\
&|T_T^L| \simeq 0.217 && \text{at} && ak_T = 1.7605.
\end{aligned}
\tag{70}
$$

It should be mentioned here that some of the peaks and plunges in (70) are very small as was the case for the previous results for the oblique incidence with $\theta = \pi/4$. Let us also obtain the critical wave numbers and the propagating wave numbers for this case. Using (62), (63), and (64), we have

$$
\begin{aligned}
(ak_T)_{cr}^L &= \frac{2\pi}{4+\sqrt{2-\sqrt{2}}} \simeq 1.3185\\
(ak_T)_{cr}^T &= \frac{\pi}{2+\sqrt{2-\sqrt{2}}} \simeq 1.1360\\
(ak_T)_L^{T(1)} &= \frac{2\pi}{4-\sqrt{2-\sqrt{2}}} \simeq 1.9425\\
(ak_T)_T^{L(1)} &= \frac{\pi}{1+\sqrt{2-\sqrt{2}}} \simeq 1.7796
\end{aligned}
\tag{71}
$$

where

$(ak_T)_{cr}^{\alpha}$—a nondimensional critical wave number for an incident α-wave

$(ak_T)_{\alpha}^{\beta(m)}$—a nondimensional propagating wave number of a β-wave of order m for an incident α-wave.

with the identifications, $L \equiv P$ and $T \equiv SV$. Again, it can be easily seen from (70) and (71) that some of the peaks and

Downloaded 03 May 2010 to 171.66.16.245. Redistribution subject to ASME license or copyright; see http://www.asme.org/terms/Terms_Use.cfm

plunges occur very close to the critical wave number or the propagating wave numbers of a respective incident wave.

It becomes apparent from the foregoing numerical results for both normal and oblique incidence that our scheme produces very accurate results with relatively few terms in Eqs. (33) and (34).

References

Achenbach, J. D., Gautesen, A. K., and McMaken, H., 1982, *Ray Methods for Waves in Elastic Solids*, Pitman, London.

Achenbach, J. D., and Kitahara, M., 1986, "Reflection and Transmission of an Obliquely Incident Wave by an Array of Spherical Cavities," *J. Acoust. Soc. Am.*, Vol. 80, pp. 1209–1214.

Achenbach, J. D., and Li, Z. L., 1986, "Reflection and Transmission of Scalar Waves by a Periodic Array of Screens," *Wave Motion*, Vol. 8, pp. 225–234.

Angel, Y. C., and Achenbach, J. D., 1985a, "Reflection and Transmission of Elastic Waves by a Periodic Array of Cracks," ASME JOURNAL OF APPLIED MECHANICS, Vol. 52, pp. 33–41.

Angel, Y. C., and Achenbach, J. D., 1985b, "Reflection and Transmission of Elastic Waves by a Periodic Array of Cracks: Oblique Incidence," *Wave Motion*, Vol. 7, pp. 375–397.

Bellman, R., 1961, *A Brief Introduction to Theta Functions*, Holt, Rinehart and Winston, New York.

Kraut, E. A., 1976, "Review of Theories of Scattering of Elastic Waves by Cracks," *IEEE Trans. Sonics and Ultrasonics*, Vol. SU-23, pp. 162–167.

Mal, A. K., 1970, "Interaction of Elastic Waves with a Griffith Crack," *Int. J. Eng. Sci.*, Vol. 8, pp. 763–776.

Mal, A. K., 1972, "A Note of The Low Frequency Diffraction of Elastic Waves by a Griffith Crack," *Int. J. Eng. Sci.*, Vol. 10, pp. 609–612.

Mikata, Y., and Achenbach, J. D., 1988a, "Interaction of Harmonic Waves with a Periodic Array of Inclined Cracks," *Wave Motion*, Vol. 10, pp. 59–72.

Mikata, Y., and Achenbach, J. D., 1988b, "Reflection and Transmission by an Infinite Array of Randomly Oriented Cracks," *J. Acoust. Soc. Am.*, Vol. 83, pp. 38–45.

Stakgold, I., 1979, *Green's Functions and Boundary Value Problems*, John Wiley and Sons, New York.

Terras, A., 1985, *Harmonic Analysis on Symmetric Spaces and Applications I*, Springer-Verlag, New York.

van den Berg, P. M., 1982, "Scattering of Two-Dimensional Elastodynamic Wave by a Rigid Plane Strip or a Plane Crack of Finite Width: The Transition Matrix," *J. Acoust. Soc. Am.*, Vol. 72, pp. 1038–1045.

van der Hijden, J. H. M. T., and Neerhoff, F. L., 1984, "Scattering of Elastic Waves by a Plane Crack of Finite Width," ASME JOURNAL OF APPLIED MECHANICS, Vol. 51, pp. 646–651.

Visscher, W. M., 1981, "Scattering of Elastic Waves from Planar Cracks in Isotropic Media," *J. Acoust. Soc. Am.*, Vol. 69, pp. 50–53.

Waterman, P. C., 1969, "New Formulation of Acoustic Scattering," *J. Acoust. Soc. Am.*, Vol. 45, pp. 1417–1429.

Downloaded 03 May 2010 to 171.66.16.245. Redistribution subject to ASME license or copyright; see http://www.asme.org/terms/Terms_Use.cfm

Interactions Among General Systems of Cracks and Anticracks: An Integral Equation Approach

K. X. Hu

A. Chandra
Mem. ASME.

Department of Aerospace and Mechanical Engineering,
The University of Arizona,
Tucson, AZ 85721

Cracks and rigid line inclusions, or anticracks, are commonly observed in many engineering materials, such as ceramics, intermetallics, etc. Interactions among these cracks and anticracks can significantly affect the load-carrying capacities and other mechanical properties of these materials. Accordingly, modeling of the interactions among general systems of cracks and anticracks subject to general loading conditions is the main thrust of this paper. An integral equation approach based on the fundamental solutions due to point loads and point dislocations in an elastic body is utilized for this purpose. A Gauss-Chebychev quadrature is used to reduce the integral equations to a system of linear equations consisting of the distributions of Burger's dislocation vectors and forces on the cracks and the anticracks, respectively. The proposed solution procedure also allows direct determination of the rigid-body rotations for the anticracks. For a collinear crack-anticrack system, the results obtained from the present analysis are verified against those obtained from a Green's function approach. Numerical results are also presented for sample systems of cracks and anticracks, and salient features of amplification and shielding of stress singularities are investigated.

1 Introduction

Most common engineering materials contain defects in the form of cracks, voids, or rigid inclusions that can significantly affect their load-carrying capacities. In recent years, various ceramic components and intermetallics, by virtue of possessing ordered superlattice structures and high activation energies for diffusion, have been found to be ideally suited for high-temperature strength and modulus retention. However, these ceramic compounds and intermetallics are generally very brittle at room temperature. In order to enhance the ductility at room temperature and to lower the brittle-ductile transition temperatures, various researchers have attempted to change the crystal structures using alloys. The alloying agents, however, introduce second-phase particles in the matrix. The networks of microdefects (voids or inclusions) introduced through alloying can significantly affect the final strength and characteristics of the products. In many material processing and structural applications, the interactions among these microdefects (voids or inclusions) have been observed to be one of the important factors in determining the macro-failure modes (e.g., Kachanov, 1985; Hori and Nemat-Nasser, 1986; Baeslack et al., 1988; Haritos et al., 1988; Jha et al., 1988).

The brittle fracture mechanisms introduced by the network of cracks and inclusions can also have benevolent effects. For ceramics and intermetallics, this network of microdefects and the associated brittle fracture modes provide crucial avenues for material removal processes. The apparent moduli of various ultrahard ceramic materials may also be reduced and controlled by inducing predetermined distributions of microcracks and inclusions in such materials. The ability to control apparent hardness and modulus has very important ramifications for various material removal processes (e.g., grinding, drilling, etc.).

Two kinds of microdefects are typically observed in a material. The first one is a microvoid, which can also be idealized as a microcrack. A crack is essentially a cut that transmits no traction across it, but allows a displacement discontinuity. The other type of microdefect is a rigid inclusion. A rigid lamella may be modeled as the opposite of a crack, i.e., it transmits tractions but prevents displacement discontinuity. Moreover, rigid lamella can undergo only rigid-body motions and no deformations. Following Dundurs and Markenscoff (1989), these rigid inclusions are called anticracks in the present work. The anticracks only admit rigid-body displacements and no deformations. There is an extensive body of literature on elastic and elastic-plastic fracture mechanics (e.g., Liebowitz, 1968; Sih, 1973; Parton and Morozov, 1989).

The problems involving anticracks have also been widely

Contributed by the Applied Mechanics Division of THE AMERICAN SOCIETY OF MECHANICAL ENGINEERS for publication in the ASME JOURNAL OF APPLIED MECHANICS.

Discussion on this paper should be addressed to the Technical Editor, Professor Lewis T. Wheeler, Department of Mechanical Engineering, University of Houston, Houston, TX 77204-4792, and will be accepted until four months after final publication of the paper itself in the ASME JOURNAL OF APPLIED MECHANICS.

Manuscript received by the ASME Applied Mechanics Division, July 26, 1991; final revision, Oct. 21, 1992. Associate Technical Editor: X. Markenscoff.

Copyright © 1993 by ASME
Downloaded 03 May 2010 to 171.66.16.245. Redistribution subject to ASME license or copyright; see http://www.asme.org/terms/Terms_Use.cfm

investigated in the context of elasticity. An extensive review of elastic problems involving inclusions is given by Mura (1987, 1988). Initial work on rigid line inclusions can be traced back to Muskheleshvili (1953) and Eshelby (1957, 1959). Since then, problems involving rigid line inclusions have been investigated by several researchers (e.g., Atkinson, 1973; Brussat and Westmann, 1975; Hasebe et al., 1984) for isotropic elastic bodies. Chou and Wang (1983) and Wang et al. (1985, 1986) considered a rigid line inclusion in an isotropic planar elastic body and derived analytical expressions for the stress field due to uniform remote loading. The same problem has also been considered by Ballarini (1987) using an integral transform method. Sendeckyj (1970) and Selvadurai (1980) investigated elastic line inclusions. Atkinson (1973) also considered elastic line inclusions using the method of Muskheleshvili (1953). He obtained an asymptotic solution for the stress fields under the assumption that the inclusion is much harder than the matrix. Erdogan and Gupta (1972) studied the more general problem of bonded materials containing a flat inclusion that may be rigid or elastic with negligible bending rigidity. They formulated the problem as a system of singular integral equations that is solved by expanding the solutions in Chebychev polynomials. Dundurs and Markenscoff (1989) provide a direct Green's function formulation for anticracks. Such a formulation is very suitable for solution by current numerical methods. They also provide pertinent fields for concentrated forces, dislocations, and couples applied on the line of the anticrack. Li and Ting (1989) investigated anticracks embedded in an anisotropic infinite elastic medium subject to uniform remote loading. Stroh's (1958, 1962) formalism is used to obtain the displacement and stress fields. They consider both rigid and elastic inclusions. A pair of singular Fredholm integral equations of the second kind is derived for the difference in the stress on both surfaces of an elastic and anisotropic inclusion. If the relative rigidity of the matrix is small compared to that of the inclusion, Li and Ting (1989) showed that the governing equations can be decoupled. For such rigid line cases, they also obtain asymptotic solutions for the traction and the rotation of the anticrack.

Most of the existing analyses of anticracks, however, consider a single rigid line inclusion. As discussed before, the problems involving interactions among anticracks and among cracks and anticracks are of crucial significance for understanding various physical phenomena ranging from failure of alloys containing second-phase particles to chip formation mechanics in ceramic grinding processes. In spite of these practical implications, problems involving interactions of cracks and anticracks have received relatively little attention so far.

Utilizing the superposition technique and the ideas of self-consistency applied to the average tractions on individual cracks, Kachanov (1985, 1987) obtained approximate analytical solutions for the stress intensity factor due to interacting elastic cracks. Also, Chen (1984) has studied problems involving multiple cracks. Broberg (1987) discussed the development of crack paths under mode I, mode II, and mode III conditions, and under a mixture of these modes. Melin (1983) and Broberg (1987) investigated the directional stability of cracks using linear elastic fracture mechanics and observed that the interactions among cracks significantly influence the directional stability and crack branching characteristics. Hori and Nemat-Nasser (1987) also used the method of Muskheleshvili to obtain a two-dimensional elasticity solution for interacting microcracks near the tip of a macrocrack. Using the dislocation approach, various researchers have also reduced the problem of a linear elastic solid with interacting cracks to a system of integral equations (e.g., Erdogan and Gupta, 1975; Chudnovsky et al., 1987; Müller, 1989). Also, Comninou (1977) obtained a pair of coupled singular integral equations for interface cracks, and Keer et al. (1983) solved for a crack near two perpendicular free surfaces.

To date, interactions among anticracks have been considered for very special cases only. Brussat and Westmann (1975) investigated the interactions among collinear rigid line inclusions subject to a uniform remote loading. For this special case, they establish a direct correspondence between the Westergaard stress function for elastic crack problems and a stress function for rigid line inclusion problems. A correspondence is also shown to exist between crack opening displacements and axial forces on the rigid inclusions.

Accordingly, development of a model for interactions among general systems of cracks and anticracks subject to general loading situations is the focus of the present paper. An integral equation approach based on the fundamental fields due to point loads and point dislocations is utilized for this purpose. A Gauss-Chebychev quadrature is used to reduce the integral equations to a linear system of equations consisting of the distribution of forces and Burger's dislocation vectors on the cracks and anticracks. The proposed solution procedure also allows direct determination of the rigid-body rotations for the anticracks.

This paper starts with a presentation of the fundamental solutions due to point loads and point dislocations. An integral equation formulation for general systems of cracks and anticracks is developed next, along with a numerical scheme for the solution of the integral equations. The numerical results obtained by the proposed technique for the special case of collinear crack-anticrack systems is first verified against the solutions obtained by using the Green's functions of Dundurs and Markenscoff (1989). General systems of cracks and anticracks subject to general loading conditions are considered next, and the proposed technique is used to investigate the interaction effects in such systems. In our analyses, the anticracks are modeled as rigid lines. It is interesting to note that, for a given configuration, the interactions between two cracks and between a crack and a rigid line bound the range of all possible interaction effects.

2 Fundamental Fields due to Point Loads and Point Dislocations

Cracks and anticracks can be modeled as continuous spatial distributions of dislocations and tractions. Accordingly, the corresponding fundamental solutions due to a point load and a point dislocation are discussed in this section. Two-dimensional problems are considered here.

For an infinite two-dimensional elastic body subjected to a concentrated force with components p_x and p_y at the location $(\xi, 0)$, the Kelvin solution (Timoshenko and Goodier, 1970) at a point (x, y) may be written as

$$2Gu_{x,x}=\frac{1}{\pi(\kappa+1)}\left[p_xH_1(x, y; \xi)+p_yH_2(x, y; \xi)\right] \quad (1a)$$

$$2Gu_{x,y}=\frac{1}{\pi(\kappa+1)}\left[p_xH_3(x, y; \xi)+p_yH_4(x, y; \xi)\right] \quad (1b)$$

$$2Gu_{y,x}=\frac{1}{\pi(\kappa+1)}\left[p_xH_5(x, y; \xi)+p_yH_6(x, y; \xi)\right] \quad (1c)$$

$$2Gu_{y,y}=\frac{1}{\pi(\kappa+1)}\left[p_xH_7(x, y; \xi)+p_yH_8(x, y; \xi)\right] \quad (1d)$$

$$\sigma_{xx}=\frac{1}{2\pi(\kappa+1)}\left[p_xH_9(x, y; \xi)+p_yH_{10}(x, y; \xi)\right] \quad (1e)$$

$$\sigma_{xy}=\frac{1}{2\pi(\kappa+1)}\left[p_xH_{11}(x, y; \xi)+p_yH_{12}(x, y; \xi)\right] \quad (1f)$$

$$\sigma_{yy}=\frac{1}{2\pi(\kappa+1)}\left[p_xH_{13}(x, y; \xi)+p_yH_{14}(x, y; \xi)\right] \quad (1g)$$

where G is the shear modulus. The constant $\kappa = (3 - 4\nu)$ for plane strain and $\kappa = (3 - \nu)/(1 + \nu)$ for plane stress, where

Downloaded 03 May 2010 to 171.66.16.245. Redistribution subject to ASME license or copyright; see http://www.asme.org/terms/Terms_Use.cfm

ν is the Poisson's ratio. The details of the kernels H_1 through H_{14} are given in the Appendix.

The fundamental solutions at (x, y) for a two-dimensional infinite body subjected to an edge dislocation with Burger's vector components b_x and b_y acting at a point $(\xi, 0)$ may also be expressed as (Read, 1953)

$$u_{x,x}=\frac{1}{2\pi(\kappa+1)}[b_xI_1(x, y; \xi)+b_yI_2(x, y; \xi)] \quad (2a)$$

$$u_{x,y}=\frac{1}{2\pi(\kappa+1)}[b_xI_3(x, y; \xi)+b_yI_4(x, y; \xi)] \quad (2b)$$

$$u_{y,x}=\frac{1}{2\pi(\kappa+1)}[b_xI_5(x, y; \xi)+b_yI_6(x, y; \xi)] \quad (2c)$$

$$u_{y,y}=\frac{1}{2\pi(\kappa+1)}[b_xI_7(x, y; \xi)+b_yI_8(x, y; \xi)] \quad (2d)$$

$$\sigma_{xx}=\frac{2G}{\pi(\kappa+1)}[b_xI_9(x, y; \xi)+b_yI_{10}(x, y; \xi)] \quad (2e)$$

$$\sigma_{xy}=\frac{2G}{\pi(\kappa+1)}[b_xI_{11}(x, y; \xi)+b_yI_{12}(x, y; \xi)] \quad (2f)$$

$$\sigma_{yy}=\frac{2G}{\pi(\kappa+1)}[b_xI_{13}(x, y; \xi)+b_yI_{14}(x, y; \xi)]. \quad (2g)$$

The details of the kernels I_1 through I_{14} are also given in the Appendix.

It is important to notice here that the displacement gradient fields and the stress fields in Eqs. (1)–(2) contain a singularity of the order of r as the distance r between the field point (x, y) and source point $(\xi, 0)$ approaches zero. The singular behavior for the point load case has been discussed widely, particularly in the boundary integral equation literature (e.g., Banerjee and Butterfield, 1981; Mukherjee, 1982; Cruse, 1988). Recently, Dundurs and Markenscoff (1989) also examined the singular behavior for the point dislocation case. A similar procedure is followed in the present work in order to represent the singular integrals in a Cauchy principal value sense.

3 An Integral Equation Formulation for General Crack-Anticrack Systems

It is assumed here that the crack, like any other void, cannot transmit any traction. Accordingly, the crack surface is required to be traction-free. For the purpose of this work, any crack closure is neglected, and it is assumed that the crack remains open throughout the application of the external load. The anticrack, like any other rigid inclusion, can only admit rigid-body motions. A perfect bonding between the rigid line and the matrix is assumed here.

A general system containing M cracks and N anticracks embedded in arbitrary orientations in an elastic body is considered here. We concentrate on the ith defect (crack or anticrack) and consider a local tangential-normal coordinate system with origin at the center of the defect, the normal direction denoted by $s^{(i)}$, and the tangential direction along the ith crack, or anticrack, denoted by $t^{(i)}$. This is schematically shown in Fig. 1. The occupancy of the ith defect is denoted as $-a^{(i)} < t^{(i)} < a^{(i)}$.

Under the preceding assumptions, the boundary conditions for cracks require that $(i = 1, \ldots, M)$

$$\sigma_{ss}^{(i)}=\sigma_{ts}^{(i)}=0 \qquad \text{for } -a^{(i)}<t^{(i)}<a^{(i)}. \quad (3)$$

The boundary conditions for the anticracks may also be expressed as $(j = 1, \ldots, N)$

$$u_t^{(j)}=\alpha^{(j)} \text{ and } u_s^{(j)}=\beta^{(j)}+\omega^{(j)}t^{(j)} \qquad \text{for } -a^{(j)}<t^{(j)}<a^{(j)} \quad (4)$$

where $\alpha^{(j)}$ and $\beta^{(j)}$ are the rigid-body translations in the $t^{(j)}$ and $s^{(j)}$ directions, respectively, and $\omega^{(j)}$ is the rigid-body rotation in the $t^{(j)} - s^{(j)}$ plane.

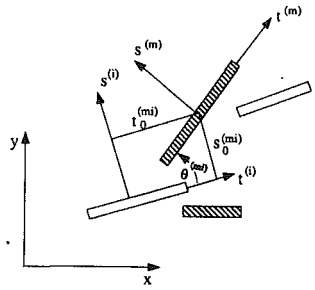


Fig. 1 Schematic diagram of a general crack-anticrack system

The rigid-body displacements may be differentiated with respect to $t^{(j)}$, yielding the boundary conditions $(j = 1, \ldots, N)$

$$\frac{\partial u_t^{(j)}}{\partial t^{(j)}}=0 \text{ and } \frac{\partial u_s^{(j)}}{\partial t^{(j)}}=\omega^{(j)} \qquad \text{for } -a^{(j)}<t^{(j)}<a^{(j)} \quad (5)$$

for the anticracks.

Let us now consider the effects of all the cracks and anticracks on the mth crack. For consistency, the stress fields associated with different cracks and anticracks are transformed to the local tangential-normal $(t^{(m)}, s^{(m)})$ coordinate system for the mth crack. For example, the stress fields associated with the ith crack may be transformed as

$$\sigma_{ss}^{(m)}=\sigma_{tt}^{(i)}\sin^2\theta^{(mi)}-2\sigma_{ts}^{(i)}\sin\theta^{(mi)}\cos\theta^{(mi)}+\sigma_{ss}^{(i)}\cos^2\theta^{(mi)} \quad (6a)$$

and

$$\sigma_{ts}^{(m)}=(\sigma_{ss}^{(i)}-\sigma_{tt}^{(i)})\sin\theta^{(mi)}\cos\theta^{(mi)}+\sigma_{ts}^{(i)}(\cos^2\theta^{(mi)}-\sin^2\theta^{(mi)}) \quad (6b)$$

where $\theta^{(mi)}$ is the angle between axes $t^{(i)}$ and $t^{(m)}$.

The N anticracks are now represented by their corresponding distributed tractions and the M cracks are represented by their corresponding distributed dislocations. Summing the effects of all cracks and anticracks on the mth crack we get $(m = 1, \ldots, M)$

$$\sum_{i=1}^{M}\int_{-a^{(i)}}^{a^{(i)}}[K_{11}(t^{(m)}, t^{(i)})b_t^{(i)}(t^{(i)})+K_{12}(t^{(m)}, t^{(i)})b_s^{(i)}(t^{(i)})]dt^{(i)}+\sum_{j=1}^{N}\int_{-a^{(j)}}^{a^{(j)}}[K_{13}(t^{(m)}, t^{(j)})p_t^{(j)}(t^{(j)})+K_{14}(t^{(m)}, t^{(j)})p_s^{(j)}(t^{(j)})]dt^{(j)}+\sigma_{ss}^{(m0)}(t^{(m)})=0 \quad (7a)$$

and

$$\sum_{i=1}^{M}\int_{-a^{(i)}}^{a^{(i)}}[K_{21}(t^{(m)}, t^{(i)})b_t^{(i)}(t^{(i)})+K_{22}(t^{(m)}, t^{(i)})b_s^{(i)}(t^{(i)})]dt^{(i)}+\sum_{j=1}^{N}\int_{-a^{(j)}}^{a^{(j)}}[K_{23}(t^{(m)}, t^{(j)})p_t^{(j)}(t^{(j)})+K_{24}(t^{(m)}, t^{(j)})p_s^{(j)}(t^{(j)})]dt^{(j)}+\sigma_{st}^{(m0)}(t^{(m)})=0 \quad (7b)$$

where the kernels K_{11} through K_{14} depend on H_9 through H_{14}, I_9 through I_{14}, and orientations of the ith and mth cracks and the jth anticrack. The details of these kernels are given in the Appendix. Here, $\sigma_{ss}^{(m0)}$ and $\sigma_{ts}^{(m0)}$ represent the stress components at the location of the mth crack, but in the absence of all cracks and anticracks.

Downloaded 03 May 2010 to 171.66.16.245. Redistribution subject to ASME license or copyright; see http://www.asme.org/terms/Terms_Use.cfm

The boundary conditions for the anticracks are considered next. Utilizing the fact that the components of the displacement gradients transform as

$$u_{t,t}^{(m)} = u_{t,t}^{(j)} \cos^2\theta^{(mj)} + u_{t,s}^{(j)} \sin\theta^{(mj)} \cos\theta^{(mj)} + u_{s,t}^{(j)} \sin\theta^{(mj)} \cos\theta^{(mj)} + u_{s,s}^{(j)} \sin^2\theta^{(mj)} \quad (8a)$$

and

$$u_{s,t}^{(m)} = -u_{t,t}^{(j)} \sin\theta^{(mj)} \cos\theta^{(mj)} - u_{t,s}^{(j)} \sin^2\theta^{(mj)} + u_{s,t}^{(j)} \cos^2\theta^{(mj)} + u_{s,s}^{(j)} \sin\theta^{(mj)} \cos\theta^{(mj)}. \quad (8b)$$

The effects of all cracks and anticracks on the mth anticrack may be expressed as ($m = 1, \ldots, N$)

$$\sum_{i=1}^{M} \int_{-a^{(i)}}^{a^{(i)}} [K_{31}(t^{(m)}, t^{(i)}) b_t^{(i)}(t^{(i)}) + K_{32}(t^{(m)}, t^{(i)}) b_s^{(i)}(t^{(i)})]dt^{(i)} + \sum_{j=1}^{N} \int_{-a^{(j)}}^{a^{(j)}} [K_{33}(t^{(m)}, t^{(j)}) p_t^{(j)}(t^{(j)}) + K_{34}(t^{(m)}, t^{(j)}) p_s^{(j)}(t^{(j)})]dt^{(j)} + u_{t,t}^{(m0)}(t^{(m)}) = 0 \quad (9a)$$

and

$$\sum_{i=1}^{M} \int_{-a^{(i)}}^{a^{(i)}} [K_{41}(t^{(m)}, t^{(i)}) b_t^{(i)}(t^{(i)}) + K_{42}(t^{(m)}, t^{(i)}) b_s^{(i)}(t^{(i)})]dt^{(i)} + \sum_{j=1}^{N} \int_{-a^{(j)}}^{a^{(j)}} [K_{43}(t^{(m)}, t^{(j)}) p_t^{(j)}(t^{(j)}) + K_{44}(t^{(m)}, t^{(j)}) p_s^{(j)}(t^{(j)})]dt^{(j)} + \omega^{(m)} + u_{s,t}^{(m0)}(t^{(m)}) = 0 \quad (9b)$$

where $u_{t,t}^{(m0)}$ and $u_{s,t}^{(m0)}$ are the displacement gradients at the location of the mth anticrack, but with no crack or anticrack present in the system. The kernels K_{41} through K_{44} depend on H_1 through H_8, I_1 through I_8, and orientations of the mth and jth anticracks and the ith crack. Details of these kernels are given in the Appendix.

It can be observed that Eqs. (7) and (9) give rise to $2(M + N)$ integral equations. In order to solve these equations completely for $b_t^{(i)}$, $b_s^{(i)}$, $p_t^{(j)}$, and $p_s^{(j)}$, however, we need to evaluate $(2M + 2N)$ additional constants of integration. It is also important to notice that we need to evaluate the rotations $\omega^{(j)}$ for the N anticracks. This requires N additional equations, bringing the total number of additional equations required to $(2M + 3N)$. The $(2M + 3N)$ additional equations may be obtained by considering the continuity of the opening shapes of the cracks and the equilibrium conditions for the anticracks.

The continuity requirements for crack opening shapes may be expressed as ($i = 1, \ldots, M$)

$$\int_{-a^{(i)}}^{a^{(i)}} b_t^{(i)}(t^{(i)})dt^{(i)} = 0 \text{ and } \int_{-a^{(i)}}^{a^{(i)}} b_s^{(i)}(t^{(i)})dt^{(i)} = 0 \quad (10)$$

Assuming that no external force or couple is applied directly on the anticrack, the equilibrium conditions for the anticracks may also be written as ($j = 1, \ldots, N$)

$$\int_{-a^{(j)}}^{a^{(j)}} p_t^{(j)}(t^{(j)})dt^{(j)} = 0, \quad \int_{-a^{(j)}}^{a^{(j)}} p_s^{(j)}(t^{(j)})dt^{(j)} = 0, \text{ and } \int_{-a^{(j)}}^{a^{(j)}} t^{(j)} p_s^{(j)}(t^{(j)})dt^{(j)} = 0. \quad (11)$$

Equations (7)–(11) now provide an integral equation representation of the interactions in a general system involving M cracks and N anticracks at arbitrary orientations. The above representation is based on the fundamental solutions due to a point load and a point dislocation in an elastic body.

Bilby and Eshelby (1969) modeled an elastic crack as a distributed dislocation and investigated its interactions with a point dislocation. Using a similar approach, Atkinson (1972a, 1972b) and Erdogan and Gupta (1975) considered interactions between a circular inclusion and a crack. Chudnovsky et al. (1987) also used a double layer potential to investigate elastic crack interactions. The solutions of Chudnovsky et al. (1987) can be obtained as a special case of the proposed scheme with no anticracks present in the system. Equations (7)–(9) can also be specialized for the case involving no cracks in the system. Such a representation can be used to investigate the collinear anticrack interactions modeled by Brussat and Westmann (1975).

4 Numerical Solution Scheme

A numerical scheme for solving the integral Eqs. (7)–(9) is presented in this section. A detailed discussion of the treatment of singular integral equations is given by Erdogan et al. (1973). In our approach, such a solution scheme for crack systems is adapted for general systems of cracks and anticracks. Particular attention is paid to the rigid-body rotations of the anticracks.

The set of integral Eqs. (7) and (9) is first reduced to a standard form by the substitutions [$i, m = 1, \ldots, (M + N)$]

$$t^{(i)} = a^{(i)} u^{(i)} \text{ and } t^{(m)} = a^{(m)} v^{(m)}. \quad (12)$$

Absorbing the new coefficient into the modified kernels, the integral Eqs. (7) and (9) may now be written as

$$\sum_{i=1}^{M} \int_{-1}^{1} [\tilde{K}_{11}(v^{(m)}, u^{(i)}) b_t^{(i)}(u^{(i)}) + \tilde{K}_{12}(v^{(m)}, u^{(i)}) b_s^{(i)}(u^{(i)})]du^{(i)} + \sum_{j=1}^{N} \int_{-1}^{1} [\tilde{K}_{13}(v^{(m)}, u^{(j)}) p_t^{(j)}(u^{(j)}) + \tilde{K}_{14}(v^{(m)}, u^{(j)}) p_s^{(j)}(u^{(j)})]du^{(j)} + \sigma_{ss}^{(m0)}(v^{(m)}) = 0 \quad \text{for } -1 < v^{(m)} < 1,\ m = 1, \ldots, M \quad (13a)$$

$$\sum_{i=1}^{M} \int_{-1}^{1} [\tilde{K}_{21}(v^{(m)}, u^{(i)}) b_t^{(i)}(u^{(i)}) + \tilde{K}_{22}(v^{(m)}, u^{(i)}) b_s^{(i)}(u^{(i)})]du^{(i)} + \sum_{j=1}^{N} \int_{-1}^{1} [\tilde{K}_{23}(v^{(m)}, u^{(j)}) p_t^{(j)}(u^{(j)}) + \tilde{K}_{24}(v^{(m)}, u^{(j)}) p_s^{(j)}(u^{(j)})]du^{(j)} + \sigma_{st}^{(m0)}(v^{(m)}) = 0 \quad \text{for } -1 < v^{(m)} < 1,\ m = 1, \ldots, M \quad (13b)$$

$$\sum_{i=1}^{M} \int_{-1}^{1} [\tilde{K}_{31}(v^{(m)}, u^{(i)}) b_t^{(i)}(u^{(i)}) + \tilde{K}_{32}(v^{(m)}, u^{(i)}) b_s^{(i)}(u^{(i)})]du^{(i)} + \sum_{j=1}^{N} \int_{-1}^{1} [\tilde{K}_{33}(v^{(m)}, u^{(j)}) p_t^{(j)}(u^{(j)}) + \tilde{K}_{34}(v^{(m)}, u^{(j)}) p_s^{(j)}(u^{(j)})]du^{(j)} + u_{t,t}^{(m0)}(v^{(m)}) = 0 \quad \text{for } -1 < v^{(m)} < 1,\ m = 1, \ldots, N \quad (13c)$$

$$\sum_{i=1}^{M} \int_{-1}^{1} [\tilde{K}_{41}(v^{(m)}, u^{(i)}) b_t^{(i)}(u^{(i)}) + \tilde{K}_{42}(v^{(m)}, u^{(i)}) b_s^{(i)}(u^{(i)})]du^{(i)} + \sum_{j=1}^{N} \int_{-1}^{1} [\tilde{K}_{43}(v^{(m)}, u^{(j)}) p_t^{(j)}(u^{(j)}) + \tilde{K}_{44}(v^{(m)}, u^{(j)}) p_s^{(j)}(u^{(j)})]du^{(j)} - \omega^{(m)} + u_{s,t}^{(m0)}(v^{(m)}) = 0 \quad \text{for } -1 < v^{(m)} < 1,\ m = 1, \ldots, N. \quad (13d)$$

Downloaded 03 May 2010 to 171.66.16.245. Redistribution subject to ASME license or copyright; see http://www.asme.org/terms/Terms_Use.cfm

The variables $b_t^{(i)}$, $b_s^{(i)}$, $p_t^{(i)}$, and $p_s^{(i)}$ contain singularities of the order of $[u^{(i)}]^{1/2}$ at the end points ($u^{(i)} = \pm 1$) of the integration. In the present work, this singularity is abstracted by expressing the solutions in terms of regular functions $B_t^{(i)}(u^{(i)})$, $B_s^{(i)}(u^{(i)})$, $P_t^{(i)}(u^{(i)})$, and $P_s^{(i)}(u^{(i)})$ along with a weighting function containing the square root singularity. This may be defined as

$$b_t^{(i)}(u^{(i)}) = \frac{B_t^{(i)}(u^{(i)})}{(1-u^{(i)^2})^{1/2}} \text{ and } b_s^{(i)}(u^{(i)}) = \frac{B_s^{(i)}(u^{(i)})}{(1-u^{(i)^2})^{1/2}} \quad i=1, \ldots, M \quad (14a)$$

$$p_t^{(j)}(u^{(j)}) = \frac{P_t^{(j)}(u^{(j)})}{(1-u^{(j)^2})^{1/2}} \text{ and } p_s^{(j)}(u^{(j)}) = \frac{P_s^{(j)}(u^{(j)})}{(1-u^{(j)^2})^{1/2}} \quad j=1, \ldots, M \quad (14b)$$

The presentation shown in Eqs. (14) also allows us to use the Gauss-Chebychev quadrature. The discretized versions of Eqs. (13) may then be expressed as

$$\sum_{i=1}^{M}\sum_{l=1}^{L}\frac{\pi}{L}[\tilde{K}_{11}(v^{(m,q)}, u^{(i,l)})B_t^{(i)}(u^{(i,l)}) + \tilde{K}_{12}(v^{(m,q)}, u^{(i,l)})B_s^{(i)}(u^{(i,l)})] + \sum_{j=1}^{N}\sum_{l=1}^{L}\frac{\pi}{L}[\tilde{K}_{13}(v^{(m,q)}, u^{(j,l)})P_t^{(j)}(u^{(j,l)}) + \tilde{K}_{14}(v^{(m,q)}, u^{(j,l)})P_s^{(j)}(u^{(j,l)})] = -\sigma_{ss}^{(m0)}(v^{(m,q)}) \quad m=1, \ldots, M \quad (15a)$$

$$\sum_{i=1}^{M}\sum_{l=1}^{L}\frac{\pi}{L}[\tilde{K}_{21}(v^{(m,q)}, u^{(i,l)})B_t^{(i)}(u^{(i,l)}) + \tilde{K}_{22}(v^{(m,q)}, u^{(i,l)})B_s^{(i)}(u^{(i,l)})] + \sum_{j=1}^{N}\sum_{l=1}^{L}\frac{\pi}{L}[\tilde{K}_{23}(v^{(m,q)}, u^{(j,l)})P_t^{(j)}(u^{(j,l)}) + \tilde{K}_{24}(v^{(m,q)}, u^{(j,l)})P_s^{(j)}(u^{(j,l)})] = -\sigma_{st}^{(m0)}(v^{(m,q)}) \quad m=1, \ldots, M \quad (15b)$$

$$\sum_{i=1}^{M}\sum_{l=1}^{L}\frac{\pi}{L}[\tilde{K}_{31}(v^{(m,q)}, u^{(i,l)})B_t^{(i)}(u^{(i,l)}) + \tilde{K}_{32}(v^{(m,q)}, u^{(i,l)})B_s^{(i)}(u^{(i,l)})] + \sum_{j=1}^{N}\sum_{l=1}^{L}\frac{\pi}{L}[\tilde{K}_{33}(v^{(m,q)}, u^{(j,l)})P_t^{(j)}(u^{(j,l)}) + \tilde{K}_{34}(v^{(m,q)}, u^{(j,l)})P_s^{(j)}(u^{(j,l)})] = -u_{t,t}^{(m0)}(v^{(m,q)}) \quad m=1, \ldots, N \quad (15c)$$

$$\sum_{i=1}^{M}\sum_{l=1}^{L}\frac{\pi}{L}[\tilde{K}_{41}(v^{(m,q)}, u^{(i,l)})B_t^{(i)}(u^{(i,l)}) + \tilde{K}_{42}(v^{(m,q)}, u^{(i,l)})B_s^{(i)}(u^{(i,l)})] + \sum_{j=1}^{N}\sum_{l=1}^{L}\frac{\pi}{L}[\tilde{K}_{43}(v^{(m,q)}, u^{(j,l)})P_t^{(j)}(u^{(j,l)}) + \tilde{K}_{44}(v^{(m,q)}, u^{(j,l)})P_s^{(j)}(u^{(j,l)})] - \omega^{(m)} = -u_{s,t}^{(m0)}(v^{(m,q)}) \quad m=1, \ldots, N \quad (15d)$$

where

$$u^{(j,l)} = u^{(i,l)} = \cos\left(\frac{2l-1}{2L}\pi\right) \quad l=1, \ldots, L \quad (15e)$$

and

$$v^{(m,q)} = \cos\left(\frac{q}{L}\pi\right) \quad q=1, \ldots, L-1. \quad (15f)$$

It should be noted here that the system of Eqs. (15) contains $2(L-1)(M+N)$ equations, but $\{2L(M+N)+N\}$ unknowns. The additional $(2M+3N)$ equations can be obtained from the discretized versions of Eqs. (10) and (11), ensuring continuity of crack-opening shapes and equilibrium of anticracks, respectively. These additional equations may be written as

$$\sum_{l=1}^{L}\frac{\pi}{L}B_t^{(i)}(u^{(i,l)}) = 0 \text{ and } \sum_{l=1}^{L}\frac{\pi}{L}B_s^{(i)}(u^{(i,l)}) = 0 \quad i=1, \ldots, M \quad (16a)$$

$$\sum_{l=1}^{L}\frac{\pi}{L}P_t^{(j)}(u^{(j,l)}) = 0, \quad \sum_{l=1}^{L}\frac{\pi}{L}P_s^{(j)}(u^{(j,l)}) = 0 \text{ and } \sum_{l=1}^{L}\frac{\pi}{L}a^{(j)}u^{(j,l)}P_s^{(j)}(u^{(j,l)}) = 0 \quad j=1, \ldots, N. \quad (16b)$$

Utilizing Eqs. (15) and (16), the values of $B_t^{(i)}$, $B_s^{(i)}$, $P_t^{(j)}$, and $P_s^{(j)}$ can be obtained at L collocation points. The crack-tip stress intensity factor may then be determined as ($i = 1, \ldots, M$)

$$K_I^{(i)}(\pm 1) = \pm 2\sqrt{\pi a^{(i)}}\frac{G}{(\kappa+1)}B_s^{(i)}(\pm 1) \text{ and } K_{II}^{(i)}(\pm 1) = \pm 2\sqrt{\pi a^{(i)}}\frac{G}{(\kappa+1)}B_s^{(i)}(\pm 1). \quad (17)$$

Here, $B_s^{(i)}(\pm 1)$ and $B_t^{(i)}(\pm 1)$ are obtained by interpolating the values of $B_s^{(i)}$ and $B_t^{(i)}$, respectively, at the collocation points.

The stress singularity coefficients for an anticrack (Wang et al., 1985) are also analogous to the stress intensity factors for a crack and can be evaluated from the solutions $P_t^{(i)}$ and $P_s^{(j)}$ in a similar fashion.

5 Numerical Results

Applications of the proposed integral equation formulation based on the fundamental solutions due to point force and point dislocation to several example problems involving interactions of cracks and anticracks are presented in this section. The proposed integral equation formulation can handle arbitrary orientations and distributions of cracks and anticracks along with arbitrary loading conditions in the context of elasticity. Thus, the proposed formulation is suitable for investigating the effects of microdefects in ceramics and intermetallics under general loading conditions.

Various researchers in the past (e.g., Comninou, 1977; Atkinson, 1972a,b; Erdogan and Gupta, 1975; He and Hutchinson, 1989; Keer et al., 1983; Müller, 1989) have pursued a Green's function approach to investigating crack problems utilizing the Green's function due to Dundurs and Mura (1964) and Dundurs and Sendeckyj (1965). Very recently, Dundurs and Markenscoff (1989) established a new Green's function for an infinite body containing an anticrack. This new Green's function can be utilized to investigate the interactions of collinear crack-anticrack systems.

In this paper, the results from the proposed scheme for a collinear crack-anticrack problem are first verified against those obtained from the Green's function approach of Dundurs and Markenscoff (1989). For this and all other examples, and $\nu = 0.3$ are used. The stress intensity factor (SIF) is also normalized with respect to $\sigma_0\sqrt{\pi a}$, where σ_0 is the remote stress and a is half of the crack length.

As shown in the inset of Fig. 2, a crack of length $2a^{(2)}$ situated collinearly at a distance b from an anticrack of length $2a^{(1)}$ is considered first. Using a Green's function approach, modeling of the anticrack boundary conditions is obviated and the traction-free conditions on the crack surface in Fig. 2 then lead to

Downloaded 03 May 2010 to 171.66.16.245. Redistribution subject to ASME license or copyright; see http://www.asme.org/terms/Terms_Use.cfm

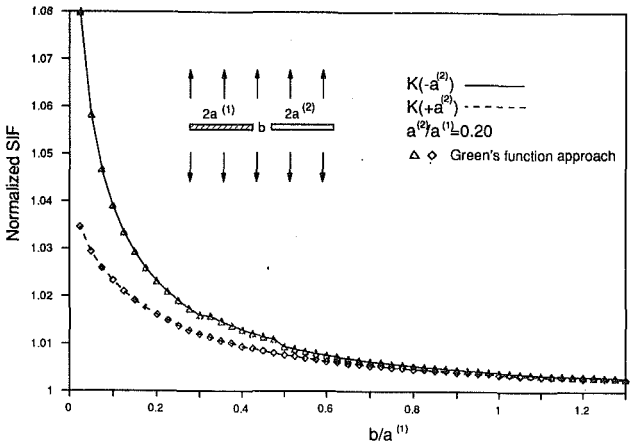


Fig. 2 Comparisons of the stress intensity factors for collinear crack-anticrack systems

$$\int_{a^{(1)}+b}^{a^{(1)}+b+2a^{(2)}} \frac{b_y(\xi_2)}{2\pi\kappa}\left[\frac{(\kappa+1)}{(x_2-\xi_2)}-\frac{(\kappa-1)^2}{(\kappa+1)}\frac{1}{\sqrt{x_2^2-a^{(1)^2}}}\times\left(1+\frac{\sqrt{\xi_2^2-a^{(1)^2}}}{x_2-\xi_2}\right)\right]d\xi_2+\sigma_{yy}^{10}=0$$

$$(a^{(1)}+b)<x_2<(a^{(1)}+b+2a^{(2)}) \quad (18a)$$

$$\int_{a^{(1)}+b}^{a^{(1)}+b+2a^{(2)}} \frac{b_x(\xi_2)}{2\pi\kappa}\left[\frac{(\kappa+1)}{(x_2-\xi_2)}+\frac{(\kappa-1)^2}{(\kappa+1)}\left[A(\xi_2)-1/(\sqrt{x_2^2-a^{(1)^2}})\left(1+A(\xi_2)x_2+\frac{\sqrt{\xi_2^2-a^{(1)^2}}}{x_2-\xi_2}\right)\right]\right]d\xi_2+\sigma_{xy}^{10}=0$$

$$(a^{(1)}+b)<x_2<(a^{(1)}+b+2a^{(2)}) \quad (18b)$$

with

$$A(\xi_2)=\frac{2}{a^{(1)^2}}[\xi_2-(\xi_2^2-a^{(1)^2})^{1/2}] \quad (18c)$$

where σ_{xy}^{10} and σ_{yy}^{10} are the stress fields in the elastic body containing the anticrack and subjected to the prescribed loading.

It should be noted here that the proposed integral equation formulation utilizes initial displacement gradient and stress fields with no crack or anticrack present in the system. Such initial fields are readily obtainable for complicated problems. Figure 2 shows the comparisons of the normalized mode-I SIF obtained by the present analysis with those obtained by the Green's function approach due to Dundurs and Markenscoff (1989). Different ratios of the separation distance (b) with respect to the anticrack length ($a^{(1)}$) are considered. Over a range of $b/a^{(1)}$ varying from 0.05 to 1.2, the numerical results obtained from the two approaches compare very well. The Green's function approach is, of course, more efficient for the collinear problem, but the integral equation approach is more general and the unknown quantities b_x, b_y, p_x, p_y, and ω are obtained directly. The Green's function approach gives b_x and b_y directly, but requires secondary calculations for obtaining p_x, p_y, and ω.

Figure 3 shows the variation of the normalized mode-I SIF for the near tip of the crack of the collinear crack-anticrack system with the ratio of the lengths between the crack and the anticrack. As $a^{(1)}/a^{(2)}$ varies from 0.05 to 10, the normalized SIFs for all $b/a^{(2)}$ ratios increase significantly. For $b/a^{(2)}$ = 0.05, the normalized SIF increases from 1.0 to 1.17 as $a^{(1)}/a^{(2)}$ goes from 0.05 to 10. The normalized SIF also increases as

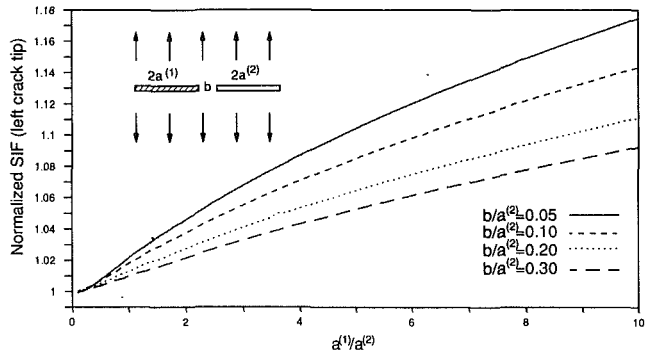


Fig. 3 Variation of the near (left) crack-tip stress intensity factor with the length of the anticrack

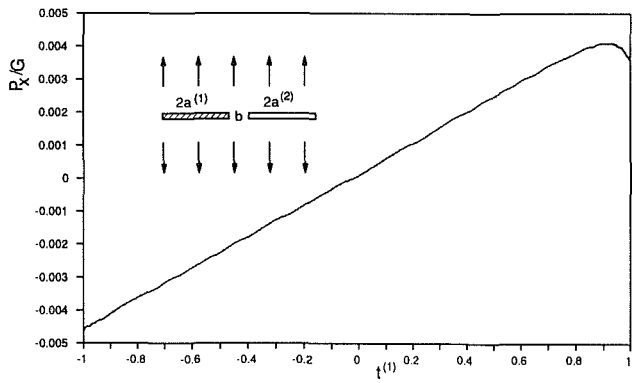


Fig. 4 Distribution of normalized shear traction (P_x/G) along the length of the anticrack

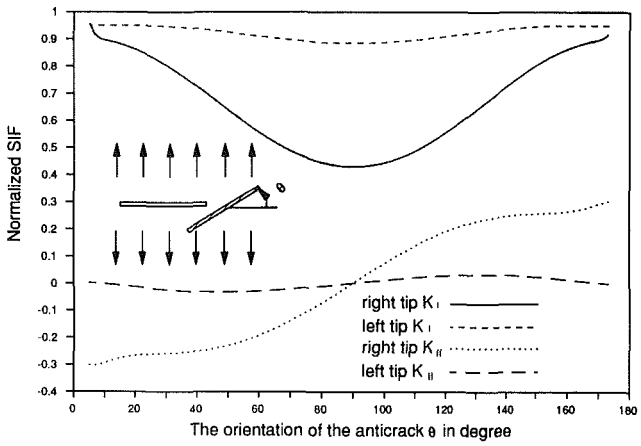


Fig. 5 Variations of the stress intensity factors with the orientation of the anticrack

$b/a^{(2)}$ decreases. As the separation decreases ($b/a^{(2)}$ goes from 0.30 to 0.05), at $a^{(1)}/a^{(2)}$ = 10 the normalized SIF changes from 1.09 to 1.17. Figure 4 shows the distribution of the normalized shear traction (for $b/a^{(2)}$ = 0.25 and $a^{(1)}/a^{(2)}$ = 1) over the length of the anticrack. As expected, P_x/G is self-equilibrating. (Note that p_x becomes singular at the tip, but P_x does not.) In the vicinity of $t^{(1)}$ = 1, it is also found to be perturbed by the presence of the crack.

A general crack-anticrack system with arbitrary orientations is considered next. The geometry of the problem is shown as an inset in Fig. 5. The crack and anticrack are of equal length. The normalized distance (w.r.t. the half-length of the crack) between the crack tip and the center of the anticrack is 0.2. As the angle of orientation θ changes from 5 deg to 90 deg,

Downloaded 03 May 2010 to 171.66.16.245. Redistribution subject to ASME license or copyright; see http://www.asme.org/terms/Terms_Use.cfm

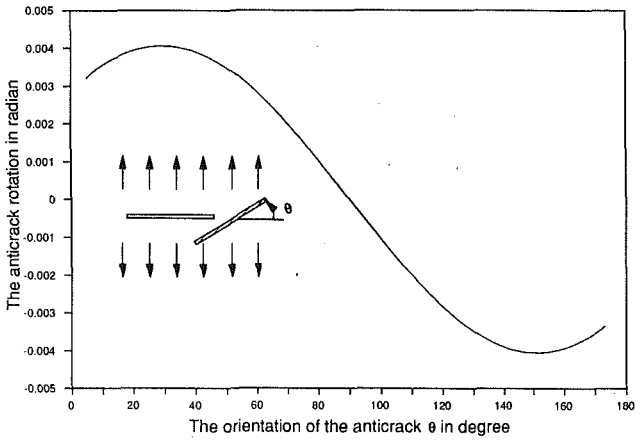


Fig. 6 Variation of the angular rotation of the anticrack with its orientation

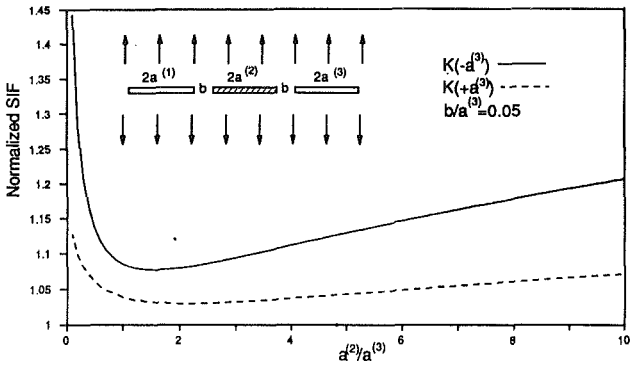


Fig. 7 Variation of the normalized stress intensity factors with the length of the anticrack for fixed separation (b) and fixed and equal crack lengths ($a^{(1)}$, $a^{(3)}$)

the near-tip mode-I SIF varies from 0.95 to a minima of 0.44. The variation is symmetric about $\theta = 90$ deg. The near-tip mode-II SIF varies from -0.3 to zero as θ goes from 5 deg to 90 deg. As expected, the sign of the mode-II SIF changes as θ increases beyond 90 deg. Variations of both far-tip mode-I and mode-II SIFs, as expected, are much smaller than their corresponding near-tip SIF variations. The angular rotation of the anticrack (shown in Fig. 6) reaches a maximum of 0.004 radians at $\theta = 28.8$ deg and drops to zero at $\theta = 90$ deg. The direction of rigid-body rotation changes as θ is increased beyond 90 deg.

A configuration involving two collinear cracks separated by an anticrack (shown as inset in Fig. 7) is considered next. The variations of the normalized SIFs for the near and far tips for a special case when $a^{(1)} = a^{(3)}$ and $b/a^{(3)} = 0.05$ are presented in Fig. 7. The ratio $a^{(2)}/a^{(3)}$ representing the relative length of the anticrack compared to that of the crack is varied from 0.05 to 10. At $a^{(2)}/a^{(3)} = 0.05$, when the anticrack is very small, the near-tip SIF is found to be 1.44 and the far-tip SIF is observed to be 1.13. With a small increase in the relative size of the anticrack, the SIFs are observed to decrease rapidly. The near-tip SIF drops to 1.08 at $a^{(2)}/a^{(3)} = 1.4$ before rising again to 1.19 at $a^{(2)}/a^{(3)} = 10$. The far-tip SIF also shows a similar profile, reaching a minimum of 1.03 at $a^{(2)}/a^{(3)} = 2$ before rising to 1.07 at $a^{(2)}/a^{(3)} = 10$. This suggests that there is an optimum ratio of $a^{(2)}/a^{(3)}$ for crack shielding in this problem. At small $a^{(2)}/a^{(3)}$, the interactions between the two cracks are dominant, while the interactions between the crack and the anticrack become more significant at large values of $a^{(2)}/a^{(3)}$. Accordingly, there exists an optimal shielding region in between these extremes.

6 Conclusions and Discussion

The fundamental solutions due to point loads and point dislocations in an elastic body are utilized in the present analysis to develop a model for interactions among cracks and rigid lines (or anticracks) in the context of elastic fracture mechanics. An integral equation approach is pursued for this purpose. The proposed technique is capable of handling general loading conditions and arbitrary orientations of cracks and anticracks. A Gauss-Chebychev quadrature is used to reduce the integral equations to a linear system of equations consisting of the distribution of forces and Burger's dislocation vectors, respectively, on the cracks and the anticracks.

The proposed integral equation approach is first verified against the solutions obtained by the Green's function approach (Dundurs and Markenscoff, 1989) for a colinear crack-anticrack system. A general crack-anticrack system with arbitrary orientations is considered next, and the effects of the relative orientation between the crack and the anticrack on the amplification and shielding of the SIFs are investigated. A system consisting of two cracks separated by an anticrack is also considered, and a criterion for optimum shielding is obtained.

Many real-life materials contain hard second-phase particles or hard second-phase lamellae. These may be treated as rigid lines or anticracks. Interactions of these anticracks with cracks determine the effectiveness of crack shielding through these rigid line inclusions. The proposed integral equation approach provides an avenue for investigating general crack-anticrack systems. Work on sensitivity studies for such systems and applications to ceramic grinding processes is currently in progress at The University of Arizona.

Acknowledgments

The authors gratefully acknowledge the financial support provided under Grant No. DMC 8657345 from the U.S. National Science Foundation.

References

Atkinson, C., 1972a, "The Interaction Between a Crack and an Inclusion," *Int. J. Engng. Sci.*, Vol. 10, pp. 127–136.

Atkinson, C., 1972b, "On Dislocation Densities and Stress Singularities Associated with Cracks and Pile Ups in Inhomogeneous Media," *Int. J. Engng. Sci.*, Vol. 10, pp. 45–71.

Atkinson, C., 1973, "Some Ribbon-Like Inclusion Problems," *Int. J. Engng. Sci.*, Vol. 11, pp. 243–266.

Baeslack, W. A., Cieslak, M. J., and Headley, T. J., 1988, "Structure, Properties and Fracture of Pulsed Nd:YAG Laser Welded Ti-14.8wt%Al-21.3wt%Nb Titanium Aluminide," *Scripta Metallurgica*, Vol. 22, pp. 1155–1160.

Baliarini, R., 1987, "An Integral Equation Approach for Rigid Line Inhomogeneity Problems," *Int. J. Fracture*, Vol. 33, pp. R23–R26.

Bilby, B. A., and Eshelby, J. D., 1969, "Dislocations and the Theory of Fracture," *Fracture*, H. Liebowitz, ed., Vol. 1, Academic Press, New York, pp. 99–182.

Broberg, K. B., 1987, "On Crack Paths," *Eng. Fracture Mechanics*, Vol. 28, pp. 663–679.

Brussat, T. R., and Westmann, R. A., 1975, "A Westergaard-Type Stress Function for Line Inclusion Problems," *Int. J. Solids Structures*, Vol. 11, pp. 665–677.

Chen, Y. Z., 1984, "Multiple Crack Problems of Antiplane Elasticity in an Infinite Body," *Eng. Fracture Mechanics*, Vol. 20, pp. 767–775.

Chou, Y. T., and Wang, Z. Y., 1983, "Stress Singularity at the Tip of a Rigid Flat Inclusion," *Recent Developments in Applied Mechanics*, F. F. Ling and I. G. Tadjbakhsh, eds., Rensselaer Press, New York, pp. 21–30.

Chudnovsky, A., Dolgopolsky, A., and Kachanov, M., 1987, "Elastic Interaction of a Crack with a Microcrack Array—Part I and II," *Int. J. Solids Structures*, Vol. 23, pp. 1–10, 11–21.

Comninou, M., 1977, "The Interface Crack," ASME JOURNAL OF APPLIED MECHANICS, Vol. 44, pp. 631–636.

Cruse, T. A., 1988, *Boundary Element Analysis in Computational Fracture Mechanics*, Kluwer Academic Publishers, Dordrecht, The Netherlands.

Dundurs, J., and Markenscoff, X., 1989, "A Green's Function Formulation of Anticracks and Their Interaction with Load-Induced Singularities," ASME JOURNAL OF APPLIED MECHANICS, Vol. 56, pp. 550–555.

Dundurs, J., and Mura, T., 1964, "Interaction Between an Edge Dislocation and a Circular Inclusion," *J. Mech. Phys. Solids*, Vol. 12, pp. 177–189.

Downloaded 03 May 2010 to 171.66.16.245. Redistribution subject to ASME license or copyright; see http://www.asme.org/terms/Terms_Use.cfm

Dundurs, J., and Sendeckyj, G. P., 1965, "Edge Dislocation Inside a Circular Inclusion," *J. Mech. Phys. Solids*, Vol. 13, pp. 141–147.

Erdogan, R., and Gupta, G. D., 1972, "Stress Near a Flat Inclusion in Bonded Dissimilar Materials," *Int. J. Solids Structures*, Vol. 8, pp. 533–547.

Erdogan, F., and Gupta, G. D., 1975, "The Crack Problem with a Crack Crossing the Boundary," *Int. J. Fracture*, Vol. 11, pp. 13–27.

Erdogan, F., Gupta, G. D., and Cook, T. S., 1973, "Numerical Solution of Singular Integral Equations," *Methods of Analysis and Solutions of Crack Problems*, G. C. Sih, ed., Noordhoff, Leyden, pp. 368–425.

Eshelby, J. D., 1957, "The Determination of the Elastic Field of an Ellipsoidal Inclusion, and Related Problems," *Proc. Royal Soc., London*, Vol. A241, pp. 376–396.

Eshelby, J. D., 1959, "The Elastic Field Outside an Ellipsoidal Inclusion," *Proc. Royal Soc.*, Vol. A252, pp. 561–569.

Haritos, G. K., Hager, J. W., Amos, A. K., Salkind, M. J., and Wang, A. S. D., 1988, "Mesomechanics: The Microstructure-Mechanics Connection," *Int. J. Solids Structures*, Vol. 24, pp. 1081–1096.

Hasebe, N., Keer, L. M., and Nemat-Nasser, S., 1984, "Stress Analysis of a Kinked Crack Initiating from a Rigid Line Inclusion; Part 1: Formulation," *Mech. of Materials*, Vol. 3, pp. 131–145.

He, M. Y., and Hutchinson, J. W., 1989, "Kinking of a Crack Out of an Interface," ASME JOURNAL OF APPLIED MECHANICS, Vol. 56, pp. 270–278.

Hori, H., and Nemat-Nasser, S., 1987, "Interacting Micro-Cracks Near the Tip in the Process Zone of a Macro-Crack," *J. Mech. Phys. Solids*, Vol. 35, pp. 601–629.

Horii, H., and Nemat-Nasser, S., 1986, "Brittle Failure in Compression: Splitting, Faulting and Brittle-Ductile Transition," *Phil. Trans. Royal Soc. Lond.*, Vol. A319, pp. 337–374.

Jha, S. C., Ray, R., and Clemm, P. J., 1988, "Microstructure of Ti3 Al + Nb Alloys Produced via Rapid Solidification," *Mat. Sci. Engng.*, Vol. 98, pp. 395–397.

Kachanov, M., 1985, "A Simple Technique of Stress Analysis in Elastic Solids with Many Cracks," *Int. J. Fracture*, Vol. 28, pp. R11–R19.

Kachanov, M., 1987, "Elastic Solids with Many Cracks: A Simple Method of Analysis," *Int. J. Solids Structures*, Vol. 23, pp. 23–43.

Keer, L. M., Lee, J. C., and Mura, T., 1983, "Stress Distribution for a Quarter Plane Containing an Arbitrarily Oriented Crack," ASME JOURNAL OF APPLIED MECHANICS, Vol. 50, pp. 43–49.

Li, Q., and Ting, T. C. T., 1989, "Line Inclusions in Anisotropic Elastic Solids," ASME JOURNAL OF APPLIED MECHANICS, Vol. 56, pp. 556–563.

Liebowitz, H., 1968, *Fracture*, Vols. 1–7, Academic Press, New York.

Melin, S., 1983, "Why Do Cracks Avoid Each Other," *Int. J. Fracture*, Vol. 23, pp. 37–45.

Mukherjee, S., 1982, *Boundary Element Methods in Creep and Fracture*, Elsevier Applied Science Publishers, Barking, Essex, U.K.

Müller, W. H., 1989, "The Exact Calculation of Stress Intensity Factor in Transformation Toughened Ceramics by Means of Integral Equations," *Int. J. Fracture*, Vol. 41, pp. 1–22.

Mura, T., 1987, *Micromechanics of Defects in Solids*, 2nd ed., Martinus Nijhoff Pub., Boston.

Mura, T., 1988, "Inclusion Problems," ASME *Appl. Mech. Rev.*, Vol. 41, pp. 15–20.

Muskhelishvili, N. I., 1953, *Some Basic Problems of the Mathematical Theory of Elasticity*, Noorhoff Ltd., Groningen, The Netherlands.

Parton, V. Z., and Morozov, E. M., 1989, *Mechanics of Elastic-Plastic Fracture*, Hemisphere, New York.

Read, W. T., 1953, *Dislocations in Crystals*, McGraw-Hill, New York.

Selvadurai, A. S. P., 1980, "The Displacements of a Flexible Inhomogeneity Embedded in a Transversely Isotropic Elastic Medium," *Fiber Science and Technology*, Vol. 14, pp. 251–259.

Sendeckyj, G. P., 1970, "Elastic Inclusion Problems in Plane Elastostatics," *Int. J. Solids Structures*, Vol. 6, pp. 1535–1543.

Sih, G. C., 1973, *Mechanics of Fracture*, Vol. 1, Noordhoff, Leyden, The Netherlands.

Stroh, A. N., 1958, "Dislocations and Cracks in Anisotropic Elasticity," *Phil. Mag.*, Vol. 3, pp. 625–646.

Stroh, A. N., 1962, "Steady-State Problems in Anisotropic Elasticity," *J. Math. Phys.*, Vol. 41, pp. 77–103.

Timoshenko, S. P., and Goodier, J. N., 1970, *Theory of Elasticity*, 3rd ed., McGraw-Hill, New York.

Wang, Z. Y., Zhang, H. T., and Chou, Y. T., 1985, "Characteristics of the Elastic Field of a Rigid Line Inhomogeneity," ASME JOURNAL OF APPLIED MECHANICS, Vol. 52, pp. 818–822.

Wang, Z. Y., Zhang, H. T., and Chou, Y. T., 1985, "Stress Singularity at the Tip of a Rigid Line Inhomogeneity Under Antiplane Shear Loading," ASME JOURNAL OF APPLIED MECHANICS, Vol. 53, pp. 459–462.

APPENDIX

The fundamental functions in Eqs. (1) and (2) are given as

$$H_1(x, y; \xi) = -(\kappa-1)\frac{x-\xi}{r^2} - \frac{(x-\xi)[(x-\xi)^2-y^2]}{r^4}$$

$$H_2(x, y; \xi) = -\frac{y[(x-\xi)^2-y^2]}{r^4}$$

$$H_3(x, y; \xi) = -\kappa\frac{y}{r} - \frac{2(x-\xi)^2 y}{r^4}$$

$$H_4(x, y; \xi) = \frac{x-\xi}{r^2} - \frac{2(x-\xi)y^2}{r^4}$$

$$H_5(x, y; \xi) = \frac{y}{r^2} - \frac{2(x-\xi)^2 y}{r^4}$$

$$H_6(x, y; \xi) = -\kappa\frac{x-\xi}{r^2} - \frac{2(x-\xi)y^2}{r^4}$$

$$H_7(x, y; \xi) = \frac{(x-\xi)[(x-\xi)^2-y^2]}{r^4}$$

$$H_8(x, y; \xi) = -(\kappa-1)\frac{y}{r^2} + \frac{y[(x-\xi)^2-y^2]}{r^4}$$

$$H_9(x, y; \xi) = -(\kappa-1)\frac{x-\xi}{r^2} - \frac{4(x-\xi)^3}{r^4}$$

$$H_{10}(x, y; \xi) = (\kappa-1)\frac{y}{r^2} - \frac{4y(x-\xi)^2}{r^4}$$

$$H_{11}(x, y; \xi) = -(\kappa-1)\frac{y}{r^2} - \frac{4(x-\xi)^2 y}{r^4}$$

$$H_{12}(x, y; \xi) = -(\kappa-1)\frac{x-\xi}{r^2} - \frac{4y^2(x-\xi)}{r^4}$$

$$H_{13}(x, y; \xi) = (\kappa-1)\frac{x-\xi}{r^2} - \frac{4(x-\xi)y^2}{r^4}$$

$$H_{14}(x, y; \xi) = -(\kappa-1)\frac{y}{r^2} - \frac{4y^3}{r^4}$$

$$I_1(x, y; \xi) = (\kappa-1)\frac{y}{r^2} + \frac{4(x-\xi)^2 y}{r^4}$$

$$I_2(x, y; \xi) = (\kappa-1)\frac{x-\xi}{r^2} - \frac{4(x-\xi)y^2}{r^4}$$

$$I_3(x, y; \xi) = (\kappa+3)\frac{x-\xi}{r^2} - \frac{4(x-\xi)y^2}{r^4}$$

$$I_4(x, y; \xi) = (\kappa-1)\frac{y}{r^2} + \frac{4(x-\xi)^2 y}{r^4}$$

$$I_5(x, y; \xi) = -(\kappa-1)\frac{x-\xi}{r^2} - \frac{4(x-\xi)y^2}{r^4}$$

$$I_6(x, y; \xi) = -(\kappa+3)\frac{y}{r^2} + \frac{4(x-\xi)^2 y}{r^4}$$

$$I_7(x, y; \xi) = -(\kappa-1)\frac{y}{r^2} - \frac{4(x-\xi)^2 y}{r^4}$$

$$I_8(x, y; \xi) = (\kappa-1)\frac{x-\xi}{r^2} + \frac{4(x-\xi)y^2}{r^4}$$

$$I_9(x, y; \xi) = -\frac{[3(x-\xi)^2+y^2]y}{r^4}$$

$$I_{10}(x, y; \xi) = \frac{(x-\xi)[(x-\xi)^2-y^2]}{r^4}$$

$$I_{11}(x, y; \xi) = \frac{[(x-\xi)^2-y^2](x-\xi)}{r^4}$$

$$I_{12}(x, y; \xi) = \frac{y[(x-\xi)^2-y^2]}{r^4}$$

$$I_{13}(x, y; \xi) = \frac{[(x-\xi)^2-y^2]y}{r^4}$$

$$I_{14}(x, y; \xi) = \frac{(x-\xi)[(x-\xi)^2+3y^2]}{r^4}$$

Downloaded 03 May 2010 to 171.66.16.245. Redistribution subject to ASME license or copyright; see http://www.asme.org/terms/Terms_Use.cfm

where

$$r^2=(x-\xi)^2+y^2.$$

The expressions of the kernels in Eqs. (7)–(9) are given as

$$K_{11}(t^{(m)}, t^{(i)}) = \frac{2G}{\pi(\kappa+1)}\{G_9(t^{(m)}, t^{(i)})\sin^2\theta^{(mi)} - 2G_{11}(t^{(m)}, t^{(i)}) \times \sin\theta^{(mi)}\cos\theta^{(mi)} + G_{13}(t^{(m)}, t^{(i)})\cos^2\theta^{(mi)}\}$$

$$K_{12}(t^{(m)}, t^{(i)}) = \frac{2G}{\pi(\kappa+1)}\{G_{10}(t^{(m)}, t^{(i)})\sin^2\theta^{(mi)} - 2G_{12}(t^{(m)}, t^{(i)}) \times \sin\theta^{(mi)}\cos\theta^{(mi)} + G_{14}(t^{(m)}, t^{(i)})\cos^2\theta^{(mi)}\}$$

$$K_{13}(t^{(m)}, t^{(i)}) = \frac{1}{2\pi(\kappa+1)}\{F_9(t^{(m)}, t^{(j)})\sin^2\theta^{(mj)} - 2F_{11}(t^{(m)}, t^{(j)})\sin\theta^{(mj)}\cos\theta^{(mj)} + F_{13}(t^{(m)}, t^{(j)})\cos^2\theta^{(mj)}\}$$

$$K_{14}(t^{(m)}, t^{(i)}) = \frac{1}{2\pi(\kappa+1)}\{F_{10}(t^{(m)}, t^{(j)})\sin^2\theta^{(mj)} - 2F_{12}(t^{(m)}, t^{(j)})\sin\theta^{(mj)}\cos\theta^{(mj)} + F_{14}(t^{(m)}, t^{(j)})\cos^2\theta^{(mj)}\}$$

$$K_{21}(t^{(m)}, t^{(i)}) = \frac{2G}{\pi(\kappa+1)}\{[G_9(t^{(m)}, t^{(i)}) + G_{13}(t^{(m)}, t^{(i)})] \times \sin\theta^{(mi)}\cos\theta^{(mi)} + G_{11}(t^{(i)}, t^{(m)})(\sin^2\theta^{(mi)} - \cos^2\theta^{(mi)})\}$$

$$K_{22}(t^{(m)}, t^{(i)}) = \frac{2G}{\pi(\kappa+1)}\{[G_{10}(t^{(m)}, t^{(i)}) + G_{14}(t^{(m)}, t^{(i)})] \times \sin\theta^{(mi)}\cos\theta^{(mi)} + G_{12}(t^{(i)}, t^{(m)})(\sin^2\theta^{(mi)} - \cos^2\theta^{(mi)})\}$$

$$K_{23}(t^{(m)}, t^{(j)}) = \frac{1}{2\pi(\kappa+1)}\{[F_9(t^{(m)}, t^{(j)}) + F_{13}(t^{(m)}, t^{(j)})] \times \sin\theta^{(mj)}\cos\theta^{(mj)} + F_{11}(t^{(m)}, t^{(j)})(\sin^2\theta^{(mj)} - \cos^2\theta^{(mj)})\}$$

$$K_{24}(t^{(m)}, t^{(j)}) = \frac{1}{2\pi(\kappa+1)}\{[F_{10}(t^{(m)}, t^{(j)}) + F_{14}(t^{(m)}, t^{(j)})] \times \sin\theta^{(mj)}\cos\theta^{(mj)} + F_{12}(t^{(m)}, t^{(j)})(\sin^2\theta^{(mj)} - \cos^2\theta^{(mj)})\}$$

$$K_{31}(t^{(m)}, t^{(i)}) = \frac{1}{2\pi(\kappa+1)}\{G_1(t^{(m)}, t^{(i)})\cos^2\theta^{(mi)} + [G_3(t^{(m)}, t^{(i)}) + G_5(t^{(m)}, t^{(i)})]\sin\theta^{(mi)}\cos\theta^{(mi)} + G_7(t^{(m)}, t^{(i)})\sin^2\theta^{(mi)}\}$$

$$K_{32}(t^{(m)}, t^{(i)}) = \frac{1}{2\pi(\kappa+1)}\{G_2(t^{(m)}, t^{(i)})\cos^2\theta^{(mi)} + [G_4(t^{(m)}, t^{(i)}) + G_6(t^{(m)}, t^{(i)})]\sin\theta^{(mi)}\cos\theta^{(mi)} + G_8(t^{(m)}, t^{(i)})\sin^2\theta^{(mi)}\}$$

$$K_{33}(t^{(m)}, t^{(j)}) = \frac{1}{2\pi G(\kappa+1)}\{F_1(t^{(m)}, t^{(j)})\cos^2\theta^{(mj)} + [F_3(t^{(m)}, t^{(j)}) + F_5(t^{(m)}, t^{(j)})]\sin\theta^{(mj)}\cos\theta^{(mj)} + F_7(t^{(m)}, t^{(j)})\sin^2\theta^{(mj)}\}$$

$$K_{34}(t^{(m)}, t^{(j)}) = \frac{1}{2\pi G(\kappa+1)}\{F_2(t^{(m)}, t^{(j)})\cos^2\theta^{(mj)} + [F_4(t^{(m)}, t^{(j)}) + F_6(t^{(m)}, t^{(j)})]\sin\theta^{(mj)}\cos\theta^{(mj)} + F_8(t^{(m)}, t^{(j)})\sin^2\theta^{(mj)}\}$$

$$K_{41}(t^{(m)}, t^{(i)}) = \frac{1}{2\pi(\kappa+1)}\{[G_7(t^{(m)}, t^{(i)}) - G_1(t^{(m)}, t^{(i)})]\sin^2\theta^{(mi)}\cos\theta^{(mi)} - [G_3(t^{(m)}, t^{(i)})\sin^2\theta^{(mi)} + G_5(t^{(m)}, t^{(i)})]\cos^2\theta^{(mi)}\}$$

$$K_{42}(t^{(m)}, t^{(i)}) = \frac{1}{2\pi(\kappa+1)}\{[G_8(t^{(m)}, t^{(i)}) - G_2(t^{(m)}, t^{(i)})]\sin\theta^{(mi)}\cos\theta^{(mi)} - G_4(t^{(m)}, t^{(i)})\sin^2\theta^{(mi)} + G_6(t^{(m)}, t^{(i)})\cos^2\theta^{(mi)}\}$$

$$K_{43}(t^{(m)}, t^{(j)}) = \frac{1}{2\pi G(\kappa+1)}\{[F_7(t^{(m)}, t^{(j)}) - F_1(t^{(m)}, t^{(j)})]\sin\theta^{(mj)}\cos\theta^{(mj)} - F_3(t^{(m)}, t^{(j)})\sin^2\theta^{(mj)} + F_5(t^{(m)}, t^{(j)})\cos^2\theta^{(mj)}\}$$

$$K_{44}(t^{(m)}, t^{(j)}) = \frac{1}{2\pi G(\kappa+1)}\{[F_8(t^{(m)}, t^{(j)}) - F_2(t^{(m)}, t^{(j)})]\sin\theta^{(mj)}\cos\theta^{(mj)} - F_4(t^{(m)}, t^{(j)})\sin^2\theta^{(mj)} + F_6(t^{(m)}, t^{(j)})\cos^2\theta^{(mj)}\}$$

where the functions $G(t^{(m)}, t^{(i)})$ and $F(t^{(m)}, t^{(i)})$ are derived from the functions of the fundamentals fields

$$F(t^{(m)}, t^{(i)}) = H(x, y; \xi) \qquad G(t^{(m)}, t^{(i)}) = I(x, y; \xi),$$

and by substitutions of x, y, and ξ,

$$x = t_0^{(mi)} + t^{(m)}\cos\theta^{(mi)}$$
$$y = s_0^{(mi)} + t^{(m)}\sin\theta^{(mi)}$$
$$\xi = t^{(i)},$$

with $t_0^{(mi)}$ and $s_0^{(mi)}$ translations of the origins of two coordinate systems $(t^{(m)}, s^{(m)})$ and $(t^{(i)}, s^{(i)})$, i.e., coordinates of the mth defect center measured in $(t^{(i)}, s^{(i)})$.

Downloaded 03 May 2010 to 171.66.16.245. Redistribution subject to ASME license or copyright; see http://www.asme.org/terms/Terms_Use.cfm

On the Mode Splitting of Degenerate Mechanical Systems Containing Cracks

I.Y. Shen
Asst. Professor,
Department of Engineering Mechanics,
University of Nebraska-Lincoln,
Lincoln, NE 68588-0347,
Mem. ASME

C. D. Mote, Jr.
Vice Chancellor and FAUNC Chair in
Mechanical Systems,
University of California,
Berkeley, CA 94720
Fellow ASME

This paper presents sufficient conditions governing mode splitting in a two-dimensional, degenerate, mechanical system whose eigensolutions satisfy the Helmholtz equation. When cracks are introduced into such systems, a pair of repeated vibration modes may remain repeated or become distinct (termed split modes) depending on the location and geometry of the cracks. Two types of split modes can occur. Split modes of the first kind are a pair of split modes in which one mode undergoes a frequency shift but the other does not. In contrast, split modes of the second kind are a pair of split modes in which both modes undergo frequency shifts. A sufficient condition for split modes of the first kind is derived through an orthogonal transformation of repeated eigenmodes of the perfect system. Sufficient conditions for repeated modes and split modes of the second kind are derived through an asymptotic analysis. Numerical examples on square and circular domains illustrate the analytical predictions on mode splitting.

1 Introduction

Degenerate machine structures possessing repeated vibration modes, such as circular plates and spinning rotors, have wide applications in industry. On some occasions, slots are introduced purposely to tune the vibration. For instance, radial rim slots are cut into circular saws to release thermal stresses induced by the cutting process and thereby improve cutting performance (Yu and Mote, 1987a). On other occasions, fatigue cracks can result from cyclic loading as in rotors of turbo engines (Mayes and Davies, 1984; Nelson and Nataraj, 1986; Wauer, 1991). The presence of slots or cracks alters the vibration response of a degenerate structure. Understanding how slots or cracks affect the eigensolutions of degenerate systems can guide design of structures or detection of emerging cracks.

A characteristic of degenerate elastic structures with imperfection is mode splitting. Upon introduction of imperfection, a pair of repeated vibration modes may remain repeated or become distinct (termed split modes) depending on the location and geometry of the imperfection. Sometimes, mode splitting will result in hazardous vibration response. For instance, Yu and Mote (1987a, b) have shown that mode splitting of a rotating, slotted, circular saw can present instability at subcritical speed, where saws are operated.

Mode splitting appears in different areas of vibration. Examples are vibration of degenerate elastic solids with elastic or viscoelastic inclusions (Shen and Mote, 1992a, b), free vibration of the rotating earth (Aki and Richards, 1980), vibration of rotationally periodic structures (Thomas, 1979), and vibration of a noncircular membrane (Nayfeh, 1981). For degenerate structures with slots or cracks, mode splitting has been demonstrated numerically by Mote (1972) and both theoretically and experimentally by Yu and Mote (1987a, b). They developed a functional perturbation method to predict mode splitting, assuming that eigenfunctions of the structure remain unchanged and continuous across the slots when the slots of infinitesimal width are introduced. In the sequel, the mode splitting addressed by Yu and Mote (1987a, b) is termed regular mode splitting.

The purpose of this paper is to derive sufficient conditions governing mode splitting of a degenerate structure, if eigenfunctions of the structure become discontinuous across the slots when the slots are introduced. Such mode splitting is termed singular mode splitting in this paper. The derivation of singular mode splitting is illustrated on a two-dimensional mechanical system whose eigensolutions are governed by the Helmholtz equation. Such systems include antiplane strain vibration of a linear elastic solid containing cracks (Mode III fracture), vibration of an elastic membrane with slots, and two-dimensional standing acoustic waves in a closed acoustic cavity with rigid obstacles. Singular mode splitting of more complicated systems, such as slotted circular saws and cracked rotors, can be predicted in a similar manner. They will not be addressed in this paper.

Two types of split modes will be discussed in this paper. Split modes of the first kind are a pair of split modes in which one mode undergoes a frequency shift, but the other does not. Split modes of the second kind are a pair of split modes in which both modes undergo frequency shifts.

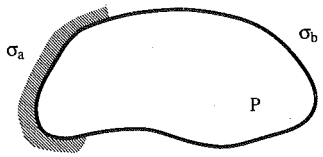
Contributed by the Applied Mechanics Division of THE AMERICAN SOCIETY OF MECHANICAL ENGINEERS for presentation at the ASME Winter Annual Meeting, New Orleans, LA, Nov. 28-Dec. 3, 1993.

Discussion on this paper should be addressed to the Technical Editor, Professor Lewis T. Wheeler, Department of Mechanical Engineering, University of Houston, Houston, TX 77204-4792, and will be accepted until four months after final publication of the paper itself in the ASME JOURNAL OF APPLIED MECHANICS.

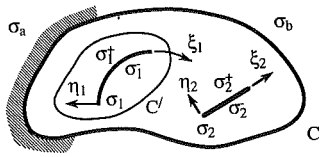
Manuscript received by the ASME Applied Mechanics Division, Jan. 22, 1992; final revision, Jan. 20, 1993. Associate Technical Editor: D. J. Inman.

Paper No. 93-WA/APM-5.

Copyright © 1993 by ASME
Downloaded 03 May 2010 to 171.66.16.245. Redistribution subject to ASME license or copyright; see http://www.asme.org/terms/Terms_Use.cfm



(a) A perfect Structure P



(b) A Structure C with Cracks

Fig. 1 *(a)* **A perfect structure** *P* **containing no cracks with eigenvalues** ω_n^2 **and eigenfunctions** $\phi_n(\mathbf{r})$, *(b)* **a cracked structure** *C* **with cracks** σ_c **of infinitesimal width**

This paper follows the approach of Shen (1993) where eigenfunctions $\psi(\mathbf{r})$ of a cracked system C are represented in terms of eigenfunctions $\phi_n(\mathbf{r})$ of a degenerate system P without the cracks. Stationarity of the Kamke quotient of C results in a Fredholm integral equation whose nontrivial solutions determine eigenvalues λ_m^2 and crack opening shapes $\Delta\psi_m$ of C. In addition, degeneracy of P implies that a pair of repeated eigenmodes of P will remain repeated under any orthogonal transformation. This additional requirement results in a sufficient condition for split modes of the first kind.

Sufficient conditions for repeated modes and split modes of the second kind, however, can only be determined through a perturbation analysis on degenerate systems with small cracks. Two numerical examples illustrate the analytic predictions on square and circular domains. Finally, a simple example explaining the difference between regular and singular mode splitting concludes this paper.

2 Formulation

Consider antiplane strain vibration of a two-dimensional degenerate linear elastic solid P with shear modulus T and density ρ occupying a finite domain τ with a fixed boundary σ_a and a free boundary σ_b. See Fig. 1(*a*). Eigenfunctions $\phi_n(\mathbf{r})$ and eigenvalues ω_n^2 of P satisfy

$$-T\nabla^2\phi_n(\mathbf{r})=\rho\omega_n^2\phi_n(\mathbf{r}),\ \mathbf{r}\in\tau \tag{1}$$

with boundary conditions

$$\phi_n(\mathbf{r})=0,\ \mathbf{r}\in\sigma_a \tag{2}$$

$$T\frac{\partial\phi_n(\mathbf{r})}{\partial n}=0,\ \mathbf{r}\in\sigma_b \tag{3}$$

and orthonormality condition

$$\int_\tau \rho\phi_m(\mathbf{r})\phi_n(\mathbf{r})d\tau=\delta_{mn}. \tag{4}$$

In addition, P possesses repeated eigenvalues $\omega_N^2=\omega_{N+1}^2$.

Consider a linear elastic solid C occupying the same domain τ with n_c cracks of zero traction. In addition, the crack width is infinitesimal. See Fig. 1(*b*). Eigenfunctions $\psi(\mathbf{r})$ and eigenvalues λ^2 of C satisfy

$$-T\nabla^2\psi(\mathbf{r})=\rho\lambda^2\psi(\mathbf{r}),\ \mathbf{r}\in\tau' \tag{5}$$

with boundary conditions

$$\psi(\mathbf{r})=0,\ \mathbf{r}\in\sigma_a \tag{6}$$

$$T\frac{\partial\psi(\mathbf{r})}{\partial n}=0,\ \mathbf{r}\in\sigma_b\cup\sigma_c. \tag{7}$$

Here $\sigma_c\equiv U_{i=1}^{n_c}\sigma_i$, where σ_i is the boundary of the ith crack, and $\tau'\equiv\tau-\sigma_c$[1].

According to Shen (1993), $\psi(\mathbf{r})$ can be represented as

$$\psi(\mathbf{r})=\sum_{n=1}^{\infty}\frac{A_n}{\lambda^2-\omega_n^2}\phi_n(\mathbf{r}),\ \mathbf{r}\in\tau' \tag{8}$$

where

$$A_n=T<\mathbf{g}_n|\Delta\Psi>. \tag{9}$$

Here $\Delta\Psi$ and $\mathbf{g}_n$ are column vectors

$$\Delta\Psi=[\Delta\psi(\xi_1),\ \Delta\psi(\xi_2),\ \ldots,\ \Delta\psi(\xi_{n_c})]^T \tag{10}$$

$$\mathbf{g}_n=\left[\frac{\partial\phi_n(\xi_1)}{\partial n},\ \frac{\partial\phi_n(\xi_2)}{\partial n},\ \ldots,\ \frac{\partial\phi_n(\xi_{n_c})}{\partial n}\right]^T \tag{11}$$

and $<\mathbf{g}_n|\Delta\Psi>$ is an inner product defined as

$$<\mathbf{g}_n|\Delta\Psi>\equiv\sum_{i=1}^{n_c}\int_{\sigma_i^+}\frac{\partial\phi_n(\xi_i)}{\partial n}\Delta\psi(\xi_i)d\sigma_i \tag{12}$$

where ξ_i is a curvilinear coordinate along the ith crack and $\Delta\psi(\xi_i)\equiv\psi(\sigma_i^+)-\psi(\sigma_i^-)$ is the crack opening shape across the ith crack in Fig. 1(*b*).

According to Shen (1993), λ^2 and $\Delta\psi$ are determined through the Fredholm integral equation

$$\mathbf{A}(\lambda^2)\Delta\Psi\equiv T^2\sum_{n=1}^{\infty}\frac{\lambda^2\mathbf{g}_n<\mathbf{g}_n|\Delta\Psi>}{\omega_n^2(\lambda^2-\omega_n^2)}+\mathbf{R}\Delta\Psi=\mathbf{0} \tag{13}$$

where $\mathbf{R}$ is a symmetric, positive definite operator satisfying

$$<\Delta\Psi|\mathbf{R}\Delta\Psi>=\int_{\tau'}T\nabla\chi(\mathbf{r})\cdot\nabla\psi(\mathbf{r})d\tau \tag{14}$$

with

$$\chi(\mathbf{r})=-\sum_{n=1}^{\infty}\frac{A_n}{\omega_n^2}\phi_n(\mathbf{r})=-T\sum_{n=1}^{\infty}\frac{<\mathbf{g}_n|\Delta\Psi>}{\omega_n^2}\phi_n(\mathbf{r}),\ \mathbf{r}\in\tau'. \tag{15}$$

The explicit expression of $\mathbf{R}$ has been determined by Shen (1993). Let $\mu(\lambda^2)$ and $\mathbf{v}(\lambda^2)$ be eigenvalues and eigenfunctions of the Fredholm operator $\mathbf{A}(\lambda^2)$. Then eigenvalues λ_m^2 of C are zeros of eigenvalue loci $\mu(\lambda^2)$ and crack opening shapes $\Delta\Psi_m$ of C are $\mathbf{v}(\lambda_m^2)$.

3 Split Modes of the First Kind

Let $\Phi_N(\mathbf{r})$ and $\Phi_{N+1}(\mathbf{r})$ be a pair of repeated, orthonormal vibration modes of P. In addition, let $\phi_N(\mathbf{r})$ and $\phi_{N+1}(\mathbf{r})$ be two orthonormal eigenfunctions of P related to $\Phi_N(\mathbf{r})$ and $\Phi_{N+1}(\mathbf{r})$ through an orthogonal transformation

$$\begin{cases}\phi_N(\mathbf{r})=\cos\theta_N\Phi_N+\sin\theta_N\Phi_{N+1}\\ \phi_{N+1}(\mathbf{r})=-\sin\theta_N\Phi_N+\cos\theta_N\Phi_{N+1}.\end{cases} \tag{16}$$

Substitute (16) into (11) to obtain

$$\begin{cases}\mathbf{g}_N=\cos\theta_N\mathbf{p}_N+\sin\theta_N\mathbf{p}_{N+1}\\ \mathbf{g}_{N+1}=-\sin\theta_N\mathbf{p}_N+\cos\theta_N\mathbf{p}_{N+1}\end{cases} \tag{17}$$

where

$$\mathbf{p}_i\equiv\left[\frac{\partial\Phi_i(\xi_1)}{\partial n},\frac{\partial\Phi_i(\xi_2)}{\partial n},\ \ldots,\ \frac{\partial\Phi_i(\xi_{n_c})}{\partial n}\right]^T,\ i=N,\ N+1. \tag{18}$$

A sufficient condition for split modes of the first kind is stated as follows.

Theorem 1. *A pair of repeated modes* $\phi_N(\mathbf{r})$ *and* $\phi_{N+1}(\mathbf{r})$

[1] Equations (1) to (7) also describe the vibration of an elastic membrane if T is the tension of the membrane. In addition, (1) to (7) will describe scattering and defraction of two-dimensional standing acoustic waves by rigid obstacles, if $c\equiv\sqrt{T/\rho}$ is the acoustic wave speed and σ_c represents the location and geometry of the obstacles.

Downloaded 03 May 2010 to 171.66.16.245. Redistribution subject to ASME license or copyright; see http://www.asme.org/terms/Terms_Use.cfm

become split modes of the first kind if $\mathbf{g}_N \| \mathbf{g}_{N+1}$ *and at least* $\mathbf{g}_N$ *or* $\mathbf{g}_{N+1}$ *is nontrivial.*

Proof. When $\mathbf{g}_N \| \mathbf{g}_{N+1}$, then (17) implies that $\mathbf{p}_N \| \mathbf{p}_{N+1}$. If θ_N is chosen such that

$$\mathbf{g}_{N+1} = -\sin\theta_N \mathbf{p}_N + \cos\theta_N \mathbf{p}_{N+1} = 0, \tag{19}$$

then ω_N^2 and

$$\psi_{N+1}(\mathbf{r}) = \phi_{N+1}(\mathbf{r}) = -\sin\theta_N \Phi_N(\mathbf{r}) + \cos\theta_N \Phi_{N+1}(\mathbf{r}) \tag{20}$$

is an eigensolution of P because they satisfy the governing Eq. (5) and the boundary conditions (6) and (7) by virtue of (19) and (20).

In contrast, $\phi_N(\mathbf{r})$ in (16) does not satisfy the boundary condition (7) because $\mathbf{g}_N$ is nontrivial and θ_N must satisfy (19). As a consequence, $\psi_N(\mathbf{r}) \neq \phi_N(\mathbf{r})$ and $\lambda_N^2 \neq \omega_N^2$. Therefore, $\phi_N(\mathbf{r})$ and $\phi_{N+1}(\mathbf{r})$ become split modes of the first kind when the cracks are introduced.

4 Asymptotic Analysis

If $\mathbf{g}_N$ and $\mathbf{g}_{N+1}$ are linearly independent and span a two-dimensional subspace S_N, the mode splitting will be determined through solutions of the Fredholm Eq. (13). Because exact solutions of (13) are difficult to obtain, an asymptotic analysis is presented in this section to predict the mode splitting when the cracks are small.

Rewrite the Fredholm operator $\mathbf{A}(\lambda^2)$ in (13) as

$$\mathbf{A}(\lambda^2) = \mathbf{A}^{(N)}(\lambda^2) + \overline{\mathbf{A}}^{(N)}(\lambda^2) \tag{21}$$

where

$$\mathbf{A}^{(N)}(\lambda^2) \equiv \frac{T^2\lambda^2[\mathbf{g}_N < \mathbf{g}_N | \bullet > + \mathbf{g}_{N+1} < \mathbf{g}_{N+1} | \bullet >]}{\omega_N^2(\lambda^2 - \omega_N^2)} \tag{22}$$

and

$$\overline{\mathbf{A}}^{(N)}(\lambda^2) \equiv T^2 \sum_{n \neq N}^{N+1} \frac{\lambda^2 \mathbf{g}_n < \mathbf{g}_n | \bullet >}{\omega_n^2(\lambda^2 - \omega_n^2)} + \mathbf{R}. \tag{23}$$

Here the notation $\Sigma_{n\neq N}^{N+1}$ denotes $\Sigma_{n=1}^{\infty}$ with $n \neq N, N+1$. For the Nth vibration mode of C, λ_N^2 is asymptotic to ω_N^2 when the cracks are small; therefore, $\mathbf{A}^{(N)}(\lambda^2)$ can always be dominant.

Consider $\mathbf{A}^{(N)}(\lambda^2)$ as an unperturbed operator. Then unperturbed eigenfunctions $\mathbf{v}(\lambda^2)$ and unperturbed eigenvalues $\mu^{(0)}(\lambda^2)$ must satisfy

$$\mathbf{A}^{(N)}(\lambda^2)\mathbf{v}(\lambda^2) = \mu^{(0)}(\lambda^2)\mathbf{v}(\lambda^2). \tag{24}$$

For eigenfunctions $\mathbf{v}(\lambda^2) \in S_N$,

$$\mathbf{v}(\lambda^2) = \mathbf{g}_N + y(\lambda^2)\mathbf{g}_{N+1}. \tag{25}$$

Substitute (22) and (25) into (24) and recall that $\mathbf{g}_N$ and $\mathbf{g}_{N+1}$ are independent to obtain

$$\mu^{(0)} y = \frac{T^2\lambda^2}{\omega_N^2(\lambda^2 - \omega_N^2)} [y < \mathbf{g}_{N+1} | \mathbf{g}_{N+1} > + < \mathbf{g}_{N+1} | \mathbf{g}_N >] \tag{26}$$

and

$$\mu^{(0)} = \frac{T^2\lambda^2}{\omega_N^2(\lambda^2 - \omega_N^2)} [y < \mathbf{g}_N | \mathbf{g}_{N+1} > + < \mathbf{g}_N | \mathbf{g}_N >]. \tag{27}$$

When

$$< \mathbf{g}_N | \mathbf{g}_N > - < \mathbf{g}_{N+1} | \mathbf{g}_{N+1} > = 0 \tag{28}$$

and

$$< \mathbf{g}_N | \mathbf{g}_{N+1} > = 0, \tag{29}$$

Eqs. (26) and (27) imply that y is arbitrary. Two unperturbed eigenfunctions $\mathbf{v}_N, \mathbf{v}_{N+1} \in S_N$ are arbitrary linear combinations of $\mathbf{g}_N$ and $\mathbf{g}_{N+1}$ with a repeated unperturbed eigenvalue

$$\mu_N^{(0)}(\lambda^2) = \mu_{N+1}^{(0)}(\lambda^2) = \frac{T^2\lambda^2 < \mathbf{g}_N | \mathbf{g}_N >}{\omega_N^2(\lambda^2 - \omega_N^2)}. \tag{30}$$

If (28) or (29) is not satisfied, $\mu^{(0)}$ in (26) and (27) can be eliminated to yield

$$y_{N,N+1} = \frac{1}{2 < \mathbf{g}_N | \mathbf{g}_{N+1} >} \{ < \mathbf{g}_{N+1} | \mathbf{g}_{N+1} > - < \mathbf{g}_N | \mathbf{g}_N > \pm \sqrt{[< \mathbf{g}_N | \mathbf{g}_N > - < \mathbf{g}_{N+1} | \mathbf{g}_{N+1} >]^2 + 4 | < \mathbf{g}_N | \mathbf{g}_{N+1} > |^2} \}. \tag{31}$$

Two unperturbed eigenfunctions in S_N are $\mathbf{v}_N = \mathbf{g}_N + y_N \mathbf{g}_{N+1}$ and $\mathbf{v}_{N+1} = \mathbf{g}_N + y_{N+1}\mathbf{g}_{N+1}$. The corresponding unperturbed eigenvalues are

$$\mu_{N,N+1}^{(0)}(\lambda^2) = \frac{T^2\lambda^2}{2\omega_N^2(\lambda^2 - \omega_N^2)} \{ < \mathbf{g}_N | \mathbf{g}_N > + < \mathbf{g}_{N+1} | \mathbf{g}_{N+1} > \pm \sqrt{[< \mathbf{g}_N | \mathbf{g}_N > - < \mathbf{g}_{N+1} | \mathbf{g}_{N+1} >]^2 + 4 | < \mathbf{g}_N | \mathbf{g}_{N+1} > |^2} \}. \tag{32}$$

Eigenvalue loci $\mu(\lambda^2)$ of $\mathbf{A}(\lambda^2)$ can be approximated as follows. Formulating the Rayleigh quotient of $\mathbf{A}(\lambda^2)$ and recalling (21) result in

$$\mu(\lambda^2) = \frac{< \Delta\Psi | \mathbf{A}^{(N)} \Delta\Psi >}{< \Delta\Psi | \Delta\Psi >} + \frac{< \Delta\Psi | \overline{\mathbf{A}}^{(N)} \Delta\Psi >}{< \Delta\Psi | \Delta\Psi >}. \tag{33}$$

When the cracks are small, $\mathbf{A}^{(N)}$ is dominant and $\Delta\Psi \approx \mathbf{v}_N$ or $\mathbf{v}_{N+1}$. Therefore, $\Delta\Psi$ in (33) can be replaced by $\mathbf{v}_N$ or $\mathbf{v}_{N+1}$, i.e.,

$$\mu_i(\lambda^2) = \mu_i^{(0)}(\lambda^2) + \mu_i^{(1)}(\lambda^2) + \ldots, \quad i = N, N+1 \tag{34}$$

where (24) has been used and

$$\mu_i^{(1)} \equiv \frac{< \mathbf{v}_i | \overline{\mathbf{A}}^{(N)} \mathbf{v}_i >}{< \mathbf{v}_i | \mathbf{v}_i >}. \tag{35}$$

Because eigenvalues λ_N^2 and λ_{N+1}^2 of C are zeros of eigenvalue loci $\mu_N(\lambda^2)$ and $\mu_{N+1}(\lambda^2)$, λ_N^2 and λ_{N+1}^2 will remain repeated asymptotically if $\mu_N(\lambda^2)$ and $\mu_{N+1}(\lambda^2)$ remain repeated asymptotically. This implies that both $\mu_i^{(0)}(\lambda^2)$, $i = N, N+1$, and $\mu_i^{(1)}(\lambda^2)$, $i = N, N+1$, remain repeated asymptotically. Based on these asymptotic properties, a sufficient condition for split modes of the second kind is derived as follows.

Theorem 2. *A pair of repeated modes* $\phi_N(\mathbf{r})$ *and* $\phi_{N+1}(\mathbf{r})$ *become split modes of the second kind asymptotically if*

$$< \mathbf{g}_N | \mathbf{g}_N > - < \mathbf{g}_{N+1} | \mathbf{g}_{N+1} > \neq 0 \tag{36}$$

or

$$< \mathbf{g}_N | \mathbf{g}_{N+1} > \neq 0. \tag{37}$$

Proof. If (36) or (37) is satisfied, then $\mu_N^{(0)} \neq \mu_{N+1}^{(0)}$ according to (32). Therefore, $\phi_N(\mathbf{r})$ and $\phi_{N+1}(\mathbf{r})$ become split modes of the second kind.

A sufficient condition for repeated modes can be derived for complex eigenfunctions $\phi_N(\mathbf{r})$ and $\phi_{N+1}(\mathbf{r})$. Generalization of the formulas above to incorporate complex eigenfunctions is addressed in Appendix A.

Theorem 3. *A pair of repeated, complex conjugate modes* $\phi_N(\mathbf{r})$ *and* $\phi_{N+1}(\mathbf{r}) \equiv \bar{\phi}_N(\mathbf{r})$ *remain repeated asymptotically if*

(1) Eqs. (28) and (29) are satisfied,

$$(2) \begin{cases} < \mathbf{g}_m | \mathbf{g}_N > = \overline{< \mathbf{g}_{m+1} | \mathbf{g}_{N+1} >} \\ < \mathbf{g}_{m+1} | \mathbf{g}_N > = \overline{< \mathbf{g}_m | \mathbf{g}_{N+1} >} \end{cases} \tag{38}$$

for every pair of repeated complex conjugate modes $\phi_m(\mathbf{r})$ and $\phi_{m+1}(\mathbf{r}) \equiv \bar{\phi}_m(\mathbf{r})$, and

$$(3)\ < \mathbf{g}_l | \mathbf{g}_N > = \overline{< \mathbf{g}_l | \mathbf{g}_{N+1} >} \tag{39}$$

for every real and distinct mode $\phi_l(\mathbf{r})$.

Proof. When (28) and (29) are satisfied, $\mu_N^{(0)}$ and $\mu_{N+1}^{(0)}$ are

Downloaded 03 May 2010 to 171.66.16.245. Redistribution subject to ASME license or copyright; see http://www.asme.org/terms/Terms_Use.cfm

repeated. In addition, y can be chosen arbitrarily. Let $\mathbf{v}_N = \mathbf{g}_N$ and $\mathbf{v}_{N+1} = \mathbf{g}_{N+1}$. Therefore,

$$<\mathbf{v}_N|\mathbf{v}_N> = <\mathbf{v}_{N+1}|\mathbf{v}_{N+1}> \tag{40}$$

by virtue of (28).

The next step is to prove $<\mathbf{v}_N|\overline{\mathbf{A}}^{(N)}\ \mathbf{v}_N> = <\mathbf{v}_{N+1}|\overline{\mathbf{A}}^{(N)}\ \mathbf{v}_{N+1}>$ so that $\mu_N^{(1)}$ and $\mu_{N+1}^{(1)}$ are repeated by (35) and (40). This requires

$$<\mathbf{g}_N|\mathbf{R}\mathbf{g}_N> = <\mathbf{g}_{N+1}|\mathbf{R}\mathbf{g}_{N+1}> \tag{41}$$

and

$$\sum_{n\neq N}^{N+1} \frac{T^2\lambda^2|<\mathbf{g}_n|\mathbf{g}_N>|^2}{\omega_n^2(\lambda^2-\omega_N^2)} = \sum_{n\neq N}^{N+1} \frac{T^2\lambda^2|<\mathbf{g}_n|\mathbf{g}_{N+1}>|^2}{\omega_n^2(\lambda^2-\omega_N^2)}. \tag{42}$$

Consider $\chi[\mathbf{g}_N]$, which is $\chi(\mathbf{r})$ evaluated at $\Delta\Psi = \mathbf{g}_N$. Rewrite $\chi[\mathbf{g}_N]$ as

$$\chi[\mathbf{g}_N] = -T\sum_m \left[\frac{<\mathbf{g}_m|\mathbf{g}_N>}{\omega_m^2}\phi_m(\mathbf{r}) + \frac{<\mathbf{g}_{m+1}|\mathbf{g}_N>}{\omega_m^2}\phi_{m+1}(\mathbf{r})\right] - T\sum_l \frac{<\mathbf{g}_l|\mathbf{g}_N>}{\omega_l^2}\phi_l(\mathbf{r}) \tag{43}$$

where Σ_m and Σ_l are summation over repeated, complex conjugate modes $\phi_m(\mathbf{r})$, $\phi_{m+1}(\mathbf{r})$, and distinct real modes $\phi_l(\mathbf{r})$, respectively. Because of (38), (39), and $\phi_m(\mathbf{r}) = \bar{\phi}_{m+1}(\mathbf{r})$, (43) can be rewritten as

$$\chi[\mathbf{g}_N] = -T\sum_l \frac{\overline{<\mathbf{g}_l|\mathbf{g}_{N+1}>}}{\omega_l^2}\phi_l(\mathbf{r}) - T\sum_m \left[\frac{\overline{<\mathbf{g}_{m+1}|\mathbf{g}_{N+1}>}}{\omega_m^2}\bar{\phi}_{m+1}(\mathbf{r}) + \frac{\overline{<\mathbf{g}_m|\mathbf{g}_{N+1}>}}{\omega_m^2}\bar{\phi}_m(\mathbf{r})\right]. \tag{44}$$

Compare (44) with (15) to obtain

$$\chi[\mathbf{g}_N] = \bar{\chi}[\mathbf{g}_{N+1}]. \tag{45}$$

Therefore, (41) holds because

$$<\mathbf{g}_N|\mathbf{R}\mathbf{g}_N> \equiv \int_{\tau'} \overline{\nabla\chi}[\mathbf{g}_N]\nabla\chi[\mathbf{g}_N] = \int_{\tau'} \nabla\chi[\mathbf{g}_{N+1}]\overline{\nabla\chi}[\mathbf{g}_{N+1}] \equiv <\mathbf{g}_{N+1}|\mathbf{R}\mathbf{g}_{N+1}>. \tag{46}$$

Equation (42) can be proved in a similar manner.

Because $\mu_N^{(0)} = \mu_{N+1}^{(0)}$ and $\mu_N^{(1)} = \mu_{N+1}^{(1)}$, a pair of repeated modes $\phi_N(\mathbf{r})$ and $\phi_{N+1}(\mathbf{r})$ remain repeated asymptotically.

The above asymptotic analysis is only valid when λ_N^2 is asymptotic to ω_N^2. When large cracks are introduced, the asymptotic analysis may not predict splitting of vibration modes where λ_N^2 is not asymptotic to ω_N^2.

5 Numerical Examples

Two numerical examples are illustrated here. The first example considers antiplane strain vibration of a linear, elastic solid occupying a square domain with dimension a; see Fig. 2(a). A crack is introduced at $x=0$ extending from $y=0$ to $y=\epsilon a$. See Fig. 2(b). Eigensolutions of the perfect system are

$$\omega_{mn}^2 = \frac{T\pi^2}{\rho a^2}(m^2+n^2) \tag{47}$$

and

$$\phi_{mn}(\mathbf{r}) = \frac{2}{\sqrt{\rho}a}\sin\frac{m\pi x}{a}\sin\frac{n\pi y}{a} \tag{48}$$

In addition; $\phi_{mn}(\mathbf{r})$ and $\phi_{nm}(\mathbf{r})$ are repeated modes if $m\neq n$. For the system with a boundary crack

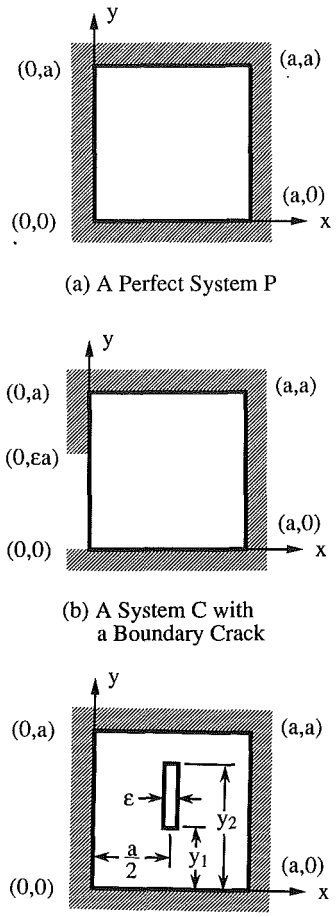


Fig. 2 (*a*) The perfect system, (*b*) the system with a boundary crack, and (*c*) the system with an internal crack

$$\mathbf{g}_{mn} = \frac{2m\pi}{\sqrt{\rho a^2}}\sin\frac{n\pi y}{a}, \tag{49}$$

and

$$\mathbf{g}_{nm} = \frac{2n\pi}{\sqrt{\rho a^2}}\sin\frac{m\pi y}{a}, \tag{50}$$

the inner product is

$$<u|v> \equiv \int_0^{\epsilon a} u(y)v(y)dy. \tag{51}$$

Therefore,

$$<\mathbf{g}_{mn}|\mathbf{g}_{mn}> = \frac{2m^2\pi^2}{\rho a^3}\left[\epsilon - \frac{\sin 2n\pi\epsilon}{2n\pi}\right] \tag{52}$$

and

$$<\mathbf{g}_{nm}|\mathbf{g}_{nm}> = \frac{2n^2\pi^2}{\rho a^3}\left[\epsilon - \frac{\sin 2m\pi\epsilon}{2m\pi}\right]. \tag{53}$$

Because $<\mathbf{g}_{mn}|\mathbf{g}_{mn}> \neq <\mathbf{g}_{nm}|\mathbf{g}_{nm}>$ for all ϵ, $\phi_{mn}(\mathbf{r})$ and $\phi_{nm}(\mathbf{r})$ will become split modes of the second kind asymptotically, when the boundary crack is introduced.

Figure 3 shows eigenvalue loci $\mu(\lambda^2)$ of $\mathbf{A}(\lambda^2)$ calculated for $a=\pi$, $\epsilon=1$, and $T=\rho=1$. The Fredholm operator $\mathbf{A}(\lambda^2)$ is first formulated through (13) with $\mathbf{g}_{mn}$ in (49) and $\mathbf{R}$ in (76) of Appendix B. $\mathbf{A}$ (λ^2) is then discretized through eigenfunction expansion (Shen, 1993) to obtain the eigenvalue loci in Fig. 3.

Downloaded 03 May 2010 to 171.66.16.245. Redistribution subject to ASME license or copyright; see http://www.asme.org/terms/Terms_Use.cfm

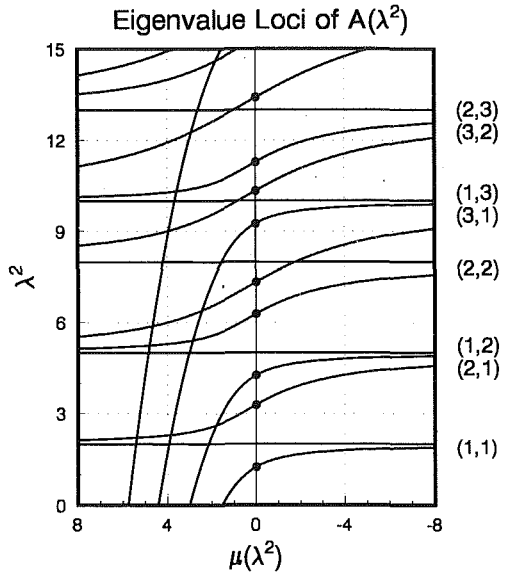
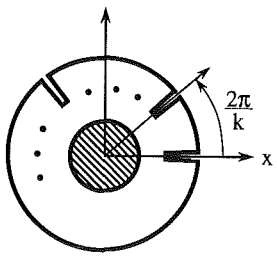


Fig. 3 Eigenvalue loci $\mu(\lambda^2)$ of the system shown in Fig. 2(*b*)



A System with
k Evenly Spaced Slots

Fig. 4 An elastic solid occupying a circular domain with *k* evenly spaced radial slots

The horizontal lines denote ω_{mn}^2 of mode (m, n) shown in (47). For every pair of repeated modes $\phi_{mn}(\mathbf{r})$ and $\phi_{nm}(\mathbf{r})$, $m \neq n$, there are two distinct eigenvalue loci, which are singular as $\lambda^2 \to (\omega_{mn}^2)^-$. Zeros of the eigenvalue loci, as dots in Fig. 3, are distinct and different from ω_{mn}^2. Therefore, $\phi_{mn}(\mathbf{r})$ and $\phi_{nm}(\mathbf{r})$ become split modes of the second kind.

Because a large crack is introduced in this numerical example ($\epsilon = 1$), the assumption that $\mathbf{A}^{(N)}$ is dominant does not hold for the (3, 1) mode for example. As a result, splitting of λ_{31}^2 and λ_{13}^2 cannot be guaranteed through the asymptotic analysis. Nevertheless, the asymptotic analysis will remain valid in depicting the splitting of the eigenvalue loci $\mu_{31}(\lambda^2)$ and $\mu_{13}(\lambda^2)$ of $\mathbf{A}(\lambda^2)$ when $\lambda^2 \to (\omega_{31}^2)^-$, which usually implies splitting of λ_{31}^2 and λ_{13}^2.

The second example considers antiplane strain vibration of a linear elastic solid occupying a circular domain with k evenly spaced radial slots. See Fig. 4. The inner rim at $r = a$ and outer rim at $r = b$ can be fixed or free. The slots are located at

$$\bar{\theta}_j = \frac{2\pi j}{k};\ j = 1, 2, \ldots, k \tag{54}$$

extending from $r = r_1$ to $r = r_2$ with $a \le r_1 < r_2 \le b$. A perfect (axisymmetric) system without the slots has complex eigenfunctions

$$\phi_{mn}(\mathbf{r}) = R_{mn}(r)e^{in\theta},\ \begin{cases} m = 1, 2, \ldots \\ n = 0, \pm 1, \pm 2, \ldots \end{cases} \tag{55}$$

where $R_{mn}(r) = R_{m,-n}(r)$ is a combination of Bessel's functions of the first and second kinds satisfying boundary conditions and orthonormality (4). In addition, $\phi_{mn}(\mathbf{r})$ and $\phi_{m,-n}(\mathbf{r})$ are repeated modes with eigenvalues ω_{mn}^2.

According to (11)

$$\mathbf{g}_{mn} = -\frac{inR_{mn}(r)}{r}\left[e^{in\bar{\theta}_1}, e^{in\bar{\theta}_2}, \ldots, e^{in\bar{\theta}_k}\right]^T \tag{56}$$

and

$$\mathbf{g}_{m,-n} = \frac{in\ R_{mn}(r)}{r}\left[e^{-in\bar{\theta}_1}, e^{-in\bar{\theta}_2}, \ldots, e^{-in\bar{\theta}_k}\right]^T. \tag{57}$$

The inner product is

$$<\mathbf{u}|\mathbf{v}> = \int_{r_1}^{r_2} \bar{\mathbf{u}}(r) \cdot \mathbf{v}(r)dr. \tag{58}$$

According to (56), (57), and (58)

$$<\mathbf{g}_{mn}|\mathbf{g}_{mn}> = <\mathbf{g}_{m,-n}|\mathbf{g}_{m,-n}> = kn^2 \int_{r_1}^{r_2} \frac{R_{mn}^2(r)}{r^2}dr, \tag{59}$$

and

$$<\mathbf{g}_{mn}|\mathbf{g}_{m,-n}> = -n^2 \int_{r_1}^{r_2} \frac{R_{mn}^2(r)}{r^2}dr \sum_{j=1}^{k} e^{-2in\bar{\theta}_j}. \tag{60}$$

Notice that $\mathbf{g}_{mn}$ and $\mathbf{g}_{m,-n}$ will satisfy (28) and (29) if

$$\sum_{j=1}^{k} e^{-2in\bar{\theta}_j} = 0. \tag{61}$$

Substitute (54) into (61) to obtain

$$\sum_{j=1}^{k} e^{-2in\bar{\theta}_j} = \frac{e^{-2\pi i(2n/k)}(1 - e^{-4\pi in})}{1 - e^{-2i\pi(2n/k)}} = \begin{cases} k, & 2n = \mathbf{M}(k) \\ 0, & 2n \neq \mathbf{M}(k) \end{cases} \tag{62}$$

where $2n = \mathbf{M}(k)$ means that $2n$ is a multiple of k.

When $2n = \mathbf{M}(k)$, (55), (56), and (57) show that $\mathbf{g}_{mn}$ and $\mathbf{g}_{m,-n}$ are linearly dependent through

$$\mathbf{g}_{mn} + \mathbf{g}_{m,-n} = 0. \tag{63}$$

Therefore, $\phi_{mn}(\mathbf{r})$ and $\phi_{m,-n}(\mathbf{r})$ become split modes of the first kind. Let Φ_{mn} be the eigenfunction defined in (55). Then (63) becomes $\mathbf{p}_{mn} + \mathbf{p}_{m,-n} = 0$ and (74) in Appendix A implies that

$$\theta_N = \frac{\pi}{2}, \frac{3\pi}{2}. \tag{64}$$

According to (55) and (73) in Appendix A, one of the split modes will be

$$\phi_{mn}^c(\mathbf{r}) = \sqrt{2}R_{mn}(r)\ \cos n\theta \tag{65}$$

with unchanged eigenvalue ω_{mn}^2.

When $2n \neq \mathbf{M}(k)$, (28) and (29) are satisfied. In addition,

$$<\mathbf{g}_{pq}|\mathbf{g}_{mn}> = \overline{<\mathbf{g}_{p,-q}|\mathbf{g}_{m,-n}>} = \int_{r_1}^{r_2} \frac{qnR_{pq}(r)R_{mn}(r)dr}{r^2} \sum_{j=1}^{k} e^{i(n-q)\bar{\theta}_j} \tag{66}$$

and

$$<\mathbf{g}_{pq}|\mathbf{g}_{m,-n}> = \overline{<\mathbf{g}_{p,-q}|\mathbf{g}_{mn}>} = -\int_{r_1}^{r_2} \frac{qnR_{pq}(r)R_{mn}(r)dr}{r^2} \sum_{j=1}^{k} e^{-i(n+q)\bar{\theta}_j} \tag{67}$$

for every pair of repeated modes $\phi_{pq}(\mathbf{r})$ and $\phi_{p,-q}(\mathbf{r})$. In addition,

$$<\mathbf{g}_{p0}|\mathbf{g}_{mn}> = \overline{<\mathbf{g}_{p0}|\mathbf{g}_{m,-n}>} = 0 \tag{68}$$

for any axisymmetric mode $\phi_{p0}(\mathbf{r})$. According to Theorem 3, $\phi_{mn}(\mathbf{r})$ and $\phi_{m,-n}(\mathbf{r})$ will remain repeated asymptotically.

Figure 5 shows the mode splitting of an elastic system with $k = 3$, $a = 0.5$, $b = 1$, $r_1 = 0.75$, $r_2 = 1.0$, and $T = \rho = 1$. The system is fixed at the inner rim and free at the outer rim. The

Downloaded 03 May 2010 to 171.66.16.245. Redistribution subject to ASME license or copyright; see http://www.asme.org/terms/Terms_Use.cfm

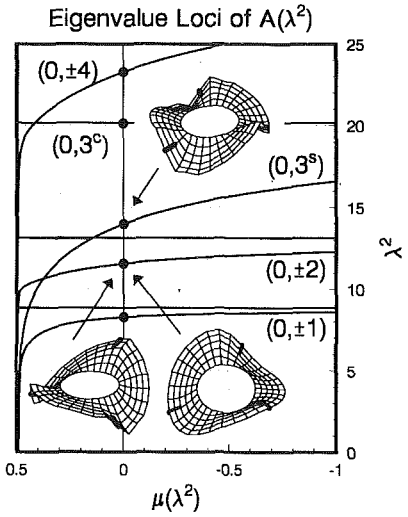


Fig. 5 Eigenvalue loci $\mu(\lambda^2)$ of the system shown in Fig. 4

eigenvalue loci in Fig. 5 are calculated through eigenfunction expansion of $\mathbf{A}(\lambda^2)$ with $\mathbf{R}$ shown in Appendix B. The horizontal lines are ω_{mn}^2 of an axisymmetric system P. For modes that remain repeated, such as $(0, \pm 1)$, $(0, \pm 2)$, and $(0, \pm 4)$ modes, there are a pair of repeated eigenvalue loci where are singular as $\lambda^2 \to (\omega_{mn}^2)^-$. Mode shapes of $(0, \pm 2)$ modes are also demonstrated. The left mode shape has one slot on an antinode while the other mode shape has one slot on a nodal line. In contrast, $(0, \pm 3)$ modes become two distinct modes: $(0, 3^c)$ with mode shape given in (65) and $(0, 3^s)$ with mode shape shown in Fig. 5.

6 Regular and Singular Mode Splitting

As mentioned earlier, the regular mode splitting by Yu and Mote (1986) requires that eigensolutions of a system remain unchanged when slots of infinitesimal width are introduced into the system. As an example, consider the elastic solid in Fig. 2(*a*) with a slot of infinitesimal width introduced at $x = 0$ extending from $y = 0$ to $y = a$ (see Fig. 2(*b*) with $\epsilon = 1$). Should the regular mode splitting be used, it would result in

$$\lambda_{mn}^2 = \omega_{mn}^2 = \frac{T\pi^2}{\rho a^2}\,(m^2 + n^2) \tag{69}$$

implying that the slot does not change the system eigenvalue. However, exact eigenvalues of the slotted system are

$$\lambda_{mn}^2 = \frac{T\pi^2}{\rho a^2}\left[\left(m - \frac{1}{2}\right)^2 + n^2\right] \tag{70}$$

which contradicts (69). When the slot is introduced, the assumption of regular mode splitting in Yu and Mote (1987a,b) is violated. In this case, the singular mode splitting should be used to predict split modes of the second kind.

Regular mode splitting occurs when the slots introduced have *finite* width. As an example, Fig. 2(*c*) shows a system with a slot of width ϵ at $x = a/2$ extending from $y = y_1$ to $y = y_2$. Consider repeated modes ϕ_{31} and ϕ_{13}. Notice that $\mathbf{g}_{31} = \mathbf{g}_{13} = 0$. Singular splitting implies that both modes will not change their eigensolutions and remain repeated if the slot width is *infinitesimal*. Therefore, regular mode splitting can be applied to determine how eigensolutions will change ϕ_{31} and ϕ_{13} as a function of the crack width ϵ.

7 Conclusions

1 When cracks are introduced into a degenerate elastic structure, a pair of repeated vibration modes can remain repeated or become distinct (termed split modes).

2 Two types of split modes can occur. For split modes of the first kind, one of the split modes undergoes an eigenvalue change and the other mode does not. A sufficient condition for split modes of the first kind is $\mathbf{g}_N \| \mathbf{g}_{N+1}$ and at least $\mathbf{g}_N$ or $\mathbf{g}_{N+1}$ is nontrivial. The orientation of the split modes must be determined through the orthogonal transformation (16) with θ_N determined by (19).

3 For split modes of the second kind, both modes undergo eigenvalue changes. A sufficient condition for split modes of the second kind is that (28) or (29) shall not hold.

4 A pair of repeated modes remain repeated asymptotically, if the conditions in Theorem 3 are satisfied.

References

Aki, K., and Richards, P., 1989, *Quantitative Seismology—Theory and Methods*, W. H. Freeman, San Francisco, CA, pp. 375–380.

Mayes, I. W., and Davies, W. G. R., 1984, "Analysis of the Response of a Multi-Rotor-Bearing System Containing a Transverse Crack in a Rotor," ASME *Journal of Vibration, Acoustics, Stress, and Reliability in Design*, Vol. 106, pp. 139–145.

Mote, C. D., Jr., 1972, "Stability Control Analysis of Rotating Plates by Finite Element: Emphasis on Slots and Holes," ASME *Journal of Dynamic Systems, Measurements, and Control*, Vol. 94, pp. 64–70.

Nelson, H. D., and Nataraj, C. 1986, "The Dynamics of a Rotor System with a Cracked Shaft," ASME *Journal of Vibration, Acoustics, Stress, and Reliability in Design*, Vol. 108, pp. 189–196.

Nayfeh, A. H., 1980, *Introduction to Perturbation Techniques*, John Wiley and Sons, New York, pp. 426–431.

Shen, I. Y., 1993, "Vibration of Structures With Cracks," ASME JOURNAL OF APPLIED MECHANICS, Vol. 60, pp. 414–421.

Shen, I. Y., and Mote, C. D., Jr., 1992a, "Dynamic Analysis of Three Dimensional, Finite, Linear, Elastic Solids Containing Small Elastic Imperfections: Theory with Application to Asymmetric Circular Plates," *Journal of Sound and Vibration*, Vol. 155, No. 3, pp. 443–466.

Shen, I. Y., and Mote, C. D., Jr., 1992b, "Dynamic Analysis of Finite, Three Dimensional, Linear, Elastic Solids With Kelvin Viscoelastic Inclusions: Theory with Applications to Asymmetrically Damped Circular Plates," *The Journal of the Acoustical Society of America*, Vol. 91, No. 3, pp. 1489–1499.

Thomas, D. L., 1979, "Dynamics of Rotationally Periodic Structures," *International Journal for Numerical Methods in Engineering*, Vol. 14, pp. 81–102.

Wauer, Jörg, 1990, "On the Dynamics of Cracked Rotors: A Literature Survey," ASME *Applied Mechanics Review*, Vol. 43, pp. 13–17.

Yu, R. C., and Mote, C. D., Jr., 1987a, "Vibration of Circular Saws Containing Slots," *Holzals Roh- und Werkstoff*, Vol. 45, pp. 155–160.

Yu, R. C., and Mote, C. D., Jr., 1987b, "Vibration and Parametric Excitation in Asymmetric Circular Plate under Moving Loads," *Journal of Sound and Vibration*, Vol. 119, pp. 409–427.

APPENDIX A

Complex Eigenfunctions

The derivation in this paper can be generalized to incorporate complex eigenfunctions. In this case, the inner product in (12) is redefined as

$$<\mathbf{g}_n | \Delta\Psi> \equiv \sum_{i=1}^{n_c} \int_{\sigma_i^+} \overline{\frac{\partial \phi_n(\xi_i)}{\partial n}} \Delta\psi(\xi_i) d\sigma_i \tag{71}$$

where the overbar denotes the complex conjugate. In addition,

$$\| \nabla\chi \|^2 = \int_{\tau'} T\overline{\nabla\chi(\mathbf{r})} \cdot \nabla\chi(\mathbf{r}) d\tau \tag{72}$$

with $\chi(\mathbf{r})$ defined in (15). The Fredholm integral Eq. (13) remains unchanged.

For split modes of the first kind, orthogonal transformation in (16) becomes

$$\begin{cases} \phi_N(\mathbf{r}) = \dfrac{1}{\sqrt{2}}\,[e^{-i\theta_N}\Phi_N + e^{i\theta_N}\Phi_{N+1}] \\ \phi_{N+1}(\mathbf{r}) = \dfrac{1}{\sqrt{2}}\,[-ie^{-i\theta_N}\Phi_N + ie^{i\theta_N}\Phi_{N+1}]. \end{cases} \tag{73}$$

Downloaded 03 May 2010 to 171.66.16.245. Redistribution subject to ASME license or copyright; see http://www.asme.org/terms/Terms_Use.cfm

In addition, θ_N is chosen such that

$$-e^{-i\theta_N}\mathbf{p}_N + e^{i\theta_N}\mathbf{p}_{N+1} = 0. \tag{74}$$

For repeated modes and split modes of the second kind, the formulas in the asymptotic analysis section still apply.

APPENDIX B

Explicit Expressions of R

This appendix is to demonstrate explicit expressions of **R**, required in formulating $\mathbf{A}(\lambda^2)$ in (13), for the square and circular domains in the numerical examples. According to Shen (1993),

$$\mathbf{R}\Delta\Psi = \mathbf{K}\Delta\Psi - \sum_{m=1}^{\infty}\sum_{n=1}^{\infty}\frac{T}{2\omega_{mn}^2}\left[\mathbf{g}_{mn}<\mathbf{b}_{mn}|\Delta\Psi> - \mathbf{b}_{mn}<\mathbf{g}_{mn}|\Delta\Psi>\right]. \tag{75}$$

Explicit expressions for **K** and $\mathbf{b}_{mn}$ can be found in Shen (1993).

For the square domain with a boundary crack,

$$\mathbf{K} = \frac{T}{a},\ \mathbf{b}_{mn}(y) = -\frac{2T}{\sqrt{\rho a}}\left(\frac{n}{m}\right)^2 \sin\left(\frac{n\pi y}{a}\right). \tag{76}$$

For the circular domain with k evenly spaced slots

$$\mathbf{K} = \frac{kT}{2\pi r}\mathbf{I}_k, \tag{77}$$

where $\mathbf{I}_k$ is a $k\times k$ identity matrix. In addition, $\mathbf{b}_{mn} = [\beta_{mn}^{(1)}(r), \ldots, \beta_{mn}^{(k)}(r)]^T$, where

$$\beta_{mn}^{(j)}(r) = \rho\omega_{mn}^2\alpha_{mn}^{(j)}(r) + \gamma_{mn}^{(j)}(r),\ j = 1, 2, \ldots, k. \tag{78}$$

Here

$$\gamma_{mn}^{(j)}(r) = -\frac{R_{mn}(r)}{r}\begin{cases} -n\sin n\bar{\theta}_j, & \phi_{mn}(\mathbf{r}) = R_{mn}(\mathbf{r})\cos n\theta,\ n\neq 0 \\ n\cos n\bar{\theta}_j, & \phi_{mn}(\mathbf{r}) = R_{mn}(r)\sin n\theta,\ n\neq 0 \\ 0 & n = 0 \end{cases} \tag{79}$$

and

$$\alpha_{mn}^{(j)}(r) = \frac{kr\,R_{mn}(r)}{2\pi}\begin{cases} -\frac{1}{n^2}[\cos n(\theta+\bar{\theta}_j)]_{\theta=-\pi/k}^{\theta=\pi/k} - \frac{2\pi}{nk}\sin n\bar{\theta}_j, & \phi_{mn}(\mathbf{r}) = R_{mn}(r)\cos n\theta \\ -\frac{1}{n^2}[\sin n(\theta+\bar{\theta}_j)]_{\theta=-\pi/k}^{\theta=\pi/k} + \frac{2\pi}{nk}\cos n\bar{\theta}_j, & \phi_{mn}(\mathbf{r}) = R_{mn}(r)\sin n\theta \\ 0 & n = 0. \end{cases} \tag{80}$$

Downloaded 03 May 2010 to 171.66.16.245. Redistribution subject to ASME license or copyright; see http://www.asme.org/terms/Terms_Use.cfm

Kuang-Chong Wu
Professor.

Fong-Tai Chang
Former Graduate Student.

Institute of Applied Mechanics,
National Taiwan University,
Taipei 107, Taiwan
Republic of China

Near-Tip Fields in a Notched Body With Dislocations and Body Forces

The dominant stress fields due to a dislocation and/or a body force near the tip of an isotropic or anisotropic notched body are derived. The structures of the near-tip stress fields for anisotropic materials are constructed by using Stroh's formalism for anisotropic elasticity. The intensity coefficients contained in the near-tip fields are determined by Betti's reciprocity theorem. Special attention is given to orthotropic and isotropic materials. Some explicit results of intensity coefficients due to concentrated forces on the notch faces and dislocations at the wedge bisector are also provided.

1 Introduction

Local stress intensification usually occurs near the tip of a notch in an elastic medium. In the theory of linear elasticity such stress intensification often manifests itself by the presence of stress singularities at the notch tip. The stress singularities generally depend on the notch angle, the elastic constants, and the boundary conditions on the notch faces. Williams (1952) investigated stress singularities resulting from various boundary conditions for notches in isotropic media. Similar investigations for anisotropic media have been done by Bogy (1972) and Ting and Chou (1981), among others. The singularity analysis, however, only determines the local fields to within some proportionality constants, which are referred to as the intensity coefficients in the present paper. The intensity coefficients are functions of the notch angle, the elastic constants, the boundary conditions on the notch faces, and the applied loading in general.

The problem of interest here is the determination of the complete near-tip fields in a notched body of general elastic anisotropy in the presence of body forces and dislocations. The configuration of the problem is shown in Fig. 1. Without loss of generality, the x_1-axis is chosen to coincide with the bisector of the notched body, such that the upper and lower notch faces are at $\theta=\alpha$ and $\theta=-\alpha$, respectively, where θ is the polar angle. The notch faces are assumed traction-free. The body force $\mathbf{F}$ and dislocation with Burgers vector $\mathbf{b}$ are located at $r=\rho$ and $\theta=\psi$. The deformations considered are two dimensional but three displacement components are allowed to coexist. The problem of dislocation-crack interaction has been extensively investigated, e.g., Atkinson (1966), Asaro (1975), Hart (1980), Rice (1985), and Wu (1988). Sternberg and Koiter (1958) obtained the solution for isotropic wedges under tractions on the wedge faces. Bogy (1972) considered the same problem studied by Sternberg and Koiter, but for anisotropic wedges. Sham and Bueckner (1988) investigated the case of piecewise homogeneous isotropic notched bodies subject to antiplane shear loading. Chang and Ohr (1985) derived the solution for an isotropic notch body with a screw dislocation.

In this paper, the near-tip fields are determined by employing the Stroh formalism for anisotropic elasticity and Betti's reciprocity theorem. The procedure adopted here is essentially the same as the weight function theory of Bueckner (1970). The weight function theory was originally developed for cracked bodies and was subsequently extended to a piecewise homogeneous notched structure under antiplane strain deformation (Sham and Bueckner, 1988). A similar procedure was also proposed by Stern (1973) for computing the stress intensity factors. Let the near-tip displacement field be proportional to r^{λ} where r is the radial distance from the notch tip and λ is a complex constant with its real part lying between 0 and 1. Application of the procedure depends critically on the existence of a fundamental displacement field that is proportional to $r^{-\lambda}$ with corresponding stresses equilibrium in the body and tractions zero on the notch faces. With the aid of Stroh formalism, it is shown in the sequel that such a fundamental field can be found for the present problem. The fundamental field and Betti's reciprocity theorem can thus be used to derive the

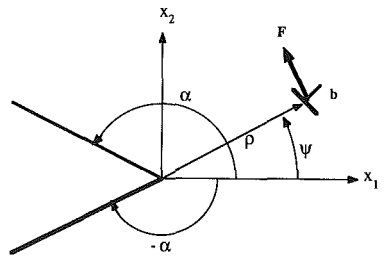


Fig. 1 A body force and dislocation in an infinite notched body

Contributed by the Applied Mechanics Division of THE AMERICAN SOCIETY OF MECHANICAL ENGINEERS for presentation at the ASME Winter Annual Meeting, New Orleans, LA, Nov. 28–Dec. 3, 1993.

Discussion on this paper should be addressed to the Technical Editor, Professor Lewis T. Wheeler, Department of Mechanical Engineering, University of Houston, Houston, TX 77204-4792, and will be accepted until four months after final publication of the paper itself in the ASME JOURNAL OF APPLIED MECHANICS.

Manuscript received by the ASME Applied Mechanics Division, Mar. 16, 1992; final revision, Dec. 3, 1992. Associate Technical Editor: R. Abeyaratne.

Paper No. 93-WA/APM-15.

Copyright © 1993 by ASME
Downloaded 03 May 2010 to 171.66.16.245. Redistribution subject to ASME license or copyright; see http://www.asme.org/terms/Terms_Use.cfm

intensity coefficients of the actual field due to the body forces and dislocations.

The plan of the paper is as follows. First, the Stroh formalism is briefly introduced in Section 2. Asymptotic analysis of the near-tip field is made in Section 3. In Section 4, the fundamental field is given and the intensity coefficients are derived. The results are specialized for orthotropic and isotropic materials in Section 5. Finally, some conclusions are given.

2 Stroh Formalism

For two-dimensional deformations dependent only on x_1 and x_2, the general expressions for the displacement $\mathbf{u}$ and stress function ϕ can be written as (Stroh, 1958)

$$\mathbf{u} = 2\Re[\mathbf{A}\mathbf{f}], \tag{1}$$

$$\phi = 2\Re[\mathbf{B}\mathbf{f}], \tag{2}$$

where $\Re$ denotes the real part, $\mathbf{f} = (f_1(z_1), f_2(z_2), f_3(z_3))^T$, with $z_\alpha = x_1 + p_\alpha x_2$. The complex constants p_α and the complex matrices $\mathbf{A}$ and $\mathbf{B}$ are functions of the elastic constants. Without loss of generality, the imaginary part of p_α is taken to be positive. The stresses are related to the stress function ϕ by

$$\sigma_{k1} = -\frac{\partial \phi_k}{\partial x_2}, \quad \sigma_{k2} = \frac{\partial \phi_k}{\partial x_1}. \tag{3}$$

The matrices $\mathbf{A}$ and $\mathbf{B}$ satisfy the following orthogonality relations:

$$\mathbf{A}^T\mathbf{B} + \mathbf{B}^T\mathbf{A} = \mathbf{I} = \overline{\mathbf{A}}^T\overline{\mathbf{B}} + \overline{\mathbf{B}}^T\overline{\mathbf{A}}, \tag{4}$$

$$\mathbf{A}^T\overline{\mathbf{B}} + \mathbf{B}^T\overline{\mathbf{A}} = \mathbf{0} = \overline{\mathbf{A}}^T\mathbf{B} + \overline{\mathbf{B}}^T\mathbf{A}, \tag{5}$$

$$\mathbf{A}\mathbf{A}^T + \overline{\mathbf{A}}\,\overline{\mathbf{A}}^T = \mathbf{0} = \mathbf{B}\mathbf{B}^T + \overline{\mathbf{B}}\,\overline{\mathbf{B}}^T, \tag{6}$$

$$\mathbf{A}\mathbf{B}^T + \overline{\mathbf{A}}\,\overline{\mathbf{B}}^T = \mathbf{0} = \mathbf{B}\mathbf{A}^T + \overline{\mathbf{B}}\,\overline{\mathbf{A}}^T, \tag{7}$$

where $\mathbf{I}$ is the identity matrix. By Eq. (6), one can let

$$\mathbf{A}\mathbf{A}^T = -\frac{i}{2}\mathbf{H} \tag{8}$$

$$\mathbf{B}\mathbf{B}^T = \frac{i}{2}\mathbf{L} \tag{9}$$

where $\mathbf{H}$ and $\mathbf{L}$ are real symmetric positive-definite matrices. Equation (7) implies

$$\mathbf{A}\mathbf{B}^T = \frac{1}{2}(\mathbf{I} - i\mathbf{S}), \tag{10}$$

where $\mathbf{S}$ is real.

3 Asymptotic Analysis

In this section, we investigate possible forms of the singular stress states near the notch tip with traction-free conditions on the notch faces $\theta = \pm\alpha$. For convenience, the complex variable z_α is expressed as $z_\alpha = r\zeta_\alpha(\theta)$, where $\zeta_\alpha(\theta) = \cos\theta + p_\alpha\sin\theta$.

Let Stroh's function $\mathbf{f}$ introduced in the previous section be of the following form:

$$\mathbf{f} = \frac{c}{2}\left(\frac{r}{\hat{r}}\right)^{\lambda}\mathbf{\Lambda}(\theta, -\alpha, \lambda)\mathbf{q} + \frac{\bar{c}}{2}\left(\frac{r}{\hat{r}}\right)^{\bar{\lambda}}\mathbf{\Lambda}(\theta, -\alpha, \bar{\lambda})\bar{\mathbf{q}}. \tag{11}$$

In Eq. (11), λ and c are complex constants, $\mathbf{q}$ a complex constant vector, $\hat{r}$ a reference length scale, the overbar denotes complex conjugate, and $\mathbf{\Lambda}$ is given by

$$\mathbf{\Lambda}(\theta, -\alpha, \lambda) = \left\langle\left(\frac{\zeta(\theta)}{\zeta(-\alpha)}\right)^{\lambda}\right\rangle\mathbf{B}^T \tag{12}$$

where

$$\left\langle\left(\frac{\zeta(\theta)}{\zeta(-\alpha)}\right)^{\lambda}\right\rangle = \mathrm{diag}\left[\left(\frac{\zeta_1(\theta)}{\zeta_1(-\alpha)}\right)^{\lambda}, \left(\frac{\zeta_2(\theta)}{\zeta_2(-\alpha)}\right)^{\lambda}, \left(\frac{\zeta_3(\theta)}{\zeta_3(-\alpha)}\right)^{\lambda}\right]$$

is a diagonal matrix and the subscript T denotes matrix transpose. The displacements and the stress functions corresponding to Eq. (11) are given by

$$\mathbf{u} = \Re\left[c\left(\frac{r}{\hat{r}}\right)^{\lambda}\mathbf{h}(\theta, -\alpha, \lambda)\right] \tag{13}$$

$$\phi = \Re\left[c\left(\frac{r}{\hat{r}}\right)^{\lambda}\mathbf{g}(\theta, -\alpha, \lambda)\right] \tag{14}$$

where

$$\mathbf{h}(\theta, -\alpha, \lambda) = (\mathbf{A}\mathbf{\Lambda}(\theta, -\alpha, \lambda) + \overline{\mathbf{A}\mathbf{\Lambda}(\theta, -\alpha, \bar{\lambda})})\mathbf{q} \tag{15}$$

$$\mathbf{g}(\theta, -\alpha, \lambda) = (\mathbf{B}\mathbf{\Lambda}(\theta, -\alpha, \lambda) + \overline{\mathbf{B}\mathbf{\Lambda}(\theta, -\alpha, \bar{\lambda})})\mathbf{q} \tag{16}$$

On account of Eq. (6), the traction $\mathbf{t}_r$ on the radial plane given by

$$\mathbf{t}_r = -\frac{\partial \phi}{\partial r} \tag{17}$$

is identically zero at $\theta = -\alpha$. The requirement that $\mathbf{t}_r$ vanish at $\theta = \alpha$ then leads to

$$c\lambda\mathbf{g}(\alpha, -\alpha, \lambda) = \mathbf{0}. \tag{18}$$

For nonzero solutions of λ, c, and $\mathbf{q}$, we must have

$$\mathbf{C}\mathbf{q} = \mathbf{0} \tag{19}$$

with

$$\Delta = |\mathbf{C}| = 0. \tag{20}$$

Here the matrix $\mathbf{C}$ is given by

$$\mathbf{C} = \mathbf{B}\mathbf{\Lambda}(\alpha, -\alpha, \lambda) + \overline{\mathbf{B}\mathbf{\Lambda}(\alpha, -\alpha, \bar{\lambda})}. \tag{21}$$

Equation (20) is the characteristic equation for λ. It is obvious that if λ is a root, so is $\bar{\lambda}$. Since the displacements in Eq. (13) are proportional to r^β, β being the real part of λ, for bounded displacements at the notch tip we must require $\beta > 0$. If $\beta < 1$, the corresponding stresses are singular. We restrict our attention to the root of λ of Eq. (20) with $0 < \beta \le 1$. For definiteness, the eigenvector is normalized such that $\mathbf{q}^T\mathbf{q} = 1$. Note that the only undetermined quantity in Eqs. (13) and (14) is the intensity coefficient c.

Up to now it is tacitly assumed that λ is a single root of Δ. If λ is a double root, Eq. (11) may have to be modified as (Ting and Chou, 1986)

$$\mathbf{f} = \frac{c}{2}\left(\frac{r}{\hat{r}}\right)^{\lambda}\mathbf{\Lambda}(\theta, -\alpha, \lambda)\mathbf{q} + \frac{\bar{c}}{2}\left(\frac{r}{\hat{r}}\right)^{\bar{\lambda}}\mathbf{\Lambda}(\theta, -\alpha, \bar{\lambda})\bar{\mathbf{q}} + \frac{d}{2}\left[\left(\frac{r}{\hat{r}}\right)^{\lambda}\mathbf{\Lambda}(\theta, -\alpha, \lambda)\mathbf{q}\right]' + \frac{\bar{d}}{2}\left[\left(\frac{r}{\hat{r}}\right)^{\bar{\lambda}}\mathbf{\Lambda}(\theta, -\alpha, \bar{\lambda})\bar{\mathbf{q}}\right]' \tag{22}$$

where d is an additional intensity coefficient and the prime denotes partial differentiation with respect to β. The notation of prime is adopted throughout the paper. The corresponding displacements and stress functions are given by

$$\mathbf{u} = \Re\left[\left(\frac{r}{\hat{r}}\right)^{\lambda}\left\{\left(c + d\log\left(\frac{r}{\hat{r}}\right)\right)\mathbf{h}(\theta, -\alpha, \lambda) + d\mathbf{h}'(\theta, -\alpha, \lambda)\right\}\right] \tag{23}$$

$$\phi = \Re\left[\left(\frac{r}{\hat{r}}\right)^{\lambda}\left\{\left(c + d\log\left(\frac{r}{\hat{r}}\right)\right)\mathbf{g}(\theta, -\alpha, \lambda) + d\mathbf{g}'(\theta, -\alpha, \lambda)\right\}\right] \tag{24}$$

where $\mathbf{h}$ and $\mathbf{g}$ are given by Eqs. (15) and (16). Note that stresses corresponding to Eqs. (23) and (24) may have logarithmic singularity for $\beta = 1$. For traction-free conditions to be satisfied, in addition to Eq. (19), we also have

$$(\mathbf{C}\mathbf{q})' = \mathbf{C}\mathbf{q}' + \mathbf{C}'\mathbf{q} = \mathbf{0}. \tag{25}$$

To investigate the necessary and sufficient condition for the existence of $\mathbf{q}$ and $\mathbf{q}'$ that satisfy Eq. (19) and (25), let δ be the eigenvalue of $\lambda\mathbf{C}$, i.e.,

$$\lambda\mathbf{C}\mathbf{q} = \delta\mathbf{q}. \tag{26}$$

Here both δ and $\mathbf{q}$ are considered to be functions of λ. For

Downloaded 03 May 2010 to 171.66.16.245. Redistribution subject to ASME license or copyright; see http://www.asme.org/terms/Terms_Use.cfm

Eq. (19) to be satisfied for a particular value of λ, say $\lambda=\lambda_0$, it is obvious that $\delta(\lambda_0)=0$. Differentiating both sides of Eq. (26) with respect to β and substituting $\lambda=\lambda_0$ leads to

$$\lambda_0(\mathbf{Cq}'+\mathbf{C}'\mathbf{q})=\delta'\mathbf{q}. \tag{27}$$

Thus Eq. (25) is satisfied if and only if $\delta(\lambda_0)=\delta'(\lambda_0)=0$. By Eq. (26), the function δ can be expressed as

$$\delta=\lambda\mathbf{q}^T\mathbf{Cq} \tag{28}$$

and by Eq. (27), δ' with $\delta=0$ can be expressed as

$$\delta'=\lambda\mathbf{q}^T\mathbf{C}'\mathbf{q}. \tag{29}$$

Equation (29) is convenient for checking the existence condition once $\mathbf{q}$ is determined.

4 Intensity Coefficients

In this section the intensity coefficients of the near-tip fields are derived for a body force $\mathbf{F}$ or a dislocation with Burgers vector $\mathbf{b}$ in the body as shown in Fig. 1. For convenience, $\hat{r}$ is taken to be ρ. The derivation will be done by using Betti's reciprocity theorem which states that

$$\int_\Gamma\left((\mathbf{u}^*)^T\mathbf{t}-(\mathbf{t}^*)^T\mathbf{u}\right)ds=0 \tag{30}$$

where $(\mathbf{u}^*,\mathbf{t}^*)$ and $(\mathbf{u},\mathbf{t})$ are the displacements and tractions of two admissible elastic states. In Eq. (30), Γ is a closed contour that encloses no elastic singularities. Equation (30) can also be expressed in an alternative form by using the relation $\mathbf{t}=-\partial\phi/\partial s$ and performing integration by parts on the second term of the left-hand side. The alternative form is given by

$$\int_\Gamma\left((\mathbf{u}^*)^T\frac{\partial\phi}{\partial s}+(\phi^*)^T\frac{\partial\mathbf{u}}{\partial s}\right)ds=0. \tag{31}$$

If there is a body force $\mathbf{F}$ and a dislocation $\mathbf{b}$ at (ξ_1,ξ_2) in the region bounded by Γ, Eq. (31) must be modified as

$$\int_\Gamma\left((\mathbf{u}^*)^T\frac{\partial\phi}{\partial s}+(\phi^*)^T\frac{\partial\mathbf{u}}{\partial s}\right)ds=-(\mathbf{u}^*(\rho,\psi)^T\mathbf{F}+\phi^*(\rho,\psi)^T\mathbf{b}). \tag{32}$$

The direction of integration in Eq. (32) is clockwise. With representations of the displacements and stress functions given by Eqs. (1) and (2), respectively, and using the orthiginality relations Eqs. (4) and (5), we can express Eq. (32) as

$$I=2\Re\left[\int_\Gamma(\mathbf{f}^*)^T\frac{\partial\mathbf{f}}{\partial s}\,ds\right]=-(\mathbf{u}^*(\rho,\psi)^T\mathbf{F}+\phi^*(\rho,\psi)^T\mathbf{b}) \tag{33}$$

where $\mathbf{f}^*$ and $\mathbf{f}$ are Stroh's functions corresponding to $(\mathbf{u}^*,\mathbf{t}^*)$ and $(\mathbf{u},\mathbf{t})$, respectively.

Let $(\mathbf{u},\mathbf{t})$ be the actual state due to a dislocation or a body force and choose the following form for $\mathbf{f}^*$:

$$\mathbf{f}^*=\frac{c^*}{2}\left(\frac{r}{\rho}\right)^{-\lambda}\mathbf{\Lambda}(\theta,\alpha,-\lambda)\mathbf{q}+\frac{\bar{c}^*}{2}\left(\frac{r}{\rho}\right)^{-\bar{\lambda}}\mathbf{\Lambda}(\theta,\alpha,-\bar{\lambda})\bar{\mathbf{q}} \tag{34}$$

with λ and $\mathbf{q}$ satisfying Eq. (19) and c^* being an arbitrary constant. The corresponding stress function ϕ^* is given by

$$\phi^*=\Re\left[c^*\left(\frac{r}{\rho}\right)^{-\lambda}\mathbf{g}(\theta,\alpha,-\lambda)\right] \tag{35}$$

where the function $\mathbf{g}$ is defined by Eq. (16). The stress function ϕ^* is identically zero on the notch face $\theta=\alpha$ by invoking Eq. (6). On the notch face $\theta=-\alpha$, ϕ^* is given by

$$\phi^*=\Re\left[c^*\left(\frac{r}{\rho}\right)^{-\lambda}\mathbf{g}(-\alpha,\alpha,-\lambda)\right]. \tag{36}$$

Since

$$\mathbf{g}(-\alpha,\alpha,-\lambda)=\mathbf{g}(\alpha,-\alpha,\lambda)=\mathbf{0}, \tag{37}$$

ϕ^* also vanishes on the notch face $\theta=-\alpha$. Note that although both ϕ and ϕ^* satisfy the traction-free conditions on the notch faces, the displacement field $\mathbf{u}$ corresponding to ϕ is proportional to r^λ whereas $\mathbf{u}^*$ corresponding to ϕ^* is proportional to $r^{-\lambda}$. The displacement field $\mathbf{u}^*$ is referred to as the fundamental field in the weight function theory of Bueckner (1970).

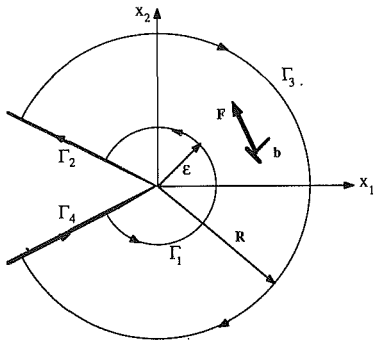


Fig. 2 Integration path for the derivation of the intensity coefficients

Consider now the integral I integrated along the path Γ shown in Fig. 2. The integration path Γ consists of four parts, Γ_k, $k=1\sim4$. Γ_1 and Γ_3 are described by $r=\epsilon$, $-\alpha<\theta<\alpha$ and $r=R$, $-\alpha<\theta<\alpha$, respectively, with ϵ and R being constants and $R>\epsilon$. Γ_2 and Γ_4 are given by $\epsilon<r<R$, $\theta=\alpha$ and $\epsilon<r<R$, $\theta=-\alpha$, respectively. I can be expressed as

$$I=\sum_{k=1}^{4}I_k \tag{38}$$

where I_k is the contribution to I as the integral is evaluated along Γ_k. Since ϕ^* as well as ϕ vanishes at $\theta=\pm\alpha$, $I_2=I_4=0$. In addition, if R is large compared to ρ, the actual stresses on Γ_3 are of the order R^{-t} with $t\geq1$ and ϕ^* is of the order of $R^{-\beta}$ with $\beta>0$. The corresponding I_3 is of the order $R^{1-t-\beta}$. As R approaches to infinity, I_3 approaches to zero. Thus, the only nonzero contribution to I is from Γ_1 so that

$$I=2\Re\left[\int_{-\alpha}^{\alpha}(\mathbf{f}^*)^T\frac{\partial\mathbf{f}}{\partial\theta}\,d\theta\right]=-(\mathbf{u}^*(\rho,\psi)^T\mathbf{F}+\phi^*(\rho,\psi)^T\mathbf{b}). \tag{39}$$

As shown in the Appendix, Eq. (39) yields

$$\frac{1}{\gamma}\Re[cc^*\delta']=\Re[c^*a] \tag{40}$$

where $\gamma=1$ if λ is real and $\gamma=2$ if λ is complex, δ' is given by Eq. (29) and a is given by

$$a=-(\mathbf{h}(\psi,\alpha,-\lambda)^T\mathbf{F}+\mathbf{g}(\psi,\alpha,-\lambda)^T\mathbf{b}). \tag{41}$$

In particular, if $\psi=\alpha$, Eq. (41) is simplified to

$$a=-\mathbf{q}^T\mathbf{F} \tag{42}$$

by using Eqs. (6) and (7). As Eq. (40) holds for arbitrary c^*, we must have

$$c=\frac{\gamma a}{\delta'}. \tag{43}$$

The expression for c is valid as long as $\delta'\neq0$. This is consistent with the fact that as $\delta'=0$, the assumed form for $\mathbf{f}$, Eq. (11), is incomplete and the modified form of Eq. (22), with the intensity coefficients c and d to be determined, must be used.

For the case $\delta'=0$, consider first $\mathbf{f}^*$ given by Eq. (34). By the same arguments discussed previously, we have

$$d=\frac{2\gamma a}{\delta''} \tag{44}$$

where δ'' is given by Eq. (A5) in the Appendix. To determine c, let $\mathbf{f}^*$ be chosen as

$$\mathbf{f}=\frac{d^*}{2}\left[\left(\frac{r}{\rho}\right)^{\lambda}\mathbf{\Lambda}(\theta,\alpha,-\lambda)\mathbf{q}\right]'+\frac{\bar{d}^*}{2}\left[\left(\frac{r}{\rho}\right)^{\bar{\lambda}}\mathbf{\Lambda}(\theta,\alpha,-\bar{\lambda})\bar{\mathbf{q}}\right]' \tag{45}$$

Downloaded 03 May 2010 to 171.66.16.245. Redistribution subject to ASME license or copyright; see http://www.asme.org/terms/Terms_Use.cfm

where d^* is an arbitrary complex constant. With this choice of $\mathbf{f}^*$, the corresponding stress function vanishes at $\theta = \pm\alpha$ by Eqs. (6) and (25). With Eq. (45) and the fact that d^* is arbitrary, Eq. (33) yields

$$\frac{\delta''}{2}c + \frac{\delta'''}{6}d = \gamma a'' \tag{46}$$

where δ''' is given by Eq. (A6) in the Appendix. Thus c is given by

$$c = \frac{2\gamma}{\delta''}\left(a' - \left(\frac{\delta''' a}{3\delta''}\right)\right). \tag{47}$$

Derivations of Eqs. (44) and (46) can be found in the Appendix.

5 Orthotropic and Isotropic Materials

In this section the results in the previous sections are specialized for orthotropic and isotropic materials. For orthotropic materials, it is assumed that the materials symmetry planes coincide with the coordinate planes so that the plane and antiplane deformations are decoupled. The case of plane deformation has been investigated by Bogy (1972). According to (Dongye and Ting, 1989), the complex constant p_3 in Stroh's formalism is imaginary and p_1, p_2 are either both imaginary or $p_1 = -\bar{p}_2$. For simplicity, we consider only the case where $p_k = il_k$ with l_k being real and positive. The case was also considered by Bogy (1972). For orthotropic materials, matrix $\mathbf{B}$ in Stroh's formalism is of the following form (Stroh, 1962):

$$\mathbf{B} = \begin{pmatrix} -p_1 B_{21} & -p_2 B_{22} & 0 \\ B_{21} & B_{22} & 0 \\ 0 & 0 & B_{33} \end{pmatrix}. \tag{48}$$

Furthermore, the matrix $\mathbf{L} = \mathrm{diag}[L_1, L_2, L_3]$ is diagonal (Dongye and Ting, 1989). Explicit expressions for L_k in terms of the elastic constants can be found in Dongye and Ting (1989). By Eq. (9), we have

$$B_{22}^2 = \frac{i}{2}\frac{l_1}{l_1 - l_2}L_2,\quad B_{21}^2 = -\frac{i}{2}\frac{l_2}{l_1 - l_2}L_2,\quad l_1 l_2 L_2 = L_1$$

$$B_{33}^2 = \frac{i}{2}L_3. \tag{49}$$

With $\mathbf{B}$ given by Eq. (48) and the relations in Eq. (49), we obtain the matrix $\mathbf{C}$ as

$$\mathbf{C} = \begin{pmatrix} \tilde{\mathbf{C}} & \mathbf{0} \\ \mathbf{0} & C_{33} \end{pmatrix} \tag{50}$$

where

$$\tilde{\mathbf{C}} = \frac{L_1}{l_1 - l_2}\sum_{k=1}^{2}(-1)^k \begin{pmatrix} l_k \sin 2\lambda\alpha_k & \cos 2\lambda\alpha_k \\ \cos 2\lambda\alpha_k & -\dfrac{\sin 2\lambda\alpha_k}{l_k} \end{pmatrix}$$

$$C_{33} = -L_3 \sin 2\lambda_3\alpha_3$$

and $\alpha_k = \tan^{-1}(l_k \tan\alpha)$. The characteristic equation for λ given by the determinant of $\mathbf{C}$ can be expressed as

$$\Delta = \Delta_1\Delta_2\Delta_3 = 0 \tag{51}$$

where

$$\Delta_1 = \frac{2L_1}{l_2 - l_1}\left(\frac{l_1}{l_2}\cos\lambda\alpha_1 \sin\lambda\alpha_2 - \sin\lambda\alpha_1 \cos\lambda\alpha_2\right) \tag{52}$$

$$\Delta_2 = -\frac{2L_1}{l_2 - l_1}\left(\frac{l_2}{l_1}\cos\lambda\alpha_1 \sin\lambda\alpha_2 - \sin\lambda\alpha_1 \cos\lambda\alpha_2\right) \tag{53}$$

$$\Delta_3 = -L_3 \sin 2\lambda_3\alpha_3. \tag{54}$$

Apart from some multiplicative constants, Eqs. (52) and (53) are in agreement with those obtained by Bogy (1972).[1] Let zeros of Δ_k with the smallest positive real parts be denoted by λ_k. λ_1 and λ_2 correspond to antisymmetric plane and symmetric plane deformations, respectively (Bogy, 1972), while $\lambda_3 = \pi/2\alpha_3$ corresponds to antiplane deformation. The vector $\mathbf{q}_k$, determined by Eq. (19) with $\mathbf{C}$ given by Eq. (50) and $\lambda = \lambda_k$, are

$$\mathbf{q}_1 = \frac{1}{\sqrt{\sin^2\lambda_1\alpha_1 + l_1^2\cos^2\lambda_1\alpha_1}}(\sin\lambda_1\alpha_1, l_1\cos\lambda_1\alpha_1, 0)^T \tag{55}$$

$$\mathbf{q}_2 = \frac{1}{\sqrt{\cos^2\lambda_2\alpha_1 + l_1^2\sin^2\lambda_2\alpha_1}}(-\cos\lambda_2\alpha_1, l_1\sin\lambda_2\alpha_1, 0)^T \tag{56}$$

$$\mathbf{q}_3 = (0,0,1)^T. \tag{57}$$

The expressions for δ_k' obtained by substituting $\lambda = \lambda_k$ and $\mathbf{q}_k$ in Eq. (29) are given by

$$\delta_1' = \lambda_1 \frac{2L_1}{l_2 - l_1}\sum_{k=1}^{2}(-1)^k \frac{l_k\alpha_k}{\sin^2\lambda_1\alpha_k + l_k^2\cos^2\lambda_1\alpha_k} \tag{58}$$

$$\delta_2' = \lambda_2 \frac{2L_1}{l_1 - l_2}\sum_{k=1}^{2}(-1)^k \frac{l_k\alpha_k}{\cos^2\lambda_2\alpha_k + l_k^2\sin^2\lambda_2\alpha_k} \tag{59}$$

$$\delta_3' = -2L_3\lambda\alpha_3\cos^2\lambda\alpha_3 = \pi L_3. \tag{60}$$

According to (Bogy, 1972), λ_1 and λ_2 are real and $\lambda_1 \le 1$, $\lambda_2 < 1$ may occur only when $2\alpha > \pi$. Furthermore, $\delta_1' = 0$ when $\lambda_1 = 1$ for the notch angle α^* satisfying

$$\alpha_1^* \sin 2\alpha_2^* = \alpha_2^* \sin 2\alpha_1^*. \tag{61}$$

For $\delta_k' \neq 0$, let the stress functions corresponding to λ_k, $k = 1,2,3$ be denoted by $\phi^{(k)}$. Since λ_k are real, $\phi^{(k)}$ as given by Eq. (14) become

$$\phi^{(k)} = c_k\left(\frac{r}{\rho}\right)^{\lambda_k}\mathbf{g}^{(k)}(\theta, -\alpha, \lambda_k) \tag{62}$$

where $\mathbf{g}^{(k)}$ as given by Eq. (16) are real. Due to decoupling of plane and antiplane deformations, $g_3^{(k)} = g_k^{(3)} = 0$, $k = 1,2$. The expressions for other $g_j^{(k)}$ are given as follows:

Antisymmetric Plane Deformation.

$$g_1^{(1)} = \frac{L_1}{l_1 - l_2}\sum_{k=1}^{2}(-1)^k\left(\frac{R_k(\theta)}{R_k(\alpha)}\right)^{\lambda_1}\frac{l_k\cos\lambda_1\theta_k}{\sqrt{\sin^2\lambda_1\alpha_k + l_k^2\cos^2\lambda_1\alpha_k}}$$

$$g_2^{(1)} = \frac{L_1}{l_2 - l_1}\sum_{k=1}^{2}(-1)^k\left(\frac{R_k(\theta)}{R_k(\alpha)}\right)^{\lambda_1}\frac{\sin\lambda_1\theta_k}{\sqrt{\sin^2\lambda_1\alpha_k + l_k^2\cos^2\lambda_1\alpha_k}}$$

Symmetric Plane Deformation.

$$g_1^{(2)} = \frac{L_1}{l_2 - l_1}\sum_{k=1}^{2}(-1)^k\left(\frac{R_k(\theta)}{R_k(\alpha)}\right)^{\lambda_2}\frac{l_k\sin\lambda_2\theta_k}{\sqrt{\cos^2\lambda_2\alpha_k + l_k^2\sin^2\lambda_2\alpha_k}}$$

$$g_2^{(2)} = \frac{L_1}{l_2 - l_1}\sum_{k=1}^{2}(-1)^k\left(\frac{R_k(\theta)}{R_k(\alpha)}\right)^{\lambda_2}\frac{\cos\lambda_2\theta_k}{\sqrt{\cos^2\lambda_2\alpha_k + l_k^2\sin^2\lambda_2\alpha_k}}$$

Antiplane Deformation.

$$g_3^{(3)} = -L_3\left(\frac{R_3(\theta)}{R_3(\alpha)}\right)^{\lambda_3}\sin\lambda_3(\theta_3 + \alpha_3)$$

where $R_k(\theta) = \sqrt{\cos^2\theta + l_k^2\sin^2\theta}$.

For $\lambda_1 = 1$, $\alpha = \alpha^*$, the vector $\mathbf{q}_1$ is obtained from Eq. (55) as

$$\mathbf{q}_1 = (\sin\alpha^*, \cos\alpha^*, 0)^T \tag{63}$$

and is independent of elastic constants. The stress functions corresponding to Eq. (24) become

[1] The parameters γ_k, ϕ_k, s used in (Bogy, 1972) are related to l_k, α_k, λ by $\gamma_k = (1 - l_k)/(1 + l_k)$, $\phi_k = \alpha_k$, $s = -\lambda - 1$.

Downloaded 03 May 2010 to 171.66.16.245. Redistribution subject to ASME license or copyright; see http://www.asme.org/terms/Terms_Use.cfm

$$\phi_j^{(1)} = d_1 \left(\frac{r}{\rho}\right)^{\lambda} g_j^{(1)}(\theta, -\alpha^*, \lambda = 1)' \tag{64}$$

for $j = 1,2$, where the fact that $g_j^{(1)}(\theta, -\alpha^*, \lambda = 1) = 0$ has been used. The explicit expressions for $(g_j^{(1)})'$ are listed as follows:

$$(g_1^{(1)})' = \frac{L_1 \cos\theta}{l_1 - l_2} \sum_{k=1}^{2} (-1)^k \left[\log\left(\frac{R_k(\theta)}{R_k(\alpha^*)}\right) - \theta_k \tan\theta_k - \alpha_k^* \cot\alpha_k^* \right]$$

$$(g_2^{(1)})' = \frac{L_1 \sin\theta}{l_1 - l_2} \sum_{k=1}^{2} (-1)^k \left[\log\left(\frac{R_k(\theta)}{R_k(\alpha^*)}\right) + \theta_k \cot\theta_k - \alpha_k^* \cot\alpha_k^* \right].$$

The quantity δ_1'' needed in determining d is obtained by differentiating δ_1' of Eq. (58) with respect to λ_1 as

$$\delta_1'' = \frac{4L_1}{l_1 - l_2} \frac{\alpha_1^* \sin 2\alpha^*}{\sin 2\alpha_1^*} (\cos 2\alpha_1^* - \cos 2\alpha_2^*). \tag{65}$$

Note that in this case the stresses are not singular.

For antiplane deformation, the results for isotropic materials can be obtained from those for orthotropic materials directly by setting $l_3 = 1$ and $L_3 = \mu$ (Bacon et al., 1973), μ being the shear modulus. For plane deformation, however, proper limits as $l_2 \to l_1 = 1$ must be evaluated to obtain the corresponding results. They are given as follows:

Antisymmetric Plane Deformation.

$\alpha \neq \alpha^*$

$$\Delta_1 = L_1(\lambda_1 \sin 2\alpha - \sin 2\lambda_1\alpha)$$

$$\mathbf{q}_1 = (\sin\lambda_1\alpha, \cos\lambda_1\alpha, 0)^T$$

$$\delta_1' = L_1\lambda_1(\sin 2\alpha - 2\alpha\cos 2\lambda_1\alpha)$$

$$g_1^{(1)} = -L_1[(\sin^2\lambda_1\alpha - \lambda_1\sin^2\alpha)\cos\lambda_1\theta + \lambda_1\sin\theta\sin(1-\lambda_1)\theta]$$

$$g_2^{(1)} = -L_1[(\cos^2\lambda_1\alpha + \lambda_1\sin^2\alpha)\sin\lambda_1\theta - \lambda_1\sin\theta\cos(1-\lambda_1)\theta]$$

$\alpha = \alpha^*$

$$2\alpha^* = \tan 2\alpha^*$$

$$\delta_1'' = 4L_1(\alpha^*)^2 \sin 2\alpha^*$$

$$(g_1^{(1)})' = -L_1[(\alpha^* \sin 2\alpha^* - \sin^2\alpha^*)\cos\theta - \theta\sin\theta]$$

$$(g_2^{(1)})' = -L_1[\theta\cos\theta - (\alpha^* \sin 2\alpha^* + \cos^2\alpha^*)\sin\theta]$$

Symmetric Plane Deformation.

$$\Delta_2 = L_1(\lambda_2 \sin 2\alpha + \sin 2\lambda_2\alpha)$$

$$\mathbf{q}_2 = (-\cos\lambda_2\alpha, \sin\lambda_2\alpha, 0)^T$$

$$\delta_1' = L_1\lambda_2(\sin 2\alpha + 2\alpha\cos 2\lambda_2\alpha)$$

$$g_1^{(2)} = L_1[(\cos^2\lambda_2\alpha - \lambda_2\sin^2\alpha)\sin\lambda_2\theta + \lambda_2\sin\theta\cos(1-\lambda_2)\theta]$$

$$g_2^{(2)} = -L_1[(\sin^2\lambda_2\alpha + \lambda_2\sin^2\alpha)\cos\lambda_2\theta - \lambda_2\sin\theta\sin(1-\lambda_2)\theta]$$

where $L_1 = \mu/(1-\nu)$ (Bacon et al., 1973) with ν being the Poisson's ratio.

For a concentrated force on the notch face $\theta = \alpha$ and a dislocation at $\theta = 0$, the intensity coefficients c_n for $\delta_n' \neq 0$ and d_1 for $\delta_1' = 0$ are obtained by Eqs. (43) and (44), respectively, as

$$c_n = \frac{a_n}{\delta_n'} \tag{66}$$

$$d_1 = -2 \frac{\sin\alpha^* F_1 + \cos\alpha^* F_2}{\delta_1''} \tag{67}$$

where a_n is given by

$$a_n = -(\mathbf{q}_n^T \mathbf{F} + \mathbf{g}^{(n)}(0, \alpha, -\lambda_n)^T \mathbf{b}) \tag{68}$$

and γ in Eq. (43) has been set to 1 as λ_k are real. The vectors $\mathbf{q}_n$ and $\mathbf{g}^{(n)}$ and the scalars δ_n' and δ_1'' in Eqs. (66) and (67) for both isotropic and orthotropic materials were listed previously in this section. It is interesting to note that if $\mathbf{F}$ is in the direction $\theta = \theta_n$ that is perpendicular to $\mathbf{q}_n$, the corresponding c_n vanishes. Consider the class of materials described by $l_1 = 1$ and $l_2 = \sqrt{c_{11}/c_{22}}$ (Dongye and Ting, 1989), where c_{ij} is the contracted notation for the elastic constants. For these materials, the vectors $\mathbf{q}_1$ and $\mathbf{q}_2$ of Eqs. (55) and (56) are simplified as

$$\mathbf{q}_1 = (\sin\lambda_1\alpha, \cos\lambda_1\alpha, 0)^T \tag{69}$$

$$\mathbf{q}_2 = (-\cos\lambda_2\alpha, \sin\lambda_2\alpha, 0)^T \tag{70}$$

and the angles θ_1 and θ_2 are given by

$$\theta_1 = \pi - \lambda_1\alpha, \quad \theta_2 = \frac{\pi}{2} - \lambda_2\alpha. \tag{71}$$

Table 1 λ_k and θ_k (in degrees), $k = 1,2$, as functions of l_2 with $l_1 = 1$

l_2	0	0.2	0.4	0.6	0.8	1.0	∞
λ_1	.667	.718	.770	.820	.867	.908	1.
θ_1	90	83.1	76.1	69.3	63.0	57.3	45.0
λ_2	0.5	.507	.515	.525	.535	.544	.667
θ_2	22.5	21.6	20.4	19.1	17.8	16.5	0

The values of λ_k, θ_k, $k = 1,2$, for various values of l_2, including $l_2 = 1$ for isotropic material, are shown in Table 1 for $\alpha = 135$ deg. It is seen that λ_1 and λ_2 increase monotonically from .667 to 1 from 0.5 to .667, respectively, as l_2 changes from 0 to ∞. The corresponding θ_1 and θ_2 also increase monotonically from 90 deg to 45 deg and from 22.5 deg to 0 deg, respectively. The result shows that for the class of materials and geometry considered λ_2 is always smaller than λ_1 and if a singular stress does exist at the notch tip, the one generated by the symmetric deformation would be more singular. Moreover, λ_1 and θ_1 exhibit wider ranges of variation than λ_2 and θ_2. The existence of θ_1 implies that if a pair of forces of the same magnitude are applied along $\theta = \theta_1$, $\theta = \pi - \theta_1$ on the face $\theta = \alpha$ and $\theta = -\alpha$, respectively, at the same distance from the notch tip, both c_1 and c_2 are zero and the stresses are finite at the notch tip. Similarly, if a pair of forces of the same magnitude are applied along $\theta = \theta_1$, $\theta = -\theta_1$ on the face $\theta = \alpha$ and $\theta = -\alpha$, respectively, at the same distance from the notch tip, the stresses are also finite at the tip.

Generalizing the concept in the elastic fracture mechanics, one can also characterize the near-tip fields by the notch stress intensity factors defined as

$$k_n = (2\pi r)^{1-\lambda_n} \sigma_{n2}^{(n)}(r, \theta = 0) \quad n = 1,2,3 \tag{72}$$

where $\sigma_{n2}^{(n)}$ is given by

$$\sigma_{n2}^{(n)}(r, \theta = 0) = \frac{\partial \phi_n^{(n)}}{\partial r}. \tag{73}$$

The relations between k_n and c_n are obtained by substituting Eq. (62) into Eq. (72) as

$$k_n = \frac{2\pi\lambda_n}{(2\pi\rho)^{\lambda_n}} g_n^{(n)}(\theta = 0) c_n. \tag{74}$$

In particular, the notch stress intensity factor k_3 for antiplane deformation is given by

$$k_3 = \frac{2\lambda_3}{(2\pi\rho)^{\lambda_3}} (R_3(\alpha)^{-\lambda_3} F_3 - L_3 b_3). \tag{75}$$

The result specialized for isotropic materials for the concentrated force agrees with that obtained by Sham and Bueckner (1988) and the result for the dislocation reduces to the one given by Ohr and Chang (1985). Equation (74) is simplified

Downloaded 03 May 2010 to 171.66.16.245. Redistribution subject to ASME license or copyright; see http://www.asme.org/terms/Terms_Use.cfm

considerably for $\alpha=\pi$ (a crack) in which case $\alpha_n=\pi$ and $\lambda_n=0.5$. The resulting stress intensity factors become

$$k_n=\frac{1}{\sqrt{2\pi\rho}}\,(F_n-L_nb_n). \tag{76}$$

This is in agreement with the existing results (Rice, 1985; Wu, 1988).

6 Concluding Remarks

The complete near-tip fields of an anisotropic or isotropic notched body due to a body force or dislocation were presented in this paper. With the aid of Stroh's formalism, we were able to express the near-tip fields in compact matrix forms and derive the intensity coefficients in closed forms. It should be emphasized that asymptotic analysis of the near-tip fields alone is not sufficient to determine if singular stress state exists for a given material and geometry. One must also consider the intensity coefficients which depend on the applied loading. Indeed, for orthotropic notch bodies, it was shown that there exist some special directions for loading applied on the notch faces. The stresses at the notch tip are finite when forces are applied in those special directions.

References

Asaro, R. J., 1975, "An Image Force Theorem for a Dislocation Near a Crack in an Anisotropic Medium," *Journal of Physics F: Metal Physics*, Vol. 5, pp. 2249–2255.

Atkinson, C., 1966, "The Interaction between a Dislocation and a Crack," *International Journal of Fracture Mechanics*, Vol. 2, pp. 576–575.

Bacon, D. J., Barnett, D. M., and Scattergood, R. O., 1973, "Anisotropic Continuum Theory of Lattice Defects," *Progress in Material Science*, Vol. 23, pp. 51–262.

Bogy, D. B., 1972, "The Plane Solution for Anisotropic Elastic Wedges under Normal and Shear Loading," ASME JOURNAL OF APPLIED MECHANICS, Vol. 39, pp. 1103–1109.

Bueckner, H. F., 1970, "A Novel Principle for the Computation of Stress Intensity Factors," *Zeitschrift Fur Angewandte Mathematik und Mechanik*, Vol. 50, pp. 529–546.

Chang, S. J., and Ohr, S. M., 1985, "Elastic Interaction of a Wedge Crack with a Screw Dislocation," *Journal of Applied Physics*, Vol. 57, No. 6, pp. 1839–1843.

Dongye, C., and Ting, T. C. T., 1989, "Explicit Expressions of Barnett-Lothe Tensors and Their Associated Tensors for Orthotropic Materials," *Quarterly Journal of Applied Mathematics*, Vol. 47, pp. 723–734.

Hart, E. W., 1980, "A Theory for Stable Crack Extension Rates in Ductile Materials," *International Journal of Solids and Structures*, Vol. 16, pp. 807–823.

Rice, J. R., 1985, "Conserved Integrals and Energetic Forces," *Fundamentals of Deformation and Fracture (Eshelby Memorial Symposium)*, B. A. Bilby, K. J. Miller and J. R. Willis, eds., Cambridge Univ. Press, Cambridge, U.K.

Sternberg, E., and Koiter, W., 1958, "The Wedge under a Concentrated Couple: A Paradox in the Two-Dimensional Theory of Elasticity," ASME JOURNAL OF APPLIED MECHANICS, Vol. 25, pp. 575–581.

Sham, T. L., and Bueckner, H. F., 1988, "The Weight Function Theory for Piecewise Homogeneous Isotropic Notches in Antiplane Strain," ASME JOURNAL OF APPLIED MECHANICS, Vol. 55, pp. 596–603.

Stern, M., 1973, "A Boundary Integral Representation for Stress Intensity Factors," *Proceedings of the 10th Anniversary Meeting of the Society of Engineering Science*, Raleigh, N.C., Nov. 5–7, 1973.

Stroh, A. N., 1958, "Dislocations and Cracks in Anisotropic Elasticity," *Philosophical Magazine*, Vol. 7, pp. 625–646.

Stroh, A. N., 1958, "Steady State Problems in Anisotropic Elasticity," *Journal of Mathematical Physics*, Vol. 41, pp. 77–103.

Ting, T. C. T., and Chou, S. C., 1981, "Edge Singularities in Anisotropic Composites," *International Journal of Solids and Structures*, Vol. 17, No. 11, pp. 1057–1068.

Williams, M. L., 1952, "Stress Singularities Resulting from Various Conditions in An Angular Corners of Plates in Extension," ASME JOURNAL OF APPLIED MECHANICS, Vol. 19, pp. 526–528.

Wu, K.-C., 1988, "Stress Intensity Factors Due to Nonelastic Strains and Body Forces for Steady Dynamic Crack Extension in an Anisotropic Elastic Material," *International Journal of Solids and Structure*, Vol. 24, No. 8, pp. 805–811.

APPENDIX

In this Appendix, Eqs. (43), (44), and (46), for determining the intensity coefficients are derived. For simplicity, λ is assumed to be real. The case when λ is complex can be derived similarly. Let $\mathbf{f}$ and $\mathbf{f}^*$ be given by

$$\mathbf{f}=c\left(\frac{r}{\rho}\right)^{\lambda}\mathbf{\Lambda}(\theta,-\alpha,\lambda)\mathbf{q}+d\left[\left(\frac{r}{\rho}\right)^{\lambda}\mathbf{\Lambda}(\theta,-\alpha,\lambda)\mathbf{q}\right]' \tag{A1}$$

$$\mathbf{f}^*=c^*\left(\frac{r}{\rho}\right)^{-\lambda}\mathbf{\Lambda}(\theta,\alpha,-\lambda)\mathbf{q}+d^*\left[\left(\frac{r}{\rho}\right)^{-\lambda}\mathbf{\Lambda}(\theta,\alpha,-\lambda)\mathbf{q}\right]' \tag{A2}$$

where c and d are the intensity coefficients, c^* and d^* are arbitrary constants, $\mathbf{\Lambda}$ is given by Eq. (12), and the prime denotes partial differentiation with respect to β (or λ as λ is real). Substituting Eqs. (A1) and (A2) into Eq. (39) yields

$$\begin{aligned}c^*a+d^*a'=&(\mathbf{q}^T\mathbf{J}_{00}\mathbf{q})c^*c+(\mathbf{q}^T\mathbf{J}_{00}\mathbf{q}'+\mathbf{q}^T\mathbf{J}_{01}\mathbf{q})c^*d\\&+[(\mathbf{q}^T)'\mathbf{J}_{00}\mathbf{q}+\mathbf{q}^T\mathbf{J}_{10}\mathbf{q}]d^*c+[(\mathbf{q}^T)'\mathbf{J}_{00}\mathbf{q}'\\&+(\mathbf{q}^T)'\mathbf{J}_{01}\mathbf{q}+\mathbf{q}^T\mathbf{J}_{10}\mathbf{q}'+\mathbf{q}^T\mathbf{J}_{11}\mathbf{q}]d^*d\end{aligned} \tag{A3}$$

where a is given by Eq. (41) and $\mathbf{J}_{mn}$ is defined as

$$\mathbf{J}_{mn}=2\Re\left[\int_{-\alpha}^{\alpha}\left(\frac{\partial^m}{\partial\lambda^m}\mathbf{\Lambda}(\theta,\alpha,-\lambda)^T\frac{\partial}{\partial\theta}\frac{\partial^n}{\partial\lambda^n}\mathbf{\Lambda}(\theta,-\alpha,\lambda)\right)d\theta\right]. \tag{A4}$$

Note that since the integral I_1 in Eq. (39) is independent of r, one needs only to consider the terms that do not contain r in deriving Eq. (A3). The integrals $\mathbf{J}_{mn}$ can be integrated as

$$\mathbf{J}_{00}=\lambda\mathbf{C}',\quad \mathbf{J}_{01}=\frac{\lambda}{2}\mathbf{C}''+\mathbf{C}'$$

$$\mathbf{J}_{01}=\frac{\lambda}{2}\mathbf{C}'',\quad \mathbf{J}_{11}=\frac{\lambda}{6}\mathbf{C}'''+\frac{1}{2}\mathbf{C}''$$

where

$$\mathbf{C}^{(n)}=2\Re\left[\mathbf{B}^T\left\langle\left(\log\frac{\zeta(\alpha)}{\zeta(-\alpha)}\right)^n\left(\frac{\zeta(\alpha)}{\zeta(-\alpha)}\right)^{\lambda}\right\rangle\mathbf{B}\right].$$

Equation (43) is obtained by letting $d^*=d=0$ with the identity for δ' given by Eq. (29). Equation (44) is obtained by setting $\delta'=0$, and $d^*=0$ with the identity

$$\delta''=\lambda(2\mathbf{q}^T\mathbf{C}'\mathbf{q}'+\mathbf{q}^T\mathbf{C}''\mathbf{q}) \tag{A5}$$

where δ is given by Eq. (28) and Eqs. (19) and (25) have been used. Finally, Eq. (46) is obtained by assuming $c^*=0$ with

$$\begin{aligned}\delta'''=&3[2(\mathbf{q}^T)'\mathbf{C}'\mathbf{q}+\mathbf{q}^T\mathbf{C}''\mathbf{q}]+\lambda[\mathbf{q}^T\mathbf{C}'''\mathbf{q}\\&+6(\mathbf{q}^T)'\mathbf{C}'\mathbf{q}'+6\mathbf{q}^T\mathbf{C}''\mathbf{q}']\end{aligned} \tag{A6}$$

where again Eqs. (19) and (25) have been used.

Downloaded 03 May 2010 to 171.66.16.245. Redistribution subject to ASME license or copyright; see http://www.asme.org/terms/Terms_Use.cfm

J. K. Good
Professor,
Mem. ASME.

Z. Wu
Research Assistant.

School of Mechanical and
Aerospace Engineering,
Oklahoma State University,
Stillwater, OK 74078

The Mechanism of Nip-Induced Tension in Wound Rolls

Models which can be used to calculate the internal stresses within wound rolls of web material have all been confirmed to the center winding technique to date. The mechanism by which a nip roller can increase the wound in tension in the outer layer of the wound roll is presented. Results of this work have been used to establish new winding models which can accurately predict the internal stresses within a center wound roll with an impinged nip.

Introduction

A web is a continuous, flexible strip of material such as paper, plastic film, metal foil, textiles, and nonwoven materials which are stored at least on an intermediate basis in wound rolls. The wound roll format is popular as it accommodates high-speed automated manufacturing operations. Much of the winding which is currently performed is accomplished via a technique which is known as center winding with an undriven nip roll, refer to Fig. 1. This technique requires that the winding torque be provided to the center (called the core) of the winding roll. An undriven nip roll follows the outside radius of the winding roll with a dual purpose. One purpose is to help exude wound-in air from the wound roll which could lead to an unstable loosely wound roll package which is apt to sustain web defects during web storage or transport. The second purpose is to provide an increased tension in the web, above the web line tension, for the web winding process. This increased tension is due to a nip mechanics mechanism which heretofore has only been understood empirically. This publication is a presentation of results of analytical and experimental investigations which provide the first basic understanding of the nip-induced tension mechanism. Some reference will be made to a machine direction which is the direction in which the web travels through the web line.

Discussion

An empirical investigation of the effect of a rolling nip upon paper stacks resulted in a landmark publication by Pfeiffer (1968). In this publication, the first quantitative data was presented which showed the effects of nip load, nip diameter, and the number of sheets in the stack upon the nip induced tensions in the stack sheets. Pfeiffer noted in his tests that the sheets nearest the nip would displace in the direction of the moving nip while some of the sheets near the bottom of the stack would travel in the opposite direction. Using photomicrographs taken from the side of the nip/stack interface, he determined that the instant center of rotation did not lie at the nip/stack interface and in fact was located beneath the interface in the stack. Sheets above the instant center would travel in the direction of the rolling nip, sheets below would travel in the opposite direction.

Engineers and scientists have long been intrigued with the mechanism of rolling friction. In a classical paper published in 1876, Reynolds (1876) proposed a theory for rolling friction in which he attributed the rolling resistance to causes essentially the same as those responsible for ordinary sliding friction. Reynolds observed that when a metal cylinder rolls over a flat rubber surface that the cylinder moves forward, in each revolution, a distance less than the circumference of the cylinder. From his earlier work regarding the slip of leather belts over cylindrical pulleys Reynolds (1874) concluded that there was a similar kind of slipping between the roller and the rubber surface. Although Reynolds' conclusions were later discounted by Tomlinson (1929) it is interesting that these experiments were very similar in setup to Pfeiffer's although certainly the goals of the experiments were dissimilar. Tabor (1955) performed similar experiments which proved that there was an extension of the flat rubber prior to the inlet of the nip contact. Furthermore, he discerned that there was no notable slip between the rubber and a steel nip during the period of contact. Tabor concluded that the mechanism of rolling friction and

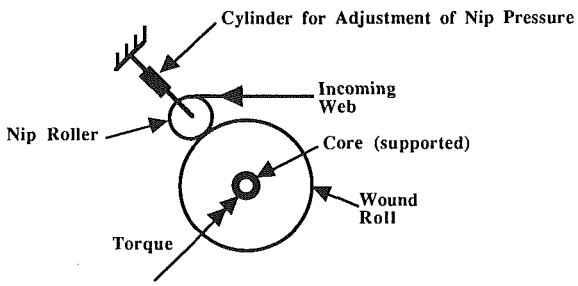


Fig. 1 A center winder with an impinging nip roller

Contributed by the Applied Mechanics Division of THE AMERICAN SOCIETY OF MECHANICAL ENGINEERS for publication in the ASME JOURNAL OF APPLIED MECHANICS.

Discussion on this paper should be addressed to the Technical Editor, Professor Lewis T. Wheeler, Department of Mechanical Engineering, University of Houston, Houston, TX 77204-4792, and will be accepted until four months after final publication of the paper itself in the ASME JOURNAL OF APPLIED MECHANICS.

Manuscript received by the ASME Applied Mechanics Division, Mar. 14, 1991; final revision, Feb. 11, 1992. Associate Technical Editor: M. E. Fourney.

Copyright © 1993 by ASME
Downloaded 03 May 2010 to 171.66.16.245. Redistribution subject to ASME license or copyright; see http://www.asme.org/terms/Terms_Use.cfm

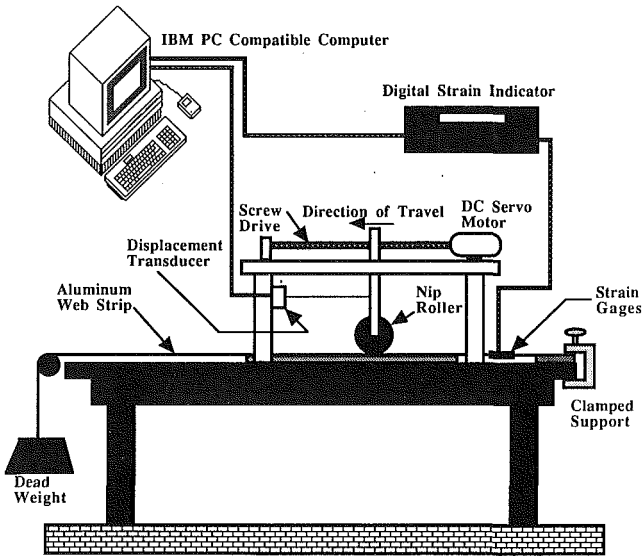


Fig. 2 Experimental apparatus

the associated energy loss was elastic hysteresis within the rubber.

The case of a nip rolling upon a web stack is fundamentally different from the case in which a nip is rolled across a relatively thick, homogenous solid such as rubber. Although slippage may not occur in the nip roll/web interface as described by Tabor, slippage can and does occur at the web sheet interfaces within the stack as will be shown. If this interlayer slippage can be determined as a function of nip load, nip diameter, and the available traction between web layers, then the nip induced tension can be determined.

An investigation was launched which began with a simple experiment. The purpose of this experiment and associated analyses was to determine the source or mechanism of the nip-induced tension.

Experimental Procedure

An experiment was designed in which the effects of elastic hysteresis would be minimal. Both Tabor and Pfeiffer had employed rubber in at least portions of their experiments. Of course the temptation to use rubber is high as Young's modulus is so low that the deformations are high, to the extent that they are visible. There is also a large amount of inherent hysteresis within rubber materials. Thus an engineering material, aluminum, was selected which would have low hysteresis but relatively high Young's modulus as the material which was to be rolled beneath the nip. Since the deformations would be small, a precise means of determining the elongation and nip-induced tensions would have to be incorporated.

The experimental apparatus is shown in Fig. 2. An aluminum strip of a UNS A92024-T3 (E = 72 GPa, ν = 0.33) material, 3.81 cm wide and 0.0254 cm thick, is rigidly clamped at one end of the test table. A dead weight was applied to the opposite end of the aluminum strip whose primary purpose was to keep the strip aligned upon the test table. Various amounts of dead weight could be applied to simulate the effect of varying the incoming web tension on the nip-induced tension. A dead weight of 22.24 N was used in all experiments which provided a pre-tension of 2.30 MPa in the strip prior to nip rolling. Aluminum nip rolls of 5.08, 10.16, 15.24, and 20.32-cm diameters were rolled across the strip at nip loads of 3.5, 7, 10.5, 14, and 17.5 N/cm (load per unit width of nip contact). The combination of a nip diameter of 5.08 cm and a nip load of 17.5 N/cm exerted the maximum Hertzian contact stress of 28.8 MPa. Since the compressive yield strength for the aluminum is 275.6 MPa, the stresses exerted upon the aluminum strip during all experiments were definitely within the elastic range. The nip-induced tension in the strip was sensed via strain gages that were oriented within a Wheatstone bridge to cancel any strains due to bending that might occur. The strain gage bridge was connected to a strain indicator. The analog output of the strain indicator was read by a data acquisition board which was resident in an IBM-PC compatible computer, thus allowing the strain from which the nip-induced tension could be inferred to be recorded. Each test for a given nip diameter and load was repeated five times and averaged to insure confidence in the data.

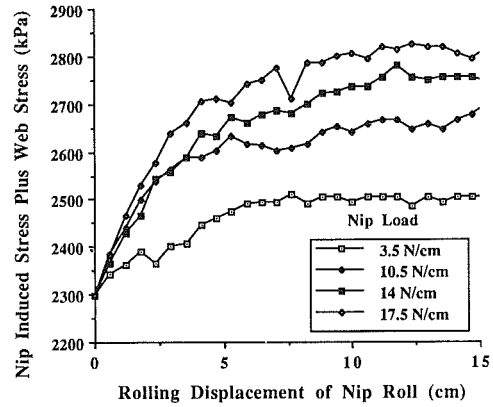


Fig. 3 Nip-induced stress versus rolling distance for a 5.08-cm diameter nip

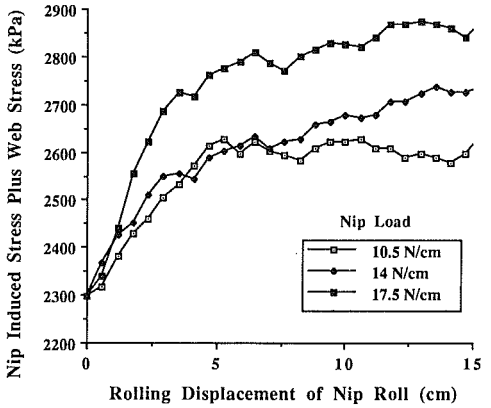


Fig. 4 Nip-induced stress versus rolling distance for a 10.16-cm diameter nip

Experimental Results

Since the stress in the strip after rolling is nominally uniform, the uniaxial form of Hooke's Law ($\sigma = E\epsilon$) was applied to convert uniaxial strains to stresses. Figures 3 and 4 show the nip-induced stresses overlaid upon the uniform pretensile stress discussed in the procedure for a 5.08 and 10.16-cm diameter nips, respectively. Data of similar form was recorded for 15.24, and 20.32-cm diameter nips as well. If a general form was given to the data presented, a relation such as

$$\sigma_x = C_1[1 - e^{-C_2 x}] + C_3 \quad (1)$$

would fit each and every curve well. In this relationship σ_x represents the total machine direction stress, C_1 represents the saturation value of the nip-induced stress, C_2 represents the growth rate of the nip-induced stress, and C_3 represents whatever pretension might have existed within the strip prior to the nip rolling.

Downloaded 03 May 2010 to 171.66.16.245. Redistribution subject to ASME license or copyright; see http://www.asme.org/terms/Terms_Use.cfm

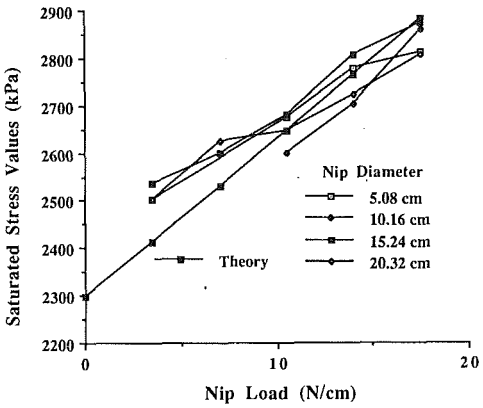


Fig. 5 Saturated values of the total induced stress

In Fig. 5 the saturation values of the total stress is shown versus nip load for various diameter nips. For each nip diameter, the saturated value of the total stress appears to be lineally dependent upon nip loading. For a differential tension to be sustained beneath the nip requires that a frictional force exists between the bottom of the aluminum strip and the steel test table which would be dependent upon the local sliding friction coefficient and the normal force or nip loading. Note that in Fig. 5 a theoretical plot of the saturated value of the total stress has been included which depicts the experimental data quite well for its simplicity. These values were obtained by measuring the coefficient of friction via a test defined by ASTM[1], multiplying the coefficient times the nip loading, dividing by the strip thickness, and adding the result to the pretension. Thus the explanation for the saturation in each of the curves in Figs. 3 and 4 is that the nip-induced tension has exceeded the product of the coefficient of sliding friction and the nip loading.

Although an explanation of why the nip-induced tension reaches a saturation value has been given, no explanation has been given as to what the mechanism is which causes the nip-induced tensions to occur prior to saturation. Finite element analyses will be employed to attempt to discern the mechanism.

Finite Element Analysis

The nip and the strip over which it is rolling might be modeled approximately as a Hertzian contact problem which was first described by Hertz (1881) and rigorously studied by Radzimovsky (1953). This indeed would be an approximation as the bodies in contact are assumed to be large in comparison to the dimensions of the compressed area. The half-width dimension of contact can commonly approach the web thickness and slippage is possible at the lower surface of the web. Thus, finite element analyses were employed such that the problem could be accurately modeled.

A model concept was formulated and is shown in Fig. 6 in which a moving, Hertzian parabolic pressure distribution would move across the upper surface of the web through time. The lower web boundary would be fully restrained vertically but only partially restrained horizontally to accommodate slippage and thereby friction.

Since the width of the tested strip was quite large compared to the thickness (3.81 cm vs 0.0254 cm), the strip was assumed to conform to plane strain conditions. The web was therefore modeled as two-dimensional plane-strain elements on COSMOS™/M[2], a finite element code which was employed for

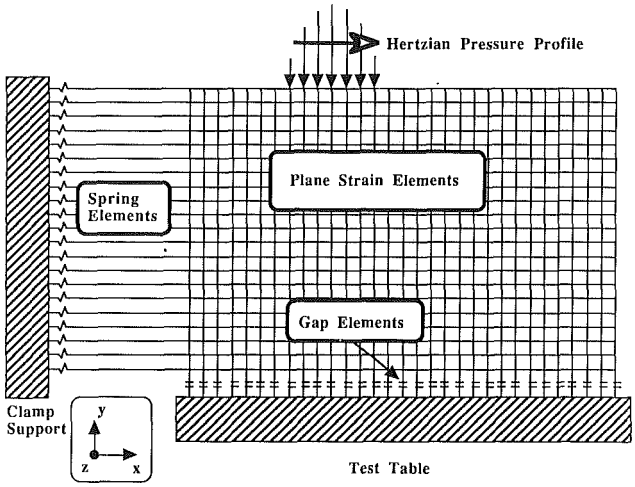


Fig. 6 The finite element model

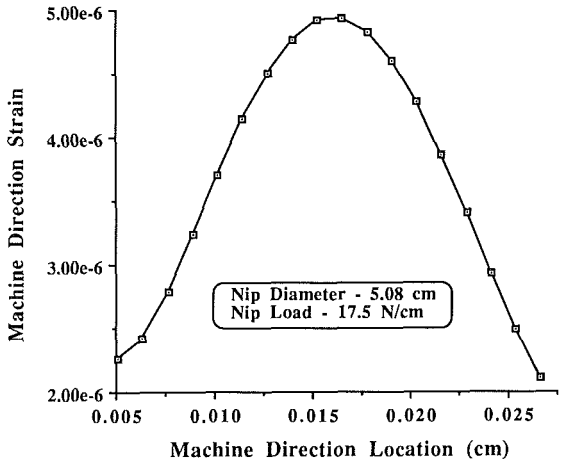


Fig. 7 Strain upon the lower surface of the web strip beneath the nip roller

the ability to solve problems involving geometric nonlinearity. Gap elements were placed upon the lower boundary to accommodate the slippage which must occur for a nip-induced tension to result. The model definition, refer to Fig. 6, portrayed the test apparatus described in the experimental procedure. The model consisted of 600 plane-strain elements (0.00127 cm × 0.00127 cm) representing the web beneath the nip, 21 spring elements which represent the axial stiffness of the web between the nip and the clamped support (a distance of 37.29 cm). 30 gap elements were employed to accommodate the slippage below the web beneath the nip. In successive time steps, the Hertzian pressure profile shown in Fig. 6 was moved to the right one element width.

Results of Finite Element Analysis

Case Study 1: A 5.08-cm Diameter Aluminum Nip With a 17.5 N/cm Nip Loading. From Radzimovsky (1953), this case yields a Hertzian half width of contact b of $3.86 * 10^{-3}$ cm and the maximum classical Hertzian contact pressure is 28.8 MPa. In perusing the results, the most interesting feature was that an elongating machine direction (x-direction) strain exists on the lower surface of the web strip. A plot of the elongating strain on the bottom surface of the web beneath the nip location is shown in Fig. 7 at the eighth time step. At the following time step the strain plot would be nearly identical except that the peak strain would have moved one nodal location to the right of the previous peak value location. Note

[1] "Standard Test Method for Static and Kinetic Coefficients of Friction in Plastic Film and Sheeting," *ASTM*, Vol. 08.02, pp. 133–137, 1989.

[2] COSMOS™/M, Structural Research and Analysis Corporation, 1661 Lincoln Boulevard, Suite 100, Santa Monica, CA, 90404.

Downloaded 03 May 2010 to 171.66.16.245. Redistribution subject to ASME license or copyright; see http://www.asme.org/terms/Terms_Use.cfm

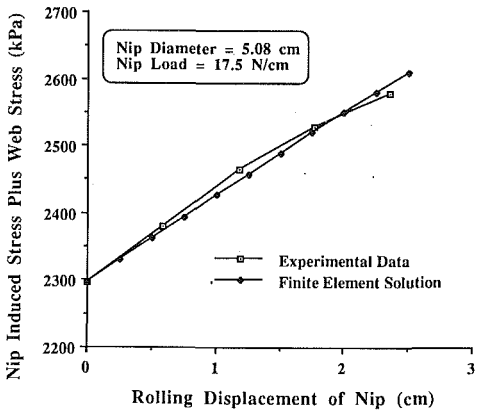


Fig. 8 Comparison of finite element analysis with experimental data—Case 1

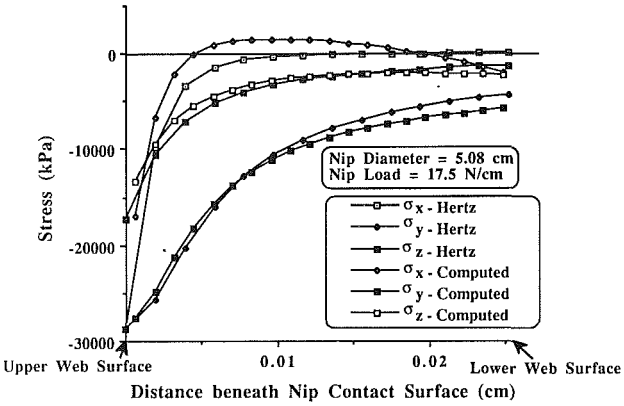


Fig. 9 Hertzian contact stresses compared to computed nip rolling stresses

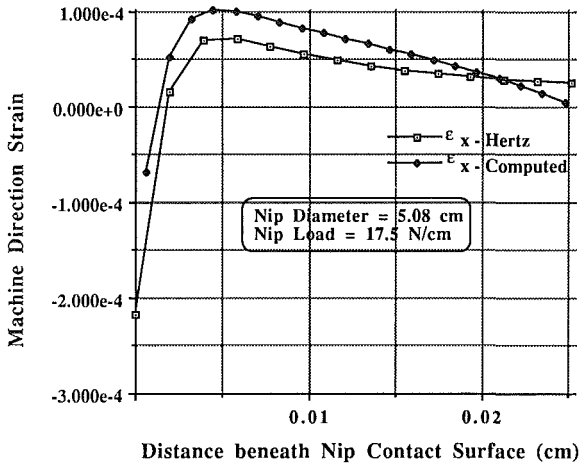


Fig. 10 Hertzian strain compared to computed nip rolling strain

as well that the strain distribution is not symmetric about the peak value location. Also note the increase in the elongating strain which exists across the nip due to the combination of the moving Hertzian pressure profile moving to the right over the upper surface of the web strip and the frictional forces on the lower surface. The maximum value of the elongating strain in Fig. 7 is 4.92 μS. Thus as the nip passes over the web strip, every point on the lower surface witnesses the elongating strain distribution shown in Fig. 7. The extension of the web strip due to the nip rolling over one finite element will be the integral of the strain, which is equivalent to the area under the curve in Fig. 7. The area under the curve, using trapezoidal rule integration, is found to be $8.665 * 10^{-8}$ cm which is the deformation contribution from the nip rolling over an element which is .00127 cm in length. The deformation of the web due to the nip roll moving 1 cm will be $8.665 * 10^{-8}$ cm * (1 cm/0.00127 cm) or $6.823 * 10^{-5}$ cm of displacement for every 1 cm of rolling distance. The strain in the web strip can be calculated using the following algorithm:

$$\epsilon_{\text{web}} = \frac{6.823 \times 10^{-5} \times \text{N.R.D.}}{L_i + \text{N.R.D.}} \tag{2}$$

where N.R.D. is the nip rolling distance (cm) and L_i is the initial distance between the clamped support and the nip roll prior to rolling (cm). Note that Eq. (2) is nonlinear with respect to the nip rolling displacement and is of the same form as Eq. (1). For large nip rolling displacements, Eq. (2) would yield that the web strain would approach a constant, however, experiments have shown that although a constant value is appropriate, the constant is dependent only upon the nip loading and the coefficient of friction as previously discussed, and not the higher strain level which would be predicted by Eq. (2). The nip-induced stress can be predicted using Eq. (2) for cases in which the saturated value of nip-induced tension has not been achieved. The nip-induced stress is calculated by multiplying the web strain by Young's modulus as the stress state in the web is unidirectional after passage of the nip. In Fig. 8 the data from Fig. 3 is presented again but note that only the first inch of rolling distance is now shown. The agreement between the experimental data and the finite element analysis is excellent. The comparison is made only over the first few centimeters of rolling distance as the slope of a curve through the experimental data begins to decrease due to slippage beginning to occur beneath the nip as the nip rolling distance increases as seen in Fig. 3.

In the finite element modeling the coefficient of traction between the aluminum web strip and the steel test table had to be selected. Early runs implemented coefficients of 0.085, which was the sliding coefficient of friction determined by tests in the laboratory. These early runs yielded nip-induced tension rates an order of magnitude higher than that reported. It became evident that an entirely different regime of friction existed during the presaturated stage of nip-induced tension than the sliding friction which was evident in the saturated stage as was discussed in the experimental results. During the presaturated stage the elongating strains on the lower surface are trapped by a high local contact pressure between the lower surface of the web strip and the test table. In this friction regime as the lower surface extends over the test table surface, it requires that surface asperities on the web strip surface and the test table surface to become dislodged requiring plastic deformation. Friction coefficients in the range of 1 to 2 have been reported for such cases by Bayer et al. (1969). Experimentation with the finite element model indicated that the elongating strain beneath the nip asymptotically approaches a minimum at coefficients near 2, a coefficient of 20 will not appreciably change the results. The coefficient of 2 was selected for reporting results since coefficients of friction higher than 2 have never been documented.

Another point of interest are the stresses which exist on a centerline beneath the point of contact between the nip roll and the web strip. The classical Hertzian contact stresses and the stresses computed by finite element analysis are shown in Fig. 9. After noting the similarity in the forms a plot of the machine direction strain was constructed for both the Hertzian and finite element stresses as shown in Fig. 10. Note that even although the classical Hertzian contact stresses are always compressive throughout much of the depth of the strip, they result in a elongating machine direction strain. This is the heart of the nip-induced tension mechanism. The three-dimensional stress-strain relationship for the machine direction strain is

Downloaded 03 May 2010 to 171.66.16.245. Redistribution subject to ASME license or copyright; see http://www.asme.org/terms/Terms_Use.cfm

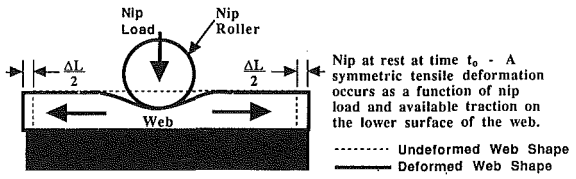


Fig. 11(*a*) Web deformation due to a static nip

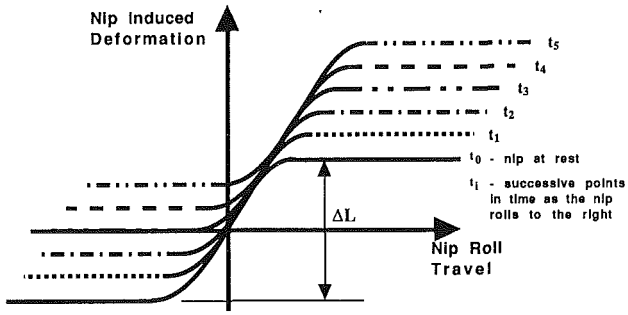


Fig. 11(*b*) Nip-induced deformations in stacks or wound rolls

$$\epsilon_x(\text{md}) = \frac{1}{E}\left[\sigma_x - \nu(\sigma_y + \sigma_z)\right] \tag{3}$$

for isotropic materials. Given that all three Hertzian contact stresses are negative compressive stresses, it is apparent that whenever the sum of the absolute values of σ_y and σ_z multiplied by Poisson's ratio is greater than σ_x, a positive machine direction strain, causing an elongation, will exist. This elongating strain distribution will proceed in the direction of rolling with material extending out in front of the nip and contacting behind the nip. If the material behind the nip is initially clamped the contraction is restrained and an increase in web strip tension between the nip and clamp will occur. This concept is shown in schematic form in Figs. 11(*a*) and 11(*b*). The classical Hertzian stresses are useful only in describing the phenomena of nip-induced tension. Finite element analyses are required if it is desired to accurately determine what the rate of nip-induced tension will be with respect to the nip rolling distance for a given nip diameter and loading, for a specific web strip geometry and web material, and for specific friction conditions.

Case Study 2: A 10.165-cm Diameter Aluminum Nip With a 10.5 N/cm Nip Loading. From Radzimovsky (1953), this case yields a Hertzian half width of contact b of $4.24 * 10^{-3}$ cm and the maximum classical Hertzian contact pressure is 15.7 MPa. As in the first case study, a coefficient of friction of 2 was implemented. A plot of the elongating strain on the bottom surface of the web beneath the nip location is shown in Fig. 12 at the eighth time step. The maximum value of the elongating strain in Fig. 12 is 2.94 μS. Thus, as the nip passes over the web strip, every point on the lower surface witnesses the elongating strain distribution shown in Fig. 12. The extension of the web strip due to the nip rolling over one finite element will be the integral of the strain, which is equivalent to the area under the curve in Fig. 12. The area under the curve using trapezoidal rule integration is found to be $5.114 * 10^{-8}$ cm, which is the deformation contribution from the nip rolling over an element which is .00127 cm in length. The deformation of the web due to the nip roll moving 1 cm will be $5.114 * 10^{-8}$ cm * (1 cm/0.00127 cm) or $4.027 * 10^{-5}$ cm of displacement for every 1 cm of rolling distance. The strain in the web strip can be calculated using the following algorithm:

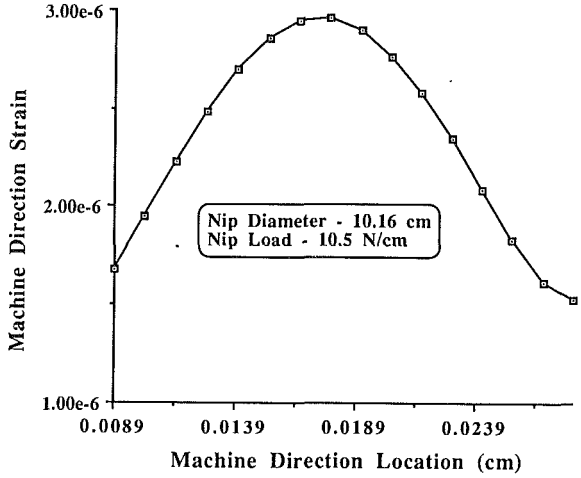


Fig. 12 Strain on the lower surface of the web strip beneath the nip roller

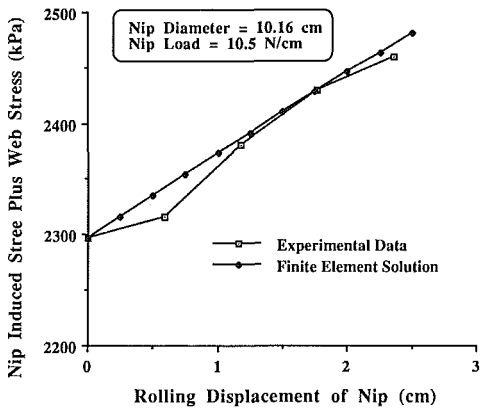


Fig. 13 Comparison of finite element analysis with experimental data—Case 2

$$\epsilon_{\text{web}} = \frac{4.027 \times 10^{-5} \times \text{N.R.D.}}{L_i + \text{N.R.D.}}. \tag{4}$$

In Fig. 13 the data from Fig. 5 is presented again but note that only the first centimeter of rolling distance is now shown. The agreement between the experimental data and the finite element analysis is excellent.

Conclusions

The mechanism which is responsible for nip-induced tension in wound rolls has been discovered. The mechanism is an elongating machine direction strain which exists beneath the nip roll location on the lower side of the web which is in intimate contact with the wound roll. This elongating strain is due to the compressive Hertzian-like contact stresses which exist through the depth of the web beneath the nip roller. As this elongating strain advances with the moving nip roll, web material attempts to advance in front of the nip and contact in towards the nip in back of the rolling nip. If the web material in back of the nip is constrained a net increase in tension will result due to the nip. The nip-induced tension cannot exceed the kinetic coefficient of traction between the outer wrap and the wrap beneath it multiplied by the nip loading. The ability to predict the nip-induced tension adds a new dimension to

Downloaded 03 May 2010 to 171.66.16.245. Redistribution subject to ASME license or copyright; see http://www.asme.org/terms/Terms_Use.cfm

the use of models for predicting internal stresses within wound rolls. These models are currently limited to centerwinding but with known nip-induced tensions can easily be extended to centerwinding with an undriven nip or to surface winding. This will be the topic of an upcoming paper by Good et al. (1992).

Acknowledgments

This publication is a result of research which was funded by the Web Handling Research Center of Oklahoma State University. The authors would like to thank the sponsors of the WHRC for supporting this research. The sponsors include the National Science Foundation, the Noble Foundation, the State of Oklahoma and an industrial consortium of which Beloit Corporation, Polaroid Corporation, Valmet-Appleton Inc., Fife Corporation, Hoescht-Celanese Corporation, 3M Company, Mobil Chemical Company, E. I. Dupont de Nemours & Co. (Inc.), ICI Americas, Kimberly-Clark Corporation, Mead Corporation, Westvaco Corporation, James River Graphics, Eastman Kodak Company, and Union Camp Corporation are members.

References

Bayer, R. G., Shalkey, A. T., and Wayson, A. R., 1969, "Design for Zero Wear," *Machine Design*, Vol. 41, Pt. I, pp. 142–151.

Good, J. K., Wu, Z., and Fikes, M. W. R., 1991, "The Internal Stresses in Wound Rolls with the Prescence of a Nip Roller," ASME JOURNAL OF APPLIED MECHANICS, submitted for publication.

Hertz, H., 1881, "Uber die Beruhrung fester elastischer Korper," *Journal fur die reine und Angewandte Mathematik*, Vol. 92, pp. 156–171.

Pfeiffer, J.D., 1968, "Mechanics of a Rolling Nip on Paper Webs," *TAPPI Journal*, Vol. 51, No. 8, pp. 77A–85A.

Radzimovsky, E. I., 1953, "Stress Distribution and Strength Condition of Two Rolling Cylinders Pressed Together," *Univ. Ill. Eng. Expt. Sta.*, Bulletin 408, pp. 1–40.

Reynolds, O., 1876, "On Rolling Friction," *Philosophical Transactions of the Royal Society of London*, Vol. 166, pp. 155–174.

Reynolds, O., 1874, "On the Efficiency of Belts or Straps as Communicators of Work," *Engineer Magazine*, p. 396.

Tabor, D., 1955, "The Mechanism of Rolling Friction II. The Elastic Range," *Proc. Roy. Soc. London*, Vol. A229, pp. 198–220.

Tomlinson, G. A., 1929, "A Molecular Theory of Friction," *The Philosophical Magazine*, Vol. 7, pp. 905–939.

Downloaded 03 May 2010 to 171.66.16.245. Redistribution subject to ASME license or copyright; see http://www.asme.org/terms/Terms_Use.cfm

Yozo Fujino
Professor,
Department of Civil Engineering,
University of Tokyo,
Bunkyo-ku, Tokyo 113, Japan

Pennung Warnitchai
Assistant Professor,
Division of Structural Engineering
and Construction,
Asian Institute of Technology,
Bangkok, Thailand

B. M. Pacheco
Structural Engineer,
Ammann and Whitney, Inc.,
New York, NY 10014-3309

Active Stiffness Control of Cable Vibration

To suppress cable vibrations, active stiffness control, *which changes the tension as a positive use of parametric excitation, is studied. An optimal algorithm is obtained from energy analysis and verified by experiment on a scale model. Numerical investigation is then made on the control of a combined system of cable and single-degree-of-freedom structure; the degree-of-freedom of the latter is along the cable axis. It is found by numerical simulation that instability occurs when the mass ratio of cable to structure is large, or when the frequency ratio of structure to cable is close to 2.0.*

Introduction

Cables are light, flexible, and low-damped and hence prone to have transverse vibrations due to winds or support motions. If cables are very long, control of such vibrations by the conventional passive dampers that are placed near the cable anchorage is very difficult (Pacheco et al., 1993). Active control at the boundary, i.e., cable anchorage, is an attractive alternate approach.

Chen (1984) showed by numerical simulations that longitudinal motion of the support of a string, which causes a time variation of transverse stiffness, can produce a damping effect on transverse vibrations; herein termed *active stiffness control.* (Some authors use the latter term to include any scheme that actively changes the stiffness of the structure.) Chen suggested an algorithm that causes the fundamental frequency of the time-varying part of the tension to be twice the frequency of free transverse vibration of the string. Natori et al. (1989) conducted a free-vibration experiment of a wire using Chen's algorithm to confirm the validity of active stiffness control, and also demonstrated an extension of the scheme to the control of membrane structures by numerical simulations.

In the present paper, we consider a taut cable (string) and follow the basic idea of Chen. Energy analysis is performed to obtain an optimal algorithm, which is subsequently implemented and verified in an experiment using a 2-m steel wire and a piezomechanical actuator. Numerical simulation is then carried out for the more realistic system of cable and single-degree-of-freedom structure, to see the effectiveness and the limitation of the active stiffness control in the presence of cable-structure interaction.

Active Stiffness Control Algorithm for Single Cable

Analytical Model. Figure 1(*a*) illustrates a cable with fixed boundary at one end and longitudinally time-varying boundary at the other. The movement of the boundary, $u(t)$, is driven by an actuator, and is assumed to be much smaller than the cable span, L. Neglecting the effect of sag, the cable is considered as a linear elastic string. The transverse vibration is considered to be confined in one plane. Axial inertia force is

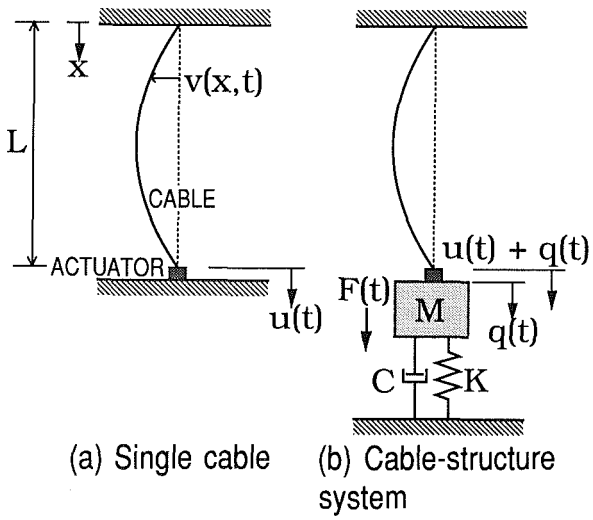


Fig. 1 Models for analysis

Contributed by the Applied Mechanics Division of THE AMERICAN SOCIETY OF MECHANICAL ENGINEERS for publication in the ASME JOURNAL OF APPLIED MECHANICS.

Discussion on this paper should be addressed to the Technical Editor, Professor Lewis T. Wheeler, Department of Mechanical Engineering, University of Houston, Houston, TX 77204-4792, and will be accepted until four months after final publication of the paper itself in the ASME JOURNAL OF APPLIED MECHANICS.

Manuscript received by the ASME Applied Mechanics Division, Dec. 26, 1991; final revision, May 11, 1992. Associate Technical Editor: R. L. Huston.

Copyright © 1993 by ASME
Downloaded 03 May 2010 to 171.66.16.245. Redistribution subject to ASME license or copyright; see http://www.asme.org/terms/Terms_Use.cfm

assumed negligible; consequently, the dynamic tension during transverse vibration is uniform over the span. This assumption is reasonable for low-order modes (Nayfeh and Mook, 1979). Employing a Lagrange formulation, with the normal modes of a fix-ended string as generalized coordinates, the governing equations of transverse motion of the taut cable can be obtained in a nondimensionalized form as (Warnitchai, 1990):

$$\frac{d^2\tilde{y}_n}{d\tau^2}+2\xi_n n\frac{d\tilde{y}_n}{d\tau}+n^2(1+\tilde{u}(\tau))\tilde{y}_n+\sum_{k=1}\tilde{\alpha}_{nk}\tilde{y}_n\tilde{y}_k^2=\tilde{F}_n(\tau) \quad (1)$$

where

$$\tilde{y}_n=\frac{y_n}{u_0},\quad \tilde{u}=\frac{u}{u_0},\quad \tau=\omega_1 t,\quad \tilde{\alpha}_{nk}=\frac{(nk\pi)^2u_0}{4L},$$

$$\tilde{F}_n=\frac{F_n}{mu_0\omega_1^2},\quad m=\frac{1}{2}\mu L,\quad \omega_n=\frac{n\pi}{L}\sqrt{\frac{T}{\mu}},$$

$$u_0=\frac{TL}{EA}\ \text{and}\ F_n=\int_0^L f(x,t)\sin\frac{n\pi x}{L}dx \quad (2a\text{–}i)$$

In the above equations, y_n is the generalized displacement of mode n; m is the generalized mass; ω_n is the undamped nth natural circular frequency; ξ_n is the corresponding critical damping ratio; α_{nk} is a cubic nonlinearity coefficient; F_n is the generalized force of mode n; u_0 is the static elongation from unstressed condition; μ is the mass per unit length; T is the static tension; E is the elastic modulus; A is the cross-sectional area; L is the cable span; and $f(x, t)$ is the distributed external transverse force.

In Eq. (1), the actuator-controlled (nondimensionalized) displacement $\tilde{u}(\tau)$ appears in the stiffness term, hence the name *active stiffness control*. The cubic nonlinearity arises from the geometrical effect of cable stretching. When considering structural cables, the dimensionless parameters n, ξ_n, u_0/L, and $\tilde{u}$ are generally of the following order of magnitude: $O(1)$, $O(10^{-3})$, $O(10^{-3})$, and $O(10^{-2})$, respectively. Since cable motion is generally large, effect of the finite motion, i.e., the nonlinearity, has to be included in Eq. (1) as will be shown in the experimental results.

Optimal Control Based on Energy Analysis. Energy analysis is conducted to clarify the mechanism and the optimal condition of the control. For simplicity, assume that the transverse vibration with active stiffness control, $\tilde{y}_n$, is harmonic with frequency, n', which is close to the undamped natural frequency n. The actuator displacement $\tilde{u}(\tau)$ is also assumed to be varied sinusoidally:

$$\tilde{y}_n(\tau)=\tilde{a}_{y_n}\cos n'\tau \quad (3)$$

$$\tilde{u}(\tau)=\tilde{a}_u\cos(sn'\tau+\gamma_{yu}) \quad (4)$$

where $\tilde{a}_u$, s, and γ_{yu} are the parameters of the control algorithm that must be selected. s is a positive constant. It is well known (Nayfeh and Mook, 1979) that parametric excitation occurs most easily when the ratio of the frequency is 2. Since n' is close to n, $s=2$ is a logical choice for Eq. (4).

Energy production, E_p, is defined here as the integral over one steady-state oscillation cycle of $\tilde{y}_n$, of the product of generalized velocity and generalized force (any term in Eq. (1)). The sign of E_p corresponding to the force may be positive or negative, corresponding to a net energy flow into the cable or out of the cable. The E_p due to the generalized force that is associated with $\tilde{u}(\tau)$, assuming $s=2$, is

$$E_p(n^2\tilde{u}\tilde{y}_n)=\int_0^{\frac{2\pi}{n'}}(-n^2\tilde{u}\tilde{y}_n)\frac{d\tilde{y}_n}{d\tau}d\tau=-\frac{1}{2}n^2\pi\,\tilde{a}_u\tilde{a}_{y_n}^2\sin\gamma_{yu}. \quad (5)$$

Meanwhile the E_p due to inherent damping is

$$E_p\left(2\xi_n n\frac{d\tilde{y}_n}{d\tau}\right)=\int_0^{\frac{2\pi}{n'}}\left(-2\xi_n n\frac{d\tilde{y}_n}{d\tau}\right)\frac{d\tilde{y}_n}{d\tau}d\tau=-2nn'\pi\xi_n\tilde{a}_{y_n}^2. \quad (6)$$

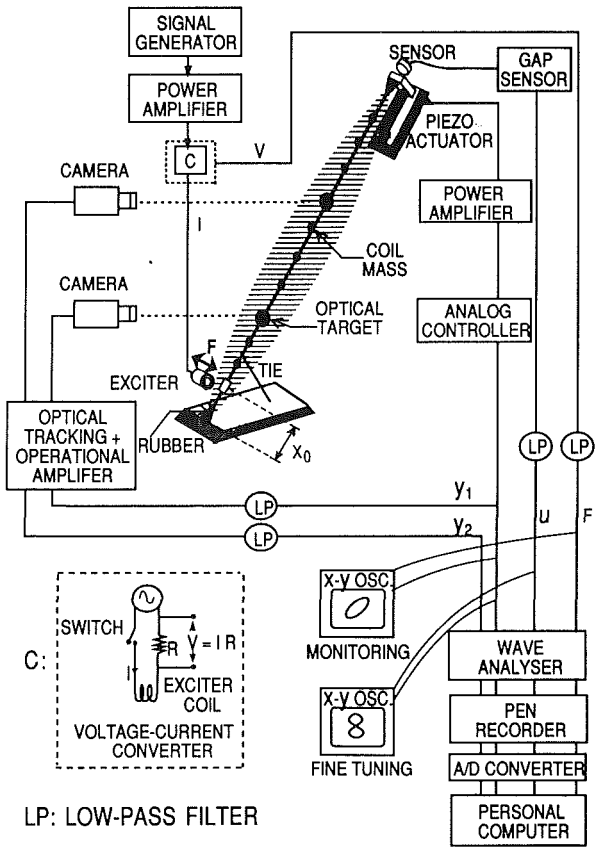


Fig. 2 Model, setup, and control components in the experiment

Equation (6) shows that a positive structural damping force always dissipates energy, since E_p is always negative. On the other hand, the boundary movement, $\tilde{u}(\tau)$, may either generate or dissipate energy, depending on the phase γ_{yu} (Eq. (5)). The energy generation is the energy source of the well-known parametric excitation, while the energy dissipation is the inverse effect that active stiffness control utilizes.

By equating the two expressions for E_p in Eqs. (5) and (6), the damping effect that is produced by stiffness variation can be evaluated in the form of equivalent additional damping ratio ξ_n^a:

$$\xi_n^a=\frac{1}{4}\frac{n}{n'}\tilde{a}_u\sin\gamma_{yu}\approx\frac{1}{4}\tilde{a}_u\sin\gamma_{yu}. \quad (7)$$

This simple relation shows that the equivalent damping ratio does not depend on oscillation amplitude, $\tilde{a}_{y_n}$; it depends on the amplitude of control, $\tilde{a}_u$, and the phase, γ_{yu}. The optimum damping can be obtained when γ_{yu} is equal to $\pi/2$.

When the frequency of $\tilde{y}_n$ varies slowly and slightly from the modal frequency n, or the amplitude is slowly varying with time, as in free vibration, the above scheme of optimal active stiffness control may be implemented through the following nonlinear feedback algorithm:

$$\tilde{u}(\tau)=\tilde{a}_u\left[\frac{2}{n'}\frac{\tilde{y}_n\cdot d\tilde{y}_n/d\tau}{\left\{\tilde{y}_n^2+\frac{(d\tilde{y}_n/d\tau)^2}{(n')^2}\right\}}\right]. \quad (8)$$

It may be easily verified that when $\tilde{y}_n$ is in fact steady and harmonic as in Eq. (3), Eq. (8) reduces to Eq. (4), with $s=2$ and $\gamma_{yu}=\pi/2$.

Experiment

Set-up. The experimental set-up shown in Fig. 2 is used to examine the actual performance of the optimal active stiffness

Downloaded 03 May 2010 to 171.66.16.245. Redistribution subject to ASME license or copyright; see http://www.asme.org/terms/Terms_Use.cfm

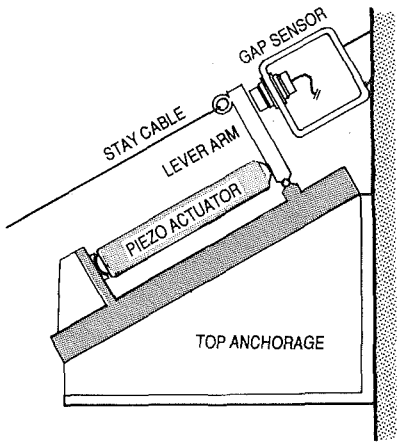


Fig. 3 Piezomechanical actuator and gap sensor for stiffness control of cable

control algorithm in a small-scale model. A stainless steel wire (SUS304 JIS) of 2.08 meter length is set to an actuator and a fixed end. Its cross-sectional area, A is 2.055×10^{-3} cm^2 and rope modulus of elasticity E is 1.74×10^{6} kgf/cm^2. To achieve proper dynamic similarities with actual structural cables, the wire is set with high initial tension ($T=83$ Newton); lumped masses at regular intervals are added on it ($m=0.07$ kg/m); and its anchorages are wrapped with rubber in order to obtain realistic inherent damping. To confine the motion of the cable in one plane, a small tie wire is installed near the lower anchorage.

Only harmonic excitation is considered in the experiment. For exciting the cable, a small steel cylinder is attached to the cable near the anchorage, and used as the attraction target for a DC electromagnet. The magnet is situated at the maximum possible gap from the target, such that the motion of the target itself is negligibly small compared with the gap. The relation between attraction force and coil current is nonlinear, and this relation is difficult to calibrate because of its sensitivity to the setting gap. Fortunately, it is found that the cable itself as a mechanical filter effectively removes all higher harmonic components of force that are created by the nonlinearity. The force calibration can be conducted indirectly by fitting experimental results with analytical prediction, without active control, as discussed as follows.

To measure the cable motion, very light optical targets were attached to the cable and their lateral movements are tracked by cameras.

An analog controller is employed in the experiment because of the high frequency requirement of the control of this model (maximum at 40 Hz). First, the frequency of observation signal is doubled. Then, using the phase-shifter, the relative phase between control signal and vibration signal is adjusted to the optimum value. (Fine adjustment of phase shift to compensate for time delay will be discussed.) Finally, the amplitude of control signal is adjusted to a specified value by amplifier.

The electrical control signal is converted to expansion of the piezomechanical actuator (see Fig. 3). By means of a lever transmission system, this expansion is magnified five times up to an axial displacement of 500 μm at the cable anchorage. The lever system also serves to apply precompression on the actuator which is rather brittle in tension. The operating frequency (maximum at 40 Hz) is much lower than the natural frequencies of this lever transmission system and actuator.

The movement of the lever arm is also directly measured by a inductive sensor (gap sensor) which is a noncontact type. This gap signal, which is proportional to $u(t)$, and the vibration signal $y(t)$, are viewed simultaneously in an x-y oscilloscope. The phase-shifter component of the analog controller

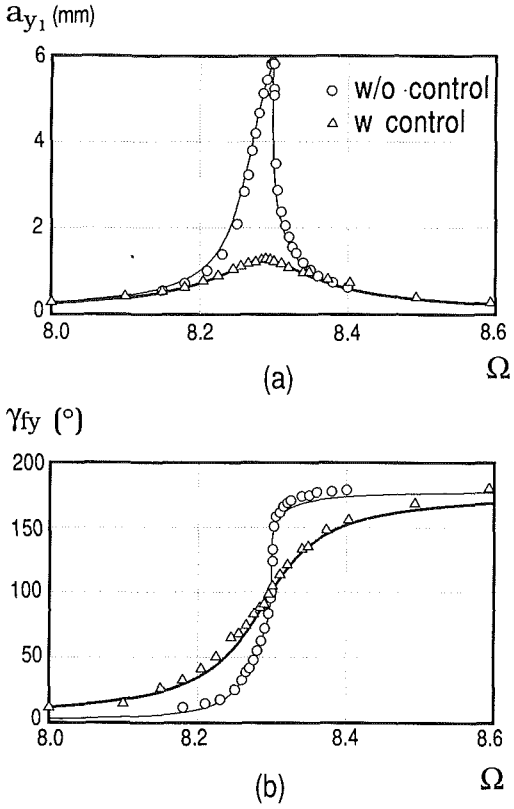


Fig. 4 Harmonic response (amplitude and phase) with and without active stiffness control

is manually adjusted until an "8" figure is displayed in the oscilloscope. This procedure compensates for the time delay due to the actuator, and ensures optimal control.

It must be pointed out that the low-pass filters are all set at the same cut-off frequency of 35.5 Hz to ensure the same phase delay in all filtered signals.

Identification of Structural Parameters. The approximate model for first mode vibration of the cable under harmonic external force can be obtained from Eq. (1) by neglecting the modal coupling terms

$$\frac{d^2\tilde{y}_1}{d\tau^2}+2\xi_1\frac{d\tilde{y}_1}{d\tau}+(1+\tilde{u}(\tau))\tilde{y}_1+\frac{\pi^2u_0}{4L}\tilde{y}_1^3 = \phi(x_0)a_f\cos\left(\frac{\Omega}{\omega_1}\tau\right) \quad (9)$$

where $\phi(x_0)=\sin\pi x_0/L$; x_0 is the point of application of the external force; a_f is the amplitude of force; and Ω is the exciting frequency.

From the free-oscillation test, $\omega_1/2\pi$ and ξ_1 are measured at 8.28 Hz and 1.6×10^{-3}, respectively. By Eq. (2g), the cable tension, T, can be computed from ω_1, and subsequently the initial strain is obtained as $u_0/L=2.43\times10^{-3}$ from Eq. (2h).

If $\tilde{u}(\tau)=0$, Eq. (9) is the well-known Duffing equation whose steady-state solutions can be analytically predicted (Nayfeh and Mook, 1979) in the following approximate form:

$$\tilde{y}_1=\tilde{a}_{y_1}\cos\left(\frac{\Omega}{\omega_1}\tau+\gamma_{fy}\right). \quad (10)$$

Steady-State Response. To investigate the frequency response of the first mode, the value of the excitation amplitude, a_f is kept constant while Ω is varied in the neighborhood of ω_1, with and without active stiffness control. The observed amplitudes at steady state are compared in Fig. 4.

The resonance curve without active stiffness control shows

Downloaded 03 May 2010 to 171.66.16.245. Redistribution subject to ASME license or copyright; see http://www.asme.org/terms/Terms_Use.cfm

a slight hardening; the peak is bent but not enough to create a jump phenomenon. The value of the excitation amplitude, a_f, is calibrated by equating the observed and predicted peak response. The thin curve in the same figure represents analytical prediction using the calibrated a_f.

With active stiffness control, $\tilde{a}_u$ and γ_{yu} are fixed at 2.27×10^{-2} (2.27 percent of initial elongation) and $\pi/2$ for all excitation frequencies Ω. Since the active stiffness control is equivalent to adding an equivalent damping ξ_1^a (Eq. (7)), the analytical prediction of steady response amplitude can be made by replacing ξ_1 by $\xi_1+\xi_1^a$ and omitting the stiffness variation term in Eq. (9). This analytical prediction is found to agree very well with the experimental results, as shown in Fig. 4.

It is experimentally confirmed that active stiffness control brings large reduction in the steady-state response even with small $\tilde{a}_u$.

The Effects of $\tilde{a}_u$ and γ_{yu}. The resonant peaks for different $\tilde{a}_u$ with optimum phase γ_{yu}, and for different phase γ_{yu} with fixed $\tilde{a}_u$ (2.27×10^{-2}), are shown in Figs. 5 and 6, respectively. Analytical predictions by Eqs. (7) and (11) are shown as full lines in the figures.

$$(a_{y_1})_{\text{peak w. control}}=\left(\frac{\xi_1}{\xi_1+\xi_1^a}\right)(a_{y_1})_{\text{peak w/o. control}} \tag{11}$$

Equation (11) is valid for linear and slightly hardening systems. The resonant frequency is slightly amplitude dependent in the latter case. In the experiment, the excitation frequency is slightly adjusted in order that this resonance peak is always reached.

The experimental results confirm that higher additional damping can be gained at higher $\tilde{a}_u$, and the damping is optimum when γ_{yu} is 90 deg ($\pi/2$). In both cases very good agreement with prediction is obtained; Eq. (7) is verified.

Control of the Second Mode. Another important feature of the active stiffness control is that it can be applied to any low-order mode. Control of the second mode with various values of the amplitude $\tilde{a}_u$ is experimentally studied under the optimal condition ($\gamma_{yu}=\pi/2$). The results are presented in Fig. 5 together with the prediction by Eq. (7) where $\xi_2=1.89\times10^{-3}$ as identified from free vibration is used. The experiment and the prediction are in very good agreement; both confirm the effectiveness of the active stiffness control.

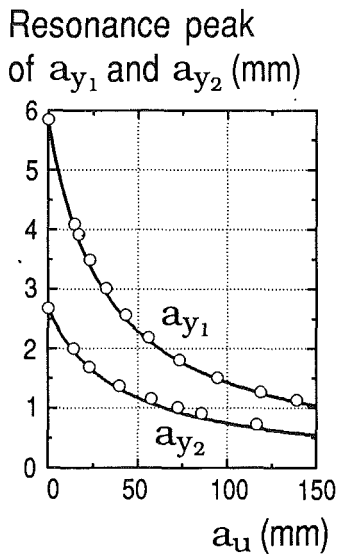


Fig. 5 Effect of control amplitude, a_u on the resonance peak amplitudes of the first and second modes

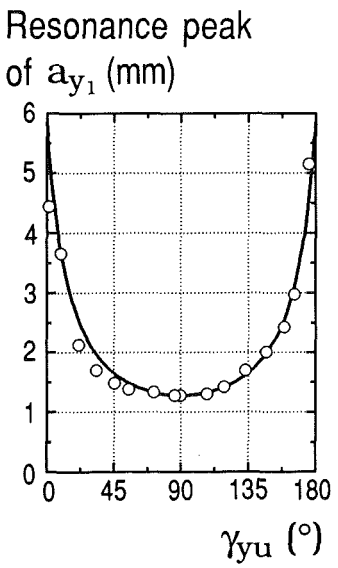


Fig. 6 Effect of phase, γ_{yu} on the resonance peak amplitude

Control of the Cable-Structure System

Analytical Model. Having verified the active stiffness control algorithm on a single-cable system, next we extend the study to a more realistic system comprising a cable and another structure as shown in Fig. 1(*b*). The previously fixed support of the cable is now attached to a single-degree-of-freedom structure that can move in the cable-axial direction. The governing equations of motion can be obtained in a nondimensionalized form as (Warnitchai, 1990) follows.

Cable mode n:

$$\frac{d^2\tilde{y}_n}{d\tau^2}+2\xi_n n\frac{d\tilde{y}_n}{d\tau}+n^2(1+\tilde{u}(\tau)+\tilde{q}(\tau))\tilde{y}_n+\sum_{k=1}\tilde{\alpha}_{nk}\tilde{y}_n\tilde{y}_k^2=\tilde{F}_n(\tau) \tag{12}$$

Structure:

$$\frac{d^2\tilde{q}}{d\tau^2}+2\xi\frac{\omega}{\omega_1}\frac{d\tilde{q}}{d\tau}+\left(\frac{\omega}{\omega_1}\right)^2\tilde{q}+\frac{1}{2}\frac{m}{M}\sum_{k=1}k^2\tilde{y}_k^2+\frac{2mL}{\pi^2Mu_0}\tilde{u}=0 \tag{13}$$

where

$$\tilde{q}=\frac{q}{u_0}\quad\text{and}\quad\omega=\sqrt{\frac{K+EA/L}{M}}. \tag{14}$$

q, M, ξ, and ω are generalized displacement, mass, damping, and circular natural frequency of the structure, respectively.

By comparing Eqs. 12 and 13 of the cable-structure system with Eq. (1) of the single-cable system, two new features can be identified. First, the structural motion $\tilde{q}$ affects the stiffness of the cable in the same way as the actuator displacement $\tilde{u}$ does. There are also feedback forces from the structure to the cable, by the term $\tilde{y}_k^2$. These are quadratic couplings which are sometimes called autoparametric couplings (Nayfeh and Mook, 1979). The coupling may generate internal resonance between $\tilde{q}$ and $\tilde{y}_n$ when $\omega=2\omega_n$, for example (Fujino et al., 1993).

Second, the actuator displacement $\tilde{u}(\tau)$ not only affects the stiffness of the cable but also provides active force on the structure. Significant structural motion may be induced by this force in certain conditions. From Eq. (13), if $\tilde{y}_k^2$ is neglected and $\tilde{u}$ is assumed to be harmonic at frequency $2\omega_n$, then the steady-state amplitude of the structural motion, $\tilde{a}_q$, can be approximated by

Downloaded 03 May 2010 to 171.66.16.245. Redistribution subject to ASME license or copyright; see http://www.asme.org/terms/Terms_Use.cfm

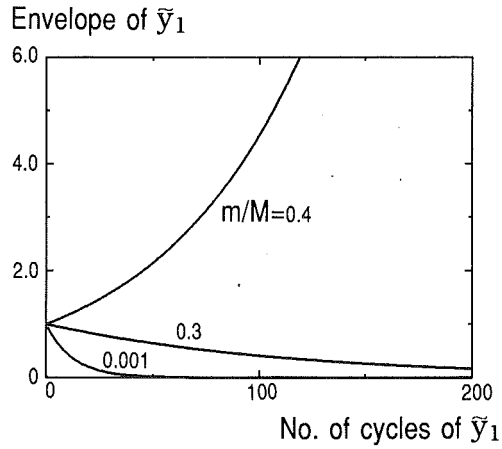


Fig. 7 Response envelopes for various mass ratios, *m/M*

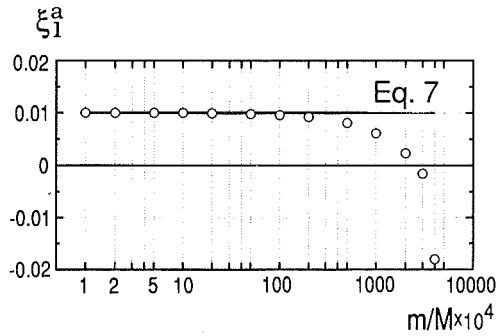


Fig. 8 Additional damping, ξ_1^a versus mass ratio, *m/M*

$$\tilde{a}_q = \left(\frac{2}{\pi^2}\frac{m}{M}\frac{L}{u_0}\tilde{a}_u\right)\left(\frac{\omega_1}{\omega}\right)^2\left(\frac{1}{\sqrt{\left(1-\left(\frac{2\omega_n}{\omega}\right)^2\right)^2+\left(\frac{4\xi\omega_n}{\omega}\right)^2}}\right). \tag{15}$$

This relation shows that large $\tilde{a}_q$ may occur when m/M is large (light structure), or when $\omega \approx 2\omega_n$ (resonance). Note that the latter condition is coincident with the internal resonance condition of quadratic coupling.

Numerical Simulation Scheme. Numerical simulation based on Eqs. (12) and (13) with the control algorithm of Eq. (8) is conducted. Only the first mode of the cable is considered together with the structure, i.e., $n=1$. Free vibration with initial condition of $\tilde{y}_1 = 1.0$ and $\tilde{q} = d\tilde{y}_1/d\tau = d\tilde{q}/d\tau = 0$ is simulated. The initial damping ξ and ξ_1 and initial strain u_0/L are specified as 3×10^{-3}, 3×10^{-3} and 2.5×10^{-3}, respectively. The amplitude of control $\tilde{a}_u$ is set to 0.04, and the phase γ_{yu} is set to the optimum value of $\pi/2$. The remaining parameters are ω/ω_1 and m/M; these are the key parameters to describe a variety of cable structure systems.

Adopting Milne's direct integration technique, approximately 100 time steps per oscillation cycle of $\tilde{y}_1$ are employed, to maintain numerical accuracy. From the free vibration history, the logarithmic decrement is calculated after every ten cycles of oscillation of $\tilde{y}_1$.

Instability When *m/M* is Large. Various simulation cases are conducted with m/M varying from 1×10^{-4} to 0.4. Time histories of envelope of $\tilde{y}_1$ for $m/M = 0.001$, 0.3 and 0.4 are presented as examples in Fig. 7. As the structure becomes light, the effectiveness of active stiffness control is very much reduced. The decay rate eventually becomes negative when the structure is too light as in the case of $m/M = 0.4$.

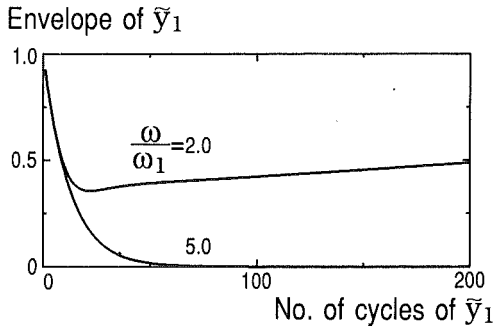


Fig. 9 Response envelopes for frequency ratios $\omega/\omega_1 = 2.0$ and 5.0

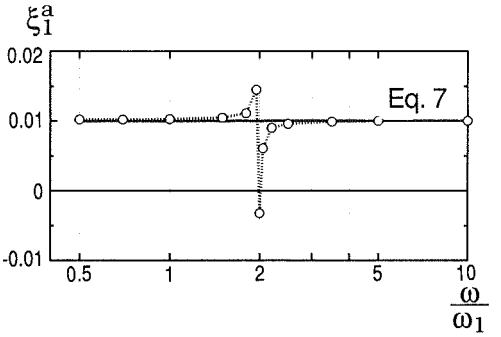


Fig. 10 Additional damping, ξ_1^a versus frequency ratio, ω/ω_1

The additional damping ξ_1^a is again computed from the logarithmic decrement of the free vibration history of $\tilde{y}_1$, subtracting the initial damping ξ_1; the results for various m/M values are plotted in Fig. 8. For small values of m/M, i.e., when the cable is light compared with the structure, the cable-structure interaction is weak. Then the cable vibration is practically an independent single-degree-of-freedom oscillation, for which the estimate of Eq. (7) is intended to be accurate. The ξ_1^a of simulated history becomes negative when $\tilde{a}_q$ as estimated by Eq. (15) becomes equal to $\tilde{a}_u$. It is apparently necessary to avoid the application of active stiffness control of cable to a cable structure system that has a light structural mass. For a civil cable-supported structure this may not be a problem, because the structure is generally massive.

Instability When $\omega/\omega_1 = 2.0$. There is another possibility that instability due to the control can be induced even though the structure is massive; that is when $\omega/\omega_1 \cong 2.0$, causing the time-varying tension to resonate with $\tilde{q}$. Therefore, various cases of ω/ω_1, from 0.5 to 10, are checked by simulation. The value of the mass ratio, m/M is specified as 1×10^{-3} in all cases.

The envelope of time history of $\tilde{y}_1$ in Fig. 9 shows that, indeed, instability occurs in the case of $\omega/\omega_1 = 2.0$; after about 50 cycles of $\tilde{y}_1$, the ξ_1^a computed from this envelope is negative. ξ_1^a for different values of ω/ω_1 are shown in Fig. 10. Significant divergence of ξ_1^a from the prediction of Eq. (7) is found only in the neighborhood of $\omega/\omega_1 = 2.0$. In this resonance zone, large $\tilde{a}_q$ is also induced as shown in Fig. 11. In this figure, the solid line is from Eq. (15); the points are from simulated history. Again it can be observed that when $\tilde{a}_q$ exceeds $\tilde{a}_u$ ($=0.04$), ξ_1^a becomes negative. Since Eq. (15) predicts $\tilde{a}_q$ well, indeed the stability limit of the other parameters in this equation may be determined by setting $\tilde{a}_q = \tilde{a}_u$.

Concluding Remarks

Active stiffness control of planar cable vibrations is experimentally and analytically studied. Optimal control algorithm

Downloaded 03 May 2010 to 171.66.16.245. Redistribution subject to ASME license or copyright; see http://www.asme.org/terms/Terms_Use.cfm

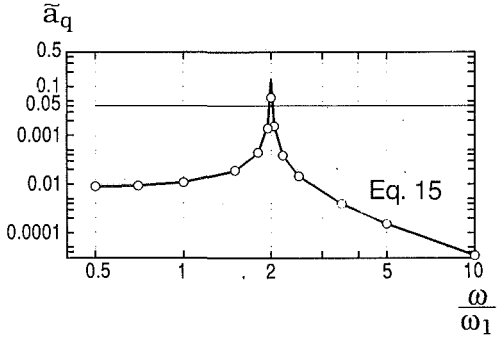


Fig. 11 Amplitude of structure, $\tilde{a}_q$ versus frequency ratio, ω/ω_1 (horizontal solid straight line corresponds to $\tilde{a}_q = \tilde{a}_u$ (= 0.04))

is obtained from energy analysis. The effectiveness and predictability of this algorithm is checked by experiment on a single cable model. The numerical study is further extended to the more realistic case: a cable structure system. Instability is found to occur when interaction between cable and structure becomes significant, i.e., when the structure is too light or is resonant with the control force. These cases have to be avoided in practical application.

Although the basic concept and effectiveness of active stiffness control are demonstrated here, for real implementation further studies are needed. These include: to control a more realistic cable which possesses three-dimensional motion and multiple modes, under realistic loading such as random force, and a more general cable-structure system where structural motion is not confined to the cable axial direction. The effects of sag on control is of concern as well.

Feasibility of the active stiffness control in engineering structures should be mentioned. In real cable structure systems such as cable-stayed bridges, hydraulic rams with servo mechanisms and pumps have been actually used during erection in order to give initial stresses to cables. This setup can be utilized for the active stiffness control as well as the active tendon control of the girder (Wanitchai et al., 1993), although some additional equipments such as accumulators might be needed to sustainedly supply high pressure fluid to actuators at high flow rate. In this sense, the authors believe that the active stiffness control is not unrealistic control means. As was shown in this paper, the dynamic force required for the active stiffness control is only a few percentages of the static tension of the cable.

Acknowledgments

The authors are grateful to T. Susumpow, R. Agret, and A. Agrawal for their assistance during the course of the experiments and numerical simulations.

References

Chen, J. C., 1984, "Response of Large Space Structures with Stiffness Control," *Journal of Spacecraft and Rockets*, AIAA 83-0344, Vol. 21, No. 5, pp. 463–467.

Fujino, Y., Wanitchai, P., and Pacheco, M. B., 1993, "An Experimental and Analytical Study of Autoparametric Resonance in a 3DOF Model of Cable-Stayed Beam," *International Journal of Nonlinear Dynamics*, No. 4, pp. 111–138.

Natori, M., et al., 1989, "Vibration Control of Membrane Space Structures Through the Change of Support Tension," *Proceedings of 40th Congress of the International Astronautical Federation*, IAF-89-335.

Nayfeh, A. H., and Mook, D. T., 1979, *Nonlinear Oscillations*, John Wiley and Sons, New York.

Pacheco, M. B., Fujino, Y., and Suekh, A., 1993, "Estimation Curve for Modal Damping in Stay Cables with Viscous Damper," *Journal of Structural Engineering*, ASCE, Vol. 119, No. 6, pp. 1961–1979.

Warnitchai, P., 1990, "Nonlinear Vibration and Active Control of Cable-Stayed Bridge," Doctoral Thesis, Department of Civil Engineering, University of Tokyo.

Warnitchai, P., Fujino, Y., Pacheco, B. M., and Agret, R., 1993, "An Experimental Study on Active Tendon Control of Cable-stayed Bridges," *Earthquake Engineering and Structural Dynamics*, Vol. 22, No. 2, pp. 93–111.

Downloaded 03 May 2010 to 171.66.16.245. Redistribution subject to ASME license or copyright; see http://www.asme.org/terms/Terms_Use.cfm

Conservation Laws in Systems With Variable Mass

L. Cveticanin
Faculty of Technical Sciences,
V. Vlahovica 3,
21000 Novi Sad,
Yugoslavia

In this paper, a method for obtaining conservation laws of dynamic systems with variable mass is developed. It is based on Noether's theorem to the existence of conservation laws and D'Alembert's variational principle. In the general case, a dynamic system with variable mass is purely nonconservative. Noether's identity for such a case is expanded by the terms that describe the mass variation. If Noether's identity if satisfied, a conservation law exists. Two groups of systems with variable mass are considered: a nonlinear vibrating machine and a rotor with variable mass. For these systems, conservation laws are obtained using the procedure developed in this paper.

1 Introduction

The conservation laws of both conservative and nonconservative dynamic systems with a finite number of degrees-of-freedom are of special interest in physics and engineering. One or more conservation laws can considerably simplify the integration of the differential equation of motion. If the number of independent conservation laws is twice the number of degrees-of-freedom, the motion of dynamic system is completely specified. The most popular up-to-date method for finding conservation laws is based on the study of the invariant properties of Hamilton's action integral with respect to infinitesimal transformations of the generalized coordinates describing the position of the system and time. This approach is based on Noether's theorem (Vujanovic, 1989). The Noetherian approach is valid only for those dynamic systems that are completely describable by means of a Lagrangian function. However, Noether's theorem does not offer any suggestion as how to find infinitesimal transformations that leave Hamilton's action integral unchanged. In several papers (Vujanovic, 1970; Djukic, 1973; Jones, 1967; Crespo de Silva, 1974), various methods for finding the aforementioned infinitesimal transformations and corresponding conservation laws are considered. In the paper of Vujanovic, Strauss, and Jones (1986), the conservation laws of purely nonconservative dynamic systems have been obtained by means of a variational principle of the Hamilton type that is suitable for nonconservative dynamic systems (variational principles with noncommutative rules (Djukic and Vujanovic, 1975) D'Alembert's differential variational principle (Vujanovic, 1978), general theory of multipliers (Djukic and Sutela, 1984)). It is of interest to see how these methods could be applied to the involving changing mass.

The aim of this paper is to find conservation laws of dynamic systems with variable mass and a finite number of degrees-of-freedom. Usually the mass variation is a function of time and position. If the mass varies in time a reactive force will take effect (Meshcherski, 1952). Depending on the form of the reactive force, two cases exist:

1 In spite of mass variation, the dynamic systems are completely describable by means of a single Lagrangian function. The Hamiltonian action integral exists, and its transformation properties, with respect to infinitesimal transformations of the generalized coordinates and time, have been the basis for finding conservation laws. This group of problems correspond to the Levi-Civita (Savin, Putjata, and Fradlin, 1964) case when the absolute velocity of mass conservation is zero. The procedure for obtaining first integrals for such systems has been developed. In Cveticanin (1993), the same method was applied to some examples of systems with variable mass.

2 The dynamic system is purely nonconservative. The system is not completely characterized by its Lagrangian. Since Hamilton's action integral does not generally exist for the case of nonconservative dynamic systems, the nonconservative effects will be included into the study of conservation laws by introducing some other basic physical invariant that correctly reflects the properties of nonconservative dynamic systems. This can be accomplished by taking D'Alembert's differential variational principle (Vujanovic, 1978) as the basic invariant. In this paper, an approach for obtaining conservation laws for such systems is developed.

2 The Equations of Motion of a Dynamical System With Variable Mass

Let us consider a dynamical system consisting of n particles with masses denoted by m_ν. The active forces operating on some point of the system are $\mathbf{F}_\nu$. Due to mass variation reactive forces $\mathbf{\Phi}_\nu$ will act, too. The virtual displacements of these points are $\delta\mathbf{r}_\nu$ ($\nu = 1, 2, \cdots, n$). D'Alembert's principle is

Contributed by the Applied Mechanics Division of THE AMERICAN SOCIETY OF MECHANICAL ENGINEERS for presentation at the ASME Winter Annual Meeting, New Orleans, LA, Nov. 28–Dec. 3, 1993.

Discussion on this paper should be addressed to the Technical Editor, Professor Lewis T. Wheeler, Department of Mechanical Engineering, University of Houston, Houston, TX 77204-4792, and will be accepted until four months after final publication of the paper itself in the ASME JOURNAL OF APPLIED MECHANICS.

Manuscript received by the ASME Applied Mechanics Division, Sept. 4, 1992; final revision, Dec. 30, 1992. Associate Technical Editor: D. J. Inman.

Paper No. 93-WA/APM-14.

Copyright © 1993 by ASME
Downloaded 03 May 2010 to 171.66.16.245. Redistribution subject to ASME license or copyright; see http://www.asme.org/terms/Terms_Use.cfm

$$\sum_{\nu=1}^{n}[m_\nu\ (d\mathbf{v}_\nu/dt)-\mathbf{F}_\nu-\mathbf{\Phi}_\nu]\delta\mathbf{r}_\nu=0 \tag{1}$$

where $\mathbf{v}_\nu$ is the velocity vector of the νth point.

Let us introduce the independent generalized coordinates q_i in such a way that each position vector can be represented as a function of these coordinates and time:

$$\mathbf{r}_\nu=\mathbf{r}_\nu(t,\ q_i),\quad \nu=1,\ \cdots,\ n,\quad i=1,\ \cdots,\ N. \tag{2}$$

Then, D'Alembert's principle is

$$\sum_{\nu=1}^{n}[m_\nu(d\mathbf{v}_\nu/dt)-\mathbf{F}_\nu-\mathbf{\Phi}_\nu]\sum_{i=1}^{N}(\partial\mathbf{r}_\nu/\partial q_i)\delta q_i=0. \tag{3}$$

Due to the relation,

$$\sum_{\nu=1}^{n}m_\nu(d\mathbf{v}_\nu/dt)\sum_{i=1}^{N}(\partial\mathbf{r}_\nu/\partial q_i)\delta q_i = \sum_{i=1}^{N}\delta q_i\sum_{\nu=1}^{n}m_\nu(dv_\nu/dt)\,(\partial\mathbf{r}_\nu/\partial q_i). \tag{4}$$

Equation (3) can be written in the form

$$\sum_{\nu=1}^{n}m_\nu(d\mathbf{v}_\nu/dt)\,(\partial\mathbf{r}_\nu/\partial q_i)=\sum_{\nu=1}^{n}[(d/dt)\,(\partial/\partial q_i)\,(m_\nu v_\nu^2/2) -(\partial/\partial q_i)\,(m_\nu v_\nu^2/2)-(dm_\nu/dt)\,(\partial/\partial\dot q_i)\,(\partial/\partial m_\nu)\,(m_\nu v_\nu^2/2) +(\partial m_\nu/\partial q_i)\,v_\nu^2/2]. \tag{5}$$

Let us introduce the kinetic energy T

$$T(t,q_i,\dot q_i)=1/2\sum_{\nu=1}^{n}m_\nu v_\nu^2, \tag{6}$$

and Eq. (5) is transformed to

$$\sum_{\nu=1}^{n}m_\nu(d\mathbf{v}_\nu/dt)\,(\partial\mathbf{r}_\nu/\partial q_i)=(d/dt)\,(\partial T/\partial\dot q_i)-\partial T/\partial q_i-D_i \tag{7}$$

where

$$D_i=\sum_{\nu=1}^{n}(\,(dm_\nu/dt)\,(\partial/\partial\dot q_i)\,(\partial/\partial m_\nu)\,(m_\nu v_\nu^2/2) -(\partial m_\nu/\partial q_i)\,v_\nu^2/2). \tag{8}$$

The forces $\mathbf{F}_\nu$ can be divided into two groups:

$$\mathbf{F}_\nu=\mathbf{F}_\nu'+\mathbf{F}_\nu''. \tag{9}$$

The forces $\mathbf{F}_\nu'$ are conservative and can be described by a force potential Π which means that

$$\sum_{\nu=1}^{n}\mathbf{F}_\nu'\,\delta\mathbf{r}_\nu=-\sum_{i=1}^{N}(\partial\Pi/\partial q_i)\delta q_i. \tag{10}$$

The forces $\mathbf{F}''$ are nonconservative and can be expressed as

$$\sum_{\nu=1}^{n}\mathbf{F}_\nu''\,\delta\mathbf{r}_\nu=\sum_{i=1}^{N}Q_i(t,q_i)\delta q_i, \tag{11}$$

where $Q_i(t,q_i)$ is a generalized force.

The reactive force is

$$\sum_{\nu=1}^{n}\Phi_\nu\,\delta\mathbf{r}_\nu=\sum_{i=1}^{N}\Delta_i(t,q_i,\dot q_i)\delta q_i. \tag{12}$$

Substituting Eqs. (7), (10), (11), and (12) into (3), the Lagrange differential equation of motion of the dynamic system with mass variable parameter is (Bessonov, 1967)

$$(d/dt)\,(\partial L/\partial\dot q_i)-\partial L/\partial q_i=D_i+Q_i+\Phi_i, \tag{13}$$

where $L=T-\Pi$ a Lagrangian function for the system.

For a single mass system, the differential equation of motion is

$$(d/dt)\,(\partial L/\partial\dot q_i)-\partial L/\partial q_i=(dm/dt)\,(\partial/\partial m)\,(\partial L/\partial\dot q_i) -(\partial m/\partial q_i)\,(\partial L/\partial m)+Q_i+\Phi_i. \tag{14}$$

If the mass variation is a function only of time t, then Eq. (13) becomes

$$(d/dt)\,(\partial L/\partial\dot q_i)-\partial L/\partial q_i =(dm/dt)\,(\partial/\partial m)\,(\partial L/\partial\dot q_i)+Q_i+\Phi_i. \tag{15}$$

Multiply Eq. (13) by δq_i and, after some transformations, we obtain

$$(d/dt)[(\partial L/\partial\dot q_i)\delta q_i]-(\partial L/\partial q_i)\delta q_i -(\partial L/\partial\dot q_i)\,(d/dt)\delta q_i=(D_i+Q_i+\Phi_i)\delta q_i. \tag{16}$$

Let us now accept the usual rule that the variation of velocity is equal to the velocity of variation

$$\delta\dot q_i=(d/dt)\,(\delta q_i). \tag{17}$$

The central Lagrangian Eq. (16) then becomes

$$(d/dt)[(\partial L/\partial\dot q_i)\delta q_i]=(\partial L/\partial q_i)\delta q_i +(\partial L/\partial\dot q_i)\delta\dot q_i+(D_i+Q_i+\Phi_i)\delta q_i. \tag{18}$$

3 Inclusion of Nonsimultaneous Variations into the Central Lagrangian Equation

The method for studying the conservative laws of dynamic systems depends on infinitesimal transformation, i.e., variations of generalized coordinates and time. The variations of generalized coordinates and time have to be introduced in the central Lagrangian equation. Let us introduce the nonsimultaneous variations (Vujanovic, 1989)

$$\delta q_i=\Delta q_i=\dot q_i\Delta t,\quad \delta\dot q_i=\Delta\dot q_i=\ddot q_i\Delta t. \tag{19}$$

Under these rules, (18) transforms to

$$d/dt[(\partial L/\partial\dot q_i)\,(\Delta q_i-\dot q_i\Delta t)]-[(\partial L/\partial\dot q_i)\Delta\dot q_i +(\partial L/\partial q_i)\Delta q_i+(\partial L/\partial t)\Delta t]+[(\partial L/\partial\dot q_i)\ddot q_i+(\partial L/\partial q_i)\dot q_i +(\partial L/\partial t)]\Delta t-(Q_i+\Phi_i+D_i)\,(\Delta q_i-\dot q_i\Delta t)=0. \tag{20}$$

Denoting

$$\Delta L=(\partial L/\partial\dot q_i)\Delta\dot q_i+(\partial L/\partial q_i)\Delta q_i+(\partial L/\partial t)\Delta t, \tag{21}$$

$$\dot L=(\partial L/\partial\dot q_i)\ddot q_i+(\partial L/\partial q_i)\dot q_i+(\partial L/\partial t), \tag{22}$$

Eq. (20) takes the form

$$d/dt[(\partial L/\partial\dot q_i)\,(\Delta q_i-\dot q_i\Delta t)+L\Delta t]-\Delta L-L(\Delta t)' -(Q_i+\Phi_i+D_i)\,(\Delta q_i-\dot q_i\Delta t)=0. \tag{23}$$

By adding and subtracting $\epsilon\dot P$, the time derivative of an arbitrary function multiplied by a small parameter ϵ, a function that depends on the generalized coordinates q_i, generalized velocities $\dot q_i$, and time t, we can rewrite Eq. (23) in the form

$$d/dt[(\partial L/\partial\dot q_i)\,(\Delta q_i-\dot q_i\Delta t)+L\Delta t-\epsilon P(\dot q_i,\ q_i,\ t)] -[\Delta L+L(\Delta t)'+(Q_i+\Phi_i+D_i)\,(\Delta q_i-\dot q_i\Delta t) =\epsilon\dot P(\dot q_i,\ q_i,\ t)]=0. \tag{24}$$

This equation represents the transformation of the central Lagrangian equation. The function $P(\dot q_i, q_i, t)$ is called the gauge function. The transformation of D'Alembert's principle (24) is the starting point for the construction of conservation laws for the system.

4 Conditions for the Existence of Conservation Laws

From Eq. (24), it is evident that if the relation

$$\Delta L+L(\Delta t)'+(Q_i+\Phi_i+D_i)\,(\Delta q_i-\dot q_i\Delta t)-\epsilon\dot P(\dot q_i,\ q_i,\ t)]=0 \tag{25}$$

is satisfied, the dynamic system with variable mass admits a conservation law of the form

Downloaded 03 May 2010 to 171.66.16.245. Redistribution subject to ASME license or copyright; see http://www.asme.org/terms/Terms_Use.cfm

$$(\partial L/\partial \dot{q}_i)\Delta q_i + [L - (\partial L/\partial \dot{q}_i)\dot{q}_i]\Delta t - \epsilon P(\dot{q}_i, q_i, t) = \text{const.} \tag{26}$$

Let us suppose that the infinitesimal transformations of the generalized coordinates and time are described by

$$\Delta q_i = \epsilon F_i(\dot{q}_i, q_i, t), \quad \Delta t = \epsilon f(\dot{q}_i, q_i, t). \tag{27}$$

Substituting these in Eq. (27), the condition for the existence of a conservation law of dynamic system with variable mass becomes

$$(\partial L/\partial \dot{q}_i)\dot{F}_i + (\partial L/\partial q_i)F_i + (\partial L/\partial t)f + [L - (\partial L/\partial \dot{q}_i)\dot{q}_i]\dot{f} + (Q_i + \Phi_i + D_i)(F_i - \dot{q}_i f) - \dot{P} = 0, \tag{28}$$

and the corresponding conservation law becomes

$$(\partial L/\partial \dot{q}_i)F_i + [L - (\partial L/\partial \dot{q}_i)\dot{q}_i]f - P(\dot{q}_i, q_i, t) = \text{const.} \tag{29}$$

Equation (28) is the basic Noether identity for the time variable mass system. For each infinitesimal transformation of the generalized coordinates and time of the form (27) and for each gauge function $P(\dot{q}_i, q_i, t)$ that satisfies condition (28) there exists a conservation law (29).

For a single mass system, the basic Noether identity becomes

$$(\partial L/\partial \dot{q}_i)\dot{F}_i + (\partial L/\partial q_i)F_i + (\partial L/\partial t)f + [L - (\partial L/\partial \dot{q}_i)\dot{q}_i]\dot{f} + [Q_i + \Phi_i + (dm/dt)(\partial/\partial m)(\partial L/\partial \dot{q}_i) - (\partial m/\partial q_i)(\partial L/\partial m)](F_i - \dot{q}_i f) - \dot{P} = 0. \tag{30}$$

If the mass variation is a function of time, then Eq. (30) simplifies to

$$(\partial L/\partial \dot{q}_i)\dot{F}_i + (\partial L/\partial q_i)F_i + (\partial L/\partial t)f + [L - (\partial L/\partial \dot{q}_i)\dot{q}_i]\dot{f} + [Q_i + \Phi_i + (dm/dt)(\partial/\partial m)(\partial L/\partial \dot{q}_i)](F_i - \dot{q}_i f) - \dot{P} = 0. \tag{31}$$

Let us prove that (29) is a conservation law.

Form the generalized basic Noether identity for the system with variable mass. Using the relation

$$d/dt[L - (\partial L/\partial \dot{q}_i)\dot{q}_i] = (\partial L/\partial t) + (\partial L/\partial q_i)\dot{q}_i - d/dt(\partial L/\partial \dot{q}_i)\dot{q}_i, \tag{32}$$

and substituting into (28), it is found that

$$d/dt\{[L - (\partial L/\partial \dot{q}_i)\dot{q}_i]f - P + (\partial L/\partial \dot{q}_i)F_i\} = (F_i - \dot{q}_i f)[d/dt(\partial L/\partial \dot{q}_i) - (\partial L/\partial q_i) - (Q_i + \Phi_i + D_i). \tag{33}$$

Under the supposition that the factor $(F - \dot{q}f)$ is different from zero, the right side of the Eq. (33) corresponds to the differential equation of motion of the system with variable mass (13). The left side of the equation represents the conservation law. This means that by satisfying Eq. (28), the relation (29) exists.

5 Conservation Law for Vibrating Machines With Variable Mass

In everyday life there are many vibrating machines where mass varies during the working period. These are the fundamental working elements of many transport machines, separators, etc., in the process industry. In Fig. 1 a model of a one-degree-of-freedom vibrating machine is shown. The description of these machines is given by Bessonov (1967). The mass of the system is varying with time. Due to the fact that the relative velocity of mass variation is different from zero, a reactive force acts. In machines in the process industry, special materials are built in. Their elastic properties are usually strongly nonlinear. For such systems, the mathematical model is (see Cveticanin, 1992)

$$m(t)\ddot{x} + x - k_3 x^3 + p(dm/dt)\dot{x} = 0, \tag{34}$$

where $m(t)$ is the variable mass, k_3 is the coefficient of nonlinear rigidity, and p is the constant coefficient of the reactive force.

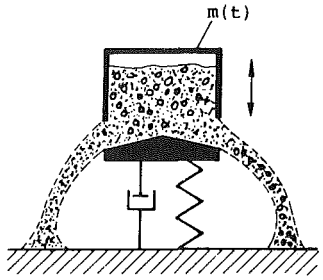


Fig. 1 Model of the vibrating machine with variable mass

The system is nonconservative. The Lagrangian and the reactive force are

$$L = m\dot{x}^2 - x^2/2 + k_3 x^4/4, \quad \Phi = -p(dm/dt)\dot{x}. \tag{35}$$

Let us suppose that the generators of the infinitesimal transformation (F and f) and the gauge function (P) are functions of x and t:

$$F = F(t, x), \quad f = f(t, x), \quad P = P(t, x). \tag{36}$$

Substituting (35) and (36) into (31) and separating the terms with the same power of $\dot{x}$, it is found that

$$(-x + k_3 x^3)F - \partial P/\partial t + (-x^2/2 + k_3 x^4/4)(\partial f/\partial t) = 0, \tag{37a}$$

$$m(\partial F/\partial t) - (p-1)(dm/dt)F - \partial P/\partial x + (-x^2/2 + k_3 x^4/4)(\partial f/\partial x) = 0, \tag{37b}$$

$$m(\partial F/\partial x) + (p - 1/2)f(dm/dt) - (m/2)(\partial f/\partial t) = 0, \tag{37c}$$

$$(1/2)(dm/dt)(\partial f/\partial x) = 0. \tag{37d}$$

Equation (37d) is identically satisfied for a function f which is independent on x. Analyzing the relation (37c), and using the previous fact it is obvious that F is a linear function of x. Examining the relation (37b) and the assumptions for the functions f and F, the function P depends on the second order of the variable x. It is concluded that the functions f, F, P may have the form

$$f = f(t), \quad F = xF_1(t), \quad P = x^2 P_1(t). \tag{38}$$

Substituting (38) into (37a-c), three equations with unknown functions f, F_1 and P_1 are obtained:

$$(-x^2 + k_3 x^4)F_1 - x^2(\partial P_1/\partial t) + (-x^2/2 + k_3 x^4/4)(\partial f/\partial t) = 0,$$
$$m(\partial F_1/\partial t) - (p-1)(dm/dt)F_1 - 2(\partial P_1/\partial x) = 0,$$
$$mF_1 + (p - 1/2)f(dm/dt) - (m/2)(\partial f/\partial t) = 0.$$

By light examination these functions are determined, and the corresponding functions (38) are

$$f = m^{(4/3)(p-1/2)}, \quad F = -(x/3)(p - 1/2)(dm/dt)m^{(4/3)(p-1/2)-1}, \quad P = -(x^2/4)m^{(4/3)(p-1/2)}. \tag{39}$$

For mass variation that satisfies the relation

$$(d^2m/dt^2) + 1/(3m)(p-2)(dm/dt)^2 = -3/(1-2p), \tag{40}$$

the conservation law is

$$m^{(4/3)(p-1/2)}[-\dot{x}x(p - 1/2)(dm/dt)/3 - m\dot{x}^2/2 - x^2/4 + k_3 x^4/4] = \text{const.} \tag{41}$$

For example, such a conservation law exists when the mass variation is given by

$$m = (\alpha + \beta t)^2, \quad \text{when } \beta = \mp 3/(1-2p),$$

which can occur in some real systems.

Let us consider some special cases:

(a) *The System is Linear.* In this case, the material properties of the system are linear ($k_3 = 0$) and the equation of motion for the system is

Downloaded 03 May 2010 to 171.66.16.245. Redistribution subject to ASME license or copyright; see http://www.asme.org/terms/Terms_Use.cfm

$$m(t)\ddot{x}+x+p(dm/dt)\dot{x}=0. \tag{42}$$

The conservation law (41) simplifies to the quadratic integral

$$m^{(4/3)(p-1/2)}[-x\dot{x}(p-1/2)(dm/dt)/3 - m\dot{x}^2/2-x^2/4]=\text{const.} \tag{43}$$

for the mass variation (40). For a singular solution of the mass Eq. (40),

$$m=(\alpha+\beta t)^2, \text{ when } \beta=\mp 3/(1-2p),$$

the conservation law (43) is valid, too.

(*b*) *Mass Variation Without Impact.* For the case when the relative velocity of mass variation is zero, the reactive force is $\Phi=0$. This means that the mass variation is without impact. The parameter p is equal to zero and the differential equation of motion becomes

$$m(t)\ddot{x}+x-k_3x^3=0. \tag{44}$$

For this dynamical system, the conservation law (41) is

$$m^{-(2/3)}[\dot{x}x(dm/dt)/6-m\dot{x}^2/2-x^2/4+k_3x^4/4]=\text{const.} \tag{45}$$

and

$$(d^2m/dt^2)-2/(3m)(dm/dt)^2=-3. \tag{46}$$

(*c*) *The Absolute Velocity of Adding or Separating Mass is Zero.* For that special case the parameter p is equal to 1 and the differential equation of motion becomes

$$(d/dt)(\dot{x}m)+x-k_3x^3=0. \tag{47}$$

This corresponds to an equation of Levi-Civita type. A conservation law exists and it is

$$m^{2/3}[\dot{x}x(dm/dt)/6-m\dot{x}^2/2-x^2/4+k_3x^4/4]=\text{const.} \tag{48}$$

when the mass is varying according to

$$(d^2m/dt^2)-1/(3m)(dm/dt)^2=3. \tag{49}$$

It is evident that the vibration properties of the machine are functions of mass variation. The results obtained in this paper can be used to construct integrals of motion for vibrating machines which satisfy the requirements of motion and mass variation.

Analyzing the differential equations of mass variation (46) and (49) it is seen that they are the members of an integrable class of equations of the form

$$(d^2m/dt^2)+f(m)(dm/dt)^2=g(m).$$

After some transformations the equation can be integrated because

$$(dm/dt)^2=2e^{-2\int f(m)dm}\int g(m)e^{[\int f(m)dm}dm+c_1e^{-2\int f(m)dm},$$

where c_1 is a constant value. So, the relation (46) is satisfied, for example, for mass variation, $m=(t^2-c_1/9)^{3/2}$, and Eq. (49) for $m=(c_1+t^2)^{3/4}$.

6 A Conservation Law for a Rotor With Time Variable Mass

Let us consider a rotor with variable mass. It is the fundamental working element of a number of machines in the process (paper, cable, textile, etc.) industry. The rotor represents a two-degree-of-freedom system. In Fig. 2 a graphical illustration of a rotor with variable mass is plotted. It is a shaft-disk system. The mass of the shaft varies in the course of time. Due to mass variation, a reactive force acts. It is a function of time. The elastic properties of the shaft material are linear. The mathematical model of the rotor is, after Cveticanin (1984),

$$m(t)\ddot{z}+cz=(dm/dt)q(t)e^{i\theta} \tag{50}$$

where $z=x+iy$ is the complex deflection of the mass center, $i=\sqrt{-1}$ is the imaginary unit, $m(t)$ is a variable mass, c is rigidity coefficient, $q(t)$ is a time variable function, $\theta=\tan^{-1}(y/x)$, and $(dm/dt)q(t)e^{i\theta}$ is the reactive force.

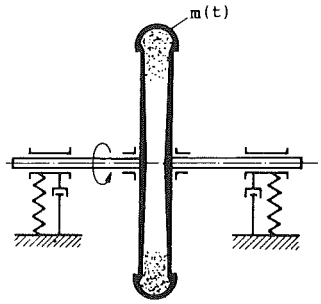


Fig. 2 Model of the rotor with time variable mass

Introducing polar coordinates r and θ, the complex function is

$$z=re^{i\theta}, \tag{51}$$

and the differential equation of motion (50) becomes a system of two differential equations

$$m(t)(\ddot{r}-r\dot{\theta}^2)+cr=(dm/dt)q(t), \tag{52a}$$

$$m(t)(2\dot{r}\dot{\theta}+r\ddot{\theta})=0. \tag{52b}$$

The second equation (52*b*) has a first integral

$$r^2\dot{\theta}=K, \tag{53}$$

where K is an arbitrary constant.

Substituting (53) into (52*a*), it follows that

$$m(t)\ddot{r}-m(t)K^2/r^3+cr=(dm/dt)q(t). \tag{54}$$

A Lagrangian function and the reactive force are

$$L=m\dot{r}^2/2-cr^2/2-mK^2/(2r^2),\quad \Phi=(dm/dt)q(t). \tag{55}$$

Using the procedure developed in this paper, the following functions can be obtained:

$$f=2t/m,\quad F=r/m,\quad P=-4rq(t), \tag{56}$$

when

$$q(t)=m^{-1/4}. \tag{57}$$

So, for

$$m(t)=t^2, \tag{58}$$

the conservation law is

$$r\dot{r}+(2t/m)[-m\dot{r}^2/2-cr^2/2-mK^2/(2r^2)] + 4rm^{-1/4}=\text{const.} \tag{59}$$

It corresponds to the case when the band is winding up on the disk.

7 Conclusions

A method for studying conservation laws of purely nonconservative dynamic systems is extended to dynamic systems with variable mass. The method is based on D'Alembert's differential variational principle and Noether's theorem. The condition for the existence of conservation laws contains terms that specify the mass variation. The form of the conservation law is the same as for purely nonconservative dynamic systems. Special attention is given to time variable mass systems where a reactive force acts. The reactive force is directly included into Noether's identity. The method developed in this paper is applied to two groups of systems: vibrating machine and rotor with variable mass. In these examples the conservation laws specify the motion of the dynamic systems completely.

Acknowledgment

Research was supported by Governments of Serbia and VANU.

Downloaded 03 May 2010 to 171.66.16.245. Redistribution subject to ASME license or copyright; see http://www.asme.org/terms/Terms_Use.cfm

References

Bessonov, A. P., 1967, *Osnovji dinamiki mehanizmovs peremennoj massoj zvenjev*, Nauka, Moscow.

Crespo de Silva, M. R. M., 1974, "A Transformation Approach for Finding First Integrals of Motion of Dynamical Systems," *Int. J. Non-Linear Mechanics*, Vol. 9, pp. 241–250.

Cveticanin, L., 1986, "Vibrations of a Textile Machine Rotor," *J. Sound and Vibration*, Vol. 97, No. 2, pp. 181–187.

Cveticanin, L, 1992, "The Influence of the Reactive Force on a Nonlinear Oscillator with Variable Parameter," *J. of Vibration and Acoustics*, Vol. 114, No. 4, pp. 578–580.

Cveticanin, L., 1993, "Some Conservation Laws for Orbits Involving Variable Mass and Linear Damping," *AIAA Journal*, Vol. 114, No. 4, pp. 578–580.

Djukic, Dj., 1973, "A Procedure for Finding First Integrals of Mechanical Systems with Gauge-Variant Lagrangians," *Int. J. Non-Linear Mechanics*, Vol. 8, pp. 479–488.

Djukic, Dj., and Vujanovic, B., 1975, "Noether's Theory in Classical Nonconservative Mechanics," *Acta Mechanica*, Vol. 23, pp. 17–27.

Djukic, Dj., and Sutela, T., 1984, "Integrating Factors and Conservation Laws for Non-Conservative Dynamical Systems," *Int. J. Non-Linear Mechanics*, Vol. 19, No. 4, pp. 331–339.

Jones, S. E., and Ames, W. F., 1967, "Similarity Variables and First Integrals of Ordinary Differential Equations," *Int. J. Non-Linear Mechanics*, Vol. 2, pp. 257–260.

Meshcherski, I. V., 1952, *Raboti po mehanike tel peremenno j massji*, Gos.izd.tehn.lit., Moscow.

Savin, G. N., Putjata, T. V., and Fradlin, B. N., 1964, *Ocherki razvitija nekotorjih fundamentalnjih problem mehaniki*, Naukova dumka, Kiev.

Vujanovic, B., 1970, "A Group-Variational Procedure for Finding First Integrals of Dynamical Systems," *Int. J. Non-Linear Mechanics*, Vol. 23, pp. 269–278.

Vujanovic, B., 1978, "Conservation Laws of Dynamical Systems Via D'Alembert's Principle," *Int. J. Non-Linear Mechanics*, Vol. 13, pp. 185–197.

Vujanovic, B., Strauss, A. M., and Jones, S. E., 1986, "On Some Conservation Laws of Conservative and Nonconservative Dynamical Systems," *Int. J. Nonlinear Mechanics*, Vol. 21, p. 489.

Vujanovic, B. D., and Jones, S. E., 1989, *Variational Methods in Nonconservative Phenomena*, Academic Press, New York.

Downloaded 03 May 2010 to 171.66.16.245. Redistribution subject to ASME license or copyright; see http://www.asme.org/terms/Terms_Use.cfm

J. B. Gómez
Graduate Student,
Departamento de Geología.

A. F. Pacheco
Professor,
ICMA and Departamento de Física.

A. J. Seguí-Santonja
Associate Professor,
Departamento de Física.

Facultad de Ciencias,
Universidad de Zaragoza,
50009 Zaragoza, España

Instability of Loaded Fractal Trees

We analyze the failure strength of loaded structures of the fractal-tree type, from a probabilistic perspective. The consideration of the intrinsic fragilities of the basic elements at each level of the tree makes the tree differ from being equivalent to a mere hierarchically organized bundle of fibers. A simple criterion for having a linear proportionality between the size of the tree and the inverse of the threshold strength for failure is found.

1 Introduction

Many natural systems remind us of the structure of fractal trees in their various modes (see the classical book by Mandelbrot, 1982). This type of structure can also be useful for different engineering designs. A few years ago, Turcotte, Smalley, and Solla (1985) (TSS) analyzed the stability of loaded fractal trees from a probabilistic point of view, concluding that there should exist a critical value for the onset of catastrophic failure, and it should appear sooner than what would be expected in terms of the mean failure probability of the constituent elements. The specific model used by TSS has recently been analyzed by Newman and Gabrielov (1991) who have proved, using computational and analytic means, that the conclusions drawn in TSS (1985) were incorrect. They "looked"at the model as a hierarchical distribution of fiber bundles (Daniels, 1945; Smith and Phoenix, 1981; McCartney and Smith, 1983) and found that, with independence of the specific failure properties of an individual element (fiber), large enough bundles always collapse; furthermore, the threshold for global failure meets a universal scaling law of the logarithmic type.

In this paper we come back to the TSS (1985) model and call attention to the fact that the only source of instability actually considered by these authors consisted of the intrinsic fragilities of the elements belonging to the first level; then, this instability propagates upwards along the whole network of the tree. This fact is more apparent after reading Smalley et al. (1985). In an actual mechanical structure of the fractal-tree type, however, the elements of the successive levels must have a non-null intrinsic probability of failure. After including the intrinsic fragilities at all levels, the model is no longer equivalent to a hierarchical distribution of fiber bundles, as analyzed in Newman and Gabrielov (1991). The quantitative consideration of this concept of intrinsic probability, which brings about an increase in the probability of general collapse, is the main goal of this paper. In the next sections, this idea will be developed in detail; the model is presented in Section 2; the results under certain specific hypotheses are gathered in Section 3, and finally, in Section 4, we state our conclusions.

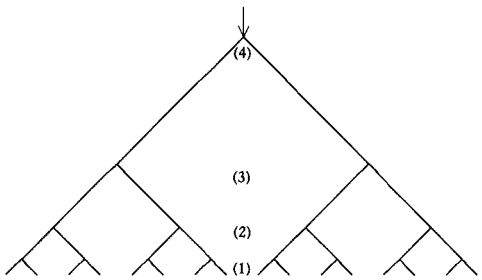


Fig. 1 Illustration of a fractal tree with $N = 4$, and a coordination number equal to two. A vertical force is applied onto the apex. The numbers in brackets denote the successive levels.

2 The Model

For maximum simplicity let us consider a two-dimensional fractal tree with a coordination number equal to 2 (two branches per knot) as shown in Fig. 1. Each level, labelled by the n index, is formed by pairs of elements—legs—linked together to one leg of the $(n+1)$ floor, which is paired likewise so that the whole structure looks like a level-independent form. In the apex of the tree $(n=N)$ we assume an applied vertical force which is supported by the successive levels, so that if no leg is broken, denoting by ${}^{(n)}\sigma_1$ the weight supported by any one of the elements of the nth level, we would have ${}^{(n+1)}\sigma_1 = 2\,{}^{(n)}\sigma_1$. In fact the term weight has been used in a generic sense; we can easily imagine the fractal tree as a fluid (electric, etc.)

Contributed by the Applied Mechanics Division of THE AMERICAN SOCIETY OF MECHANICAL ENGINEERS for publication in the JOURNAL OF APPLIED MECHANICS.

Discussion on this paper should be addressed to the Technical Editor, Professor Lewis T. Wheeler, Department of Mechanical Engineering, University of Houston, Houston, TX 77204-4792, and will be accepted until four months after final publication of the paper itself in the JOURNAL OF APPLIED MECHANICS.

Manuscript received by the ASME Applied Mechanics Division, Nov. 13, 1991; final revision, June 25, 1992. Associate Technical Editor: R. M. Bowen.

Copyright © 1993 by ASME
Downloaded 03 May 2010 to 171.66.16.245. Redistribution subject to ASME license or copyright; see http://www.asme.org/terms/Terms_Use.cfm

distribution network with an analogous pressure (current, etc.) partition.

Having specified what the typical weight supported by the legs on each level is, now we will assume that the intrinsic probability of failure of a leg at the nth level, ${}^{(n)}p_a$, when it bears a weight ${}^{(n)}\sigma_a = a\,{}^{(n)}\sigma_1$ fulfills a cumulative Weibull distribution (see, for example, Johnson and Leone, 1977), i.e.,

$$ {}^{(n)}p_a = 1 - e^{-\left[\frac{{}^{(n)}\sigma_a}{{}^{(n)}\sigma_0}\right]^m} \tag{1} $$

where ${}^{(n)}\sigma_0$ is a reference strength for that level and m (the index or shape parameter) is typically a number between 1 and 10. As is well known, this distribution fulfills the condition ${}^{(n)}p_{2a} = 1 - [1 - {}^{(n)}p_a]^2$. Obviously, the properties of ${}^{(n)}p_a$, expressed by Eq. (1), are characteristic of that leg without any reference to the specifications of the fractal tree where that leg is inserted, like the coordination number, the position in the vertical ranking, etc.

It is clear that because of being located in the tree, the failure of the leg at level n materializes not only as a result of the mentioned intrinsic probabilities, but also because of the failure of the pair of legs under it, at level $(n-1)$. This second probability of breakage will be denoted by ${}^{(n)}p'$. Hence, we will have

$$ {}^{(n)}P_a = {}^{(n)}p_a + [1 - {}^{(n)}p_a]\,{}^{(n)}p'_a, \tag{2} $$

${}^{(n)}P$ being the total probability of failure of a leg at the nth level and Eq. (2) expresses that p and p' are independent.

We will assume the principle of equal weight sharing (Daniels, 1945); in our case this simply implies that if a leg fails the load it is bearing, in general ${}^{(n)}\sigma_a$ is transferred to its pair mate and then this leg may suffer an induced failure, which is described by the conditional probability ${}^{(n)}P_{2a,a}$, given by

$$ {}^{(n)}P_{2a,a} = \frac{{}^{(n)}P_{2a} - {}^{(n)}P_a}{1 - {}^{(n)}P_a}. \tag{3} $$

Then it is easy to compute ${}^{(n+1)}p'_a$ in terms of ${}^{(n)}P_a$:

$$ {}^{(n+1)}p'_a = {}^{(n)}P_a^2 + 2\,{}^{(n)}P_a[1 - {}^{(n)}P_a]\,{}^{(n)}P_{2a,a} $$
$$ = 2\,{}^{(n)}P_{2a}\,{}^{(n)}P_a - {}^{(n)}P_a^2. \tag{4} $$

The aim of the paper is to compute the global instability of the tree, i.e., ${}^{(N)}P_1$. It will be determined by Eqs. (1), (2), and (4), after fixing m and the successive reference strengths ${}^{(n)}\sigma_0$. In this respect, note that if ${}^{(n)}\sigma_0$ for all $n>1$ is taken as infinity, then that would be equivalent to considering that only the first level has an intrinsic probability of failure. In this case, which is exactly the one considered in TSS (1985) and later reanalized by Newman and Gabrielov (1991), the only probability of failure transmitted upwards through the renormalization relations reflects this initial and unique input of fragility coming from the first level. But, as mentioned, we will consider ${}^{(n)}\sigma_0$ as finite at all levels. Note that if we want to maintain a constant ratio, for all n, between the typical load ${}^{(n)}\sigma_1$ and ${}^{(n)}\sigma_0$, the rule would be ${}^{(n)}\sigma_0 = 2^{n-1}\,{}^{(1)}\sigma_0$. However, because of the fact that ${}^{(N)}P_1$ grows considerably because of the non-null small p's, we have considered it convenient to introduce a progressive intrinsic strengthening of the legs as one moves upwards. We will parameterize this concept through the relation:

$$ {}^{(n)}\sigma_0 = \frac{2^{n-1}\,{}^{(1)}\sigma_0}{\alpha^{n-1}}. \tag{5} $$

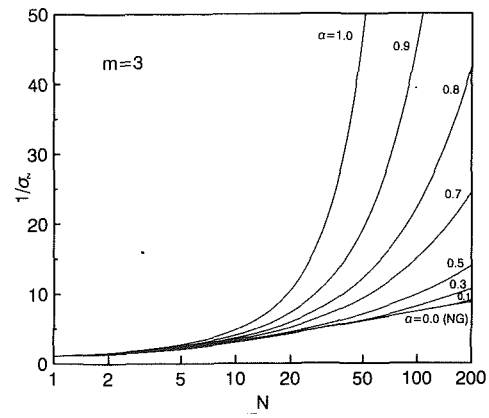


Fig. 2 Reciprocal value of the failure threshold versus the tree height, N, for different values of α

Thus TSS corresponds to the case $\alpha = 0$, i.e., the reference strengths are infinite except that of level $n=1$. For $\alpha \neq 0$, ${}^{(n)}\sigma_0$ increases in a geometric progression of ratio equal to $2/\alpha$. We will explore the range $0 \leq \alpha \leq 1$, i.e., up to the situation in which the ratio $({}^{(n)}\sigma_1 / {}^{(n)}\sigma_0)$ is constant for all n.

3 Results

We will denote by σ_N the value of ${}^{(1)}\sigma_1$, which leads to a ${}^{(N)}P_1$ equal to a given value, 0.5 for example. Thus σ_N acts as a threshold strength for the failure of a fractal tree of size N (let us take ${}^{(1)}\sigma_0 = 1$ to simplify the notation). Then the task consists in computing the following chain:

$$ {}^{(1)}P_1 \dashrightarrow \left.\begin{matrix} {}^{(2)}p'_1 \\ {}^{(2)}p_1 \end{matrix}\right) \dashrightarrow {}^{(2)}P_1 \dashrightarrow \left.\begin{matrix} {}^{(3)}p'_1 \\ {}^{(3)}p_1 \end{matrix}\right) \dashrightarrow {}^{(3)}P_1 \dashrightarrow \left.\begin{matrix} {}^{(4)}p'_1 \\ {}^{(4)}p_1 \end{matrix}\right) \dashrightarrow {}^{(4)}P_1 \dashrightarrow \ldots $$

using the previous equations. This process stops at the previously decided N. The resulting ${}^{(N)}P_1$ is compared with 0.5, and the initial input ${}^{(1)}P_1$ is moved up or down until it matches the agreed ${}^{(N)}P_1$. But it is obvious from the structure of Eq. (4) that the computation of ${}^{(n)}p'_1$ demands the knowledge of ${}^{(n-1)}p'_1$ and ${}^{(n-1)}p'_2$. Stepping backwards in the chain, it would involve ${}^{(n-2)}p'_1$, ${}^{(n-2)}p'_2$ and ${}^{(n-2)}p'_4$, and so on. Hence, we infer, along with Newman and Gabrielov (1991), that the computation of ${}^{(N)}P_1$ requires the previous computation of ${}^{(1)}P_{20}$, ${}^{(1)}P_{21}$. . . ${}^{(1)}P_{2N}$, i.e., a vector of $(N+1)$ components. At the second level the corresponding vector would have N components, etc. As we reach typical heights of N being equal to several hundreds, these numerical vectors are handled with total ease.

In Fig. 2 we plot $1/\sigma_N$ versus log (N), first to appreciate the finding of Newman and Gabrielov (1991), i.e., the linear proportionality between $1/\sigma_N$ and log (N) for the $\alpha = 0$ case. We then see there how a small non-null α implies an increase in the global failure probability. The Weibull index used in this figure was $m=3$.

Now we face the challenge of finding regularities in the asymptotic behavior of these curves for $\alpha \neq 0$. Using the Weibull distribution we have found that the results, in general, do not show any clear asymptotic trend. However, we have in fact been able to identify a condition which leads to straight lines i.e., $1/\sigma_N \propto N$. This condition, for a fractal tree with coordination number equaling two, reads

$$ \alpha^* = \left(\frac{1}{2}\right)^{1/m}. \tag{6} $$

With this precise rate of intrinsic strengthening ($\alpha = \alpha^*$), the

Downloaded 03 May 2010 to 171.66.16.245. Redistribution subject to ASME license or copyright; see http://www.asme.org/terms/Terms_Use.cfm

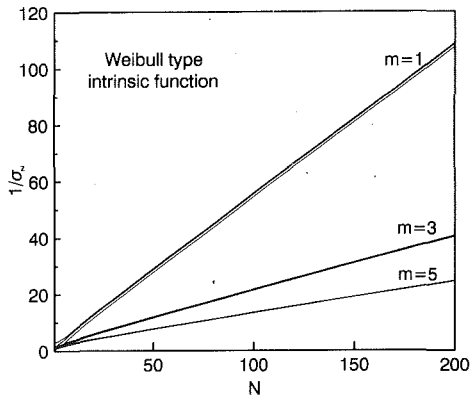


Fig. 3 Reciprocal value of the failure threshold versus N, in the case of fulfilling the linear proportionality condition (Eq. (6)) for an intrinsic probability function of the Weibull type. The three components of the lines correspond to different values of ${}^{(N)}P_1$. See the text for details.

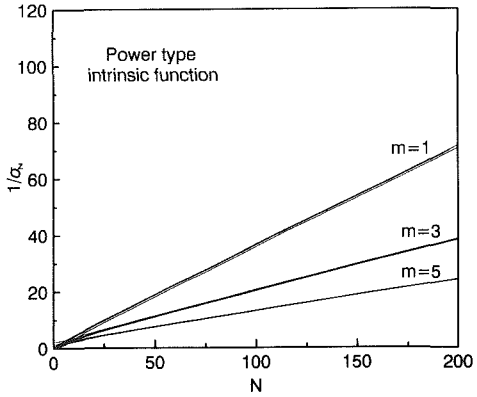


Fig. 4 Reciprocal value of the failure threshold versus N, in the case of fulfilling the linear proportionality condition (Eq. (6)) for an intrinsic probability function of the potential type. The three components of the lines correspond to different values of ${}^{(N)}P_1$. See the text for details.

increase of the inverse threshold strength is proportional to the tree height. This condition is independent of the specific value assumed for ${}^{(N)}P_1$. This is illustrated in Fig. 3 where for several values of m (1, 3 and 5), the α given by Eq. (6) leads to the constant-slope behavior previously mentioned. The "fine structure" observed corresponds to the three values taken for ${}^{(N)}P_1$, specifically 0.3, 0.5, and 0.9.

It is important to emphasize that this linear proportionality is also found when instead of Weibull functions, one uses power-like distributions for the intrinsic probability of failure of the legs, namely if the upward strengthening is again accomplished by Eq. (5), and α is fixed by Eq. (6). These results are shown in Fig. 4.

4 Conclusions

In this paper we have carried out a probabilistic analysis of the instability of a loaded structure of the fractal-tree type. The natural inclusion of intrinsic fragilities at all levels makes it differ from being mere hierarchically organized bundles of fibers. The intrinsic probabilities considered are either of the Weibull type, or of the potential type, with an equal index at all levels. The reference strengths at the different levels have been allowed to vary on inducing, by means of a parameter

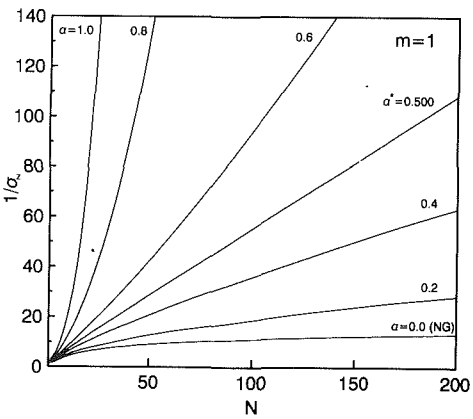


Fig. 5 Characteristic behavior of $1/\sigma_N$, for ${}^{(N)}P_1 = 0.5$, $m = 1$ and different values of α. See the separating role played by the critical value $\alpha = \alpha^*$. Weibull functions have been used.

called α, a progressive strengthening in the vertical direction. We have been able to identify a precise strengthening rate, $\alpha = \alpha^*$, to have linear proportionality between the global threshold strength and the tree height, N. This result is interesting because it classifies the asymptotic behaviors: for $\alpha < \alpha^* (\alpha > \alpha^*)$ $1/\sigma_N$ grows less than (more than) proportionally with respect to N (see Fig. 5, for $m = 1$). This may be a useful guide when designing mechanical structures of the fractal-tree type.

To conclude, it is pertinent to remember that these results are model dependent in two basic aspects: (i) We have restricted our analysis to the case of a fractal tree with a coordination number of 2. The generalization to other coordinations would be certainly interesting. And (ii) the progressive vertical strengthening of the tree elements have been done in the specific way expressed in Eq. (5). In a future paper we will try to generalize these results to other models and probability realizations.

Acknowledgments

This work was supported in part by the Spanish DGICYT, under grant PB90-0916.

References

Daniels, H. E., 1945, "The Statistical Theory of Strengths of Bundles of Threads," *Proceedings Royal Society, London*, Vol. A183, pp. 404–435.

Johnson, N. L., and Leone, F. C., 1977, *Statistics and Experimental Design in Engineering and the Physical Sciences*, Vol. 1, 2nd ed., John Wiley and Sons, New York.

Mandelbrot, B., 1982, *The Fractal Geometry of Nature*, Freeman, San Francisco, CA.

McCartney, L. N., and Smith, R. L., 1983, "Statistical Theory of the Strength of Fiber Bundles," ASME Journal of Applied Mechanics, Vol. 105, pp. 601–608.

Newman, W. I., and Gabrielov, A. M., 1991, "Failure of Hierarchical Distributions of Fibre Bundles. I," *International Journal of Fracture*, Vol. 50, pp. 1–14.

Smalley, R. F., Turcotte, D. L., and Solla, S. A., 1985, "A Renormalization Group Approach to the Stick-Slip Behavior of Faults," *Journal of Geophysical Research*, Vol. 90, pp. 1894–1900.

Smith, R. L., and Phoenix, S. L., 1981, "Asymptotic Distributions for the Failure of Fibrous Materials Under Series-Parallel Structure and Equal Load-Sharing," ASME Journal of Applied Mechanics, Vol. 48, pp. 75–82.

Turcotte, D. L., Smalley, R. F., and Solla, S. A., 1985, "Collapse of Loaded Fractal Trees," *Nature*, Vol. 313, pp. 671–672.

Downloaded 03 May 2010 to 171.66.16.245. Redistribution subject to ASME license or copyright; see http://www.asme.org/terms/Terms_Use.cfm

A Conservation Theorem for Constrained Multibody Systems

J. T. Wang
Staff Research Engineer,
Engineering Mechanics Department,
General Motors R & D Center,
Warren, MI 48090-9055
Mem. ASME

This paper presents a general conservation theorem for multibody systems subject to simple nonholonomic constraints. It is applicable to both conservative and nonconservative systems. The derivation of this theorem is based on Kane's equations with undetermined multipliers. A power equation and a first integral of motion have been derived. They emerge in physically meaningful forms and include expressions for evaluating the power and energy flowing into the system. Like Kane's equations, the power equation and the first integral of motion are derived in matrix form. This makes them particularly useful for the computer formulation and solution of multibody system dynamics.

1 Introduction

Power equations play a very important role in dynamical investigations and in answering many questions of physics. The integral of a power equation is a constant called the first integral of the equations of motion. For example, the *Hamiltonian* of a conservative system is the integral of the power equation of the system. It leads to the well-known canonical (or Hamilton's) equations of motion.

Recently, progress has been made in deriving the power equation of simple nonholonomic systems. Kane and Banerjee (1983) presented a formulation to obtain the power equation of mechanical systems subject to homogeneous simple nonholonomic constraints. The extension of this effort to nonhomogeneous simple nonholonomic constraints was then made by Kane and Levinson (1985, 1988). The power equation was used in the latter study for testing numerical integrations of equations of motion of mechanical systems. However, their formulation is not general and certain conditions must be satisfied (e.g., see Table 7.2.1, Kane and Levinson, 1985).

More recently, Papastavridis (1991) presented a power equation for general simple nonholonomic systems. Papastavridis' formulation was derived based on the equations of Boltzmann/Hamel and is free from the limiting conditions in Kane and Levinson's formulation. However, the equations of Boltzmann/Hamel are not known as an efficient formalism for solving the problem of multibody systems. Moreover, the final form of Papastavridis' power equation is not physically meaningful in view of energy conservation. For example, the power flowing into the system due to the contribution of constraint forces is not explicitly presented in his power equation. He also erroneously concluded that the reason why Kane and Levinson's power equations are not general is due to the synonymous treatment of nonholonomic constraints and holonomic constraints in Kane's equations.

In this paper, we will derive a power equation for simple nonholonomic systems based on Kane's equations with undetermined multipliers (Wang and Huston, 1987). We will show that although the nonholonomic and holonomic constraints are treated similarly in Kane's equations, it is still possible to obtain a correct and physically meaningful power equation. Like Kane's equations, this new power equation will be derived in matrix form. This form makes it especially useful for computer implementation and solution for large mechanical systems. In what follows, we will first review some basic concepts on constrained multibody dynamics and the matrix notation. A conservation theorem for simple nonholonomic system will then be derived. Examples and an extension of this theorem will also be presented.

2 Constrained Multibody Dynamics

Consider a system S, of N bodies whose permissible configurations in a Newtonian reference frame G can be specified by $n(n \leq 6N)$ generalized coordinates $q \stackrel{D}{=} (q_1, \ldots, q_n)^T$, and which is subject to motion constraints such that the $m(m \leq n)$ equations

$$Av + b = 0, \tag{1}$$

are satisfied throughout every motion of S in G. Here the $m \times 6N$ and $m \times 1$ matrices A and b are functions of the generalized coordinates q and time t. The vector of body velocity $v \stackrel{D}{=} (v_1, \ldots, v_{6N})^T$, including three translations and three rotations for each body, can be expressed as

$$v = R\dot{q} \tag{2}$$

where the elements of the $6N \times n$ matrix R are a function of q and time t, and the generalized speeds, $\dot{q}$, are the derivatives

Contributed by the Applied Mechanics Division of THE AMERICAN SOCIETY OF MECHANICAL ENGINEERS for presentation at the ASME Winter Annual Meeting, New Orleans, La., Nov. 28–Dec. 3, 1993.
Discussion on this paper should be addressed to the Technical Editor, Professor Lewis T. Wheeler, Department of Mechanical Engineering, University of Houston, Houston, TX 77204-4792, and will be accepted until four months after final publication of the paper itself in the ASME JOURNAL OF APPLIED MECHANICS.
Manuscript received by the ASME Applied Mechanics Division, Feb. 28, 1992; final revision, Aug. 31, 1992. Associate Technical Editor: P. D. Spanos.
Paper No. 93-WA/APM-2.

Copyright © 1993 by ASME
Downloaded 03 May 2010 to 171.66.16.245. Redistribution subject to ASME license or copyright; see http://www.asme.org/terms/Terms_Use.cfm

of the generalized coordinates q with respect to time. Of these n generalized speeds, only $(n-m)$ of them are linearly independent due to the m motion constraints. Similarly, we may also view the velocity v as a set of generalized speeds, where only $(n-m)$ out of $6N$ generalized speeds are linearly independent variables.

Here we purposely choose to express all translational velocities in terms of three mutually perpendicular unit vectors fixed in the inertial reference frame G, and to express the angular velocity of body $B_k (k=1, \ldots, N)$ in terms of three mutually perpendicular unit vectors fixed in the body, which coincide with the axes of principal moments of inertia of the body. Although it is not necessary for our analysis to use this specific set of unit vectors for expressing velocities, it allows us to directly differentiate velocity without involving the differentiation of unit vectors.

The choice of describing a multibody system in the form of Eqs. (1) and (2) has effectively separated motion constraints from configuration constraints. The m motion constraints are explicitly expressed in Eq. (1), while the $(6N - n)$ configuration constraints, which are due to joints between adjacent bodies, are implicitly included in Eq. (2). That is, there exists additional $(6N - n)$ configuration constraints based on Eq. (2) and they can be written in the form of

$$Jv = 0, \tag{3}$$

where the $(6N - n) \times 6N$ matrix J is a function of q and t, and it is chosen in such a way that

$$JR \equiv 0. \tag{4}$$

Note that the matrix J is known as the orthogonal complement matrix of R (Wang and Huston, 1987).

The above treatment is not necessary for our analysis. For example, we may treat both configuration and motion constraints the same way. In this case, we will have a total of $m + (6N - n)$ kinematic constraint equations in the form of Eq. (1). However, since the constraint forces due to the configuration constraints are reaction forces or moments which will not do work on the system, whether or not to explicitly express the configuration constraints is irrelevant to the energy conservation analysis. On the other hand, separating these two types of constraints enables us to focus on the motion constraint.

It is well known that a system with constraints in the form of Eqs. (1) or (3) is called a simple nonholonomic system if there is no way of integrating the constraint equations to yield a relation containing the generalized coordinates and time only. Otherwise it is called a holonomic system. In this paper we are studying multibody systems with motion constraints in the form of Eq. (1), whether or not the constraint equations are integrable. Therefore, this study is applicable to both holonomic and nonholonomic systems.

By substituting from Eq. (2) into Eq. (1), we may obtain an alternative form of the motion constraint equation in the space spanned by n generalized speeds, $\dot{q}$:

$$\hat{A}\dot{q} + b = 0 \tag{5}$$

where

$$\hat{A} = AR. \tag{6}$$

We see that the size of the matrix $\hat{A}$ is $m \times n$, and that again it is a function of the generalized coordinates q and time t.

Now introduce a set of new generalized speeds, $u \stackrel{D}{=} (u_1, \ldots, u_{n-m})^T$, which can be the derivatives of either real coordinates or quasi-coordinates. The transformation between the new and old generalized speeds is defined as

$$\dot{q} = \hat{R}u + \hat{b} \tag{7}$$

where the $n \times (n - m)$ and $n \times 1$ matrices $\hat{R}$ and $\hat{b}$ are functions of q and time t, and they are chosen in such a way that

$$\hat{A}\hat{R} \equiv 0 \tag{8}$$

and

$$\hat{A}\hat{b} \equiv -b. \tag{9}$$

Equation (8) is essentially saying that $\hat{R}$ is the orthogonal complement matrix of $\hat{A}$. Considering their close and complemental relationship, we call Eqs. (5) and (7), respectively, the first and the second form of simple nonholonomic constraints corresponding to a pair of complemental generalized speeds, $\dot{q}$ and u. Recall that Eqs. (3) and (2) possess a similar relationship, i.e., Eq. (3) is the first form of constraint equations, while Eq. (2) is the second form of constraint equations, corresponding to a pair of generalized speeds, v and $\dot{q}$. The first and the second form constraint equations provide the necessary and sufficient rule for transforming the system from one generalized speed space to another, e.g., from an n-dimensional space of $\dot{q}$ to an $(n - m)$-dimensional space of u.

The substitution from Eq. (7) into Eq. (2) then yields

$$v = \tilde{R}u + v_t \tag{10}$$

where

$$\tilde{R} = R\hat{R} \tag{11}$$

and

$$v_t = R\hat{b}. \tag{12}$$

Recall that the previous choice of a specific set of unit vectors allows us to directly differentiate Eq. (10) without involving the differentiation of unit vectors. Accordingly, we obtain the body translational and angular accelerations:

$$\bar{a} = \dot{v} = \dot{\tilde{R}}u + \tilde{R}\dot{u} + \dot{v}_t. \tag{13}$$

Furthermore, the mass matrix M of the system S can be expressed in a partitioned form:

$$M = \left(\begin{array}{c|c} m & 0 \\ \hline 0 & I \end{array}\right) \tag{14}$$

where the $3N \times 3N$ submatrices m and I, respectively, represent the concentrated mass and principal moments of inertia of each body of the system S, respectively. Note that the matrix M is a diagonal matrix and independent of time, i.e., $dM/dt = 0$, due to our choice of this specific set of unit vectors.

We now separate the translational and angular velocities in our equations by matrix partitioning. We obtain the following equations:

$$R = \begin{pmatrix} R_1 \\ \hline R_2 \end{pmatrix} \tag{15}$$

$$\tilde{R} = \begin{pmatrix} \tilde{R}_1 \\ \hline \tilde{R}_2 \end{pmatrix} = \begin{pmatrix} R_1 \hat{R} \\ \hline R_2 \hat{R} \end{pmatrix} \tag{16}$$

$$v = \begin{pmatrix} \bar{v} \\ \hline \bar{\omega} \end{pmatrix} = \begin{pmatrix} \tilde{R}_1 \\ \hline \tilde{R}_2 \end{pmatrix} (u) + \begin{pmatrix} \bar{v}_t \\ \hline \bar{\omega}_t \end{pmatrix} \tag{17}$$

and

$$v_t = \begin{pmatrix} \bar{v}_t \\ \hline \bar{\omega}_t \end{pmatrix} \tag{18}$$

where $\bar{v}$ and $\bar{\omega}$ represent the $3N$ translational velocities at each mass center of N bodies and the $3N$ angular velocities of N bodies, respectively. Observe that the velocity v is now a function of the quasi-coordinate derivatives "u," the real coordinates "q," and time t.

The inertia force vector F^* of the system S corresponding to the $\bar{v}$ and $\bar{\omega}$ can now be obtained:

$$F^* = -M\bar{a} - \begin{pmatrix} 0 \\ \hline \Omega I \bar{\omega} \end{pmatrix} \tag{19}$$

Downloaded 03 May 2010 to 171.66.16.245. Redistribution subject to ASME license or copyright; see http://www.asme.org/terms/Terms_Use.cfm

where the $3N \times 3N$ matrix Ω is the "dual matrix" of the angular velocity vector (Huston, 1990). The generalized inertia force vectors $\hat{F}^*$ and $\tilde{F}^*$, corresponding to the generalized speeds $\dot{q}$ and u, respectively, are

$$\hat{F}^* = \frac{\partial v}{\partial \dot{q}} \cdot F^* = R^T F^* \tag{20}$$

and

$$\tilde{F}^* = \hat{R}^T \hat{F}^* = \hat{R}^T R^T F^* = \tilde{R}^T F^* \tag{21}$$

where the expression $\partial v/\partial \dot{q}$ is the partial velocity of the system associated with the generalized speed $\dot{q}$ (Kane and Levinson, 1985), and is equal to the transpose of the matrix R.

Similarly, if the active force vector corresponding to $\bar{v}$ and $\bar{\omega}$ is denoted as F, the generalized active force vectors $\hat{F}$ and $\tilde{F}$, corresponding to the generalized speeds $\dot{q}$ and u, respectively, become

$$\hat{F} = R^T F \tag{22}$$

and

$$\tilde{F} = \hat{R}^T \hat{F} = \hat{R}^T R^T F = \tilde{R}^T F. \tag{23}$$

Finally, depending on which set of generalized speeds is chosen the equations of motion of the system S can be written in the form of Kane's equations with undetermined multipliers (Wang and Huston, 1987):

$$F^* + F + F' = 0 \tag{24}$$

or

$$\hat{F}^* + \hat{F} + \hat{F}' = 0 \tag{25}$$

where F' and $\hat{F}'$ are the generalized constraint forces. Making use of Eqs. (1) and (3), or (5), we have

$$F' = (A^T | J^T) \begin{pmatrix} \lambda \\ --- \\ \lambda_b \end{pmatrix} \tag{26}$$

and

$$\hat{F}' = \hat{A}^T \lambda \tag{27}$$

where λ and λ_b are $m \times 1$ and $(6N - n) \times 1$ matrices of undetermined multipliers. Equations (24) and (25) can be further reduced to the standard form of Kane's equations in the space spanned by the $(n - m)$ generalized speeds, u. We have

$$\tilde{F}^* + \tilde{F} = \tilde{R}^T (F^* + F) = 0. \tag{28}$$

The constraint forces play a central role in a simple nonholonomic system. Historically, constraint forces are thought to be nonworking forces. This statement is only valid if we view the problem in the $(n - m)$-dimensional space of the generalized speeds u. Since constraint forces are orthogonal to u, the work done on the system by the constraint forces in every dimension of this space is zero. However, the above observation is not complete. Since there are m constraint displacements in the same dimensional space in which the constraint forces act, the constraint forces will and must do work on the system along these displacements. Let the work done on the system S from time t_1 to t_2 by the constraint force be denoted as W'. Then we may write the expression of the work done on the system S as either

$$W' = \int_{t_1}^{t_2} v^T F' \, dt \tag{29}$$

or

$$W' = \int_{t_1}^{t_2} \dot{q}^T \hat{F}' \, dt. \tag{30}$$

By substituting from Eq. (26) into Eq. (29), or from Eq. (27) into Eq. (30), and then making use of Eqs. (1) or (5), the result is

$$W' = -\int_{t_1}^{t_2} b^T \lambda \, dt. \tag{31}$$

This equation shows that in general the work done on the system S by constraint forces will not vanish, unless

$$b = 0. \tag{32}$$

Whenever Eq. (32) is satisfied, the system is then said to be catastatic and the constraint equations become homogeneous:

$$Av = 0 \text{ or } \hat{A}\dot{q} = 0. \tag{33}$$

If there is no dissipating energy involved in a catastatic system, this constrained multibody system is a conservative system. The first integral of the equations of motion of both holonomic and nonholonomic conservative systems is a constant. The derivative of the first integral, known as the power equation, vanishes. For example, different forms of power equations for conservative nonholonomic systems have been given by Neimark and Fufaev (1972) and Kane and Banerjee (1983).

On the other hand, a system that is not catastatic is called acatastatic. An acatastatic system is a nonconservative system, since the constraint forces do work on the system as shown in Eq. (31).

3 Conservation Theorem

In order to derive an energy conservation theorem for acatastatic systems, we need to subtract from the system's internal energy the work done to the system due to the constraint forces. Furthermore, if there are nonpotential active forces acting on the system, we need to add the energy dissipated from the system, or to subtract the work done to the system, due to the nonpotential active forces. Alternatively, this can be done by subtracting the net power flowing into the system from the internal power of the system. That is, hypothetically a power equation should be in the form of

$$\dot{E} = \dot{K} + \dot{V} - \dot{Q} = 0 \tag{34}$$

where $\dot{E}$, $\dot{K}$, and $\dot{V}$, are the time derivative of the adjusted total energy, kinetic energy, and potential energy of the system, respectively, and Q is the net power flowing into the system. The integral of this power equation is a constant, i.e., it is the first integral of motion of the system. Here a positive Q signifies that the net power is flowing into the system and, conversely, a negative Q indicates that the net power is flowing out of the system. In what follows, we will show that the above conservation theorem is true and that Eq. (34) is the power equation for acatastatic systems with nonpotential active forces.

Consider the system S again. Premultiplying Eq. (28) with the generalized speeds vector u^T yields

$$u^T (\tilde{F}^* + \tilde{F}) = 0. \tag{35}$$

Its first and second terms are the power contributed by generalized inertia and active forces, respectively, in the space spanned by the generalized speeds, u. Immediately, we realize that Eq. (35) is the power equation of the system S, because its integral is a constant. Next, we will show the equivalence of this power equation and Eq. (34).

The kinetic energy of the system S can be expressed as a function of the derivatives of quasi-coordinates u, real coordinates q, and time t:

$$K = \frac{1}{2} v^T M v = \frac{1}{2} (u^T \tilde{R}^T M \tilde{R} u + 2 v_t^T M \tilde{R} u + v_t^T M v_t). \tag{36}$$

Downloaded 03 May 2010 to 171.66.16.245. Redistribution subject to ASME license or copyright; see http://www.asme.org/terms/Terms_Use.cfm

As shown in Eq. (36), the expression for the kinetic energy K consists of three terms,

$$K = K_2 + K_1 + K_0, \tag{37}$$

where K_2 is a quadratic function of the generalized speeds u,

$$K_2 \overset{D}{=} \frac{1}{2} u^T \tilde{R}^T M \tilde{R} u = \frac{1}{2} (v - v_t)^T M (v - v_t). \tag{38}$$

K_1 is a linear function of the generalized speeds u,

$$K_1 \overset{D}{=} v_t^T M \tilde{R} u = v_t^T M (v - v_t), \tag{39}$$

and K_0 is a function of the generalized coordinates q and time t,

$$K_0 \overset{D}{=} \frac{1}{2} v_t^T M v_t. \tag{40}$$

Differentiating Eqs. (38) through (40) with respect to time, we have

$$\dot{K}_2 = u^T \tilde{R}^T M \tilde{R} u + u^T \tilde{R}^T M \tilde{R} \dot{u} \tag{41}$$

$$\dot{K}_1 = \dot{v}_t^T M \tilde{R} u + v_t^T M \dot{\tilde{R}} u + v_t^T M \tilde{R} \dot{u} \tag{42}$$

and

$$\dot{K}_0 = v_t^T M \dot{v}_t. \tag{43}$$

We now rewrite the active forces into two terms, the potential force, F_V, and nonpotential force, F_D:

$$F = F_V + F_D. \tag{44}$$

Based on the definition of the potential energy, we have

$$\dot{V} \overset{D}{=} -v^T F_V. \tag{45}$$

Considering the first term of Eq. (35), we obtain

$$\begin{aligned} -u^T \tilde{F}^* &= -u^T \tilde{R}^T F^* \\ &= u^T \tilde{R}^T M \dot{\tilde{R}} u + u^T \tilde{R}^T M \tilde{R} \dot{u} + u^T \tilde{R}^T M \dot{v}_t + u^T \tilde{R}_2^T \Omega I \bar{\omega} \\ &= \frac{d}{dt} \left(\frac{1}{2} u^T \tilde{R}^T M \tilde{R} u \right) + u^T \tilde{R}^T M \dot{v}_t + (\bar{\omega} - \bar{\omega}_t)^T \Omega I \bar{\omega} \\ &= \dot{K}_2 + (v - v_t)^T M \dot{v}_t + (\bar{\omega} - \bar{\omega}_t)^T \Omega I \bar{\omega}. \end{aligned} \tag{46}$$

Note that

$$\bar{\omega}^T \Omega I \bar{\omega} = \bar{\omega} \cdot \bar{\omega} \times (I \cdot \bar{\omega}) = \bar{\omega} \times \bar{\omega} \cdot (I \cdot \bar{\omega}) \equiv 0. \tag{47}$$

Equation (46) may now be reduced to

$$-u^T \tilde{F}^* = \dot{K}_2 - \dot{K}_0 + v^T M \dot{v}_t - \bar{\omega}_t^T \Omega I \bar{\omega}. \tag{48}$$

Similarly, premultiplying Eq. (23) and making use of Eq. (10) results in a new form for the second term of Eq. (35):

$$-u^T \tilde{F} = -u^T \tilde{R}^T F = -(v - v_t)^T F. \tag{49}$$

Now, substituting from Eq. (44) and (45) into Eq. (49) yields

$$-u^T \tilde{F} = \dot{V} - v^T F_D + v_t^T F. \tag{50}$$

Finally, substituting from Eqs. (48) and (50) into Eq. (35) gives

$$\dot{K}_2 - \dot{K}_0 + v^T M \dot{v}_t - \bar{\omega}_t^T \Omega I \bar{\omega} + \dot{V} - v^T F_D + v_t^T F \equiv 0. \tag{51}$$

Thus, the power equation of the system S may then be written in a form similar to the one given by Kane and Levinson (1988):

$$\dot{K}_2 - \dot{K}_0 + \dot{V} + \dot{Z} = 0 \tag{52}$$

where

$$\dot{Z} = v^T M \dot{v}_t - \bar{\omega}_t^T \Omega I \bar{\omega} - v^T F_D + v_t^T F. \tag{53}$$

Integrating this power equation with respect to time leads to the expression

$$K_2 - K_0 + V + Z = \text{constant}. \tag{54}$$

Observe that the $\dot{Z}$ term of Eq. (53) is different from the expression given by Kane and Levinson (1988). Equations (52) through (54) have been derived without imposing any conditions on the analysis. Hence, unlike Kane and Levinson's power equation, they hold always for any catastatic and acatastatic systems (i.e., for any homogeneous and nonhomogeneous simple nonholonomic systems).

Since Eq. (52) is derived based on a known power equation, i.e., Eq. (35), there is no doubt that it is another form of the power equation of the system S. However, there is little evidence to support this claim by viewing Eq. (52) alone. Several questions can be raised here: (1) Why is K_1 not included in the equation? (2) Why is K_0 negative? and (3) What is the physical meaning of the $\dot{Z}$ term, if any? To answer these questions and to obtain a power equation in the form of Eq. (34), further analysis is necessary.

By making use of Eqs. (10), (18), (19), and (41) through (43), the power contributed by the generalized inertia force, i.e., Eq. (48), can be rewritten as

$$\begin{aligned} -u^T \tilde{F}^* &= \dot{K} - (v_t^T M \dot{\tilde{R}} u + v_t^T M \tilde{R} \dot{u} + v_t^T M \dot{v}_t) - \bar{\omega}_t^T \Omega I \bar{\omega} \\ &= \dot{K} - v_t^T M \left[\frac{d}{dt} (\tilde{R} u) + \dot{v}_t \right] - \bar{\omega}_t^T \Omega I \bar{\omega} \\ &= \dot{K} - v_t^T M \left[\frac{d}{dt} (v - v_t) + \dot{v}_t \right] - \bar{\omega}_t^T \Omega I \bar{\omega} \\ &= \dot{K} - v_t^T M \dot{v} - \bar{\omega}_t^T \Omega I \bar{\omega} \\ &= \dot{K} - v_t^T M \bar{a} - (\bar{v}_t^T \mid \bar{\omega}_t^T) \begin{pmatrix} 0 \\ \hline \Omega I \bar{\omega} \end{pmatrix} \\ &= \dot{K} + v_t^T F^*. \end{aligned} \tag{55}$$

With the help of Eqs. (10) and (21), Eq. (55) leads to an alternative definition for system's kinetic energy:

$$\dot{K} \overset{D}{=} -v^T F^*. \tag{56}$$

Equation (56) is a definition for the kinetic energy analogous to the definition of the potential energy as given in Eq. (45).

By combining Eqs. (50) and (55), we can now express the power equation in the form of Eq. (34):

$$\dot{K} + \dot{V} - \dot{Q} = 0 \tag{57}$$

where

$$\dot{Q} = -v_t^T (F^* + F) + v^T F_D. \tag{58}$$

An energy conservation equation, i.e., a first integral, can be obtained by integrating Eq. (57),

$$K + V - Q = E, \tag{59}$$

where the adjusted total energy of the system, E, is a constant. We have thus successfully verified the validity of our hypothetical energy conservation theorem by showing the equivalence of Eqs. (34) and (35).

Several remarks can be made about Eqs. (57) through (59). The physical meaning of the second term on the right-hand side of Eq. (58) can be easily understood based on its contents. It is simply the power flowing into the system S due to nonpotential active forces, denoted as $\dot{Q}_D$:

$$\dot{Q}_D \overset{D}{=} v^T F_D. \tag{60}$$

On the other hand, the physical meaning of the first term in Eq. (58) is not clear. We see that it is proportional to the sum of the inertia and active forces in the space spanned by the $6N \times 1$ generalized speed matrix v. We also note that if b vanishes, then v_t and $\hat{b}$ as well as this first term will all vanish. However, its physical meaning is still not clear. In what follows, we will further clarify this term's meaning.

Making use of Eqs. (10) and (35) yields

$$(v - v_t)^T (F^* + F) = 0. \tag{61}$$

Now, by premultiplying Eq. (24) by v^T, we obtain

$$v^T (F^* + F + F') = 0 \tag{62}$$

or

Downloaded 03 May 2010 to 171.66.16.245. Redistribution subject to ASME license or copyright; see http://www.asme.org/terms/Terms_Use.cfm

$$-v^T(F^* + F) = v^T F'. \tag{63}$$

Rearranging Eq. (61) and substituting it into Eq. (63) gives

$$-v_t^T(F^* + F) = v^T F' \tag{64}$$

Now, differentiating Eq. (29) with respect to time reveals

$$\dot{W}' = \frac{d}{dt}\int v^T F'\,dt = v^T F'. \tag{65}$$

We see that the right-hand side of Eq. (64) is actually the time derivative of the work (i.e., the power) done to the system by the constraint force,

$$-v_t^T(F^* + F) = \dot{W}'. \tag{66}$$

Based on Eqs. (58), (60), and (66), we conclude

$$\dot{Q} = \dot{W}' + \dot{Q}_D. \tag{67}$$

To this end, we see that Eq. (57), indeed, provides a conservation theorem. That is, we have shown that by subtracting $\dot{Q}$, i.e., the net power contributed by both constraint forces and nonpotential active forces, from $\dot{K} + \dot{V}$ or the system's internal power, we have successfully established a conservation theorem for simple nonholonomic systems. We also see that Eq. (58) provides a convenient means to evaluate the net power flowing into the system without the need to evaluate the constraint force as needed in Eq. (65).

A relationship between the quantities $\dot{Z}$ and $\dot{Q}$ can be established by comparing Eqs. (52) and (57). We have

$$\dot{Z} = \dot{K}_1 + 2\dot{K}_0 - \dot{Q}. \tag{68}$$

We learn that $\dot{K}_1$ is not included in Eq. (52) because it is embedded in $\dot{Z}$ as shown in Eq. (68), and that since there are two times $\dot{K}_0$ embedded in $\dot{Z}$, together with the negative $\dot{K}_0$ explicitly expressed in Eq. (52), we learn that $\dot{K}_0$ is actually not a negative term in the power equation. Apparently, Eq. (52) and the quantity $\dot{Z}$ carry physically indistinct information about the system, whereas Eq. (57) clearly shows the power conservation of the system in terms of the total kinetic power $\dot{K}$, potential power $\dot{V}$, and the power added and dissipated from the system, $\dot{Q}$. That is, the power equation in the form of Eq. (57) is superior to the forms of both Eq. (52) and the power equation given by Papastavridis (1991).

4 Examples

We will now work on some examples to illustrate the use of the new power equation. Specifically, we will revisit the problems previously evaluated by Papastavridis (1991) and Kane and Levinson (1988).

We first consider the problem studied by Papastavridis (1991) in which a homogeneous sphere D, of mass m and radius r, rolls without slipping on a rough horizontal plane P. The plane P spins about its Z-axis, which is perpendicular to the plane, with a constant angular velocity ω in the inertial reference frame G.

A set of three mutually perpendicular unit vectors, which is fixed in G, is chosen for expressing the translational velocity of the mass center of the sphere and its angular velocity,

$$v^T = (\dot{x}\ \ \dot{y}\ \ \dot{z}\ \ \omega_x\ \ \omega_y\ \ \omega_z). \tag{69}$$

We now introduce a set of generalized speeds

$$\dot{q}^T = (\dot{x}\ \ \dot{y}\ \ \dot{\phi}\ \ \dot{\theta}\ \ \dot{\psi}) \tag{70}$$

where ϕ, θ, and ψ are the Eulerian angles defining the precession, nutation, and spin of the sphere D relative to the inertial reference frame G. Recall that the transformation between v and $\dot{q}$ is defined by Eq. (2), and the transformation matrix R is

$$R = \begin{pmatrix} 1 & 0 & 0 & 0 & 0 \\ 0 & 1 & 0 & 0 & 0 \\ 0 & 0 & 0 & 0 & 0 \\ 0 & 0 & 0 & c\phi & s\theta s\phi \\ 0 & 0 & 0 & s\phi & -s\theta c\phi \\ 0 & 0 & 1 & 0 & c\theta \end{pmatrix} \tag{71}$$

where "s" and "c" denote "sin" and "cos," respectively.

Since the sphere rolls without slipping on the plane, the system is subject to two motion constraints in the form of Eq. (1) and one configuration constraint in the form of Eq. (3). The coefficient matrices of the motion constraint equation are

$$A = \begin{pmatrix} 1 & 0 & 0 & 0 & -r & 0 \\ 0 & 1 & 0 & r & 0 & 0 \end{pmatrix} \tag{72}$$

and

$$b = \begin{pmatrix} y\omega \\ -x\omega \end{pmatrix}. \tag{73}$$

This motion constraint is due to the pure rolling, in which the velocity of both sphere and plane must be identical at their common contact point. The configuration constraint is due to the fact that the sphere is restrained by the plane to roll on the X-Y plane only, i.e., the translational velocity $\dot{z}$ is always equal to zero. Note that this configuration constraint will do no work on the system, and it is not necessary to explicitly include it in our analysis.

The coefficient matrix $\hat{A}$ for the alternative form of constraint equations is the matrix product of A and R as defined in Eq. (6)

$$\hat{A} = \begin{pmatrix} 1 & 0 & 0 & -rs\phi & rs\theta c\phi \\ 0 & 1 & 0 & rc\phi & rs\theta s\phi \end{pmatrix}. \tag{74}$$

Now, introduce a set of new generalized speeds

$$u^T = (\omega_x\ \ \omega_y\ \ \omega_z) \tag{75}$$

such that

$$\hat{R} = \begin{pmatrix} 0 & r & 0 \\ -r & 0 & 0 \\ -s\phi\,\dfrac{c\theta}{s\theta} & -c\phi\,\dfrac{c\theta}{s\theta} & 1 \\ c\phi & s\phi & 0 \\ \dfrac{s\phi}{s\theta} & \dfrac{-c\phi}{s\theta} & 0 \end{pmatrix} \tag{76}$$

and

$$\hat{b}^T = (-y\omega\ \ x\omega\ \ 0\ \ 0\ \ 0). \tag{77}$$

It can be easily verified that Eqs. (8) and (9) are satisfied for those $\hat{A}$, $\hat{R}$, and $\hat{b}$ as given in Eqs. (72), (74), and (75).

The inertia and active forces acting on the sphere are

$$F^* = \begin{pmatrix} m & 0 & 0 & 0 & 0 & 0 \\ 0 & m & 0 & 0 & 0 & 0 \\ 0 & 0 & m & 0 & 0 & 0 \\ 0 & 0 & 0 & I_x & 0 & 0 \\ 0 & 0 & 0 & 0 & I_x & 0 \\ 0 & 0 & 0 & 0 & 0 & I_x \end{pmatrix} \begin{pmatrix} \ddot{x} \\ \ddot{y} \\ \ddot{z} \\ \dot{\omega}_x \\ \dot{\omega}_y \\ \dot{\omega}_z \end{pmatrix} \text{ and } F = \begin{pmatrix} 0 \\ 0 \\ -mg \\ 0 \\ 0 \\ 0 \end{pmatrix}. \tag{78}$$

Note that the three principal moments of inertia of a homogeneous sphere are identical. They are denoted as I_x in Eq. (78). Also note that since no dissipative forces are involved in this problem, we have $F_D = 0$ and $F = F_V$.

The velocity of the mass center of the sphere and its angular velocity in terms of the generalized speeds, u, can now be

Downloaded 03 May 2010 to 171.66.16.245. Redistribution subject to ASME license or copyright; see http://www.asme.org/terms/Terms_Use.cfm

obtained by substituting Eqs. (71), (76), and (77) into Eqs. (11) and (12). We express them in the partitioned form as given in Eq. (17):

$$v=\begin{pmatrix}\overline{v}\\ ----\\ \overline{\omega}\end{pmatrix}=\begin{pmatrix}\dot{x}\\ \dot{y}\\ \dot{z}\\ ----\\ \omega_x\\ \omega_y\\ \omega_z\end{pmatrix}=\begin{pmatrix}0 & r & 0\\ -r & 0 & 0\\ 0 & 0 & 0\\ - & - & -\\ 1 & 0 & 0\\ 0 & 1 & 0\\ 0 & 0 & 1\end{pmatrix}\begin{pmatrix}\omega_x\\ \omega_y\\ \omega_z\end{pmatrix}+\begin{pmatrix}-y\omega\\ x\omega\\ 0\\ ----\\ 0\\ 0\\ 0\end{pmatrix}. \tag{79}$$

Comparing Eqs. (18) and (79), we obtain

$$v_t=\begin{pmatrix}\overline{v}_t\\ ----\\ \overline{\omega}_t\end{pmatrix}=\begin{pmatrix}-y\omega\\ x\omega\\ 0\\ ----\\ 0\\ 0\\ 0\end{pmatrix}. \tag{80}$$

We are now ready to evaluate the quantity $\dot{Z}$. The four terms in the right-hand side of Eq. (53) are first evaluated:

$$v^T M\dot{v}_t = m\dot{x}\cdot(-\dot{y}\omega)+m\dot{y}\cdot\dot{x}\omega=0 \tag{81}$$

$$\overline{\omega}_t^T\Omega I\overline{\omega}=0 \tag{82}$$

$$v^T F_D=0 \tag{83}$$

and

$$v_t^T F=0\cdot(-mg)=0. \tag{84}$$

Substituting the preceding four quantities into Eq. (53) results in

$$\dot{Z}=v^T M\dot{v}_t-\overline{\omega}_t^T\Omega I\overline{\omega}-v^T F_D+v_t^T F=0. \tag{85}$$

The potential energy of this system is a constant:

$$V=mgr. \tag{86}$$

Hence we have

$$\dot{V}=0. \tag{87}$$

Finally, substituting Eqs. (85) and (87) into (52) leads to an equation identical to that obtained by Papastavridis (1991):

$$\dot{K}_2-\dot{K}_0=0. \tag{88}$$

The power flowing into the system, i.e., the power contributed by the spinning plane to the sphere, can be directly evaluated by using Eq. (58) with the absence of nonpotential forces

$$\dot{Q}=\dot{W}'=-v_t^T(F^*+F)=m\omega(x\ddot{y}-y\ddot{x}). \tag{89}$$

Recall that this useful information is not provided by the power equation given by Papastavridis (1991).

Next, we apply our conservation theorem to the example problems presented by Kane and Levinson (1988). For convenience, we follow their symbols and notation. In their first example (see Fig. 1), the motion of a particle P, of mass m, is constrained to remain on a circular wire W, of radius R, which is made to rotate with an angular speed Ω about a fixed, vertical axis passing through the center of the circular wire O and lying in the plane of W. The relative angle between the vertical axis and the vector OP (a vector from the center O to the particle P) is denoted as q_1.

It can be easily verified that identical results as given in their Eqs. (32) and (31) can be obtained by using Eqs. (52) and (53). Additionally, the power flowing into the system, which is not provided by their power equation, can now be computed based on Eq. (68):

$$\dot{Q}=0+2\frac{d}{dt}\left[\frac{1}{2}m(R\Omega\sin q_1)^2\right]-mR^2\Omega\dot{\Omega}\sin^2 q_1$$

$$=mR^2\Omega\sin q_1(\dot{\Omega}\sin q_1+2\Omega\dot{q}_1\cos q_1). \tag{90}$$

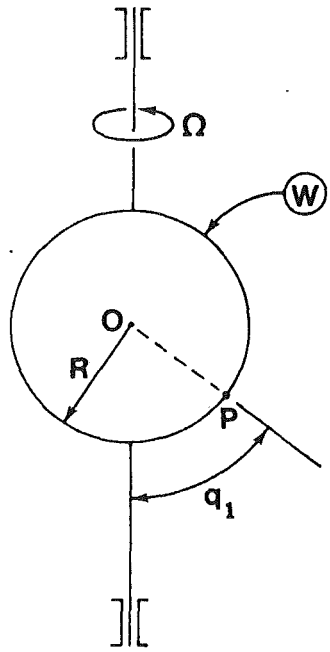


Fig. 1 Particle on a rotating circular wire (after Kane and Levinson, 1988)

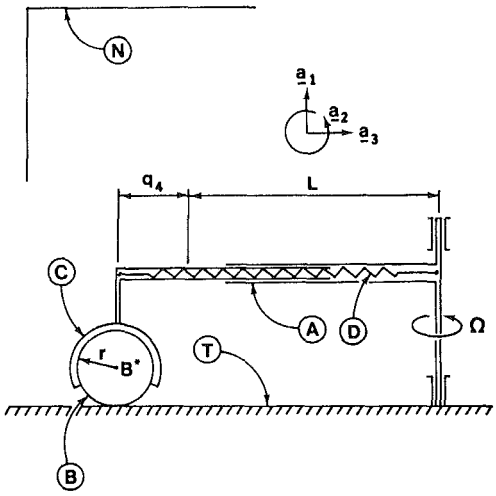


Fig. 2 A three-body dissipative system (after Kane and Levinson, 1988)

In their second example, Kane and Levinson (1988) studied a three-body dissipative system (see Fig. 2). Again, it can be easily verified that identical results as given in their Eqs. (60) and (61) can be obtained by using Eq. (53) and (52). We further evaluate the power flowing into and dissipating from the system by using Eqs. (68), (66), and (60). We obtain

$$\dot{W}'=\frac{7}{5}M\Omega(L+q_4)[\dot{\Omega}(L+q_4)+2\Omega\dot{q}_4] \tag{91}$$

and

$$\dot{Q}_D=-\delta[(u_1-\Omega)u_1+u_2^2]. \tag{92}$$

The net power flowing into the system, $\dot{Q}$, is then the sum of these two quantities. The results presented in Eqs. (90) through (92) can never be obtained by using Kane and Levinson's power equation.

5 A Remark About the *Hamiltonian*

The rolling sphere problem presents an interesting special case, in which $\dot{Z}$ in Eq. (52) vanishes to result in

Downloaded 03 May 2010 to 171.66.16.245. Redistribution subject to ASME license or copyright; see http://www.asme.org/terms/Terms_Use.cfm

$$\dot{K}_2 - \dot{K}_0 + \dot{V} = 0. \tag{93}$$

The integral of Eq. (93) is the well-known *Hamiltonian* of S in G. Observe that Eq. (93) is equal to Eq. (57) if

$$\dot{Q} = \dot{K}_1 + 2\dot{K}_0. \tag{94}$$

Whenever Eq. (93) is satisfied, provided that $v_t \neq 0$, the system S is generally nonconservative and the power flowing into the system can be computed using Eq. (94).

Equation (94) can be further simplified by using Eq. (39) and (40). We have

$$K_1 = v_t^T M v - v_t^T M v_t = v_t^T M v - 2K_0. \tag{95}$$

Differentiating Eq. (95) and then substituting it into Eq. (94) yields

$$\dot{Q} = \frac{d}{dt}(v_t^T M v) - 2\dot{K}_0 + 2\dot{K}_0 = \frac{d}{dt}(v_t^T M v). \tag{96}$$

Accordingly, we may now obtain the power supplied to the system satisfying Eq. (93) by either evaluating Eq. (94) or (96). For example, by using Eq. (96) for the rolling sphere problem, we obtain

$$\begin{aligned}\dot{Q} &= \frac{d}{dt}(v_t^T M v) \\ &= \frac{d}{dt}(-m\omega y\dot{x} + m\omega x\dot{y}) \\ &= m\omega(x\ddot{y} - y\ddot{x})\end{aligned} \tag{97}$$

which is identical to the result obtained by using Eq. (57) as given in Eq. (89). We have, thus, verified Eqs. (94) and (96).

Now, since Eq. (93) can be replaced by the power equation derived in this paper, i.e., Eq. (57), if Eq. (94) is satisfied, we see that its first integral is the *Hamiltonian* of this system. We redefined the *Hamiltonian* into a more meaningful form:

$$Hamiltonian \stackrel{D}{=} K + V - Q' \tag{98}$$

where

$$Q' \stackrel{D}{=} Q - Z = K_1 + 2K_0. \tag{99}$$

Like the original form of the *Hamiltonian*, this new expression asserts that the *Hamiltonian* of a multibody system subject to simple nonholonomic constraints is always a constant, if

$$Z = \text{constant} \tag{100}$$

is satisfied. In addition, this new form provides physical meaning for the system S. It says that whenever Eq. (100) is satisfied, the *Hamiltonian* of the system S is actually the total energy of the initial state of the system, and that the amount of energy flowing into the system S is given in Eq. (99).

For example, the rolling sphere system satisfies Eq. (100). The *Hamiltonian* of the sphere system hence is equivalent to the total energy of the initial state of the system as defined in Eq. (98). The Q' term in Eq. (98) becomes

$$Q' = K_1 + 2K_0 = v_t^T M v = -m\omega(y\dot{x} - x\dot{y}), \tag{101}$$

which is the net energy flowing into the system.

6 Generalized Power Equations

The power equation in the form of Eq. (52) is only valid in the space spanned by those $(n - m)$ generalized speeds, u, since its first and second terms, i.e., K_2 and K_0, are functions of u as defined in Eqs. (40) and (42). Note that although we may express the total kinetic energy of the system S in the inertial reference frame G in any sets of generalized speeds, the contents of its three components, K_2, K_1, and K_0, will vary for different generalized speeds. Hence Eq. (52) is not a general formulation.

On the other hand, considering the power equation in the form of Eq. (57) we see that the first two terms are the derivatives of the system's total kinetic and potential energy, which are independent of the choice of generalized speeds. This is also the case for the third term, $\dot{Q}$, since it is given in the space spanned by the $6N$ body velocities, v, as shown in Eq. (58), which can be expressed in any sets of generalized speeds. For example, this term could be presented in the space spanned by the n generalized speeds, $\dot{q}$. By making use of Eqs. (2), (7), and (12), Eq. (58) becomes

$$\begin{aligned}\dot{Q} &= -v^T(F^* + F_V) \\ &= -\dot{q}^T(\hat{F}^* + \hat{F}_V) \\ &= -\dot{b}^T(\hat{F}^* + \hat{F}) + \dot{q}^T\hat{F}_D\end{aligned} \tag{102}$$

where

$$\hat{F}_D \stackrel{D}{=} R^T F_D \quad \text{and} \quad \hat{F}_V \stackrel{D}{=} \hat{F} - \hat{F}_D. \tag{103}$$

Furthermore, with the help of Eqs. (7) and (28), it is possible to partially express this term in the $(n - m)$-dimensional space u:

$$\dot{Q} = -u^T(\tilde{F}^* + \hat{F}_V) - \dot{b}^T(\hat{F}^* + \hat{F}_V) = -\dot{b}^T(\hat{F}^* + \hat{F}_V) + u^T\tilde{F}_D \tag{104}$$

where

$$\hat{F}_D \stackrel{D}{=} \hat{R}^T\hat{F}_D \quad \text{and} \quad \tilde{F}_V \stackrel{D}{=} \tilde{F} - \tilde{F}_D. \tag{105}$$

Equations (58), (102), and (104) are equivalent and should lead to identical results. Based on the above discussion, we conclude that the power equation in the form of Eq. (57) is totally independent of the choice of generalized speeds. Therefore, it is more general than both Eq. (52) and the power equation given by Papastavridis (1991). We call Eq. (57) with these various forms of $\dot{Q}$ the generalized power equation with respect to a specific set of generalized speeds.

7 Conclusion

Based on Kane's equations with undetermined multipliers, a conservation theorem for constrained multibody systems subject to a simple nonholonomic constraint has been developed. This conservation theorem asserts the existence of an energy conservation equation for a simple nonholonomic system, even if the system itself is nonconservative. The energy conservation equation is the first integral of motion and differentiating this equation leads to the power equation of the system. Two alternative forms of the power equation have been derived. Equation (52) is the power equation in a form similar to the one obtained in many previous studies; e.g., Neimark and Fufaev (1972), Kane and Levinson (1988), Papastavridis (1991). However, this power equation is only valid in the space spanned by the $(n - m)$ generalized speeds, u, and it provides little intuition for interpreting the power (or the energy) exchanging activities in the system. On the other hand, Eq. (57) is a power equation in a form independent of the choice of generalized speeds, and including all the power exchanging activities. It also provides a convenient means, i.e., Eq. (58), for evaluating the net power flowing into the system. Clearly, we have shown that the power equation in the form of Eq. (57) is superior to Eq. (52) and those derived by Kane and Levinson (1985, 1988) and Papastavridis (1991). We have also furnished three alternative forms, i.e., Eqs. (57), (102), and (104), for evaluating the net power flowing into the system in different generalized speed spaces. Moreover, based on this conservation theorem we have redefined the *Hamiltonian* into a physically meaningful expression. This new definition asserts that the *Hamiltonian* of a multibody system subject to simple nonholonomic

Downloaded 03 May 2010 to 171.66.16.245. Redistribution subject to ASME license or copyright; see http://www.asme.org/terms/Terms_Use.cfm

constraints is always a constant, if "Z = constant" is satisfied. In this case, the *Hamiltonian* is actually the total energy of the initial state of the system.

Indeed, we have developed a general conservation theorem for multibody systems subject to simple nonholonomic constraints. Like Kane's equations, the power equation of this conservation theorem is derived in matrix form. This makes it especially useful for computer formulation and solution for large multibody systems. This power equation is also applicable to holonomic systems and to those systems including nonpotential active forces.

Acknowledgment

I would like to thank Dr. Ellen Kock and Dr. Jim Bennett for their helpful comments about this paper.

References

Huston, R. L., 1990, *Multibody Dynamics*, Butterworth-Heinemann, Stoneham, MA, pp. 46–47.

Kane, T. R., and Banerjee, A. K., 1983, "A Conservation Theorem for Simple Nonholonomic Systems," ASME JOURNAL OF APPLIED MECHANICS, Vol. 50, pp. 647–651.

Kane, T. R., and Levinson, D. A., 1985, *DYNAMICS: Theory and Applications*, McGraw-Hill, New York, pp. 45–50, 130–157, 193–194.

Kane, T. R., and Levinson, D. A., 1988, "A Method for Testing Numerical Integrations of Equations of Motion of Mechanical Systems," ASME JOURNAL OF APPLIED MECHANICS, Vol. 55, pp. 711–715.

Neimark, J. I., and Fufaev, N. A., 1972, *Dynamics of Nonholonomic Systems*, American Mathematical Society, Providence, RI, pp. 131–135.

Papastavridis, J. G., 1991, "On Energy Rate Theorems for Linear First-Order Nonholonomic Systems," ASME JOURNAL OF APPLIED MECHANICS, Vol. 58, pp. 536–544.

Wang, J. T., and Huston, R. L., 1987, "Kane's Equations with Undetermined Multipliers-Application to Constrained Multibody Systems," ASME JOURNAL OF APPLIED MECHANICS, Vol. 54, pp. 424–429.

Downloaded 03 May 2010 to 171.66.16.245. Redistribution subject to ASME license or copyright; see http://www.asme.org/terms/Terms_Use.cfm

Analytical Solutions for a Spinning Rigid Body Subject to Time-Varying Body-Fixed Torques, Part I: Constant Axial Torque

J. M. Longuski
Assoc. Professor.

P. Tsiotras
Ph.D. Candidate.

School of Aeronautics and Astronautics,
Purdue University,
West Lafayette, IN 47907

Analytic solutions are derived for the general attitude motion of a near-symmetric rigid body subject to time-varying torques in terms of certain integrals. A methodology is presented for evaluating these integrals in closed form. We consider the case of constant torque about the spin axis and of transverse torques expressed in terms of polynomial functions of time. For an axisymmetric body with constant axial torque, the resulting solutions of Euler's equations of motion are exact. The analytic solutions for the Eulerian angles are approximate owing to a small angle assumption, but these apply to a wide variety of practical problems. The case when all three components of the external torque vector vary simultaneously with time is much more difficult and is treated in Part II.

1 Introduction

Many numerical simulations are often necessary in order to understand the attitude response and control characteristics of a rigid-body vehicle. In fact, sensitivity and/or error analyses, using numerical integration, may be prohibitively expensive and time consuming, especially when a large number of problem parameters are involved. Analytical models can be of great help in obtaining a *qualitative* understanding of the complex dynamical behavior; even simple heuristic analytical results may provide a fast and relatively accurate model for maneuver analysis. This approach has been proved to be very useful in the past (Hintz and Longuski, 1985; Kia and Longuski, 1984; Longuski, Kia and Breckenridge, 1989). Moreover, for future applications it appears that the trend for autonomous on-board guidance control schemes dictates the use of compact, simple, analytical expressions modeling the attitude evolution. The development of such analytic solutions for the attitude history of rotating bodies thus provides a cornerstone for the advent of autonomous, closed-loop navigation. Even for the case of optimal open-loop control laws, analytic solutions can be very helpful in the associated two-point boundary value problem, providing a first guess for shooting-method algorithms. Analytic solutions are also important in the area of attitude reconstruction, where modern satellite telescopes require a precision of a few milliseconds of arc for the success of the mission (Bois, 1986). In such cases attitude reconstruction by numerical integration is not suitable; it is necessary to have analytical representations, using as few parameters as possible. Thus, the revival of interest in analytic solutions for the rigid-body dynamics problem comes as no surprise. In fact, attitude evolution of a rigid body has been extensively studied over the past few decades.

Analytic solutions for the attitude motion of a rigid body have been obtained recently for the *constant body-fixed torque problem* by Longuski (1980, 1991) and Tsiotras and Longuski (1991a). By this term, we mean the problem of a rotating rigid body under the influence of an external torque vector, which has *constant* components along the axes of a coordinate frame fixed in the body. Practical applications of this problem include the case of spinning satellites in space, where the torques are created internally in the body, e.g., as a result of a thruster firing. This problem is often referred to in the literature as the *self-excited rigid-body problem* and includes all the cases when the acting torques do not depend on the actual orientation of the body in inertial space. It does include, however, the case when the acting torques have a prescribed time-varying behavior in a reference frame fixed in the body. This is exactly the case that we are interested in. In this paper we assume that the transverse torques vary continuously with time, and are modeled as polynomials, or more generally, as truncated Taylor series expansions of analytic functions. The axial torque is assumed to be constant. This restriction can be relaxed, although a different procedure is necessary in order to handle the more complex integrals arising in this case (see Part II). The solution for the angular velocities is *exact* for symmetric rigid bodies, and very accurate for near-symmetric rigid bodies. In the case of the Eulerian angles, the solutions are always approximate because of a small angle assumption. We use the

Contributed by the Applied Mechanics Division of THE AMERICAN SOCIETY OF MECHANICAL ENGINEERS for publication in the JOURNAL OF APPLIED MECHANICS.

Discussion on this paper should be addressed to the Technical Editor, Professor Lewis T. Wheeler, Department of Mechanical Engineering, University of Houston, Houston, TX 77204-4792, and will be accepted until four months after final publication of the paper itself in the JOURNAL OF APPLIED MECHANICS.

Manuscript received by the ASME Applied Mechanics Division, Apr. 10, 1992; final revision, Oct. 22, 1992. Associate Technical Editor: R. L. Huston.

Copyright © 1993 by ASME
Downloaded 03 May 2010 to 171.66.16.245. Redistribution subject to ASME license or copyright; see http://www.asme.org/terms/Terms_Use.cfm

term *symmetric* (or equivalently, *axisymmetric*) for bodies with two equal principal moments of inertia. The term *near-symmetric* will refer to bodies with two principal moments of inertia that do not differ "too much." When the body is symmetric or nearly symmetric, we will also assume that the spinning axis is the third principal axis, being perpendicular to the plane defined by the two principal axes with equal (or nearly equal) moments of inertia.

Since every torque that varies continuously with time can be approximated to any desired degree of accuracy by polynomials, the analysis permits one to develop more realistic models of spacecraft torques and forces; these then may be applied to a variety of current and future problems involving chemical, ion, and solar sail propulsion. Another work by the authors (Tsiotras and Longuski, 1991b) examines the closely related problem when the acting torques are periodic functions of time, or alternatively, torques that can be expressed in terms of Fourier expansions. In such cases, solutions have been obtained for both the angular velocities and Eulerian angles; however, the analysis is more involved because the frequency of the acting transverse torques generates a two-parameter family of integrals, the explicit evaluation of which is very tedious. Since Fourier and Taylor expansions are the most common techniques of functional approximations, the results can be used in many applications. One, of course, would expect that the results of Tsiotras and Longuski (1991b) will be more helpful for discontinuous torques, or when the torques exhibit some kind of periodicity. For most of the other cases, however, the results of the current work will be more relevant and easier to apply.

2 Analytic Solution of Euler's Equations of Motion

Euler's equations of motion for principal axes at the center of mass are

$$M_x = I_x\dot{\omega}_x + (I_z - I_y)\omega_y\omega_z \tag{1}$$

$$M_y = I_y\dot{\omega}_y + (I_x - I_z)\omega_z\omega_x \tag{2}$$

$$M_z = I_z\dot{\omega}_z + (I_y - I_x)\omega_x\omega_y. \tag{3}$$

In these equations M_x, M_y, and M_z are the torque vector components, ω_x, ω_y, and ω_z are the angular velocity vector components, and I_x, I_y, and I_z are the principal moments of inertia. As usual, a dot represents differentiation with respect to time. No explicit analytic solutions of this system of nonlinear differential equations are known to exist for arbitrary functions of the external torques M_x, M_y, and M_z. In fact, no exact solutions are known, without the need of some simplifying assumptions, even for the case of M_x, M_y, and M_z being constant. Assuming that only M_z is constant and that the last term of Eq. (3) is small (either because of near symmetry or because of the product $\omega_x\omega_y$ being small) we obtain

$$\omega_z(t) \approx (M_z/I_z)t + \omega_{z0}, \quad \omega_{z0} \triangleq \omega_z(0). \tag{4}$$

This approximation has been proved very useful in previous developments (Longuski, 1980; Longuski, 1991; Tsiotras and Longuski, 1991a) and is *exact* for the case of a *symmetric* rigid body (defined here by $I_x = I_y$). Surely this approximation is very accurate also for the case of a spin-stabilized spacecraft, when both ω_x and ω_y tend to remain small, even when no symmetry assumption can be made. This approximation in the solution of Eq. (3) allows one to decouple the third-order system of nonlinear differential Eqs. (1)–(3). Therefore, assuming the validity of Eq. (4), one can merely concentrate on Eqs. (1) and (2), which now become a set of two coupled, but linear time-varying differential equations. The use of the change to the new independent variable

$$\tau(t) \triangleq \omega_z(t) \tag{5}$$

and the transformation of the dependent variables

$$\Omega_x \triangleq \omega_x\sqrt{k_y}, \quad \Omega_y \triangleq \omega_y\sqrt{k_x} \tag{6}$$

where $k_x \triangleq (I_z - I_y)/I_x$, $k_y \triangleq (I_z - I_x)/I_y$, $k \triangleq \sqrt{k_x k_y}$ allows one to combine both Eqs. (1) and (2) into the following scalar, linear but *complex* differential equation with a time-varying coefficient

$$\frac{d\Omega}{d\tau} - i\rho\tau\Omega = F. \tag{7}$$

In Eq. (7) we have

$$\Omega \triangleq \Omega_x + i\Omega_y, \quad \rho \triangleq k(I_z/M_z), \quad F \triangleq F_x + iF_y \tag{8}$$

$$F_x \triangleq (M_x/I_x)(I_z/M_z)\sqrt{k_y}, \quad F_y \triangleq (M_y/I_y)(I_z/M_z)\sqrt{k_x} \tag{9}$$

where $F = F(\tau)$ is now considered as a function of τ. It is assumed, without loss of generality, that the spin axis is the axis of the largest moment of inertia I_z, and for the sake of consistency we will assume that $I_z > I_x > I_y$. This choice will imply stable motion about the spin axis. The following procedure can be applied with a few modifications to the case when the z-axis is the minor principal axis, as well. The case when I_z represents the intermediate axis will not be considered, since it always results in unstable motion. The solution for the transverse angular velocities can be written immediately as follows:

$$\Omega(\tau) = \Omega_0 \exp\left(i\frac{\rho}{2}\tau^2\right) + \exp\left(i\frac{\rho}{2}\tau^2\right)\int_{\tau_0}^{\tau}\exp\left(-i\frac{\rho}{2}u^2\right)F(u)\,du \tag{10}$$

where $\Omega_0 \triangleq \Omega(\tau_0)\exp[-(i\rho/2)\tau_0^2]$ and $\Omega(\tau_0)$ is the initial condition in the new independent variable τ. The only difficulty that arises in the computation of the solution for the transverse angular velocities ω_x and ω_y comes from the integral of the nonhomogeneous part of the solution, due to the forcing function $F(\tau)$. We are, therefore, merely interested in computing the integral appearing in (10), that is,

$$I_\omega(\tau_0, \tau; \rho) \triangleq \int_{\tau_0}^{\tau}\exp\left(-i\frac{\rho}{2}u^2\right)F(u)\,du \tag{11}$$

for the special case when the transverse torques, M_x and M_y, are assumed to take the form of polynomials. Using the affinity of the transformation (4) and (5), one can assume, without loss of generality, the following expression for M_x and M_y in the new independent variable τ

$$M_x(\tau) = \sum_{n=0}^{m}\overline{M}_{x,n}\tau^n, \quad M_y(\tau) = \sum_{n=0}^{m}\overline{M}_{y,n}\tau^n \tag{12}$$

where $\overline{M}_{x,n}$ and $\overline{M}_{y,n}$ are constants, and some of them can be zero. (Therefore, there is no loss of generality in assuming that both M_x and M_y are polynomials of the same degree.) Equation (12) implies that because of the simple character of the transformation (5), polynomial functions in the original independent variable t, correspond to polynomials in the new independent variable τ. This is not the case, however, when M_z is not constant, and the relationship between the two expressions is not that obvious. Part II of the paper addresses this problem. Using Eqs. (8), (9), and (12) one can now write the following expression for the forcing function $F(\tau)$:

$$F(\tau) = \sum_{n=0}^{m}F_n\tau^n \tag{13}$$

where the coefficients F_n in the above expression are complex constants, given by $F_n \triangleq F_{x,n} + iF_{y,n}$ and $F_{x,n} \triangleq (\overline{M}_{x,n}/I_x)(I_z/M_z)\sqrt{k_y}$, $F_{y,n} \triangleq (\overline{M}_{y,n}/I_y)(I_z/M_z)\sqrt{k_x}$. Substitution of this rep-

Downloaded 03 May 2010 to 171.66.16.245. Redistribution subject to ASME license or copyright; see http://www.asme.org/terms/Terms_Use.cfm

resentation into Eq. (11) allows one to rewrite the integral as follows:

$$\int_{\tau_0}^{\tau} \exp\left(-i\frac{\rho}{2}u^2\right)F(u)du = \sum_{n=0}^{m} F_n \int_{\tau_0}^{\tau} \exp\left(-i\frac{\rho}{2}u^2\right)u^n du = \sum_{n=0}^{m} F_n \bar{I}_n(\tau_0, \tau;\rho) \tag{14}$$

where for convenience the following integrals have been introduced:

$$\bar{I}_n(\tau_0, \tau;\rho) \triangleq \int_{\tau_0}^{\tau} \exp\left(-i\frac{\rho}{2}u^2\right)u^n du, \quad n=0,1,2, \ldots, m. \tag{15}$$

Integrals of the form

$$I_n(x;\rho) \triangleq \int_0^x \exp\left(-i\frac{\rho}{2}u^2\right)u^n du \tag{16}$$

can be evaluated easily by means of the recurrence formula

$$\int_0^x \exp\left(-i\frac{\rho}{2}u^2\right)u^n du = i\frac{x^{n-1}}{\rho}\exp\left(-i\frac{\rho}{2}x^2\right) - i\frac{n-1}{\rho}\int_0^x \exp\left(-i\frac{\rho}{2}u^2\right)u^{n-2}du, \quad n=2,3,4, \ldots. \tag{17}$$

To obtain all the integrals from (17) one needs to find the first two terms of the sequence. This can be done using the following expressions:

$$I_0(x;\rho) \triangleq \int_0^x \exp\left(-i\frac{\rho}{2}u^2\right)du = \sqrt{\pi/\rho}\,\mathrm{sgn}\,(x)E\left(\sqrt{\rho/\pi}x\right) \tag{18}$$

$$I_1(x;\rho) \triangleq \int_0^x \exp\left(-i\frac{\rho}{2}u^2\right)u\,du = \frac{i}{\rho}\left[\exp\left(-i\frac{\rho}{2}x^2\right)-1\right] \tag{19}$$

where $E(x)$ represents the complex Fresnel integral function of the *first kind* defined by

$$E(x) \triangleq \int_0^x \exp\left(-i\frac{\pi}{2}u^2\right)du. \tag{20}$$

There exists also the complex Fresnel integral function of the *second kind* defined by

$$E_2(x) \triangleq \frac{1}{\sqrt{2\pi}}\int_0^x \frac{\exp(-iu)}{\sqrt{u}}\,du. \tag{21}$$

The foregoing two functions are related by $E(x) = E_2[(\pi/2)x^2]$. Series and asymptotic representations of these functions can be found, for instance, in Abramowitz and Stegun (1972). We have assumed, without loss of generality, that in Eq. (18) ρ is positive (which corresponds to a spin-up), since from (16) one sees that for ρ negative (spin-down) one merely takes the complex conjugate of Eq. (18), that is, $I_0^*(x;\rho) = I_0(x;-\rho)$ where the asterisk denotes complex conjugation. Both cases can be handled at the same time by defining the function

$$\bar{E}(x) \triangleq \begin{cases} E(x) & \text{if } \rho > 0 \\ E^*(x) & \text{if } \rho < 0. \end{cases} \tag{22}$$

Since we have assumed that $I_z > I_x > I_y$ the case of $\rho = 0$ is of no concern to us, since it corresponds to either $I_z = I_y$ or $I_z = I_x$, and in either case the problem reduces to the axisymmetric case. Therefore, one can solve exactly for one of the components of the angular velocities (ω_x if $I_z = I_y$ or ω_y if $I_z = I_x$) and substitute in the other two. It is clear that by relabeling the axes, the problem can be cast into the current framework of analysis. On the other hand, if $I_z = I_x = I_y$, then the solution of the system of the differential Eqs. (1)–(3) becomes trivial. Hence, in any case we can assume, without loss of generality, that $\rho \neq 0$. Using (22), we have that for *both* spin-up and spin-down, the integral $I_0(x;\rho)$ can be evaluated by

$$I_0(x;\rho) = \sqrt{\pi/|\rho|}\,\mathrm{sgn}\,(x)\bar{E}\left(\sqrt{|\rho|/\pi}x\right). \tag{23}$$

In this expression sgn denotes the signum function such that $\mathrm{sgn}\,(x) = 1$, for $x > 0$, $\mathrm{sgn}\,(x) = -1$, for $x < 0$, and $\mathrm{sgn}\,(x) = 0$, for $x = 0$. Therefore, Eqs. (10) and (14) give the complete solution for the transverse components of the angular velocity vector ω_x and ω_y in terms of complex Fresnel integrals (20). The solution for ω_z was found in (4).

3 Analytic Solution of Attitude Motion

We use Eulerian angles to describe the attitude orientation of a rotating body. Although other descriptions of the attitude are also available (Euler parameters, direction cosines) the Eulerian angles have the advantage of directly representing physical quantities, making them amenable to engineering insight. We have chosen to use Eulerian angles in the present analysis mainly for this reason. Using a 3-1-2 Eulerian angle sequence (Wertz, 1980; Kane et al., 1983), the kinematics obey the following set of differential equations:

$$\dot{\phi}_x = \omega_x \cos\phi_y + \omega_z \sin\phi_y \tag{24}$$

$$\dot{\phi}_y = \omega_y - (\omega_z \cos\phi_y - \omega_x \sin\phi_y)\tan\phi_x \tag{25}$$

$$\dot{\phi}_z = (\omega_z \cos\phi_y - \omega_x \sin\phi_y)\sec\phi_x. \tag{26}$$

Under this parameterization of the kinematics, the orientation of the local body-fixed reference frame with respect to the inertial reference frame is found by first rotating the body about its z-axis through an angle ϕ_z, then rotating about its x-axis with an angle ϕ_x and finally by rotating about its y-axis by an angle ϕ_y. Note that a singularity exists in Eqs. (25) and (26) for $\phi_x = \pm\pi/2$. For a 3-1-2 sequence, ϕ_x and ϕ_y describe the attitude deviation of the spin axis from its initial orientation (assumed to be the inertial Z-axis), that is caused from the application of disturbances. For a spin-stabilized body these represent unwanted deviation of the spin axis and are often referred to as the *attitude error components*.

A small angle approximation for ϕ_x, ϕ_y is therefore quite reasonable for a spin-stabilized body, and together with the assumption that the product $\phi_y\omega_x$ in Eq. (26) is usually small compared to ω_z, reduces the previous system of equations, (24)–(26), to the following reduced system of three linear time-varying differential equations:

$$\dot{\phi}_x = \omega_x + \phi_y\omega_z \tag{27}$$

$$\dot{\phi}_y = \omega_y - \phi_x\omega_z \tag{28}$$

$$\dot{\phi}_z = \omega_z. \tag{29}$$

The solution for ϕ_z is given immediately by

$$\phi_z(t) = \int_0^t \omega_z(u)\,du + \phi_z(0) = \frac{1}{2}(M_z/I_z)t^2 + \omega_{z0}t + \phi_{z0}, \quad \phi_{z0} \triangleq \phi_z(0). \tag{30}$$

Since the solution of ω_z is known from (4), one can combine the two equations (27) and (28) into the following single complex scalar equation:

$$\dot{\phi} + i\omega_z\phi = \omega \tag{31}$$

where the complex variables $\phi(t) \triangleq \phi_x(t) + i\phi_y(t)$ and $\omega(t) \triangleq \omega_x(t) + i\omega_y(t)$ have been introduced. Using the new independent variable τ as was done in Eq. (5), one gets that

Downloaded 03 May 2010 to 171.66.16.245. Redistribution subject to ASME license or copyright; see http://www.asme.org/terms/Terms_Use.cfm

$$\frac{d\phi}{d\tau} + i\lambda\tau\phi = \lambda\omega, \tag{32}$$

where λ is defined by $\lambda \triangleq \rho/k = I_z/M_z$. Equation (32) is a linear time-varying differential equation in the complex plane. The complex angle ϕ represents a measure of the total deviation of the spin axis. The differential equation for ϕ has the solution

$$\phi(\tau) = \phi_0 \exp\left(-i\frac{\lambda}{2}\tau^2\right) + \lambda \exp\left(-i\frac{\lambda}{2}\tau^2\right)\int_{\tau_0}^{\tau} \exp\left(i\frac{\lambda}{2}u^2\right)\omega(u)\,du \tag{33}$$

where $\phi_0 \triangleq \phi(\tau_0)\exp[i(\lambda/2)\tau_0^2]$ and $\phi(\tau_0)$ represents the initial condition for the transverse angles ϕ_x and ϕ_y in the new independent variable. The solution involves an expression for $\omega(\tau)$ instead of $\Omega(\tau)$, which has been already found in Eq. (10). However, it is easy to see that $\omega(\tau)$ can be expressed in terms of the already known solution of $\Omega(\tau)$ to obtain

$$\omega(\tau) = \Omega(\tau)\frac{\sqrt{k_x}+\sqrt{k_y}}{2k} + \Omega^*(\tau)\frac{\sqrt{k_x}-\sqrt{k_y}}{2k}. \tag{34}$$

Therefore, in order to solve for the Eulerian angles, one needs to evaluate the two integrals

$$I_{\phi_1}(\tau_0,\tau;\lambda,\rho) \triangleq \int_{\tau_0}^{\tau} \exp\left(i\frac{\lambda}{2}u^2\right)\Omega(u)\,du \tag{35}$$

$$I_{\phi_2}(\tau_0,\tau;\lambda,\rho) \triangleq \int_{\tau_0}^{\tau} \exp\left(i\frac{\lambda}{2}u^2\right)\Omega^*(u)\,du. \tag{36}$$

Recall that from Eqs. (10) and (11) the solution for $\Omega(\tau)$ is given by

$$\Omega(\tau) = \Omega_0 \exp\left(i\frac{\rho}{2}\tau^2\right) + \exp\left(i\frac{\rho}{2}\tau^2\right) I_\omega(\tau_0,\tau;\rho) \tag{37}$$

where, from Eq. (14), $I_\omega(\tau_0,\tau;\rho) = \sum_{n=0}^{m} F_n \bar{I}_n(\tau_0,\tau;\rho)$ and $\bar{I}_n(\tau_0,\tau;\rho)$ was given in Eq. (15). If one substitutes (37) into (35) and (36), after carrying out the algebra, one obtains

$$I_{\phi_1}(\tau_0,\tau;\lambda,\rho) = \left[\Omega_0 - \sum_{n=0}^{m} F_n I_n(\tau_0;\rho)\right]\int_{\tau_0}^{\tau} \exp\left(i\frac{\mu}{2}u^2\right)du + \sum_{n=0}^{m} F_n \int_{\tau_0}^{\tau} \exp\left(i\frac{\mu}{2}u^2\right) I_n(u;\rho)\,du \tag{38}$$

$$I_{\phi_2}(\tau_0,\tau;\lambda,\rho) = \left[\Omega_0^* - \sum_{n=0}^{m} F_n^* I_n^*(\tau_0;\rho)\right]\int_{\tau_0}^{\tau} \exp\left(i\frac{\kappa}{2}u^2\right)du + \sum_{n=0}^{m} F_n^* \int_{\tau_0}^{\tau} \exp\left(i\frac{\kappa}{2}u^2\right) I_n^*(u;\rho)\,du \tag{39}$$

where $\mu \triangleq \lambda + \rho = \lambda(1+k)$ and $\kappa \triangleq \lambda - \rho = \lambda(1-k)$. The first integral in (38) is computed by

$$\int_{\tau_0}^{\tau} \exp\left(i\frac{\mu}{2}u^2\right)du = \bar{I}_0(\tau_0,\tau;-\mu). \tag{40}$$

In similar way one handles the first integral in (39). The second integrals appearing in Eqs. (38) and (39) are of the same form and can be handled simultaneously. Therefore, we present next how one computes the second integral in (38), with the provision that the computation of the corresponding integral in (39) is found by taking the complex conjugate. Let the integral in Eq. (38) be denoted by

$$J_n(\tau_0,\tau;\mu,\rho) \triangleq \int_{\tau_0}^{\tau} \exp\left(i\frac{\mu}{2}u^2\right) I_n(u;\rho)du,\ n=0,1,2,\ \ldots,\ m. \tag{41}$$

From the recurrence formula for $I_n(u;\rho)$ given in Eq. (17), one can easily verify the following recurrence formula for $J_n(\tau_0,\tau;\mu,\rho)$:

$$J_n(\tau_0,\tau;\mu,\rho) = \frac{i}{\rho}\int_{\tau_0}^{\tau} \exp\left(i\frac{\lambda}{2}u^2\right)u^{n-1}du - i\frac{n-1}{\rho}J_{n-2}(\tau_0,\tau;\mu,\rho),\quad n=2,3,4,\ \ldots. \tag{42}$$

Since one readily computes

$$\int_{\tau_0}^{\tau} \exp\left(i\frac{\lambda}{2}u^2\right)u^{n-1}du = \bar{I}_{n-1}(\tau_0,\tau;-\lambda), \tag{43}$$

the use of the above recurrence formula allows one to reduce the evaluation of the integral $J_n(\tau_0,\tau;\mu,\rho)$ to the evaluation of the first two unknown terms of the sequence, given by

$$J_0(\tau_0,\tau;\mu,\rho) \triangleq \int_{\tau_0}^{\tau} \exp\left(i\frac{\mu}{2}u^2\right) I_0(u;\rho)\,du \tag{44}$$

$$J_1(\tau_0,\tau;\mu,\rho) \triangleq \int_{\tau_0}^{\tau} \exp\left(i\frac{\mu}{2}u^2\right) I_1(u;\rho)\,du. \tag{45}$$

The integral in (45) can easily be computed using Eq. (19) as

$$J_1(\tau_0,\tau;\mu,\rho) = \frac{i}{\rho}\left[\int_{\tau_0}^{\tau} \exp\left(i\frac{\lambda}{2}u^2\right)du - \int_{\tau_0}^{\tau} \exp\left(i\frac{\mu}{2}u^2\right)du\right] = \frac{i}{\rho}\left[\bar{I}_0(\tau_0,\tau;-\lambda) - \bar{I}_0(\tau_0,\tau;-\mu)\right]. \tag{46}$$

Using (23), the integral $J_0(\tau_0,\tau;\mu,\rho)$ takes the form

$$J_0(\tau_0,\tau;\mu,\rho) = \sqrt{\pi/|\rho|}\int_{\tau_0}^{\tau} \sin(u)\exp\left(i\frac{\mu}{2}u^2\right)\bar{E}\left(\sqrt{|\rho|/\pi}\,u\right)du. \tag{47}$$

By the change of variable $\bar{u} \triangleq \sqrt{|\rho|/\pi}\,u$, the above integral simplifies to

$$J_0(\tau_0,\tau;\mu,\rho) = (\pi/|\rho|)\int_{\bar{\tau}_0}^{\bar{\tau}} \sin(\bar{u})\exp\left(i\frac{\bar{\mu}}{2}\bar{u}^2\right)\bar{E}(\bar{u})d\bar{u} \triangleq (\pi/|\rho|)\bar{J}_0(\bar{\tau}_0,\bar{\tau};\bar{\mu}) \tag{48}$$

where $\bar{\tau}_0 \triangleq \sqrt{|\rho|/\pi}\,\tau_0$, $\bar{\tau} \triangleq \sqrt{|\rho|/\pi}\,\tau$, and $\bar{\mu} \triangleq \mu\pi/|\rho|$. If one now also drops for notational convenience the bars from the arguments of $\bar{J}_0$, one has merely to examine the integral

$$\bar{J}_0(\tau_0,\tau;\mu) \triangleq \int_{\tau_0}^{\tau} \operatorname{sgn}(u)\exp\left(i\frac{\mu}{2}u^2\right)\bar{E}(u)\,du. \tag{49}$$

The above is an integral that appears in the problem when the forcing transverse torques are constants, and has been thoroughly evaluated by Tsiotras and Longuski (1991a), where series expansions of the Fresnel integral $\bar{E}(u)$ were used, in order to integrate (49) termwise. A very accurate representation of the Fresnel integral was used (Boersma, 1960) based on the τ-method of Lanczos (1956). It is interesting to note that $\bar{J}_0(\tau_0,\tau;\mu)$ is closely related to integrals appearing in the mathematical theory of rocket flight (Rosser et al., 1947). Summing up, we have that $I_{\phi_1}(\tau_0,\tau;\lambda,\rho)$ and $I_{\phi_2}(\tau_0,\tau;\lambda,\rho)$ are computed by

Downloaded 03 May 2010 to 171.66.16.245. Redistribution subject to ASME license or copyright; see http://www.asme.org/terms/Terms_Use.cfm

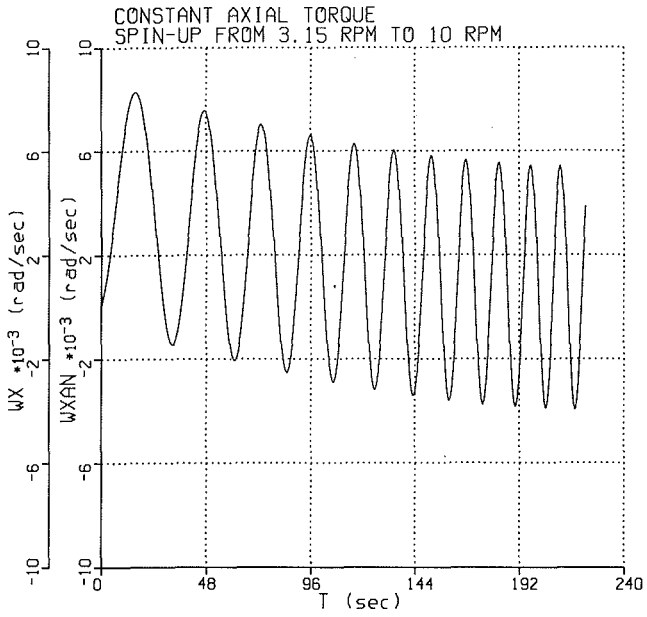


Fig. 1 Exact and analytic solutions for $\omega_x(t)$

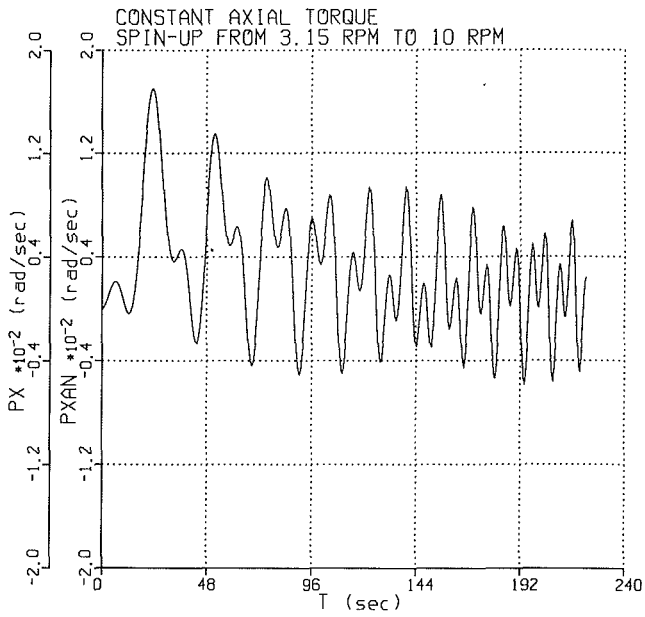


Fig. 2 Exact and analytic solutions for $\phi_x(t)$

$$I_{\phi_1}(\tau_0,\tau;\lambda,\rho)=\left[\Omega_0-\sum_{n=0}^{m}F_nI_n(\tau_0;\rho)\right]\bar{I}_0(\tau_0,\tau;-\mu)+\sum_{n=0}^{m}F_nJ_n(\tau_0,\tau;\mu,\rho) \tag{50}$$

$$I_{\phi_2}(\tau_0,\tau;\lambda,\rho)=\left[\Omega_0^*-\sum_{n=0}^{m}F_n^*I_n^*(\tau_0;\rho)\right]\bar{I}_0(\tau_0,\tau;-\kappa)+\sum_{n=0}^{m}F_n^*J_n^*(\tau_0,\tau;-\kappa,\rho). \tag{51}$$

The above relations along with (33)–(36) and (30), provide the *complete* analytical solution to the differential Eqs. (29) and (31), for the orientation of a near-symmetric spinning rigid body, when the forcing transverse torques are polynomial functions of time.

4 Numerical Example

A numerical example is used in order to demonstrate the accuracy of the analytic solutions. The inertia parameters are based on the Galileo spacecraft (Longuski, 1991) and are given by $I_x=2985$ kg-m^2, $I_y=2729$ kg-m^2, and $I_z=4183$ kg-m^2. The Galileo spacecraft is a dual spin vehicle. It can operate in an all-spin mode in which the rotor and the stator revolve together, or a dual-spin mode with the stator fixed in inertial frame. The above values correspond to its all-spin mode, i.e., when the stator and the rotor are locked and are rotating with the same spin velocity. We consider first a *spin-up maneuver* from $\omega_z(0)=3.15$ rpm to $\omega_z(t_f)=10$ rpm. For the purpose of illustration, the transverse torques M_x and M_y are assumed to be given by

$$M_x(t)=1.0+2.7\times10^{-2}t-2.4\times10^{-4}t^2+5.7\times10^{-7}t^3\text{N-m} \tag{52}$$

$$M_y(t)=-1.5-9.0\times10^{-3}t+1.2\times10^{-4}t^2-3.0\times10^{-7}t^3\text{N-m}. \tag{53}$$

The coefficients of the corresponding polynomials of M_x and M_y in terms of τ in Eq. (12) can then be computed, using (4) and (5).

The initial conditions for ω_x, ω_y, ϕ_x, ϕ_y, and ϕ_z are all assumed to be zero. The spin-up maneuver is simulated with a

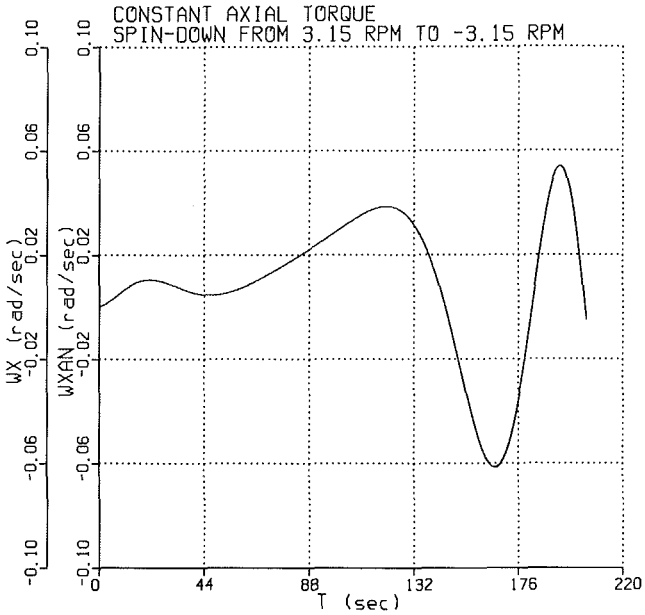


Fig. 3 Exact and analytic solutions for $\omega_x(t)$

constant M_z torque of 13.5 N-m. The results are shown in Figs. 1 and 2. In these figures the captions refer to the *exact* solution which means a precise numerical integration of the original differential equations (Eqs. (1)–(3) and Eqs. (24)–(26)). As shown in the figures, the analytic solutions are very close to the exact solutions for the case of a spin-up maneuver. In fact, the analytic solutions are indistinguishable from the exact solutions when presented on the same plot. Only the ω_x and ϕ_x solutions are plotted since ω_y and ϕ_y exhibited similar behavior.

A spin-down maneuver through zero spin rate, is considered next, from $\omega_z(0)=3.15$ rpm to $\omega_z(t_f)=-3.15$ rpm, with all other initial conditions set to zero, as before. The torque M_z is considered to be constant at $M_z=-13.5$ N-m. The transverse torques are given again by Eqs. (52) and (53). The results are shown in Figs. 3 through 5. Once again, we see that the analytic solutions for the angular velocities cannot be differentiated from the exact solutions when plotted in the same figure. The

Downloaded 03 May 2010 to 171.66.16.245. Redistribution subject to ASME license or copyright; see http://www.asme.org/terms/Terms_Use.cfm

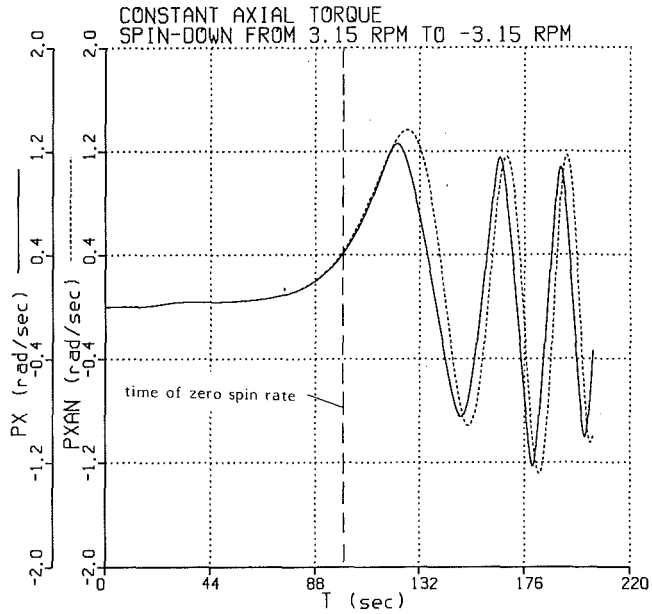


Fig. 4 Exact and analytic solutions for $\phi_x(t)$

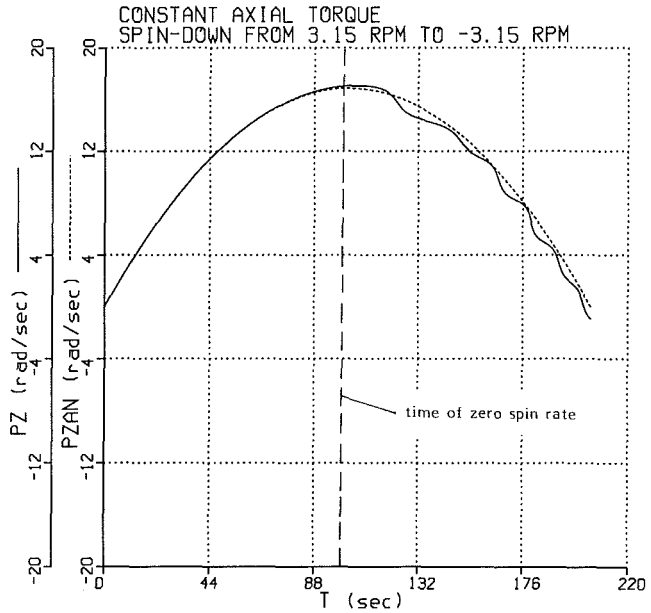


Fig. 5 Exact and analytic solutions for $\phi_z(t)$

spin-down maneuver represents a much more difficult case for the analytic solutions of the Eulerian angles when zero spin rate is reached, because the stabilizing effect of spinning about the maximum principal axis of inertia vanishes, and the transverse torques cause the angles to grow suddenly, as can be seen in Fig. 4. At this point the small angle assumption begins to break down and nonlinear behavior is exhibited. This is clear from Figs. 4 and 5 where the solid line indicates the exact solution, while the dotted line represents the analytic solution. It is interesting to note, however, that even though the value of ϕ_x exceeds 1 radian in Fig. 4, the general behavior is still qualitatively predicted by the analytic solution. For a further discussion of the large angle problem see Tsiotras and Longuski (1992).

5 Conclusions

Approximate analytic solutions have been derived for the attitude motion of a near-symmetric spinning rigid body, under the influence of transverse time-varying torques, expressed as polynomial functions. The torque about the spinning axis is assumed to remain constant. Analytic solutions were derived for both the angular velocity vector and the Eulerian angles. These solutions were shown to be very accurate when compared with the exact solutions for typical spacecraft maneuvers in a numerical example. In fact, the solution of the angular velocities are exact when the rigid body is axisymmetric. The solutions for the Eulerian angles are always approximate due to a small angle assumption, but they remain valid for a large class of practical applications. Part II of the paper extends the preceding results to include cases when all *three* components of the external torque vector are time-varying.

Acknowledgment

This research has been supported by the National Science Foundation under Grant No. MSS-9114388 (NSF program official Elbert L. Marsh).

References

Abramowitz, M., and Stegun, I. A., 1972, *A Handbook of Mathematical Functions*, Dover Publications Inc., New York.

Boersma J., 1960, "Computation of Fresnel Integrals," *Math. Comp.*, Vol. 14, p. 380.

Bois, E., 1986, "First-Order Theory of Satellite Attitude Motion Application to Hipparcos," *Celest. Mech.*, Vol. 39, pp. 309–327.

Hintz, G. R., and Longuski, J. M., 1985, "Error Analysis for the Delivery of a Spinning Probe to Jupiter," *Journal of Guidance, Control, and Dynamics*, Vol. 8, No. 3, pp. 384–390.

Kane, T. R., Likins, P. W., and Levinson, P. A., 1983, *Spacecraft Dynamics*, McGraw-Hill, New York.

Kia, T., and Longuski, J. M., 1984, "Error Analysis of Analytic Solutions for Self-Excited Near Symmetric Rigid Bodies: A Numerical Study," AIAA Paper 84-2018, AIAA/AAS Astrodynamics Conference, Seattle, WA, Aug. 20–22.

Lanczos C., 1956, *Applied Analysis*, Prentice-Hall, Englewood Cliffs, NJ.

Longuski, J. M., 1980, "Solution of Euler's Equations of Motion and Eulerian Angles for Near Symmetric Rigid Bodies Subject to Constant Moments," AIAA Paper 80-1642, AIAA/AAS Astrodynamics Conference, Danvers, MA, Aug. 11–13.

Longuski, J. M., 1991, "Real Solutions for the Attitude Motion of a Self-Excited Rigid Body," *Acta Astron.*, Vol. 25, No. 3, pp. 131–140.

Longuski, J. M., Kia, T., and Breckenridge, W. G., 1989, "Annihilation of Angular Momentum Bias During Thrusting and Spinning-up Maneuvers," *J. Astron. Sci.*, Vol. 37, No. 4, pp. 433–450.

Rosser, J. B., Newton, R. R., and Gross, G. L., 1947, *Mathematical Theory of Rocket Flight*, McGraw-Hill, New York.

Tsiotras, P., and Longuski, J. M., 1991a, "Complex Analytic Solution for the Attitude Motion of a Near-Symmetric Rigid Body Under Body-Fixed Torques," *Celest. Mech.*, Vol. 51, pp. 281–301.

Tsiotras, P., and Longuski, J. M., 1991b, "Analytic Solutions for the Attitude Motion of Spinning Rigid Bodies Subject to Periodic Torques," AAS Paper 91-404, AAS/AIAA Astrodynamics Conference, Durango, CO, Aug. 19–22.

Tsiotras, P., and Longuski, J. M., 1992, "On the Large Angle Problem in Rigid Body Attitude Dynamics," IAF Paper 92-0034, 43rd Congress of the International Astronautical Federation, Washington, D.C., Aug. 28–Sept. 5.

Wertz, J. R., 1980, *Spacecraft Attitude Determination and Control*, D. Reidel Publishing Company, Dordrecht, Holland.

Downloaded 03 May 2010 to 171.66.16.245. Redistribution subject to ASME license or copyright; see http://www.asme.org/terms/Terms_Use.cfm

P. Tsiotras
Ph. D. Candidate.

J. M. Longuski
Assoc. Professor.

School of Aeronautics and Astronautics,
Purdue University,
West Lafayette, IN 47907

Analytic Solutions for a Spinning Rigid Body Subject to Time-Varying Body-Fixed Torques, Part II: Time-Varying Axial Torque

In this paper we extend the methodology developed in Part I in order to accommodate the case of an axial time-varying torque (in addition to the two transverse time-varying torques) acting on a rotating rigid body. The analytic solutions thus derived describe the general attitude motion of a near-symmetric rigid body subject to time-varying torques about all three body-fixed axes.

1 Introduction

The problem of attitude motion of a rotating rigid body is a very difficult one, and no general solution is known to exist. This comes as no surprise since the equations of motion consist of a system of six nonlinear, coupled differential equations and one cannot expect to find solutions to these equations without some simplifying assumptions. Typically such assumptions include axial symmetry of the body (see the survey by Janssens, 1980), a torque-free body (Junkins et al., 1973; Cochran and Shu, 1983; Kane and Levinson, 1987), or a weakly perturbed torqued body (Kraige and Junkins, 1976). For the case of a *self-excited* rigid body (Leimanis, 1965; Longuski, 1984), the general problem of forced motion is somewhat alleviated because the acting torques do not depend on the body orientation. Considerable progress has been achieved in recent years in developing analytic and semi-analytic solutions for this particular problem. Up to now, only rigid bodies subject to *constant* torques have been considered (Longuski, 1980; Van der Ha, 1984; Tsiotras and Longuski, 1991a). Solutions like these can help us better understand the underlying behavior of the dynamics of rotating rigid bodies under the influence of external torques, but they do not address the more complicated problem when the external torques vary with time. The purpose of this paper is to extend previous solutions to include cases when the torques are no longer required to be constants. Part I examined the case when the transverse torques were modeled as *polynomial* functions of time. Part II extends these results to include a time-varying axial torque, as well. This study is complementary to the study by Tsiotras and Longuski (1991b), where the transverse torques are modeled as *periodic* functions or can be expressed in terms of Fourier series. In such models, virtually all physically realizable torques can be accommodated.

We outline the general analytic procedure as follows. In the case of an axial time-varying torque, with the two transverse time-varying torques, the same simplifying assumptions made in Part I are used to reduce the solution of the problem to quadratures. The integrals appearing, however, are much more complicated than those in the constant axial-torque case, and there is no a priori guarantee that one can evaluate these integrals in closed form; the success of this task depends on each particular problem at hand. In many cases, a judicious choice of a new independent variable allows one to avoid much of the work involved in the evaluation of these integrals. When such a choice is not possible or difficult, a general method that allows approximate evaluation of a very large class of integrals is provided that can accommodate most of the cases of practical interest. The main difficulty of this method relies upon the construction of an explicit representation of the inverse transformation between the new independent variable and the original independent variable, i.e. time. Sufficient conditions when this is possible are discussed and a method to find this inverse transformation in terms of series expansions is also presented. The method of analytic continuation is used to extend the solution for all times outside the initial interval of the convergence of the series. Numerical simulations provide an indication of the accuracy and the validity of the solutions for both the angular velocity vector and the Eulerian angles.

2 Solution for the Angular Velocities and Eulerian Angles

The analysis in Part I was based on the assumption that the axial torque M_z is constant. The case when M_z is a function of the independent variable is much more complicated and the ability to find closed-form expressions for the solution in such a case is not assured. To be more specific, using the near-symmetry assumption $I_x \approx I_y$ in the differential equation for the spin velocity ω_z, one can readily find ω_z by simple integration as

Contributed by the Applied Mechanics Division of THE AMERICAN SOCIETY OF MECHANICAL ENGINEERS for publication in the ASME JOURNAL OF APPLIED MECHANICS.

Discussion on this paper should be addressed to the Technical Editor, Professor Lewis T. Wheeler, Department of Mechanical Engineering, University of Houston, Houston, TX 77204-4792, and will be accepted until four months after final publication of the paper itself in the JOURNAL OF APPLIED MECHANICS.

Manuscript received by the ASME Applied Mechanics Division, Apr. 10, 1992; final revision, Oct. 22, 1992. Associate Technical Editor: R. L. Huston.

Copyright © 1993 by ASME
Downloaded 03 May 2010 to 171.66.16.245. Redistribution subject to ASME license or copyright; see http://www.asme.org/terms/Terms_Use.cfm

$$\omega_z(t) \approx \int_0^t \frac{M_z(u)}{I_z}\, du + \omega_z(0). \tag{1}$$

In general, M_z in the above expression is not constant, but it is given as a prescribed function of time. According to the analysis presented in Part I, the transverse components of the angular velocity ω_x and ω_y can be found by solving the following linear differential equation:

$$\frac{d\Omega}{dt} - ik\omega_z\Omega = M(t) \tag{2}$$

where the variables in the above expression have been introduced in Part I, and the forcing function $M(t)$ is given by $M(t) \triangleq (M_x(t)/I_x)\sqrt{k_y} + i(M_y(t)/I_y)\sqrt{k_x}$. One then can easily give the solution for the transverse angular velocities from (2) as

$$\Omega(t) = \Omega_0 \exp\left[ik\int_0^t \omega_z(u)du\right] + \exp\left[ik\int_0^t \omega_z(u)du\right]\int_0^t M(u)\exp\left[-ik\int_0^u \omega_z(v)dv\right]du. \tag{3}$$

It is clear from (3), that although the calculation of Ω and therefore for ω_x and ω_y has been reduced to quadratures, the practical applicability of the solution is limited by one's ability, ingenuity, or even luck to calculate these integrals in closed form. The same statement holds for the analytic solution of the Eulerian angles, as well. As shown in Part I, a small angle assumption reduces the problem of the kinematics to the solution of the two linear differential equations $\dot{\phi} = \omega_z$ and $\dot{\phi} + i\omega_z\phi = \omega$, the solution of which can be given in terms of quadratures by

$$\phi_z(t) = \int_0^t \omega_z(u)du + \phi_z(0) \tag{4}$$

$$\phi(t) = \phi_0 \exp\left[-i\int_0^t \omega_z(u)\,du\right] + \exp\left[-i\int_0^t \omega_z(u)\,du\right]\int_0^t \omega(u)\exp\left[i\int_0^u \omega_z(v)dv\right]du \tag{5}$$

where $\phi \triangleq \phi_x + i\phi_y$ and $\omega \triangleq \omega_x + i\omega_y$. For the special case when all three acting torques are constant, it can be shown that the evaluation of (3) can be performed exactly in terms of Fresnel integrals; the evaluation of (5) is more complicated, but very accurate approximations have been found by Tsiotras and Longuski (1991a). No general statements can be made however about the form of the solutions, when the acting external torques are arbitrary functions of time. Nevertheless, when ω_z does not become zero, one can apply the methodology developed in Part I for the constant M_z case, with a few modifications, to develop solutions that approximate the angular velocity vector solution for the time-varying M_z case as accurately as one may wish. The case of a nonvanishing spin rate ω_z could be, for example, the case of a spin-up maneuver ($M_z > 0$) from a positive value of initial spin rate ($\omega_z(0) > 0$), or the case of a spin-down maneuver ($M_z < 0$) from a negative value of initial spin rate ($\omega_z(0) < 0$). We proceed now to the development of the analysis for such a case.

2.1 Transformation of Independent Variable. Assuming hereafter that $\omega_z(t) \neq 0$ (for all t), we introduce the new independent variable $\tau = \tau(t)$ by

$$\tau \triangleq \int_0^t \omega_z(u)du. \tag{6}$$

In most instances we will suppress the explicit dependence of τ on t, but one should always keep in mind Eq. (6). When for reasons of clarity we need to stress this dependence, we will do so. The previous expression implies in particular that $d\tau/dt = \omega_z$. Therefore, one can write the differential Eq. (2) that governs the behavior for Ω, in terms of the new independent variable τ as follows:

$$\frac{d\Omega}{d\tau} - ik\Omega = F(\tau) \tag{7}$$

where now, however, the forcing function F has to be considered in terms of the new independent variable, that is,

$$F(\tau) \triangleq \frac{M(t(\tau))}{\omega_z(t(\tau))}. \tag{8}$$

In such a case, the solution for $\Omega(\tau)$ is given by

$$\Omega(\tau) = \Omega_0 \exp(ik\tau) + \exp(ik\tau)\int_0^\tau F(u)\exp(-iku)\,du. \tag{9}$$

It should be mentioned that the integral in (9) is equivalent to the integral in (3); however, the integration, now performed with respect to the new independent variable τ, has simplified the form of the integrand significantly. The difficulty of the aforementioned methodology relies, however, upon the explicit evaluation of the forcing term $F(\tau)$ in Eq. (7), or equivalently, upon our ability to express M/ω_z as a function of the new independent variable τ as in Eq. (8). This is, in general, not a trivial task and it is not assured that one can find such an analytic representation for F. There are cases, however, that such an expression is readily available by the nature of the problem. Hence, one can evaluate the complete solution of Ω without the need to express t as a function of τ, but one can use his intuition, or the physics of the problem in order to introduce, where possible, new variables that will simplify the problem considerably. For example, in a number of problems, the underlying behavior of the external torques is based on ϕ_z, so the choice of ϕ_z as our new independent variable can reduce the problem to the evaluation of elementary functions. In fact, as was shown by Bois (1986), in many cases involving spinning satellites the external torque depends upon the rotation angle of the satellite ϕ_z, or one can expand the dominating torque in terms of ϕ_z alone. For all these cases, the choice of ϕ_z as the new independent variable looks very promising. In general, however, it is not possible to express the acting torques as a function of the new independent variable directly, so a more general procedure is required that will encompass all the cases of practical interest. This will involve solving for t in terms of τ from Eq. (6). Sufficient conditions that allow one to obtain such an expression are given by the Inverse Function Theorem, and are discussed later on.

2.2 Angular Velocities. At this point, we will make the assumption that the external axial torques M_x, M_y, and M_z are *analytic* functions of time, that is, have convergent power series expansions about each point over their domain of definition. In other words, we assume that M_x, M_y, and M_z can be represented by the power series expansions

$$M_x(t) = \sum_{n=0}^{\infty} M_{x,n}t^n, \quad M_y(t) = \sum_{n=0}^{\infty} M_{y,n}t^n, \quad M_z(t) = \sum_{n=0}^{\infty} M_{z,n}t^n. \tag{10}$$

In these expressions the variable t should be considered as a variable in the *complex* plane even though, physically, t represents the real variable time. This is necessary, because the singularities that determine the convergence properties of power series lie in the complex plane and thus, power series have to be introduced having a complex argument. From analytic function theory (Knopp, 1956) it is known that the convergence of the above series is *absolute* and *uniform*. The importance of

Downloaded 03 May 2010 to 171.66.16.245. Redistribution subject to ASME license or copyright; see http://www.asme.org/terms/Terms_Use.cfm

the absolute convergence is the fact, that one can operate with absolutely convergent series for the most part, as with ordinary sums. That is, one can add, subtract, and take (Cauchy) products, and rearrange the terms of absolutely convergent series without worrying about convergence, i.e., completely *formally*. On the other hand, uniform convergence of the series will imply, among other things, that one is allowed to integrate the series termwise, and the sum of the integrals will converge to the integral of the function that this series represents.

Using Eqs. (1), (6), and (10) we have that

$$\omega_z(t) = \sum_{n=0}^{\infty} \omega_{z,n} t^n, \quad \text{with } \omega_{z,n} = \frac{M_{z,n-1}}{I_z n} \tag{11}$$

for $n = 1,2,3, \ldots$ and $\omega_{z,0} \triangleq \omega_z(0)$ and

$$\tau(t) = \sum_{n=0}^{\infty} b_n t^n, \quad \text{with } b_n = \frac{\omega_{z,n-1}}{n} \tag{12}$$

for $n = 1,2,3, \ldots$ and $b_0 \triangleq 0$.

Of course, for the special case when M_z is a polynomial in t, the foregoing series terminate after a finite number of terms. In order to write F as a function of the new independent variable τ, one has to invert Eq. (6) to write t as a function of τ and then compose this function into F. From the previous discussion, and Eqs. (8) and (10), it follows that one can represent the function M/ω_z with a power series

$$\frac{M(t)}{\omega_z(t)} = F(t) = \sum_{n=0}^{\infty} \bar{f}_n t^n \quad \text{for } |t| < r \tag{13}$$

where r is the radius of convergence of the series. Inside the disk of radius r (t considered complex), the series converges absolutely and uniformly. It is clear that, in general, F will have a finite radius of convergence, since any zeros of ω_z will be singular points of F in the complex plane. In fact, the radius of convergence equals the minimum distance to the origin of any zero of ω_z. It is clear that because of the assumption that $\omega_z(t) \neq 0$, none of the singularities of F can lie on the real axis. This assumption is essential, because later we will allow the use of analytic continuation in order to extend the solution to arbitrary time intervals. Nevertheless, there are singularities on the complex plane and for the case when M_z is a polynomial of order n, there are exactly $n+1$ singularities of F in the complex plane, all of which are *poles*. In general, the inverse function of (6) does not exist globally, unless the function $\tau = \tau(t)$ is bijective (one-to-one and onto). The Inverse Function Theorem states, however, that one is always able to invert a function in the vicinity of points where the derivative does not vanish. For our problem a *sufficient* condition for this to be true is that ω_z does not change sign inside the domain of its definition. This implies that $\tau(t)$ is monotonic, and thus (in fact globally) invertible. Therefore, inverting Eq. (12) we get

$$t(\tau) = \sum_{n=1}^{\infty} c_n \tau^n \tag{14}$$

where the coefficients of the inverted series can be calculated recursively, from the relationships (Knopp, 1956)

$$\begin{aligned}
&c_1 = 1/b_1, \quad c_2 = -b_2/b_1^3, \quad c_3 = (2b_2^2 - b_1 b_3)/b_1^5 \\
&c_4 = (5b_1 b_2 b_3 - b_1^2 b_4 - 5b_2^3)/b_1^7 \\
&c_5 = (6b_1^2 b_2 b_4 + 3b_1^2 b_3^2 + 14 b_2^4 - b_1^3 b_5 - 21 b_1 b_2^2 b_3)/b_1^9 \\
&c_6 = (7b_1^3 b_2 b_5 + 7b_1^3 b_3 b_4 + 84 b_1 b_2^3 b_3 \\
&\quad - b_1^4 b_6 - 28 b_1^2 b_2^2 b_4 - 28 b_1^2 b_2 b_3^2 - 42 b_2^5)/b_1^{11} \\
&\vdots
\end{aligned} \tag{15}$$

Notice that the choice of $b_0 = 0$, which is arbitrary at this point, results in $c_0 = 0$, a condition that will be explained in detail later. Substitution now of Eq. (14) into Eq. (13) results in the following power series of F in terms of the new independent variable τ

$$F(t(\tau)) = \sum_{n=0}^{\infty} f_n \tau^n \text{ for } |\tau| < R \tag{16}$$

where R is the radius of convergence of the composed series, completely determined by r.

A necessary and sufficient condition for the composition of $t(\tau)$ into F in (16) is that $|c_0| < r$, where as mentioned earlier r is the radius of convergence of (13). We therefore see that the choice of $c_0 = 0$ in (14) was more than a simple convenience, but rather it was imposed so that the method is well defined for every r. For a more complete analysis on the inversion and composition of power series as well as in general analytic function theory, see Knopp (1956) and Hille (1973).

Using Eq. (16) one can compute the required integral in (9) by

$$\int_0^{\tau} F(u) \exp(-iku)\, du = \sum_{n=0}^{\infty} f_n \int_0^{\tau} u^n \exp(-iku)\, du. \tag{17}$$

Integrals of this form can be evaluated using the recurrence formula

$$\int u^n \exp(-iu) du = iu^n \exp(-iu) - in \int u^{n-1} \exp(-iu) du \qquad n = 1,2,3, \ldots . \tag{18}$$

Therefore, the complete solution for Ω is given by

$$\Omega(\tau) = \Omega_0 \exp(ik\tau) + \exp(ik\tau) \sum_{n=0}^{\infty} f_n I_n(\tau;k) \tag{19}$$

where

$$I_n(\tau;k) \triangleq \int_0^{\tau} u^n \exp(-iku)\, du, \quad n = 0,1,2, \ldots . \tag{20}$$

2.3 Eulerian Angles. Using the transformation introduced in (6) and the relationship between ω and Ω established in Part I, one writes the solution for the Eulerian angles (5) in the form

$$\begin{aligned}
\phi(\tau) &= \phi_0 \exp(-i\tau) + \exp(-i\tau) \int_0^{\tau} \frac{\omega(u)}{\omega_z(t(u))} \exp(iu) du \\
&= \phi_0 \exp(-i\tau) + \exp(-i\tau) \left[k_1 \int_0^{\tau} \frac{\Omega(u)}{\omega_z(t(u))} \exp(iu) du \right. \\
&\qquad \left. + k_2 \int_0^{\tau} \frac{\Omega^*(u)}{\omega_z(t(u))} \exp(iu) du \right]
\end{aligned} \tag{21}$$

where

$$k_1 \triangleq \left(\sqrt{k_x} + \sqrt{k_y} \right)/2k \text{ and } k_2 \triangleq \left(\sqrt{k_x} - \sqrt{k_y} \right)/2k.$$

Thus, the following two integrals need to be evaluated,

$$\int_0^{\tau} \frac{\Omega(u)}{\omega_z(t(u))} \exp(iu) du, \quad \int_0^{\tau} \frac{\Omega^*(u)}{\omega_z(t(u))} \exp(iu) du, \tag{22}$$

where the solution for Ω has been found from (19). Recall now, that according to the discussion for the solution for the angular velocities, $1/\omega_z(t)$ is analytic along the real line and using Eq. (14) we can write its expansion in terms of τ in the form of a power series

$$\frac{1}{\omega_z(t(\tau))} = \sum_{m=0}^{\infty} a_m \tau^m \quad \text{for } |\tau| < R. \tag{23}$$

If we substitute the above expression into (21) then after some

Downloaded 03 May 2010 to 171.66.16.245. Redistribution subject to ASME license or copyright; see http://www.asme.org/terms/Terms_Use.cfm

straightforward algebraic manipulation, we may write for the first integral in (22)

$$\int_0^\tau \frac{\Omega(u)}{\omega_z(t(u))} \exp(iu)\,du = \Omega_0 \sum_{m=0}^{\infty} a_m I_m^*(\tau;k+1) + \sum_{n=0}^{\infty}\sum_{m=0}^{\infty} F_n a_m J_n^m(\tau;k) \quad (24)$$

where

$$J_n^m(\tau;k) \triangleq \int_0^\tau u^m \exp[i(k+1)u] I_n(u;k)\,du \quad (25)$$

and $I_m^*(\tau;k+1)$ can be computed by Eqs. (18) and (20). Using also the recurrence formula for $I_n(\tau;k)$ given in (18) one gets for fixed m, a recurrence formula for $J_n^m(\tau;k)$ as follows:

$$J_n^m(\tau;k) = \frac{i}{k}\int_0^\tau u^{n+m}\exp(iu)\,du - i\frac{n}{k}\int_0^\tau u^m \exp[i(k+1)u] I_{n-1}(u;k)\,du = \frac{i}{k} I_{n+m}^*(\tau;1) - i\frac{n}{k} J_{n-1}^m(\tau;k) \quad (26)$$

for $n=1,2,3,\ldots$ and $m=0,1,2,\ldots$.

For $n=0$ and for some fixed integer m, the first term of the sequence of the integrals $J_n^m(\tau;k)$ is computed by

$$J_0^m(\tau;k) = \int_0^\tau u^m \exp[i(k+1)u] I_0(u;k)\,du = \frac{i}{k}[I_m^*(\tau;1) - I_m^*(\tau;k+1)],\quad m=0,1,2,\ldots \quad (27)$$

because from (20) we have

$$I_0(\tau;k) = \int_0^\tau \exp(-iku)\,du = \frac{i}{k}[\exp(-ik\tau)-1]. \quad (28)$$

It is not difficult to show that the second integral in (22), required for the solution of the Eulerian angles, is given similarly by

$$\int_0^\tau \frac{\Omega^*(u)}{\omega_z(t(u))}\exp(iu)\,du = \Omega_0^* \sum_{m=0}^{\infty} a_m I_m^*(\tau;k-1) + \sum_{n=0}^{\infty}\sum_{m=0}^{\infty} F_n^* a_m J_n^m(\tau;-k). \quad (29)$$

Equation (21) along with Eqs. (22), (24), and (29) give the solution to the Eulerian angles. In practice, one has to approximate the solution by truncating the infinite series in (24) and (29); however, because of the established absolute convergence of these series, the approximation can be made as accurately as one wishes. For most practical applications this will suffice.

3 Extension of the Solution

As mentioned at the beginning of the present analysis, the series representation of F in (13) has in general a finite radius of convergence r, which is determined by the zero of ω_z closest to the origin in the complex plane. It is therefore clear that one cannot expect the previous methodology to still be valid for time $t \geq r$. In fact, as we approach this value $t=r$ the rate of convergence of the series (16) becomes slower and slower, and therefore more and more terms are needed in order to achieve the same accuracy. One way to circumvent this difficulty is to use the principle of *analytic continuation* for F in order to find $F(t)$ for all t.

In short, the methodology goes as follows. Since, by assumption, ω_z has no zero on the real axis, one can choose a time $t_1 < r$ and expand F about $t=t_1$. The resulting series has a radius of convergence r_1 and therefore we can choose time t_2 such that $t_1 < t_2 < t_1 + r_1$ and expand F about $t=t_2$, etc. In general, given an expansion of F about a point t_n with radius of convergence r_n, we can find a point t_{n+1} such that $t_n < t_{n+1} < t_n + r_n$ and such that if we expand F in a power series about this point, the series will have a radius of convergence r_{n+1} which will be determined by the closest zero to t_{n+1} of ω_z in the complex plane.

Formalizing the method, we assume that given a time T, we seek the value of the solution (2) for all $t \in [0, T]$. It is obvious from (3) and (9) that the solution merely consists of evaluating the integral in (17)

$$R(\tau) \triangleq \int_0^\tau F(u)\exp(-iku)\,du \quad (30)$$

where $\tau = \tau(t)$. As a first step, we partition the interval $[0, T]$ into N subintervals $[t_n, t_{n+1}]$, $n=0, 1, 2, \ldots, N-1$, such that $t_0 = 0$ and $t_N = T$. The time points $t_1, t_2, \ldots, t_{N-1}$ have been chosen by the procedure explained in the previous paragraph. Now given $t \in [0, T]$, let $t \in [t_n, t_{n+1}]$ for some n. Then we can write $R(\tau)$ as follows:

$$R(\tau) = R(\tau_n) + \int_{\tau_n}^{\tau} F(u)\exp(-iku)\,du \quad (31)$$

where $\tau_n = \tau(t_n)$. If we now let $\tau = \tau_n + \Delta\tau$, we can write

$$R(\tau) = R(\tau_n) + \int_0^{\Delta\tau} F(\tau_n + u)\exp[-ik(\tau_n+u)]\,du = R(\tau_n) + \exp(-ik\tau_n)\int_0^{\Delta\tau} F(\tau_n+u)\exp(-iku)\,du. \quad (32)$$

It is easy to show that $\Delta\tau$ is related to $\Delta t = t - t_n$ by

$$\Delta\tau = \int_0^{\Delta t} \omega_z(t_n+u)\,du. \quad (33)$$

Therefore, if we expand $M(t)/\omega_z(t)$ about $t=t_n$ and use the series inversion formula for (33) we can write $F(\tau_n+\Delta\tau)$ in terms of $\Delta\tau$, that is, we obtain an expansion of $F(\tau)$ about τ_n. Substitution of this expansion in (9) will give for the solution of Ω

$$\Omega(\tau) = [\Omega_0 + R(\tau_n)]\exp(ik\tau) + \exp(ik\Delta\tau)\int_0^{\Delta\tau} F_n(u)\exp(-iku)\,du \quad (34)$$

where the explicit dependence of τ on t has been suppressed and F_n represents the series expansion of $F(\tau)$ about τ_n, that is, $F(\tau_n+\Delta\tau) = F_n(\Delta\tau) = \sum_{m=0}^{\infty} F_{n,m}(\Delta\tau)^m$. It is important to keep in mind that for $t_n \leq t \leq t_{n+1}$, or equivalently for $0 < \Delta\tau \leq \tau_{n+1} - \tau_n$ the independent variable in (34) is $\Delta\tau$. In order to stress this point we can rewrite (34) in the equivalent form

$$\Omega(\tau_n+\Delta\tau) = \Omega_{0,n}\exp(ik\Delta\tau) + \exp(ik\Delta\tau)\int_0^{\Delta\tau} F_n(u)\exp(-iku)\,du = \Omega_{0,n}\exp(ik\Delta\tau) + \exp(ik\Delta\tau)\sum_{m=0}^{\infty} F_{n,m} I_m(\Delta\tau;k) \quad (35)$$

where $\Omega_{0,n} \triangleq [\Omega_0 + R(\tau_n)]\exp(ik\tau_n)$ is constant for $t \in [t_n, t_{n+1}]$. The last equation is of the same form as Eq. (19). The explicit representation of the solution for Ω in terms of $\Delta\tau$ has an advantage that will become clear shortly, when we seek analytic solutions for the Eulerian angles.

In accordance with the previous discussion, it is necessary to extend also the solution for the Eulerian angles for all t using analytic continuation, since the expansion (23) is limited

Downloaded 03 May 2010 to 171.66.16.245. Redistribution subject to ASME license or copyright; see http://www.asme.org/terms/Terms_Use.cfm

by the singularities of $1/\omega_z$ in the complex plane. To be more precise, given a time T, we are interested in the evaluation of the integral (36) for all $t\in[0, T[$:

$$Q(\tau)\triangleq\int_0^{\tau}\frac{\Omega(u)}{\omega_z(t(u))}\exp(iu)du. \tag{36}$$

The methodology to compute $Q(\tau)$ is along the same lines used for the evaluation of $R(\tau)$. Since the singularities of F in (13) are completely determined by the singularities of $1/\omega_z$, it will suffice to use the *same partition* of the interval $[0, T]$ into N subintervals $[t_n, t_{n+1}]$, $n=0, 1, 2, \ldots, N-1$, as before. Now given $t\in[t_n, t_{n+1}]$, for some n, one writes $Q(\tau)$ as follows:

$$Q(\tau)=Q(\tau_n)+\exp(i\tau_n)\int_0^{\Delta\tau}\frac{\Omega(\tau_n+u)}{\omega_z(t(\tau_n+u))}\exp(iu)du. \tag{37}$$

By expanding ω_z about $t=t_n$ and using (33) we get the following expansion of $1/\omega_z$ about τ_n

$$\frac{1}{\omega_z(t(\tau_n+\Delta\tau))}=\sum_{m=0}^{\infty}a_{n,m}(\Delta\tau)^m \tag{38}$$

where the subscript n denotes expansion about τ_n. Using the previous equation along with Eqs. (37) and (35) we get that

$$\int_0^{\Delta\tau}\frac{\Omega(\tau_n+u)}{\omega_z(t(\tau_n+u))}\exp(iu)du=\Omega_{0,n}\sum_{m=0}^{\infty}a_{n,m}I_m^*(\Delta\tau;k+1)+\sum_{p=0}^{\infty}\sum_{m=0}^{\infty}F_{n,p}a_{n,m}J_p^m(\Delta\tau;k). \tag{39}$$

This expression is of the same form as the one in (24) and can be computed using the recursive formulas (18) and (26). We mention in passing that for the second integral in (22) one has, similarly,

$$\int_0^{\Delta\tau}\frac{\Omega^*(\tau_n+u)}{\omega_z(t(\tau_n+u))}\exp(iu)du=\Omega_{0,n}^*\sum_{m=0}^{\infty}a_{n,m}I_m^*(\Delta\tau;k-1)+\sum_{p=0}^{\infty}\sum_{m=0}^{\infty}F_{n,p}^*a_{n,m}J_p^m(\Delta\tau;-k). \tag{40}$$

4 Criticism of the Analytic Solutions

We have described a methodology that gives the solution for the angular velocity components in a body-fixed frame, and the solution for the Eulerian angles, for the case when arbitrary transverse and axial torques act simultaneously on the body. The sole hypothesis made is that the rotating rigid body be nearly symmetric about its spin axis; an additional mild assumption is that the acting torques are analytic functions of time. In practice, one usually approximates the acting torques with polynomials, or equivalently, by truncating the power series expansions until a desired degree of accuracy is achieved. Therefore, the model of polynomial torques for the acting torques encompasses a large class of applications. The methodology consists of introducing a new independent variable in order to simplify the arising integrals. In many cases, a judicious choice of the new independent variable will eliminate most of the tedious calculations, however, in general one will require the use of the inverse transformation (14) to express the forcing function in (7) in terms of the new independent variable. For the case when the spin rate ω_z does not vanish, one can introduce ω_z as the new independent variable. Then the inverse transformation is given in the form of an infinite power series, and this is true even when the actual torques are exact polynomials. Because in practice one has to truncate the infinite series (14) an error is always present in the solution. Even worse, since the series representation of the function F has a finite radius of convergence, one cannot expect to obtain a globally valid solution for all t. However, the theory of analytic continuation can be used to circumvent this difficulty and extend the previous analytic solution for all t, as demonstrated above. Moreover, because the series in (35), (39), and (40) converge absolutely and uniformly, the general procedure allows one to approximate the solution as accurately as one desires.

Next we shall demonstrate with a numerical example the accuracy of the derived analytic solutions, for a typical practical application involving a spinning spacecraft subject to external disturbing torques about all three axes.

5 Numerical Example

We consider the simplest case when the axial torque M_z is *linearly increasing with time* from $M_z(0)=0$ to $M_z(t_f)=28$ N−m for $t_f=200$ s. That is, it is assumed that

$$M_z(t)=0.1273\ t\ \text{N}-\text{m}. \tag{41}$$

The transverse torques M_x and M_y, are assumed to be the same as for the constant axial torque example, and are given in Part I. The rigid-body mass properties, as well as the initial conditions for the angular velocity vector, remain the same as for the constant axial torque case. Under these assumptions, one can compute $\tau(t)$ by Eq. (12), and $t(\tau)$ and $F(\tau)$ from (14) and (16). (In other words, we begin with $M_{x,n}$, $M_{y,n}$ and $M_{z,n}$ from Eqs. (10), we find b_n from Eqs. (11) and (12), $\bar{f}_n$ from Eq. (13), c_n from Eqs. (14) and (15) and ultimately f_n from Eq. (16).) For the given values, ω_z is a quadratic polynomial which has two conjugate imaginary roots at approximately $\pm i\,147$. Therefore, the method of analytic continuation has been used to extend the solution beyond the bound of 147 s, as described earlier in the paper. Three points have been chosen in the interval $0\le t\le 200$; at $t_1=60$, $t_2=110$, and $t_3=160$ seconds, respectively. The operations with the power series were performed using the symbolic language manipulation software package MAPLE (Char et al., 1991). The results of the numerical simulations are depicted in Figs. 1 and 2. Only the ω_x (Fig. 1) and ϕ_x (Fig. 2) solutions are shown here, since ω_y and ϕ_y exhibit similar behavior. It is clear that upon the construction of the analytic solutions, a compromise must be made between the number of the terms kept in the power series in (16) and (23) and in the number of partition intervals for the analytical continuation of the solution. It is an unfortunate fact that decreasing the number of intervals required for con-

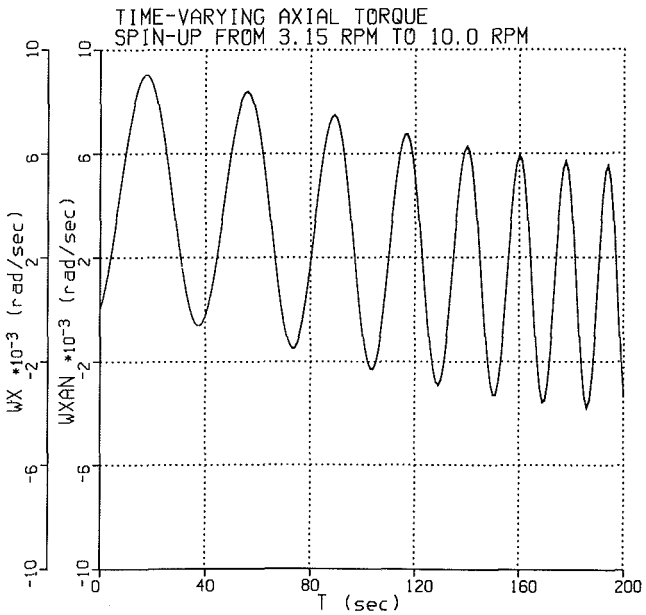


Fig. 1 Exact and analytic solutions for $\omega_x(t)$

Downloaded 03 May 2010 to 171.66.16.245. Redistribution subject to ASME license or copyright; see http://www.asme.org/terms/Terms_Use.cfm

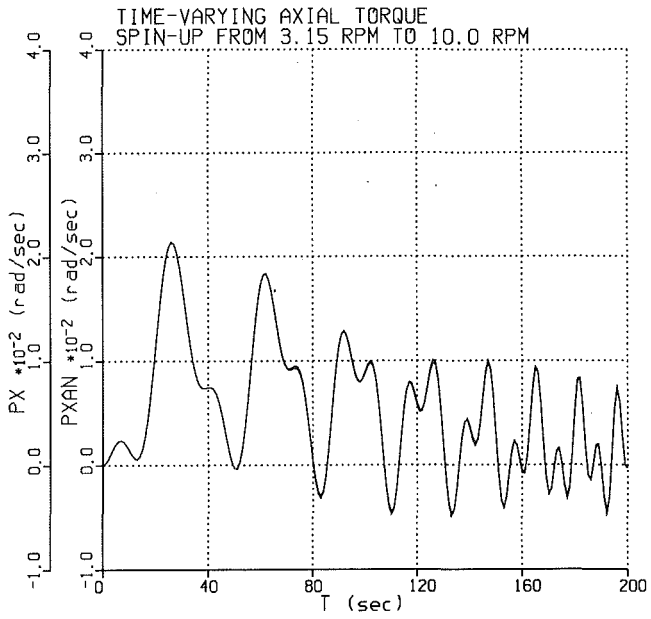


Fig. 2 Exact and analytic solutions for $\phi_x(t)$

tinuation of the solution beyond the bound determined by the singularities of $1/\omega_z$ comes at the expense of increasing the number of terms in the series expansion of F and $1/\omega_z$. In the example presented here, the first six terms were kept in the expansions of F and $1/\omega_z$ about each t_n, for $n=0,1,2,3$.

6 Conclusions

Approximate analytic solutions have been derived for the attitude motion of a near-symmetric spinning rigid body, under the influence of transverse and axial time-varying torques, expressed as polynomial functions of time. In essence, the theory of Part I has been extended to include cases when all three components of the external torque vector vary with time. The difficulty of the method relies on expressing the external torques as functions of a new independent variable. Since the external torques are known functions of time, this involves the construction of the inverse transformation between the two independent variables. This is achieved using a series inversion lemma. As a consequence, the evaluation of the required integrals is always approximate, but because of the established convergence of the series, the approximation can be made arbitrarily accurate.

Acknowledgment

This research has been supported by the National Science Foundation under Grant No. MSS-9114388 (NSF program official Elbert·L. Marsh).

References

Bois, E., 1986, "First-Order Theory of Satellite Attitude Motion Application to Hipparcos," *Celest. Mech.*, Vol. 39, pp. 309–327.

Char, B. W., Geddes, K. O., Gonnet, G. H., Leong, B. L., Monagan, M. B., and Watt, S. M., 1991, *Maple Language Reference Manual*, Waterloo Maple Publishing.

Cochran, J. E., and Shu, P. H., 1983, "Attitude Motion of Spacecraft with Skewed Internal Angular Momenta," *J. Astron. Sci.*, Vol. 31, pp. 203–215.

Hille, E., 1973, *Analytic Function Theory*, Chelsea, New York.

Janssens, F., 1980, "Nutation of a Symmetric Rigid Body under Continuous Thrusting; Application to METEOSAT-2," ESTEC Working Paper No. 1247, Noordwijk, The Netherlands.

Junkins, J. L., Jacobson, I. D., and Blanton, J. N., 1973, "A Nonlinear Oscillator Analog of Rigid Body Dynamics," *Celest. Mech.*, Vol. 7, pp. 397–407.

Kane, T. R., and Levinson, D. A., 1987, "Approximate Description of Attitude Motions of a Torque-Free, Nearly Axisymmetric Rigid Body," *J. Astron. Sci.*, Vol. 35, pp. 435–446.

Knopp, K., 1956, *Infinite Sequences and Series*, Dover Publications, New York.

Kraige, L. G., and Junkins, J. L., 1976, "Perturbation Formulations for Satellite Attitude Dynamics," *Celest. Mech.*, Vol. 13, pp. 39–64.

Leimanis, E., 1965, *The General Problem of the Motion of Coupled Rigid Bodies About a Fixed Point*, Springer-Verlag, New York.

Longuski, J. M., 1980, "Solution of Euler's Equations of Motion and Eulerian Angles for Near Symmetric Rigid Bodies Subject to Constant Moments," AIAA Paper 80-1642, AIAA/AAS Astrodynamics Conference, Danvers, MA, Aug. 11–13.

Longuski, J. M., 1984, "On the Attitude Motion of a Self-Excited Rigid Body," *J. Astron. Sci.*, Vol. 32, pp. 463–473.

Tsiotras, P., and Longuski, J. M., 1991a, "Complex Analytic Solution for the Attitude Motion of a Near-Symmetric Rigid Body Under Body-Fixed Torques," *Celest. Mech.*, Vol. 51, pp. 281–301.

Tsiotras, P., and Longuski, J. M., 1991b, "Analytic Solutions for the Attitude Motion of Spinning Rigid Bodies Subject to Periodic Torques," AAS Paper 91-404, AAS/AIAA Astrodynamics Conference, Durango, CO, Aug. 19–22.

Van der Ha, J. F., 1984, "Perturbation Solution of Attitude Motion Under Body-Fixed Torques," IAF Paper 84-357, 35th Congress of the International Astronautical Federation, October 7–13, Lausanne, Switzerland.

Downloaded 03 May 2010 to 171.66.16.245. Redistribution subject to ASME license or copyright; see http://www.asme.org/terms/Terms_Use.cfm

The Incremental Variational Principles for Frictional Contact Problems of Linear Elasticity

G. Zboinski
Institute of Fluid Flow Machinery,
Polish Academy of Sciences,
80-952 Gdansk, Poland

Four types of the most frequently used variational functionals are employed in order to form the inequality principles of the kineto-static contact problem of two elastic bodies in the common relative motion. As the general case, the principle based on the Hu-Washizu functional is proposed. The principles formed with the Reissner type, potential energy, and complementary energy functionals are derived as the special cases.

1 Introduction

Variational principles of the contact mechanics are formulated either in the classical (nonincremental) form or incremental description of the problem is applied. The former case includes slip definition of the bodies in contact in terms of total displacements (Panagiotopoulos, 1975; Oden and Pires, 1983; Kikuchi and Oden, 1988) or velocities (Michalowski and Mróz, 1978; Kalker, 1986a,b; Klarbing, 1990). For the latter case the slip definition is based on the displacement increments and two possibilities exist. Either one can apply fully incremental approach with the linear elasticity and contact mechanics equations in the incremental form (Frederiksson, 1976; Torstenfelt, 1983) or only contact mechanics equations take the incremental form (Zboiński, 1990). The last approach, which is also applied in the paper, is a bit similar to Kalker's formulation. One of the main differences is application of the slip increments in this paper instead of Kalker's time increments and velocities.

2 Variational Formulations of the Problem

The paper presents variational formulations of the incremental kineto-static frictional contact problem for two linear thermoelastic bodies a ($a = 1, 2$) in a relative motion due to small deformations. Initial volumes, Vo, initially loaded and constrained parts Po and Qo of the surfaces of the bodies are shown in Fig. 1. The motion of the bodies is described in the same reference configuration for both the bodies, as the common transportation motion with a known acceleration a^i is assumed. The same curvilinear coordinates ξ^i ($i, j, k, l = 1, 2, 3$) with the corresponding metric tensor g^{ij} are applied. The alternative may be the use of two different reference configurations moving with respect to each other with a known displacement increment. The initial, current, and searched configurations of any point of the bodies are denoted Mo, M', and M, respectively.

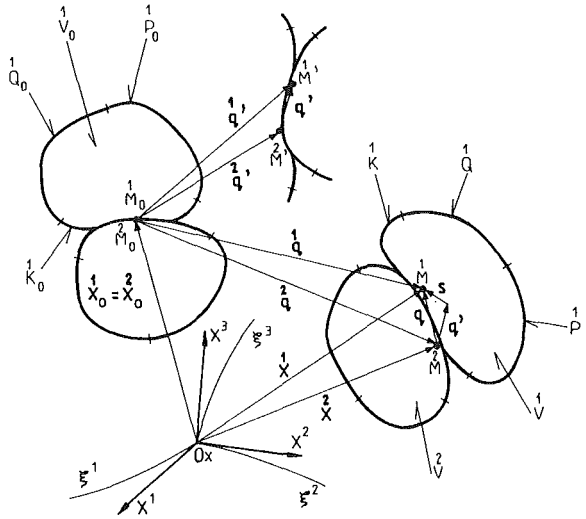


Fig. 1 Incremental deformation of two elastic bodies in contact

We apply standard nomenclature throughout the paper. Terms D^{ijkl}, σ^{ij}, ϵ_{ij} are the elastic constants, stress, and strain tensors, respectively. Displacements and stress reactions are denoted by q^i and r^i while terms f^i, d^i, and p^i are known vectors of the body forces, surface displacements, and surface tractions. The unit exterior normal vector of each body is denoted ν^i. Quantities ρ, α, and T represent the mass density, the thermal expansion coefficient, and the stationary temperature field, respectively.

We apply the following notation of the quantities defined within the initial potential contact area Ko. For any point of Ko, we introduce a local system with one axis n ($n = 1$) normal and two axes t or s ($t, s = 1, 2$) tangent to the surface of the first body ($a = 1$). The directions of the local surface system are defined by the unit exterior normal vector n^i of the first

Contributed by the Applied Mechanics Division of THE AMERICAN SOCIETY OF MECHANICAL ENGINEERS for publication in the ASME JOURNAL OF APPLIED MECHANICS.

Discussion on this paper should be addressed to the Technical Editor, Professor Lewis T. Wheeler, Department of Mechanical Engineering, University of Houston, Houston, TX 77204-4792, and will be accepted until four months after final publication of the paper itself in the ASME JOURNAL OF APPLIED MECHANICS.

Manuscript received by the ASME Applied Mechanics Division, July 5, 1991; final revision, May 5, 1992. Associate Technical Editor: A. K. Noor.

Copyright © 1993 by ASME
Downloaded 03 May 2010 to 171.66.16.245. Redistribution subject to ASME license or copyright; see http://www.asme.org/terms/Terms_Use.cfm

body and the pseudo-tensor t_{is} of two unit tangents of the same body. The normal and tangential components of the contact stress reactions of the first body are denoted by r_n and r_t. Quantities ho_n and h_n represent the initial and searched gap between the bodies, while s_t is the slip increment vector defined with the tangential displacement difference increment vector Δq_t. The normal and tangential components of the differences of displacements of the bodies in contact are denoted q_n and q_t.

The local formulation of the contact problem under consideration is based on the nonincremental elasticity equations and incremental contact mechanics equations. We assume that the tangential traction bound $b = \mu p_n$ is known and defined by the Coulomb friction coefficient μ and a function p_n, which may represent the given contact pressure. This pressure may be updated iteratively to converge towards the unknown contact normal reaction, r_n as proposed by Panagiotopulos (1975) or Kalker (1990).

2.1 The Hu-Washizu Functional. The following contact mechanics relations of the local formulation (not included in the variational principle)

$$\left.\begin{aligned} &h_n r_n = 0\\ &h_n \le 0\\ &(s_t s_t)^{1/2}[(r_t r_t)^{1/2} + \mu p_n] = 0\\ &(s_t s_t)^{1/2} \ge 0 \end{aligned}\right\}, \quad \xi^i \in K, \tag{1}$$

have to be applied in order to complete the problem description (Zboiński, 1990).

As the inequality terms due unilateral constraints and tangential traction bound appear in the functional defining the problem, the variational principle takes the inequality form. The sign of the inequality is unknown, as the individual variations applied in the principle are neither kinematically nor statically admissible but arbitrary. For the kineto-static problem, the kinetic energy is defined as a virtual work of the d'Alembert force. Thus we have

$$\delta J_{h\text{-}w} \lessgtr 0, \tag{2}$$

where the Hu-Washizu functional $J_{h\text{-}w}$ is given by the formula

$$J_{h\text{-}w} = \sum_{a=1}^{2} \left(\overset{a}{Vo} \int \left\{ \overset{a}{D}{}^{ijkl} \left(\frac{1}{2}\epsilon_{ij} - g_{ij} \overset{a}{\alpha} T \right) \epsilon_{kl} - \sigma^{ij} [\epsilon_{ij} - 1/2(q_{i,j} + q_{j,i})] - (f^i - \overset{a}{\rho} a^i) q_i \right\} d\overset{a}{Vo} - \overset{a}{Po} \int P^i q_i d\overset{a}{Po} - \overset{a}{Qo} \int r^i (q_i - d_i) d\overset{a}{Qo} \right) - {}_K\!\int [r_n (q_n - h_n + ho_n) + r_t (\Delta q_t - s_t) + \mu p_n (s_t s_t)^{1/2}] dK. \tag{3}$$

We assume that the functional (2) is a function of independent arguments q_i (or q_n and q_t), ϵ_{ij}, r^i (or r_n and r_t), σ^{ij} as well as h_n and s_t. Thus, the final form of the principle can be obtained by summation of the right-hand side terms of (4) after application of Gauss proposition and integration by parts

$$\partial J_{h\text{-}w}/\partial q_i \cdot \delta q_i = -\sum_{a=1}^{2} \{ \overset{a}{Vo} \int (\sigma^{ij}_{\ j} + f^i - \overset{a}{\rho} a^i) \delta q_i d\overset{a}{Vo} + \overset{a}{Po} \int (\sigma^{ij} \nu_j - p^i) \delta q_i d\overset{a}{Po} - \overset{a}{Qo} \int (\sigma^{ij} \nu_j - r^i) \delta q_i d\overset{a}{Qo} \},$$

$$\partial J_{h\text{-}w}/\partial \epsilon_{ij} \cdot \delta \epsilon_{ij} = \sum_{a=1}^{2} \overset{a}{Vo} \int [\overset{a}{D}{}^{klij} (\epsilon_{kl} - g_{kl} \overset{a}{\alpha} T) - \sigma^{ij}] \delta \epsilon_{ij} d\overset{a}{Vo},$$

$$\partial J_{h\text{-}w}/\partial r^i \cdot \delta r^i = -\sum_{a=1}^{2} \overset{a}{Qo} \int (q_i - d_i) \delta r^i d\overset{a}{Qo},$$

$$\partial J_{h\text{-}w}/\partial \sigma^{ij} \cdot \delta \sigma^{ij} = -\sum_{a=1}^{2} \overset{a}{Vo} \int [\epsilon_{ij} - 1/2(q_{i,j} + q_{j,i})] \delta \sigma^{ij} d\overset{a}{Vo},$$

$$\partial J_{h\text{-}w}/\partial q_n \cdot \delta q_n = {}_K\!\int (\sigma^{ij} \nu_j n_i - r_n) \delta q_n dK,$$

$$\partial J_{h\text{-}w}/\partial q_t \cdot \delta q_t = {}_K\!\int (\sigma^{ij} \nu_j t_{is} \delta_{st} - r_t) \delta q_t dK,$$

$$\partial J_{h\text{-}w}/\partial r_n \cdot \delta r_n = -{}_K\!\int (q_n - h_n + ho_n) \delta r_n dK,$$

$$\partial J_{h\text{-}w}/\partial r_t \cdot \delta r_t = -{}_K\!\int (\Delta q_t - s_t) \delta r_t dK,$$

$$\partial J_{h\text{-}w}/\partial h_n \cdot \delta h_n = {}_K\!\int r_n \delta h_n dK,$$

$$\partial J_{h\text{-}w}/\partial s_t \cdot \delta s_t = {}_K\!\int [r_t \delta s_t - \mu p_n \delta (s_t s_t)^{1/2}] dK. \tag{4}$$

2.2 The Hellinger-Reissner Functional. As it can be seen from (4), the above variational functional of Hu-Washizu has the feature that one can replace all the equations of the local formulation of the problem apart from relations (1) with only one integral relation (3). The simplified approaches are also admissible in which one can assume that some of the local equations hold a priori. Thus, these equations can be omitted in the variational functional of the problem.

Having the above feature in mind, let us assume that the inverse of the constitutive relation, the stress reaction, and other conditions of the local formulation are valid a priori

$$\epsilon_{ij} - g_{ij} \overset{a}{\alpha} T = \overset{a}{D}{}^{-1}_{ijkl} \sigma^{kl}, \quad \xi^i \in \overset{a}{Vo}.$$

$$\left.\begin{aligned} &q^i = d^i\\ &\sigma^{ij} \nu_j = r^i \end{aligned}\right\}, \quad \xi^i \in \overset{a}{Qo}, \tag{5}$$

$$\left.\begin{aligned} &\sigma^{ij} \nu_j n_i = r_n\\ &\sigma^{ij} \nu_j t_{is} \delta_{st} = r_t\\ &q_n = h_n - ho_n\\ &h_n r_n = 0\\ &r_n \le 0\\ &s_t = \Delta q_t\\ &(s_t s_t)^{1/2}[(r_t r_t)^{1/2} + \mu p_n] = 0\\ &(s_t s_t)^{1/2} \ge 0 \end{aligned}\right\}, \quad \xi^i \in K.$$

Thus, the functional $J_{h\text{-}w}$ from relation (3) is equivalent to the Hellinger-Reissner functional J_r. The sign of the variational inequality is unknown again as the individual variations applied in the principle are still neither kinematically nor statically admissible but arbitrary. Having all the above in mind we can write the following inequality:

$$\delta J_r \lessgtr 0. \tag{6}$$

The term J_r can be obtained from $J_{h\text{-}w}$ with relations (5)

$$J_r = \sum_{a=1}^{2} \left\{ \overset{a}{Vo} \int \left[-\frac{1}{2} \overset{a}{D}{}^{-1}_{ijkl} \sigma^{ij} \sigma^{kl} - g_{ij} \overset{a}{\alpha} T \sigma^{ij} + \overset{a}{D}{}^{ijkl} g_{ij} g_{kl} \overset{a}{\alpha}{}^2 T^2 + \frac{1}{2} \sigma^{ij} (q_{i,j} + q_{j,i}) - (f^i - \overset{a}{\rho} a^i) q_i \right] d\overset{a}{Vo} - \overset{a}{Po} \int p^i q_i d\overset{a}{Po} \right\} - {}_K\!\int [\sigma^{ij} \nu_j n_i (q_n + ho_n) + \sigma^{ij} \nu_j t_{is} \delta_{st} (\Delta q_t - s_t) + \mu p_n (s_t s_t)^{1/2}] dK. \tag{7}$$

We assume that the functional (6) is a function of independent arguments q_i (or q_n), σ^{ij}, and s_t. Thus, the final form of the principle can be obtained by summation of the right-hand side terms of (8), remembering the last but one Eq. (5), and applying the Gauss proposition and integration by parts

Downloaded 03 May 2010 to 171.66.16.245. Redistribution subject to ASME license or copyright; see http://www.asme.org/terms/Terms_Use.cfm

$$\partial J_r/\partial q_i \cdot \delta q_i = -\sum_{a=1}^{2} \{ \overset{a}{Vo} \int (\sigma^{ij}_{,j} + f^i - \overset{a}{\rho} a^i)\delta q_i d\overset{a}{Vo} + \overset{a}{Po} \int (\sigma^{ij}\nu_j - p^i)\delta q_i d\overset{a}{Po} \},$$

$$\partial J_r/\partial \sigma^{ij} \cdot \delta\sigma^{ij} = -\sum_{a=1}^{2} \overset{a}{Vo} \int \left[\frac{1}{2} \overset{a}{D}{}^{-1}_{ijkl}\sigma^{kl} + g_{ij}\overset{a}{\alpha}T - 1/2(q_{i,j} + q_{j,i}) \right] \delta\sigma^{ij} d\overset{a}{Vo},$$

$$\partial J_r/\partial \sigma^{ij} \cdot \delta\sigma^{ij} = -{}_K\int (q_n + ho_n) n_i \nu_j \delta\sigma^{ij} dK - {}_K\int (\Delta q_t - s_t)\delta_{ts} t_{si} \nu_j \delta\sigma^{ij} dK,$$

$$\partial J_r/\partial q_n \cdot \delta q_n = 0,$$

$$\partial J_r/\partial s_t \cdot \delta s_t = {}_K\int [\sigma^{ij}\nu_j t_{is}\delta_{st}\delta s_t - \mu p_n \delta (s_t s_t)^{1/2}] dK.$$

2.3 The Potential Energy Functional. Let us assume now that the following equations of the local formulation are valid a priori:

$$\left.\begin{aligned} \epsilon_{ij} &= 1/2(q_{i,j} + q_{j,i}) \\ \sigma^{ij} &= \overset{a}{D}{}^{ijkl}(\epsilon_{kl} - g_{kl}\overset{a}{\alpha}T) \end{aligned}\right\}, \quad \xi^i \in \overset{a}{Vo},$$

$$\left.\begin{aligned} q^i &= d^i \\ \sigma^{ij}\nu_j &= r^i \end{aligned}\right\}, \quad \xi^i \in \overset{a}{Qo}, \tag{9}$$

$$\left.\begin{aligned} &\sigma^{ij}\nu_j n_i = r_n \\ &\sigma^{ij}\nu_j t_{is}\delta_{st} = r_t \\ &q_n = h_n - ho_n \\ &h_n r_n = 0 \\ &h_n \le 0 \\ &s_t = \Delta q_t \\ &(s_t s_t)^{1/2}[(r_t r_t)^{1/2} + \mu p_n] = 0 \\ &(s_t s_t)^{1/2} \ge 0 \end{aligned}\right\}, \quad \xi^i \in K.$$

Thus, the functional $J_{h\text{-}w}$ from relation (2) is equal to the potential energy J_p and we can write

$$\delta J_p \ge 0, \tag{10}$$

where the term J_p equals

$$J_p = \sum_{a=1}^{2} \left\{ \overset{a}{Vo} \int \left[\overset{a}{D}{}^{ijkl} \left(\frac{1}{2}\epsilon_{ij} - g_{ij}\overset{a}{\alpha}T \right) \epsilon_{kl} - (f^i - \overset{a}{\rho} a^i) q_i \right] d\overset{a}{Vo} - \overset{a}{Po} \int p^i q_i d\overset{a}{Po} \right\} + {}_K\int [-\mu p_n (s_t s_t)^{1/2}] dK. \tag{11}$$

The individual variations applied in the principle are all kinematically admissible. Thus the sign of the inequality (10) due to unilateral constraints and is tangential traction-bound can be uniquely defined.

The functional (10) can be treated as a function of the arguments q_i (or q_n) and s_t. It needs application of the relations $\delta\epsilon_{kl} = \delta u_{k,l}$ and $\delta s_t = \delta(\Delta q_t) = \delta(q_t - q_t') = \delta q_t$, where q_t' refers to the previous incremental step that arise from relations (9). Thus the final form of the principle can be obtained by summation of the right-hand side terms of (12) after application of the Gauss proposition and integration by parts

$$\partial J_p/\partial q_i \cdot \delta q_i = -\sum_{a=1}^{2} \{ \overset{a}{Vo} \int (\sigma^{ij}_{,j} + f^i - \overset{a}{\rho} a^i)\delta q_i d\overset{a}{Vo} + \overset{a}{Po} \int (\sigma^{ij}\nu_j - p^i)\delta q_i d\overset{a}{Po} \},$$

$$\partial J_p/\partial q_n \cdot \delta q_n = {}_K\int \sigma^{ij}\nu_j n_i \delta q_n dK,$$

$$\partial J_p/\partial s_t \cdot \delta s_t = {}_K\int [\sigma^{ij}\nu_t t_{is}\delta_{st}\delta s_t - \mu p_n \delta (s_t s_t)^{1/2}] dK. \tag{12}$$

2.4 The Complementary Energy Functional. Let us assume now that the following local relations are valid a priori:

$$\left.\begin{aligned} &\sigma^{ij}_{,j} + f^i - \overset{a}{\rho} a^i = 0 \\ &\epsilon_{ij} = 1/2(q_{i,j} + q_{j,i}) \\ &\epsilon_{ij} - g_{ij}\overset{a}{\alpha}T = \overset{a}{D}{}^{-1}_{ijkl}\sigma^{kl} \end{aligned}\right\}, \quad \xi^i \in \overset{a}{Vo}.$$

$$\left.\begin{aligned} &\sigma^{ij}\nu_j = p^i, \quad \xi^i \in \overset{a}{Po}, \\ &\sigma^{ij}\nu_j = r^i, \quad \xi^i \in \overset{a}{Qo}, \end{aligned}\right. \tag{13}$$

$$\left.\begin{aligned} &\sigma^{ij}\nu_j n_i = r_n \\ &\sigma^{ij}\nu_j t_{is}\delta_{st} = r_t \\ &q_n = h_n - ho_n \\ &h_n r_n = 0 \\ &r_n \le 0 \\ &s_t = \Delta q_t \\ &(s_t s_t)^{1/2}[(r_t r_t)^{1/2} + \mu p_n] = 0 \\ &(r_t r_t)^{1/2} + \mu p_n \le 0 \end{aligned}\right\}, \quad \xi^i \in K,$$

Thus, the functional $J_{h\text{-}w}$ from relation (2) becomes the complementary energy J_c. We can write

$$\delta J_c \le 0, \tag{14}$$

where the term J_c is defined as follows:

$$J_c = \sum_{a=1}^{2} \left[\overset{a}{Vo} \int \left(-\frac{1}{2} \overset{a}{D}{}^{-1}_{ijkl}\sigma^{ij}\sigma^{kl} - g_{ij}\overset{a}{\alpha}T\sigma^{ij} + \overset{a}{D}{}^{ijkl} g_{ij} g_{kl} \overset{a}{\alpha}{}^2 T^2 \right) d\overset{a}{Vo} + \overset{a}{Qo} \int \sigma^{ij}\nu_j d_i d\overset{a}{Qo} \right] - {}_K\int (\sigma^{ij}\nu_j n_i ho_n - \sigma^{ij}\nu_j t_{is}\delta_{st} q_t')\, dK. \tag{15}$$

The individual variation applied in the principle is statically admissible. Thus, the sign of the terms due unilateral constraints from inequality (14) can be defined. It is worth noting that the tangential traction terms do not appear in (15). It is a consequence of the last two a priori relations (13).

As the functional (14) is a function of independent argument σ^{ij}, the final form of the principle can be obtained by taking the right-hand side term of (16) gained with the Gauss proposition and integration by parts after substituting the second and third Eq. (13) into (15). We have to notice that $\delta\sigma^{ij}_{,j} = 0$ that arises from the first Eq. (13). We apply the relation $\Delta q_t = q_t - q_t'$. Thus we get

$$\partial J_c/\partial \sigma^{ij} \cdot \delta\sigma^{ij} = \sum_{a=1}^{2} [\overset{a}{Vo} \int q_i \delta\sigma^{ij}_{,j} d\overset{a}{Vo} - \overset{a}{Qo} \int (q_i - d_i)\nu_j \delta\sigma^{ij} d\overset{a}{Qo}] - {}_K\int [(q_n + ho_n) n_i \nu_j \delta\sigma^{ij} + s_t \delta_{ts} t_{si} \nu_j \delta\sigma^{ij}] dK. \tag{16}$$

The displacements applied in the above and other principles of the paper are not generally large as the contact problem of two bodies in the common rigid transportation motion is considered. In the case of a sliding or rolling contact problem where the displacements are generally large, although the deformations are small, it may be useful to decompose the total displacements of each body on the potential contact area into a given rigid-body displacement and the small reminder ones as proposed by Kalker (1990)).

3 The Existence and Uniqueness Theory

The existence and uniqueness of the solution for the frictionless contact of the elastic body and rigid foundation (Signorini problem) have been proved by Fichera (1972). The same problem has been also investigated by Knops and Payne (1971). Duvaut and Lions (1976) proved the existence of the solution for the static problem of the same body in the case of the

Downloaded 03 May 2010 to 171.66.16.245. Redistribution subject to ASME license or copyright; see http://www.asme.org/terms/Terms_Use.cfm

Coulomb friction when the tangential tractions are prescribed. They also formulated the terms for the uniqueness of the solution. The uniqueness for the same problem has also been investigated by Turner (1979). The existence and uniqueness of the solution for the same elastic bodies with the tangential tractions not known in advance (Signorini problem with friction) have been investigated by Duvault and Lions (1976), but they have not achieved the proper proofs. The special case of such a problem of little practical importance has been successfully solved by Nečas et al. (1980). Oden and Pires (1983) presented the proper proof of existence of such a problem for nonlocal friction law in the case of regularized normal pressures. They proved the existence of the solution for sufficiently small coefficients of friction.

All the above works refer to the nonincremental potential energy formulation of the problem. The same formulation as well as the nonincremental complementary energy and Reissner functional formulations have been used by Kikuchi and Oden (1988) to establish the existence and uniqueness of the solution of the Signorini problem.

An attempt to obtain the proper proof of existence and uniqueness has been done by Frederiksson (1976) for the case of fully incremental potential energy formulation. It corresponds only with the case when the geometry and normal loading of the contact area are defined in advance. The proof of the existence and uniqueness of the solution corresponding with the incremental potential energy formulation presented above have been established by this author (Zboiński, 1990) for the case of two elastic bodies when the tangential tractions are known in advance. The proof takes advantage of the considerations by Duvault and Lions (1976) as well as Kikuchi and Oden (1988).

4 Conclusions

There exist Hu-Washizu and Hellinger-Reissner functionals for the incremental frictional contact problem of two elastic bodies moving together.

The functional of Hu-Washizu forming the most general variational principle of the problem can be applied to derivation of the corresponding principles based on the Reissner, potential energy, and complementary energy functionals.

References

Duvaut, G., and Lions, J. L., 1972, *Inequalities in Mechanics and Physics*, Springer-Verlag, Berlin.

Fichera, G., 1964, "Existence Theorems in Elasticity: Boundary Value Problems of Elasticity with Unilateral Constraints," *Encyclopedia of Physics*, Vol. VI, Springer-Verlag, Berlin, pp. 347–427.

Frederiksson, B., 1976, "On Elastostatic Contact with Friction," Ph.D. Thesis, Linköping Inst. Technol., Linköping.

Kalker, J. J., 1986a, "The Principle of Virtual Work and Its Dual for Contact Problems in Elasticity," *Ing. Arch.*, No. 56, pp. 453–467.

Kalker, J. J., 1986b, "Mathematical Models for Contact Problems in Elasticity," *Wear*, No. 113, pp. 61–77.

Kalker, J. J., 1990, *Three-Dimensional Elastic Bodies in Rolling Contact*, Kluwer, Dordrecht, The Netherlands.

Kikuchi, N., and Oden, J. T., 1988, *Contact Problems in Elasticity: A Study of Variational Inequalities and Finite Element Methods*, SIAM, Philadelphia.

Klarbing, A., 1990, "Examples of Non-Uniqueness and Non-Existence of Solutions to Quasistatic Contact Problems with Friction," *Ing. Arch.*, No. 60, pp. 529–541.

Knops, R. J., and Payne, L. E., 1971, *Uniqueness Theorems in Linear Elasticity*, Springer-Verlag, Berlin.

Michałowski, R., and Mróz, Z., 1978, "Associated and Non-Associated Sliding Rules in Contact Friction Problems," *Arch. Mech.*, No. 30, pp. 259–276.

Nečas, J., Jurašek, J., and Haslinger, J., 1980, "On the Solution of the Variational Inequality to the Signorini Problem with Small Friction," *Boll. Un. Mat. Ital.*, No. 17, pp. 796–811.

Oden, J. T., and Pires, E. B., 1983, "Nonlocal and Nonlinear Friction Laws and Variational Principles for Contact Problems in Elasticity," ASME JOURNAL OF APPLIED MECHANICS, pp. 67–76.

Panagiotopoulos, P. D., 1975, "A Nonlinear Programming Approach to the Unilateral Contact- and Friction-Boundary Value Problem in the Theory of Elasticity," *Ing. Arch.*, No. 44, pp. 421–432.

Torstenfelt, B., 1983, "Contact Problems with Friction in General Purpose Finite Element Computer Programs," *Comput. Struct.*, No. 16, pp. 487–493.

Turner, J. R., 1979, "The Frictional Unloading Problem on a Linear Elastic Space," *J. Inst. Math. Appl.*, No. 24, pp. 439–469.

Zboiński, G., 1990, "Numerical Analysis of Kineto-Static Stresses and Strains in the Turbomachinery Blade Attachments," Ph.D. Thesis, Gdańsk Techn. Univ., Gdańsk, Poland.

Downloaded 03 May 2010 to 171.66.16.245. Redistribution subject to ASME license or copyright; see http://www.asme.org/terms/Terms_Use.cfm

G. Meda

S. F. Hoysan

P. S. Steif
Mem. ASME.

Department of Mechanical Engineering,
Carnegie Mellon University,
Pittsburgh, PA 15213

The Effect of Fiber Poisson Expansion in Micro-Indentation Tests

The fiber micro-indentation push-in test is studied in detail for the case of a Coulomb friction interface law. Using an integral equation method, as well as a finite element method, we investigate the "Poisson effect"; that is, the tendency for the loading to raise the normal stresses at the interface which can, in turn, augment the shear stresses. Results of the detailed analyses are compared with those of an approximate analysis which neglects the induced normal stresses and with one that includes them. A favorable comparison with the latter approximation enables us to assess the effect of material parameters on the strength of the "Poisson effect."

Introduction

The properties of fiber-reinforced composites depend in large measure on the fiber-matrix interface. For ceramic-matrix composites, in particular, little or no bonding is preferable, though some frictional resistance to interfacial sliding is necessary for adequate stiffness and strength. Consequently, a variety of tests have been proposed for deducing interface properties. Tests most often employed involve pushing on fibers with a micro-indentor and observing the consequent sliding of the fiber with respect to the matrix. For example, the so-called push-in test, which was first proposed by Marshall (1984), involves a specimen which is very thick in comparison with the fiber radius. In this test, the fiber load and the relative displacement (the slip) at the fiber-matrix interface are measured. The test is typically interpreted by assuming that the resistance at the fiber-matrix interface is characterized by a constant frictional shear stress τ_f. The commonly used approximate analysis of this test leads to the following relationships between the applied pressure p, the slip zone length L_s, and the relative displacement between the fiber and the matrix at the surface Δu_z:

$$p=\frac{2L_s\tau_f}{R} \tag{1a}$$

$$\Delta u_z=\frac{p^2R}{4E_f\tau_f} \tag{1b}$$

where E_f is elastic modulus of the fiber, and R is the fiber radius.

If the interface suffers frictional slippage, then the friction might be of the Coulomb type; that is, the shear stress may not be constant, but may depend on the local normal stress. This possibility was, in fact, explored by Takaku and Arridge (1973) for the case of the *pull-out* test. They introduced a modified shear lag analysis that accounts approximately for the alteration in the interfacial normal stress which accompanies Poisson contraction of the pulled fiber. This modified shear lag analysis was adapted by Shetty (1988) to the case of the fiber being pushed instead of pulled; the Poisson effect results in the fiber expanding radially which, due to the presence of the matrix, increases the normal pressure at the interface. Shetty's analysis, which is reviewed in the Appendix, would lead to the following relations between the relevant variables:

$$p=\frac{\sigma_0}{k}\left[\exp\left(\frac{2\mu kL_s}{R}\right)-1\right] \tag{2a}$$

$$\frac{\Delta u_z}{R}=\frac{(1-2\nu_f k)\sigma_0}{kE_f}\left\{\frac{1}{2\mu k}\left[\exp\left(\frac{2\mu kL_s}{R}\right)-1\right]-\frac{L_s}{R}\right\} \tag{2b}$$

where μ is the friction coefficient, σ_0 is the residual compressive stress at the interface (before loading), and k is defined by

$$k=\frac{E_m\nu_f}{E_f(1+\nu_m)+E_m(1-\nu_f)}. \tag{3}$$

E and ν are the Young's modulus and Poisson ratio, respectively, and subscripts refer to the fiber or matrix as appropriate. (Equation (2*b*) giving the relative displacement was not presented by Shetty.) Since two parameters, μ and σ_0, must be determined, measurements need to be taken for several applied loads. Note that $\mu\sigma_0$ is a nominal friction stress, which is the friction stress that would prevail if the load were to induce no additional normal stress on the interface.

Now, imagine that the load and the relative displacement are extracted from a push-in test. As seen in the results section to follow, the friction stress τ_f that one would infer through

Contributed by the Applied Mechanics Division of THE AMERICAN SOCIETY OF MECHANICAL ENGINEERS for publication in the ASME JOURNAL OF APPLIED MECHANICS.

Discussion on this paper should be addressed to the Technical Editor, Professor Lewis T. Wheeler, Department of Mechanical Engineering, University of Houston, Houston, TX 77204-4792, and will be accepted until four months after final publication of the paper itself in the ASME JOURNAL OF APPLIED MECHANICS.

Manuscript received by the ASME Applied Mechanics Division, Dec. 16, 1991; final revision, Aug. 14, 1992. Associate Technical Editor: G. J. Dvorak.

Copyright © 1993 by ASME
Downloaded 03 May 2010 to 171.66.16.245. Redistribution subject to ASME license or copyright; see http://www.asme.org/terms/Terms_Use.cfm

the use of Eqs. (1) can be quite different from the nominal friction stress $\mu\sigma_0$ inferred using Eqs. (2); that is, the assumptions of constant friction and Coulomb friction lead to different conclusions. Certainly it is likely to remain an open question as to whether the interfacial friction is really of the Coulomb type. While further experimentation is necessary to answer this question, it is also important to have a reliable means of interpreting these experiments. Hence, this paper addresses the following question: If the interface can be characterized by Coulomb friction, is the widely used (Bright, Shetty, Griffin and Limaye, 1989; Kerans and Parthasarathy, 1991) Shetty analysis accurate?

To judge the accuracy of the Shetty analysis, we analyze precisely the problem that his analysis is intended to address. A circular fiber is embedded in an infinite half-space, with slippage at the fiber-matrix interface characterized by Coulomb friction; a pressure is applied to the top of the fiber. First, a highly accurate integral equation technique is employed which is applicable *only* to the case of equal fiber and matrix moduli. This method represents the slip at the fiber-matrix interface with a continuous distribution of prismatic dislocation loops; it is a generalization of the two-dimensional analysis of the push-in test presented by Dollar and Steif (1988). Next, the problem is solved using a commercial finite element code, with the equal modulus case constituting a test of the finite element code's ability to handle the Coulomb friction interface. Finally, with its accuracy demonstrated, the finite element method is applied to the same problem, but with distinct fiber and matrix moduli; this provides additional comparisons with the Shetty analysis.

There appear to be relatively few *detailed* studies of the effects of friction during fiber pull-out or push-in. Besides the work of Dollar and Steif (1988), there appears only to be the short note by Faber, Advani, Lee, and Jinn (1986) in which the variation of the shear stress distribution with friction coefficient was investigated using a finite element method. Grande, Mandell, and Hong (1988) analyzed the push-in test with a finite element method, though not with an interface which can suffer frictional slippage.

Finally, we note that Shetty proposed his analysis to be applied to interpret the micro-indentation *push-out* test. This test features a specimen ranging in thickness from 10 to 100 times the fiber radius. Indentor loads are applied which are sufficient to cause complete slippage at the fiber-matrix interface; the fiber is actually pushed out the bottom of the specimen. Due to the exponential term in Eq. (2), Shetty's analysis predicts that the pressure to push a fiber out does not increase linearly with specimen thickness, but exponentially. In fact, a nonlinear increase in the load to cause complete slippage has been observed (Eldridge, Bhatt, and Kiser, 1991). Without an analysis of the finite specimen configuration, including the pushed-out fiber, it is difficult to judge the accuracy of applying Shetty's approach to this test. Nevertheless, one suspects that if the Shetty analysis is reasonably accurate when applied to a fiber embedded in a half-space, then it may also be of some value when applied to the push-out test, provided the specimen is relatively thick.

Problem Statement

A schematic of the configuration under consideration is shown in Fig. 1. A semi-infinite circular fiber of radius R and isotropic elastic moduli E_f and ν_f is embedded in a half-space of matrix material having isotropic elastic moduli E_m and ν_m. The exposed surface of the fiber is subjected to a uniform pressure $\sigma_{zz} = -p$ and zero shear stress σ_{rz}; the surface of the matrix is free of tractions. The resulting deformations are axisymmetric, with nonzero displacements u_r and u_z, and nonzero stresses σ_{rr}, $\sigma_{\theta\theta}$, σ_{zz}, and σ_{rz}. It is assumed that the pressure p applied to the fiber is increased monotonically. Along the

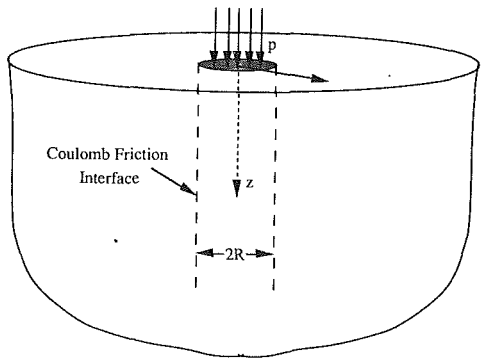


Fig. 1 Loading of fiber embedded in a half-space

fiber-matrix interface at $r = R$, a Coulomb friction interface law is assumed to hold. Since opening of the interface does not occur under applied pressure, the two relevant states of the interface are

$$\text{stick condition} \quad \sigma<0,\ |\tau|<\mu|\sigma|,\ \frac{dg}{dt}=0 \tag{4a}$$

$$\text{slip condition} \quad \sigma<0,\ |\tau|=\mu|\sigma|,\ \operatorname{sgn}\left(\frac{dg}{dt}\right)=\operatorname{sgn}(\tau) \tag{4b}$$

where $\sigma = \sigma_{rr}$, $\tau = \sigma_{rz}$, μ is the friction coefficient, and g is the displacement jump defined by

$$g=\lim_{\epsilon\to 0^+}\left[u_z(R+\epsilon,\ z)-u_z(R-\epsilon,\ z)\right]. \tag{5}$$

The quantity t is any time-like parameter which increases as the loading proceeds, and the condition $\operatorname{sgn}(dg/dt) = \operatorname{sgn}(\tau)$ enforces positive energy dissipation during slip; i.e., the instantaneous slip increment should be in the same direction as the shear stress. (Enforcement of this condition is trivial for the case of monotonically increasing loading considered here.) It is further assumed that there exists, prior to loading, a residual stress state associated with, say, the fabrication. At the interface, this stress state involves a normal pressure $\sigma_{rr} = -\sigma_0$ and zero shear stress. Thus, the stresses in the friction law (4) are the total stresses including the residual pressure. Both the residual stress σ_0 and the friction coefficient μ are taken to be constant along the interface.

With such an interface law, the monotonically increasing loading produces a slip zone, $0 < z < L_s$, in which there is relative slip. For $z > L_s$, the fiber and matrix are still sticking. Note that the slip length L_s depends on the pressure p, as well as on material parameters such as σ_0 and the elastic moduli. For the push-in test, the quantities of interest are the slip length L_s and the relative displacement at the surface as a function of the pressure applied to the fiber.

Methods of Analysis

Herein, we present first the integral equation method for analyzing the case of *equal* fiber and matrix elastic moduli. The method is based on the observation that the displacement u_z is discontinuous along those portions of the interface which have undergone slip. By contrast, the tractions and the normal displacement are continuous across the interface. The varying displacement discontinuity is equivalent to a distribution of circular prismatic dislocation loops of varying intensity (Burgers vector) along the interface. This is analogous to the more familiar use of dislocations to represent two-dimensional cracks, and it is a direct three-dimensional generalization of the two-dimensional analysis by Dollar and Steif (1988) of the push-in test.

To ensure the correct boundary conditions at the surface of the half-space a superposition procedure is used. The total solution consists of two parts:

Downloaded 03 May 2010 to 171.66.16.245. Redistribution subject to ASME license or copyright; see http://www.asme.org/terms/Terms_Use.cfm

(i) pressure p applied at $0 < r < R$, $z = 0$, with complete continuity of displacements at the interface;
(ii) a distribution of prismatic dislocation loops along the interface, with each dislocation giving rise to zero tractions on $z = 0$.

The solution for a circular patch of pressure p applied to the surface of a half-space is given by Sneddon (1951). Of interest are the associated normal stress and shear stress at the interface, which we denote by $\sigma^p_{rr}(r, z)$ and $\sigma^p_{rz}(r, z)$; they are given by

$$\frac{\sigma^p_{rr}(r, z)}{p} = -I^0_0\left(\frac{r}{R}, \frac{z}{R}\right) + \frac{z}{R} I^1_0\left(\frac{r}{R}, \frac{z}{R}\right) + \frac{R}{r}(1-2\nu) I^{-1}_1\left(\frac{r}{R}, \frac{z}{R}\right) - \frac{z}{R} I^0_1\left(\frac{r}{R}, \frac{z}{R}\right) \quad (6a)$$

$$\frac{\sigma^p_{rz}(r, z)}{p} = -\frac{z}{R} I^1_1\left(\frac{r}{R}, \frac{z}{R}\right) \quad (6b)$$

where the functions $I^n_m(\rho, \xi)$ are defined by

$$I^n_m(\rho, \xi) = \int_0^\infty t^n J_m(t\rho) J_1(t) e^{-t\xi}\, dt \quad (7)$$

and $J_m(x)$ is the Bessel function of the first kind of order m.

The kernel dislocation solution, featuring a prismatic dislocation loop of radius R centered at $(r, z) = (0, z')$ in a half-space with a traction-free surface, satisfies the following conditions:

$$\sigma_{rz}(r, 0) = 0, \quad \sigma_{zz}(r, 0) = 0, \quad 0 < r < \infty \quad (8a, b)$$

$$b = \lim_{\epsilon \to 0^+} [u_z(r, z' + \epsilon) - u_z(r, z' - \epsilon)] \neq 0 \quad 0 < r < R \quad (8c)$$

where the Burgers vector b is constant. A solution to this dislocation problem is given by Bastecka (1964), who utilized Kroupa's (1960) solution for a prismatic dislocation loop in an infinite space. Kroupa's solution technique employed the Hankel transform to convert the equations of three-dimensional axisymmetric elasticity into a single ordinary differential equation. This equation can be solved by forcing the field quantities to vanish at infinity and satisfy the appropriate jump and continuity conditions at the plane of the loop. The solution to the related problem of a ring of point forces in an infinite space was given by Selvadurai and Rajapakse (1985).

To obtain her solution for the loop in a half-space, Bastecka (1964) started with a dislocation loop, of Burgers vector b, centered at $(r, z) = (0, z')$ in an infinite medium. To eliminate normal tractions, σ_{zz} at $z = 0$, she added an image loop of opposite Burgers vector at $(0, -z')$. To eliminate the remaining shear traction, σ_{rz}, on $z = 0$, she used Sneddon's (1951) general solution for a half-space with prescribed shear tractions on the surface.

Therefore, the relevant stress components associated with a prismatic loop of unit Burgers vector in a half-space, $\sigma^d_{rr}(r, z; z')$ and $\sigma^d_{rz}(r, z; z')$, can be expressed in the form

$$\sigma^d_{rr}(r, z; z')b = [\sigma^I_{rr}(r, z; z') + \sigma^{II}_{rr}(r, z; z') + \sigma^F_{rr}(r, z; z')]b$$

$$\sigma^d_{rz}(r, z; z')b = [\sigma^I_{rz}(r, z; z') + \sigma^{II}_{rz}(r, z; z') + \sigma^F_{rz}(r, z; z')]b. \quad (9a, b)$$

The first terms are given by

$$\sigma^I_{rr}(r, z; z')b = \frac{bG}{2R(1-\nu)}\left\{I^1_0\left(\frac{r}{R}, \frac{|z-z'|}{R}\right) - \frac{|z-z'|}{R} I^2_0\left(\frac{r}{R}, \frac{|z-z'|}{R}\right) - \frac{(1-2\nu)}{r/R} I^0_1\left(\frac{r}{R}, \frac{|z-z'|}{R}\right) + \frac{|z-z'|}{r} I^1_1\left(\frac{r}{R}, \frac{|z-z'|}{R}\right)\right\} \quad (10a)$$

$$\sigma^I_{rz}(r, z; z')b = \frac{bG}{2R(1-\nu)} \frac{z-z'}{R}\left(I^2_1\left(\frac{r}{R}, \frac{|z-z'|}{R}\right)\right. \quad (10b)$$

and represent the stresses at field point (r, z) in an infinite medium containing a prismatic dislocation loop of radius R, centered at $(r, z) = (0, z')$; the second terms are

$$\sigma^{II}_{rr}(r, z; z') = -\sigma^I_{rr}(r, z; -z') \qquad \sigma^{II}_{rz}(r, z; z') = -\sigma^I_{rz}(r, z; -z') \quad (11a, b)$$

representing the stresses associated with the image loop centered at $(r, z) = (0, -z')$; the final terms are

$$\sigma^F_{rr}(r, z; z')b = \frac{-z'bG}{R^2(1-\nu)}\left\{2I^2_0\left(\frac{r}{R}, \frac{z'+z}{R}\right) - \frac{z}{R} I^3_0\left(\frac{r}{R}, \frac{z'+z}{R}\right) - \frac{2(1-\nu)}{r/R} I^1_1\left(\frac{r}{R}, \frac{z'+z}{R}\right) + \frac{z}{r} I^2_1\left(\frac{r}{R}, \frac{z'+z}{R}\right)\right\} \quad (12a)$$

$$\sigma^F_{rz}(r, z; z')b = \frac{z'bG}{R^2(1-\nu)}\left\{I^2_1\left(\frac{r}{R}, \frac{z'+z}{R}\right) - \frac{z}{R} I^3_1\left(\frac{r}{R}, \frac{z'+z}{R}\right)\right. \quad (12b)$$

representing the stresses associated with eliminating the remaining shear stresses on $z = 0$.

With the kernel dislocation solutions, one can derive the governing integral equation by asserting $\sigma_{rz} = \mu|\sigma_0 + \sigma_{rr}|$ over the segment $0 < z < L_s$, where stresses σ_{rz} and σ_{rr} are those associated with the loading. The resulting equation is given by

$$\sigma^p_{rz}(R, z) + \int_0^{L_s} \sigma^d_{rz}(R, z; z')\eta(z')dz' = \mu\left\{\sigma_0 - \sigma^p_{rr}(R, z) - \int_0^{L_s} \sigma^d_{rr}(R, z; z')\eta(z')dz'\right\} \quad (13)$$

where the Burgers vector b has been replaced by $\eta(z')dz'$, where $\eta(z)$ is the dislocation density. Consistent with the nonsingular stress at the surface and the Coulomb friction law at the interface, the dislocation density $\eta(z)$ vanishes at $z = 0$ and $z = L_s$ (Dundurs and Comninou, 1979).

The only unusual feature of the problem is the need to determine the upper limit of the integral, i.e., the slip length L_s. An inverse approach was taken in which a value for the slip length was chosen. Then, for arbitrary values of p, there will, in general, be a singularity in the dislocation density (and the stress) at $z = L_s$. As is typical for problems involving a singularity, the dislocation density $\eta(z)$ is conveniently replaced by the form

$$\eta(z) = \frac{\beta(z)}{\sqrt{L_s - z}} \quad (14)$$

which incorporates the singularity, leaving the function $\beta(z)$ to be nonzero at $z = L_s$. (We still enforce $\beta(0) = 0$.) The solution for $\beta(z)$ is found for various values of applied pressure p; the value of p at which $\beta(L_s) = 0$ is the one which satisfies the Coulomb friction law, while producing a slip length L_s.

The integral equation is solved with a relatively standard collocation procedure. The domain $0 < z < L_s$ is discretized into N intervals, and the function $\beta(z)$ is approximated as piecewise linear within each interval. The function $\beta(z)$ is then found by enforcing the integral equation midway along each interval. Except for the Cauchy singular term which is integrated analytically, the other terms are integrated numerically. The integrals in Eq. (7) involving Bessel functions can be converted to elliptic integrals. For I^0_0, I^1_0, I^{-1}_1, I^0_1, and I^1_1, this has been done by Eason, Noble, and Sneddon (1955); for I^2_1, I^3_1,

Downloaded 03 May 2010 to 171.66.16.245. Redistribution subject to ASME license or copyright; see http://www.asme.org/terms/Terms_Use.cfm

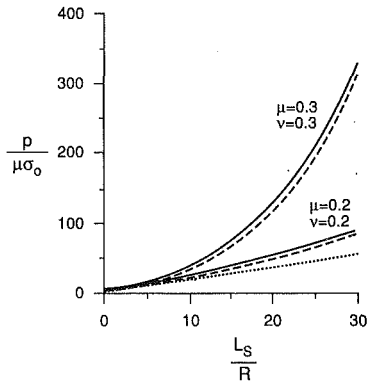


Fig. 2 Pressure versus slip length for homogeneous elastic moduli (— integral equation method; --- Takaku and Arridge approximation; · · · · constant shear stress approximation)

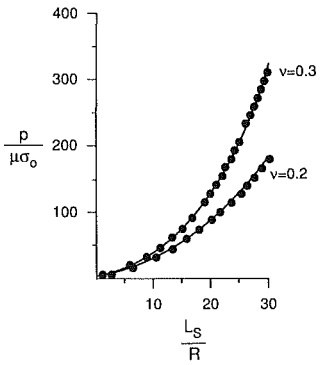


Fig. 3 Pressure versus slip length for homogeneous elastic moduli (— integral equation method; • finite element method; $\mu = 0.3$)

I_0^2, and I_0^3, this has been done by Luk and Keer (1979), using identities given by Eason, Noble, and Sneddon (1955).

To analyze the push-in test when the fiber and matrix have *distinct* moduli, the commercial finite element code ABAQUS, developed by Hibbit, Karlsson, and Sorenson, was used. The finite domain analyzed occupied $0 < r < 50\,R$ and $0 < z < 50\,R$. The mesh consisted of 2835 axisymmetric solid elements, and 80 interface elements. This mesh was developed specifically for analyzing long slip lengths, and it is not expected to give particularly accurate results for slip lengths smaller than the fiber radius. (Other finite element calculations, not presented here, using a more detailed mesh near the surface, gave results which are consistent with the integral equation method results for short slip lengths.)

Results

First, we consider results for the case of equal fiber and matrix moduli. In Fig. 2, the pressure normalized by $\mu\sigma_0$ is plotted as a function of the slip length L_s. The solid curves represent the results of the integral equation method, the dashed curves are the Takaku and Arridge approximation given by Eq. (2*a*), and the dotted line is the constant shear stress approximation (CSSA) given by Eq. (1*a*). Note that the CSSA is independent of the friction coefficient μ and the Poisson ratio ν; it is given by $p/\mu\sigma_0 = 2L_s/R$. In contrast, the Takaku and Arridge approximation depends on both of these parameters. The deviation from the CSSA (and the obvious nonlinearity of the curves corresponding to $\nu = 0.3, \mu = 0.3$) indicates that there can be a substantial Poisson effect. Interestingly, the Takaku and Arridge approximation handles the Poisson effect quite well; for large slip lengths it agrees with the integral equation method to within five to ten percent. The deviation from the CSSA depends strongly on the friction coefficient and on the Poisson ratio (the parameter k equals $\nu/2$ for the case of homogeneous moduli), because both of these appear in the argument of the exponential term in Takaku and Arridge's approximation.

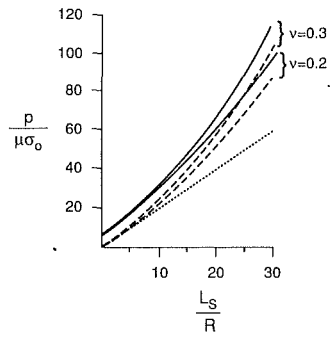


Fig. 4 Pressure versus slip length for dissimilar elastic moduli (— finite element method; --- Takaku and Arridge approximation; · · · · constant shear stress approximation; $E_f/E_m = 3.54$; $\mu = 0.3$)

Since our calculations for distinct moduli are based on a finite element analysis, it was deemed necessary to establish the accuracy of the finite element method. To this end, we reconsidered the homogeneous case and compared the integral equation results (solid curves) with the finite element results (data points). These results are shown in Fig. 3 for friction coefficient 0.3 and for two values of Poisson ratio ($\nu = 0.2$ and $\nu = 0.3$). Since the finite element code indicates which nodes are slipping and which are sticking, it is possible to determine the slip length only to within an element length. For example, in the range $0 < L_s < 30$, the slip length associated with a given load can be determined only to within 0.25 R. Nevertheless, the comparison between the finite element method and the integral equation method suggests that the finite element code is reasonably accurate.

We now consider cases of dissimilar fiber and matrix moduli. Figure 4 compares finite element results (solid curves) with those of the Takaku and Arridge approximation (dashed curves) for the case of $\mu = 0.3$, $E_f/E_m = 3.54$ and $\nu_f = \nu_m = 0.3$ and $\nu_f = \nu_m = 0.2$. The ratio of Young's moduli correspond to silicon carbide fibers in a matrix of silicon nitride. First, it should be noted that the Poisson effect is diminished when the fiber is stiff in comparison with the matrix; for fixed friction coefficient and Poisson ratios, the deviation from the CSSA (dotted line) is not as significant as when $E_f/E_m = 1.0$. Secondly, the Takaku and Arridge approximation still gives a decent approximation to the load-displacement curve, again underestimating it slightly. The curves in Fig. 4 suggest that the discrepancy between the finite element results and the Takaku and Arridge approximation can be mostly attributed to the difference in the *initiating* loads. In the finite element solution slip does not initiate at zero load, while slip initiates immediately in the Takaku and Arridge approximation. The curves appear to track one another with roughly a constant difference between them.

[For the case of equal fiber and matrix moduli, it is certain that frictional slip does not begin until $p/\mu\sigma_0$ reaches some critical finite value. The reason for this is that the stresses as $z \to 0$ along the interface are finite if displacement continuity is enforced; therefore, with a nonzero σ_0, the shear stress will always be less than μ times the *total* normal stress if p is below a critical value. However, when the moduli differ, there is, in general, a weak stress singularity (Bogy, 1970) if displacement continuity is enforced; hence, one cannot rule out slip for arbitrarily small values of p. Nevertheless, the finite element result for values of slip length on the order of one suggest that the response is practically as if slip required a finite value of p for initiation.]

Finally, we present results for the relative displacement Δu_z between the fiber and matrix at the surface, including a com-

Downloaded 03 May 2010 to 171.66.16.245. Redistribution subject to ASME license or copyright; see http://www.asme.org/terms/Terms_Use.cfm

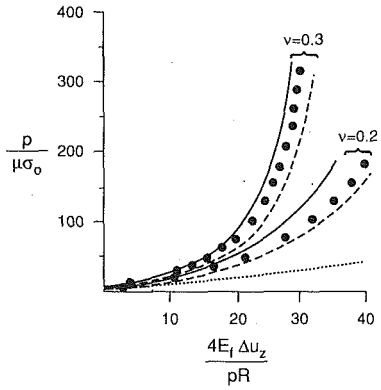


Fig. 5 Pressure versus relative displacement at the interface for homogeneous elastic moduli (— integral equation method; • finite element method; --- Takaku and Arridge approximation; · · · · constant shear stress approximation; μ = 0.3)

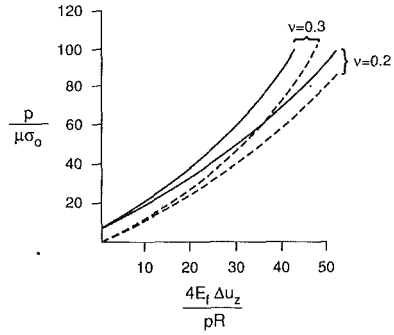


Fig. 6 Pressure versus relative displacement at the interface for dissimilar elastic moduli (— finite element method; --- Takaku and Arridge approximation; E_f/E_m = 3.54; μ = 0.3)

parison between the numerical solutions and the approximate estimates (1*b*) and (2*b*). For the case of equal fiber and matrix moduli, we compare in Fig. 5 the results of four separate calculations of the load-displacement relation: the integral equation method (solid curves); the FEM (data points); the Takaku and Arridge approximation Eq. (2*b*) (dashed curves); and, the CSSA Eq. (1*b*) (dotted line). First, note that there can be a very substantial Poisson effect: for $\nu_f = \nu_m = 0.3$, the integral equation method and the CSSA predict loads which differ by more than a factor of 10 for the same displacement. Hence, if the CSSA were used to interpret such experimental data, the inferred shear stress would be in error by a factor of 10. Secondly, note that the load predicted by the Takaku and Arridge approximation Eq. (2*b*) is always less than the FEM prediction, which is always less than the integral equation method, all for the same displacement Δu_z. Therefore, based on the reliabilities of the different analyses, it would appear fair to assume that Eq. (2*b*) leads to a slight overestimation of the frictional shear stress.

Results are presented in Fig. 6 showing a comparison between the FEM (solid curves) and the Takaku and Arridge approximation (dashed curves) for a case of dissimilar elastic moduli (E_f/E_m = 3.54). Now the discrepancy between the CSSA and methods which account for the Poisson effect is not as severe, consistent with the previous results for slip length. It is also apparent from this figure that the Takaku and Arridge approximation tracks the FEM rather well, once the different pressures to initiate slip are included.

Conclusions

Fiber micro-indentation tests are used to assess interface properties, including situations in which the shear stress at the interface is believed to be frictional in origin. Two approaches to inferring the interfacial shear resistance have been reported in the literature: one in which the frictional shear stress is assumed to be constant, and one in which the shear stress is proportional to the normal stress. The difference between the predictions of these approaches stems from the presence of a Poisson effect, in which the fiber expansion is resisted by the matrix, giving rise to enhanced normal stresses and, hence, enhanced shear stresses. In the present paper we have explored in detail the consequences of assuming the interface can be characterized by Coulomb friction. In particular, we have studied this effect using an integral equation method as well as a finite element method.

It was found that the load to produce slip over a given length is predicted to be larger when the shear stress depends on the normal stress than when the interfacial shear stress is assumed to have a constant value. This load enhancement decreases as the ratio E_f/E_m increases; also, not surprisingly, the load enhancement increases with the friction coefficient and with the fiber Poisson ratio. In general, the approximate one-dimensional analysis put forth by Takaku and Arridge (1973), which was adapted specifically to the push-in test by Shetty (1988), captures the load enhancement rather well. The modest degree to which this approximate analysis overestimates the frictional shear stress seems to be attributable to differences in the initial stages of interfacial slip. The Poisson effect is also evident in the curves of load versus relative displacement at the surface, which are crucial to an interpretation of the push-in test. An extension of the Takaku and Arridge analysis to predict the relative displacement yields similarly good agreement with the more detailed methods of analysis.

Acknowledgments

We are indebted to H. O. K. Kirchner for bringing the work of Kroupa and Bastecka to our attention and to P. Byrne for assisting in the finite element computations. We also wish to thank Hibbit, Karlsson, and Sorenson, Inc., for the use of ABAQUS. G. Meda and P. S. Steif were supported by the Air Force Office of Scientific Research under grant 890548 and S. F. Hoysan was supported by the Department of Energy under grant DE-FG02-89ER45404. Support by the Department of Mechanical Engineering, Carnegie Mellon University is also gratefully acknowledged.

References

Bastecka, J., 1964, "Interaction of Dislocation Loop with Free Surface," *Czech. J. Phys.*, Vol. B14, pp. 430-441.

Bogy, D. B., 1970, "On the Problem of Edge-Bonded Elastic Quarter-Planes Loaded at the Boundary," *Int. J. Sol. Structures*, Vol. 6, pp. 1287-1313.

Bright, J. D., Shetty, D. K., Griffin, C. W., and Limaye, S. Y., 1989, "Interfacial Bonding and Friction in Silicon Carbide (Filament)-Reinforced Ceramic- and Glass-Matrix Composites," *J. Am. Ceram. Soc.*, Vol. 72, pp. 1891-1898.

Dollar, A., and Steif, P. S., 1988, "Load Transfer in Composites with a Coulomb Friction Interface," *Int. J. Sol. Structures*, Vol. 24, pp. 789-803.

Dundurs, J., and Comninou, M., 1988, "Some Consequences of the Inequality Conditions in Contact and Crack Problems," *J. Elasticity*, Vol. 9, pp. 71-82.

Eason, G., Noble, B., and Sneddon, I. N., 1955, "On Certain Integrals of Lipschitz-Hankel Type Involving Products of Bessel Functions," *Philos. Trans. R. Soc.*, London, Vol. A247, pp. 529-551.

Eldridge, J. I., Bhatt, R. T., and Kiser, J. D., 1991, "Investigation of Interfacial Shear Strength in SiC/Si_3N_4 Composites," *Ceram. Eng. Sci. Proc.*, Vol. 12, pp. 1152-1171.

Faber, K. T., Advani, S. H., Lee, J. K., and Jinn, J.-T., 1986, "Frictional Stress Evaluation Along the Fiber-Matrix Interface in Ceramic Matrix Composites," *J. Am. Ceram. Soc.*, Vol. 69, No. 9, pp. C-208-C-209.

Grande, D. H., Mandell, J. F., and Hong, K. C. C., 1988, "Fiber-Matrix Bond Strength Studies of Glass, Ceramic and Metal Matrix Composites," *J. Mater. Sci.*, Vol. 23, pp. 311-328.

Kerans, R. J., and Parthasarathy, T. A., 1991, "Theoretical Analysis of the Fiber Pull-Out and Push-Out Tests," *J. Am. Ceram. Soc.*, Vol. 74, pp. 1585-1596.

Downloaded 03 May 2010 to 171.66.16.245. Redistribution subject to ASME license or copyright; see http://www.asme.org/terms/Terms_Use.cfm

Kroupa, F., 1960, "Circular Edge Dislocation Loop," *Czech. J. Phys.*, Vol. B10, pp. 284–293.

Luk, V. K., and Keer, L. M., 1979, "Stress Analysis for an Elastic Half Space Containing an Axially-Loaded Rigid Cylindrical Rod," *Int. J. Solids Structures*, Vol. 15, pp. 805–827.

Marshall, D. B., 1984, "An Indentation Method for Measuring Matrix-Fiber Frictional Stresses in Ceramic Composites," *J. Am. Ceram. Soc.*, Vol. 67, pp. C-259–C-260.

Selvadurai, A. P. S., and Rajapakse, R. K. N. D., 1985, "On the Load Transfer from a Rigid Cylindrical Inclusion Upon an Elastic Half Space," *Int. J. Solids Structures*, Vol. 21, pp. 1213–1229.

Shetty, D. K., 1988, "Shear-lag Analysis of Fiber Pushout (Indentation) Test for Estimating Interfacial Friction Stress in Ceramic-Matrix Composites," *J. Am. Cer. Soc.*, Vol. 71, pp. C-107–C-109.

Sneddon, I. N., 1951, *Fourier Transforms*, McGraw-Hill, New York.

Takaku, A., and Arridge, R. G. C., 1973, "The Effect of Interfacial Radial and Shear Stresses on Fibre Pull-out in Composite Materials," *J. Phys. D: Appl. Phys.*, Vol. 6, pp. 2038–2047.

APPENDIX

Herein the one-dimensional analysis of Takaku and Arridge (1973), as adapted by Shetty (1988) to the indentation test, is reviewed, and the resulting relative displacement at the surface is computed.

Prior to loading the composite, there is a pre-existing radial compression σ_0 at the interface; other residual stress components do not enter the analysis, and the displacements are taken to be zero. The analysis of the response under an indenting load is based on the free-body diagrams shown in Fig. 7. Due to the loading, the fiber element under consideration sustains an axial stress $\sigma_{zz} = -p$ and a radial stress $\sigma_{rr} = -q$; this radial stress also acts on the matrix.

The shear stresses at the interface are given by the Coulomb friction rule

$$\sigma_{rz} = \mu(\sigma_0 + q).$$

Furthermore, by equilibrium of the fiber element, the axial pressure is related to the shear stress by

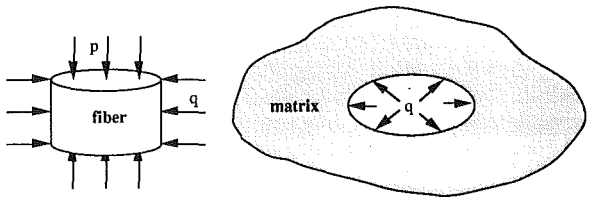


Fig. 7 Free-body diagrams of fiber and matrix elements

$$\frac{dp}{dz} = \frac{2}{R}\,\sigma_{rz}.$$

The final relation is derived from the condition that the radial displacements be continuous across the fiber-matrix interface; i.e., $(u_r)_{\text{fiber}} = (u_r)_{\text{matrix}}$. Neglecting the effects of the shear stresses on u_r, and assuming the axial and radial stresses in the fiber element are uniform, one finds

$$(u_r)_{\text{fiber}} = \frac{R}{E_f}\,[-(1-\nu_f)q + \nu_f p].$$

The displacement on the matrix side is derived from the assumption that the axial strain (ϵ_{zz}) in the matrix is negligible; that is, the matrix element is an infinite slab, deforming in plane strain, which contains a hole with internal pressure equal to the local value of q. Under these assumptions, one finds

$$(u_r)_{\text{matrix}} = \frac{Rq(1+\nu_m)}{E_m}.$$

With the condition that $p = 0$ at the end of the slip zone $z = L_s$, the first-order ordinary differential equation for p

$$\frac{dp}{dz} = \frac{2\mu}{R}\,[\sigma_0 + kp]$$

is integrated to yield Eq. (2). (The constant k is given by Eq. (3).) The relative displacement at the free surface, given by Eq. (2*b*), is equal the integral of the fiber axial strain, since the matrix is assumed to have zero axial strain.

Downloaded 03 May 2010 to 171.66.16.245. Redistribution subject to ASME license or copyright; see http://www.asme.org/terms/Terms_Use.cfm

Stress and Notch-Stress Concentration Induced by Slight Depressions and Protrusions

C. H. Wu
Professor,
Department of Civil Engineering, Mechanics, and Metallurgy,
University of Illinois at Chicago,
P.O. Box 4348,
Chicago, IL 60680
Fellow ASME

The presence of a smooth depression on the surface of a stretched half-plane magnifies the surface stress at the trough of the depression. Similarly, the stress at the foot of a smooth protrusion is also magnified. The associated stress concentration factors are determined, via a regular perturbation procedure, in terms of a small aspect ratio that measures the slight unevenness of the surface. When the depression/protrusion profile has corners, the method of matched asymptotic expansions is used to obtain the desired analytic solution. The case of a shallow notch, as well as that of a triangular protrusion, is solved explicitly.

1 Introduction

Stress concentration effects caused by slightly undulating surfaces have been recently studied by Gao (1991a,b). Using the aspect ratio, ϵ, of a shallow dimple as the small parameter, he has devised a procedure that is capable of generating uniformly valid asymptotic solutions accurate to the order of ϵ. While not explicitly stipulated by Gao, the slightly uneven surface profile must have continuous derivative in order for the first-order perturbation solution to be uniformly valid throughout the region of consideration. It is perhaps for this reason that only sinusoidally wavy surfaces and isolated sinusoidal dimples have been considered by Gao.

In this paper and in the context of plane elasticity, the aforementioned problem is more fully developed and new singular solutions are obtained. First, the perturbation procedure is extended in a systematic manner so that asymptotic solutions of any order may be obtained by solving a system of well-defined Cauchy problems. This procedure is then applied to sinusoidally wavy surfaces of elastic half-planes. For a four-term expansion, it is found that the associated stress concentration factor (SCF) is

$$\text{SCF} = 1 + \pi\epsilon - \frac{3}{16}(\pi\epsilon)^3 + \cdots \tag{1}$$

where the first two terms have been obtained by Gao, who used $(\epsilon/4)$ as his small parameter. Our analysis shows that the ϵ^2-term is identically zero even though the associated stress field is not. Moreover, the availability of the ϵ^3-term enables us to propose the plausible limitation that

$$\epsilon < \frac{4}{3\pi} = 0.424, \tag{2}$$

as the above SCF is expected to be nondecreasing in ϵ.

The stress at the trough of a smooth depression is magnified and so is the stress at the foot of a protrusion. The latter situation, while intuitively obvious in some way, has rarely been emphasized. For the case of a single depression given by $x_2 = \epsilon(1 - x_1^2)^2$ on the surface of the upper half-plane $(x_2 > 0)$, the stress concentration factor is

$$\text{SCF} = 1 + \epsilon\frac{32}{3\pi} + \cdots, \tag{3}$$

which is to be compared with (1). On the other hand, the SCF associated with a single protrusion $x_2 = -\epsilon(1 - x_1^2)^2$ is

$$\text{SCF} = 1 + \epsilon\frac{16}{3\pi} + \cdots, \tag{4}$$

which occurs at $x_1 = \pm 1$.

The perturbation procedure associated with the above calculations is a regular one in that all asymptotic expressions are uniformly valid throughout the half-plane under consideration. This is impossible if the surface unevenness has discontinuous tangent. The situation is typified by the geometry of a shallow notch for which a singular perturbation approach must be used. Such an analysis is accomplished in this paper, and the "strength" of the notch-tip singularity is explicitly determined. Similarly, at the foot of a triangular or even parabolic protrusion the stress field is also singular. The solution to the latter may be deduced from that to a depression in a straightforward manner if only a first-order approximation is desired.

2 A Half-Plane With an Almost Perfectly Straight Boundary

Let l be a characteristic length of a surface irregularity to be studied in this paper and μ the shear modulus. We shall use l and μl^2 as the length and force scales throughout this

Contributed by the Applied Mechanics Division of THE AMERICAN SOCIETY OF MECHANICAL ENGINEERS for presentation at the ASME Winter Annual Meeting, New Orleans, LA, Nov. 28–Dec. 3, 1993.

Discussion on this paper should be addressed to the Technical Editor, Professor Lewis T. Wheeler, Department of Mechanical Engineering, University of Houston, Houston, TX 77204-4792, and will be accepted until four months after final publication of the paper itself in the ASME JOURNAL OF APPLIED MECHANICS.

Manuscript received by the ASME Applied Mechanics Division, Jan. 9, 1992; final revision, Oct. 16, 1992. Associate Technical Editor: R. Abeyaratne.

Paper No. 93-WA/APM-4.

Copyright © 1993 by ASME
Downloaded 03 May 2010 to 171.66.16.245. Redistribution subject to ASME license or copyright; see http://www.asme.org/terms/Terms_Use.cfm

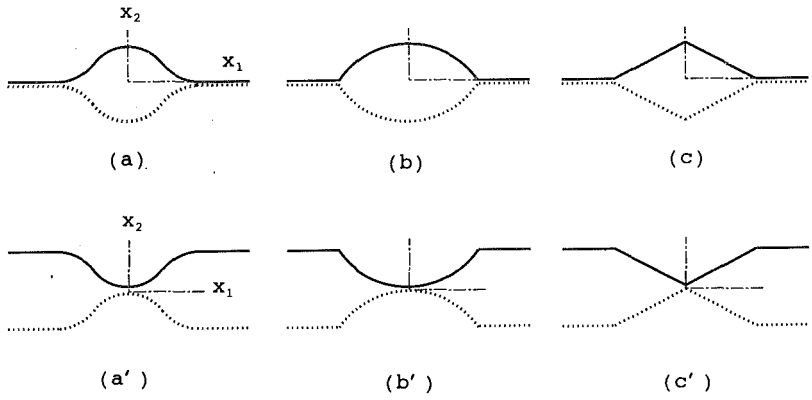


Fig. 1 Surface depressions and protrusions

paper, so that all quantities are nondimensional relative to these two parameters.

Let x_i $(i=1, 2, 3)$ be (dimensionless) rectangular Cartesian coordinates and $\mathbf{e}_i$ the associated unit vectors. We consider plane elasticity problems so that the (dimensionless) displacements u_α, (dimensionless) stresses $\tau_{\alpha\beta}$ are functions of x_β where Greek subscripts range from 1 to 2. The elastic upper half-plane S^+ is assumed to have a traction-free boundary so that if $u_\alpha^{(0)}(x_1, x_2)$ and $\tau_{\alpha\beta}^{(0)}(x_1, x_2)$ represent an appropriate solution then

$$\tau_{2\alpha}^{(0)}(x_1, 0)=0. \tag{5}$$

It is clear that the surface stress $\tau_{11}^{(0)}(x_1, 0)$ is in general neither constant nor zero.

Attention is now given to the cases where the $x_2=0$ boundary is not perfectly straight but is actually prescribed by

$$x_2=\epsilon A(x_1), \quad (\epsilon \ll 1), \tag{6}$$

where ϵ is a small dimensionless parameter and

$$0\le A(x_1)\le 1. \tag{7}$$

The first inequality indicates that the actual upper half-plane S_ϵ^+ is contained in S^+, and the second inequality implies that the maximum amplitude of the deviation from a straight boundary is ϵ (Fig. 1). It is clear that the normal to the new traction-free surface (6) is not longer $-\mathbf{e}_2$.

The conditions that were applied on S^+ to produce $u_\alpha^{(0)}(x_1, x_2)$ and $\tau_{\alpha\beta}^{(0)}(x_1, x_2)$ are now applied on S_ϵ^+. Let $u_\alpha(x_1, x_2; \epsilon)$ and $\tau_{\alpha\beta}(x_1, x_2; \epsilon)$ be the desired solution. Our objective is to determine these unknown functions asymptotically in terms of the small parameter ϵ as ϵ tends to zero. In, Case A, (x_1), together with its first derivative, is continuous, the desired expansion may be expressed in powers of ϵ as follows:

$$u_\alpha(x_1, x_2; \epsilon)\sim \sum_{n=0}^{\infty}\frac{\epsilon^n}{n!}u_\alpha^{(n)}(x_1, x_2), \tag{8}$$

$$\tau_{\alpha\beta}(x_1, x_2; \epsilon)\sim \sum_{n=0}^{\infty}\frac{\epsilon^n}{n!}\tau_{\alpha\beta}^{(n)}(x_1, x_2), \tag{9}$$

which are uniformly valid for all x_1 and x_2. The solutions given by Gao (1991a,b) are of this type. In, Case A, (x_1) has a discontinuous derivative, additional boundary layer expansions are needed to complete the solution. We have found it convenient to formulate the class of problems via a complex formulation.

Let $z=x_1+ix_2$ be the complex variable. The following four two-dimensional regions are defined (c.f., (6), (7), and Fig. 1) as follows:

$$S^{\pm}: x_2\gtrless 0, \quad S_\epsilon^{\pm}: x_2\gtrless \pm\epsilon A(x_1). \tag{10}$$

The elastic half-plane of our interest is S_ϵ^+. Let $W(z)\equiv W(z; \epsilon)$ be a complex function holomorphic in both S_ϵ^+ and S_ϵ^-. Then the so-called stress continuation (England, 1971) yields

$$2(u_1+iu_2)=\kappa W(z)+W(\bar z)+(\bar z-z)\overline{W'(z)}, \tag{11}$$

$$\tau_{11}+\tau_{22}=2[W'(z)+\overline{W'(z)}], \tag{12}$$

$$\tau_{22}-i\tau_{12}=W'(z)-W'(\bar z)+(z-\bar z)\overline{W''(z)}, \tag{13}$$

where

$$\kappa=\begin{cases}3-4\nu & \text{plane strain}\\ (3-\nu)/(1+\nu) & \text{plane stress}\end{cases} \tag{14}$$

and ν is Poisson's ratio. We recall that the variables z, u_α, $\tau_{\alpha\beta}$, and W are all dimensionless. The integrated form of the traction vector along a curve $z=z_c$ is the so-called resultant vector R and

$$iR=W(z_c)-W(\bar z_c)+(z_c-\bar z_c)\overline{W'(z_c)}, \tag{15}$$

which may be set to zero if $z=z_c$ is traction-free.

Let $W_0(z)$ be the complex function associated with $u_\alpha^{(0)}$ of (5), which was defined on S^+. Then (5) and the above lead to the conclusion that

$$W_0^+(x_1)-W_0^-(x_1)=0 \tag{16}$$

where $W_0^{\pm}(x_1)\equiv W_0(x_1\pm i0)$. The solution to the above, together with certain other applied conditions, is a holomorphic function $W_0(z)$ that is defined on both S^+ and S^-.

Consider now the function $W(z)\equiv W(z; \epsilon)$ associated with $S_\epsilon^{\pm}$. The traction-free condition may be obtained by letting

$$z_c=x_1+i\epsilon A(x_1) \tag{17}$$

in (15), viz.

$$W(z_c; \epsilon)-W(\bar z_c; \epsilon)+\epsilon i2A(x_1)\overline{W'(z_c; \epsilon)}=0, \tag{18}$$

which suggests the expansion

$$W(z; \epsilon)\sim \sum_{n=0}^{\infty}\frac{\epsilon^n}{n!}W_n(z). \tag{19}$$

Substituting the above into (18) and setting $\epsilon=0$, we recover (16). It follows that the first approximation to the function $W(z; \epsilon)$, which is defined on $S_\epsilon^{\pm}$, is just the function W_0 which is defined on $S^{\pm}$. In fact, all the functions $W_n(z)$ are defined on the half-planes $S^{\pm}$ via the conditions

$$W_p^+-W_p^-=-p!\sum_{n=0}^{p-1}\frac{(iA)^{p-n}}{n!(p-n)!}\Big[W_n^{(p-n)+}-(-1)^{p-n}W_n^{(p-n)-}-2(p-n)(-1)^{p-n}\overline{W_n^{(p-n)+}}\Big] \tag{20}$$

where

$$W_n^{(p-n)\pm}\equiv\frac{\partial^{p-n}}{\partial z^{p-n}}W_n(z)\,|_{z=x_1\pm i0}. \tag{21}$$

Downloaded 03 May 2010 to 171.66.16.245. Redistribution subject to ASME license or copyright; see http://www.asme.org/terms/Terms_Use.cfm

Thus, the desired expansion may be obtained by solving a sequence of Cauchy problems in a systematic manner. In Case A, $'(x_1)$ is not continuous, special homogeneous solutions will be added to W_n to facilitate matching to yet additional inner expansions.

3 Smoothly Perturbed Free Surfaces

The upper half-plane S^+ is assumed to be stretched by $\tau_{11}^{(0)} = T$ with $\tau_{22}^{(0)} = \tau_{12}^{(0)} = 0$, so that

$$W_0^+(x_1) - W_0^-(x_1) = 0, \tag{22}$$

and

$$W_0(z) = \frac{T}{4} z. \tag{23}$$

Sinusoidally Wavy Surface. The amplitude function $A(x_1)$ of (16) is given by

$$A(x_1) = \frac{1}{2}(1 + \cos \pi x_1) \quad (-\infty < x_1 < \infty). \tag{24}$$

This problem has been studied by Gao (1991a). To illustrate the usefulness of (20), we have extended Gao's two-term solution to four terms. This is summarized in the Appendix, and the associated stress concentration factor (SCF) is

$$\mathrm{SCF} \equiv \tau_{11}(0, \epsilon; \epsilon)/T = \frac{2}{T}[W'(i\epsilon) + \overline{W'(i\epsilon)}] \sim 1 + \pi\epsilon - \frac{3}{16}(\pi\epsilon)^3 + \cdots, \tag{25}$$

where the first two terms have been obtained by Gao who used $(\epsilon/4)$ as his small parameter. Our four-term result indicates that the ϵ^2-term is identically zero. Moreover, the plausible suggestion that (25) should be nondecreasing in ϵ leads to the limitation that

$$\epsilon < \frac{4}{3\pi} = 0.424. \tag{26}$$

We shall now restrict our attention to a first-order perturbation analysis. The pertinent two-term solution is

$$W(z; \epsilon) \sim \frac{T}{4} z + \epsilon W_1(z) + \cdots \tag{27}$$

where

$$W_1^+ - W_1^- = -iTA(x_1). \tag{28}$$

We recall once again that (27) is uniformly valid if $A'(x_1)$ is continuous. Finally, for stress calculations it is more expedient to use the differentiated form of (28), i.e.,

$$W_1'^+ - W_1'^- = -iTA'(x_1). \tag{29}$$

A Single Smooth Depression. The case of a single isolated shallow depression may be defined by

$$A(x_1) = A_d(x_1) = \begin{cases} D(x_1) & (|x_1| < 1) \\ 0 & (|x_1| > 1) \end{cases} \tag{30}$$

where $A_d(\pm 1) = A_d'(\pm 1) = 0$. It follows from (29) that

$$W_1'(z) = W_D'(z) \equiv -\frac{T}{2\pi} \int_{-1}^{+1} \frac{D'(x)\,dx}{x - z} \tag{31}$$

which is just the integral obtained by Gao (1991a). We have

$$\mathrm{SCF}(x_1) \equiv \frac{1}{T}\tau_{\alpha\alpha}(x_1, \epsilon A(x_1); \epsilon) \sim 1 + \epsilon \frac{4}{T} \mathrm{Re}\, W_1'(x_1) + \cdots \tag{32}$$

where $\mathrm{SCF}(x_1) \cdot T$ is just the surface stress along the slightly uneven surface.

Let us now consider the depression profile defined by (Fig. 1(*a*))

$$D(x_1) = (1 - x_1^2)^2. \tag{33}$$

Substituting the above into (31) we get

$$W_1'(z) = W_D'(z) \equiv \frac{2T}{\pi}\left\{2(1 - z^2) + z(1 - z^2)\ln\frac{z - 1}{z + 1} - \frac{2}{3}\right\}, \tag{34}$$

which is holomorphic in $S^{\pm}$, and tends to z^{-2} as $z \to \infty$. The surface stress assumes a maximum at $(x_1 = 0, x_2 = \epsilon)$ and

$$\mathrm{SCF}(0) \sim 1 + \epsilon \frac{32}{3\pi} + \cdots, \tag{35}$$

which is to be compared with the first two terms of (25).

A Single Smooth Protrusion. The single complex function formulation of Section 2 requires that the physical upper half-plane S_ϵ^+ be contained in the mathematical upper half-plane S^+ (c.f. (7)). The case of a single isolated protrusion may therefore be defined by (Fig. 1(*a'*))

$$A(x) = A_p(x) = \begin{cases} 1 - D(x_1) & (|x_1| < 1) \\ 1 & (|x_1| > 1) \end{cases} \tag{36}$$

where $D(x_1)$ may be thought of as that given in (30). It follows from (29), (36), and (34) that

$$W_1'(z) = -W_D'(z). \tag{37}$$

The surface stress at the root of the protrusion is found to be large, and

$$\mathrm{SCF}(\pm 1) \sim 1 + \epsilon \frac{16}{3\pi} + \cdots. \tag{38}$$

The requirement that A and A' be continuous ensures that the two-term expansion (27) is uniformly valid for all z in S_ϵ^+. What happens if $A'(x_1)$ is not continuous? The following profiles illustrate the typical singular situations:

Parabolic Profile. (Figs. 1(*b*) and 1(*b'*)).

$$D(x_1) = 1 - x_1^2, \tag{39}$$

$$W_1'(z) = \pm\frac{T}{\pi}\left\{2 + z\ln\frac{z - 1}{z + 1}\right\}, \tag{40}$$

Triangular Profile. (Figs. 1(*c*) and 1(*c'*)).

$$D(x_1) = \begin{cases} 1 + x_1 & (-1 < x_1 < 0) \\ 1 - x_1 & (0 < x_1 < 1), \end{cases} \tag{41}$$

$$W_1'(z) = \pm\frac{T}{2\pi}\ln\{(z^2 - 1)/z^2\}, \tag{42}$$

where the plus signs apply to depressions and minus signs to protrusions. For the case of a parabolic profile, the logarithmic singularities at $z = \pm 1$ do not reflect the true behavior of the solution and special inner expansions must be constructed to complete the solution. For a triangular profile, the function $A'(x_1)$ has an additional discontinuity at $x_1 = 0$ and hence $W_1'(z)$ is also logarithimically singular at $z = 0$. Thus the complete asymptotic expansion associated with a triangular profile actually consists of an outer expansion and three inner expansions. The desired inner expansions are just the well-known wedge-apex solutions.

4 Wedge-Apex Solution and Related Properties.

Let ζ_R be a dimensionless boundary layer complex variable defined by

$$\zeta_R = \frac{z - z_R}{\epsilon} \tag{43}$$

where z_R is a complex constant. In terms of the polar representation (Fig. 2)

Downloaded 03 May 2010 to 171.66.16.245. Redistribution subject to ASME license or copyright; see http://www.asme.org/terms/Terms_Use.cfm

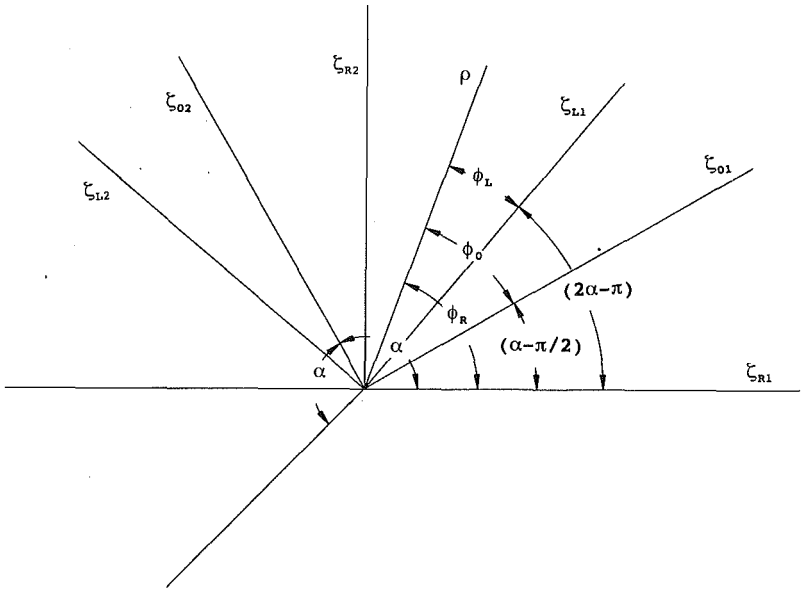


Fig. 2 Coordinate systems associated with a wedge of wedge angle 2α

$$\zeta_R = \zeta_{R1} + i\zeta_{R2} = \rho e^{i\phi_R}, \tag{44}$$

a traction-free elastic wedge of wedge angle 2α may be defined by

$$S_R^+ : 0 < \phi_R < 2\alpha, \quad \rho > 0. \tag{45}$$

Let us use the stress continuation Eqs. (11)–(16) and seek a solution in the form

$$W = \Omega_R(\zeta_R) = F_R \zeta_R^{1-\lambda} \tag{46}$$

where F_R and λ are constants, and the expression is assumed to hold for $-2\alpha < \phi_R < 2\alpha$ by the requirements of continuation. The traction-free condition along $\phi_R = 0$ is identically satisfied, and that along $\phi_R = 2\alpha$ yields

$$[\sin 2(1-\lambda)\alpha] F_R + [(1-\lambda)\sin 2\alpha] e^{i2\lambda\alpha} \overline{F}_R = 0, \tag{47}$$

where $\overline{F}_R$ denotes complex conjugate of F_R. Taking the complex conjugate of the above and considering F_R and $\overline{F}_R$ as two constants, we conclude that F_R must vanish unless $\lambda = \lambda^{(\pm)}$ is a root of

$$\sin 2(1-\lambda^{(\pm)})\alpha \pm (1-\lambda^{(\pm)})\sin 2\alpha = 0. \tag{48}$$

In that case

$$F_R = F e^{i\lambda^{(+)}\alpha}, \quad F_R = iF e^{i\lambda^{(-)}\alpha}, \tag{49}$$

where F is real.

The roots of (48) have been extensively studied in the literature (Williams, 1952; England, 1971; Moffatt and Duffy, 1980). We find the summary information of Ting (1984, 1985) most lucid and complete. Let $\lambda = \lambda_1, \lambda_2, \cdots$ be the roots, ordered in such a way that $+1 > \mathrm{Re}\lambda_1 > \mathrm{Re}\lambda_2 > \cdots$. For our present purpose the wedge angle 2α is almost π and

$$\lambda_1^{(+)} = \frac{2}{\pi}(2\alpha - \pi) - \left[\frac{2}{\pi}(2\alpha - \pi)\right]^2 + \cdots,$$

$$\lambda_2^{(+)} = -1 - \frac{1}{\pi}(2\alpha - \pi)^3 + \cdots,$$

$$\lambda_1^{(-)} = -1 + \frac{4}{\pi}(2\alpha - \pi) + \cdots, \tag{50}$$

where the two-term approximation for $\lambda_1^{(+)}$ is fairly accurate for (c.f., Fig. 1 of Ting, 1984)

$$-\frac{\pi}{8} < 2\alpha - \pi < \frac{\pi}{4}. \tag{51}$$

Thus, for a one-term wedge-apex expansion we have

$$W = \Omega_R(\zeta_R) = F e^{i\lambda\alpha} \zeta_R^{1-\lambda} \quad (-2\alpha < \phi_R < 2\alpha) \tag{52}$$

where $\lambda = \lambda_1^{(+)}$.

Let ζ_L be another complex variable defined by (Fig. 2)

$$\zeta_L = \zeta_R e^{-i(2\alpha - \pi)}, \quad \zeta_L = \zeta_{L1} + i\zeta_{L2} = \rho e^{i\phi_L}. \tag{53}$$

Then the same traction-free wedge of wedge angle 2α may be defined by

$$S_L^+ : -(2\alpha - \pi) < \phi_L < \pi, \quad \rho \geq 0. \tag{54}$$

The associated solution may be obtained as follows:

$$W = \Omega_L(\zeta_L) = -\overline{\Omega_R(\zeta_R)}\,|_{\zeta_R = \rho e^{i(\pi - \phi_L)}}$$

$$= F e^{-i\lambda(\alpha - \pi)} \zeta_L^{1-\lambda} \quad (\pi - 2\alpha < \phi_L < \pi + 2\alpha). \tag{55}$$

Similarly, let ζ_0 be yet another complex variable defined by (Fig. 2)

$$\zeta_0 = \zeta_R e^{-i\left(\alpha - \frac{\pi}{2}\right)}, \quad \zeta_0 = \zeta_{01} + i\zeta_{02} = \rho e^{i\phi_0}. \tag{56}$$

The same wedge may be defined by

$$S_0 : \frac{\pi}{2} - \alpha < \phi_0 < \frac{\pi}{2} + \alpha, \tag{57}$$

and hence neither one of the traction-free boundary coincides with the real axis ζ_{01}. The required W function may be obtained from the transformation (Muskhelishrili, 1953)

$$W = \Omega_0(\zeta_0) = \Omega_R[\zeta_0 e^{i(\alpha - \pi/2)}] e^{-i(\alpha - \pi/2)}$$

$$= F e^{i\lambda\pi/2} \zeta_0^{1-\lambda} \left(\frac{\pi}{2} - \alpha < \phi_0 < \frac{\pi}{2} + \alpha\right) \tag{58}$$

which is not analytically continued beyond S_0 of (47). It may be straightforwardly shown, however, that the other complex function $w(z)$ is

$$w = \omega_0(\zeta_0) = [\cos 2(1-\lambda)\alpha + (1-\lambda)\cos 2\alpha]\Omega_0(\zeta_0). \tag{59}$$

5 Singularly Perturbed Free Surfaces

The surface defined by (16) is said to be singularly perturbed if $A'(x_1)$ is discontinuous. The simpliest of all such cases are the parabolic depression and protrusion depicted in Figs. 1(*b*,

Downloaded 03 May 2010 to 171.66.16.245. Redistribution subject to ASME license or copyright; see http://www.asme.org/terms/Terms_Use.cfm

b'). The triangular configurations of Figs. 1(c, c'), however, appear to be more general and are treated in great detail in this section.

(1) Shallow Notch. The depression profile is defined by

$$A(x_1)=A_d(x_1)=\begin{cases}D(x_1) & (|x_1|<1)\\ 0 & (|x_1|>1),\end{cases} \tag{60}$$

where

$$D(x_1)=\begin{cases}1+x_1 & (-1<x_1<0)\\ 1-x_1 & (0<x_1<1).\end{cases} \tag{61}$$

It is noted that $A'(x_1)$ is discontinuous at $x_1=-1,\ 0,\ +1$. The solution is to be obtained in terms of four expansions. Since the expansions must be matched, it is more convenient to deal with $W(z)$, instead of $W'(z)$.

The two-term *outer expansion* obtained from (27), (28), (60), and (61) is

$$W(z;\ \epsilon)\sim\frac{T}{4}z+\epsilon\frac{T}{2\pi}\left\{z\ln\frac{z^2-1}{z^2}+\ln\frac{z+1}{z-1}\right\}+\cdots. \tag{62}$$

The stress field associated with the above is logarithmically singular at $z=\pm1$, where the wedge angle is smaller than 180 deg. It is also logarithmically singular at $z=0$, but $z=0$ is not in S_ϵ^+, the physical half-plane. The notch tip is at $z=i\epsilon$ where, according to (62), the solution is mathematically regular even though the wedge angle is now greater than 180 deg. It follows that the above solution cannot be valid for $0\le|z\pm1|\ll1$ and $0\le|z-i\epsilon|\ll1$.

For z in the immediate neighborhood of $z=1$, the geometric boundary[1] is that of a wedge of wedge angle

$$2\alpha=\pi-\tan^{-1}\epsilon=\pi-\epsilon+\cdots. \tag{63}$$

The appropriate boundary layer complex variable is

$$\zeta_R=\frac{z-1}{\epsilon}=\zeta_{R1}+i\zeta_{R2}=\rho e^{i\phi_R}, \tag{64}$$

so that the elastic wedge is given by

$$0<\phi_R<2\alpha,\quad \rho\ge0. \tag{65}$$

The leading terms of the *inner expansion* are

$$W\sim\Omega_R(\zeta_R;\ \epsilon)\sim C_R(\epsilon)+iB_R(\epsilon)\zeta_R+F_R(\epsilon)e^{i\lambda\alpha}\zeta_R^{1-\lambda}+\cdots\quad\left(\lambda=-\frac{2}{\pi}\epsilon\right), \tag{66}$$

where C_R, B_R, and F_R are constants and the latter two must be real. The first two terms constitute a rigid-body displacement in the complex ζ_R-plane. All three unknown constants are to be determined by matching.

Before proceeding it is perhaps important to note that homogeneous solutions of the type z^{-n} could be added to the W_1-term of the outer expansion, as $z=0$ is not in $S_\epsilon^+ + S_\epsilon^-$. The constants associated with these terms, however, would turn out to be zero from matching.

The following is a suitable matching variable (Cole, 1968; Van Dyke, 1975):

$$\zeta=\frac{z-1}{\epsilon^{1/2}}. \tag{67}$$

It follows that

$$z=1+\epsilon^{1/2}\zeta,\quad \zeta_R=\zeta/\epsilon^{1/2}. \tag{68}$$

The desired matching will be conducted for ζ fixed and $\epsilon\to0$. The *inner expansion of the outer expansion* is obtained by substituting the first of (68) into (62). We have

$$W(z;\ \epsilon)|_{z=1+\epsilon^{1/2}\zeta}\sim\frac{T}{4}+\epsilon^{1/2}\frac{T}{4}\zeta+\epsilon\frac{T}{\pi}\ln2+(\epsilon^{3/2}\ln\epsilon^{1/2})\frac{T}{2\pi}\zeta+\epsilon^{3/2}\frac{T}{2\pi}[\zeta\ln\zeta+(\ln2-1)\zeta]+\cdots. \tag{69}$$

Substituting the second of (68) into (66) we get the *outer expansion of the inner expansion*

$$\Omega_R(\zeta_R;\ \epsilon)|_{\zeta_R=\zeta/\epsilon^{1/2}}\sim C_R(\epsilon)+i[B_R(\epsilon)/\epsilon^{1/2}]\zeta+F_R(\epsilon)e^{-i\epsilon}[\zeta/\epsilon^{1/2}]^{1+2/\pi\epsilon}+\cdots. \tag{70}$$

Using the identity

$$x^\epsilon=\exp[\epsilon\ln x]=1+\epsilon\ln x+\cdots, \tag{71}$$

we obtain from equating (69) to (70) the conclusion that

$$F_R(\epsilon)\sim\frac{T}{4}\left[1+\epsilon\frac{2}{\pi}(\ln2-1)+\cdots\right]\epsilon^{1+2/\pi\epsilon+\cdots},$$

$$B_R(\epsilon)\sim\frac{T}{4}\epsilon^2+\cdots,\quad C_R(\epsilon)\sim\frac{T}{4}+\epsilon\frac{T}{\pi}\ln2+\cdots.$$

Substituting the above back into (66), we finally conclude that

$$W\sim\frac{T}{4}+\epsilon\left[\frac{T}{\pi}\ln2+i\frac{T}{4}(z-1)\right]+\frac{T}{4}\left[1+\epsilon\frac{2}{\pi}(\ln2-1)+\cdots\right]e^{-i\epsilon}(z-1)^{1+2/\pi\epsilon}+\cdots, \tag{73}$$

which is valid for $0\le|z-1|\ll1$ where the inclusion of the equality is to be emphasized. A similar inner expansion may be obtained for $0\le|z+1|\ll1$ by applying the operation used in deriving (55).

Turning now to the notch tip at $z=i\epsilon$, we have

$$2\alpha=\pi+2\epsilon+\cdots, \tag{74}$$

$$\zeta_0=\frac{z-i\epsilon}{\epsilon}=\zeta_{01}+i\zeta_{02}=\rho e^{i\phi_0}, \tag{75}$$

and the wedge region is defined by

$$S_0:\ -\epsilon<\phi_0<\pi+\epsilon,\quad \rho\ge0. \tag{76}$$

The leading terms of the associated inner expansion is

$$W\sim\Omega_0(\zeta_0;\ \epsilon)\sim C_0(\epsilon)+iB_0(\epsilon)\zeta_0+F_0(\zeta)e^{i\lambda\pi/2}\zeta_0^{1-\lambda}\quad\left(\lambda\simeq\frac{4}{\pi}\epsilon\right). \tag{77}$$

The new matching variable is

$$\zeta=\frac{z-i\epsilon}{\epsilon^{1/2}}. \tag{78}$$

Using the above, we obtain from (62) and (77)

$$W(z;\ \epsilon)|_{z=\epsilon^{1/2}\zeta+i\epsilon}\sim\epsilon^{1/2}\frac{T}{4}\zeta-\epsilon i\frac{T}{4}-(\epsilon^{3/2}\ln\epsilon^{1/2})\frac{T}{\pi}\zeta+\epsilon^{3/2}\frac{T}{\pi}[\zeta-\zeta\ln\zeta+i\pi\zeta]+\cdots, \tag{79}$$

$$\Omega_0(\zeta_0;\ \epsilon)|_{\zeta_0=\zeta/\epsilon^{1/2}}\sim C_0(\epsilon)+i[B_0(\epsilon)/\epsilon^{1/2}]\zeta+F_0(\epsilon)e^{i2\epsilon}[\zeta/\epsilon^{1/2}]^{1-4/\pi\epsilon}+\cdots. \tag{80}$$

The results of matching are

$$F_0(\epsilon)\sim\frac{T}{4}\left(1+\epsilon\frac{4}{\pi}+\cdots\right)\epsilon^{1-4/\pi\epsilon+\cdots},$$

$$B_0(\epsilon)\sim-\epsilon^2\frac{T}{4}+\cdots,\quad C_0(\epsilon)\sim-\epsilon i\frac{T}{4}+\cdots, \tag{81}$$

and

[1] A curvilinear wedge of the type discussed by Ting (1985) would be involved for a parabolic depression.

Downloaded 03 May 2010 to 171.66.16.245. Redistribution subject to ASME license or copyright; see http://www.asme.org/terms/Terms_Use.cfm

$$W \sim -\epsilon i\frac{T}{4} - \epsilon\frac{T}{2} i(z - i\epsilon) + \frac{T}{4}\left(1 + \epsilon\frac{4}{\pi} + \cdots\right) e^{i2\epsilon}(z - i\epsilon)^{1-4/\pi\epsilon} + \cdots, \quad (82)$$

which is valid for $0 \le |z - i\epsilon| \ll 1$. We conclude this part of the analysis by noting that inverse powers of ζ will appear in (79) if higher order terms are included. Thus, homogeneous solutions should be included in the outer expansion starting from W_3.

Finally, the notch-stress intensity factor is explicitly captured in (82). In view of (74) and the right-hand side of (51), we conclude that

$$2\epsilon < \frac{\pi}{4}, \quad \epsilon < \frac{\pi}{8} = 0.393, \quad (83)$$

which is to be compared with (26). The asymptotic expression (82) should be applicable to $2\alpha < 225$ deg.

(2) Triangular Protrusion. The protrusion profile is

$$A(x_1) = A_p(x_1) = 1 - A_d(x_1) \quad (84)$$

where $A_d(x_1)$ is just the function defined by (60) and (61). The immediate impression one gets is that a sign modification on the notch solution would yield the desired new solution. That this observation is not strictly correct follows from the fact that the regions formed by the two sets of $S_\epsilon^{\pm}$,s are completely different (Fig. 1). For the present case, homogeneous solutions that are appropriate for inclusion in the outer expansion are

$$(z - 1 - i\epsilon)^{-n} \text{ and } (z + 1 - i\epsilon)^{-n} \quad (85)$$

which, however, will not be needed until the term $\epsilon^3 W_3(z)$.

The two-term approximation is summarized as follows:

Outer Expansion.

$$W(z;\epsilon) \sim \frac{T}{4} z - \epsilon\frac{T}{2\pi}\left\{ z \ln\frac{z^2 - 1}{z^2} + \ln\frac{z+1}{z-1}\right\} + \cdots \quad (86)$$

Inner Expansion (Tip of Protrusion).

$$W \sim \cdots + \frac{T}{4}\left(1 - \epsilon\frac{4}{\pi} + \cdots\right) e^{-i2\epsilon} z^{1+4/\pi\epsilon\cdots} + \cdots \quad (87)$$

Inner Expansion (Foot of Protrusion).

$$W \sim \cdots + \frac{T}{4}\left[1 - \epsilon\frac{2}{\pi}(\ln 2 - 1) + \cdots\right] \times e^{i\epsilon}(z - 1 - i\epsilon)^{1-2/\pi\epsilon+\cdots} + \cdots \quad (88)$$

which are to be compared with (62), (82), and (73), respectively.

References

Cole, J. D., 1968, *Perturbation Methods in Applied Mathematics*, Blaisdell Publishing Company.

England, A. H., 1971a, *Complex Variable Methods in Elasticity*, John Wiley and Sons, New York.

England, A. H., 1971b, "On Stress Singularities in Linear Elasticity," *Int. J. Eng. Sci.*, Vol. 9, pp. 571–585.

Gao, H., 1991a, "Stress Concentration at Slightly Undulating Surfaces," *J. Mech. Phys. Solids*, Vol. 39, No. 4, pp. 443–458.

Gao, H., 1991b, "Morphological Instabilities Along Surfaces of Anisotropic Solids," *Modern Theory of Anisotropic Elasticity and Applications*, J. J. Wu, T. C. T. Ting, and D. M. Barnett, pp. 139–150.

Moffatt, H. K., and Duffy, B. R., 1980, "Local Similarity Solutions and Their Limitations," *J. Fluid Mech.*, Vol. 96, pp. 299–313.

Muskhelishvili, N. I., 1953, *Some Basic Problems of the Mathematical Theory of Elasticity*, (translated by J. R. M. Redok), Noordhoff.

Ting, T. C. T., 1984, "The Wedge Subjected to Tractions: A Parador Re-examined," *J. Elasticity*, Vol. 14, pp. 235–247.

Ting, T. C. T., 1985, "Asymptotic Solution Near the Apex of an Elastic Wedge with Curved Boundaries," *Q. Appl. Math.*, Vol. 00, pp. 467–476.

Van Dyke, M., 1975, *Perturbation Methods in Fluid Mechanics*, Parabolic Press.

Williams, M. L., 1952, "Stress Singularities Resulting From Various Boundary Conditions in Angular Corners of Plates in Extension," ASME JOURNAL OF APPLIED MECHANICS, Vol. 19, pp. 526–528.

APPENDIX

A Four-Term Asymptotic Solution for Sinusoidally Wavy Surface

We being by exhibiting the first three Cauchy conditions deduced from (20) as follows:

$$W_1^+ + W_1^- = -iA[W_0'^+ + W_0'^- + \overline{2W_0'^+}], \quad (A1)$$

$$W_2^+ - W_2^- = A^2[W_0''^+ - W_0''^- - \overline{4W_0''^+}] - 2iA[W_1' + W_1'^- + \overline{2W_1'^+}], \quad (A2)$$

$$W_3^+ - W_3^- = iA^3[W_0'''^+ + W_0'''^- + \overline{6W_0'''^+}] + 3A^2[W_1'''^+ - W_1'''^- - \overline{4W_1'''^+}] - 3iA[W_2'^+ + W_2'^- + \overline{2W_2'^+}], \quad (A3)$$

where $W_0(z)$ and $A(x_1)$ are defined by (23) and (24).

The Cauchy condition for W_1, (A1), now becomes

$$W_1^+ - W_1^- = -\frac{iT}{2}\left[1 + \frac{1}{2}(e^{i\pi x_1} + e^{-i\pi x_1})\right]. \quad (A4)$$

The solution to the above is

$$W_1(z) = \begin{cases} -\dfrac{iT}{2}\left[\dfrac{1}{1+\kappa} + \dfrac{1}{2}e^{i\pi z}\right] & (z\epsilon S^+) \\ \dfrac{iT}{2}\left[\dfrac{\kappa}{1+\kappa} + \dfrac{1}{2}e^{-i\pi z}\right] & (z\epsilon S^-). \end{cases} \quad (A5)$$

where the constant terms are fixed in such a way that S^+ has a zero rigid-body displacement.

The result of substituting all the known relation into (A2) is

$$W_2^+ - W_2^- = -\frac{i\pi T}{8}\{4 + 2e^{i\pi x_1} + e^{i2\pi x_1} + 6e^{-i\pi x_1} + 3e^{-i2\pi x_1}\}, \quad (A6)$$

and hence

$$W_2(z) = \begin{cases} -\dfrac{i\pi T}{8}\left\{\dfrac{4}{1+\kappa} + 2^{i\pi z} + e^{i2\pi z}\right\} & (z\epsilon S^+) \\ \dfrac{i\pi T}{8}\left\{\dfrac{4\kappa}{1+\kappa} + 6e^{-i\pi z} + 3e^{-i2\pi z}\right\} & (z\epsilon S^-). \end{cases} \quad (A7)$$

This process is continued one step further via (A3) and the net result is

$$W_3^+ - W_3^- = \frac{3i\pi^2 T}{64}\{-e^{i\pi x_1} - 8e^{i2\pi x_1} - 3e^{i3\pi x_1} - 29e^{-i\pi x_1} - 40e^{-i2\pi x_1} - 15e^{-i3\pi x_1}\}. \quad (A8)$$

It follows that

$$W_3(z) = \begin{cases} -\dfrac{3i\pi^2 T}{64}\{e^{i\pi z} + 8e^{i2\pi z} + 3e^{i3\pi z}\} \\ \dfrac{3i\pi^2 T}{64}\{29e^{-i\pi z} + 40e^{-i2\pi z} + 15e^{-i3\pi z}\}. \end{cases} \quad (A9)$$

This formally completes a 4-term asymptotic solution accurate to the order of ϵ^3.

Finally, the desired SCF is calculated from

$$W'(i\epsilon) \sim W_0'(0) + \epsilon[W_1'(0) + iW_0''(0)] + \frac{1}{2}\epsilon^2[W_2'(0) + 2iW_1''(0) - W_0'''(0)] + \frac{1}{3!}\epsilon^3[W_3'(0) + 3iW_2''(0) - 3W_1'''(0) - W_0''''(0)] + \cdots. \quad (A10)$$

Downloaded 03 May 2010 to 171.66.16.245. Redistribution subject to ASME license or copyright; see http://www.asme.org/terms/Terms_Use.cfm

Free Vibration Analysis of Rectangular Plates with Nonuniform Lateral Elastic Edge Support

D. J. Gorman
Professor,
Department of Mechanical Engineering,
University of Ottawa,
Ottawa, Ontario K1N 6N5
Canada

The method of superposition is utilized to obtain a solution for the free vibration of thin rectangular plates resting on non-uniform lateral elastic edge supports. The stiffness of the elastic supports may have any desired distribution along the edges, including discontinuities and local concentrations. Convergence is found to be rapid. Graphical results are plotted for square plates in order to verify that proper frequency limits are approached as the edge stiffness approach limits of zero and infinity. Results are tabulated for square and nonsquare plates in order that other researchers will have data against which they can compare their results.

1 Introduction

Numerous papers related to the free vibration of rectangular plates resting on uniform elastic edge supports have appeared in the literature. The term "uniform" implies that along each edge the elastic coefficients of the edge support do not vary. It has long been recognized that among such problems there are essentially two families. In the first, and simpler family, the plates have two opposite edges free of elastic restraint and with simple edge support. Such problems can be resolved by means of a Lévy-type solution. In the more general family of problems where all edges may have elastic support, solutions are more difficult to obtain. Series-type solutions have been achieved by energy methods and, more recently, the author has obtained highly accurate solutions by means of the superposition method (Gorman, 1989, 1990).

A search of the literature quickly reveals that little work has been devoted to the problem of plates resting on elastic edge support where the stiffness varies along the edges. An exception is the work of Leissa et al. (Leissa, 1980), where a limited set of problems with variable rotational elastic support along one opposite pair of edges has been analyzed. It is pointed out that this is the first published work in this area. It also appears that little, if any, such work has been performed since that time.

In this paper the problem of rectangular plates resting on elastic lateral edge support, where the elastic coefficients can vary along each edge, is addressed. It will be appreciated that this problem, which has arisen in recent industrial applications, presents the analyst with a considerably greater challenge. Again, the problem is solved by the superposition method and rapid convergence to exact eigenvalues is obtained. A number of problems are solved in order to demonstrate that correct limits are approached as the elastic distribution coefficients are allowed to approach their natural limits of infinity and zero. They also help demonstrate the computational procedure. A limited amount of computed data is tabulated in digital form so that other researchers will have data with which they may compare their results.

2 Development of Mathematical Model

In order to resolve the problem of interest by means of the superposition method, two distinct sets of solutions, or building blocks, are required. Each set is described separately.

(1) Building Blocks Driven by Harmonic Vertical Edge Reactions. This set of building blocks is represented schematically in Fig. 1. The digits 1 to 4 on the reference block to the left of the figure are used to designate the various plate edges. It will be noted that the digit 1 will be incorporated into Fourier coefficients and elastic stiffnesses related to the edge 1, etc. Each building block has three edges which are given slip-shear support, i.e., slope taken normal to the edge, as well as vertical edge reaction, is everywhere zero. This condition is indicated by two small circles adjacent to the edge. The driven edge of each building block in the set also has a condition of zero slope imposed. In addition, this edge is driven by a distributed harmonic vertical edge reaction. The zero slope condition is indicated by two solid circular dots adjacent to the edge.

Contributed by the Applied Mechanics Division of THE AMERICAN SOCIETY OF MECHANICAL ENGINEERS for presentation at the ASME Winter Annual Meeting, New Orleans, LA, Nov. 28–Dec. 3, 1993.

Discussion on this paper should be addressed to the Technical Editor, Professor Lewis T. Wheeler, Department of Mechanical Engineering, University of Houston, Houston, TX 77204-4792, and will be accepted until four months after final publication of the paper itself in the ASME JOURNAL OF APPLIED MECHANICS.

Manuscript received by the ASME Applied Mechanics Division, Jan. 29, 1992; final revision, Dec. 23, 1992. Associate Technical Editor: F. Y. M. Wan.

Paper No. 93-WA/APM-6.

Copyright © 1993 by ASME
Downloaded 03 May 2010 to 171.66.16.245. Redistribution subject to ASME license or copyright; see http://www.asme.org/terms/Terms_Use.cfm

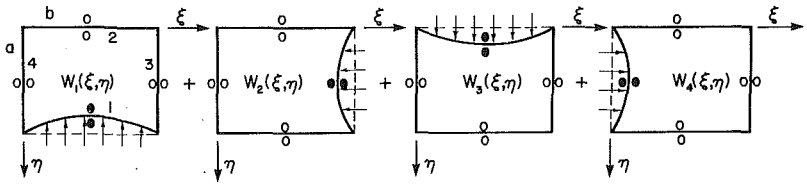


Fig. 1 Building blocks utilized to satisfy vertical edge reaction equilibrium

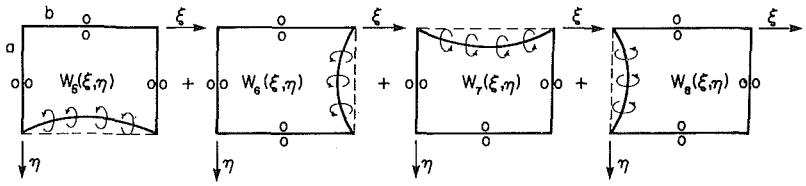


Fig. 2 Building blocks utilized to neutralize bending moments on edge of plate

Focusing attention on the first building block, it is seen that its solution can be written as

$$W_1(\xi, \eta) = \sum_{m=0,1}^{\infty} Y_m(\eta) \cos m\pi\xi \tag{1}$$

where ξ and η are spatial coordinates nondimensionalized with respect to edge lengths a and b. $W(\xi, \eta)$ is the plate lateral displacement divided by edge length a.

In view of the boundary conditions enforced along the edge, $\eta = 0$ and the nature of the dynamic plate equilibrium equation, it is shown that we may write, for $\lambda^2 > (m\pi)^2$,

$$Y_m(\eta) = \{A_m \cosh \beta_m\eta + B_m \cos \gamma_m\eta\}, \tag{2}$$

and, for $\lambda^2 < (m\pi)^2$,

$$Y_m(\eta) = \{A_m \cosh \beta_m\eta + B_m \cosh \gamma_m\eta\}, \tag{3}$$

where $\beta_m^2 = \phi^2[\lambda^2 + (m\pi)^2]$, and $\gamma_m^2 = \phi^2[\lambda^2 - (m\pi)^2]$, or $\phi^2[(m\pi)^2 - \lambda^2]$, whichever is real, and A_m and B_m are constants to be evaluated. λ^2, the plate eigenvalue, equals $\omega a^2\sqrt{\rho/D}$, where ω is the circular frequency of vibration, ρ is the mass per unit area of the plate, and D is the plate flexural rigidity. ϕ, the plate aspect ratio, equals b/a.

We choose to represent the dimensionless amplitude of the harmonic vertical edge reaction along the edge, $\eta = 1$, in series form as

$$\frac{V(\xi)b^3}{aD} = \sum_{m=0,1}^{\infty} E_1(m) \cos m\pi\xi \tag{4}$$

where the $E_1(m)$'s are Fourier coefficients to be determined later.

Enforcing the condition of zero slope and the harmonic vertical edge reaction of Eq. (4) along the edge, $\eta = 1$, it is shown that Eqs. (2) and (3) become, respectively,

$$Y_m(\eta) = E_1(m)\{\theta_{11_m} \cosh \beta_m\eta + \theta_{13_m} \cos \gamma_m\eta\} \tag{5}$$

and

$$Y_m(\eta) = E_1(m)\{\theta_{22_m} \cosh \beta_m\eta + \theta_{23_m} \cosh \gamma_m\eta\} \tag{6}$$

where

$$\theta_{11_m} = \frac{-1}{\beta_m(ZZ3 + ZZ4)\sinh \beta_m},$$

$$\theta_{13_m} = \frac{-1}{\gamma_m(ZZ3 + ZZ4)\sinh \gamma_m},$$

with

$$ZZ3 = \beta_m^2 - \nu^*\phi^2(m\pi)^2$$

and

$$ZZ4 = \gamma_m^2 + \nu^*\phi^2(m\pi)^2$$

and

$$\theta_{22_m} = \frac{-1}{\beta_m(ZZ3 - ZZ4)\sinh \beta_m},$$

$$\theta_{23_m} = \frac{1}{\gamma_m(ZZ3 - ZZ4)\sinh \gamma_m},$$

with

$$ZZ4 = \gamma_m^2 - \nu^*\phi^2(m\pi)^2$$

where ν = Poisson's ratio and $\nu^* = 2 - \nu$.

It will be apparent that solutions for all other building blocks in this set are easily extracted from the first. The solution for the second building block is obtained through an interchange of the variables ξ and η and replacement of the aspect ratio by its inverse. Solution for the third building block is obtained by simply replacing the variable η by the quantity $(1 - \eta)$, etc.

(2) Building Blocks Driven by Harmonic Edge Moments. This set of building blocks is depicted in Fig. 2. It differs from the first set only in that the driven edges are free of vertical edge reaction and are subjected to a dimensionless harmonic bending moment which is expressed in a form similar to that of Eq. (4) as

$$\frac{M(\xi)b^2}{aD} = \sum_{m=0,1}^{\infty} G_1(m) \cos m\pi\xi. \tag{7}$$

The solution for the first building block of this set is identical in form to that of the first building block of the first set (Eqs. (1), (5), and (6)) except that the quantities θ_{13_m}, etc., will be different. Their symbols are slightly modified here to avoid confusion and they are given as

$$\theta_{11_{mp}} = \frac{-1}{(ZZ3\,XX1 + ZZ1\,ZZ4\,YY1/ZZ2)\sinh \beta_m}$$

$$\theta_{13_{mp}} = \frac{1}{(ZZ2 * ZZ3 * XX1/ZZ1 + ZZ4\,YY1)\sin \gamma_m}$$

where

$$ZZ3 = \beta_m^2 - \nu\phi^2(m\pi)^2, \quad ZZ4 = \gamma_m^2 + \nu\phi^2(m\pi)^2$$
$$ZZ1 = \beta_m ZZ3, \quad ZZ2 = \gamma_m ZZ4$$

Downloaded 03 May 2010 to 171.66.16.245. Redistribution subject to ASME license or copyright; see http://www.asme.org/terms/Terms_Use.cfm

$$XX1 = \frac{\cosh \beta_m}{\sinh \beta_m}, \quad \text{and} \quad YY1 = \frac{\cos \gamma_m}{\sin \gamma_m}$$

and

$$\theta_{22_{mp}} = \frac{-1}{(ZZ3\ XX1 - ZZ1\ ZZ4\ YY1/ZZ2)\sinh \beta_m}$$

$$\theta_{23_{mp}} = \frac{1}{(ZZ2\ ZZ3\ XX1/ZZ1 - ZZ4\ YY1)\sinh \gamma_m}$$

where

$$ZZ4 = \gamma_m^2 - \nu\phi^2 (m\pi)^2$$

$$XX1 = \frac{\cosh \beta_m}{\sinh \beta_m}, \quad \text{and} \quad YY1 = \frac{\cosh \gamma_m}{\sinh \gamma_m}.$$

Solutions for the remaining building blocks of this set are extracted from the first building block in a manner identical to that described for the first set.

3 Development of the Eigenvalue Matrix

Contributions of First Set of Building Blocks. We begin by considering the situation when all four building blocks of the first set (Fig. 1) are superimposed, one upon the other. Consider the edge $\eta = 1$. Let this edge rest on lateral elastic edge support whose dimensionless distribution is given as $K_1(\xi)$, where $K_1(\xi) = kb^3/D$, k being the lateral elastic stiffness per unit edge length. Then letting $W(\xi, \eta)$ represent the net lateral displacement of the combined building block set we have

$$\frac{V(\xi)b^3}{aD} = -K_1(\xi)\ W(\xi, \eta)|_{\eta=1.} \tag{8}$$

The left-hand side of Eq. (8) is already available in the form of a cosine series (Eq. 4). For convenience, the quantity $K_1(\xi)$ is easily made available in a Fourier series; we choose a cosine series. We can thus expand the total right-hand side of Eq. (8) in a further cosine series. We will then be able to utilize Eq. (8) to write homogeneous algebraic equations relating all the unknown Fourier coefficients appearing in the building blocks.

Let us consider the nth term in the expansion of the right-hand side of Eq. (8). Let us also, for the moment, include only the contribution of $W_1(\xi, \eta)$ toward the net displacement. We consider the quantity $K_1(\xi)$ to be expanded in series form as

$$K_1(\xi) = \sum_{i=0,1}^{\infty} EL1(i) \cos i\pi\xi \tag{9}$$

Referring to Eqs. (5) and (6), we introduce the symbol H_m as

$$H_m = \theta_{11_m} \cosh \beta_m\eta + \theta_{13_m} \cos \gamma_m\eta\,|_{\eta=1} \tag{10}$$

or

$$H_m = \theta_{22_m} \cosh \beta_m\eta + \theta_{23_m} \cosh \gamma_m\eta\,|_{\eta=1}$$

whichever is appropriate.

We now refer to Eqs. (4), (5), (6), (8), and (9). It follows that equating the nth terms in the expansion of Eq. (8), as just discussed, leads to the equality

$$E_1(n) = -2 \sum_{m=0,1}^{\infty} E_1(m) \sum_{i=0,1}^{\infty} EL1(i) \times \int_0^1 H_m \cos m\pi\xi \cos i\pi\xi \cos n\pi\xi\, d\xi. \tag{11}$$

In this particular case, where only the contribution of $W_1(\xi, \eta)$ is included, the quantities H_m will not be functions of ξ and the exact required integrals are easily provided by a computer algorithm. It will be observed that, in fact, Eq. (11) is a homogeneous linear algebraic equation relating the set of Fourier coefficients $E_{1(m)}$. If the total number of coefficients utilized with each building block equals K, then K such equations can be written.

We consider next the situation when all four building blocks are superimposed. It will be obvious that three more summations will appear on the right-hand side of Eq. (11) because of the contributions to displacement along the edge, $\eta = 1$, of the additional building blocks. The integrals of Eq. (11) will be quite similar for the contributions of the first and third building blocks. It will be evident that for the other two building blocks, the integrals will be slightly changed as the quantity $H_m \cos m\pi\xi$ will be replaced with some multiples of hyperbolic or trigonometric functions of the variable ξ.

It is seen that we now have $4K$ unknown Fourier coefficients in each of the K-equations. $3K$ additional equations are, of course, available by enforcing the counterpart of Eq. (11) on each of the other three edges.

In fact, as will be seen later, if we wish only to investigate the free vibration frequencies and mode shapes of a plate resting on distributed elastic lateral edge support, and with slope taken normal to the edges forbidden, we now have all the equations necessary to construct the eigenvalue matrix. Our main purpose here, however, is to solve the problem where bending moment, instead of slope is forbidden along these edges. We achieve this goal by combining the first and second sets of building blocks already described.

Let us now consider the four building blocks of Fig. 2 to be superimposed on those of the first set. The net displacement will be composed of the contributions of all eight building blocks. Accordingly, the right-hand side of Eq. (11) will contain eight summations instead of one. A typical equation, upon evaluation of the integrals, will provide us with a linear homogeneous algebraic equation relating the $8K$ unknown Fourier coefficients. Of course, K equations can be written for each of the four edges resulting in a set of $4K$ simultaneous equations. We still need another $4K$ equations and we obtain those by requiring vanishing of the net moment along each of the four edges.

This final set of equations is obtained by following well-established procedures. Along each edge we expand the net bending moment in a Fourier series, here we will utilize a cosine series. Some of the moments will already be available in this series. We then require that each coefficient in this series expansion should vanish. Employing K terms in the series results in a set of K homogeneous algebraic equations relating the $8K$ unknowns. Of course, we obtain K equations for each edge, resulting in $4K$ additional equations. We now have the required set of $8K$ equations required for constructing the eigenvalue matrix.

A schematic representation of this matrix, based on three-term expansions for the building blocks, is presented in Fig. 3. The first segment composed of three rows of the matrix arises because of the requirement that the vertical edge reaction equilibrium condition should be satisfied along the edge, $\eta = 1$. Inserts to the right of the figure indicate the edge on which equilibrium is enforced. There are of course four such segments of the matrix, one related to each edge of the plate.

The final four segments of the matrix result from enforcement of the condition of zero net bending moment along each of the four edges. Again, the edge to which each segment is related is indicated in the inserts to the right of the figure.

It will be appreciated that, because of the nature of Eq. (11), a relatively simple computer program can be constructed to generate contributions to the matrix elements resulting from the right-hand side of this equation. The same is true regarding contributions of the building blocks toward edge moment distributions. This simplicity arises because there are really only two basic building blocks utilized in the entire analysis.

Contributions associated with the left-hand side of Eq. (11)

Downloaded 03 May 2010 to 171.66.16.245. Redistribution subject to ASME license or copyright; see http://www.asme.org/terms/Terms_Use.cfm

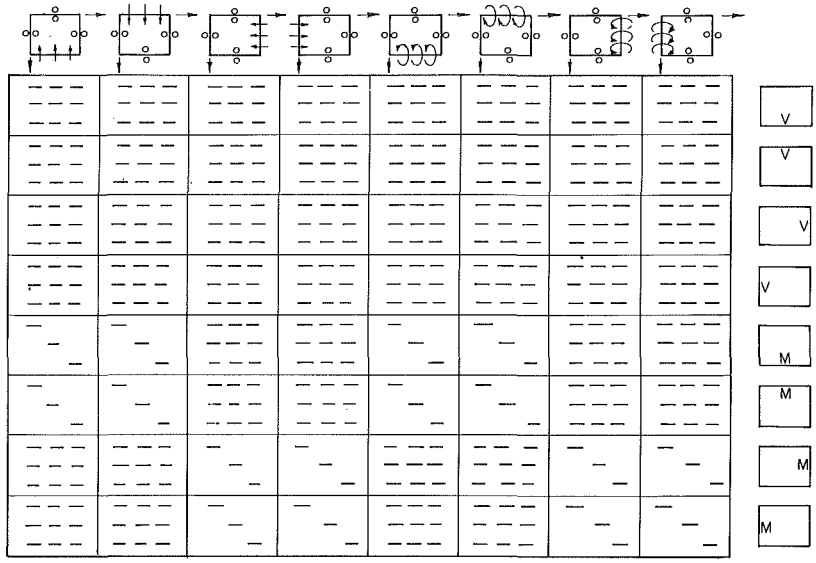


Fig. 3 Schematic representation of eigenvalue matrix based on three-term building block expansions

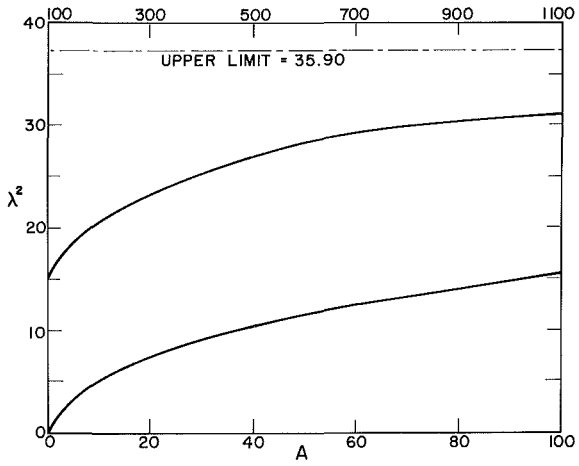


Fig. 4 First mode eigenvalue versus amplitude A of parabolically distributed elastic edge support, for square plate with slope forbidden normal to edges. Equal stiffness on all edges.

are easily incorporated into the matrix. This is done by simply adding $+1$ to each diagonal element of the matrix in the first four segments. This added quantity will always be positive in view of the transformations utilized to extract solutions for the third and fourth building blocks from the first and second. Finally, it will be appreciated that by setting any one of the nonzero Fourier coefficients equal to unity, the set of equations leading to the eigenvalue matrix becomes nonhomogeneous. We may then solve, for the vibrating plate, the mode shape associated with any eigenvalue.

4 Presentation of Computed Results

With the plate aspect ratio selected as well as distributions for the lateral elastic edge support the eigenvalue matrix can be constructed, and a search can be conducted to determine those values of λ^2 which cause the determinant of the matrix to vanish (the eigenvalues). It will be evident that an infinity of results could be generated. In order to keep the problem manageable and to permit certain verification tests to be performed, we choose to limit our study to two cases of dimensionless elastic stiffness distributions. In the first case, the distribution will be uniform along all edges. In the second case, the stiffness will be parabolically distributed. The fundamental stiffness, k, will be maintained the same for each edge, regardless of plate aspect ratio.

For parabolic distributions, the dimensionless stiffness along the edge, $\eta = 1$ is written as

$$K_1(\xi) = 4A\xi(1-\xi). \tag{12}$$

It is seen that the stiffness goes to zero at each extremity of the edge and has a magnitude A midway along the edge. This type of distribution is similar to that employed by Leissa et al. (1990) in their study of plates resting on edges with rotational elastic stiffness.

A preliminary study of the matrix (Fig. 3) indicates that the right lower quadrant alone permits free vibration analysis of the completely free plate. Tests have therefore been performed to verify that, in fact, the known eigenvalues for the completely free plate are obtained in this way.

It will also be apparent that the upper left quadrant of the matrix permits analysis of a rectangular plate resting on elastic lateral edge supports with slope taken normal to the edges forbidden. In Fig. 4 the computed first-mode eigenvalue for a square plate of this type with equal parabolically distributed lateral stiffness along each edge is presented. In this figure, as in Figs. 5, 6, and 7, the values of the abscissa for the upper curve are to be taken from the upper edge of the figure. Maximum amplitude of the stiffness distribution along the edges is given by the symbol A as defined in Eq. (12). It is seen that the eigenvalue approaches the known first-mode limits of zero and 35.90, as the parameter A is allowed to approach zero, and infinity, respectively. Extensions of the graphs presented show a continuation of this approach. The upper limit is, of course, that of a fully clamped plate. We can never quite arrive at this upper limit as our stiffness at the corners will always be zero. This is due to our choice of a parabolic distribution of the stiffness.

In Fig. 5 the first mode eigenvalue for a square plate with equal uniform stiffness along all edges is plotted against the dimensionless stiffness coefficient K_1 for the general problem where edge moment is forbidden. In this analysis only the first term of the cosine series representing the stiffness distribution is utilized. The analysis is based on the full matrix of Fig. 3. It is seen that the limits of $2\pi^2$ and zero for the eigenvalue are approached. In fact, with proper coordinate transformation,

Downloaded 03 May 2010 to 171.66.16.245. Redistribution subject to ASME license or copyright; see http://www.asme.org/terms/Terms_Use.cfm

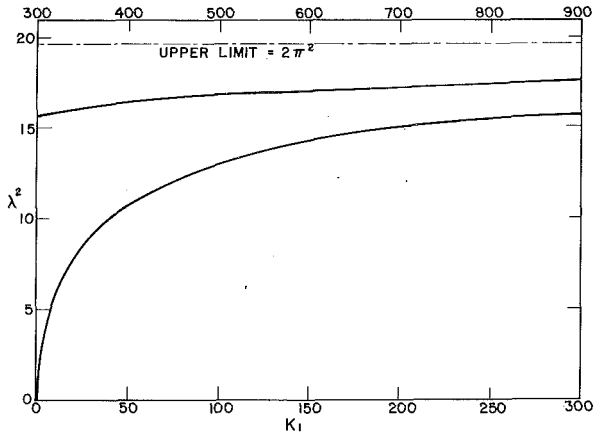


Fig. 5 First mode eigenvalue versus uniform stiffness coefficient K_1 for square plate with equal stiffnesses along all edges

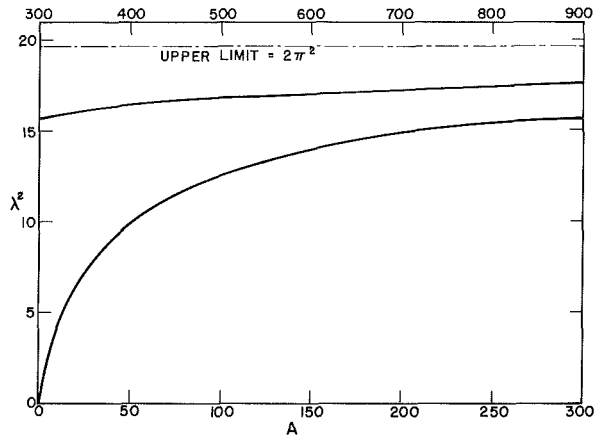


Fig. 6 First-mode eigenvalue versus amplitude A of parabolically distributed elastic edge support for a square plate. Equal stiffness on all edges.

the curve of this figure fits exactly on top of the corresponding curve (Fig. 5) of Gorman (1989). We do not need the much more general and sophisticated computational procedure of the current analysis to solve this uniform elastic distribution problem, but the exercise serves as a valuable verification test. Here we should appreciate that in the upper limit case, concentrated forces act at the corners. Because our stiffness is uniform, we can never generate these concentrated forces and hence can never quite reach the upper limit of Fig. 5.

In Fig. 6 the foregoing analysis is repeated, but this time an equal parabolic distribution of stiffness, of maximum amplitude A, is distributed along each edge. Again, the correct limits of zero and $2\pi^2$ for the eigenvalue are approached. It will be noted, on closer examination, that the curve of Fig. 6 lies slightly below that of Fig. 5. This is to be expected, as the parabolic distribution does not offer as much resistance to lateral displacement as the uniform distribution with the same amplitude.

Finally, in Fig. 7 the second-mode eigenvalue for a rectangular plate of aspect ratio 1.2 is plotted as a function of A, the amplitude (maximum value) of parabolically distributed lateral stiffness along the edge $\eta = 1$. Identical stiffness is distributed along the edge $\eta = 0$. Dimensionless stiffness parameters along the other two edges are modified so as to give the same fundamental stiffness, k, on all four edges. Again, correct frequency limits are approached.

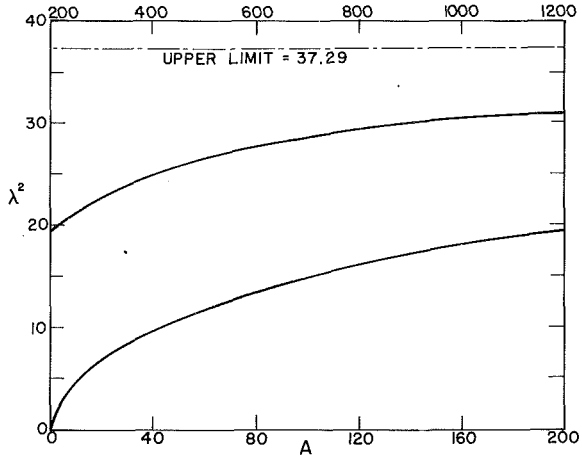


Fig. 7 Second-mode eigenvalue versus amplitude A of parabolically distributed elastic edge support along the edge $\eta = 1$ of a rectangular plate $\phi = 1.20$. Fundamental stiffness k is equal on all edges.

Table 1 Tabulated first mode eigenvalue versus amplitude A of a parabolically distributed lateral elastic edge support for a square plate. Equal stiffness on all edges.

A:	2.5	5.0	10	20	30	50
λ^2:	2.563	3.599	5.018	6.896	8.210	10.03
A:	75	100	150	200	500	1000
λ^2:	11.52	12.55	13.88	14.71	16.77	17.81

Table 2 Tabulated second mode eigenvalue versus amplitude A of parabolically distributed lateral elastic edge support along edge, $\eta = 1$, of a rectangular plate. $\phi = 1.20$ k is equal on all edges.

A:	2.5	5.0	10	20	30	50
λ^2:	2.442	3.449	4.864	7.265	8.335	10.64
A:	75	100	150	200	500	1000
λ^2:	12.85	14.64	17.44	19.60	26.46	30.37

It is further appreciated that a useful role which can be fulfilled by a paper of this type is to provide digital data against which other researchers can compare their results. Accordingly, in Tables 1 and 2, computed eigenvalues are tabulated for the problems of Figs. 6 and 7. The stiffness intervals in these tables have been selected so as to give approximately equal intervals in the tabulated eigenvalues.

Numerous convergence tests were conducted before computing the results reported here. It will be evident that two series limits must be chosen, one related to the expansion of the distributed stiffnesses and one related to the number of terms to be utilized in the building block solution expansions. It has generally been found that a value of 15 for the former, and 9 for the latter, leads to an accuracy of four significant digits in the computed results. These are the series upper limits utilized in the work reported here.

It will be recalled that each term of each solution series satisfies exactly the governing differential equation, hence, the solution built on these series also satisfies exactly the differential equation. It should be pointed out that the solution to this boundary value problem can be further verified by examining the solution to ensure that both of the prescribed boundary conditions are satisfied along each of the four edges. In fact, this verification test has been carried out and all boundary conditions are found to have been satisfied.

5 Discussion and Conclusions

The superposition method has been exploited to obtain a highly accurate and comprehensive solution for the free vi-

Downloaded 03 May 2010 to 171.66.16.245. Redistribution subject to ASME license or copyright; see http://www.asme.org/terms/Terms_Use.cfm

bration of rectangular plates resting on variable lateral elastic edge supports. Convergence is found to be rapid. Any elastic distribution may be prescribed along any edge. Concentrated lateral spring stiffness may be imposed through use of the Dirac function. Lateral elastic support with step discontinuities in stiffness distribution, a problem of current interest, may also be imposed.

Numerous verification tests have been performed. These involved verifying that correct solutions were obtained when problems related to certain subsections of the eigenvalue matrix were resolved. They also involved demonstrating, in numerous cases, that known correct eigenvalue limits were approached as the stiffnesses were permitted to approach their natural limits of zero and infinity.

It is shown that, insofar as only two basic building block solutions are utilized in the entire analysis, the computational procedure for generating the eigenvalue matrix is relatively simple. This appears to be the first comprehensive analytical solution for this general problem to appear in the literature.

Acknowledgment

The author is indebted to Dr. Isaac Elishakoff, Associate Director, Center for Applied Stochastics Research, Florida Atlantic University, for proposing the vibration study reported here.

References

Gorman, D. J., 1989, "A Comprehensive Study of the Free Vibration of Rectangular Plates Resting on Symmetrically Distributed Uniform Elastic Edge Support," ASME JOURNAL OF APPLIED MECHANICS, Vol. 56, pp. 893–899.

Gorman, D. J., 1990, "A General Solution for the Free Vibration of Rectangular Plates Resting on Uniform Elastic Edge Supports," *Journal of Sound and Vibration*, Vol. 139, No. 2, pp. 325–335.

Leissa, A. W., Laura, P. A. A., and Gutierrez, R., 1980, "Vibrations of Rectangular Plates with Nonuniform Elastic Edge Supports," ASME JOURNAL OF APPLIED MECHANICS, Vol. 47, pp. 891–895.

Downloaded 03 May 2010 to 171.66.16.245. Redistribution subject to ASME license or copyright; see http://www.asme.org/terms/Terms_Use.cfm

Transfer Function Formulation of Constrained Distributed Parameter Systems, Part I: Theory

C. A. Tan
Assistant Professor,
Assoc. Mem. ASME.

C. H. Chung
Graduate Research Assistant.

Department of Mechanical Engineering,
Wayne State University,
Detroit, MI 48202

Analysis of constrained distributed parameter systems by the transfer function formulation is presented. The methodology is suitable for symbolic computation coding. The distributed system is an assembly of distributed elements. A generalized displacement method (GDM) is developed to evaluate the free and forced responses of the system. It is shown that, while classical methods require the satisfaction of both the displacement and force boundary conditions at the subsystem interfaces, GDM only needs to impose generalized force constraints. The continuity of generalized displacements at the interfaces is embedded in the present formulation. Thus, computation efforts are greatly reduced, in particular, for systems with a large number of distributed subsystems. Eigenfunctions of constrained systems are obtained by solving a finite-dimensional eigenvalue problem governing the generalized coordinate vector. The formulation can be applied to damped and non-self-adjoint systems.

1 Introduction

The dynamic response of constrained distributed parameter systems are studied. Constrained dynamic systems refer to subsystems under pointwise and/or distributed constraints, and complex systems composed of subsystems coupled by geometric compatibility and force constraints applied at the subsystem interfaces. The dynamics of systems under pointwise constraints has been studied extensively; notably by Dowell (1971, 1972, 1979), Bergman and Nicholson (1985), Bergman and McFarland (1988); and Nicholson and Bergman (1986a, b). Examples of distributed constraints are found in several important applications such as the use of bearing forces in the vibration control of bands and tapes (Tan et al., 1990, 1993).

Interest in the study of constrained distributed systems was initiated by analyzes of periodic structures using finite difference, transfer matrix, and wave propagation methods (e.g., Lin, 1969; Mead, 1971; Miles, 1956). To date, most research efforts have concentrated on the dynamics of combined linear structures that are interconnected at discrete points and/or along lines. Dowell (1979), Grief and Chung (1975), and Kerstens (1981) applied the Lagrange multipliers method to impose the constraints through a discrete formulation. While this method is useful, it requires the knowledge of the normal modes of the unconstrained structures in the analysis. Moreover, their technique is not extended to systems composed of subsystems. Bergman and colleagues (1985, 1988), Nicholson and Bergman (1986a,b) combined Green's function and separation of variables techniques in their analyzes. However, the Green's functions they considered are primarily for undamped distributed systems with symmetric operators and no formulation was presented for gyroscopic systems. It is noted that the transfer matrix method is also not suitable for problems with nonseparable operators. A similar technique, the receptance method, has also been employed to study constrained systems (Soedel, 1981).

An approach to analyze a complex system is to partition it into subsystems by the component modes method (Hurty, 1960, 1965). A major difficulty of this method is that substructure modes are not easily obtained. Meirovitch and Hale (1981) proposed the substructure synthesis method in which the substructure motions are described by a set of admissible functions.

The transfer function of a distributed system is the Laplace transform of the Green's function with respect to time (Butkovskiy, 1983), which contains all information required to predict the system spectrum, the response of the system under any initial and external disturbances, and the stability. As shown by Yang and Tan (1992), it is advantageous to formulate the problems of interest by the transfer function method because it can be used for damped, non-self-adjoint problems without increasing computational complexity. Moreover, the stability of the constrained system (closed loop) can be established by examining the poles and zeros of the transfer function of the unconstrained system (open loop). Closed-form transfer functions are well known for second-order and fourth-order symmetric systems (Butkovskiy, 1982; Bergman and Hyatt,

Contributed by the Applied Mechanics Division of THE AMERICAN SOCIETY OF MECHANICAL ENGINEERS for presentation at the ASME Winter Annual Meeting, New Orleans, LA, Nov. 28–Dec. 3, 1993.

Discussion on this paper should be addressed to the Technical Editor, Professor Lewis T. Wheeler, Department of Mechanical Engineering, University of Houston, Houston, TX 77204-4792, and will be accepted until four months after final publication of the paper itself in the ASME JOURNAL OF APPLIED MECHANICS.

Manuscript received by the ASME Applied Mechanics Division, Apr. 17, 1992; final revision, Mar. 10, 1993. Associate Technical Editor: D. J. Inman.

Paper No. 93-WA/APM-11.

Copyright © 1993 by ASME
Downloaded 03 May 2010 to 171.66.16.245. Redistribution subject to ASME license or copyright; see http://www.asme.org/terms/Terms_Use.cfm

1989). Recently Yang and Tan (1992) developed a technique to evaluate transfer functions for general one-dimensional distributed parameter systems. Closed-form transfer functions are more useful than classical eigenfunction expansions (Laurent series of transfer functions). For example, the expansion series requires a knowledge of the exact eigensolutions and converges slowly for second-order systems. Moreover, series truncation can lead to spill-over instability in the active control of distributed systems. The transfer function approach bypasses these problems.

The dynamics of the basic distributed subsystem (element) is first described in Section 2. A systematic formulation for the analysis of one-dimensional distributed parameter systems under pointwise constraints or having many subsystems is then presented in the frequency domain. The formulation leads to the generalized displacement method (GDM) for determining eigensolutions of the constrained system, and algorithms that are suitable for symbolic and numeric computations. Applications of this formulation are demonstrated in Part II of this paper (Chung and Tan, 1993).

2 Analysis of the Basic Distributed Subsystem

The response $w(x, t)$ of the basic distributed parameter subsystem is governed by the nth order linear partial differential equation

$$L[w(x, t)] = \left[A_2 \frac{\partial^2}{\partial t^2} + A_1 \frac{\partial}{\partial t} + A_0 \right] w(x, t) = f_e(x, t), \quad x \in (a, b), \quad t > 0, \quad (1)$$

with inhomogeneous boundary conditions

$$M_j[w(a, t)] + N_j[w(b, t)] = \gamma_{Bj}(t), \quad t \geq 0, \quad j = 1, 2, \ldots, n. \quad (2)$$

Here $f_e(x, t)$ is the external excitation force. A_i are spatial differential operators of the form

$$A_i = \sum_{k=0}^{n} A_{ik} \frac{\partial^k}{\partial x^k}, \quad i = 0, 1, 2, \quad (3)$$

where A_{ik} are constants, and $\Sigma_{i=0}^{2} |A_{in}|^2 \neq 0$. M_j and N_j are temporal-spatial, linear differential operators of proper order, and $\gamma_{Bj}(t)$ describe the inhomogeneous boundary conditions, e.g., due to an end moment or a transverse motion applied to a flexible structure. The initial conditions are

$$w(x, t = 0) = w_0(x), \quad w_{,t}(x, t = 0) = v_0(x). \quad (4)$$

Assume the initial boundary value problem (1–4) is well posed and admits a unique solution.

Equation (1), which may be of hyperbolic, parabolic, elliptic, or mixed type, describes the dynamics of many important physical processes such as diffusion, heat conduction, vibration, and wave propagation. For example, in describing the vibration of a continuum, (1) is an hyperbolic equation. The operator $A_2 \partial^2/\partial t^2$ is associated with the inertia of the continuum, $A_1 \partial/\partial t$ results from material viscous damping ($\partial/\partial t$ term) and/or Coriolis acceleration ($\partial^2/\partial x\, \partial t$ term), and A_0 is related to stiffness, centrifugal, and circulatory forces. For the heat diffusion problem, (1) is a parabolic equation. The operator $A_2 = 0$ and A_0 describes the normal flow of heat flux.

The response of (1) subjected to (2), (4) is obtained in the Laplace domain. First transform the global coordinate x to a local coordinate $z = (x - a)/(b - a)$. Equation (1) becomes

$$L[w(z, t)] = \left[a_2 \frac{\partial^2}{\partial t^2} + a_1 \frac{\partial}{\partial t} + a_0 \right] w(z, t) = f_e(z, t), \quad z \in (0, 1), \quad t > 0, \quad (5)$$

where a_i are spatial operators in z of the form of (3). The Laplace transform of (5) and (2) gives

$$[s^2 a_2 + s a_1 + a_0] \bar{w}(z, s) = \bar{f}_{el}(z, s), \quad (6a)$$

$$\bar{f}_{el}(z, s) \equiv \bar{f}_e(z, s) + (s a_2 + a_1) w_0(z) + a_2 v_0(z), \quad (6b)$$

$$\bar{M}_j[\bar{w}(0, s)] + \bar{N}_j[\bar{w}(1, s)] = \bar{\gamma}_j(s) \equiv \bar{\gamma}_{Bj}(s) + \bar{\gamma}_{Ij}(s), \quad j = 1, 2, \ldots, n, \quad (7)$$

where $\bar{M}_j$ and $\bar{N}_j$ are M_j and N_j with $\partial/\partial t$ and $\partial^2/\partial t^2$ replaced by s and s^2, respectively, and $\partial^k/\partial x^k$ replaced by $(\partial^k/\partial z^k)/(b - a)^k$. $\bar{\gamma}_{Ij}(s)$ is a polynomial function representing the initial conditions at the boundaries $z = 0$ and 1. Symbolically, the solution of (6a) and (7) is (Roach, 1981)

$$\bar{w}(z, s) = \int_0^1 G_0(z, \xi, s) \bar{f}_{el}(\xi, s) d\xi + h_1(z, s) \gamma(s), \quad (8a)$$

$$h_1^T(z, s) \in C^n, \quad \gamma(s) = \{\bar{\gamma}_1(s)\ \bar{\gamma}_2(s) \ldots \bar{\gamma}_n(s)\}^T \in C^n, \quad (8b)$$

where $G_0(z, \xi, s)$ is the transfer function of the distributed parameter subsystem, and the boundary transfer function $h_1(z, s)$ represents the influence of the inhomogeneous boundary conditions on the system response. $G_0(z, \xi, s)$ for second-order and fourth-order symmetric systems are well known. For general distributed systems, detailed derivations of $G_0(z, \xi, s)$ and $h_1(z, s)$ are given by Yang and Tan (1992). Cast (6a) and (7) into a state space form

$$\frac{\partial}{\partial x} \eta(z, s) = F(s) \eta(z, s) + q(z, s), \quad z \in (0, 1), \quad (9a)$$

$$M(s) \eta(0, s) + N(s) \eta(1, s) = \gamma(s), \quad (9b)$$

where

$$\eta(z, s) = \left\{ \bar{w}(z, s)\ \frac{\partial}{\partial z} \bar{w}(z, s) \ldots \frac{\partial^{n-1}}{\partial z^{n-1}} \bar{w}(z, s) \right\}^T \in C^n, \quad (9c)$$

and $M(s)$ and $N(s)$ are n by n complex matrices composed of the differential operators $\bar{M}_j$ and $\bar{N}_j$. Define the generalized displacement and force vectors of a distributed parameter subsystem as

$$\eta_d(z, s) = \left\{ \bar{w}(z, s)\ \frac{\partial}{\partial z} \bar{w}(z, s) \ldots \frac{\partial^{\frac{n}{2}-1}}{\partial z^{\frac{n}{2}-1}} \bar{w}(z, s) \right\}^T \in C^{n/2}, \quad (10a)$$

$$\eta_f(z, s) = \left\{ \frac{\partial^{\frac{n}{2}}}{\partial z^{\frac{n}{2}}} \bar{w}(z, s) \ldots \frac{\partial^{n-1}}{\partial z^{n-1}} \bar{w}(z, s) \right\}^T \in C^{n/2}. \quad (10b)$$

The term "generalized" is consistent with the context of analytical mechanics. For example, when considering the response of an elastic beam, $n = 4$, η_d contains the transverse displacement and slope, and the elements of η_f have dimensions of moment and shear force divided by the flexural rigidity. For the heat diffusion problem, $n = 2$, η_d is the temperature and η_f is related to the heat flux. The solution to (9a,b) is

$$\eta(z, s) = \int_0^1 \Gamma(z, \xi, s) q(\xi, s) d\xi + H(z, s) \gamma(s), \quad z \in (0, 1), \quad (11a)$$

where the matrix transfer function $\Gamma(z, \xi, s)$ is

$$\Gamma(z, \xi, s) = \begin{cases} H(z, s) M(s) \Phi(-\xi, s), & \xi < z \\ -H(z, s) N(s) \Phi(1 - \xi, s), & \xi > z \end{cases}, \quad (11b)$$

and

$$H(z, s) = \Phi(z, s)[M(s) + N(s) \Phi(1, s)]^{-1} \equiv \Phi(z, s) P^{-1}(s). \quad (11c)$$

Downloaded 03 May 2010 to 171.66.16.245. Redistribution subject to ASME license or copyright; see http://www.asme.org/terms/Terms_Use.cfm

Here $\Phi(z, s) = e^{F(s)z}$ is the system fundamental matrix. Comparing (8*a*) and (11*a*), we have

$$G_0(z, \xi, s) = \frac{\Gamma_{1n}(z, \xi, s)}{s^2 a_{2n} + s a_{1n} + a_{0n}}, \tag{12}$$

where $\Gamma_{1n}(z, \xi, s)$ is the $(1, n)$ element of $\Gamma(z, \xi, s)$, and $h_1(z, s)$ is the first row of $H(z, s)$. Note that the coordinate transformation simplifies the computation of $P(s)$; $M(s)\Phi(a, s) \rightarrow M(s)$, where we have used the property $\Phi(0, s) = \mathrm{I}$. The derivatives of $\overline{w}(z, s)$ are

$$\frac{\partial^k}{\partial x^k}\overline{w}(z, s) = \int_0^1 G_k(z, \xi, s)\bar{f}_{el}(\xi, s)d\xi + h_{k+1}(z, s)\gamma(s), \tag{13a}$$

where

$$G_k(z, \xi, s) = \frac{\Gamma_{(k+1)n}(z, \xi, s)}{s^2 a_{2n} + s a_{1n} + a_{0n}}, \quad k = 1, \ldots, n-1. \tag{13b}$$

Combining (8*a*), (12), and (13*a*, *b*), define

$$\begin{Bmatrix} \eta_d(z, s) \\ \eta_f(z, s) \end{Bmatrix} = \int_0^1 \begin{Bmatrix} G_d(z, \xi, s) \\ G_f(z, \xi, s) \end{Bmatrix} \bar{f}_{el}(\xi, s)d\xi + \begin{bmatrix} H_d(z, s) \\ H_f(z, s) \end{bmatrix}\gamma(s). \tag{14}$$

Equations (8*a*), (11*a–c*), and (12) give the formal, closed-form response solution of the distributed parameter subsystem. The method presented is exact; no truncation or approximation is involved. An algorithm can be constructed to evaluate $G_0(z, \xi, s)$ and $h_1(z, s)$, and hence the system response. A computational advantage of this formulation is that solution for a different problem requires only changes in $F(s)$, $M(s)$, $N(s)$, and $\gamma(s)$, but not in the algorithm. Also, the required calculations are relatively simple because $n \leq 4$ in general (e.g., vibration and wave propagation in elastic continua), and $M(s)$, $N(s)$ are sparse matrices. The formulation is also applicable to non-self-adjoint systems. For damped systems we only need to modify the state matrix $F(s)$, and the algorithm is again unchanged. The characteristic equation of the distributed parameter subsystem is given by the singular condition of $G_0(z, \xi, s)$ or $h_1(z, s)$

$$\det[P(s)] = \det[M(s) + N(s)\Phi(1, s)] = 0. \tag{15}$$

The roots of (15) are the eigenvalues (open loop poles); denoted by λ_i, $i = 1, 2, \ldots$.

Although (1) describes the dynamics of a uniformly distributed subsystem, this analysis is also applicable to nonuniformly distributed systems. In (3), A_{ik} becomes $A_{ik}(x)$. The characteristic equation is again given by (15). However, the evaluation of $\Phi(z, s)$ is generally difficult for nonuniformly distributed systems. For uniformly distributed systems, a simple algorithm for evaluating $e^{F(s)z}$ using the diagonalization approach was developed (Yang and Tan, 1992).

Consider the excitation force and inhomogeneous boundary conditions given by

$$f_e(z, t) = \sum_k f_k(z)e^{i\omega_k t}, \quad \gamma_j(t) = \sum_k \gamma_{jk}e^{i\Omega_k t}, \tag{16}$$

where $\bar{\gamma}_j(s)$ is the Laplace transform of $\gamma_j(t)$; see (7). From (8*a*), the response $w(z, t)$ is obtained using the inversion formula

$$w(z, t) = \sum_k \int_0^1 G_0(z, \xi, i\omega_k)f_k(\xi)d\xi e^{i\omega_k t} + \sum_k \sum_{j=1}^n H_{1j}(z, i\Omega_k)\gamma_{jk}e^{i\Omega_k t} + \sum_{i=1}^\infty \operatorname*{Res}_{s=\lambda_i}\left[\int_0^1 G_0(z, \xi, s)\bar{f}_{el}(\xi, s)d\xi\right]e^{\lambda_i t} + \sum_{i=1}^\infty \sum_{j=1}^n \operatorname*{Res}_{s=\lambda_i}[H_{1j}(z, s)\bar{\gamma}_j(s)]e^{\lambda_i t}, \tag{17a}$$

where Res denotes the residue and $H_{1j}(z, s)$ is the $(1, j)$ element of $H(z, s)$. If the homogeneous system is asymptotically stable, the steady-state solution is

$$w_{ss}(z, t) = \sum_k \int_0^1 G_0(z, \xi, i\omega_k)f_k(\xi)d\xi e^{i\omega_k t} + \sum_k \sum_{j=1}^n H_{1j}(z, i\Omega_k)\gamma_{jk}e^{i\Omega_k t}. \tag{17b}$$

Hence the transfer function formulation leads to a simple and compact closed-form expression for $w_{ss}(z, t)$. The third and fourth terms on the right-hand side of (17*a*) represent the transient solution. When the homogeneous system is just stable, all terms in (17*a*) persist indefinitely as $t \rightarrow \infty$. The resonance conditions due to excitation forces and boundary excitations are $G_0(z, \xi, i\omega_k) \rightarrow \infty$ and $H_{1j}(z, i\Omega_k) \rightarrow \infty$, respectively. The response solution may also be expressed in the convolution form in terms of the Green's function

$$w(z, t) = \int_0^1 \int_0^t g_0(z, \xi, t-\tau)f_e(\xi, \tau)d\tau d\xi + \int_0^1 g_0(z, \xi, t)[a_1(w_0(\xi)) + a_2(v_0(\xi))]d\xi + \int_0^1 \frac{dg_0(z, \xi, t)}{dt}a_2(w_0(\xi))d\xi + \sum_{j=1}^n \int_0^t h_{1j}(z, t-\tau)\gamma_j(\tau)d\tau, \tag{18}$$

where $g_0(z, \xi, t)$ and $h_{1j}(z, t)$ are the inverse transform of $G_0(z, \xi, s)$ and $H_{1j}(z, s)$, respectively. However, identification of $w_{ss}(z, t)$ is not so straightforward using (18) (Hsu and Cheng, 1974). While the present formulation does not offer a more efficient approach in the evaluation of the transient solution compared with classical methods such as the modal truncation method, (17*a*) and (18) are valid for both the proportionally and nonproportionally damped subsystems.

3 Subsystems Under Pointwise Constraints

Consider a distributed parameter subsystem constrained at m discrete points. Bergman and colleagues (1985, 1988) and Yang (1992) have studied similar combined dynamic systems.

$$L[w(z, t)] = f_e(z, t) + f_c(z, t), \; z \in (0, 1), \; t > 0, \tag{19}$$

and appropriate boundary conditions are assumed. Here $f_c(z, t)$ is the sum of all constraint forces. From (8*a*), the response of the subsystem is

$$\overline{w}(z, s) = \int_0^1 G_0(z, \xi, s)(\bar{f}_{el}(\xi, s) + \bar{f}_c(\xi, s))d\xi + h_1(z, s)\gamma(s). \tag{20}$$

The constraint force is expressed in terms of the generalized displacements

$$\bar{f}_c(z, s) = \sum_{i=1}^m \beta_i^T(z, s)\eta_{rd}^{(i)}(s), \tag{21}$$

where $\eta_{rd}^{(i)}(s)$ and $\beta_i(z, s)$ are the reduced generalized displacement and stiffness vectors at the ith constraint location z_i. Consider the beam vibration example ($n = 4$), then

$$\beta_i^T(z, s) = \{-k_i\delta(z - z_i)\}, \quad \eta_{rd}^{(i)}(s) = \{\overline{w}(z_i, s)\}, \tag{22a}$$

Downloaded 03 May 2010 to 171.66.16.245. Redistribution subject to ASME license or copyright; see http://www.asme.org/terms/Terms_Use.cfm

if a linear spring of stiffness k_i constrains the displacement at z_i, and

$$\beta_i^T(z, s) = \{ -c_i s\delta(z-z_i) \quad -k_{\theta_i}\delta'(z-z_i) \},$$

$$\{\eta_{rd}^{(i)}(s)\}^T = \{\overline{w}(z_i, s)\ \overline{w}_{,z}(z_i, s)\}, \quad (22b)$$

if the displacement and slope are constrained by a damper and a torsional spring at z_i, respectively. The formulation is also suitable for structures that are supported at discrete points. For example, if a structure is simply supported at z_i with displacement constraint $w(z_i, t) = 0$, then β_i is given by (22*a*) with k_i approaches infinity. While Dowell (1971) considered only holonomic displacement constraints, (21) represents constraints on generalized forces and displacements. For combined dynamical systems such as a lumped spring-mass system attached to a distributed subsystem at z_i,

$$\beta_i = \left\{ -\frac{k_i s^2}{s^2+\Omega^2}\,\delta(z-z_i) \right\};\ \Omega^2 = \sqrt{\frac{k_i}{m_i}}. \quad (23)$$

The constraint forces (21) are viewed as feedback control forces. In the foregoing examples, the control forces are locally applied at z_i. For problems such as robot manipulators (Sakawa and Luo, 1989) where the control force effect is distributed, $\beta_i(z, s)$ is represented by functions other than $\delta(z)$.

Substitution of (21) into (20) gives

$$\overline{w}(x, s) = \int_0^1 [G_0(z, \xi, s) b_0^T(z, \xi, s)] \begin{Bmatrix} \bar{f}_{el}(\xi, s) \\ \overline{w}_d(s) \end{Bmatrix} d\xi + h_1(z, s)\gamma(s), \quad (24)$$

where

$$\overline{w}_d^T(s) = \{ (\eta_{rd}^{(1)}(s))^T \ \dots\ (\eta_{rd}^{(m)}(s))^T \},\ \overline{w}_d \in C^p, \quad (25a)$$

$$b_0^T(z, \xi, s) = \{ G_0(z, \xi, s)\beta_1^T(\xi, s) \ \dots\ G_0(z, \xi, s)\beta_m^T(\xi, s) \}. \quad (25b)$$

The p-dimensional generalized coordinate vector $\overline{w}_d(s)$ is an array of the reduced generalized displacement vectors. From (14) and (24), the solutions for the elements of $\overline{w}_d(s)$ are obtained by letting $z = z_i$

$$\eta_{rd}^{(i)}(s) = \int_0^1 [G_{rd}(z_i, \xi, s)\ b_{rd}^T(z_i, \xi, s)] \begin{Bmatrix} \bar{f}_{el}(\xi, s) \\ \overline{w}_d(s) \end{Bmatrix} d\xi + H_{rd}(z_i, s)\gamma(s), \quad (26)$$

where

$$b_{rd}^T(z_i, \xi, s) = \{ G_{rd}(z_i, \xi, s)\beta_1^T(\xi, s) \ \dots\ G_{rd}(z_i, \xi, s)\beta_m^T(\xi, s) \}, \quad (27)$$

and $G_{rd}(z_i, \xi, s)$, $H_{rd}(z_i, s)$ are the appropriate reduced forms of $G_d(z_i, \xi, s)$ and $H_d(z_i, s)$ defined in (14). From (26), the solution for $\overline{w}_d(s)$ is

$$\overline{w}_d(s) = \int_0^1 \begin{bmatrix} G_{rd}(z_1, \xi, s) & b_{rd}^T(z_1, \xi, s) \\ \vdots & \vdots \\ G_{rd}(z_m, \xi, s) & b_{rd}^T(z_m, \xi, s) \end{bmatrix} \begin{Bmatrix} \bar{f}_{el}(\xi, s) \\ \overline{w}_d(s) \end{Bmatrix} d\xi + \begin{bmatrix} H_{rd}(z_1, s) \\ \vdots \\ H_{rd}(z_m, s) \end{bmatrix} \gamma(s), \quad (28a)$$

or

$$\overline{w}_d(s) = A(s)\overline{w}_d(s) + \int_0^1 C_1(\xi, s)\bar{f}_{el}(\xi, s)d\xi + C_2(s)\gamma(s);\ C_1 \in C^p,\ C_2 \in C^{p\times n}. \quad (28b)$$

For free-vibration analysis, consider the homogeneous problem with $\bar{f}_{el}(z, s) = 0$ and $\gamma(s) = 0$.

$$\overline{w}_d(s) = A(s)\overline{w}_d(s), \quad A(s) \in C^{p\times p} \quad (29)$$

For nontrivial solution of (29), it is required that

$$\det[\mathrm{I} - A(s)] = 0. \quad (30)$$

The foregoing equation is the characteristic equation of the constrained subsystem (closed loop), and the closed-loop eigenvalues s_k are the roots of (30) or $s_k = \lambda_k$ for some k if (i) the constraints have zeros cancelling λ_k, (ii) the constraints are applied at the nodal points of the kth mode of the unconstrained system (see Appendix A). These two conditions are related to the controllability of distributed parameter systems by pointwise constraints (Yang and Mote, 1991) in which the constraints do not change the open loop poles λ_k.

Consider the case of one constraint on the displacement applied at $z = z_1$. Let

$$\bar{f}_c(z, s) = -k_1 \frac{N(s)}{D(s)}\,\delta(z-z_1)\overline{w}(z_1, s). \quad (31)$$

From Appendix B, the characteristic equation is

$$D(s) + k_1 N(s) G_0(z_1, z_1, s) = 0. \quad (32)$$

The closed-loop poles are the roots of

$$D_0(s)D(s) + k_1 N(s) N_0(z_1, z_1, s) = 0;$$

$$G_0(z, \xi, s) = \frac{N_0(z, \xi, s)}{D_0(s)}, \quad (33)$$

or $D_0(s) = 0$ if for some k, $N(\lambda_k) = 0$ (pole-zero cancellation) or $N_0(z_1, z_1, \lambda_k) = 0$ (z_1 is a nodal point for the kth unconstrained mode). Moreover, (32) shows that the open-loop poles are the closed-loop poles when $k \to \infty$. This idea is used to obtain the eigenvalues of a simply supported beam from those of the unconstrained free-free beam; see Part II of this paper. Note that for a subsystem constrained by m linear springs, the general structure of $A(s)$ is

$$[A(s)]_{ij} = -k_i(s) G_0(z_i, z_j, s). \quad (34)$$

For systems in which $G_0(z_i, z_j, s)$ are separable (e.g., beams), the determinant and the inverse of (I—$A(s)$) can easily be obtained using the matrix inversion lemma (Astrom and Wittenmark, 1984); see Appendix C. This computational advantage has not been observed before.

The eigenfunctions of the constrained system are obtained in the following manner. Consider the jth eigenvalue s_j and the eigenvalue problem (29). Let w_{dj} be the eigenvector

$$[\mathrm{I} — A(s_j)]w_{dj} = 0. \quad (35)$$

From (24), the eigenfunction of the constrained distributed parameter system is then given by

$$w_j(z) = b_0^T(z, s_j)w_{dj}. \quad (36)$$

The idea of GDM is clear from (35) and (36). Once the eigenvector w_{dj} is obtained, i.e., the relative displacements between $\eta_{rd}^{(i)}(s_j)$ and $\eta_{rd}^{(l)}(s_j)$, $i \neq l$, $i, l = 1, \dots, m$, are known, then there exists only one function $w_j(z)$ that would interpolate w_{dj} and satisfy the equation of motion and the homogeneous boundary conditions simultaneously. This function must be the eigenfunction corresponding to the eigenvalue s_j. The concept is graphically shown in Fig. 1.

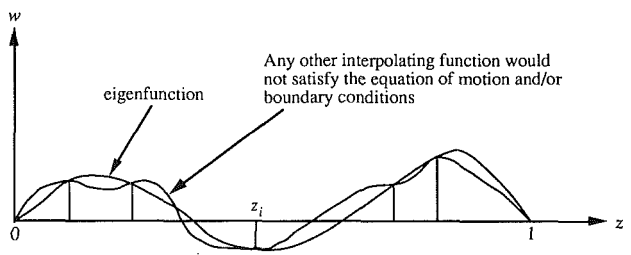


Fig. 1 Graphical illustration of the GDM idea to determine the eigenfunctions of a constrained distributed parameter dynamic system

Downloaded 03 May 2010 to 171.66.16.245. Redistribution subject to ASME license or copyright; see http://www.asme.org/terms/Terms_Use.cfm

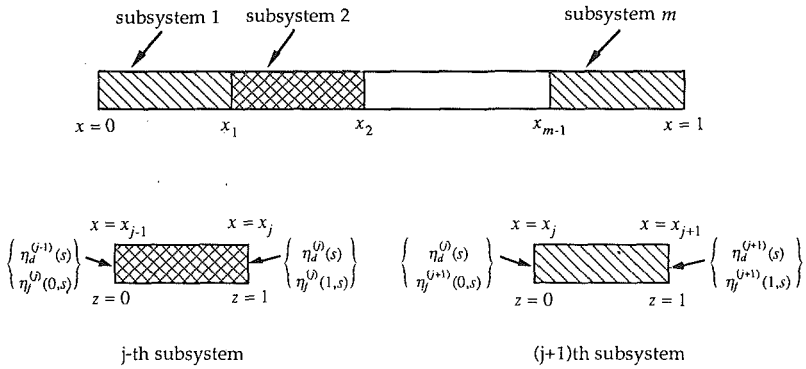


Fig. 2 Description of a distributed parameter system consisting of m subsystems

The present approach provides a systematic and straightforward computation algorithm for the direct evaluation of the eigenfunctions. As a corollary, we can apply this idea to determine the eigenfunctions of the unconstrained system. For example, constrain the subsystem by a linear spring at z_1. Then the open-loop eigenfunction is the closed-loop eigenfunction as k approaches zero. In this case, the generalized displacement at z_1 may be viewed as a *pseudo*-generalized displacement. An example is illustrated in Part II to demonstrate this idea. From (28*b*), $\overline{w}_d(s)$ can be obtained in terms of the external force, initial conditions, and inhomogeneous boundary conditions. Substitute this result into (24) yields the response solution of the constrained system. Note that this procedure also produces the closed-loop system and boundary transfer functions which determine the dynamic characteristics of the constrained system. The system response in the time domain can be obtained in a similar manner as (17*a*) or (18).

4 Formulation of Multiple Subsystems

Consider a system consisting of m distributed parameter subsystems. Assume that each subsystem is unconstrained. The analysis of multiple constrained subsystems can be done by combining the theories presented in this and the previous sections. The purpose here is to show how to impose the boundary conditions at the interface between two adjacent subsystems by applying the concept of GDM.

In Fig. 2, each subsystem is connected to the adjacent ones at its ends. There are $(m-1)$ sets of constraint conditions and two sets of physical boundary conditions at $x = 0, 1$ that must be satisfied simultaneously. Note that the generalized displacement and force vectors are unknown at each interface and their effects on the response of each subsystem are treated as inhomogeneous boundary conditions. Since the generalized displacement vector is *continuous* at each interface boundary, then only the generalized force constraints need to be considered if one chooses

$$\gamma^{(i)}(s) = \begin{Bmatrix} \eta_d^{(i-1)}(s) \\ \eta_d^{(i)}(s) \end{Bmatrix}, \quad \eta_d^{(i)}(s) = \eta_d(x_i, s), \quad i = 2, \ldots, m-1, \tag{37}$$

where $\gamma^{(i)}(s)$ describes the inhomogeneous boundary conditions for the ith subsystem. For $i = 1$ and m, the physical boundary conditions must be included. Let

$$\gamma^{(1)}(s) = \begin{Bmatrix} \gamma_0(s) \\ \eta_d^{(1)}(s) \end{Bmatrix}, \qquad \gamma^{(m)}(s) = \begin{Bmatrix} \eta_d^{(m-1)}(s) \\ \gamma_1(s) \end{Bmatrix}, \ \gamma_0(s), \gamma_1(s) \in C^{n/2}, \tag{38}$$

where $\gamma_0(s)$ and $\gamma_1(s)$ describe the inhomogeneous boundary conditions at $x = 0$ and 1. Define the local coordinate for the ith subsystem

$$z = \frac{x - x_{i-1}}{x_i - x_{i-1}} = \frac{x - x_{i-1}}{d_i}, \ i = 1, \ldots, m, \ x \in [x_{i-1}, x_i], \tag{39}$$

where $x_0 = 0$ and $x_m = 1$. The state vector is expressed in terms of the local coordinate

$$\{\eta^{(i)}(x, s)\} = \begin{Bmatrix} \eta_d^{(i)}(x, s) \\ \eta_f^{(i)}(x, s) \end{Bmatrix} = \begin{Bmatrix} J_d^{(i)} \eta_d^{(i)}(z, s) \\ J_f^{(i)} \eta_f^{(i)}(z, s) \end{Bmatrix}, \tag{40}$$

where $J_d^{(i)}$, $J_f^{(i)}$ are coordinate transformation factors. The corresponding governing equations of motion for each subsystem with state matrices $F^{(i)}(s)$ are given by (9*a*). The transfer function for each subsystem $G_0^{(i)}(z, \xi, s)$ is defined by (12). From (14), the response is

$$\begin{Bmatrix} \eta_d^{(i)}(z, s) \\ \eta_f^{(i)}(z, s) \end{Bmatrix} = \int_0^1 \begin{Bmatrix} G_d^{(i)}(z, \xi, s) \\ G_f^{(i)}(z, \xi, s) \end{Bmatrix} \bar{f}_{el}(\xi, s) d\xi + \begin{bmatrix} H_d^{(i)}(z, s) \\ H_f^{(i)}(z, s) \end{bmatrix} \gamma^{(i)}(s), \ i = 1, \ldots, m. \tag{41}$$

For free-vibration analysis, $\bar{f}_{el} = 0$. Then (37) and (41) give

$$\begin{Bmatrix} \eta_d^{(i)}(z, s) \\ \eta_f^{(i)}(z, s) \end{Bmatrix} = \begin{bmatrix} H_d^{(i)}(z, s) \\ H_f^{(i)}(z, s) \end{bmatrix} \begin{Bmatrix} \eta_d^{(i-1)}(s) \\ \eta_d^{(i)}(s) \end{Bmatrix}. \tag{42}$$

Apply the force constraint conditions at $x = x_i$ which can be written as

$$\hat{Q}_2^{(i)}(s)\eta_f^{(i)}(x_i, s) + \hat{Q}_1^{(i+1)}(s)\eta_f^{(i+1)}(x_i, s) = \beta^{(i)}(s)\eta_d^{(i)}(s); \qquad \beta^{(i)}, \hat{Q}_2^{(i)}, \hat{Q}_1^{(i+1)} \in C^{n/2 \times n/2}, \tag{43}$$

where $\hat{Q}_2^{(i)}$ and $\hat{Q}_1^{(i+1)}$ are constraint operators and $\beta^{(i)}$ is a generalized stiffness operator. These matrices are known and are determined from the generalized force boundary conditions imposed at the interface x_i. Applying (40), (43) is expressed in terms of the local coordinate in the form

$$Q_2^{(i)}(s)\eta_f^{(i)}(z=1, s) + Q_1^{(i+1)}(s)\eta_f^{(i+1)}(z=0, s) = \beta^{(i)}(s)\eta_d^{(i)}(s); \quad Q_k^{(i)}(s) = J_f^{(i)}\hat{Q}_k^{(i)}(s). \tag{44}$$

From (42), (44) we obtain

$$\left(Q_2^{(i)}(s) \begin{bmatrix} H_f^{(i)}(1, s) \\ 0 \end{bmatrix} + Q_1^{(i+1)}(s) \begin{bmatrix} 0 \\ H_f^{(i+1)}(0, s) \end{bmatrix} - \begin{bmatrix} 0 \\ \beta^{(i)}(s) \\ 0 \end{bmatrix} \right) \begin{Bmatrix} \eta_d^{(i-1)}(s) \\ \eta_d^{(i)}(s) \\ \eta_d^{(i+1)}(s) \end{Bmatrix} = 0, \tag{45a}$$

Downloaded 03 May 2010 to 171.66.16.245. Redistribution subject to ASME license or copyright; see http://www.asme.org/terms/Terms_Use.cfm

$$\Rightarrow [T^{(i)}(s)] \begin{Bmatrix} \eta_d^{(i-1)}(s) \\ \eta_d^{(i)}(s) \\ \eta_d^{(i+1)}(s) \end{Bmatrix} = 0,\ i = 1, \ldots, m-1. \quad (45b)$$

Summing the above equation over the $(m - 1)$ interfaces to get

$$\sum_{i=1}^{m-1} [T_{(s)}^{(i)}] \begin{Bmatrix} \eta_d^{(i-1)}(s) \\ \eta_d^{(i)}(s) \\ \eta_d^{(i+1)}(s) \end{Bmatrix} = 0 \Rightarrow [T(s)] \begin{Bmatrix} \gamma_0(s) \\ \overline{w}_d(s) \\ \gamma_1(s) \end{Bmatrix} = 0, \quad (46a)$$

where

$$\overline{w}_d^T(s) = \{ (\eta_d^{(1)}(s))^T \ldots (\eta_d^{(m-1)}(s))^T \}, \quad (46b)$$

is an array of the $(m - 1)$ generalized displacement vectors at the interfaces. For the free-vibration problem, we also need to set $\gamma_0(s) = 0$ and $\gamma_1(s) = 0$. Then (46*a*) gives

$$[T_c(s)]\overline{w}_d(s) = 0. \quad (47)$$

The characteristic equation of the constrained distributed parameter system is

$$\det[T_c(s)] = 0. \quad (48)$$

Note that the dimension of $T_c(s)$ is at most $(m - 1)n/2$. Classical methods impose all the generalized displacement and force boundary conditions at the interfaces and the boundaries, and hence the characteristic equation requires the evaluation of the determinant of a $mn \times mn$ matrix. Thus, the GDM reduces the number of algebraic constraint equations in (47). This is advantageous for dynamic systems with a large number of subsystems.

This formulation is also useful for supported structures. Consider a beam-type structure which is simply supported at r locations. The system thus has $(r + 1)$ subsystems (spans) of which the geometric and material properties may differ from one subsystem to another. Since $w(x_i, t) = 0$, $i = 1, \ldots, r$, only the slopes at x_i need to be included in $\overline{w}_d(s)$ in (46*b*). The dimension of $T_c(s)$ is thus r. Moreover, $T_c(s)$ is a tri-diagonal matrix (Tan and Chung, 1992). In the paper by Bergman and McFarland (1988), the response of a four-span beam was studied. However, their technique is not applicable when the spans have different geometric and/or material properties. Moreover, the matrix whose vanishing determinant gives the characteristic equation is a full matrix.

The eigenfunctions of the distributed parameter system are obtained in a similar manner as discussed in the previous section. From (47), for $s = s_j$, the eigenvector of (47) is first determined

$$w_d^T(s_j) = \{ (\eta_d^{(1)}(s_j))^T \ldots (\eta_d^{(m-1)}(s_j))^T \}. \quad (49)$$

From (8*a*) and (42), the jth eigenfunction for $x \in [x_{i-1}, x_i]$ is

$$w(x, s_j) = [h_1^{(i)}(z, s_j)]\gamma^{(i)}(s_j),\ i = 1, \ldots, m, \quad (50)$$

with $\gamma_0(s)$ and $\gamma_1(s)$ set to zero at the boundaries $x = 0$ and 1, respectively. Note that GDM requires no integration to obtain the eigenfunctions, and only algebraic equations are involved.

As an illustrating example, consider a string translating across a uniform, elastic foundation that stretches from $x = x_1$ to $x = 1$. A point spring with stiffness $\hat{k}$ is also attached at x_1. The system is non-self-adjoint with equations of motion

$$\left[\frac{\partial^2}{\partial t^2} + 2c\frac{\partial^2}{\partial x \partial t} + (c^2 - 1)\frac{\partial^2}{\partial x^2}\right] w(x, t) = f_e(x, t),\ x \in (0, x_1), \quad (51a)$$

$$\left[\frac{\partial^2}{\partial t^2} + 2c\frac{\partial^2}{\partial x \partial t} + (c^2 - 1)\frac{\partial^2}{\partial x^2} + k\right] w(x, t) = f_e(x, t),\ x \in (x_1, 1), \quad (51b)$$

where c is the translation speed and k is the foundation stiffness. There are two subsystems for this problem. Assume fixed-fixed boundary conditions. Then

$$\gamma^{(1)}(s) = \begin{Bmatrix} 0 \\ \overline{w}(x_1, s) \end{Bmatrix},\ \gamma^{(2)}(s) = \begin{Bmatrix} \overline{w}(x_1, s) \\ 0 \end{Bmatrix}. \quad (52)$$

The constraint on generalized forces at $x = x_1$ is

$$(1 - c^2)[-\overline{w}_{,x}(x_1^-, s) + \overline{w}_{,x}(x_1^+, s)] - \hat{k}\overline{w}(x_1, s) = 0. \quad (53)$$

Applying (43)–(47), the (one-by-one) matrix $T_c(s)$ is easily obtained:

$$T_c(s) = -\hat{k} - \frac{1 - c^2}{x_1} H_{22}^{(1)}(1, s) + \frac{1 - c^2}{1 - x_1} H_{21}^{(2)}(0, s). \quad (54)$$

Evaluating the boundary transfer functions in (54) gives

$$T_c(s) = -\hat{k} - s\coth(a) - r\coth(b), \quad (55a)$$

where

$$a = \frac{sx_1}{1 - c^2},\ b = \frac{r(1 - x_1)}{1 - c^2},\ r = \sqrt{s^2 + k(1 - c^2)}. \quad (55b)$$

Note that, as $\hat{k} \to \infty$, the characteristic equation yields two sets of eigenvalues corresponding to the natural frequencies of the *uncoupled* subsystems

$$\sinh(a) = 0 \Rightarrow \omega_n = \frac{n\pi(1 - c^2)}{x_1},\ n = 1, 2, \ldots, \quad (56a)$$

$$\sinh(b) = 0 \Rightarrow \omega_l = \sqrt{\frac{l^2\pi^2(1 - c^2)^2}{(1 - x_1)^2} + k(1 - c^2)},\ l = 1, 2, \ldots. \quad (56b)$$

Discussion of the dynamics of coupled distributed parameter systems is presented in Part II.

5 Discussion and Summary

The transfer function formulation of constrained distributed parameter systems is presented. The methodology can be applied to analyze the responses of complex dynamic systems composed of many subsystems. The subsystems are coupled by imposing suitable geometric compatibility and force constraint conditions at the interfaces. Comparing with the ideas of the finite element method (FEM), it is noted that each subsystem is a *distributed element* whose geometric and material properties are continuous functions in space and its dynamics in the local coordinate is described in Section 2.

Consider a free-free beam constrained by linear springs at its ends. The problem may be studied by three different approaches. First, the constrained beam is considered as one distributed subsystem with the spring constraints appearing in the boundary condition operators. Hence, the theory discussed in Section 2 is employed. Second, the spring forces can be treated as constraint forces (feedback forces) and the analysis of Section 3 is suitable for this formulation. Third, the constrained beam is treated as a fixed-constrained substructure with the undetermined generalized displacements at both ends being treated as inhomogeneous boundary terms. This is the GDM. Application of these approaches is discussed in Part II.

The methodology presented here leads to systematic, symbolic, and numeric computation algorithms. The solution for a different problem requires only changes in $F(s)$, $M(s)$, $N(s)$, and $\gamma(s)$, but not in the algorithm. It can also be used to study the dynamics of damped and non-self-adjoint systems and the effects of inhomogeneous boundary conditions on the system response. The eigenfunctions of the constrained system are obtained from solving a finite-dimensional eigenvalue problem governing the generalized coordinate vector. Using the GDM,

Downloaded 03 May 2010 to 171.66.16.245. Redistribution subject to ASME license or copyright; see http://www.asme.org/terms/Terms_Use.cfm

only algebraic equations are involved to obtain the eigenfunctions.

Acknowledgment

The authors gratefully acknowledge the partial support of the National Science Foundation and the American Natural Resources Pipeline Company for this research.

References

Astrom, K. J., and Wittenmark, B., 1984, *Computer Controlled Systems Theory and Design*, Prentice-Hall, Englewood Cliffs, N.J.

Bergman, L. A., and Nicholson, J. W., 1985, "Forced Vibration of a Damped Combined Linear System," ASME *Journal of Vibration, Acoustics, Stress, and Reliability in Design*, Vol. 107, pp. 275–281.

Bergman, L. A., and McFarland, D. M., 1988, "On the Vibration of a Point-Supported Linear Distributed System," ASME *Journal of Vibration, Acoustics, Stress, and Reliability in Design*, Vol. 110, pp. 485–492.

Bergman, L. A., and Hyatt, J. E., 1989, "Green Functions for Transversely Vibrating Uniform Euler-Bernoulli Beams Subject to Constant Axial Preload," *Journal of Sound and Vibration*, Vol. 134, No. 1, pp. 175–180.

Butkovskiy, A. G., 1982, *Green's Functions and Transfer Functions Handbook*, Halsted Press, New York.

Butkovskiy, A. G., 1983, *Structural Theory of Distributed Systems*, Ellis Horwood, New York.

Chung, C. H., and Tan, C. A., 1993, "Transfer Function Formulation of Constrained Distributed Parameter Systems, Part II: Applications," ASME JOURNAL OF APPLIED MECHANICS, Vol. 60.

Dowell, E. H., 1971, "Free Vibrations of a Linear Structure With Arbitrary Support Conditions," ASME JOURNAL OF APPLIED MECHANICS, Vol. 38, pp. 595–600.

Dowell, E. H., 1972, "Free Vibrations of an Arbitrary Structure in Terms of Component Modes," ASME JOURNAL OF APPLIED MECHANICS, Vol. 39, pp. 727–732.

Dowell, E. H., 1979, "On Some General Properties of Combined Dynamical Systems," ASME JOURNAL OF APPLIED MECHANICS, Vol. 46, pp. 206–209.

Grief, R., and Chung, H., 1975, "Vibrations of Constrained Cylindrical Shells," *AIAA Journal*, Vol. 13, pp. 1190–1198.

Hodges, C. H., 1982, "Confinement of Vibration by Structural Irregularity," *Journal of Sound and Vibration*, Vol. 82, No. 3, pp. 411–424.

Hsu, C. S., and Cheng, W. H., 1974, "Steady-State Response of a Dynamical System Under Combined Parametric and Forcing Excitations," ASME JOURNAL OF APPLIED MECHANICS, Vol. 41, pp. 371–378.

Hurty, W. C., 1960, "Vibrations of Structural Systems by Component Modes Synthesis," *ASCE Journal of Engineering Mechanics*, Aug., pp. 51–69.

Hurty, W. C., 1965, "Dynamic Analysis of Structural Systems Using Component Modes," *AIAA Journal*, Vol. 3, No. 4, Apr., pp. 678–685.

Kerstens, J. G. M., 1981, "Vibration of Complex Structures: The Modal Constraint Method," *Journal of Sound and Vibration*, Vol. 76, No. 4, pp. 467–480.

Lin, Y. K., and McDaniel, T. J., 1969, "Dynamics of Beam-Type Periodic Structures," ASME *Journal of Engineering for Industry*, pp. 1133–1141.

Mead, D. J., 1971, "Vibration Response and Wave Propagation in Periodic Structures," ASME *Journal of Engineering for Industry*, pp. 783–792.

Meirovitch, L., and Hale, A. L., 1981, "On the Substructure Synthesis Method," *AIAA Journal*, Vol. 19, No. 7, July, pp. 940–947.

Miles, J. W., 1956, "Vibrations of Beams on Many Supports," *ASCE Journal of Engineering Mechanics*, EM1, Jan., pp. 1–9.

Nicholson, J. W., and Bergman, L. A., 1986a, "Free Vibration of Combined Dynamical Systems," *ASCE Journal of Engineering Mechanics*, Vol. 112, pp. 1–13.

Nicholson, J. W., and Bergman, L. A., 1986b, "Vibration of Damped Plate-Oscillator Systems," *ASCE Journal of Engineering Mechanics*, Vol. 112, pp. 14–30.

Roach, G. F., 1981, *Green's Functions*, Cambridge University Press, Cambridge, U.K.

Sakawa, Y., and Luo, Z. H., 1989, "Modeling and Control of Coupled Bending and Torsional Vibrations of Flexible Beams," *IEEE Transactions on Automatic Control*, Vol. 34, No. 9, Sept., pp. 970–977.

Soedel, W., 1981, *Vibrations of Shells and Plates*, Marcel Dekker, New York.

Tan, C. A., and Chung, C. H., 1992, "A New Computation Algorithm for Analysis of Complex Distributed Parameter Systems," *AIAA 33rd Structures, Structural Dynamics, and Materials Conference*, AIAA Paper No. 92-2328, Dallas, TX.

Tan, C. A., Yang, B., and Mote, C. D., Jr., 1990, "On the Vibration of a Translating String Coupled to Hydrodynamic Bearings," ASME *Journal of Vibration and Acoustics*, Vol. 112, pp. 337–345.

Tan, C. A., Yang, B., and Mote, C. D., Jr., 1993, "Dynamic Response of an Axially Moving Beam Coupled to Hydrodynamic Bearings," ASME *Journal of Vibration and Acoustics*, Vol. 115, pp. 9–15.

Yang, B., and Mote, C. D., Jr., 1991, "Controllability and Observability of Distributed Gyroscopic Systems," ASME *Journal of Dynamic Systems, Measurement, and Control*, Vol. 113, No. 1, March, pp. 11–17.

Yang, B., and Tan, C. A., 1992, "Transfer Functions of One-Dimensional Distributed Parameter Systems," ASME JOURNAL OF APPLIED MECHANICS, Vol. 59, No. 4, pp. 1009–1014.

Yang, B., 1992, "Transfer Functions of Constrained/Combined One-Dimensional Continuous Dynamic Systems," *Journal of Sound and Vibration*, Vol. 156, No. 1, July, pp. 425–443.

APPENDIX A

Eigenvalues of Subsystems Under Pointwise Constraints

Denote

$$D_c(s) = \det[I - A(s)], \tag{A1}$$

and $\hat{B}(s)$ as the adjoint matrix of $I - A(s)$. From (20), the closed-loop system and boundary transfer functions $G_c(z, \xi, s)$ and $h_c(z, s)$ can be obtained as

$$G_c(z, \xi, s) = \frac{D_c(s)G_0(z, \xi, s) + \tilde{C}_1(z, \xi, s)}{D_c(s)}, \tag{A2}$$

and

$$h_c(z, s) = \frac{D_c(s)h_1(z, s) + \tilde{C}_2(z, s)}{D_c(s)}, \; h_c^T(z, s) \in C^n, \tag{A3}$$

where

$$\tilde{C}_1(z, \xi, s) = \left[\int_0^1 b_0^T(z, \sigma, s)d\sigma\right]\hat{B}(s)\begin{Bmatrix} G_{rd}(z_1, \xi, s) \\ \vdots \\ G_{rd}(z_m, \xi, s)\end{Bmatrix}, \tag{A4}$$

$$\tilde{C}_2(z, s) = \left[\int_0^1 b_0^T(z, \sigma, s)d\sigma\right]\hat{B}(s)\begin{bmatrix} H_{rd}(z_1, s) \\ \vdots \\ H_{rd}(z_m, s)\end{bmatrix}. \tag{A5}$$

(i) If $\int_0^1 b_0^T(z, \sigma, \lambda_k)d\sigma = 0$, then the constraints have zeros cancelling the kth eigenvalue λ_k of the unconstrained subsystem, and

$$G_c(z, \xi, \lambda_k) = G_0(z, \xi, \lambda_k) \text{ and } h_c(z, \lambda_k) = h_1(z, \lambda_k). \tag{A6}$$

Hence λ_k is a closed-loop pole.

(ii) Consider

$$\begin{Bmatrix} G_{rd}(z_1, \xi, s) \\ \vdots \\ G_{rd}(z_m, \xi, s)\end{Bmatrix} = \begin{bmatrix} H_{rd}(z_1, s) \\ \vdots \\ H_{rd}(z_m, s)\end{bmatrix} = 0. \tag{A7}$$

Again, λ_k is a closed-loop pole. Physically, (A7) says that there is no response at z_i, $i = 1, \ldots, m$ for any external force or boundary excitation. This is only possible if all of z_i are nodal points of the kth mode of the unconstrained system. Besides conditions (i) and (ii), the other closed-loop poles can only be the roots of $D_c(s) = 0$.

APPENDIX B

Derivation of (32)

The constraint force is given by (31). From (A1),

$$D_c(s) = 1 + k_1 \frac{N(s)}{D(s)} G_0(z_1, z_1, s) = 0. \tag{B1}$$

Downloaded 03 May 2010 to 171.66.16.245. Redistribution subject to ASME license or copyright; see http://www.asme.org/terms/Terms_Use.cfm

The closed-loop system and boundary transfer functions are

$$G_c(z, \xi, s) = \frac{D(s)G_0(z, \xi, s) - k_1N(s)[G_0(z, z_1, s)G_0(z_1, \xi, s) + G_0(z_1, z_1, s)G_0(z, \xi, s)]}{D(s) + k_1N(s)G_0(z_1, z_1, s)} \quad \text{(B2)}$$

$$h_c(z, s) = \frac{D(s)h_1(z, s) - k_1N(s)[G_0(z_1, z_1, s)h_1(z, s) + G_0(z, z_1, s)h_1(z_1, s)]}{D(s) + k_1N(s)G_0(z_1, z_1, s)} \quad \text{(B3)}$$

APPENDIX C

Determinant and Inverse of (I-$A(s)$)

From (34) and consider systems with

$$G_0(z_i, z_j, s) = g_1(z_i, s)g_2(z_j, s). \quad \text{(C1)}$$

Then the determinant and inverse of I—$A(s)$ are

$$\det[\text{I}—A(s)] = D_c(s) = 1 + \sum_{i=1}^{m} k_i(s)G_0(z_i, z_i, s), \quad \text{(C2)}$$

$$[\text{I}—A(s)]_{ij}^{-1} = \delta_{ij} - \frac{k_i(s)g_1(z_i, s)g_2(z_j, s)}{D_c(s)}, \quad \text{(C3)}$$

where δ_{ij} is the Kronecker-Delta symbol.

Downloaded 03 May 2010 to 171.66.16.245. Redistribution subject to ASME license or copyright; see http://www.asme.org/terms/Terms_Use.cfm

Transfer Function Formulation of Constrained Distributed Parameter Systems, Part II: Applications

C. H. Chung
Graduate Research Assistant.

C. A. Tan
Assistant Professor.
Assoc. Mem. ASME.

Department of Mechanical Engineering,
Wayne State University,
Detroit, MI 48202

In this paper, the application of the transfer function formulation and the generalized displacement method (GDM) to the analysis of constrained distributed parameter systems is illustrated. Two kinds of classical examples are considered. In the constrained free-free beam example, it is shown how the GDM gives the eigensolutions without requiring knowledge of the normal modes of the unconstrained beam. In the string on a partial elastic foundation example, mode localization and eigenvalue loci veering phenomena are examined. It is shown that mode localizaation can occur in spatially symmetric systems and for modes whose frequency loci do not veer.

1 Introduction

The dynamics of complex structures has been studied by many researchers. The general methodology is to consider the structure as an assembly of substructures that are connected together by imposing certain geometric compatibility and force constraint conditions at the internal boundaries or interfaces between the substructures. Hence, the dynamic analysis of complex structures may be regarded as the study of *constrained* dynamic systems which is the subject of this work. The dynamic systems considered here are composed of many subsystems and/or subject to pointwise constraints.

The idea of partitioning a complex structure into substructures was first developed by Hurty in the component modes method (1960, 1965). Dowell (1971, 1972, 1979) developed another method by expressing the constraints on generalized coordinates using the Lagrange multipliers. While this method is useful, it requires the knowledge of the normal modes of the unconstrained structure in the analysis. Moreover, no transient solution was presented. Bergman and Nicholson (1985) and Nicholson and Bergman (1986a, b) examined the dynamics of combined linear systems by employing the Green's function technique and classical modal analysis. Yang (1992) studied similar systems by the transfer function method.

In Part I of this work (Tan and Chung, 1993), analysis of one-dimensional, constrained, distributed parameter systems by the transfer function formulation was presented. Closed-form expressions of the transfer functions are given by Yang and Tan (1992). The formulation leads to the development of the generalized displacements method (GDM). With this method, the state vector in the frequency domain $\eta(x, s)$ is decomposed into two subvectors, the generalized displacement vector $\eta_d(x, s)$ and the generalized force vector $\eta_f(x, s)$. The $\eta_d(x, s)$ at the subsystem interfaces are assembled to form the generalized coordinate vector $\overline{w}_d(s)$ of the system. The basic idea is to express the response and eigensolutions of the constrained distributed system in terms of $\overline{w}_d(s)$. Because the formulation does not involve any modal truncation, the solutions are exact. Moreover, since $\overline{w}_d(s)$ is composed of $\eta_d(x, s)$ at the interfaces, geometric compatibility conditions are readily satisfied at the interfaces, and only force constraint conditions are included in the formulation. The present formulation also leads to systematic and efficient algorithms suitable for symbolic and numeric computations and can be applied to non-self-adjoint, damped systems.

In this paper, the methodology is applied to two kinds of examples. In Section 2, we study the free vibration response of a free-free beam constrained by linear springs at its ends (Dowell, 1971). Three different approaches based on the transfer function formulation are presented and discussed. With the GDM, no knowledge of the normal modes of the unconstrained (free-free) beam is required to obtain the modes of the constrained system. Indeed, GDM also generates the modes of the free-free beam. In Sections 3 and 4, we examine the dynamic characteristics of an elastic structure on a partial elastic foundation by applying the GDM. The system is treated as an assembly of substructures. Coupling between substructures is discussed, and conditions and physical interpretations for eigenvalue loci veering and mode localization in such systems are given.

2 Free Vibration Analysis of a Constrained Free-Free Beam

Consider an elastic beam constrained by linear springs of stiffness k at both ends. We present three approaches to analyze

Contributed by the Applied Mechanics Division of THE AMERICAN SOCIETY OF MECHANICAL ENGINEERS for presentation at the ASME Winter Annual Meeting, New Orleans, LA, Nov. 28–Dec. 3, 1993.

Discussion on this paper should be addressed to the Technical Editor, Professor Lewis T. Wheeler, Department of Mechanical Engineering, University of Houston, Houston, TX 77204-4792, and will be accepted until four months after final publication of the paper itself in the ASME JOURNAL OF APPLIED MECHANICS.

Manuscript received by the ASME Applied Mechanics Division, Apr. 17, 1992; final revision, Mar. 7, 1993. Associate Technical Editor: D. J. Inman.

Paper No. 93-WA/APM-12.

Copyright © 1993 by ASME
Downloaded 03 May 2010 to 171.66.16.245. Redistribution subject to ASME license or copyright; see http://www.asme.org/terms/Terms_Use.cfm

the free vibration problem using the transfer function formulation and the GDM. The Laplace transform of the nondimensional beam equation is

$$\overline{w}_{,xxxx} + s^2 \overline{w}(x,s) = \overline{f}_{el}(x,s), \quad x \in [0,1]. \tag{1}$$

The state matrix as defined in (I.9a)[1] is

$$F(s) = \begin{bmatrix} 0 & 1 & 0 & 0 \\ 0 & 0 & 1 & 0 \\ 0 & 0 & 0 & 1 \\ -s^2 & 0 & 0 & 0 \end{bmatrix}. \tag{2}$$

(A) The spring constraints appear in boundary condition operators, and the problem has homogeneous boundary conditions. This approach treats the beam and the springs as a whole system and the theory presented in Section 2 of Part I is applied. The boundary conditions are

$$\begin{aligned} \overline{w}_{,xxx}(0,s) + k\overline{w}(0,s) &= 0 \\ \overline{w}_{,xxx}(1,s) - k\overline{w}(1,s) &= 0. \end{aligned} \tag{3}$$

From (3), the boundary condition operators, $M(s)$, $N(s)$, and $\gamma(s)$ as defined in (I.9b), are given by (A2) in Appendix A. From (I.15), the characteristic equation is given by $\det[P(s)] = 0$, where $P(s) = M(s) + N(s)\Phi(1,s)$ and $\Phi(x,s) = e^{F(s)x}$ is the fundamental matrix.

The characteristic equation can be shown to be

$$2\alpha^6[1 - \cos(\alpha)\cosh(\alpha)] + 4k^2\sin(\alpha)\sinh(\alpha) + 4\alpha^3 k[\cos(\alpha)\sinh(\alpha) - \sin(\alpha)\cosh(\alpha)] = 0 \tag{4}$$

where $\alpha^4 = -s^2$. When k is equal to zero, the constraint forces are zero and the beam has free-free boundary conditions. The characteristic equation

$$\alpha^6[1 - \cos(\alpha)\cosh(\alpha)] = 0 \tag{5}$$

is obtained. Note that the zero eigenvalue corresponds to rigid-body modes. When k approaches infinity, the beam becomes simply supported and the characteristic equation is

$$\sin(\alpha) = 0. \tag{6}$$

These results agree with classical solutions (Meirovitch, 1967).

(B) The second approach considers the substructure as an unconstrained free-free beam with spring constraint forces applied at both ends. The theory presented in Section 3 of Part I is employed here. In Dowell's approach (1971), the system is a free-free beam subjected to constraint conditions (boundary conditions) which lead to the Lagrange multipliers. The mode shapes of the free-free beam are used in the modal expansion to determine the eigenvalues of the constrained beam. Note that Dowell considered only the infinitely constrained case (simply supported beam), while analysis for arbitrary spring stiffness can be done by the present formulation. Moreover, no information of the free-free beam mode shapes is required to determine the eigenvalues of the constrained beam.

The generalized displacements at both ends form the generalized coordinate vector

$$\overline{w}_d(s) = \{\overline{w}(0,s)\ \ \overline{w}(1,s)\}^T. \tag{7}$$

The constraint force, contributed by the two pointwise constraints at both ends, is

$$\overline{f}_c(x,s;\overline{w}) = -k\delta(x-0)\overline{w}(0,s) - k\delta(x-1)\overline{w}(1,s). \tag{8}$$

The boundary condition operators are given by (A3). For free vibration analysis, the system response is

$$\overline{w}(x,s) = [-kG_0(x,0,s)\ \ -kG_0(x,1,s)]\overline{w}_d(s) \tag{9}$$

where $G_0(x,\xi,s)$ is the transfer function of the free-free beam. From (9), the solution for $\overline{w}_d(s)$ is given by

$$\overline{w}_d(s) = A(s)\overline{w}_d(s);$$

where $A(s) = \begin{bmatrix} -kG_0(0,0,s) & -kG_0(0,1,s) \\ -kG_0(1,0,s) & -kG_0(1,1,s) \end{bmatrix}$. (10)

The expressions for the elements of $A(s)$ are given by (A4). For nontrivial solution of (10), it is required that

$$\det(I - A(s)) = 0. \tag{11}$$

The characteristic Eq. (11) is the same as (4).

To determine the eigenfunctions, let $s_j \neq 0$ be the jth eigenvalue. Find the eigenvector $\overline{w}_d(s)$ of (10), and substitute back into (9) to determine the mode shape

$$\overline{w}(x,s_j) = c\{k^2[G_0(x,0,s_j)G_0(0,1,s_j) - G_0(x,1,s_j)G_0(0,0,s_j)] - kG_0(x,1,s_j)\} \tag{12}$$

where c is a normalization constant. As k approaches infinity, (12) gives the mode shapes

$$\overline{w}(x,s_j) \to \{G_0(x,0,s_j)G_0(0,1,s_j) - G_0(x,1,s_j)G_0(0,0,s_j)\}, \to \sin(\alpha_j x) \tag{13}$$

of the simply supported beam, where $\alpha_j^4 = -s_j^2$. When k is zero, the flexible mode shapes of the free-free beam are obtained

$$\begin{aligned} \overline{w}(x,s_j) &\to -G_0(x,1,s_j) \\ &\to [(\cos(\alpha_j) - \cosh(\alpha_j))(\sin(\alpha_j x) + \sinh(\alpha_j x)) \\ &\quad - (\sin(\alpha_j) - \sinh(\alpha_j))(\cos(\alpha_j x) + \cosh(\alpha_j x))]. \end{aligned} \tag{14}$$

These results are identical with classical solutions.

(C) The third approach is a direct application of GDM which considers the beam as a fixed-constrained substructure. The undetermined generalized displacements of both ends are treated as inhomogeneous boundary terms.

The generalized coordinate vector $\overline{w}_d(s)$ is given by (7). The beam is considered as fixed-constrained at both ends, and hence the substructure can be treated as a clamped-clamped or simply supported beam. The simply supported beam is chosen because its transfer function is simpler. The boundary operators and the inhomogeneous boundary vectors are given by (A5). The theory presented in Section 4 of Part I is employed here.

The free vibration response is

$$\eta(x,s) = \begin{Bmatrix} H_d(x,s) \\ H_f(x,s) \end{Bmatrix}\gamma(s) = \Phi(x,s)(M(s) + N(s)\Phi(1,s))\gamma(s). \tag{15}$$

The constraint equation is given by (4), which can be written in matrix form in terms of $\overline{w}_d(s)$

$$Q_2(s)\eta_f(0,s) + Q_1(s)\eta_f(1,s) = \beta(s)\overline{w}_d(s). \tag{16}$$

The constraint operators $Q_2(s)$, $Q_1(s)$, and the generalized stiffness operator $\beta(s)$ are given by (A6). Combining (15), (16) gives

$$[T(s)]\overline{w}_d(s) = 0 \tag{17a}$$

where

$$T(s) = \begin{bmatrix} H_{41}(0,s) + k & H_{43}(0,s) \\ H_{41}(1,s) & H_{43}(1,s) - k \end{bmatrix}. \tag{17b}$$

The characteristic equation is $\det[T(s)] = 0$, which is identical with (4). To determine the mode shapes, let $s_j \neq 0$ be the jth eigenvalue. Find the eigenvector $\overline{w}_d(s)$ of (17a) and note that the inhomogeneous boundary vector $\gamma(s_j)$ is composed of $\overline{w}_d(s)$; see (A5). Substituting $\gamma(s_j)$ back into (15) gives the mode shapes

[1](I.9a) refers to Eq. (9a) in Part I of this work.

Downloaded 03 May 2010 to 171.66.16.245. Redistribution subject to ASME license or copyright; see http://www.asme.org/terms/Terms_Use.cfm

$$\overline{w}(x,s_j) = c\{H_{11}(x,s_j)H_{43}(0,s_j) - H_{13}(x,s_j)H_{41}(0,s_j) - kH_{13}(x,s_j)\}, \quad (18)$$

where c is a normalization constant. As k approaches infinity, (18) gives the mode shapes

$$\overline{w}(x,s_j) \to H_{13}(x,s_j) \to \sin(\alpha_j x), \quad \alpha_j^4 = -s_j^2 \quad (19)$$

of the simply supported beam. When k is zero, the flexible mode shapes of the free-free beam are obtained:

$$\overline{w}(x,s_j) \to \{H_{11}(x,s_j)H_{43}(0,s_j) - H_{13}(x,s_j)H_{41}(0,s_j)\} \to [(\cos(\alpha_j) - \cosh(\alpha_j))(\sin(\alpha_j x) + \sinh(\alpha_j x)) - (\sin(\alpha_j) - \sinh(\alpha_j))(\cos(\alpha_j x) + \cosh(\alpha_j x))]. \quad (20)$$

Equations (19), (20) are identical with (13), (14).

From (5), there exists zero eigenvalue ($s = 0$) that corresponds to the rigid-body modes of free-free beam. It can be shown that $[T(0)]$ is a null matrix when $k = 0$ and $s = 0$. Hence, the eigenvectors $\overline{w}_d(s)$ are any two linearly independent vectors in $\mathbf{R}^2$. Choose one eigenvector as $\{1\ 1\}^T$, and the other eigenvector as $\{1\ -1\}^T$. Substitute these two eigenvectors back into (15) and evaluate the mode shapes as s approaches zero. The translational mode shape is

$$\overline{w}(x,0) = \lim_{s\to 0}[H_{11}(x,s)\ H_{12}(x,s)\ H_{13}(x,s)\ H_{14}(x,s)]\begin{pmatrix}1\\0\\1\\0\end{pmatrix} = 1. \quad (21a)$$

The rotational mode shape is

$$\overline{w}(x,0) = \lim_{s\to 0}[H_{11}(x,s)\ H_{12}(x,s)\ H_{13}(x,s)\ H_{14}(x,s)]\begin{pmatrix}1\\0\\-1\\0\end{pmatrix} = 1-2x. \quad (21b)$$

Note that the rigid-body modes (21a, b) could have been obtained by observation. The eigenvector $\overline{w}_d(0) = \{1\ 1\}^T$ means that the two ends move with the same amplitude. This corresponds to the rigid-body mode $\overline{w}(x, 0) = 1$. Alternatively, one can choose another set of eigenvectors such as $\{1\ 0\}^T$ and $\{0\ 1\}^T$. These lead to $\overline{w}(x, 0) = 1 - x$ and $\overline{w}(x, 0) = x$, respectively, which are a linear combination of the modes given by (21a, b).

The three approaches show that the transfer function formulation provides different ways to analyze a problem, and leads to systematic algorithms. Solutions for different problems require only changes in the boundary operators and state matrices but not in the algorithms. Furthermore, the methodology does not involve modal expansion so that information of the unconstrained mode shapes is not needed. The result of this technique is exact and requires little computational effort. Comparing the three approaches, the GDM (Approach C) is the most versatile in analysis.

3 Analysis of a String on a Partial Elastic Foundation

Consider a fixed-fixed string constrained by an elastic foundation of stiffness k extending from x_1 to x_2; see Fig. 1. The string is also constrained by two point springs at x_1 and x_2. The system can be regarded as being composed of three substructures. Note that the partial foundation is a distributed constraint which may represent some kind of pressure forces acting on the flexible structure. Hence, results of this study have potential implications in the dynamic characteristics and passive vibration control of structures where fluid loadings are important. The vibration control of axially moving continua by bearing forces has recently been studied by the transfer function method (Tan et al., 1990, 1993).

According to GDM, the boundary operators are

$$M^{(i)}(s) = \begin{bmatrix}1 & 0\\0 & 0\end{bmatrix}, \quad N^{(i)}(s) = \begin{bmatrix}0 & 0\\1 & 0\end{bmatrix}, \quad i = 1,2,3. \quad (22)$$

The generalized displacements at the substructure interfaces are treated as inhomogeneous boundary terms. Hence,

$$\gamma^{(1)}(s) = \begin{Bmatrix}0\\\overline{w}(x_1,s)\end{Bmatrix}, \quad \gamma^{(2)}(s) = \begin{Bmatrix}\overline{w}(x_1,s)\\\overline{w}(x_2,s)\end{Bmatrix}, \quad \gamma^{(3)}(s) = \begin{Bmatrix}\overline{w}(x_2,s)\\0\end{Bmatrix}, \quad (23)$$

where we have used the zero displacement boundary conditions at $x = 0, 1$. The generalized coordinate vector $\overline{w}_d(s) = \{\overline{w}(x_1, s)\ \overline{w}(x_2, s)\}^T$. Define local coordinates

$$z = \frac{x}{x_1} \text{ for } x \in [0,x_1], \quad z = \frac{x-x_1}{x_2-x_1} \text{ for } x \in [x_1,x_2], \quad z = \frac{x-x_2}{1-x_2} \text{ for } x \in [x_2,1] \quad (24)$$

and transform the equations of motion from the global coordinate to the local coordinates. For free vibrations, the responses of the substructures are

$$\{\eta^{(i)}(z,s)\} = \begin{Bmatrix}\eta_d^{(i)}(z,s)\\\eta_f^{(i)}(z,s)\end{Bmatrix} = \begin{Bmatrix}H_d^{(i)}(z,s)\\H_f^{(i)}(z,s)\end{Bmatrix}\gamma^{(i)}(s), \quad i = 1,2,3. \quad (25)$$

From the free-body diagram shown in Fig. 1, the constraint equations at $x = x_1$ are

$$\overline{w}(x_1^-,s) = \overline{w}(x_1^+,s) \quad (26a)$$

$$\overline{w}_{,x}(x_1^+,s) - \overline{w}_{,x}(x_1^-,s) = \hat{k}\overline{w}(x_1,s). \quad (26b)$$

Note that the construction of $\gamma^{(i)}(s)$ and $\overline{w}_d(s)$ has implicitly assumed the continuity of generalized displacement across the subsystem boundaries. Hence, the geometric compatibility (26a) is readily satisfied. The constraint equation (26b) on the generalized force is expressed in terms of local coordinates

$$Q_2^{(1)}(s)\eta_f^{(1)}(z=1,s) + Q_1^{(2)}(s)\eta_f^{(2)}(z=0,s) = \beta^{(1)}(s)\eta_d(x_1,s). \quad (27)$$

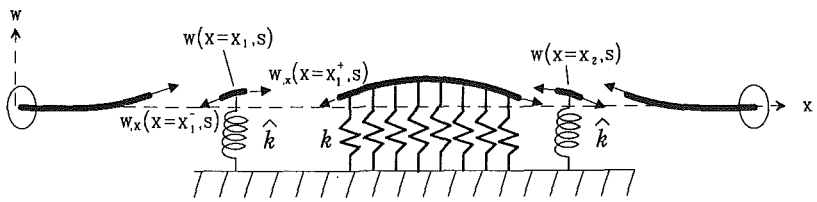


Fig. 1 Free-body diagram of a string on an elastic foundation

Downloaded 03 May 2010 to 171.66.16.245. Redistribution subject to ASME license or copyright; see http://www.asme.org/terms/Terms_Use.cfm

Applying similar procedures leads to another constraint equation at $x = x_2$.

The state matrices $F^{(i)}(s)$, constraint and stiffness operators $Q_j^{(i)}(s)$, and $\beta^{(k)}(s)$ are given in Appendix B. Combining the constraint equations and using (23) and (25) leads to a homogeneous algebraic equation in $\overline{w}_d(s)$,

$$[T_c(s)]\overline{w}_d(s) = 0, \tag{28a}$$

where

$$T_c(s) = \begin{bmatrix} -\hat{k} - \gamma \coth(\gamma(x_2 - x_1)) - s \coth(sx_1) & \dfrac{\gamma}{\sinh(\gamma(x_2 - x_1))} \\ \dfrac{\gamma}{\sinh(\gamma(x_2 - x_1))} & -\hat{k} - \gamma \coth(\gamma(x_2 - x_1)) - s \coth(s(1 - x_1)) \end{bmatrix} \tag{28b}$$

and $\gamma^2 = s^2 + k$. The characteristic equation is $\det[T_c(s)] = 0$. Note that classical methods would lead to the expansion of a 6×6 matrix (two boundary and four constraint conditions) for the characteristic equation.

3.1 Spatially Symmetric Systems. Consider the case of an elastic foundation that is symmetrically located along the span of the string. Denote $d = x_2 - x_1$ as the length of the foundation. From (28*b*) and the relation $x_1 + x_2 = 1$, the characteristic equation is reduced to

$$\hat{k}^2 - \Omega^2 + \frac{f_3^2(\omega,d)}{f_2^2(\omega,d)} + 2\hat{k}\frac{f_4(\Omega,d)}{f_1(\Omega,d)} + 2\hat{k}\frac{f_3(\omega,d)}{f_2(\omega,d)} + 2\frac{f_3(\omega,d)f_4(\Omega,d)}{f_1(\Omega,d)f_2(\omega,d)} = 0 \tag{29}$$

where

$$f_1(\Omega,d) = \sin(d\Omega), \quad f_2(\omega,d) = \sin(x_1 w) = \sin\left(\frac{(1-d)\omega}{2}\right)$$

$$f_3(\omega,d) = \omega\cos(x_1\omega) = \omega\cos\left(\frac{(1-d)\omega}{2}\right), \quad f_4(\Omega,d) = \Omega\cos(d\Omega)$$

$$s = i\omega, \ \gamma = i\Omega, \ \Omega^2 = \omega^2 - k. \tag{30}$$

The parameter ω is the natural frequency of the system. Note that for $k = \hat{k} = 0$, (29) becomes

$$-\sin(d\omega)\sin^2(x_1\omega) + \cos^2(x_1\omega)\sin(d\omega) + 2\cos(d\omega)\cos(x_1\omega)\sin(x_1\omega) = 0, \tag{31}$$

which can be simplified to yield $\sin(\omega) = 0$. The roots $\omega_n = n\pi$ are the natural frequencies of the string without the elastic foundation and the springs.

For the limiting case of $\hat{k} \to \infty$, the characteristic equation reduces to

$$f_1(\Omega,d)f_2^2(\omega,d) = 0, \tag{32}$$

which yields three sets (two of them repeated) of natural frequencies

$$f_2(\omega,d) = 0 \Rightarrow \omega_n = \frac{2n\pi}{1-d}, \quad n = \pm 1, \pm 2, \cdots \tag{33a}$$

$$f_1(\Omega,d) = 0 \Rightarrow \Omega_m = \frac{m\pi}{d}; \ \omega_m = \sqrt{\frac{m^2\pi^2}{d^2} + k}, \quad m = \pm 1, \pm 2, \cdots. \tag{33b}$$

Referring to Fig. 1 and the problem formulation (Eqs. (22)–(25), (B4)), three subsystems can be identified. The natural frequencies of the subsystems are those of (33*a*, *b*). These subsystems are coupled through constraint equations of the form (27). As $\hat{k} \to \infty$, $\overline{w}(x_1, s)$ and $\overline{w}(x_2, s)$ approach zero, and the subsystems become uncoupled with fixed-fixed boundary conditions. The parameter $1/\hat{k}$ is thus a coupling factor. When $\hat{k}$ is large, the subsystems are weakly coupled. A similar coupling phenomenon has been reported in disordered systems with internal coupling (Bendikson, 1987; Hodges, 1982; Pierre and Dowell, 1987; Pierre, 1988; Pierre and Cha, 1989; Perkins and Mote, 1986; Gottlieb, 1987).

Figure 2(*a*) shows the loci of the natural frequencies as a function of the length of the elastic foundation for $\hat{k} = k = 50$; see (29). Equations (33*a*, *b*) are also plotted for comparison (dashed curves in the figure). Note that as $d \to 1$, we have a complete foundation and the frequencies ω_m approach the limit $\sqrt{m^2\pi^2 + k}$ (Eq. (33*b*)). For $d \to 0$, we recover the results for a point spring located at $x = 0.5$. In this case, as the spring

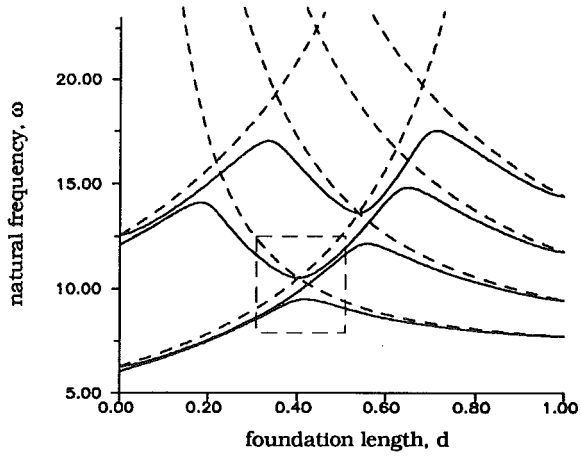


Fig. 2(*a*) Loci of the natural frequencies of a string on an elastic foundation for $k = \hat{k} = 50$; solid curves are the exact solutions, and the dashed curves are the natural frequency loci of the uncoupled subsystems $\omega_n = 2n\pi/(1-d)$ and $\omega_m = \sqrt{\frac{m^2\pi^2}{d^2} + k}$. Box indicates a representative region of curve veering, and comparison with perturbation solution is shown in Fig. 2(*b*).

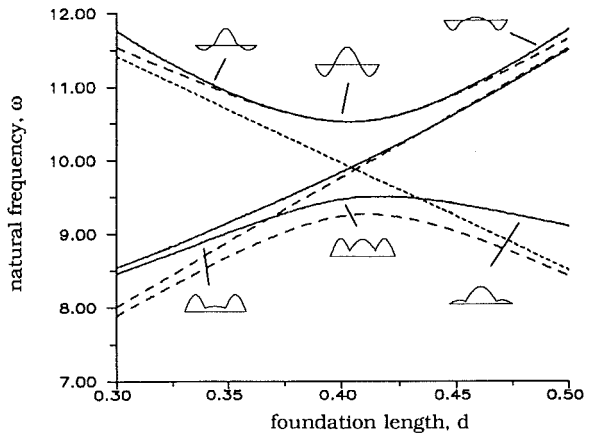


Fig. 2(*b*) Perturbation solution for the representative region of curve veering; solid curves are the exact solutions; dashed curves are the perturbation results (represented by two hyperbola curves and a straight line) with the dashed line being an asymptote of the hyperbola. The dotted line represents the other asymptote of the hyperbola. Some mode shapes are also shown.

Downloaded 03 May 2010 to 171.66.16.245. Redistribution subject to ASME license or copyright; see http://www.asme.org/terms/Terms_Use.cfm

stiffness approaches infinity, we have two identical uncoupled subsystems with natural frequencies $\omega_n = 2n\pi$. Note that, for any given mode, the natural frequencies of the uncoupled subsystems form an upper bound for the corresponding frequencies of the coupled system.

In Fig. 2(*a*), it is seen that the frequency loci of the uncoupled subsystems cross each other. At crossing points (ω^*, d^*), we have from (33*a*, *b*)

$$(m^2\pi^2 + kd^{*2})(1-d^*)^2 = 4n^2\pi^2 d^{*2}, \quad m,n = 1,2,3. \tag{34}$$

Near the crossings, the system frequency loci (solid curves) either *veer away* from each other with high local curvature or *veer together*. It is noted that the frequency loci of the system pass through (ω^*, d^*) regardless of the degree of coupling (Schajer, 1984). There are two branches that bifurcate from the dashed curve governed by (33*a*) due to the spatial symmetry of the problem with (33*a*) representing two sets of repeated eigenvalues. Eigenvalue loci veering has been studied extensively for disordered systems in both structural dynamics and physics (Leissa, 1974; Kuttler and Sigillito, 1981). It was shown that for self-adjoint problems, eigenvalue loci veering and strong mode localization are two manifestations of the same physical phenomenon (Pierre, 1988). However, eigenvalue loci veering for *spatially symmetric* systems is reported here for the first time.

The first and second brace brackets in (38) represent the equations of a straight line and a general hyperbola in the $(\tilde{\omega}, \tilde{d})$ plane near (ω^*, d^*), respectively. The approximate characteristic Eq. (36) thus leads to three distinct branches. The straight line is also an asymptote of the hyperbola. The intersection point of the asymptotes of the hyperbola is (ω_1, d_1) given in (39*a*, *b*). The slope of the line is $-b_2/a_2$ which is locally tangent to $f_2(\omega, d) = 0$ at (ω^*, d^*). Hence, the local characteristic of one branch of $f_2(\omega, d) = 0$ curves is a straight line which accounts for the veering together phenomenon. The other two branches (curve veering), which are locally described by the hyperbola, evolve from regions of loci crossings which are locally governed by the degenerate form of the hyperbola, $\Lambda = 0$ in (38). From (33*a*, *b*), perturb around $m = n = 1$; see the boxed region in Fig. 2(*a*). The comparison of exact solutions (solid curves) and perturbation results (dashed curves) are shown in Fig. 2(*b*). The preceding analysis shows that evolution of regions of loci veering and veering together can be described by perturbations of the characteristic equation around the loci crossings. Cheng and Perkins (1991) employed a similar analysis to examine the loci veering characteristics of a friction-guided, translating string.

Mode shapes of the representative loci veering region are also shown in Fig. 2(*b*). Applying GDM, the eigenfunction that corresponds to eigenvalue $s_j = i\omega_j$ is

$$\overline{w}(x,\omega_j) = \begin{cases} \dfrac{\sin(\omega_j x)}{\sin(\omega_j x_1)}\,\overline{w}(x_1,\omega_j), & x \in [0,x_1] \\ \dfrac{\sin(\Omega_j(x_2-x))}{\sin(\Omega_j d)}\,\overline{w}(x_j,\omega_j) + \dfrac{\sin(\Omega_j(x-x_1))}{\sin(\Omega_j d)}\,\overline{w}(x_2,\omega_j), & x \in [x_1,x_2] \\ \dfrac{\sin(\omega_j(1-x))}{\sin(\omega_j(1-x_2))}\,\overline{w}(x_2,\omega_j), & x \in [x_2,1] \end{cases} \tag{40}$$

A perturbation analysis of (29) is employed here to highlight the evolution of regions of curve veering. Define $\epsilon = 1/\hat{k}$ as a coupling factor and perturbation parameter. Equation (29) becomes

$$(1+\epsilon-\omega^2\epsilon^2)f_1f_2^2 + \epsilon^2 f_3^2 f_1 + 2\epsilon f_4 f_2^2 + 2\epsilon f_1 f_2 f_3 + 2\epsilon^3 f_2 f_3 f_4 = 0. \tag{35}$$

Let $\omega = \omega^* + \epsilon\tilde{\omega}$ and $d = d^* + \epsilon\tilde{d}$, where both $\tilde{\omega}$ and $\tilde{d}$ are of $O(1)$. Expanding the functions in (35) in a Taylor series, and retaining up to $O(\epsilon^3)$ terms (since we have three branches), gives

$$(a_1\tilde{\omega}+b_1\tilde{d})(a_2\tilde{\omega}+b_2\tilde{d})^2 + (f_3^*)^2(a_1\tilde{\omega}+b_1\tilde{d}) + 2f_4^*(a_2\tilde{\omega}+b_2\tilde{d})^2 + 2f_3^*(a_1\tilde{\omega}+b_1\tilde{d})(a_2\tilde{\omega}+b_2\tilde{d}) + 2f_3^*f_4^*(a_2\tilde{\omega}+b_2\tilde{d}) = 0 \tag{36}$$

where

$$a_i = \left.\frac{\partial f_i}{\partial\omega}\right|_{(\omega^*,d^*)}; \quad b_i = \left.\frac{\partial f_i}{\partial d}\right|_{(\omega^*,d^*)}, \quad i = 1,2 \tag{37a}$$

$$f_3^* = f_3(\omega^*,d^*), \quad f_4^* = f_4(\omega^*,d^*). \tag{37b}$$

Equation (36) can be factored into

$$\{a_2(\tilde{\omega}-\omega_1)+b_2(d_1-\tilde{d})\}\cdot\{[a_1(\tilde{\omega}-\omega_1)+b_1(d_1-\tilde{d})][a_2(\tilde{\omega}-\omega_1)+b_2(d_1-\tilde{d})-\Lambda]\} = 0 \tag{38}$$

where

$$\omega_1 = (f_3^*b_1 - 2f_4^*b_2)/(a_1b_2 - a_2b_1), \tag{39a}$$

$$d_1 = (2f_4^*a_2 - f_3^*a_1)/(a_1b_2 - a_2b_1), \tag{39b}$$

$$\Lambda = 2f_3^*f_4^*. \tag{39c}$$

where $\overline{w}(x_1, \omega_j)$ and $\overline{w}(x_2, \omega_j)$ are elements of $\overline{w}_d(\omega_j)$ obtained by solving (28*a*). For this symmetric system $\overline{w}_d(\omega_j) = \{1\ 1\}^T$ for odd modes and $\overline{w}_d(\omega_j) = \{1\ -1\}^T$ for even modes. From (40), the resonance conditions of the mode shape in each segment are governed by (33*a*, *b*). Hence, for frequency loci very near the crossings (ω^*, d^*), the amplitudes of the mode shape in each segment are relatively the same, and no mode localization is expected. This is clearly indicated by the mode shapes shown in Fig. 2(*b*) for $d \cong 0.42$. However, for frequency loci away from (ω^*, d^*) where the branches are distinctly apart, mode localization becomes eminent. In Fig. 2(*b*) for $d \cong 0.34$, the lower branches stay close to $f_2(\omega, d) = 0$ and the upper branch is close to $f_1(\Omega, d) = 0$. Hence the amplitude of the third mode (upper branch) is much larger in the mid-segment while the amplitude of the first mode is relatively larger in the two outer segments. However, at $d \cong 0.48$, the resonance conditions in the segments are reversed because of loci veering away, and a "mode exchange" characteristic is observed. This characteristic of loci veering has been observed by several researchers, but the physical meanings have seldom been examined.

It is thus important to realize that modes near loci veering can be highly localized and a small change in d can produce large changes in the modal response magnitude. By carefully selecting design parameters, the system can be passively controlled utilizing the mode localization phenomenon. Note that no approximation is used in revealing and explaining the frequency loci veering and mode localization phenomena in the spatially symmetric physical system considered here.

Figure 3 shows the loci of the natural frequencies as a function of k with $x_1 = 0.3$, $x_2 = 0.7$, $\hat{k} = 50$. The dashed curves which represent the natural frequencies of the uncoupled subsystems are determined from (33*a*, *b*) and (40)

Downloaded 03 May 2010 to 171.66.16.245. Redistribution subject to ASME license or copyright; see http://www.asme.org/terms/Terms_Use.cfm

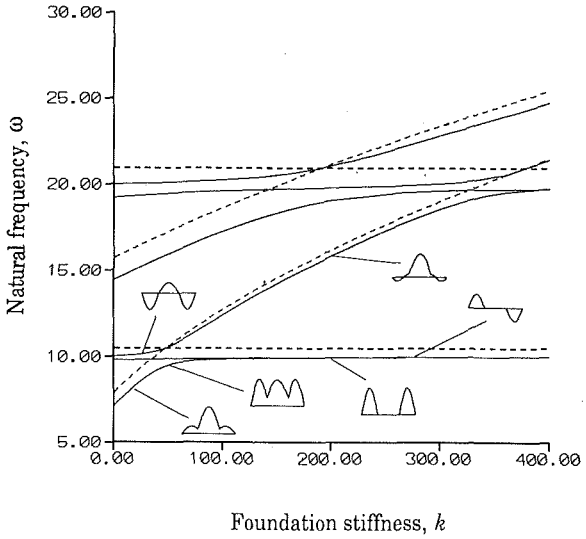


Fig. 3 Loci of the first six natural frequencies of a string on an elastic foundation extending from $x_1 = 0.3$ to $x_2 = 0.7$ for $\hat{k} = 50$; dashed curves are the natural frequency loci of the uncoupled subsystems. Some mode shapes are shown. Curve veering and mode localization is clearly observed.

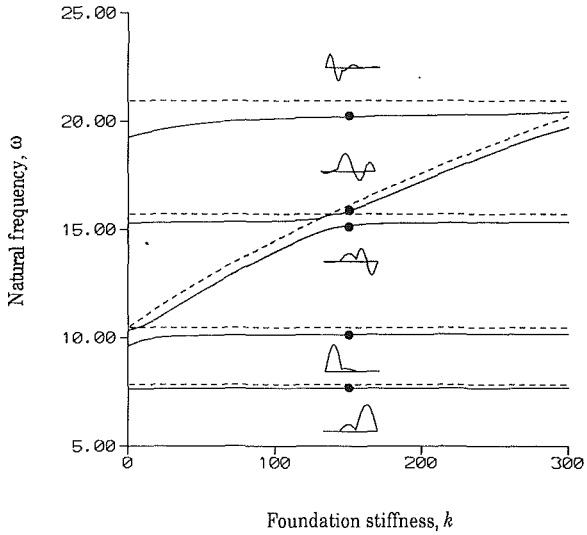


Fig. 4 Loci of the first five natural frequencies of a string on an elastic foundation extending from $x_1 = 0.3$ to $x_2 = 0.6$ (asymmetrically located case) for $\hat{k} = 95$. Dashed curves are the natural frequency loci of the uncoupled subsystems. Some mode shapes are shown, and mode localization is observed.

$$\omega_n = \frac{2n\pi}{1-d} = \frac{n\pi}{0.3}, \tag{41a}$$

$$\omega_m = \sqrt{\frac{m^2\pi^2}{d^2} + k} = \sqrt{\frac{m^2\pi^2}{0.16} + k}. \tag{41b}$$

The loci crossings (ω^*, k^*) are located by equating the above two equations. Near (ω^*, k^*), the frequency loci either veer away or veer together. The veering away phenomenon always involves three distinct branches, while only two branches are involved in the veering together. This is due to the spatial symmetry of the problem which causes (41*a*) to bifurcate into two branches.

Examine the loci of the lowest three frequencies. As k becomes large, i.e., $k > k^*$, the first and second frequency loci become asymptotically close to each other (veering together) and their frequencies approach $\omega_\infty = \pi/0.3$ using (41*a*). This is the weakly coupled situation. From (40), the modal amplitudes of the first and second modes in the mid-segment are thus significantly smaller than those in the outer two segments. The mid-segment appears to be a rigid foundation and the system is basically decoupled with a pair of symmetric and antisymmetric modes. The mechanism of mode localization is again related to the modal resonance conditions of the substructures for weakly coupled systems.

In Fig. 3, it is seen that the third frequency locus continues to follow the dashed curve (41*b*) after the first veering away. The modal amplitude of mid-segment is now significantly larger than those of the outer two segments, and mode localization is resulted. Similar loci veering and mode localization phenomena can be predicted for higher modes. Moreover, for a particular mode, the minimum stiffness above which the mid-segment appears to be a rigid foundation can be estimated. The elastic foundation does not behave as rigid for all the modes at any given value of k.

3.2 Spatially Asymmetric Systems. Consider the spatially asymmetric case. Figure 4 shows the frequency loci versus k for $x_1 = 0.3$, $x_2 = 0.6$, and $\hat{k} = 95$. Because of the spatial asymmetry, three distinct uncoupled subsystems with natural frequencies

$$\omega_l = \frac{l\pi}{x_1} = \frac{l\pi}{0.3}, \tag{42a}$$

$$\omega_m = \sqrt{\frac{m^2\pi^2}{d^2} + k} = \sqrt{\frac{m^2\pi^2}{0.16} + k}, \tag{42b}$$

$$\omega_n = \frac{n\pi}{1-x_2} = \frac{n\pi}{0.4}, \tag{42c}$$

are identified. These are represented by the dashed curves in the figure. An immediate consequence of having distinct uncoupled subsystems is that no veering together phenomenon can occur. This is clearly observed in Fig. 4. Moreover, at the crossings of the frequency loci of the uncoupled subsystems, only two modes are involved in the veering away process. Note that the frequencies of the first and second modes approach $\omega_\infty = n\pi/0.4$ (Eq. (42*c*)) and $\omega_\infty = l\pi/0.3$ (Eq. (42*a*)), respectively.

Figure 4 also shows the first five mode shapes for $k = 150$. From (40), since the ω_1 locus is asymptotic to the branch (42*c*) for $n = 1$, the shape of the first mode is then highly localized in the end segment. Similar explanations for the mode localization behavior in other modes can be given. Note that mode localizations occur for the first and second modes whose frequency loci do not veer. This is in contrast to what Pierre (1988) concluded for self-adjoint, slightly disordered systems. Nevertheless, mode localization is found only in weakly coupled systems when the frequency locus of a particular mode is close to some frequency loci of the uncoupled subsystems.

4 Analysis of a Beam on a Partial Elastic Foundation

Consider a similar system of a beam, but with $x_1 = 0.5$, $x_2 = 1$. The system has two substructures. Because of page limitation, we shall focus on how the transfer function formulation simplifies the computation. Physical characteristics of the system will be discussed in another paper.

The boundary operators, $M^{(i)}(s)$ and $N^{(i)}(s)$, and the inhomogeneous boundary vectors, $\gamma^{(i)}(s)$, are listed in Appendix C. Applying the following constraint equation (see (C3) for details),

$$Q_2^{(1)}(s)\eta_f^{(1)}(z=1,s) + Q_1^{(2)}(s)\eta_f^{(2)}(z=0,s) = \beta(s)\eta_d(x_1,s), \tag{43}$$

and combining with (C1), (C2), and (25), lead to a homogeneous algebraic equation in $\overline{w}_d(\omega_j)$ in the form of (28*a*) where

Downloaded 03 May 2010 to 171.66.16.245. Redistribution subject to ASME license or copyright; see http://www.asme.org/terms/Terms_Use.cfm

$$T_c(s) = \begin{bmatrix} \frac{1}{d^3} H_{41}^{(2)}(0,s) - \frac{1}{x_1^3} H_{43}^{(1)}(1,s) + k & \frac{1}{d^3} H_{44}^{(2)}(0,s) - \frac{1}{x_1^3} H_{42}^{(1)}(1,s) \\ \frac{1}{d^2} H_{33}^{(2)}(0,s) - \frac{1}{x_1^2} H_{31}^{(1)}(1,s) & \frac{1}{d^2} H_{34}^{(2)}(0,s) - \frac{1}{x_1^2} H_{32}^{(1)}(1,s) \end{bmatrix}. \quad (44)$$

$H_{jk}^{(i)}(z, s)$ is the (j, k) element of $H^{(i)}(z, s)$ which can either be obtained in closed form or evaluated numerically. The characteristic equation is $\det[T_c(s)] = 0$.

With the present formulation, evaluation of the characteristic equation requires the expansion of the 2×2 matrix. Classical methods impose four physical boundary conditions and four internal boundary conditions, and a 8×8 matrix is resulted. GDM also leads to systematic algorithms for the response analysis of different physical problems. For example, (44) remains unchanged for a damped, axially translating beam model. The axial translation of the beam renders the problem non-self-adjoint. The only changes are in $H_{jk}^{(i)}(z, s)$ whose closed-form solution is given by (I.11*c*). In contrast, classical methods do not offer the advantages described above.

5 Summary and Conclusions

The application of the transfer function formulation and the GDM for analysis of one-dimensional, constrained distributed parameter systems is illustrated. The present formulation leads to systematic algorithms, and solutions for different problems require only changes in the boundary operators and state matrices but not in the algorithms.

In the first example, the free vibration response of an elastic beam under pointwise spring constraints applied at its ends is examined. Three different approaches are presented. In each approach, the exact characteristic equation is obtained. Unlike the Lagrange multipliers method, the constraint force approach (Approach B) and the GDM (Approach C) give exact mode shapes of the constrained beam for arbitrary spring stiffness without requiring information of the mode shapes of the unconstrained free-free beam.

In the second example, we study the dynamic characteristics of constrained elastic structures (strings and beams) on a partial elastic foundation by applying the GDM. This example represents a system that is composed of several subsystems. It is shown that the characteristic equation can be obtained in a simpler way compared with classical methods. For the string example, eigenvalue loci veering away and mode localization are observed in both spatially symmetric and asymmetric systems, while loci veering together can occur only in the spatially symmetric case. A perturbation approach is employed to highlight the loci veering process. It is shown that curve veering and mode localization phenomena are manifestations of the coupling between the subsystems, in particular, in weakly coupled systems when the frequency locus of a particular mode is close to some frequency loci of the uncoupled subsystems. Moreover, mode localization can occur in modes whose frequency loci do not veer. For sufficiently large foundation stiffness, the elastic foundation appears to be rigid for some modes. This behavior is related to the conditions for eigenvalue loci veering and mode localization.

Acknowledgment

The authors gratefully acknowledge the partial support of the National Science Foundation and the American Natural Resources Pipeline Company for this research.

References

Bendikson, O. O., 1987, "Mode Localization Phenomena in Large Space Structures," *AIAA Journal*, Vol. 25, No. 9, Sept., pp. 1241–1248.

Bergman, L. A., and Nicholson, J. W., 1985, "Forced Vibration of a Damped Combined Linear System," ASME *Journal of Vibration, Acoustics, Stress, and Reliability in Design*, Vol. 107, pp. 275–281.

Cheng, S. P., and Perkins, N. C., 1991, "The Vibration and Stability of a Friction-Guided, Translating String," *Journal of Sound and Vibration*, Vol. 144, No. 2, pp. 281–292.

Dowell, E. H., 1971, "Free Vibrations of a Linear Structure With Arbitrary Support Conditions," ASME JOURNAL OF APPLIED MECHANICS, Vol. 38, pp. 595–600.

Dowell, E. H.., 1972, "Free Vibrations of an Arbitrary Structure in Terms of Component Modes," ASME JOURNAL OF APPLIED MECHANICS, Vol. 39, pp. 727–732.

Dowell, E. H., 1979, "On Some General Properties of Combined Dynamical Systems," ASME JOURNAL OF APPLIED MECHANICS, Vol. 46, pp. 206–209.

Gottlieb, H. P. W., 1987, "Extension of a Textbook Problem to Curve Veering for Coupled Pendulums," *Journal of Sound and Vibration*, Vol. 113, No. 1, pp. 185–187.

Hodges, C. H., 1982, "Confinement of Vibration by Structural Irregularity," *Journal of Sound and Vibration*, Vol. 82, No. 3, pp. 411–424.

Hurty, W. C., 1960, "Vibrations of Structural Systems by Component Mode Synthesis," *ASCE Journal of Engineering Mechanics*, Aug., pp. 51–69.

Hurty, W. C., 1965, "Dynamic Analysis of Structural Systems Using Component Modes," *AIAA Journal*, Vol. 3, No. 4, Apr., pp. 678–685.

Kuttler, J. R., and Sigillito, V. G., 1981, "On Curve Veering," *Journal of Sound and Vibration*, Vol. 75, No.4, pp. 585–588.

Leissa, A. W., 1974, "On a Curve Veering Aberration," *ZAMP*, Vol. 25, pp. 99–111.

Meirovitch, L., 1967, *Analytical Methods in Vibrations*, Macmillan, New York.

Nicholson, J. W., and Bergman, L. A., 1986a, "Free Vibration of Combined Dynamical Systems," *ASCE Journal of Engineering Mechanics*, Vol. 112, pp. 1–13.

Nicholson, J. W., and Bergman, L. A., 1986b, "Vibration of Damped Plate-Oscillator Systems," *ASCE Journal of Engineering Mechanics*, Vol. 112, pp. 14–30.

Perkins, N. C., and Mote, C. D., Jr., 1986, "Comments on Curve Veering in Eigenvalue Problems," *Journal of Sound and Vibration*, Vol. 106, No. 3, pp. 451–463.

Pierre, C., 1988, "Mode Localization and Eigenvalue Loci Veering Phenomena in Disordered Structures," *Journal of Sound and Vibration*, Vol. 126, No. 3, pp. 485–502.

Pierre, C., and Cha, P. D., 1989, "Strong Mode Localization in Nearly Periodic Disordered Structures," *AIAA Journal*, Vol. 27, No. 2, Feb., pp. 227–241.

Pierre, C., and Dowell, E. H., 1987, "Localization of Vibrations by Structural Irregularity," *Journal of Sound and Vibration*, Vol. 114, No. 3, pp. 549–564.

Schajer, G. S., 1984, "The Vibration of a Rotating Circular String Subject to a Fixed End Restraint," *Journal of Sound and Vibration*, Vol. 92, pp. 11–19.

Tan, C. A., and Chung, C. H., 1993, "Transfer Function Formulation of Constrained Distributed-Parameter Systems, Part I: Theory," ASME JOURNAL OF APPLIED MECHANICS, Vol. 60.

Tan, C. A., Yang, B., and Mote, C. D., Jr., 1990, "On the Vibration of a Translating String Coupled to Hydrodynamic Bearings," ASME *Journal of Vibration and Acoustics*, Vol. 112, pp. 337–345.

Tan, C. A., Yang, B., and Mote, C. D., Jr., 1993, "Dynamic Response of an Axially Moving Beam Coupled to Hydrodynamic Bearing," ASME *Journal of Vibration and Acoustics*, Vol. 115, pp. 9–15.

Yang, B., 1992, "Transfer Functions of Constrained/Combined One-Dimensional Continuous Dynamic Systems," *Journal of Sound and Vibration*, Vol. 156, No. 1, July, pp. 425–433.

Yang, B., and Tan, C. A., 1992, "Transfer Functions of One-Dimensional Distributed Parameter Systems," ASME JOURNAL OF APPLIED MECHANICS, Vol. 59, pp. 1009–1014.

APPENDIX A

List of Transfer Functions and Operators Used in Section 2

The matrix transfer function is

$$\Gamma(x,\xi,s) = \begin{cases} \Phi(x,s)\,(M(s)+N(s)\Phi(1,s))^{-1}M(s)\Phi(-\xi,s), & \xi<x \\ -\Phi(x,s)\,(M(s)+N(s)\Phi(1,s))^{-1}N(s)\Phi(1-\xi,s), & \xi>x. \end{cases} \quad (A1)$$

Downloaded 03 May 2010 to 171.66.16.245. Redistribution subject to ASME license or copyright; see http://www.asme.org/terms/Terms_Use.cfm

The boundary condition operators and inhomogeneous boundary terms are given as follows.

Approach A:

$$M(s)=\begin{bmatrix} k & 0 & 0 & 1 \\ 0 & 0 & 1 & 0 \\ 0 & 0 & 0 & 0 \\ 0 & 0 & 0 & 0 \end{bmatrix}, \quad N(s)=\begin{bmatrix} 0 & 0 & 0 & 0 \\ 0 & 0 & 0 & 0 \\ -k & 0 & 0 & 1 \\ 0 & 0 & 1 & 0 \end{bmatrix},$$

$$\gamma(s)=\begin{Bmatrix} 0 \\ 0 \\ 0 \\ 0 \end{Bmatrix}. \quad \text{(A2)}$$

Approach B:

$$M(s)=\begin{bmatrix} 0 & 0 & 1 & 0 \\ 0 & 0 & 0 & 1 \\ 0 & 0 & 0 & 0 \\ 0 & 0 & 0 & 0 \end{bmatrix}, \quad N(s)=\begin{bmatrix} 0 & 0 & 0 & 0 \\ 0 & 0 & 0 & 0 \\ 0 & 0 & 1 & 0 \\ 0 & 0 & 0 & 1 \end{bmatrix},$$

$$\gamma(s)=\begin{Bmatrix} 0 \\ 0 \\ 0 \\ 0 \end{Bmatrix}, \quad \text{(A3)}$$

and the transfer function of the free-free beam is

$$G_0(x,0,s)=B(x,0,\alpha)/\Delta \qquad \text{(A4)}$$
$$G_0(x,1,s)=B(x,1,\alpha)/\Delta, \quad \alpha^4=-s^2$$

where

$$B(x,0,\alpha)=-\sin(\alpha x)-\sin(\alpha-\alpha x)-\sin(\alpha)\cosh(\alpha-\alpha x)$$
$$+\cos(\alpha-\alpha x)\sinh(\alpha)+\sinh(\alpha x)+\cos(\alpha)\sinh(\alpha-\alpha x),$$
$$B(x,1,\alpha)=-\sin(\alpha-\alpha x)-\sin(\alpha x)\cosh(\alpha)-\sin(\alpha)\cosh(\alpha x)$$
$$+\cos(\alpha x)\sinh(\alpha)+\cos(\alpha)\sinh(\alpha x)+\sinh(\alpha-\alpha x),$$
$$\Delta=2\alpha^3-2\alpha^3\cos(\alpha)\cosh(\alpha).$$

Approach C:

$$M(s)=\begin{bmatrix} 1 & 0 & 0 & 0 \\ 0 & 0 & 1 & 0 \\ 0 & 0 & 0 & 0 \\ 0 & 0 & 0 & 0 \end{bmatrix}, \quad N(s)=\begin{bmatrix} 0 & 0 & 0 & 0 \\ 0 & 0 & 0 & 0 \\ 1 & 0 & 0 & 0 \\ 0 & 0 & 1 & 0 \end{bmatrix},$$

$$\gamma(s)=\begin{Bmatrix} \overline{w}(0,s) \\ 0 \\ \overline{w}(1,s) \\ 0 \end{Bmatrix}, \quad \text{(A5)}$$

and the constraint operators and generalized stiffness operators are

$$Q_2(s)=\begin{bmatrix} 0 & 1 \\ 0 & 0 \end{bmatrix}, \quad Q_1(s)=\begin{bmatrix} 0 & 0 \\ 0 & 1 \end{bmatrix}, \quad \beta(s)=\begin{bmatrix} -k & 0 \\ 0 & k \end{bmatrix}. \qquad \text{(A6)}$$

APPENDIX B

List of Equations and Operators Used in Section 3

The state matrices in local coordinates are

$$F^{(1)}(s)=\begin{bmatrix} 0 & 1 \\ s^2x_1^2 & 0 \end{bmatrix}, \quad F^{(2)}(s)=\begin{bmatrix} 0 & 1 \\ (s^2+k)(x_2-x_1)^2 & 0 \end{bmatrix},$$

$$F^{(3)}(s)=\begin{bmatrix} 0 & 1 \\ s^2(1-x_2)^2 & 0 \end{bmatrix}. \quad \text{(B1)}$$

The constraint operators and generalized stiffness operators at $x = x_1$ are

$$Q_2^{(1)}(s)=\begin{bmatrix} -\dfrac{1}{x_1} \end{bmatrix}, \quad Q_1^{(2)}(s)=\begin{bmatrix} \dfrac{1}{x_2-x_1} \end{bmatrix}, \quad \beta^{(1)}(s)=\hat{k}. \quad \text{(B2)}$$

The constraint operators and generalized stiffness operators at $x = x_2$ are

$$Q_2^{(1)}(s)=\begin{bmatrix} -\dfrac{1}{x_2-x_1} \end{bmatrix}, \quad Q_1^{(2)}(s)=\begin{bmatrix} \dfrac{1}{1-x_2} \end{bmatrix},$$

$$\beta^{(2)}(s)=\hat{k}. \quad \text{(B3)}$$

APPENDIX C

List of Operators Used in Section 4

The boundary operators and inhomogeneous boundary terms for each substructure are:

Substructure 1:

$$M^{(1)}(s)=\begin{bmatrix} 1 & 0 & 0 & 0 \\ 0 & 0 & 1 & 0 \\ 0 & 0 & 0 & 0 \\ 0 & 0 & 0 & 0 \end{bmatrix}, \quad N^{(1)}(s)=\begin{bmatrix} 0 & 0 & 0 & 0 \\ 0 & 0 & 0 & 0 \\ 1 & 0 & 0 & 0 \\ 0 & 1 & 0 & 0 \end{bmatrix},$$

$$\gamma^{(1)}(s)=\begin{Bmatrix} 0 \\ 0 \\ \overline{w}(x_1,s) \\ \overline{w}_{,x}(x,s) \end{Bmatrix}, \quad (C1)$$

Substructure 2:

$$M^{(2)}(s)=\begin{bmatrix} 1 & 0 & 0 & 0 \\ 0 & 1 & 0 & 0 \\ 0 & 0 & 0 & 0 \\ 0 & 0 & 0 & 0 \end{bmatrix}, \quad N^{(2)}(s)=\begin{bmatrix} 0 & 0 & 0 & 0 \\ 0 & 0 & 0 & 0 \\ 1 & 0 & 0 & 0 \\ 0 & 0 & 1 & 0 \end{bmatrix},$$

$$\gamma^{(2)}(s)=\begin{Bmatrix} \overline{w}(x_1,s) \\ \overline{w}_{,x}(x_1,s) \\ 0 \\ 0 \end{Bmatrix}. \quad \text{(C2)}$$

The constraint and stiffness operators are

$$Q_2^{(1)}(s)=\begin{bmatrix} \dfrac{1}{x_1^3} & 0 \\ 0 & \dfrac{1}{x_1^2} \end{bmatrix}, \quad Q_1^{(2)}(s)=\begin{bmatrix} -\dfrac{1}{(1-x_1)^3} & 0 \\ 0 & -\dfrac{1}{(1-x_1)^2} \end{bmatrix},$$

$$\beta(s)=\begin{bmatrix} \hat{k} & 0 \\ 0 & 0 \end{bmatrix}. \quad \text{(C3)}$$

Downloaded 03 May 2010 to 171.66.16.245. Redistribution subject to ASME license or copyright; see http://www.asme.org/terms/Terms_Use.cfm

B. Tabarrok

Liyong Tong

Department of Mechanical Engineering,
University of Victoria,
P.O. Box 3055
Victoria, BC, V8W 3P6, Canada

Dualities in Free Vibration of Minimum Surface Membranes

For the linear free vibration of minimum surface membranes, the governing equations and the associated variational functional are derived. Using the basic geometrical characteristics of any two minimum surface membranes, the analysis brings to light the existence of geometrically different surface membranes with identical surface areas, natural frequencies, and vibrating modes.

1 Introduction

The celebrated minimum surface problem may be stated as follows: find the surface of the minimum area bounded by one or more given closed curves in space. This problem was first cast into a variational statement by Lagrange and later Euler showed that all such surfaces must be saddle-shaped, with their mean curvature equal to zero. Minimum surfaces find applications in design of tension structures.

Since the governing equations for minimum surfaces are nonlinear partial differential equations, they do not admit general closed-form solutions. However, Plateau found "physical" solutions for a large variety of boundary contours by dipping wire frames of various shapes into soap film solutions. More recently, the minimum surface problem has been analyzed numerically by the finite difference and finite element methods (Greenspan, 1965, 1967; Conus, 1967; Hinata et al., 1977; Wagner 1977; Hewgill, 1984; Tabarrok and Xiong, 1991; Tabarrok and Tong, 1991, 1992).

In this study the vibration equations of minimum surface membranes are derived through Hamilton's principle. These equations are then linearized and simplified using the characteristics of the minimum surface. Dualities in free vibration of dual minimum surfaces are investigated, and it is shown that dual surfaces, which are geometrically different, have not only identical surface areas but also the same natural frequencies and vibrating modes. An example is given to illustrate the dualities between the catenoid and the helicoid surfaces.

2 Dual Minimum Surfaces

2.1 Minimum Surfaces. Let a surface S, with its bounding curve ∂S, be described by a position vector $\mathbf{r}_1$ as

$$\mathbf{r}_1 = x_1\mathbf{e}_1 + y_1\mathbf{e}_2 + z_1\mathbf{e}_3 \tag{1}$$

where $\mathbf{e}_i (i = 1, 2, 3)$ are the unit vectors of the three-dimensional Euclidean space. Since the tip of $\mathbf{r}_1$ must stay on the surface, x_1, y_1, and z_1 in Eq. (1) are not independent; they are related through the equation of the surface which we describe parametrically as

$$x_1 = f_1(\alpha,\beta) \quad y_1 = f_2(\alpha,\beta) \quad z_1 = f_3(\alpha,\beta) \tag{2}$$

The functions $f_i (i = 1, 2, 3)$ are single-valued and continuous functions of parameters α and β. Thus,

$$\mathbf{r}_1 = f_1\mathbf{e}_1 + f_2\mathbf{e}_2 + f_3\mathbf{e}_3 \tag{3}$$

and

$$d\mathbf{r}_1 = \frac{\partial \mathbf{r}_1}{\partial \alpha}\, d\alpha + \frac{\partial \mathbf{r}_1}{\partial \beta}\, d\beta. \tag{4}$$

Further,

$$d\mathbf{r}_1 \cdot d\mathbf{r}_1 = Ed\alpha^2 + 2Fd\alpha d\beta + Gd\beta^2 \tag{5}$$

where E, F, and G are the first fundamental surface coefficients given by

$$E = \frac{\partial \mathbf{r}_1}{\partial \alpha}\cdot\frac{\partial \mathbf{r}_1}{\partial \alpha} \quad F = \frac{\partial \mathbf{r}_1}{\partial \alpha}\cdot\frac{\partial \mathbf{r}_1}{\partial \beta} \quad G = \frac{\partial \mathbf{r}_1}{\partial \beta}\cdot\frac{\partial \mathbf{r}_1}{\partial \beta}. \tag{6}$$

Consider now a small region bounded by curves $(\alpha, \alpha + d\alpha)$, and $(\beta, \beta + d\beta)$. The area of this parallelogram is given by

$$dA = \left|\frac{\partial \mathbf{r}_1}{\partial \alpha} \times \frac{\partial \mathbf{r}_1}{\partial \beta}\right| d\alpha d\beta = \sqrt{EG - F^2}\, d\alpha d\beta. \tag{7}$$

For the sake of simplicity, we employ orthogonal curvilinear coordinates and thereby we set F equal to zero. In that case, the total area bounded by a closed curve ∂S may be written as

$$A = \int_\alpha \int_\beta \sqrt{EG}\, d\alpha d\beta = \int_\alpha \int_\beta \sqrt{(\mathbf{r}_{1,\alpha}\cdot\mathbf{r}_{1,\alpha})(\mathbf{r}_{1,\beta}\cdot\mathbf{r}_{1,\beta})}\, d\alpha d\beta. \tag{8}$$

Now minimizing A with respect to $\mathbf{r}_1$, we have

$$\delta A = -\int_\alpha \int_\beta \left\{ \frac{\partial}{\partial \alpha}\left[\sqrt{\frac{(\mathbf{r}_{1,\beta}\cdot\mathbf{r}_{1,\beta})}{(\mathbf{r}_{1,\alpha}\cdot\mathbf{r}_{1,\alpha})}}\, \mathbf{r}_{1,\alpha}\right] + \frac{\partial}{\partial \beta}\left[\sqrt{\frac{(\mathbf{r}_{1,\alpha}\cdot\mathbf{r}_{1,\alpha})}{(\mathbf{r}_{1,\beta}\cdot\mathbf{r}_{1,\beta})}}\, \mathbf{r}_{1,\beta}\right]\right\} \cdot \delta\mathbf{r}_1 d\alpha d\beta$$

Contributed by the Applied Mechanics Division of THE AMERICAN SOCIETY OF MECHANICAL ENGINEERS for presentation at the ASME Winter Annual Meeting, New Orleans, LA, Nov. 28–Dec. 3, 1993.

Discussion on this paper should be addressed to the Technical Editor, Professor Lewis T. Wheeler, Department of Mechanical Engineering, University of Houston, Houston, TX 77204-4792, and will be accepted until four months after final publication of the paper itself in the ASME JOURNAL OF APPLIED MECHANICS.

Manuscript received by the ASME Applied Mechanics Division, Mar. 30, 1992; final revision, Oct. 7, 1992. Associate Technical Editor: A. K. Noor.

Paper No. 93-WA/APM-3.

Copyright © 1993 by ASME

Downloaded 03 May 2010 to 171.66.16.245. Redistribution subject to ASME license or copyright; see http://www.asme.org/terms/Terms_Use.cfm

$$+\oint_{\partial S}\left(n_\alpha\sqrt{\frac{(\mathbf{r}_{1,\beta}\cdot\mathbf{r}_{1,\beta})}{(\mathbf{r}_{1,\alpha}\cdot\mathbf{r}_{1,\alpha})}}\,\mathbf{r}_{1,\alpha}+n_\beta\sqrt{\frac{(\mathbf{r}_{1,\alpha}\cdot\mathbf{r}_{1,\alpha})}{(\mathbf{r}_{1,\beta}\cdot\mathbf{r}_{1,\beta})}}\,\mathbf{r}_{1,\beta}\right)\cdot\delta\mathbf{r}ds=0. \tag{9}$$

Since $\mathbf{r}_1$ is prescribed as $\mathbf{r}_{1p}$ along the boundary, then $\delta\mathbf{r}_1 = 0$ along ∂S and Eq. (8) yields the following Euler-Lagrange equation in the domain:

$$\frac{\partial}{\partial\alpha}\left[\sqrt{\frac{(\mathbf{r}_{1,\beta}\cdot\mathbf{r}_{1,\beta})}{(\mathbf{r}_{1,\alpha}\cdot\mathbf{r}_{1,\alpha})}}\,\mathbf{r}_{1,\alpha}\right]+\frac{\partial}{\partial\beta}\left[\sqrt{\frac{(\mathbf{r}_{1,\alpha}\cdot\mathbf{r}_{1,\alpha})}{(\mathbf{r}_{1,\beta}\cdot\mathbf{r}_{1,\beta})}}\,\mathbf{r}_{1,\beta}\right]=0. \tag{10}$$

To develop the complementary formulation, let us define the following pseudo-stress vectors:

$$\sigma=\sqrt{\frac{(\mathbf{r}_{1,\beta}\cdot\mathbf{r}_{1,\beta})}{(\mathbf{r}_{1,\alpha}\cdot\mathbf{r}_{1,\alpha})}}\,\mathbf{r}_{1,\alpha}\quad\tau=\sqrt{\frac{(\mathbf{r}_{1,\alpha}\cdot\mathbf{r}_{1,\alpha})}{(\mathbf{r}_{1,\beta}\cdot\mathbf{r}_{1,\beta})}}\,\mathbf{r}_{,\beta}, \tag{11}$$

or on inversion

$$\mathbf{r}_{1,\alpha}=\sqrt{\frac{(\tau\cdot\tau)}{(\sigma\cdot\sigma)}}\,\sigma\quad\mathbf{r}_{1,\beta}=\sqrt{\frac{(\sigma\cdot\sigma)}{(\tau\cdot\tau)}}\,\tau. \tag{12}$$

These equations have the appearance of some constitutive relations connecting the pseudo-stress vectors to the gradients of the position vector. A further analogy with the theory of elasticity is brought to light if the condition for minimum area, as given in Eq. (10), is expressed in terms of the stress vectors as follows:

$$\frac{\partial\sigma}{\partial\alpha}+\frac{\partial\tau}{\partial\beta}=0. \tag{13}$$

Equation (13) has the appearance of an equilibrium equation.

Now let us develop a complementary expression for the infinitesimal area, through a Legendre transformation, as follows:

$$a^*=\sigma\cdot\mathbf{r}_{1,\alpha}+\tau\cdot\mathbf{r}_{1,\beta}-dA. \tag{14}$$

On integrating this expression by parts, we obtain

$$\int_\alpha\int_\beta\sqrt{EG}\,d\alpha d\beta+\int_\alpha\int_\beta a^*d\alpha d\beta$$
$$+\int_\alpha\int_\beta(\sigma_{,\alpha}+\tau_{,\beta})\cdot\mathbf{r}_1d\alpha d\beta-\oint_{\partial S}(n_\alpha\sigma+n_\beta\tau)\cdot\mathbf{r}_1ds=0. \tag{15}$$

The first term is of course the area A. The third term can be eliminated if σ and τ are constrained such that equilibrium Eq. (13) is identically satisfied. Then we may express Eq. (15) as

$$A+A^*=0, \tag{16}$$

where

$$A^*=\int_\alpha\int_\beta a^*d\alpha d\beta-\oint_{\partial S}(\mathbf{r}_{1p}\cdot\sigma_n)ds, \tag{17}$$

where

$$\sigma_n=n_\alpha\sigma+n_\beta\tau. \tag{18}$$

Equation (16) also reveals that when A is minimized, A^* is maximized. Evidently, A^* will be a function of σ and τ. However, these variables are not independent and are required to satisfy the equilibrium Eq. (13) identically. To this end we introduce a vector stress function $\mathbf{r}_2(\alpha,\beta)$ as follows:

$$\mathbf{r}_2(\alpha,\beta)=x_2(\alpha,\beta)\mathbf{e}_1+y_2(\alpha,\beta)\mathbf{e}_2+z_2(\alpha,\beta)\mathbf{e}_3 \tag{19}$$

such that

$$\sigma=-\frac{\partial\mathbf{r}_2}{\partial\beta}\quad\tau=\frac{\partial\mathbf{r}_2}{\partial\alpha}. \tag{20}$$

From this definition it is evident that only the gradients of $\mathbf{r}_2$ control the surface A^* and we may arbitrarily set $\mathbf{r}_2$ equal to a constant, say zero, at one point on the surface. Now eliminating the variable $\mathbf{r}_1$ from a^* in Eq. (14), via (12) and expressing of σ and τ in terms of $\mathbf{r}_2$, we may write A^* as

$$A^*=\int_\alpha\int_\beta\sqrt{(\mathbf{r}_{2,\alpha}\cdot\mathbf{r}_{2,\alpha})(\mathbf{r}_{2,\beta}\cdot\mathbf{r}_{2,\beta})}d\alpha d\beta-\oint_{\partial S}(\mathbf{r}_{1p}\cdot\mathbf{r}_{2,s})ds. \tag{21}$$

Since the area integral in Eq. (21) is identical in form to that in Eq. (8), one can see that the Euler-Lagrange equation of the above functional will be identical in form to that given in Eq. (10). Thus the $\mathbf{r}_2$ and $\mathbf{r}_1$ surfaces are governed by the same differential equation. However, the boundary conditions for the two surfaces are different. For the $\mathbf{r}_1$ surface the boundary is prescribed as $\mathbf{r}_{1p}$ along ∂S, while for the $\mathbf{r}_2$ surface the boundary condition is of the natural type, i.e., $\mathbf{r}_2$ is free along ∂S. This boundary condition, found from extremum condition of the functional in Eq. (21), is given by

$$n_\alpha\sqrt{\frac{(\mathbf{r}_{2,\beta}\cdot\mathbf{r}_{2,\beta})}{(\mathbf{r}_{2,\alpha}\cdot\mathbf{r}_{2,\alpha})}}\,\mathbf{r}_{2,\alpha}+n_\beta\sqrt{\frac{(\mathbf{r}_{2,\alpha}\cdot\mathbf{r}_{2,\alpha})}{(\mathbf{r}_{2,\beta}\cdot\mathbf{r}_{2,\beta})}}\,\mathbf{r}_{2,\beta}+\mathbf{r}_{1p,s}=0. \tag{22}$$

Through Eqs. (12) and (20), we may readily interpret the Euler-Lagrange equation and the boundary condition for the $\mathbf{r}_2$ surface. The boundary condition, in Eq. (22), implies that

$$n_\alpha\mathbf{r}_{1,\beta}-n_\beta\mathbf{r}_{1,\alpha}+\mathbf{r}_{1p,s}=0. \tag{23}$$

The governing Eq. (10), when expressed in terms of $\mathbf{r}_2$ implies that

$$\frac{\partial}{\partial\alpha}(\mathbf{r}_{1,\beta})+\frac{\partial}{\partial\beta}(-\mathbf{r}_{1,\alpha})=0. \tag{24}$$

Now we can see that the extremum conditions for A^* express some compatibility requirements along the boundary and in the domain.

The two minimum surfaces in terms of $\mathbf{r}_1$ and $\mathbf{r}_2$ form a dual set (Tabarrok and Tong, 1991, 1992).

2.2 Illustrative Example. To illustrate the foregoing theory, let us obtain the dual surface to the catenoid. Taking advantage of the symmetry, we consider half a catenoid. The position vector $\mathbf{r}_1$ on the half catenoid, shown in Fig. 1, may be explicitly expressed in cylindrical coordinates as

$$\mathbf{r}_1=d\cosh\left(\frac{z-h}{d}\right)(\cos\theta\,\mathbf{e}_1+\sin\theta\,\mathbf{e}_2)+z\mathbf{e}_3$$
$$(0\le\theta\le2\pi,\ 0\le z\le h) \tag{25}$$

where the radius at the bottom end of the half catenoid surface is taken as unity and the radius at the upper end is $d = 0.84834$. The height of the half catenoid is $h = 0.5$. To find its dual surface, we need to introduce the following orthogonal curvilinear coordinate system

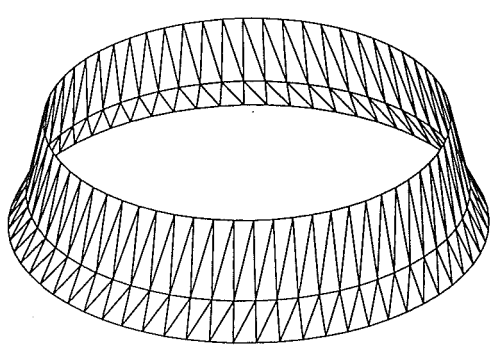


Fig. 1 Catenoid surface

Downloaded 03 May 2010 to 171.66.16.245. Redistribution subject to ASME license or copyright; see http://www.asme.org/terms/Terms_Use.cfm

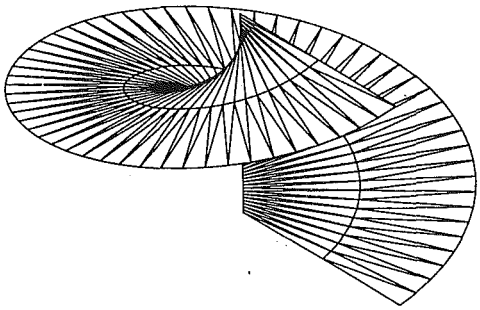


Fig. 2 Helicoid surface

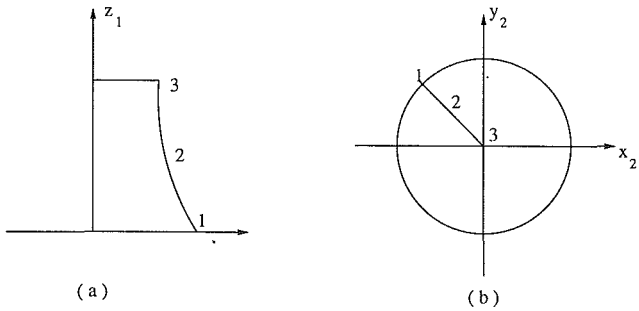


Fig. 3 Duality between r_1 and r_2 for a given α

$$\alpha = \theta \qquad (0 \le \theta \le 2\pi) \qquad (26)$$

$$\beta = d\left[\sinh\left(\frac{z-h}{d}\right) + \sinh\left(\frac{h}{d}\right)\right] \qquad (0 \le z \le h) \qquad (27)$$

where α is along the circumferential and β along the meridian directions, respectively. Thus, the position vector for the catenoid surface may be rewritten as follows:

$$\mathbf{r}_1 = f(\beta)\cos\alpha\,\mathbf{e}_1 + f(\beta)\sin\alpha\mathbf{e}_2 + \left\{h + d\sinh^{-1}\left[\frac{\beta}{d} - \sinh\left(\frac{h}{d}\right)\right]\right\}\mathbf{e}_3$$

$$(0) \le \alpha \le 2\pi,\ 0 \le \beta \le d\sinh\left(\frac{h}{d}\right). \qquad (28)$$

Hence

$$f_1 = f(\beta)\cos\alpha$$

$$f_2 = f(\beta)\sin\alpha$$

$$f_3 = \left\{h + d\sinh^{-1}\left[\frac{\beta}{d} - \sinh\left(\frac{h}{d}\right)\right]\right\}$$

where

$$f(\beta) = \sqrt{d^2 + \left[\beta - d\sinh\left(\frac{h}{d}\right)\right]^2}. \qquad (29)$$

It is worth noting that the defining domain in the α and β coordinate system is a rectangle with α ranging from 0 to 2π and β taking values between 0 and $d\sinh(h/d)$.

The derivatives of $\mathbf{r}_1$ with respect to α and β may be written as

$$\mathbf{r}_{1,\alpha} = -f(\beta)\sin\alpha\,\mathbf{e}_1 + f(\beta)\cos\alpha\,\mathbf{e}_2$$

$$\mathbf{r}_{1,\beta} = f_{,\beta}(\beta)\cos\alpha\,\mathbf{e}_1 + f_{,\beta}(\beta)\sin\alpha\,\mathbf{e}_2 + f_{3,\beta}(\beta)\mathbf{e}_3 \qquad (30)$$

where

$$f_{,\beta}(\beta) = \frac{\beta - d\sinh\left(\frac{h}{d}\right)}{f(\beta)}$$

$$f_{3,\beta}(\beta) = \frac{d}{f(\beta)}. \qquad (31)$$

The first fundamental coefficients of the catenoid surface are given by

$$(\mathbf{r}_{1,\alpha}\cdot\mathbf{r}_{1,\alpha}) = f^2(\beta) \quad (\mathbf{r}_{1,\beta}\cdot\mathbf{r}_{1,\beta}) = 1. \qquad (32)$$

According to the definition of dual surface in Eqs. (11) and (20), the dual surface to the catenoid may be obtained by solving the following equations:

$$\mathbf{r}_{2,\beta} = -\frac{1}{f(\beta)}\mathbf{r}_{1,\alpha}$$

$$\mathbf{r}_{2,\alpha} = f(\beta)\mathbf{r}_{1,\beta}. \qquad (33)$$

Substituting Eqs. (30) into Eqs. (33) and using Eqs. (29) and (31), we find

$$\mathbf{r}_{2,\beta} = \sin\alpha\,\mathbf{e}_1 - \cos\alpha\,\mathbf{e}_2$$

$$\mathbf{r}_{2,\alpha} = \left[\beta - d\sinh\left(\frac{h}{d}\right)\right](\cos\alpha\,\mathbf{e}_1 + \sin\alpha\,\mathbf{e}_2) + d\mathbf{e}_3. \qquad (34)$$

Integration of Eqs. (34), the defining domain of which is identical to that of Eqs. (28), implies that

$$\mathbf{r}_2 = \beta(\sin\alpha\,\mathbf{e}_1 - \cos\alpha\,\mathbf{e}_2) + \mathbf{g}_1(\alpha) \qquad (35)$$

and

$$\mathbf{r}_2 = \left[\beta - d\sinh\left(\frac{h}{d}\right)\right](\sin\alpha\,\mathbf{e}_1 - \cos\alpha\,\mathbf{e}_2) + d\,\alpha\,\mathbf{e}_3 + \mathbf{g}_2(\beta) \qquad (36)$$

where $\mathbf{g}_1(\alpha)$ and $\mathbf{r}_2(\beta)$ are the integration functions to be determined later. To match all terms of $\mathbf{r}_2$ in Eqs. (35) and (36), we have that

$$\mathbf{g}_1(\alpha) = -d\sinh\left(\frac{h}{d}\right)(\sin\alpha\,\mathbf{e}_1 - \cos\alpha\,\mathbf{e}_2) + d\,\alpha\,\mathbf{e}_3 + \mathbf{g}_0 \qquad (37)$$

$$\mathbf{g}_2(\beta) = \mathbf{g}_0 \qquad (38)$$

where $\mathbf{g}_0$ is an arbitrarily unknown constant vector. By taking

$$\mathbf{g}_0 = \mathbf{0}, \qquad (39)$$

we arrive at the dual surface of the catenoid described by the position vector $\mathbf{r}_2$, as

$$\mathbf{r}_2 = \left[\beta - d\sinh\left(\frac{h}{d}\right)\right](\sin\alpha\,\mathbf{e}_1 - \cos\alpha\,\mathbf{e}_2) + d\,\alpha\,\mathbf{e}_3. \qquad (40)$$

This is the helicoid surface, shown in Fig. 2.

It is worth noting that the defining domain in the α and β coordinate system for the helicoid is identical to that for the catenoid, namely $(0 \le \alpha \le 2\pi,\ 0 \le \beta \le d\sinh(h/d))$. This may be explained as

- when β ranges from 0 to $d\sinh(h/d)$ for a given α, $\mathbf{r}_1$ moves along a meridian line $\overline{123}$ on the catenoid surface from bottom to the upper edge (see Fig. 3(*a*)), and $\mathbf{r}_2$ moves along the radius line $\overline{123}$ on the helicoid towards its center from the outer edge (see Fig. 3(*b*));
- when α takes values from 0 to 2π for a given β, $\mathbf{r}_1$ follows the circumferential line $\overline{12341}$ on the catenoid surface (see Fig. 4(*a*)), and $\mathbf{r}_2$ follows the circumferential line $\overline{12341}$ on the helicoid surface but with a 90-deg lag (see Fig. 4(*b*)).

Thus the circles in the catenoid transform to the helices in the helicoid and likewise the catenaries transform to straight radial lines.

2.3 Characteristics of Dual Minimum Surfaces. Consider dual minimum surfaces S_1 and S_2, bounded by curves ∂S_1 and ∂S_2. Let the positions on the surface S_1 and S_2 be denoted by vectors $\mathbf{r}_1$ and $\mathbf{r}_2$, respectively. Let vectors $\mathbf{r}_{1p}$ and $\mathbf{r}_{2p}$ represent, respectively, prescribed positions on the two bounding curves ∂S_1 and ∂S_2 of the dual surfaces S_1 and S_2. Since S_1 and S_2 are dual surfaces, they have the following characteristics:

Downloaded 03 May 2010 to 171.66.16.245. Redistribution subject to ASME license or copyright; see http://www.asme.org/terms/Terms_Use.cfm

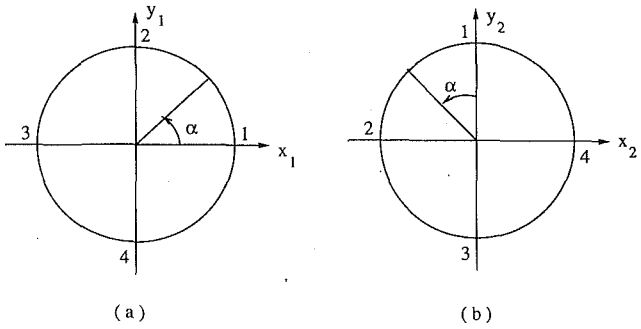


Fig. 4 Duality between r_1 and r_2 for a given β

- The surface areas of dual minimum surfaces are identical.
- The partial derivatives of the position vectors $\mathbf{r}_1$ and $\mathbf{r}_2$ on dual surfaces S_1 and S_2 with respect to the curvilinear coordinates α and β are related according to the definition of the complementary surfaces, see Eqs. (11) and (20),

$$\mathbf{r}_{2,\beta} = -\sqrt{\frac{(\mathbf{r}_{1,\beta}\cdot\mathbf{r}_{1,\beta})}{(\mathbf{r}_{1,\alpha}\cdot\mathbf{r}_{1,\alpha})}}\,\mathbf{r}_{1,\alpha} \quad \mathbf{r}_{2,\alpha} = \sqrt{\frac{(\mathbf{r}_{1,\alpha}\cdot\mathbf{r}_{1,\alpha})}{(\mathbf{r}_{1,\beta}\cdot\mathbf{r}_{1,\beta})}}\,\mathbf{r}_{1,\beta}. \tag{41}$$

Now evaluating the dot products $\mathbf{r}_{2,\alpha}\cdot\mathbf{r}_{2,\alpha}$ and $\mathbf{r}_{2,\beta}\cdot\mathbf{r}_{2,\beta}$, we find

$$\mathbf{r}_{1,\alpha}\cdot\mathbf{r}_{1,\alpha} = \mathbf{r}_{2,\alpha}\cdot\mathbf{r}_{2,\alpha} \quad \mathbf{r}_{1,\beta}\cdot\mathbf{r}_{1,\beta} = \mathbf{r}_{2,\beta}\cdot\mathbf{r}_{2,\beta}. \tag{42}$$

Through Eqs. (6) these two equations may be interpreted as the first fundamental coefficients E_1 and G_1 of surface S_1 being equal to the first fundamental coefficients E_2 and G_2 of surface S_2, respectively. Using Eqs. (42), Eqs. (41) may be rewritten as follows:

$$\mathbf{r}_{1,\alpha} = -\sqrt{\frac{(\mathbf{r}_{2,\alpha}\cdot\mathbf{r}_{2,\alpha})}{(\mathbf{r}_{2,\beta}\cdot\mathbf{r}_{2,\beta})}}\,\mathbf{r}_{2,\beta} \quad \mathbf{r}_{1,\beta} = \sqrt{\frac{(\mathbf{r}_{2,\beta}\cdot\mathbf{r}_{2,\beta})}{(\mathbf{r}_{2,\alpha}\cdot\mathbf{r}_{2,\alpha})}}\,\mathbf{r}_{2,\alpha}. \tag{43}$$

- Since $\mathbf{r}_2$ may be obtained by integrating Eqs. (41), the defining domain of $\mathbf{r}_2$ in α and β coordinate system must be the same as that of Eqs. (41). Noting that the right-hand side terms in Eqs. (41) are only related to $\mathbf{r}_1$, the defining domain of Eqs. (41) must be identical to that of the surface vector $\mathbf{r}_1$. Therefore, we conclude that $\mathbf{r}_1$ and $\mathbf{r}_2$ have identical defining domains.
- The "normal" directional derivative of one minimum surface along its boundary curve is related to the prescribed position vector of its dual through the following equations:

For the $\mathbf{r}_1$ surface

$$n_\alpha\sqrt{\frac{(\mathbf{r}_{2,\beta}\cdot\mathbf{r}_{2,\beta})}{(\mathbf{r}_{2,\alpha}\cdot\mathbf{r}_{2,\alpha})}}\,\mathbf{r}_{2,\alpha} + n_\beta\sqrt{\frac{(\mathbf{r}_{2,\alpha}\cdot\mathbf{r}_{2,\alpha})}{(\mathbf{r}_{2,\beta}\cdot\mathbf{r}_{2,\beta})}}\,\mathbf{r}_{2,\beta} + \mathbf{r}_{1p,s} = 0, \tag{44}$$

and for the $\mathbf{r}_2$ surface,

$$n_\alpha\sqrt{\frac{(\mathbf{r}_{1,\beta}\cdot\mathbf{r}_{1,\beta})}{(\mathbf{r}_{1,\alpha}\cdot\mathbf{r}_{1,\alpha})}}\,\mathbf{r}_{1,\alpha} + n_\beta\sqrt{\frac{(\mathbf{r}_{1,\alpha}\cdot\mathbf{r}_{1,\alpha})}{(\mathbf{r}_{1,\beta}\cdot\mathbf{r}_{1,\beta})}}\,\mathbf{r}_{1,\beta} + \mathbf{r}_{2p,s} = 0 \tag{45}$$

where n_α and n_β are the directional cosines of the normal along the boundary of the defining domain of curvilinear coordinates α and β. Through Eqs. (41) and (43), the boundary condition in Eqs. (44) and (45) imply that

for the $\mathbf{r}_1$ surface,

$$n_\alpha\mathbf{r}_{1,\beta} - n_\beta\mathbf{r}_{1,\alpha} + \mathbf{r}_{1p,s} = 0, \tag{46}$$

and for the $\mathbf{r}_2$ surface,

$$n_\alpha\mathbf{r}_{2,\beta} - n_\beta\mathbf{r}_{2,\alpha} + \mathbf{r}_{2p,s} = 0. \tag{47}$$

3 Vibration Equations for a Minimum Surface Membrane

Consider now a minimum surface membrane S bounded by ∂S as described in the previous section. Let $\mathbf{w}$ denote the position vector of the vibrating surface membrane, measured from the original minimum surface membrane. As for $\mathbf{r}$, we may express $\mathbf{w}$ as follows:

$$\mathbf{w} = w_x\mathbf{e}_1 + w_y\mathbf{e}_2 + w_z\mathbf{e}_3 \tag{48}$$

where $\mathbf{e}_i (i = 1, 2, 3)$ are the unit vectors of the three-dimensional Euclidean space, and w_x, and w_y, and w_z are single-valued functions and are expressed, in terms of the curvlinear coordinates α and β on the original minimum surface membrane S, as

$$w_x = g_1(\alpha,\beta) \quad w_y = g_2(\alpha,\beta) \quad w_z = g_3(\alpha,\beta). \tag{49}$$

Now let an initial uniformly distributed membrane tension Γ, be acting in the surface membrane. We assume that Γ is relatively large and it remains constant as the surface membrane executes small oscillations. Thus the product of the change of surface area and the membrane tension Γ yields the potential energy

$$\Pi_p = \int_t\int_\alpha\int_\beta \Gamma\{\sqrt{[(\mathbf{r}_{,\alpha}+\mathbf{w}_{,\alpha})\cdot(\mathbf{r}_{,\alpha}+\mathbf{w}_{,\alpha})][(\mathbf{r}_{,\beta}+\mathbf{w}_{,\beta})\cdot(\mathbf{r}_{,\beta}+\mathbf{w}_{,\beta})]} - \sqrt{(\mathbf{r}_{,\alpha}\cdot\mathbf{r}_{,\alpha})(\mathbf{r}_{,\beta}\cdot\mathbf{r}_{,\beta})}\}\,d\alpha\,d\beta\,dt. \tag{50}$$

If the surface membrane has a constant density ρ_o per unit area, then the complementary kinetic energy of the surface membrane may be computed by

$$\Pi_k = \frac{1}{2}\int_t\int_\alpha\int_\beta \rho_o\sqrt{(\mathbf{r}_{,\alpha}\cdot\mathbf{r}_{,\alpha})(\mathbf{r}_{,\beta}\cdot\mathbf{r}_{,\beta})}\;(\dot{\mathbf{w}}\cdot\dot{\mathbf{w}})\,d\alpha\,d\beta\,dt \tag{51}$$

where $\dot{\mathbf{w}}$ is the velocity vector.

Now the Lagrangian

$$L = \Pi_k - \Pi_p \tag{52}$$

may be extremized, with respect to $\mathbf{w}$, to yield

$$\delta L = \int_t\int_\alpha\int_\beta \Gamma\left\{\frac{\partial}{\partial\alpha}\left[\sqrt{\frac{(\mathbf{r}_{,\beta}+\mathbf{w}_{,\beta})\cdot(\mathbf{r}_{,\beta}+\mathbf{w}_{,\beta})}{(\mathbf{r}_{,\alpha}+\mathbf{w}_{,\alpha})\cdot(\mathbf{r}_{,\alpha}+\mathbf{w}_{,\alpha})}}\,(\mathbf{r}_{,\alpha}+\mathbf{w}_{,\alpha})\right] + \frac{\partial}{\partial\beta}\left[\sqrt{\frac{(\mathbf{r}_{,\alpha}+\mathbf{w}_{,\alpha})\cdot(\mathbf{r}_{,\alpha}+\mathbf{w}_{,\alpha})}{(\mathbf{r}_{,\beta}+\mathbf{w}_{,\beta})\cdot(\mathbf{r}_{,\beta}+\mathbf{w}_{,\beta})}}\,(\mathbf{r}_{,\beta}+\mathbf{w}_{,\beta})\right] - \rho_o\sqrt{(\mathbf{r}_{,\alpha}\cdot\mathbf{r}_{,\alpha})(\mathbf{r}_{,\beta}\cdot\mathbf{r}_{,\beta})}\;\ddot{\mathbf{w}}\right\}\cdot\delta\mathbf{w}\,d\alpha\,d\beta\,dt$$

$$-\int_t\oint_{\partial S}\left(n_\alpha\left[\sqrt{\frac{(\mathbf{r}_{,\beta}+\mathbf{w}_{,\beta})\cdot(\mathbf{r}_{,\beta}+\mathbf{w}_{,\beta})}{(\mathbf{r}_{,\alpha}+\mathbf{w}_{,\alpha})\cdot(\mathbf{r}_{,\alpha}+\mathbf{w}_{,\alpha})}}\,(\mathbf{r}_{,\alpha}+\mathbf{w}_{,\alpha})\right] + n_\beta\left[\sqrt{\frac{(\mathbf{r}_{,\alpha}+\mathbf{w}_{,\alpha})\cdot(\mathbf{r}_{,\alpha}+\mathbf{w}_{,\alpha})}{(\mathbf{r}_{,\beta}+\mathbf{w}_{,\beta})\cdot(\mathbf{r}_{,\beta}+\mathbf{w}_{,\beta})}}\,(\mathbf{r}_{,\beta}+\mathbf{w}_{,\beta})\right]\right)\cdot\delta\mathbf{w}\,ds\,dt$$

$$-\int_\alpha\int_\beta \rho_o\sqrt{(\mathbf{r}_{,\alpha}\cdot\mathbf{r}_{,\alpha})(\mathbf{r}_{,\beta}\cdot\mathbf{r}_{,\beta})}\;\dot{\mathbf{w}}\cdot\delta\mathbf{w}\,d\alpha\,d\beta\Big|_{t_0}^{t} = 0. \tag{53}$$

As is customary, we assume that $\delta\mathbf{w} = 0$ at t_0 and t and therefore the last term in Eqs. (53) drops out. Equations (53) yield the governing equations and the associated boundary conditions along ∂S as follows.

Governing equations (in the domain S):

Downloaded 03 May 2010 to 171.66.16.245. Redistribution subject to ASME license or copyright; see http://www.asme.org/terms/Terms_Use.cfm

$$\frac{\partial}{\partial\alpha}\left[\sqrt{\frac{(\mathbf{r}_{,\beta}+\mathbf{w}_{,\beta})\cdot(\mathbf{r}_{,\beta}+\mathbf{w}_{,\beta})}{(\mathbf{r}_{,\alpha}+\mathbf{w}_{,\alpha})\cdot(\mathbf{r}_{,\alpha}+\mathbf{w}_{,\alpha})}}\,(\mathbf{r}_{,\alpha}+\mathbf{w}_{,\alpha})\right]$$

$$+\frac{\partial}{\partial\beta}\left[\sqrt{\frac{(\mathbf{r}_{,\alpha}+\mathbf{w}_{,\alpha})\cdot(\mathbf{r}_{,\alpha}+\mathbf{w}_{,\alpha})}{(\mathbf{r}_{,\beta}+\mathbf{w}_{,\beta})\cdot(\mathbf{r}_{,\beta}+\mathbf{w}_{,\beta})}}\,(\mathbf{r}_{,\beta}+\mathbf{w}_{,\beta})\right]$$

$$=\rho\sqrt{(\mathbf{r}_{,\alpha}\cdot\mathbf{r}_{,\alpha})(\mathbf{r}_{,\beta}\cdot\mathbf{r}_{,\beta})}\;\ddot{\mathbf{w}} \quad (54)$$

where $\rho = \rho_o/\Gamma$.

The associated boundary conditions for the minimum surface membrane S, takes two forms: i) prescribed position vectors $\mathbf{r}_p$ along the boundary curve ∂S, this implies that

$$\delta\mathbf{w}=\mathbf{0}, \quad (55)$$

i.e.,

$$\mathbf{w}=\mathbf{w}_p \quad \text{(prescribed)}. \quad (56)$$

The other is the natural boundary condition, namely

$$n_\alpha\left[\sqrt{\frac{(\mathbf{r}_{,\beta}+\mathbf{w}_{,\beta})\cdot(\mathbf{r}_{,\beta}+\mathbf{w}_{,\beta})}{(\mathbf{r}_{,\alpha}+\mathbf{w}_{,\alpha})\cdot(\mathbf{r}_{,\alpha}+\mathbf{w}_{,\alpha})}}\,(\mathbf{r}_{,\alpha}+\mathbf{w}_{,\alpha})\right]$$

$$+n_\beta\left[\sqrt{\frac{(\mathbf{r}_{,\alpha}+\mathbf{w}_{,\alpha})\cdot(\mathbf{r}_{,\alpha}+\mathbf{w}_{,\alpha})}{(\mathbf{r}_{,\beta}+\mathbf{w}_{,\beta})\cdot(\mathbf{r}_{,\beta}+\mathbf{w}_{,\beta})}}\,(\mathbf{r}_{,\beta}+\mathbf{w}_{,\beta})\right]+\mathbf{r}_p=0 \quad (57)$$

where $\mathbf{r}_p$ is the prescribed vector of the dual surface membrane along the boundary ∂S.

Equations (54) and (57) are nonlinear and difficult to solve. To linearize, let us assume that $\mathbf{w}$ is a small quantity compared with $\mathbf{r}$, thus dropping the terms of $\mathbf{w}_{,\alpha}$ and $\mathbf{w}_{,\beta}$ under the square root, we obtain the corresponding linearized equations:

$$\frac{\partial}{\partial\alpha}\left[\sqrt{\frac{(\mathbf{r}_{,\beta}\cdot\mathbf{r}_{,\beta})}{(\mathbf{r}_{,\alpha}\cdot\mathbf{r}_{,\alpha})}}\,(\mathbf{r}_{,\alpha}+\mathbf{w}_{,\alpha})\right]+\frac{\partial}{\partial\beta}\left[\sqrt{\frac{(\mathbf{r}_{,\alpha}\cdot\mathbf{r}_{,\alpha})}{(\mathbf{r}_{,\beta}\cdot\mathbf{r}_{,\beta})}}\,(\mathbf{r}_{,\beta}+\mathbf{w}_{,\beta})\right]$$

$$=\rho\sqrt{(\mathbf{r}_{,\alpha}\cdot\mathbf{r}_{,\alpha})(\mathbf{r}_{,\beta}\cdot\mathbf{r}_{,\beta})}\;\ddot{\mathbf{w}} \quad (58)$$

and

$$n_\alpha\left[\sqrt{\frac{(\mathbf{r}_{,\beta}\cdot\mathbf{r}_{,\beta})}{(\mathbf{r}_{,\alpha}\cdot\mathbf{r}_{,\alpha})}}\,(\mathbf{r}_{,\alpha}+\mathbf{w}_{,\alpha})\right]$$

$$+n_\beta\left[\sqrt{\frac{(\mathbf{r}_{,\alpha}\cdot\mathbf{r}_{,\alpha})}{(\mathbf{r}_{,\beta}\cdot\mathbf{r}_{,\beta})}}\,(\mathbf{r}_{,\beta}+\mathbf{w}_{,\beta})\right]+\mathbf{r}_p=0. \quad (59)$$

Since the surface membrane is a minimum surface, the position vector $\mathbf{r}$ satisfies the governing Eqs. (10) and the associated boundary conditions (22). Thus, Eqs. (54) and (57) may be simplified to

$$\frac{\partial}{\partial\alpha}\left[\sqrt{\frac{(\mathbf{r}_{,\beta}\cdot\mathbf{r}_{,\beta})}{(\mathbf{r}_{,\alpha}\cdot\mathbf{r}_{,\alpha})}}\,\mathbf{w}_{,\alpha}\right]+\frac{\partial}{\partial\beta}\left[\sqrt{\frac{(\mathbf{r}_{,\alpha}\cdot\mathbf{r}_{,\alpha})}{(\mathbf{r}_{,\beta}\cdot\mathbf{r}_{,\beta})}}\,\mathbf{w}_{,\beta}\right]$$

$$=\rho\sqrt{(\mathbf{r}_{,\alpha}\cdot\mathbf{r}_{,\alpha})(\mathbf{r}_{,\beta}\cdot\mathbf{r}_{,\beta})}\;\ddot{\mathbf{w}} \quad (60)$$

and

$$n_\alpha\left[\sqrt{\frac{(\mathbf{r}_{,\beta}\cdot\mathbf{r}_{,\beta})}{(\mathbf{r}_{,\alpha}\cdot\mathbf{r}_{,\alpha})}}\,\mathbf{w}_{,\alpha}\right]+n_\beta\left[\sqrt{\frac{(\mathbf{r}_{,\alpha}\cdot\mathbf{r}_{,\alpha})}{(\mathbf{r}_{,\beta}\cdot\mathbf{r}_{,\beta})}}\,\mathbf{w}_{,\beta}\right]=0. \quad (61)$$

Equations (60) are second-order differential equations with variable coefficients. For a flat plane, which is a special case of minimum surface membranes ($\mathbf{r}_{,\alpha}\cdot\mathbf{r}_{,\alpha}=\mathbf{r}_{,\beta}\cdot\mathbf{r}_{,\beta}=$ *constant*), Eqs. (60) simplify to the classical membrane vibration equation (Tabarrok and Tong, 1993), if only the transverse motion is to be taken into account.

To study the free vibration of minimum surface membranes, let us assume a solution of the form

$$\mathbf{w}=\mathbf{w}_o e^{i\omega t} \quad (62)$$

where $i=\sqrt{-1}$, and ω is the natural frequency. Substituting into Eqs. (60), and dropping the subscript o for sake of simplicity, we obtain

$$\frac{\partial}{\partial\alpha}\left[\sqrt{\frac{(\mathbf{r}_{,\beta}\cdot\mathbf{r}_{,\beta})}{(\mathbf{r}_{,\alpha}\cdot\mathbf{r}_{,\alpha})}}\,\mathbf{w}_{,\alpha}\right]+\frac{\partial}{\partial\beta}\left[\sqrt{\frac{(\mathbf{r}_{,\alpha}\cdot\mathbf{r}_{,\alpha})}{(\mathbf{r}_{,\beta}\cdot\mathbf{r}_{,\beta})}}\,\mathbf{w}_{,\beta}\right]$$

$$+\rho\omega^2\sqrt{(\mathbf{r}_{,\alpha}\cdot\mathbf{r}_{,\alpha})(\mathbf{r}_{,\beta}\cdot\mathbf{r}_{,\beta})}\;\mathbf{w}=0. \quad (63)$$

The associated boundary conditions are the same as those in Eqs. (56) and (61) for prescribed and natural boundary conditions respectively, and for free vibration $\mathbf{w}_p = 0$.

It is relatively easy to show that the variational functional for the linearized free vibration of minimum surface membranes may be written as

$$\Pi=\frac{1}{2}\int_\alpha\int_\beta\left\{\sqrt{\frac{(\mathbf{r}_{,\beta}\cdot\mathbf{r}_{,\beta})}{(\mathbf{r}_{,\alpha}\cdot\mathbf{r}_{,\alpha})}}\,(\mathbf{w}_{,\alpha}\cdot\mathbf{w}_{,\alpha})+\sqrt{\frac{(\mathbf{r}_{,\alpha}\cdot\mathbf{r}_{,\alpha})}{(\mathbf{r}_{,\beta}\cdot\mathbf{r}_{,\beta})}}\,(\mathbf{w}_{,\beta}\cdot\mathbf{w}_{,\beta})\right.$$

$$\left.+\rho\omega^2\sqrt{(\mathbf{r}_{,\alpha}\cdot\mathbf{r}_{,\alpha})(\mathbf{r}_{,\beta}\cdot\mathbf{r}_{,\beta})}\,(\mathbf{w}\cdot\mathbf{w})\right\}d\alpha\,d\beta. \quad (64)$$

4 Free Vibration of Dual Minimum Surface Membranes

Let us use the energy functional described in the previous section to study the free vibration of dual surface membranes. The vectors $\mathbf{w}_1$ and $\mathbf{w}_2$ denote the vibrating displacement vectors on the dual minimum surface membranes, respectively. For the minimum surface membrane S_1, the governing equations and the associated boundary conditions are

$$\frac{\partial}{\partial\alpha}\left[\sqrt{\frac{(\mathbf{r}_{1,\beta}\cdot\mathbf{r}_{1,\beta})}{(\mathbf{r}_{1,\alpha}\cdot\mathbf{r}_{1,\alpha})}}\,\mathbf{w}_{1,\alpha}\right]+\frac{\partial}{\partial\beta}\left[\sqrt{\frac{(\mathbf{r}_{1,\alpha}\cdot\mathbf{r}_{1,\alpha})}{\mathbf{r}_{1,\beta}\cdot\mathbf{r}_{1,\beta})}}\,\mathbf{w}_{1,\beta}\right]$$

$$+\rho\omega^2\sqrt{(\mathbf{r}_{1,\alpha}\cdot\mathbf{r}_{1,\alpha})(\mathbf{r}_{1,\beta}\cdot\mathbf{r}_{1,\beta})}\;\mathbf{w}_1=0 \quad (65)$$

and

$$n_\alpha\left[\sqrt{\frac{(\mathbf{r}_{1,\beta}\cdot\mathbf{r}_{1,\beta})}{(\mathbf{r}_{1,\alpha}\cdot\mathbf{r}_{1,\alpha})}}\,\mathbf{w}_{1,\alpha}\right]+n_\beta\left[\sqrt{\frac{(\mathbf{r}_{1,\alpha}\cdot\mathbf{r}_{1,\alpha})}{(\mathbf{r}_{1,\beta}\cdot\mathbf{r}_{1,\beta})}}\,\mathbf{w}_{1,\beta}\right]=0. \quad (66)$$

or

$$\mathbf{w}_1=0. \quad (67)$$

For the free vibration of the minimum surface membrane S_2, which is the dual surface membrane to S_1, we may write the governing equations and the related boundary conditions as follows:

$$\frac{\partial}{\partial\alpha}\left[\sqrt{\frac{(\mathbf{r}_{2,\beta}\cdot\mathbf{r}_{2,\beta})}{(\mathbf{r}_{2,\alpha}\cdot\mathbf{r}_{2,\alpha})}}\,\mathbf{w}_{2,\alpha}\right]+\frac{\partial}{\partial\beta}\left[\sqrt{\frac{(\mathbf{r}_{2,\alpha}\cdot\mathbf{r}_{2,\alpha})}{(\mathbf{r}_{2,\beta}\cdot\mathbf{r}_{2,\beta})}}\,\mathbf{w}_{2,\beta}\right]$$

$$+\rho\omega^2\sqrt{(\mathbf{r}_{2,\alpha}\cdot\mathbf{r}_{2,\alpha})(\mathbf{r}_{2,\beta}\cdot\mathbf{r}_{2,\beta})}\;\mathbf{w}_2=0 \quad (68)$$

and

$$n_\alpha\left[\sqrt{\frac{(\mathbf{r}_{2,\beta}\cdot\mathbf{r}_{2,\beta})}{(\mathbf{r}_{2,\alpha}\cdot\mathbf{r}_{2,\alpha})}}\,\mathbf{w}_{2,\alpha}\right]+n_\beta\left[\sqrt{\frac{(\mathbf{r}_{2,\alpha}\cdot\mathbf{r}_{2,\alpha})}{(\mathbf{r}_{2,\beta}\cdot\mathbf{r}_{2,\beta})}}\,\mathbf{w}_{2,\beta}\right]=0 \quad (69)$$

or

$$\mathbf{w}_2=0. \quad (70)$$

It is worth noting that the governing equations and the related boundary conditions for the free vibration of dual minimum surface membranes take the same form. If $\mathbf{w}_1$ and $\mathbf{w}_2$ are replaced by $\mathbf{w}$, thus the only difference is the variable coefficients, which are the first fundamental coefficients of the surface. Using Eqs. (26) and noting Eqs. (28) and (29) in Section 2.2, the governing equations and the associated boundary conditions for both minimum surface membranes may be rewritten as

Downloaded 03 May 2010 to 171.66.16.245. Redistribution subject to ASME license or copyright; see http://www.asme.org/terms/Terms_Use.cfm

$$\frac{\partial}{\partial\alpha}\left[F_1(\alpha,\beta)\mathbf{w}_{i,\alpha}\right]+\frac{\partial}{\partial\beta}\left[\frac{1}{F_1(\alpha,\beta)}\,\mathbf{w}_{i,\beta}\right]+\rho\omega^2F_2(\alpha,\beta)\mathbf{w}_i=0 \quad (71)$$

and

$$n_\alpha\left[F_1(\alpha,\beta)\mathbf{w}_{i,\alpha}\right]+n_\beta\left[\frac{1}{F_1(\alpha,\beta)}\,\mathbf{w}_{i,\beta}\right]=0 \quad (72)$$

or

$$\mathbf{w}_i=0 \quad (73)$$

where the subscript i of $\mathbf{w}$ denotes the vibrating displacement vectors of minimum surface membrane S_1 ($i = 1$) and its dual minimum surface S_2 ($i = 2$), respectively, and

$$F_1(\alpha,\beta)=\sqrt{\frac{(\mathbf{r}_{1,\beta}\cdot\mathbf{r}_{1,\beta})}{(\mathbf{r}_{1,\alpha}\cdot\mathbf{r}_{1,\alpha})}}=\sqrt{\frac{(\mathbf{r}_{2,\beta}\cdot\mathbf{r}_{2,\beta})}{(\mathbf{r}_{2,\alpha}\cdot\mathbf{r}_{2,\alpha})}} \quad (74)$$

$$F_2(\alpha,\beta)=\sqrt{(\mathbf{r}_{1,\beta}\cdot\mathbf{r}_{1,\beta})(\mathbf{r}_{1,\alpha}\cdot\mathbf{r}_{1,\alpha})}=\sqrt{(\mathbf{r}_{2,\beta}\cdot\mathbf{r}_{2,\beta})(\mathbf{r}_{2,\alpha}\cdot\mathbf{r}_{2,\alpha})}. \quad (75)$$

Now it is evident that the governing equations and the associated boundary conditions for the surface membrane S_1 are identical to those for the dual surface membrane S_2. Noting that "the defining domain of the curvilinear coordinates α and β and its boundary are the same," we conclude that the minimum surface membranes S_1 and S_2 have identical natural frequencies and vibrating modes, if both surface membranes have either prescribed (namely, boundary condition in Eq. (73)) or "free" (namely, boundary condition in Eq. (72)), along the same boundary in the defining domain of the curvilinear coordinates $\alpha - \beta$. This conclusion may be stated as: dual minimum surface membranes not only have the same surface areas but also have the same natural frequencies and modes of vibration.

5 A Numerical Example

In this section we investigate the free vibration of two minimum surface membranes, the catenoid and the helicoid, as an illustration of the foregoing theory.

5.1 Governing Equation. Taking advantage of the symmetry of these surfaces, we consider half a catenoid and half a helicoid. The position vectors $\mathbf{r}_1$ and $\mathbf{r}_2$ on the half catenoid and helicoid surfaces, respectively, are given in Eqs. (28) and (40). As discussed in the previous section, it is evident that the defining domain of the catenoid $\mathbf{r}_1$ and the helicoid $\mathbf{r}_2$ on $\alpha - \beta$ plane are identical that is, α varies from 0 to 2π and β ranges from 0 to $d\sinh(h/d)$. The boundary curves in the $\alpha - \beta$ plane: α ranges from 0 to 2π while β takes 0, which corresponds to the bottom edge of the half catenoid and the outer edge of the half helicoid, and $d\sinh(h/d)$, which corresponds to the upper edge of the half catenoid and the inner edge of the half helicoid.

Now let us compute the first fundamental coefficients of the catenoid and the helicoid. Using Eqs. (30) and (34), we find

$$(\mathbf{r}_{1,\alpha}\cdot\mathbf{r}_{1,\alpha})=f^2(\beta)\quad(\mathbf{r}_{1,\beta}\cdot\mathbf{r}_{1,\beta})=1. \quad (76)$$

$$(\mathbf{r}_{2,\alpha}\cdot\mathbf{r}_{2,\alpha})=f^2(\beta)\quad(\mathbf{r}_{2,\beta}\cdot\mathbf{r}_{2,\beta})=1. \quad (77)$$

Thus, the first fundamental coefficients of the half catenoid are identical to those of the half helicoid, namely,

$$(\mathbf{r}_{1,\alpha}\cdot\mathbf{r}_{1,\alpha})=(\mathbf{r}_{2,\alpha}\cdot\mathbf{r}_{2,\alpha})=f^2(\beta)\,(\mathbf{r}_{1,\beta}\cdot\mathbf{r}_{1,\beta})=(\mathbf{r}_{2,\beta}\cdot\mathbf{r}_{2,\beta})=1, \quad (78)$$

and the free vibration equations for both the catenoid and the helicoid can be rewritten as

$$\frac{\partial}{\partial\alpha}\left[\frac{1}{f(\beta)}\,\mathbf{w}_{,\alpha}\right]+\frac{\partial}{\partial\beta}\left[f(\beta)\mathbf{w}_{,\beta}\right]+\rho\omega^2f(\beta)\mathbf{w}=0. \quad (79)$$

Let us assume

$$\mathbf{w}=\mathbf{u}\cos n\alpha \quad (80)$$

where n is the circumferential wave number of the vibrating mode. Substituting into Eq. (79), we have

$$\frac{d}{d\beta}\left[f(\beta)\frac{d\mathbf{u}}{d\beta}\right]+\left[\rho\omega^2f(\beta)-\frac{n^2}{f(\beta)}\right]\mathbf{u}=0. \quad (81)$$

The associated prescribed or free boundary conditions are given, respectively, by

$$\mathbf{u}=0\quad\text{at}\quad\beta=0,\quad\text{and}\quad\beta=d\sinh\left(\frac{h}{d}\right) \quad (82)$$

or

$$\frac{d\mathbf{u}}{d\beta}=0\quad\text{at}\quad\beta=0,\quad\text{and}\quad\beta=d\sinh\left(\frac{h}{d}\right). \quad (83)$$

The eigenvalues ω and the associated eigenfunctions of Eq. (81) may be computed using Eq. (82) if the surface membranes are clamped or Eq. (83) if the surface membranes are free.

5.2 Solution. To solve, let us introduce the following transformation:

$$x=\sinh^{-1}\left[\frac{\beta}{d}-\sinh\left(\frac{h}{d}\right)\right]-\frac{h}{d} \quad (84)$$

Substituting into Eq. (81) and taking note of Eq. (29), we have

$$\frac{d^2\mathbf{u}}{dx^2}+\left[\rho\omega^2d^2\cosh^2\left(x-\frac{h}{d}\right)-n^2\right]\mathbf{u}=0\left(0\le x\le l=\frac{h}{d}\right). \quad (85)$$

Equation (85) may be solved using the Galerkin method. For the "clamped" boundary condition, let us assume

$$\mathbf{u}=c_0\sin\frac{m\pi x}{l} \quad (86)$$

Substituting into Eq. (85), we obtain the frequency parameter as follows:

$$\lambda=\rho\omega^2=\frac{4(l^2n^2+m^2\pi^2)\,(l^2+m^2\pi^2)}{ld^2[2l(l^2+m^2\pi^2)+m^2\pi^2\sinh 2l]}. \quad (87)$$

The frequency parameter λ versus the circumferential wave number n is plotted in Fig. 5, and Table 1 gives the frequency parameter λ versus the circumferential wave number n and the longitudinal wave number m. It is worth noting that the axi-

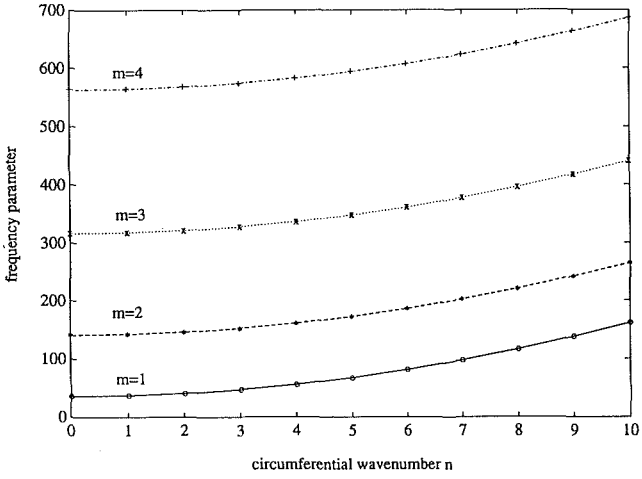


Fig. 5 Frequency parameter versus circumferential wave number

Downloaded 03 May 2010 to 171.66.16.245. Redistribution subject to ASME license or copyright; see http://www.asme.org/terms/Terms_Use.cfm

Table 1 Frequency parameters ρw^2

n	$m=1$	$m=2$	$m=3$	$m=4$	$m=5$	$m=6$
0	35.795	141.163	316.763	562.602	878.680	1264.998
1	37.055	142.405	318.002	563.840	879.917	1266.234
2	40.835	146.131	321.718	567.552	883.628	1269.945
3	47.134	152.342	327.912	573.740	889.814	1276.128
4	55.954	161.036	336.583	582.404	898.473	1284.786
5	67.292	172.215	347.732	593.542	909.607	1295.917
6	81.151	185.879	361.359	607.156	923.214	1309.521
7	97.530	202.026	377.463	623.245	939.296	1325.599
8	116.428	220.658	396.045	641.809	957.852	1344.151
9	137.846	241.774	417.104	662.848	978.882	1365.176
10	161.783	265.374	440.640	686.362	1002.386	1388.674
11	188.241	291.458	466.655	712.352	1028.365	1414.646
12	217.218	320.027	495.147	740.817	1056.817	1443.092
13	248.715	351.079	526.116	771.757	1087.743	1474.011
14	282.732	384.616	559.563	805.172	1121.144	1507.404
15	319.268	420.638	595.487	841.063	1157.019	1543.270

symmetric vibration mode with $m = 1$ gives the lowest frequency. This is due to the fact that the minimal surface membrane is an isostress surface, and does not have bending stiffness. Thus, the vibrating mode corresponding to the lowest frequency will result in negligible variation in the isostress state.

6 Concluding Remarks

The salient points of this investigation include: (1) the linear free vibration equations for minimum surface membrane are derived; (2) it is shown that dual minimum surface membranes not only have the same surface areas but also have identical natural frequencies and vibrating modes under the same boundary conditions, (3) the free vibrations of a half catenoid and a half helicoid are investigated in an illustrative example.

References

Conus, P., 1967, "Numerical Solutions of the Minimal Surfaces," *Math. Comp.*, Vol. 21, pp. 340–350.

Greenspan, D., 1965, "On Approximating Extremals of Functions. I: The Method and Examples for Boundary Value Problems," *ICC Bull.*, Vol. 4, pp. 99–120.

Greenspan, D., 1967, "On Approximating Extremals of Functions. II. Theory and Generalization Related to Boundary Value Problems for Nonlinear Differential Equations," *Int. J. Eng. Sci.*, Vol. 5, pp. 571–588.

Hewgill, D. E., 1984, "Computing Surfaces of Constant Mean Curvature With Singularities," *Computing*, Vol. 32, pp. 81–92.

Hinata, M., Shimasaki, M., and Kiyono, T., 1977, "Numerical Solution of Plateau's Problem," *Math. Comp.*, Vol. 19, pp. 35–58.

Tabarrok, B., and Xiong, Y., 1991, "Some Variational Formulations for Minimal Surfaces," *Acta Mechanica*, Vol. 89, pp. 33–43.

Tabarrok, B., and Tong, L., 1991, "Dualities in Minimum Surfaces," *The Finite Element Method in the 1990's* (A book dedicated to O. C. Zienkiewicz), E. Onate, J. Periaux, and A. Samuelsson, Springer-Verlag, New York, pp. 565–573.

Tabarrok, B., and Tong, L., 1992, "New Variational Formulations for Minimal Surfaces," *Int. Journal for Numerical Methods in Engineering*, Vol. 35, pp. 491–502.

Volterra, E., and Zachmanoglou, E. C., 1965, "Dynamics of Vibrations," Charles E. Merrill, Columbus, Ohio, p. 272.

Wagner, H.-J., 1977, "A Contribution to the Numerical Approximation of Minimal Surfaces," *Computing*, Vol. 19, pp. 35–58.

Downloaded 03 May 2010 to 171.66.16.245. Redistribution subject to ASME license or copyright; see http://www.asme.org/terms/Terms_Use.cfm

B. C. Yang[1]

F. B. Cheung[2]
Mem. ASME

Department of Mechanical Engineering,
The Pennsylvania State University,
University Park, PA 16802

J. H. Koo
Naval Systems Division,
FMC Corporation,
Minneapolis, MN 55421

Modeling of One-Dimensional Thermomechanical Erosion of High-Temperature Ablatives

A one-dimensional material erosion model has been developed to describe the simultaneous processes of thermochemical ablation and mechanical erosion of ablatives exposed to high-temperature particle-laden flows. The model accounts for the effect of mechanical erosion due to thermochemical weakening of the material and the influence of particle impact on the thermochemical ablation. Numerical calculations of the erosion depth (i.e., surface recession) have been made for various thermal and particle loading conditions. The predicted results are found to agree reasonably well with available experimental data.

1 Introduction

The thermal, mechanical, and chemical performance of ablatives in a hostile environment, typical of those produced by solid rocket exhaust, is of important concern in the design of advanced missile launching systems. Previous studies of erosion of ablatives have been focused primarily on thermochemical ablation (i.e., thermal decomposition and thermal erosion) due to direct rocket exhaust impingement. However, severe erosion problems could also result from mechanical erosion (i.e., direct particle impacts on the ablative). To assure the integrity and prolong the lifetime of the launcher, suitable ablatives need to be selected to protect the interior structure of the launching system. This goal can be accomplished by first achieving a better understanding of the erosion pattern of the candidate ablatives subjected to thermal and mechanical attack of solid rocket exhaust.

Mechanical erosion is a special form of wear that occurs when high-speed solid particles impact against an ablative. When an ablative is subjected to the attack of an impinging particle at a small impact angle (say 0 deg $\leq \theta \leq$ 5 deg), a compressive force is introduced by the impact (Soo, 1983; Kitron, Eljerin and Tamir, 1989). Material erosion would occur in the albative when the compressive stress F_b/A_m is greater than the compression yielding stress σ_b of the ablative. This so-called deformation wear usually occurs in brittle materials (Finnie 1960; Nielson and Gilchrist 1968). The erosion mechanism associated with deformation wear involves a constant battering or fatigue of the target surface leading eventually to subsurface cracking or spalling of the target. On the other hand, when an ablative is subjected to the attack of an impinging particle at a large impact angle (say 60 deg $\leq \theta \leq$ 70 deg), a machining force is introduced by the impact. Material erosion would occur in the ablative when the shearing stress F_d/A_m is greater than the shear yielding stress σ_d of the ablative. This so-called cutting wear usually occurs in ductile materials (Finnie 1960; Neilson and Gilchrist 1968). The erosion mechanism associated with cutting wear involves cutting or micromachining of the target surface with the sharp corner of particles acting as a miniature single-point machine tool. For a brittle and ductile material, the total mechanical erosion can be obtained as a linear combination of the deformation wear and cutting wear as suggested by Soo (1977). This is true especially when the behavior of the particle impact deviates only slightly from elastic.

When the surface of an ablative is attacked thermally and mechanically by a high-temperature particle-laden flow, both thermochemical ablation and mechanical erosion could take place simultaneously and interact with one another (Koo et al., 1991, 1992). So far no physical model has been developed that includes both thermochemical ablation and mechanical erosion. The only reported modeling effort is that by Mockenhaupt and Wickman (1983), who studied the subsonic erosion in rocket nozzles using the "G-law" approach, where G is the ratio of mass flux of target material removed to mass flux of particle incident on the surface. This approach, however, is largely empirical and has no theoretical basis. The objective of this study is to develop an overall material erosion model. The goal is to relate the erosion rate to the thermal and mechanical properties of the ablative and the erosion parameters of the system. The ablative will be treated as ductile and brittle, allowing both deformation wear and cutting wear to take place simultaneously.

2 Mathematical Formulation

Consider an impinging particle at a velocity v and an angle

[1]Presently with the Energy Resources Laboratories, ITRI, Taiwan, R.O.C.
[2]To whom correspondence should be addressed.

Contributed by the Applied Mechanics Division of THE AMERICAN SOCIETY OF MECHANICAL ENGINEERS for presentation at the ASME Winter Annual Meeting, New Orleans, LA., Nov. 28–Dec. 3, 1993.

Discussion on this paper should be addressed to the Technical Editor, Professor Lewis T. Wheeler, Department of Mechanical Engineering, University of Houston, Houston, TX 77204-4792, and will be accepted until four months after final publication of the paper itself in the ASME JOURNAL OF APPLIED MECHANICS.

Manuscript received by the ASME Applied Mechanics Division, Feb. 12, 1992; final revision, Sept. 29, 1992. Associate Technical Editor: R. M. Bowen.

Paper No. 93-WA/APM-1.

Copyright © 1993 by ASME
Downloaded 03 May 2010 to 171.66.16.245. Redistribution subject to ASME license or copyright; see http://www.asme.org/terms/Terms_Use.cfm

θ impacting on an ablative. The compressive (F_b) and tangential (F_d) forces acting on the ablative due to the particle impact can be expressed by Hertz equation (Timoshenko and Goodier, 1969):

$$F_b = \left[\frac{4\sqrt{r_p}}{3\pi(K_p+K_w)}\right]^{2/5}\left[\frac{1+\epsilon}{2}\frac{5m}{4}v_i^2\cos\theta\right]^{3/5} \quad (1)$$

$$F_d = \eta_w F_b + F_b \tan\theta, \quad (2)$$

where r_p is the radius of the particle, m the particle mass, v_i the particle impact velocity, θ the impact angle, ϵ the coefficient of restitution, η_w the coefficient of friction between the particle and the ablative, and K_p, K_w are the coefficients for the particle and the ablative defined, respectively, by

$$K_p = \frac{1-v_p^2}{\pi E_p} \text{ and } K_w = \frac{1-v_w^2}{\pi E_w}. \quad (3)$$

In the above equation, v_p is the Poisson's ratio of the particle, v_w the Poisson's ratio of the ablative, E_p the elastic modulus of the particle, and E_w the elastic modulus of the ablative.

In the brittle mode of erosion, the prevailing mechanism is the deformation wear caused by the compressive force F_b. The volume loss per impact can be expressed as (Soo, 1983)

$$W_b = \frac{\eta_b\left[C_b\frac{F_b}{A_m}-\sigma_b\right](v_i\cos\theta)A_m t_d}{\epsilon_b}, \quad (4)$$

where η_b is the deformation efficiency of impact including the effects of gliding, scattering, and lifting of the particle by the gas stream, C_b the deformation wear correction factor for the nonsphericity of the actual particles, stress concentration at sharp edge, roughness of the target surface and nonspecular reflection of an actual surface, $A_m (= \pi r_c^2)$ the maximum contact area during the impact, σ_b the compression yielding stress, t_d the duration of impact, and ϵ_b the erosion energy for the deformation wear.

According to Soo (1983), the radius of the maximum contact area r_c and the duration of the impact t_d are given, respectively, by

$$r_c = \left[\frac{3\pi}{4}F_b(K_p+K_w)r_p\right]^{1/3}$$

$$\text{and } t_d = \frac{1.47}{v_i\cos\theta}\left[\frac{1+\epsilon}{2}\frac{5m}{4n}v_i^2\cos\theta\right]^{2/5} \quad (5)$$

where the quantity n is defined as

$$n = \frac{4\sqrt{r_p}}{3\pi(K_p+K_w)}. \quad (6)$$

In the ductile mode of erosion, the prevailing mechanism is the cutting wear caused by the tangential force F_d. The volume loss per impact can be expressed as (Soo, 1983)

$$W_d = \frac{\eta_d\left[C_d\frac{F_d}{A_m}-\sigma_d\right](v_i\sin\theta)A_m t_d}{\epsilon_d}, \quad (7)$$

where η_d is the cutting efficiency of impact including the effects of gliding, scattering, and lifting of the particle by the gas stream; C_d the cutting wear correction factor for the nonsphericity of the actual particles, stress concentration at sharp edge, roughness of the target surface, and nonspecular reflection of an actual surface; σ_d, the shear yielding stress; and ϵ_d, the erosion energy for the cutting wear.

For most ablatives, the mechanical erosion can be treated as a linear combination of the ductile and brittle modes (Soo, 1977). Hence, the extent of erosion caused by particle impact can be written as

$$W_t = W_b + W_d \quad (8)$$

where W_t is the total volume loss per impact. By defining δ_m as the equivalent surface recession due to mechanical erosion, f_v the fraction of particle contributed to the mechanical erosion, and N the number of particles impacing on the ablative per unit area and time, we have

$$\frac{\partial\delta_m}{\partial t} = f_v N(W_d + W_b) = f_v N W_t \quad (9)$$

where the incoming particles are assumed to have the same size. This assumption can be relaxed in future modeling effort by using a suitable probability density function to describe the poly-dispersed particle size distribution.

To determine the total material erosion, including both the thermochemical ablation and mechanical erosion, two sequential phases are considered.

2.1 Developing Phase. Consider a small control volume of the ablative. From the conservation of mass, the following continuity equation can be derived:

$$-\frac{\partial\rho_s}{\partial t} = \frac{\partial}{\partial x}(\rho_g v_x) + \frac{\partial\rho_g}{\partial t} = \frac{\partial}{\partial x}(\dot{m}_x'') + \frac{\partial\rho_g}{\partial t} \quad (10)$$

where ρ_s is the local density of the ablative, ρ_g the density of the decomposition gases accumulated inside the ablative, v_x the velocity of the decomposition gases flowing through the ablative, and $\dot{m}_x''$ the rate of mass flux of the decomposition gases. The rate of mass change in the ablative can be calculated from the kinetic rate equation:

$$\frac{1}{\rho_0}\frac{\partial\rho_s}{\partial t} = -A_j\left(\frac{\rho_s-\rho_{f_j}}{\rho_0}\right)^{n_j}\exp\left(-\frac{E_j}{RT}\right), \quad (11)$$

where ρ_0 is the initial density of the ablative, ρ_{f_j} the final density of the ablative, A_j the pre-exponential factor, n_j the order of reaction, E_j the activation energy, R the universal gas constant, and T the local temperature of the ablative. In the above terms, the subscript $j(=1, 2)$ stands for the virgin material and char residue.

Within the porous char layer, the velocity of the decomposition gases is relatively small compared to the incident gas flow (i.e., the rocket exhaust) as the erosion process is relatively slow. Thus, the mass fluxes of the decomposition gases can be derived from the Darcy's law (Collins, 1961). This is

$$\dot{m}_x'' = -\frac{\gamma_s\rho_g}{\mu_g\phi}\frac{\partial p}{\partial x}, \quad (12)$$

where γ_s is the permeability of the ablative, ϕ the porosity of the ablative, p the gas pressure, and μ_g the viscosity of the decomposition gases. The gas pressure (p) can be calculated from the equation of state, i.e.,

$$p = \frac{\rho_g RT}{M\phi}, \quad (13)$$

where M is the molecular weight of the gases. By performing an energy balance on the control volume, we get

$$\dot{q}_s = \dot{q}_{\text{cond}} + \dot{q}_{\text{chem}} + \dot{q}_{\text{conv}} \quad (14)$$

where $\dot{q}_s$ is the net rate of energy change in the ablative, $\dot{q}_{\text{cond}}$ the rate of heat transfer by conduction, $\dot{q}_{\text{chem}}$ the rate of chemical heat generation, and $\dot{q}_{\text{conv}}$ the rate of convection heat transfer due to the flow of the decomposition gases through the ablative. These quantities are given by

$$\dot{q}_s = \frac{\partial}{\partial t}(\rho_s h_s + \rho_g h_g)$$

$$= (\rho_c C_{p_s} + \rho_g C_{p_g})\frac{\partial T}{\partial t} + h_s\frac{\partial\rho_s}{\partial t} + k_g\frac{\partial\rho_g}{\partial t} \quad (15)$$

$$\dot{q}_{\text{cond}} = \frac{\partial}{\partial x}\left\{[k_s(1-\phi)+k_g\phi]\frac{\partial T}{\partial x}\right\} \quad (16)$$

Downloaded 03 May 2010 to 171.66.16.245. Redistribution subject to ASME license or copyright; see http://www.asme.org/terms/Terms_Use.cfm

$$\dot{q}_{\text{chem}} = -Q_s \frac{\partial \rho_s}{\partial t} \tag{17}$$

$$\dot{q}_{\text{conv}} = k_g \frac{\partial \rho_s}{\partial t} - C_{p_g}\left(\dot{m}'' \frac{\partial T}{\partial x}\right) + h_g \frac{\partial \rho_g}{\partial t} \tag{18}$$

where h_s is the enthalpy of the ablative, h_g is the enthalpy of the decomposition gases, C_{p_s} the specific heat of the ablative, C_{p_g} the specific heat of the decomposition gases, k_s the conductivity of the ablative, k_g the conductivity of the decomposition gases, and Q_s the heat of decomposition of the ablative.

An overall energy equation for the process is obtained by substituting Eqs. (15)–(18) into Eq. (14):

$$(\rho_s C_{p_s} + \rho_g C_{p_g}) \frac{\partial T}{\partial t} = \frac{\partial}{\partial x}\left\{[k_s(1-\phi) + k_g\phi] \frac{\partial T}{\partial x}\right\} - (Q_s + h_s - k_g) \frac{\partial \rho_s}{\partial t} - C_{p_g}\left(\dot{m}_x'' \frac{\partial T}{\partial x}\right). \tag{19}$$

The term on the left-hand side of Eq. (19) represents the enthalpy change of the ablative, the first term on the right-hand side represents the conduction heat transfer along the x-axis, the second term represents the energy variation associated with the mass change, and the last term represents the energy variation due to gas flux (i.e., convection effect).

Thermal expansion of the ablative due to the temperature variation and material decomposition can be calculated using the expansion equation proposed by Buch (1982):

$$\frac{1}{L_o}\frac{\partial L}{\partial t} = \beta_v f \frac{\partial T}{\partial t} + \beta_c (1-f) \frac{\partial T}{\partial t} + \frac{\eta}{\rho_0}\frac{\partial \rho_s}{\partial t}, \tag{20}$$

where L_o is the initial length of the ablative, L the instantaneous length of the ablative, β_v the coefficient of linear expansion of the virgin material, β_c the coefficient of linear expansion of the char material, η a dimensionless decomposition expansion factor, and f the instantaneous mass fraction of the reactable material remaining. The last quantity is defined by

$$f = \frac{\rho_s - \rho_f}{\rho_o - \rho_f}, \tag{21}$$

where ρ_f is the final density of the ablative. The initial conditions for the process are

$$t = 0\text{: } \dot{m}_x'' = 0,\ p = p_0,\ T = T_0,\ \rho_s = \rho_0. \tag{22}$$

In the developing phase there is no thermochemical ablation, i.e., $\delta_t = 0$. The overall material erosion δ is due to mechanical erosion alone, i.e., $\delta = \delta_m$. The boundary condition at the eroded surface can be determined by performing an interfacial energy balance. The result is at $x = \delta$,

$$\dot{q}'' = \frac{1}{2} N m v_i^2 (1-\epsilon^2) = f_v N(\epsilon_d W_d + \epsilon W_b) - \left[k_s(1-\phi) + k_g\phi\right] \frac{\partial T}{\partial x}\bigg|_{x=\delta} \tag{23}$$

where $\dot{q}''$ is the input heat flux from the flow to the surface.

2.2 Developed Phase. Equations (10) to (21) which describe the various processes occurring inside the ablative still apply in this phase. Major differences arise due to the surface recession by thermochemical ablation. In the developed phase, both kinds of erosion (i.e., mechanical erosion and thermochemical ablation) would take place simultaneously in the ablative. The overall material erosion in this fully developed phase is given by

$$\delta = \delta_t + \delta_m. \tag{24}$$

The initial conditions are

$$t = t_1\text{: } \delta_t = 0,\ \delta = \delta_m \tag{25}$$

where t_1 is the time corresponding to the onset of surface recession due to thermochemical ablation.

The boundary condition at the eroded surface is obtained by adding the energy required for removing the char residue by thermochemical ablation into Eq. (23). This gives

$$\dot{q}'' = \frac{1}{2} N m v_i^2 (1-\epsilon^2) = f_v N(\epsilon_d W_d + \epsilon_b W_b) - [k_s(1-\phi) + k_g\phi] \frac{\partial T}{\partial x}\bigg|_{x=\delta} + \rho_s \Delta H_e \frac{\partial \delta_t}{\partial t} \tag{26}$$

where ρ_s is the instantaneous density of the ablative at the surface and ΔH_e the erosion energy (i.e., enthalpy change) due to the thermochemical ablation.

3 Numerical Solution

The system of equations governing the developing and developed phases are solved numerically using an implicit finite difference method. A variable grid structure is employed in the numerical analysis to account for the large temperature gradients near the front surface and relatively small temperature gradients in the subsurface region. Owing to surface recession caused by mechanical erosion and thermochemical ablation as well as thermal expansion caused by temperature variation and decomposition of the solid material, the total length of the computational domain is not a constant. To facilitate numerical computations, the total number of nodes is kept constant by allowing the grid size to change with time. Thus, the coordinate of the first node represents the surface recession.

The finite difference equations for the interior nodes are obtained using an implicit scheme with backward difference in time and central difference in space. On the other hand, the finite difference equations for the boundary nodes are obtained by taking forward difference in time and one-side difference in space. In doing so, a system of linear algebraic equations can be set up to represent the resulting finite difference equations as follows:

$$[A][T] = [R] \tag{27}$$

where the coefficient matrix $[A]$ is a tri-diagonal matrix, $[T]$ the temperature distribution, and $[R]$ a constant vector defined by

$$A = \begin{pmatrix} a_{11} & a_{12} & 0 & 0 & 0 & \cdots & 0 \\ a_{21} & a_{22} & a_{23} & 0 & 0 & \cdots & 0 \\ 0 & a_{32} & a_{33} & a_{34} & 0 & \cdots & 0 \\ \vdots & \vdots & \ddots & \ddots & \ddots & \vdots & \vdots \\ 0 & 0 & 0 & a_{(u-2),(u-3)} & a_{(u-2),(u-2)} & a_{(u-2),(u-1)} & 0 \\ 0 & 0 & 0 & 0 & a_{(u-1),(u-2)} & a_{(u-1),(u-1)} & a_{(u-1),u} \\ 0 & 0 & 0 & 0 & 0 & a_{(u),(u-1)} & a_{u,u} \end{pmatrix} \tag{28}$$

$$[T] = (T_1, T_2, \ldots\ldots, T_u)^T \tag{29}$$

$$[R] = (r_1, r_2, \ldots\ldots, r_u)^T \tag{30}$$

where u is the number of the nodes.

All the properties and rate of mass flux used in the equations are calculated by the temperature distribution from the previous time step. In this way, we can maintain the updated values and avoid too many interloops in the numerical procedure. Only two interloops are included in each computational step. One is for solving the Darcy's law, the continuity equation, and the equation of state. This is employed to obtain consistent values for the $\dot{m}_x''$, ρ_g and p. The other is for calculating thermochemical recession (δ_t). The goal is to calculate consistent values for δ_t and the temperature distribution. The

Downloaded 03 May 2010 to 171.66.16.245. Redistribution subject to ASME license or copyright; see http://www.asme.org/terms/Terms_Use.cfm

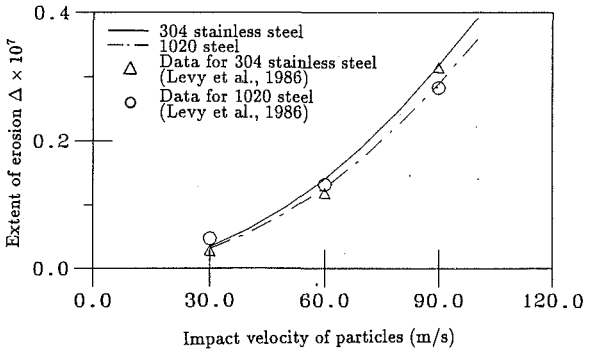


Fig. 1 Comparison of the predicted mechanical erosion with the experimental data for different impact velocities

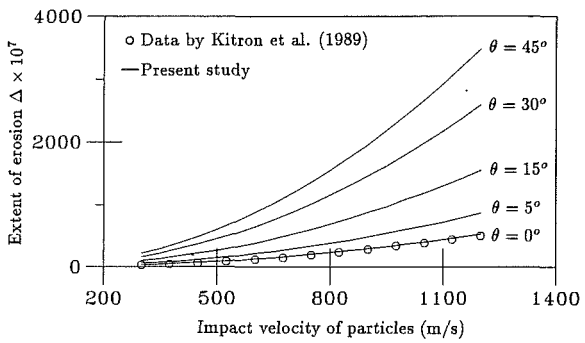


Fig. 2 Effect of impact angle on the extent of mechanical erosion

Table 1 Comparison between the predicted mechanical erosion and observed results

Material	Predicted results (m^3/kg)	Experimental data (m^3/kg)
1020 steel	3.074×10^{-8}	$(2.82 \pm 0.48) \times 10^{-8}$
304 stainless steel	3.739×10^{-8}	$(3.24 \pm 0.68) \times 10^{-8}$

first interloop is applied after the pyrolysis reaction begins at each node whereas the second is applied after the onset of surface recession due to thermochemical ablation.

The first interloop is obtained by substituting the equation of state and the Darcy's law into the continuity equation to eliminate the terms representing the mass flux and the mass of decomposition gases. In so doing, a system of equations is derived which can be represented by the following finite difference equations:

$$[AA][PP] = [RR] \tag{31}$$

where the coefficient matrix $[AA]$ is a tri-diagonal matrix, $[PP]$ the pressure at each node, and $[RR]$ a constant vector. Their definitions are similar to those given in Eqs. (28) to (30). A detailed description of the numerical work is given by Yang (1992).

4 Results and Discussion

To partially validate the computer model, the extent of mechanical erosion is calculated for the case of a uniform gas flow containing Al_2O_3 particles ($r_p = 50\ \mu m$) with a total mass of 0.3 kg impacting on: (i) type 1020 steel and (ii) type 304 stainless steel at different impact velocities. The impact angle used in the calculation is 60 deg. The predicted results are compared with the experimental data reported by Levy et al. (1986) in Fig. 1. In this figure, the extent of erosion, Δ(m^3/kg), is expressed in terms of the total volume of ablative eroded per kilogram of particles. Evidently, Δ is a strong function of the impact velocity. Below the velocity of 20 m/s (not shown in the figure), however, the predicted erosion is almost negligible. Overall, the predicted results agree favorably with the experimental data.

To further validate the computer model, another series of simulations is performed for the same particle and target material. The mass flow rate of Al_2O_3 is 2.0×10^{-3} kg/min and the mean particle radius is 25μm. The particles are impinging at a normal angle on the target plate with a constant velocity of 70 m/s for ten minutes. The predicted results are compared with the experimental data (Ruff, 1986) in Table 1. In view of the uncertainties in the shape and size distribution of the particles, the agreement is considered to be quite satisfactory. Note that the difference between the predicted results and the experimental data are on the same order of the experimental error.

Figure 2 illustrates the effect of impact angle on the extent of mechanical erosion for the case of silica particles with a radius of 0.5 mm and a total mass of 5×10^{-5} kg impacting on a steel plate at various impact angles and impact velocities. The results obtained by Kitron et al. (1989) for the special case of $\theta = 0$ deg (i.e., the normal impact) are also shown in the figure for comparison. In general, the value of Δ increases with increasing impact angle and impact velocity. The fact that Δ is a strong function of the impact angle clearly demonstrates the importance of the cutting wear in this case. Comparison of the results presented in Figs. 1 and 2 shows that the extent of mechanical erosion is strongly related to the impact velocity and particle size. The velocity of the silica particles is about ten times larger than the Al_2O_3 particles and the mean radius of the silica particles is also about ten times larger than that of Al_2O_3 particles. As a result, the extent of erosion is much larger for the case of silica particles.

The thermochemical ablation of MXBE-350, a high-temperature ablative currently used in the uptake section of a vertical launching system, is studied for the case of a constant input heat flux, using the properties reported by Henderson and Wiecek (1988). MXBE-350 is a composite material consisting of approximately 42 percent phenolic resin, 43 percent glass fibers, and 15 percent glass powder. Various values for the pyrolysis temperature, T_p, failure temperature, T_e, and erosion energy, ΔH_e are assumed in the numerical calculations to cover the range of uncertainties in these properties. The predicted recession distances (i.e., erosion depth) and elongation for different values of T_p, T_e, and ΔH_e are summarized in Table 2. The experimental data provided by Koo et al. (1991) are also shown in the table for comparison. It is found that (i) δ_i decreases with an increase in T_e (this means that an increase in the value of T_e would not only delay the onset of thermochemical ablation but also slow down the surface recession); (ii) there is a significant increase in the value of δ_i with a decrease in ΔH_e (this means that an increase in the value of ΔH_e would slow down the surface recession due to the consumption of a large portion of the input heat flux); (iii) an increase in the value of T_p would delay the pyrolysis reaction but the effect on the surface recession is small. Evidently, ΔH_e and T_e have more significant effects on the thermochemical ablation than T_p.

According to Koo et al. (1991), the values of T_p and T_e are taken to be approximately equal to 523K and 1273K, respectively. Calculations have been made for the thermochemical ablation of three different high-temperature ablatives, i.e., MXBE-350, H41N, and MXB-360. H41N is a composite material consisting of 39.5 percent phenolic resin and approximately 60.5 percent short glass fiber and talc. MXBE-360 is a composite material consisting of 42 percent phenolic resin and 58 percent glass fiber and powder. The calculated results are summarized in Table 3. Also given in the table are the data

Downloaded 03 May 2010 to 171.66.16.245. Redistribution subject to ASME license or copyright; see http://www.asme.org/terms/Terms_Use.cfm

Table 2 Summary of the predicted results for thermochemical ablation of MXBE-350

	T_p (K)	T_e (K)	ΔH_e (kJ/kg)	δ_t** (m)	Recession Rate*** (m/s)	Elongation**** (%)
1	623	1400	4324	4.124×10^{-3}	7.93×10^{-4}	8.93
2	573	1400	4324	4.150×10^{-3}	7.98×10^{-4}	9.03
3	523	1400	4324	4.177×10^{-3}	8.03×10^{-4}	9.15
4	523	1323	4324	4.471×10^{-3}	8.60×10^{-4}	8.09
5	523	1273	4324	4.651×10^{-3}	8.94×10^{-4}	7.46
6	523	1400	3924	4.450×10^{-3}	8.56×10^{-4}	9.11
7	523	1400	4724	3.935×10^{-3}	7.57×10^{-4}	9.23
8	523	1400	5124	3.715×10^{-3}	7.14×10^{-4}	9.27

* Simulation conditions :
Input heat flux = 7380 (kW/m^2), Duration of thermal attack Δt = 5.2 s, Dimension of material = 0.1017- by 0.1017- by 0.0127- m thick
** Experimental data provided by Koo et al (1991) : 4.72×10^{-3} (m) at peak
***Recession rate = δ_t / Δt
**** Definition of elongation :
(final length + surface recession)/(initial length)

Table 3 Comparison of the predicted thermochemical ablation with experimental data for high-temperature ablatives

Type	T_p (K)	T_e (K)	ΔH_e** (kJ/kg)	$\delta_t(\times10^{-2}m)$ Prediction	Data**	Elongation (%)
MXBE-350	523	1273	4724	0.437	0.472	7.47
H41N	523	1273	14418	0.146	0.147	17.32
MXB-360	523	1273	21173	0.100	0.099	9.11

* Simulation conditions :
Input heat flux = 7380 (kW/m^2), Duration of thermal attack Δt = 5.2 s,
** Experimental value reported by Koo et al (1991)

reported by Koo et al. (1991). The agreement of the erosion depth between the predicted results and experimental data for H41N and MXB-360 is surprisingly well. This indicates that the choice of T_p and T_e is reasonable for these two kinds of ablatives, but may be a little higher for MXBE-350. Note that in the absence of particle impact, both MXB-360 and H41N outperform MXBE-350.

When an ablative (say, MXBE-350) is exposed to hot rocket exhaust, both thermochemical ablation and mechanical erosion would take place simultaneously. These two erosion modes could mutually interact with each other, thus greatly modify the overall rate of material erosion. In order to account for this mutual interaction, all the parameters used in the calculations are treated as linear functions of temperature from the onset of pyrolysis until the beginning of thermochemical ablation (i.e., over the temperature range of $T_p \le T \le T_e$). The effects of thermal and mechanical properties of the ablative are studied parametrically by arranging them into four groups: (i) E_w, σ_b, and σ_d; (ii) η_w, υ_w, and ϵ; (iii) ϵ_b and ϵ_d; (iv) η_b, η_d, C_b and C_d. In the parametric study the input heat flux is fixed at 7380kW/m^2, the impact velocity of particles at 976 m/s, and the duration of simulation at 5.2 sections. The above conditions are deduced from the experimental conditions employed by Koo et al. (1991). The impact angle is chosen to be $\theta = 5$ deg to simulate the experimental conditions used by Koo et al. (1991). This is done by assuming an average particle impact angle for the entire experiment. The ablative used in this series of study is MXBE-350.

Regarding the three parameters in the first group (E_w, σ_b, and σ_d), a sensitivity study is performed by varying each parameter by ± 50 percent from the baseline case while keeping

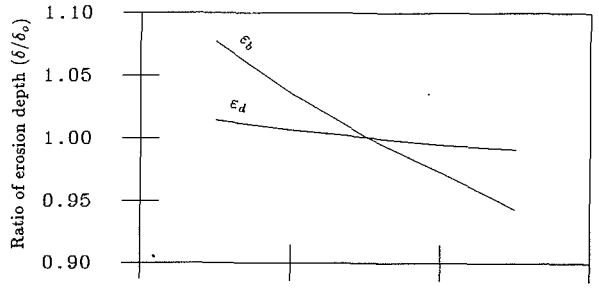


Fig. 3(*a*)

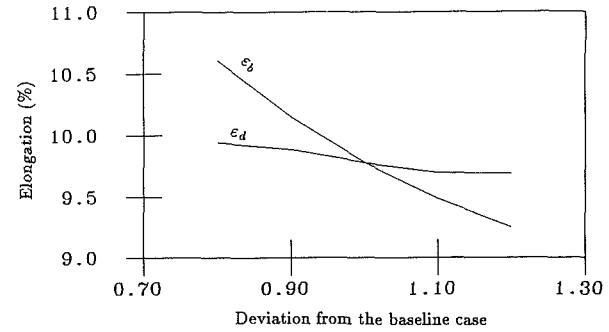


Fig. 3(*b*)

Fig. 3 Effects of erosion energy for particle impact (ϵ_b and ϵ_d) on the ratio of erosion depth and elongation

the others at the same values as those for the baseline case. It is found that these three parameters do not significantly affect the overall material erosion. A decrease of 50 percent in the elastic modulus of the ablative only results in a 0.5 percent decrease in the erosion depth. The variations of σ_b and σ_d have even less influence on the erosion depth. Regarding the three parameters in the second group (η_w, ϵ, and υ_w), a parametric study is performed by varying each parameter by ± 20 percent from the baseline case while keeping the others constant. It is found that a decrease in the value of any one parameter would reduce the extent of material erosion. However, the reduction is less than one percent.

Regarding the two parameters in the third group, a sensitivity study is made by varying one of them by $\pm$ 20 percent from the baseline case at a time while keeping the others at the same values. The results are shown in Fig. 3. It is found that the lower the erosion energy, the higher the erosion rate and elongation become. A small variation of ϵ_b or ϵ_d can result in a large change of mechanical erosion. Note that ϵ_b has more significant effect than ϵ_d. This is not generally true because the impact angle in the present calculation is fixed at 5 deg and at this angle the deformation wear plays a dominated role.

The four correction coefficients in the last group have similar effects as the parameters in the third group. A sensitivity study is performed by varying each parameter by -30 percent to 10 percent from the baseline case while keeping the others at the same values as those for the baseline case. The results are shown in Fig. 4. The effects of these four correction coefficients on the erosion depth and elongation of material are very significant. It is found that η_b and C_b have almost the same influence on the overall material erosion. The same conclusion applied to η_d and C_d. Among the 12 parameters explored in this study, the erosion energies for particle impact (ϵ_b and ϵ_d) and the correction coefficients (η_b, η_d, C_b, and C_d) have more significant effects than the others.

Table 4 summarizes the calculated and observed material erosion and elongation for the cases with and without particle impact for MXBE-350. It can be seen that particle impact greatly enhances the material erosion and elongation. The over-

Downloaded 03 May 2010 to 171.66.16.245. Redistribution subject to ASME license or copyright; see http://www.asme.org/terms/Terms_Use.cfm

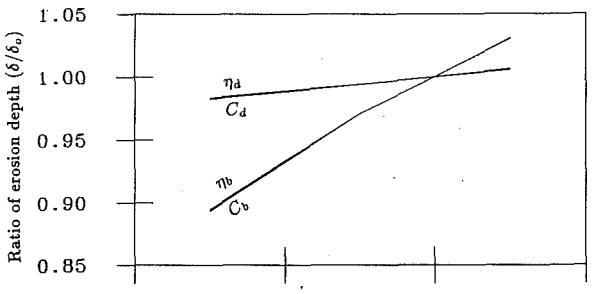


Fig. 4(*a*)

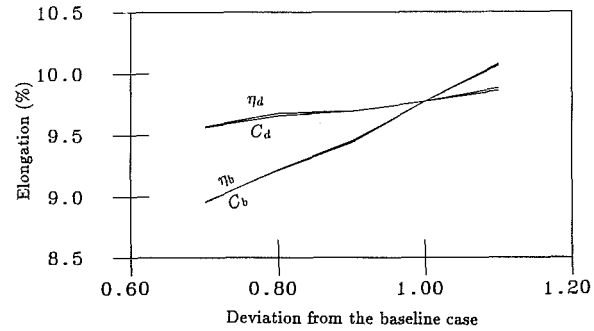


Fig. 4(*b*)

Fig. 4 Effects of the correction coefficients on the ratio of erosion depth and elongation

Table 4 Comparison of material erosion and elongation for the cases with and without particle impact for MXBE-350

Type	Without particle impact*	With particle impact*
Erosion depth (cm)	0.4370 (0.472)	0.9503 (0.998)
Elongation (%)	7.47	9.77

* The numbers in the parenthesis are the experimental data provided by Koo et al (1991).

all material erosion is almost twice the erosion due to thermochemical ablation only and the total elongation about 30.8 percent more. Overall, the prediction agrees well with the experimental data of Koo et al. (1991).

4 Conclusions

Based on the results of this study, the following conclusions can be made:

1 When a high-temperature ablative is exposed to solid rocket exhaust, the effect of mechanical wear on the overall material erosion is as important as the thermochemical effect. Thus, ignoring the effect of particle impact could lead to a significant error in evaluating the ablative performance.

2 Among the various thermal properties, the erosion energy ΔH_e of the ablative and failure temperature T_e of the ablative have dominant effects on the extent of the thermochemical ablation.

3 The major mechanical properties of the ablative that have significant influence on the extent of mechanical erosion are the erosion energies for particle impact, ϵ_b and ϵ_d, and the correction coefficients, η_b, η_d, C_b, and C_d. Improved resistance of the ablative to mechanical wear at high-temperatures can be obtained by decreasing the value of the correction coefficients or increasing the values of the erosion energies for particle impact.

4 The processes of particle-impact erosion and thermochemical ablation are strongly coupled. The mutual interaction between these two processes needs to be considered in predicting the overall material erosion.

Acknowledgment

The authors wish to thank Dr. Y. C. Pan of Argonne National Laboratory for his interest and encouragement in this research. This work was funded by the Naval Systems Division of FMC Corporation through the IR&D 423 Project on Launcher Protection Technology.

References

Buch, J. D., 1982, "Thermal Expansion Behavior of a Thermally Degrading Organic Matrix Composite," *Thermochemical Behavior of High-Temperature Composite*, ASME Publication AD-04, pp. 35–49.

Collins, R. E., 1961, *Flow of Fluids Through Porous Materials*, Reinhold Publishing Corporation, New York, pp. 1–20.

Finnie, I., 1960, "Erosion of Surface by Solid Particles," *Wear*, Vol. 3, pp. 87–103.

Henderson, J. B., and Wiecek, T. E., 1988, "A Numerical Study of the Thermal-Induced Response of Decomposing, Expanding Polymer Composites," *Warme-und Stouffubertragung*, Vol. 22, pp. 275–284.

Kitron, A. K., Eljerin, T., and Tamir, A., 1989, "Monte Carlo Analysis of Wall Erosion and Direct Contact Heat Transfer by Impinging Two-Phase Jet," *Journal of Thermophysics*, Vol. 3, pp. 112–122.

Koo, J. H., Lin, S., Kneer, M., and Miller, M., 1991, "Comparison of Ablative Materials in a Simulated Solid Rocket Exhaust Environment," AIAA-91-0978, *32nd SDM Structure, Dynamics, and Materials Conference*, Baltimore, MD.

Koo, J. H., Lin, S., Kneer, M., and Boyer, C. T., 1992, "Performance of High-Temperature Composite Ablatives under a Hostile Environment," *37th International SAMPE Symposium and Exhibition*, Anaheim, CA.

Levy, A., Aghazadeh, M., and Hickey, G., 1986, "The Effects of Test Variables on the Platelet Mechanism of Erosion," *Wear*, Vol. 108, pp. 23–41.

Mockenhaupt, J. D., and Wickman, J. H., 1983, "Particle Impact Erosion, Volume II: Erosion Model Development," AFRPL TR-83-013, *Air Force Rocket Propulsion Laboratory*.

Neilson, J. H., and Gilthrist, A., 1968, "Erosion by a Stream of Solid Particles," *Wear*, Vol. 11, pp. 111–122.

Ruff, A. W., 1986, "Analysis of Interlaboratory Test Results of Solid Particle Impingement Erosion," *Wear*, Vol. 108, pp. 323–335.

Soo, S. L., 1983, "Dynamic Interactions of Granular Materials," *Advances in the Mechanics of the Flow of Granular Materials*, Vol. II, M. Shaninpoor, ed., pp. 675–698.

Soo, S. L., 1977, "A Note on Erosion by Moving Dust Particles," *Powder Technology*, Vol. 17, pp. 259–263.

Timoshenko, S. P., and Goodier, J. N., 1969, *Theory of Elasticity*, 3rd ed., McGraw-Hill, New York, pp. 409–422.

Yang, B. C., 1992, "A Theoretical Study of Thermo-Mechanical Erosion of High-Temperature Ablatives," Ph.D. Dissertation, The Pennsylvania State University, University Park, PA.

Downloaded 03 May 2010 to 171.66.16.245. Redistribution subject to ASME license or copyright; see http://www.asme.org/terms/Terms_Use.cfm

G. W. Hunt

M. K. Wadee

N. Shiacolas

Department of Civil Engineering,
Imperial College of Science,
Technology, and Medicine,
London SW7 2BU, U.K.

Localized Elasticae for the Strut on the Linear Foundation

Localized solutions, for the classical problem of the nonlinear strut (elastica) on the linear elastic foundation, are predicted from double-scale analysis, and confirmed from nonlinear volume-preserving Runge-Kutta runs. The dynamical phase-space analogy introduces a spatial Lagrangian function, valid over the initial post-buckling range, with kinetic and potential energy components. The indefinite quadratic form of the spatial kinetic energy admits unbounded solutions, corresponding to escape from a potential well. Numerical experimentation demonstrates that there is a fractal edge to the escape boundary, resulting in spatial chaos.

1 Introduction

The elastic strut on elastic foundation has played a major heuristic role in the development of our understanding of the buckling process (Timoshenko and Gere, 1963). Both linear and nonlinear studies abound in the literature (e.g., Hetényi, 1946; Bolotin, 1958; Lekkerkerker, 1962; Thompson and Hunt, 1973). The linear eigenvalue problem suggests a buckle pattern that is harmonic along the length, and post-buckling theory and analysis provide information on the amplitudes of these fluctuations.

To explore the post-buckling range successfully, nonlinear terms are thus required in the potential energy function, and correspondingly in the underlying differential equation. Such terms arise naturally in the large-deflection range, as in the classical elastica analysis (Euler, 1744). It is well known that, for a stiff foundation or long strut, buckling occurs at an unstable-symmetric point of bifurcation (Thompson and Hunt, 1973), and it has generally been assumed that the periodic solution that emerges from this critical point is unique. But this is in stark contrast with recent results for the simpler case of a linearized strut on a destabilizing nonlinear foundation, where localized forms of buckling are known to occur (Potier-Ferry, 1983; Hunt and Wadee, 1991; Amick and Toland, 1992b; Champneys and Toland, 1992).

This paper reports on the successful search for localized elastica solutions to the strut on the linear foundation. Comparison of the differential equation with the simpler case demonstrates the extra complexity involved, yet the responses are very similar. A foundation nonlinearity might be seen as an artificial contrivance, but the same cannot be said for the nonlinearities associated with the elastica, which are an integral part of the formulation.

Solutions are sought using double-scale Fourier perturbation analysis, and checked against numerical runs of the full fourth-order differential equation. As for the simpler case, a multiplicity of localized post-buckling solutions occurs, associated with a fractal escape boundary in the four-dimensional phase space of the differential equation; this in turn is linked to an indefinite quadratic form of "spatial" kinetic energy, which appears when this conservative Hamiltonian system is seen in the light of the Lagrange equations (Hunt and Lucena Neto, 1991; Hunt and Wadee, 1991).

2 Slow Space Fourier Analysis

A localized buckle pattern in the strut on the linear elastic foundation is first suggested by double-scale perturbation analysis, and confirmed by the four-dimensional runs which follow. We consider a typical section of an infinitely long, axially loaded strut of bending stiffness EI, resting on a linear foundation ($c=0$) of stiffness k, and vertically displaced an amount $y(x)$ where x measures along the displaced shape of the strut, part of which is shown in Fig. 1. As the strut deflects, the foundation force remains vertical and of magnitude ky. A total potential energy functional can be written:

$$\mathbf{V}=\frac{1}{2}EI\int_{-\infty}^{\infty}\ddot{y}^2(1-\dot{y}^2)^{-1}dx - P\int_{-\infty}^{\infty}[1-(1-\dot{y}^2)^{1/2}]dx+\frac{1}{2}k\int_{-\infty}^{\infty}y^2dx, \quad (1)$$

where, with a dot denoting differentiation with respect to x, the first term is the strain energy, the second is the work done

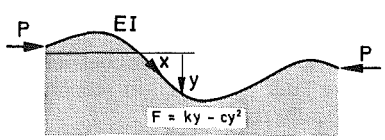


Fig. 1 An axially loaded strut on an elastic (linear or nonlinear) foundation

Contributed by the Applied Mechanics Division of THE AMERICAN SOCIETY OF MECHANICAL ENGINEERS for publication in the ASME JOURNAL OF APPLIED MECHANICS.

Discussion on this paper should be addressed to the Technical Editor, Professor Lewis T. Wheeler, Department of Mechanical Engineering, University of Houston, Houston, TX 77204-4792, and will be accepted until four months after final publication of the paper itself in the ASME JOURNAL OF APPLIED MECHANICS.

Manuscript received by the ASME Applied Mechanics Division, Mar. 26, 1992; final revision, Oct. 26, 1992. Associate Technical Editor: D. J. Inman.

Copyright © 1993 by ASME
Downloaded 03 May 2010 to 171.66.16.245. Redistribution subject to ASME license or copyright; see http://www.asme.org/terms/Terms_Use.cfm

by the load, and the third is the foundation energy. The expressions remain valid over large deflections. A straightforward application of the calculus of variations (Thompson and Hunt, 1973) gives the fourth-order Euler-Lagrange equation in x

$$EI[\dddot{y}+4\,\ddot{y}\dot{y}\,\dot{y}(1-\dot{y}^2)^{-1}+\ddot{y}^3(1+3\dot{y}^2)(1-\dot{y}^2)^{-2}] + P\ddot{y}(1-\dot{y}^2)^{-1/2}+ky(1-\dot{y}^2)=0. \quad (2)$$

We compare this in passing with the simplified strut equation used earlier to illustrate localized buckling (Hunt and Wadee, 1991)

$$EI\dddot{y}+P\ddot{y}+ky-cy^2=0, \quad (3)$$

where the strain energy and work done by load are linearized, and a nonlinearity ($c\neq 0$) is introduced into the foundation.

Double-scale analysis can be initiated either from the Euler-Lagrange equation (Hunt et al., 1989), or directly from the energy functional (Hunt and Wadee, 1991). Here we take the latter course, and start by expanding the nonlinear functions of $\mathbf{V}$ as power series

$$\mathbf{V}=\frac{1}{2}EI\int_{-\infty}^{\infty}(\ddot{y}^2+\ddot{y}^2\dot{y}^2+\ddot{y}^2\dot{y}^4+\cdots)dx - P\int_{-\infty}^{\infty}\left(\frac{1}{2}\dot{y}^2+\frac{1}{8}\dot{y}^4+\frac{1}{16}\dot{y}^6+\cdots\right)dx+\frac{1}{2}k\int_{-\infty}^{\infty}y^2dx. \quad (4)$$

We then introduce a load-dependent rescaling of the spatial dimension by writing

$$X=sx, \quad (5)$$

where X is the so-called slow space, and s measures progress out from the first critical point C, at the well-known critical load of $P^C=2\sqrt{kEI}$, encountered in the flat fundamental state under increasing load (Thompson and Hunt, 1973). We suppose y can be written

$$y=\sum_{i=0}^{\infty}A_i(X)\cos i\omega x, \quad (6)$$

where the critical value of ω is determined later from linear eigenvalue analysis. Derivatives with respect to x then become

$$\dot{y}=\sum_{i=0}^{\infty}(-A_i i\omega\sin i\omega x+sA_i'\cos i\omega x),$$

$$\ddot{y}=\sum_{i=0}^{\infty}(-A_i i^2\omega^2\cos i\omega x-2sA_i'\,i\omega\sin i\omega x+s^2A_i''\cos i\omega x) \quad (7)$$

etc., where a prime denotes differentiation with respect to X.

Substitution of the necessary derivatives into the expanded form (4) of $\mathbf{V}$ leads to a set of energy integrals involving products of A_i and its derivatives, together with harmonic functions. For periodic responses, amplitudes A_i can be taken outside the integral sign, leading to conventional nonlinear Rayleigh-Ritz analysis (Thompson and Hunt, 1973). For localized responses, we integrate by parts and write the energy as

$$\mathbf{V}=\frac{1}{2}\sum_{i=0}^{\infty}\left(V_{ii}\int_{-\infty}^{\infty}A_i^2dx+V_{i'i'}\int_{-\infty}^{\infty}A_i'^2dx+V_{ii''}\int_{-\infty}^{\infty}A_iA_i''dx\right) + \frac{1}{24}V_{ijkl}\int_{-\infty}^{\infty}A_iA_jA_kA_l dx+\text{h.o.t.}, \quad (8)$$

where the Einstein summation convention is employed on the final term only, terms with coefficients of the order s^4 are dropped (Hunt and Wadee, 1991) and the higher-order terms (h.o.t.) include quartics with s in the coefficients. Anticipating the results of the later perturbation scheme, the coefficients which are specifically required are

$$V_{00}=k,\ V_{ii}=\frac{1}{2}(EIi^4\omega^4-Pi^2\omega^2+k)\ \text{ for }\ i\neq 0,$$

$$V_{0'0'}=-s^2P,\ V_{i'i'}=\frac{1}{2}s^2(4EIi^2\omega^2-P)\ \text{ for }\ i\neq 0,$$

$$V_{ii''}=-s^2EIi^2\omega^2,$$

$$V_{iiii}=\frac{3}{2}i^4\omega^4\left(EIi^2\omega^2-\frac{3}{4}P\right). \quad (9)$$

The harmonic fluctuations are thus removed. Coefficients without primes are the same as for constant amplitude periodic study (Thompson and Hunt, 1973), while those with primes given explicitly above are the same as for the simplified strut (Hunt and Wadee, 1991).

To obtain the important amplitude modulation equation for localized responses we apply the calculus of variations, writing a small increment of $\mathbf{V}$ as

$$\delta\mathbf{V}=\sum_{i=0}^{\infty}\int_{-\infty}^{\infty}\left[\frac{1}{2}V_{ii''}A_i\delta A_i''+V_{i'i'}A_i'\delta A_i' + \left(V_{ii}A_i+\frac{1}{2}V_{ii''}A_i''+\frac{1}{6}V_{ijkl}A_jA_kA_l\right)\delta A_i\right]dx+\text{h.o.t.} \quad (10)$$

where the summation convention is again employed over j, k, and l, but suspended over i. The order of differentiation of the first two terms can be reversed ($\delta A_i'=d(\delta A_i)/dX$, etc.) and integration by parts gives

$$\delta\mathbf{V}=\sum_{i=0}^{\infty}\left\{\frac{1}{2s}\left[V_{ii''}A_i\delta A_i'-V_{ii''}A_i'\delta A_i-2V_{i'i'}A_i'\delta A_i\right]_{-\infty}^{\infty} + \int_{-\infty}^{\infty}\left((V_{ii''}-V_{i'i'})A_i''+V_{ii}A_i+\frac{1}{6}V_{ijkl}A_jA_kA_l\right)\delta A_i dx+\text{h.o.t.}\right\}. \quad (11)$$

Periodic, periodically modulated, and localized solutions can all co-exist. For periodic solutions, the first three terms above must vanish, since $A_i'=\delta A_i'=0$. For localized solutions they again mush vanish, since the entirely flat state $A_i=A_i'=0$ is approached as $X\to\pm\infty$. Finally, periodic modulation of an amplitude A_i is again enough to ensure that these boundary terms vanish at $X\to\pm\infty$, if we take it that the system is at identical stages in its cycle of modulation as it crosses the two boundaries.

For $\delta\mathbf{V}$ to be zero under any δA_i, we thus have the Euler equation in slow space

$$(V_{ii''}-V_{i'i'})A_i''+V_{ii}A_i+\frac{1}{6}V_{ijkl}A_jA_kA_l+\text{h.o.t.}=0. \quad (12)$$

The lowest critical load is linked to the amplitude A_1 by setting $V_{11}^C=0$, which, using Eq. (9), gives $\omega^2=\sqrt{(k/EI)}$ and $P^C=2\sqrt{(kEI)}$. These in turn give the remaining *stability coefficients*

$$V_{00}^C=k;\quad V_{ii}^C=\frac{1}{2}k(i^2-1)^2\ \text{ for }\ i\neq 0, \quad (13)$$

which are nonzero for $i\neq 1$. These coefficients are independent of s, while those for the leading term of the Euler Eq. (12) depend on s^2 (see Eq. (9)). Close to C, therefore, where s is small, the second term of Eq. (12) for $i\neq 1$ dominates the leading term. If, in addition, the lowest possible order of nonlinear term is included, passive mode amplitudes A_i ($i\neq 1$) then must be of the order of A_1^3 or higher, just as for the periodic case (Thompson and Hunt, 1973), and we need consider them no further in an initial post-buckling study.

For the special (critical) case of $i=1$, we finally give a physical significance to the parameter s by defining

$$s=\sqrt{(P^C-P)}. \quad (14)$$

Downloaded 03 May 2010 to 171.66.16.245. Redistribution subject to ASME license or copyright; see http://www.asme.org/terms/Terms_Use.cfm

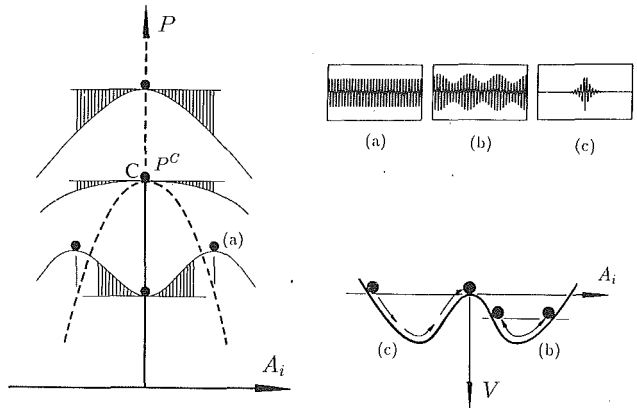


Fig. 2 The rolling ball analogy applied to (*a*) periodic, (*b*) modulated, and (*c*) localized solutions

We suppose also that A_1 and its derivatives initially are of the order of s, and ignore all terms of s^4 and higher in the slow space Euler equation for $i=1$. After a little manipulation, this gives the *second-order differential equation for amplitude modulation in slow space*

$$16EIA_1'' - 4A_1 + kA_1^3 = 0, \tag{15}$$

which, from amongst other solutions, is satisfied completely by the localized form

$$A_1 = 2\sqrt{\frac{2}{k}}\,\mathrm{sech}\left(\frac{1}{2\sqrt{EI}}X\right). \tag{16}$$

The slow space Euler Eq. (12) can be seen as an example of the Lagrange equation

$$\frac{d}{dX}\left(\frac{\partial \mathcal{L}}{\partial A'}\right) - \frac{\partial \mathcal{L}}{\partial A} = 0, \tag{17}$$

if the Lagrangian $\mathcal{L}(A_i, A_i', P) = T(A_i', P) - V(A_i, P)$ is defined by

$$T = \frac{1}{2}\sum_{i=0}^{\infty} T_{ii}A_i'^2, \quad \text{where} \quad T_{ii} = V_{ii}'' - V_{i'i'}$$

$$V = \frac{1}{2}\sum_{i=0}^{\infty} V_{ii}A_i^2 + \frac{1}{24}V_{ijkl}A_iA_jA_kA_l + \text{h.o.t.} \tag{18}$$

with a present restriction to the initial post-buckling, as terms in s^4 have been ignored (Hunt and Wadee, 1991).

This new breakdown of the total energy integral **V** into potential (V) and kinetic (T) "spatial" components which are local to a point in X, leads to the dynamical analogy of Fig. 2. A periodic solution (a) corresponds to a state of statical equilibrium, with a ball resting at the bottom of a potential well, the latter being represented by $-V$ since the kinetic energy coefficients T_{ii} ($i \neq 0$) turn out to be negative. Modulated solutions (b) are then modeled by the ball rolling backwards and forwards in the well, "spatial" kinetic energy now contributing. Modulations build to the fully localized solution (c), where the potential energy V at maximum amplitude, on the symmetric section $A_i' = 0$ where also $T = 0$, has the same value as in the flat fundamental state. This so-called "zero energy" amplitude provides a valuable extra condition for localization from amongst all possible solutions (Toland, 1986; Amick and Toland, 1992a; Hunt and Wadee, 1991; Hunt and Lucena Neto, 1991).

We note that the first-order kinetic energy coefficients T_{ii} are identical to those found earlier for the linearized strut on the nonlinear foundation, and come directly from the linearized strain-energy-of-bending and work-done-by-load terms of the integrand of **V** (Hunt and Wadee, 1991). As noted earlier, they are negative for $i \neq 0$, but T_{00} is positive. The diagonalized quadratic form for T is thus indefinite, and "escape" from the multi-degree-of-freedom potential well described by $V(A_i)$ is possible, provided that the bias amplitude A_0 is involved; this corresponds to a disturbance in the underlying order, to the point of spatial chaos, as seen below.

For the strut on the nonlinear (asymmetric) foundation, A_0 is involved from the outset of the post-buckling. In the present symmetric case, it would not appear to play the same role. Its involvement, or that of some higher-order terms in T, is to be suspected, however, in that spatially chaotic behavior is again found at loads below P^C.

3 Dynamical Phase-Space Analogy

The above perturbation analyis is asymptotic in nature. This is demonstrated in Fig. 3, which sets the variation of Eq. (16) against numerical runs of a fourth-order *symplectic* (volume-preserving) Runge-Kutta scheme (Sanz-Serna, 1988; Hunt and Wadee, 1991). The quality of the predicted amplitude variation, with accuracy improving as $s = \sqrt{P^C - P}$ approaches zero, is clear to see.

The choice of a Runge-Kutta scheme over the more usual structural tools of finite element or finite difference analysis stems from the philosophy of the dynamical phase-space analogy (Hunt et al., 1989; Hunt and Wadee, 1991); the shape adopted by the structure in the spatial variable x is viewed as a response in phase space, in this case involving the four dimensions of y, $\dot{y}$, $\ddot{y}$, and $\dddot{y}$ (Thompson and Stewart, 1986). For the earlier, simpler problem, we can then identify forms for spatial kinetic and potential energies, different from the slow-space T and V above, such that the strut appears as a two-degree-of-freedom Lagrangian system, in the so-called *fast-space* representation (Hunt and Wadee, 1991). Such a full description remains elusive for the nonlinear integrand of (1), although the same linearized forms are of course useful over the initial post-buckling range.

In common with the slow-space T of Eq. (18), the kinetic energy has an indefinite quadratic form, which not only allows solutions to "escape" to $y = \pm\infty$ from the potential well formed by V, but gives the edge between such unbounded solutions, and those that are bounded and hence physically realizable, the fractal quality seen in Fig. 4; in the limit, the response is chaotic, admitting an infinite number of possible localized and semi-localized solutions.

The phase space being four dimensional, the dynamical analogy demands four initial conditions. The structural nature of the problem supplies two in the form of boundary conditions, so we can take it that all localized forms for the strut typically appear in the bundle of paths which emerge from a two-dimensional (blanket) set of starts enclosing the origin. Figure 4 shows the results from such a series, with states leading to escape by a certain test length x_{div} shown in white, and those remaining bounded by this length shown in black; over 800,000 runs are included, with the four different test lengths shown, all important numerical data being as given in the figure caption. Escape is here defined by the condition $|\dot{y}| \geq 1$, the differential equation then becoming singular; we note that this presumably includes as a subset, the realizable solutions where simultaneously $\ddot{y} = 0$ and the strut physically curves back on itself (Thompson and Virgin, 1988; El Naschie, 1989) but such complications are left for future study.

Figure 4(*a*), at $x_{\text{div}} = 50$, has two fingers of unbounded escaping solutions (white) intruding into the black region of starting states that remain bounded by this length. By $x_{\text{div}} = 70$, the sharp edges of the first picture start to break up as extra thin fingers appear; a small central region of Fig. 4(*b*) will match Fig. 4(*a*) precisely, the system responding linearly for longer, the closer a particular start is to the origin. Figure 4(*c*), at $x_{\text{div}} = 100$, shows the developing fractal edge, while by $x_{\text{div}} = 180$, the space of starts has apparently turned to dust, as

Downloaded 03 May 2010 to 171.66.16.245. Redistribution subject to ASME license or copyright; see http://www.asme.org/terms/Terms_Use.cfm

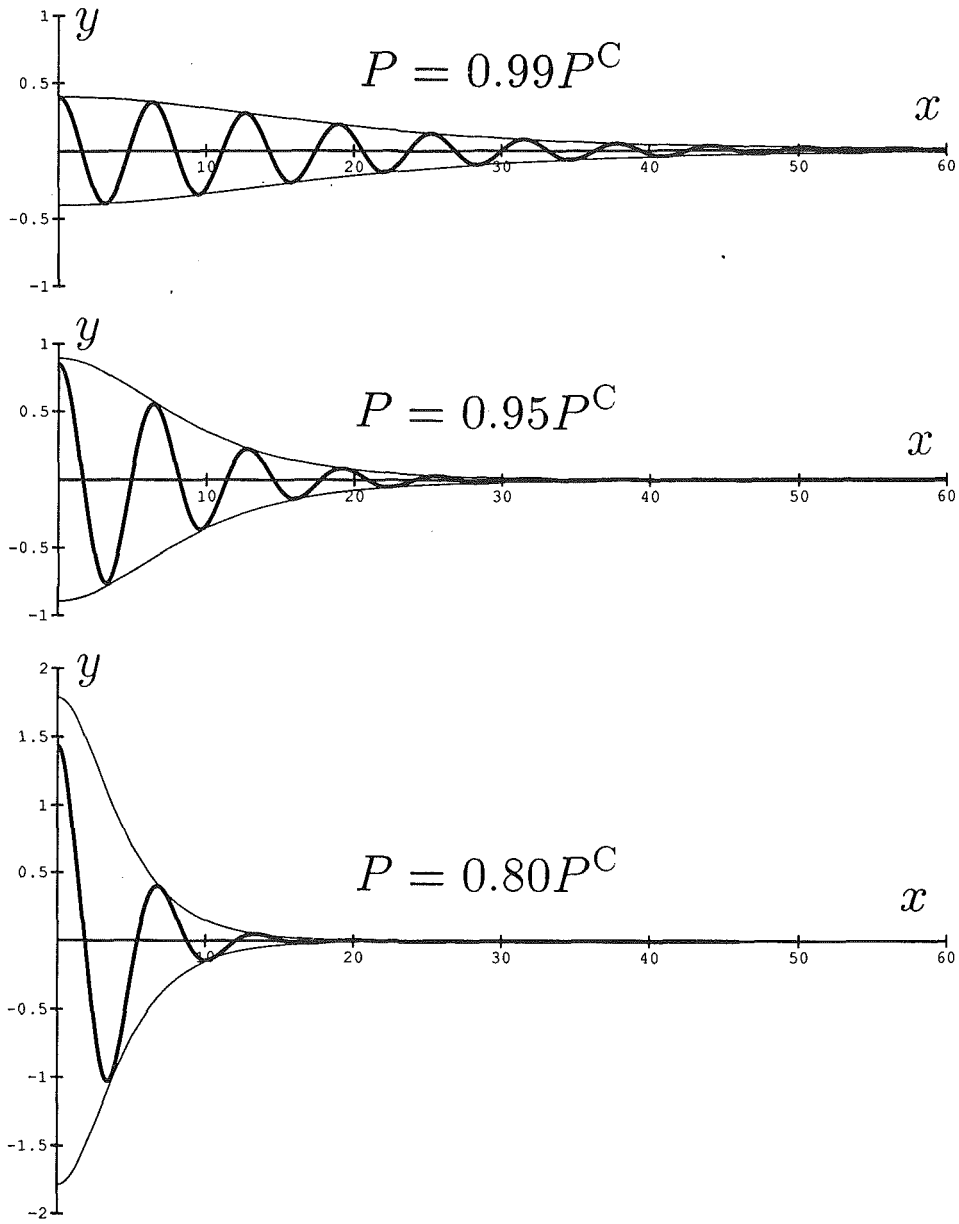


Fig. 3 Amplitude modulation of Eq. (16) (thin line), set against Runge-Kutta solutions of the full fourth-order Eq. (2) (thick line)

seen in Fig. 4(*d*); the close-up plots of Fig. 5, however, show that this dust actually comprises a subtle mixture of thin and fat lines.

In the nature of fractals, the more closely an area of the space of starts is explored, the more fine details emerges, as seen in Fig. 5. As the intruding fingers develop and multiply, sandwiched between the white spirals of escape are black spirals representing the bounded solutions, which of course include the localized forms. Search routines lead typically to the seven such examples of Fig. 6, stemming from the small area in the space of starts as shown in Fig. 5. Each form can be shifted along the x-axis by a spiral adjustment in the space of starts, so that all are identifiable for any particular long-but-finite strut, as described in our earlier paper (Hunt and Wadee, 1991). Here we present a complementary view, which underlines the chaotic quality of the response by demonstrating a profound sensitivity to initial starting conditions.

Unlike time, the spatial measure x is necessarily reversible, and the system is then by its nature Hamiltonian or conservative. The object of Fig. 5 thus takes the form of a "fat fractal," which, unlike the well-known Cantor set, exhibits finite-thickness regions of both white and black. Several different measures of the so-called fractal dimension have been suggested (Peitgen and Saupe, 1988). The standard technique for measuring the box or capacity dimension (Guckenheimer and Holmes, 1983; Moon, 1987) tends to come up with near integer values for fat fractals, and the alternative measure proposed by Umberger and Farmer (1985) seems more useful. They hypothesize that a fat fractal scales as

$$\mu(\epsilon) \approx \mu(0) + A\epsilon^{\beta} \tag{19}$$

where $\mu(\epsilon)$ is a course-grained count of the black regions, ϵ is an appropriate measurement of scale, and A is a constant. For thin fractals, $\mu(0)$ is zero, but for Hamiltonian systems it is nonzero and represents the finite area taken up by the black regions as the length scale tends to zero; in this way, β provides an estimate of the modified fractal dimension (Hanson, 1987).

Course estimates of the quantity β for the present system indicate that $\beta \approx 0.5 \pm 0.1$, the error term being a subjective but conservative estimate of the variation found over a number of test counts. For a fat fractal, $\beta < 1$, while for a Euclidean

Downloaded 03 May 2010 to 171.66.16.245. Redistribution subject to ASME license or copyright; see http://www.asme.org/terms/Terms_Use.cfm

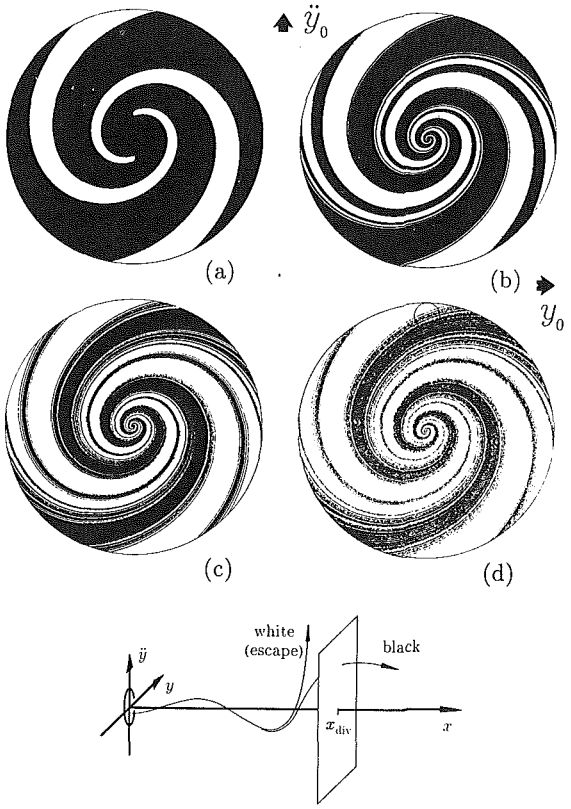


Fig. 4 Fractal edge to the escape boundary. For Eq. (2), $EI = k = 1$, $P = 1.7$, $\Delta x = 0.01$, and the illustrated radius of starts = 0.00001 (*a*) $x_{div} = 50$; (*b*) $x_{div} = 70$; (*c*) $x_{div} = 100$; (*d*) $x_{div} = 180$. The circled region in (*d*) is detailed in Fig. 5.

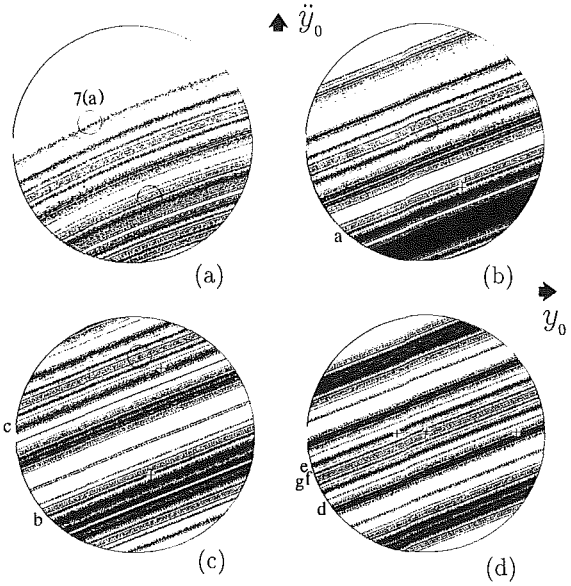


Fig. 5 Scrutiny of fractal edge. (*b*) is lower circled region in (*a*), (*c*) is circled region in (*b*), etc.

set, β computes the unity. This confirms that the map of bouned trajectories does indeed take the form of a fat fractal.

4 Numerics Versus Dynamics

Fractal boundaries and chaos can be generated numerically as well by a nonlinear dynamical process, so it is important to determine whether the above has numerical overtones. Useful checks are for robustness against changes in Δx, and in the choice of numerical solution scheme. All the forms shown in

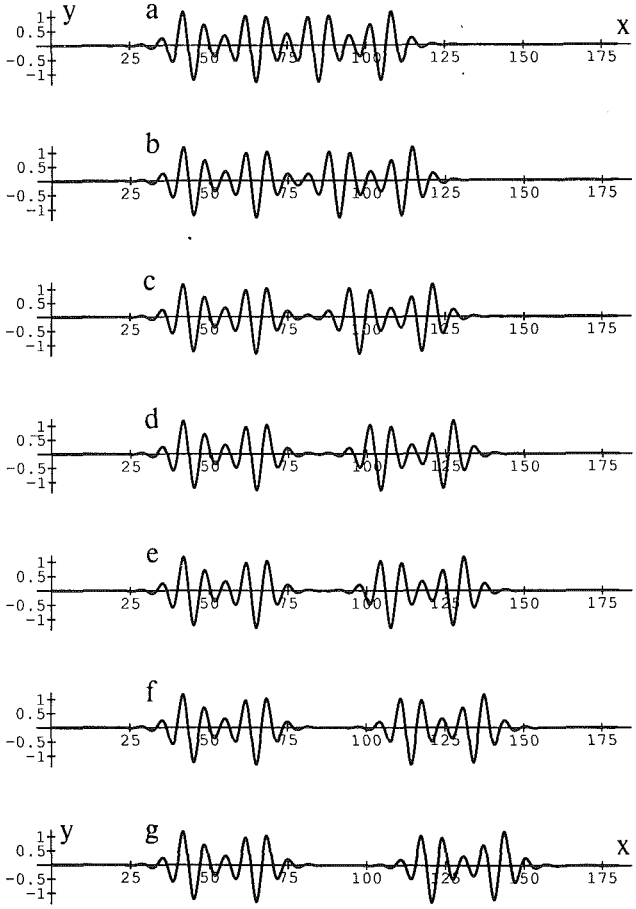


Fig. 6 Localization modes, with starts as indicated in Fig. 5

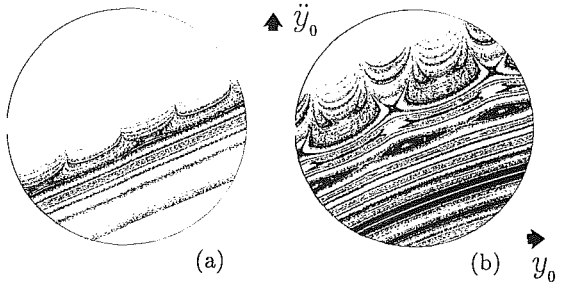


Fig. 7 Numerically induced distortion of space of starts with $x_{div} = 180$. (*a*) $\Delta x = 0.01$: upper circled region in Fig. 5(*a*). (*b*) $\Delta x = 0.1$: similar region to (*a*) scaled by a factor of 10.

Fig. 6 seem to pass these tests; they have been found for three different step sizes, and when the fourth-order Runge-Kutta scheme is replaced with a simple trapezium rule which is likewise volume preserving. We can then propose with some confidence that the modes of Fig. 6 are genuinely part of the dynamics, and would appear in a continuous system.

There is further apparent evidence, however, in the particular forms of Fig. 6. This set of responses is produced by seeking passage through the *symmetric section* $\dot{y} = \ddot{y} = 0$, from which forward and backwards runs give mirror images (Hunt and Wadee, 1991), and which occurs somewhere in the range $70 < x < 100$ (7000 to 10000 steps at $\Delta x = 0.01$) for each of the plots. What appears is a process by which the complex localized form at the top splits into the two, separated, mirror-image localized modes at the bottom. This separation is clearly linked to the oscillatory wavelength, which itself is part of the dy-

Downloaded 03 May 2010 to 171.66.16.245. Redistribution subject to ASME license or copyright; see http://www.asme.org/terms/Terms_Use.cfm

namics. This strongly suggests that the multiplicity of solution is dynamically rather numerically induced. We note that this apparent interaction of two localized modes is strongly reminiscent of inverse-scattering phenomena for solitons (Drazin and Johnson, 1989), but such consideration are left for further study.

Numerically induced modes can also appear, however. Figure 7 shows comparative regions of the space of starts, within which distortions due to finite step size are evident. Numerically induced forms appear within such regions; the distortion varies considerably with changes in step size, and hence these modes lack robustness against such changes. (Note that the region used for Fig. 7(a) is at a tenth of the scale of Fig. 7(b), the step size being reduced by the same factor.)

5 Concluding Remarks

Double-scale analysis, leading to a slow space Lagrangian function for the initial buckling of a nonlinear strut on a linear foundation, is synthesized from two separate developments; potential energy is the same as under a periodic formulation (Thompson and Hunt, 1973), while the spatial kinetic energy matches to first order that of the linearized strut (Hunt and Wadee, 1991). Higher-order equations, possibly involving phase as well as amplitude modulation, of course will reflect the differences.

The indefinite form of the spatial kinetic energy means that escape from the corresponding potential well, leading to unbounded solutions even though the total energy remains bounded, is possible. The edge between unbounded and bounded solution has a complex fractal structure, which is only made apparent when initial rather than boundary conditions, according to the dynamical phase-space analogy, are employed. Many possible forms of localized solution exist; along with the symmetric modes seen in Fig. 3 and at the top of Fig. 6, antisymmetric modes also appear for this symmetric system (although not for the earlier asymmetric system of Hunt and Wadee (1991)), and we find also localized solutions without any obvious symmetries (e.g., the fully separated modes at the bottom of Fig. 6). The overall picture is apparently one of infinite variety, typical of fully developed chaos.

The form of spatial chaos found here differs from earlier examples, in that it is not imperfection induced. The multiplicity of possible solutions appears here in a single passage around a homoclinic loop (Hunt et al., 1989), within a potential well, broken up by the phenomenon of escape; earlier models (Thompson and Virgin, 1988; El Naschie, 1989) employ multiple approaches to the saddle point represented by the flat state $y=0$, broken up by periodic imperfections. Both kinds are of intereset phenomenologically, but it does seem that the present form is the more important from the practical point of view.

Earlier studies of struts on elastic foundations have focused on periodic solutions, but a localized form is the most likely in practice. All post-buckling responses are unstable under dead load, while under a rigid load of magnitude less than P^C they represent allowable alternative equilibrium states that can be triggered from the flat fundamental state by an extra input of energy. On a plot of load against its corresponding deflection, the post-buckling state lying closest to the fundamental equilibrium path requires the least triggering energy (Hunt et al., 1989), and thus provides the expected response under random disturbance. For the long strut considered here, this is the simple localized form of Fig. 3.

The existence of periodic solutions has thus effectively masked the more practically significant, but analytically more complex, localized behavior. Exactly the same effect has been found recently in a classical shell buckling problem (Hunt and Lucena Neto, 1991, 1992).

Acknowledgment

Financial support for M. K. W. was provided by a U.K. Science and Engineering Research Council research studentship.

References

Amick, C. J., and Toland, J. F., 1992a, "Global Uniqueness of Homoclinic Orbits for a Class of Fourth Order Equations," *Z. Angew Math. Phys.*, Vol. 43, pp. 591–597.

Amick, C. J., and Toland, J. F., 1992b, "Homoclinic Orbits in the Dynamic Phase-Space Analogy of an Elastic Strut," *European J. Appl. Maths.*, Vol. 3, pp. 97–114.

Bolotin, V. V., 1958, "Nonlinear Theory of Elasticity and Stability in the Case of Large Deflections," *Raschety na Prochnost*, No. 3, Mashgiz, Moscow.

Champneys, A. R., and Toland, J. F., 1993, *Bifurcation of a Plethora of Large Amplitude Homoclinic Orbits for Hamiltonian Systems*, to be published.

Drazin, P. G., and Johnson, R. S., 1989, *Solitons: An Introduction*, Cambridge University Press, Cambridge, U.K.

El Naschie, M. S., 1989, "On Certain Homoclinic Soliton in Elastic Stability," *Journal of the Physical Society of Japan*, Vol. 58, No. 12, pp. 4310–4321.

Euler, L., 1744, "De Curvis Elasticis," *Methodus inveniedi lineas curvas maximi minimive proprietate gaudentes*, Lausanne and Geneva, Appendix.

Guckenheimer, J., and Holmes, P. J., 1983, *Nonlinear Oscillations, Dynamical Systems, and Bifurcations of Vector Fields*, Springer-Verlag, New York.

Hanson, J. D., 1987, "Fat-Fractal Scaling Exponent of Area-Preserving Maps," *Phys. Rev.*, Vol. 35, No. 3, pp. 1470–1473.

Hetényi, M., 1946, *Beams on Elastic Foundation*, The University of Michigan Press, Ann Arbor, MI.

Hunt, G. W., and Lucena Neto, E., 1991, "Localized Buckling in Long Axially-Loaded Cylindrical Shells," *J. Mech. Phys. Solids*, Vol. 39, No. 7, pp. 881–894.

Hunt, G. W., and Lucena Neto, E., 1993, "Maxwell Critical Loads for Axially Loaded Cylindrical Shells," ASME JOURNAL OF APPLIED MECHANICS, Vol. 60, pp. 702–706.

Hunt, G. W., and Wadee, M. K., 1991, "Comparative Lagrangian Formulations for Localized Buckling," *Proc. R. Soc. Lond.*, Vol. A434, pp. 485–502.

Hunt, G. W., Bolt, H. M., and Thompson, J. M. T., 1989, "Structural Localization Phenomena and the Dynamical Phase-Space Analogy," *Proc. R. Soc. Lond.*, Vol. A425, pp. 245–267.

Lekkerkerker, J. G., 1962, "On the Stability of an Elastically Supported Beam Subjected to its Smallest Buckling Load," *Proc. K. ned. Akad. Wet.*, Series B, Vol. 65, No. 190.

Moon, F. C., 1987, *Chaotic Vibrations*, John Wiley & Sons, New York.

Peitgen, H.-O., and Saupe, D., eds., 1988, *The Science of Fractal Images*, Springer-Verlag, New York.

Potier-Ferry, M., 1983, "Amplitude Modulation and Localization of Buckling Patterns," Thompson, J. M. T., and Hunt, G. W., eds., *Collapse: The Buckling of Structures in Theory and Practice*, Cambridge University Press, Cambridge, U.K.

Sanz-Serna, J. M., 1988, "Runge-Kutta Schemes for Hamiltonian Systems," *BIT*, Vol. 28, pp. 877–883.

Thompson, J. M. T., and Hunt, G. W., 1973, *A General Theory of Elastic Stability*, Wiley, London, U.K.

Thompson, J. M. T., and Stewart, J. B., 1986, *Nonlinear Dynamics and Chaos*, Wiley, London, U.K.

Thompson, J. M. T., and Virgin, L. N., 1988, "Spatial Chaos and Localization Phenomena in Nonlinear Elasticity," *Physics Letters A*, Vol. 126, No. 8,9, pp. 491–496.

Timoshenko, S. P., and Gere, J. M., 1963, *Theory of Elastic Stability*, 2nd ed., McGraw-Hill, New York.

Toland, J. F., 1986, "Existence of Symmetric Homoclinic Orbits for Systems of Euler-Lagrange Equations," *Proc. Symposia in Pure Mathematics*, Vol. 45, Part 2, pp. 447–459.

Umberger, D. K., and Farmer, J. D., 1985, "Fat Fractals on the Energy Surface, Phys. Rev. Lett, Vol. 55, pp. 661–664.

Downloaded 03 May 2010 to 171.66.16.245. Redistribution subject to ASME license or copyright; see http://www.asme.org/terms/Terms_Use.cfm

J. A. Peck
Graduate Research Assistant.

W. P. Schonberg
Associate Professor,
Assoc. Mem. ASME.

Civil and Environmental
Engineering Department,
The University of Alabama in Huntsville,
Huntsville, AL 35899

Asymmetric Indentation of a Finite Elastically Supported Beam

This paper presents the results of an investigation into the behavior of an elastic beam that is loaded by a frictionless cylindrical indenter. Results are obtained using a solution which incorporates both local contact behavior as well as global beam behavior. The solution is obtained by superposing an elastic layer solution derived through the use of integral transforms and the cylindrical bending solution for a flat plate. The problem reduces to two coupled Fredholm integral equations of the second kind which are solved numerically. Local contact stresses and load-deflection relations are examined in detail for various geometric and contact parameters. The results are compared to Hertz theory contact stresses and beam theory deflection predictions.

Introduction

Contact between mechanical elements occurs in virtually all structural systems and generally serves the purpose of transmitting loads from one element to another. This results in stresses and deformations in the members involved. Traditionally, the global consequences of mechanical contact are analyzed using a "strength of materials" approach while the local effects are modeled using theory of elasticity methods. When contact occurs on a beam, the common method of analysis is to model the overall load-displacement relationship using Bernoulli-Euler beam theory and then employ a Hertzian contact solution to calculate the local stresses near the contact site. However, such a method of solution is applicable only in a limited class of contact problems. Prior static indentation studies (Keer and Miller, 1983; Keer and Schonberg, 1986a,b) in which the local and global effects were coupled have shown that the local contact stresses will differ significantly from Hertzian distributions when the contact region is relatively large. These studies illustrated some of the limitations of the traditional approach and set bounds on the ranges of various geometric parameters for which more refined techniques are needed.

The problem considered in this paper is that of a finite elastic beam of thickness h and length L that is asymmetrically loaded by a smooth cylindrical indenter on its upper surface (Fig. 1). While the symmetric case was investigated previously by Keer and Miller (1983), the analysis herein produces a more general solution in that it allows the indenter to be placed at any point between the beam supports. The method of solution is one that superposes an elasticity layer solution with a cylindrical bending solution for a flat plate. Layer solution loads at the ends of the beam are canceled by cylindrical bending loads in a manner such that the boundary conditions there are satisfied. In the enforcement of these conditions, it is assumed that thickness effects are negligible at the ends of the beam. This superposition and matching of boundary conditions leads to two coupled Fredholm integral equations which are solved numerically. By varying appropriate beam parameters and the location of the indenter, an extensive study of the response of an asymmetrically loaded finite elastic beam is performed. In the analysis, the quantities of interest are the stress distribution under the indenter and the load-deflection relationship. These quantities are used to evaluate the ranges of various geometric parameters for which beam theory solutions and Hertzian contact stresses do not apply.

Theoretical Development

The problem to be solved is that of the smooth, rigid, cylindrical indentation of the isotropic elastic beam of length L and thickness h shown in Fig. 1. The beam is supported at its ends by elastic springs with spring constants k. Although the equations developed allow any value of the spring constant k to be used, two support conditions are considered specifically: simply supported ($k = 0$) and fixed ($k = \infty$). The solution of the problem is obtained by the superposition of an

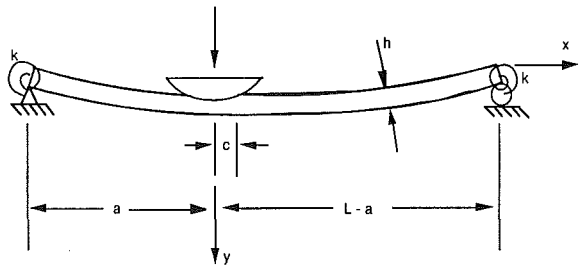


Fig. 1 Problem configuration

Contributed by the Applied Mechanics Division of THE AMERICAN SOCIETY OF MECHANICAL ENGINEERS for presentation at the ASME Winter Annual Meeting, New Orleans, LA, Nov. 28–Dec. 3, 1993.

Discussion on this paper should be addressed to the Technical Editor, Professor Lewis T. Wheeler, Department of Mechanical Engineering, University of Houston, Houston, TX 77204-4792, and will be accepted until four months after final publication of the paper itself in the ASME JOURNAL OF APPLIED MECHANICS.

Manuscript received by the ASME Applied Mechanics Division, Feb. 21, 1992; final revision, Feb. 3, 1993. Associate Technical Editor: F. Y. M. Wan.

Paper No. 93-WA/APM-7.

Copyright © 1993 by ASME
Downloaded 03 May 2010 to 171.66.16.245. Redistribution subject to ASME license or copyright; see http://www.asme.org/terms/Terms_Use.cfm

elasticity solution and a cylindrical bending solution. The boundary conditions for the elasticity solution corresponding to an infinite elastic layer loaded on its upper surface by a frictionless cylindrical indenter with radius R are

$$\sigma_{xy}=\sigma_{yy}=0 \qquad y=h, \quad |x|<\infty \qquad (1a, b)$$

$$\sigma_{xy}=0 \qquad y=0, \quad |x|<\infty \qquad (1c)$$

$$\sigma_{yy}=0 \qquad y=0, \quad |x|>c \qquad (1d)$$

$$u_y=\Delta-x^2/2R \qquad y=0, \quad |x|<c \qquad (1e)$$

where c is semi-contact length. The support conditions for the beam ends are

$$M-k\theta=0 \quad @\ x=-a \quad \text{and} \quad x=L-a \qquad (2a)$$

$$u_y=0 \quad @\ x=-a \quad \text{and} \quad x=L-a \qquad (2b)$$

where M is the moment and θ is the average value of the slope measured through the thickness given by

$$\theta=(1/h)\int_0^h (\partial u_y/\partial x)dy. \qquad (2c)$$

A suitable elasticity solution that represents general loading on the upper surface of an isotropic elastic layer with no loading on its lower surface is found using Fourier transforms (Sneddon, 1951) and is given as follows:

$$\sigma_{xy}=(2/\pi)\int_0^\infty [E_s(\xi)\sin(\xi x)-E_a(\xi)\cos(\xi x)]f_{xy}(\xi,y)d\xi \qquad (3)$$

$$\sigma_{yy}=(2/\pi)\int_0^\infty [E_s(\xi)\cos(\xi x)+E_a(\xi)\sin(\xi x)]f_{yy}(\xi,y)d\xi \qquad (4)$$

$$\sigma_{xx}=(2/\pi)\int_0^\infty [E_s(\xi)\cos(\xi x)+E_a(\xi)\sin(\xi x)]f_{xx}(\xi,y)d\xi \qquad (5)$$

$$u_y=(2/\pi)\int_0^\infty [E_s(\xi)\cos(\xi x)+E_a(\xi)\sin(\xi x)] \times [K_{12}f_{xy}(\xi,y)-K_{11}g(\xi,y)]d\xi/\xi \qquad (6)$$

$$u_x=(2/\pi)\int_0^\infty [E_s(\xi)\sin(\xi x)-E_a(\xi)\cos(\xi x)] \times [K_{11}f_{xx}(\xi,y)-K_{12}f_{yy}(\xi,y)]d\xi/\xi \qquad (7)$$

where $K_{12}=-\nu(1+\nu)/E$ and $K_{11}=(1-\nu^2)/E$; the functions fxx, fxy, fyy, and g are found through application of the method in Sneddon (1951) and are listed in Peck (1991).

The moments and shears resulting from the elastic layer solution are

$$M_E(x)=\int_0^h y\sigma_{xx}dy=-(2/\pi)\int_0^\infty [E_s(\xi)\cos(\xi x) + E_a(\xi)\sin(\xi x)]d\xi/\xi^2 \qquad (8)$$

$$V_E(x)=\int_0^h \sigma_{xy}dy=(2/\pi)\int_0^\infty [E_s(\xi)\sin(\xi x) - E_a(\xi)\cos(\xi x)]d\xi/\xi. \qquad (9)$$

We note that Eqs. (8), (9) satisfy the relationship $V = dM/dx$. Using Eq. (2c), the average slope through the elastic layer thickness is given by

$$\theta_E(x)=-(2/\pi)\int_0^\infty [E_s(\xi)\sin(\xi x)-E_a(\xi)\cos(\xi x)]\{K_{12} - K_{11}[3\sinh(\alpha)-\alpha]/[\sinh(\alpha)-\alpha]\}d\xi/\alpha \qquad (10)$$

where $\alpha = \xi h$. For the cylindrical bending solution, the displacement is assumed to be of the form

$$u_y^B=a_3x^3+a_2x^2+a_1x+a_0. \qquad (11)$$

Assuming that plane sections which are perpendicular to the neutral axis of the beam remain planar and normal, the bending stress is given by

$$\sigma_{xx}^B=(1/K_{11})(\partial u_x^B/\partial x)=(1/K_{11})(6a_3x+2a_2)(h/2-y) \qquad (12)$$

where

$$u_x^B=(\partial u_y^B/\partial x)(h/2-y)=(3a_3x^2+2a_2x+a_1)(h/2-y). \qquad (13)$$

Using these equations, the moments, shears, and slope for the cylindrical bending solution may be written as

$$M_B(x)=\int_0^h y\sigma_{xx}^B dy=-h^3(3a_3x+a_2)/6K_{11} \qquad (14)$$

$$V_B(x)=\partial M_B/\partial x=-h^3a_3/2K_{11} \qquad (15)$$

$$\theta_B(x)=\partial u_y^B/\partial x=3a_3x^2+2a_2x+a_1. \qquad (16)$$

Thus, the solution sought will be a superposition of the elasticity solution given by Eqs. (3)–(10) and the cylindrical bending solution given by Eqs. (11)–(16). The two solutions are matched properly when the boundary conditions, Eqs. (1a–e) and (2a, b), are all satisfied. Since the elasticity solution satisfies boundary conditions (1a) through (1d), these conditions will automatically be satisfied in the superposed solution. All that remains is to satisfy Eqs. (1e) and (2a, b). This is done by first using Eqs. (2a, b) to solve for the constants in Eq. (11). Finally, Eq. (1e) will be applied which will create a system of equations in terms of unknown transform functions.

To satisfy Eqs. (2a, b), end moments, rotations, and displacements are written as the sum of corresponding elasticity and cylindrical bending solutions. This yields the following set of equations:

$$u_y^E(-a,0)+u_y^B(-a)=0 \qquad (17)$$

$$u_y^E(L-a,0)+u_y^B(L-a)=0 \qquad (18)$$

$$M_E(-a)+M_B(-a)-k[\theta_E(-a)+\theta_B(-a)]=0 \qquad (19)$$

$$M_E(L-a)+M_B(L-a)-k[\theta_E(L-a)+\theta_B(L-a)]=0. \qquad (20)$$

Substituting the appropriate expressions for the elasticity and cylindrical bending moments, slopes, and displacements allows the solution of the constants a_0 through a_3 (Peck, 1991). The final boundary condition to be satisfied is that of the displacement under the indenter, Eq. (1e). Applying Eq. (1e) to the displacement under the indenter, we have

$$u_y^E(x,0)+u_y^B(x)=\Delta-x^2/2R. \qquad (21)$$

Taking the derivative of Eq. (21) with respect to x and separating the result into symmetric and antisymmetric components yields

$$\partial u_y^E(x,0)/\partial x|_s+3a_3x^2+a_1=0 \qquad (22)$$

$$\partial u_y^E(x,0)/\partial x|_a+2a_2x=-x/R \qquad (23)$$

Introducing the auxiliary functions $\psi(t)$ and $\phi(t)$ defined as

Downloaded 03 May 2010 to 171.66.16.245. Redistribution subject to ASME license or copyright; see http://www.asme.org/terms/Terms_Use.cfm

$$E_s(\xi)=\int_0^c J_0(\xi t)\psi(t)dt \quad \text{and} \quad E_a(\xi)=\int_0^c J_1(\xi t)\phi(t)dt, \tag{24, 25}$$

substituting for u_y^E, a_1, a_2, a_3 into Eqs. (22), (23), and combining terms in $\psi(t)$ and $\phi(t)$ results in the following two coupled integral equations in terms of $\psi(t)$ and $\phi(t)$:

$$\int_0^c \psi(t)\int_0^\infty J_0(\xi t)\{[K_{11}I(\alpha)/H(\alpha)]\sin(\xi x) + x\lambda_1(\xi)\cos(\xi a)+x\lambda_2(\xi)\cos[\xi(L-a)]+x\lambda_3(\xi)\sin(\xi a) - xUVk\lambda_0(\xi)\sin[\xi(L-a)]/J\}d\xi dt + \int_0^c \phi(t)\int_0^\infty J_1(\xi t)\{x\lambda_3(\xi)\cos(\xi a)+x\lambda_2(\xi)\sin[\xi(L-a)] - x\lambda_1(\xi)\sin(\xi a)+xUVk\lambda_0(\xi)\cos[\xi(L-a)]/J\}d\xi dt = -\pi x/4R \tag{26}$$

$$\int_0^c \psi(t)\int_0^\infty J_0(\xi t)\{[3x^2S(\xi)-\lambda_7(\xi)]\cos(\xi a) + [3x^2T(\xi)+\lambda_6(\xi)]\cos[\xi(L-a)]+[3x^2k\lambda_0(\xi)(N+1/J) - \lambda_9(\xi)]\sin(\xi a)+[3x^2k\lambda_0(\xi)/J+\lambda_8(\xi)]\sin[\xi(L-a)]\}d\xi dt + \int_0^c \phi(t)\int_0^\infty J_1(\xi t)\{[-2K_{11}I(\alpha)/H(\alpha)]\cos(\xi x) - [3x^2S(\xi)-\lambda_7(\xi)]\sin(\xi a)+[3x^2T(\xi)+\lambda_6(\xi)]\sin[\xi(L-a)] + [3x^2k\lambda_0(\xi)(N+1/J)-\lambda_9(\xi)]\cos(\xi a)-[3x^2k\lambda_0(\xi)/J + \lambda_8(\xi)]\cos[\xi(L-a)]\}d\xi dt = 0 \tag{27}$$

where the constants J, N, U, V and functions H, I, S, T, and λ_0 through λ_9 are as defined in Peck (1991).

In order to be able to solve Eqs. (26), (27) numerically, the kernels must be bounded at the lower limit and approach zero at the upper limit. Performing an asymptotic analysis of the kernels in Eqs. (26), (27) as $\xi \to 0$ shows that the integrands are indeed bounded at the lower limit. However, the term $I(\alpha)/H(\alpha)$ approaches unity as $\xi \to \infty$. This improper behavior is corrected by adding and subtracting the terms

$$K_{11_0}\int_0^c \psi(t)\int_0^\infty J_0(\xi t)\sin(\xi x)d\xi dt,$$

$$2K_{11_0}\int_0^c \phi(t)\int_0^\infty J_1(\xi t)\cos(\xi x)d\xi dt$$

in Eqs. (26), (27), respectively. After some manipulation (Peck, 1991) Eqs. (26), (27) are reduced to the following Fredholm integral equations:

$$K_{11}\psi(x)+\int_0^c \psi(t)K_1(x,t)dt + \int_0^c \phi(t)K_2(x,t)dt = -\pi x/4R \tag{28}$$

$$K_{11}\phi(x)+\int_0^c \phi(t)K_3(x,t)dt+\int_0^c \psi(t)K_4(x,t)dt=0 \tag{29}$$

where

$$K_1(x,t)=x\int_0^\infty J_0(\xi t)\{K_{11}[I(\alpha)/H(\alpha)-1]\xi J_0(\xi x) + \lambda_1(\xi)\cos(\xi a)+\lambda_2(\xi)\cos[\xi(L-a)]+\lambda_3(\xi)\sin(\xi a) - UVk\lambda_0(\xi)\sin[\xi(L-a)]/J\}d\xi \tag{30}$$

$$K_2(x,t)=x\int_0^\infty J_1(\xi t)\{\lambda_3(\xi)\cos(\xi a)+\lambda_2(\xi)\sin[\xi(L-a)] - \lambda_1(\xi)\sin(\xi a)+UVk\lambda_0(\xi)\cos[\xi(L-a)]/J\}d\xi \tag{31}$$

$$K_3(x,t)=(x^2/2)\int_0^\infty J_1(\xi t)\{2K_{11}[I(\alpha)/H(\alpha)-1](\xi/x)J_1(\xi x) - 3S(\xi)\sin(\xi a)+3T(\xi)\sin[\xi(L-a)] + 3k\lambda_0(\xi)(N+1/J)\cos(\xi a)-3k\lambda_0\cos[\xi(L-a)]/J\}d\xi \tag{32}$$

$$K_4(x,t)=(x^2/2)\int_0^\infty J_0(\xi t)\{3S(\xi)\cos(\xi a) + 3T(\xi)\cos[\xi(L-a)]+3k\lambda_0(\xi)(N+1/J)\sin(\xi a) + 3k\lambda_0(\xi)\sin[\xi(L-a)]/J\}d\xi. \tag{33}$$

Equations (28), (29) are solved simultaneously for the unknown auxiliary functions $\psi(t)$ and $\phi(t)$ by assuming a value of the semi-contact length c. Once these functions are known, all quantities of interest may be calculated as functions of c. For example, surface contact stresses may be obtained by substituting Eqs. (24), (25) into Eq. (4), which gives

$$\sigma_{yy}(x,0)=(2/\pi)\int_0^c \psi(t)/\sqrt{t^2-x^2}dt + (2x/\pi)\int_x^c \phi/t\sqrt{t^2-x^2}dt. \tag{34}$$

The load due to the symmetric contact stresses on the surface is given by

$$P=\int_{-c}^{c}\sigma_{yy}(x,0)\Big|_s dx=-2\int_0^c \psi(t)dt \tag{35}$$

Similarly, the moment due to the antisymmetric surface stresses is given by

$$M=\int_{-c}^{c}x\sigma_{yy}(x,0)\Big|_a dx=-2\int_0^c t\phi(t)dt. \tag{36}$$

Finally, the total displacement of the beam under the center of the indenter corresponding to a specified semi-contact length c is given by

$$\Delta=u_y^E(0,0)+u_y^B(0) = -(4/\pi)\int_0^\infty E_s(\xi)[K_{11}I(\alpha)/H(\alpha)]d\xi/\xi+a_0. \tag{37}$$

Downloaded 03 May 2010 to 171.66.16.245. Redistribution subject to ASME license or copyright; see http://www.asme.org/terms/Terms_Use.cfm

Table 1 Verification of central indentation results

	c/h	Δ' present study	Δ' Keer & Miller 1983	P' present study	P' Keer & Miller 1983	σ* present study	σ* Keer & Miller 1983
Fixed Ends L/h = 10	0.25	1.900	1.912	0.0831	0.0834	0.635	0.635
	0.5	3.503	3.506	0.1550	0.1548	0.619	0.622
	1.0	4.831	4.807	0.2211	0.2197	0.556	0.560
	2.0	6.515	6.527	0.3616	0.3606	0.985	0.981
Fixed Ends L/h = 20	0.25	10.17	10.23	0.0575	0.0578	0.635	0.635
	0.5	14.95	15.02	0.0848	0.0851	0.619	0.622
	1.0	17.28	17.83	0.1017	0.1018	0.556	0.560
	2.0	21.10	21.22	0.1266	0.1271	0.985	0.981
Simple Supports L/h = 10	0.25	5.159	5.177	0.0403	0.0404	0.635	0.635
	0.5	7.568	7.575	0.0594	0.0594	0.619	0.622
	1.0	8.935	8.939	0.0714	0.0712	0.556	0.560
	2.0	10.26	10.35	0.0911	0.0908	0.985	0.978
Simple Supports L/h = 20	0.25	25.25	25.34	0.0252	0.0251	0.635	0.635
	0.5	31.50	31.57	0.0315	0.0314	0.619	0.622
	1.0	34.29	34.46	0.0346	0.0344	0.556	0.559
	2.0	36.97	37.55	0.0386	0.0384	0.985	0.980

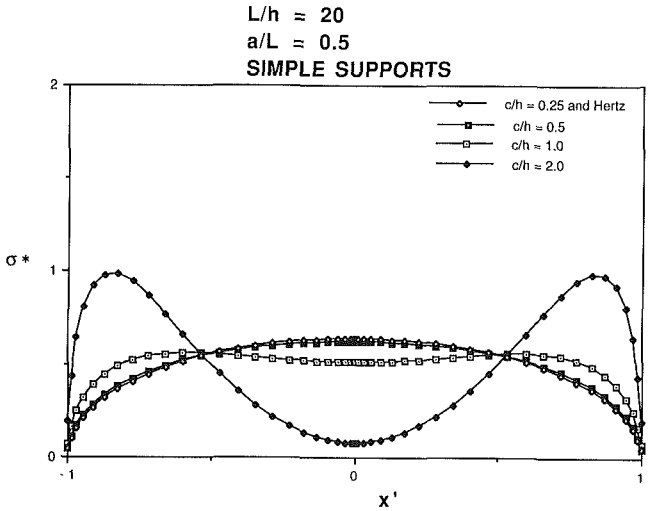


Fig. 2 Contact stress distribution (*L/h* = 20, *a/L* = 0.5, simply supported beam)

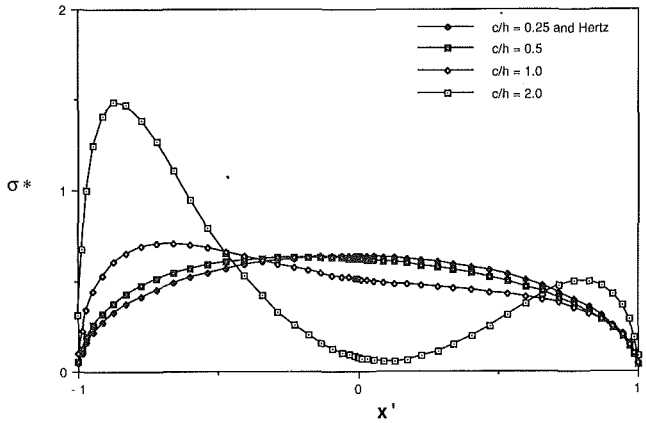


Fig. 3 Contact stress distribution (*L/h* = 20, *a/L* = 0.25, simply supported beam)

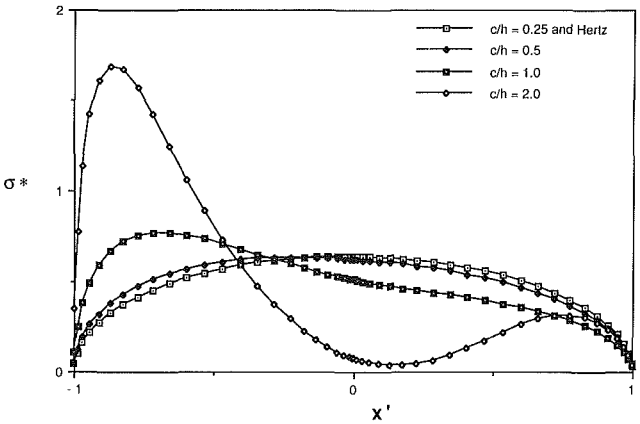


Fig. 4 Contact stress distribution (*L/h* = 20, *a/L* = 0.15, simply supported beam)

After substituting for a_0, replacing $E_s(\xi)$ and $E_a(\alpha)$ with $\phi(t)$ and $\psi(t)$, and collecting like terms, Eq. (37) becomes

$$\Delta = \int_0^c \psi(t)K_5(t)dt + \int_0^c \phi(t)K_6(t)dt \tag{38}$$

where

$$K_5(t) = (2/\pi)\int_0^\infty J_0(\xi t)\{[-2K_{11}I(\alpha)/H(\alpha)]$$
$$\times[\cos(\xi a)-1]/\xi + [a\lambda_6(\xi) - a^2\lambda_2(\xi) + a^3T(\xi)]\cos[\xi(L-a)]$$
$$-[a\lambda_7(\xi) + a^2\lambda_1(\xi) - a^3S(\xi)]\cos(\xi a) + [a\lambda_8(\xi)$$
$$+a^2UVk\lambda_0(\xi)/J + a^3k\lambda_0(\xi)/J]\sin[\xi(L-a)] - [a\lambda_9(\xi)$$
$$+a^2\lambda_3(\xi) - a^3k\lambda_0(\xi)(N+1/J)]\sin(\xi a)\}d\xi \tag{39a}$$

$$K_5(t) = (2/\pi)\int_0^\infty J_1(\xi t)\{[a\lambda_6(\xi) - a^2\lambda_2(\xi)$$
$$+a^3T(\xi)]\sin[\xi(L-a)] + [a\lambda_7(\xi) + a^2\lambda_1(\xi) - a^3S(\xi)$$
$$-2K_{11}I(\alpha)/\xi H(\alpha)]\sin(\xi a) - [a\lambda_8(\xi) + a^2UVk\lambda_0(\xi)/J$$
$$+a^3k\lambda_0(\xi)/J]\cos[\xi(L-a)] - [a\lambda_9(\xi) + a^2\lambda_3(\xi)$$
$$-a^3k\lambda_0(\xi)(N+1/J)]\cos(\xi a)\}d\xi. \tag{39b}$$

An asymptotic analysis shows that the kernels of Eq. (39*a*, *b*) are bounded as $\xi \to 0$ and, as $\xi \to \infty$, the terms in (39*a*, *b*) approach zero. Thus, Eq. (38) and its kernels can be evaluated numerically without any further adjustments.

Numerical Results and Discussion

In order to solve Eqs. (28), (29) for the unknown auxiliary functions $\psi(t)$ and $\phi(t)$ and to evaluate the displacement of the beam using Eq. (38), a specific value of the spring constant k must be chosen. Thus, while all of the equations developed have been written in terms of an arbitrary spring constant k, in order to perform the numerical solution and analysis, the kernels for Eqs. (28), (29), (38) are reduced using two specific values of k, that is, those corresponding to simply supported ($k=0$) and fixed ($k=\infty$) end conditions. The simplified forms of the kernels for these two cases can be found in Peck (1991).

Solutions to the indentation problem are obtained for two beam aspect ratios: $L/h = 10$ and $L/h = 20$. For each aspect ratio, three indentation locations are considered: $a/L = 0.15$, 0.25, 0.5; and, for each indentation location, four c/h values are used ($c/h = 0.25$, 0.5, 1.0, 2.0), each corresponding to a different amount of indentation. It is noted that for $a/L = 0.15$ and $L/h = 10$, a value of $c/h = 2.0$ would imply that the contact length would extend past the support. Hence for $a/L = 0.15$, a value of $c/h = 2.0$ is not considered. Finally, all calculations are performed with a Poisson's ratio of 0.3.

Downloaded 03 May 2010 to 171.66.16.245. Redistribution subject to ASME license or copyright; see http://www.asme.org/terms/Terms_Use.cfm

Table 2 Maximum normalized stress under the indenter

		Simply Supported		Fixed	
	c/h	L/h = 10	L/h = 20	L/h = 10	L/h = 20
a/L = 0.15	0.25	0.6354	0.6354	0.6355	0.6355
	0.50	0.6304	0.6302	0.6362	0.6350
	1.00	0.7761	0.7693	0.8271	0.8132
	2.00	x	1.688	x	1.780
a/L = 0.25	0.25	0.6353	0.6353	0.6354	0.6353
	0.50	0.6250	0.6249	0.6299	0.6292
	1.00	0.7112	0.7067	0.7693	0.7567
	2.00	1.564	1.490	1.726	1.640
a/L = 0.5	0.25	0.6352	0.6352	0.6351	0.6352
	0.50	0.6192	0.6192	0.6192	0.6192
	1.00	0.5558	0.5558	0.5558	0.5558
	2.00	0.9848	0.9848	0.9848	0.9848

Table 1 compares the numerical results for center indentation ($a/L = 0.5$) to those obtained in the previous symmetric indentation study of Keer and Miller (1983). In Table 1, P' and Δ' are nondimensional load and displacement values. As can be seen, the equations derived here yield results which closely match the results of Keer and Miller. Furthermore, the coupled integral equations reduce exactly to the corresponding equation used in Keer and Miller when $a/L = 0.5$. For both the simply supported and fixed cases, the coupling terms $K_2(x, t)$ and $K_4(x, t)$ vanish. This leaves two uncoupled equations, one for $\psi(t)$ and one for $\phi(t)$. The equation for $\psi(t)$ reduces to the corresponding equation of Keer and Miller while the equation for $\phi(t)$ yields the desired trivial solution. Therefore, any differences in Table 1 are numerical and due to the fact that different computers were used in the numerical solution of the integral equations and in the calculation of loads, displacements, and contact stresses.

Typical stress distributions under the indenter are shown in Figs. 2 through 4. In these figures, $\sigma^* = \sigma_{yy}c/P$ and $x' = x/c$ are the nondimensional stress and position along the contact surface, respectively. Each plot corresponds to a particular value of a/L, L/h, and k, and shows curves for the four different c/h values. The Hertzian contact stress distribution (Timoshenko and Goodier, 1970) is also plotted. Figures 5 through 7 illustrate typical load-displacement relationships. Examination of the figures reveals that for small values of c/h, the Hertzian distribution approximates the stress under the indenter quite well. As c/h is increased, the distribution changes significantly. For central indentation, as c/h is increased, the location of the peak stress shifts away from the center towards the two edges of the contact zone. In these cases, the stress distribution is severely non-Hertzian and begins to resemble the stress distributions under a flat stamp. This result is identical to that obtained in the symmetric indentation study of Keer and Miller (1983).

The results for asymmetric indentation (i.e., when the indenter is placed closer to one of the supports) are in some manner similar to those obtained in previous investigations of cantilever beam indentation by Keer and Schonberg (1986a, b). For example, in an asymmetric indentation in which the indenter is to the left of center of the beam, as c/h is increased, the peak stress shifts to the left and the distribution became less and less parabolic. The major difference between the contact stresses for the asymmetric indentation of a beam supported on both ends and those for a cantilever beam occurs for large c/h values. In those cases, while the contact stresses in the cantilever beam decrease steadily from the peak stress, those in the asymmetrically loaded beam have a second peak. This is because a beam with two supports wraps around the indenter while a cantilever beam bends away from the indenter.

A comparison of corresponding plots for simply supported and fixed end conditions reveals that the end conditions have very little effect on the normalized stress distributions for central (i.e., symmetric) indentation. For the off-center indentations, a small difference can be found between the curves for the two different end conditions when the contact length was relatively large (i.e., $c/h \geq 1$). This difference can be attributed to the higher moment induced by the fixed end supports. In a manner similar to the effect of changing end conditions, changing the values of the parameters a/L and L/h also has very little effect on the stress distributions for small c/h values. For large c/h values, decreasing the value of a/L causes an expected increase in the resultant moment, which increases the antisymmetric nature of the stress distributions. Also reducing the L/h ratio further exaggerated this antisymmetric behavior. Thus aside from the slight variations due to changes in aspect ratio or support condition, contact stress distributions are indeed a highly localized effect, but are strongly dependent on the contact length-to-layer thickness ratio (c/h). This is further illustrated in Table 2, which lists the maximum contact stress for different aspect ratios and for the two support conditions considered. From this table it can

Table 3 Load-displacement values (simple supports)

				Elementary Beam Theory	Modified Beam Theory	Superposition Solution
a/L	c/h (1)	P′ (2)	M′ (3)	Δ′ (4)	Δ′ (5)	Δ′ (6)
0.5	L/h = 10					
	0.25	0.0403	0.0	5.036	5.019	5.159
	0.50	0.0594	0.0	7.430	7.385	7.568
	1.00	0.0714	0.0	8.907	8.770	8.935
	2.00	0.0911	0.0	11.38	10.24	10.26
	L/h = 20					
	0.25	0.0252	0.0	25.16	25.09	25.25
	0.50	0.0315	0.0	31.49	31.39	31.50
	1.00	0.0346	0.0	34.57	34.39	34.29
	2.00	0.0386	0.0	38.60	37.76	36.97
0.25	L/h = 10					
	0.25	0.0474	0.0001	3.337	3.323	3.448
	0.50	0.0766	0.0012	5.407	5.324	5.499
	1.00	0.0994	0.0129	7.234	6.587	6.751
	2.00	0.1638	0.1235	13.83	7.770	7.758
	L/h = 20					
	0.25	0.0310	0.0000	17.43	17.38	17.52
	0.50	0.0412	0.0006	23.24	23.06	23.16
	1.00	0.0470	0.0059	26.90	25.84	25.74
	2.00	0.0573	0.0374	35.03	28.46	27.67
0.15	L/h = 10					
	0.25	0.0572	0.0001	1.862	1.851	1.957
	0.50	0.1059	0.0023	3.485	3.371	3.535
	1.00	0.1593	0.0290	5.699	4.499	4.659
	2.00	x	x	x	x	x
	L/h = 20					
	0.25	0.0399	0.0001	10.37	10.33	10.45
	0.50	0.0586	0.0013	15.34	15.10	15.19
	1.00	0.0719	0.0127	19.62	17.63	17.53
	2.00	0.1071	0.0979	34.85	19.66	18.74

Table 4 Load-displacement values (fixed supports)

				Elementary Beam Theory	Modified Beam Theory	Superposition Calculation
a/L	c/h (1)	P′ (2)	M′ (3)	Δ′ (4)	Δ′ (5)	Δ′ (6)
0.5	L/h = 10					
	0.25	0.0831	0.0	1.817	1.809	1.900
	0.50	0.1550	0.0	3.390	3.359	3.503
	1.00	0.2211	0.0	4.837	4.675	4.831
	2.00	0.3616	0.0	7.910	6.468	6.515
	L/h = 20					
	0.25	0.0575	0.0	10.07	10.04	10.17
	0.50	0.0848	0.0	14.85	14.78	14.95
	1.00	0.1017	0.0	17.80	17.63	17.28
	2.00	0.1266	0.0	22.15	21.11	21.10
0.25	L/h = 10					
	0.25	0.1032	0.0002	0.9531	0.9475	1.017
	0.50	0.2437	0.0051	2.264	2.204	2.327
	1.00	0.4568	0.0808	4.448	3.756	3.870
	2.00	1.609	1.551	19.31	7.141	6.400
	L/h = 20					
	0.25	0.0747	0.0001	5.808	5.787	7.864
	0.50	0.1404	0.0028	10.40	10.28	10.39
	1.00	0.1935	0.0324	14.66	13.65	13.73
	2.00	0.2992	0.2549	25.02	17.18	16.98
0.15	L/h = 10					
	0.25	0.124	0.0002	0.3612	0.3579	0.4072
	0.50	0.403	0.0108	1.194	1.127	1.219
	1.00	1.452	0.3215	4.948	3.307	3.204
	2.00	x	x	x	x	x
	L/h = 20					
	0.25	0.1050	0.0002	2.438	2.427	2.477
	0.50	0.2532	0.0065	5.937	5.783	5.862
	1.00	0.4774	0.1006	12.00	9.969	9.974
	2.00	1.398	1.443	45.64	17.65	16.43

Downloaded 03 May 2010 to 171.66.16.245. Redistribution subject to ASME license or copyright; see http://www.asme.org/terms/Terms_Use.cfm

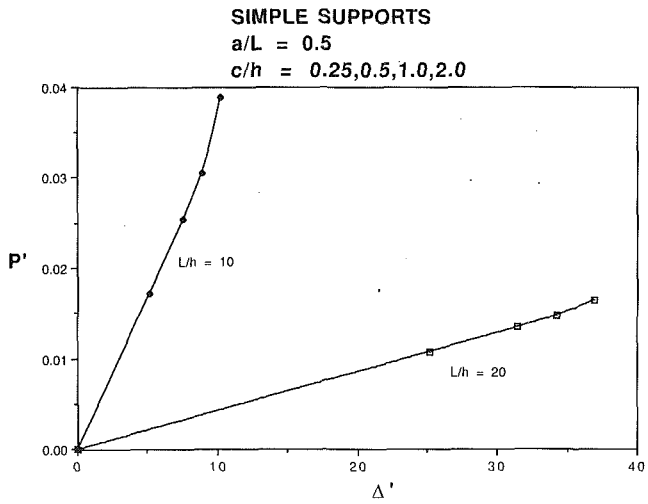


Fig. 5 Load-displacement curves (L/h = 10, 20, a/L = 0.5, simply supported beam)

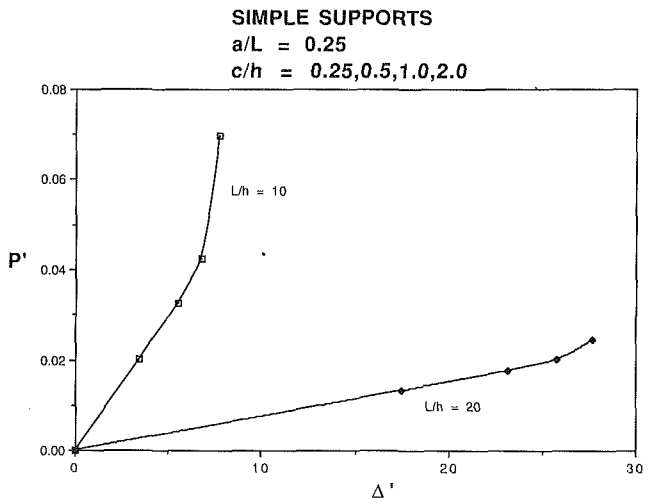


Fig. 6 Load-displacement curves (L/h = 10, 20, a/L = 0.25, simply supported beam)

be seen that for any given value of a/L, the effect of changing the L/h ratio or the support conditions is small compared to that of changing the c/h ratio.

Tables 3 and 4 compare displacement values calculated using the method developed herein with those obtained from elementary and modified beam theory. The parameters P' and Δ' are nondimensional load and displacement parameters, where $P' = (1 - \nu)RP/h^2\mu$ or $RP/h^2\mu$ for the simply supported and clamped cases, respectively, and $\Delta' = \Delta R/h^2$ for both end conditions. The nondimensional moment parameter is given by $M' = (1 - \nu)RP/h^3\mu$ for simply supported and $RP/h^3\mu$ for fixed end conditions. In this nondimensional scheme, $\mu = E/2(1 + \nu)$. The elementary beam theory values were obtained by using the concentrated load and moment resulting from the contact stresses in appropriate elementary beam theory equations for a simply supported or clamped beam loaded by a point load and moment. As can be seen from Tables 3 and 4, the elementary beam theory values for Δ' are in good agreement with those obtained from the superposition solution for central indentation and when $c/h < 1.0$; even when $c/h = 2.0$, there is only approximately a ten percent difference. However, as a/L is decreased, the agreement between elementary beam theory and numerical results becomes increasingly poor when c/h exceeded 1.0 for both the simply supported and fixed ends. This is due to the distributed nature of the actual loads when $c/h \geq 1.0$ and the fact that the centroid of the area under the contact stress distribution curves shifts away from $x = 0$ as the loading becomes increasingly asymmetric.

Alternatively, there was good agreement between superposition solution displacement values and those obtained using a modified beam theory. Modified beam theory displacements are obtained by approximating the numerically calculated stress distributions as a set of 48 point loads, calculating the displacements for each load using basic beam theory equations, and then summing the resulting displacements. The fact that the displacement values obtained using the modified beam theory follow the nonlinear behavior of those obtained from the numerical calculations suggest that this behavior is indeed a result of the distributed nature of the contact stresses. Although the modified beam theory results are in general agreement with those of the numerical calculations, several cases show more of difference than others. The highest differences occur for indenter locations closest to a support, i.e., small a/L. At these locations, the trigonometric terms in the coupled equations for $\psi(t)$ and $\phi(t)$ and in the equation for Δ have the greatest difference in frequency which makes the kernels more erratic and difficult to integrate numerically. In addition,

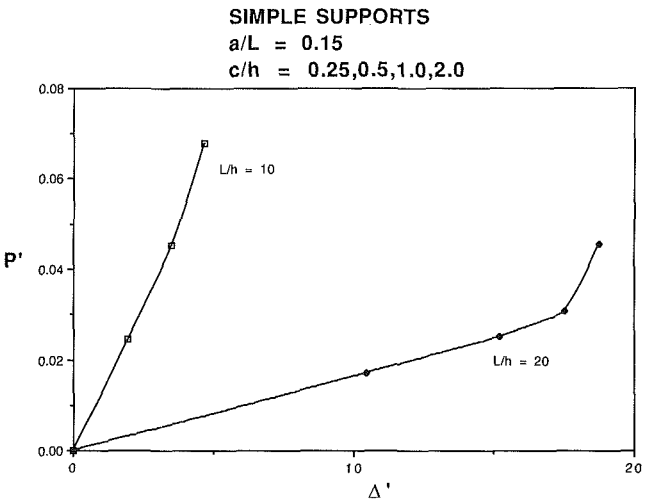


Fig. 7 Load-displacement curves (L/h = 10, 20, a/L = 0.15, simply supported beam)

decreasing the value of L/h increased the amplitude of all trigonometric terms which further contributes to the difficulties. However, the most significant factor that affects the numerical integration of the kernels is the choice of end conditions. As can be seen by comparing the kernels for the simply supported and fixed end conditions, the kernels for simply supported ends converge at a rate of $1/\xi^2$, while those for fixed ends converge at the much slower rate of $1/\xi$. Although a high level of accuracy was maintained in evaluating the kernels for both end conditions, it was not physically possible to integrate the kernels for the fixed end equations to exactly the same accuracy as those of the simply supported cases due to the limited computer time available.

The data in Tables 3 and 4 are plotted in Figs. 5 through 7 to illustrate the load-deflection relationships for various geometric and indentation parameters. These plots show a linear behavior for small c/h values (i.e., $c/h < 1.0$) and a nonlinear response for large c/h (i.e., $c/h > 1.0$). The nonlinear section of these curves indicate a region in which the distributed nature of the actual contact loading becomes significant.

Conclusions

Based on the results obtained in this investigation, it is apparent that Hertzian distributions can be used to model contact stress distributions for central indentation if $c/h < 1.0$. For

Downloaded 03 May 2010 to 171.66.16.245. Redistribution subject to ASME license or copyright; see http://www.asme.org/terms/Terms_Use.cfm

large c/h values, (i.e., $c/h \geq 1.0$) contact stress distributions become significantly non-Hertzian with increased maximum values located near the edge of the contact region. A study of the load-displacement relationships indicated that elementary beam theory is sufficient to predict displacement due to contact loads that result in small contact lengths (i.e., $c/h < 0.5$ to 1.0) and that are due to near-central indentation. For large contact lengths ($c/h \geq 1.0$), elementary beam theory overpredicts actual displacement values. The amount of overprediction increases as c/h increases and a/L decreases. Off-center indentation with large c/h values results in nonlinear load-displacement response.

Acknowledgments

The authors are grateful for the support of the University of Alabama in Huntsville College of Engineering and the NASA/Marshall Space Flight Center.

References

Keer, L. M., and Miller, G. R., 1983, "Smooth Indentation of a Finite Layer," *Journal of Engineering Mechanics*, Vol. 109, No. 3, pp. 706–717.

Keer, L. M., and Schonberg, W. P., 1986a, "Smooth Indentation of an Isotropic Cantilever Beam," *International Journal of Solids and Structures*, Vol. 22, No. 1, pp. 87–106.

Keer, L. M., and Schonberg, W. P., 1986b, "Smooth Indentation of a Transversely Isotropic Cantilever Beam," *International Journal of Solids and Structures*, Vol. 22, No. 9, pp. 1033–1053.

Peck, J. A., 1991, *Asymmetric Indentation of a Finite Elastically Supported Beam*, Master's Thesis, University of Alabama in Huntsville, Huntsville, AL.

Sneddon, I. N., 1951, *Fourier Transforms*, McGraw-Hill, New York.

Timoshenko, S. P., and Goodier, J. N., 1970, *Theory of Elasticity*, 3rd ed., McGraw-Hill, New York.

Downloaded 03 May 2010 to 171.66.16.245. Redistribution subject to ASME license or copyright; see http://www.asme.org/terms/Terms_Use.cfm

Journal of Applied Mechanics

Brief Notes

A Brief Note is a short paper that presents a specific solution of technical interest in mechanics but which does not necessarily contain new general methods or results. A Brief Note should not exceed 1500 words *or equivalent* (a typical one-column figure or table is equivalent to 250 words; a one line equation to 30 words). Brief Notes will be subject to the usual review procedures prior to publication. After approval such Notes will be published as soon as possible. The Notes should be submitted to the Technical Editor of the JOURNAL OF APPLIED MECHANICS. Discussions on the Brief Notes should be addressed to the Editorial Department, ASME, United Engineering Center, 345 East 47th Street, New York, N. Y. 10017, or to the Technical Editor of the JOURNAL OF APPLIED MECHANICS. Discussions on Brief Notes appearing in this issue will be accepted until two months after publication. Readers who need more time to prepare a Discussion should request an extension of the deadline from the Editorial Department.

The Dynamic Energy Release Rate of Delaminations Based on Midlin-Type Nonlinear Plate Theory

A. E. Giannakopoulos[1] and K. -F. Nilsson[1]

The delamination will be taken to be between two plates and bounded by a curve, $\partial\Omega$, on the reference midplane $x_3 = 0$. The delamination is assumed to grow in its own reference plane (x_1, x_2). At time t, the instaneous velocity of $\partial\Omega$ in the normal outward direction, along its line coordinate s, is $v(s, t)$. It is our objective to derive an expression for the dynamic energy release rate including the transverse shear effect, in analogy with the expression derived by Storakers and Andersson (1988) for the static case, and by Giannakopoulos (1991) for the dynamic case with von Karman kinematics. There are, of course, other plate theories that can be used in such problems. Higher order plate theories closer approach the full three-dimensional theory. However, the complexity increases, especially when it comes to model the corresponding boundary conditions. We therefore believe that a first-order plate theory is sufficient to describe the small strains and the large rotations that dominate in very thin plate problems.

The plate theory adopted is of Mindlin type (K. -F. Nilsson, 1991). The displacements are given in cartesian coordinates as

$$u_\alpha(x_1, x_2, x_3, t) = \bar{u}_\alpha(x_1, x_2, t) + x_3\theta_\alpha(x_1, x_2, t) \tag{1a}$$

$$u_3(x_1, x_2, x_3, t) = \bar{u}_3(x_1, x_2, t). \tag{1b}$$

Greek indices run from 1 to 2 and Latin indices from 1 to 3. In Eq. (1), the bar indicates midplane displacements, and θ_α denotes the rotation of a transverse material fiber which is taken to remain straight and inextensional during deformation (Cosserat solid).

[1]Department of Solid Mechanics, The Royal Institute of Technology, S-10044 Stockholm, Sweden.

Contributed by the Applied Mechanics Division of THE AMERICAN SOCIETY OF MECHANICAL ENGINEERS for publication in the ASME JOURNAL OF APPLIED MECHANICS. Manuscript received by the ASME Applied Mechanics Division, Oct. 7, 1991; final revision, Aug. 17, 1992. Associate Technical Editor: F. Y. M. Wan.

In-plane rotations are assumed negligible. Then the Green-Lagrange strains of interest are (Wempner, 1981)

$$e_{\alpha\beta} = (\bar{u}_{\alpha,\beta} + \bar{u}_{\beta,\alpha} + \bar{u}_{3,\alpha}\bar{u}_{3,\beta})/2 + x_3(\theta_{\alpha,\beta} + \theta_{\beta,\alpha})/2$$
$$= e^0_{\alpha\beta} + e^b_{\alpha\beta} \tag{2a}$$

$$e_{\alpha 3} = (\bar{u}_{\alpha,3} + \theta_\alpha)/2 \tag{2b}$$

The comma indicates differentiation with respect to x_i coordinates.

In the sequel, we will use $(e^0_{\alpha\beta}, e^b_{\alpha\beta}/x_3, 2e_{\alpha 3})$ as eight independent variables rather than three displacements $(\bar{u}_i)$ and two rotations (θ_α). We need eight Gauss-Codazzi compatibility equations:

$$e^0_{11,11} - 2e^0_{12,12} + e^0_{22,22} + (2e_{13,1} - e^b_{11}/x_3)(2e_{23,2} - e^b_{22}/x_3)$$
$$- (e_{13,2} + e_{23,1} - e^b_{12}/x_3)^2 = 0 \tag{3a}$$

$$e^b_{11,11} - 2e^b_{12,12} + e^b_{22,22} = 0 \tag{3b}$$

$$e_{\gamma 3,\alpha\beta} - e_{\gamma 3,\beta\alpha} = 0. \tag{3c}$$

A hyperelastic type of material can be modeled assuming a free energy, W, per unit of undeformed area of the reference midsurface. This potential (internal energy) is a function of the generalized strains

$$W = W(e^0_{\alpha\beta}, 2e_{\alpha 3}, e^b_{\alpha\beta}/x_3). \tag{4}$$

Then the constitutive equations for the work conjugate forces can be stated as (Wempner, 1981) follows:

$$N_{\alpha\beta} = \partial W/\partial e^0_{\alpha\beta} \quad \text{(membrane forces)} \tag{5a}$$

$$M_{\alpha\beta} = \partial W/\partial (e^b_{\alpha\beta}/x_3) \quad \text{(bending moments)} \tag{5b}$$

$$Q_\alpha = \partial W/\partial(2e_{\alpha 3}) \quad \text{(transverse forces)}. \tag{5c}$$

All the generalized forces are taken per unit length of the undeformed midplane configuration, and are, of course, functions of time t.

The five dynamic equilibrium equations of an infinitesimal undeformed plate element with distributed forces, p_i, acting on the midsurface are

$$N_{\alpha\beta,\beta} + p_\alpha = \rho\partial^2\bar{u}_\alpha/\partial t^2 \tag{6a}$$

$$Q_{\alpha,\alpha} + N_{\alpha\beta,\alpha}\bar{u}_{3,\beta} + p_3 = \rho\partial^2\bar{u}_3/\partial t^2 \tag{6b}$$

$$M_{\alpha\beta,\beta} - Q_\alpha = I_{\alpha\beta}\partial^2\theta_\beta/\partial t^2. \tag{6c}$$

Repeated indices indicate summation over the appropriate range. $I_{\alpha\beta}(= I_{\beta\alpha})$ is the rotational inertia density and ρ is the

Copyright © 1993 by ASME
Downloaded 03 May 2010 to 171.66.16.245. Redistribution subject to ASME license or copyright; see http://www.asme.org/terms/Terms_Use.cfm

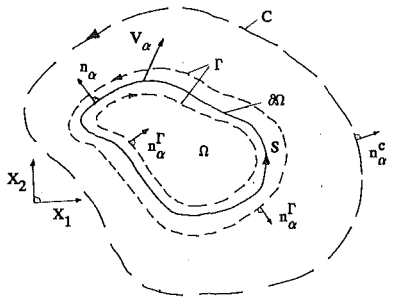


Fig. 1 Embedded delamination Ω advancing in its plane $x_1 - x_2$

mass density per unit area of the undeformed midsurface. $\partial(\ )/\partial t$ stands for velocity, and $\partial^2(\ )/\partial t^2$ for acceleration. The five generalized displacements $(\bar{u}_i, \theta_\alpha)$ and the corresponding velocities should conform with the imposed boundary and initial conditions.

The equilibrium of an edge plate element requires

$$N_{\alpha\beta} n_\beta^* = T_\alpha^* \tag{7a}$$

$$Q_\alpha n_\alpha^* + N_{\alpha\beta} n_\alpha^* \bar{u}_{3,\beta} = Q^* \tag{7b}$$

$$M_{\alpha\beta} n_\alpha^* = M_\alpha^* \epsilon_{\alpha\beta}. \tag{7c}$$

The star indicates boundary values and n_α^* is the boundary outward normal. $\epsilon_{\alpha\beta}$ is the permutation tensor. Equations (6) and (7) can also be derived from the variation of the Hamiltonean of the plate.

Let us denote the kinetic energy density of the system by

$$T = (\rho/2)\partial\bar{u}_i/\partial t \partial\bar{u}_i/\partial t + (I_{\alpha\beta}/2)\partial\theta_\alpha/\partial t \partial\theta_\beta/\partial t. \tag{8}$$

Take the inner product of the equilibrium equations with the generalized velocities. Then the differential form of the power balance becomes

$$p_i \partial\bar{u}_i/\partial t - \partial(W+T)/\partial t + \partial(\partial\bar{u}_\beta/\partial t N_{\alpha\beta} + \partial\bar{u}_3/\partial t Q_\alpha + \partial\theta_\beta/\partial t M_{\alpha\beta})/\partial x_\alpha = 0 \tag{9}$$

Consider a delaminated region enclosed by a curve C. A double contour Γ closely and completely surrounds the delamination front $\partial\Omega$ (Fig. 1). Contours C, Γ, and $\partial\Omega$ are sufficiently smooth. The contour Γ is fixed in size and orientation with the delamination front $\partial\Omega$ as it expands in the reference frame (x_1, x_2). Time t is treated as a spacial coordinate.

We integrate Eq. (9) with respect to the volume in the (x_1, x_2, t) space, as described previously by Nakamura et al. (1985). We then apply the divergence theorem and the Reynolds transport theorem to obtain the corresponding theorem of virtual velocities. It can be shown that the work done on the delamination increases the internal energy and advances the delamination front during the time interval (t_1, t_2). The instantaneous rate of the energy flow through Γ (dissipative power due to delamination advance) is

$$F(\Gamma) = \int_\Gamma (\partial\bar{u}_\beta/\partial t N_{\alpha\beta} + \partial\bar{u}_3/\partial t Q_\alpha + \partial\theta_\beta/\partial t M_{\alpha\beta} + (W+T)\delta_{\alpha\gamma} v n_\gamma^\Gamma) n_\alpha^\Gamma d\Gamma \tag{10}$$

where n_α^Γ is the unit normal to Γ, as shown in Fig. 1, and $\delta_{\alpha\beta}$ is Kroneker's delta.

Suppose that the generalized displacement field satisfies

$$\partial(\ )/\partial t \to -v n_\gamma \partial(\ )/\partial x_\gamma \text{ as } n_\alpha^\Gamma \to n_\alpha \tag{11}$$

where n_α is the unit outward normal of $\partial\Omega$. Condition (11) stands for the asymptotic steady-state delamination. This condition ensures the path independency of $F(\Gamma)$ (Giannakopoulos, 1991). Then, the dynamic energy release rate (energy released from the delamination per unit delamination advance) is defined as

$$G = \lim_{\Gamma \to \partial\Omega} F(\Gamma)/v = \int_{\partial\Omega} \|P_{\alpha\gamma}\| n_\alpha n_\gamma ds \tag{12}$$

with

$$P_{\alpha\beta} = (W+T)\delta_{\alpha\beta} - N_{\alpha\gamma}\bar{u}_{\gamma,\beta} - Q_\alpha \bar{u}_{3,\beta} - M_{\alpha\gamma}\theta_{\alpha,\beta} \tag{13}$$

where $\| \ \|$ denotes the jump across $\partial\Omega$. Aligning a coordinate direction to always be normal to the delamination front ($n_1 = 1$, $n_2 = 0$), we obtain

$$\|P_{\alpha\gamma}\| n_\alpha n_\gamma = \|P_{11}\| = \| (W+T) - N_{1\alpha}\bar{u}_{\alpha,1} - Q_1 \bar{u}_{3,1} - M_{1\alpha}\theta_{\alpha,1} \|. \tag{14}$$

Equation (14) is the local expression of the energy release rate and depends on s and $v(s)$. The result (14) resembles the one derived by Giannakopoulos (1991) for von Karman kinematics, provided that $\theta_{\alpha,1}$ has to be replaced by $-\bar{u}_{3,\alpha 1}$, and T in Eq. (8) should contain only the first term. Moreover, Eq. (14) is a simple algebraic expression based on generalized displacements and forces. It can be easily incorporated into a FEM code, as was done by Nilsson and Giannakopoulos (1990) for the static case.

A typical dynamic type of Griffith fracture criterion may be associated with the dynamic energy release rate

$$\|P_{11}\| = G_c(v) \ \rightarrow \text{growth at point } s \text{ of } \partial\Omega. \tag{15}$$

Here $G_c(v)$ characterizes the dynamic fracture of the material interface pointwise under specific environmental conditions. Equation (15) actually determines the delamination front motion. In case of small-scale yielding, bridging, contact, etc., a local analysis should be performed to reveal the relevant shielding effect, with $\|P_{11}\|$ serving as the far-field strength to the crack tip.

A more general approach to this problem would be by taking the power balance equation as

$$\rho\dot{e} = M_{\alpha\beta}\dot{e}_{\alpha\beta}^b + N_{\alpha\beta}\dot{e}_{\alpha\beta}^0 + 2Q_\alpha \dot{e}_{\alpha 3} - (\dot{h}_{\alpha,\alpha} + H_{\alpha\beta}\dot{h}_{\alpha,3\beta}), \tag{16}$$

with the dots indicating partial differentiation with respect to time. Here e is the internal energy per unit mass of the plate and h_α is the average heat flux of the midsurface. $H_{\alpha\beta}(=H_{\beta\alpha})$ are the heat flux first moment coefficients that depend on the plate's properties across its thickness, and are, with respect to the midsurface. It can be easily derived that in place of (13) we have

$$P_{\alpha\beta} = (e+T)\delta_{\alpha\beta} - N_{\alpha\gamma}\bar{u}_{\gamma,\beta} - Q_\alpha \bar{u}_{3,\beta} - M_{\alpha\gamma}\theta_{\gamma,\beta} + (h_{\alpha,\beta} + H_{\alpha\gamma}h_{\gamma,3\beta}) \tag{17}$$

a result similar to Kostrov and Nikitin (1970).

Acknowledgment

The authors want to thank Prof. F. Nilsson for bringing to our attention the general formulation of the power balance equation.

References

Giannakopoulos, A. E., 1991, "The Energy Release Rate of Dynamic Delamination," submitted for publication.

Kostrov, B. V., and Nikitin, L. V., 1970, "Some General Problems of Mechanics of Brittle Fracture," *Arch. Mech. Stos.*, Vol. 22, pp. 749–776.

Nakamura, T., Shih, C.-F., and Freund, L. B., 1985, "Computational Methods Based on Energy Integral in Dynamic Fracture," *Int. J. of Fracture*, Vol. 27, pp. 229–243.

Nilsson, K.-F., 1991, private communication.

Nilsson, K.-F., and Giannakopoulos, A. E., 1990, "Finite Element Simulation of Delamination Growth," *Proceedings of the First International Conference on Computer-Aided Assessment and Control of Localized Damage*, Vol. 2, M. H. Aliabadi, C. A. Brebbia, and D. J. Cartwright, eds., Springer-Verlag, New York, pp. 299–313.

Storakers, B., and Andersson, B., 1988, "Nonlinear Plate Theory Applied to Delamination in Composites," *J. Mech. Phys. Solids*, Vol. 36, pp. 689–718.

Wempner, G., 1981, *Mechanics of Solids with Applications to Thin Bodies*, Sijthoff and Noordhoff, Netherlands.

Downloaded 03 May 2010 to 171.66.16.245. Redistribution subject to ASME license or copyright; see http://www.asme.org/terms/Terms_Use.cfm

Eshelby Tensor for an Elastic Inclusion With Slightly Weakened Interface

Jianmin Qu[2]

The Eshelby tensor for an ellipsoidal inclusion in an elastic matrix of infinite extent is considered in this paper. Instead of assuming perfect bonding between the inclusion and the matrix, the interface between the inclusion and the matrix is modeled by a spring layer of vanishing thickness. The inclusion-matrix interface is said to be slightly weakened if the compliance of the spring layer is much smaller than that of the matrix material. By virtue of the Betti-Rayleigh reciprocal identity in linear elasticity, an integral representation for the displacement field due to an elastic inclusion with a spring layer interface is derived. Explicit expressions of the Eshelby tensor for an ellipsoidal inclusion with slightly weakened interface are obtained through an iteration procedure developed from the integral representation.

1 Introduction

In this paper, an elastic *inclusion* is defined as a subdomain Ω in a homogeneous elastic matrix over which a distribution of eigenstrain (stress-free transformation strain) is prescribed. The elastic moduli for the inclusion and the matrix are assumed the same.

It was shown by Eshelby (1957) that the total strain in an ellipsoidal inclusion is uniform if the eigenstrain distribution is uniform, namely,

$$\epsilon_{ij} = S_{ijkl}\epsilon^*_{kl}, \tag{1}$$

where ϵ^*_{kl} is the uniform eigenstrain, ϵ_{ij} is the total strain in the inclusion, and S_{ijkl} is referred to the Eshelby inclusion tensor.

The inclusions and inhomogeneities studied by Eshelby are perfectly bonded to the matrix. However, the condition of perfect bonding is sometimes inadequate. Inclusions in high-strength steel, for example, are easily debonded after a few cyclic loadings. Grain boundary sliding in polycrystals and granular materials are common phenomena. Fiber-matrix interfaces in ceramic matrix composites are designed to debond for higher toughness. Defects and damage may also develop on the fiber-matrix interfaces and consequently the interfaces become nonperfect.

In this paper, an attempt is made to incorporate some of the interface properties into the solution of the inclusion problem. The inclusion-matrix interface is characterized by a thin layer of distributed springs. In the limit of vanishing layer thickness, the interfacial traction remains continuous, but the displacements at the two sides of the spring layer become discontinuous. This linear spring layer model has been explored by several investigators in some other context (e.g., Benveniste, 1985; Steif and Dollar, 1988; Achenbach and Zhu, 1989; Bassani and Qu, 1990; Pagano and Tandon, 1990; Jasiuk and Tong, 1989, etc.). The main objective of this paper is to derive an explicit expression of the Eshelby tensor for inclusions with slightly weakened interfaces. An interface is said to be slightly weakened if the compliance of the spring layer is much smaller than that of the matrix material.

2 Integral Representation

Consider a homogeneous, linearly elastic body, V. If an eigenstrain distribution ϵ^*_{ij} is given in V, the displacement equations of equilibrium in the Cartesian coordinate system (x_1, x_2, x_3) can be written as (Mura, 1987)

$$L_{ijkl}u_{k,lj} - L_{ijkl}\epsilon^*_{kl,j} = 0, \quad \mathbf{x}\in V \tag{2}$$

where u_i is the displacement component and L_{ijkl} is the fourth-order elasticity tensor. It relates the stress tensor, σ_{ij}, to the elastic strain tensor, ϵ_{kl}, through Hooke's law

$$\sigma_{ij} = L_{ijkl}(\epsilon_{kl} - \epsilon^*_{kl}) = L_{ijkl}(u_{k,l} - \epsilon^*_{kl}). \tag{3a,b}$$

In (2)-(3) and the sequel, a comma stands for partial differentiation. It is obvious from (2) that the presence of eigenstrains is equivalent to a body force $f_i = -L_{ijkl}\epsilon^*_{kl,j}$.

By virtue of the Betti-Rayleigh reciprocal identity, one can derive an integral representation of the displacement field u_i for the eigenstrain problem (2)

$$\int_S L_{jlmn}[\phi_{ji}(\xi - \mathbf{x})u_{m,n}(\xi) - u_j(\xi)\phi_{mi,n}(\xi - \mathbf{x})]n_l\, ds(\xi)$$

$$-\int_V L_{jlmn}\epsilon^*_{mn,l}(\xi)\phi_{ji}(\xi - \mathbf{x})\, dv(\xi) = \begin{cases} u_i(\mathbf{x}) & \mathbf{x}\in V \\ 0 & \mathbf{x}\notin V \end{cases} \tag{4a,b}$$

where $\phi_{ji}(\xi - \mathbf{x})$ is the Green's function in an infinite domain. This integral representation will be used to develop the solution of the inclusion problem in the following sections.

3 Ellipsoidal Inclusion

Consider an ellipsoidal subdomain Ω in a homogeneous, linearly elastic solid of infinite extent D. The subdomain Ω is called an inclusion when eigenstrain $\epsilon^*_{mn} \neq 0$ is prescribed in Ω. The interface between the inclusion and the matrix is assumed nonperfect. A spring layer of vanishing thickness will be used to characterize the nonperfect bonding. In this model, the interfacial traction is still continuous, but displacement discontinuity may occur at the interface. The jump in displacement at the interface is related to the interfacial traction. Although some nonlinear relations between the interfacial traction and displacement jumps may be proposed, a liner spring layer model will be explored in this paper.

If S and n_i are used, respectively, to denote the interface and its unit outward normal vector, the interfacial conditions may be written as

$$\Delta\sigma_{ij}n_j = [\sigma_{ij}(\mathbf{x})|_{S^+} - \sigma_{ij}(\mathbf{x})|_{S^-}]n_j = 0, \tag{5}$$

$$\Delta u_i = u_i(\mathbf{x})|_{S^+} - u_i(\mathbf{x})|_{S^-} = \eta_{ij}\sigma_{jk}n_k, \tag{6}$$

where $u_i(\mathbf{x})|_{S^+}$ and $u_i(\mathbf{x})|_{S^-}$ are the values of $u_i(\mathbf{x})$ as $\mathbf{x}$ approaching the interface from outside and inside of the inclusion, respectively, so are $\sigma_{ij}(\mathbf{x})|_{S^+}$ and $\sigma_{ij}(\mathbf{x})|_{S^-}$. In (6), the second-order tensor η_{ij} represents the compliance of the interface (spring layer). For simplicity, it is assumed in this paper that η_{ij} is symmetric and positive definite. It is also clear from (6) that $\eta_{ij} = 0$ corresponds to a perfect interface, while $\eta_{ij} \to \infty$ represents complete debond ($\sigma_{jk}n_k = 0$ on S). From this point of view, a slightly weakened interface may be modeled by small η_{ij}.

[2]George W. Woodruff School of Mechanical Engineering, Georgia Institute of Technology, Atlanta, GA 30332-0405. Assoc. Mem. ASME.

Contributed by the Applied Mechanics Division of THE AMERICAN SOCIETY OF MECHANICAL ENGINEERS for publication in the ASME JOURNAL OF APPLIED MECHANICS. Manuscript received by the ASME Applied Mechanics Division, Nov. 19, 1991; final revision, Aug. 14, 1992. Associate Technical Editor: X. Markenscoff.

Copyright © 1993 by ASME
Downloaded 03 May 2010 to 171.66.16.245. Redistribution subject to ASME license or copyright; see http://www.asme.org/terms/Terms_Use.cfm

A special form of η_{ij} that has some physical significance is given by

$$\eta_{ij} = \alpha\delta_{ij} + (\beta - \alpha)n_i n_j. \tag{7}$$

It can be easily shown that α and β represent the compliance in the tangential and normal directions of the interface, respectively, i.e.,

$$\Delta u_i(\delta_{ik} - n_i n_k) = \alpha\sigma_{ij}n_j(\delta_{ik} - n_i n_k), \tag{8a}$$

$$\Delta u_i n_i = \beta\sigma_{ij}n_j n_i. \tag{8b}$$

When $\beta = 0$, this constitutive characterization of the interface allows relative sliding between the two surfaces, but not separation. Furthermore, the free-sliding case studied by Mura (1987) can be achieved by setting $\alpha \to \infty$ with $\beta = 0$. Therefore, solutions to the case of small α with $\beta = 0$ provide the approximation in contrast to the sliding interface. It also should be mentioned here that material interpenetration may take place when $\beta \neq 0$, which is a violation of the compatibility requirement. Further discussions on this issue may be found in Achenbach and Zhu (1989).

When the region V is taken to be the inclusion Ω, the integral representation (4*a*) is readily applicable to yield the displacement field inside the inclusion,

$$u_i(\mathbf{x}) = \int_{S^-} L_{jlmn}\{\phi_{ji}(\xi - \mathbf{x})[u_{m,n}(\xi) - \epsilon^*_{mn}(\xi)] - u_j(\xi)\phi_{mi,n}(\xi - \mathbf{x})\}n_l\, ds(\xi) + \int_\Omega L_{jlmn}\epsilon^*_{mn}(\xi)\phi_{ji,l}(\xi - \mathbf{x})dv(\xi), \quad \text{for } \mathbf{x}\in\Omega. \tag{9}$$

Next we take V to be the region exterior to Ω, i.e., $V = D - \Omega$. Then for $\mathbf{x}$ inside Ω, or equivalently, for $\mathbf{x}$ outside V, (4*b*) yields

$$\int_{S^+} L_{jlmn}[\phi_{ji}(\xi - \mathbf{x})u_{m,n}(\xi) - u_j(\xi)\phi_{mi,n}(\xi - \mathbf{x})]n_l\, ds(\xi) = 0. \tag{10}$$

Note that both (9) and (10) are valid for $\mathbf{x} \in \Omega$. Thus it follows from subtracting (10) from (9) and making use of (5) that

$$u_i(\mathbf{x}) = \int_\Omega L_{jlmn}\epsilon^*_{mn}(\xi)\phi_{ji,l}(\xi - \mathbf{x})dv(\xi) + \int_S L_{jlmn}\Delta u_j(\xi)\phi_{mi,n}(\xi - \mathbf{x})n_l\, ds(\xi). \tag{11}$$

An integral equation for u_i can be obtained by letting the point $\mathbf{x}$ approach the boundary S in (11). In general, the integral equation cannot be solved analytically. Numerical solutions to the integral equation are discussed elsewhere (Qu, 1992). We proceed here to discuss some special cases of (11) and develop approximate and asymptotic solutions.

First, we assume the eigenstrain ϵ^*_{ij} is uniform in Ω. It then follows from (11) that

$$\epsilon_{ij}(\mathbf{x}) = -\epsilon^*_{kl}L_{klmn}\int_\Omega G_{ijmn}(\xi - \mathbf{x})dv(\xi) - L_{klmn}\int_S \Delta u_k(\xi)G_{ijmn}(\xi - \mathbf{x})n_l\, ds(\xi), \tag{12}$$

where

$$G_{ijmn}(\mathbf{x}) = \frac{1}{4}[\phi_{mi,nj}(\mathbf{x}) + \phi_{mj,ni}(\mathbf{x}) + \phi_{ni,mj}(\mathbf{x}) + \phi_{nj,mi}(\mathbf{x})]. \tag{13}$$

It can be shown that the volume integral in (12) is independent of $\mathbf{x}$, and furthermore,

$$-L_{klmn}\int_\Omega G_{ijmn}(\xi - \mathbf{x})dv(\xi) = S_{ijkl}, \; x\in\Omega, \tag{14}$$

where S_{ijkl} is the original Eshelby inclusion tensor. Expressions of S_{ijkl} for both isotropic and anisotropic materials can be found in Mura's book (1987). Substituting (14) into (12) yields

$$\epsilon_{ij}(\mathbf{x}) = S_{ijkl}\epsilon^*_{kl} - L_{klmn}\int_S \Delta u_k(\xi)G_{ijmn}(\xi - \mathbf{x})n_l\, ds(\xi). \tag{15a}$$

An alternative expression of (15*a*) can be obtained by using the jump condition (6),

$$\epsilon_{ij}(\mathbf{x}) = S_{ijkl}\epsilon^*_{kl} - L_{klmn}\int_S \eta_{kp}\sigma_{pq}(\xi)G_{ijmn}(\xi - \mathbf{x})n_q n_l\, ds(\xi). \tag{15b}$$

Clearly, the first term in (15) is identical to the original Eshelby solution. The effect of spring-layer interface comes in through the surface integral involving the displacement jump at the interface. Since perfect (interface) bonding corresponds to $\eta_{ij} = 0$, a slightly weakened (interface) bonding may be modeled by very small η_{ij}. Thus (15) provides a convenient basis to construct asymptotic solutions for slightly weakened interfaces.

To this end, we replace $\sigma_{pq}(\xi)$ in (15*b*) by the right-hand side of (3*a*)

$$\epsilon_{ij}(\mathbf{x}) = S_{ijkl}\epsilon^*_{kl} + L_{klmn}L_{pqst}\epsilon^*_{st}\int_S \eta_{kp}G_{ijmn}(\xi - \mathbf{x})n_q n_l\, ds(\xi) - L_{klmn}L_{pqst}\int_S \eta_{kp}\epsilon_{st}(\epsilon)G_{ijmn}(\xi - \mathbf{x})n_q n_l\, ds(\xi). \tag{16}$$

An iteration procedure can now be formulated

$$\epsilon^{(n)}_{ij}(\mathbf{x}) = S_{ijkl}\epsilon^*_{kl} + L_{klmn}L_{pqst}\epsilon^*_{st}\int_S \eta_{kp}G_{ijmn}(\xi - \mathbf{x})n_q n_l\, ds(\xi) - L_{klmn}L_{pqst}\int_S \eta_{kp}\epsilon^{(n-1)}_{st}(\xi)G_{ijmn}(\xi - \mathbf{x})n_q n_l\, ds(\xi), \quad n = 1, 2, \ldots \tag{17}$$

where one may take the initial value to be

$$\epsilon^{(o)}_{ij} = S_{ijkl}\epsilon^*_{kl}.$$

The leading order solution for small η_{kp} can then be obtained

$$\epsilon_{kl}(\mathbf{x}) \approx \epsilon^{(1)}_{ij}(\mathbf{x}) = S_{ijkl}\epsilon^*_{kl} + T_{ijst}(\mathbf{x})(I_{stkl} - S_{stkl})\epsilon^*_{kl}, \tag{18}$$

where

$$T_{ijst}(\mathbf{x}) = L_{klmn}L_{stpq}\int_S \eta_{kp}G_{ijmn}(\xi - \mathbf{x})n_q n_l\, ds(\xi). \tag{19}$$

An alternative form of (18) may be written as

$$\epsilon_{ij}(\mathbf{x}) = S^o_{ijkl}(\mathbf{x})\epsilon^*_{kl}, \tag{20}$$

where

$$S^o_{ijkl}(\mathbf{x}) = S_{ijkl} + T_{ijst}(\mathbf{x})(I_{stkl} - S_{stkl}). \tag{21}$$

This $S^o_{ijkl}(\mathbf{x})$ may be defined as the modified Eshelby inclusion tensor for an ellipsoidal inclusion with slightly weakened interface.

Equation (20) provides the first-order asymptotic solution for the total strain field inside an ellipsoidal inclusion with slightly weakened interface. It is seen that the strains are no longer uniform in this general case.

In Fig. 1, the asymptotic strain field inside an ellipsoidal inclusion is presented. The surface of the ellipsoid is given by $(x_1/a_1)^2 + (x_2/a_2)^2(x_3/a_3)^2 = 1$, where $a_3/a_1 = a_3/a_2 = 0.6$. The numerical calculation is based on an isotropic solid with bulk modulus K and shear modulus μ, where $K/\mu = 1.7$. The eigenstrain distribution is a simple shear $\epsilon^*_{ij} = \delta_{i1}\delta_{j2} + \delta_{j1}\delta_{i2}$. In this case, the total strain inside the inclusion is also a simple shear,

Downloaded 03 May 2010 to 171.66.16.245. Redistribution subject to ASME license or copyright; see http://www.asme.org/terms/Terms_Use.cfm

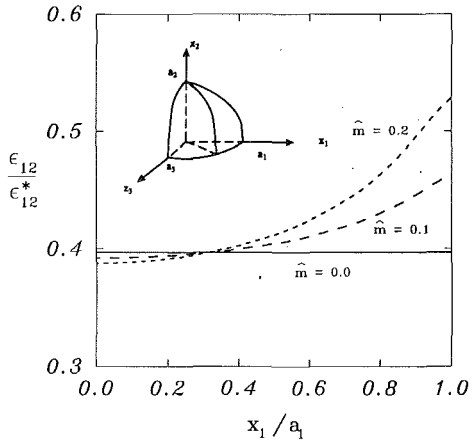


Fig. 1 Strain distribution in an ellipsoidal inclusion, $(x_1/a_1)^2+(x_2/a_1)^2+(x_3/a_3)^2=1$, where $a_3/a_1=0.6$, $\hat{m}=\mu\alpha/a_1$

$\epsilon_{ij}=(\delta_{i1}\delta_{j2}+\delta_{j1}\delta_{i2})\epsilon_{12}$. The distribution of $\epsilon_{12}/\epsilon^*_{12}$ for various values of $\hat{m}=\mu\alpha/a_1$ and $\beta=0$ is plotted in Fig. 1 for $x_2=x_3=0$, $0\le x_1<a_1$.

4 Summary

The Eshelby tensor for an ellipsoidal inclusion with a spring-layer interface has been studied in this paper. An integral representation for the strain field inside an elastic inclusion (of arbitrary shape) with a spring-layer interface is derived, which can be used to establish an integral equation for the inclusion problem. An iteration procedure is developed for the solution of the Eshelby tensor for an ellipsoidal inclusion with slightly weakened interface, and the explicit first-order expression of the Eshelby tensor is given.

Acknowledgments

This work is partially supported by the NSF under Grant MSS-9119291.

References

Achenbach, J. D., and Zhu, H., 1989, "Effect of Interfacial Zone on Mechanical Behavior and Failure of Fiber-Reinforced Composites," *J. Mech. Phys. Solids*, Vol. 37, pp. 381–393.

Bassani, J. L., and Qu, J., 1990, "Interfacial Discontinuities and Average Bimaterial Properties," *Acta/Scripta Metall.* Proc. Ser., Vol. 4, pp. 401–406.

Benveniste, Y., 1985, "The Effective Mechanical Behavior of Composite Materials with Imperfect Contact between the Constituents," *Mechanics of Materials*, Vol. 4, pp. 197–208.

Eshelby, J. D., 1957, "The Determination of the Elastic Field of an Ellipsoidal Inclusion, and Related Problems," *Proc. Roy. Soc., London*, Vol. A241, pp. 376–396.

Jasiuk, I., and Tong, Y., 1989, "The Effect of Interface on the Elastic Stiffness of Composites," *Mechanics of Composite Materials and Structures*, Proc. of the Third Joint ASCE/ASME Conference, pp. 49–54.

Mura, T., 1987, *Micromechanics of Defects in Solids*, Martinus Nijhoff Pub., Boston.

Pagano, N. J., and Tandon, G. P., 1990, "Modeling of Imperfect Bonding in Fiber Reinforced Brittle Matrix Composites," *Mechanics of Materials*, Vol. 9, pp. 49–64.

Qu, J., 1993, "Effects of Slightly Weakened Interfaces on the Overall Elastic Properties of Composite Materials," *Mechanics of Materials*, Vol. 14, pp. 269–281.

Steif, P. S., and Dollar, A., 1988, "Longitudinal Shearing of a Weakly Bonded Fiber Composite," ASME JOURNAL OF APPLIED MECHANICS, Vol. 55, pp. 618–623.

End Shortening Relation and Stability of Columns on Nonlinear Foundation

M. O. Oyesanya[3]

We derive the end shortening relations for both the primary and secondary bifurcation states of columns on nonlinear foundation and use Budiansky's pictorial stability theorem to show the instability of these states.

1 Introduction

The axially compressed columns on nonlinear "softening" elastic foundations is an imperfection-sensitive structure that exhibits all the interesting features of such structures and yet is governed by tractable boundary value problem.

Amazigo and Oyesanya (1986) showed the existence of secondary bifurcation states for columns on nonlinear "softening" elastic foundation. In that paper it was shown that for values of the length that are slightly different from the critical value, the multiple primary point splits into simple primary points and secondary bifurcation points. The corresponding secondary states bifurcate subcritically showing existence of secondary bifurcation loads which are lower than the classical buckling.

The stability analysis of this important structure was not undertaken in that paper. In this paper we undertake this analysis using the end shortening relations and Budiansky's pictorial stability theorem (Budiansky, 1974).

We show that both the primary and the secondary states are unstable. The primary state exchanges its stability with the secondary state and exhibits a "mode jumping" phenomenon at the secondary bifurcation point.

2 Formulation and Post-Buckling Analysis

The nondimensional form of the boundary value problem for the lateral displacement $w(x)$ of a perfect elastic column supported laterally by a continuous nonlinear elastic foundation consists of

$$L_\alpha[w,\lambda]\equiv\alpha^2 w''''+2\lambda\alpha w''+w=w^3,\quad 0<x<\pi \tag{1}$$

$$w=w''=0 \quad \text{at} \quad x=0,\ \pi. \tag{2}$$

The nondimensional axial coordinate x, lateral displacement $w(x)$, and the axial load parameter λ are related to the corresponding physical quantities by

[3]Department of Mathematics, University of Nigeria, Nsukka, Nigeria.

Contributed by the Applied Mechanics Division of THE AMERICAN SOCIETY OF MECHANICAL ENGINEERS for publication in the ASME JOURNAL OF APPLIED MECHANICS. Manuscript received by the ASME Applied Mechanics Division, Aug. 21, 1991; final revision, Aug. 17, 1992. Associate Technical Editor: P. D. Spanos.

Downloaded 03 May 2010 to 171.66.16.245. Redistribution subject to ASME license or copyright; see http://www.asme.org/terms/Terms_Use.cfm

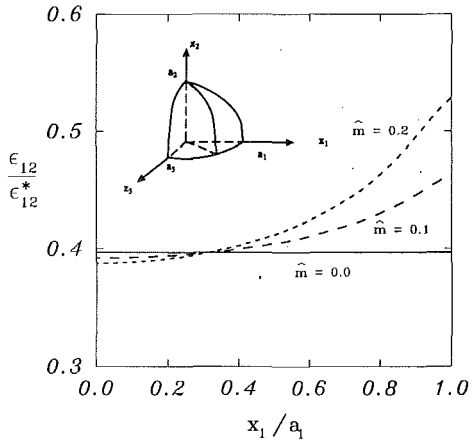


Fig. 1 Strain distribution in an ellipsoidal inclusion, $(x_1/a_1)^2 + (x_2/a_1)^2 + (x_3/a_3)^2 = 1$, where $a_3/a_1 = 0.6$, $\hat{m} = \mu\alpha/a_1$

$\epsilon_{ij} = (\delta_{i1}\delta_{j2} + \delta_{j1}\delta_{i2})\epsilon_{12}$. The distribution of $\epsilon_{12}/\epsilon^*_{12}$ for various values of $\hat{m} = \mu\alpha/a_1$ and $\beta = 0$ is plotted in Fig. 1 for $x_2 = x_3 = 0$, $0 \le x_1 < a_1$.

4 Summary

The Eshelby tensor for an ellipsoidal inclusion with a spring-layer interface has been studied in this paper. An integral representation for the strain field inside an elastic inclusion (of arbitrary shape) with a spring-layer interface is derived, which can be used to establish an integral equation for the inclusion problem. An iteration procedure is developed for the solution of the Eshelby tensor for an ellipsoidal inclusion with slightly weakened interface, and the explicit first-order expression of the Eshelby tensor is given.

Acknowledgments

This work is partially supported by the NSF under Grant MSS-9119291.

References

Achenbach, J. D., and Zhu, H., 1989, "Effect of Interfacial Zone on Mechanical Behavior and Failure of Fiber-Reinforced Composites," *J. Mech. Phys. Solids*, Vol. 37, pp. 381–393.

Bassani, J. L., and Qu, J., 1990, "Interfacial Discontinuities and Average Bimaterial Properties," *Acta/Scripta Metall.* Proc. Ser., Vol. 4, pp. 401–406.

Benveniste, Y., 1985, "The Effective Mechanical Behavior of Composite Materials with Imperfect Contact between the Constituents," *Mechanics of Materials*, Vol. 4, pp. 197–208.

Eshelby, J. D., 1957, "The Determination of the Elastic Field of an Ellipsoidal Inclusion, and Related Problems," *Proc. Roy. Soc., London*, Vol. A241, pp. 376–396.

Jasiuk, I., and Tong, Y., 1989, "The Effect of Interface on the Elastic Stiffness of Composites," *Mechanics of Composite Materials and Structures*, Proc. of the Third Joint ASCE/ASME Conference, pp. 49–54.

Mura, T., 1987, *Micromechanics of Defects in Solids*, Martinus Nijhoff Pub., Boston.

Pagano, N. J., and Tandon, G. P., 1990, "Modeling of Imperfect Bonding in Fiber Reinforced Brittle Matrix Composites," *Mechanics of Materials*, Vol. 9, pp. 49–64.

Qu, J., 1993, "Effects of Slightly Weakened Interfaces on the Overall Elastic Properties of Composite Materials," *Mechanics of Materials*, Vol. 14, pp. 269–281.

Steif, P. S., and Dollar, A., 1988, "Longitudinal Shearing of a Weakly Bonded Fiber Composite," ASME JOURNAL OF APPLIED MECHANICS, Vol. 55, pp. 618–623.

End Shortening Relation and Stability of Columns on Nonlinear Foundation

M. O. Oyesanya[3]

We derive the end shortening relations for both the primary and secondary bifurcation states of columns on nonlinear foundation and use Budiansky's pictorial stability theorem to show the instability of these states.

1 Introduction

The axially compressed columns on nonlinear "softening" elastic foundations is an imperfection-sensitive structure that exhibits all the interesting features of such structures and yet is governed by tractable boundary value problem.

Amazigo and Oyesanya (1986) showed the existence of secondary bifurcation states for columns on nonlinear "softening" elastic foundation. In that paper it was shown that for values of the length that are slightly different from the critical value, the multiple primary point splits into simple primary points and secondary bifurcation points. The corresponding secondary states bifurcate subcritically showing existence of secondary bifurcation loads which are lower than the classical buckling.

The stability analysis of this important structure was not undertaken in that paper. In this paper we undertake this analysis using the end shortening relations and Budiansky's pictorial stability theorem (Budiansky, 1974).

We show that both the primary and the secondary states are unstable. The primary state exchanges its stability with the secondary state and exhibits a "mode jumping" phenomenon at the secondary bifurcation point.

2 Formulation and Post-Buckling Analysis

The nondimensional form of the boundary value problem for the lateral displacement $w(x)$ of a perfect elastic column supported laterally by a continuous nonlinear elastic foundation consists of

$$L_\alpha[w, \lambda] \equiv \alpha^2 w'''' + 2\lambda\alpha w'' + w = w^3, \quad 0 < x < \pi \tag{1}$$

$$w = w'' = 0 \quad \text{at} \quad x = 0, \pi. \tag{2}$$

The nondimensional axial coordinate x, lateral displacement $w(x)$, and the axial load parameter λ are related to the corresponding physical quantities by

[3]Department of Mathematics, University of Nigeria, Nsukka, Nigeria.

Contributed by the Applied Mechanics Division of THE AMERICAN SOCIETY OF MECHANICAL ENGINEERS for publication in the ASME JOURNAL OF APPLIED MECHANICS. Manuscript received by the ASME Applied Mechanics Division, Aug. 21, 1991; final revision, Aug. 17, 1992. Associate Technical Editor: P. D. Spanos.

Copyright © 1993 by ASME
Downloaded 03 May 2010 to 171.66.16.245. Redistribution subject to ASME license or copyright; see http://www.asme.org/terms/Terms_Use.cfm

$$x=\frac{\pi X}{L}, \qquad w=\left(\frac{k_3}{k_4}\right)^{1/2} W$$
$$\lambda=\frac{P}{(2EIk_1)^{1/2}}, \quad \alpha=\left(\frac{EI}{k_1}\right)^{1/2}\left(\frac{\pi}{L}\right)^2 \tag{3}$$

where EI is the bending stiffness of the column, P is the applied axial loading, and $\alpha^{-1/2}$ is a measure of the length L of the column. The lateral deflection W of the column is restrained by a continuous elastic "softening" foundation that produces a nonlinear restraining force per unit length of $k_1W-k_3W^3$ for $k_1,\ k_3>0$.

The classical primary, and secondary buckling analysis were thoroughly analyzed in Amazigo and Oyesanya (1986). Since we need the results of that paper in our stability analysis we briefly review some salient aspects of the paper.

We solve the classical problem

$$L_\alpha[w;\ \lambda]=0 \quad \text{subject to (2)}$$

with the eigenvalues $\lambda_n(\alpha)$ and the corresponding eigenfunctions ϕ_n given by

$$\lambda=\lambda_n(\alpha)=\frac{1}{2\alpha n^2}(1+\alpha^2n^4) \tag{4}$$

$$w=\phi_n=\left(\frac{2}{\pi}\right)^{1/2}\sin nx \quad n=1,\ 2,\ \ldots. \tag{5}$$

We note from (4) that if

$$\alpha=\frac{1}{kp}=\bar{\alpha}, \quad k\neq p, \tag{6}$$

then

$$\lambda_k(\bar{\alpha})=\lambda_p(\bar{\alpha})=\frac{1}{2}\left(\frac{p}{k}+\frac{k}{p}\right)\equiv\bar{\lambda}. \tag{7}$$

The primary buckled states for this case are obtained by assuming for (1) and (2) perturbation solution

$$w^p(x,\epsilon)=w^c(x)\epsilon+w_2(x)\epsilon^2+w_3(x)\epsilon^3+\ldots \tag{8}$$
$$\lambda^p(\epsilon)=\bar{\lambda}_n(\alpha)+\bar{\lambda}_1\epsilon+\bar{\lambda}_2\epsilon^2+\ldots \tag{9}$$

where

$$\epsilon^2=\langle w^p,\ w^p\rangle, \quad w^c=a_p\phi_p+a_k\phi_k$$
$$a_p^2+a_k^2=1 \ \text{ and } \ \langle u,\ v\rangle=\int_0^\pi uv\,dx.$$

We solve the sequence of equations ensuing from equating like powers of ϵ.

We next obtain the secondary bifurcation points by solving the linearized problem

$$\alpha^2u''''+2\alpha\lambda^pu''+u=3(w^p)^2u, \quad 0<x<\pi$$
$$u=u''=0 \ \text{ at } \ x=0,\ \pi.$$

We assume perturbation solution in the form

$$u=u_o+u_1\delta+u_2\delta^2+\ldots$$
$$\epsilon=\epsilon_1\delta+\epsilon_2\delta^2+\ldots$$

where δ is a small parameter defined by $\alpha-\bar{\alpha}=b\delta^2$ and $b=1$ for $\alpha>\bar{\alpha}$ and $b=-1$ for $\alpha<\bar{\alpha}$. Imposing a solvability condition on the equations ensuring by equating like powers of δ gives the result, for $p\sqrt{2}>k$,

$$(\epsilon_1^{(p)})^2-\frac{4\pi}{3}\frac{p(p+1)(2p+1)}{(p-1)^2-2}=0 \tag{10}$$

which specify the secondary bifurcation points.

Further application of perturbation procedures in the amplitude parameter η defined by

$$\eta^2=\langle w,\ w^ps,\ w-w^ps\rangle$$

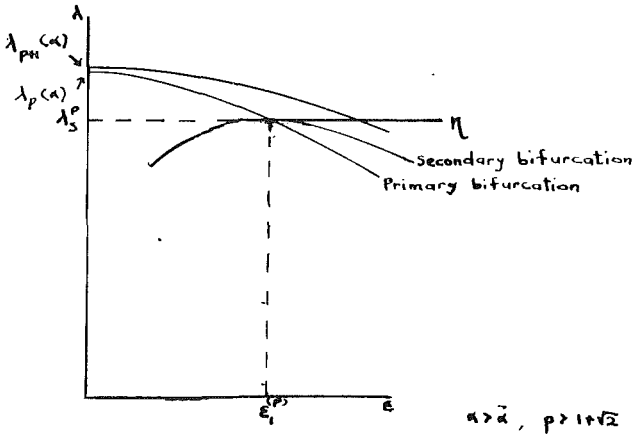


Fig. 1 Subcritical bifurcation states

gives the secondary bifurcation state emanating from the lowest primary state as

$$w(x,\ \delta,\ \eta)=\epsilon_1^{(p)}\phi_p(x)\delta+\phi_{p+1}(x)\eta+0(\delta^2,\ \delta\eta,\ \eta^2) \tag{11}$$

$$\lambda(\delta,\ \eta)=\bar{\lambda}+\left\{\frac{1}{2}\left(p^2-\frac{1}{\bar{\alpha}^2p^2}\right)-\frac{3}{4\pi\bar{\alpha}p^2}(\epsilon_1^{(p)})^2\right\}\delta^2$$
$$-\frac{3}{2\pi}\frac{1}{\bar{\alpha}p^2}\eta^2+0(\delta^3,\ \delta\eta^2). \tag{12}$$

We note that

$$w^ps=w(x,\ \delta,\ o)=\epsilon_1^{(p)}\phi_n(x)\delta+\epsilon_2^{(p)}\phi_n(x)\delta^2+\ldots. \tag{13}$$

The primary and secondary bifurcation states are shown in Fig. 1.

3 End Shortening Relations

The end shortening is given by

$$\Delta=\int_0^L\left[1+\left(\frac{dW}{dx}\right)^2\right]^{1/2}dX-L. \tag{14}$$

That is,

$$\Delta\cong\frac{1}{2}\int_0^L\left(\frac{dW}{dx}\right)^2dX \ \text{ for } \ |W'|\ll 1. \tag{15}$$

Using (3) in (15) gives

$$\Delta=\frac{1}{2}\frac{\pi}{L\beta}\int_0^\pi\left(\frac{dw}{dx}\right)^2dx \tag{16}$$

where

$$\beta=\left(\frac{k_3}{k_1}\right)^{1/2}.$$

If we now substitute (11) into (16) and evaluate the integral we have, neglecting terms with powers of δ, η higher than 2,

$$\frac{2L\beta}{\pi}\Delta=(\epsilon_1^{(p)}p\delta)^2+[(p+1)\eta]^2. \tag{17}$$

For $\eta=0$, that is, primary state at the secondary bifurcation point, (17) gives

$$\frac{2L\beta}{\pi}\Delta=(\epsilon_1^{(p)}p\delta)^2. \tag{18}$$

This gives, using (12),

$$\lambda=\lambda_s^p=\bar{\lambda}+\bar{p}\Delta, \tag{19}$$

where

Downloaded 03 May 2010 to 171.66.16.245. Redistribution subject to ASME license or copyright; see http://www.asme.org/terms/Terms_Use.cfm

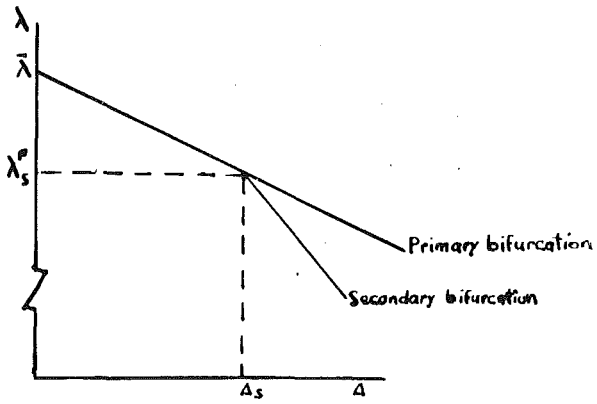


Fig. 2 End-shortening relation

$$\bar{p}=\left[\frac{1}{2}\left(p^2-\frac{1}{\bar{\alpha}^2p^2}\right)-\frac{3(\epsilon_1^{(p)})^2}{4\pi\bar{\alpha}p^2}\right]\frac{2L\beta}{\pi p^2(\epsilon_1^{(p)})^2}. \tag{20}$$

For fixed $\delta\neq 0$ we specify the secondary state

$$\eta^2=\frac{1}{(p+1)^2}\left[\frac{2L\beta\Delta}{\pi}-(\epsilon_1^{(p)}p\delta)^2\right], \tag{21}$$

so that from (12) we have

$$\lambda=\lambda_s^p-\frac{3}{2\pi p(p+1)}\left[\frac{2L\beta\Delta}{\pi}-(\epsilon_1^{(p)}p\delta)^2\right], \tag{22}$$

where λ_s^p is given by (19).

4 Stability Analysis

Budiansky (1974) proved a pictorial stability theorem which we shall use in this analysis.

Theorem 4.1: If on a load-shortening curve $(\lambda-\Delta)$ the slope is negative then the equilibrium state is unstable, that is, $d\lambda/d\Delta<0$ implies instability under prescribed loading.

Proof: See Budiansky (1974).

We note that since (22) is linear in Δ the sign of $d\lambda/d\Delta$ will depend on the sign of the coefficient of Δ and hence on the sign of $\bar{p}$.

Using (6) for $k=p+1$ and (10) in (20) show that $\bar{p}<0$ and hence $d\lambda/d\Delta<0$, which, using Theorem 4.1, shows that the primary state at the secondary bifurcation point is unstable and will therefore exhibit "mode jumping" phenomenon with the secondary state.

Equation (22) with (19) also show that, for the secondary state, $d\lambda/d\Delta<0$, since $\bar{p}<0$, showing instability of the secondary state.

The end-shortening relation is shown in Fig. 2.

5 Concluding Remarks

We have shown that for the column on a nonlinear elastic "softening" foundation, a highly imperfection-sensitive structure, both the primary and secondary states, are unstable. The primary state exhibits mode jumping instability as well as the secondary state at the secondary bifurcation point.

References

Amazigo, J. C., and Oyesanya, M. O., 1986, "Secondary Bifurcation and Imperfection Sensitivity of Columns on Nonlinear Foundations," *J. Nigerian Math. Soc.*, Vol. 5, pp. 47–62.

Budiansky, B., 1974, "Theory of Buckling and Postbuckling Behaviour of Elastic Structure," *Adv. in Appl. Mech.*, C. S. Yih, ed., Vol. 14, pp. 1–65.

Multilayer Material With an Interface Crack

Pei Gu[4]

1 Introduction

Multilayer material specimens are important for understanding interfacial fracture phenomenon. A special class of layered materials consists of a thin layer sandwiched between two homogeneous isotropic bulk materials of identical elastic properties. The crack can reside along one of the two interfaces. A universal relation between local stress intensity factors and remote stress intensity factors as well as the phase shift has been obtained by Suo and Hutchinson (1989). In this paper their approach is extended to a multilayer geometry, as shown in Fig. 1. Two substrates and the thin layer are three different materials. A universal relation appropriate to multilayer materials is derived in Section 2. The dominance zone of a crack-tip singular field is discussed in Section 3. It is shown that the zone dominated by the complex stress intensity factor depends on material combination. The zone of dominance is smaller if the difference of elastic constants between the thin layer and the two substrates becomes larger. An integral equation is formulated to solve this problem.

2 Universal Relation

The typical crack geometry is shown in Fig. 1(*a*). We solve the asymptotic problem depicted in Fig. 1(*b*). The two substrates and the thin layer are assumed to be isotropic, homogeneous, linear elastic. The thin layer has a thickness h and a semi-infinite crack is on the top interface. The prescribed boundary condition is a K field of bimaterial interface crack without the thin layer. The specimen is under plane deformation. Unlike a sandwich specimen (only two Dundur's parameters in the case), there are six Dundur's parameters (Dundurs, 1969) involved in the stress field of the multilayer structure shown in Fig. 1(*b*), which are

$$\alpha_{13}=\frac{\Gamma_{13}(\kappa_3+1)-(\kappa_1+1)}{\Gamma_{13}(\kappa_3+1)+(\kappa_1+1)}$$

$$\beta_{13}=\frac{\Gamma_{13}(\kappa_3-1)-(\kappa_1-1)}{\Gamma_{13}(\kappa_3+1)+(\kappa_1+1)}$$

$$\alpha_{32}=\frac{\Gamma_{32}(\kappa_2+1)-(\kappa_3+1)}{\Gamma_{32}(\kappa_2+1)+(\kappa_3+1)}$$

$$\beta_{32}=\frac{\Gamma_{32}(\kappa_2-1)-(\kappa_3-1)}{\Gamma_{32}(\kappa_2+1)+(\kappa_3+1)}$$

$$\alpha_{12}=\frac{\Gamma_{12}(\kappa_2+1)-(\kappa_1+1)}{\Gamma_{12}(\kappa_2+1)+(\kappa_1+1)}$$

$$\beta_{12}=\frac{\Gamma_{12}(\kappa_2-1)-(\kappa_1-1)}{\Gamma_{12}(\kappa_2+1)+(\kappa_1+1)} \tag{1}$$

where $\Gamma_{13}=\mu_1/\mu_3$, $\Gamma_{32}=\mu_3/\mu_2$, $\Gamma_{12}=\mu_1/\mu_2$, $\mu_i(i=1,2,3)$ is the shear modulus; $\kappa_i=3-4\nu_i$ for plane strain; $\kappa_i=(3-\nu_i)/(1+\nu_i)$ is for plane stress; $\nu_i(i=1,2,3)$ is the Poisson's ratio. Subscripts 1, 2, and 3 refer to materials shown in Fig.

[4]Division of Engineering, Brown University, Providence, RI 02912.

Manuscript received by the ASME Applied Mechanics Division, Sept. 26, 1991; final revision, Oct. 22, 1992. Associate Technical Editor: G. J. Dvorak.

Downloaded 03 May 2010 to 171.66.16.245. Redistribution subject to ASME license or copyright; see http://www.asme.org/terms/Terms_Use.cfm

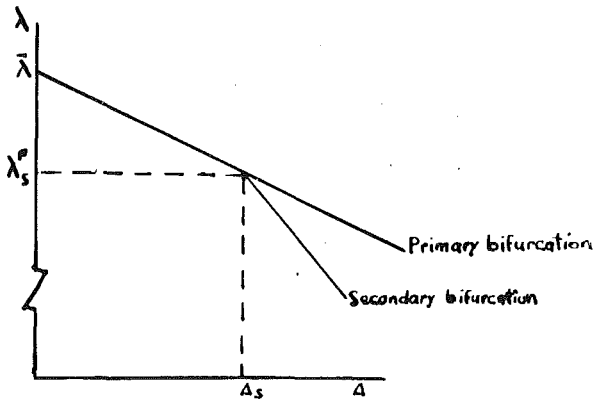


Fig. 2 End-shortening relation

$$\bar{p}=\left[\frac{1}{2}\left(p^2-\frac{1}{\bar{\alpha}^2p^2}\right)-\frac{3(\epsilon_1^{(p)})^2}{4\pi\bar{\alpha}p^2}\right]\frac{2L\beta}{\pi p^2(\epsilon_1^{(p)})^2}. \tag{20}$$

For fixed $\delta\neq 0$ we specify the secondary state

$$\eta^2=\frac{1}{(p+1)^2}\left[\frac{2L\beta\Delta}{\pi}-(\epsilon_1^{(p)}p\delta)^2\right], \tag{21}$$

so that from (12) we have

$$\lambda=\lambda_s^p-\frac{3}{2\pi p(p+1)}\left[\frac{2L\beta\Delta}{\pi}-(\epsilon_1^{(p)}p\delta)^2\right], \tag{22}$$

where λ_s^p is given by (19).

4 Stability Analysis

Budiansky (1974) proved a pictorial stability theorem which we shall use in this analysis.

Theorem 4.1: If on a load-shortening curve $(\lambda-\Delta)$ the slope is negative then the equilibrium state is unstable, that is, $d\lambda/d\Delta<0$ implies instability under prescribed loading.

Proof: See Budiansky (1974).

We note that since (22) is linear in Δ the sign of $d\lambda/d\Delta$ will depend on the sign of the coefficient of Δ and hence on the sign of $\bar{p}$.

Using (6) for $k=p+1$ and (10) in (20) show that $\bar{p}<0$ and hence $d\lambda/d\Delta<0$, which, using Theorem 4.1, shows that the primary state at the secondary bifurcation point is unstable and will therefore exhibit "mode jumping" phenomenon with the secondary state.

Equation (22) with (19) also show that, for the secondary state, $d\lambda/d\Delta<0$, since $\bar{p}<0$, showing instability of the secondary state.

The end-shortening relation is shown in Fig. 2.

5 Concluding Remarks

We have shown that for the column on a nonlinear elastic "softening" foundation, a highly imperfection-sensitive structure, both the primary and secondary states, are unstable. The primary state exhibits mode jumping instability as well as the secondary state at the secondary bifurcation point.

References

Amazigo, J. C., and Oyesanya, M. O., 1986, "Secondary Bifurcation and Imperfection Sensitivity of Columns on Nonlinear Foundations," *J. Nigerian Math. Soc.*, Vol. 5, pp. 47–62.

Budiansky, B., 1974, "Theory of Buckling and Postbuckling Behaviour of Elastic Structure," *Adv. in Appl. Mech.*, C. S. Yih, ed., Vol. 14, pp. 1–65.

Multilayer Material With an Interface Crack

Pei Gu[4]

1 Introduction

Multilayer material specimens are important for understanding interfacial fracture phenomenon. A special class of layered materials consists of a thin layer sandwiched between two homogeneous isotropic bulk materials of identical elastic properties. The crack can reside along one of the two interfaces. A universal relation between local stress intensity factors and remote stress intensity factors as well as the phase shift has been obtained by Suo and Hutchinson (1989). In this paper their approach is extended to a multilayer geometry, as shown in Fig. 1. Two substrates and the thin layer are three different materials. A universal relation appropriate to multilayer materials is derived in Section 2. The dominance zone of a crack-tip singular field is discussed in Section 3. It is shown that the zone dominated by the complex stress intensity factor depends on material combination. The zone of dominance is smaller if the difference of elastic constants between the thin layer and the two substrates becomes larger. An integral equation is formulated to solve this problem.

2 Universal Relation

The typical crack geometry is shown in Fig. 1(*a*). We solve the asymptotic problem depicted in Fig. 1(*b*). The two substrates and the thin layer are assumed to be isotropic, homogeneous, linear elastic. The thin layer has a thickness h and a semi-infinite crack is on the top interface. The prescribed boundary condition is a K field of bimaterial interface crack without the thin layer. The specimen is under plane deformation. Unlike a sandwich specimen (only two Dundur's parameters in the case), there are six Dundur's parameters (Dundurs, 1969) involved in the stress field of the multilayer structure shown in Fig. 1(*b*), which are

$$\alpha_{13}=\frac{\Gamma_{13}(\kappa_3+1)-(\kappa_1+1)}{\Gamma_{13}(\kappa_3+1)+(\kappa_1+1)}$$

$$\beta_{13}=\frac{\Gamma_{13}(\kappa_3-1)-(\kappa_1-1)}{\Gamma_{13}(\kappa_3+1)+(\kappa_1+1)}$$

$$\alpha_{32}=\frac{\Gamma_{32}(\kappa_2+1)-(\kappa_3+1)}{\Gamma_{32}(\kappa_2+1)+(\kappa_3+1)}$$

$$\beta_{32}=\frac{\Gamma_{32}(\kappa_2-1)-(\kappa_3-1)}{\Gamma_{32}(\kappa_2+1)+(\kappa_3+1)}$$

$$\alpha_{12}=\frac{\Gamma_{12}(\kappa_2+1)-(\kappa_1+1)}{\Gamma_{12}(\kappa_2+1)+(\kappa_1+1)}$$

$$\beta_{12}=\frac{\Gamma_{12}(\kappa_2-1)-(\kappa_1-1)}{\Gamma_{12}(\kappa_2+1)+(\kappa_1+1)} \tag{1}$$

where $\Gamma_{13}=\mu_1/\mu_3$, $\Gamma_{32}=\mu_3/\mu_2$, $\Gamma_{12}=\mu_1/\mu_2$, $\mu_i(i=1,2,3)$ is the shear modulus; $\kappa_i=3-4\nu_i$ for plane strain; $\kappa_i=(3-\nu_i)/(1+\nu_i)$ is for plane stress; $\nu_i(i=1,2,3)$ is the Poisson's ratio. Subscripts 1, 2, and 3 refer to materials shown in Fig.

[4]Division of Engineering, Brown University, Providence, RI 02912.

Manuscript received by the ASME Applied Mechanics Division, Sept. 26, 1991; final revision, Oct. 22, 1992. Associate Technical Editor: G. J. Dvorak.

Copyright © 1993 by ASME
Downloaded 03 May 2010 to 171.66.16.245. Redistribution subject to ASME license or copyright; see http://www.asme.org/terms/Terms_Use.cfm

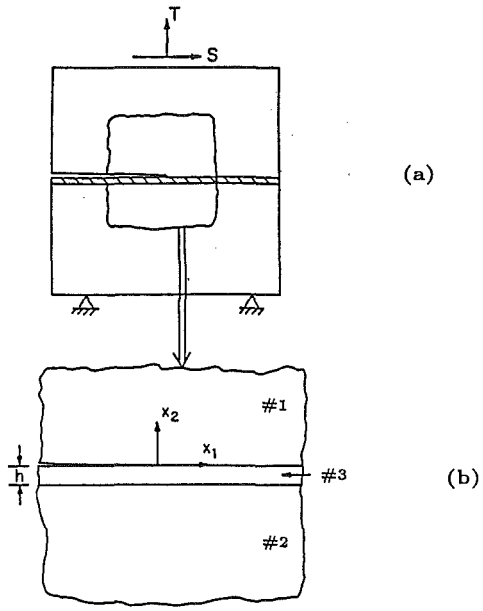


Fig. 1 Multilayer geometry; (*a*) finite crack geometry, (*b*) asymptotic problem of a semi-infinite crack

1. The last two in (1), α_{12}, β_{12}, are those that appeared in the bimaterial solution, which is the prescribed boundary condition of Fig. 1(*b*). Of the six Dundur's parameters, five may be independently chosen. This is because an additional relation

$$\Gamma_{13}\Gamma_{32}=\Gamma_{12} \tag{2}$$

holds among the six equations in (1). In practice, Poisson's ratios are close to 0.3 for a lot of materials. If we can take all three Poisson's ratios as 0.33, then only two parameters are independent and the rest can be expressed in terms of the two.

The stresses ahead of the crack tip and the displacements behind the crack tip are given by

$$\sigma_{22}+i\sigma_{12}=\frac{Kr^{i\epsilon_{13}}}{(2\pi r)^{1/2}} \tag{3}$$

$$\delta_2+i\delta_1=\frac{1}{2}\sqrt{\frac{r}{2\pi}}\,\frac{(c_1+c_3)Kr^{i\epsilon_{13}}}{(1+2i\epsilon_{13})\cosh(\pi\epsilon_{13})} \tag{4}$$

where $K = K_1 + iK_2$ is a complex stress intensity factor; $c_i = (\kappa_i + 1)/\mu_i$, $(i = 1, 2, 3)$. The energy release rate for the crack extending along the interface is given by

$$\mathcal{G}=\frac{c_1+c_3}{16\cosh^2(\pi\epsilon_{13})}\,|K|^2. \tag{5}$$

The far field is characterized by a complex stress intensity factor K^∞. Crack-tip stress and displacement fields are given by

$$\sigma_{22}+i\sigma_{12}=\frac{K^\infty r^{i\epsilon_{12}}}{(2\pi r)^{1/2}} \tag{6}$$

$$\delta_2+i\delta_1=\frac{1}{2}\sqrt{\frac{r}{2\pi}}\,\frac{(c_1+c_2)K^\infty r^{i\epsilon_{12}}}{(1+2i\epsilon_{12})\cosh(\pi\epsilon_{12})} \tag{7}$$

and the energy release rate is

$$\mathcal{G}=\frac{c_1+c_2}{16\cosh^2(\pi\epsilon_{12})}\,|K^\infty|^2. \tag{8}$$

The right-hand side of (5) and (8) must be equal by the application of a *J*-integral. Therefore, we obtain

$$|K|=\rho|K^\infty| \tag{9}$$

where

$$\rho=\sqrt{\frac{(1-\alpha_{13})(1-\beta_{12}^2)}{(1-\alpha_{12})(1-\beta_{13}^2)}}. \tag{10}$$

Dimension and linearity consideration lead to the following universal relation:

$$Kh^{i\epsilon_{13}}=\rho K^\infty h^{i\epsilon_{12}}e^{i\omega} \tag{11}$$

where ω is a phase shift which is related to α_{13}, β_{13}, α_{32}, β_{32}. For a sandwich specimen, $\epsilon_{12} = 0$, and (11) reduces to the universal relation obtained by Suo and Hutchinson (1989),

$$Kh^{i\epsilon_{13}}=\rho K^\infty e^{i\omega} \tag{12}$$

with

$$\rho=\sqrt{\frac{(1-\alpha_{13})}{(1-\beta_{13}^2)}}. \tag{13}$$

The universal relation can also be written in another way. Using the following two relations

$$Kh^{i\epsilon_{13}-i\epsilon_{12}}=|K|e^{i\psi} \tag{14}$$

and

$$K^\infty=|K^\infty|e^{i\phi}, \tag{15}$$

we restate (11) as

$$|K|=\rho|K^\infty|,\quad \psi=\phi+\omega \tag{16}$$

where ψ is a phase angle.

The phase shift ω may be solved by an integral equation which is similar to the one given by Suo and Hutchinson (1989). Numerical values of ω for several cases are presented as follows:

(a) Al/epoxy/glass

$$\alpha_{13}=0.895,\quad \alpha_{32}=-0.888,\quad \beta_{13}=0.217,\quad \beta_{32}=-0.210$$
$$\omega=-13.03 \text{ deg}$$

(b) $E_1/E_2=10$, $E_3/E_2=5$, $\nu_1=0.2$, $\nu_2=0.3$, $\nu_3=0.25$

$$\alpha_{13}=0.323,\quad \alpha_{32}=0.658,\quad \beta_{13}=0.093,\quad \beta_{32}=0.18$$
$$\omega=7.8 \text{ deg}$$

(c) $E_1/E_2=0.1$, $E_3/E_2=0.5$, $\nu_1=0.3$, $\nu_2=0.2$, $\nu_3=0.25$

$$\alpha_{13}=-0.658,\quad \alpha_{32}=-0.323,\quad \beta_{13}=-0.18,\quad \beta_{32}=-0.093$$
$$\omega=-1.4 \text{ deg}$$

(d) glass/Cu/glass

$$\alpha_{13}=-\alpha_{32}=-0.327,\quad \beta_{13}=-\beta_{32}=-0.147$$
$$\omega=3.02 \text{ deg}$$

(e) Cu/glass/Cu

$$\alpha_{13}=-\alpha_{32}=0.327,\quad \beta_{13}=-\beta_{32}=0.147$$
$$\omega=-3.88 \text{ deg}$$

(f) glass/epoxy/glass

$$\alpha_{13}=-\alpha_{32}=0.888,\quad \beta_{13}=-\beta_{32}=0.210$$
$$\omega=-12.58 \text{ deg}.$$

The values of α and β given previously are based on the following elastic constants: Aluminum, $E = 70.6$ GPa, $\nu = 0.345$; Epoxy: $E = 3.9$ GPa, $\nu = 0.34$; Glass: $E = 70.3$ GPa, $\nu = 0.24$; Copper: $E = 129.8$ GPa, $\nu = 0.343$, where E is the Young's modulus and ν is the Poisson's ratio. Those constants are taken from Suga et al. (1988). As shown by Dundurs (1969), α and β are within a parallelogram enclosed by $\alpha = \pm 1$ and $\alpha - 4\beta = \pm 1$ in the (α, β) plane. For a homogeneous solid, $\alpha = 0$, $\beta = 0$.

In case (a), despite the strong material dissimilarity as characterized by large values of α's and β's, the phase shift is small—$\omega = 13.03$ deg. For the broad range of α and β considered, the absolute value of the phase shift is less than about 15 deg, and this is in agreement with the results by Suo and Hutchinson (1989) for sandwich specimens.

Downloaded 03 May 2010 to 171.66.16.245. Redistribution subject to ASME license or copyright; see http://www.asme.org/terms/Terms_Use.cfm

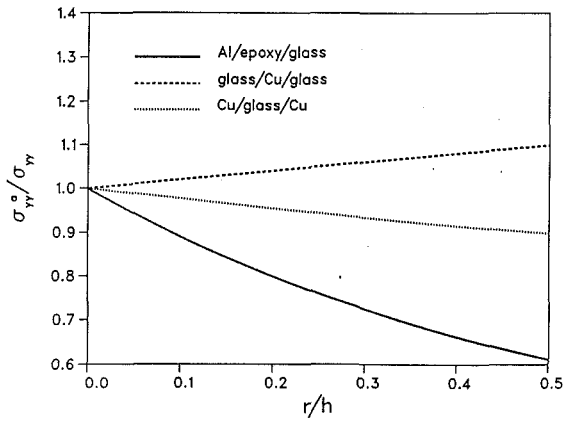


Fig. 2 Comparison of a hoop stress based on the asymptotic solution with the full-field solution for several layered material systems

The effect of crack location on the phase shift is examined. Consider a material system where material 1 is stiffer than material 2 and the stiffness of material 3 is between material 1 and material 2. In one case the crack lies between material 1 and material 3 (case (b)) and the other case the crack lies between material 3 and material 2 (note that this is case (c)). We find that $\omega = 7.8$ deg for the crack on the top interface and $\omega = -1.4$ deg for the crack on the bottom interface. The example reveals the effect of the dissimilarity of the moduli of the two bulk materials.

All the numerical results presented here satisfy the consistency test. Using (11) the solution for the real and imaginary parts of K provides independent results for $\cos\omega$ and $\sin\omega$. However, the latter quantities must satisfy the identity $\sin^2\omega + \cos^2\omega = 1$. This provides a consistency test of the numerical solution for ω. The agreement of our results with the above equation is better than an error of 0.3 percent.

3 Dominance Zone

To estimate the zone of dominance we compare σ_{yy} based on the K-field solution with σ_{yy} from the full-field solution. Figure 2 is a plot of $\sigma_{yy}^a/\sigma_{yy}$ versus the distance ahead of the crack tip normalized by layer thickness, where σ_{yy}^a is the crack-tip asymptotic solution and σ_{yy} is the full-field solution. At a distance of $r/h = 0.1$ (ahead of a crack tip on the interface), $\sigma_{yy}^a/\sigma_{yy} \approx 0.98$ for Cu/glass/Cu, $\sigma_{yy}^a/\sigma_{yy} \approx 1.02$ for glass/Cu/glass and $\sigma_{yy}^a/\sigma_{yy} \approx 0.89$ for Al/epoxy/glass. The comparison shows that the zone of K-dominance depends on the mismatch of material moduli. The large mismatch of material moduli reduces the size of the K-dominance zone.

Acknowledgments

Guidance by Prof. C. F. Shih and support provided by the Office of Naval Research through ONR Grant N00014-90-J1380 is gratefully acknowledged.

References

Dundurs, J., 1969, "Edge-Bonded Dissimilar Orthogonal Elastic Wedges Under Normal and Shear Loading," ASME JOURNAL OF APPLIED MECHANICS, Vol. 36, pp. 650-652.

Suo, Z., and Hutchinson, J. W., 1989, "Sandwich Test Specimens for Measuring Interface Crack Toughness," *Materials Science and Engineering*, Vol. A107, pp. 135-143.

Suta, T., Elssner, G., and Schmauder, S., 1988, "Composite Parameters and Mechanical Compatibility of Material Joints," *Journal of Composite Materials*, Vol. 22, pp. 917-934.

Stresses in Narrow Regions

J. B. Keller[5]

A method for calculating the stress distribution in a narrow region of an elastic plate is presented. It consists in treating the narrow region by beam theory, treating the rest of the plate by any computational or analytical method, and matching the results of these two calculations. It is illustrated by finding the stress distribution in the narrow region of a plate, between a straight edge and a nearby hole, when the plate is under tension. The same method can be applied to three-dimensional bodies with thin plate-like or shell-like regions.

1 Introduction

It is difficult to calculate numerically the stress distribution in a narrow region of an elastic plate because the stresses and their gradients are much larger there than elsewhere. Consequently, mesh refinement must be employed in such a region when direct numerical methods are employed. The narrower the region, the finer the mesh must be, and the more pronounced are the attendant difficulties.

To avoid these difficulties, we shall separate the calculation into two parts, one for the narrow region and another for the rest of the plate. In the narrow part we determine the stress distribution by beam theory, while in the rest of the plate we can use any computational or analytical method. The solutions in the two regions must match with one another where the regions meet. Matching determines the boundary conditions which are needed to determine uniquely the stresses in each part.

This method can be derived systematically as an asymptotic expansion of the solution with respect to the small slenderness ratio of the narrow part. Two expansions are required, one in the narrow part and another in the rest of the plate, and they must be matched together. The procedure described above corresponds to determining the leading term in each of the two expansions. Further terms can be found by continuing the expansion procedure. This interpretation in terms of matched asymptotic expansions shows that the leading terms become a better approximation as the slenderness ratio decreases. This is just when the direct computation becomes more difficult, so this method complements that of direct computation. To determine higher order terms, an additional expansion may be needed in the junction between the other two expansions.

In Section 2, we determine the stress in a curved nonuniform beam, which is needed for the narrow region. The solution involves three constants, the force components (F_x, F_y) applied to one end of the beam and the bending moment $G(0)$ applied about some point 0 of the beam. In Section 3, we apply the result of Section 2 to the narrow region between the straight edge of a plate and a nearby circular hole with the plate under tension. This problem was solved by Mindlin (1948), and from his solution we determine the constants F_x, F_y, and $G(0)$. With them, the solution of Section 2 explains the peculiar stress distribution he obtained along the straight edge.

In general, the constants F_x, F_y, and $G(0)$ must be found from the displacements and rotations of the ends of the beam, in the manner explained in Section 4. These displacements and

[5]Departments of Mathematics and Mechanical Engineering, Stanford University, Stanford, CA 94305.

Manuscript received by the ASME Applied Mechanics Division, Aug. 31, 1992; final revision, Oct. 2, 1992. Associate Technical Editor: X. Markenscoff.

Downloaded 03 May 2010 to 171.66.16.245. Redistribution subject to ASME license or copyright; see http://www.asme.org/terms/Terms_Use.cfm

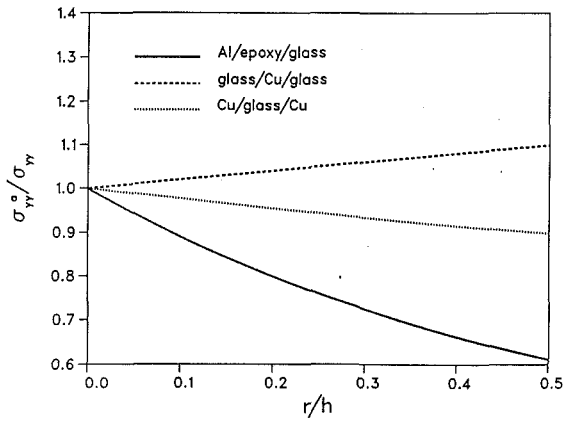


Fig. 2 Comparison of a hoop stress based on the asymptotic solution with the full-field solution for several layered material systems

The effect of crack location on the phase shift is examined. Consider a material system where material 1 is stiffer than material 2 and the stiffness of material 3 is between material 1 and material 2. In one case the crack lies between material 1 and material 3 (case (b)) and the other case the crack lies between material 3 and material 2 (note that this is case (c)). We find that $\omega = 7.8$ deg for the crack on the top interface and $\omega = -1.4$ deg for the crack on the bottom interface. The example reveals the effect of the dissimilarity of the moduli of the two bulk materials.

All the numerical results presented here satisfy the consistency test. Using (11) the solution for the real and imaginary parts of K provides independent results for $\cos\omega$ and $\sin\omega$. However, the latter quantities must satisfy the identity $\sin^2\omega + \cos^2\omega = 1$. This provides a consistency test of the numerical solution for ω. The agreement of our results with the above equation is better than an error of 0.3 percent.

3 Dominance Zone

To estimate the zone of dominance we compare σ_{yy} based on the K-field solution with σ_{yy} from the full-field solution. Figure 2 is a plot of $\sigma_{yy}^a/\sigma_{yy}$ versus the distance ahead of the crack tip normalized by layer thickness, where σ_{yy}^a is the crack-tip asymptotic solution and σ_{yy} is the full-field solution. At a distance of $r/h = 0.1$ (ahead of a crack tip on the interface), $\sigma_{yy}^a/\sigma_{yy} \approx 0.98$ for Cu/glass/Cu, $\sigma_{yy}^a/\sigma_{yy} \approx 1.02$ for glass/Cu/glass and $\sigma_{yy}^a/\sigma_{yy} \approx 0.89$ for Al/epoxy/glass. The comparison shows that the zone of K-dominance depends on the mismatch of material moduli. The large mismatch of material moduli reduces the size of the K-dominance zone.

Acknowledgments

Guidance by Prof. C. F. Shih and support provided by the Office of Naval Research through ONR Grant N00014-90-J1380 is gratefully acknowledged.

References

Dundurs, J., 1969, "Edge-Bonded Dissimilar Orthogonal Elastic Wedges Under Normal and Shear Loading," ASME JOURNAL OF APPLIED MECHANICS, Vol. 36, pp. 650-652.

Suo, Z., and Hutchinson, J. W., 1989, "Sandwich Test Specimens for Measuring Interface Crack Toughness," *Materials Science and Engineering*, Vol. A107, pp. 135-143.

Suta, T., Elssner, G., and Schmauder, S., 1988, "Composite Parameters and Mechanical Compatibility of Material Joints," *Journal of Composite Materials*, Vol. 22, pp. 917-934.

Stresses in Narrow Regions

J. B. Keller[5]

A method for calculating the stress distribution in a narrow region of an elastic plate is presented. It consists in treating the narrow region by beam theory, treating the rest of the plate by any computational or analytical method, and matching the results of these two calculations. It is illustrated by finding the stress distribution in the narrow region of a plate, between a straight edge and a nearby hole, when the plate is under tension. The same method can be applied to three-dimensional bodies with thin plate-like or shell-like regions.

1 Introduction

It is difficult to calculate numerically the stress distribution in a narrow region of an elastic plate because the stresses and their gradients are much larger there than elsewhere. Consequently, mesh refinement must be employed in such a region when direct numerical methods are employed. The narrower the region, the finer the mesh must be, and the more pronounced are the attendant difficulties.

To avoid these difficulties, we shall separate the calculation into two parts, one for the narrow region and another for the rest of the plate. In the narrow part we determine the stress distribution by beam theory, while in the rest of the plate we can use any computational or analytical method. The solutions in the two regions must match with one another where the regions meet. Matching determines the boundary conditions which are needed to determine uniquely the stresses in each part.

This method can be derived systematically as an asymptotic expansion of the solution with respect to the small slenderness ratio of the narrow part. Two expansions are required, one in the narrow part and another in the rest of the plate, and they must be matched together. The procedure described above corresponds to determining the leading term in each of the two expansions. Further terms can be found by continuing the expansion procedure. This interpretation in terms of matched asymptotic expansions shows that the leading terms become a better approximation as the slenderness ratio decreases. This is just when the direct computation becomes more difficult, so this method complements that of direct computation. To determine higher order terms, an additional expansion may be needed in the junction between the other two expansions.

In Section 2, we determine the stress in a curved nonuniform beam, which is needed for the narrow region. The solution involves three constants, the force components (F_x, F_y) applied to one end of the beam and the bending moment $G(0)$ applied about some point 0 of the beam. In Section 3, we apply the result of Section 2 to the narrow region between the straight edge of a plate and a nearby circular hole with the plate under tension. This problem was solved by Mindlin (1948), and from his solution we determine the constants F_x, F_y, and $G(0)$. With them, the solution of Section 2 explains the peculiar stress distribution he obtained along the straight edge.

In general, the constants F_x, F_y, and $G(0)$ must be found from the displacements and rotations of the ends of the beam, in the manner explained in Section 4. These displacements and

[5]Departments of Mathematics and Mechanical Engineering, Stanford University, Stanford, CA 94305.

Manuscript received by the ASME Applied Mechanics Division, Aug. 31, 1992; final revision, Oct. 2, 1992. Associate Technical Editor: X. Markenscoff.

Copyright © 1993 by ASME
Downloaded 03 May 2010 to 171.66.16.245. Redistribution subject to ASME license or copyright; see http://www.asme.org/terms/Terms_Use.cfm

rotations are determined by the solution for the rest of the plate. To calculate that solution requires boundary conditions on the small surfaces introduced by removing the narrow part. Generally the appropriate conditions are that these surfaces are traction-free because the narrow part can exert only negligible tractions on the rest of the plate. However, in special cases the narrow part exerts non-negligible traction on the rest of the plate, and then the appropriate conditions must be found by matching using an additional expansion.

The same method can be applied to three-dimensional elastic bodies which have thin plate-like, shell-like, or beam-like regions. Then a plate shell, or beam theory, can be used in the thin region, and any method can be used to solve the three-dimensional problem in the rest of the body. Again the surfaces introduced by removing the plate, shell, or beam must be treated as traction-free. The resulting displacement and rotation of these surfaces provides the boundary conditions at the edge of the plate or shell or at the ends of the beam.

Markenscoff and Dundurs (1992) have examined the stresses in the narrow parts of plates, which they call thin ligaments, in four examples. They have pointed out that these ligaments behave like beams and transmit forces and bending moments.

2 Stress in a Curved Nonuniform Beam

Let us consider a nonuniform beam lying in the x, y-plane with the undeformed centerline $x(s)$, $y(s)$ where s is arclength from some point on this line. Let $T(s)$, $N(s)$, and $G(s)$ denote the tensile force, shear force, and bending moment about the z-axis, respectively. Then beam theory shows that the stress component $\sigma_{ss}(s, n)$ at the normal distance n from the centerline, positive toward the center of curvature, is given by

$$\sigma_{ss}(s,n)=\frac{T(s)}{A(s)}-\frac{nG(s)}{I(s)}. \tag{1}$$

Here $I(s)$ is the moment of inertia about the z-axis of the cross-section at s and $A(s)$ is the width of that cross-section.

We assume that the only loads on the beam are a force $(-F_x, -F_y)$ and a moment G_0 on the end of the beam at $s = 0$ and an equilibrating load at the other end $s = L$. Then the equations of equilibrium of the beam yield

$$T(s)=F_x\cos\theta(s)+F_y\sin\theta(s) \tag{2}$$

$$N(s)=-F_x\sin\theta(s)+F_y\cos\theta(s) \tag{3}$$

$$G(s)=G_0+F_x[y(s)-y(0)]-F_y[x(s)-x(0)]. \tag{4}$$

Now (1) can be written

$$\sigma_{ss}(s,n)=\frac{1}{A(s)}\left[F_x\cos\theta(s)+F_y\sin\theta(s)\right]-\frac{n}{I(s)}\left\{G_0+F_x[y(s)-y(0)]-F_y[x(s)-x(0)]\right\}. \tag{5}$$

This result (5) gives $\sigma(s, n)$ in terms of the three constants F_x, F_y, and G_0 and the geometrical properties of the beam.

3 A Plate With a Hole Near an Edge

We shall now apply (5) to a plate lying in the half-plane $y < 0$ with a circular hole of radius R and center $x = 0$, $y = -R - d$ near the straight edge $y = 0$. The boundary of the hole nearest the edge is given by $y = -R - d + (R^2 - x^2)^{1/2}$ where d is the distance from the edge to the hole. For a uniform tension T_0 parallel to the x-axis applied to the plate, the stress distribution has been determined by Mindlin (1948). He showed that the force F_x applied to that part of the plate between the hole and the edge is $F_x = T_0[(R + d)^2 - R^2]^{1/2} = T_0(2dR)^{1/2}[1 + 0(d/R)]$, where the expansion applies for d/R small. The force $F_y = 0$ by symmetry. He did not evaluate G_0, but we can obtain it from his result for σ_{xx} at the origin, which is the point on the straight edge nearest the hole.

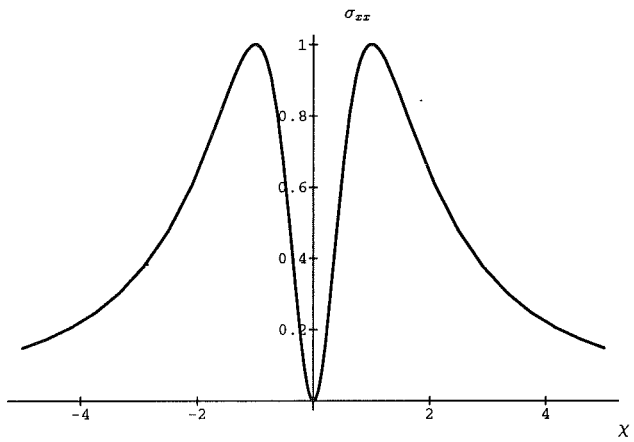


Fig. 1 A graph of the dimensionless stress $(d/2R)^{1/2}T_0^{-1}\sigma_{xx}(x, 0)$ along the edge of the plate at $y = 0$ as a function of $\chi = x(2dR)^{-1/2}$, based upon (7).

His numerical results show that this stress tends to zero as $d \to 0$.

To use his result we consider the narrow strip of the plate, between the hole and the edge, to be a beam. We shall set $s = 0$ at $x = 0$ and then in (5) G_0 denotes the bending moment at $x = 0$. At $x = 0$ the beam width is $A(0) = d$, its centerline is at $y(0) = -d/2$, its slope angle is $\theta(0) = 0$, and its moment of inertia there is $I(0) = d^3/12$. The origin is at $s = 0$, $n = d/2$ so we have $\sigma_{ss}(0, d/2) \sim 0$ for $d/R \ll 1$. Upon using these values in (5) and solving for G_0 we get $G_0 \sim F_x d/6 \sim T_0(2dR)^{1/2}d/6$. Then we can use this value in (5) to determine $\sigma_{ss}(s, n)$ throughout the narrow strip. In particular at the point on the hole nearest the edge, (5) yields $\sigma_{ss}(0, -d/2) \sim 2(2R/d)^{1/2}T_0$. This result was obtained before, using Mindlin's solution, by Duan, Kienzler, and Herrmann (1986) and by Callias and Markenscoff (1989), while the expression for G_0 was also found by Markenscoff and Dundurs (1992).

It is quite remarkable that $\sigma_{xx} = 0$ at $x = 0$, $y = 0$ on the plate edge since the plate is in tension. Our result shows that this is a consequence of the positive moment applied to the beam, so that the two terms in (2) cancel. Because the beam is curved downward, a tensile force applied to its ends produces a positive moment. This produces a compressive stress along the upper edge, which just cancels the tensile stress due to F_x at $x = 0$, $y = 0$. On the upper edge of the hole, the moment produces a tensile stress, which adds to that produced by F_x and yields the large stress there.

To write (5) explicitly we approximate the centerline of the beam by $y(x) = 1/2[-R - d + (R^2 - x^2)^{1/2}] \sim -d/2 - x^2/4R$ and its width by $A(x) = 2|y(x)|$. Then $I(x) = A^3/12 = 2|y^3(x)|/3$, $\cos\theta(x) = (1 + [y'(x)]^2)^{-1/2} \sim 1$, $n \approx y - y(x)$, and (5) becomes, with $\chi = x/(2dR)^{1/2}$,

$$T_0^{-1}\sigma_{xx}(x,y)\approx\left(\frac{2R}{d}\right)^{1/2}\left\{\frac{1}{1+\chi^2}+\frac{(3\chi^2-1)}{(1+\chi^2)^3}(1+\chi^2+2y/d)\right\}. \tag{6}$$

This result gives σ_{xx} throughout the narrow region of the plate.

At the edge of the plate $y = 0$, (6) yields

$$\left(\frac{d}{2R}\right)^{1/2}T_0^{-1}\sigma_{xx}(x,0)=\frac{4\chi^2}{(1+\chi^2)^2}. \tag{7}$$

The right side of (7) is an even function of the single dimensionless position variable χ. It increases from the value zero at $\chi = 0$ to the maximum value one at $\chi = 1$, and then decreases to zero at $\chi = \infty$. See Fig. 1. This agrees qualitatively with Mindlin's numerical evaluation of the exact solution for $d/R = 0.2$.

Similarly, we can apply (5) to the strip between two holes

Downloaded 03 May 2010 to 171.66.16.245. Redistribution subject to ASME license or copyright; see http://www.asme.org/terms/Terms_Use.cfm

separated by a distance d, with radii of curvature R_1 and R_2 at $x = 0$ where they are closest together. Let the middle curve be $y(x) = -d/2 + (R_1^{-1} - R_2^{-1})x^2/4 + \ldots$ and $A(x) = d + (R_1^{-1} + R_2^{-1})x^2/2 + \ldots$. Then, when $F_y = 0$, we can write (5) as

$$\sigma_{xx}(x,y) = \frac{F_x/d}{1+(R_1^{-1}+R_2^{-1})x^2/2d} + \frac{(3F_x/d)(R_2^{-1}-R_1^{-1})\dfrac{x^2}{2d} - 6G_0/d^2}{[1+(R_1^{-1}+R_2^{-1})x^2/2d]^3} \times \left[1+(R_2^{-1}-R_1^{-1})\frac{x^2}{2d}+\frac{2y}{d}\right] \quad (8)$$

This reduces to (6) when $R_1^{-1} = 0$, $R_2^{-1} = R^{-1}$ and F_x and $G(0)$ have the appropriate values. To use (8) in other cases it is necessary to solve the problem in the rest of the plate, and from it to determine the displacements and rotation of the ends of the narrow part. From them F_x and G_0 can be found by the method explained in the next section.

4 Determination of F_x, F_y, and G_0

In general we must determine F_x, F_y and G_0 in (5) from the displacements and rotations of the ends of the beam. Thus we suppose that the end of the beam at $s = 0$ is displaced by the small vector (a_0, b_0) and rotated by the small angle φ_0, while the end at $s = L$ is displaced by (a_L, b_L) and rotated by φ_L. As a consequence the centerline will be strained by the small amount $e(s)$ and rotated by the small angle $\varphi(s)$, which are determined by the equations

$$e(s) = E^{-1}T(s), \quad (9)$$

$$\varphi'(s) = \frac{G(s)}{EI(s)}. \quad (10)$$

Then the beam will be deformed to the new position $x(s) + \delta x(s), y(s) + \delta y(s)$ where δx and δy are given by the following expressions to first order in e and φ:

$$\delta x(s) = a_0 + \int_0^s [e(s')\cos\theta(s') - \varphi(s')\sin\theta(s')]ds', \quad (11)$$

$$\delta y(s) = b_0 + \int_0^s [e(s')\sin\theta(s') + \varphi(s')\cos\theta(s')]ds'. \quad (12)$$

We now integrate by parts the terms in (11) and (12) containing φ, recalling that $\sin\theta = y_s$ and $\cos\theta = x_s$. Then we set $s = L$ and obtain

$$a_L - a_0 = \varphi_0 y(0) - \varphi_L y(L) + \int_0^L [e(s)\cos\theta(s) + y(s)\varphi'(s)]ds, \quad (13)$$

$$b_L - b_0 = \varphi_L x(L) - \varphi_0 x(0) + \int_0^L [e(s)\sin\theta(s) - x(s)\varphi'(s)]ds. \quad (14)$$

We also integrate $\varphi'(s)$ given by (10) from 0 to L to get

$$\varphi_L - \varphi_0 = \int_0^L \frac{G(s)}{EI(s)}\,ds. \quad (15)$$

Next we substitute (9) and (10) into (13)–(15) and use (2) for $T(s)$ and (4) for $G(s)$. In this way we obtain three linear equations for F_x, F_y, and G_0 in terms of known geometrical quantities. By solving these equations and using the results in (5) we can determine $\sigma_{ss}(s, n)$ completely.

Acknowledgment

This work was supported in part by AFOSR, ONR, and NSF.

References

Callias, C. J., and Markenscoff, X., 1989, "Singular Asymptotics Analysis for the Singularity at a Hole Near a Boundary," *Quart. Appl. Math.*, Vol. 47, pp. 233-245.

Duan, Z.-P., Kienzler, R., and Herrmann, G., 1986, "An Integral Equation Method and Its Application to Defect Mechanics," *J. Mech. Phys. Solids*, Vol. 36, pp. 539-562.

Markenscoff, X., and Dundurs, J., 1992, "Amplification of Stresses in Thin Ligaments," *Int. J. Solids Structures*, Vol. 29, pp. 1883-1888.

Mindlin, R. D., 1948, "Stress Distribution Around a Hole Near the Edge of a Plate Under Tension," *Proc. Soc. Exptl. Stress Anal.*, Vol. 5, pp. 56-67.

On Neutral Holes in Tailored, Layered Sheets

B. Budiansky[6,8], J. W. Hutchinson[6,8], and A. G. Evans[7]

It has been suggested that multilayered sheets, in which alternating layers have different elastic moduli, might lend themselves to *tailoring* to reduce, or even eliminate, harmful stress concentrations at holes or other stress raisers. Such tailoring could be implemented by making the sheet thickness spatially nonuniform, varying the *number* of layers, but keeping the layering pattern unchanged; or, keeping the total thickness unchanged, by varying the pattern of layer locations and thicknesses; or by a combination of these two approaches. We will call the first method "thickness tailoring," and the second "modulus tailoring." Tailored fabrication of such nonuniform layered sheets seems particularly well suited to masked deposition techniques.

This Note provides a preliminary analytical assessment of the theoretical feasibility of designing a tailored, layered sheet that would alleviate the stress concentration induced by a circular hole in a field of balanced biaxial tension (see Fig. 1). If the stress concentration is actually eliminated, the result is a so-called "neutral" hole (Mansfield, 1950). It should be emphasized at the outset that reducing the *average* circumferential stress at the boundary of the hole is definitely not necessarily the desired goal. As we shall see, if modulus tailoring with constant overall thickness is exploited, and only the relative volumes of the layer constituents are changed, the stresses within the individual layers can be reduced while the average stress goes up! (This seemingly paradoxical result takes a little getting used to; the reason it's right is that while the stress in the stiffer material drops, there is more of it, so the average rises.) Conversely, a misguided reduction of the average hole-boundary stress by means of modulus tailoring can lead to higher stress concentrations within the layers.

We consider a two-constituent layered sheet, with Young's moduli E_α ($\alpha = 1, 2$) in the alternating layers, and for simplicity, we assume the same Poisson's ratio ν in each layer. The effective sheet modulus is $E = f_1E_1 + f_2E_2$, where the f's are vol-

[6] Division of Applied Sciences, Harvard University, Cambridge, MA 02138.
[7] Materials Department, University of California, Santa Barbara, CA 93106.
[8] Fellow ASME.

Contributed by the ASME Applied Mechanics Division, Aug. 14, 1992; final revision, Nov. 18, 1992. Associate Technical Editor: S. K. Datta.

Downloaded 03 May 2010 to 171.66.16.245. Redistribution subject to ASME license or copyright; see http://www.asme.org/terms/Terms_Use.cfm

separated by a distance d, with radii of curvature R_1 and R_2 at $x = 0$ where they are closest together. Let the middle curve be $y(x) = -d/2 + (R_1^{-1} - R_2^{-1})x^2/4 + \ldots$ and $A(x) = d + (R_1^{-1} + R_2^{-1})x^2/2 + \ldots$. Then, when $F_y = 0$, we can write (5) as

$$\sigma_{xx}(x,y) = \frac{F_x/d}{1+(R_1^{-1}+R_2^{-1})x^2/2d} + \frac{(3F_x/d)(R_2^{-1}-R_1^{-1})\dfrac{x^2}{2d} - 6G_0/d^2}{[1+(R_1^{-1}+R_2^{-1})x^2/2d]^3} \times \left[1+(R_2^{-1}-R_1^{-1})\frac{x^2}{2d}+\frac{2y}{d}\right] \quad (8)$$

This reduces to (6) when $R_1^{-1} = 0$, $R_2^{-1} = R^{-1}$ and F_x and $G(0)$ have the appropriate values. To use (8) in other cases it is necessary to solve the problem in the rest of the plate, and from it to determine the displacements and rotation of the ends of the narrow part. From them F_x and G_0 can be found by the method explained in the next section.

4 Determination of F_x, F_y, and G_0

In general we must determine F_x, F_y and G_0 in (5) from the displacements and rotations of the ends of the beam. Thus we suppose that the end of the beam at $s = 0$ is displaced by the small vector (a_0, b_0) and rotated by the small angle φ_0, while the end at $s = L$ is displaced by (a_L, b_L) and rotated by φ_L. As a consequence the centerline will be strained by the small amount $e(s)$ and rotated by the small angle $\varphi(s)$, which are determined by the equations

$$e(s) = E^{-1}T(s), \quad (9)$$

$$\varphi'(s) = \frac{G(s)}{EI(s)}. \quad (10)$$

Then the beam will be deformed to the new position $x(s) + \delta x(s), y(s) + \delta y(s)$ where δx and δy are given by the following expressions to first order in e and φ:

$$\delta x(s) = a_0 + \int_0^s [e(s')\cos\theta(s') - \varphi(s')\sin\theta(s')]ds', \quad (11)$$

$$\delta y(s) = b_0 + \int_0^s [e(s')\sin\theta(s') + \varphi(s')\cos\theta(s')]ds'. \quad (12)$$

We now integrate by parts the terms in (11) and (12) containing φ, recalling that $\sin\theta = y_s$ and $\cos\theta = x_s$. Then we set $s = L$ and obtain

$$a_L - a_0 = \varphi_0 y(0) - \varphi_L y(L) + \int_0^L [e(s)\cos\theta(s) + y(s)\varphi'(s)]ds, \quad (13)$$

$$b_L - b_0 = \varphi_L x(L) - \varphi_0 x(0) + \int_0^L [e(s)\sin\theta(s) - x(s)\varphi'(s)]ds. \quad (14)$$

We also integrate $\varphi'(s)$ given by (10) from 0 to L to get

$$\varphi_L - \varphi_0 = \int_0^L \frac{G(s)}{EI(s)}\,ds. \quad (15)$$

Next we substitute (9) and (10) into (13)–(15) and use (2) for $T(s)$ and (4) for $G(s)$. In this way we obtain three linear equations for F_x, F_y, and G_0 in terms of known geometrical quantities. By solving these equations and using the results in (5) we can determine $\sigma_{ss}(s, n)$ completely.

Acknowledgment

This work was supported in part by AFOSR, ONR, and NSF.

References

Callias, C. J., and Markenscoff, X., 1989, "Singular Asymptotics Analysis for the Singularity at a Hole Near a Boundary," *Quart. Appl. Math.*, Vol. 47, pp. 233–245.

Duan, Z.-P., Kienzler, R., and Herrmann, G., 1986, "An Integral Equation Method and Its Application to Defect Mechanics," *J. Mech. Phys. Solids*, Vol. 36, pp. 539–562.

Markenscoff, X., and Dundurs, J., 1992, "Amplification of Stresses in Thin Ligaments," *Int. J. Solids Structures*, Vol. 29, pp. 1883–1888.

Mindlin, R. D., 1948, "Stress Distribution Around a Hole Near the Edge of a Plate Under Tension," *Proc. Soc. Exptl. Stress Anal.*, Vol. 5, pp. 56–67.

On Neutral Holes in Tailored, Layered Sheets

B. Budiansky[6,8], J. W. Hutchinson[6,8], and A. G. Evans[7]

It has been suggested that multilayered sheets, in which alternating layers have different elastic moduli, might lend themselves to *tailoring* to reduce, or even eliminate, harmful stress concentrations at holes or other stress raisers. Such tailoring could be implemented by making the sheet thickness spatially nonuniform, varying the *number* of layers, but keeping the layering pattern unchanged; or, keeping the total thickness unchanged, by varying the pattern of layer locations and thicknesses; or by a combination of these two approaches. We will call the first method "thickness tailoring," and the second "modulus tailoring." Tailored fabrication of such nonuniform layered sheets seems particularly well suited to masked deposition techniques.

This Note provides a preliminary analytical assessment of the theoretical feasibility of designing a tailored, layered sheet that would alleviate the stress concentration induced by a circular hole in a field of balanced biaxial tension (see Fig. 1). If the stress concentration is actually eliminated, the result is a so-called "neutral" hole (Mansfield, 1950). It should be emphasized at the outset that reducing the *average* circumferential stress at the boundary of the hole is definitely not necessarily the desired goal. As we shall see, if modulus tailoring with constant overall thickness is exploited, and only the relative volumes of the layer constituents are changed, the stresses within the individual layers can be reduced while the average stress goes up! (This seemingly paradoxical result takes a little getting used to; the reason it's right is that while the stress in the stiffer material drops, there is more of it, so the average rises.) Conversely, a misguided reduction of the average hole-boundary stress by means of modulus tailoring can lead to higher stress concentrations within the layers.

We consider a two-constituent layered sheet, with Young's moduli E_α ($\alpha = 1, 2$) in the alternating layers, and for simplicity, we assume the same Poisson's ratio ν in each layer. The effective sheet modulus is $E = f_1E_1 + f_2E_2$, where the f's are vol-

[6] Division of Applied Sciences, Harvard University, Cambridge, MA 02138.
[7] Materials Department, University of California, Santa Barbara, CA 93106.
[8] Fellow ASME.

Contributed by the ASME Applied Mechanics Division, Aug. 14, 1992; final revision, Nov. 18, 1992. Associate Technical Editor: S. K. Datta.

Copyright © 1993 by ASME
Downloaded 03 May 2010 to 171.66.16.245. Redistribution subject to ASME license or copyright; see http://www.asme.org/terms/Terms_Use.cfm

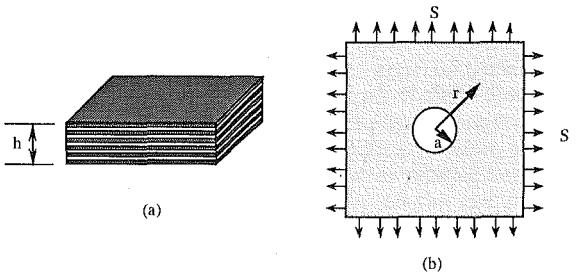


Fig. 1 *(a)* Layered sheet; *(b)* hole in sheet under balanced biaxial tension

ume fractions. At each r, denote the average radial and circumferential stresses by σ_r and σ_θ, and let $\sigma_r^{(\alpha)}$, $\sigma_\theta^{(\alpha)}$ $(\alpha = 1, 2)$ be the stresses in the layers. The stress-strain relations are

$$\epsilon_r = \frac{\sigma_r^{(\alpha)} - \nu\sigma_\theta^{(\alpha)}}{E_\alpha} = \frac{\sigma_r - \nu\sigma_\theta}{E(r)}$$
$$\epsilon_\theta = \frac{\sigma_\theta^{(\alpha)} - \nu\sigma_r^{(\alpha)}}{E_\alpha} = \frac{\sigma_\theta - \nu\sigma_r}{E(r)}. \tag{1}$$

Let

$$\sigma_r = \frac{E(r)}{E(\infty)} s_r, \quad \sigma_\theta = \frac{E(r)}{E(\infty)} s_\theta \tag{2}$$

where $E(\infty)$ is the untailored sheet modulus far from the hole. Then

$$\sigma_r^{(\alpha)} = \frac{E_\alpha}{E(\infty)} s_r, \quad \sigma_\theta^{(\alpha)} = \frac{E_\alpha}{E(\infty)} s_\theta \tag{3}$$

and so the layer stresses are proportional to s_r and s_θ. Hence, it is the value of s_θ at $r = a$ that we must seek to lower by tailoring $E(r)$, or the sheet thickness $h(r)$, or both. Note that while the stress concentration factor (SCF) for the *average* sheet stress σ_θ is $\sigma_\theta(s)/S$, the *layer* concentration factors are

$$\frac{\sigma_\theta^{(\alpha)}(a)}{\sigma_\theta^{(\alpha)}(\infty)} = \frac{s_\theta(a)}{s_\theta(\infty)} = \frac{s_\theta(a)}{S}. \tag{4}$$

For a *uniform* layered sheet, these layer concentration factors are equal to the classical stress concentration factor $\sigma_\theta(a)/S = 2$.

The equations of equilibrium and compatibility are

$$\frac{d(rh\sigma_r)}{dr} = h\sigma_\theta \tag{5}$$

and

$$\frac{d(r\epsilon_\theta)}{dr} = \epsilon_r, \tag{6}$$

respectively. These may be rewritten as

$$[\lambda\rho s_r]' = \lambda s_\theta \tag{7}$$

$$[\rho(s_\theta - \nu s_r)]' = s_r - \nu s_\theta \tag{8}$$

in terms of $\rho \equiv r/a$, and the *tailoring function*, defined by

$$\lambda(r) \equiv \frac{E(r)}{E(\infty)} \frac{h(r)}{h(\infty)}. \tag{9}$$

Primes denote derivatives with respect to ρ.

We proceed in a semi-inverse fashion by asserting the spatial distribution

$$s_r = S(1 - \rho^{-n}) \tag{10}$$

and solving the compatibility Eq. (8) for s_θ to get

$$s_\theta = S\left[1 + \frac{1 - \nu(n-1)}{(n-1-\nu)\rho^n} - \frac{C}{\rho^{(1+\nu)}}\right] \tag{11}$$

where C is a constant. The only value of C that leads to a bounded tailoring function is

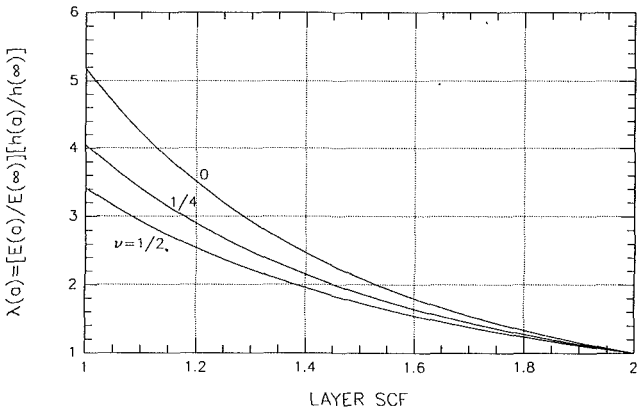


Fig. 2 Tailoring function at hole boundary versus layer stress concentration factor

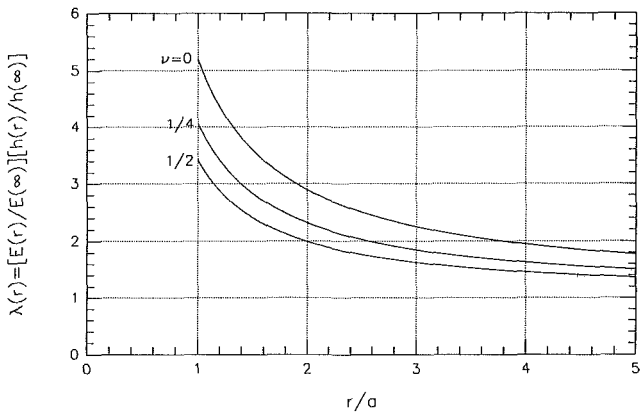


Fig. 3 Spatial variation of tailoring function for a neutral hole

$$C = \frac{2n - n^2}{n - 1 - \nu} \tag{12}$$

and this gives the *layer* stress concentration factor $s_\theta/S = n$ at $\rho = 1$. The tailoring formula

$$\lambda(r) = \exp\left[\frac{n(2-n)}{n-1-\nu}\int_0^{a/r} \frac{x^\nu - x^{n-1}}{1 - x^n} dx\right] \tag{13}$$

follows from the equilibrium Eq. (7). In all cases the peak value of $\lambda(r)$, as expected, occurs at $r = a$, and is given by

$$\lambda(a) = \exp\left[\frac{n(2-n)}{n-1-\nu}\int_0^1 \frac{x^\nu - x^{n-1}}{1 - x^n} dx\right] \quad (n \neq 1 + \nu)$$
$$= \exp\left[-(1-\nu^2)\int_0^1 \frac{x^\nu \log x}{1 - x^n} dx\right] \quad (n = 1 + \nu). \tag{14}$$

For $\nu = 0$ this last result equals $\exp(\pi^2/6)$.

Figure 2 shows how the peak tailoring magnitude varies with the layer stress concentration factor n, for several values of ν. We remark that if only thickness tailoring is used, the SCF for average stress is the same as that for the layers, and so is also reduced below 2. But for pure modulus tailoring, the SCF for the average stress is given by $n\lambda(a)$, and this always exceeds 2 for $n < 2$.

To get a neutral hole, we set $n = 1$ in the formula for $\lambda(r)$, and find

$$\lambda_{\text{neutral}}(r) = \exp\left[\frac{1}{\nu}\int_0^{a/r} \frac{1 - x^\nu}{1 - x} dx\right]. \tag{15}$$

For $\nu = 0$, this result becomes

Downloaded 03 May 2010 to 171.66.16.245. Redistribution subject to ASME license or copyright; see http://www.asme.org/terms/Terms_Use.cfm

$$\lambda_{\text{neutral}}(r) = \exp\left[-\int_0^{a/r} \frac{\log x}{1-x} dx \right] \quad (\nu = 0). \tag{16}$$

Figure 3 shows how λ_{neutral} varies with r/a for $\nu = 0$, 1/4, and 1/2.

We should check the values of $\sigma_\theta^{(\alpha)}(r)/\sigma_\theta^{(\alpha)}(\infty) = s_\theta(r)/S$ away from the hole. In the case of the neutral hole, we find

$$s_\theta/S = 1 - (\rho^{-1} - \rho^{-(1+\nu)})/\nu \quad (\nu \neq 0)$$
$$= 1 - \rho^{-1}\log\rho \quad (\nu = 0) \tag{17}$$

and so the peak layer stress does indeed occur at the hole.

Acknowledgments

This work was supported by DARPA's Defense Sciences Research Council, under contract to the University of Michigan, by a DARPA URI grant to the University of California at Santa Barbara, and by the Division of Applied Sciences, Harvard University.

References

Mansfield, E. H., 1950, "Neutral Holes in a Plane Sheet: Reinforced Holes Which are Elastically Equivalent to the Uncut Sheet," R.A.E. Report Structures 90, Reports and Memoranda No. 2815.

The Coefficient of Restitution for a Planar Two-Body Eccentric Impact

G. G. Adams[9,11] and D. N. Tran[10,11]

1 Introduction

The coefficient of restitution (e), along with the equations of linear and angular impulse and momentum, provide a simple procedure for predicting the motion of two colliding rigid bodies immediately after impact. A typical planar rigid-body impact is shown in Fig. 1. Such collisions may be classified as normal if the velocity of point C_1 with respect to point C_2 is normal to the contact plane, and oblique if the relative velocity has a tangential component. Additionally, the impact is central if the normal impulse causes changes solely in the normal velocity difference, while the tangential impulse produces changes only in the relative tangential velocity. Thus in a central impact the quantity $d_1 h_1/m_1 r_1^2 + d_2 h_2/m_2 r_2^2$ is equal to zero, whereas in an eccentric impact that expression does not vanish. Originally e was introduced by Newton as a velocity constraint, i.e., the ratio of the separation velocity to the approach velocity. Subsequently, Poisson defined the coefficient of restitution as the impulse during the restitution phase of the collision divided by the impulse during deformation. More recently, Kane (1984) discovered that the use of the coefficient of restitution in certain types of rigid-body collisions can result in a predicted increase in the kinetic energy of a rigid-body

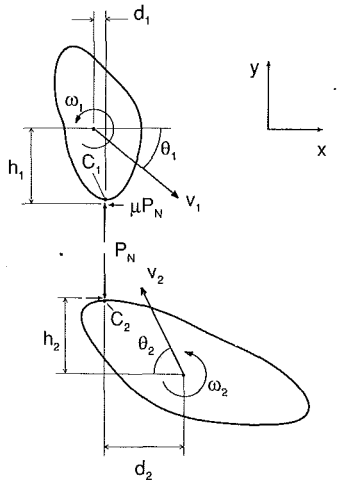


Fig. 1 A planar two-body eccentric impact

system. This unrealistic result is a consequence of friction which, when a slip condition is utilized, can cause a reversal in the direction of slip velocity in an eccentric collision. Papers by Brach (1984, 1989), Keller (1986), Smith (1991), and Stronge (1990, 1991) address the issues of friction, slip reversal, and energy loss. In particular, Stronge (1990) defines the coefficient of restitution in terms of energy dissipation and shows that the three definitions of e are consistent except for an eccentric impact in which the slip direction changes or halts during the collision.

Originally, the coefficient of restitution was thought to be a material property. Recently, however, attention has been given to the determination of e from the material properties, approach velocities, and the geometry of the colliding bodies. The model introduced by Johnson (1985) uses elastic Hertz contact followed by fully plastic deformation during the loading (deformation) phase. Unloading (restitution) is elastic with both the force and contact area continuous at the instant that the deformation phase is succeeded by restitution. Tabor (1951) also predicts e, but bases his method on equating the energy of the permanent indentation to the difference between the energy of the impact and the energy of rebound. Chang and Ling (1992) use an elastic-plastic model based on volume conservation in order to determine the coefficient of restitution for normal impacts. They also compare their model with those of Johnson and Tabor. The three methods described above are based upon central impacts. Experimental determinations of e (e.g., Goldsmith, 1960) generally involve the central impact of a sphere colliding with a flat surface. The results of Johnson, Tabor, Chang, and Ling, and Goldsmith all indicate that the coefficient of restitution decreases with increasing normal approach velocity. This is because in a normal impact of, for example, a translating sphere with a large stationary flat body, the sphere must be brought to rest just prior to the initiation of restitution. Hence at that instant of time, all of the kinetic energy of the sphere has been converted into elastic strain energy and plastic work. Higher initial velocities cause greater energy dissipation in the form of increased plastic deformation which is not recovered during restitution.

The *eccentric* impact of two rigid bodies has not been addressed from the point of view of determining an appropriate value of e. In fact, it appears to have been tacitly assumed that the value of the coefficient of restitution, determined for a specific pair of rigid bodies at a specified approach velocity, can also be used for an eccentric impact of the same bodies at the same approach velocity. It is the purpose of this paper to demonstrate that *a different value of the coefficient of*

[9]Professor, Mem. ASME.
[10]Graduate Student.
[11]Department of Mechanical Engineering, Northeastern University, Boston, MA 02115.

Contributed by the Applied Mechanics Division for publication in the ASME JOURNAL OF APPLIED MECHANICS. Manuscript received by the ASME Applied Mechanics Division, Aug. 10, 1992; final revision, Dec. 3, 1992. Associate Technical Editor: R. L. Huston.

Downloaded 03 May 2010 to 171.66.16.245. Redistribution subject to ASME license or copyright; see http://www.asme.org/terms/Terms_Use.cfm

$$\lambda_{\text{neutral}}(r) = \exp\left[-\int_0^{a/r} \frac{\log x}{1-x} dx \right] \quad (\nu = 0). \tag{16}$$

Figure 3 shows how λ_{neutral} varies with r/a for $\nu = 0$, 1/4, and 1/2.

We should check the values of $\sigma_\theta^{(\alpha)}(r)/\sigma_\theta^{(\alpha)}(\infty) = s_\theta(r)/S$ away from the hole. In the case of the neutral hole, we find

$$s_\theta/S = 1 - (\rho^{-1} - \rho^{-(1+\nu)})/\nu \quad (\nu \neq 0)$$
$$= 1 - \rho^{-1}\log\rho \quad (\nu = 0) \tag{17}$$

and so the peak layer stress does indeed occur at the hole.

Acknowledgments

This work was supported by DARPA's Defense Sciences Research Council, under contract to the University of Michigan, by a DARPA URI grant to the University of California at Santa Barbara, and by the Division of Applied Sciences, Harvard University.

References

Mansfield, E. H., 1950, "Neutral Holes in a Plane Sheet: Reinforced Holes Which are Elastically Equivalent to the Uncut Sheet," R.A.E. Report Structures 90, Reports and Memoranda No. 2815.

The Coefficient of Restitution for a Planar Two-Body Eccentric Impact

G. G. Adams[9,11] and D. N. Tran[10,11]

1 Introduction

The coefficient of restitution (e), along with the equations of linear and angular impulse and momentum, provide a simple procedure for predicting the motion of two colliding rigid bodies immediately after impact. A typical planar rigid-body impact is shown in Fig. 1. Such collisions may be classified as normal if the velocity of point C_1 with respect to point C_2 is normal to the contact plane, and oblique if the relative velocity has a tangential component. Additionally, the impact is central if the normal impulse causes changes solely in the normal velocity difference, while the tangential impulse produces changes only in the relative tangential velocity. Thus in a central impact the quantity $d_1 h_1/m_1 r_1^2 + d_2 h_2/m_2 r_2^2$ is equal to zero, whereas in an eccentric impact that expression does not vanish. Originally e was introduced by Newton as a velocity constraint, i.e., the ratio of the separation velocity to the approach velocity. Subsequently, Poisson defined the coefficient of restitution as the impulse during the restitution phase of the collision divided by the impulse during deformation. More recently, Kane (1984) discovered that the use of the coefficient of restitution in certain types of rigid-body collisions can result in a predicted increase in the kinetic energy of a rigid-body

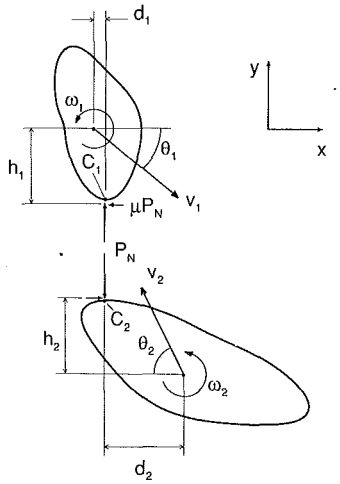


Fig. 1 A planar two-body eccentric impact

system. This unrealistic result is a consequence of friction which, when a slip condition is utilized, can cause a reversal in the direction of slip velocity in an eccentric collision. Papers by Brach (1984, 1989), Keller (1986), Smith (1991), and Stronge (1990, 1991) address the issues of friction, slip reversal, and energy loss. In particular, Stronge (1990) defines the coefficient of restitution in terms of energy dissipation and shows that the three definitions of e are consistent except for an eccentric impact in which the slip direction changes or halts during the collision.

Originally, the coefficient of restitution was thought to be a material property. Recently, however, attention has been given to the determination of e from the material properties, approach velocities, and the geometry of the colliding bodies. The model introduced by Johnson (1985) uses elastic Hertz contact followed by fully plastic deformation during the loading (deformation) phase. Unloading (restitution) is elastic with both the force and contact area continuous at the instant that the deformation phase is succeeded by restitution. Tabor (1951) also predicts e, but bases his method on equating the energy of the permanent indentation to the difference between the energy of the impact and the energy of rebound. Chang and Ling (1992) use an elastic-plastic model based on volume conservation in order to determine the coefficient of restitution for normal impacts. They also compare their model with those of Johnson and Tabor. The three methods described above are based upon central impacts. Experimental determinations of e (e.g., Goldsmith, 1960) generally involve the central impact of a sphere colliding with a flat surface. The results of Johnson, Tabor, Chang, and Ling, and Goldsmith all indicate that the coefficient of restitution decreases with increasing normal approach velocity. This is because in a normal impact of, for example, a translating sphere with a large stationary flat body, the sphere must be brought to rest just prior to the initiation of restitution. Hence at that instant of time, all of the kinetic energy of the sphere has been converted into elastic strain energy and plastic work. Higher initial velocities cause greater energy dissipation in the form of increased plastic deformation which is not recovered during restitution.

The *eccentric* impact of two rigid bodies has not been addressed from the point of view of determining an appropriate value of e. In fact, it appears to have been tacitly assumed that the value of the coefficient of restitution, determined for a specific pair of rigid bodies at a specified approach velocity, can also be used for an eccentric impact of the same bodies at the same approach velocity. It is the purpose of this paper to demonstrate that *a different value of the coefficient of*

[9]Professor, Mem. ASME.
[10]Graduate Student.
[11]Department of Mechanical Engineering, Northeastern University, Boston, MA 02115.

Contributed by the Applied Mechanics Division for publication in the ASME JOURNAL OF APPLIED MECHANICS. Manuscript received by the ASME Applied Mechanics Division, Aug. 10, 1992; final revision, Dec. 3, 1992. Associate Technical Editor: R. L. Huston.

Copyright © 1993 by ASME
Downloaded 03 May 2010 to 171.66.16.245. Redistribution subject to ASME license or copyright; see http://www.asme.org/terms/Terms_Use.cfm

restitution should be used for an eccentric impact. Furthermore, a simple equation is presented which gives an *effective approach velocity* in terms of the actual approach velocity, the coefficient of friction, and the location of the impact point with respect to the mass centers. This effective approach velocity can be used along with a relationship between e and the actual approach velocity (determined for central impact), in order to obtain the appropriate value of the coefficient of restitution for an *eccentric* impact. This analysis is restricted to cases in which slip occurs during the entire impact process, i.e., the coefficient of friction is less than its maximum possible value for continuous slip (e.g., Brach, 1989).

2 Problem Description

Consider the planar collision of two rigid bodies as depicted in Fig. 1. The x and y-directions are chosen to be tangent and normal to the bodies at the contact point as shown. Without loss of generality the bodies are assumed to slip such that the contact point C_1 slides to the right with respect to the contact point C_2. The principles of linear and angular impulse and momentum can be applied in order to obtain six equations (e.g., Brach, 1984). There are, however, eight unknowns—two components of linear velocity and one component of angular velocity for each body after the collision as well as the normal and tangential impulses acting between the two bodies. With continuous slip, an additional condition is that the tangential impulse is equal to the product of the normal impulse and the friction coefficient. A restitution law is then used in order to supply the final equation. The coefficient of restitution can be expressed as a velocity constraint, an impulse relation, or as energy dissipation. For the case considered here all descriptions are equivalent (Stronge, 1990) and the velocity form will be utilized.

Newton's laws of motion for the planar rigid-body collision are written as

$$\ddot{y}_1 = P_N/m_1, \quad \dot{\omega}_1 = (d_1 - \mu h_1)P_N/I_1,$$
$$\ddot{y}_2 = -P_N/m_2, \quad \dot{\omega}_2 = (d_2 - \mu h_2)P_N/I_2, \quad (1)$$

where y_i, ω_i, m_i, and I_i are the normal displacement of the mass center, the angular velocity, the mass, and the mass moments of inertia, respectively, of body i. It is noted that y_i is measured from the position of body i at the instant immediately prior to impact. The only forces considered during the short time period of the collision ($0 \le t \le t_2$) are the impact and frictional forces (P_N, μP_N) which depend upon the rigid-body interference (δ) of the two colliding bodies. Several contact deformation laws exist (e.g., Johnson, 1985; Tabor, 1951; Chang and Ling, 1992) which assume Hertz contact until the onset of plastic yielding, followed by an elastic-plastic or fully plastic deformation law which holds until the time at which the deformation phase ends (i.e., $t = t_1$). Unloading proceeds elastically with deformation energy converted into rigid-body kinetic energy. Let the contact deformation law be represented by

$$P_N(\delta) = \begin{cases} F_1(\delta), & 0 \le t \le t_1, \\ F_2(\delta), & t_1 \le t \le t_2. \end{cases} \quad (2)$$

It is noted that the path during unloading depends upon the maximum deformation $\delta(t_1)$ which defines the transition from deformation to restitution. Also the effect of the frictional shear stresses on the normal stress distribution is neglected.

From rigid-body kinematics, the interference (δ) is related to the rigid-body motion by

$$\ddot{\delta} = \ddot{y}_{C_2} - \ddot{y}_{C_1} = \ddot{y}_2 - \ddot{y}_1 - \dot{\omega}_2 d_2 - \dot{\omega}_1 d_1 \quad (3)$$

in which the usual assumption of small angular displacements has been made and the contribution of the centripetal acceleration during impact has been neglected. Substitution of (1) into (3), and multiplication by $d\phi$ yields

$$\overline{m}\ddot{\delta}d\delta = \overline{m}\,\dot{\delta}\,d\dot{\delta} = -\alpha P_N(\delta)d\delta, \quad \overline{m} = \frac{m_1 m_2}{m_2 + m_2}, \quad (4)$$

where

$$\alpha = 1 + \frac{m_2 d_1 (d_2 - \mu h_1)}{(m_1 + m_2) r_1^2} + \frac{m_1 d_2 (d_2 - \mu h_2)}{(m_1 + m_2) r_2^2}, \quad (5)$$

and r_i is the radius of gyration of body i. Equation (4) gives the relationship between the normal relative acceleration of the contact points of the two bodies and the contact force. This result can be integrated during the deformation phase, and then during restitution, in order to obtain

$$\frac{\overline{m}}{2\alpha}\dot{\delta}_0^2 = \int_0^{\delta_1} F_1(\delta)d\delta, \quad \frac{\overline{m}}{2\alpha}\dot{\delta}_2^2 = \int_{\delta_2}^{\delta_1} F_2(\delta)d\delta, \quad (6)$$

where $\delta_i = \delta(t_i)$, and $\dot{\delta}_0$ and $-\dot{\delta}_2$ are the normal approach and separation velocities of the contact points, respectively.

Consider a central impact which is often used in order to determine a coefficient of restitution either theoretically or experimentally. The result is known to depend upon approach velocity, material properties, and geometry at impact. As can be seen from

$$e^2 = \left(\frac{\dot{\delta}_2}{\dot{\delta}_0}\right)^2 = \frac{\int_{\delta_2}^{\delta_1} F_2(\delta)d\delta}{\int_0^{\delta_1} F_1(\delta)d\delta}, \quad (7)$$

the coefficient of restitution depends upon the deformation law and the maximum interference. From $(6)_1$, the maximum interference (δ_1) depends upon the energy absorbed during deformation, which in turn depends upon the quantity

$$\frac{1}{2}\overline{m}\frac{\dot{\delta}_0^2}{\alpha} = \frac{1}{2}\overline{m}v_e^2, \; v_e = \dot{\delta}_0/\sqrt{\alpha}. \quad (8)$$

Thus, for an eccentric impact, the appropriate coefficient of restitution depends upon an *effective approach velocity* (v_e) defined by (8) and (5). Alternatively, it is also possible to view $\overline{m}/\alpha$ as an effective mass.

3 Results and Conclusions

As an example, the coefficient of restitution will be determined using the model of Chang and Ling (1992) which, along with $(6)_1$, determines e according to

$$e^2 = \frac{(8/15)\,ER^{1/2}\delta^*(2\delta_1 - \delta^*)^{3/2}}{\overline{m}\,\dot{\delta}_0^2/2\alpha} \quad (9)$$

where

$$\delta^* = \left(\frac{\pi KY}{2E}\right)^2 R, \; K = 1.282 + 1.158\nu, \; KY = \min(K_1 Y_1, K_2 Y_2),$$
$$\frac{1}{R} = \frac{1}{R_1} + \frac{1}{R_2}, \quad \frac{1}{E} = \frac{(1-\nu_1^2)}{E_1} + \frac{(1-\nu_2^2)}{E_2}, \quad (10)$$

and R_i, E_i, ν_i, Y_i are the radius of curvature, Young's modulus, Poisson's ratio, and yield strength of body i. The Poisson's ratio (ν) used in order to define K in (10), is that of the material with the lower value of KY. Furthermore, δ^* is the largest value of the interference for which the collision is fully elastic. Finally, the maximum interference (δ_1) is determined from the solution of

$$\pi KYR\delta_1(\delta_1 - \delta^*) + \frac{8}{15}ER^{1/2}\delta^{*5/2} - \overline{m}\,\dot{\delta}_0^2/2\alpha = 0. \quad (11)$$

The above model of Chang and Ling was developed for the normal central impact of two translating spheres, and was then used as a basis for the study of the impact of rough surfaces. In the present investigation, (9)-(11) will, with appropriate

Downloaded 03 May 2010 to 171.66.16.245. Redistribution subject to ASME license or copyright; see http://www.asme.org/terms/Terms_Use.cfm

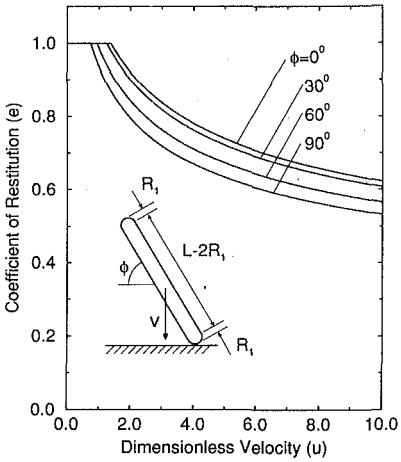


Fig. 2 The coefficient of restitution (e) versus dimensionless velocity (u) for the normal eccentric frictionless impact of a rod onto a flat surface with R_1/L = 0.05 and various angles of inclination (ϕ)

modifications, be used to model the eccentric impact of two rigid bodies which are each locally spherical in the region of the contact points. First, however, (11) is used in order to solve for δ_1 which is then substituted into (9) yielding

$$e=\left(\frac{8\alpha}{15u^2}\right)^{1/2}\left(\frac{2u^2}{\alpha}-\frac{1}{15}\right)^{3/8}, \quad u^2=\frac{\overline{m}\,\dot{\delta}_0^2}{2ER^3}\left(\frac{2E}{\pi KY}\right)^5, \qquad (12)$$

where u is the dimensionless approach velocity. It is noted that (9)–(12) applies only if $\delta_1 \geq \delta^*$, i.e., $u \geq \sqrt{8\alpha/15}$; otherwise no energy is lost and $e = 1$.

Now consider the normal eccentric impact of a translating rod ($v_1 = v$, $\omega_1 = 0$, $\theta_1 = \pi/2$) onto a frictionless fast surface (Fig. 2). The cylindrical rod has mass m, total length L, hemispherical ends of radius R_1, and makes an angle ϕ with the flat surface at impact. Figure 2 shows a plot of the coefficient of restitution (e) versus dimensionless approach velocity u for various angles of inclination (ϕ). Alternatively, Fig. 2 could be used with only the central impact curve ($\phi = \pi/2$) and with the dimensionless velocity u replaced by the dimensionless effective velocity ($u/\sqrt{\alpha}$). It is seen that lower values of ϕ correspond to higher values of e because such impacts involve greater eccentricity, and hence produce greater α and lower effective approach velocity.

A central impact of the rod causes the normal velocity of the center of mass to be zero at the instant that restitution begins. However, an eccentric impact allows the mass center to have a finite normal velocity due to rotational effects. Hence a smaller amount of kinetic energy is absorbed during the deformation phase of the eccentric collision, resulting in less energy dissipation and a higher value of the coefficient of restitution. It is shown that a relationship between the coefficient of restitution and the approach velocity, obtained for central impact, can also be used for an eccentric impact provided that the approach velocity is replaced by an effective approach velocity.

4 References

Brach, R. M., 1984, "Friction, Restitution, and Energy Loss in Planar Collisions," ASME JOURNAL OF APPLIED MECHANICS, Vol. 51, pp. 164–170.

Brach, R. M., 1989, "Rigid Body Collisions," ASME JOURNAL OF APPLIED MECHANICS, Vol. 56, pp. 133–138.

Chang, W. R., and Ling, F. F., 1992, "Normal Impact Model of Rough Surfaces," ASME *Journal of Tribology*, Vol. 114, pp. 439–447.

Goldsmith, W., 1960, *Impact*, Edward Arnold Publishers Ltd., London, 1960.

Johnson, K. L.,1985, *Contact Mechanics*, Cambridge University Press, Cambridge, pp. 361–363.

Kane, T. R., 1984, "A Dynamics Puzzle," *Stanford Mechanics Alumni Club Newsletter*.

Keller, J. B., 1986, "Impact With Friction," ASME JOURNAL OF APPLIED MECHANICS, Vol. 53, pp. 1–4.

Smith, C. E., 1991, "Predicting Rebounds Using Rigid-Body Dynamics," ASME JOURNAL OF APPLIED MECHANICS, Vol. 58, pp. 754–758.

Stronge, W. J., 1990, "Rigid Body Collisions With Friction," *Proceedings of the Royal Society, London*, Vol. A431, pp. 169–181.

Stronge, W. J., 1991, "Unraveling Paradoxical Theories for Rigid Body Collisions," ASME JOURNAL OF APPLIED MECHANICS, Vol. 58, pp. 1049–1055.

Tabor, D., 1951, *The Hardness of Metals*, Oxford University Press, London, pp. 115–130.

Downloaded 03 May 2010 to 171.66.16.245. Redistribution subject to ASME license or copyright; see http://www.asme.org/terms/Terms_Use.cfm

Journal of Applied Mechanics

Discussion

Authors' Closure[1]

The purpose of our paper is to document necessary and sufficient conditions under which the coefficient matrices of a linear nonconservative system can be diagonalized or upper triangularized by a common similarity transformation. Computational algorithms for determining solvability were not addressed in our paper. Thus the discussion by Dr. S. M. Shahruz[2] is rather irrevelant.

In the literature, there are alternative conditions of sufficiency for checking the solvability of a matrix Lie algebra. Efficient schemes for computations involving commutator products are also available. These issues were simply not addressed in our paper. In Example 2, the coefficient matrices M, C, and K cannot be diagonalized by a common similarity transformation. Among other things, M itself is not diagonalizable by similarity transformation because there is only one eigenvector $[1, 1]^T$ associated with the repeated eigenvalue 1. However, these matrices are still closely connected in structure because $L^{(2)} = \{0\}$. That is the simple reason why a nonsingular transformation on M, C, and K leads to three matrices which can be diagonalized simultaneously.

Singular Plastic Fields in Steady Penetration of a Rigid Cone[3]

H. S. Yu.[4] As an application of their asymptotic analysis, the authors have used their solution to predict the axial force for deep penetration of an elastic-perfectly plastic solid by a conically tipped circular rod of semi-infinite length. It was assumed that the hydrostatic pressure at the shoulder point ($r = R$, $\theta = \beta$) equals the limit pressure required to expand a cylindrical cavity in an elastic-perfectly plastic solid. It is noted that the authors' prediction is about 23–36 percent lower than the measured penetration pressure.

The writer wishes to suggest a method that can be used to improve the prediction of the measured penetration pressure with the singular plastic stress fields developed by the authors.

In agreement with actual measurements, a strain path analysis presented by Teh and Houlsby (1991) indicates that there is a significant reduction in normal pressure immediately above the shoulder. A further study of the stress field at the shoulder of a cone penetrometer by Sagaseta and Houlsby (1992) provides an approximate relation between the hydrostatic stress at the shoulder along the direction of cone face and that along the shaft. For the case when the shaft roughness can be ignored, this relation may be expressed as follows:

$$\frac{p_c - p_s}{k} = \pi + 2\alpha + \arcsin(m) \tag{1}$$

where p_c and p_s are used to denote the hydrostatic pressures at the shoulder point along the cone face and shaft directions, respectively. According to the experimental work of Lehane and Jardine (1992), the hydrostatic pressure along the shaft may be assumed to be the average of the three stresses (i.e., radial, hoop, and vertical stresses) required to expand a cylindrical cavity, namely:

$$\frac{p_s}{k} = \ln \frac{E}{3k} \tag{2}$$

where E is Young's modulus. Combining Eqs. (1) and (2) leads to the expression for the hydrostatic pressure at ($r = R$, $\theta = \beta$):

$$\frac{p_c}{k} = \pi + 2\alpha + \arcsin(m) + \ln \frac{E}{3k}. \tag{3}$$

Using Eq. (3), the averaged penetration pressure on the conical head can be obtained as

Table 1 Comparison of predicted penetration pressure with measured value for work-hardened copper, from Bishop et al. (1945)

		Rough Cone $m = 1$	Smooth Cone $m = 0$
$\alpha = 20°$ $\frac{\bar{p}}{\sigma_0}$	Measured	7.4	4.8
	Predicted by Eq. (49) in the paper	5.7	3.5
	Error	−23%	−27%
	Predicted by Eq. (4) in the discussion	8.28	5.1
	Error	12%	6%
$\alpha = 30°$ $\frac{\bar{p}}{\sigma_0}$	Measured	6.8	5.5
	Predicted by Eq. (49) in the paper	5.2	3.5
	Error	−24%	−36%
	Predicted by Eq. (4) in the discussion	7.9	5.3
	Error	16%	−3.6%

[1]By T. K. Caughey and F. Ma. Paper originally published in the Mar. 1993 issue of the ASME JOURNAL OF APPLIED MECHANICS, Vol. 60, pp. 26–28.

[2]By S. M. Shahruz and published in the Sept. 1993 issue of the ASME JOURNAL OF APPLIED MECHANICS, Vol. 60, p. 787.

[3]By D. Durban and N. A. Fleck, and published in the Dec. 1992 issue of the ASME JOURNAL OF APPLIED MECHANICS, Vol. 59, pp. 706–710.

[4]Department of Civil Engineering and Surveying, The University of Newcastle, N.S.W. 2308, Australia.

Copyright © 1993 by ASME
Downloaded 03 May 2010 to 171.66.16.245. Redistribution subject to ASME license or copyright; see http://www.asme.org/terms/Terms_Use.cfm

$$\frac{\bar{p}}{\sigma_0}=\frac{1}{\sqrt{3}}\left[\pi+2\alpha+\arcsin(m)+\ln\frac{E}{\sqrt{3}\sigma_0}+\frac{D}{2}+m\cot\alpha-\sqrt{1-m^2}\right]. \quad (4)$$

The predicted penetration pressure using this solution is compared with the measured values reported by Bishop et al. (1945) in Table 1. By comparison, it is found that Eq. (4) tends to give a much better prediction on the actual measured cone penetration pressure. The agreement is best for the case of a perfectly smooth cone face ($m = 0$) where the actual pressure can be predicted to within about a few percent.

References

Lehane, B., and Jardine, R., 1992, "The Behavior of a Displacement Pile in Bothkennar Clay," *Proc. Wroth Memorial Symp. on Predictive Soil Mechanics*, Vol. 2, pp. 306–317.

Sagaseta, C., and Houlsby, G. T., 1992, "Stresses Near the Shoulder of a Cone Penetrometer in Clay," *Proc. 3rd Int. Conf. on Computational Plasticity: Fundamentals and Applications*, pp. 895–906.

Teh, C. I., and Houlsby, G. T., 1991, "An Analytical Study of the Cone Penetration Test in Clay," *Geotechnique*, Vol. 41, pp. 17–34.

Authors' Closure[5]

The authors are grateful for the helpful comments by Dr. Yu. We want to emphasize that the asymptotic analysis in our paper provides only the essential features of the singular plastic zone near the tip of a penetrating cone. As such it has a limited range of validity. Nevertheless, the predictions of the shear shock orientation and penetration pressure are surprisingly accurate. Any matching with the unknown remote field is not uniquely defined and is speculative in nature. A more complete analysis (accounting for strain hardening, nonproportional loading and far-field conditions) is needed in order to understand the full details about the active plastic zone in the cone-penetration process.

[5]N. A. Fleck, Department of Engineering, Cambridge University, Trumpington Street, Cambridge, CB2 1PZ, U.K. and D. Durban, Faculty of Aerospace Engineering, Technion—Israel Institute of Technology, Haifa 32000, Israel.

Copyright © 1993 by ASME
Downloaded 03 May 2010 to 171.66.16.245. Redistribution subject to ASME license or copyright; see http://www.asme.org/terms/Terms_Use.cfm

Journal of Applied Mechanics

Book Review

Stress Intensity Factors Handbook, Vol. 3, edited by Y. Murakami. The society of Materials Science, Japan, and Pergamon Press, Kyoto, Japan, 1992. 1100 pages.

REVIEWED BY L. M. KEER[1]

This valuable handbook follows the two volumes previously published in 1987. Although the objectives of the present volume are the same as the preceding ones, all solutions are new and a new chapter, Chapter 18, reflects some of the current interest of researchers in the field of composite materials and structures.

The first two volumes were very useful in providing in one location known solutions to important boundary value problems involving cracks. They also provided a useful service in making available solutions that were in the Japanese journals that might not be well-known to western researchers. The 18 handbook chapters are listed below:

1 Fracture Mechanics Test Specimens
2 Finite Width Plate Containing Two-Dimensional Cracks
3 Cracks in a Semi-Infinite Plate
4 Cracks in an Infinite Plate
5 Cracks at Stress Concentration (Two-Dimensional Problem)
6 Cracks in a Circular Plate or in a Cylinder
7 Nonlinear Shaped Cracks in an Infinite Plate
8 Interface Cracks and Cracks in Inhomogeneous Materials
9 Three-Dimensional Surface and Interior Crack
10 Mixed Mode and Mode III Cracks
11 Thermoelastic Crack Problem
12 Cracks Under Contact Stress Field
13 Cracks in Welded Joints
14 Cracks in Residual Stress Field or Magnetic Field and Cracks in Anisotropic Plate
15 Plate Bending Problems
16 Cracks in a Shell
17 Dynamic Crack Problem
18 Stress Singularity for Notch at Bimaterial Interface

It should be noted that the policy of this handbook is to publish only the solutions for which free copyright permission has been granted by the publisher. Thus a few references have not been included because citing fees were required. Journals for which copyright permission was granted were The Japan Society of Mechanical Engineers, Engineering Fracture Mechanics, International Journal of Solids and Structures, and International Journal of Engineering Science.

[1]Professor, Department of Mechanical Engineering, Northwestern University, Evanston, IL 60208. Fellow ASME.

Copyright © 1993 by ASME
Downloaded 03 May 2010 to 171.66.16.245. Redistribution subject to ASME license or copyright; see http://www.asme.org/terms/Terms_Use.cfm